SANDIA REPORT

SAND93—2675 • UC—814
Unlimited Release
Printed April 1994

Yucca Mountain Site Characterization Project

Total-System Performance Assessment for Yucca Mountain – SNL Second Iteration (TSPA-1993)

Executive Summary

Michael L. Wilson, John H. Gauthier, Ralston W. Barnard, George E. Barr, Holly A. Dockery, Ellen Dunn, Roger R. Eaton, David C. Guerin, Ning Lu, Mario J. Martinez, Robert Nilson, Christopher A. Rautman, Thomas H. Robey, Benjamin Ross, Eric E. Ryder, Albert R. Schenker, Sharon A. Shannon, Lee H. Skinner, William G. Halsey, James D. Gansemer, Lynn C. Lewis, Alan D. Lamont, Inés R. Triay, Arend Meijer, David E. Morris

Prepared by
Sandia National Laboratories
Albuquerque, New Mexico 87185 and Livermore, California 94550
for the United States Department of Energy
under Contract DE-AC04-94AL85000

"Prepared by Yucca Mountain Site Characterization Project (YMSCP) participants as part of the Civilian Radioactive Waste Management Program (CRWM). The YMSCP is managed by the Yucca Mountain Project Office of the U.S. Department of Energy, DOE Field Office, Nevada (DOE/NV). YMSCP work is sponsored by the Office of Geologic Repositories (OGR) of the DOE Office of Civilian Radioactive Waste Management (OCRWM)."

Issued by Sandia National Laboratories, operated for the United States Department of Energy by Sandia Corporation.

Available to DOE and DOE contractors from
Office of Scientific and Technical Information
PO Box 62
Oak Ridge, TN 37831

Prices available from (615) 576-8401, FTS 626-8401

Available to the public from
National Technical Information Service
US Department of Commerce
5285 Port Royal Rd
Springfield, VA 22161

NTIS price codes
Printed copy: A04
Microfiche copy: A01

Distribution Category
UC-814

SAND93-2675
Unlimited Release
Printed April, 1994

Total-System Performance Assessment for Yucca Mountain — SNL Second Iteration (TSPA-1993)

Executive Summary

Michael L. Wilson, John H. Gauthier†, Ralston W. Barnard,
George E. Barr, Holly A. Dockery, Ellen Dunn, Roger R. Eaton, David C. Guerin‡,
Ning Lu*, Mario J. Martinez, Robert Nilson, Christopher A. Rautman,
Thomas H. Robey†, Benjamin Ross*, Eric E. Ryder, Albert R. Schenker‡,
Sharon A. Shannon, Lee H. Skinner†
(Sandia National Laboratories)

William G. Halsey, James D. Gansemer, Lynn C. Lewis, Alan D. Lamont
(Lawrence Livermore National Laboratory)

Inés R. Triay, Arend Meijer§, David E. Morris
(Los Alamos National Laboratory)

† Spectra Research, Inc.
‡ Los Alamos Technical Associates, Inc.
* Disposal Safety, Inc.
§ Jacobs Engineering, Inc.

Abstract

Sandia National Laboratories has completed the second iteration of the periodic total-system performance assessments (TSPA-93) for the Yucca Mountain Site Characterization Project (YMP). These analyses estimate the future behavior of a potential repository for high-level nuclear waste at the Yucca Mountain, Nevada, site under consideration by the Department of Energy. TSPA-93 builds upon previous efforts by emphasizing YMP concerns relating to site characterization, design, and regulatory compliance.

Scenarios describing expected conditions (aqueous and gaseous transport of contaminants) and low-probability events (human-intrusion drilling and volcanic intrusion) are modeled. The hydrologic processes modeled include estimates of the perturbations to ambient conditions caused by heating of the repository resulting from radioactive decay of the waste. Hydrologic parameters and parameter probability distributions have been derived from available site data. Possible future climate changes are modeled by considering two separate groundwater infiltration conditions: "wet", with a mean flux of 10 mm/yr, and "dry", with a mean flux of 0.5 mm/yr. Two alternative waste-package designs and two alternative repository areal thermal power densities are investigated. One waste package is a thin-wall container emplaced in a vertical borehole, and the second is a container designed with corrosion-resistant and corrosion-allowance walls emplaced horizontally in the drift. Thermal power loadings of 57 kW/acre (the loading specified in the original repository conceptual design) and 114 kW/acre (a loading chosen to investigate effects of a "hot repository") are considered.

TSPA-93 incorporates significant new detailed process modeling, including two- and three-dimensional modeling of thermal effects, groundwater flow in the saturated-zone aquifers, and gas flow in the unsaturated zone. The saturated-zone model is used to estimate travel times for contaminants through layered, dipping formations. Coupled calculations of gas and heat flow are used to estimate travel times for gaseous CO_2. Time-dependent temperature distributions in the rock surrounding the potential repository are calculated, using the four repository layouts. A phenomenological model for waste-package degradation is implemented; the model includes temperature-dependent corrosion, fuel alteration, and dissolution.

Probabilistic analyses are performed for aqueous and gaseous flow and transport, human intrusion, and basaltic magmatic activity. Repository performance estimates are sensitive to assumptions made about unsaturated-zone water flow and contact with waste. Two conceptual models of unsaturated-zone water flow are considered — the composite-porosity model, which treats fracture and matrix flow as being strongly coupled; and the weeps model, which allows for flow only through locally saturated zones. The weeps aqueous releases and the human-intrusion direct releases are sensitive to the size of the waste packages that are affected: the larger horizontally-emplaced containers produce greater releases. Releases are generally insensitive to repository thermal effects: a hotter thermal loading protects parts of the repository from contact with liquid water, but other parts experience enhanced water flow due to condensation and diversion. The volcanic scenario, which investigates the effects of magmatic volatiles on the degradation of the waste packages, does not contribute significantly to releases.

Results of the calculations done for TSPA-93 lead to a number of recommendations concerning studies related to site characterization. Primary among these are the recommendations to obtain better information on percolation flux at Yucca Mountain, on the presence or absence of flowing fractures, and on physical and chemical processes influencing gaseous flow. Near-field thermal and chemical processes, and waste-container degradation are also areas where additional investigations may reduce important uncertainties. Recommendations resulting from TSPA-93 for repository and waste-package design studies are: 1) to evaluate the performance implications of large-size containers, and 2) to investigate in more detail the implications of high repository thermal power output on the adjacent host rock and on the spent fuel.

If future repository performance regulations are based on individual dose rather than cumulative release, results suggest that future site-characterization efforts should emphasize investigations of groundwater contact with waste packages in the unsaturated zone and examinations of saturated-zone flow paths. Because dose rates are dependent on the rate of radionuclide releases, it would be useful to investigate container designs that fail "slowly" over long periods of time.

Volume 1
contains Chapters 1 through 12

Volume 2
contains Chapters 13 through 25
and the Appendices

This report was prepared under the Yucca Mountain Site Characterization Project WBS 1.2.5.4.1. QAGR 1.2.3.4.1 was applied, however, the information and data documented in the report were not developed to meet quality-affecting standards. Not all the work activities were subject to QA controls. The information in this report is not qualified and is not to be used for licensing.

Contents

Part II: Data Development

Contents of Volume 2

Figures

Tables

(This page left intentionally blank)

Executive Summary

1 Introduction

Yucca Mountain is being investigated by the U.S. Department of Energy (DOE) as the potential site for the permanent disposal of spent fuel from nuclear reactors and high-level radioactive waste generated by the U.S. Department of Defense. Yucca Mountain is located in a sparsely populated, arid region of the U.S., approximately 120 km northwest of Las Vegas, Nevada, on the border of the DOE's Nevada Test Site. To take advantage of less groundwater, a potential repository at the site would be mined in the unsaturated zone of the mountain, about 300 m below the surface, but over 200 m above the water table (Figure ES-1).

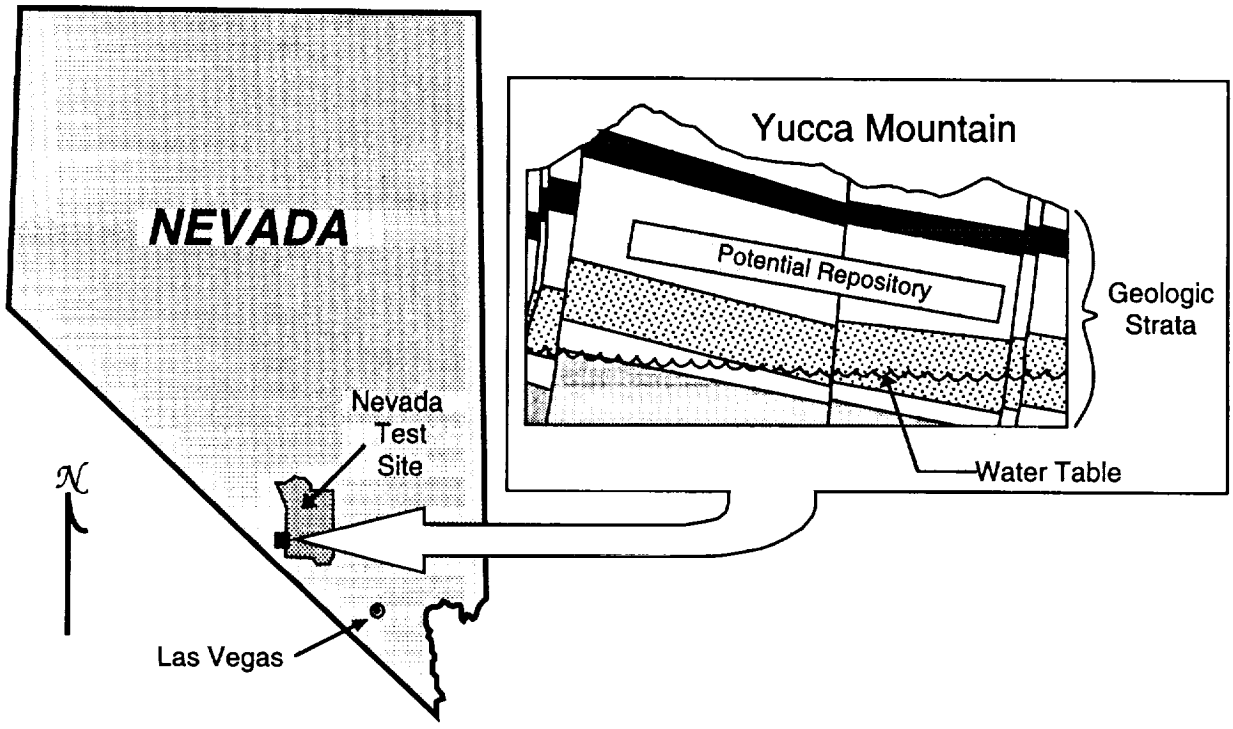

Figure ES-1. Location of Yucca Mountain and a potential high-level radioactive-waste repository.

A repository at Yucca Mountain will have to meet a number of Federal regulations, including regulations concerning long-term waste isolation promulgated by the U.S. Environmental Protection Agency (EPA) and the U.S. Nuclear Regulatory Commission. To determine long-term waste isolation, the Yucca Mountain Site Characterization Project (YMP) of DOE has begun a series of total-system performance assessments (TSPAs). The work described in this report—TSPA-93—is part of the second full iteration in the series (Figure ES-2).

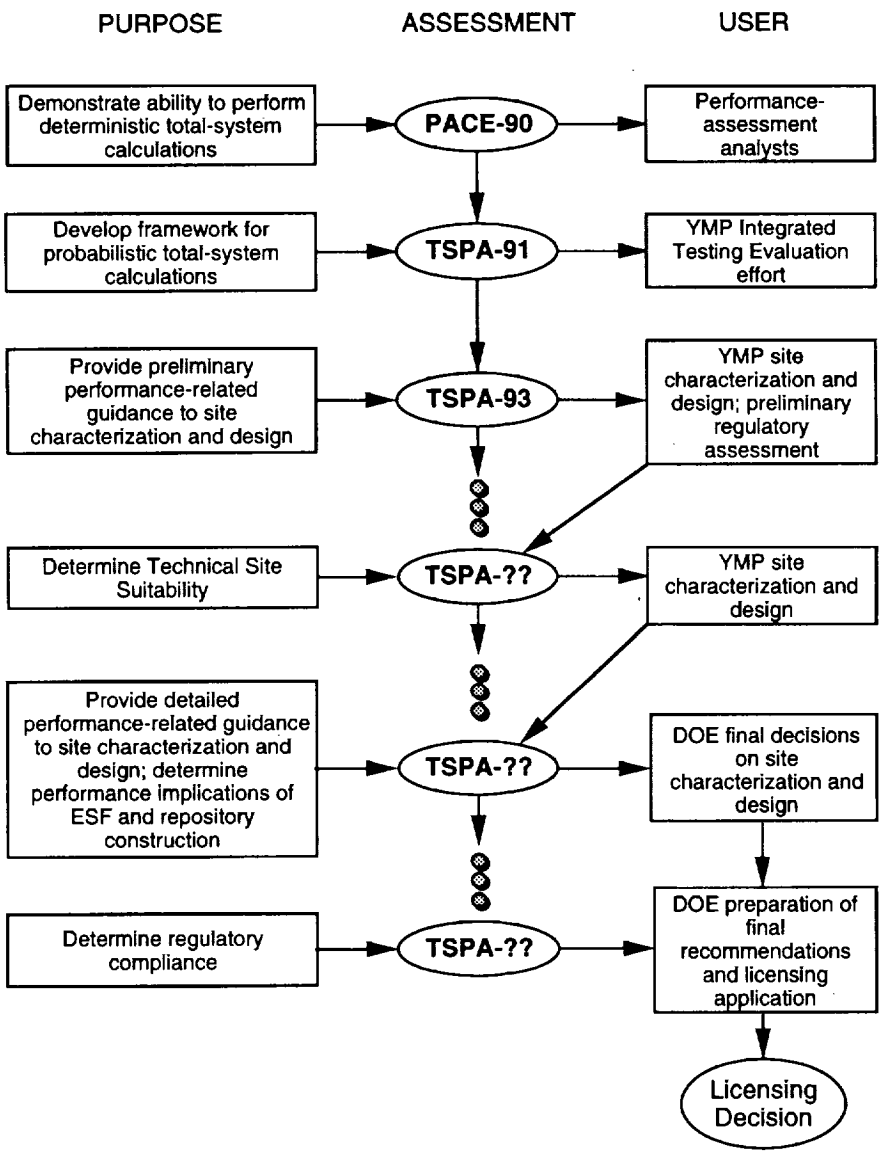

Figure ES-2. Progression of TSPA analyses.

TSPA-93 differs from previous analyses in several important respects. Significant new detailed modeling is undertaken, including three-dimensional geostatistical modeling of the stratigraphy, three-dimensional modeling of the saturated zone, and modeling of repository thermal effects. A phenomenological source term developed by Lawrence Livermore National Laboratory (LLNL) and climate change extrapolated from the paleoclimatic record are included in the probabilistic models. Several different repository designs with different containers and different thermal loadings are evaluated.

Two performance measures are considered in this TSPA iteration: normalized cumulative release, as defined by the EPA in 40 CFR 191.13, and radiation dose to a maximally exposed individual. The Energy Policy Act of 1992 dictates that 40 CFR Part 191 no longer

applies to Yucca Mountain, and sets a course of action for specifying a new standard. Individual dose is examined in TSPA-93 to determine the potential impact of such a standard on the performance assessment. To study the impact of longer time periods on repository performance, both cumulative-releases and dose results were calculated for a million-year time period in addition to the typical 10,000-year period.

In one respect, the results of TSPA-93 tend to confirm previous work: cumulative releases from all investigated sources are generally below the EPA standard (40 CFR 191.13), except for gaseous releases of ^{14}C. However, a significant new result is that future peak doses from drinking water in the area could be substantially above background radiation levels. Also, some of the models indicate that larger containers (e.g., the multipurpose container) and hotter repository configurations could lead to worse long-term performance, although a great deal of uncertainty is associated with these results.

1.1 TSPA-93 purpose

The ultimate goal of the TSPA process is to determine compliance of a repository with applicable regulations and to support a license application for construction and operation of a repository. However, at this point in the process, the primary goal of TSPA-93 is to provide feedback to YMP particpants on the significance of design and site-characterization information to regulatory compliance. Secondary goals of TSPA-93 involve progress toward performance assessments that are scientifically justified and acceptable for a license application, including refinement of mathematical models of physical processes, features, and events that could influence repository performance; consideration of an individual-dose performance measure; and calculation of conditional estimates of compliance with performance measures for scientific review. A final goal of TSPA-93 is to involve several different organizations within the project in production of a TSPA for Yucca Mountain. Table ES-1 shows the participants who provided input to TSPA-93. In addition, researchers from the Waste Isolation Pilot Project (WIPP) contributed to an independent review of this work.

1.2 Scenarios

A TSPA is based on a risk-assessment methodology that contains the following major steps: (1) develop and screen scenarios, (2) develop models of important features, events, and processes, (3) estimate parameter values and uncertainties, (4) make calculations using the models and parameter values, and (5) interpret results. A summary of models, parameters, and results is contained in the following sections. Development and screening of scenarios are independent efforts and are described in separate documents; a brief disscussion follows.

Table ES-1. Information sources for TSPA-93 analyses.

Component	Contributors
Stratigraphy and Hydrogeologic Parameters	*LBL* (C. Wittwer, G. Bodvarsson) *USGS* (A. Flint, L. Flint, R. Spengler, E. Weeks, R. Luckey, A. Geldon, D. Appel, D. Hoxie) *SNL* (A. Schenker, T. Robey, C. Rautman, D. Guerin)
Climate Change	*USGS* (A. Flint, L. Flint, D. Hobson, R. Forester, Z. Peterman) *WIPP* (P. Swift) *SNL* (J. Gauthier, M. Wilson)
Geochemistry	*LANL* (I. Triay, D. Morris, A. Meijer, M. Ebinger) *SNL* (M. Siegel)
Thermal Effects	*LLNL* (G. Johnson, T. Buscheck, L. Lewis) *TRW* (J. King) *B&W Fuel* (T. Doering, R. Bahney, A. Thompson) *SNL* (E. Ryder, E. Dunn, J. Holland)
Saturated Zone	*USGS* (R. Luckey) *SNL* (G. Barr)
Gas Flow	*DSI* (B. Ross, N. Lu) *SNL* (M. Wilson)
Source Term and EBS Processes	*LLNL* (A. Lamont, J. Gansemer, W. Halsey, L. Lewis, R. Stout, D. McCright) *Iowa State University* (D. Bullen) *ORNL* (A. Croff) *SNL* (R. Barnard, J. Gauthier, M. Wilson)

A scenario consists of an organized list of features, events, and processes (FEPs) that could lead to releases of radionuclides to the accessible environment—either the ground surface or a subsurface boundary 5 km from the repository. Scenario categories consist of groupings of similar scenarios. The general scenario categories considered in TSPA-93 include cases with an undisturbed repository (the "nominal" case), and with a disrupted repository (the "disturbed" cases).

For TSPA-93, the nominal case consists of a heat-generating repository that is subjected to climate-dependent groundwater flow. Two alternative conceptual models of groundwater flow in the unsaturated zone are considered. Waste containers within the repository degrade by a variety of mechanisms, but the most important mechanism is aqueous-induced corrosion. If and when containers fail, radionuclides are available for gaseous or aqueous transport to the accessible environment. For gaseous transport, radionuclides move upward through the unsaturated zone to the ground surface. For aqueous transport, radionuclides

move downward through the unsaturated zone, then laterally through the saturated zone past the 5-km subsurface boundary. Radionuclides are tracked in terms of (1) cumulative releases to the accessible environment and (2) the dose an individual might recieve by drinking contaminated water pumped from the saturated zone at the accessible environment.

For TSPA-93, two disturbed cases are investigated: (1) inadvertant human intrusion by exploratory drilling, and (2) volcanic activity that introduces corrosion-enhancing heat and volatiles into the repository. For human intrusion, radionuclides exhumed with the drill core and the drilling fluids contribute to releases. For indirect volcanic effects, magmatic-induced corrosion of containers allows earlier releases of radionuclides that are transported in groundwater flowing as described in the nominal case. (Direct volcanic releases were evaluated in TSPA-91.)

2 Data development

2.1 Repository

The design limit for a repository at Yucca Mountain is 70,000 metric tons of radioactive waste. The approximately 63,000 metric tons of spent fuel emplaced in the repository is considered to be aged 25 years, with burnups of 30,000 MWd/MTU for boiling-water-reactor fuel and 40,000 MWd/MTU for pressurized-water-reactor fuel. The approximately 7,000 metric tons of defense high-level waste is considered to have many of the heavy metal products removed and to be encased in a vitrified waste form. A study performed in conjuction with TSPA-93 examined the significance of each radionuclide contained in the wastes in terms of its potential for contributing to contamination at the accessible environment. Based on this study, the human-intrusion analyses in TSPA-93 consider a broad suite of 43 radionuclides. Nominal case and indirect volcanic effects consider 8 radionuclides, chosen for their transport characteristics (low retardation) or their potential contribution to individual dose.

The waste forms are enclosed in containers; container designs have not been finalized, but those investigated to date consist of cylindrical metal containers with gas-tight closures. Two container types are considered in TSPA-93 (Figure ES-3): (1) a smaller, "vertically emplaced" container proposed in the Site Characterization Plan (SCP) Conceptual Design of 1987, and (2) a larger, "in-drift" container which approximates the multipurpose container (MPC) presently being considered by the Yucca Mountain Project. Vertically emplaced containers are modeled with a surrounding air gap that is sometimes filled with rubble. In-drift containers are modeled with a surrounding backfill, provided to prevent drift collapse. (Consequences of adding a backfill are an increased potential for water pathways to the waste container, and higher container temperatures caused by the backfill acting as a thermal

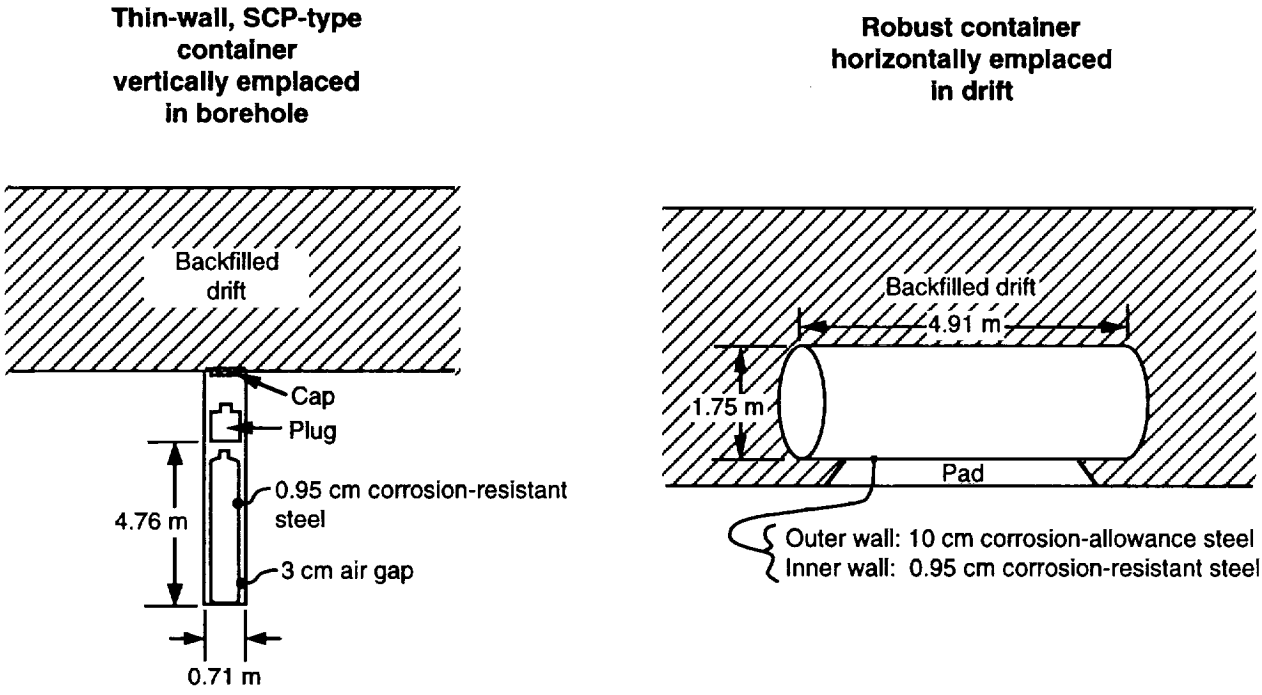

Figure ES-3. The two container types and emplacement strategies considered in TSPA-93.

insulator.) A 70,000-metric-ton repository requires the use of about 35,000 of the vertically emplaced containers or about 8,500 of the in-drift containers.

The repository layout incorporated in TSPA-93 consists of a series of emplacement drifts that run perpendicular to a main access drift. Length and proximity of the drifts to one another depend on the rock mass and the thermal characteristics of the repository. Decay of the radioactive waste produces heat: approximately 1 kW of heat for every metric ton (at emplacement—heat generation decreases over time). While the heat output depends primarily on the spent-fuel burnup and on the waste-acceptance schedule, the temperatures within the repository depend on the local areal power density (LAPD, expressed in terms of kW/acre), which is primarily a function of the waste-container spacing. It has been proposed that temperatures above boiling could produce a dry environment that would enhance the long-term performance of the repository. The SCP Conceptual Design specified an LAPD of 57 kW/acre (Figure ES-4). More recently, LAPDs up to 114 kW/acre have been considered by the YMP in order to attempt to induce a larger dryout zone.

Four combinations of container/thermal loadings are examined in TSPA-93. A 57-kW/acre repository with vertically emplaced containers is the baseline analysis case for TSPA-93, and most like the design described in the SCP and evaluated in TSPA-91. Also

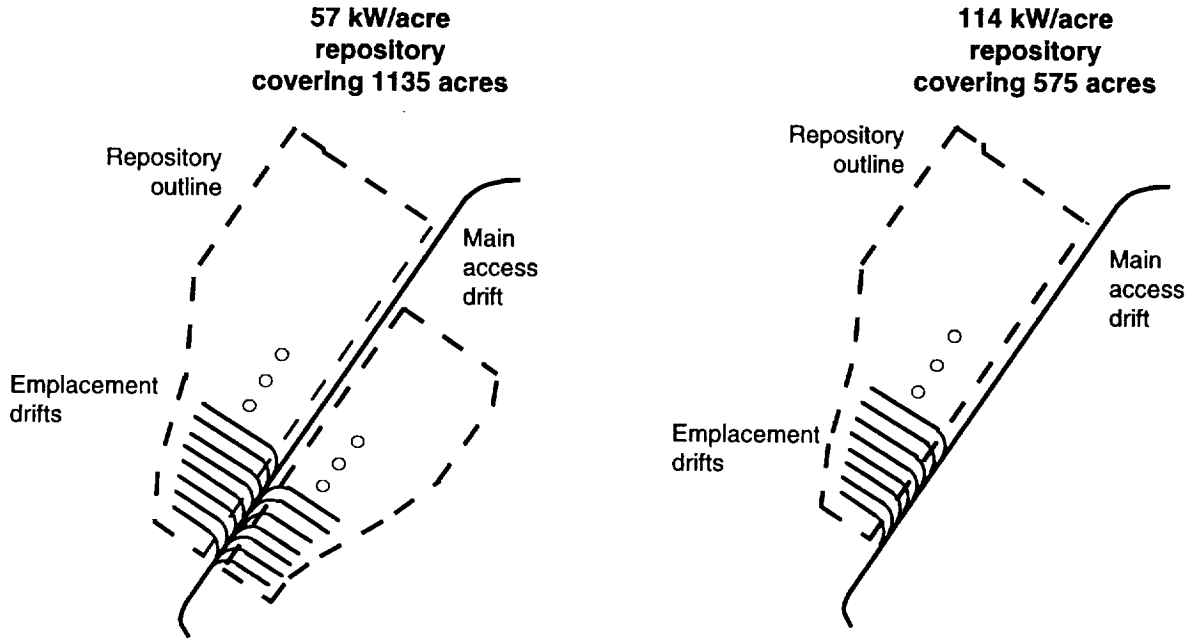

Figure ES-4. Repository layouts for the two thermal loadings considered in TSPA-93.

examined are a 114-kW/acre repository with vertically emplaced containers, a 57-kW/acre repository with in-drift containers, and a 114-kW/acre repository with in-drift containers.

2.2 Stratigraphy

A fully three-dimensional stratigraphic model of the potential repository region is developed for TSPA-93. The model uses geostatistics to reduce dependence on qualitative approaches by incorporating as much site-specific information as possible. The model was developed with the long-term goal of determining whether the thicknesses of the strata at the site are important to the modeled performance. For TSPA-93, probabilistic calculations (see below) are conducted using a reference stratigraphy selected from 10 geostatistical simulations performed with this approach.

The model incorporates lithologic data from 22 deep drillholes within or near the potential repository region in an indicator simulation to determine boundaries between welded and nonwelded layers of tuff. More regular structures—the Topopah Spring vitrophyre and the boundary between the vitric and zeolitized Calico Hills layers—are added separately.

Despite the welded/nonwelded indicator having horizontal correlation lengths on the order of kilometers, significant variation is seen in the strata contacts within the repository block for the 10 geostatistical outcomes. The implication is that the lithologic-data drillholes are not spaced closely enough for accurate predictions.

2.3 Hydrogeologic parameters

A performance-assessment data base is produced for TSPA-93 for the purpose of standardizing available data and generating probability distributions of parameters used in both the detailed and the probabilistic models. Data are categorized for 15 hydrologic properties (e.g., porosity, hydraulic conductivity, etc.) in 10 strata, both in the unsaturated and saturated formations. Each of the 10 modeled strata is considered homogeneous, and one probability density function (PDF) is developed for each hydrologic property in each layer. Each PDF is either derived directly from available data (where data are abundant), or is derived based on maintaining maximum informational entropy (where data are sparse), in order to minimize the chance of biasing the results. PDFs are also adjusted from lab scale to site scale to make them more representative.

A new accomplishment with this effort is the development of a method for determining fracture characteristics that are consistent with site data. Distributions of bulk-permeability, fracture-frequency, and fracture-dip data from drillholes are used as input to a parallel-plate model, allowing calculation of fracture apertures, hydraulic conductivities, porosities, etc.

2.4 Climate change

Groundwater flow could be the most important process affecting the performance of a repository at Yucca Mountain (analysis of TSPA-91 and TSPA-93 results show a significant sensitivity to the groundwater-flux parameter). Although the present groundwater flow through Yucca Mountain is thought to be relatively insignificant, few quantitative data are available. The strategy for TSPA-93 is to examine the paleoclimatic record and data from analog sites, then extrapolate future infiltration and percolation at Yucca Mountain. The paleoclimatic record shows that an ice-age cycle of 100,000 years has existed during the recent Pleistocene, and researchers have noted that Yucca Mountain experienced probably 40% but perhaps up to 200% more annual precipitation during the last ice age. Recent data from the U. S. Geological Survey (USGS) has also indicated that the water table under Yucca Mountain was higher by 85 m or more during the last ice age.

For TSPA-93, a series of "wet" (ice-age) and "dry" (interglacial) climates are specified, with a cycle of 100,000 years, but with the dividing time between wet and dry selected at random. Flow is modeled as a sequence of steady states. Infiltration rates average 10 mm/yr for wet climates, and 0.5 mm/yr for dry climates. The water table is allowed to rise up to 120 m during wet climates. These values are greater than what often is believed for the region. Percolation from meteoric sources is assumed to equal infiltration in the TSPA model that describes groundwater flow in fractures (the weeps model) but, for the model that describes

flow in both matrix and fractures (the composite-porosity model), percolation is reduced to account for lateral diversion of flow above the repository. For TSPA-93, groundwater mobilized by a repository thermal pulse (see below) is added onto the direct meteoric influx and both are diverted around the dried region where temperatures are above boiling.

2.5 Solubility and sorption parameters

Distributions of solubility and sorption parameters for TSPA-93 were obtained through elicitation of experts from Los Alamos National Laboratory (LANL) and Sandia National Laboratories (SNL). Their decisions are based primarily on laboratory data, while keeping in mind that solubility and sorption characteristics of radionuclides are especially dependent on site-specific groundwater chemistry and somewhat dependent on temperature. The experts reaffirmed that most of the actinides are relatively insoluble and highly sorbing in conditions typical of Yucca Mountain. However, neptunium does not adsorb well to tuffs and under oxidizing conditions is relatively soluble. The solubility and sorption values offered by the experts resulted in neptunium often being a major contributor to aqueous releases and doses for the nominal-case scenarios.

3 Detailed calculations

3.1 Thermal effects

It has become increasingly apparent over the last few years that heat generated by radioactive decay within a repository will influence the environment around it. For TSPA-93, thermal effects related to the thermal dryout, perturbation of the flow field, container corrosion, and spent-fuel alteration are considered.

For TSPA-93, three-dimensional heat-flow calculations were performed to determine parameters thought to be the most critical in defining the impact of the repository thermal pulse. Only heat conduction was considered in the calculations; hydrologic and mechanical effects were not explicitly modeled. All four repository configurations were explicitly modeled, however, accounting for each container location, container thermal output, and container emplacement time. In addition, LLNL supplied TSPA-93 with results of two-dimensional hydrothermal calculations with a smeared heat source for comparison (see below).

Critical parameters that are produced relate to the extent that the thermal pulse protects the repository from groundwater by forming a region above boiling temperature (called the protected, or "dryout fraction," of the repository), as well as the extent that it perturbs the environment by displacing vaporized water (water is displaced from the "dryout volume") and diverting meteoric water. In addition, container-wall temperatures and internal waste

tempertures are produced. The parameters are used in the probabilistic calculations to redistribute groundwater flow and to adjust the source term. For example, the source term used in the probabilistic calculations allows aqueous corrosion of a container only when liquid water is contacting the container and the container-wall temperature is below 100°C.

Some major results of the thermal modeling are as follows. The boiling isotherm, and therefore the perturbation in the environment, reaches substantial proportions around both the 57-kW/acre repositories and the 114-kW/acre repositories, although more so for the higher thermal loading (Figure ES-5). (For a period, at 114-kW/acre, the entire repository is dried out.) Comparison of the SNL and LLNL thermal modeling shows that repository geometry and the discrete nature of the heat sources are important: the center of 114-kW/acre repositories drops below boiling at around 5000 years with a discretely modeled repository, but at around 9000 years when the repository is modeled as a smeared heat source. Also, the in-drift containers are large discrete heat sources that produce a nonuniform dryout zone at early times. Thermal loading, backfill, and container size have a significant effect on container temperatures: the in-drift containers could see temperatures well above 500°C under certain conditions in a 114 kW/acre repository; the vertically emplaced containers reach temperatures slightly above 200°C in a 57 kW/acre repository.

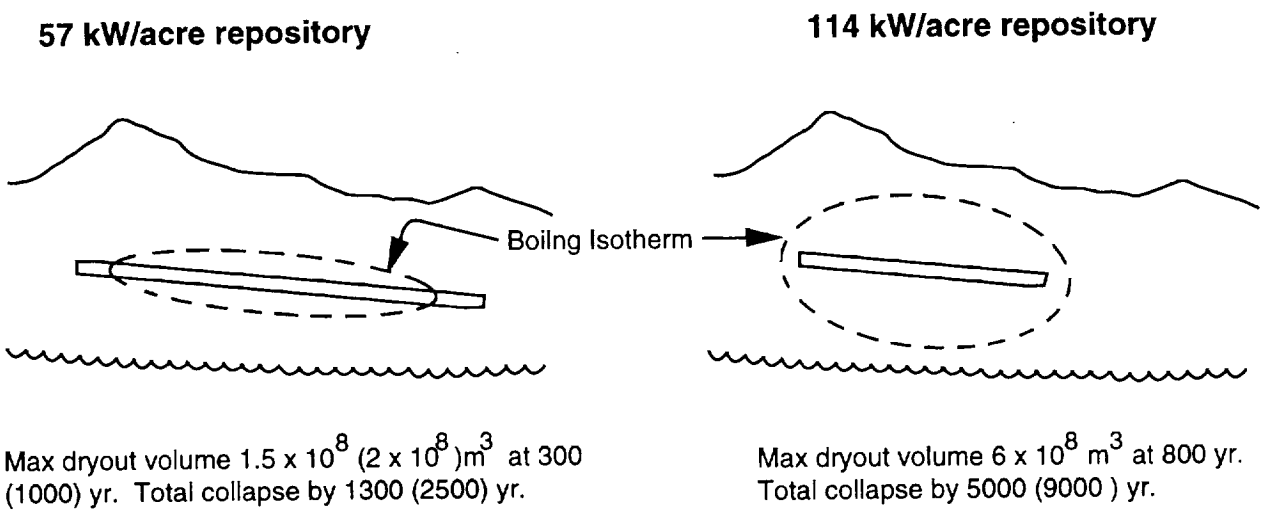

Figure ES-5. Extent and duration of the volume encompassed by the boiling isotherm (the dryout volume). Where different, the values calculated with a smeared heat source are shown in parentheses.

3.2 Saturated zone

A three-dimensional model of steady-state groundwater flow in the saturated zone is constructed for TSPA-93. Geometry for the model consists of an approximately 8-km square

section extending from the water table down 200 m. Five strata are included, which because of the tilt of the units intersect the water table at an angle. Two different flow models are superimposed on this geometry: nondiversionary flow, where all fluid entering the "high-gradient region" (to the northeast of the repository block) in the tuff aquifers continues to move through the tuff aquifers; and diversionary flow, where part of the fluid entering the high-gradient region is diverted from the saturated tuff downward to continue its flow path in the carbonate aquifers. Flow boundary conditions are taken from a regional saturated-zone flow model. Both the nondiversionary and the diversionary models calibrate to within a meter of water-table elevation at almost all drillholes.

Tracer transport times through the complicated three-dimensional structure are estimated for both models by transport calculations. The calculations involve a nonsorbing tracer released at various points under the repository block. Transport-time distributions are changed to velocity distributions for use in the probabilistic models.

Model calculations indicate that tracer transport times over the 5 km to the accessible environment tend to be less than 1000 years, and they tend to be shorter for the diversionary flow model than for the nondiversionary model. The short transport times, as well as the structure exhibited by the tracer concentrations during transport, indicate that three-dimensional modeling is important in the saturated zone. Accurate calibration of the flow systems required that reduced hydraulic conductivities be assigned to the Solitario Canyon fault and the Drill Hole Wash fault; these faults should be investigated for these properties.

3.3 Gas flow

A two-dimensional, nonisothermal, transient model of gas flow and $^{14}CO_2$ transport provide gaseous-transport-time distributions for use in the TSPA-93 probabilitic models. Geometry for the model is taken from three parallel east-west cross sections that incorporate the latest information about site topography and stratigraphy. Only a 57-kW/acre repository is considered. For each calculation, transport times are determined for gas particles traveling from points distributed throughout the repository area to the ground surface. Transport-time distributions for $^{14}CO_2$ particles are output at 1000-year intervals.

Major results of the gas-flow calculations indicate that $^{14}CO_2$ transport times are short enough to have only marginal effect on cumulative releases. Gas flow depends primarily on temperature and the bulk-permeability distribution within the mountain. Retardation by exchange of $^{14}CO_2$ with bicarbonate in the groundwater is included in the model, and significantly slows transport—typically by an order of magnitude or more. Adsorption onto minerals in the rock is not included, but is potentially important.

4 Probabilistic modeling

The models for probabilistic analyses are abstractions of process models. The input parameters for these models come primarily from the data development and detailed modeling activities discussed above. To address uncertainty in parameters, the probabilistic models are used to perform thousands of calculations with parameters picked from probability distributions (the Monte Carlo method). To address uncertainty in models, two alternative conceptual models of groundwater flow in the unsaturated zone are analyzed. To simplify the process, aqueous, gaseous, human-intrusion, and basaltic-volcanism releases are modeled separately.

4.1 Nominal-case models

Two alternative conceptual models of flow in the unsaturated zone form the foundation of the nominal-case calculations. These two models were used in TSPA-91, but are refined for TSPA-93 to include an abstracted thermal-effects model (based on the results of the detailed thermal-effects calculations discussed above) and climate change. To calculate aqueous releases and doses, each of these models incorporates: (1) a phemonenological source-term model to calculate radionuclide releases from containers, (2) a transport model to calculate spread of radionuclides through the groundwater, (3) a simplified saturated-zone model (using parameters from the detailed saturated-zone calculations discussed above), (4) a simple drinking-water-dose model, and (5) a simplified gas-flow model (based on the detailed gas-flow modeling discussed above).

4.1.1 The composite-porosity model

The composite-porosity model (also known as the equivalent-continuum model) describes flow through an equivalent porous medium of matrix and fractures using Darcy's law. The major assumption in the model is that a local pressure equilibrium tightly couples flow in the matrix and flow in the fractures; thus, groundwater flow is dominated by capillary forces and only occurs in the fractures when the matrix is saturated. The result is a relatively uniform flow (Figure ES-6). Radionuclide transport also is modeled assuming tight coupling between matrix and fracture transport; thus, when fracture flow does occur in the calculations, diffusion of radionuclides into the matrix slows the transport considerably. At the onset of a climate change, the water table is modeled to rise abruptly, and all radionuclides in the inundated part of the unsaturated zone are transfered immediately to the saturated zone, shortly thereafter forming a spike in the releases at the accessible environment.

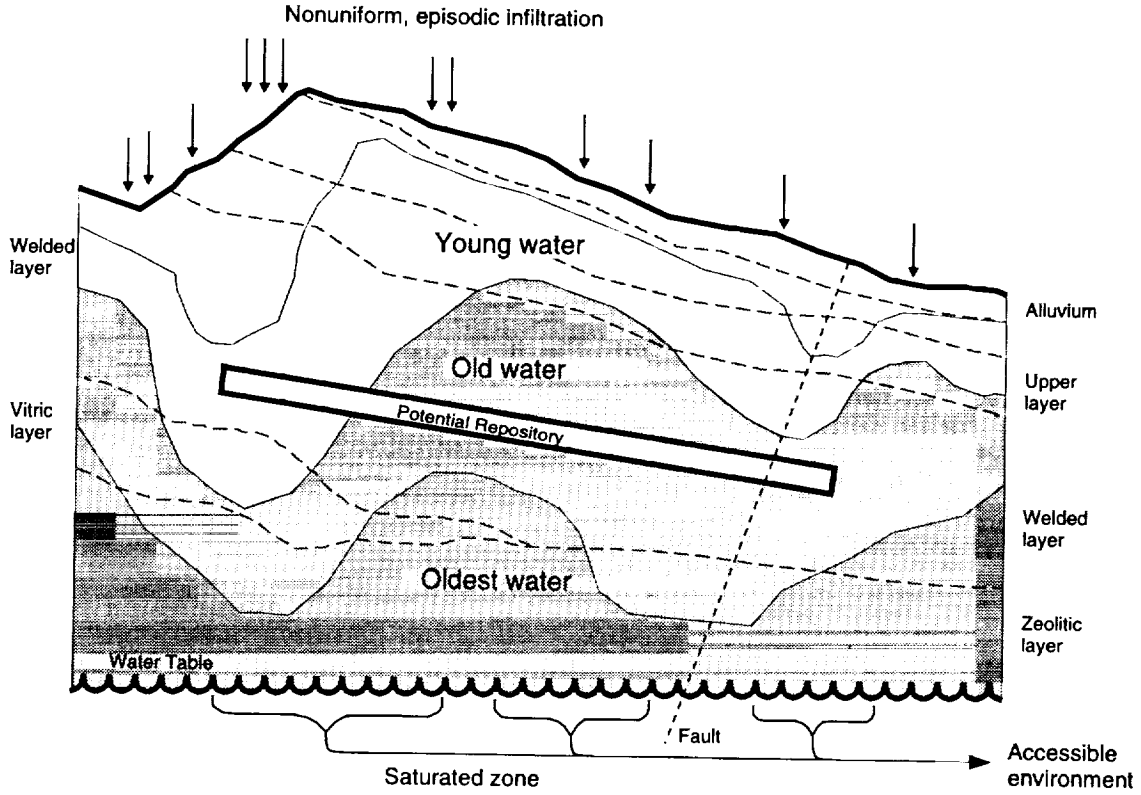

Figure ES-6. The composite-porosity model (large-scale regular percolation).

For TSPA-93, flow and transport through the unsaturated zone is modeled in 8 (for the 57-kW/acre repositories) or 5 (for the 114-kW/acre repositories) vertical flow tubes. Each unsaturated-zone flow tube is matched with a horizontal flow tube in the saturated zone.

Calculations using the composite-porosity model indicate that a relatively uniform flow pattern causes a large number of containers to be in a moist or a wet environment. Subsequent aqueous corrosion of these containers leads to widespread failure. (With the source-term being used, most aqueous corrosion occurs during the collapse of the repository thermal pulse, when water contacts containers that are near 100°C—see below.) Slow, constant percolation causes slow, constant leaching of waste from the failed waste containers. Long travel times afforded by the slowly percolating water in the unsaturated zone limit cumulative releases over 10,000 years, but are not sufficient to significantly limit peak doses that could occur in a 1,000,000-year period.

The parameters most important to performance depend on the performance measure applied, i.e., cumulative releases or individual dose. For the EPA measure from 40 CFR 191.13, percolation flux is the dominant parameter; when cumulative releases are measured at 10,000 years, the leading edge of a long-term pulse of releases is being measured, and the percolation flux determines how much of that leading edge crosses the boundary to

the accessible environment within 10,000 years. For the individual-dose measure, without any time limit, dilution in the environment is most important, but parameters relating to releases from containers are also important. For example, backfill allows more water contact with in-drift containers, causing a substantial number of failures and subsequent radioactive releases.

4.1.2 The weeps model

The weeps model describes groundwater flow restricted to locally saturated fractures, which only contact the repository at discrete points (Figure ES-7). Weep location in time and space depends on thermal effects and climate change, and is treated as an inherently probabilistic process. Degradation of containers and releases of radionuclides are limited to the intersections of weeps and containers. Transport of radionuclides through the unsaturated zone is assumed to be instantaneous. The saturated zone is modeled with a single flow tube.

Weeps-model calculations indicate that flowing fractures contacting containers are relatively rare occurrences, and that many containers within a repository remain relatively dry

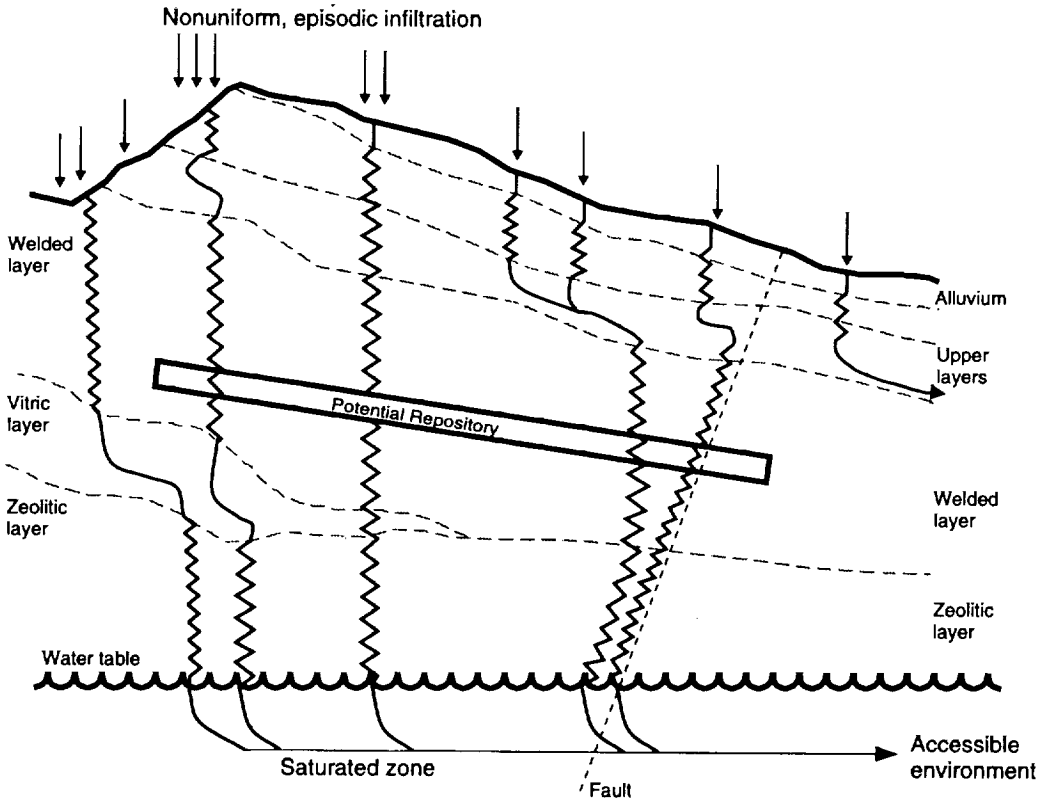

Figure ES-7. The weeps model (episodic pulses of flow in locally saturated zones, e.g. fractures).

and intact. In-drift containers present a larger cross section to vertical weeps than vertically emplaced containers, and are more readily contacted. Most contacts occur because of the flow perturbation from repository thermal effects or during a wet climate. Although it is typically of shorter duration, the flow perturbation caused by thermal effects is more significant in terms of releases than the increased flow caused by a wet climate. The reason is because the waste containers are susceptible to corrosion primarily when their temperature is above ambient (about 25°C), and especially when near 100°C, which occurs during the collapse of the thermal pulse. At later times when climate change is most often modeled to occur, container temperatures have fallen to levels where the corrosion rates are insignificant. Releases during wet climates typically only occur from a few previously failed containers. Consequently, peak doses occur most often within the first 20,000 years of repository life, and cumulative releases do not increase much after this time.

4.1.3 Radionuclide source-term model

For TSPA-93, the YMIM source-term model, developed at LLNL, is directly incorporated into the nominal-case probabilistic models. YMIM is a phenomenological model that calculates container corrosion (including oxidation, general aqueous corrosion, and localized corrosion—pitting), oxidation alteration of spent fuel, and dissolution of radionuclides within spent fuel. Temperature dependence of these processes is included in the model, although the temperature dependence of solubility is not considered in TSPA-93. Inputs include near-field hydrology, container and fuel-rod temperature, and water chemistry. Defective or mechanically failed containers (known as juvenile failures) are consider probabilistically. Several important processes (e.g., steam corrosion and cathodic protection of containers) are not yet included in YMIM.

Use of YMIM within the composite-porosity and weeps models provides two important results: (1) dry oxidation destroys the corrosion-allowance steel outer wall of the in-drift containers during the high-temperature period following backfill, and (2) aqueous corrosion is only significant while container temperatures are above ambient (about 25°C), and it can be especially rapid while temperatures are near 100°C.

4.2 Disturbed-case models

4.2.1 Human intrusion

The human-intrusion analysis is based on a FEP sequence involving exploratory drilling, waste container breakage, and radionuclide release via extracted drill core and entrainment in the drilling fluid. Extraction of contaminated rock from a near miss of a failed container is also considered. Present-day drilling technology is assumed. Drilling

frequency is based on guidance given in 40 CFR Part 191. A more comprehensive source term that distinguishes between spent-fuel and defense-high-level-waste containers is used in TSPA-93 than was used in TSPA-91. The only performance measure calculated is normalized cumulative release—individual doses are not considered.

Because of the more detailed source term, more variation is seen in the results when compared with the results for TSPA-91. As with TSPA-91, drilling frequency is the most important parameter (and one of the most difficult to predict). The in-drift containers, being larger, are more often hit by drilling and lead to greater releases; however, if it is assumed that only part of the container is exhumed commensurate with the size of the drill, then releases from in-drift containers are similar to releases from vertically emplaced containers.

4.2.2 Indirect volcanic effects

For TSPA-91, direct releases of radionuclides caused by intrusion of a basaltic dike into the repository were investigated; for TSPA-93, indirect releases are investigated. The FEP sequence modeled addresses magma intruding rock units near the repository and accelerating waste-container degradation because of the effects of heat and aggressive volatiles. These effects result in changes to the aqueous-transport source term. Dike length, location, and thickness are calculated probabilistically. The temperature of rock adjacent to a magmatic intrusion is calculated as a function of basaltic dike temperature and thickness, distance into the rock, and time. Waste-container corrosion rates are adjusted 10^4 higher to account for aggressive magmatic volatiles. This value is consistent with sulfidization rates.

Analysis results show penetration of heat from a dike only on the order of a few meters. Magmatic volatiles are assumed to intrude only the same distance. Also, the probability of magmatic intrusion, based on geologically realistic values for the volcanic recurrence rate in the Yucca Mountain region and scaled for the two possible areas of the repository, is extremely low over 10,000 years ($\sim 10^{-4}$ probability of occurrence), and even when extrapolated to 1,000,000 years ($\sim 10^{-2}$ probability of occurrence). Thus, little contribution from indirect volcanic effects to the nominal-case aqueous releases is observed.

5 Results

Results of the TSPA-93 probabilistic modeling are in the form of conditional complementary cumulative distribution functions (CCDFs). The CCDFs show the probability of exceeding a given value of either the EPA sum (i.e., the cumulative release normalized as specified in 40 CFR 191.13) or peak individual dose for a given realization of a probabilistic model. The distributions are conditional because they do not as yet include all possible scenarios.

Figure ES-8 shows calculated CCDFs of 10,000-year normalized cumulative release using the composite-porosity model, for all modeled release mechanisms. Only results for a 57-kW/acre repository with vertically emplaced containers are shown; however, with the composite-porosity model, all repository configurations produce similar results (see below). Gaseous releases are predicted to be the most significant, exceeding the EPA standard. Several factors contribute to the large gaseous releases: relatively uniform flow causes a large number of containers to be contacted by water when they are warm (near 100°C) and susceptible to corrosion; upon container failure, $^{14}CO_2$ is readily released (there is a sizable prompt fraction of ^{14}C, but also, when temperatures are elevated, oxidation alteration of spent fuel proceeds rapidly and allows ^{14}C to escape); and $^{14}CO_2$ has a short transport time to the ground surface. Releases caused by human intrusion and nominal-case aqueous releases are important, but do not violate the standard. Indirect releases caused by volcanism are both few and low; direct releases caused by volcanism (a TSPA-91 result) are low primarily because the probability of a basaltic dike intruding in the repository in 10,000 years is very low.

As mentioned, the composite-porosity model predicts little influence of the four repository designs on performance. Container size is immaterial because slow, uniform percolation

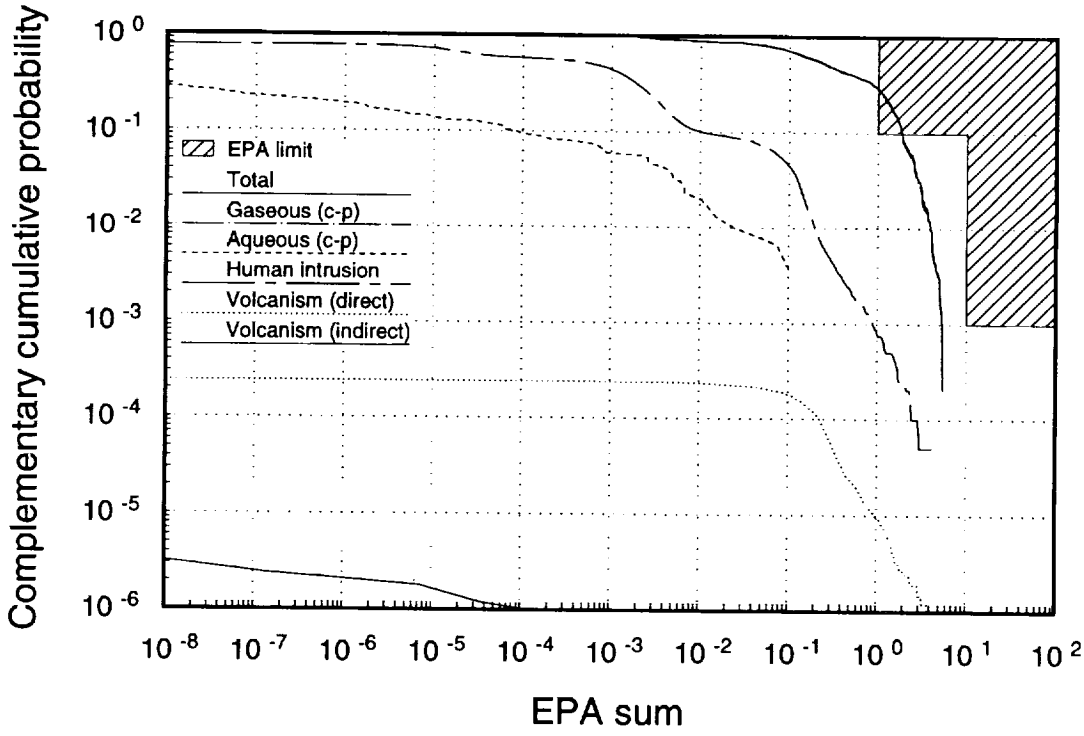

Figure ES-8. Base-case normalized cumulative release predicted by the composite-porosity model.

of groundwater leads to widescale contact irrespective of size. A slight effect is seen in the normalized cumulative releases over 10,000 years, where the dryout zone created by the hotter repositories results in a several thousand year increase in container lifetime. But for dose calculations over 1,000,000 years, container lifetime and thermal perturbations are too short to make much difference.

The CCDFs of 10,000-year normalized cumulative release calculated using the weeps model are shown in Figure ES-9. Normalized cumulative releases are predicted to be lower for the weeps model than for the composite-porosity model (compare total releases in Figure ES-8 with those shown in Figure ES-9). Releases caused by human intrusion are often predicted to be greater than the nominal-case releases predicted by the weeps model. The reason is that weeps rarely contact waste containers. And within 10,000 years, most weep contacts are caused by groundwater shed around the dryout volume onto unprotected parts of the repository (although many of the resulting contacts are for short periods of time). Gaseous releases are greater than aqueous releases at the highest probabilities because of juvenile failures that release $^{14}CO_2$ without weep contact. Indirect releases caused by volcanism are not calculated for the weeps model and do not appear in the figure. (This figure only represents the base-case design; repository design does influence releases predicted by the weeps model, as discussed below.)

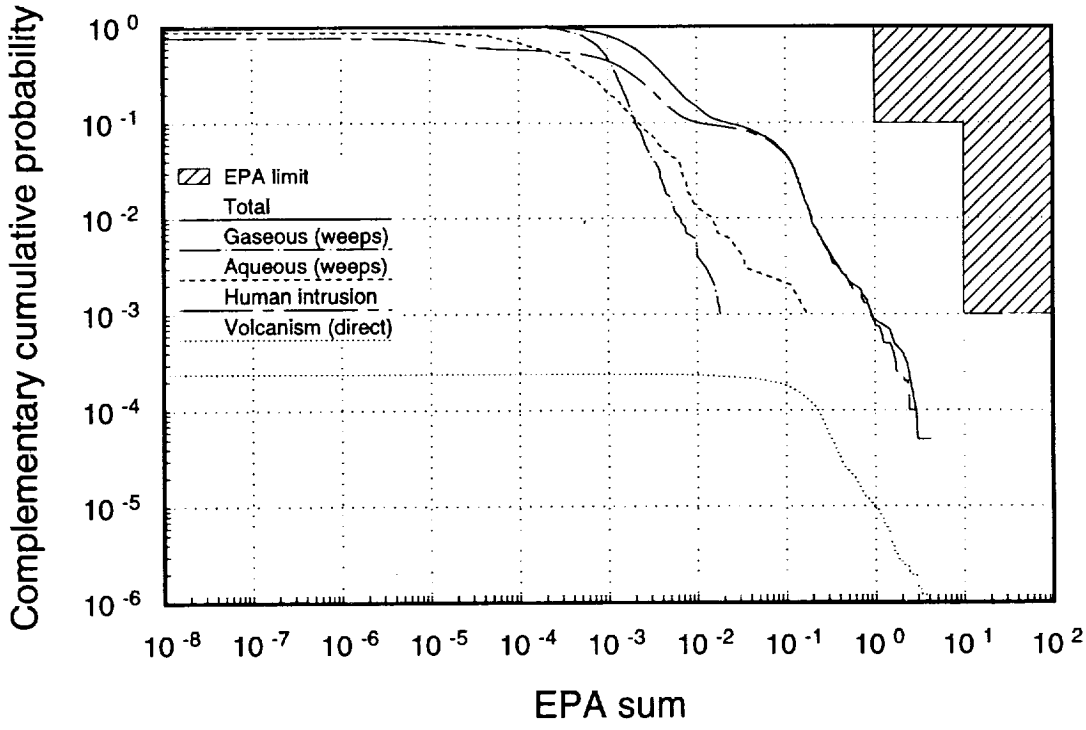

Figure ES-9. Base-case normalized cumulative release predicted by the weeps model.

A comparison of peak individual doses for the two unsaturated-zone flow models is shown in Figure ES-10. The doses shown are for drinking water only and are the peak doses realized within a 1,000,000-yr period. The figure shows that both models predict doses from the repository at levels above background dose (approximately 300 mrem/yr): over 90% of the composite-porosity realizations and about 1% of the weeps model realizations exceed background. These doses are primarily caused by neptunium. Peak doses predicted by the composite-porosity model typically occur because of high percolation rates and water-table rise of a wet climate; those predicted by the weeps model typically occur because of water shed on easily corroded containers (the number of containers contacted by water is a probabilistic result) as the repository thermal perturbation dissipates.

Because transport time is not an issue (except that some actinides decay away before they reach the accessible environment), peak doses are primarily a function of radionuclide release rate from the repository and dilution in the environment. Arid environments typically have little dilution. The release rate is greater, and thus the doses are greater, for the composite-porosity model than for the weeps model because of the larger number of containers that are contacted by water and fail.

Figure ES-11 presents weeps-model peak doses calculated for the four repository designs. The weeps model predicts that larger containers, because of the larger cross section

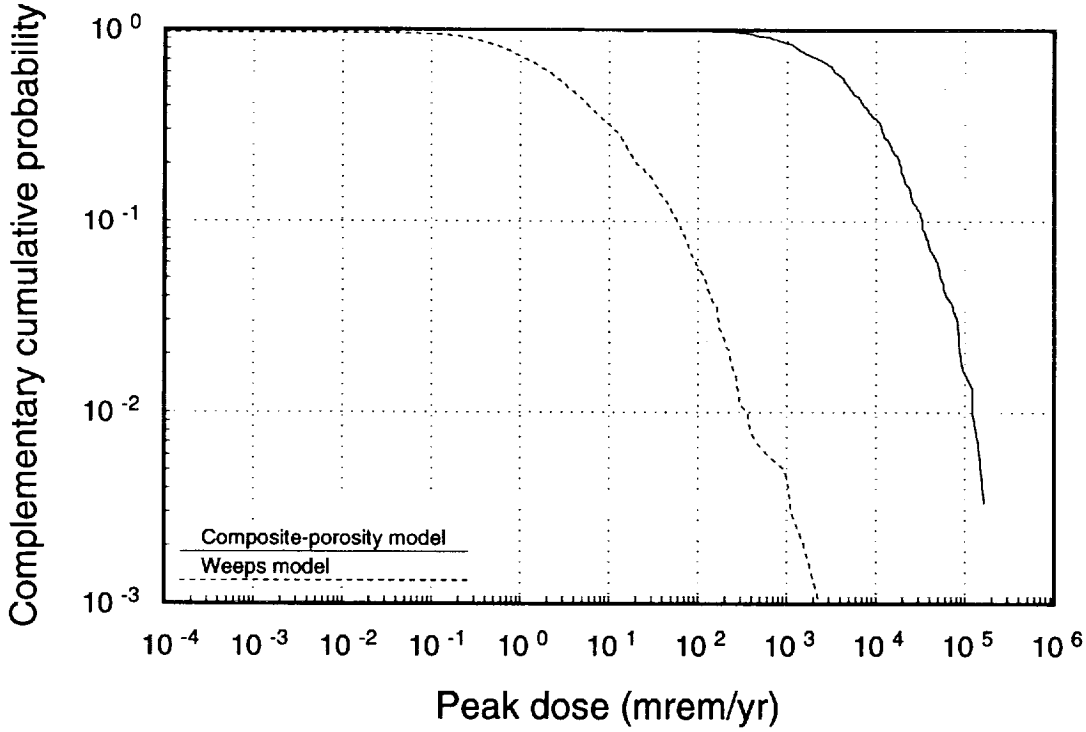

Figure ES-10. Peak drinking-water dose within 1,000,000 years.

they offer for vertical weeps, have worse performance. A secondary effect is that hotter repositories cause worse performance, because hotter repositories cause a greater perturbation in groundwater flow and an increased probability of containers being contacted by weeps. (These findings are predicated on a number of factors, including that the repository drifts do not divert or concentrate weep flow, that flow returns to the dryout volume coincident with its collapse, etc.) The weeps model predicts similar behavior with the EPA performance measure, although none of the repository designs violate this standard.

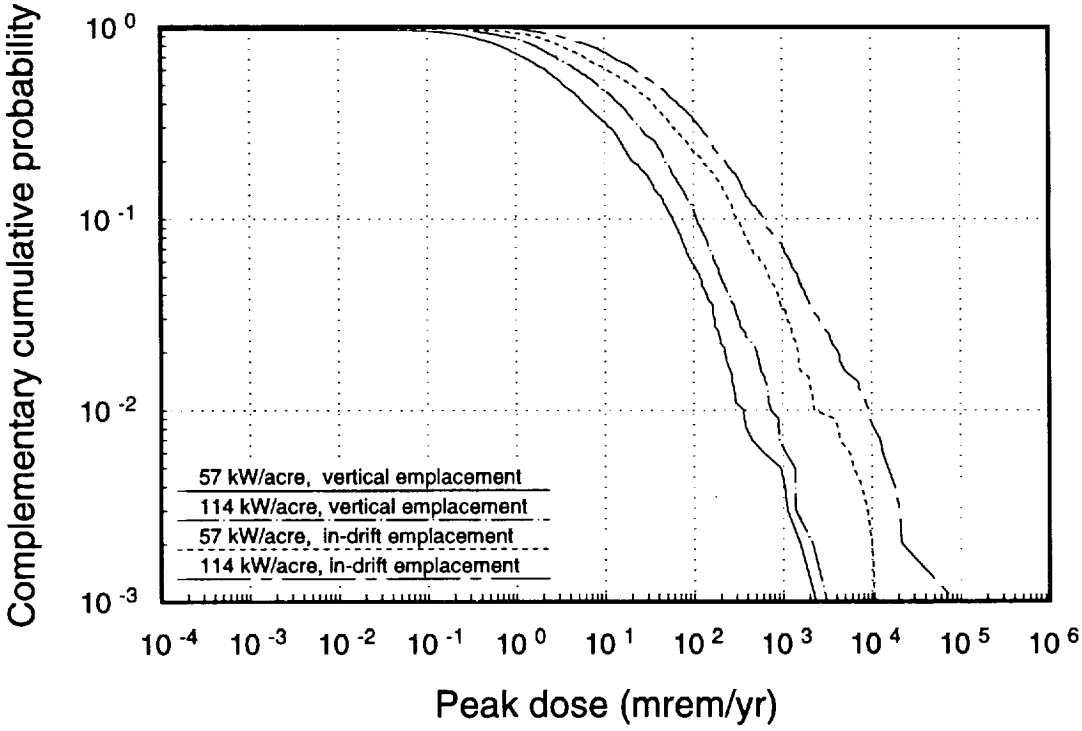

Figure ES-11. Peak doses for four repository configurations as predicted by the weeps model.

6 Conclusions and recommendations

The large difference in the results of the alternative conceptual models leads to questions about what model best approximates the behavior of the groundwater flow system. Calculations of peak individual drinking-water dose over 1,000,000 years indicate that radionuclides released from a Yucca Mountain repository could experience little dilution, and extremely low release rates from the repository—either from a highly engineered waste container or a system for reducing water contact with containers—might be needed to achieve low individual dose rates. Two possible impacts of repository design on long-term performance are also identified: (1) larger containers could be more readily contacted by weeps and drilling; (2) hotter repositories could cause a greater perturbation in the flow field, resulting in more containers being contacted by weeps. Results from the composite-porosity model

indicate that normalized cumulative releases and doses are relatively insensitive to thermal loading and container size and emplacement. The YMIM corrosion models used by both the composite-porosity model and the weeps model predict that most container failures significant to performance occur during decay of the repository thermal pulse—within the first few thousand years. A 10-cm corrosion-allowance overpack for in-drift containers is predicted to be oxidized away within a few hundred years, with no contribution to performance. (The overpack could be more important than indicated because of processes not included in the models currently being used.) Indirect releases from volcanic activity are not found to be significant contributors to overall releases.

Recommendations regarding site-data needs derive primarily from nominal-condition results because human-intrusion results are largely site-independent and volcanism results are comparatively insignificant. The following recommendations are made acknowledging limitations and assumptions in the present models, as well as uncertainities in our knowledge of physical conditions within Yucca Mountain and future events. It should also be mentioned that data are being collected in a number of these areas and an effort is being made to ascertain that the data are useful to determining long-term performance.

- Because of the substantial difference between the results of the two groundwater flow models, the first priority should be the determination of the dominant flow mechanisms (in both time and space) operating in the unsaturated zone at Yucca Mountain.
- Concerning gaseous releases, more data are needed on the spatial distribution of bulk permeability throughout Yucca Mountain and on adsorption of CO_2 to tuff.
- Concerning aqueous releases, characterization at the repository horizon of percolation-flux magnitude and distribution (in both time and space) is a high priority.
- Concerning individual doses, a high priority is characterization of the amount of horizontal and vertical dispersion (factors in dilution) in the saturated zone.
- Additional hydrogeologic data from new drillholes are also needed, as is research on scaling of properties and hydraulic characterization of unsaturated fractures in the rock matrix.
- Additional information is needed on heterogeneity and spatial correlations for geostatistical modeling and on cross-correlations among parameters.
- Thermal and hydraulic properties of proposed backfill materials should be determined, and fault-zone hydrogeologic properties should be characterized.
- To develop reliable models of near-field interactions, integrated testing is needed in the areas of waste-container/groundwater contact, radionuclide transport from degraded

containers, coupled thermal-mechanical-hydrologic-chemical processes, and the interactions between natural and man-made system components.

- Further work is also recommended on waste-form alteration and container corrosion under realistic conditions.

Repository design must meet a number of requirements, with long-term performance being but one. Recommendations concerning long-term performance typically come from models that contain a number of limitations. Acknowledging this situation, the following design-related recommendations are made based on the TSPA-93 results.

- Calculated waste-container temperatures are very high for the in-drift cases, well above the thermal goals defined in the SCP. To approach the thermal goals, any backfill used with in-drift emplacement needs to be designed to allow for heat transfer.
- The biggest difference in the performance measures for the four repository configurations that are considered is a result of the difference in container "target size." Reduction in target size or engineered measures to reduce contact between containers and weeps or drilling paths is recommended.
- Container emplacement should be designed to reduce moisture contact with containers (both weeps and uniformly percolating water). Borehole emplacement attempts to achieve this reduction by specifying an air gap surrounding the container. For in-drift emplacement, backfill or a system within the backfill could possibly be engineered to control water contact.

Regulatory change could affect performance assessment for radioactive-waste disposal. If the radioactive-release standard changes to a measure based on individual dose rates over a time period much longer than 10,000 years, significant changes in site-characterization program priorities might be needed, with more emphasis on determining radionuclide release rates. If the standard is changed to an individual-dose standard but the regulated time period remains at 10,000 years, impact on the site-characterization needs would be lessened. Dose calculations require more information than cumulative-release calculations and would require additional characterization of the biosphere in the vicinity of Yucca Mountain. Information extrapolated into the distant future will introduce additional uncertainty into the calculations.

YUCCA MOUNTAIN SITE CHARACTERIZATION PROJECT
DISTRIBUTION LIST

1 D.A. Dreyfus (RW-1)
Director
OCRWM
US Department of Energy
1000 Independence Avenue SW
Washington, DC 20585

1 L.H. Barrett (RW-2)
Acting Deputy Director
OCRWM
US Department of Energy
1000 Independence Avenue SW
Washington, DC 20585

1 J.D. Saltzman (RW-4)
Office of Strategic Planning and International Programs
OCRWM
US Department of Energy
1000 Independence Avenue SW
Washington, DC 20585

1 J.D. Saltzman (RW-5)
Office of External Relations
OCRWM
US Department of Energy
1000 Independence Avenue SW
Washington, DC 20585

1 Samuel Rousso (RW-10)
Office of Program and Resource Mgt.
OCRWM
US Department of Energy
1000 Independence Avenue SW
Washington, DC 20585

1 J. C. Bresee (RW-10)
OCRWM
US Department of Energy
1000 Independence Avenue SW
Washington, DC 20585

1 R.M. Nelson (RW-20)
Office of Geologic Disposal
OCRWM
US Department of Energy
1000 Independence Avenue, SW
Washington, DC 20585

1 S. J. Brocoum (RW-22)
Analysis and Verification Division
OCRWM
US Department of Energy
1000 Independence Avenue SW
Washington, DC 2585

1 D. Shelor (RW-30)
Office of Systems and Compliance
OCRWM
US Department of Energy
1000 Independence Avenue, SW
Washington, DC 20585

1 J. Roberts (RW-33)
Director, Regulatory Compliance Division
OCRWM
US Department of Energy
1000 Independence Avenue, SW
Washington, DC 20585

1 G. J. Parker (RW-332)
Reg. Policy/Requirements Branch
OCRWM
US Department of Energy
1000 Independence Avenue, SW
Washington, DC 20585

1 R. A. Milner (RW-40)
Office of Storage and Transporation
OCRWM
US Department of Energy
1000 Independence Avenue, SW
Washington, DC 20585

1 S. Rousso (RW-50)
Office of Contract Business Management
OCRWM
US Department of Energy
1000 Independence Avenue, SW
Washington, DC 20585

1 T. Wood (RW-52)
Director, M&O Management Division
OCRWM
US Department of Energy
1000 Independence Avenue, SW
Washington, DC 20585

4 Victoria F. Reich, Librarian
Nuclear Waste Technical Review Board
1100 Wilson Blvd, Suite 910
Arlington, VA 22209

5 R.M. Nelson Jr, Acting Project Manager
Yucca Mountain Site Characterization Office
US Department of Energy
P.O. Box 98608--MS 523
Las Vegas, NV 89193-8608

1 C. L. West, Director
Office of External Affairs
DOE Nevada Field Office
US Department of Energy
P.O. Box 98518
Las Vegas, NV 89193-8518

8 Technical Information Officer
DOE Nevada Field Office
US Department of Energy
P.O. Box 98518
Las Vegas, NV 89193-8518

1 P. K. Fitzsimmons, Technical Advisor
Office of Assistant Manager for Environmental Safety and Health
DOE Nevada Field Office
US Department of Energy
P.O. Box 98518
Las Vegas, NV 89193-8518

1 D. R. Elle, Director
Environmental Protection and Division
DOE Nevada Field Office
US Department of Energy
P.O. Box 98518
Las Vegas, NV 89193-8518

1 Repository Licensing & Quality Assurance
Project Directorate
Division of Waste Management
US NRC
Washington, DC 20555

1 Senior Project Manager for Yucca Mountain
Repository Project Branch
Division of Waste Management
US NRC
Washington, DC 20555

1 NRC Document Control Desk
Division of Waste Management
US NRC
Washington, DC 20555

1 Philip S. Justus
NRC Site Representive
301 E Stewart Avenue, Room 203
Las Vegas, NV 89101

1 E. P. Binnall
Field Systems Group Leader
Building 50B/4235
Lawrence Berkeley Laboratory
Berkeley, CA 94720

1 Center for Nuclear Waste Regulatory Analyses
6220 Culebra Road
Drawer 28510
San Antonio, TX 78284

3 W. L. Clarke
Technical Project Officer - YMP
Attn: YMP/LRC
Lawrence Livermore National Laboratory
P.O. Box 5514
Livermore, CA 94551

1 J. A. Blink
Deputy Project Leader
Lawrence Livermore National Laboratory
101 Convention Center Drive
Suite 820, MS 527
Las Vegas, NV 89109

4 J. A. Canepa
Technical Project Officer - YMP
N-5, Mail Stop J521
Los Alamos National Laboratory
P.O. Box 1663
Los Alamos, NM 87545

1 H. N. Kalia
Exploratory Shaft Test Manager
Los Alamos National Laboratory
Mail Stop 527
101 Convention Center Dr., #820
Las Vegas, NV 89101

1 N. Z. Elkins
Deputy Technical Project Officer
Los Alamos National Laboratory
Mail Stop 527
101 Convention Center Dr., #820
Las Vegas, NV 89101

5 L. E. Shephard
Technical Project Officer - YMP
Sandia National Laboratories
Organization 6302, M/S 1333
P.O. Box 5800
Albuquerque, NM 87185

1 J. F. Devine
Asst Director of Engineering Geology
US Geological Survey
106 National Center
12201 Sunrise Valley Drive
Reston, VA 22092

1 L. R. Hayes
Technical Project Officer
Yucca Mountain Project Branch
MS 425
US Geological Survey
P.O. Box 25046
Denver, CO 80225

1 V. R. Schneider
Asst. Chief Hydrologist--MS 414
Office of Program Coordination and Technical Support
US Geological Survey
12201 Sunrise Valley Drive
Reston, VA 22092

1 J. S. Stuckless
Geologic Division Coordinator
MS 913
Yucca Mountain Project
US Geological Survey
P.O. Box 25046
Denver, CO 80225

1 D. H. Appel, Chief
Hydrologic Investigations Program
MS 421
US Geological Survey
P.O. Box 25046
Denver, CO 80225

1 E. J. Helley
Branch of Western Regional Geology
MS 427
US Geological Survey
345 Middlefield Road
Menlo Park, CA 94025

1 R. W. Craig, Chief
Nevada Operations Office
US Geological Survey
101 Convention Center Drive
Suite 860, MS 509
Las Vegas, NV 89109

1 D. Zesiger
US Geological Survey
101 Conventional Center Drive
Suite 860, MS 509
Las Vegas, NV 89109

1 G. L. Ducret, Associate Chief
Yucca Mountain Project Division
US Geological Survey
P.O. Box 25046
421 Federal Center
Denver, CO 80225

1 A. L. Flint
US Geological Survey
MS 721
P.O. Box 327
Mercury, NV 89023

1 D. A. Beck
Water Resources Division, USGS
6770 S Paradise Road
Las Vegas, NV 89119

1 P. A. Glancy
US Geological Survey
Federal Building, Room 224
Carson City, NV 89701

1 Sherman S.C. Wu
US Geological Survey
2255 N. Gemini Drive
Flagstaff, AZ 86001

1 J. H. Sass - USGS
Branch of Tectonophysics
2255 N Gemini Drive
Flagstaff, AZ 86001

1 DeWayne Campbell
Technical Project Officer - YMP
US Bureau of Reclamation
Code D-3790
P.O. Box 25007
Denver, CO 80225

1 J. M. LaMonaca
Records Specialist
US Geological Survey
421 Federal Center
P.O. Box 25046
Denver, CO 80225

1 W. R. Keefer - USGS
913 Federal Center
P.O. Box 25046
Denver, CO 80225

1 M. D. Voegele
Technical Project Officer - YMP
SAIC
101 Convention Center Drive
Suite 407
Las Vegas, NV 89109

2 L. D. Foust
Nevada Site Manager
TRW Environmental Safety Systems
101 Convention Center Drive
Suite 540, MS 423
Las Vegas, NV 89109

1 C. E. Ezra
YMP Support Office Manager
EG&G Energy Measurements Inc
MS V-02
P.O. Box 1912
Las Vegas, NV 89125

1 E. L. Snow, Program Manager
Roy F. Weston Inc
955 L'Enfant Plaza SW
Washington, DC 20024

1 Technical Information Center
Roy F. Weston Inc
955 L'Enfant Plaza SW
Washington, DC 20024

1 D. Hedges, Vice President, QA
Roy F. Weston Inc
4425 Spring Mountain Road
Suite 300
Las Vegas, NV 89102

1 D. L. Fraser, General Manager
Reynolds Electrical & Engineering Co, Inc
MS 555
P.O. Box 98521
Las Vegas, NV 89193-8521

1 B. W. Colston, President and General Manager
Las Vegas Branch
Raytheon Services Nevada
MS 416
P.O. Box 95487
Las Vegas, NV 89193-5487

1 R. L. Bullock
Technical Project Officer - YMP
Raytheon Services Nevada
Suite P-250, MS 403
101 Convention Center Drive
Las Vegas, NV 89109

1 Paul Eslinger, Manager
PASS Program
Pacific Northwest Laboratory
P.O. Box 999
Richland, WA 99352

1 A. T. Tamura
Science and Technology Division
OSTI
US Department of Energy
P.O. Box 62
Oak Ridge, TN 37831

1 Carlos G. Bell Jr
Professor of Civil Engineering
Civil and Mechanical Engineering Dept.
University of Nevada, Las Vegas
4505 S Maryland Parkway
Las Vegas, NV 89154

1 P. J. Weeden, Acting Director
Nuclear Radiation Assessment Div.
US EPA
Environmental Monitoring Systems Lab
P.O. Box 93478
Las Vegas, NV 89193-3478

1 ONWI Library
Battelle Columbus Laboratory
Office of Nuclear Waste Isolation
505 King Avenue
Columbus, OH 43201

1 T. Hay, Executive Assistant
Office of the Governor
State of Nevada
Capitol Complex
Carson City, NV 89710

3 R. R. Loux
Executive Director
Agency for Nuclear Projects
State of Nevada
Evergreen Center, Suite 252
1802 N. Carson Street
Carson City, NV 89710

1 C.H. Johnson
Technical Program Manager
Agency for Nuclear Projects
State of Nevada
Evergreen Center, Suite 252
1802 N. Carson Street
Carson City, NV 89710

1 John Fordham
Water Resources Center
Desert Research Institute
P.O. Box 60220
Reno, NV 89506

1 David Rhode
Desert Research Institute
P.O. Box 60220
Reno, NV 89506

1 Eric Anderson
Mountain West Research-
Southwest Inc
2901 N Central Avenue #1000
Phoenix, AZ 85012-2730

1 The Honorable Cyril Schank
Chairman
Churchill County Board of
Commissioners
190 W First Street
Fallon, NV 89406

1 Dennis Bechtel, Coordinator
Nuclear Waste Division
Clark County Department of
Comprehensive Planning
301 E Clark Avenue, Suite 570
Las Vegas, NV 89101

1 Juanita D. Hoffman
Nuclear Waste Repository
Oversight Program
Esmeralda County
P.O. Box 490
Goldfield, NV 89013

1 Eureka County Board of
Commissioners
Yucca Mountain Information
Office
P.O. Box 714
Eureka, NV 89316

1 Brad Mettam
Inyo County Yucca Mountain
Repository Assessment Office
Drawer L
Independence, CA 93526

1 Lander County Board of
Commissioners
315 South Humbolt
Battle Mountain, NV 89820

1 Vernon E. Poe
Office of Nuclear Projects
Mineral County
P.O. Box 1026
Hawthorne, NV 89415

1 Les W. Bradshaw
Program Manager
Nye County Nuclear Waste
Repository Program
P.O. Box 153
Tonopah, NV 89049

1 Florindo Mariani
White Pine County Nuclear
Waste Project Office
457 Fifth Street
Ely, NV 89301

1 Judy Foremaster
City of Caliente Nuclear Waste
Project Office
P.O. Box 158
Caliente, NV 89008

1 Phillip A. Niedzielski-Eichner
Nye County Nuclear Waste
Repository Project Office
P.O. Box 221274
Chantilly, VA 22022-1274

1 Jason Pitts
Lincoln County Nuclear Waste
Project Office
Lincoln County Courthouse
Pioche, NV 89043

1 Economic Development Dept.
City of Las Vegas
400 E. Stewart Avenue
Las Vegas, NV 89101

1 Commmunity Planning and Development
City of North Las Vegas
P.O. Box 4086
North Las Vegas, NV 89030

1 Community Development and Planning
City of Boulder City
P.O. Box 61350
Boulder City, NV 89006

1 Commission of the European Communities
200 Rue de la Loi
B-1049 Brussells
BELGIUM

2 M. J. Dorsey, Librarian
YMP Research and Study Center
Reynolds Electrical & Engineering Co Inc
MS 407
P.O. Box 98521
Las Vegas, NV 89193-8521

1 Amy Anderson
Argonne National Laboratory
Building 362
9700 S Cass Avenue
Argonne, IL 60439

1 Steve Bradhurst
P.O. Box 1510
Reno, NV 89505

1 Michael L. Baughman
35 Clark Road
Fiskdale, MA 01518

1 Glenn Van Roekel
Director of Community Development
City of Caliente
P.O. Box 158
Caliente, NV 89008

1 Ray Williams, Jr
P.O. Box 10
Austin, NV 89310

1 Nye County District Attorney
P.O. Box 593
Tonopah, NV 89049

1 William Offutt
Nye County Manager
Tonopah, NV 89049

1 Charles Thistlethwaite, AICP
Inyo County Planning Department
Drawer L
Independence, CA 93526

1 R. F. Pritchett
Technical Project Officer - YMP
Reynolds Electrical & Engineering Company Inc
MS 408
P.O. Box 98521
Las Vegas, NV 89193-8521

1 Dr. Moses Karakouzian
1751 E Reno #125
Las Vegas, NV 89119

3 Brenda Bailey White
CCS
5301 Central NE
Suite 1520
Albuquerque, NM 87108

1 Clarence R. Allen
NWTRB
1000 E. California Blvd.
Pasadena, CA 91106

1 Johan Andersson
SKI
Division of Nuclear Waste
Sehlstedtgatan II
Box 27106
S-102 52 Stockholm
SWEDEN

1 Michael J. Apted
Intera Sciences
3609 S. Wadsworth Blvd
Denver, CO 80235

1 Dwayne Chesnut
Lawrence Livermore National Laboratory
P.O. Box 808
M/S L202
Livermore, CA 94551

1 Richard Codell
US Nuclear Regulatory Commission
M/S 4-H-3
Washinton, DC 20555

1 Seth M. Coplan
US Nuclear Regulatory Commission
M/S 4-H-3
Washington, DC 20555

1 Kevin Coppersmith
Geomatrix Consultants
100 Pine Street, 10th Floor
San Francisco, CA 94111

1 C.F. Costa
Nuclear Radiation Assessment Division
US EPA
Environmental Monitoring Systems Laboratory
P.O. Box 93478
Las Vegas, NV 89193-3478

1 Allen G. Croff
Chemical Technology Division
Oak Ridge National Laboratory
4500N, MS-6235
P.O. Box 2008
Oak Ridge, TN 37831-6235

1 Bruce M. Crowe
Los Alamos National Laboratory
101 Convention Center Drive
Suite 820
Las Vegas, NV 89109

1 Department of Comprehensive Planning
Clark County
225 Bridger Avenue, 7th Floor
Las Vegas, NV 89155

1 D.W. Engel
Pacific Northwest Laboratory
P.O. Box 999
M/S K7-34
Richland, WA 99352

1 Leonard J. Fiorenzi
P.O. Box 257
Eureka, NV 89316

1 A.B. Gureghian
CNWRA
6220 Culebra Road
San Antonio, TX 78228-0510

5 William G. Halsey
Lawrence Livermore National Laboratory
P.O. Box 808
M/S L-204
Livermore, CA 94551

1 M.E. Harr
School of Civil Engineering
Purdue University
1284 Civil Engineering Building
West Lafayette, IN 47907-1284

1 Dwight Hoxie
US Geological Survey
101 Convention Center Drive
Suite 860
Las Vegas, NV 89109

1 Edwin E. Kinter
Bradley Hill Road
P.O. Box 682
Nortwich, VT 05055

1 Donald Langmuir
Nuclear Waste Technical Review Board
109 So. Lookout Mountain Cr.
Golden, CO 80401

1 Lincoln County Commission
Lincoln County
P.O. Box 90
Pioche, NV 89043

1 Ian Miller
Golder Associates Inc
4104 148 Avenue NE
Redmond, WA 98052

1 R.W. Nelson
INTERA-M&O
101 Convention Center Drive
Suite P110
Las Vegas, NV 89109

1 Claudia Newbury
Yucca Mountain Project Office
US Department of Energy
P.O. Box 98608
M/S 523
Las Vegas, NV 89193-8518

1 D. Warner North
NWTRB
Decision Focus Inc
4984 El Camino Real
Los Altos, CA 94062

2 William J. O'Connell
Lawrence Livermore National Laboratory
P.O. Box 808, M/S L-195
Livermore, CA 94551

1 Michael Revelli
Lawrence Livermore National Laboratory
P.O. Box 808
M/S L-206
Livermore, CA 94551

1 Benjamin Ross
Disposal Safety Inc
1660 L STreet NW, Suite 314
Washington, DC 20036

2 SAIC-T & MSS Library
101 Convention Center Drive
Suite 407
Las Vegas, NV 89109

1 Frank W. Schwartz
195 Thornbury Lane
Powell, OH 43065

1 Bjorn Selinder
190 W. First Street
Fallon, NV 89406

1 Ardyth Simmons
Yucca Mountain Project
US DOE
P.O. Box 98608
M/S 523
Las Vegas, NV 89193-8518

1 Scott Sinnock
TRW
101 Convention Center Drive
Suite P110
Las Vegas, NV 89109

1 Ellis D. Verink
Nuclear Waste Technical Review Board
4401 NW 18th Place
Gainesville, FL 32605

1 Joseph Wang
Lawrence Berkeley Laboratory
Earth Sciences Division
1 Cyclotron Road
Berkeley, CA 94720

1 R.V. Watkins, Chief
Project Planning and Management
USGS
P.O. Box 25046
421 Federal Center
Denver, CO 80225

1 Ed Weeks -USGS
P.O. Box 25046
Federal Center M/S 413
Lakewood, CO 80225

1 C.L. West, Director
Office of External Affairs
DOE Field Office, Nevada
US DOE
P.O. Box 98518
Las Vegas, NV 89193-8518

1 Robert F. Williams
EPRI Nuclear Power Division
P.O. Box 10412
Palo Alto, CA 94303

1 George Zyvoloski
Geoanalysis Group
Los Alamos National Lab
M/S F665
Los Alamos, NM 87545

1 Jean Younker
TRW
101 Convention Center Drive
Suite P110
Las Vegas, NV 89109

1 Dr. June Fabryka-Martin
Los Alamos National Lab
MS J-514
Los Alamos, NM 87545

1 Dr. F. Owen Hoffman
Oak Ridge National Lab
P.O. Box 2008
Oak Ridge, TN 37831-6036

1 Dr. Arjun Makhijani
Institute for Energy and Environmental Research
6935 Laurel Avenue
Takoma Park, MD 20912

1 Dr. James E. Martin
Assistant Professor of
Radiological Health
University of Michigan
School of Public Health
Ann Arbor, MI 48109

1 Dr. H. Robert Meyer
C.N.S.I.
750 East Park Drive
Suite 200
Harrisburg, PA 17111

1 Jess Riley
Heinman Research Labs
P.O. Box 35457
Charlotte, NC 28207

1 James E. Watson Jr
Environ. Science and Engineering
Campus Box 7400
University of North Carolina
Chapel Hill, NC 27599-7400

1 Dr. William M. Murphy
Center for Nuclear Waste
Regulatory Analyses
Southwest Research Institute
6220 Culebra Road
San Antonio, TX 78238-5166

1 Miroslav Kucerka, Consultant
Radioactive Waste Management
Botevova 3104
143 00 Praha 4
Czech Republic

1 Dr. John Kessler
Nuclear Power Division
EPRI
P.O. Box 10412
Palo Alto, CA 94303-0813

1 Per-Eric Ahlstrom
Research Director
Swedish Nuclear Fuel and
Waste Management Co
Box 5864 S-102 48
Stockholm, Sweden

1 W.A. Seddon
AECL Technologies
9210 Corporate Boulevard
Suite 410
Rockville, MD 20850

1 Dr. Wilfried Albert
NAGRA
Hardstrasse 73
CH-5430 Wettingen
Switzerland

1 Runo Barrdahl
Swedish Radiation Protection
Institute
P.O. Box 60204
S-104 01 Stockholm
Sweden

1 Dr. John E. Gale
Fracflow Consultants Inc
36 Pearson Street
St. John's, Newfoundland
Canada A1A 3R1

1 Dr. Furruccio Gera
ISMES S.P.S.
Via dei Crociferi 44
00187 Rome, Italy

1 Dr. Gunnar Gustafson
Department of Geology
Chalmers University of Technology
and University of Goteborb
S-412 96 Goteborg
Sweden

1 Dr. Alan W. Herbert
AEA Technology
Theoretical Studies Department
Harwell Laboratory B424.4
Oxfordshire OX11 ORA
United Kingdom

1 David Hodgkinson
INTERA
Chiltern House
45 Station Road
Henley-on-Thames, Oxon
RG9 1AT
United Kingdom

1 Dr. Yong Soo Hwang
Korea Atomic Energy
Research Institute
P.O. Box 7
Daeduk-Danji
Taejeon, Korea

1 Dr. Katsumi Kamemura
Shinozuka Research Institute
5F Maguna Kogyo Building 1-31-13
Yoyogi, Shibuya-ku
Tokyo, 151, Japan

1 Dr. Bill Lanyon
Geo-Science Limited
Falmouth Business Park
Bickland Water Road
Falmouth, Cornwall
TR11 4SZ, United Kingdom

1 Dr. Jussi Palmu
Imatran Voima Oy
Rajatorpantie 8
P.O. Box 112
SF-01601 Vantaa, Finland

1 Dr. Carmen Bajos Parada
ENRESA
Emilio Vargas 7
28043 Madrid, Spain

1 Dr. Gunnar Ramqvist
ELTEKNO AB
Gruvvagen 1
S-714 00 Kopparberg
Sweden

1 Dr. Robert Rundberg
Los Alamos National Lab
Mail Stop J-514
Los Alamos, NM 87545

1 James A. Steadman
Building Research Establishment
Structural Performance Division
Garston, Watford WD2 7JR
United Kingdom

1 Dr. Ove Stephansson
Department of Engineering Geology
Royal Institute of Technology
S-100 44 Stockholm, Sweden

1 Dr. Juhani Vira
Teollisuuden Voiman Oy
Annankatu 42 C
SF-00100 Helsinki
Finland

1 Peter Wallman
Golder Associates
4104 148 Avenue NE
Redmond WA 98052

1 Minoro Yamakuma
Geoscience Research Project
PNC Tokyo, Japan

1 David Leaver
Polestar
Four Main Street
Los Altos, CA 94022

1 James Gansemer
Lawrence Livermore National Laboratory
P.O. Box 808
Livermore, CA 94551

1 Lynn C. Lewis
Lawrence Livermore National Laboratory
P.O. Box 808
Livermore, CA 94551

1 Alan D. Lamont
Lawrence Livermore National Laboratory
P.O. Box 808
Livermore, CA 94551

1 Ines Triay
Los Alamos National Laboratory
P.O. Box 1663
Los Alamos, NM 87545

1 David Morris
Los Alamos National Laboratory
P.O. Box 1663
Los Alamos, NM 87545

1 Ning Lu
USGS
P.O. Box 25046, MS 421
Denver Federal Center
Lakewood, CO 80225

1 Gary LeCain
USGS
P.O. Box 25046
Denver Federal Center
Lakewood, CO 80225

1 Edward Kwicklis
USGS
P.O. Box 25046
Denver Federal Center
Lakewood, CO 80225

1 Jerry McNeish
INTERA
M/S 423
101 Convention Center Drive
Las Vegas, NV 89109

1 April V. Gil
Yucca Mountain Project
M/S 523
101 Convention Center Drive
Las Vegas, NV 89109

1 Joseph J. Dlugosz
Yucca Mountain Project
M/S 523
101 Convention Center Drive
Las Vegas, NV 89109

1 Wendy R. Dixon
Yucca Mountain Project
M/S 523
101 Convention Center Drive
Las Vegas, NV 89109

1 Jeanne C. Nesbit
Yucca Mountain Project
M/S 523
101 Convention Center Drive
Las Vegas, NV 89109

1 Susan B. Jones
Yucca Mountain Project
M/S 523
101 Convention Center Drive
Las Vegas, NV 89109

1 William B. Simecka
Yucca Mountain Project
M/S 523
101 Convention Center Drive
Las Vegas, NV 89109

1 Dennis R. Williams
Yucca Mountain Project
M/S 523
101 Convention Center Drive
Las Vegas, NV 89109

1 C. Thomas Statton
Yucca Mountain Project
M&O/WCFS
M/S 423
101 Convention Center Drive
Las Vegas, NV 89109

1 Yvonne Tsang
Lawrence Berkeley Laboratory
Earth Sciences Division
1 Cyclotron Road
Berkeley, CA 94720

1 Tom Bjerstedt
Yucca Mountain Project
US DOE
P.O. Box 98608
M/S 523
Las Vegas, NV 89193-8518

1 Maxwell Blanchard
Yucca Mountain Project
P.O. Box 98608
M/S 523
Las Vegas, NV 89193-8518

2 Jeremy Boak
Yucca Mountain Project
US DOE
P.O. Box 98608
M/S 523
Las Vegas, NV 89193-8518

1 Garry D. Brewer
Nuclear Waste Technical Review Board
University of Michigan
Dana Bldg, Room 3516
Ann Arbor, MI 48109-1115

1 Daniel B. Bullen
Iowa State University
P.O. Box 1768
Ames, IA 50010

1 Thomas A. Buscheck
Lawrence Livermore National Laboratory
P.O. Box 808
M/S L206
Livermore, CA 94550

1 John E. Cantlon, Chairman
Nuclear Waste Technical Review Board
1795 Bramble Drive
East Lansing, MI 48823

1 K.W. Causseaux
NHP Reports Chief
U.S. Geological Survey
421 Federal Center
P.O. Box 25046
Denver, CO 80225

1 Pat Domenico
NWTRB
1100 Wilson Boulevard, Suite 910
Arlington, VA 22209

2 A.L. Dudley
SPECTRA Research Institute
1603 University NE
Albuquerque, NM 87102

1 William Dudley
US Geological Survey
P.O. Box 25046
M/S 425
Denver, CO 80225

1 J. Russell Dyer
Yucca Mountain Project Office
US DOE
P.O. Box 98608
M/S 425
Las Vegas, NV 89193-8518

1 Norman A. Eisenberg
US Nuclear Regulatory Commission
M/S 4-H-3
Washington, DC 20555

1 W.W.-L. Lee
Environmental Evaluation Group
7007 Wyoming NE
Suite F-2
Albuquerque, NM 87109

1 R.E. Lowder
MAC Tec
101 Conventional Center Drive
Suite 1100
Las Vegas, NV 89109

1 R.R. Luckey
USGS
Building 53
Denver Federal Center
Room H2314/MS 5421
Denver, CO 80225

1 Annette MacIntyre
Lawrence Livermore National Laboratory
P.O. Box 808
M/S L-194
Livermore, CA 94551

1 Edward A. Mason
Amoco Resource Center
P.O. Box 451
46 Admirals Lane
Osterville, MA 02655-0451

1 Russell McFarland
NWTRB
100 Wilson Blvd, Suite 910
Arlington, VA 22209

1 Robin McGuire
Risk Engineering Inc
5255 Pine Ridge Road
Golden, CO 80403

1 John J. McKetta
NWTRB
Department of Chemical Engineering
CRE Building 1450
Austin, TX 78712-1062

1 Ian McKinley
NAGRA
Hardstrasse 73
Wettingen, CH-5430
SWITZERLAND

1 Fred W. McLafferty
Department of Chemistry
Cornell University
2600 Baker Laboratory
Ithaca, NY 14853-1301

1 Arend Meijer
GCX Inc
P.O. Box 87198-2427
Albuquerque, NM 87198

1 Dr. Martin Mifflin
Water Resources Center
Desert Research Center
2505 Chandler Avenue, Suite 1
Las Vegas, NV 89120

1 Suresh Pahwa
INTERA
6850 Austin Center Blvd
Suite 300
Austin, TX 78731

1 Planning Department
Nye County
P.O. Box 153
Tonopah, NV 89049

1 F. Joseph Pearson Jr
1304 Walnut Hill Lane
Suite 210
Irving, TX 75038

1 Chris Pflum
SAIC
101 Conventional Center Drive
Las Vegas, NV 89109

1 T.H. Pigford
University of California
Department of Nuclear Engineering
Berkeley, CA 94720

1 P.T. Prestholt
NRC Site Representative
301 E. Stewart Avenue, Room 203
Las Vegas, NV 89101

1 Dennis L. Price
NWTRB
1011 Evergreen Way
Blackburg, VA 24060

1 Karsten Pruess
Lawrence Berkeley Laboratory
Earth Sciences Division
1 Cyclotron Road
Berkeley, CA 94720

1 Norman C. Rasmussen
MIT
Department of Nuclear Engineering
Bldg 24-205
Cambridge, MA 02139

1 Leon Reiter
NWTRB
1100 Wilson Blvd, Suite 910
Arlington, VA 22209-2297

1 Everett Springer
Los Alamos National Laboratory
P.O. Box 1663
M/S J495
Los Alamos, NM 87545

1 Roger Staehle
University of Minnesota
Department of Chemical Engineering
and Materials Science
22 Red Fox Road
North Oaks, MN 55127

1 Jane Summerson
US DOE
Forrestal RW-22, 7F-091/FORS
Washington, DC 20555

1 Aaron Thode
Los Alamos National Lab
M/S F607
P.O. Box 1663
Los Alamos, NM 87545

1 K.T. Thomas
National Academy of Sciences
2001 Wisconsin Ave NW
Harris Bldg, Room 456
Washington, DC 20007

1 C.F. Tsang
Lawrence Berkeley Laboratory
Earth Sciences Division
1 Cyclotron Road
Berkeley, CA 94720

1 Greg Valentine
Los Alamos National Lab
P.O. Box 1663
M/S F665
Los Alamos, NM 87545

1 Richard Van Konynenburg
Lawrence Livermore National Lab
P.O. Box 808
Livermore, CA 94551

1 Abraham Van Luik
Intera-M&O
101 Convention Center Drive
Suite #P110
Las Vegas, NV 89109

1 C. John Mann
Department of Geology
245 Natural History Building
1301 West Green Street
Urbana, Illinois 61801

1 Henry Loo
Westinghouse Idaho Nuclear Co.
P.O. Box 4000
M/S 5219
Idaho Falls, ID 83415

1 Kjell Andersson
Karinta-Konsult
P.O. Box 6048
S-183 06
Taby, Sweden

1 Dr. G. Ross Heath
College - Ocean/Fishery Sciences
583 Henderson Hall
University of Washington
Seattle, WA 98195

1 Carl Anderson
National Academy of Sciences
2101 Constitution Ave NW
Harris Building, Room 456
Washington, DC 20418

1 Dorothy M. Clark
Secretary, Science Advisory Board
US EPA
401 M Street SW, A-101F
Washington, DC 20460

1 Kathleen W. Conway
Science Advisory Board - EPA
401 M Street SW, A-101F
Washington, DC 20460

1 Dr. Chris Whipple
Clement International
160 Spear Street
Suite 1380
San Francisco, CA 94105-1535

13 Priscilla Bunton
US DOE, OCRWM (RW-331)
1000 Independence Ave SW
Washington, DC 20585

1 Linda Desell
US DOE, OCRWM (RW-331)
Suite 200
1000 Independence Ave SE
Washington, DC 20585

1 Robert J. Budnitz, President
Future Resources Associates Inc
2000 Center Street, Suite 418
Berkeley, CA 94704

1 Thomas A. Cotton
JK Research Associates Inc
4429 Butterworth Place, NW
Washington, DC 20016

1 Srikanta Mishra
M&O/ INTERA
M/S 423
101 Convention Center Drive
Las Vegas, NV 89109

200 Eric Smistad
Yucca Mountain Project
M/S 523
101 Convention Center Drive
Las Vegas, NV 89109

1 Margaret Federline
Nuclear Regulatory Commission
Washington, DC 20555-0001

1 Dr. Alan Hooper
United Kingdom Nirex Limited
Curie Avenue, Harwell
Didcot, Oxfordshire OX11 0RH
United Kingdom

1 Dr. Michael J. Bell
IAEA
Wagramerstrasse 5
P.O. Box 100
A-1400 Vienna
Austria

1 Dr. Neil Chapman
INTERA
Park View House
14B Burton Street
Melton Mowbray, Leicestershire
United Kingdom LE13 1AE

1 Dr. James G.T. Chyr
Taiwan Power Company
AF 2 Alley 15
Lane 196 Sec 4
Roosevelt Road
Taipei, Taiwan
Republic of China

1 Dr. Nestor R. Correa
NAGRA
Hardstrasse 73
CH-5430 Wettingen
Switzerland

1 Kenneth W. Dormuth, AECL
Whiteshell Laboratories
Pinawa, Manitoba
Canada ROE 1L0

1 Dr. Esko Eloranta
Finnish Centre for Radiation
P.O. Box 268
SF-00101 Helsinki
Finland

1 Dr. Helmut D. Fuchs
Gesellschaft fur Nuklear-
Service mbH
Lange Laube 7
D-3000 Hannover 1
Germany

1 Ito Fumio
c/o Prof. Swoboda
University of Innsbruck
Technikerstr 13
A-6020 Innsbruck
Austria

1 Dr. Hilkka Leino-Forsman
VTT, Technical Research
Centre of Finland
Otakaari 3 A
P.O. Box 200
SF-02151 Espoo, Finland

1 Dr. Robert W. Lieb
NAGRA
Hardstrasse 73
CH-5430 Wettingen
Switzerland

1 Dr. J.W. Lloyd
School of Earth Sciences
Edgbaston, Birmingham
B 15 2TT, United Kingdom

1 D. Ganpat S. Lodha, AECL
Whiteshell Laboratories
Pinawa, Manitoba
Canada ROE 1L0

1 Douglas E. Metcalfe
Waste Management Division
P.O. Box 1046, Station B
270 Albert Street
Ottawa, Canada K1P 5S9

1 Dr. Ivars Neretnieks
Department of Chemical
Engineering
Royal Institute of Technology
Teknikringen 26
S-100 44 Stockholm
Sweden

1 Dr. Jean-Pierre Olivier
OECD/NEA
12 Boulevard des Iles
92130 Issy Les Molineaux
France

1 Dr. Olle Olsson
Conterra AB
P.O. Box 493
S-751 06 Uppsala, Sweden

1 Maria Onofrei, AECL
Whiteshell Laboratories
Pinawa, Manitoba
Canada ROE 1L0

1 Dr. Liu Wen-Chung
Radwaste Adminstration
Atomic Energy Council
6F 65 Lane 144 Keeling Load
Section 4 Taipei
Taiwan

1 Dr. Sidney H. Whitaker
AECL
Whiteshell Laboratories
Pinawa, Manitoba
Canada ROE 1L0

1 Dr. Roger Yearsley
Inspectorate of Pollution
Room A5.02
Romney House
43 Marsham Street
London SW1P 3Py
United Kingdom

1 Dr. Piet Zuidema
NAGRA
Hardstrasse 73
CH-543o Wettingen
Switzerland

1 Dr. Arthur Motta
Nuclear Engineering Department
Pennsylvania State University
231 Sackett Building
University Park, PA 16802

1 Dr. M.R. Chandratillake
Capcis March Limited
Bainbridge House, Granby Row
Manchester M1 2PW
United Kingdom

1 Serge Runge
Eurisys Consultants S.A.
14 rue du Printemps
74017 Paris, France

1 Peter Suci
Montana State University
Bozeman, MT

1 Dr. David Kreamer
Geoscience Department - UNLV
4505 South Maryland Parkway
Las Vegas, NV 89159

1 Richard Forester
USGS
P.O. Box 25046
Denver Federal Center
Lakewood, CO 80225

1 Zell Peterman
USGS
P.O. Box 25046
Denver Federal Center
Lakewood, CO 80225

1 Kevin McCoy
B&W Fuel Company
101 Convention Center Drive
Suite P110
Las Vegas, NV 89109

1 John Nitao
Lawrence Livermore National Laboratory
P.O. Box 808
Livermore, CA 94551

1 Anne-Marie Meike
Lawrence Livermore National Laboratory
P.O. Box 808
Livermore, CA 94551

1 G.S. Bodvarsson
Lawrence Berkeley Laboratory
1 Cyclotron Road
Berkeley, CA 94720

1 Jiamin Wan
Lawrence Berkeley Laboratory
1 Cyclotron Road
Berkeley, CA 94720

1 Robert Andrews
INTERA
M/S 423
101 Convention Center Drive
Las Vegas, NV 89109

1 Tim Dale
INTERA
M/S 423
101 Convention Center Drive
Las Vegas, NV 89109

1 Dan McCright
Lawrence Livermore National Laboratory
P.O. Box 808
M/S L-204
Livermore, CA 94551

1 Ray Stout
Lawrence Livermore National Laboratory
P.O. Box 808
M/S L-204
Livermore, CA 94551

INTERNAL DISTRIBUTION

	MS	
4	1330	G. M. Gerstner-Miller, 6352 100/12541/SAND93-2675/QA
20	1330	WMT Library, 6352
1	0827	P. J. Hommert, 1502
1	1375	D. A. Dahlgren, 4400
5	0899	Technical Library, 7141
1	0619	Technical Publications, 7151
10	1119	Document Processing for DOE/OSTI, 7613-2
1	9018	Central Technical Files, 8523-2
1	0827	J. C. Cummings, 1502
1	0827	J. S. Rottler, 1511
1	0827	P. L. Hopkins, 1511
1	0827	M. J. Martinez, 1511
1	0835	R. R. Eaton, 1513
1	0835	R. D. Skocypec, 1513
1	1324	P. D. Davies, 6115
1	1324	R. J. Glass, 6115
1	1324	C. A. Rautman, 6115
1	1324	V. C. Tidwell, 6115
1	1324	C. Ho, 6115
1	1320	M. D. Siegel, 6119
1	1333	F. J. Schelling, 6302
10	1326	H. A. Dockery, 6312
10	1326	R. W. Barnard, 6312
10	1326	G. E. Barr, 6312
10	1326	J. H. Gauthier, 6312
1	1326	P. G. Kaplan, 6312
1	1326	T. H. Robey, 6312
1	1326	L. H. Skinner, 6312
1	1326	W. G. Perkins, 6312
1	1326	A. R. Schenker, 6312
1	1326	S. A. Shannon, 6312
60	1326	M. L. Wilson, 6312
1	1325	L. S. Costin, 6313
1	1325	R. E. Finley, 6313
1	1325	E. Dunn, 6313
1	1325	J. F. Holland, 6313
1	1325	J. Pott, 6313
1	1325	C. S. Chocas, 6313
1	1325	E. E. Ryder, 6313
1	1325	S. R. Sobolik, 6313
1	1330	M. C. Brady, 6314
1	1345	T. J. Brown, 6331

1	1328	M. E. Fewell, 6342
1	1328	C. T. Stockman, 6342
1	1328	R. P. Rechard, 6342
1	1328	M. G. Marietta, 6342
1	0755	B. D. Zak, 6612
1	1315	T. E. Blejwas, 7500
1	9043	R. Nilson, 8745

SAND93-2675

The number in the lower right-hand corner is an accession number used for Office of Civilian Radioactive Waste Management purposes only. It should not be used when ordering this publication.

Org.	Bldg.	Name	Rec'd by	Org.	Bldg.	Name	Rec'd by

Sandia National Laboratories

SANDIA REPORT

SAND93–2675
Unlimited Release
Printed April 1994

Yucca Mountain Site Characterization Project

Total-System Performance Assessment for Yucca Mountain – SNL Second Iteration (TSPA-1993)

Volume 1

Michael L. Wilson, John H. Gauthier, Ralston W. Barnard, George E. Barr, Holly A. Dockery, Ellen Dunn, Roger R. Eaton, David C. Guerin, Ning Lu, Mario J. Martinez, Robert Nilson, Christopher A. Rautman, Thomas H. Robey, Benjamin Ross, Eric E. Ryder, Albert R. Schenker, Sharon A. Shannon, Lee H. Skinner, William G. Halsey, James D. Gansemer, Lynn C. Lewis, Alan D. Lamont, Inés R. Triay, Arend Meijer, David E. Morris

Prepared by
Sandia National Laboratories
Albuquerque, New Mexico 87185 and Livermore, California 94550
for the United States Department of Energy
under Contract DE-AC04-94AL85000

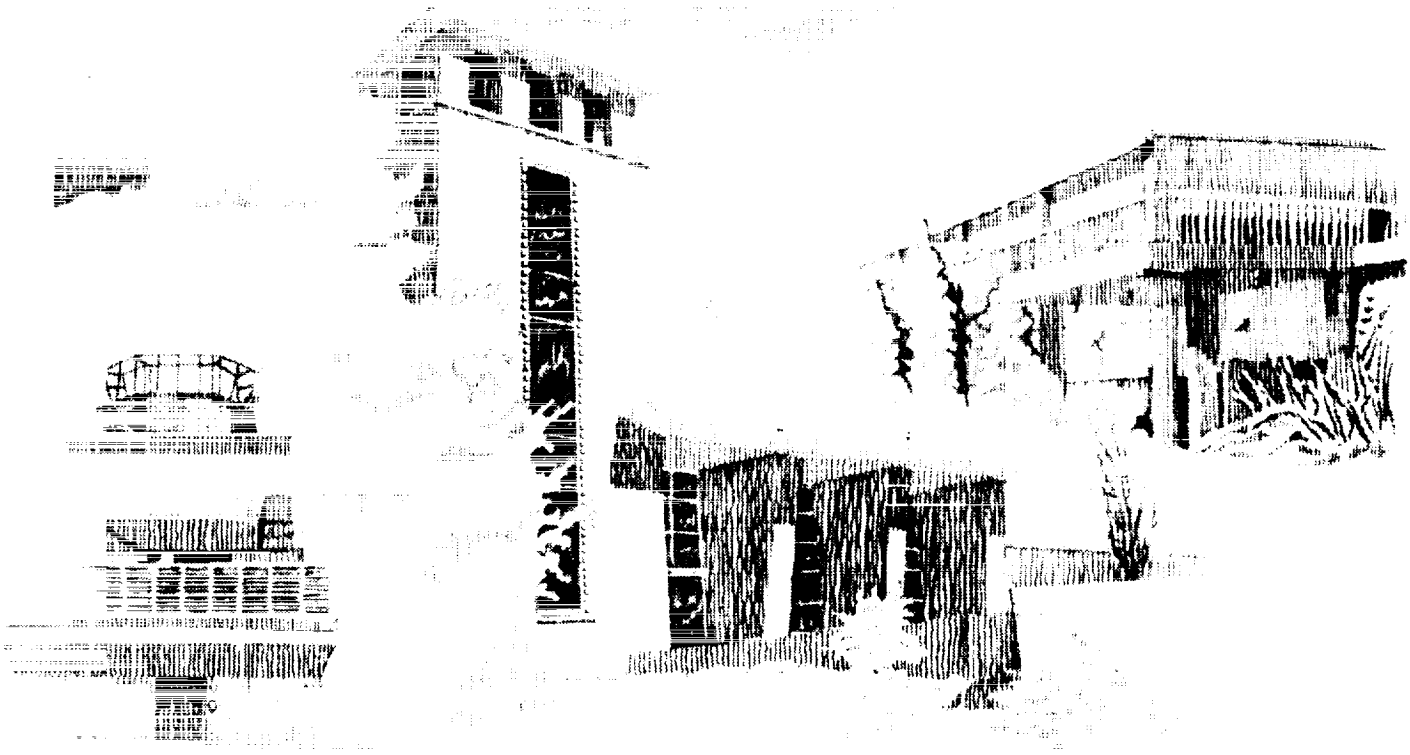

Issued by Sandia National Laboratories, operated for the United States Department of Energy by Sandia Corporation.

Available to DOE and DOE contractors from
Office of Scientific and Technical Information
PO Box 62
Oak Ridge, TN 37831

Prices available from (615) 576-8401, FTS 626-8401

Available to the public from
National Technical Information Service
US Department of Commerce
5285 Port Royal Rd
Springfield, VA 22161

NTIS price codes
Printed copy: A07
Microfiche copy: A01

Distribution Category
UC-814

SAND93-2675
Unlimited Release
Printed April, 1994

Total-System Performance Assessment for Yucca Mountain — SNL Second Iteration (TSPA-1993)

Volume 1

Michael L. Wilson, John H. Gauthier†, Ralston W. Barnard,
George E. Barr, Holly A. Dockery, Ellen Dunn, Roger R. Eaton, David C. Guerin‡,
Ning Lu*, Mario J. Martinez, Robert Nilson, Christopher A. Rautman,
Thomas H. Robey†, Benjamin Ross*, Eric E. Ryder, Albert R. Schenker‡,
Sharon A. Shannon, Lee H. Skinner†
(Sandia National Laboratories)

William G. Halsey, James D. Gansemer, Lynn C. Lewis, Alan D. Lamont
(Lawrence Livermore National Laboratory)

Inés R. Triay, Arend Meijer§, David E. Morris
(Los Alamos National Laboratory)

† Spectra Research, Inc.
‡ Los Alamos Technical Associates, Inc.
* Disposal Safety, Inc.
§ Jacobs Engineering, Inc.

Abstract

Sandia National Laboratories has completed the second iteration of the periodic total-system performance assessments (TSPA-93) for the Yucca Mountain Site Characterization Project (YMP). These analyses estimate the future behavior of a potential repository for high-level nuclear waste at the Yucca Mountain, Nevada, site under consideration by the Department of Energy. TSPA-93 builds upon previous efforts by emphasizing YMP concerns relating to site characterization, design, and regulatory compliance.

Scenarios describing expected conditions (aqueous and gaseous transport of contaminants) and low-probability events (human-intrusion drilling and volcanic intrusion) are modeled. The hydrologic processes modeled include estimates of the perturbations to ambient conditions caused by heating of the repository resulting from radioactive decay of the waste. Hydrologic parameters and parameter probability distributions have been derived from available site data. Possible future climate changes are modeled by considering two separate groundwater infiltration conditions: "wet", with a mean flux of 10 mm/yr, and "dry", with a mean flux of 0.5 mm/yr. Two alternative waste-package designs and two alternative repository areal thermal power densities are investigated. One waste package is a thin-wall container emplaced in a vertical borehole, and the second is a container designed with corrosion-resistant and corrosion-allowance walls emplaced horizontally in the drift. Thermal power loadings of 57 kW/acre (the loading specified in the original repository conceptual design) and 114 kW/acre (a loading chosen to investigate effects of a "hot repository") are considered.

TSPA-93 incorporates significant new detailed process modeling, including two- and three-dimensional modeling of thermal effects, groundwater flow in the saturated-zone aquifers, and gas flow in the unsaturated zone. The saturated-zone model is used to estimate travel times for contaminants through layered, dipping formations. Coupled calculations of gas and heat flow are used to estimate travel times for gaseous CO_2. Time-dependent temperature distributions in the rock surrounding the potential repository are calculated, using the four repository layouts. A phenomenological model for waste-package degradation is implemented; the model includes temperature-dependent corrosion, fuel alteration, and dissolution.

Probabilistic analyses are performed for aqueous and gaseous flow and transport, human intrusion, and basaltic magmatic activity. Repository performance estimates are sensitive to assumptions made about unsaturated-zone water flow and contact with waste. Two conceptual models of unsaturated-zone water flow are considered — the composite-porosity model, which treats fracture and matrix flow as being strongly coupled; and the weeps model, which allows for flow only through locally saturated zones. The weeps aqueous releases and the human-intrusion direct releases are sensitive to the size of the waste packages that are affected: the larger horizontally-emplaced containers produce greater releases. Releases are generally insensitive to repository thermal effects: a hotter thermal loading protects parts of the repository from contact with liquid water, but other parts experience enhanced water flow due to condensation and diversion. The volcanic scenario, which investigates the effects of magmatic volatiles on the degradation of the waste packages, does not contribute significantly to releases.

Results of the calculations done for TSPA-93 lead to a number of recommendations concerning studies related to site characterization. Primary among these are the recommendations to obtain better information on percolation flux at Yucca Mountain, on the presence or absence of flowing fractures, and on physical and chemical processes influencing gaseous flow. Near-field thermal and chemical processes, and waste-container degradation are also areas where additional investigations may reduce important uncertainties. Recommendations resulting from TSPA-93 for repository and waste-package design studies are: 1) to evaluate the performance implications of large-size containers, and 2) to investigate in more detail the implications of high repository thermal power output on the adjacent host rock and on the spent fuel.

If future repository performance regulations are based on individual dose rather than cumulative release, results suggest that future site-characterization efforts should emphasize investigations of groundwater contact with waste packages in the unsaturated zone and examinations of saturated-zone flow paths. Because dose rates are dependent on the rate of radionuclide releases, it would be useful to investigate container designs that fail "slowly" over long periods of time.

The Executive Summary
is in a separate volume

Volume 1
contains Chapters 1 through 12

Volume 2
contains Chapters 13 through 25,
References,
and the Appendices

(This page left intentionally blank)

Acknowledgments

The SNL TSPA-93 authors would like to thank the large number of people whose contributions have benefited this document.

A formal review team was formed for this document. The entire document was revised and improved in response to the comments provided by this team of reviewers. The members of that team included Polly Hopkins and Steven Sobolik, who performed the functions required for YMP technical review; Dwight Hoxie, who provided a review on behalf of the USGS; Melvin Marietta and Merton Fewell (both of the Waste Isolation Pilot Plant [WIPP] Project), who provided both technical review, as well as information on the perspective of a different group involved in work similar to that reported here; Marilyn Gruebel (Tech Reps) who provided general support to the team; and George Perkins, who coordinated the entire interaction between the team, the authors, and the technical editors.

Additional reviewers who provided substantial comments included Laurence Costin and Les Shephard, who were the management reviewers for the report, and Richard Luckey (USGS) who reviewed the chapter on saturated-zone modeling.

Felton Bingham was the SNL manager guiding the first half of the TSPA effort. Also, he authored Chapter 2 of TSPA-91, from which portions were taken and included in Chapter 3 of TSPA-93, and he reviewed sections of this document.

Tim Peterson of Tech Reps was the very capable technical writer who reviewed the entire document for consistency and clarity; he also helped to write the executive summary. Brenda Bailey White from Creative Computer Services was the technical editor for this report and provided support in arranging word processing and drafting, and performing all the duties that led to successful production of all of the interim versions.

Drafting of the various figures was a major effort. The people who contributed computer graphics for TSPA-93 were Dominic Martinez, Mary Heerdt, Corrine Taylor, Vickie Greenier, and David Eley.

Richard Thompson, William Chambers, and Edward Boucheron helped the TSPA analysts obtain access to additional computers that allowed a substantial decrease in the amount of time required to complete their release calculations. In addition, William Chambers did the initial gridding of the water-table model used in the saturated-zone modeling, and performed considerable debugging on the STAFF3D code used for the analysis.

John Holland performed a number of the thermal-modeling analyses for Chapter 10 of this document. Tom Doering, Bob Bahney, and Al Thompson (M&O/B&W Fuel) performed the fuel rod temperature calculations for the in-drift configurations, and Gary Johnson and Lynn Lewis (LLNL) performed those calculations for the vertical-emplacement cases.

This report was prepared under the Yucca Mountain Site Characterization Project WBS 1.2.5.4.1. QAGR 1.2.3.4.1 was applied, however, the information and data documented in the report were not developed to meet quality-affecting standards. Not all the work activities were subject to QA controls. The information in this report is not qualified and is not to be used for licensing.

Contents

Part II: Data Development

Contents of Volume 2

Figures

Tables

Glossary

A_{Repos}	area of the repository
AML	areal mass loading
APD	areal power density
BF	Bullfrog Member
BFn	Bullfrog Member, nonwelded
BFw	Bullfrog Member, welded
BP	barometric pumping
BWR	boiling-water reactor
C	contaminant concentration
<C>	average concentration of contaminant
^{14}C	carbon-14
cal	calorie
CCDF	complementary cumulative distribution function
CDB	Characteristics Data Base
CDF	cumulative distribution function
CFR	Code of Federal Regulations
CH	Tuffaceous Beds of the Calico Hills
CHn	Tuffaceous Beds of the Calico Hills, nonwelded
CHnv	Tuffaceous Beds of the Calico Hills, nonwelded vitric
CHnz	Tuffaceous Beds of the Calico Hills, nonwelded zeolitic
Ci	Curies
CLIMAP	Climate Mapping and Prediction Project
CO_2	carbon dioxide
$^{14}CO_2$	carbon dioxide composed of carbon-14
COHMAP	Cooperative Holocene Mapping Project
COVE-2A	Code Verification, Case 2A
c-p	composite porosity
CV	coefficient of variation
D	devitrified tuff
D	darcies
DB	double-blended
DOE	U. S. Department of Energy
DSI	Disposal Safety Incorporated
EBS	engineered barrier system
Eh	emf of hydrogen
EPA	U. S. Environmental Protection Agency
EPRI	Electric Power Research Institute
ESF	Experimental Studies Facility
E[x]	expected value
Fe	iron; descriptor for iron-oxide rock type
FEP	feature, event, or process

GRIP	Greenland Ice-Core Project
GWd	gigawatt-day
HANF	Hanford Site, Washington
HLW	defense high-level waste
HYDROCOIN	Hydrologic Code Intercomparison Project
ICPP	Idaho Chemical Processing Plant
ICRP	International Commission on Radiological Protection
ID	inside diameter
IDB	Integrated Data Base
IGIS	Interactive Graphics Information System
K	hydraulic conductivity
k_b	bulk permeability
K_d	sorption coefficient
K_f	fracture conductivity
K_m	matrix conductivity
kPa	kiloPascal
K_{sp}	solubility product
L	length
LANL	Los Alamos National Laboratory
LAPD	local areal power density
LBL	Lawrence Berkeley Laboratory
LLNL	Lawrence Livermore National Laboratory
M^*	cumulative contaminant outflow
$\dot{M}^*$	fractional outflow of contaminant per year
MCi	megaCuries
MGDS	mined geologic disposal system
MKS	meter-kilogram-second
MOL	method of lines
MPA	Mission Plan Amendment
MPC	multi-purpose container
MRS	monitored retrieval and storage system
MTHM	metric tons of heavy metal
MTU	metric tons of uranium
MWd	megawatt-days
NAS	National Academy of Sciences
NCRP	National Council on Radiation Protection and Measurements
^{237}Np	neptunium-237
N_{Pkg}	number of packages
NTS	Nevada Test Site
NRC	U. S. Nuclear Regulatory Commission
NWPA	Nuclear Waste Policy Act
^{18}O	oxygen-18
ODE	ordinary differential equation

ORNL	Oak Ridge National Laboratory
PA	performance assessment
Pa	Pascal
PADB	Performance Assessment Data Base
PACE-90	Performance Assessment Calculational Exercises, 1990
PDE	partial differential equation
PDF	probability distribution (density) function
pH	negative logarithm of the effective hydrogen ion concentration
P_{hit}	probability of a drill hitting a waste package
PI	principal investigator
PNL	Battelle Pacific Northwest Laboratory
PP	Prow Pass Member
PPn	Prow Pass Member, nonwelded
PPw	Prow Pass Member, welded
PTn	Paintbrush nonwelded interval
PZ	paleozoic units
PWR	pressurized water reactor
QA	quality assurance
QAGR	QA grading report
R	retardation factor
RHS	right-hand side
RIB	Yucca Mountain Reference Information Base
SCP	Site Characterization Plan
SCP-CDR	Site Characterization Plan Conceptual Design Report
SCV	scaled coefficient of variation
SD	standard deviation
SEPDB	Yucca Mountain Site and Engineering Properties Data Base
SNF	spent nuclear fuel
SNL	Sandia National Laboratories
SolWOG	Radionuclide Solubility Working Group
SRS	Savannah River Site, South Carolina
SZ	saturated zone
TBM	tunnel boring machine
TCw	Tiva Canyon Member, welded
TS	Topopah Spring Member
TSA	total system analyzer
TSPA	total system performance assessment
TSPA-91	Total System Performance Assessment, 1991
TSPA-93	Total System Performance Assessment, 1993
TSw	Topopah Spring Member, welded
TSw1	Topopah Spring Member, lithophysae-rich
TSw2	Topopah Spring Member, lithophysae-poor
TSw3	Topopah Spring Member, vitrophyre

UO_2	uranium dioxide
USGS	U. S. Geological Survey
UZ	unsaturated zone
V	vitric tuff
$\dot{V}^*$	fractional outflow of gas per year
WSA	Waste Stream Analysis
WBS	work breakdown structure
WIPP	Waste Isolation Pilot Plant
WP	waste package
WT	water table
wt. %	percent by weight
WVDP	West Valley Demonstration Project, New York
YFF	youngest fuel first
YM	Yucca Mountain
YMP	Yucca Mountain Site Characterization Project
Z	zeolitic tuff

(This page left intentionally blank)

Part I

Overview

Chapter 1
Introduction
(Dockery)

The development of a repository for highly radioactive waste requires technical analyses of many kinds. Total-system performance assessments (TSPAs) are among the most important analyses in the work of the Yucca Mountain Site Characterization Project (YMP), an activity of the U. S. Department of Energy (DOE) that is examining the suitability of a potential repository site at Yucca Mountain, Nevada. A TSPA estimates the behavior of all the natural and engineered components of a repository system for thousands of years after it has received waste and been closed. The TSPA reported in this document estimates the behavior a repository system might exhibit if it were built at the potential Yucca Mountain site.

The ultimate use for Yucca Mountain TSPAs will be in determining whether a repository there will meet the regulatory standards set by the U. S. Environmental Protection Agency (EPA). For this reason, later TSPAs in the series of which this is one step will resemble a document that can be submitted to demonstrate compliance with regulatory criteria. It is important, however, to make TSPAs even in the current early stages of repository development—during site characterization and repository design. This document, intended to meet the needs of the early stages, is not a preliminary compliance document. Its purposes are the following:

- To aid in setting priorities for the tests that help characterize the potential repository site.
- To help in early determinations of the site's suitability.
- To help guide decisions related to repository design (although it will not form the basis for any final design decisions, because it was not performed under the quality-assurance procedures that govern such decisions).
- To develop the methods that will eventually be used to make the ultimate assessment of compliance with the EPA standards.

Although this TSPA does not demonstrate compliance, it does exercise an indispensable process that all the future TSPAs must carry out: the process of abstracting the essential information from the great masses of data that a repository-development program must gather. To fully describe the long-term behavior of a repository system, a

TSPA requires information describing a vast range of natural phenomena. For example, a TSPA must have information about phenomena that range from large-scale processes like regional tectonic movement to small-scale processes like the microscopic complexation of radionuclides. The information must also describe the thermal and chemical behavior of the waste package and the waste form, as well as the temporally and spatially variable behavior of the rest of the engineered system. A TSPA makes its estimates of the system's future behavior by using this information in mathematical models that are developed primarily from field and laboratory data and observations. For studying individual and coupled processes, the models are detailed and quite complex. For a TSPA, which studies the entire system, the models cannot be so elaborate; not every aspect of the system can be modeled in the high level of detail appropriate for individual processes. A TSPA therefore attempts to capture the principal features described by the detailed models. It abstracts those features by considering their likelihoods and the degree to which the system's behavior is sensitive to them.

A principal task of this TSPA, then, is to develop ways to do this abstraction—methods that will be acceptable to regulators and other parties interested in the final compliance demonstration.

1.1 Evolution of SNL total-system performance assessments for Yucca Mountain

Sandia National Laboratories (SNL) has participated in three major performance-assessment modeling exercises within the past 4 years. These exercises reflect the progression in the degree of sophistication analysts have acquired to simulate processes at Yucca Mountain. PACE-90 (Barnard and Dockery, 1991) was a hydrologic flow and transport modeling exercise for Yucca Mountain that used the knowledge gained from a series of previous hydrologic flow simulations, such as the COVE2A studies (Dykhuizen and Barnard, 1992) and modeling done as part of the HYDROCOIN international studies (Prindle and Hopkins, 1990). PACE-90 might be considered the "zeroth order" iteration of TSPA, since it laid the foundation for the subsequent series of calculational exercises. In 1991, SNL used the simulations from PACE-90 as a basis to construct the first in a series of total-system performance assessments for the Yucca Mountain Site Characterization Project, TSPA-91 (Barnard *et al.*, 1992). After completion of that exercise, the next iteration was begun. This document reports the development and results of this effort, called Total-System Performance Assessment-1993 (TSPA-93). The process leading to the production of TSPA-93, essentially the same as that for TSPA-91, is described in Chapter 3. That chapter describes the evaluation pro-

cess defined in the SCP, the concept of a hierarchy of models, and the specific steps followed in both total-system performance assessments, TSPA-91 and TSPA-93.

Future total-system performance assessments will continue to address the needs of YMP in areas such as site suitability, design, and assessment of regulatory issues. As the YMP proceeds with site characterization, future performance-assessment analyses may stress different aspects, such as technical site suitability or sensitivity studies of site properties. Figure 1-1 reviews the purposes and users of the previous performance-assessment analyses and suggests possible goals of future TSPAs.

1.1.1 PACE-90

PACE-90 was a calculational exercise defined to simulate nominal-case groundwater flow and transport. The problem was specified to calculate "expected performance" of a potential repository at Yucca Mountain over a modeling period of 100,000 years. Deterministic analyses were run by SNL, Pacific Northwest Laboratory (PNL), and Los Alamos National Laboratory (LANL) in both one and two dimensions. A set of four radionuclides was used to represent classes of long-lived radionuclides present in the inventory. The percolation flux at the repository horizon was modeled using a single value of 0.01 mm/yr. The source term allowed mobilization of waste from two primary water contact modes: "wet-drip" and "moist-continuous." The nuclides then moved through a 19-layer hydrostratigraphy that was developed from limited information derived from 4 boreholes. No nuclides reached the water table within the specified period, and for that reason, the saturated zone was not explicitly modeled. Gaseous releases and thermal effects were not modeled.

1.1.2 TSPA-91

TSPA-91 built upon PACE-90 by modeling both nominal conditions and disturbances to the system by basaltic volcanism, human intrusion, and climate change. For TSPA-91, SNL ran a set of one-dimensional calculations, and PNL performed two-dimensional analyses. It was the first set of stochastic TSPA analyses run by YMP participants. All of the hydrogeologic parameters were represented by distributions developed from site and analog data. The radionuclide inventory was expanded from PACE-90 to include nuclides that were prevalent in the inventory and also to include those expected to be important contributors to dose. Gaseous flow of ^{14}C was included for the first time. The saturated zone was also modeled, and for the first time the calculations were run to the 5 km accessible-environment boundary. For the SNL analyses, a range of values for percolation flux thought to encompass broad changes in future climactic con-

ditions was sampled. Aqueous flow was analyzed using two alternate conceptual models in order to assess the relative effects of fracture and matrix flow.

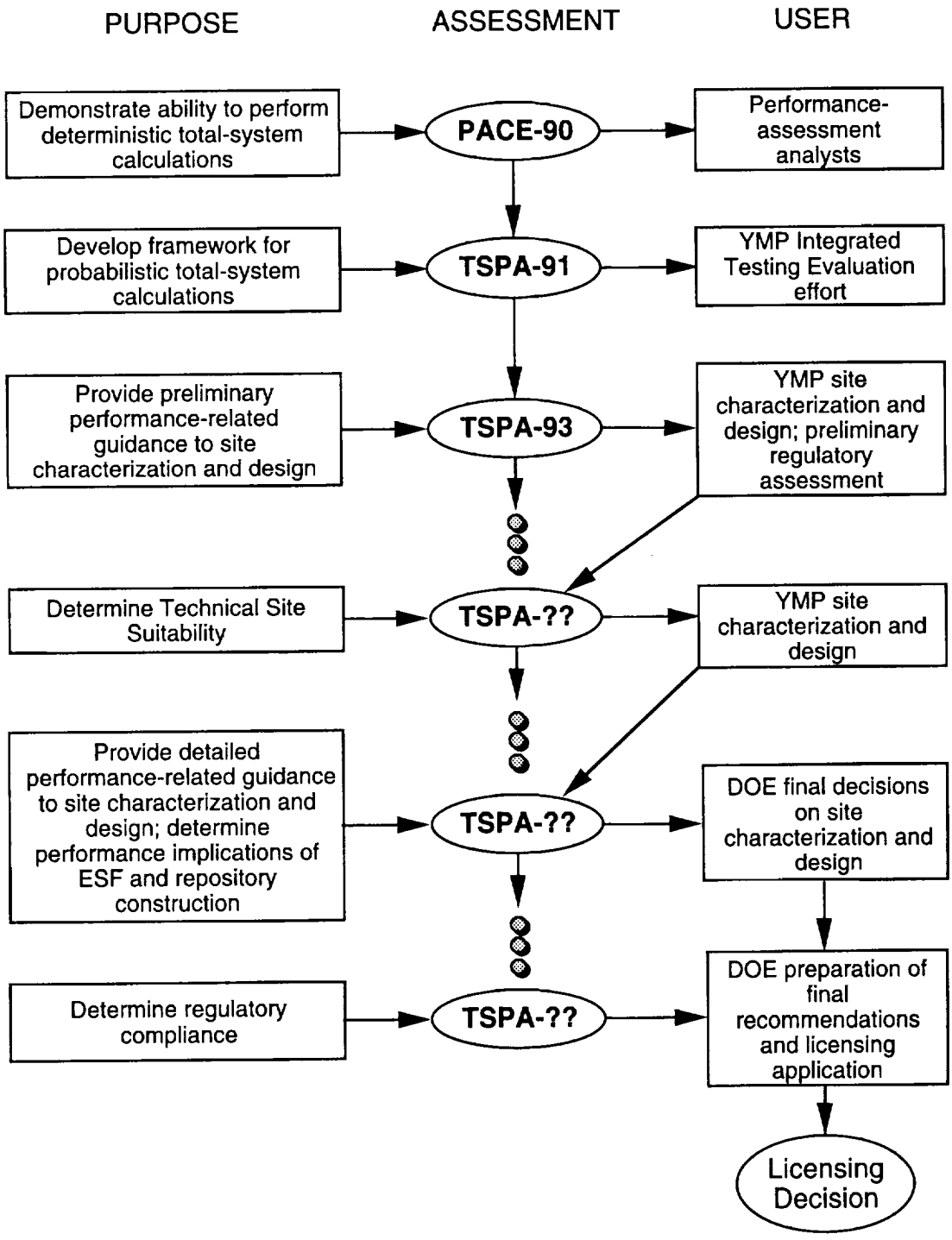

Figure 1-1. Illustration of the purposes and users of iterative performance assessments.

1.2 TSPA-93

The TSPA-93 analyses are based on the calculational components developed during PACE-90 and TSPA-91. These analyses, performed by SNL, included the following expansions and improvements:

- The model domain was expanded to be more geographically representative of the entire repository block. (TSPA-91 used information only from the northern part of the repository area.)

- For the first time, a three-dimensional stratigraphy was developed for the unsaturated zone; it was based on geostatistical correlations of units.

- Hydrogeologic parameter distributions were based on an expanded site-data set. The data set also expressly included fracture properties from site measurements, rather than surrogate properties.

- Future, wetter climatic conditions were explicitly included as a distribution of percolation-flux values separate from the distribution used for the current, drier conditions, (in contrast to including the range of climate effects in one distribution).

- A more sophisticated model was developed for the saturated zone. Instead of using a composite of all of the rock units to represent the tuffs below the water table, each unit was discretely modeled. Water velocities, and thus transport times, therefore differed among the units.

- More-comprehensive distributions on geochemical parameters related to retardation and to sorption were elicited from a group of LANL and SNL experts.

- The models included parameters showing thermal dependence. Repository system response was analyzed for two thermal loads resulting from areal power densities of 57 and 114 kW/acre.

- The fracture-flow (weeps) model was altered to allow spatial and temporal variations in fracture apertures.

- A more sophisticated source-term model was included, based on LLNL's YMIM model. The YMIM model includes phenomenological waste-package failure due to corrosion and to dry oxidation, as well as waste-form dissolution and oxidation models. The hy-

drothermal processes that drive source-term releases reflect the thermal history of the waste package and waste form.

- Supporting calculations were performed to assess the effects of moisture movement through Yucca Mountain caused by changes in barometric pressure. Such "barometric pumping" may, in turn, influence the amount of water that can infiltrate into the mountain and be available to percolate down to the repository level. In addition, the effects of barometric pumping were also investigated for its possible influence on movements of gaseous contaminants to the surface.

- Two types of waste-packages were modeled—thin-walled containers emplaced in boreholes, as envisioned by the SCP design, and large multipurpose containers placed in the repository drifts.

- The assumed radionuclide inventory contained both spent fuel and vitrified high-level defense waste. Moreover, it was constructed to reflect the waste-receipt schedule.

1.2.1 Caveats

To estimate the future behavior of the repository system, the TSPA uses mathematical and conceptual models of the natural and engineered components that make up the total system. These models are discussed in more detail in Chapter 3. The calculations estimate the performance of these components under two different basic assumptions: (1) that the site remains undisturbed for 10,000 years, and (2) the site is disturbed by unlikely but possible natural phenomena and human activities. The YMP has acquired additional data from the site since TSPA-91 was completed, and, where possible, these data have been incorporated into TSPA-93. Although TSPA-93 enlarges significantly upon previous overall performance-assessment efforts for Yucca Mountain, it does not cover all of the elements necessary to support the license application.

Because of the limited number of components included, the TSPA-93 performance estimate is not intended to constitute an evaluation of Yucca Mountain as a site for a potential radioactive-waste repository. However, the study may be regarded as an update of certain aspects of previous studies of total-system performance because the performance measures produced in this study were derived from data available as of the summer of 1993. It is important to remember, however, that many data are yet to be obtained for Yucca Mountain, several important choices among conceptual models are yet to be made, and formal methods for using abstraction and expert judgment are yet to be

developed. Because much work remains, the results of this study are not direct measures of the higher-level suitability of the Yucca Mountain site under the system criteria of 10 CFR Part 960 (DOE 1984), as described by Younker *et al.* (1992). A more appropriate use of these results is as guidance for site characterization and design and for the next iterations of total-system performance assessment, as discussed above.

A further explanation may be useful for readers familiar with the series of TSPAs currently being done at Sandia National Laboratories for the Waste Isolation Pilot Plant (WIPP) Project The most recent report of those studies (WIPP Performance Assessment Department, 1992) closely approximates a compliance document. Such documentation is appropriate for the WIPP, which is in a much later stage of development than the Yucca Mountain Site Characterization Project and expects to apply for certification within a few years. The YMP, on the other hand, has only recently begun to systematically perform the tests described in its Site Characterization Plan (DOE, 1988a). In addition, its underground Experimental Studies Facility is in early stages of construction. Documents approximating a compliance demonstration will be appropriate for the YMP only after considerably more characterization and testing have been done.

1.3 Issues considered when planning TSPA-93

One of the goals for TSPA-93 is to address the deficiencies of TSPA-91. Insufficient time and resources available for TSPA-91 required the omission of several components perceived by the analysts to be quite important. Chapter 11 of TSPA-91 ("Areas for Future Work") discussed the priorities for the next TSPA in detail and formed the primary planning basis for the next iteration. Some components that needed further assessment were recognized later from further study of the results of TSPA-91 and subsequent sensitivity studies. These studies also helped determine the structure and content of TSPA-93.

The decision about which components were to be included in TSPA-93 was influenced by both data availability and by the current project needs (discussed in Chapter 3). The three project needs that ultimately controlled the selection of the components that constituted TSPA-93 were (1) setting priorities for site characterization efforts, (2) analysis of current design options, and (3) evaluation of potential alternatives for repository-performance regulations. Therefore, the most important goal of TSPA-93 was to attempt to construct a set of analyses, using as much site-specific information as possible, such that the results could be used by YMP to help with decisions related to the three issues listed above. An example of how each of these issues was addressed is shown in the remainder of this section.

1.3.1 Addressing issues related to site characterization

Many of the suggestions for future work originating from TSPA-91 were directed toward obtaining specific information from site-characterization activities and from studies of waste-package degradation. In particular, sensitivity studies performed as a follow-on to TSPA-91 (Wilson, 1993) showed that the aqueous-flow results were most sensitive to a few specific parameters. The studies also showed that different conceptual models were sensitive to different parameters. The most sensitive parameters for the composite-porosity model were: percolation flux, gaseous-transport time, container lifetime, and fuel-matrix-alteration rate. For the weeps model, the results were most sensitive to fracture properties (fracture aperture and fracture connectivity), percolation flux, and amount of water available during episodic flows.

Based on the sensitivities identified above, one major effort of TSPA-93 was the attempt to acquire additional insight regarding the effects of the variation of percolation flux at the repository horizon. Not only is the current percolation flux unknown, the effects of future climate are also unknown. Whereas site data may give us bounds on current flux, the connection of climate change to infiltration rates at Yucca Mountain is poorly understood. There are widely differing views concerning how to relate the amount of water falling on the surface of Yucca Mountain to the amount of fluid flow that actually occurs at the deeper levels. To gain an understanding of the influences of past and future climates, a number of discussions were held with members of the United States Geological Survey (USGS) working on this problem for YMP. Staff from the Waste Isolation Pilot Project (WIPP) were also contacted for input to the model used in TSPA-93. The final TSPA-93 model includes two distinct alternating intervals—wet and dry—that represent climate changes occurring in response to glacial advances and retreats. Each interval has a different distribution of values for percolation flux. Details on the development of these distributions are found in Chapter 8. The results of TSPA-93 continue to show a strong sensitivity to percolation flux. Therefore, the TSPA-93 guidance to site characterization continues to give high priority to tests leading to an enhanced understanding of percolation flux through the repository horizon.

1.3.2 Addressing issues related to design

Design issues were also important for determining which new components would be incorporated in TSPA-93. In particular, TSPA-93 assessed the usefulness of the "hot repository" concept in enhancing long-term performance and the feasibility of large, multipurpose containers (MPC). (See Chapter 4 for more detailed information on the waste packages.) In 1992 and 1993, a large effort has been under way in YMP to exam-

ine whether increased areal power densities (APD) could lead to an extended dryout zone that would protect the containers from aqueous flow and ultimately result in better repository performance (Buscheck and Nitao, 1992; Ryder, 1993). In support of these efforts, TSPA-93 included the first nonisothermal calculations that are part of the TSPA cycle. These analyses, described in Chapter 10, develop the repository-scale temperature distributions (in time and space) that might be expected for different emplacement configurations and different waste-package types. The different distributions produce different amounts of dryout in the rock surrounding the waste packages. To a limited degree, the effects on performance of the SCP waste-package designs were compared with the MPC (DOE, 1993a) design. These studies of different waste package design and APD were used to produce source terms for the aqueous and gaseous transport calculations that reflected the assumed thermal conditions.

As Chapter 14 explains, little difference is observed in the release curves for the different APDs and different waste packages under the assumptions in the matrix-dominated aqueous-flow model. Conversely, the results from the aqueous model for fracture-dominated flow (Chapter 15) and for human intrusion (Chapter 16) show that waste packages with larger horizontal profiles produce higher releases. The enhanced releases occur because the probability that an individual package will be affected by either a flowing fracture or a drill bit is directly related to the area the package subtends in the horizontal plane. Rather than being a robust conclusion that could guide engineering decisions regarding the APDs and waste packages, the results are more likely to be an indicator that the models were overly simplified. Considerations that are probably important were not included, because of a lack of data on site-specific natural processes and waste-package degradation processes. Despite our uncertainty regarding the models, the implications of container design on the performance-assessment results must be considered. Chapter 19 proposes a number of studies that might provide the information needed for future analyses to provide more clear-cut guidance to design.

1.3.3 Addressing issues related to regulation assessment

The effects of potential changes in the EPA regulations concerning repository performance were also investigated. A discussion of the regulations and the possible changes is in Section 2.3. A module was added to the aqueous-flow calculations to assess the dose obtained through drinking water, given the release calculated with the various models. The results of this analysis show how important our understanding of the saturated zone would become if the potential Yucca Mountain repository is regulated by a dose-based standard. The amount of dilution in the saturated zone becomes a

critical piece of information for dose, but is less important if the site is regulated solely by a release-based standard.

1.4 Participants in SNL TSPA-93

SNL made a concerted effort to involve as many participants as possible in the process of setting up TSPA-93 simulations. Information was solicited from both field and laboratory workers as well as other analysts. Table 1-1 shows the participants involved in helping develop the various components of TSPA-93.

Table 1-1 Information sources for TSPA-93 analyses.

Component	Contributors
Stratigraphy and Hydrogeologic Parameters	LBL (C. Wittwer, G. Bodvarsson) USGS (A. Flint, L. Flint, R. Spengler, E. Weeks, R. Luckey, A. Geldon, D. Appel, D. Hoxie) SNL (A. Schenker, T. Robey, C. Rautman, D. Guerin)
Climate Change	USGS (A. Flint, L. Flint, D. Hobson, R. Forester, Z. Peterman) WIPP (P. Swift) SNL (J. Gauthier, M. Wilson)
Geochemistry	LANL (I. Triay, D. Morris, A. Meijer, M. Ebinger) SNL (M. Seigel)
Thermal Effects	LLNL (G. Johnson, T. Buscheck, L. Lewis) TRW (J. King) B&W Fuel (T. Doering, R. Bahney, A. Thompson) SNL (E. Ryder, J. Holland, E. Dunn)
Saturated Zone	USGS (R. Luckey) SNL (G. Barr)
Gas Flow	DSI (B. Ross, N. Lu) SNL (M. Wilson)
Source Term and EBS Processes	LLNL (A. Lamont, J. Gansemer, W. Halsey, L. Lewis, R. Stout, D. McCright) Iowa State University (D. Bullen) ORNL (A. Croff) SNL (R. Barnard, J. Gauthier, M. Wilson)

For each of the model parameters, SNL tried to obtain the most current information available from YMP participants and workers outside of YMP. As part of this effort, SNL participated in DOE-sponsored technical interchanges at LANL and at the USGS. These meetings with LANL and the USGS contributed greatly to the information that was used in TSPA-93.

1.5 Organization of the TSPA-93 report

This report is organized to mirror the PA analysis methods. Since the primary goal of this exercise is to provide guidance for other work in YMP, information contained in the chapters on input and process modeling is of equal importance with that in the chapters showing results of the probabilistic calculations.

This report has been divided into six major parts. The groupings of chapters in each of these parts represents a block of work accomplished for TSPA-93. Part I (Overview) introduces TSPA-93 and gives the background behind the formulation of the problem set for the SNL TSPA-93. In general it contains an overview of the site, the repository system, the regulations against which TSPA-93 makes comparisons, and the scenarios selected for study. Part II (Data Development) contains information on the development of hydrogeologic parameters and the geostatistically based stratigraphy used in the subsequent calculations. Part III (Detailed Modeling and Abstraction) provides the information on the detailed process modeling done specifically for TSPA-93. Process models (thermal effects, saturated-zone flow, and gaseous flow) are all areas in which significant new work was accomplished. This work ultimately led to significant enhancements to the abstracted models used for the one-dimensional probabilistic calculations described in Part IV (Probabilistic Modeling and Results). Part IV includes the calculations of radionuclide release from aqueous and gaseous flow, human intrusion, and basaltic magmatic activity. Part V (Summary and Conclusions) discusses the conclusions of TSPA-93, including guidance for various other YMP activities and for future TSPA work. Part VI (Ancillary Calculations) contains information on several supporting calculational exercises that were performed to test the process of abstraction. The appendices include additional detail that may be useful for reference purposes, but that would be distracting if included in the text. Appendix A shows all of the information used to develop the geostatistically based stratigraphy and all of the individual stratigraphic columns generated for possible use in the one-dimensional simulations. Appendix B shows all the probability distribution functions generated for sorption and solubility. Appendix C provides additional information on the thermal-modeling approaches.

Figure 1-2 illustrates the relationships among the various elements of TSPA-93. The input parameters are identified in the square boxes, and they represent actual data. The octagonal boxes show the information or parameters that were derived from the input values, and are then used as input for subsequent calculations. The diamonds identify the detailed process models; some of these models represent significant increases in modeling complexity over elements included in TSPA-91. Probabilistic, abstracted mod-

els are shown in the circles. Results, in the ovals, include release to the accessible environment and dose.

This figure can also be used as a "road map" for the analyses and the document. Figure 1-2 illustrates the interrelationships among the various elements comprising TSPA-93. Chapter numbers are shown in order to help the reader trace each analysis from start to finish.

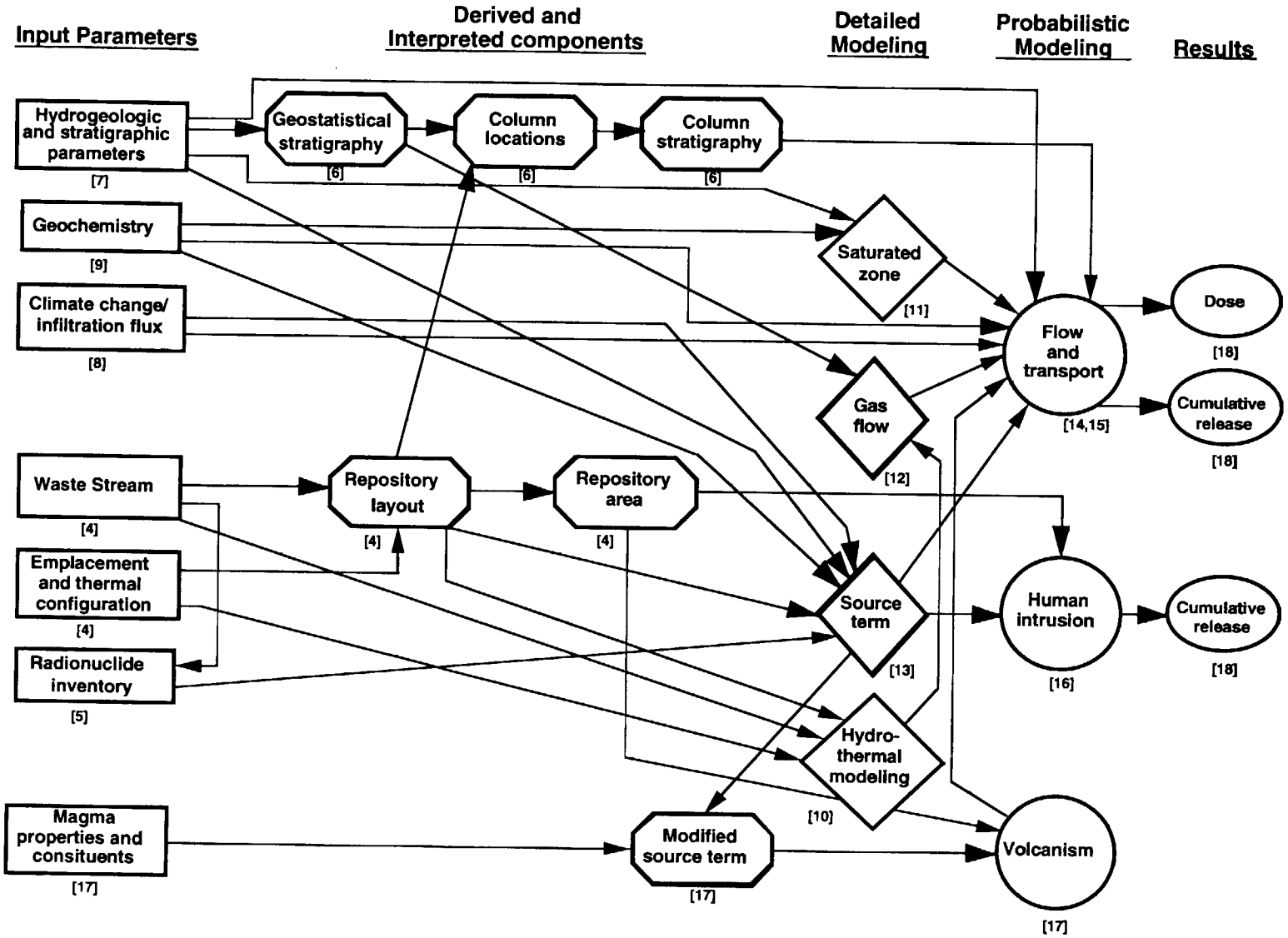

Figure 1-2. Elements of TSPA-93 analyses, showing chapters in this report where they are discussed.

Chapter 2
Site Description and Regulatory Context

(Dockery, Barnard, Wilson, Rautman)

2.1 Physical setting

Yucca Mountain is located in Nye County, southern Nevada. It is on the southwestern boundary of the Nevada Test Site (NTS), approximately 120 km northwest of Las Vegas, Nevada (Figure 2-1). The region is part of the southwestern Nevada volcanic field in the southern Basin-and-Range physiographic province. The region is characterized by linear mountain ranges and intervening valleys whose orientation is primarily controlled by north-trending normal faults. Elevations range from approximately 350 m to 1,600 m above sea level.

The area is semiarid, receiving an average of approximately 17 cm of precipitation per year (Flint *et al.*, 1993), mostly as winter snowfall, although brief summer thunderstorms also contribute to the annual precipitation. Consequently, the region has little vegetation and is sparsely populated.

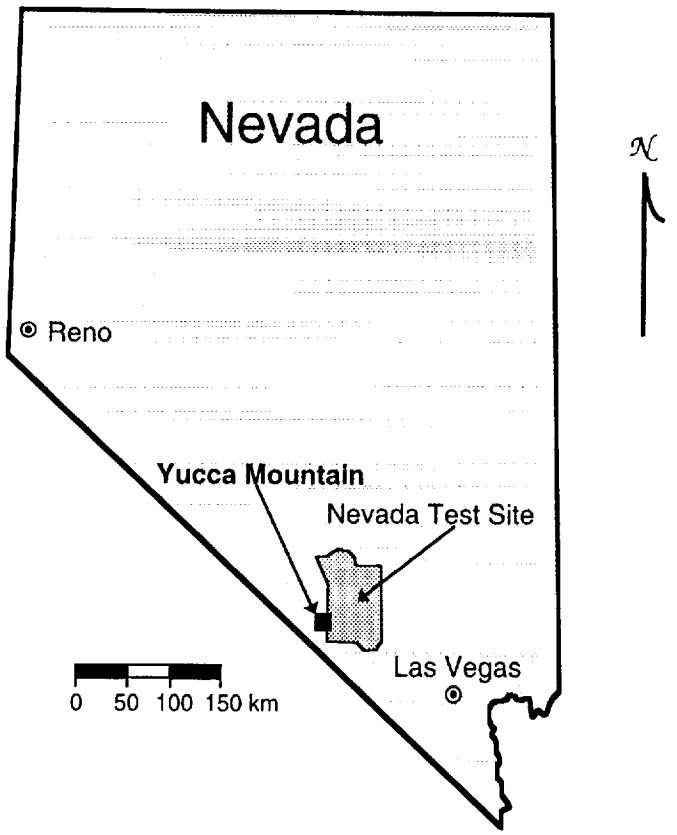

Figure 2-1. Map showing location of Yucca Mountain region adjacent to the Nevada Test Site in southern Nevada.

2.1.1 Geology

The rock units of the Yucca Mountain region include Paleozoic sediments and metasediments, several late Mesozoic quartz monzonitic and granodioritic intrusions, Cenozoic silicic and basaltic volcanic sequences, and recent alluvial deposits. A summary of regional stratigraphic units occurring in the Yucca Mountain area is presented in Table 2-1.

The basement rocks at Yucca Mountain consist of Paleozoic clastic and carbonate units. These units were subjected to at least one major compressional tectonic event during the Mesozoic (e.g., Eckel, 1968), resulting in folding and thrust faulting of the Paleozoic units. The late-Mesozoic intrusions are volumetrically small and are probably related to the emplacement of the Sierra Nevada batholith, 91 to 101 million years ago (Naeser and Maldonado, 1981). The Mesozoic units have not been observed under Yucca Mountain.

Table 2-1. Generalized stratigraphy, at Nevada Test Site/Yucca Mountain region (modified after Carr, 1988).

Approximate Age (M. y.)	Unit
0.27, 1.2, 3.8	Younger Basalts
8.5–10.5	Older Basalts (Kiwi, Skull Mountain)
9	Shoshone Rhyolite Lava
11	Timber Mountain Tuff Ammonia Tanks Member Rainier Mesa Member
12	Rhyolite Lavas (Fortymile, Windy Wash)
12.5–13	Paintbrush Tuff Tiva Canyon Member (TCw) Yucca Mountain Member Pah Canyon Member Topopah Spring Member (TSw)[a]
13	Tuffs and Lavas of Calico Hills (CHn)
13.5	Crater Flat Tuff Prow Pass Member (PPw) Bullfrog Member Tram Member
14	Lithic Ridge Tuff
14–16	"Older Tuffs"
Paleozoic (240)–570 Precambrian > 570	Upper Clastic Aquitard (Eleana Formation) Lower Carbonate Aquifer (Bonanza King, etc.) Lower Clastic Aquitard (Zabriskie, Wood Canyon, etc.)

[a]Location of potential repository.

The rock units underlying the site that are of most interest to the Yucca Mountain Project are dominated by the Miocene silicic ash-flow and air-fall tuffs erupted from the Timber Mountain–Oasis Valley caldera complex. This structure occurs immediately north of the potential repository site. The emissions from this caldera complex form a thick sequence of volcanic rocks ranging from 9.5 to 16 million years in age (Byers *et al.*, 1976; Christiansen *et al.*, 1977). In Table 2-1, the formation-level subdivisions (i.e., Timber Mountain Tuff, Paintbrush Tuff, etc.) generally represent completely different magmatic systems with significantly different petrologic histories. The individual member-level stratigraphic units correspond to major volcanic eruptions related to the collapse of a caldera system.

The tabular sheets of alternating welded and nonwelded tuffs are relatively uniform in thickness (Figure 2-2). These ash-flow units are typically several hundreds of meters thick, and they can be traced laterally throughout the NTS region. The major welded ash-flow tuffs are usually separated by thinner intervals of nonwelded or poorly welded ash flows, air-fall tuffs, and reworked tuffaceous materials.

In the vicinity of the potential repository, the tuffs have been gently tilted toward the east by generally north-trending, Basin-and-Range-style block faulting. Yucca Mountain itself consists of a relatively unfaulted large block capped with surficial exposures of welded ash-flow tuffs belonging to the Tiva Canyon Member of the Paintbrush Tuff (Scott and Bonk, 1984). The intact main block of Yucca Mountain is bordered to the west by the Solitario Canyon fault, a major (300-plus meters displacement) normal fault, and on the east by a more diffuse zone of normal faulting (Figure 2-2). The repository block is transected from north to south by the Ghost Dance fault, interpreted as a scissors fault. The sense of displacement on the Ghost Dance fault within the repository block is down to the west with a few tens of meters maximum displacement (Spengler and Chornak, 1984).

The dip-slope of the repository block has been dissected by a number of sub-parallel, east-trending drainages. A more substantial southeast-trending drainage, Drill Hole Wash, marks the northeastern boundary of the potential repository area, and may be controlled by a northwest–southeast-trending structural zone with a possible strike-slip component to the movement. Units below the Tiva Canyon Member of the Paintbrush Tuff are locally exposed in the bottoms of the deeper washes. Generally, nonwelded tuffs equivalent to the Yucca Mountain and Pah Canyon Members ("Paintbrush nonwelded" unit) crop out at the base of the washes. Surficial exposures of the potential repository-host unit, the Topopah Spring Member of the Paintbrush Tuff, are uncommon except along the Solitario Canyon fault scarp. Strata below the level of the Paintbrush Tuff are not exposed in the immediate vicinity of Yucca Mountain (Lipman and McKay, 1965).

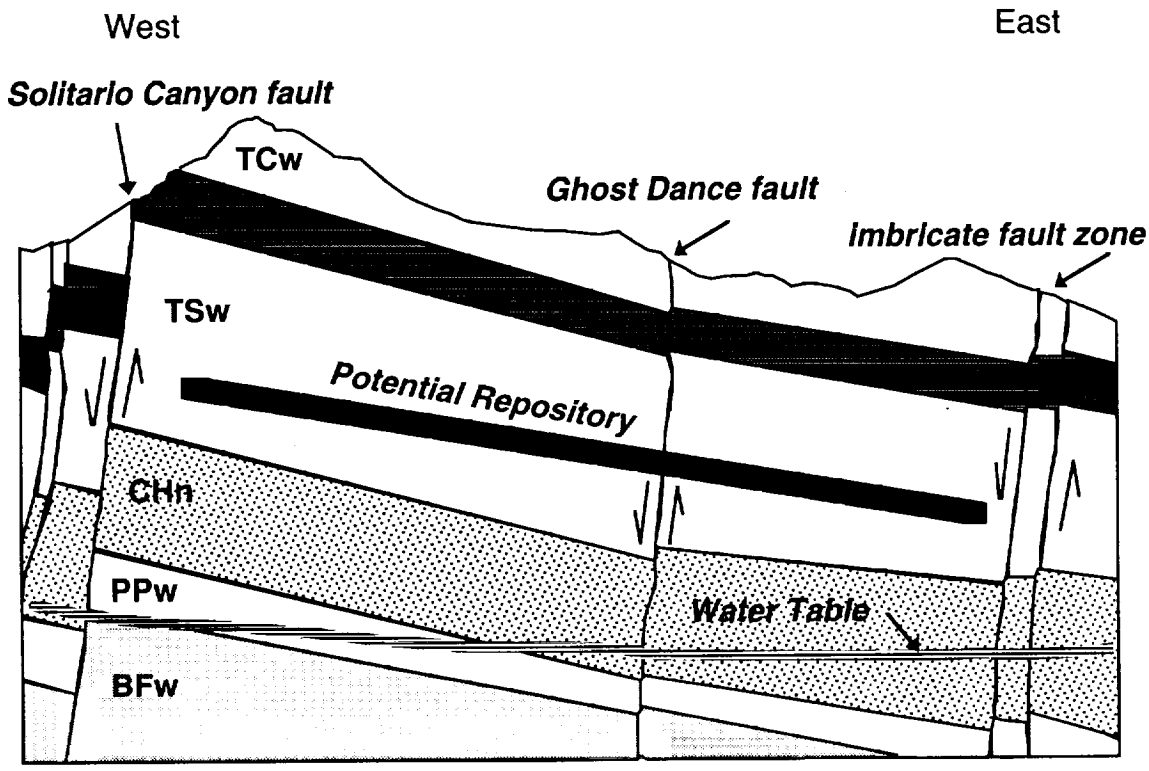

Figure 2-2. Schematic cross section of the potential Yucca Mountain repository region showing location of the repository horizon and static water table with respect to the thermal/mechanical stratigraphic units defined by Ortiz *et al.* (1985). TCw: Tiva Canyon welded unit; PTn: Paintbrush nonwelded unit; TSw: Topopah Spring welded unit; CHn: Calico Hills nonwelded unit; PPw: Prow Pass welded unit; BFw: Bullfrog welded unit.

Basaltic volcanism occurs in the vicinity of Yucca Mountain as younger post-caldera events, probably related to a change in the style of Basin and Range faulting (Dockery, 1984). Evidence of basaltic volcanism is observed in the Crater Flat volcanic center to the southeast of Yucca Mountain near Lathrop Wells (e.g., Crowe, 1990). The hawaiite-type basalts were erupted as polycyclic events from a series of north-northeast-trending cinder cones (Vaniman *et al.*, 1982). The age of these basalts is currently estimated as ranging from 105,000 years (Crowe, 1990 and Wells *et al.*, 1990) to 130,000 years (Turrin and Champion, 1991) for the older sequences to late Pleistocene to Holocene (1.8 million years to 100,000 years, respectively) for the younger sequences (Crowe, 1990; Wells *et al.*, 1990). The young basalts are of interest because of the perceived possibility that the mechanisms related to basaltic magma production are still active. Assessment of the probability of such an eruption occurring in the repository block and the consequences of any resulting releases of radionuclides is part of TSPA-93 (Chapter 17).

2.1.2 Geohydrology

The unsaturated zone beneath Yucca Mountain consists of stratified units of welded and nonwelded tuffs of contrasting hydrologic properties. Some of the units are more highly fractured, which may influence the flow of groundwater. In addition, both the faults bounding the Yucca Mountain block, and the Ghost Dance fault within the block, also may be either pathways for flow or impediments to flow. The downward percolation may be offset by upward flow of water vapor.

A small fraction of the precipitation at Yucca Mountain that falls on the surface flows generally downward through the unsaturated units, past the repository horizon to the water table (Flint, 1989; Norris, 1989). The static groundwater table underlies Yucca Mountain at depths of 600 to 800 meters, depending upon topography, producing a very thick unsaturated zone within the volcanic section (Robison, 1984). The water table beneath the potential repository block is nearly flat-lying; however, the water level rises markedly to the north and northwest (Fridrich *et al.*, 1991). The saturated zone can be divided regionally into two principal aquifer systems, one in the volcanic section and the other in the Lower Paleozoic carbonate sequence (Craig and Robison, 1984). In the Yucca Mountain region, the dominant saturated flow appears to be generally southerly, from higher elevations in the northern NTS to discharge areas in the Amargosa Desert to the south (Czarnecki and Waddell, 1984). In the tuffs, fractures may provide paths for water flow. Although the tuffs are fractured, their dip, offsets, and variation in physical properties between layers cause fractures in adjacent units to not necessarily be aligned. Thus, fracture flow may not be continuous. Groundwater within the volcanic aquifer at the site may be largely separate from the regional flow system (Craig and Robison, 1984).

2.1.3 Climate

The Yucca Mountain site experiences a variety of climate effects that have been characterized as falling into two National Weather Service climatological zones: those typical of southwestern deserts at lower elevations, and those typical of mid-latitude deserts at higher elevations. The lower regions are characterized by hot summers, mild winters, and limited amounts of precipitation. Higher elevations experience large annual and diurnal fluctuations in temperatures and significant variability in year-to-year amounts of precipitation.

The salient features of Yucca Mountain climate are summarized in the Site Characterization Plan (SCP) (DOE, 1988a). During the winter months, the major air masses affecting the region originate at the Pacific coast. In their passage eastward over the Sierra Nevada mountains, they lose most of their moisture. Consequently, Yucca

Mountain lies in the rain shadow of the Sierra and receives little winter moisture from this direction. The precipitation that reaches Yucca Mountain comes from the collision of warm, moist air masses from the southwest with cold air masses from the north. Low-pressure cells off southern California (caused by a dipping of the jet stream to the south) can produce this situation. Average precipitation during the fall and winter months (November–February) is about 18 mm/month, although as much as 100 mm has fallen in one month.

During the summer months, a thermally induced low-pressure system develops over the southwestern deserts. Prevailing winds are from the south and southwest, occasionally bringing Pacific moisture to the Yucca Mountain area, where it precipitates as thunderstorms. Average monthly precipitation for the spring and summer months (March through October) is about 9 mm.

2.2 The repository

Yucca Mountain is being characterized by the DOE as the site for a potential mined geologic disposal system (MGDS). The design and operating goals of the MGDS are to emplace radioactive waste safely, to retain the option to retrieve the waste, and to provide long-term containment and isolation of the waste (DOE, 1988a). Containment and isolation are to be achieved by the use of multiple barriers to mobilization and transport of the contaminants—waste containers that resist degradation, and the location of the repository in a geologic setting that reduces the probability that both expected and unforeseen processes and events can make the contaminants accessible to humans.

An underground repository for nuclear waste has several components. One description of the components of a potential repository at Yucca Mountain is given in the SCP (DOE, 1988a). Ventilation equipment, waste-receiving, and safety and access control facilities are located at the ground surface. Accesses to the underground workings are by gentle-grade ramps for moving the waste packages. Currently design specifies an access ramp at the north and south ends of the repository. The repository itself is bisected by two or three main tunnels (drifts) that provide ventilation and access for waste-emplacement operations. A perimeter drift runs around the periphery of the emplacement area. Waste is located in emplacement drifts that run between the main access drift and the perimeter drift. Waste is transported from the surface to depth in dedicated vehicles. Figure 2-3 is a visualization of an MGDS.

The repository is expected to remain open for over 25 years while waste is emplaced. During the operational period, the drifts are ventilated and accessible to humans. At a later time, (approximately 75 years from start of operations) the repository will be sealed by backfilling the drifts and placing engineered sealing structures at each emplacement drift.

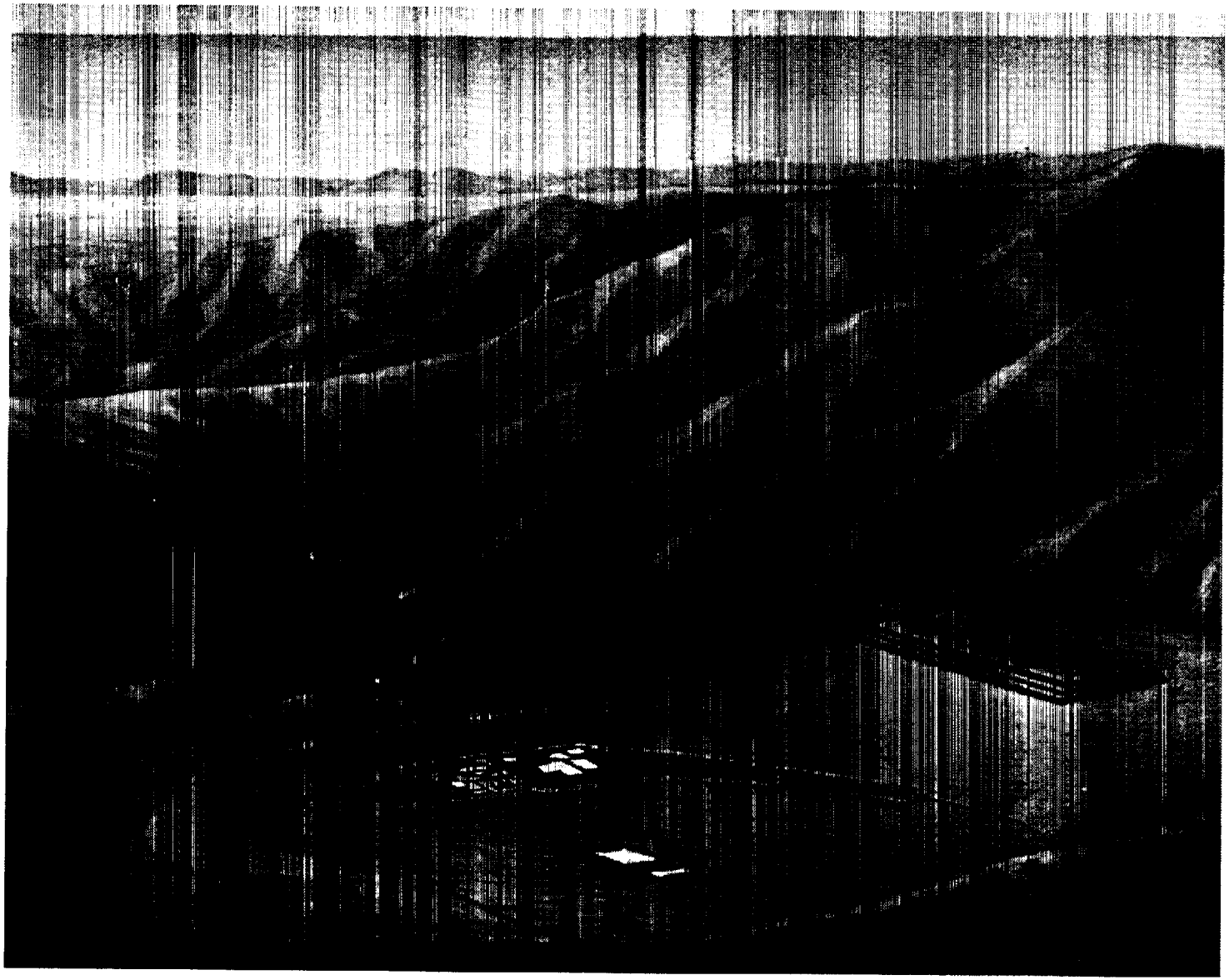

Figure 2-3. Visualization of the potential Yucca Mountain repository and associated surface facilities (after DOE, 1988a).

The designed capacity of the repository is 70,000 metric tons of high-level waste. Of this amount, 63,020 tons are spent nuclear fuel and the balance is defense high-level waste (HLW). The amount of spent fuel is expressed in terms of the amount of uranium originally contained in the nuclear fuel—metric tons of uranium (MTU). The reprocessing operations that produce HLW make its expression in terms of MTU difficult. A discussion of the amount of HLW representing the 6,980-MTU repository capacity is given in Chapter 5.

2.2.1 Site

The Yucca Mountain site was chosen for characterization because the sequence of unsaturated geologic units would make exposure of the waste to pervasive groundwater unlikely (DOE, 1988a). Distances of several hundred meters from the surface to the potential repository horizon, and from the repository horizon to the water table, would present barriers to rapid groundwater travel and contaminant transport. Furthermore, the site is thought to be relatively geologically stable, and relatively free of economically desirable resources. Figure 2-2 shows the location of the potential repository in the Yucca Mountain block.

2.2.2 Waste package

The waste package is part of an engineered barrier system (EBS) that may include the waste form (i.e., reactor-fuel assemblies or vitrified high-level defense waste), internal stabilizers, the container, and backfill or standoffs between the container and the adjacent rock. Container design contributes to retrievability and emplacement and acts as a barrier to the release of contaminants.

Several waste-package designs have been considered by the DOE. All consist of a cylindrical metal container into which the waste is placed. The container is sealed with a gas-tight closure. The capacity of the waste container and the amount of radiation shielding are design issues. The SCP design specified stainless-steel waste containers each holding the equivalent of about 2 metric tons of nuclear fuel. Alternative waste-package designs that contain between 7 and 9 metric tons are being considered. Details of the waste packages modeled in TSPA-93 are given in Chapters 4 and 10.

2.2.3 Emplacement

The original design for a potential repository specified in the Site Characterization Plan–Conceptual Design Report (SCP–CDR) (SNL, 1987) stipulated that the smaller containers be placed in either vertical boreholes drilled in the floor of the repository emplacement drifts, or horizontally in boreholes drilled into the walls of the drifts. For either emplacement configuration, an air gap surrounds the sides of the container. Since the publica-

tion of the SCP–CDR, only the vertical configuration has been given much further consideration. In TSPA-93, we only consider the "vertical-emplacement" or "borehole-emplacement" configuration discussed in the SCP–CDR. Alternative emplacements being considered are based on studies of the entire nuclear-waste cycle—from offloading from the reactor to emplacement in the repository. These alternatives consider containers that can be used for all aspects of the cycle; these larger packages are placed horizontally on the floors of the emplacement drifts. This configuration is called the "in-drift" emplacement. Chapters 4 and 10 also discuss these issues.

2.2.4 Waste description

The potential repository is designed to hold the highly radioactive spent nuclear fuel from nuclear reactors and high-level waste resulting from activities at DOE defense facilities. The spent fuel consists of assemblies from both boiling water reactors (BWRs) and pressurized water reactors (PWRs). The assemblies include not only the uranium oxide fuel, but also the fuel cladding and support hardware, all of which are radioactive due to activation or intrinsic radioactivity. Options for the waste form include intact or chopped-up assemblies. The HLW consists of products resulting from physical and chemical processes associated with the separation of fissile materials for defense needs. These waste products are immobilized in a glass or calcine matrix.

2.2.5 TSPA-93 modeling domains

The physical domains through which contaminants released from the potential repository must travel to the accessible environment include both the unsaturated tuffs (the unsaturated zone—UZ) in which the repository is located and the saturated formations below the repository block (the saturated zone—SZ). In later chapters of this document, the modeling processes for the contaminant-transport pathways through both the UZ and SZ are discussed. In addition to pathways associated with the hydrologic features discussed in the previous section, releases from the potential repository may also occur by gaseous transport. Both the aqueous and gaseous releases may occur even if the site remains undisturbed for long periods; other pathways may develop if the site is disturbed by events such as human or volcanic intrusions. Figure 2-4 illustrates the pathways investigated in TSPA-93.

Regardless of the transport pathway, the modeling domain can be divided into two parts: the near field and the far field. The far field is defined as that part of the model domain where the geological and environmental parameters are not significantly disturbed by the presence of the repository. In contrast, the near field is that part of the model domain where repository perturbations may temporarily or permanently occur. Depending on what

parameter or model is being considered, the extent of disturbance to the repository system varies. Furthermore, the extent of the disturbance can vary with time. As an example, when considering rock-mechanical stresses, the near field (i.e., the region in which rock stresses deviate from the ambient stresses in the rock) may extend at most a few meters from the repository drifts. In contrast, to identify the bounds of near-field thermal conditions, (e.g., the region where thermal processes such as temperature and convection have altered the ambient water content of the rock) the extent of the disturbance can be many tens of meters, and will vary according to the time that the driving thermal effects have been present. Thus, the definition of the near field is imprecise: it is the portion of the model domain where disruptive effects from the presence of the repository make themselves evident on the host environment.

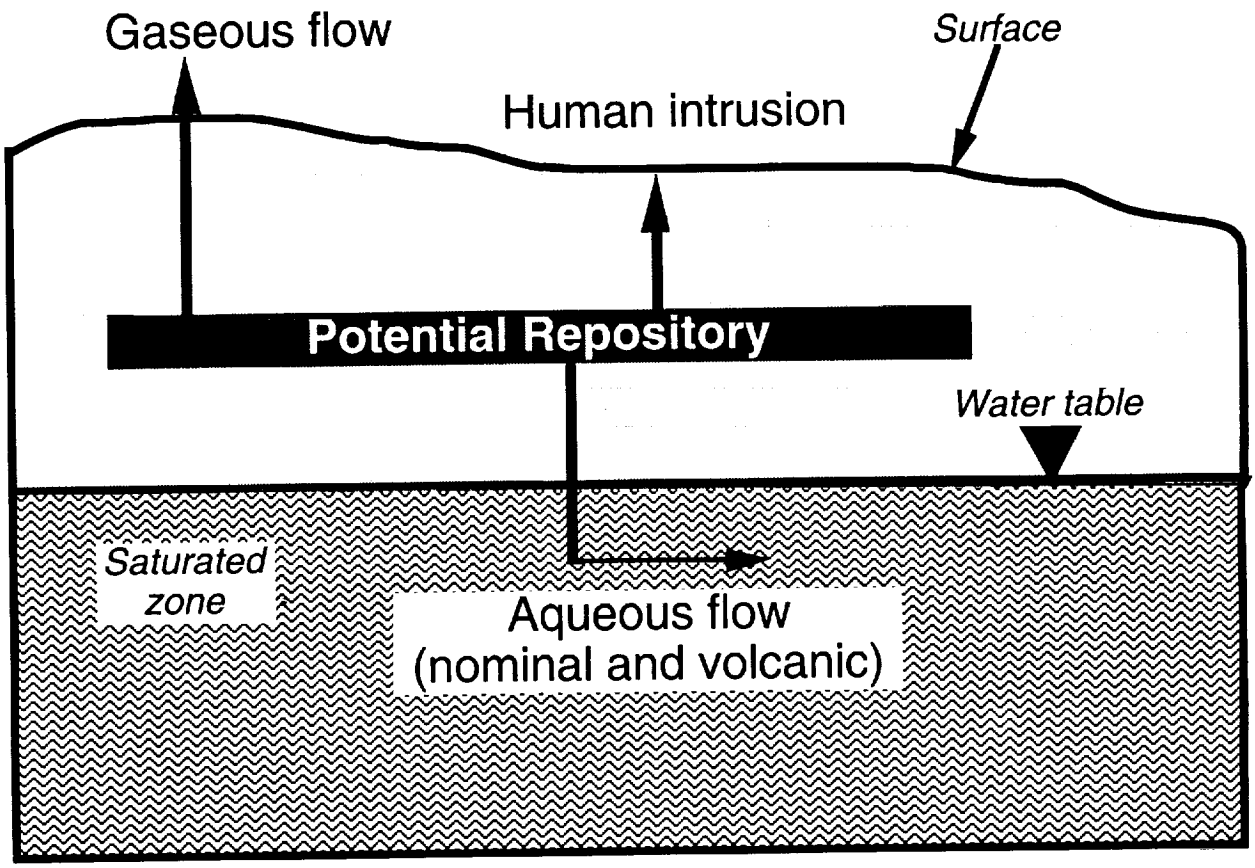

Figure 2-4. Release pathways arising from expected and unanticipated processes at Yucca Mountain.

2.3 Regulatory context

The basic policy in the United States regarding disposal of radioactive waste was set forth in the Nuclear Waste Policy Act of 1982 (Public Law 97-425, 1982). The Act outlined

the procedure to be followed for choosing, characterizing, and approving a site for storage of radioactive waste. The Act has been implemented in regulations of the U. S. Department of Energy (DOE), the U. S. Nuclear Regulatory Commission (NRC), and the U. S. Environmental Protection Agency (EPA).

General siting guidelines were defined by the DOE in 10 CFR Part 960 (DOE, 1984). Sites are to be evaluated against a number of criteria having to do with favorable or unfavorable site characteristics. For example, some favorable conditions are "conditions such that the pre-waste-emplacement ground-water travel time along any path of likely radionuclide travel from the disturbed zone to the accessible environment would be more than 10,000 years" and "low population density in the general region of the site." Some potentially adverse conditions are "geochemical processes or conditions that could reduce the sorption of radionuclides or degrade the rock strength" and "evidence that the water table could rise sufficiently over the next 10,000 years to saturate the underground facility in a previously unsaturated host rock." Comparison of the Yucca Mountain site against the guidelines in 10 CFR Part 960 are not discussed in this report, but a detailed evaluation of "site suitability" against those guidelines was made recently by Younker *et al.* (1992).

If the Yucca Mountain site is determined to be a suitable location for a radioactive-waste repository according to the 10 CFR Part 960 guidelines and other assessments, the DOE would apply to the NRC for authorization to construct the repository and for a license to operate it. The NRC regulations governing repositories for high-level radioactive waste are given in 10 CFR Part 60 (NRC, 1983). The regulation covers many aspects of repository siting, design, operation, and post-closure performance. Of relevance here are four post-closure performance objectives given in 10 CFR 60.112 and 60.113. Section 60.112 states that the repository system must conform to applicable EPA standards, and Section 60.113 introduces three additional performance objectives relating to particular barriers:

- Containment of high-level waste within the waste packages must be "substantially complete" for a period of 300 to 1000 years.

- The release rate from the EBS following the containment period must not exceed a given rate (one part in 100,000 per year of the inventory at 1000 years following repository closure, with some important exceptions).

- The pre-waste-emplacement groundwater travel time along the "fastest path of likely radionuclide travel" from the disturbed zone to the accessible environment must be at least 1000 years.

These individual-barrier goals are discussed in the TSPA-91 report, but for TSPA-93 they are not considered. We concentrate our attention on long-term post-closure performance of the repository system as a whole.

The regulations governing such performance have, in the past, been given by 40 CFR Part 191 (EPA, 1985). However, the Energy Policy Act of 1992 (Public Law 102-486, 1992) requires new standards to be promulgated for the Yucca Mountain site. The Act specifies that a study be conducted by the National Academy of Sciences (NAS) and that the EPA then set standards for Yucca Mountain consistent with the recommendations of the NAS. The Act states that the standards "shall prescribe the maximum annual effective dose equivalent to individual members of the public from releases to the accessible environment from radioactive materials stored or disposed of in the repository." The Act requires the NRC to make its standards consistent with the EPA's new standards and with the recommendations of the NAS.

Since the EPA containment requirements in 40 CFR 191.13 are based on cumulative releases of radioactivity to the accessible environment over 10,000 years, a new standard based on individual radiation doses would be a significant change. In this TSPA, we are faced with making a preliminary assessment of repository performance without knowing what performance measure will be applicable to the site when the repository is licensed.

Appendix A of 40 CFR Part 191 defines a performance measure that will be referred to here as "normalized cumulative release" or "EPA sum," which is calculated by taking the cumulative release of radioactivity to the accessible environment over 10,000 years for each radionuclide, dividing by a given limit (called the "EPA limit") for that nuclide, and summing over all radionuclides with half-lives greater than 20 years:

$$E = \sum_i R_i / L_i , \tag{2.1}$$

where E is the EPA sum, R_i is the cumulative release for nuclide i, and L_i is the EPA limit for nuclide i. With this definition, the containment requirements from 40 CFR 191.13 specify a reasonable expectation that the EPA sum shall (1) have a likelihood of less than one chance in 10 of exceeding 1, and (2) have a likelihood of less than one chance in 1000 of exceeding 10.

The "accessible environment," as defined by the EPA, includes the atmosphere, land surface, surface waters, and all rock and groundwater outside the "controlled area." The controlled area is also defined by the EPA; the controlled area for Yucca Mountain is depicted in Figure 2-5. The controlled area is defined so that the accessible environment is 5 km away from the repository in the direction of expected saturated-zone water flow.

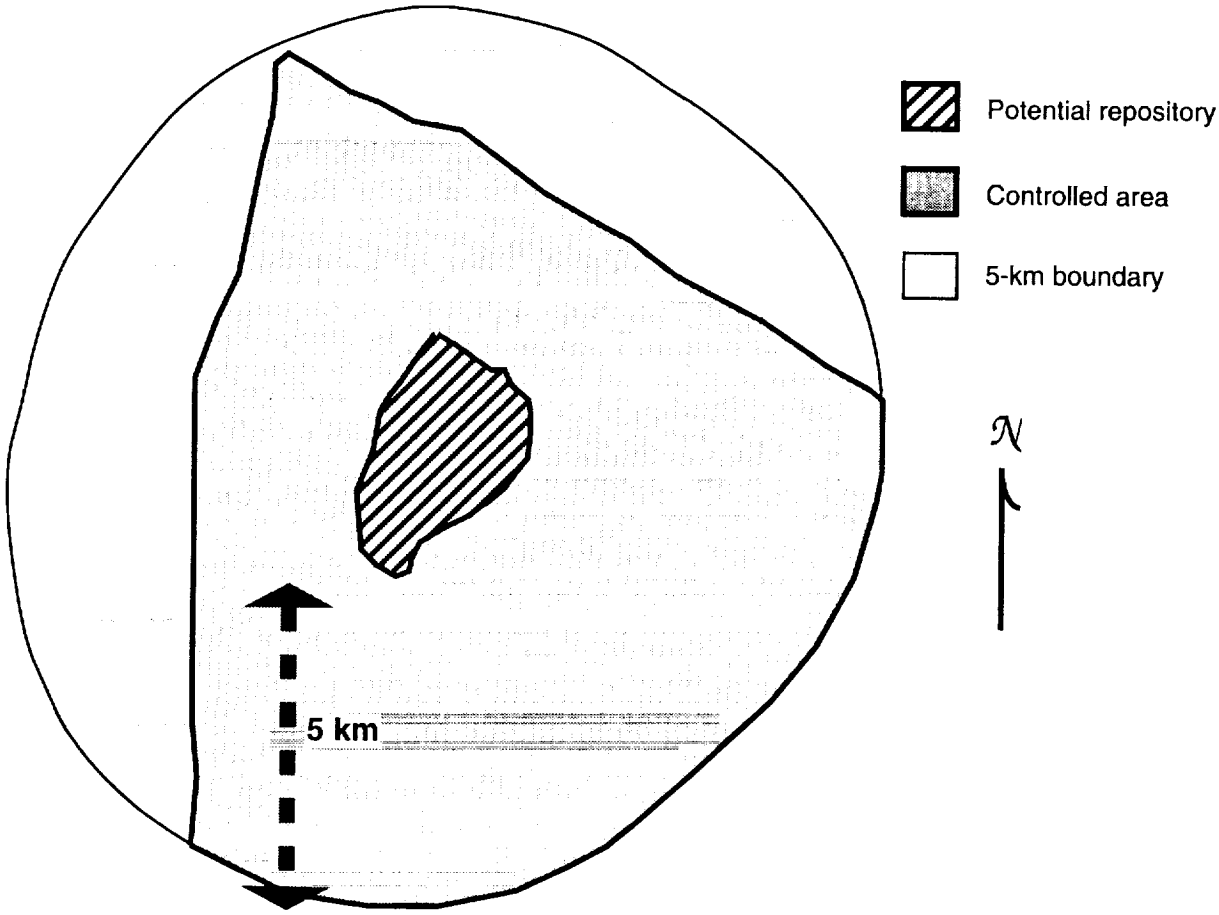

Figure 2-5. Map of region surrounding the potential repository at Yucca Mountain; the area outside the shaded region is the accessible environment. (After Figure 9 of Rautman *et al.*, 1987).

Although 40 CFR Part 191 no longer applies to Yucca Mountain, two other performance requirements defined there are relevant to the form a new individual-dose standard might take. The individual-protection requirements in Section 191.15 state that, for undisturbed repository performance, there should be a reasonable expectation for 10,000 years that annual committed effective dose from the disposal system to any member of the public in the accessible environment will not exceed 15 mrem. This limitation originally was 25 mrem and applied for only 1,000 years, but 40 CFR 191.15 was amended recently to reduce the limit and to increase the period of applicability. The groundwater-protection requirements also were amended recently, and now state (Section 191.24) that, for undisturbed performance, there should be a reasonable expectation for 10,000 years that levels of radioactivity in any underground source of drinking water in the accessible environment shall not exceed the limits specified in 40 CFR Part 141. "Undisturbed performance" is defined as "the predicted behavior of a disposal system, including consideration of the uncertainties

in predicted behavior, if the disposal system is not disrupted by human intrusion or the occurrence of unlikely natural events." The standards for drinking water in the U. S. are contained in 40 CFR Part 141 (EPA, 1975), and they limit the radiation dose from drinking water to 4 mrem/yr (40 CFR 141.16).

The radioactive-waste regulations in most other countries are based on individual radiation doses. The International Commission on Radiological Protection has recommended a maximum dose rate of 100 mrem/yr for members of the general public (ICRP, 1985; 1991), but that limit includes exposures from other sources (e.g., medical procedures) in addition to any doses from a radioactive-waste repository. Furthermore, no time limit is specified on the dose limit, so it applies indefinitely in the future.

Because we have no way of knowing what form the new standards for Yucca Mountain will take, our approach is to consider several possibilities so that relevant information is available to those who are involved in defining the standards. We continue to consider the EPA cumulative-release performance measure of 40 CFR 191.13 because it affords comparison with past work (such as TSPA-91) that was done using that performance measure. In addition, we calculate individual drinking-water dose rates for some scenarios, for reference and to examine the implications of different performance measures on model sensitivities. Doses are not calculated for exposure pathways other than drinking water in this study. We also consider longer time periods in addition to the 10,000-year time period of 40 CFR Part 191. Most calculations are made for time periods of one million years because that is the period of time needed to capture the peak dose rate in the aqueous-release calculations (see Chapters 14 and 15). Gaseous-release calculations are carried out for only 10,000 years because the only nuclide considered in them is ^{14}C, which has a half-life of 5,730 years. (The gas-flow calculations were carried out to 20,000 years, so the gaseous-release calculations could be extended to 20,000 years in follow-on work.)

Releases from human-intrusion drilling activities are calculated for both 10,000 and one million years. Given the lack of success that futurists have had in the past predicting human behavior and technology, the assumptions made in TSPA-93 that present-day technology will continue to be used for long periods in the future is hard to justify. However, such assumptions have been used in the past (as was done in TSPA-91), because 40 CFR Part 191 specifically directs that present-day technology be assumed for 10,000-year release estimates. The estimations of million-year performance for human intrusion should not be interpreted as support for regulating this aspect of repository performance over such a long period.

The fact that we make release simulations for one-million-year periods should not be taken as a recommendation on our part to consider such long time periods in the radioac-

tive-waste standard. We simply provide the results so that more information is available on which to base decisions. The results of this report should not be used without becoming familiar with the assumptions and uncertainties that underlie them.

Chapter 3
Method

(Wilson, Barr, Barnard, Gauthier, Dockery)

In this chapter, we (1) present a short introduction to performance assessment (PA) and explain how the parts of this report relate to the performance-assessment method; (2) discuss "scenarios" and the features, events, and processes (FEPs) that are considered in this TSPA; (3) discuss the models used to simulate those FEPs; and (4) discuss the methods used to incorporate uncertainty into the computed results of the models.

3.1 Performance assessment

The fundamental purpose, or function, of PA is to evaluate how well a system complies with given criteria. Thus, in Section 8.3.5.13 of the Yucca Mountain Site Characterization Plan (SCP; DOE, 1988a) a strategy was established for assessing performance of the potential Yucca Mountain repository site with respect to applicable Nuclear Regulatory Commission (NRC) and Environmental Protection Agency (EPA) regulations. Given successful completion of the Yucca Mountain Site Characterization Project (YMP), the end product of PA would be used as evidence in support of an application to the NRC to license the repository.

At this stage of the project, when site characterization and repository design are still ongoing, PA serves another function—to use preliminary estimates of repository performance to provide input to the site-characterization and repository-design programs concerning the performance implications of their results and options, and to guide future PA work.

Both the evaluation and guidance functions influence current PA work. The second function is primary at the present time; the focus of this report is on the implications of TSPA to other parts of the project. Those implications are summed up as recommendations in Chapter 19. Secondarily, TSPA-91 and TSPA-93 are iterations toward the ultimate goal of assessing compliance of the potential repository system with applicable regulations. The current work should be regarded as developmental, however. PA is only in the early stages of the process described in SCP Section 8.3.5.13; the FEPs that are significant to repository performance are still being determined. Additional PA work that is crucial to further development of capabilities (so that future TSPA iterations will be closer to the ultimate compliance assessment) is listed in Chapter 20.

The following list gives the major steps of performance assessment (see Figure 3-1). This list contains the same basic information as lists given in Section 8.3.5.13 of the SCP and in Chapter 2 of the TSPA-91 report (Barnard *et al.*, 1992), though the order and the number of steps listed is somewhat different in each place.

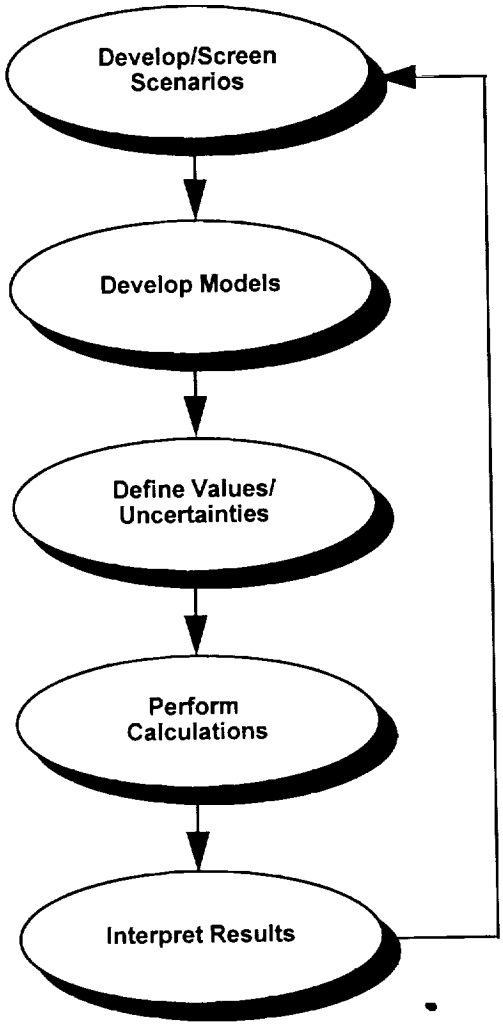

Figure 3-1. Major steps of performance assessment.

1. *Develop and screen scenarios.* To "develop scenarios" means to make organized lists of potentially important FEPs. As is shown in the next section, we organize the lists into tree-like "FEP diagrams." To "screen scenarios" means to eliminate any that can be shown to be unimportant. The screening can be based on common sense, on data that show a suspected feature or process to be nonexistent or insignificant, or on results of the models discussed in subsequent steps.

2. *Develop models of important FEPs.* These models are usually implemented in computer programs. Alternative models are developed, where applicable, to account for uncertainty as to the appropriate model (referred to as "conceptual-model uncertainty"). Models including different levels of detail are useful for different purposes—see the discussion of "the hierarchy of models" in Chapter 2 of the TSPA-91 report. Here,

the hierarchy will be collapsed into "detailed models" and "system models." Detailed models contain as much complexity as possible, and their purpose is to provide understanding of physical processes at a fundamental level. Because of their complexity, detailed models are typically used to perform a limited number of deterministic calculations. System models contain fewer details, but are still expected to reproduce the essential phenomena. System models are used for probabilistic analyses, in which many realizations of the system are computed to examine the statistical properties of the results (e.g., What is the mean release? What is the range of releases? What is the probability that releases are above the regulatory limit?).

Constructing these system models is not necessarily a simple task. Although Section 8.3.5.13 of the SCP describes the simplification in general terms, the actual construction of the system models has to proceed by a series of iterations. Calculations using more detailed process models explore the effects of phenomena, and effects that prove significant are incorporated into the system models. Moreover, the understanding gained from this work allows the system models to handle quantitatively the uncertainties associated with the results of the explorations. Calculations with the system models help analysts identify phenomena and uncertainties to which estimates of system performance are most sensitive; this information helps to guide the next iteration of studies with the detailed process models. We refer to the development of such system models as "abstraction" because the development proceeds by extracting the essential features from detailed calculations done with the process models—i.e., by abstracting those calculations.

3. *Estimate parameter values and the uncertainties in them.* For studies using detailed process models, normally only a few "representative" values are used for any given parameter because of the time and cost required to obtain solutions. For studies using system models, the uncertainty in each parameter (or, perhaps, in each key parameter) is quantified by defining a probability density function (PDF). Probabilities of occurrence may also need to be defined for some FEPs (e.g., the probability that a volcanic intrusion will occur in a given period of time).

4. *Make calculations using the models and parameter values.* For detailed process models, a calculation typically includes only a subset of the repository system. The calculation produces predictions that can be compared with laboratory or field data, used to guide repository or test design, or used for abstraction into system models. For system models, a calculation produces predictions of regulatory performance measures and the uncertainty in the performance measures caused by the parameter and model

uncertainties included in the analysis. The predictions can be used to assess regulatory compliance or to determine to which parameters and models the performance measures are most sensitive.

5. *Interpret results.* The results can be used to screen scenarios, guide testing or design work, or direct future model development. When models and data are sufficiently mature, the results can be used to determine whether the system satisfies regulatory requirements.

These steps are not necessarily sequential; they can be performed in parallel. The entire process is iterative, and individual steps can also be iterated within themselves. In all steps, PA works with project participants and with the external scientific community.

The preceding discussion can be used as a framework to explain the structure of this report. After the introductory chapters are five major parts. Part II, "Data Development," describes the development of data sets for the model parameters and the quantification of their uncertainty by defining PDFs (Step 3 above). Part III, "Detailed Modeling and Abstraction," describes detailed process modeling and abstraction of the results into simpler system models, an essential part of the long-term PA process (Step 2). Part IV, "Probabilistic Modeling and Results," describes the application of system models to calculate radionuclide releases probabilistically, so that uncertainty in the release estimates is included (Step 4). Part V, "Summary and Conclusions," summarizes the results, with interpretation and recommendations for future work (Step 5). Part VI, "Ancillary Calculations," describes additional detailed process modeling that has not yet been abstracted for use by system models. The ancillary calculations are part of the exploration process discussed above in Step 2, in which phenomena are modeled to determine whether they are significant.

Although Step 1 is not explicit as one of the major divisions of the report, an introduction to scenarios for Yucca Mountain follows in the next section, and FEPs are discussed within the report as appropriate. Conceptual-model uncertainty, mentioned above in Step 2, is exemplified by the consideration of two different conceptual models of unsaturated-zone groundwater flow and transport (Chapters 14 and 15).

Before going on to a discussion of scenarios for a potential Yucca Mountain repository, let us briefly describe other PA efforts. Several groups have contributed to Yucca Mountain performance assessment. The Electric Power Research Institute (EPRI; McGuire *et al.*, 1990, 1992), the NRC (Codell *et al.*, 1992), Golder Associates (Miller *et al.*, 1992), Pacific Northwest Laboratory (PNL; Eslinger *et al.*, 1993), and INTERA (1993) have all produced preliminary TSPAs. The methods used by the different groups vary in degree of detail included in the models. EPRI, Golder, and INTERA all use highly abstracted system models for their

assessments, whereas PNL uses detailed multidimensional models of flow and transport for its calculations. The NRC is intermediate, as is SNL (TSPA-91 and TSPA-93). The difference is reflected in the number of realizations used. PNL calculates flow and transport for a limited number of representative parameter values, whereas the others generally put more emphasis on probability distributions and exploring the sensitivity of the results to parameter variations.

The NRC uses a method similar to that used for the Waste Isolation Pilot Plant site (WIPP Performance Assessment Department, 1992), in which the assessment is broken into separate calculations, depending on the occurrence or non-occurrence of disruptive events such as human intrusion. The method differs from that used for this study and for TSPA-91 in that each of the calculations is complete, including nominal releases as well as releases due to the disruptive event(s). In TSPA-91 and TSPA-93, we take the disruptive events to be independent from nominal conditions and from each other, as a means of simplifying the calculations. PNL uses a method that combines some aspects of both methods. Golder and INTERA use a method that simulates the entire system at once. During each realization, there is some probability of a disruptive event taking place. "Importance sampling" is used to increase the number of realizations with low-probability disruptive events. The method used by EPRI is different from all the others in being based on a logic-tree formalism. In the EPRI method, probability distributions are not defined for uncertain parameters, but rather a logic tree is defined, with branches representing a few discrete values of some of the uncertain parameters. Disruptive events are also represented with branches in the logic tree.

3.2 Scenarios

As discussed in the previous section, the process of determining which phenomena are to be modeled in a TSPA analysis begins with a screening of the scenarios. This process is done to determine, systematically, what a TSPA should model in order to meet its purposes. Figure 3-2 illustrates the types of scenarios that could affect performance of a potential repository at Yucca Mountain. "Nominal" flow and transport, perturbed by the presence of the repository, are the expected release mechanisms, proceeding whether or not disruptive events occur (though there is great uncertainty about the details of the flow and transport). Disruptive events such as human intrusion, volcanism, and tectonism may occur in addition to nominal flow and transport, and their effects can be of two types: direct release of radioactivity to the surface, or alteration of the nominal flow and transport system, thereby altering the amount of aqueous or gaseous release. Unexpected perturbations to the system

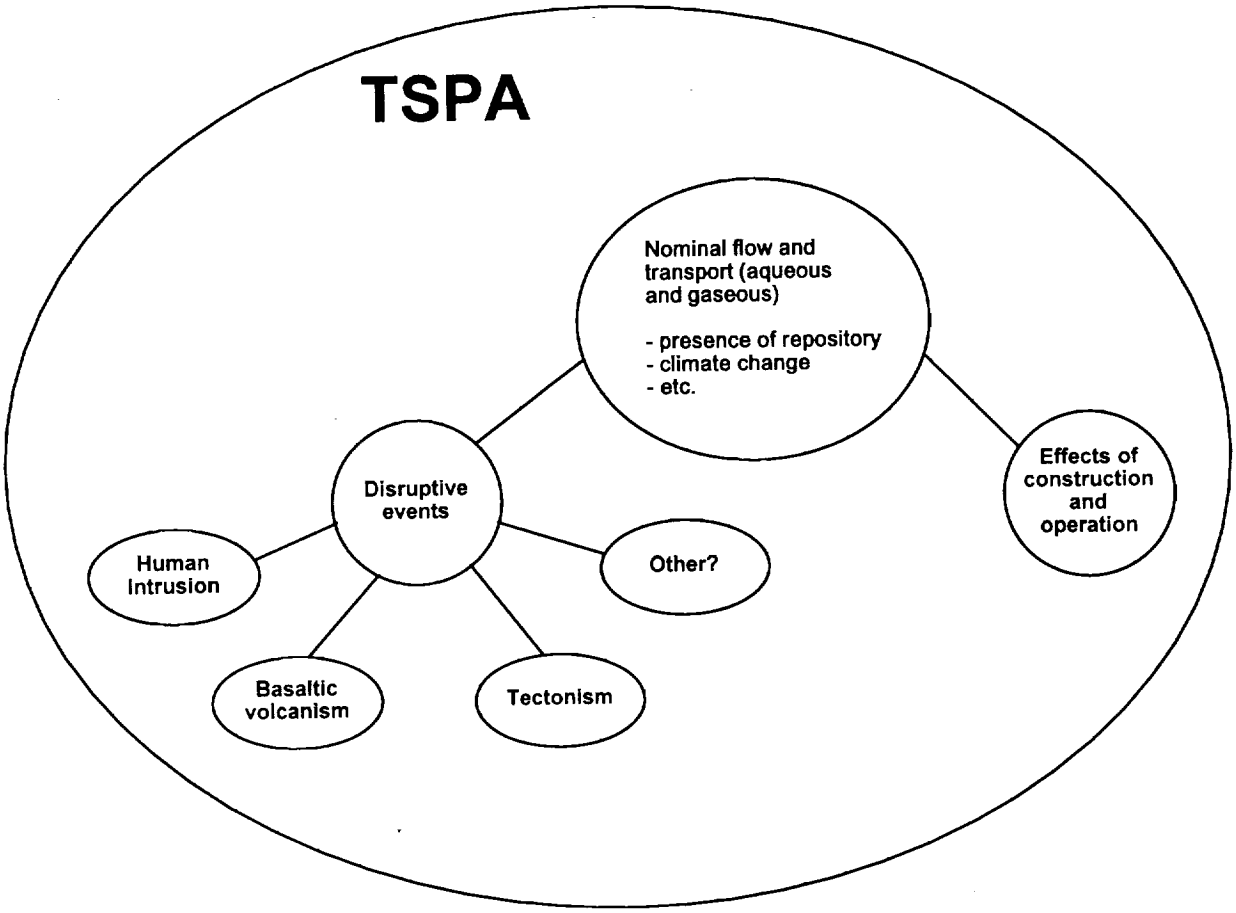

Figure 3-2. Categories of scenarios that must be considered in predicting the performance of a potential repository at Yucca Mountain.

due to accidents during repository construction and operation or due to defects in design or materials must also be considered.

The scenario categories shown in Figure 3-2 are at different levels of maturity in their consideration by performance assessment. Sequences, or trees, of potentially important features, events, and processes have been developed for basaltic volcanism by Barr *et al.* (1993). A report on FEPs for nominal aqueous flow and transport is in preparation. Detailed FEP diagrams for other scenario categories are in development, but are not as far along. The FEP diagrams contain many FEPs whose importance and likelihood are uncertain. The purpose of the diagrams is to catalog physically reasonable FEPs so that their significance can be investigated systematically. In addition, detailed FEP diagrams are useful to promote communication among YMP principal investigators (PIs) and performance assessors.

A scenario is a well-defined sequence of FEPs. A scenario can be thought of as a possible future history of the repository system, and can be represented by one or more paths through the FEP diagrams. Because the branches of FEP diagrams are not mutually exclusive, more

than one path may be active at the same time during the future history of the system; also, different paths may be active at different times or at different spatial locations. Additional discussion of these points may be found in Chapter 3 of the TSPA-91 report.

Currently, PA analyses are exploring various scenarios, chosen with some advice from PIs, in order to establish what FEPs are important to radionuclide release from a potential repository located at Yucca Mountain. As experience grows with these analyses, it will become possible to recognize the most essential FEPs.

Each of the diagrams included in the subsequent subsections shows an overview of the general FEPs used to construct the TSPA-93 analyses. A full diagram contains an extremely large amount of information, as shown in the reports cited above. However, only a small portion of a given diagram is actually modeled in this TSPA and only the modeled segments are shown here. In some cases, a number of FEP boxes (or elements) within a segment have been collapsed into a single representative box. A number under a FEP element in the diagrams indicates the chapter in this report in which information on that FEP is located.

3.2.1 Nominal flow

The scenarios describing groundwater and gas flow and transport were developed from the FEP diagram for "Nominal flow in the presence of a repository," which is in preparation. The diagram shown in Figure 3-3 is a condensed version included to provide an overview of the FEPs modeled in TSPA-93. It describes aqueous and gaseous radionuclide transport to the accessible environment, perturbed by transient thermal effects caused by the hot waste in the repository.

The diagram begins with "Nominal flow" and proceeds to "Percolation flux to the repository." In the full diagram, a great deal of additional detail concerning the processes contributing to percolation flux at depth is included in several branches. However, for the TSPA-93 simulations, these details are not modeled explicitly. Instead, assumptions about the cumulative effects are contained in the distribution of flux values used as boundary conditions for the simulations (Chapter 8).

Below "Percolation flux to the repository," the diagram branches to describe the effects of the repository during and after the thermal pulse. The "Hot repository" branch examines the processes occurring during the period when the emplaced waste has elevated the temperature of the adjacent rock so that the boiling isotherm is outside the waste containers (see Chapter 10). The "Cold repository" branch describes the system either before the rock temperatures have been elevated or after the thermal pulse has dissipated and the container surface temperatures have dropped below the temperature for local vaporization.

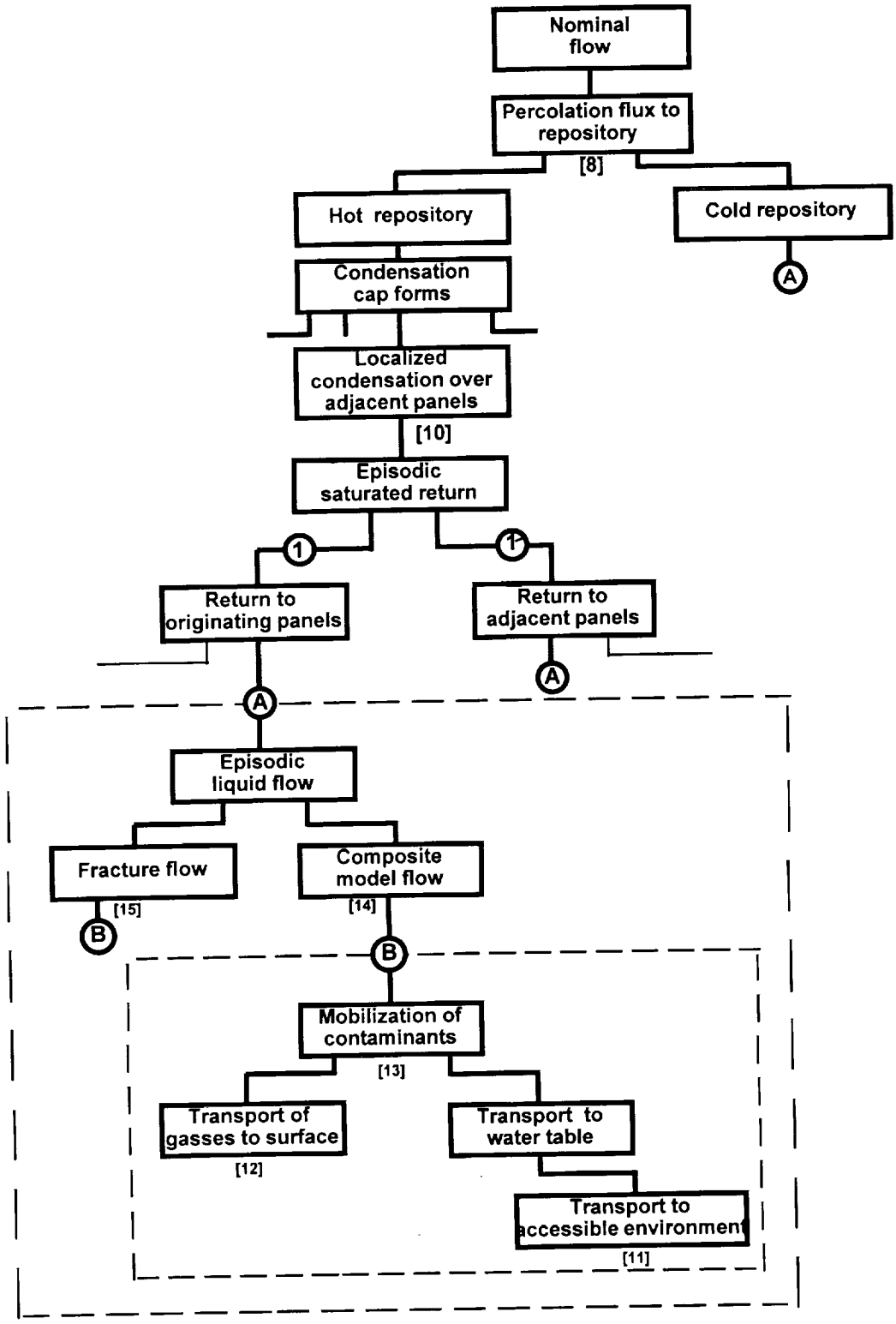

Figure 3-3. Condensed FEP diagram for nominal flow in the presence of a repository. (Chapter numbers are shown in brackets.)

Below the "Hot repository" element, "Condensation cap forms" also contains more detail than we are modeling. In the abstracted hydrothermal model (Chapter 10), a condensation cap is assumed to form and shed water onto the repository, but details of convection and other processes are not included. "Localized condensation over adjacent panels" indicates that the power density of emplaced containers is sufficient to move water vapor at rates and volumes large enough to form a zone of condensation that extends over adjacent panels, but not necessarily over the entire repository including the unusable areas. An issue depicted lower in the diagram is fluid movement between waste-emplacement panels. "Episodic saturated return" is intended to describe periodic return flow from the condensation zone that occurs because accumulation exceeds the capacity of the matrix and thus feeds fractures or other locally saturated flow mechanisms. The accumulation can develop from continued condensation driven by repository heat or from locally saturated flow due to percolation from the surface. As the liquid flows down from the condensation cap, it may either be shed off of the margins of the cap ("Return to adjacent panels") or, as the heat decreases and the condensation cap begins to collapse, the liquid will begin to "Return to originating panels."

After describing the generation of saturated conditions near the repository, the FEP diagram treats alternatives for the return of liquid to the immediate vicinity of the waste packages. Note that the FEPs in the outer dashed box are to be repeated wherever (A) appears, and similarly with the inner dashed box and (B). The liquid moves episodically into either "Fracture flow," as modeled using the weeps model (Chapter 15) or "Composite model flow" (Chapter 14). "Mobilization of contaminants" encompasses waste-package and waste-form degradation as well as movement of the contaminants through the engineered barrier system. This element represents the information in the YMIM model (Chapter 13). One branch below this element shows that, after release from the waste package, volatile ^{14}C moves upward through Yucca Mountain to the surface and is released to the accessible environment (Chapter 12). The other branch shows movement of the nuclides first through the unsaturated zone to the water table (Chapters 14 and 15), and then out through saturated-zone flow paths to the 5-km accessible-environment boundary (Chapter 11).

3.2.2 Human intrusion

The human-intrusion scenarios included in this TSPA analysis were developed from the FEP diagram for human intrusion given in Chapter 6 of the TSPA-91 report. Figure 3-4 shows the portion of the FEP diagram that includes the FEPs captured in the TSPA-93 calculations, which include only direct release at the surface due to drilling into a waste container or contaminated rock.

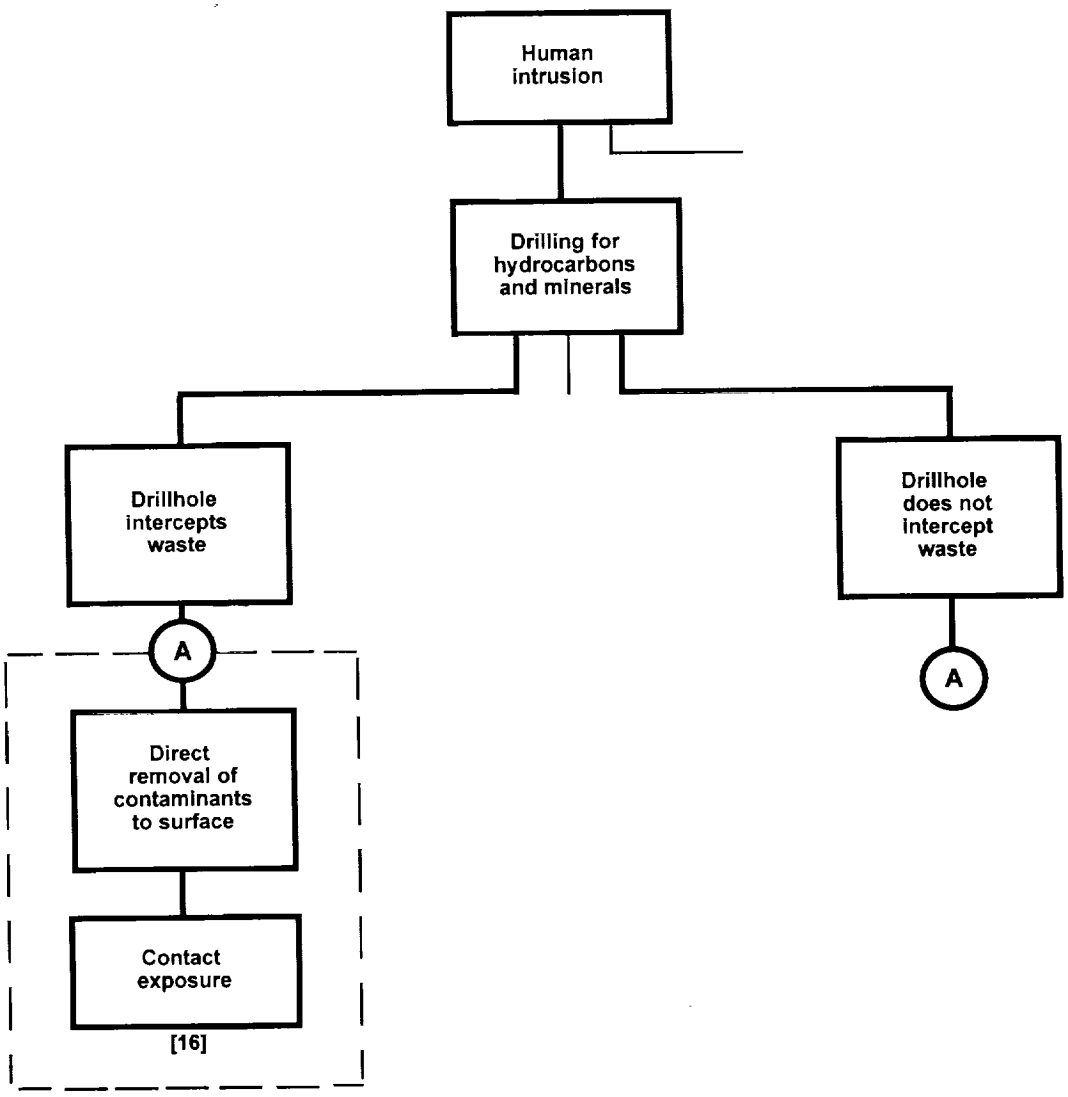

Figure 3-4. Condensed FEP diagram for human intrusion. (Chapter numbers are shown in brackets.)

The TSPA analysis considers only drilling events. Specifying "hydrocarbon and mineral exploration" rather than "scientific exploration" has implications about the size of the holes that are drilled. The drillhole is assumed either to intercept a waste container directly or to intercept only surrounding rock, which may be contaminated with radionuclides that have escaped from a waste package. In both cases, the direct removal of contaminants to the surface is calculated (Chapter 16). This scenario category is included again, after having been considered in TSPA-91, primarily to investigate the effects of alternative waste-package designs on repository performance.

3.2.3 Basaltic volcanism

Basaltic volcanism is used as a convenient label to describe scenarios developed for basaltic igneous activity (Barr *et al.*, 1993). In particular, the FEP diagram of interest for Chapter 17 (Figure 3-5) examines the case of intrusion of a dike through the repository but not directly contacting any waste containers. (Another branch—direct contact of waste containers—was considered in TSPA-91 but is not repeated for TSPA-93.) Some details have been simplified and condensed from the more complete diagram for this case. The intent of this diagram segment is to examine the influence of heat and magmatic volatiles on waste and waste containers that have no direct contact with the magma.

In Chapter 17, the effects of a dike are discussed for the case of no contact with waste along its entire length. In reality, an intrusion would be expected to make contact with some containers and to miss others along its length. The somewhat contrived situation of missing all containers is intended to maximize the number of waste packages exposed only to volatiles. The expectation is that such interaction will cause the affected waste packages and waste forms to degrade rapidly, producing a source that has considerably more mobile components. Consideration is given to the physical state of a container at the time of dike intrusion because the period in which the dike is exsolving aggressive volatiles is limited. "Degraded containers" would have fuel rods or glass waste already exposed for interaction, whereas "undegraded containers" must be breached before the magmatic processes can act upon the waste. Since the processes are rate- and volume-dependent (on volatiles and waste containers), so are the amounts of mobilized contaminants. After interaction with the magma, waste is available at the containers to provide a local source of contaminants to the flow field. The diagram segments then continue as for the nominal-flow FEP diagram at points (1) and (1′) (Figure 3-3).

3.3 Processes, models, and computer programs

To evaluate scenarios and determine which FEPs are significant to repository performance, mathematical models must be developed for the important FEPs. These mathematical models are usually solved by implementing them in computer models. This section provides an overview of important FEPs included in this TSPA and the computer programs used to model them. The interconnections between programs are also discussed.

Probably the most important processes to understand for Yucca Mountain are those concerning nominal conditions (without disruptive events). Those processes include precipitation and infiltration, including effects of climate changes; groundwater flow in both unsaturated and saturated zones; air and vapor flow in the unsaturated zone; aqueous and gaseous transport of radionuclides and heat; geochemical processes that affect flow and

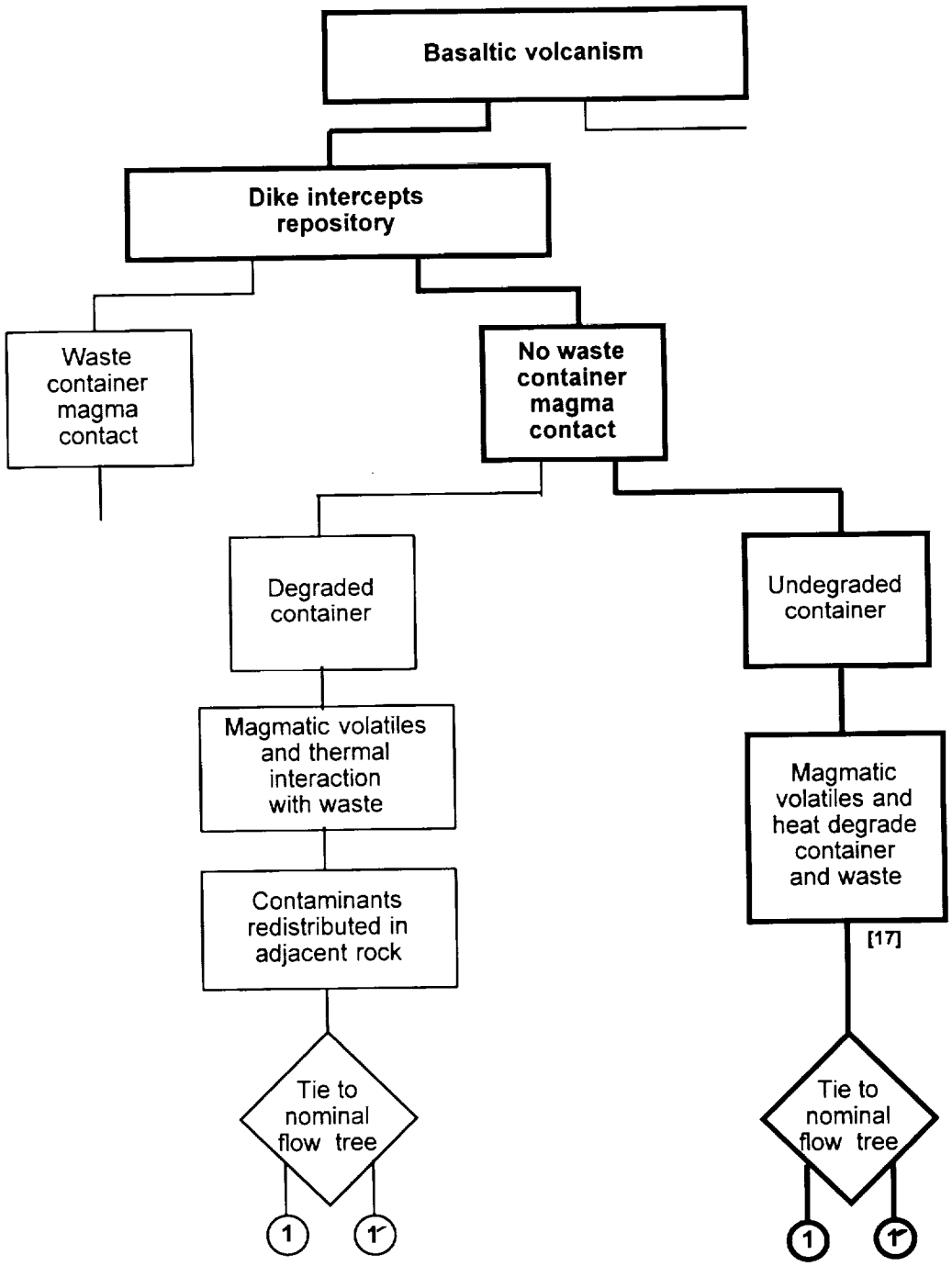

Figure 3-5. Condensed FEP diagram for basaltic volcanism. (Chapter numbers are shown in brackets.)

transport; corrosion and other failure mechanisms of waste containers and fuel-rod cladding; alteration of the waste form (spent fuel or glass waste); and dissolution and mobilization of radionuclides.

We consider two different models of unsaturated-zone (UZ) flow in order to explore the performance implications of different assumptions about water movement through fractures in the unsaturated zone. The composite-porosity model (Chapter 14) assumes pressure equilibrium between matrix and fracture flows, whereas the weeps model (Chapter 15) assumes that water flows in locally saturated fractures with no matrix/fracture interaction. The composite-porosity model is implemented by a computer program called TOSPAC (Dudley *et al.*, 1988; Gauthier *et al.*, 1992), which solves flow and transport in one spatial dimension. (The applicability of one-dimensional calculations to Yucca Mountain is discussed in Chapter 23. In many cases, the use of one spatial dimension is more rigorous than previously assumed.) The weeps model is implemented by a computer program called WEEPTSA (see Chapter 15). WEEPTSA is probabilistic in nature, its basic calculation being the probability of a flowing fracture contacting a waste container. Both of these programs are coupled to a radionuclide source program called YMIM (see Chapter 13), which calculates container failure, waste-form alteration, and radionuclide dissolution and release. YMIM is actually incorporated within TOSPAC and WEEPTSA as a subroutine because the flow, source release, and transport routines share a great quantity of information. In addition to these three central programs, information from many other programs is used in the course of a nominal-release calculation. Flow charts showing the programs and the flow of information are depicted in Figures 3-6 and 3-7, for the composite-porosity model and the weeps model, respectively. Much information is common to the two models, so large sections of Figures 3-6 and 3-7 are the same.

Starting at the top of the figures, temperature (T_c = container temperature, T_f = fuel temperature) and dryout (f_d = dryout fraction, V_d = dryout volume; these parameters are used to characterize the extent of thermal perturbation to the nominal flow system) information is calculated as discussed in Chapter 10. The major models used are a computer implementation of a three-dimensional analytical heat-conduction solution (see Appendix C) and COYOTE (Gartling, 1982), a finite-element program for solving nonlinear heat-conduction problems. The COYOTE container temperatures are thought to be more accurate at early times and the analytical container temperatures are thought to be more accurate at late times, so the solutions are merged to give a composite container-temperature curve, which is used by YMIM for modeling temperature-dependent corrosion processes. WEEPTSA does some preliminary analysis of corrosion rates before passing a given parameter set to YMIM. The composite container temperature is also used as a boundary condition for calculation of

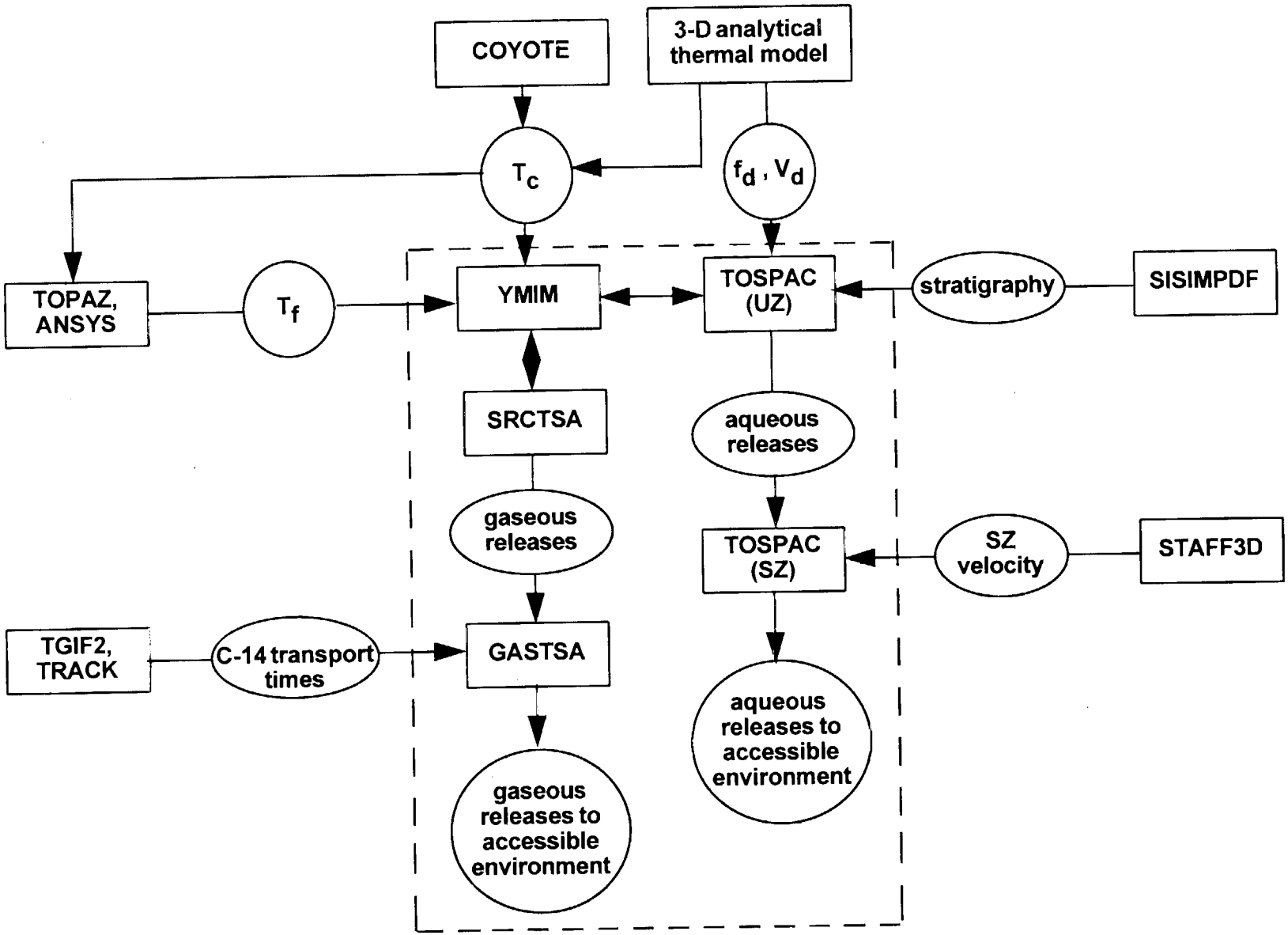

Figure 3-6. Flow chart showing computer programs used for calculation of nominal releases with the composite-porosity model. Programs within the dashed box are run for each Monte Carlo realization.

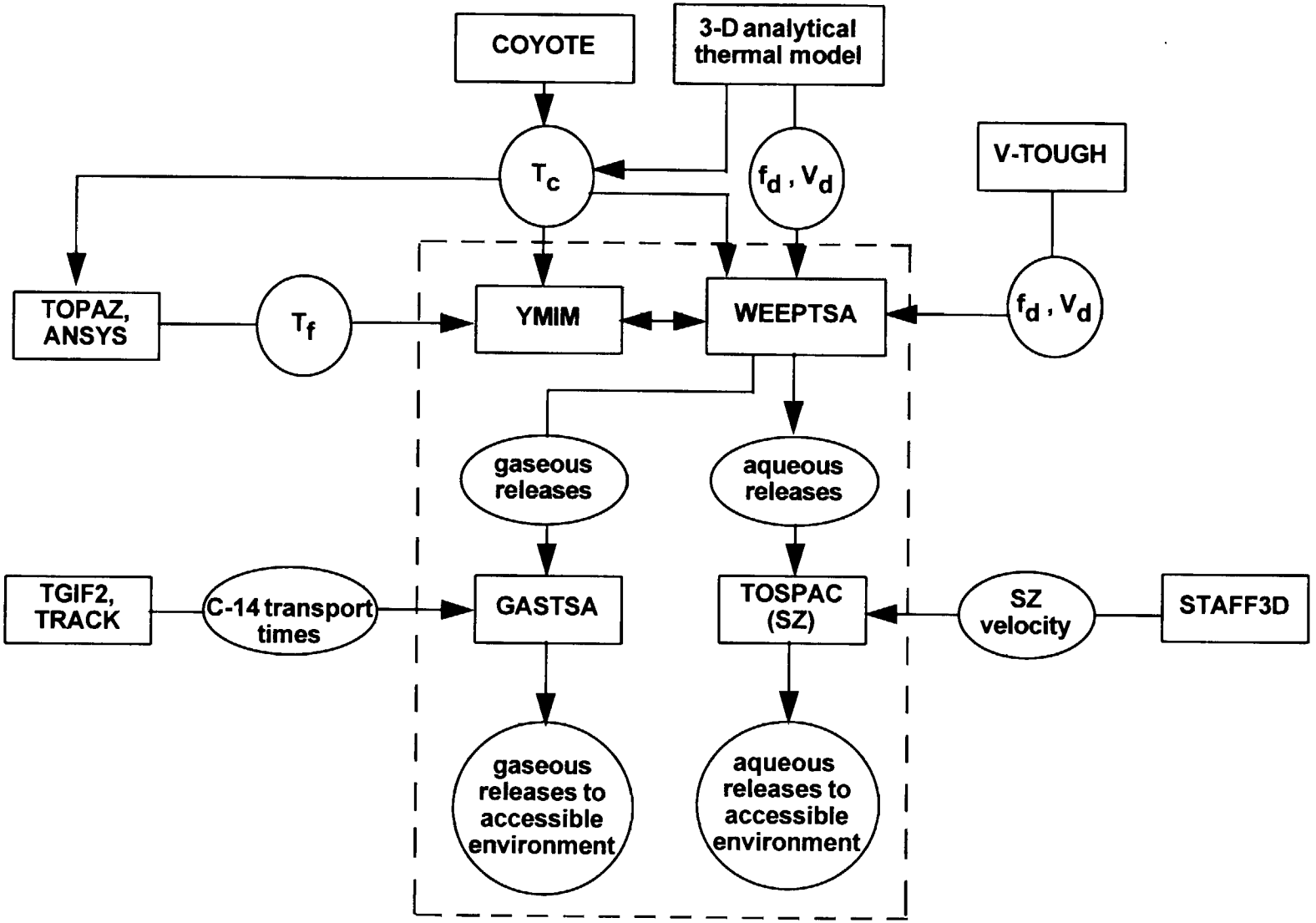

Figure 3-7. Flow chart showing computer programs used for calculation of nominal releases with the weeps model. Programs within the dashed box are run for each Monte Carlo realization.

internal waste-package temperatures. For the SCP-type containers, TOPAZ (Shapiro and Edwards, 1990) is used to calculate the internal temperatures, and for the multipurpose-type containers, ANSYS, a commercial program, is used. In both cases, heat flow within the detailed geometry of fuel assemblies in a waste package is modeled. The resulting fuel temperatures are used by YMIM for modeling temperature-dependent fuel-rod-cladding failure, spent-fuel alteration, and radionuclide dissolution.

In addition, dryout fraction and dryout volume are abstracted from V-TOUGH (Nitao, 1989) results. V-TOUGH calculates multiphase fluid flow coupled with heat transfer. These results are only used in weeps simulations (see Chapters 10 and 15).

Another part of the calculations that is common to composite-porosity and weeps simulations is the calculation of radionuclide transport through the saturated zone (SZ). The composite-porosity model is used by both models for the saturated zone, implemented by one-dimensional TOSPAC calculations for the aqueous-release simulations. In those calculations, the SZ water velocity is not calculated, but is an input parameter. The range of values to use for SZ water velocity and dispersivity is abstracted from three-dimensional simulations of saturated-zone flow and transport using STAFF3D (Huyakorn *et al.*, 1992). The detailed modeling and the abstraction process are discussed in Chapter 11.

Also common to composite-porosity and weeps simulations is the calculation of gaseous ^{14}C transport to the ground surface. The calculation is performed by a program called GASTSA by means of a convolution integral described in Section 12.4. The convolution combines the source release rate for ^{14}C with distributions of transport times derived by detailed calculations using computer models TGIF2 and TRACK (see Chapter 12). The detailed calculations are two-dimensional simulations of coupled gas and heat flow, assuming 100% humidity to eliminate the necessity of simulating water flow as well. The source term for ^{14}C is produced directly by the WEEPTSA/YMIM combination, but for the composite-porosity model a program called SRCTSA is used with YMIM. SRCTSA is a subset of TOSPAC, containing only the parts of TOSPAC (and YMIM) necessary for a source calculation, and excluding the flow and transport parts (see Chapter 14).

The last item shown in Figure 3-6 is the geostatistics program SISIMPDF (Deutsch and Journel, 1992), which is used to generate stratigraphic realizations from known borehole data (see Chapter 6). Geostatistical methods are used to incorporate uncertainty about unit-interface locations into the calculations, and properly belong in the next section on "incorporation of uncertainty." They are included here to show a difference between the composite-porosity and weeps models (the weeps model does not use stratigraphic information) and because in this study we only use a single stratigraphic realization, so the stratigraphic uncertainty is not included.

Some of the basic structure of the nominal-flow FEP diagram (Figure 3-3) can be distinguished in Figures 3-6 and 3-7. The split below (A) in the FEP diagram is represented by the existence of two basic models and two flow charts for nominal release. The split below (B) is the split between aqueous release and gaseous release that is apparent in Figures 3-6 and 3-7, with different computational models used for the different processes. The FEPs above (A) in the FEP diagram are not represented in the flow charts except by the dryout parameters (f_d and V_d). The processes of condensation and shedding are represented in the simulations by an abstracted hydrothermal model (see Chapter 10) that is programmed into TOSPAC, WEEPTSA, and SRCTSA.

In addition to nominal releases, releases resulting from human intrusion (exploratory drilling) and basaltic volcanism are considered in TSPA-93.

A flow chart is not given for human-intrusion models because releases due to human intrusion are calculated with a single stand-alone computer program called DRILL (see Chapter 16). DRILL calculates the probability that a drill will intercept a waste container or contaminated rock outside a waste container, and then uses a probabilistic calculation to determine the amount of radioactive waste brought to the surface by the drilling.

A flow chart for the basaltic-volcanism models is shown in Figure 3-8. The basaltic-volcanism simulations done for this TSPA concern the modification of container degradation and radionuclide releases resulting from high temperatures and corrosive gases near a dike intrusion, but with no direct contact between the magma and waste containers. As indicated on the flow chart, the effect modeled is a modification of the radionuclide source term for a period of time after the intrusion (see Chapter 17). The actual release calculation is a composite-porosity aqueous-release calculation, as depicted in Figure 3-6. (Gaseous releases are not calculated for the magmatic intrusions, nor are weeps-model releases.)

As shown in the flow chart, two computer models are used for calculation of magmatic releases, in addition to the nominal-release models. VOLCAN is used to calculate the number of waste containers affected by a dike intrusion, and ROCKTEMP models the temperature excursion caused by the dike. These two models implement the algorithms discussed in Chapter 17. VOLCAN can also be used in a stand-alone mode to calculate releases from direct magma/waste-container interactions, as was done for TSPA-91. As indicated, ROCKTEMP requires input of information on nominal container temperatures, which are the same as discussed above.

As a simplification, the major processes are treated independently for this TSPA. Thus, the aqueous- and gaseous-release parts of the nominal-condition simulations are performed separately, and the disruptive-event simulations (human intrusion and basaltic volcanism)

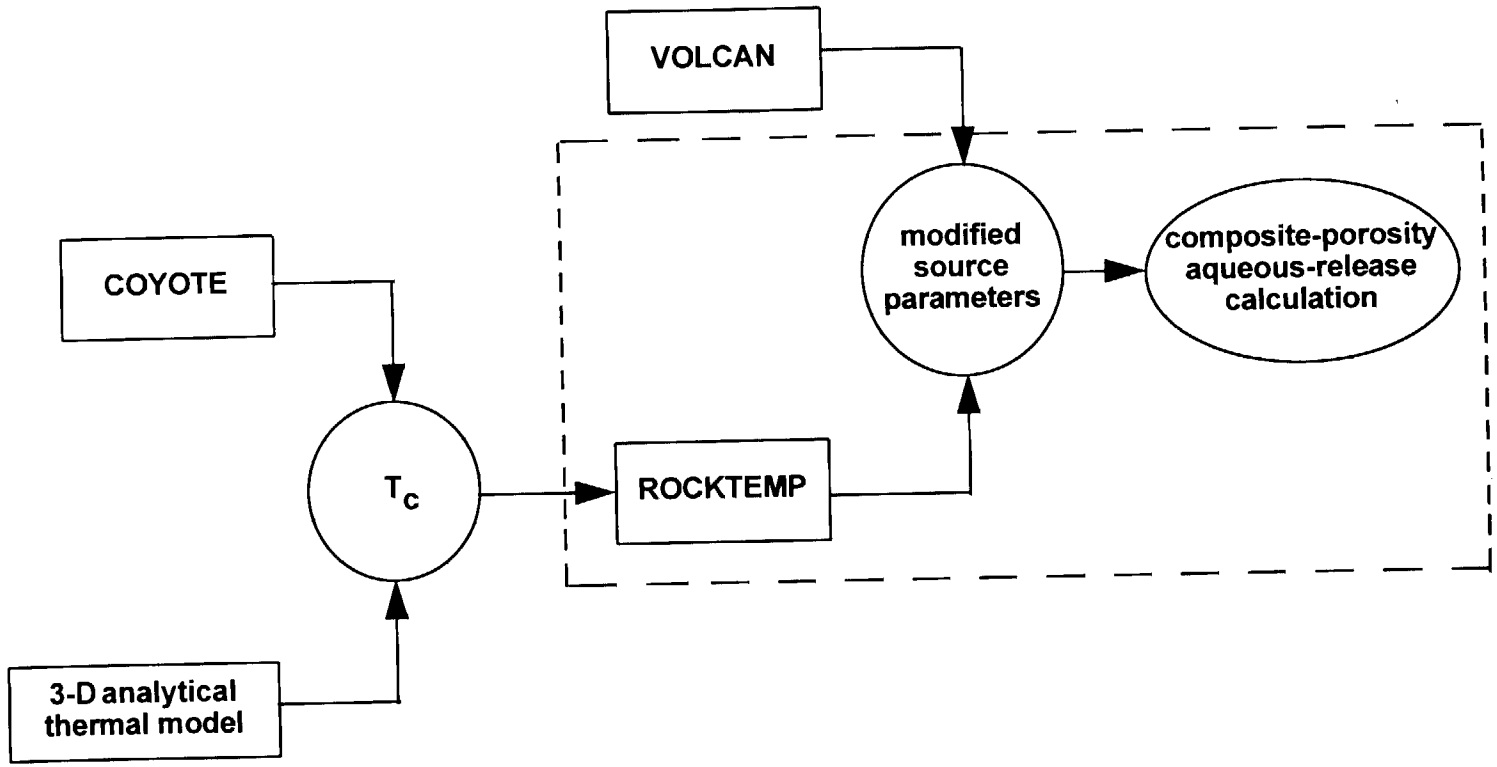

Figure 3-8. Flow chart showing computer programs used for calculation of basaltic-volcanism releases. Programs within the dashed box are run for each Monte Carlo realization.

are performed separately from each other and from the nominal simulations. This separation is made for convenience, and should be reconsidered in future TSPAs.

Note that this discussion includes only the major computer models used. Many subsidiary programs are used for data analysis, for pre- and post-processing, and for translating the output of one program into the form required for input to another. Such operations are largely straightforward and not necessary to discuss here.

3.4 Incorporation of uncertainty

A key part of a systems analysis is an examination of the uncertainty in the data available and an analysis of how that uncertainty affects the predictions of performance measures (that is, how uncertainty is propagated through the system from inputs to outputs).

Generally speaking, we recognize four types of uncertainty:

- *Measurement uncertainty.* In any laboratory measurement or field test, there is always some error, leading to uncertainty about the true value of the measured quantity. In natural systems, the measurement uncertainty can be significant because of the necessity of taking measurements on time and spatial scales short compared to the times and distances of interest. Note that measurement uncertainty includes uncertainty in the appropriate model to use for interpretation of measurements.

- *Spatial variability of material properties and boundary conditions.* In a natural system such as Yucca Mountain there is considerable spatial variability, and because the system cannot be sampled exhaustively, uncertainty about the spatial variability will always remain.

- *Temporal variability of material properties and boundary conditions.* Similarly, there is considerable temporal variability, especially over the long time periods of interest (thousands of years). We cannot predict the future with precision, so uncertainty about the temporal variability will always remain.

- *Model uncertainty.* Because of the limitations discussed in the previous items, there is uncertainty as to the appropriate conceptual model to use for some processes. Once again, some model uncertainty will probably always remain.

The uncertainties listed above are not, in and of themselves, of serious concern. What is of concern is how much uncertainty in the predictions of performance is caused by the above uncertainties. If a particular parameter has a possible range of several orders of magnitude, but estimates of performance are nearly the same when the parameter is varied over that range, then the parameter uncertainty is not important. However, even though a parameter

or model, when varied by itself, has no significant effect on performance, synergistic effects are still possible when it is varied in concert with some other parameter or model.

We use the following methods to incorporate uncertainties into the system simulations in Chapters 14 through 17.

- PDFs are developed for many parameters, based on available data, on results of detailed modeling, or on expert judgment. Discussion of data and PDF-development is concentrated in Chapters 7, 8, and 9, with additional discussion in Chapters 11 through 17. The different methods of PDF development are illustrated as follows. The PDFs discussed in Chapter 7 were developed using an objective method, from hydrogeologic data that have been compiled into a performance-assessment data base. The PDFs discussed in Chapter 9 were developed using a semi-formal expert-elicitation method. The PDFs discussed in Chapter 8 (and Chapters 12 through 17) were developed by the PA analysts themselves, with informal input from other experts. Some of the PDFs discussed in Chapter 11 were developed by analyzing the results of detailed-model calculations and considering the range of abstracted values.

- Two conceptual models of unsaturated-zone groundwater flow are considered (see Chapters 14 and 15), and the performance measures are calculated separately for the two models. Comparison of the results of the two models shows the uncertainty in the performance measures arising from the conceptual-model uncertainty considered (see Section 18.2). Two conceptual models of saturated-zone groundwater flow are also considered (see Chapter 11). This uncertainty is not carried all the way through the systems analysis, as the UZ model uncertainty is, but rather is incorporated into uncertainty of a system parameter (see Section 11.6).

  The treatment of the four repository cases (two thermal loads combined with two container/emplacement options) is akin to the treatment of conceptual-model uncertainty, only the four cases do not represent uncertainty but rather multiple design options.

- The method used to propagate parameter uncertainty through to performance-measure uncertainty is the Monte Carlo method, in which multiple equally likely "realizations" of the system are generated by sampling parameter values from their PDFs. The performance measures are computed for each realization, leading to distributions of performance-measure values. A general illustration of the method is shown in Figure 3-9.

Because of independent development of models for different release categories (e.g., nominal, human intrusion, volcanism), we do not use a single system code for the Monte Carlo simulations; there are three.

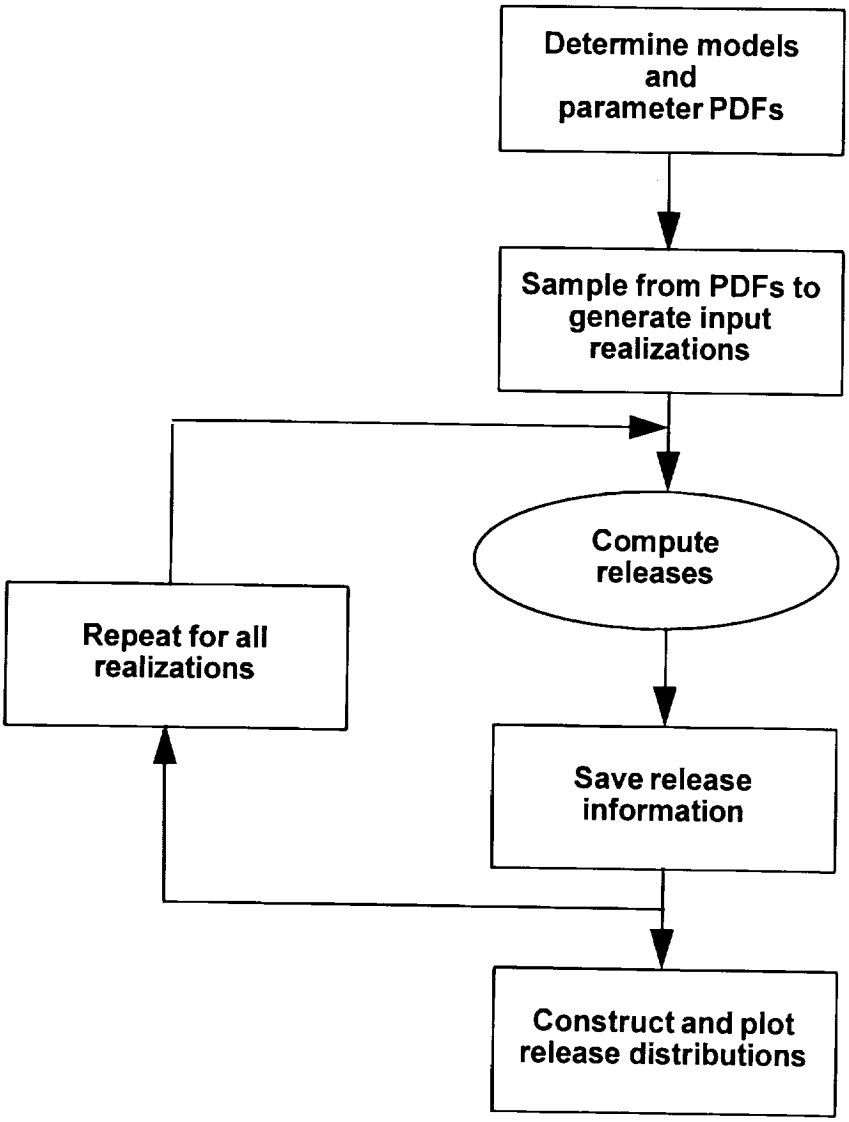

Figure 3-9. Flow chart illustrating the Monte Carlo method. The step called "Compute releases" corresponds to a run of the programs inside the dashed box in Figure 3-6, 3-7, or 3-8.

Monte Carlo simulation of nominal releases is done with the total-system analyzer (TSA; Wilson *et al.*, 1991, Wilson, 1992). The TSA is a shell (written in the UNIX C-shell language) for running multiple realizations of stand-alone programs. It is very flexible: it takes only minutes to develop a TSA shell to run a particular sequence of programs, unless a new translation program is needed for converting the output of a program to the form needed for input to another program. The LHS program (Iman and Shortencarier, 1984), an implementation of the Latin-hypercube sampling method, is used to generate the realizations

from the input PDFs. Depending on the analysis, TOSPAC, WEEPTSA, SRCTSA, and/or GASTSA may be run within the TSA.

Monte Carlo simulation of human intrusion is done using the DRILL program. In addition to its role as a model for calculating human-intrusion releases, DRILL also contains its own sampling routines and can calculate releases for a large number of drilling realizations efficiently. DRILL contains its own random-sampling routine and also uses the LHS program (converted to a callable subroutine) for sampling.

Monte Carlo simulation of direct releases due to volcanism is done using the VOLCAN program. Direct volcanism releases are not simulated for this TSPA, but were simulated for TSPA-91. VOLCAN is similar to DRILL, and in fact they share many routines. For simulation of indirect magmatic releases, VOLCAN is run separately to generate the number of containers affected for each realization, and then the TSA is run with ROCKTEMP linked to TOSPAC to calculate aqueous releases with a modified source term.

Part II

Data Development

Chapters 4 through 9 deal with input data needed for the computer models of release processes. (The computer models used are introduced in Chapter 3. Details are given in later chapters as the computations are discussed.)

Chapter 4 introduces the potential repository and emplacement configurations considered for TSPA-93 and provides data on the repository area and the waste stream. Chapter 5 provides data on the radionuclide inventory. Chapter 6 discusses a geostatistical model that is used to generate the hydrogeologic stratigraphy for Yucca Mountain, and shows the model stratigraphies. Chapter 7 provides data on hydrogeologic parameters and discusses the methods used to develop probability distributions for them. Chapter 8 discusses infiltration, percolation, and climate change, and gives the assumptions used to model them. Chapter 9 provides data on geochemical parameters.

Below is a duplication of the document "road map" (Figure 1-1), with the items for this part highlighted.

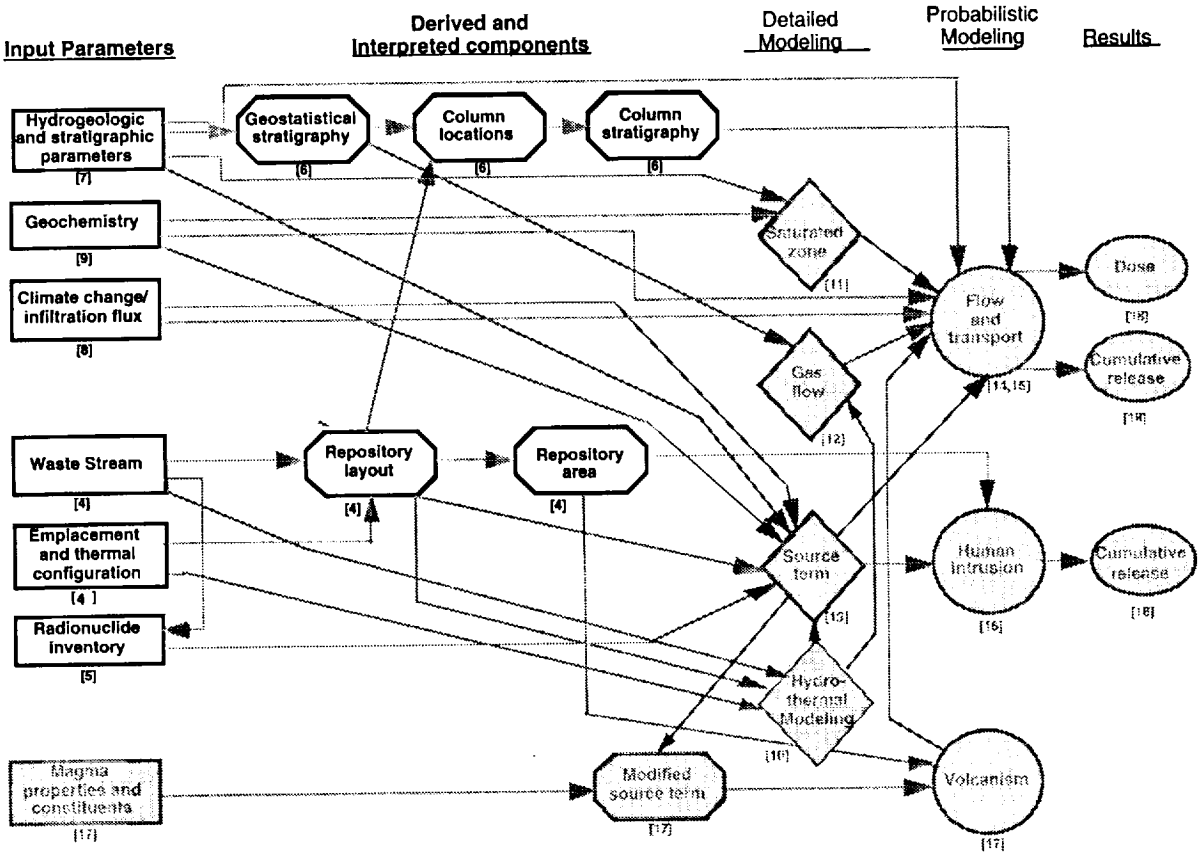

Chapter 4
Repository Areas and Layouts

(Barnard, Ryder, Halsey)

The original conceptual design for a potential nuclear-waste repository at the Yucca Mountain site is described in the Site Characterization Plan–Conceptual Design Report (SCP–CDR) (SNL, 1987). The conceptual design specifies waste-package design, mode of emplacement, nominal areal thermal power density, expected age of the waste, and total mass of the waste. The conceptual design forms the basis for investigations of design alternatives and their potential impact on radionuclide releases. YMP is currently investigating alternative waste-package designs (e.g., larger capacity, different shielding), modes of emplacement (e.g., in-drift *vs.* vertical-borehole), and areal thermal power densities ("thermal loading"). Some of the alternatives can affect the underground space required for a repository through a reduction in heated-area requirements and the layout of the repository.

For TSPA-93, two waste-package designs, two emplacement modes, and two repository thermal-loading options have been analyzed in limited combinations with respect to their effects on releases and doses.

4.1 Design changes

The purpose of exploring alternative designs is to provide greater confidence in meeting waste-package containment requirements, as set forth in 10 CFR Part 60. The focus has been on two issues, the container design and the thermal power density of the repository.

Since completion of the SCP–CDR, there has been interest in investigating higher-performance waste packages that would provide greater confidence in meeting the containment requirements. The approach to these alternative waste packages includes the principles of defense in depth and redundant barriers, as recognized by the NRC in reactor licensing. There are two classes of containers being considered—a "robust" container and a multipurpose container (MPC). The robust container has a greater capacity, and has more shielding than the designs described in the SCP–CDR. The MPC is a container that could be loaded at each reactor site, could be used for interim storage, for transportation, and for disposal. Overpacks, tailored to each application are feasible for each of these alternatives (as well as for the SCP–CDR design). These ideas are being examined in a series of waste-package design and MPC system studies addressing cost/benefit issues. Because these alternative designs could affect repository performance, it was decided to analyze a representative large robust waste package and a design representative of those discussed in the

SCP–CDR in TSPA-93. (The MPC can at this stage in design be considered a special case of the robust container.)

The second design change devolves from the issue of thermal power density for the loading of the repository. Analyses of experimental data obtained from G-Tunnel heater tests (Zimmerman *et al.*, 1986; Ramirez *et al.*, 1991) and modeling studies of idealized representations of Yucca Mountain (Buscheck and Nitao, 1991; 1993) have led to the suggestion that dryout of moisture in the mountain, and its return, can be controlled by changing the local thermal power density, e.g., by emplacing containers closer together. Increasing the power density reduces the underground area of the repository and may influence the layout. Since the studies apply to an idealized repository and mountain, how their results change for more detailed, less idealized representations is a matter of current study. Furthermore, the extent of the dryout may be a function of the hydrothermal model used. Questions arise regarding operational thermal problems and uncertainties regarding the persistence of an extended thermal transient on the properties of the natural system. These issues are being addressed in a series of studies investigating repository thermal behavior. Because the thermal loading could change repository performance, it was decided to include as much thermal dependence as practical in TSPA-93 and to examine both SCP-design and elevated thermal-loading cases. The thermal analyses are discussed in Chapter 10.

4.2 Waste-package design

4.2.1 SCP configuration

The SCP conceptual design was envisioned as a repository containing 70,000 metric tons of high-level radioactive waste, consisting primarily spent nuclear-reactor fuel. The SCP reference waste-package design is one that is based on fuel-assembly consolidation (although other options involving non-consolidation were also considered). With the decision by YMP not to consolidate, the alternative designs presented in the SCP are now being evaluated. The alternative spent-fuel package proposed in the SCP is a thin-walled circular cylinder constructed of a corrosion-resistant high-nickel alloy (such as Alloy 825). The waste container has an outer diameter of 0.71 m, wall thickness of 0.95 cm, and an overall length of 4.76 m. This package is capable of handling either 4 fuel assemblies from a pressurized water reactor (PWR), 10 fuel assemblies from a boiling water reactor (BWR), or a combination of 3 PWR and 4 BWR assemblies (Figure 4-1). The container can hold the equivalent of about 2 metric tons of spent fuel (expressed as the quantity of uranium originally in the fuel assembly—MTU). The overall weight of the package would be on the order of 5 metric tons, depending on the specific assemblies chosen.

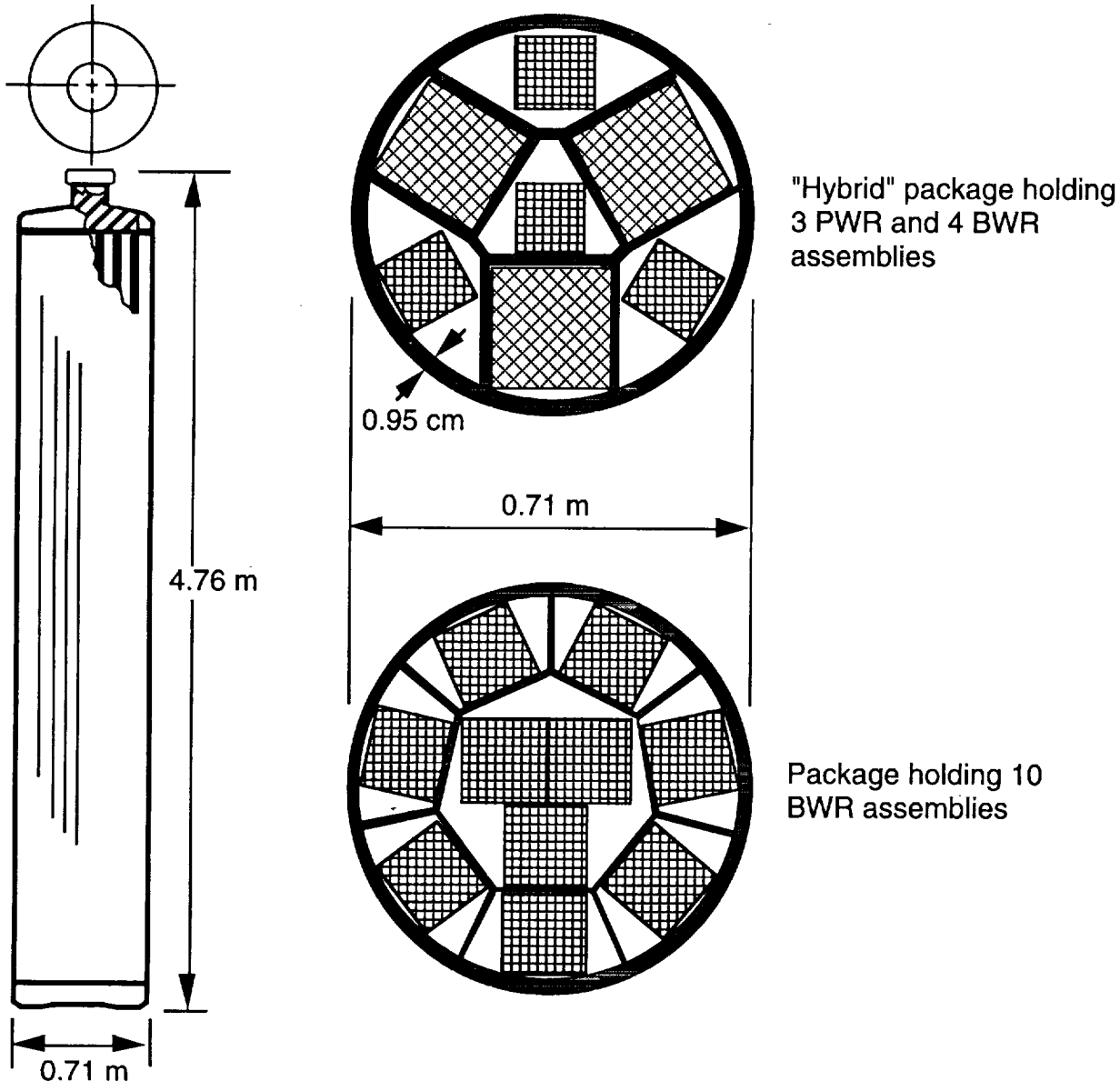

Figure 4-1. SCP waste-package design (after DOE, 1988a).

4.2.2 Alternative configuration

The recent YMP emphasis has been on examining waste-package designs that have a greater waste capacity than the SCP container. The designs examined have included containers not only with increased capacity, but also with two or more layers of corrosion-allowance and/or corrosion-resistant materials. One of these designs has been incorporated into the TSPA-93 analyses. It is a non-self-shielded, metallic multi-barrier concept proposed to hold either 21 PWR or 40 BWR assemblies (see Figure 4-2). With an inner diameter of 1.52 m and an outer diameter of 1.75 m, this design has a support-wall thickness of

3.0 cm and a 0.95-cm-thick first barrier (made of corrosion-resistant Alloy 825 separated by 0.6 cm from a 10-cm mild steel outer barrier. The length of this package is 4.91 m and, depending on loading, could weigh in excess of 50 metric tons. It is designed to hold about 7.5 MTU of BWR spent fuel, or 9.2 MTU of PWR spent fuel, depending on the reactor fuel assemblies chosen.

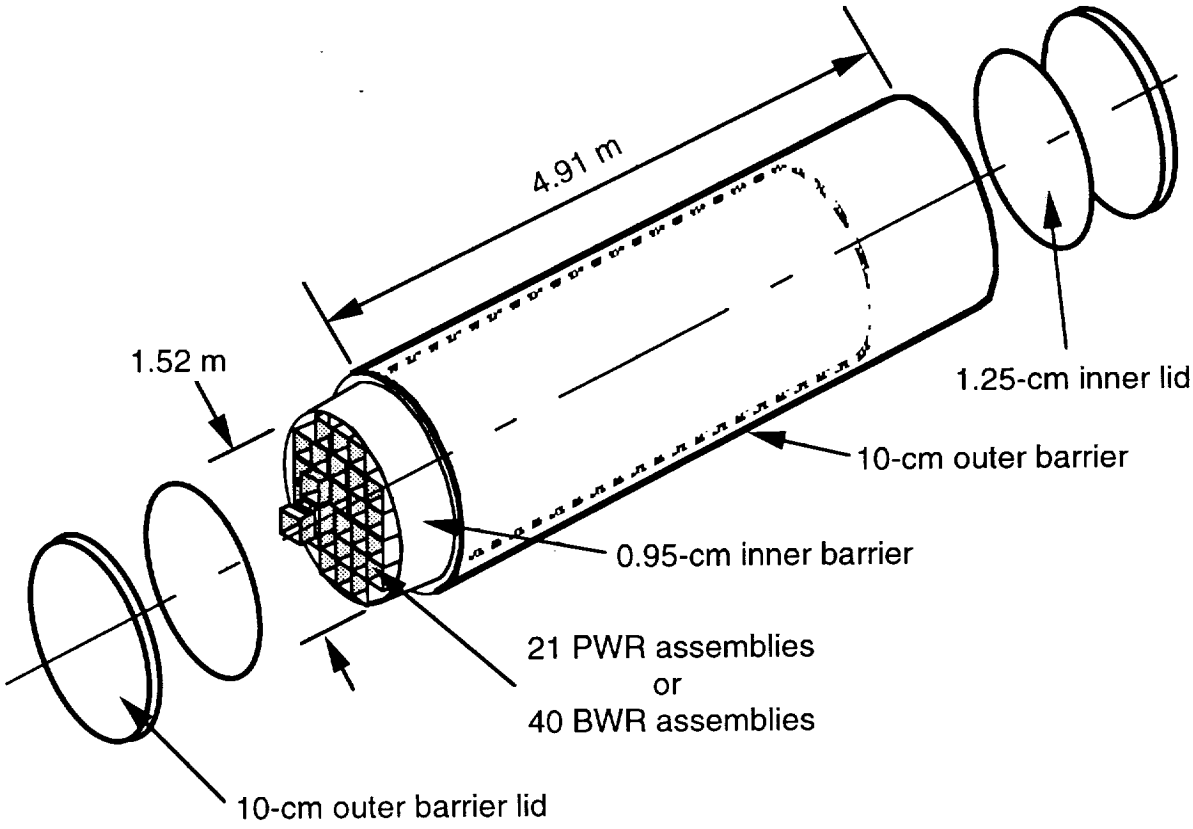

Figure 4-2. In-drift waste-package design (after DOE, 1993a).

4.3 Emplacement

4.3.1 SCP emplacement

According to the SCP design, the waste containers are placed in the repository in boreholes (either drilled vertically into the floor or horizontally into the walls of the em placement drifts). The vertical emplacement has been given the most consideration, and it is only that orientation that is modeled here. Figure 4-3 shows that the SCP design assumes 7.62-m (25 ft) deep boreholes for spent-fuel disposal, allowing for a 3.05-m (10 ft) separation between the top of a waste package and the drift floor. Such a disposal technique requires that the packages be of a size and weight that can be tilted and lowered into (or retrieved from) a borehole. It would require in excess of 30,000 SCP-style containers to

hold the 70,000 metric tons of waste. This emplacement configuration is called "borehole," or "vertical" emplacement in this document.

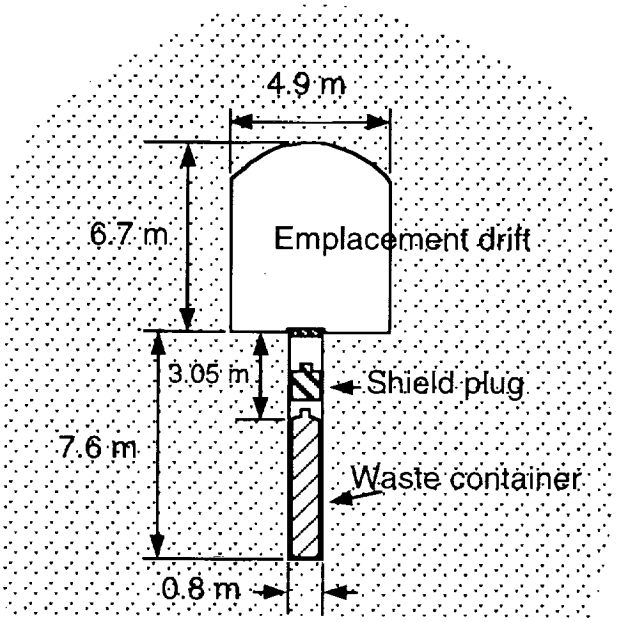

Figure 4-3. Borehole-emplacement configuration.

4.3.2 Alternative emplacement

The larger waste-package size leads to consideration of horizontal emplacement of waste packages on the floors of the repository drifts (Figure 4-4). It may be impractical to expect to be able to retrieve such large packages from boreholes. This method of emplacement has received attention in the past (Gram *et al.*, 1985), and is currently being pursued as an option during the advanced conceptual design of the repository. This configuration is called "in-drift" emplacement in this document.

4.4 Other issues affecting thermal loading

The decay of the radioactive waste can produce considerable heat. The accumulated heat from all the packages in the repository creates repository-scale thermal effects (e.g., heating, dryout, etc.) in the surrounding rock (see Sections 10.1 and 10.2). The amount of heat produced varies with time, and is a function of the time that the radioisotopes have decayed (fuel "age") and the original irradiation of the fuel in the nuclear reactors (fuel "burnup"). Burnup depends on many factors associated with reactor design, fuel-assembly design, and most importantly, with reactor operation and fuel management. Burnup is described in terms of megawatt-days/MTU (MWd/MTU), and is a measure of the number of fissions the fuel has undergone. This controls the amount of fission products and fission-

produced actinides in the spent fuel. It is the radioactive products that decay and produce heat.

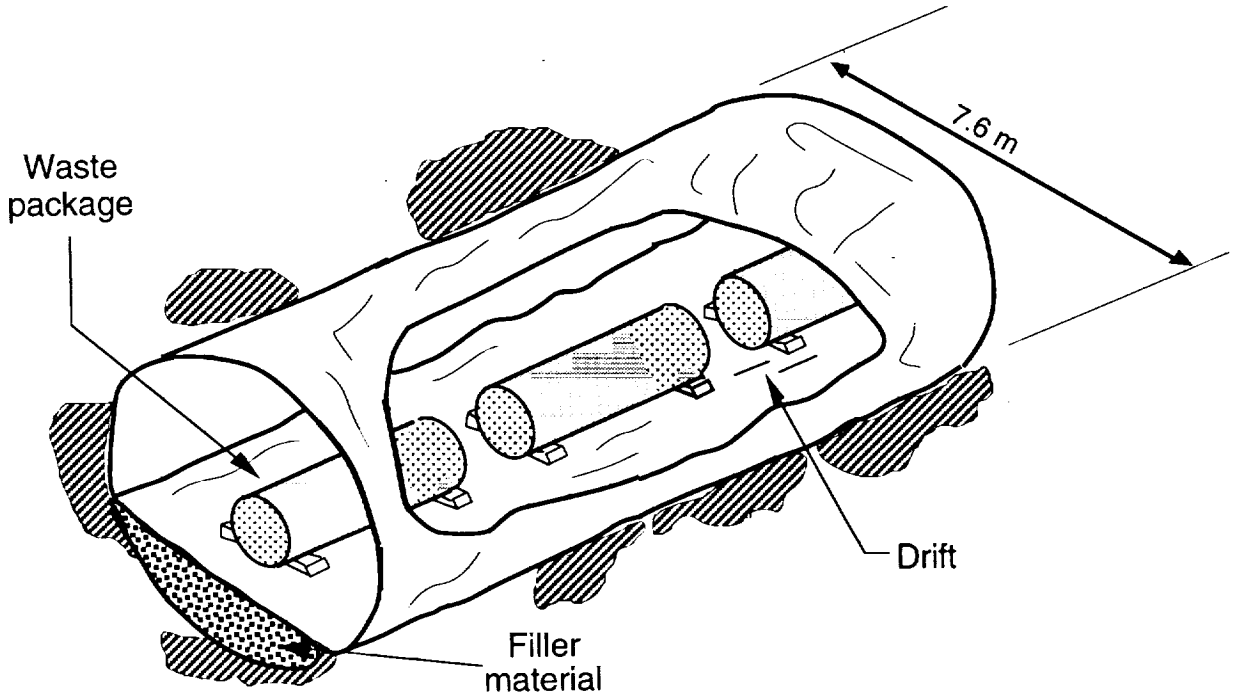

Figure 4-4. In-drift emplacement configuration.

4.4.1 Waste-acceptance schedule

In addition to waste-package design, the rate at which waste is placed in a repository (considerations for operations and access) and its age and amount of burnup (both of which affect thermal output) also influence the required repository area. The waste-acceptance schedule ("waste stream") is a detailed characterization of the yearly receipt of waste.

As reported by the DOE Energy Information Administration (DOE, 1992a), historical and projected data on spent fuel indicate that approximately 87,000 metric tons of spent fuel will be available for permanent disposal by the end of discharge year 2037. This inventory of spent fuel represents the discharge from approximately 115 commercial reactors and assumes a "No New Orders–Extended Burnup" projection scenario. For this scenario it is assumed that there will be no future orders for domestic reactors, and that any reactor not currently under construction (or granted a license for construction) has been canceled. Furthermore, it is assumed that in the future fuel used in existing reactors will be designed to operate to higher levels of burnup.

Although approximately 87,000 tons of spent fuel will ultimately be available for disposal, the Mission Plan Amendment (MPA) (DOE, 1988b) specifies that 63,020 metric tons

of spent fuel and 6,980 metric tons of defense high-level waste (HLW) are to be emplaced in the nation's first repository. Emplacement is assumed to start in the year 2010 and continue for 25 years. The yearly rate of emplacement increases during the first 6 years, and decreases for the final 2 years. Table 4-1 lists the MPA acceptance schedule.

Table 4-1. Waste-receipt schedule based on the DOE Mission Plan Amendment.

Emplacement Year	Schedule of Receipt (MTU)	Emplacement Year	Schedule of Receipt (MTU)
2010	400	2023	3000
2011	400	2024	3000
2012	400	2025	3000
2013	900	2026	3000
2014	1800	2027	3000
2015	3000	2028	3000
2016	3000	2029	3000
2017	3000	2030	3000
2018	3000	2031	3000
2019	3000	2032	3000
2020	3000	2033	2700
2021	3000	2034	2420
2022	3000		
Total			**63020**

The tonnage requirements of the MPA represent only one of the constraints that must be adhered to when defining a waste stream for the repository. In addition to the tonnage constraints of the MPA, there are allocation and pickup priorities that must be observed. *Allocations* provide each reactor site the right to deliver a specified number of assemblies to the federal waste management system, but do not identify the specific assemblies that must be delivered. When these constraints are coupled with additional considerations such as the possible existence of a monitored retrievable storage facility (MRS), emergency scenarios that alter pickup priorities, specific waste-package designs, and the constraint that spent fuel must be aged at least 5 years before pickup, a myriad of repository waste-stream characteristics can be defined.

For TSPA-93 analyses, a "double-blended" waste stream (as generated using the WSA code) is assumed (Andress and McLeod, 1988). This waste stream assumes complete freedom to select fuel at reactors and assumes the ability to fully blend both PWR and BWR fuels of all ages at the MRS. No alteration in pickup priorities is considered and the MPA tonnage schedule is observed.

Tables 4-2 and 4-3 list the schedules for the receipt of spent fuel for the waste streams for both the borehole-emplacement and in-drift-emplacement repositories. As the tables

show, the double-blended waste streams for both emplacement configurations do not greatly deviate from the MPA schedule. The difference between the waste stream for vertical-borehole emplacement and the in-drift emplacement arises because of yearly differences in availability of the proper amounts of waste to fill the packages.

Table 4-2. Waste-acceptance schedule for borehole-emplacement waste packages.

Emplacement Year	BWR Spent Fuel			PWR Spent Fuel			Total MTU	Departure from MPA
	Quantity (MTU)	Decay Age (years)	Burnup (MWd/MTU)	Quantity (MTU)	Decay Age (years)	Burnup (MWd/MTU)		
2010	12.70	40.85	11553.07	347.89	18.12	36873.70	360.59	-9.9%
2011	0.00	0.00	0.00	363.39	19.72	37412.03	363.39	-9.2%
2012	158.20	24.74	24641.83	259.25	17.59	42084.23	417.45	4.4%
2013	324.25	25.44	24788.13	594.23	19.36	39161.90	918.48	2.1%
2014	589.57	21.91	30773.48	1206.41	22.13	38599.01	1795.98	-0.2%
2015	1005.58	25.69	28191.15	2006.08	21.40	38597.37	3011.66	0.4%
2016	1294.64	24.84	29453.85	1734.03	21.26	39787.53	3028.67	1.0%
2017	899.96	26.20	29403.35	2092.99	21.50	39901.46	2992.95	-0.2%
2018	1050.26	23.87	31209.80	1951.87	22.63	39358.13	3002.13	0.1%
2019	1179.53	26.26	31758.24	1818.78	22.54	39668.91	2998.31	-0.1%
2020	1046.86	24.14	32581.97	1891.56	23.52	40304.66	2938.42	-2.1%
2021	749.77	24.27	33172.17	2242.64	25.98	37920.59	2992.41	-0.3%
2022	1156.78	28.19	31348.07	1876.58	24.74	40664.22	3033.36	1.1%
2023	1187.81	27.32	32882.31	1826.69	23.72	41207.96	3014.50	0.5%
2024	1074.23	27.45	32940.98	1915.53	25.30	41636.73	2989.76	-0.3%
2025	1177.16	28.96	32518.56	1787.87	24.78	43655.57	2965.03	-1.2%
2026	1213.31	28.71	31475.13	1818.01	26.22	42819.62	3031.32	1.0%
2027	1096.45	26.78	32801.30	1890.08	26.70	41881.96	2986.53	-0.4%
2028	1087.87	28.40	29929.91	1904.57	26.87	43342.75	2992.44	-0.3%
2029	1204.51	22.41	31350.01	1789.89	27.60	42354.09	2994.40	-0.2%
2030	538.91	30.62	32529.54	2457.02	26.14	41107.32	2995.93	-0.1%
2031	1089.51	28.97	31115.83	1956.25	26.62	43027.55	3045.76	1.5%
2032	940.34	27.17	33912.42	2027.64	29.89	40924.41	2967.98	-1.1%
2033	832.84	30.18	33292.34	1908.15	35.38	37079.19	2740.99	1.5%
2034	1336.57	22.30	33672.74	1081.61	39.99	34883.40	2418.18	-0.1%
Totals	**22247.6**			**40749.0**			**62996.6**	**0.0%**

The use of the double-blended waste stream implies that as the repository is filled, the waste being emplaced has fairly constant thermal-power output and radionuclide inventory. Illustrations of the uniformity of the thermal-power output and waste age are given in Figure 10-3 in Chapter 10 for the in-drift containers. Our modeling of the TSPA-93 source-term inventory and the thermal behavior is simplified if these characteristics do not vary greatly at different times, or at different locations in the repository. We therefore assume that the waste has constant nuclear and thermal properties at the time of emplacement, which makes the calculations applicable over the entire repository.

Table 4-3. Waste-acceptance schedule for in-drift-emplacement waste packages.

Emplacement Year	BWR Spent Fuel			PWR Spent Fuel			Total MTU	Departure from MPA
	Quantity (MTU)	Decay Age (years)	Burnup (MWd/MTU)	Quantity (MTU)	Decay Age (years)	Burnup (MWd/MTU)		
2010	5.58	41.11	12613.16	344.65	18.13	36779.78	350.23	-12.4%
2011	0.00	0.00	0.00	358.60	19.75	37426.82	358.60	-10.4%
2012	157.29	25.33	24237.30	259.80	17.61	42073.38	417.09	4.3%
2013	323.09	25.46	24771.58	591.27	19.38	39184.34	914.36	1.6%
2014	582.50	21.94	30724.76	1203.59	22.14	38538.80	1786.09	-0.8%
2015	1005.43	25.70	28181.27	2003.59	21.40	38595.47	3009.02	0.3%
2016	1295.29	24.84	29455.44	1732.08	21.28	39755.07	3027.37	0.9%
2017	899.96	26.20	29401.96	2089.11	21.50	39892.38	2989.07	-0.4%
2018	1044.90	23.90	31178.82	1945.92	22.64	39353.89	2990.82	-0.3%
2019	1178.88	26.27	31739.72	1810.06	22.52	39626.57	2988.94	-0.4%
2020	1038.25	24.17	32567.00	1894.64	23.54	40309.07	2932.89	-2.2%
2021	754.70	24.27	33160.96	2240.09	25.97	37930.76	2994.79	-0.2%
2022	1148.80	28.25	31295.66	1876.99	24.77	40649.53	3025.79	0.9%
2023	1185.37	27.35	32859.06	1822.51	23.73	41177.14	3007.88	0.3%
2024	1067.33	27.52	32911.06	1911.08	25.32	41589.04	2978.41	-0.7%
2025	1175.17	28.97	32472.49	1776.30	24.83	43597.54	2951.47	-1.6%
2026	1210.28	28.74	31454.05	1814.20	26.24	42758.88	3024.48	0.8%
2027	1084.64	26.86	32736.66	1871.21	26.77	41774.06	2955.85	-1.5%
2028	1083.60	28.44	29918.28	1893.81	26.93	43239.89	2977.41	-0.8%
2029	1204.70	22.42	31355.11	1788.32	27.61	42347.38	2993.02	-0.2%
2030	538.58	30.47	32553.29	2457.08	26.13	41108.64	2995.66	-0.1%
2031	1090.49	29.02	31089.58	1948.30	26.63	43007.34	3038.79	1.3%
2032	941.91	27.15	33902.88	2027.92	29.94	40922.64	2969.83	-1.0%
2033	835.75	30.17	33312.50	1908.09	35.34	37070.12	2743.84	1.6%
2034	1330.10	22.35	33642.15	1077.22	39.97	34856.19	2407.32	-0.5%
Totals	**22182.6**			**40646.4**			**62829.0**	**-0.3%**

4.4.2 Waste-emplacement density

The waste packages have a heat output at time of emplacement that depends on the burnup and decay of the spent fuel. Their spacing in the repository at emplacement therefore determines the local areal power density (LAPD—given in kilowatts/acre). At the time of emplacement, thermal areal power densities are achieved by controlling the spacing among nearest-neighbor waste packages. The waste streams in Section 4.4.1 are levelized streams, chosen to minimize fluctuations in the thermal power of the as-received waste.

The heat output from HLW canisters is considered to be negligible; since these canisters make little contribution to the heat generation, they generally do not require additional area for emplacement, and often can be located between spent-fuel containers. Because the in-drift containers hold more waste than the borehole containers (7 to 9 MTU *vs.* 2 MTU), there are fewer containers required. However, to maintain a specified thermal loading they must be spaced farther apart because of their greater initial heat output.

4.4.3 Repository layout assumptions

In the SCP–CDR, a repository composed of a series of emplacement panels is described. Emplacement panels are approximately rectangular in shape and extend from the outer main drift to the perimeter of the repository (Figure 4-5). The principal access to the emplacement panels are provided by three main drifts that run the length of the repository. Panel-access drifts lead from the main drifts to the emplacement drifts within the panels.

YMP has chosen to use a tunnel-boring machine (TBM) for the construction of the repository, in place of a drill-and-blast construction method described in the SCP–CDR. Consequently, several changes in repository layout have been proposed. First, the panel structure documented in the SCP–CDR has been abandoned in favor of a series of emplacement drifts that run approximately perpendicular to the main access drifts (Figure 4-6). Depending on the repository area required, the emplacement drifts can be located on both sides of the main drift, or only on one side. The emplacement drifts are assumed to be 7.62 m in diameter, with a centerline spacing of 25.4 m between drifts.

4.5 Emplacement/thermal-loading cases analyzed in TSPA-93

A goal of the TSPA-93 analyses is to include waste-package design and emplacement options and thermal-loading configurations representative of the alternatives described above, and reflective of current YMP interests. Both the thin-walled borehole-emplacement waste package and the alternative in-drift-emplacement package are included. The double-blended waste stream, with local areal power densities of 57 kW/acre and 114 kW/acre, is examined. The former value is that specified in the SCP–CDR, whereas the latter has been used in some of the studies of alternative thermal loadings discussed in Section 4.1. Lastly, a repository layout based on the TBM construction method has been chosen. Table 4-4 lists the analysis cases and some of the attributes of the waste packages.

Table 4-4. Emplacement/thermal-loading cases analyzed.

Emplacement Mode	Thermal Loading (kW/acre)	Container Description	Waste Capacity
Vertical, in-borehole	57	Thin-wall, corrosion-resistant high-nickel alloy	4 BWR + 3 PWR, or 10 BWR, or 4 PWR; 2 MTU/container
Vertical, in-borehole	114	Thin-wall, corrosion-resistant high-nickel alloy	4 BWR + 3 PWR, or 10 BWR, or 4 PWR; 2 MTU/container
Horizontal, in-drift	57	Mild-steel corrosion-allowance overpack with thin-wall high-nickel alloy inner layer	40 BWR, or 21 PWR; 8 MTU/container
Horizontal, in-drift	114	Mild-steel corrosion-allowance overpack with thin-wall high-nickel alloy inner layer	40 BWR, or 21 PWR; 8 MTU/container

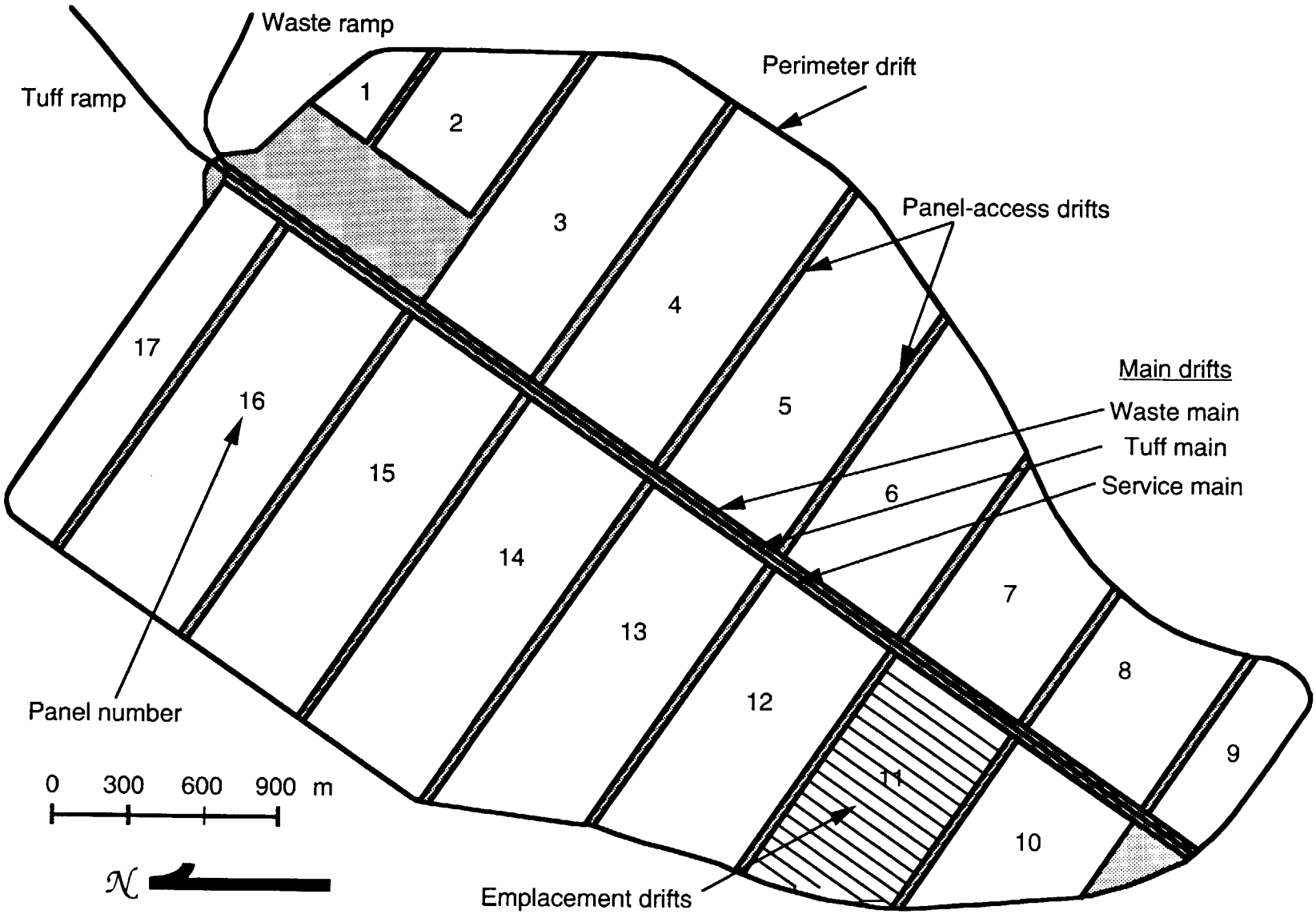

Figure 4-5. SCP-CDR repository layout (after DOE, 1988a).

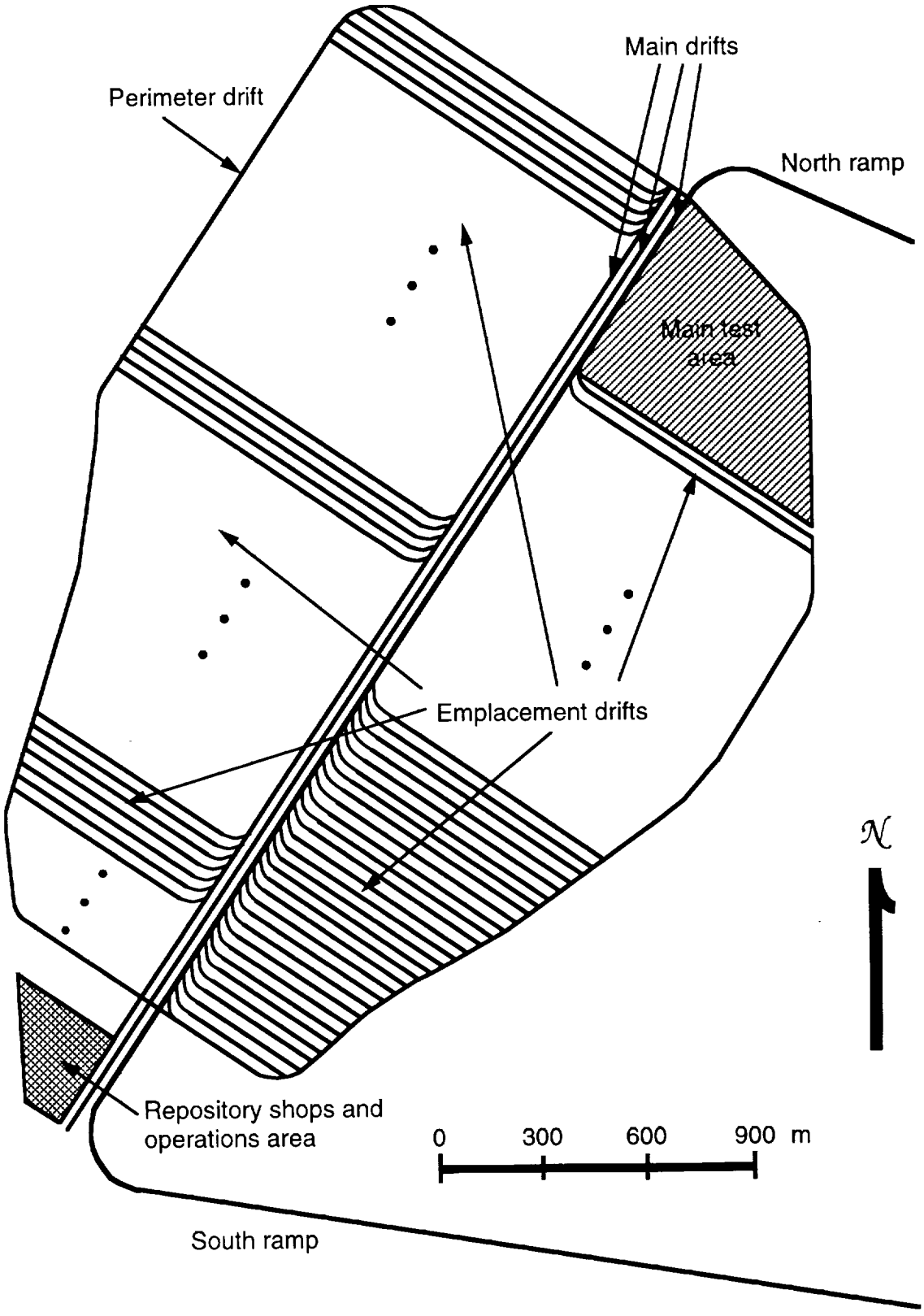

Figure 4-6. Alternative repository layout based on tunnel-boring machine construction.

4.6 Repository areas

The factor used to describe the physical extent of the various repository configurations for modeling purposes is the repository heated area. This is the underground area necessary to contain the waste that has been emplaced in a specified waste-package design at a specified LAPD. It is the area that creates the heat source for the thermal calculations described in Chapter 10. It does not include support areas such as shops, testing areas, etc. It is the heated area that is the major factor in the hydrothermal calculations; the gross repository area is not considered in our calculations, even though inclusion of these areas could affect some aspects of repository behavior. In general, the heated area of a repository is described by the waste stream and the specified thermal loading. The gross area is controlled by the waste stream, the thermal loading and the layout. Throughout this document, references to repository area are to the heated area, unless otherwise noted.

For TSPA-93, the two thermal loadings—57 kW/acre and 114 kW/acre—and the two waste-package designs produce four repository areas. Figure 4-7 shows the modeled repository heated area for the borehole, 57-kW/acre case (indicated by the shading). The repository area is divided into two main sections, separated by a corridor where the main drifts are located. (The gross repository area for this configuration is somewhat larger than the heated area because it includes the main-drift corridor, and support and testing areas.) Also shown on Figure 4-7 is the perimeter drift that determines the gross area of the SCP conceptual design of the potential Yucca Mountain repository. The differences between the two areas arise because of different assumptions about the total thermal output of the waste to be emplaced, and because of the changes in the assumptions about layout of the repository. Specifically, the SCP assumed a waste stream that had about 40 to 50 MW thermal output, while the double-blended waste stream has an output of about 60 MW; the greater thermal output requires a larger repository heated area to produce the same thermal loading. Redesign of the of the repository to incorporate the concept of ramp access has required setting aside area in the southern end of the repository block previously intended in the SCP for waste emplacement, thus reducing the area available for waste.

Figure 4-8 shows the repository area for the in-drift, 114-kW/acre case. The higher thermal loading means that the waste packages are spaced sufficiently close to each other that they all fit on one side of the main-drift corridor shown in Figure 4-7. Figure 4-9 shows the area for the in-drift, 57-kW/acre case. It requires approximately the same area as for the vertical-borehole case of the same thermal loading.

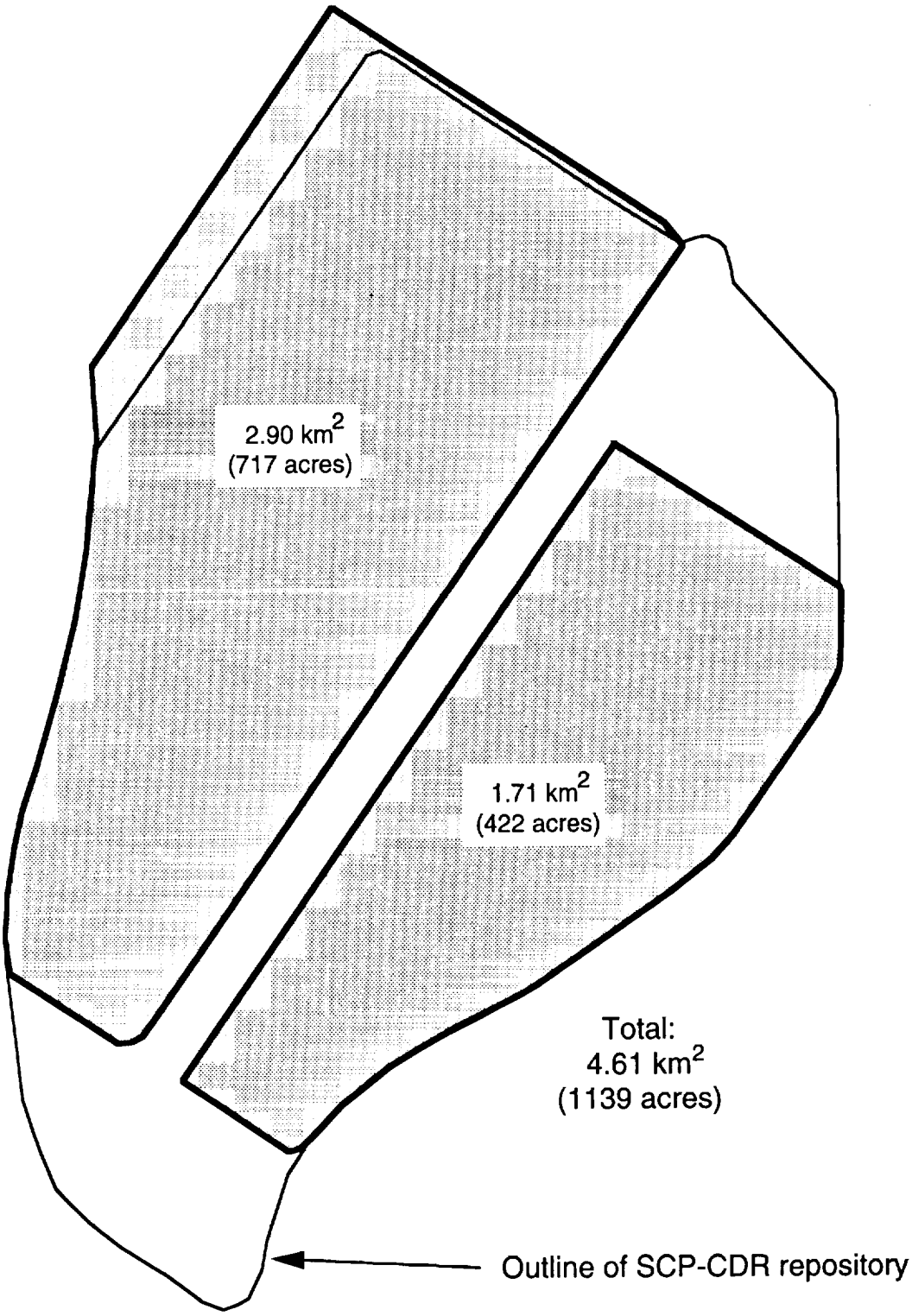

Figure 4-7. Repository area for 57-kW/acre borehole emplacement case.

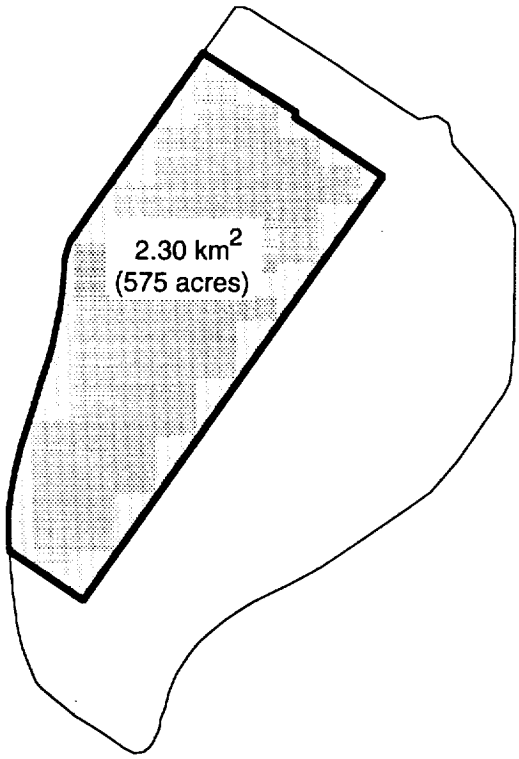

Figure 4-8. Repository area for 114-kW/acre in-drift emplacement case.

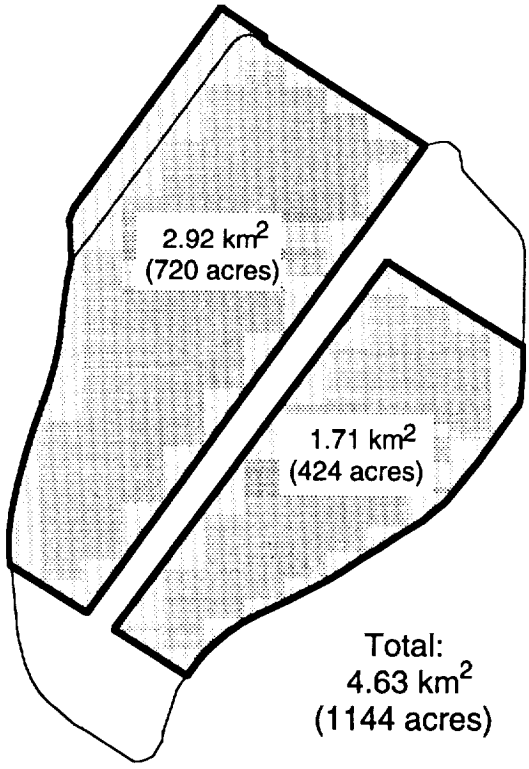

Figure 4-9. Repository area for 57-kW/acre in-drift emplacement case.

For all but the borehole, 114-kW/acre case, there is enough room between emplaced containers to locate the HLW canisters. Thus, the HLW does not increase the repository area in these cases. For this exceptional case, additional area must be provided. Assuming the same emplacement spacing for HLW canisters as for the spent-fuel containers, approximately seventy 1,500-ft drifts are needed to accommodate the HLW. This represents 840,000 m^2, or 200 acres, based on a 25.4-m drift spacing. This layout is shown in Figure 4-10. The extra area is only used for the human-intrusion analyses, since the repository area is a major factor in calculating releases. For the aqueous-release analyses, the area containing the spent fuel alone is used.

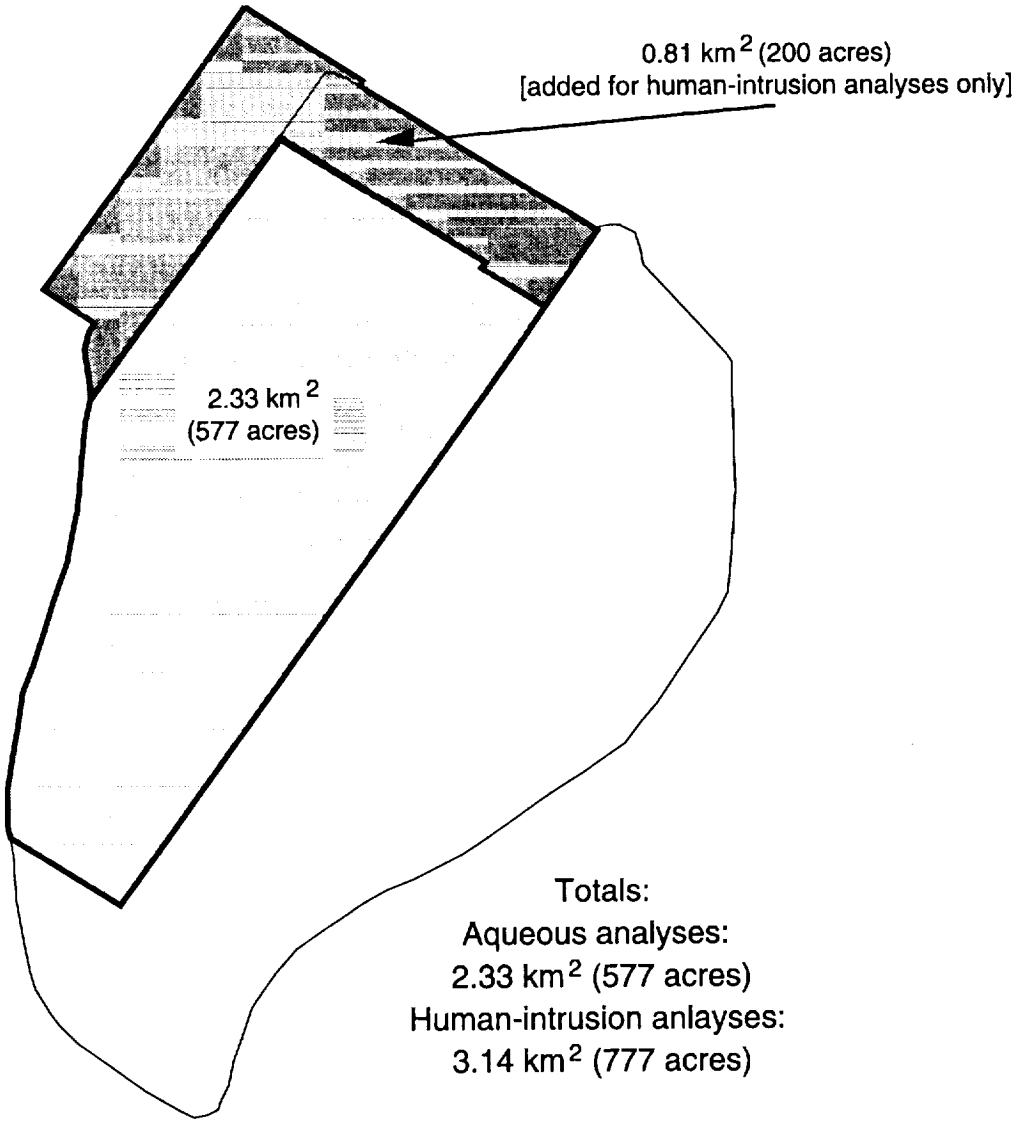

Figure 4-10. Repository area for 114-kW/acre borehole emplacement case, showing extra area needed for high-level waste canisters.

Table 4-5 lists the repository heated areas and waste-package spacings for the four cases. Because repository heated area is primarily controlled by the assumed emplacement density, the areas are almost the same for the two emplacement configurations at the same thermal loading.

Table 4-5. Repository areas and waste-package spacings for four emplacement configurations.

Emplacement Configuration	Heated Area (km^2)	Heated Area (acres)	Spacing (m)
Borehole, 57 kW/Ac	4.61	1139	5.6
Borehole, 114 kW/Ac	3.14[a]	777[a]	2.8
In-drift, 57 kW/Ac	4.63	1144	23.2
In-drift, 114 kW/Ac	2.33	575	11.6

[a] 2.33 km^2 (577 acres) for spent fuel, 0.81 km^2 (200 acres) for HLW.

Chapter 5
Radionuclide Inventory
(Barnard)

This chapter discusses the selection of radionuclides included in the source terms for the TSPA-93 analyses. Both reactor spent fuel and vitrified high-level waste are included in the inventory. In addition to using all the types of waste expected to be in the potential repository, a more realistic specification of the spent-fuel characteristics is used. The TSPA-91 inventory consisted only of spent fuel.

5.1 Spent Fuel

5.1.1 Spent-fuel inventory

The spent-fuel component of the radionuclide inventory used for the TSPA source term is based on the "double-blended" waste stream described in Section 4.4.1. It consists of the equivalent of approximately 63,000 metric tons of spent fuel (expressed as metric tons of uranium in the fuel as fabricated—MTU), from both boiling water reactors (BWRs) and pressurized water reactors (PWRs). Using the data from the waste stream given in Tables 4-2 and 4-3, we calculate the weighted average age and burnup (given in megawatt-days per MTU—MWd/MTU), for both the vertical-borehole and in-drift emplacement schemes. These values are given in Table 5-1. The weighted averages are constructed from the ages and burnups for each year of receipt for each reactor type, weighted by the quantities of spent fuel received from each type of reactor.

Table 5-1. Weighted-average age and burnup of spent fuel.

Reactor Type	Amount of Waste (MTU)	Percentage of Total Spent Fuel	Weighted-Average Age (years)	Weighted-Average Burnup (MWd/MTU)	Numbers of Packages: Hybrid (mixed types)	Numbers of Packages: Single-Type
			Borehole Emplacement			
BWR	22248	35.3	26.3	31550	28057	1215
PWR	40749	64.7	25.5	40461	–	2750
Totals	**62996**	**100**	–	–	**32022**	
			In-Drift Emplacement			
BWR	22183	35.3	26.4	31533	–	3109
PWR	40646	64.7	25.5	40433	–	4531
Totals	**62829**	**100**	–	–		**7640**

As was noted in Section 4.4.1, the total amount of spent fuel emplaced following the double-blended waste stream is very close to the amount specified in the Mission Plan Amendment. The differences in the amounts of PWR and BWR fuel for the two emplacement schemes are small, and they arise from differences in availability of the proper types of waste packages in some years.

Since the burnups and ages of each waste type for the two emplacement schemes are so similar, the borehole-emplacement waste stream has been used as the basis for constructing the inventory. For the purposes of determining the radiological properties of the spent fuel, both the BWR and PWR fuels are considered to have an age of 25 years, and burnups of 30,000 MWd/MTU and 40,000 MWd/MTU, respectively.

The weighted-average inventory (and other characteristics) are given in Table 5-2. The weighted average has been constructed from the percentages of the two sources of fuels. The table lists the inventories for fuels from BWRs and PWRs for the given decay ages and burnups. These inventories have been taken from the *Characteristics Data Base* (CDB) (DOE, 1992b). CDB data are generated from ORIGEN2 computer simulations (e.g., Roddy *et al.*, 1986) that calculate the depletion, buildup and decay of isotopes resulting from nuclear-reactor fuel operational cycles. To construct the database, ORIGEN2 models two reference reactors, a PWR and a BWR; the database lists radionuclide inventories for various burnup values and decay ages, based on appropriate values of initial fuel enrichment.

Table 5-2. Spent-fuel inventory and characteristics.

Isotope	Half Life (years)	Activity (Ci/mole)	EPA Limit (Ci/MTU)	25-yr, 30,000-MWd/MTU BWR Inventory (Ci/MTU)	25-yr, 40,000-MWd/MTU PWR Inventory (Ci/MTU)	Weighted-Average Spent-Fuel Inventory (Ci/MTU)
^{238}U	4.468×10^{9}	8.00×10^{-5}	0.1	3.18×10^{-1}	3.13×10^{-1}	3.15×10^{-1}
^{246}Cm	4.731×10^{3}	7.56×10^{1}	0.1	1.08×10^{-2}	4.39×10^{-2}	3.22×10^{-2}
^{242}Pu	3.869×10^{5}	9.24×10^{-1}	0.1	1.18×10^{0}	2.05×10^{0}	1.74×10^{0}
^{242m}Am	1.520×10^{2}	2.35×10^{3}	0.1	8.38×10^{0}	1.03×10^{1}	9.62×10^{0}
^{238}Pu	8.774×10^{1}	4.07×10^{3}	0.1	1.61×10^{3}	2.87×10^{3}	2.43×10^{3}
^{234}U	2.445×10^{5}	1.46×10^{0}	0.1	1.41×10^{0}	1.56×10^{0}	1.51×10^{0}
^{230}Th	7.700×10^{4}	4.64×10^{0}	0.01	3.53×10^{-4}	3.72×10^{-4}	3.65×10^{-4}
^{226}Ra	1.600×10^{3}	2.23×10^{2}	0.1	2.19×10^{-6}	2.24×10^{-6}	2.22×10^{-6}
^{210}Pb	2.230×10^{1}	1.60×10^{4}	1.0	5.34×10^{-7}	5.37×10^{-7}	5.36×10^{-7}
^{243}Cm	2.850×10^{1}	1.25×10^{4}	0.1	7.21×10^{0}	1.61×10^{1}	1.30×10^{1}
^{243}Am	7.380×10^{3}	4.84×10^{1}	0.1	1.00×10^{1}	2.09×10^{1}	1.71×10^{1}
^{239}Pu	2.406×10^{4}	1.49×10^{1}	0.1	2.97×10^{2}	3.53×10^{2}	3.33×10^{2}
^{235}U	7.038×10^{8}	5.08×10^{-4}	0.1	2.25×10^{-2}	2.30×10^{-2}	2.28×10^{-2}
^{231}Pa	3.277×10^{4}	1.09×10^{1}	0.1	3.53×10^{-5}	3.82×10^{-5}	3.72×10^{-5}
^{227}Ac	2.177×10^{1}	1.64×10^{4}	0.1	1.70×10^{-5}	1.85×10^{-5}	1.80×10^{-5}
^{245}Cm	8.499×10^{3}	4.21×10^{1}	0.1	6.24×10^{-2}	2.20×10^{-1}	1.64×10^{-1}

Table 5-2. Spent-fuel inventory and characteristics (continued).

Isotope	Half Life (years)	Activity (Ci/mole)	EPA Limit (Ci/MTU)	25-yr, 30,000-MWd/MTU BWR Inventory (Ci/MTU)	25-yr, 40,000-MWd/MTU PWR Inventory (Ci/MTU)	Weighted-Average Spent-Fuel Inventory (Ci/MTU)
^{241}Pu	$1.440x10^{1}$	$2.49x10^{4}$	—	$3.09x10^{4}$	$4.61x10^{4}$	$4.07x10^{4}$
^{241}Am	$4.322x10^{2}$	$8.27x10^{2}$	0.1	$2.50x10^{3}$	$3.67x10^{3}$	$3.26x10^{3}$
^{237}Np	$2.140x10^{6}$	$1.67x10^{-1}$	0.1	$2.87x10^{-1}$	$4.27x10^{-1}$	$3.78x10^{-1}$
^{233}U	$1.585x10^{5}$	$2.26x10^{0}$	0.1	$4.30x10^{-5}$	$6.57x10^{-5}$	$5.77x10^{-5}$
^{229}Th	$7.339x10^{3}$	$4.87x10^{1}$	0.1	$2.07x10^{-7}$	$3.66x10^{-7}$	$3.10x10^{-7}$
^{244}Cm	$1.811x10^{1}$	$1.98x10^{4}$	—	$3.52x10^{2}$	$9.86x10^{2}$	$7.62x10^{2}$
^{240}Pu	$6.537x10^{3}$	$5.47x10^{1}$	0.1	$4.64x10^{2}$	$5.34x10^{2}$	$5.09x10^{2}$
^{236}U	$2.341x10^{7}$	$1.53x10^{-2}$	0.1	$2.66x10^{-1}$	$3.37x10^{-1}$	$3.12x10^{-1}$
^{232}U	$7.200x10^{1}$	$4.97x10^{3}$	0.1	$1.79x10^{-2}$	$4.16x10^{-2}$	$3.32x10^{-2}$
^{151}Sm	$8.999x10^{1}$	$3.97x10^{3}$	1.0	$2.80x10^{2}$	$3.66x10^{2}$	$3.36x10^{2}$
^{137}Cs	$3.000x10^{1}$	$1.19x10^{4}$	1.0	$5.19x10^{4}$	$6.96x10^{4}$	$6.33x10^{4}$
^{135}Cs	$2.300x10^{6}$	$1.55x10^{-1}$	1.0	$4.32x10^{-1}$	$5.04x10^{-1}$	$4.79x10^{-1}$
^{129}I	$1.570x10^{7}$	$2.28x10^{-2}$	0.1	$2.75x10^{-2}$	$3.74x10^{-2}$	$3.39x10^{-2}$
^{126}Sn	$1.000x10^{5}$	$3.58x10^{0}$	1.0	$6.26x10^{-1}$	$9.01x10^{-1}$	$8.04x10^{-1}$
^{121m}Sn	$4.997x10^{1}$	$7.15x10^{3}$	1.0	$9.52x10^{-1}$	$6.08x10^{-1}$	$7.29x10^{-1}$
^{108m}Ag	$1.270x10^{2}$	$2.81x10^{3}$	1.0	$9.82x10^{-3}$	$1.14x10^{-2}$	$1.08x10^{-2}$
^{107}Pd	$6.496x10^{6}$	$5.50x10^{-2}$	1.0	$8.70x10^{-2}$	$1.28x10^{-1}$	$1.14x10^{-1}$
^{99}Tc	$2.130x10^{5}$	$1.68x10^{0}$	10.0	$1.22x10^{1}$	$1.55x10^{1}$	$1.43x10^{1}$
^{93}Mo	$3.498x10^{3}$	$1.02x10^{2}$	1.0	$5.56x10^{-4}$	$2.76x10^{-2}$	$1.80x10^{-2}$
^{94}Nb	$2.030x10^{4}$	$1.76x10^{1}$	1.0	$2.95x10^{-2}$	$1.41x10^{0}$	$9.22x10^{-1}$
^{93}Zr	$1.530x10^{6}$	$2.34x10^{-1}$	1.0	$1.98x10^{0}$	$2.36x10^{0}$	$2.23x10^{0}$
^{90}Sr	$2.912x10^{1}$	$1.23x10^{4}$	1.0	$3.79x10^{4}$	$4.91x10^{4}$	$4.51x10^{4}$
^{79}Se	$6.496x10^{4}$	$5.50x10^{0}$	1.0	$3.73x10^{-1}$	$4.96x10^{-1}$	$4.53x10^{-1}$
^{63}Ni	$9.200x10^{1}$	$3.89x10^{3}$	1.0	$1.23x10^{2}$	$5.44x10^{2}$	$3.95x10^{2}$
^{59}Ni	$8.000x10^{4}$	$4.47x10^{0}$	1.0	$1.01x10^{0}$	$4.21x10^{0}$	$3.08x10^{0}$
^{36}Cl	$3.010x10^{5}$	$1.19x10^{0}$	1.0	$1.04x10^{-2}$	$1.14x10^{-2}$	$1.10x10^{-2}$
^{14}C	$5.729x10^{3}$	$6.24x10^{1}$	0.1	$1.43x10^{0}$	$1.46x10^{0}$	$1.45x10^{0}$

5.1.2 Inventory parameters for the source-term module

The source-term module YMIM (described in Chapter 13) requires as inputs the inventory expressed in grams of radionuclide per fuel rod and the radiological activity in Curies per gram. The quantities data base section of the CDB lists the number of fuel assemblies at the various reactors, and the number of fuel rods per assembly. Table 5-3 lists the reactor fuel assemblies and numbers of rods. The average number of rods per assembly for PWRs is calculated to be 231, and for BWRs is 60. A weighted average value for the MTU per rod has been calculated. For BWRs, there is 0.0030 MTU/rod, and for PWRs the amount is 0.0019 MTU/rod. Other parameters needed by YMIM are listed in Tables 5-4 and 5-5. Data have been obtained from the CDB.

Table 5-3. Description of reactor fuel assemblies.

	PWR			BWR		
Assembly Class	Number of Assemblies	Total Weight (MTU)	Rods/ Assembly	Number of Assemblies	Total Weight (MTU)	Rods/ Assembly
B&W 15 X 15	10359	4808.9	208	–	–	–
B&W 17 X 17	3131	1429.4	264	–	–	–
CE 14 X 14	9783	3717.1	166	–	–	–
CE 16 X 16	8141	3334.9	224	–	–	–
CE SYSTEM 80	8134	3425.0	220	–	–	–
GE BWR/2,3	–	–	–	35319	6325.8	60
GE BWR/4-6	–	–	–	125211	22603.2	60
WE 14 X 14	7785	2886.0	179	–	–	–
WE 15 X 15	14884	6753.6	204	–	–	–
WE 17 X 17	58599	25953.9	264	–	–	–
Big Rock Point	–	–	–	635	83.6	100
Dresden 1	–	–	–	892	90.9	35
Ft. Calhoun	1138	407.3	168	–	–	–
Humboldt Bay	–	–	–	390	28.9	40
Haddam Neck	1500	585.0	204	–	–	–
Indian Point	160	30.6	170	–	–	–
Lacrosse	–	–	–	333	38	98
Palisades	1518	607.1	210	–	–	–
St. Lucie 2	1878	726.3	224	–	–	–
San Onofre 1	1036	381.7	180	–	–	–
South Texas	3071	1661.0	250	–	–	–
Yankee Rowe	721	170.7	231	–	–	–
Grand Totals	131838	56878.5		162780	29170.4	

Table 5-4. Numbers of fuel rods per package.

Emplacement configuration/ package type	Fuel rods/ package
Borehole Emplacement	
Hybrid Package	933
BWR-Fuel Package	600
PWR-Fuel Package	924
In-Drift	
BWR-Fuel Package	2,400
PWR-Fuel Package	4,851

Table 5-5. Fuel-rod parameters.

Reactor Type	Fuel-Rod Length (m)	Fuel-Rod Diameter (cm)
BWR	3.759	1.252
PWR	3.658	0.950

5.2 Vitrified high-level waste

5.2.1 Vitrified high-level waste stream

Vitrified high-level waste (HLW) has been generated from reprocessing of defense and commercial reactor fuel at four sites. These sites are Savannah River, SC (listed as SRS in the CDB), Hanford, WA (HANF), Idaho Chemical Processing Plant, ID (ICPP), and West Valley, NY (WVDP). The first three sites listed produce defense HLW, and WVDP produced commercial HLW. The amounts and characteristics of each HLW inventory are described in the *Integrated Data Base Projections* (IDB) (DOE, 1991a).

The mass of radionuclides in the HLW cannot directly be translated into the units used to describe repository inventory (i.e., MTU). After reprocessing, it is difficult to relate the radionuclides in the HLW to the amount of uranium originally present in the source fuel. Because of the lack of direct connection with spent fuel, the amounts of HLW are often expressed as metric tons of heavy metal (MTHM).

From the IDB, we get the total mass of radionuclides and the total radioactivity in the HLW. The MPA implies that each defense HLW canister represents about 0.5 MTHM, and that each WVDP canister represents about 2.1 MTHM. There is great uncertainty in this value, since it is so difficult to relate the original mass of heavy metal to the final vitrified waste. Nevertheless, these factors are used to calculate the number of waste packages corresponding to the allowable amount of HLW. Data derived from the CDB, IDB, and the MPA are summarized in Table 5-6.

Table 5-6. Sources of high-level waste.

Source	Number of Canisters	Volume of HLW in Canister (m^3)	Density of HLW (Mg/m^3)	Mass of HLW (kg/ canister)	Mass of Radio-nuclides (kg/ canister)	Total Mass of Radio-nuclides (MT)[a]	Max. Radio-activity (Ci/can)[b]	Max. Total Radio-activity (MCi)
SRS	5,282	0.616	2.73	1,682	34	179	234,400	1,238
WVDP	275	0.7	2.71	1,900	70	19	114,700	31.5
ICPP	7,800	0.57	3.20	1,825	0.83	6.5	108,900	856
HANF	1,960	0.626	2.64	1,650	14	27	298,000	584
Totals	**15,317**	-	-	-	-	**231.5**	-	**2,709.5**

[a] Maximum values are approximately twice as great as average values.
[b]Mass in metric tons.

Assuming 63,000 MTU of spent fuel is emplaced, then 7,000 MTHM of HLW can be emplaced to reach the repository capacity given in the MPA. Using the assumptions for the equivalent MTHM represented by the HLW, the 15,317 canisters represent about 8,100 MTHM. Thus, the total HLW identified above is greater than the capacity of the repository

by 1,100 MTHM. To emplace only 7,000 MTHM of HLW, we can assume that 2,197 canisters from ICPP are not included. (Since this site has the plans that are least firmly defined, making this assumption probably reduces the uncertainties in the inventory.) The canisters used represent about 86% of the entire HLW radioactivity. The assumed configuration is then described in Table 5-7.

Table 5-7. HLW waste stream used for TSPA analyses.

Source	Number of Canisters	Total Inventory (MTHM)	Maximum Total Radioactivity (MCi)
SRS	5,282	2,641	1,238
WVDP	275	577	31.5
ICPP	5,603	3,241	615
HANF	1,960	980	584
Totals	**13,957**	**7,000**	**2,468.5**

5.2.2 High-level waste inventory

We assume that the inventory will decay between now and when it is emplaced. For lack of better information, we assume that it will be another 30 years (on average) until emplacement. The activity figures quoted in IDB are for 1990, so it is necessary to age the inventory by 30 years to make it consistent with the spent-fuel inventory. This has been done by using ORIGEN2 data for BWR fuel of 30,000 MWd/MTU burnup and taking the ratios of inventories of the appropriate nuclides for 1-year decay and 30-year decay. Although the burnup of the spent fuel producing the HLW is unknown, this does not seriously affect the adjustment for decay. Radionuclides decay predictably, so the decay of single radionuclides is not affected by burnup. Because the amounts of isotopes that are part of decay chains depend on the amounts of the parent isotopes, variations due to burnup anywhere in the chain affect all members below in that chain. For example, assuming that the spent fuel comprising the HLW had a burnup of only 7,500 MWd/MTU, the ratios for the isotopes at the ends of the decay chains (i.e., ^{210}Pb, ^{227}Ac, ^{226}Ra, ^{231}Pa, etc.) show differences as compared to the nominal 30,000-MWd/MTU spent fuel. The ratios are listed in Table 5-8.

The inventories for the four waste streams were taken from the CDB. Generally, the waste streams contain many more radionuclides than those considered for the TSPA, but most of those not included in the TSPA inventory have short half-lives, and thus no EPA limit. In a few cases, there are some isotopes that have EPA limits, but all of these are present in such small amounts that they have not been included. The SRS isotopes that have EPA limits not included in the source term are given in Table 5-9. (There are more of these from SRS than from any other stream.) They can be seen to be of little significance from a radionuclide-inventory standpoint.

Table 5-8. Comparison of HLW inventories at two burnups.

Isotope	Half-Life (years)	30-yr/1-yr Inventory Ratio at 30,000 MWd/MTU	30-yr/1-yr Inventory Ratio at 7,500 MWd/MTU
^{238}U	4.468×10^{9}	1.00×10^{0}	1.00×10^{0}
^{246}Cm	4.731×10^{3}	9.96×10^{-1}	9.96×10^{-1}
^{242}Pu	3.869×10^{5}	1.00×10^{0}	1.00×10^{0}
^{242m}Am	1.520×10^{2}	8.76×10^{-1}	8.76×10^{-1}
^{238}Pu	8.774×10^{1}	8.13×10^{-1}	8.14×10^{-1}
^{234}U	2.445×10^{5}	1.19×10^{0}	1.03×10^{0}
^{230}Th	7.700×10^{4}	7.81×10^{0}	1.73×10^{1}
^{226}Ra	1.600×10^{3}	4.69×10^{1}	2.89×10^{2}
^{210}Pb	2.230×10^{1}	1.45×10^{2}	2.50×10^{3}
^{243}Cm	2.850×10^{1}	4.94×10^{-1}	4.94×10^{-1}
^{243}Am	7.380×10^{3}	9.97×10^{-1}	9.97×10^{-1}
^{239}Pu	2.406×10^{4}	9.99×10^{-1}	9.99×10^{-1}
^{235}U	7.038×10^{8}	1.00×10^{0}	1.00×10^{0}
^{231}Pa	3.277×10^{4}	1.53×10^{0}	6.99×10^{0}
^{227}Ac	2.177×10^{1}	1.21×10^{1}	7.55×10^{1}
^{245}Cm	8.499×10^{3}	9.97×10^{-1}	9.98×10^{-1}
^{241}Pu	1.440×10^{1}	2.48×10^{-1}	2.48×10^{-1}
^{241}Am	4.322×10^{2}	8.93×10^{0}	1.30×10^{1}
^{237}Np	2.140×10^{6}	1.07×10^{0}	1.19×10^{0}
^{233}U	1.585×10^{5}	4.31×10^{0}	3.53×10^{0}
^{229}Th	7.339×10^{3}	1.57×10^{0}	9.71×10^{0}
^{244}Cm	1.811×10^{1}	3.30×10^{-1}	3.30×10^{-1}
^{240}Pu	6.537×10^{3}	1.01×10^{0}	9.97×10^{-1}
^{236}U	2.341×10^{7}	1.00×10^{0}	1.00×10^{0}
^{232}U	7.200×10^{1}	1.52×10^{0}	2.11×10^{0}
^{151}Sm	8.999×10^{1}	8.00×10^{-1}	8.00×10^{-1}
^{137}Cs	3.000×10^{1}	5.12×10^{-1}	5.11×10^{-1}
^{135}Cs	2.300×10^{6}	1.00×10^{0}	1.00×10^{0}
^{129}I	1.570×10^{7}	1.00×10^{0}	1.00×10^{0}
^{126}Sn	1.000×10^{5}	1.00×10^{0}	1.00×10^{0}
^{121m}Sn	4.997×10^{1}	6.69×10^{-1}	6.69×10^{-1}
^{108m}Ag	1.270×10^{2}	8.53×10^{-1}	8.54×10^{-1}
^{107}Pd	6.496×10^{6}	1.00×10^{0}	1.00×10^{0}
^{99}Tc	2.130×10^{5}	1.00×10^{0}	1.00×10^{0}
^{93}Mo	3.498×10^{3}	9.94×10^{-1}	9.94×10^{-1}
^{94}Nb	2.030×10^{4}	9.99×10^{-1}	9.99×10^{-1}
^{93}Zr	1.530×10^{6}	1.00×10^{0}	1.00×10^{0}
^{90}Sr	2.912×10^{1}	5.01×10^{-1}	5.01×10^{-1}
^{79}Se	6.496×10^{4}	1.00×10^{0}	9.99×10^{-1}
^{63}Ni	9.200×10^{1}	8.04×10^{-1}	8.04×10^{-1}
^{59}Ni	8.000×10^{4}	1.00×10^{0}	1.00×10^{0}
^{36}Cl	3.010×10^{5}	1.00×10^{0}	1.00×10^{0}
^{14}C	5.729×10^{3}	9.97×10^{-1}	9.96×10^{-1}

Table 5-9. High-level waste radionuclides with EPA limits not included in TSPA inventory.

Isotope	Inventory (Ci/canister)	EPA Limit (Ci/MTHM)
^{142}Ce	9.61×10^{-6}	1
^{87}Rb	8.72×10^{-7}	1
^{236}Np	1.74×10^{-8}	1
^{147}Sm	2.00×10^{-6}	0.1
^{144}Nd	4.86×10^{-10}	0.1
^{148}Sm	5.79×10^{-12}	0.1
^{149}Sm	1.78×10^{-12}	0.1
^{248}Cm	6.86×10^{-13}	0.1
^{247}Cm	6.60×10^{-13}	0.1

The combined vitrified HLW inventory is a weighted average of the four waste streams. The 30,000 MWd/MTU decay ratio has been applied to each isotope in the waste stream matching the list used for the spent-fuel inventory. These values have been weighted by the contribution of the streams to the total (7,000 MTHM) inventory. Although the four waste streams in the HLW inventory are each lacking many of the isotopes present in spent fuel, the combined HLW inventory has almost all the same constituents as spent fuel. The total HLW inventory is given in Table 5-10.

5.3 Combined inventory

The vitrified HLW inventory represents 10% of the total repository. If the HLW is combined with the spent fuel (using the waste stream for borehole emplacement), the combined weighted-average inventory is given in Table 5-11.

5.4 Radionuclides used in analyses

The direct-release analyses use the 43 radionuclides and the combined spent-fuel–HLW inventories listed in Table 5-11. The aqueous analyses use fewer radionuclides that are chosen for their transport characteristics or their contributions to dose effects. The radionuclides chosen are listed in Table 5-12, along with their combined spent-fuel–HLW inventory values. Based on results of TSPA-91 and other analyses, any radionuclide with a relatively high retardation factor (i.e., with a sorption coefficient, K_d, greater than 10 or 20 ml/g) contributes a negligible amount to releases and doses. Thus, releases from nuclides such as ^{243}Am, ^{135}Cs, ^{126}Sn, and ^{59}Ni are not considered. Although ^{239}Pu also falls into this category, its releases have been included as being representative of the above group. Certainly, if additional retardation data identify other radionuclides with low K_d values, they too would be considered. The prior analyses also showed that ^{235}U was a moderate

Table 5-10. Combined high-level waste inventory.

Isotope	Decay-Adjusted Inventories (Ci/canister)				Weighted Average (Ci/MTHM)
	HANF	SRS	WVDP	ICPP	
^{238}U	3.51×10^{-3}	1.05×10^{-2}	3.14×10^{-3}	1.28×10^{-11}	8.98×10^{-3}
^{246}Cm	0	5.32×10^{-7}	3.91×10^{-4}	0	6.19×10^{-5}
^{242}Pu	7.61×10^{-5}	1.22×10^{-2}	6.37×10^{-3}	2.30×10^{-3}	1.16×10^{-2}
^{242m}Am	0	1.27×10^{-2}	1.02×10^{0}	0	1.70×10^{-1}
^{238}Pu	3.60×10^{-1}	1.21×10^{3}	2.65×10^{1}	7.27×10^{1}	9.27×10^{2}
^{234}U	5.46×10^{-3}	4.09×10^{-2}	1.97×10^{-2}	6.56×10^{-7}	3.40×10^{-2}
^{230}Th	0	0	1.84×10^{-3}	0	2.90×10^{-4}
^{226}Ra	0	0	0	0	0
^{210}Pb	0	0	0	0	0
^{243}Cm	0	2.75×10^{-3}	2.60×10^{-1}	0	4.29×10^{-2}
^{243}Am	3.78×10^{-2}	5.77×10^{-3}	1.36×10^{0}	1.06×10^{-2}	2.36×10^{-1}
^{239}Pu	1.17×10^{0}	1.29×10^{1}	6.38×10^{0}	8.93×10^{-1}	1.13×10^{1}
^{235}U	1.91×10^{-4}	1.57×10^{-4}	3.54×10^{-4}	2.30×10^{-6}	2.22×10^{-4}
^{231}Pa	0	0	9.13×10^{-2}	0	1.44×10^{-2}
^{227}Ac	0	0	3.92×10^{-3}	0	6.17×10^{-4}
^{245}Cm	0	6.69×10^{-6}	3.45×10^{-3}	0	5.47×10^{-4}
^{241}Pu	3.12×10^{0}	4.13×10^{2}	7.85×10^{1}	5.06×10^{1}	3.49×10^{2}
^{241}Am	2.53×10^{3}	9.84×10^{1}	1.87×10^{3}	1.04×10^{1}	1.05×10^{3}
^{237}Np	1.67×10^{-1}	9.52×10^{-3}	9.82×10^{-2}	6.55×10^{-5}	6.69×10^{-2}
^{233}U	0	6.82×10^{-6}	1.53×10^{-1}	6.60×10^{-9}	2.41×10^{-2}
^{229}Th	0	0	1.30×10^{-3}	0	2.04×10^{-4}
^{244}Cm	1.66×10^{0}	3.55×10^{1}	9.89×10^{0}	2.19×10^{-1}	2.77×10^{1}
^{240}Pu	3.96×10^{-1}	8.74×10^{0}	4.71×10^{0}	8.36×10^{-1}	7.77×10^{0}
^{236}U	4.22×10^{-4}	1.13×10^{-3}	1.10×10^{-3}	1.28×10^{-5}	1.11×10^{-3}
^{232}U	0	2.04×10^{-2}	4.14×10^{-2}	0	2.12×10^{-2}
^{151}Sm	5.58×10^{2}	1.98×10^{2}	2.65×10^{2}	1.74×10^{2}	4.66×10^{2}
^{137}Cs	1.85×10^{4}	2.22×10^{4}	1.45×10^{4}	8.50×10^{3}	2.97×10^{4}
^{135}Cs	2.02×10^{-1}	9.94×10^{-2}	6.34×10^{-1}	9.58×10^{-2}	2.98×10^{-1}
^{129}I	1.29×10^{-5}	0	0	0	3.44×10^{-6}
^{126}Sn	3.65×10^{-1}	4.42×10^{-1}	4.09×10^{-1}	4.09×10^{-2}	5.10×10^{-1}
^{121m}Sn	5.19×10^{-2}	5.28×10^{-2}	4.59×10^{-2}	0	5.91×10^{-2}
^{108m}Ag	0	0	0	0	0
^{107}Pd	3.02×10^{-2}	1.47×10^{-2}	4.33×10^{-2}	2.55×10^{-3}	2.74×10^{-2}
^{99}Tc	7.51×10^{0}	3.08×10^{0}	4.28×10^{-1}	2.68×10^{0}	6.33×10^{0}
^{93}Mo	0	0	0	0	0
^{94}Nb	0	9.63×10^{-5}	0	0	6.93×10^{-5}
^{93}Zr	1.05×10^{0}	1.12×10^{0}	1.07×10^{0}	3.96×10^{-1}	1.55×10^{0}
^{90}Sr	1.49×10^{4}	2.34×10^{4}	1.32×10^{4}	8.32×10^{3}	2.93×10^{4}
^{79}Se	3.15×10^{-3}	1.70×10^{-1}	1.38×10^{-2}	8.17×10^{-2}	1.88×10^{-1}
^{63}Ni	9.73×10^{0}	2.39×10^{0}	2.43×10^{1}	0	8.13×10^{0}
^{59}Ni	1.09×10^{-1}	2.40×10^{-2}	4.16×10^{-1}	0	1.12×10^{-1}
^{36}Cl	0	0	0	0	0
^{14}C	0	0	0	0	0

Table 5-11. Combined (spent-fuel and high-level waste) inventory (in Ci/MTHM)

Isotope	BWR Inventory	PWR Inventory	HLW Inventory	Combined Weighted Average
^{238}U	3.18×10^{-1}	3.13×10^{-1}	8.98×10^{-3}	2.84×10^{-1}
^{246}Cm	1.08×10^{-2}	4.39×10^{-2}	6.19×10^{-5}	2.90×10^{-2}
^{242}Pu	1.18×10^{0}	2.05×10^{0}	1.16×10^{-2}	1.57×10^{0}
^{242m}Am	8.38×10^{0}	1.03×10^{1}	1.70×10^{-1}	8.68×10^{0}
^{238}Pu	1.61×10^{3}	2.87×10^{3}	9.27×10^{2}	2.28×10^{3}
^{234}U	1.41×10^{0}	1.56×10^{0}	3.40×10^{-2}	1.36×10^{0}
^{230}Th	3.53×10^{-4}	3.72×10^{-4}	2.90×10^{-4}	3.58×10^{-4}
^{226}Ra	2.19×10^{-6}	2.24×10^{-6}	0	2.00×10^{-6}
^{210}Pb	5.34×10^{-7}	5.37×10^{-7}	0	4.82×10^{-7}
^{243}Cm	7.21×10^{0}	1.61×10^{1}	4.29×10^{-2}	1.17×10^{1}
^{243}Am	1.00×10^{1}	2.09×10^{1}	2.36×10^{-1}	1.54×10^{1}
^{239}Pu	2.97×10^{2}	3.53×10^{2}	1.13×10^{1}	3.01×10^{2}
^{235}U	2.25×10^{-2}	2.30×10^{-2}	2.22×10^{-4}	2.06×10^{-2}
^{231}Pa	3.53×10^{-5}	3.82×10^{-5}	1.44×10^{-2}	1.47×10^{-3}
^{227}Ac	1.70×10^{-5}	1.85×10^{-5}	6.17×10^{-4}	7.79×10^{-5}
^{245}Cm	6.24×10^{-2}	2.20×10^{-1}	5.47×10^{-4}	1.48×10^{-1}
^{241}Pu	3.09×10^{4}	4.61×10^{4}	3.49×10^{2}	3.67×10^{4}
^{241}Am	2.50×10^{3}	3.67×10^{3}	1.05×10^{3}	3.04×10^{3}
^{237}Np	2.87×10^{-1}	4.27×10^{-1}	6.69×10^{-2}	3.46×10^{-1}
^{233}U	4.30×10^{-5}	6.57×10^{-5}	2.41×10^{-2}	2.46×10^{-3}
^{229}Th	2.07×10^{-7}	3.66×10^{-7}	2.04×10^{-4}	2.07×10^{-5}
^{244}Cm	3.52×10^{2}	9.86×10^{2}	2.77×10^{1}	6.89×10^{2}
^{240}Pu	4.64×10^{2}	5.34×10^{2}	7.77×10^{0}	4.59×10^{2}
^{236}U	2.66×10^{-1}	3.37×10^{-1}	1.11×10^{-3}	2.81×10^{-1}
^{232}U	1.79×10^{-2}	4.16×10^{-2}	2.12×10^{-2}	3.20×10^{-2}
^{151}Sm	2.80×10^{2}	3.66×10^{2}	4.66×10^{2}	3.49×10^{2}
^{137}Cs	5.19×10^{4}	6.96×10^{4}	2.97×10^{4}	6.00×10^{4}
^{135}Cs	4.32×10^{-1}	5.04×10^{-1}	2.98×10^{-1}	4.61×10^{-1}
^{129}I	2.75×10^{-2}	3.74×10^{-2}	3.44×10^{-6}	3.05×10^{-2}
^{126}Sn	6.26×10^{-1}	9.01×10^{-1}	5.10×10^{-1}	7.75×10^{-1}
^{121m}Sn	9.52×10^{-1}	6.08×10^{-1}	5.91×10^{-2}	6.62×10^{-1}
^{108m}Ag	9.82×10^{-3}	1.14×10^{-2}	0	9.76×10^{-3}
^{107}Pd	8.70×10^{-2}	1.28×10^{-1}	2.74×10^{-2}	1.05×10^{-1}
^{99}Tc	1.22×10^{1}	1.55×10^{1}	6.33×10^{0}	1.35×10^{1}
^{93}Mo	5.56×10^{-4}	2.76×10^{-2}	0	1.62×10^{-2}
^{94}Nb	2.95×10^{-2}	1.41×10^{0}	6.93×10^{-5}	8.30×10^{-1}
^{93}Zr	1.98×10^{0}	2.36×10^{0}	1.55×10^{0}	2.16×10^{0}
^{90}Sr	3.79×10^{4}	4.91×10^{4}	2.93×10^{4}	4.36×10^{4}
^{79}Se	3.73×10^{-1}	4.96×10^{-1}	1.88×10^{-1}	4.26×10^{-1}
^{63}Ni	1.23×10^{2}	5.44×10^{2}	8.13×10^{0}	3.57×10^{2}
^{59}Ni	1.01×10^{0}	4.21×10^{0}	1.12×10^{-1}	2.78×10^{0}
^{36}Cl	1.04×10^{-2}	1.14×10^{-2}	0	9.94×10^{-3}
^{14}C	1.43×10^{0}	1.46×10^{0}	0	1.30×10^{0}

contributor to releases and doses, but its aqueous-transport characteristics are the same as those of ^{234}U; since its releases are about an order of magnitude below those of ^{234}U, it was felt that little additional information would be gained by including it.

Table 5-12. Radionuclides and modified inventories used for aqueous and gaseous analyses

Isotope	Initial inventory used (Ci/MTU)
^{234}U	$2.19x10^{0}$
^{239}Pu	$3.04x10^{2}$
^{231}Pa	$3.10x10^{-2}$
^{237}Np	$1.21x10^{0}$
^{129}I	$3.05x10^{-2}$
^{99}Tc	$1.35x10^{1}$
^{79}Se	$4.26x10^{-1}$
^{14}C	$9.09x10^{-1}$

Because YMIM does not calculate ingrowth of daughter nuclides from chain decay, the initial inventories of the four actinides listed in Table 5-12 have been adjusted. For ^{239}Pu, ^{237}Np, and ^{234}U, the starting inventories are determined by adding in all of the ingrowth from the beginning, that is, summing the inventories (in moles) of all parents. Table 5-13 illustrates the adjustment done for ^{237}Np. For ^{231}Pa, this procedure is not appropriate because its parent, ^{235}U, has a half-life of almost a billion years. ^{231}Pa attains secular equilibrium with ^{235}U within a million years, so ^{231}Pa is assigned the same inventory, in curies, as ^{235}U. Also, the half-life of ^{231}Pa is changed to equal that of ^{235}U. At times long enough that secular equilibrium has been obtained (somewhere between 100,000 and 1,000,000 years), this approximation results in the correct inventory of ^{231}Pa. At earlier times, the ^{231}Pa inventory is exaggerated.

Table 5-13. Illustration of adjustment of inventory for ^{237}Np.

Isotope	Activity (Ci/mole)	Combined Weighted Average Inventory (Ci/MTU)	Inventory expressed as mole/MTU	Adjusted Inventory (Ci/MTU)
^{245}Cm	$4.21x10^{1}$	$1.48x10^{-1}$	$3.52x10^{-3}$	
^{241}Pu	$2.49x10^{4}$	$3.67x10^{4}$	$1.47x10^{0}$	
^{241}Am	$8.27x10^{2}$	$3.04x10^{3}$	$3.68x10^{0}$	
^{237}Np	$1.67x10^{-1}$	$3.46x10^{-1}$	$2.07x10^{0}$	
Total			**$7.23x10^{0}$**	**$1.21x10^{0}$**

The gaseous analyses used only ^{14}C. Rather than using the inventory listed in Table 5-11, the ^{14}C inventory was based on the work of Van Konynenburg (1991). Van Konynenburg re-examined some of the assumptions regarding ^{14}C that were made in ORIGEN calculations which form the basis of the CDB, and he estimated a reduced inventory of 1.01 Ci/MTU for ^{14}C. (This value is for a 65%/35% mixture of PWR/BWR spent fuel.) For the TSPA-93 calculations, Van Konynenburg's value was further reduced by 10%, since the HLW contains essentially no ^{14}C, to obtain the value listed in Table 5-12.

5.5 Comparisons

5.5.1 Comparison of Inventories for TSPA-93 and TSPA-91

We can compare both the TSPA-93 spent-fuel inventory and the overall combined inventory with that used for the TSPA-91 analyses. The latter inventory consisted of 60% PWR and 40% BWR fuel that was 10 years old at emplacement. In TSPA-91, only the spent-fuel inventory was used for the analyses (with the amounts scaled up from 63,000 to 70,000 MTU).

Because the release mechanisms (i.e., container failure, dissolution, etc.), due to groundwater interactions for spent fuel and HLW are assumed to be different, the nominal-case analyses do not specifically model HLW. Instead, the source term is assumed to be entirely composed of spent fuel, but with the overall combined inventory of radionuclides. However, the overall combined inventory is used for the human-intrusion drilling analyses, since the interactions between the drilling and the waste packages can be modeled for both types of waste. The ratios of the inventories, both spent-fuel and combined, are given in Table 5-14.

The largest components of aqueous releases in TSPA-91 (^{99}Tc, ^{129}I, and ^{79}Se) all have about 15% to 20% higher amounts in the TSPA-93 spent-fuel inventory. Of the major contributors to direct surface releases in TSPA-91 (^{240}Pu, ^{241}Am, and ^{239}Pu), ^{241}Am has double the inventory, while the other two are essentially equal to the TSPA-91 values. There is only a slightly smaller amount of ^{14}C (significant for gaseous releases) in the TSPA-93 spent-fuel inventory. The major difference between the two inventories occurs for ^{210}Pb (about 11 times more in the TSPA-93 inventory than previously), but this is a minor component. Comparing the TSPA-93 combined (i.e., spent fuel and HLW) inventory with the TSPA-91 (spent fuel only) inventory shows smaller differences between the two for the important radionuclides discussed above. However, some of the minor components have significantly larger amounts in the combined inventory.

Table 5-14. Comparisons of TSPA-91 and TSPA-93 inventories.

Isotope	Weighted-Average TSPA-93 Spent-Fuel Inventory (Ci/MTU)	TSPA-93 Spent-Fuel Inventory/ TSPA-91 Inventory	TSPA-93 Combined Inventory/ TSPA-91 Inventory
^{238}U	$3.15x10^{-1}$	0.99	0.89
^{246}Cm	$3.22x10^{-2}$	1.25	1.12
^{242}Pu	$1.74x10^{0}$	1.09	0.98
^{242m}Am	$9.62x10^{0}$	1.29	1.16
^{238}Pu	$2.43x10^{3}$	1.14	1.07
^{234}U	$1.51x10^{0}$	1.33	1.20
^{230}Th	$3.65x10^{-4}$	2.83	2.77
^{226}Ra	$2.22x10^{-6}$	6.06	5.45
^{210}Pb	$5.36x10^{-7}$	11.38	10.24
^{243}Cm	$1.30x10^{1}$	0.84	0.76
^{243}Am	$1.71x10^{1}$	1.10	0.99
^{239}Pu	$3.33x10^{2}$	1.08	0.98
^{235}U	$2.28x10^{-2}$	1.36	1.22
^{231}Pa	$3.72x10^{-5}$	1.92	75.75
^{227}Ac	$1.80x10^{-5}$	3.46	15.00
^{245}Cm	$1.64x10^{-1}$	1.30	1.17
^{241}Pu	$4.07x10^{4}$	0.55	0.49
^{241}Am	$3.26x10^{3}$	1.99	1.85
^{237}Np	$3.78x10^{-1}$	1.31	1.20
^{233}U	$5.77x10^{-5}$	2.27	96.73
^{229}Th	$3.10x10^{-7}$	2.21	147.57
^{244}Cm	$7.62x10^{2}$	0.66	0.60
^{240}Pu	$5.09x10^{2}$	1.00	0.90
^{236}U	$3.12x10^{-1}$	1.30	1.17
^{232}U	$3.32x10^{-2}$	1.33	1.28
^{151}Sm	$3.36x10^{2}$	1.06	1.10
^{137}Cs	$6.33x10^{4}$	0.83	0.78
^{135}Cs	$4.79x10^{-1}$	1.37	1.32
^{129}I	$3.39x10^{-2}$	1.15	1.03
^{126}Sn	$8.04x10^{-1}$	1.12	1.08
^{121m}Sn	$7.29x10^{-1}$	0.81	0.73
^{108m}Ag	$1.08x10^{-2}$	0.91	0.82
^{107}Pd	$1.14x10^{-1}$	1.08	1.00
^{99}Tc	$1.43x10^{1}$	1.17	1.10
^{93}Mo	$1.80x10^{-2}$	1.13	1.02
^{94}Nb	$9.22x10^{-1}$	1.16	1.05
^{93}Zr	$2.23x10^{0}$	1.18	1.15
^{90}Sr	$4.51x10^{4}$	0.85	0.82
^{79}Se	$4.53x10^{-1}$	1.19	1.12
^{63}Ni	$3.95x10^{2}$	0.87	0.78
^{59}Ni	$3.08x10^{0}$	0.87	0.78
^{36}Cl	$1.10x10^{-2}$	0.93	0.84
^{14}C	$1.45x10^{0}$	0.94	0.85

5.5.2 Comparison of HLW and spent-fuel inventories

The HLW inventory differs from the TSPA-93 spent-fuel inventory in several ways. Overall, it has only about 40% of the activity per MTHM of spent fuel. Most isotopes in HLW have activities of only a fraction of those in spent fuel. Four notable exceptions are ^{233}U, ^{231}Pa, ^{229}Th, and ^{227}Ac, which have many times the spent-fuel inventories. However, the absolute amounts of these nuclides are small (~10^{-2} Ci/MTHM). Of the radionuclides that contributed most to aqueous releases in TSPA-91 (^{129}I, ^{99}Tc, and ^{79}Se), the HLW contains almost no ^{129}I, and only about 45% of the inventories of the other two radionuclides. Table 5-15 compares the radionuclide inventories of HLW and spent fuel.

Table 5-15. Comparison of spent-fuel and HLW inventories.

Isotope	HLW Weighted Average (Ci/MTHM)	Spent-Fuel Weighted Avg. (Ci/MTHM)	Ratio (HLW/Spent Fuel)
^{238}U	8.98×10^{-3}	3.15×10^{-1}	0.03
^{246}Cm	6.19×10^{-5}	3.22×10^{-2}	0.00
^{242}Pu	1.16×10^{-2}	1.74×10^{0}	0.01
^{242m}Am	1.70×10^{-1}	9.62×10^{0}	0.02
^{238}Pu	9.27×10^{2}	2.43×10^{3}	0.38
^{234}U	3.40×10^{-2}	1.51×10^{0}	0.02
^{230}Th	2.90×10^{-4}	3.65×10^{-4}	0.79
^{226}Ra	0	1.01×10^{-6}	0.00
^{210}Pb	0	5.36×10^{-7}	0.00
^{243}Cm	4.29×10^{-2}	1.30×10^{1}	0.00
^{243}Am	2.36×10^{-1}	1.71×10^{1}	0.01
^{239}Pu	1.13×10^{1}	3.33×10^{2}	0.03
^{235}U	2.22×10^{-4}	2.28×10^{-2}	0.01
^{231}Pa	1.44×10^{-2}	3.72×10^{-5}	386.29
^{227}Ac	6.17×10^{-4}	1.80×10^{-5}	34.33
^{245}Cm	5.47×10^{-4}	1.64×10^{-1}	0.00
^{241}Pu	3.49×10^{2}	4.07×10^{4}	0.01
^{241}Am	1.05×10^{3}	3.26×10^{3}	0.32
^{237}Np	6.69×10^{-2}	3.78×10^{-1}	0.18
^{233}U	2.41×10^{-2}	5.77×10^{-5}	416.94
^{229}Th	2.04×10^{-4}	3.10×10^{-7}	657.72
^{244}Cm	2.77×10^{1}	7.62×10^{2}	0.04
^{240}Pu	7.77×10^{0}	5.09×10^{2}	0.02
^{236}U	1.11×10^{-3}	3.12×10^{-1}	0.00
^{232}U	2.12×10^{-2}	3.32×10^{-2}	0.64
^{151}Sm	4.66×10^{2}	3.36×10^{2}	1.39
^{137}Cs	2.97×10^{4}	6.33×10^{4}	0.47
^{135}Cs	2.98×10^{-1}	4.79×10^{-1}	0.62
^{129}I	3.44×10^{-6}	3.39×10^{-2}	0.00
^{126}Sn	5.10×10^{-1}	8.04×10^{-1}	0.63

Table 5-15. Comparison of spent-fuel and HLW inventories (continued).

Isotope	HLW Weighted Average (Ci/MTHM)	Spent-Fuel Weighted Avg. (Ci/MTHM)	Ratio (HLW/Spent Fuel)
^{121m}Sn	5.91×10^{-2}	7.29×10^{-1}	0.08
^{108m}Ag	0	1.08×10^{-2}	0.00
^{107}Pd	2.74×10^{-2}	1.14×10^{-1}	0.24
^{99}Tc	6.33×10^{0}	1.43×10^{1}	0.44
^{93}Mo	0	1.80×10^{-2}	0.00
^{94}Nb	6.93×10^{-5}	9.22×10^{-1}	0.00
^{93}Zr	1.55×10^{0}	2.23×10^{0}	0.70
^{90}Sr	2.93×10^{4}	4.51×10^{4}	0.65
^{79}Se	1.88×10^{-1}	4.53×10^{-1}	0.41
^{63}Ni	8.13×10^{0}	3.95×10^{2}	0.02
^{59}Ni	1.12×10^{-1}	3.08×10^{0}	0.04
^{36}Cl	0	1.10×10^{-2}	0.00
^{14}C	0	1.45×10^{0}	0.00
Totals	**6.18×10^{4}**	**1.57×10^{5}**	**0.39**

The aqueous analyses described in Chapters 14 and 15 use inventory values given in Section 5.4. These values are based on the combined weighted-average inventory, and therefore include the contributions from HLW. As can be seen from Table 5-15 above, one of the largest divergences between spent fuel and HLW occurs for ^{231}Pa, a component of the aqueous source term. Because of the necessity in YMIM to specifically account for the ingrowth of ^{231}Pa in the decay chains, the ^{231}Pa inventory is closer to the HLW value than to the combined weighted-average value.

Chapter 6
Geostatistically Based Stratigraphic Model

(Rautman, Robey)

The details of the properties of various individual hydrologic units underlying Yucca Mountain may prove very important to estimates of site performance. However, the stratigraphic models used in previous simulations were developed from very limited lithologic information. For example, Dudley *et al.* (1988) used information from drillhole USW G-4 to develop the stratigraphic section used in their calculations. PACE-90 (Barnard and Dockery, 1991) simulated flow and transport through one- and two-dimensional cross sections constructed using data from four drillholes. TSPA-91 used data from three drillholes, along with limited analog information, to construct a two-dimensional cross-section that formed the basis for the six one-dimensional columns used for the stochastic simulations. These simplistic approaches to modeling the geologic framework of Yucca Mountain limited the generality of the flow and transport simulations. The final calculations did not fully represent the entire geographic area, nor did they allow any analysis of sensitivity that might be related to changing thicknesses of individual units.

Geostatistical methods can be used to provide a systematic representation of the lithology; starting from available data, realizations of the lithology for the entire domain can be constructed in a manner that includes uncertainty in the locations and extent of individual units. One objective for this TSPA effort is to use geostatistical techniques for the first time to generate stratigraphic representations of the potential repository region. These techniques can help reduce dependence on qualitative or subjective approaches and aid in incorporating as much quantitative, site-specific information as possible. Because the actual site-specific subsurface data will always be limited, any model of site geology will be uncertain. Geostatistical methods help to assess the uncertainty in the geometry of unit contacts and thicknesses of stratigraphic units in a rigorous, quantitative manner. Uncertainty in the site description will then be propagated to the modeled releases of radionuclides. Although the geostatistically generated hydrogeologic stratigraphy is not fully incorporated into these TSPA-93 simulations, the work reported here lays the groundwork for an important tool that will be used in future sensitivity studies to more fully investigate the effects of geologic uncertainty on total-system performance.

Models used in total-system performance assessments require simplification to be computationally tractable. However, these simplifications must preserve the signifi-

cant properties of the site itself. In developing a lithologic model of the site for TSPA-93, the initial differentiation of the units is based on the observed occurrence of alternating layers of welded and nonwelded tuff. Degree of welding influences the porosity and permeability of the rock, which affects groundwater flow through the rock. A secondary subdivision is based on whether the tuffs are zeolitic or vitric. The presence of zeolites may increase the sorption of contaminants into the rock matrix, and may also change the flow properties of the rock. The welded/nonwelded rock characteristics have been geostatistically modeled, while the zeolitic/vitric characteristics have been modeled deterministically.

Thus, the goal of the geologic modeling portion of TSPA-93 is to find a modeling method that (1) is fully three-dimensional, (2) incorporates as much site data as possible in a rigorous manner, (3) adequately represents the distinctions between welded, nonwelded, and zeolitic rock types, and (4) allows quantification within the limits of existing knowledge. Geostatistical methods, described below, appear to meet these requirements.

The stratigraphic columns derived in this chapter are used by the composite-porosity model in simulating unsaturated-zone groundwater flow and transport (Chapter 14). These columns have been extracted from ten complete and fully three-dimensional geostatistical lithologic simulations. Each of the simulations is statistically consistent with the available data (drillholes and spatial continuity patterns) provided as input to the simulation process. Because of time considerations, performance assessment calculations for TSPA-93 use only one of these simulations as the geologic description of the unsaturated zone portion of the site. Had this limitation been anticipated earlier, it probably would have been better to use indicator kriging (rather than simulation) to develop the expected locations of the stratigraphic contacts used in the performance-assessment calculations. However, simulation is a more rigorous and robust approach because it allows uncertainty assessment.

The intent of the TSPA analyses is to eventually assess the impact of characterization uncertainty with respect to stratigraphic contacts. Future calculations will investigate in a systematic fashion the sensitivity of the performance results to variations in stratigraphic thickness using the remaining realizations; all ten stratigraphic realizations for the columns are therefore provided in this report for such future calculations.

6.1 Geostatistical methods

Geostatistical techniques (Journel and Huijbregts, 1978; Clarke, 1979) provide a quantitative and reproducible way to combine geologic information from many drillholes. The information is combined into a coherent three-dimensional model from which

the simplified one- or two-dimensional profiles needed for complex performance-assessment calculations can be extracted. There is no requirement that computations be based on cross sections or profiles that pass exactly through a drillhole in order to incorporate field data. Information is propagated away from each known location in accordance with a mathematical model of spatial continuity deduced from the physical measurements. Because the underlying model is fully three dimensional, profiles with their associated material properties for flow and transport calculations can be extracted in any desired location and orientation.

Geostatistical simulation (Journel, 1989; Journel and Alabert, 1989; Rautman and Treadway, 1991) provides a powerful technique for quantifying the uncertainty associated with numerical models representing geologic units. Simulation produces an arbitrary number of realizations, each consistent with the measured data, yet varying at locations away from those data in a manner controlled by the quantitative pattern of spatial continuity. Statistically, this variability represents the uncertainty that results from less-than-exhaustive site information. By evaluating the performance consequences in a Monte Carlo approach using a suite of these simulations, the impact of characterization uncertainty—that is, a lack of actual site knowledge—can be propagated through the performance-assessment process in a manner similar to the more usual propagation of uncertainty in material properties. (For a more subjective but non-stochastic approach to characterization uncertainty, see Buesch *et al.*, 1993).

A subset of geostatistical methods is uniquely suited to the representation of categorical variables (in contrast with continuously varying variables; e.g., porosity), such as the hydrogeologic rock types of primary interest in this performance assessment. Known as indicator techniques (Journel, 1983), this approach substitutes a transformed indicator variable, $I(x)$, for the original category or verbal classification of each rock type, $Z(x)$, at a specific location, x. Thus:

$$I(x) = \begin{cases} 1 : Z(x) \text{ is welded} \\ 0 : Z(x) \text{ is not welded} \end{cases} \qquad (6.1)$$

In the current exercise, the rock types in each drillhole are categorized at regular intervals as either welded or nonwelded. Each category is then transformed using equation 6.1. For practical reasons related to the need to distinguish particular welded rock types within the Crater Flat Tuff, welded rocks of the Prow Pass Member were coded separately from the more generic welded category when used as conditioning data (see Section 6.5.4). However, all welded hydrogeologic rock types are assumed to possess the same spatial continuity pattern.

6.2 Lithologic data

As mentioned previously, the degree of welding is the primary indicator used to characterize the tuffs of Yucca Mountain. There is an inverse correlation between the degree of welding and the porosity and permeability of the rock (Figure 6-1): more densely welded materials have lower matrix porosities, and consequently lower matrix permeabilities, than nonwelded or poorly welded materials. The secondary distinction of the presence or absence of zeolitization is applied to the nonwelded tuffs. It is generally true that nonwelded zeolitic materials are less permeable than nonwelded vitric tuffs because of the post-depositional growth of zeolitic minerals in the pores. Devitrification of glass in welded tuffs tends to lead to the formation of stable mineral phases; precluding subsequent zeolitization.

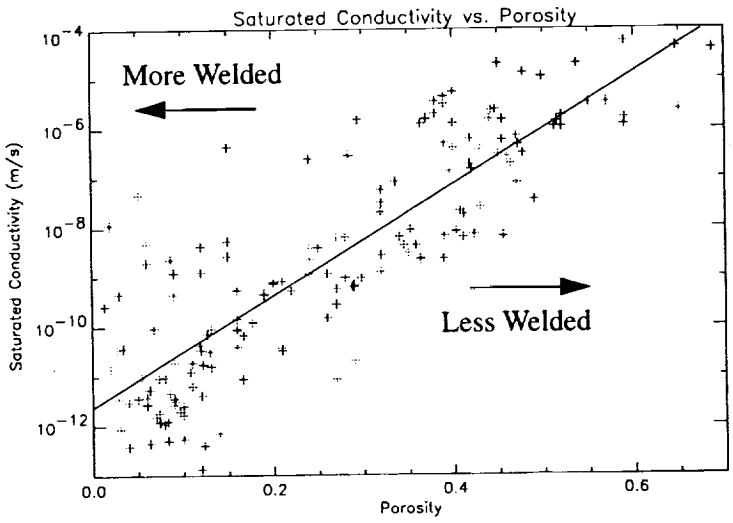

Figure 6-1. Correlation between matrix porosity and matrix permeability for non-zeolitic welded and nonwelded tuffs from Yucca Mountain (from Rautman and Robey, 1993).

Data are available for 22 deep drillholes within the potential repository region as shown in Figure 6-2. The spatial distribution is uneven, with fewer drillholes in the western portion of the area. Drillholes in the eastern part of the area tend to be clustered in the washes at lower elevations. Not all drillholes extend below the water table, which leads to more sparse data at deeper stratigraphic levels.

Published drillhole lithologic logs are used as the primary sources of information (tabulated in Schenker *et al.*, 1994). Lithologic descriptions are reviewed and summarized into welded and nonwelded categories. For purposes of the indicator coding, welded materials are inferred from any description of the rock as "moderately" or

"densely" welded. Intervals described as "nonwelded" or "partially" welded are classified as nonwelded, as are the so-called "bedded tuffs" that occur between the major ash-flow units. Intermediate descriptions, such as those described as "partially to moderately welded" generally are classified as welded, but can be classified as nonwelded if supporting information, such as porosity measurements, indicate this categorization is appropriate.

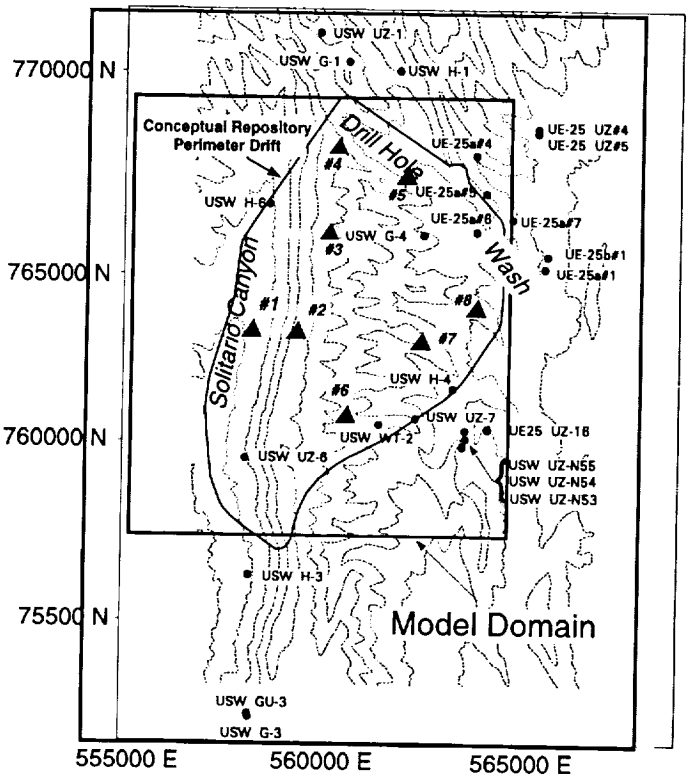

Figure 6-2. Map showing locations of deep drillholes (dots) used in developing the simulated stratigraphic models and of the desired stratigraphic columns (triangles) at Yucca Mountain (coordinates are given in Nevada State Plane Coordinates in feet).

Geophysical logs (documented in Schenker *et al.*, 1994) are used to cross-check the major lithologic changes inferred from the lithologic logs. In some cases, there is excellent correlation between the geophysical and descriptive lithologic logs. For other intervals, the correlation is weak or lacking. In the WT-series holes for which no substantiating lithologic log is available, geophysical logs are the primary source of information. These interpretations are checked against lithologic logs from nearby drillholes. Other sources of information used to create or confirm the indicator coding include core photographs and quantitative measurements of porosity and permeability from core sam-

ples (where available). All indicator-coded drillhole data used in the geostatistical modeling are tabulated in Schenker *et al.* (1994).

6.3 Spatial continuity

Geostatistical simulation begins with definition of a grid covering the region for which the simulated variable is to be generated. The specific value at any particular grid node is obtained by sampling from the local probability density function, which is derived from the surrounding data used to condition the simulation. Grid nodes close to high data values (or to indicator values representing a particular lithologic category) statistically will tend to resemble those data. Conversely, nodes close to low data values (or alternative indicator categories) will tend to resemble those values. Computation of exactly what constitutes geostatistical "closeness" requires a mathematical description of how the property varies in space.

Spatial continuity (also referred to as spatial correlation or correlation length) of a property is determined by computing the sample variogram, $\gamma(\bar{h})$, which statistically represents the difference in value of a property among pairs of data as the vector distance, $\bar{h}$, between the members of the pairs increases. For mathematical reasons, this statistical difference is expressed in the form of a variance (Journel and Huijbregts, 1978):

$$2\gamma(\bar{h}) \equiv Var\left\{I(x+\bar{h}) - I(x)\right\} = E\left\{\left[I(x+\bar{h}) - I(x)\right]^2\right\} = \frac{1}{N}\sum_{i=1}^{N(\bar{h})}\left[I(x+\bar{h}) - I(x)\right]^2, \quad (6.2)$$

where x is a particular spatial location, N is the number of samples, and $I(x)$ is the categorical property observed at that location (as determined in equation 6.1). $E[...]$ is the expectation operator and $Var[...]$ is the variance operator.

The variogram is based upon the intuition that two sample values located close together generally are more similar than two values located further apart. In other words, the average squared difference of pairs of values separated by a given distance is expected to be smaller at short distances. A specific functional relationship is fitted to the sample variogram to provide a complete description of spatial continuity in all directions and for all distances. This mathematical variogram model is described by the orientation of its major and minor axes, the range of correlation, the sill or absolute magnitude of the sample variance, and any nugget effect representing irresolvable small-scale variability at short separation distances.

Continuity of a property need not be the same in all directions. In a layered sequence, such as that at Yucca Mountain, considerable anisotropy may exist. In three dimensions, a conceptual surface of equal continuity may be thought of as forming a triaxial ellipsoid in which the axes of different lengths represent the range of spatial continuity or correlation in that direction. More than one functional relationship or model may be nested to represent continuity structures of more than one origin with different ranges.

Normal geostatistical practice involves computing sample variograms from the sample values that will eventually be used to condition, or constrain, the resulting model. However, the current density of drilling at Yucca Mountain is inadequate to derive a model of spatial continuity between drillholes. As a surrogate, the stratigraphic units identified on published geologic cross sections, which are presented as welded and nonwelded rock types (Scott and Bonk, 1984) have been digitized, and this information has been converted to discrete three-dimensional points, associated with the appropriate lithologic category (welded or nonwelded), using a gridding algorithm. These data have been used to compute the sample variograms.

Geologic knowledge of the Yucca Mountain site is also used to guide development of the spatial continuity model. Across the region of interest, stratigraphic units generally strike north-south and dip gently eastward at approximately 5 to 6 degrees. The cross-section data are also arranged spatially to capture this geologic context (Figure 6-3). The initial search strategy used in the variogram computations to locate data pairs focuses on these orientations. The principal search directions are then varied incrementally away from the conceptual orientations to confirm the applicability of geologic intuition.

Figure 6-4 presents sample variograms that are computed from the digitized cross section data looking horizontally (i.e., dip = 0°) in the north-south direction and at dips of 5° toward N 90° E and 85° toward N 90° W. These latter directions are essentially parallel and perpendicular to typical stratification. Superimposed on the figure are the results of a single, nested three-dimensional variogram model computed in the appropriate directions. Given the assumptions involved in the cross-sectional surrogate data set and in the indicator coding of this thick stratigraphic interval, the model is judged a good fit to the sampled data. The parameters of the fitted model, in the shorthand notation of Isaaks and Srivastava (1989), are as follows:

$$\gamma(h) = 0.1 \cdot Sph_{3,000}(h_1) + 0.225 \cdot Sph_{50,000}(h_2), \qquad (6.3)$$

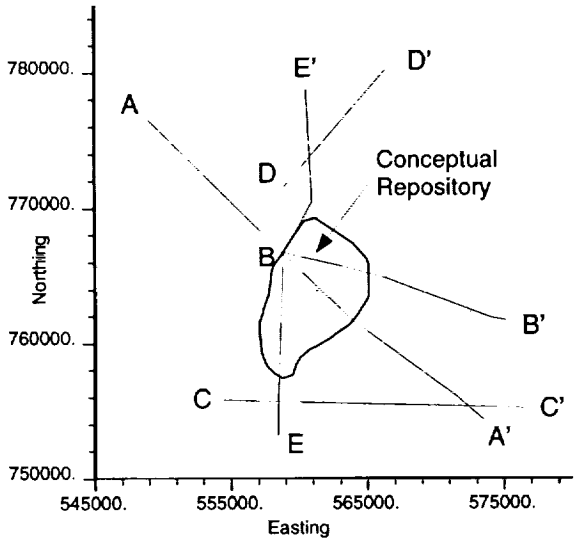

Figure 6-3. Map showing the locations of the digitized cross sections used to develop the spatial continuity model of lithology (from Scott and Bonk, 1984). (Nevada State Plane Coordinate System in feet.)

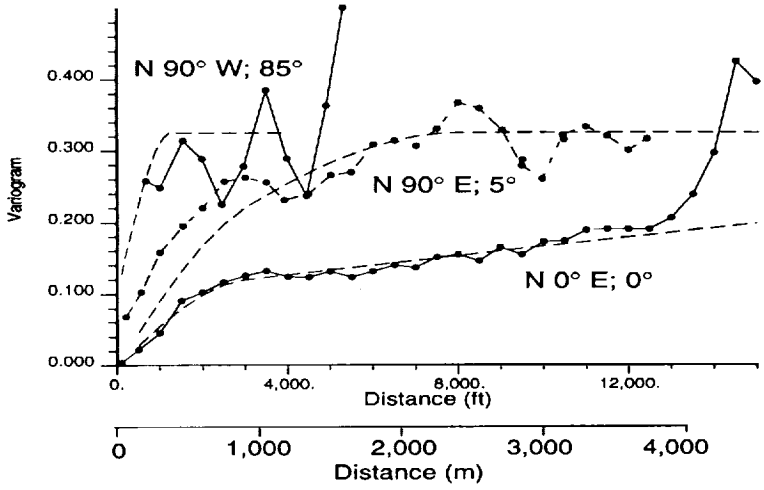

Figure 6-4. Sample variograms (dots) computed in the indicated directions from the digitized cross sections shown in Figure 6-3. Smooth curves are the variogram model, computed in the appropriate direction, from equation 6.3.

where

$$h_1 = \sqrt{\left[\frac{h_{x'}}{3000}\right]^2 + \left[\frac{h_{y'}}{3000}\right]^2 + \left[\frac{h_{z'}}{300}\right]^2}, \tag{6.4}$$

$$h_2 = \sqrt{\left[\frac{h_{x'}}{50000}\right]^2 + \left[\frac{h_{y'}}{50000}\right]^2 + \left[\frac{h_{z'}}{3000}\right]^2}, \tag{6.5}$$

and $s_i \cdot Sph_a(h_i)$ represents the i^{th} nested spherical variogram model with sill s, and range a. In Equations (6.4) and (6.5), $h_{x'}$, $h_{y'}$, and $h_{z'}$ are the separation distances in the rotated x, y, and z directions, respectively. The parameters of the nested model are presented in tabular form in Table 6-1.

Table 6-1. Summary of modeled variogram parameters.

	Major Axis Range (ft)	Sill	Anisotropy Ratio 1[a]	Anisotropy Ratio 2[a]	Rotation Angle[b]
Nugget	–	0.000	–	–	Angle 1: 0°
Structure 1	3,000	0.100	1.00	0.10	Angle 2: 0°
Structure 2	50,000	0.225	0.16	0.04	Angle 3: -5°

[a] The anisotropy ratios represent the length of the secondary and minor axes relative to the major axis for a conceptual triaxial ellipsoid; see Deutsch and Journel (1992).

[b] The rotation angles 1 and 2 are applied to the "principal direction" or major axis of the continuity ellipsoid, first in the x-y plane and then in the horizontally rotated x'-z plane. Rotation angle 3 is then applied to the resultant y' and z' axes clockwise when looking toward the origin; see Deutsch and Journel (1992).

A schematic representation of this nested variogram model is presented in Figure 6-5. Spatial models are enhanced by a reasonable geologic interpretation. A reasonable interpretation of this model follows. The shorter of the two structures appears to be related principally to the vertical extent of the stratigraphic units. The 90 m (300 ft) vertical range (the 910 m [3,000 ft] major-axis range times the 0.1 anisotropy ratio) seems to be a composite value related to the presence of thick (100 to 300 m, [350 to 1,000 ft]) welded units interbedded with significantly thinner (6 to 60 m, [20 to 120 ft]) nonwelded tuffs. Rautman and Flint (1992) reported a range of 30 m (100 ft) for a vertical composite of the Paintbrush Tuff and of 60 m (200 ft) for the Topopah Spring Member. This origin of this same structure is less obvious in plan view, but presumably it represents a first-order degree of continuity related to welding intensity, perhaps accentuated by the smaller-volume, welded ash-flow tuffs, the Pah Canyon and Yucca Mountain Members

of the Paintbrush Tuff, which are present in the northern portion of the Yucca Mountain region. No obvious anisotropy is apparent for this structure in plan view; hence the anisotropy factor of 1.0. The longer-range structure (approximately 15 km or 50,000 ft) appears to be related to the overall extent of the ash-flow sheets, which extend southward some tens of kilometers from a northern source caldera. The specific anisotropy observed in plan (0.16) may be partially a function of the extent of these units in the dip direction, which is limited both by normal faulting and by the construction of the cross sections. The extreme anisotropy ratio for this longer structure in cross-sectional view (0.04) reflects the layered nature of the tuffs themselves. Without vertical exaggeration, an ash-flow sheet is exactly that: a thin sheet of large lateral extent. The limited east-west extent of the modeled region limits the practical effect of this long-range structure in all directions other than those close to north-south, as indicated by the modeled variograms of Figure 6-4.

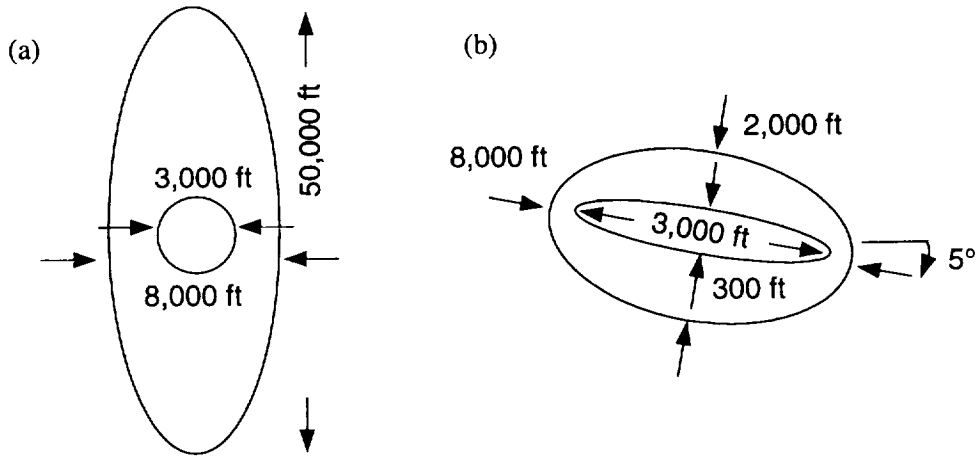

Figure 6-5. Conceptual representation in two directions of the fitted, two-part nested variogram model: (a) plan view; (b) cross-sectional view from west to east. Ranges and degree of anisotropy are schematic and not to scale.

6.4 Simulations

The simulated model is based on a gridded representation of the volume containing the potential Yucca Mountain repository, extending from Solitario Canyon on the west to beyond the eastern edge of the proposed perimeter drift, and from the surface to below the static water level. Boundaries of the model are Nevada State Plane Coordinates (defined in feet) 555,205 and 565,155 East, and 757,620 and 769,520 North. Elevations within the model range from 2,350 ft to 4,840 ft. The grid spacings of 100 ft N-S, 50 ft E-W, and 10 ft vertically, define 6 million nodes.

6.4.1 Sequential simulation algorithm

The simulations produced for this modeling exercise are intended to include two lithologic types, welded and nonwelded. Because hydrologic properties must eventually be assigned to these lithologies for use in flow and transport calculations, and because the specific hydrologic properties vary with the member-level subdivisions (see Section 6.5.4), the welded lithologic category has been subdivided into two subclasses to distinguish a particular interval in which two different stratigraphic units (welded phases of the Prow Pass and Bullfrog Members of the Crater Flat Tuff) may come into contact. The same spatial continuity model is applied to each indicator class.

To construct a specific simulation, a random path is defined through the model that will visit each node once and only once. At each unsampled location, the probability of encountering a welded or a nonwelded rock type is estimated using the computer code, SISIMPDF (Deutsch and Journel, 1992), given the surrounding conditioning data and the inferred model of spatial continuity. That location is then assigned a rock type randomly, based upon the locally conditioned probability. The simulation process then moves to the next node along the random path. At each point, the local probability is conditioned both to the original lithologic codes and to any nearby previously simulated grid nodes. If there is no information within the range of spatial correlation specified by the continuity model, the rock type is assigned randomly based upon the overall proportion of different rock types. For the current model, the marginal percentages of each category are 61% welded, 36% nonwelded, and 3% Prow Pass welded.

As the grid is filled, grid nodes in regions near conditioning data will tend to be assigned rock types resembling those data; an unsampled node stratigraphically close to a thick welded unit generally will be simulated as welded. However, there is a non-zero probability of generating a nonwelded value at the same location. Conversely, at grid nodes in regions remote from any conditioning data, the initial probability of generating a particular lithology is close to the overall proportion of that lithology defined for the model as a whole. As the simulation proceeds, subsequent nodes in that same region will be constrained by the previously generated values. This simulation mechanism produces individual realizations that collectively reflect geologic uncertainty. Close to measured data, there is little uncertainty, and replicate simulations will appear similar. Far from data, there is great uncertainty, and equivalent images extracted from alternative models may appear substantially different in character. Note that because of anisotropy, "close" and "far" refer to the geologic context: a point 100 m away along the plane of depositional layering is generally much "closer" geologically than a point 10 m away perpendicular to that layering.

The search radius determines how far away to search for data in computing the probability distribution for each node and greatly affects the amount of time required for computing the geostatistical simulations. The search radius used for these simulations is 2,438 m (8,000 ft) in the direction of strike (also the direction with maximum range). For the calculation of local conditional probability function at each simulated node, a maximum of two data points from each octant (in three dimensions) is allowed. This strategy forces consideration of data in all possible directions and prevents locally clustered data in one octant from dominating the computation. A maximum total of eight conditioning nodes (data plus previously simulated) are used in estimating the probability density function. Complete specification of the simulation parameters is code-specific (Deutsch and Journel, 1992).

6.4.2 Empirical modification of the inferred spatial model

The choice of dip angle affects the ability of the simulation algorithm to resolve the more significant normal faults known to offset the stratigraphic units at Yucca Mountain. The digitized cross sections incorporated offsets related to the faults interpreted on the USGS cross sections (Scott and Bonk, 1984). Currently no adequate mechanism exists to reverse the effect of the faulting when computing the sample variograms. Thus, the dip identified by the variography (Table 6-1) includes the influence of the numerous relatively small offsets present within the mapped area. Given the relative magnitudes of the horizontal and vertical distances reflected in the cross sections and the surrogate nature of the cross-section data itself, this simplification is not believed to be significant. However, when generating the actual simulations, effective propagation of the conditioning data into unsampled volumes is dependent upon the dip of the actual rocks units. Evaluation of the Scott and Bonk (1984) map and cross sections coupled with numerical experimentation (varying the rotation angle input to the simulation algorithm; angle 3 in Table 6-1) results in a final choice of 6.7° for the statistical dip of the units within the model.

If the model parameters of Table 6-1 are used without further modification, the sequential simulation algorithm tends to introduce stratigraphic units that are less laterally extensive (more ellipsoidal) and more complexly interfingered (Figure 6-6a) than the generally accepted, "layer-cake" conceptual model of the stratigraphy of Yucca Mountain. This computational artifact is particularly evident for the massively welded units of the Paintbrush Tuff that form the dominant surface exposures at the site. The interfingering is more pronounced where the model is not well constrained by conditioning data. An example is the discontinuity of the nonwelded rock types appearing in the

upper portion of Figure 6-6a. Although the resulting pinching and swelling may be a better representation of the less consistently welded Crater Flat tuffs, such interfingering is disconcerting to the observer familiar with the field geology of Yucca Mountain, which is dominated by exposures of the Paintbrush Tuff.

Figure 6-6. Representative west-to-east cross-section of Yucca Mountain illustrating the tendency of simulated welded and nonwelded lithologies to pinch and swell and to interfinger in a more complex fashion than is believed reasonable based on field observations. (a) Profile simulated directly using the anisotropy ratios from Table 6-1. (b) The same profile simulated by adjusting anisotropy ratio 2 to 0.025 (40:1).

Computing variograms for properties that exhibit markedly different correlation ranges in different directions typically leads to underestimation of anisotropy ratio(s), particularly for data that are not regularly arranged in space. This tendency is compounded in the present example by the fact that many of the data used in the variography exercise are located preferentially along cross sections (Figure 6-3) that are located at an angle to the major and minor axes of anisotropy. Deutsch and Journel (1992) recommend empirical adjustment of the anisotropy ratios in such cases. Thus the anisotropy ratios (ratio 2 in Table 6-1) inferred from the cross-section data have been arbitrarily adjusted by trial-and-error to 40:1 (0.025), which eliminated most of the more obvious numerical artifacts. Figure 6-6b is a simulated profile at the same location as Figure 6-6a, produced by increasing the anisotropy ratio as described.

Another phenomenon may also be operating to produce post-adjustment simulations that still appear to interfinger more than called for by the layered conceptual

model. Without sufficient drillhole data to condition the simulations adequately, the non-zero probabilities associated with all rock types at unsampled locations can lead to the generation of random (numerical) lithologic artifacts at grid locations far from conditioning data, which then propagate for some distance before being overwhelmed by the propagation of actual data. In the present case, the residual interfingering exhibited by Figure 6-6b is a direct result of the limited number of drillholes that serve as the conditioning data. Incorporation of additional soft data (or future drillholes) would work to alleviate this type of remnant numerical artifact. Although additional empirical adjustments to the anisotropy ratios could be performed to "tinker" with the cross-sectional appearance of the geostatistical models, we elect to simulate lithology using the adjusted 40:1 anisotropy ratio and then manually simplify the cross sections to derive the one-dimensional profiles at the desired locations for performance computations.

6.5 Development of stratigraphic columns for performance-assessment modeling

The generally accepted layered-geology conceptual model of Yucca Mountain implies that a vertical profile (stratigraphic column) will encounter only a limited number of major welded-to-nonwelded transitions that correspond approximately to the major member-level and formation-level stratigraphic contacts. Figure 6-7 presents a composite vertical profile of the model of Yucca Mountain that incorporates the major lithologic transitions expected. Interval thicknesses and general lithologic classes are patterned after information from drillhole USW G-4 (Spengler and Chornack, 1984); however, the details are a composite of all drillholes and the resulting indicator model. Column (a) of Figure 6-7 shows the locations of the welded-to-nonwelded indicators; column (b) shows the hydrogeologic units. Definitions of the hydrogeologic units are given in Table 6-2. Also shown for comparison and reference are the corresponding formal geologic units in column (c) (summarized from Scott and Bonk, 1984) and thermal/mechanical units (from Ortiz *et al.*, 1985) that have been used in some previous performance assessment exercises (column (d)).

6.5.1 Column locations

TSPA-91 (Barnard *et al.*, 1992) considered a two-dimensional transect with six vertical columns in the northern part of the potential repository. The six columns along the transect represented equal-area subregions. The simplicity of this transect approach was useful, but it did not have representation from the southern part of the potential repository block.

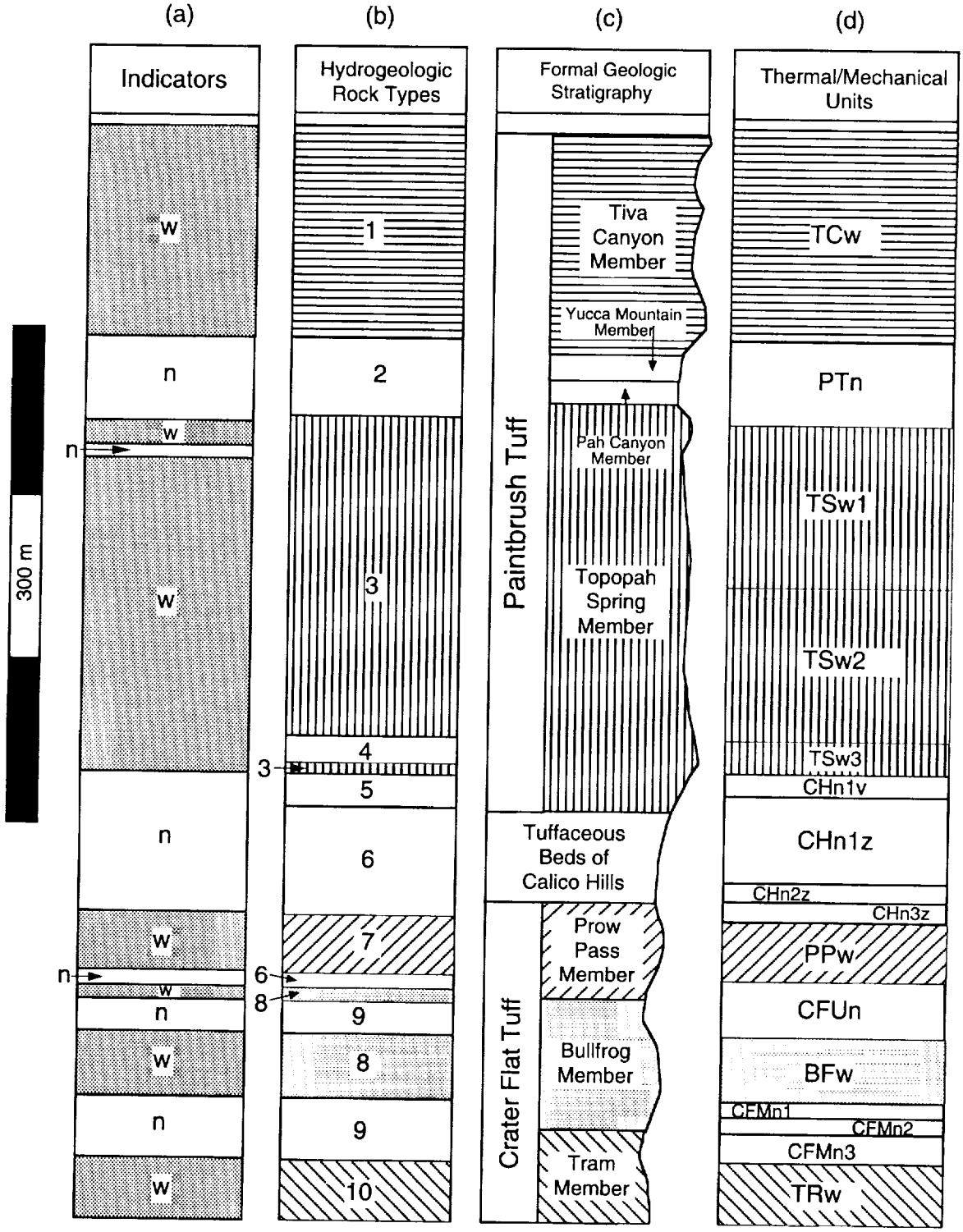

Figure 6-7. Composite vertical profile of Yucca Mountain showing approximate correspondence of indicator lithologic categories (column (a)) with thermal/mechanical units of Ortiz *et al.* (1985) (column (d)), and formal geologic nomenclature as modified from Scott and Bonk (1984) (column (c)). Column (b) shows the hydrogeologic units used in TSPA-93. (Not all of the thin zones at the bottom of Column (b) were modeled.)

Table 6-2. Descriptions of the ten hydrogeologic units used in TSPA-93.

Unit Number	Hydrogeologic Unit	Description
1	Tiva Canyon welded	Moderately to densely welded, devitrified ash-flow tuffs belonging to the Tiva Canyon member of the Paintbrush Tuff
2	Paintbrush nonwelded	Nonwelded to partially welded, vitric and locally devitrified tuffs belonging to the lowermost Tiva Canyon Member, Yucca Mountain Member, Pah Canyon Member and uppermost Topopah Spring Member of the Paintbrush Tuff; also includes air-fall tuffs, "bedded tuffs," and intercalcated re-worked tuffaceous sediments. The Yucca Mountain and Pah Canyon Members are locally welded in the northern part of the modeled area.
3	Topopah Spring welded	Moderately to densely welded, devitrified ash-flow tuffs including the upper vitrophyre belonging to the Topopah Spring Member of the Paintbrush Tuff.
4	Topopah Spring vitrophyre	Densely welded basal vitrophyre belonging to the Topopah Spring Member of the Paintbrush Tuff.
5	Calico Hills/Prow Pass nonwelded vitric	Nonwelded to partially welded, vitric and argillic ash-flow, bedded, and reworked tuffs belonging to the lowermost part of the Topopah Spring Member of the Paintbrush Tuff, the tuffaceous beds of Calico Hills, and the nonwelded portion of the Prow Pass Member of the Crater Flat Tuff.
6	Calico Hills/Prow Pass nonwelded zeolitic	Same as unit 5, but specifically identifying the zeolitized portions of these units.
7	Prow Pass welded	Partially to moderately welded, devitrified and locally zeolitic ash-flow tuffs belonging to the Prow Pass Member of the Crater Flat Tuff.
8	Bullfrog welded	Moderately to densely welded, devitrified ash-flow tuffs belonging to the Bullfrog Member of the Crater Flat Tuff.
9	Bullfrog nonwelded	Nonwelded to partially welded, argillic, zeolitic, and devitrified ash-flow tuffs and minor "bedded tuffs" belonging to the upper and lower portions of the Bullfrog Member of the Crater Flat Tuff.
10	Tram welded	Moderately to densely welded, devitrified ash-flow tuffs belonging to the Tram Member of the Crater Flat Tuff.

The approach for TSPA-93 takes advantage of being able to extract a stratigraphic profile at any location within the three-dimensional geostatistical simulations in order to improve upon TSPA-91. Choosing representative columns for modeling in TSPA-93 is complicated by thermal emplacement configurations that may use only part of the potential repository area and by changes that the four configurations considered have undergone as more information is gathered and calculations are updated. The four config-

urations include a 1,139-acre design region divided by the main drift and a 575-acre region located entirely to the northwest of the main drift (illustrated in Figures 4-7 through 4-10). For the 1,139-acre area, the estimated ratio of the area northwest of the main drift to the area to the southeast is 5:3. Thus, five areas have been chosen for modeling the northwestern part, which are also used in calculations for the 575-acre scenario, and three areas are used for modeling the southeastern part. Figures 6-8 and 6-9 show the column locations for the 1,139-acre (57 kW/acre) and the 575-acre (114 kW/acre) cases respectively.

To represent the potential repository properly with these eight columns, each column should represent an approximately equal portion of the repository. One chosen representative area is Ghost Dance Fault; thus fault-zone properties can be specified in columns 5 and 7 in Figure 6-8 (or column 5 only in Figure 6-9). Another area (column 1 in Figure 6-8) is chosen to represent the Solitario Canyon slope. The remaining areas are roughly aligned with the expected intersections of the Bullfrog, Prow Pass, and Calico Hills geologic units with the water table (the shaded areas in Figures 6-8 and 6-9). Because of structural dip, a different number of stratigraphic units are expected to be included in these columns.

The column locations are based on the 1,139-acre potential repository layout. The equal areas are determined by superimposing a 50-meter-square grid over the potential repository and counting squares. After the areas are chosen, the representative columns are located at the approximate center of each area. The same eight columns are used for both 57-kW/acre cases. The 114-kW/acre cases use only the first five columns. Although the areas represented by the five columns do not exactly overlie the northwestern part of the 1,139-acre repository (and the areas they represent are not quite the same as in the 57-kW/acre cases), the same five columns are used to allow better comparisons between the cases and to reduce computation. Column locations are tabulated in Table 6-3.

6.5.2 Conceptual model and data uncertainty issues

Given the conceptual geologic model of Yucca Mountain assumed for the performance assessment models, extreme interfingering of welded and nonwelded rock types within a single stratigraphic column is considered unrealistic and unacceptable. Although the empirical adjustment of anisotropy ratios (Section 6.4.2) eliminated many features in the simulations interpreted as numerical artifacts of the simulation algorithm, the characteristics illustrated in Figure 6-6b tend to persist, particularly in the deeper stratigraphic units. Simplification of the stratigraphic columns extracted di-

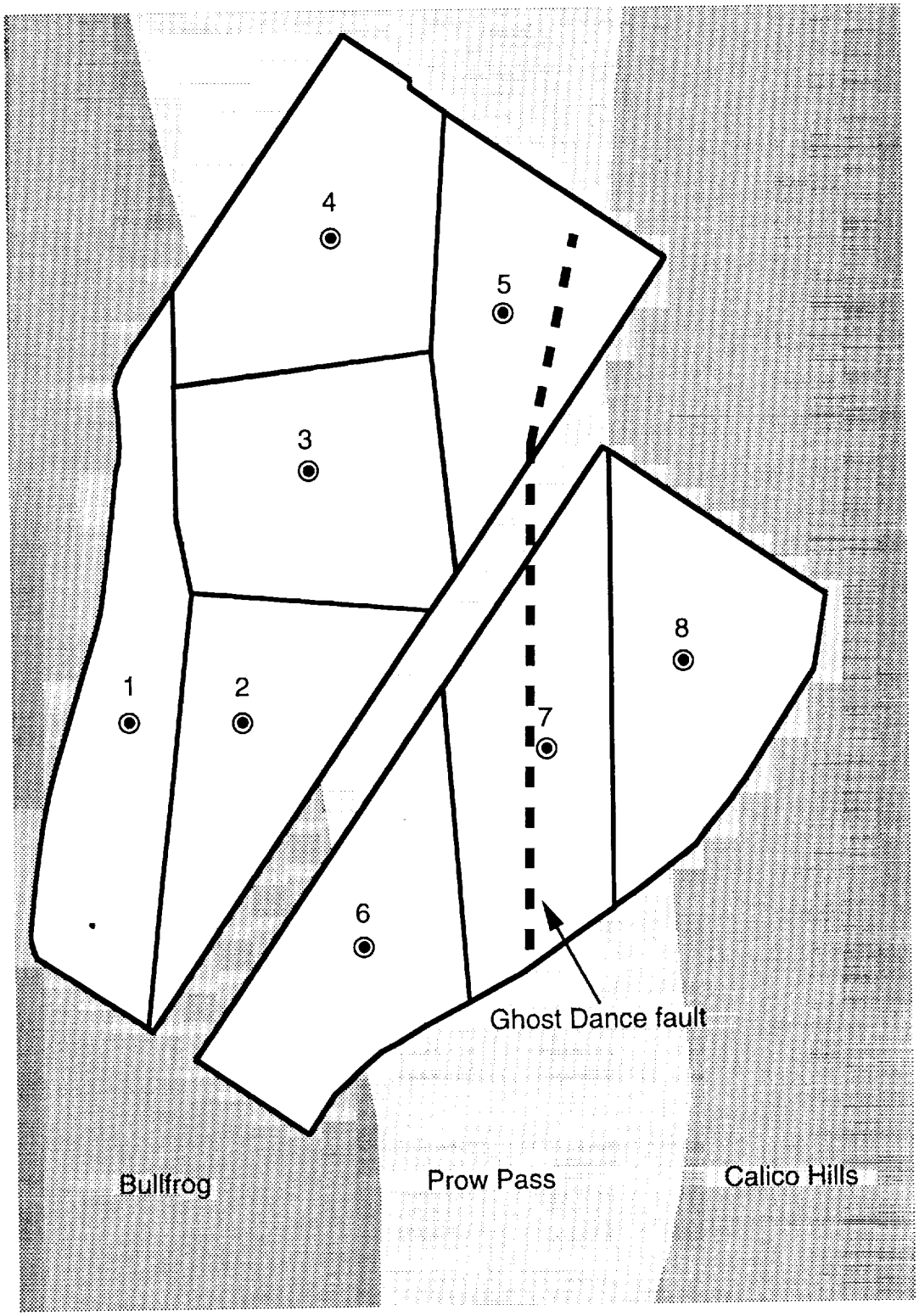

Figure 6-8. Columns and associated areas for the 1,139-acre (57 kW/acre) repository model

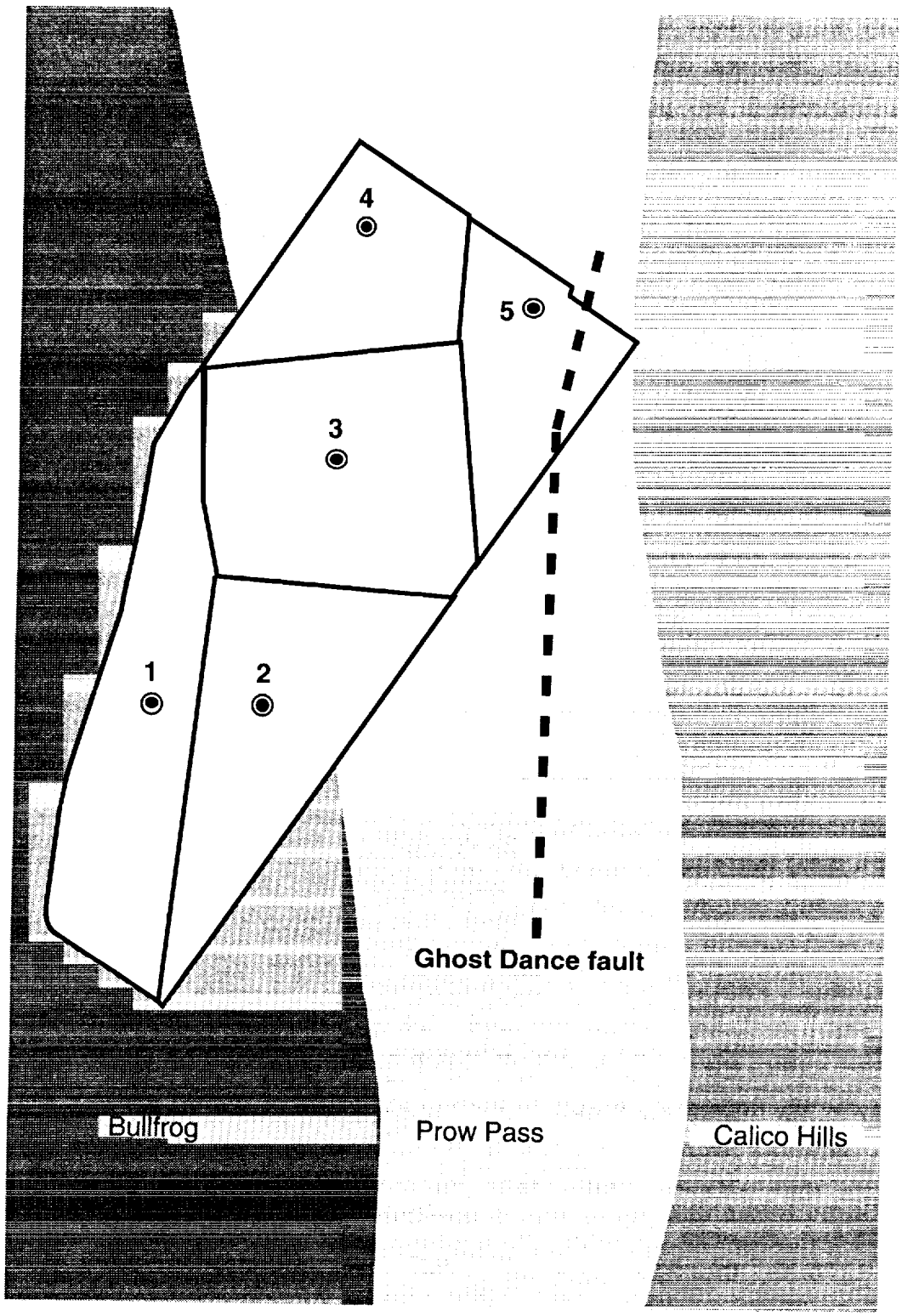

Figure 6-9. Columns and associated areas for the 575-acre (114 kW/acre) repository model

rectly from the stochastic models was judged necessary. This process is described in Section 6.5.3. However, there are several factors which indicate that the "interfingering" of lithologies is not purely an artifact of the geostatistical simulation process. These factors suggest that there is greater uncertainty associated with the conceptual model of Yucca Mountain than may generally be appreciated, and the existence of these questions suggests avenues for further site characterization.

Table 6-3. TSPA-93 column locations (Nevada state plane coordinates converted from feet).

Column	Easting (m)	Northing (m)
1	170,156.12	232,538.02
2	170,506.64	232,538.02
3	170,720.00	233,330.50
4	170,796.20	234,062.02
5	171,329.60	233,818.18
6	170,872.40	231,836.98
7	171,451.52	232,446.58
8	171,878.24	232,720.90

It is unclear that the current conceptual model of Yucca Mountain is necessarily as strongly layered as is often assumed. Figure 6-7 portrays some apparent discrepancies with the conceptual representation of entirely massive welded intervals separated by equally massive, if somewhat thinner, nonwelded sections. For example, in the upper portion of the Topopah Spring welded sequence of drillhole USW G-4, Spengler and Chornack (1984) describe the occurrence of a "nonwelded to partially welded" interval from 85.3 to 86.2 m (280.0 to 284.5 ft) underlying more than 11 m (37 ft) of "densely to moderately welded" tuff. According to the indicator coding scheme adopted for TSPA-93 (Schenker *et al.*, 1994), there is a definite change in rock type within the supposedly massive Topopah Spring welded sequence. Similar mixing or interfingering of rock types occurs within the Crater Flat Tuff, which is characterized by significant internal variability in the degree of welding as evidenced by the published geologic logs of the drill core (data and references in Schenker *et al.*, 1994), contrary to the homogeneity implicit in the thermal/mechanical stratigraphy of Ortiz *et al.* (1985). An example is the occurrence of a "partially welded" interval from 602.4 to 632.1 m (1976.5 to 2073.9 ft) in drillhole USW G-1 (Spengler *et al.*, 1981; additional evidence in Nelson *et al.*, 1991) sandwiched within a more "partially to moderately welded" section extending upward to 568.9 m (1866.6 ft) and downward to 655.9 m (2152.0 ft). This style of variability has been captured by the additional, lower interval of "Prow Pass welded" rock type (indicator category 3, unit 7 of Table 6-2) shown in the composite vertical profile of

Figure 6-7. This material is genetically part of the Prow Pass Member of the Crater Flat Tuff, as indicated by its inclusion in that formal geologic unit.

These examples indicate that there is definite geologic evidence for interlayered rock types, which, when coded into indicator categories and used to condition the geostatistical simulation process, propagates according to the variogram model. This propagation, which is particularly evident in the lateral dimension because of the inferred anisotropy ratios, produces undesirable mixing of rock types in the resulting stratigraphic columns. Thus, the geostatistical modeling process has identified the existence of conceptual model uncertainty: Yucca Mountain may not be as simplistically layered as is frequently assumed.

A second factor tending to create interfingered lithologic units in the simulated models is data uncertainty. Data uncertainty is used here in the sense of the quantity of information available to inform the many grid nodes composing the numerical lithologic model. There are regions within the model domain in which the general density of drillholes is greater or less than elsewhere. Cursory evaluation of the data content of the model from Figure 6-2 indicates that stratigraphic column 1, which represents the portion of the repository region adjacent to Solitario Canyon, and stratigraphic column 2 exhibit the greatest variability, in large part because there are fewer drillholes in the western portion of the modeled volume. The geologic interpretation in this region is uncertain at best. Stratigraphic columns 4 and 5 exhibit the least variability among simulations because they border Drill Hole Wash, so named because of the many exploration drillholes located in this region. Additionally, fewer drillholes reach to the deeper stratigraphic levels, thus increasing geologic uncertainty at depth. Not surprisingly, variability among simulations is high at the deeper levels in the model, reflecting that lack of knowledge. This latter circumstance interacts with the previously documented lithologic variability of the Crater Flat Tuff to produce apparent highly heterogeneous intervals for these deep stratigraphic zones.

Actual measurement errors in the conditioning data obviously are another source of uncertainty. However, in geostatistical studies, measurement error is generally assumed to be substantially less important in estimating or simulating an unsampled location than the uncertainty resulting from the absence of information at that point.

A third factor affecting the simulated models is the presence of faults in the field that are only partially approximated by the operation of the simulation algorithm described in Section 6.4.1. Where sufficient conditioning data exist, a more-or-less definitive offset of simulated rock types can be observed. More generally, however, the conditioning data are not sufficient, and some interfingering appears to result as the logic of

a hard-coded mathematical formulation attempts to deal with the apparent logical inconsistency of differing lithologies on opposite sides of a deterministic break. A future challenge in geostatistical modeling is to incorporate external information, such as fault locations, into the more stochastic modeling process. Incorporation of other "soft" information not considered in this modeling exercise would further reduce the tendency to propagate artifacts generated as a consequence of local ignorance.

6.5.3 Simplification of the stratigraphic columns for further analyses

The persistence of presumed excessive interfingering of welded and nonwelded rock types in the final simulated models, even after adjustment of the anisotropy ratios, requires manual simplification to produce stratigraphic columns suitable for the TSPA-93 calculations. The degree of subjectivity is probably no greater than that involved in the original indicator coding of the descriptive drillhole logs (e.g., Schenker *et al.*, 1994).

For purposes of simplifying the raw stratigraphic columns, the boundaries between hydrogeologic rock types are interpreted where there is a major vertical change in overall appearance from a relatively massive simulated rock type (welded or nonwelded) to a more interfingered style. Where the geostatistical simulations exhibit relatively distinct boundaries between the inferred hydrogeologic units, efforts are made not to alter significantly the overall proportion of the different lithologic types, although this is not performed in a rigorous manner. Nearby drillhole evidence (if any) is also used to guide the selection of appropriate contact elevations. Away from conditioning data, the hydrogeologic units are not as distinctly defined, and the thermal/mechanical model of Ortiz *et al.* (1985) is used as an initial guide in determining the interfaces.

6.5.4 Introduction of deterministic stratigraphic features

Examination of the underlying geologic data (references in Schenker *et al.*, 1994) and of many profiles extracted from the ten stochastic indicator realizations leads to the composite profile of Figure 6-7. Essentially, this represents a conceptual stratigraphic framework to be imposed deterministically upon the simulated welded/nonwelded realizations. Fundamental aspects of this deterministic overprint include a member-level, formal lithostratigraphic designation (e.g., Tiva Canyon, Bullfrog) and supplemental lithologic identification (nonwelded vitric, nonwelded zeolitic, welded vitrophyre). These unit designations and other, non-simulated contacts (e.g., the basal Topopah Spring vitrophyre) were added based on previous modeling of similar features by Ortiz *et al.* (1985). An expanded description of the ten inferred hydrogeologic units subsequently used in the flow-and-transport modeling of TSPA-93 is presented in Table 6-2.

Imposition of these deterministic stratigraphic attributes, external to the stochastic simulation process, is a prerequisite to the assignment of matrix and fracture material properties to the units in preparation for the flow and transport calculations that compose the objective of TSPA-93. Not all welded (or nonwelded) rock types possess identical material properties. As discussed in Chapter 7, the properties assigned to a specific interval in a stratigraphic column for performance computations have been sampled from univariate distributions appropriate to that deterministic unit.

It is this requirement to assign appropriate material properties that led to the subdivision of the "welded" category into generic "welded" and "Prow Pass welded" subcategories. Although in general the major welded units are separated by substantial enough nonwelded intervals that identification of the member-level lithostratigraphic equivalence is not difficult, there are portions of the Yucca Mountain region in which the welded portion(s) of the Prow Pass Member of the Crater Flat Tuff almost directly overlie welded rocks of the Bullfrog Member. To prevent confusion of these two rock types, or the imposition of excessively subjective interpretation, the Prow Pass welded rock type is coded separately in the conditioning data. In this manner, simulated welded rocks that should be assigned material properties characteristic of the Prow Pass Member are clearly identified separately from those otherwise identical, simulated welded rocks that should receive Bullfrog properties.

6.5.5 Contact Uncertainty

The final, simplified stratigraphic columns thus generated from the stochastic indicator realizations are presented graphically in Figures 6-10 through 6-17. The actual elevations associated with each stratigraphic column are given in Appendix A.

The complete set of simulated stratigraphic columns is shown in Figures 6-10 through 6-17; each figure shows the ten simulations performed for that column, as well as the thermal/mechanical stratigraphy of Ortiz *et al.* (1985). To help visualize the effects of the geostatistical simulations, it is instructive to consider the uncertainty associated with one particular contact, the top of unit 5 (approximately equivalent to the tuffaceous beds of Calico Hills), as shown in Figure 6-18. In this illustration, the ten simulated contacts have been displayed in histogram format, classified into 10-m vertical intervals. The histogram for stratigraphic column 1 is relatively broad, extending over a gross interval of 100 m, indicating considerable uncertainty in location. By contrast, the histogram for column 4 is significantly more tightly clustered, extending over a range of only 30 m. The implication is that the simulated models are much better constrained in the vicinity of column 4 (near Drill Hole Wash;) than near column 1.

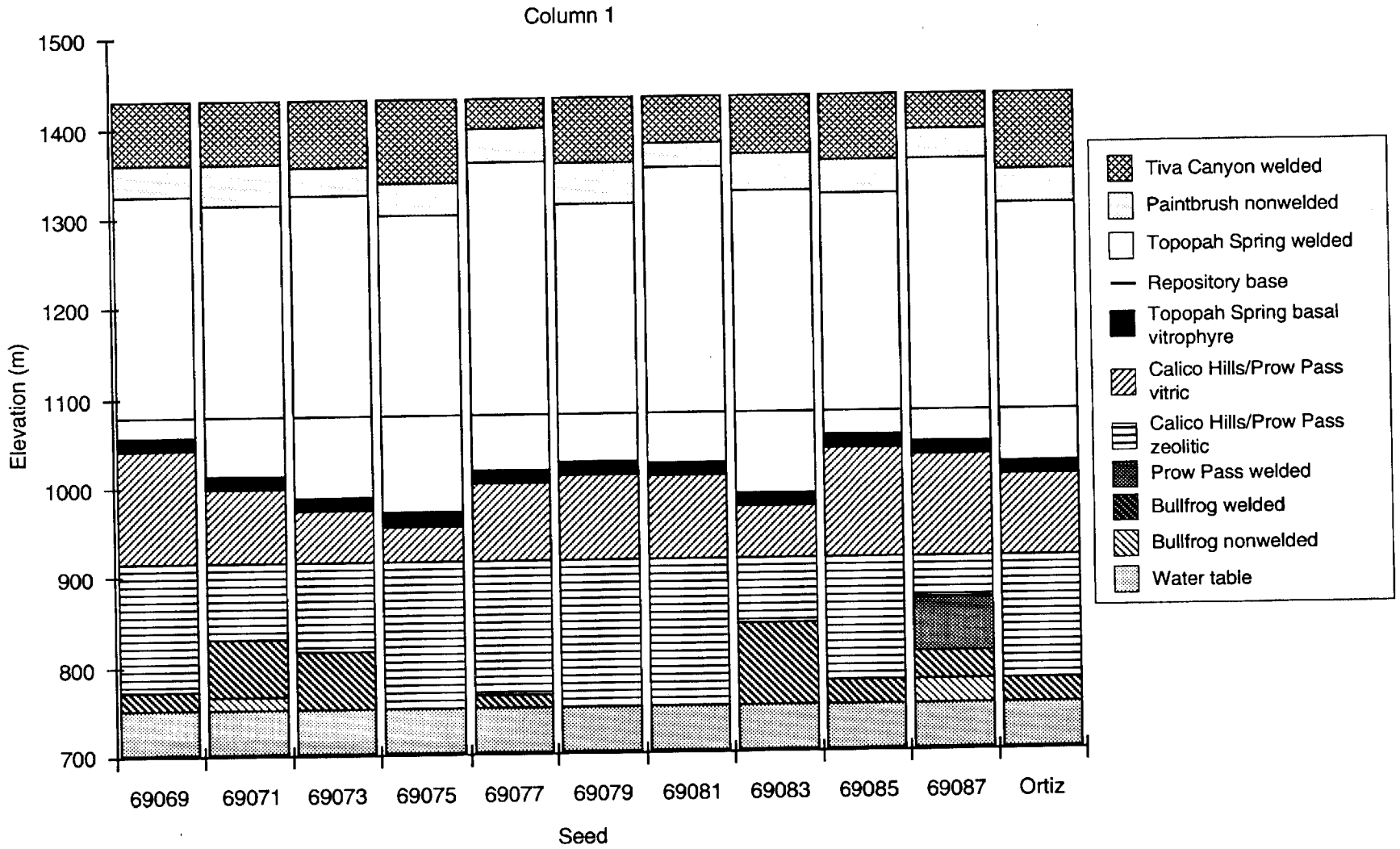

Figure 6-10. Ten simplified stochastic realizations of stratigraphic column 1 extracted from the three-dimensional indicator simulations. Note the presence of the Prow Pass welded unit only in simulation 69087. For comparison, the approximately equivalent thermal/mechanical stratigraphy of Ortiz *et al.* (1985) is shown at the right.

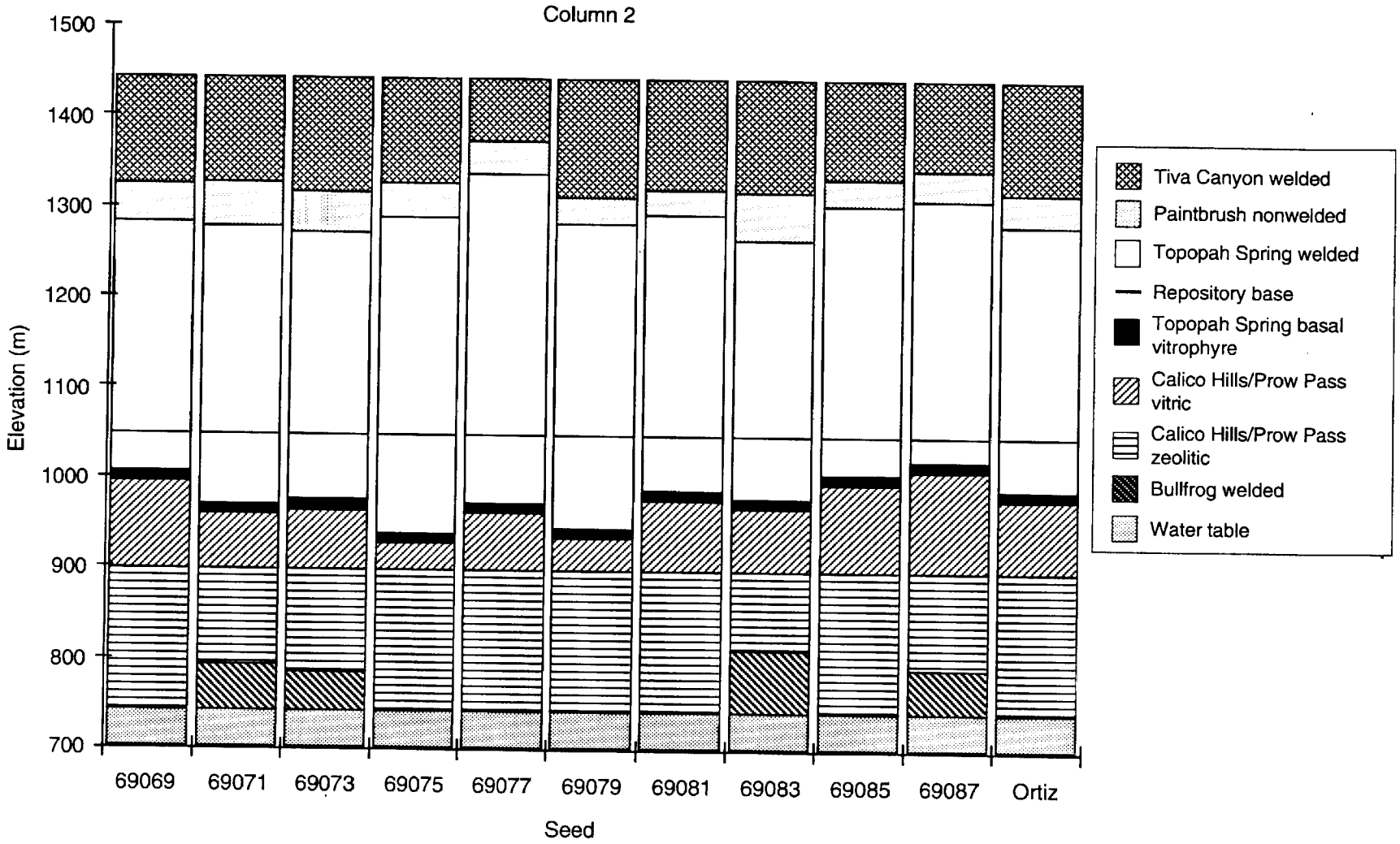

Figure 6-11. Ten simplified stochastic realizations of stratigraphic column 2 extracted from the three-dimensional indicator simulations. Note the absence of the Prow Pass welded and the Bullfrog nonwelded units from all simulations. The approximately equivalent thermal/mechanical stratigraphy for column 2 of Ortiz *et al.* (1985) is at the right.

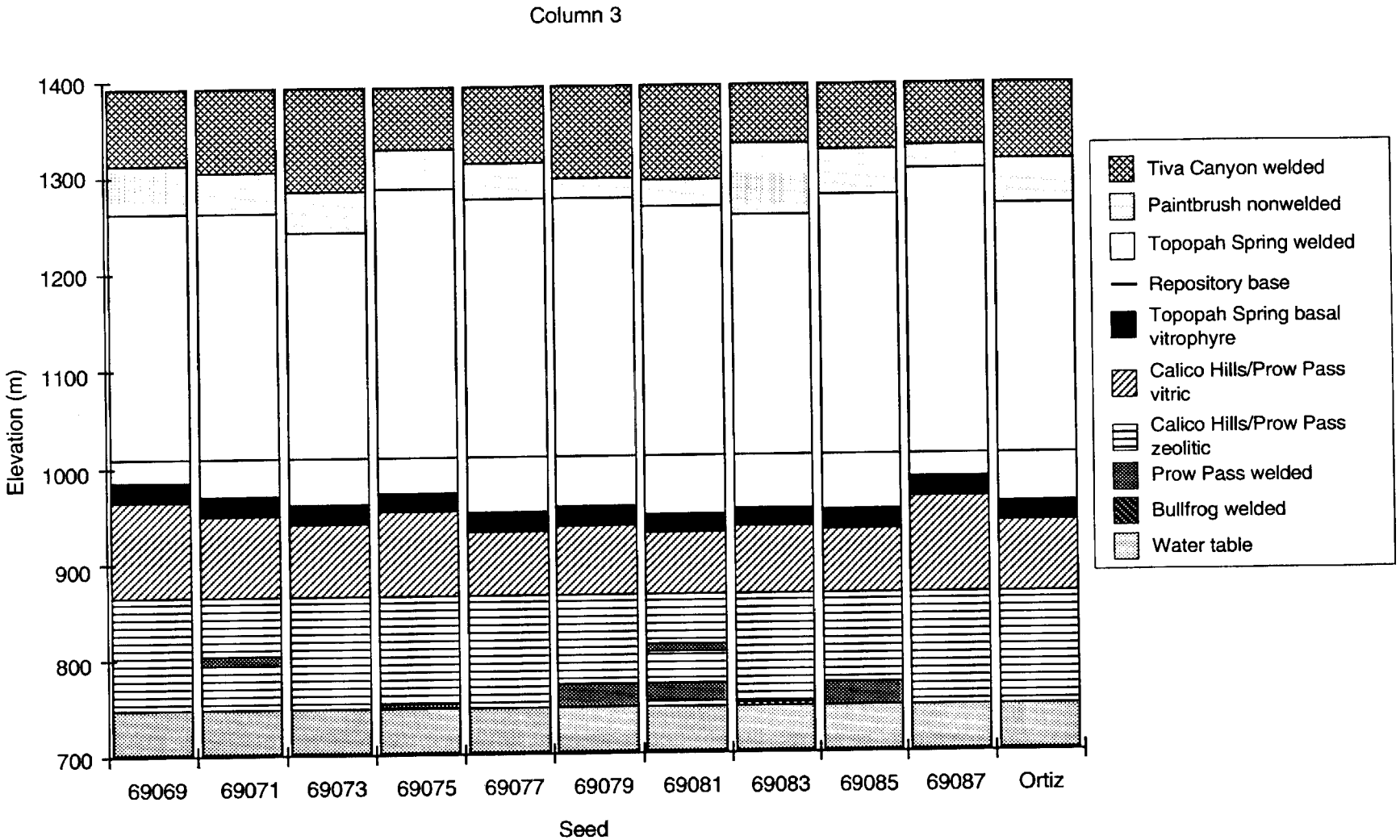

Figure 6-12. Ten simplified stochastic realizations of stratigraphic column 3 extracted from the three-dimensional indicator simulations. Note the appearance of the Prow Pass welded unit twice in simulation 69081, and the presence of the Bullfrog welded only in simulation 69083. The approximately equivalent thermal/mechanical stratigraphy for column 3 of Ortiz *et al.* (1985) is at the right.

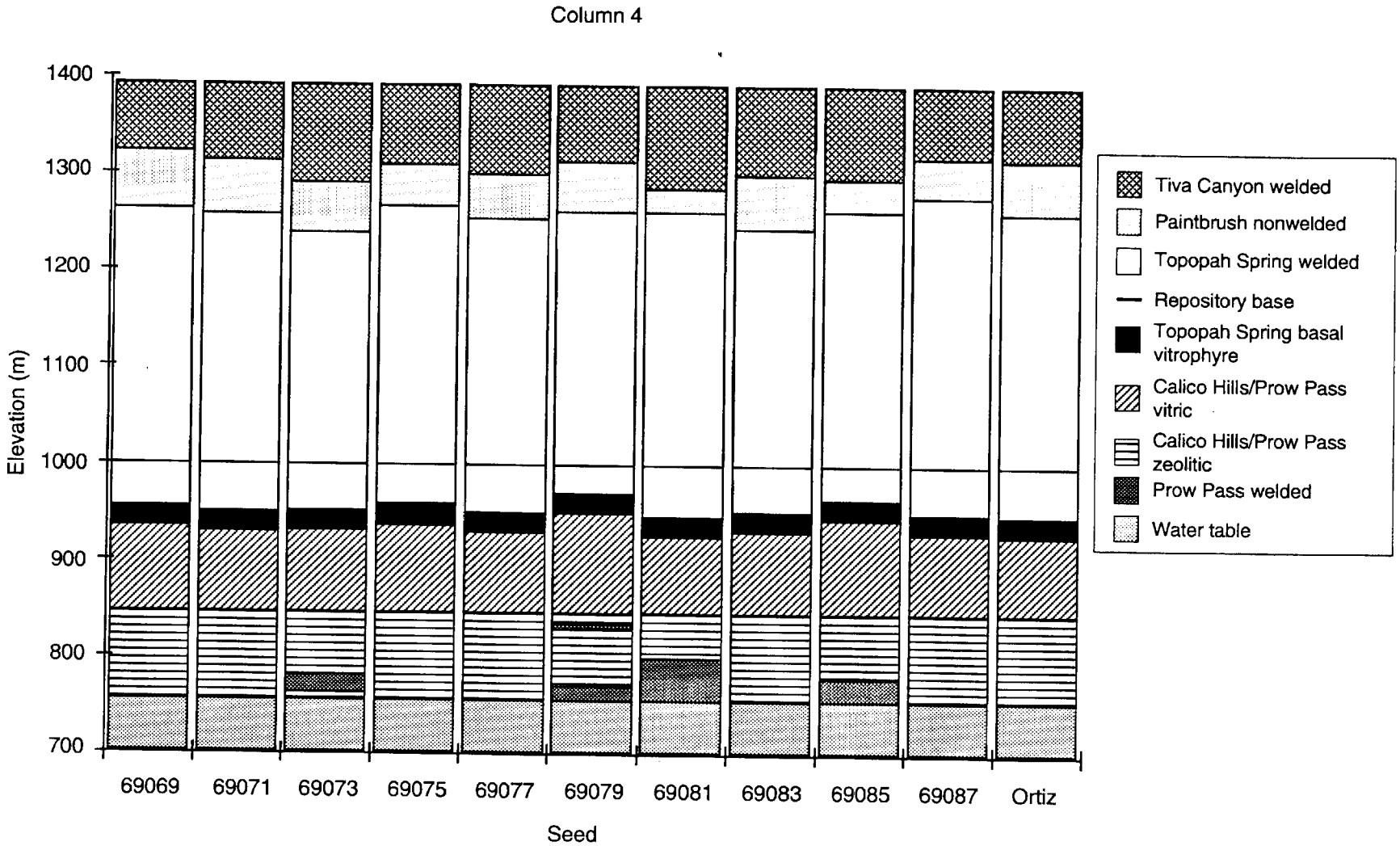

Figure 6-13. Ten simplified stochastic realizations of stratigraphic column 4 extracted from the three-dimensional indicator simulations. Note the appearance of the Prow Pass welded unit twice in simulation 69079. The approximately equivalent thermal/mechanical stratigraphy for column 4 of Ortiz *et al.* (1985) is at the right.

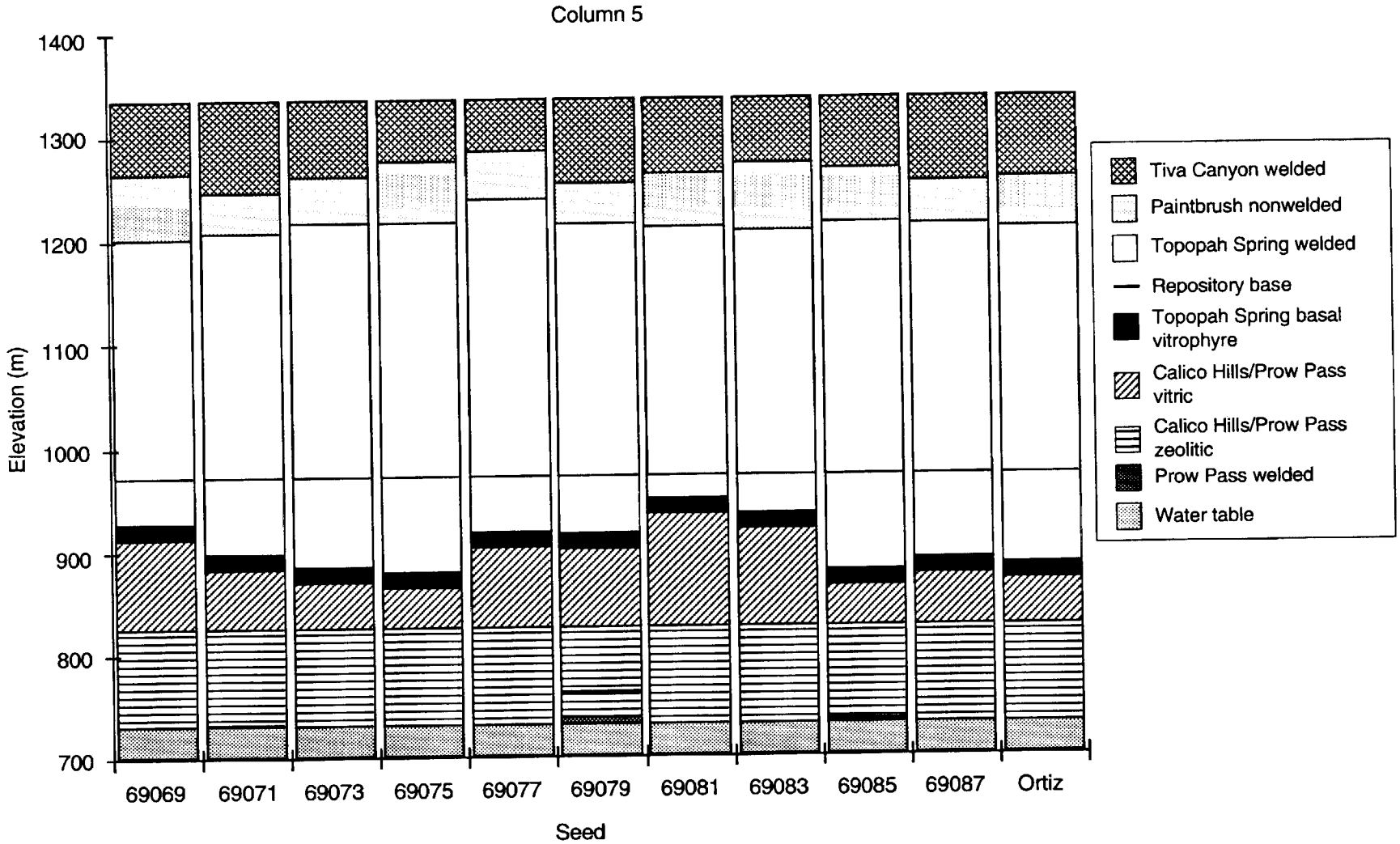

Figure 6-14. Ten simplified stochastic realizations of stratigraphic column 5 extracted from the three-dimensional indicator simulations. Note the appearance of the Prow Pass welded unit only in simulations 69071, 69079, and 69085. The approximately equivalent thermal/mechanical stratigraphy for column 5 of Ortiz *et al.* (1985) is at the right.

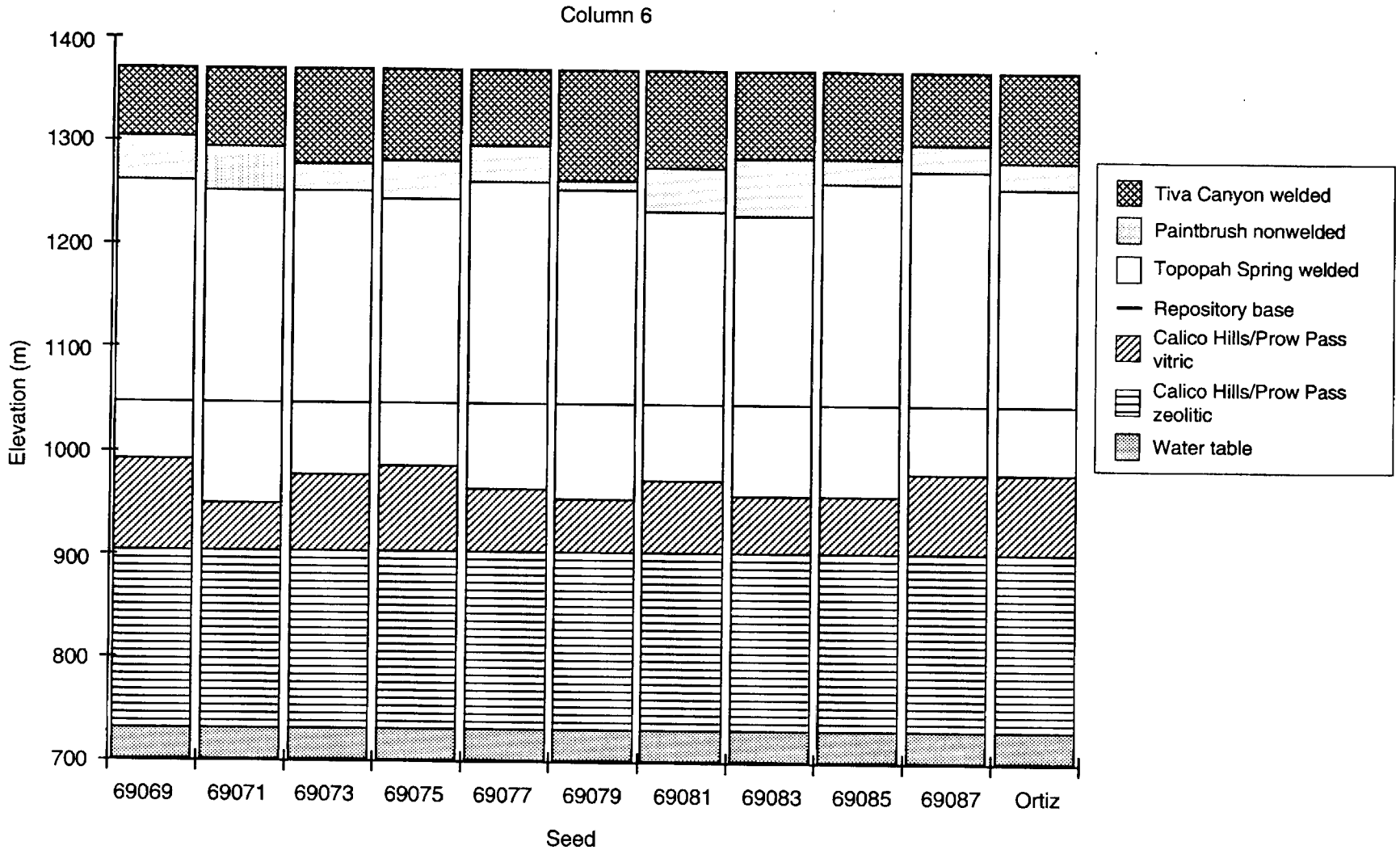

Figure 6-15. Ten simplified stochastic realizations of stratigraphic column 6 extracted from the three-dimensional indicator simulations. Note the absence of the Topopah Spring basal vitrophyre, the Prow Pass welded, and the Bullfrog units from this column. The thermal/mechanical stratigraphy for column 6 of Ortiz *et al.* (1985) is at the right.

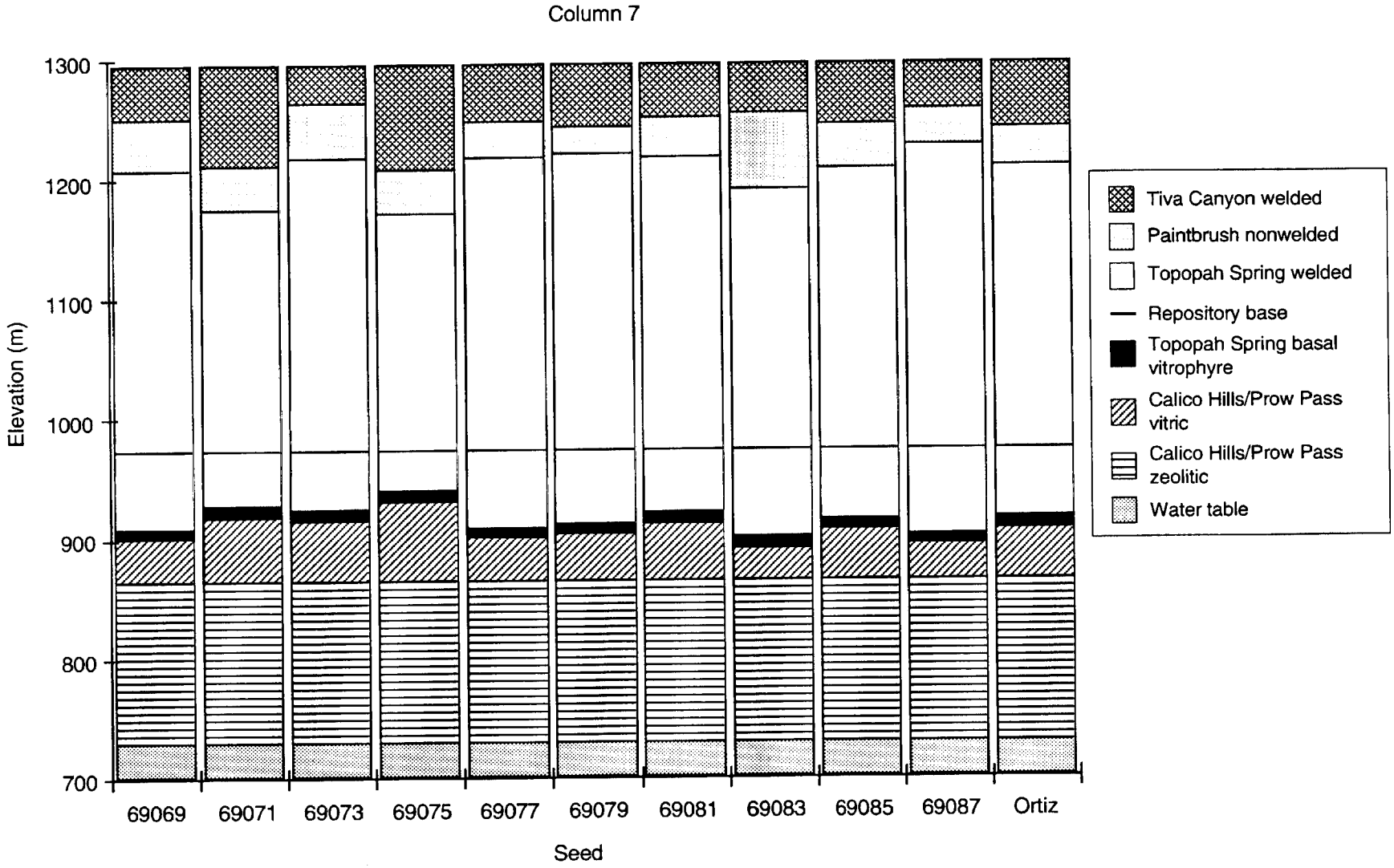

Figure 6-16. Ten simplified stochastic realizations of stratigraphic column 7 extracted from the three-dimensional indicator simulations. Note the absence of the Prow Pass welded and the Bullfrog units from this column. The thermal/mechanical stratigraphy for column 7 of Ortiz *et al.* (1985) is at the right.

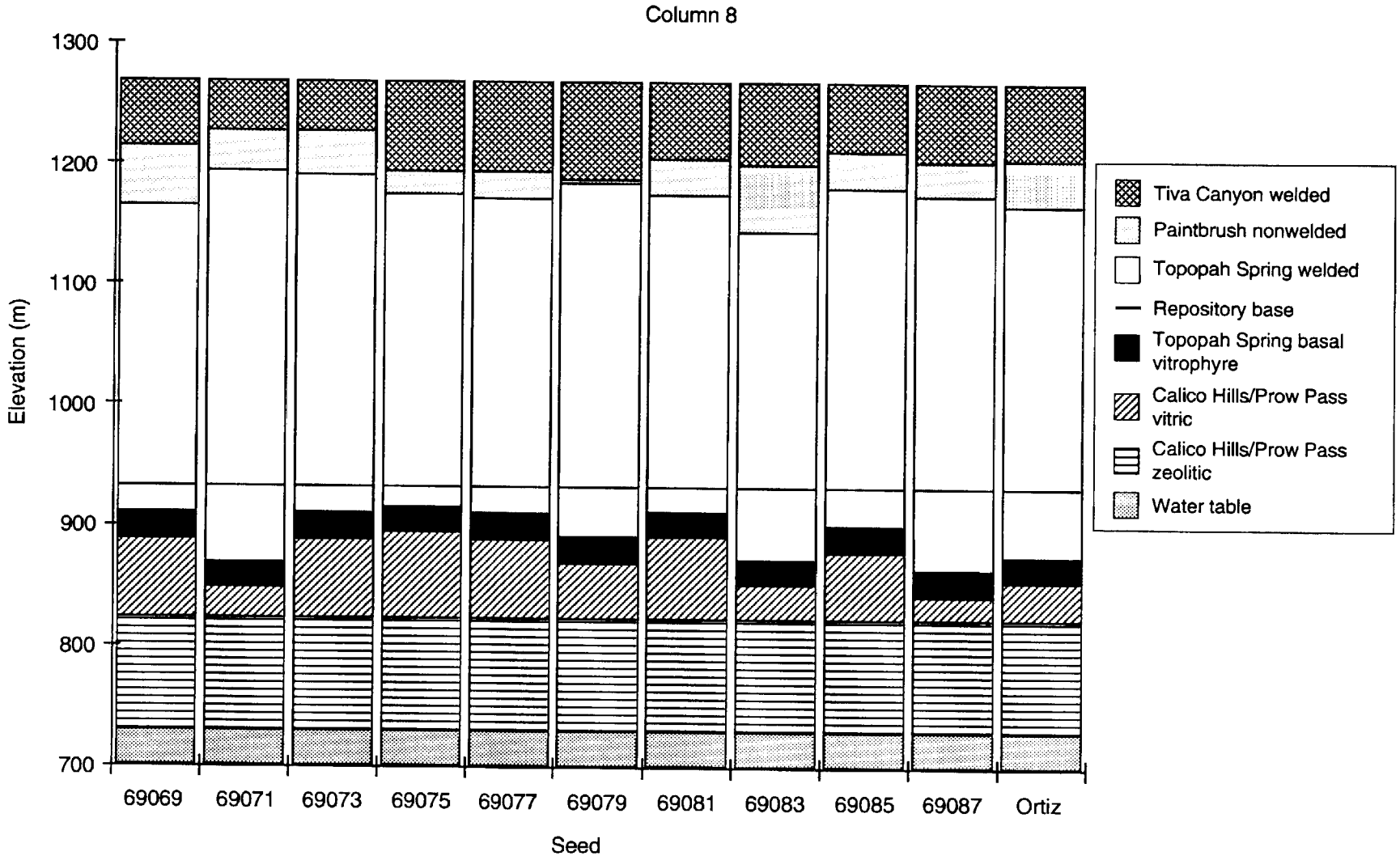

Figure 6-17. Ten simplified stochastic realizations of stratigraphic column 8 extracted from the three-dimensional indicator simulations. Note the thicker Topopah Spring basal vitrophyre, and the absence of the Prow Pass welded and the Bullfrog units. The thermal/mechanical stratigraphy for column 8 of Ortiz *et al.* (1985) is at the right.

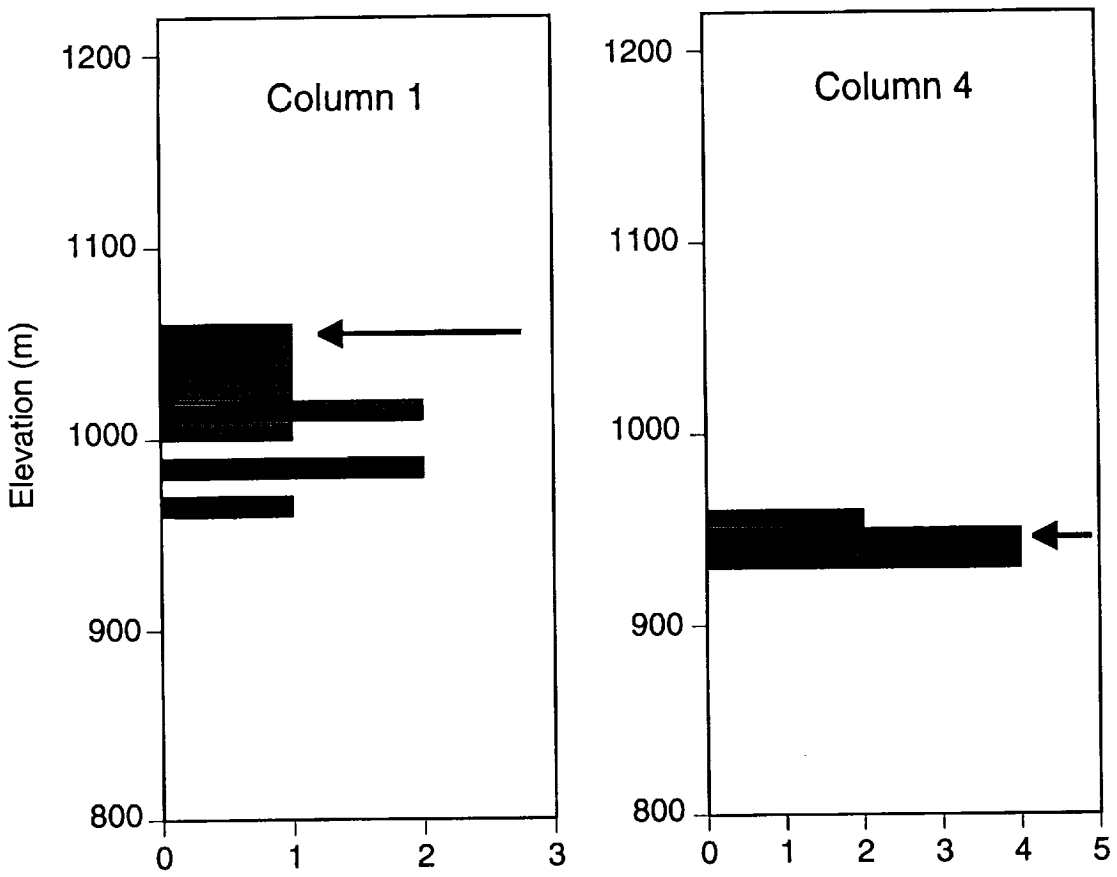

Figure 6-18. Histograms summarizing the uncertainty associated with the upper contact of unit 5 at the location of (a) stratigraphic column 1, and (b) stratigraphic column 4. Arrow indicates contact elevation from the single simulation randomly selected and used for the TSPA-93 calculations.

Also shown in Figure 6-18 is the location of the contact corresponding to the one particular simulation that was selected (at random) as the basis for the detailed TSPA-93 performance-assessment calculations. Note that in general, the position of a contact from this single model may be near the center of the distribution of potential contacts, near the extreme range of that distribution, or somewhere in between. The sensitivity of the performance-assessment results to this relative position has not yet been addressed systematically. However, such a systematic evaluation of sensitivity will be performed at a later date. It is important, however, to remember that all of the contacts represented by an individual simulation are fully consistent with one another and with the drillhole data used as input.

6.6 Use of stratigraphic simulations

Using geostatistical methods to characterize the geologic uncertainty resulting from less-than-exhaustive site information is an important initial step in the performance assessment process. To quantify fully the effects of such geologic uncertainty, a number of stratigraphic simulations must be used as input to the transfer function which then propagates that uncertainty into the selected performance measure (Journel, 1989). As in any Monte Carlo process, it is necessary to sample adequately the underlying probability function(s). For total-system performance assessment calculations, the complexity and number of the computer codes that collectively compose the transfer function may impose limitations on the use of multiple simulations generated as described in this chapter. In the present instance, the time available to execute the multiple runs of the performance computations for all the replicate stochastic images of the site prevent the complete evaluation of stratigraphic uncertainty. As discussed briefly in Section 6.5, only one of the simulations was used for the full total-system performance assessment. Future calculations will address the sensitivity of the performance results to the variation in stratigraphic thickness.

Chapter 7
Hydrogeologic Parameter Development

(Schenker, Robey, Guerin, Barnard)

This chapter is an abbreviated description of the work presented in Schenker *et al.* (1994). In that document the development of the performance-assessment data base (PADB) is discussed in detail. The PADB includes the sources of hydrogeologic properties data, the parameters derived from those data, and the probability density functions (PDFs) developed from the hydrogeologic parameters. We define "properties" as the hydrologic characteristics described by the raw source data (the quantitative measurements). A "parameter" is the resulting statistical descriptive value derived from the properties data. The PDFs are then developed from the hydrogeologic parameters. A probability density function gives the likelihood of a value when the function is randomly sampled.

Derivation of the parameter PDFs for TSPA-93 is based on the approach developed for TSPA-91 (Barnard *et al.*, 1992). Because of the scarcity of data available for TSPA-91, the PDFs were not constrained by the observed data ranges. Instead, the PDFs attempted to reflect both the observed data and the analysts' estimates of the variability and uncertainty of those data. In contrast, we have analyzed an extensive range of hydrogeologic data from the Yucca Mountain site and have incorporated them into TSPA-93. The parameters developed here are descriptive of the actual geology and hydrogeology at Yucca Mountain to the extent that the underlying data are representative. Where there are insufficient data to derive PDFs with acceptable confidence, analogs have been developed from appropriately similar site data to model those parameters.

7.1 Overview of parameter development

Most of the parameter distributions derived in this chapter are used for the simulation of unsaturated-zone groundwater flow and transport using the composite-porosity model (see Chapter 14). The fracture-aperture distributions are used in the modeling of unsaturated-zone groundwater flow using the weeps model (Chapter 15). The bulk hydraulic conductivity distributions are used in the gas-flow modeling (Chapter 12). Additionally, equivalent-porous-medium bulk hydraulic-conductivity values are used as starting values in the saturated-zone modeling (Chapter 11).

As is discussed in Chapter 6, the repository area for flow and transport modeling is described by either five or eight columns, each representing an equal portion of the repository, and each with stratigraphies characteristic of that portion. Each column contains up to ten hydrogeologic units from the land surface of Yucca Mountain to the

water table. (The undifferentiated overburden or alluvium is not modeled in the transport simulations, and is therefore not included in the columns.) Only five layers (from the repository to the water table) are used for the unsaturated flow and transport modeling, however the units from the repository to the surface are used for the gas-flow analyses. Figure 7-1 shows the locations and thicknesses of the hydrogeologic units in the eight columns. Note that some units are missing from some columns due to variations and uncertainties in the thicknesses of the units. The hydrogeologic parameters developed in this chapter are used to characterize the eight analysis columns.

Hydrogeologic properties data are available from numerous sources. There are many data for some properties for some hydrogeologic units. For other properties at other locations the data are much more sparse. In the cases where there are many data, the parameters can be derived directly. Where data are minimal, we use a fitting routine that develops a population distribution from the sample data.

In Chapter 6, geostatistical techniques are used to develop spatial distributions of the thicknesses of the hydrogeologic units. Although the thicknesses of the units can vary by up to 50% between realizations, the hydrologic parameters associated with the units are assumed to be almost independent of thickness. Thus, all materials properties are grouped according to hydrogeologic unit and are analyzed without regard to specific location of the measurement. The flow models assume that the parameters are applicable throughout a hydrogeologic unit. Thus, for each property in each of the ten hydrogeologic units listed in Table 6-2, we have developed a single PDF that is assumed to be descriptive of the entire unit.

7.1.1 Hydrologic properties considered

The hydrogeologic properties used to develop the parameter distributions fall in three major categories: matrix, bulk hydraulic, and fracture. The parameters are determined from the properties listed in Table 7-1.

7.1.2 Development method

The goal in developing PDFs is to represent the data with the least possible amount of interpretation to minimize the chance of biasing the results. Five steps are performed to develop the required PDFs for input to the flow and transport models. These are: identification of data, inclusion of the data in the PADB, preparation for analysis, statistical reduction to determine parameters, and definition of probability density functions from the parameters.

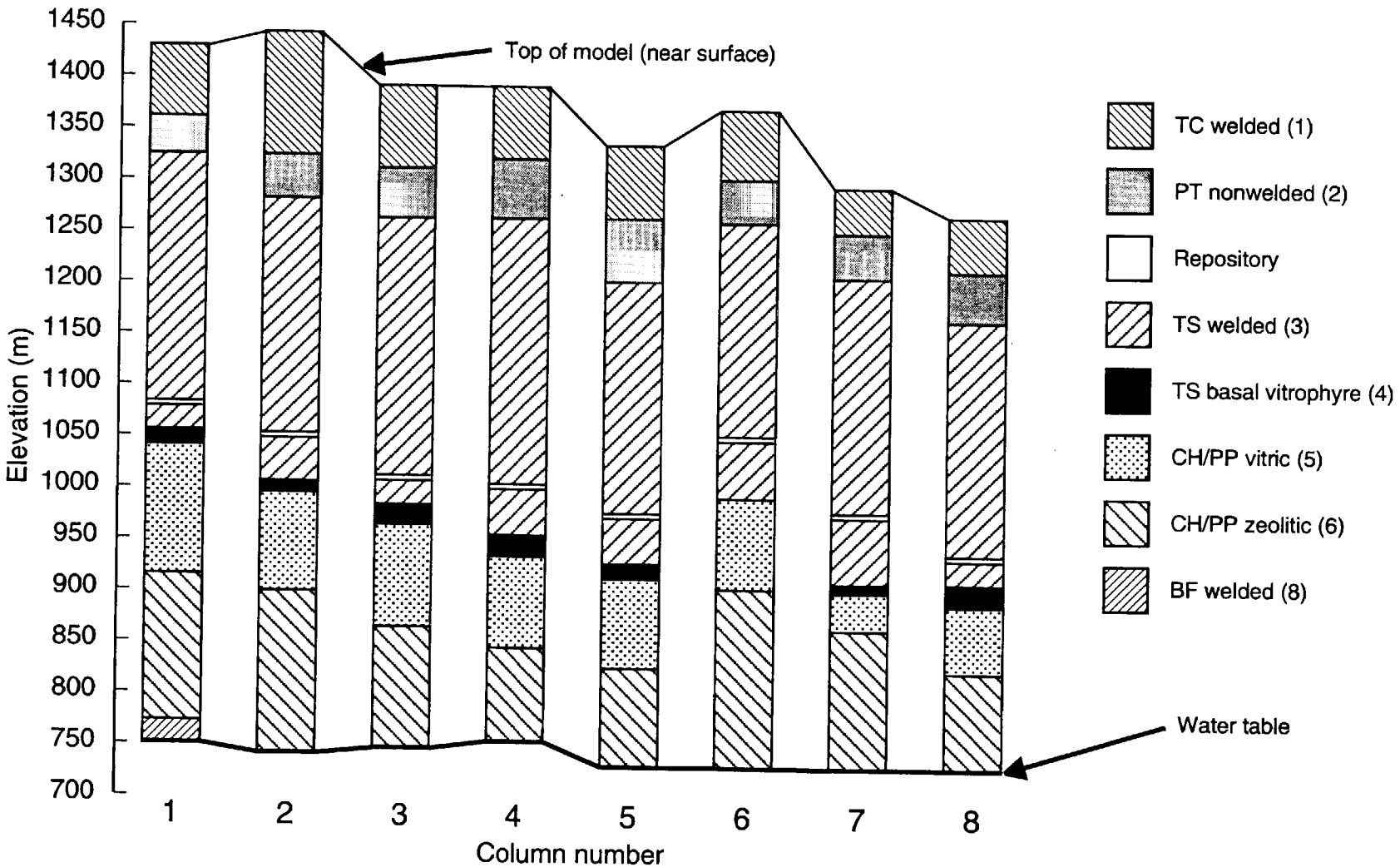

Figure 7-1. TSPA-93 unsaturated-zone hydrostratigraphy, from the top of the model domain (near the earth's surface) to the water table. Note that the column heights and water-table elevations vary because the columns are located at different points at Yucca Mountain.

Table 7-1. Hydrogeologic properties used to determine parameter distribution functions for TSPA-93.

Matrix Properties	Bulk Properties	Fracture Properties
Porosity (ϕ)	Bulk saturated hydraulic conductivity (K_{bs})	Frequency (F_f)
Rock bulk density (ρ_b)	Gas permeability (K_{bg})	Orientation (θ_f)
Saturated hydraulic conductivity (K_s)	Combined saturated hydraulic conductivities (bulk and gas)	Spacing (a_f)
Water retention (van Genuchten): air-entry (α_{vG}), saturation/desaturation (β_{vG}), and residual degree of saturation (S_r)		Hydraulic aperture (b_f)
		Porosity (ϕ_f)
		Saturated hydraulic conductivity (K_f)
		Water retention (van Genuchten): air-entry (α_{vG_f})

7.1.2.1 Data manipulation

The basic data, as identified from different sources, are sorted and grouped to correspond with each of the modeled hydrogeologic units. As data are entered into the PADB, they are evaluated for reasonableness. If there are questions of interpretation, an attempt has been made to confirm their validity. As the data are prepared for analyses, they are converted to consistent units. The parameters calculated for each data set are the expected value, $E[x]$, (the mean), the high and low values (Max and Min), and the standard deviation (SD). The coefficient of variation (CV) is also determined:

$$CV = \left| SD / E[x] \right|. \tag{7.1}$$

7.1.2.2 Description of probability density functions

The functional form of the PDFs is given by the beta function (Harr, 1987). The beta function is defined by (1) the minimum value, (2) the maximum value, (3) the mean, and (4) the coefficient of variation of the variable. The beta function can produce PDFs with many shapes (e.g., uniform, exponential, normal, bathtub). When combined with

the principle of maximum informational entropy (Jaynes, 1957), the shape of the beta function is dictated by the data available. For example, knowing only the minimum and maximum values of a property requires that the PDF be a uniform distribution across the minimum-to-maximum range.

Some of the types of distributions commonly used to fit the data are uniform, unimodal (i.e., "peaked"), and skewed (e.g., exponential). Because of the ability of the beta function to represent all these distribution types, we have chosen to use this function to generate all the PDFs. Over the range $[a,b]$, the beta function produces a PDF, $p(x)$, given by

$$p(x) = C(x-a)^{\alpha}(b-x)^{\beta}, \tag{7.2}$$

where α and β define the shape of the distribution, and C is a normalizing constant. The normalizing constant is undefined for values of α and β less than -1. When the α and β parameters are less than 0, this often is an indication that the range of the parameter is underestimated; in this case, the PDF does not have a mode in the interior of the range, but the greatest probability density occurs at one or both extremes.

7.1.2.3 Considerations when describing data with PDFs

Where the data are numerous, the parameters of the data set can be used directly to determine a beta-function PDF. It is possible that the range of the parameters may not encompass the actual range of the property; thus, this approach may not be used for all large data sets. Some properties, such as porosity, have a physical range that can be determined independently of the available data; the minimum and maximum values of porosity are defined to be 0.0 and 1.0. This extension of the range of data to the theoretical range is intended to recognize that the finite sample size is not exhaustive, and that values outside the sample are possible. Note that the probability of sampling a value near the theoretical maximum or minimum may be very unlikely, if the area under the PDF near those points is insignificant.

For some properties where the data are not extensive and no physical restrictions exist on the range of the parameter, a beta distribution is fit using a nonlinear entropy fitting program. See Schenker *et al.* (1994), Chapter 3, for a complete description of the use of the entropy fit routine. This fitting procedure attempts to infer the properties of the entire population from the limited sample. Not only does the PDF reflect the shape of the frequency distribution of the data, but it also has a range dependent upon the structure of data. For example, if data are all closely grouped at one end of the observed range, the entropy fit would interpret this as a physical limit to the property (as is

illustrated in Figure 7-2 by the behavior of the fit near the parameter value 0.1). If, on the other hand, the data at the end of the range are quite scattered the entropy fit would produce a tail on the probability distribution, implying the physical range of the data is greater than the observed range (as shown in Figure 7-2 near the value 0.8). Although the entropy fit helps in interpreting limited data sets, it does not reduce the inherent uncertainty due to small amounts of data.

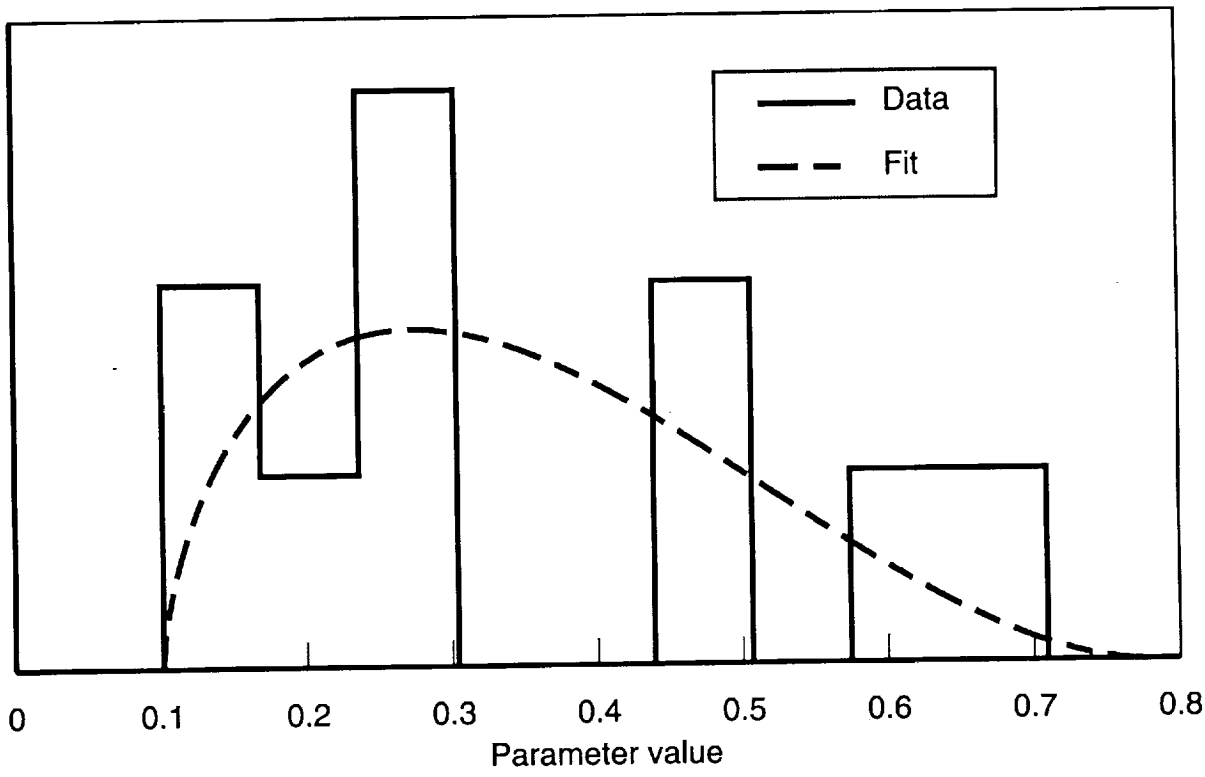

Figure 7-2. Fit to limited data using the entropy-fit routine.

The entropy fit uses nonlinear optimization to determine the best fit. Nonlinear optimization can be sensitive to the initial choices for the parameters. When the endpoints of the distribution are near the minimum and maximum of the data range, high values for the entropy and high gradients result; this sometimes causes numerical difficulties. Where such numerical difficulties exist, increasing the initial choices for the range from that of the data range circumvents the numerical problems. However, the choice of too large values for the endpoints may result in beta-function exponents that are excessively large. This also causes numerical problems.

Limited data on fractures require a different approach to determine the modeling parameters. Only two fracture properties—frequency and orientation—are available

from actual measurements of down-hole data. The remaining fracture parameters must be derived using functional relationships. Details of this derivative approach are fully described in Section 7.4.

Because there are insufficient data, PDFs cannot be developed for bulk saturated hydraulic conductivity in three of the hydrogeologic units, and for fracture orientation in six of the hydrogeologic units. In this case we select an existing hydrogeologic unit that most closely represents the hydrogeologic unit for which data are missing. Analog distributions are then created with adjustments to account for uncertainty. To make these adjustments for uncertainty, either the coefficient of variation is increased or the range is adjusted. Range adjustment is often done by setting the minimum and maximum to one or more standard deviations about the mean. This allows for more scatter around the expected value—a concession to our lack of knowledge.

In the cases where the α and β parameters of the beta function are both calculated to be less than 0 (which results in a "bathtub" shape to the PDF), we review the properties data to see if this PDF shape is physically reasonable. If it is not, the PDFs are recalculated by adjusting the range of the parameter.

Some properties (such as hydraulic conductivity) are typically distributed log-normally. Other properties have been transformed to log space if PDFs generated from the untransformed data are not well behaved. The beta distribution is able to approximate both linear and log-transformed data.

7.1.3 Scaling

Once the parameters have been determined, the matrix parameters require one additional modification. Geologic materials are known to be heterogeneous but are modeled in performance-assessment analyses as being homogeneous. Therefore, what is needed for the models is the average value of the property over the entire unit thickness. When matrix properties are determined from small core samples in a laboratory, the question that must be asked is: to what degree do the small-scale samples represent the entire hydrogeological unit? Properties values that are obtained from only a few small samples may have greater variability in the measured values (averaged over the sample) than an average taken over the entire unit. Therefore, to compensate, we reduce the variability of the parameters derived from the observed data to make them more representative of the average over the entire thickness.

The approach we use to scale parameters is an initial attempt at addressing this question. We adjust the coefficient of variation (a measure of the spread in the data) calculated for the sample to better reflect the distribution of values over the unit to be

modeled. The formula (Dagan, 1989) we use scales the coefficient of variation (CV) for either the untransformed or $\log_{10}$-transformed data to give a scaled coefficient of variation (SCV):

$$SCV = CV\sqrt{\lambda / \bar{t}}, \lambda > \bar{t}. \tag{7.3}$$

where CV is the unscaled coefficient of variation, λ is the vertical correlation length and, $\bar{t}$ is the mean thickness of the entire hydrogeologic unit. Because λ is greater than $\bar{t}$, the SCV is smaller than the CV, meaning that the variation in the mean value of the property over the entire unit thickness is reduced.

To illustrate the effect of scaling, consider the PDFs shown in Figure 7-3. This PDF is used to represent a property such as porosity over an entire hydrogeologic unit. For the original unscaled data (the solid line in Figure 7-3), the expected value of the parameter is 0.139, with an effective range (defined as probability densities greater than about 15% of the maximum probability density) from 0.01 to 0.36. This implies that the parameter value can lie between the values 0.01 or 0.36 for the entire unit. After applying the scaling transformation, the mean of the parameter is the same (0.139), but the *Min* and *Max* values change to approximately 0.03 and 0.29 (the dashed line in Figure 7-3). Thus, the range of the PDF has narrowed and increased the probability density around the expected value.

7.1.4 Hydrologic units parameterized

The hydrogeologic units for which PDFs for matrix properties are derived are shown in Table 7-2. In order to perform the scaling transformation discussed above, both the vertical correlation length and the mean thicknesses of the units must be known. The vertical correlation length is set to 30 meters based on a composite vertical porosity variogram: λ = 40+190Sph(30) (Rautman and Flint, 1992). The unit thicknesses given in Ortiz *et al.* (1985) are used as the bases for scaling the data and are listed in Table 7-2.

The unsaturated flow calculations use only the units from the repository down to unit 8. Hydrogeologic unit 3 (the Topopah Spring-welded), in which the potential repository is located, includes a subunit (3R) running from the base of the repository to the top of the basal vitrophyre, to properly scale the PDFs for the portion of the unit used in the modeling. Scaling is done for both the repository subunit (3R), as well as the complete Topopah Spring welded unit (3C). Parameter scaling is done for all units with mean thicknesses greater than the 30-meter vertical correlation length.

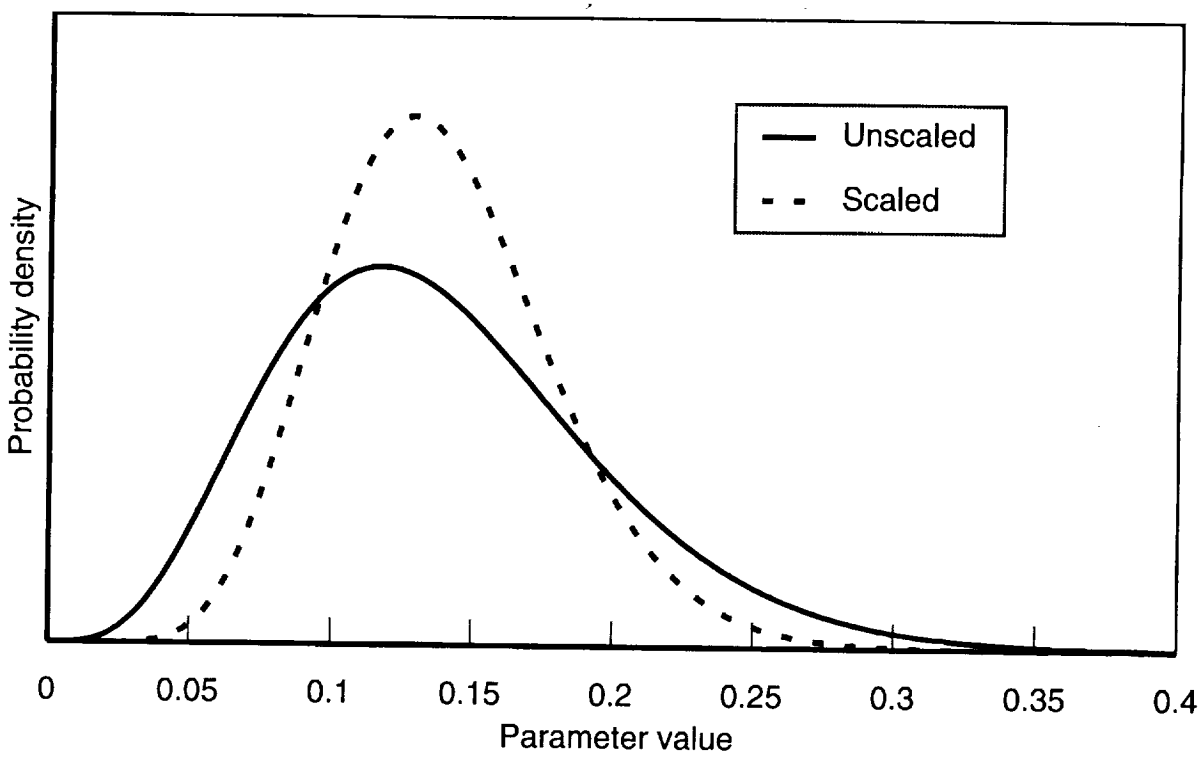

Figure 7-3. Comparison of unscaled and scaled parameter distributions.

Table 7-2. Hydrogeologic units and their mean thicknesses.

Unit	Hydrogeologic Unit and Lithology	Mean Thickness ($\bar{t}$)[a]
1	Tiva Canyon welded	81.00
2	Paintbrush nonwelded	39.43
3C	Topopah Spring welded–composite	237.80
3R	Topopah Spring welded–repository	61.20
4	Topopah Spring vitrophyre	14.63[b]
5	Calico Hills/Prow Pass nonwelded-vitric	63.99
6	Calico Hills/Prow Pass nonwelded-zeolitic	126.88
7	Prow Pass welded	c
8	Bullfrog welded	c
9	Bullfrog nonwelded	d
10	Tram welded	d

[a] Determined from Ortiz *et al.* (1985).

[b] The mean thickness is less than the vertical correlation length.

[c] Thicknesses for these units are not reported by Ortiz *et al.* (1985); PDFs were not scaled.

[d] These units do not occur in the unsaturated-zone models.

7.2 Matrix parameter distributions

The following sections present compilations of data contained in the PADB for the matrix hydrogeologic parameters. As is discussed above, the hydrogeologic units are assumed to be homogeneous, and matrix property data have been assigned to the units

without regard to the location within the units from which they were measured. At the interfaces of units, it may occasionally be uncertain to which unit a datum belongs. After compiling the data for a unit, the minimum and maximum are determined; if there are enough data to make the calculations meaningful, the mean and variance of the data are also determined.

7.2.1 Porosity (ϕ)

Porosity data for the ten hydrogeologic units (described in Table 6-2) have been obtained from the sources listed in the PADB. Porosity data are among the most extensive (1234 individual measurements for the hydrogeologic units) used for the TSPA. Table 7-3 presents the parameters for matrix porosity data in three representations: basic statistics, beta probability-distribution parameters, and the scaled beta-distribution parameters. Included in the basic statistics for each unit are the number of data and the parameters required to generate the beta probability distributions. Because the theoretical limits of the porosity are known (i.e., porosity is defined from 0.0 to 1.0), these values are used to determine the unscaled beta-function PDFs. Thus, the maxima and minima for the PDFs have been adjusted beyond the limits of the observed data.

For most units, the unscaled beta probability distributions for porosity are determined using the theoretical minima and maxima. When units 3C and 6 were scaled, the initial α and β values were very large, resulting in numerical problems. These beta functions have been recalculated with the ranges expressed as multiples of the standard deviation about the mean. Using the rule of thumb devised for the TSPA-91 PDFs, ranges based on four standard deviations above and below the mean have been chosen. This constraint has no practical impact, since virtually no area is under the porosity PDF curves outside four standard deviations. For unit 3C, only the maximum has been adjusted and the minimum remains at 0.0. For both units 3C and 6, it is likely that the maximum observed porosity values are statistical outliers; their presence has skewed the beta distributions. The choice of a maximum for unit 3C that is less than the observed maximum supports this observation.

7.2.2 Matrix bulk density (ρ_b)

Rock bulk density values from matrix core samples are statistically analyzed for each of the ten hydrogeologic units. Bulk density is one of the most comprehensive sets available, with 2644 data for the ten hydrogeologic units. Because data are very abundant for this property, the basic statistics (range, mean and standard deviation) can be calculated directly. Table 7-4 gives the statistics and the parameters.

Table 7-3. Matrix porosity statistics, unscaled beta and scaled beta distribution parameters.

Unit	Basic Statistics					Beta Distribution Parameters				Scaled Beta-Distribution Parameters		
	n	$E[x]$	$CV[x]$	Min	Max	Min	Max	Alpha	Beta	$SCV[x]$	Alpha	Beta
1	290	0.087	0.634	0.033	0.450	0.000	1.000	1.183	21.823	0.386	5.043	62.183
2	205	0.421	0.248	0.132	0.650	0.000	1.000	7.992	11.361	0.216	10.950	15.428
3C	300	0.139	0.412	0.004	0.480	0.000	0.368[a]	3.934	29.567	0.146	27.682	46.255
3R	300	0.139	0.412	0.004	0.480	0.000	1.000	3.934	29.567	0.288	9.209	62.234
4	26	0.065	0.656	0.014	0.177	0.000	1.000	1.107	29.134	–	–	–
5	117	0.331	0.271	0.097	0.510	0.000	1.000	7.775	16.720	0.186	18.093	37.555
6	127	0.306	0.209	0.141	0.470	0.050[a]	0.562[a]	14.573	34.254	0.102	32.317	32.315
7	70	0.292	0.239	0.101	0.430	0.000	1.000	11.110	28.422	–	–	–
8	26	0.165	0.361	0.058	0.231	0.000	1.000	5.243	30.601	–	–	–
9	41	0.261	0.193	0.174	0.380	0.000	1.000	18.578	54.428	–	–	–
10	32	0.191	0.306	0.018	0.280	0.000	1.000	7.445	34.691	–	–	–

[a] These values are used for the scaled beta distribution parameters to obtain the fits; for unscaled PDFs, a range of 0.0 to 1.0 is used.
– These units are not scaled.

Table 7-4. Rock bulk density statistics, and beta and scaled beta distribution parameters.

Unit	Basic Statistics					Beta-Distribution Parameters		Scaled Beta-Distribution Parameters		
	n	$E[x]$ (kg/m^3)	$CV[x]$	Min (kg/m^3)	Max (kg/m^3)	Alpha	Beta	$SCV[x]$	Alpha	Beta
1	618	2366	0.058	1410	2530	5.253	0.073	0.035	17.334	2.145
2	388	1714	0.292	850	2620	0.037	0.088	0.255	0.517	0.591
3C	782	2258	0.063	1686	2830	11.877	5.625	0.022	62.580	62.580
3R	782	2258	0.063	1360	2720	11.877	5.625	0.044	25.955	12.868
4	59	2308	0.026	2090	2400	2.213	0.356	–	–	–
5	241	1838	0.195	1050	3020	1.500	2.750	0.134	4.786	7.680
6	198	1746	0.110	1300	2230	1.327	1.525	0.053	10.390	11.360
7	121	1993	0.187	1440	3120	0.148	1.339	–	–	–
8	61	2260	0.071	1800	2510	1.246	0.221	–	–	–
9	92	2021	0.090	1600	2320	0.640	0.165	–	–	–
10	84	2185	0.065	1800	2470	1.551	0.889	–	–	–

– These units are not scaled.

Figure 7-4 shows the histogram of the data and the beta-function PDF for unit 3 (Topopah Spring welded). The PDF shown in Figure 7-4 is typical of the nature of the fit by a beta function to numerous data. Because the ordinates of the two graphs are arbitrary, an important characteristic of the fit is for the modes to coincide and for the widths of the peaks to be similar. The modes of the two curves appear to be almost coincident; the two curves show slight skewing to the left (skewness = -1.1).

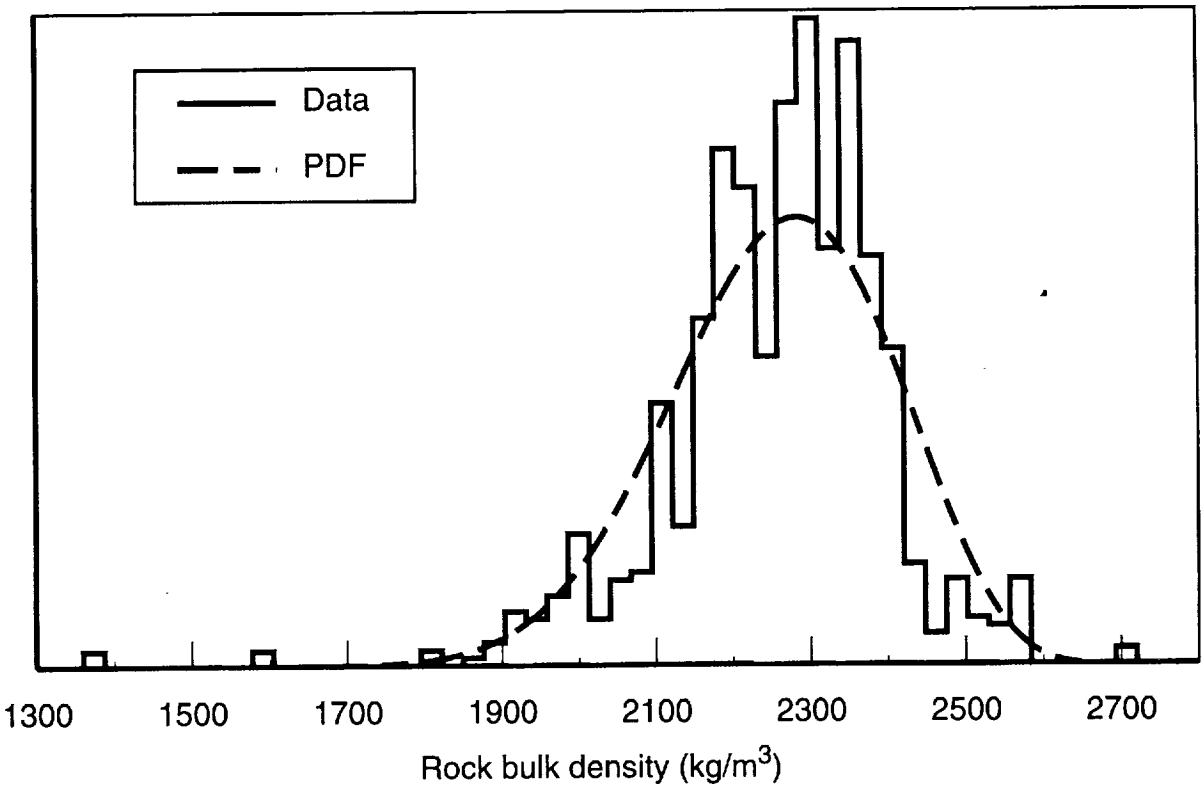

Figure 7-4. PDF fit to the rock bulk density data for unit 3 (Topopah Spring welded).

7.2.3 Matrix saturated hydraulic conductivity (K_S)

A total of 257 matrix saturated hydraulic conductivity values applicable to the modeled hydrogeologic units are used in the matrix saturated hydraulic conductivity analysis. Other published data (Yucca Mountain Project, 1992a), not incorporated in the PADB, are also part of this data set.

Matrix saturated hydraulic conductivity is best represented and analyzed in log space. For this study, the data are analyzed as a beta distribution in base-10 log space. Tables 7-5a and 7-5b shows the basic statistics, $\log_{10}$ statistics, and entropy-fit beta and scaled beta probability distribution parameters. Due to the sparseness of data, the entropy-fit routine has been used to derive the beta-function parameters. Because a nonlinear fitting procedure is sensitive to the choice of endpoints of the data range being fit, it is sometimes necessary to adjust the range to obtain reasonable beta-function PDFs. Units 1, 2, 3C, 3R, 5, 7, and 8 have been fitted with the entropy fit routine using initial endpoints based on the ranges of the basic data. Unit 10 has been fitted using an initial minimum and maximum of two standard deviations (95.46% of the data encompassed in a normal distribution) about the mean. Units 4, 6, and 9 required initial ranges set to three standard deviations about the mean to obtain reasonable fits.

The histogram of the basic data for unit 2 (Paintbrush Tuff nonwelded) is clearly bimodal (see Figure 7-5). This may occur because the matrix saturated hydraulic conductivity properties for this unit are spatially varying, or because the unit should be subdivided vertically into two units. Two values for the matrix saturated hydraulic conductivity are listed in Table 7-5b. (Because this unit is not used in the unsaturated-zone aqueous-flow analyses, the choice of PDF is moot.) Other parameters for unit 2 are also bimodal, as is indicated in the following sections.

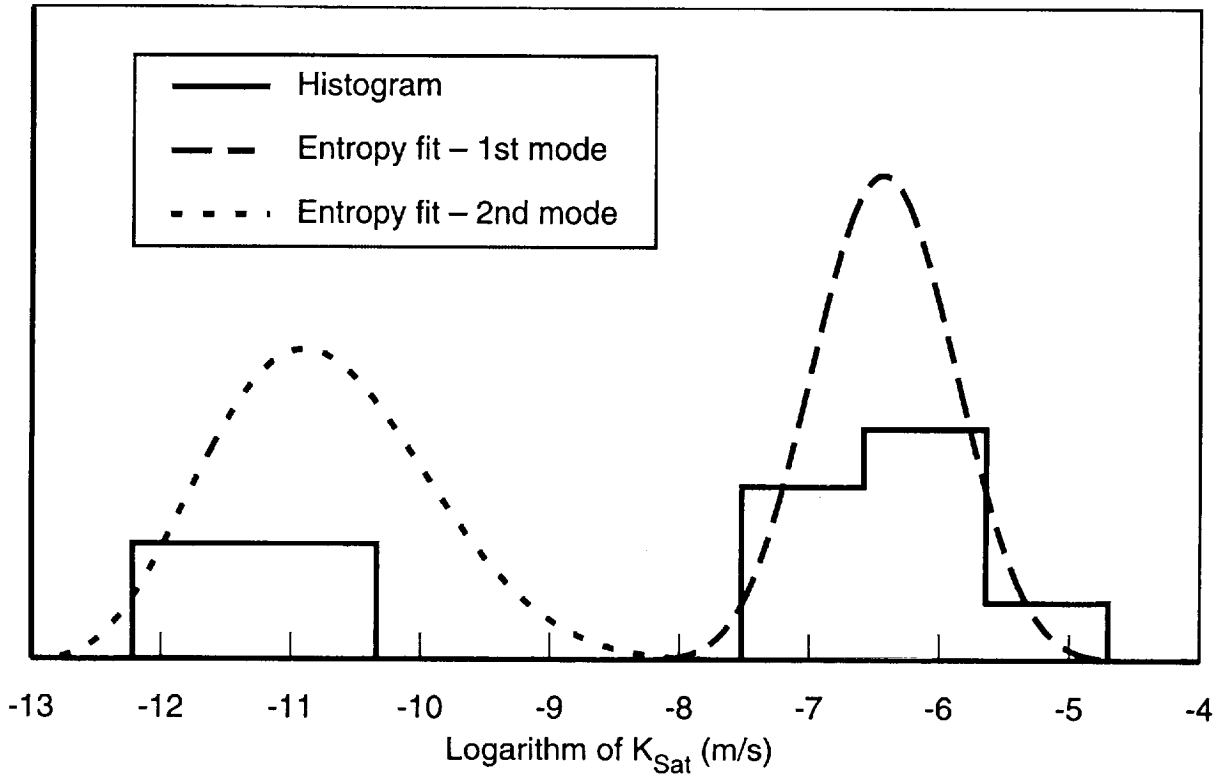

Figure 7-5. Log-transformed data and PDF for unit 2 (Paintbrush Tuff nonwelded).

The matrix saturated hydraulic conductivities from the drillhole UE-25a #1 appear to be higher than for the other drillholes. Statistical test are unable to unequivocally show that the data are different. For units 1, 3, and 6, there is a 95% confidence that the data are different; for units 2, 5, 7, and 9, the differences are not statistically significant. Therefore, the data have been included as part of the analyses. Higher conductivity values from UE-25a #1 can skew higher the overall expected values for the distribution. Suggested causes for higher matrix saturated hydraulic conductivity in the UE-25a #1 samples are (1) increased microfracturing, since this drillhole is in the imbricate fault zone, or (2) differences in laboratory testing methods or techniques.

Table 7-5a. Matrix saturated hydraulic conductivity statistics, and $\log_{10}$ statistics.

Unit	Basic Statistics					Log_{10} Statistics			
	n	$E[x]$ (m/s)	$CV[x]$	Min (m/s)	Max (m/s)	E[x] (m/s)	$CV[x]$	Min (m/s)	Max (m/s)
1	14	$3.86\text{x}10^{-10}$	3.32	$7.00\text{x}10^{-13}$	$4.83\text{x}10^{-9}$	-10.90	0.098	-12.16	-8.32
2	12	$5.47\text{x}10^{-7}$	1.46	$2.86\text{x}10^{-12}$	$2.35\text{x}10^{-6}$	-7.96	0.302	-11.54	-5.63
3C	66	$2.37\text{x}10^{-10}$	3.57	$3.05\text{x}10^{-13}$	$5.23\text{x}10^{-9}$	-10.71	0.084	-12.52	-8.28
3R	66	$2.37\text{x}10^{-10}$	3.57	$3.05\text{x}10^{-13}$	$5.23\text{x}10^{-9}$	-10.71	0.084	-12.52	-8.28
4	7	$2.26\text{x}10^{-11}$	1.11	$1.52\text{x}10^{-12}$	$6.95\text{x}10^{-11}$	-11.00	0.062	-11.82	-10.16
5	44	$1.82\text{x}10^{-8}$	3.27	$5.13\text{x}10^{-12}$	$2.92\text{x}10^{-7}$	-8.99	0.115	-11.29	-6.54
6	51	$1.93\text{x}10^{-10}$	3.01	$2.37\text{x}10^{-14}$	$3.14\text{x}10^{-9}$	-10.79	0.093	-13.63	-8.50
7	13	$2.58\text{x}10^{-9}$	1.28	$9.61\text{x}10^{-12}$	$8.95\text{x}10^{-9}$	-9.10	0.101	-11.02	-8.05
8	8	$4.92\text{x}10^{-10}$	0.661	$1.97\text{x}10^{-11}$	$9.26\text{x}10^{-10}$	-9.51	0.061	-10.71	-9.03
9	26	$4.20\text{x}10^{-9}$	0.950	$2.31\text{x}10^{-10}$	$1.35\text{x}10^{-8}$	-8.62	0.061	-9.64	-7.87
10	16	$1.78\text{x}10^{-9}$	1.00	$2.31\text{x}10^{-11}$	$5.79\text{x}10^{-9}$	-9.14	0.083	-10.64	-8.24

Table 7-5b. Matrix saturated hydraulic conductivity entropy-fit parameters and, scaled beta probability distribution parameters.

Unit	Entropy-Fit Beta Distribution Parameters ($\log_{10}$)						Scaled Beta-Distribution Parameters ($\log_{10}$)		
	$E[x]$ (m/s)	$CV[x]$	Min (m/s)	Max (m/s)	Alpha	Beta	$SCV[x]$	Alpha	Beta
1	-10.69	0.085	-12.20	-8.21	0.263	1.128	0.052	3.259	5.961
2-1st mode[a]	-6.42	0.081	-8.93	-3.76	10.478	11.213	0.071	14.230	15.208
2-2nd mode[a]	-10.75	0.076	-13.16	-6.06	4.491	9.634	0.066	6.253	13.051
3C	-10.68	0.087	-12.54	-7.97	0.980	1.875	0.031	17.491	25.854
3R	-10.68	0.087	-12.54	-7.97	0.980	1.875	0.061	3.456	5.471
4	-11.01	0.046	-12.57	-9.65	2.899	2.400	–	–	–
5	-8.96	0.116	-11.40	-5.98	1.590	2.152	0.079	5.029	6.337
6	-10.80	0.096	-14.17	-7.97	3.294	2.598	0.047	18.900	15.705
7	-9.04	0.073	-12.39	-7.95	4.567	0.807	–	–	–
8	-9.56	0.049	-10.71	-9.03	0.231	-0.431	–	–	–
9	-8.60	0.051	-10.36	-7.70	3.732	1.432	–	–	–
10	-9.12	0.069	-10.86	-8.24	0.889	-0.042	–	–	–

[a] Area for 1st mode is 66%; area for 2nd mode is 34%.
– These units are not scaled.

7.2.4 Matrix water-retention parameters (van Genuchten model)

The van Genuchten model (van Genuchten, 1978) of water retention in unsaturated rock is described by an air-entry parameter (α_{vG}), a saturation/ desaturation parameter (β_{vG}), and a residual-saturation parameter (S_r). These are used to fit a curve of saturation (%) *vs.* pressure head (m).

For each unit, we have derived water-retention curves from the original data. We have used pressure-head and saturation data from Peters *et al.* (1984), Rutherford *et al.* (1992), Flint and Flint (1990), and Voss (1993). Prior determinations of the water-retention curves have generally produced a single curve for a hydrologic unit by averaging

data taken from multiple cores from that unit. For example, Peters *et al.* (1984) developed water-retention curves for each unit from the averages of two or three data sets.

Water-retention data are available for only units 1 through 9. Before determining the basic statistics and PDFs, the data are assigned to their respective hydrogeologic units. Initial determinations of the matrix air-entry and matrix saturation/desaturation parameter distributions produced beta-function distributions that have negative exponents, and are therefore "bathtub" shaped. By transforming the data to $\log_{10}$ values and using the entropy-fit routine, satisfactory PDFs are generated for these parameters. Matrix residual degree of saturation data has been fit with the beta function without any data transformation. Tables 7-6, 7-7, and 7-8 give the parameters of the PDFs for α_{vG}, β_{vG}, and S_r, respectively.

Table 7-6a. Matrix air-entry parameter statistics and $\log_{10}$ statistics.

Unit	Basic Statistics					$\log_{10}$ Statistics			
	n	*E*[*x*] (m^{-1})	*CV*[*x*]	Min (m^{-1})	Max (m^{-1})	E[*x*] (m^{-1})	*CV*[*x*]	Min (m^{-1})	Max (m^{-1})
1	19	0.0218	1.6870	0.0003	0.1338	-2.094	0.325	-3.523	-0.874
2	43	0.2485	1.4987	0.0104	1.6690	-1.134	0.636	-1.983	0.222
3C	51	0.0299	2.1728	0.0021	0.4244	-1.885	0.265	-2.678	-0.372
3R	51	0.0299	2.1728	0.0021	0.4244	-1.885	0.265	-2.678	-0.372
4	10	0.0032	0.6392	0.0002	0.0077	-2.624	0.167	-3.699	-2.114
5	24	0.0531	1.7839	0.0054	0.3752	-1.644	0.302	-2.268	-0.426
6	50	0.0193	2.1957	0.0004	0.2355	-2.270	0.275	-3.398	-0.628
7	8	0.0180	0.4319	0.0085	0.0344	-1.777	0.100	-2.071	-1.463
8	–	0.0299	2.1728	0.0021	0.4244	-1.885	0.265	-2.678	-0.372
9	6	0.0208	0.5565	0.0098	0.0356	-1.739	0.142	-2.009	-1.449

– No data; unit 8 is considered analogous to unit 3.

Table 7-6b. Matrix air-entry parameter entropy fit parameters, and scaled beta-distribution parameters.

Unit	Entropy-Fit Beta Distribution Parameters ($\log_{10}$)						Scaled Beta-Distribution Parameters ($\log_{10}$)		
	E[*x*] (m^{-1})	*CV*[*x*]	Min (m^{-1})	Max (m^{-1})	Alpha	Beta	*SCV*[*x*]	Alpha	Beta
1	-2.102	0.327	-3.587	-0.859	0.583	0.324	0.199	4.199	3.350
2–1st mode	-0.255	0.960	-0.744	0.235	1.500	1.500	0.837	1.129	1.129
2–2nd mode	-1.498	0.199	-2.040	-0.764	0.474	0.995	0.174	1.070	1.803
3C	-1.868	0.274	-2.678	-0.301	0.315	1.545	0.097	11.788	23.741
3R	-1.868	0.274	-2.678	-0.301	0.315	1.545	0.192	2.038	4.878
4	-2.659	0.138	-3.755	-2.114	1.278	0.135	–	–	–
5	-1.555	0.298	-2.765	0.045	2.454	3.570	0.204	6.854	9.392
6	-2.226	0.290	-3.405	-0.504	0.576	1.301	0.141	6.977	10.647
7	-1.795	0.081	-2.071	-1.453	0.565	0.945	–	–	–
8	-1.868	0.411	-3.403	-0.301	0.525	0.556	–	–	–
9	-1.700	0.085	-2.009	-1.449	0.485	0.212	–	–	–

Table 7-7a. Matrix saturation/desaturation statistics and $\log_{10}$ statistics.

Unit	Basic Statistics					Log_{10} Statistics			
	n	$E[x]$ (m/s)	$CV[x]$	Min (m/s)	Max (m/s)	E[x] (m/s)	$CV[x]$	Min (m/s)	Max (m/s)
1	19	1.620	0.129	1.349	2.085	0.206	0.259	0.130	0.319
2	43	2.611	0.740	1.187	11.800	0.347	0.647	0.074	1.072
3C	51	1.793	0.395	1.155	5.363	0.233	0.523	0.063	0.729
3R	51	1.793	0.395	1.155	5.363	0.233	0.523	0.063	0.729
4	10	2.437	0.459	1.377	4.473	0.349	0.539	0.139	0.651
5	24	2.750	0.683	1.249	9.888	0.373	0.614	0.097	0.995
6	50	1.752	0.403	1.184	5.914	0.223	0.540	0.073	0.772
7	8	7.014	0.649	2.442	16.980	0.775	0.341	0.388	1.230
8	–	1.793	0.395	1.155	5.363	0.233	0.523	0.063	0.729
9	6	3.179	0.353	2.036	4.775	0.479	0.323	0.309	0.679

– No data; unit 8 is considered analogous to unit 3.

Table 7-7b. Matrix saturation/desaturation entropy fit, and scaled beta-distribution parameters.

Unit	Entropy-Fit Beta Distribution Parameters ($\log_{10}$)						Scaled Beta-Distribution Parameters ($\log_{10}$)		
	$E[x]$ (m/s)	$CV[x]$	Min (m/s)	Max (m/s)	Alpha	Beta	$SCV[x]$	Alpha	Beta
1	0.210	0.228	0.130	0.328	0.257	0.864	0.139	3.088	5.030
2	0.375	0.558	0.074	1.080	0.147	1.673	0.487	0.603	2.759
3C	0.255	0.506	0.063	0.768	0.346	2.578	0.180	11.545	32.448
3R	0.255	0.506	0.063	0.768	0.346	2.578	0.354	2.015	7.054
4	0.348	0.400	0.101	0.777	0.628	1.835	–	–	–
5	0.391	0.510	0.095	1.020	0.182	1.519	0.349	1.881	5.116
6	0.232	0.527	0.073	0.777	0.077	2.713	0.256	4.287	17.168
7	0.770	0.270	0.369	1.240	0.554	0.832	–	–	–
8	0.255	0.557	0.063	0.768	0.057	1.825	–	–	–
9	0.445	0.257	0.238	0.778	0.630	1.631	–	–	–

– These units are not scaled.

7.3 Bulk hydraulic-parameter development

In developing parameters, an effort has been made to include representations of the bulk hydraulic properties that provide a realistic view of the total coupled matrix and fracture hydrogeologic processes. In the flow process, bulk saturated hydraulic conductivity (K_{bs}) and gas permeability (K_{bg}) are controlling features that dominate matrix-controlled properties.

The properties data for the bulk saturated hydraulic conductivities are obtained from bulk hydraulic pump tests and barometric-fluctuation measurements (which measure gas permeabilities for the vadose zone). The bulk saturated hydraulic conductivity values come from pump tests in drillholes USW G-4, H-1, H-3, and H-4, UE-25b #1 and UE-25p #1, and J-13. Holes USW UZ-1 and UE-25a #4 are used for air permeability data

derived from barometric fluctuations, as reported in Montazer *et al.* (1986). Where there are insufficient data available for a unit, analog units with similar lithologic and matrix properties are used. The basic data are statistically reduced and beta probability distributions produced for all hydrogeologic units.

Table 7-8. Matrix residual degree of saturation statistics, and beta and scaled beta distribution parameters.

	Basic Statistics					Beta-Distribution Parameters		Scaled Beta-Distribution Parameters		
Unit	n	$E[x]$	$CV[x]$	Min	Max	Alpha	Beta	$SCV[x]$	Alpha	Beta
1	19	0.0212	2.5807	0.0000	1.0000	-0.8742	4.8066	0.9558	0.0502	47.4869
2	43	0.1540	1.1088	0.0000	1.0000	-0.4659	1.9342	0.8436	0.0347	4.6842
3C	51	0.0453	1.3418	0.0000	1.0000	-0.5150	9.2206	0.1693	32.2722	700.214
3R	51	0.0453	1.3418	0.0000	1.0000	-0.5150	9.2206	0.6577	1.1614	44.5525
4	10	0.1180	1.4167	0.0000	1.0000	-0.6785	1.4027	–	–	–
5	24	0.0968	1.4114	0.0000	1.0000	-0.6434	2.3273	0.6617	0.9660	17.3443
6	50	0.1207	1.4172	0.0000	1.0000	-0.6829	1.3101	0.3351	6.7103	55.1698
7	8	0.0688	0.5631	0.0000	1.0000	1.8680	37.8178	–	–	–
8	[a]	0.0453	1.3418	0.0000	1.0000	-0.5150	9.2206	–	–	–
9	6	0.0571	0.1855	0.0000	1.0000	0.5030	0.5030	–	–	–

[a] No data; unit 8 is considered analogous to unit 3.
– These units are not scaled.

The data reported in the USGS reports for the bulk saturated hydraulic conductivity data are presented as transmissivity values. These values are converted to bulk saturated hydraulic conductivities (K_{bs}) by:

$$K_{bs} = T/b, \tag{7.3}$$

where T is the transmissivity (m^2/s), and b is the thickness of the tested interval (m).

Data that are characteristic of a single hydrogeologic unit are required for our analyses. Because many of the intervals for the bulk saturated hydraulic conductivity measurements cover more than one of the hydrogeologic units, over half the data have been eliminated. The representativeness of the data from the pump testing is limited because the tests are designed to determine the hydrogeologic flow properties only in the saturated zones. For the most part, the data pertain just to the hydrogeologic units from the lower sequences of Topopah Spring downward. Only a few tests are reported above this horizon. These tests were made in drillholes located farther down-dip, where the higher units are below the water table. The hydrologic characteristics may differ with distance from the repository region. To supplement the information for the saturated zones and provide values at hydrogeologic units higher in the sequence in the un-

saturated zone, data derived from vadose zone barometric fluctuations are used. Much of the data from these holes also cross hydrogeologic unit boundaries and only a limited number of observations are applicable to single hydrogeologic units. Despite these concerns, the data are used to derive PDFs, since so little other information is available.

The same general approach used for matrix PDF development is used for the bulk saturated hydraulic conductivity analyses. The results from the tabulated pump tests are sorted into the corresponding hydrogeologic units of our model. Even though we expect that the data must be transformed to log space, the usual approach (i.e., making initial beta-distribution fits to untransformed data) to analyzing and reducing the data has been taken, thereby maintaining consistency and minimizing bias. The distributions are not scaled because the data have been from measurements made over unit thicknesses similar to the those in our model.

7.3.1 Bulk saturated hydraulic conductivity (K_{bs})

Among the available data from pump tests in the saturated zone near Yucca Mountain, the only hydrogeologic unit information suitable for compilation comes from hydrogeologic units 6 through 10. The amount of data available for each unit ranges from four data points for unit 7, to 15 data points for unit 6. The single datum available for unit 3 is not considered useful by itself. It is, however, consistent with the values from the barometric pumping tests (see below); therefore, it has been added to that data set and considered in the subsequent evaluation. Table 7-9a shows the data as both basic statistics and log-transformed values for hydrogeologic units 6 through 10.

Table 7-9a. Bulk saturated hydraulic conductivity basic statistics and $\log_{10}$ statistics.

Unit	Basic Statistics					Log_{10} Statistics			
	n	$E[x]$ (m/s)	$CV[x]$	Min (m/s)	Max (m/s)	E[x] (m/s)	$CV[x]$	Min (m/s)	Max (m/s)
6	15	$2.81\text{x}10^{-6}$	1.30	$5.21\text{x}10^{-8}$	$1.35\text{x}10^{-5}$	-5.93	0.114	-7.28	-4.87
7	4	$5.48\text{x}10^{-5}$	1.86	$2.31\text{x}10^{-8}$	$2.08\text{x}10^{-4}$	-5.69	0.304	-7.64	-3.68
8	7	$8.00\text{x}10^{-6}$	1.25	$5.16\text{x}10^{-8}$	$2.50\text{x}10^{-5}$	-5.69	0.163	-7.29	-4.60
9	8	$2.15\text{x}10^{-7}$	1.39	$3.40\text{x}10^{-9}$	$9.26\text{x}10^{-7}$	-7.04	0.103	-8.47	-6.03
10	11	$5.57\text{x}10^{-6}$	1.19	$4.63\text{x}10^{-8}$	$1.76\text{x}10^{-5}$	-5.75	0.155	-7.33	-4.75

Analyses of the basic statistics show that the data are highly skewed. Consequently, the statistics have been transformed to log space. The limited number of data require the use of the entropy-fit routine to determine the exponents for the beta distribution. Table 7-9b lists the parameters for units 6 through 10 for bulk saturated hydraulic conductivity.

Table 7-9b. Bulk saturated hydraulic conductivity probability-distribution parameters from an entropy fit.

Unit	Entropy-Fit Beta Distribution Parameters (log_{10})					Beta-Distribution Parameters	
	n	*E*[*x*] (m/s)	*CV*[*x*]	Min (m/s)	Max (m/s)	Alpha	Beta
6	15	-5.93	0.100	-7.36	-4.87	0.886	0.413
7	4	-5.73	0.188	-8.05	-2.28	1.35	2.50
8	7	-5.56	0.121	-7.82	-4.60	1.68	0.128
9	8	-7.06	0.837	-8.52	-6.03	0.941	0.367
10	11	-5.83	0.115	-7.56	-4.59	1.20	0.580

7.3.2 Gas conductivity (K_{bg})

Bulk saturated hydraulic conductivity values for units 2 and 3 of the model hydrogeologic units are developed from the data acquired by Montazer *et al.* (1986). These researchers measured air permeabilities for the unsaturated zone, using measurements of barometric pumping at Yucca Mountain. This approach was first used by Montazer *et al.* (1986) and Weeks (1978) to measure the changes in soil-gas pressure fluctuations as climatic pressure systems move across the Yucca Mountain area. From the measurements of unsaturated fluid potentials in the matrix, Montazer *et al.* were able to determine the soil gas pressure fluctuations at depth and infer gas permeabilities for Yucca Mountain. The two drillholes tested, USW UZ-1 and UE-25a #4, yield results for the Tiva Canyon member down to the Topopah Spring member. Unfortunately, as with saturated zone-bulk saturated hydraulic conductivity testing, some measurements cross hydrogeologic unit boundaries and can not be used in the analysis.

Montazer *et al.* (1986) converted the air permeabilities to equivalent saturated hydraulic conductivity values using the viscosity and density of water at standard conditions. The results are limited, but provide enough data to determine bulk saturated hydraulic conductivities for units 2 and 3, the Paintbrush nonwelded and the Topopah Spring welded units, as listed in Tables 7-10a and 7-10b. As mentioned earlier, one bulk saturated hydraulic conductivity value is included with these data for unit 3.

Table 7-10a. Barometric pumping statistics expressed as bulk saturated conductivities for units 2 and 3.

Unit	Basic Statistics					Log_{10} Statistics			
	n	*E*[*x*] (m/s)	*CV*[*x*]	Min (m/s)	Max (m/s)	E[*x*] (m/s)	*CV*[*x*]	Min (m/s)	Max (m/s)
2	4	2.67×10^{-5}	1.22	2.31×10^{-7}	6.94×10^{-5}	-5.22	0.218	-6.64	-4.16
3	4	3.70×10^{-5}	1.43	7.00×10^{-6}	1.16×10^{-4}	-4.74	0.119	-5.16	-3.94

Table 7-10b. Barometric pumping beta probability distribution parameters from an entropy fit.

Unit	Beta Probability Distribution Parameters (log_{10})					Beta-Distribution Parameters	
	n	$E[x]$ (m/s)	$CV[x]$	Min (m/s)	Max (m/s)	Alpha	Beta
2	4	-5.27	0.130	-6.75	-3.63	1.00	1.21
3	4	-4.74	0.068	-5.32	-3.94	0.466	1.05

The gas conductivities appear to be highly skewed, although there are little data. Thus, the gas conductivities have been converted to log_{10} values and the PDFs are calculated using the entropy fit routine. Table 7-10b provides the barometric pumping beta probability distribution parameters. Comparing Tables 7-10a and 7-10b, we see that the parameters of the beta function determined from the entropy fit differ from the log_{10} statistics. This is a consequence of the entropy-fit procedure, which may expand the range of the data or change the skewness of the distribution peak.

7.3.3 Analog bulk saturated hydraulic conductivity

There are not enough data for units 1, 4, and 5 of the model hydrogeologic units to generate PDFs for bulk saturated hydraulic conductivity. Consequently, we have created analog data by selecting from the other seven units an existing unit that most closely represents the hydrogeologic unit for which data are missing. To account for the greater uncertainty in the properties of these units, we have increased the coefficient of variation to allow for more scatter around the expected value.

Unit 1 (Tiva Canyon welded), has only one published gas permeability value. Units 3 (Topopah Spring welded) and 8 (Bullfrog welded) appear to be likely analog candidates. Table 7-11 lists the comparisons of the major matrix parameters and fracture frequencies made between unit 1 and units 3 and 8. Although most parameters are similar, some differences are observed. The single bulk saturated hydraulic conductivity value for unit 1 lies in the range for K_{bs} in unit 8 (Table 7-9a), but is below the minimum for unit 3 (Table 7-10a). The single measured value of K_{bs} for unit 3 is listed in the table. Three geologic differences between the units lead to rejection of the Bullfrog welded unit as an analog for the Tiva Canyon unit. One, the Bullfrog welded unit is much deeper in the stratigraphy and is in the saturated rather than the unsaturated zone. Two, the depth of burial of the Bullfrog would subject it to much higher lithologic stresses, and three, the saturated environment would introduce significantly different alteration and mineralization in the unit (Ortiz *et al.*, 1985). Therefore, the Topopah Spring welded has been chosen as an analog to the Tiva Canyon welded.

The range of barometric permeability for unit 3 is 7.00×10^{-6} m/s to 1.16×10^{-4} m/s (Table 7-10a), and the one applicable value for unit 1 is 2.31×10^{-7} m/s. Since this value is below the minimum for unit 3, it has been chosen as the minimum value for this unit as a conservative estimate. The value 1.16×10^{-4} m/s is retained as the maximum. Using this range and a CV of one standard deviation about the mean, the entropy fit has been used to generate a PDF parameters for unit 1, as is listed in Table 7-12.

Unit 4 (Topopah Spring basal vitrophyre), appears to most closely resemble unit 3 (Topopah Spring welded). In Table 7-11, the matrix properties (porosity, saturated hydraulic conductivity, and the van Genuchten air-entry parameter) and the fracture frequency (F_f) (discussed in the following section) are all smaller than those of unit 3. We assume that the matrix properties of the bulk saturated hydraulic conductivity parameters for unit 4 are basically similar to those of unit 3. The difference between the units depends on fracture frequency, which is a consequence of the vitric characteristic of unit 4. To acknowledge our increased uncertainty, we have increased the coefficient of variation for unit 3 by 10%. The values generated are shown in Table 7-12.

Table 7-11. Hydrogeologic unit matrix, bulk-hydraulic, and fracture parameters comparison for analog bulk saturated hydraulic conductivity.

Unit Unknown Analog	Matrix				Bulk		Fracture	
	ϕ	K_s	α_{vG}	β_{vG}	ρb (g/cm3)	K_{bs} (m/s)	F_f [a] (1/m)	F_f [b] (1/m)
Unit 1 (TCw)	0.087	3.86×10^{-10}	0.0218	1.62	2.366	2.31×10^{-7}	4.50	7.70
Unit 3 (TSw)	0.139	2.37×10^{-11}	0.0299	1.793	2.258	1.17×10^{-5}	3.00	4.25
Unit 8 (BFw)	0.165	4.92×10^{-10}	–	–	2.26	8.00×10^{-6}	3.00	–
Unit 4 (TSwv)	0.065	2.26×10^{-11}	0.0032	2.437	2.308	–	2.50	3.40
Unit 3 (TSw)	0.139	2.37×10^{-10}	0.0299	1.793	2.258	1.17×10^{-5}	3.00	4.25
Unit 5 (CHnv/PPnv)	0.331	1.82×10^{-8}	0.0531	2.75	1.838	–	1.40	0.20
Unit 2 (PTn)	0.421	5.47×10^{-7}	0.2485	2.611	1.714	2.67×10^{-5}	1.40	1.00
Unit 6 (CHnz/PPnz)	0.306	1.93×10^{-10}	0.0193	1.752	1.746	2.81×10^{-6}	1.10	0.20

[a] Data are from Section 7.4 of this document.
[b] Data are from Lin *et al.* (1993).
– Data are either unavailable or inapplicable.

Two possibilities exist for analogs to unit 5 (Calico Hills/Prow Pass nonwelded-vitric)—unit 6, (Calico Hills/Prow Pass nonwelded-zeolitic), and unit 2, (Paintbrush nonwelded). For both analogs, the matrix and fracture frequency parameters are generally in close agreement. The Paintbrush nonwelded has been chosen as the analog because it is not zeolitized and therefore appears to be the more representative unit. The param-

eters for unit 5 are listed in Table 7-12. As for unit 4, the coefficient of variation is increased by 10% to account for increased uncertainties.

Table 7-12. Bulk saturated hydraulic conductivity parameters for units 1, 4, and 5 (based on analogs).

Unit	Basic Statistics			Log_{10} Statistics				Beta PDF Parameters	
	E[x] (m/s)	Max (m/s)	Min (m/s)	E[x] (m/s)	CV[x]	Max (m/s)	Min (m/s)	Alpha	Beta
1	1.81×10^{-5}	2.31×10^{-7}	1.16×10^{-4}	-4.74	0.135	-6.64	-3.94	0.8978	-0.1915
4	1.81×10^{-5}	4.79×10^{-6}	1.16×10^{-4}	-4.74	0.074	-5.32	-3.94	0.1389	0.5930
5	5.40×10^{-6}	1.78×10^{-7}	2.36×10^{-4}	-5.27	0.142	-6.75	-3.63	0.5717	0.7382

Table 7-13 summarizes for all the units the PDF parameters for K_{bs}. The table combines the parameters derived from aqueous K_{bs} measurements, barometric gas conductivity measurements, and the analog values.

Table 7-13. Summary of K_{bs} parameters.

Unit	Entropy-Fit Beta Distribution Parameters (log_{10})					Beta-Distribution Parameters	
	n	E[x] (m/s)	CV[x]	Min (m/s)	Max (m/s)	Alpha	Beta
1	1	-4.7424	0.1354	-6.6364	-3.9355	0.8978	-0.1915
2	4	-5.2675	0.1297	-6.7506	-3.6273	1.0015	1.2136
3	4	-4.7424	0.0677	-5.3193	-3.9355	0.4656	1.0499
4	4	-4.7424	0.0745	-5.3193	-3.9355	0.1389	0.5930
5	4	-5.2675	0.1426	-6.7506	-3.6273	0.5717	0.7382
6	15	-5.9311	0.1003	-7.3599	-4.8697	0.8862	0.4127
7	4	-5.7307	0.1884	-8.0453	-2.2818	1.3474	2.4977
8	7	-5.5563	0.1205	-7.8195	-4.6038	1.6807	0.1282
9	8	-7.0625	0.0837	-8.5240	-6.0334	0.9413	0.3670
10	11	-5.8305	0.1150	-7.5619	-4.5893	1.2035	0.5797

7.4 Fracture parameter development

7.4.1 Approach

The fracture parameters required for the TSPA-93 flow and transport models are frequency, F_f, spacing, a_f, porosity, ϕ_f, air-entry parameter, α_{vGf}, aperture, b_f, angle/orientation, θ_f, and hydraulic conductivity, K_f. Of these parameters, only two—fracture frequency and orientation—are available from actual measurements of down-hole properties. The remainder are derived by assuming that the fractures can be modeled as parallel plates (Snow, 1968; referenced in Freeze and Cherry, 1979). Details of the development of the fracture parameters are given in Schenker *et al.* (1994).

7.4.2 Available fracture data

Fracture properties are tabulated from four drillholes: USW G-1, USW GU-3, USW G-4, and UE 25a #1. Although other researchers have performed similar fracture studies, the four drillholes we used are the same that Lin *et al.* (1993) incorporated in their fracture analysis. These holes give us a starting data set to which we have added additional information. The four holes bound the potential repository area and provide a limited but geographically broad distribution of fracture frequencies at the potential repository area. Other drillholes do have fracture frequency information, but partly due to resource limitations are not included in this study.

We have determined the fracture frequencies for each of the ten hydrogeologic units from the lithologic logs for each hole. Fracture-orientation data are only available for units 1 through 9. The data consist of the fracture count (number/m) and the fracture orientation (dip angles).

7.4.2.1 Frequency (F_f)

Fracture frequencies are determined from the down-hole fracture-count data for drillholes USW G-1 (Spengler *et al.*, 1981), G-4 (Spengler and Chornack, 1984), GU-3 (Scott and Castellanos, 1984), and UE-25a #1 (Spengler *et al.*, 1979). The data are reported as the number of fractures per 10-foot interval down the drillholes. They have been converted to number of fractures per 1-meter interval, and grouped according to hydrogeologic unit.

The basic statistics for the fracture frequencies all have coefficients of variation that are near 1.0 (see Table 7-14). By definition, the exponential distribution has a CV of 1.0; therefore, we assume that all the distributions can be represented by the beta-function PDFs that approximate exponential distributions. For the exponential distribution, the minimum is zero and the maximum is infinity. To approximate an exponential PDF by a beta function requires that the maximum be set to a value less than infinity, so 30 times the mean value has been chosen. The resulting beta distribution is reasonably close to the desired exponential (see the TSPA-91 document for a discussion of the approximation of an exponential by a beta function). Because the maximum is a constant multiplicative factor of the mean, the alpha and beta exponents for *all* the hydrogeologic units are the same. Table 7-14 lists the statistics and the approximated beta-distribution exponents for fracture frequency.

Table 7-14. Fracture frequency statistics and beta distribution approximation of the exponential.

Unit	Basic Statistics					Approximated Exponential Distribution Parameters				
	n	$E[x]$ (m^{-1})	$CV[x]$	Min (m^{-1})	Max (m^{-1})	$CV[x]$	Min (m^{-1})	Max (m^{-1})	Alpha	Beta
1	57	4.5	0.7	0.3	14.8	1.00	0.00	135.00	-0.067	26.067
2	12	1.4	0.8	0.7	3.9	1.00	0.00	42.00	-0.067	26.067
3	323	3.0	1.0	0.2	23.3	1.00	0.00	90.00	-0.067	26.067
4	23	2.5	0.7	0.3	6.2	1.00	0.00	75.00	-0.067	26.067
5	59	1.4	0.9	0.2	4.9	1.00	0.00	42.00	-0.067	26.067
6	70	1.1	1.1	0.2	7.5	1.00	0.00	33.00	-0.067	26.067
7	33	1.0	0.8	0.3	4.3	1.00	0.00	30.00	-0.067	26.067
8	77	3.0	0.8	0.3	10.8	1.00	0.00	90.00	-0.067	26.067
9	43	1.0	0.7	0.3	2.6	1.00	0.00	30.00	-0.067	26.067
10	71	1.3	0.8	0.3	4.6	1.00	0.00	39.00	-0.067	26.067

7.4.2.2 Orientation (θ_f)

Fracture orientation data are available for units 1, 2, 3, and 5. Because no single drillhole supplied sufficient data to cover all the units, the four units with data serve as analogs for the remaining units analyzed. Unit 10 is not considered. The descriptive statistics for degree of welding and fracture frequency are used to select analogs for missing fracture-orientation data. Table 7-15 provides comparisons between the missing units and the analog units. Unit 3 is used as an analog for units 4 and 8 because all three are welded units, and the fracture frequency for unit 3 is quite similar to the frequencies for units 4 and 8. Fracture frequencies for the other units differ from those for units 3, 4, and 8. Unit 6 is considered analogous to unit 5 because both are nonwelded units and both units were deposited during the same geologic event. The main difference between the two is that unit 6 has been zeolitized (Ortiz *et al.*, 1985; Broxton *et al.*, 1986). The fracture frequencies of the two units are similar. Units 7 and 9 are considered analogous to unit 2 mainly based on the similarities of the expected values of their fracture frequencies. If only degree of welding is considered, no analog would be obvious for unit 7.

Table 7-15. Analog units used for fracture orientation missing units.

Missing Unit	Analog Unit	Fracture Frequency: Missing Unit (m^{-1})	Fracture Frequency: Analog Unit (m^{-1})	Degree of Welding: Analog Unit	Degree of Welding: Missing Unit
4	3C	2.5	3.0	Welded	Welded
8	3C	3.0	3.0	Welded	Welded
6	5	1.1	1.5	Nonwelded	Nonwelded
7	2	1.0	1.4	Welded	Welded
9	2	1.0	1.4	Welded	Nonwelded

The orientations are compiled as percentages for each 10-degree increment between 0 and 90 degrees from vertical. Table 7-16 summarizes the statistics and the beta-distribution exponents for the nine units.

Table 7-16. Fracture angle/orientation statistics and beta-distribution parameters.

Unit	Basic Statistics					Beta-Distribution Parameters	
	n	$E[x]$ (degrees)	$CV[x]$	Min (degrees)	Max (degrees)	Alpha	Beta
1	300	48.900	0.546	0.000	90.000	-0.010	-0.168
2	100	41.400	0.702	0.000	90.000	-0.365	-0.255
3	399	58.183	0.478	0.000	90.000	-0.100	-0.508
4[a]	399	58.183	0.478	0.000	90.000	-0.100	-0.508
5	400	57.650	0.474	0.000	90.000	-0.043	-0.463
6[b]	400	57.650	0.474	0.000	90.000	-0.043	-0.463
7[c]	100	41.400	0.702	0.000	90.000	-0.365	-0.255
8[a]	399	58.183	0.478	0.000	90.000	-0.100	-0.508
9[c]	100	41.400	0.702	0.000	90.000	-0.365	-0.255

[a] Analog to unit 3.
[b] Analog to unit 5.
[c] Analog to unit 2.

Fracture orientations shown in the YMP Reference Information Base for welded tuffs have predominantly near-vertical dip angles, with a secondary grouping that is nearly horizontal. For the hydrogeologic units defined for TSPA-93, the fracture angles also follow this trend, although the distributions we generate are not as strongly bimodal. A rose diagram showing the distribution of fracture orientations is given in Figure 7-6 for the Calico Hills nonwelded unit. Because the fracture orientations are grouped at high and low angles, the probability distribution is "U shaped" or "bathtub shaped," and a typical PDF is shown in Figure 7-7.

7.4.3 Derived parameters

Fractures are modeled as a parallel array of planar fractures; this assumption permits the determination of fracture-model parameters that cannot be measured (i.e., spacing, hydraulic aperture, porosity, hydraulic conductivity, and air entry) in terms of the ones that are—bulk saturated hydraulic conductivity, K_{bs}, fracture frequency, F_f, and fracture orientation, θ_f. The relationship between porosity and bulk saturated hydraulic conductivity established by Snow (1968), as cited by Freeze and Cherry (1979), gives the fracture porosity ϕ_f and the permeability k (in m^2) for an array of parallel planar fractures:

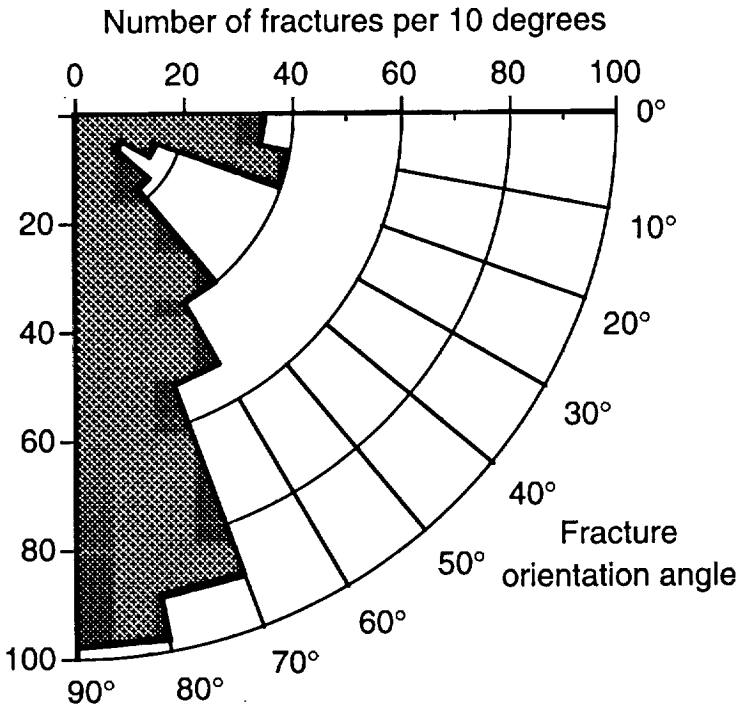

Figure 7-6. Distribution of fracture orientations for unit 5.

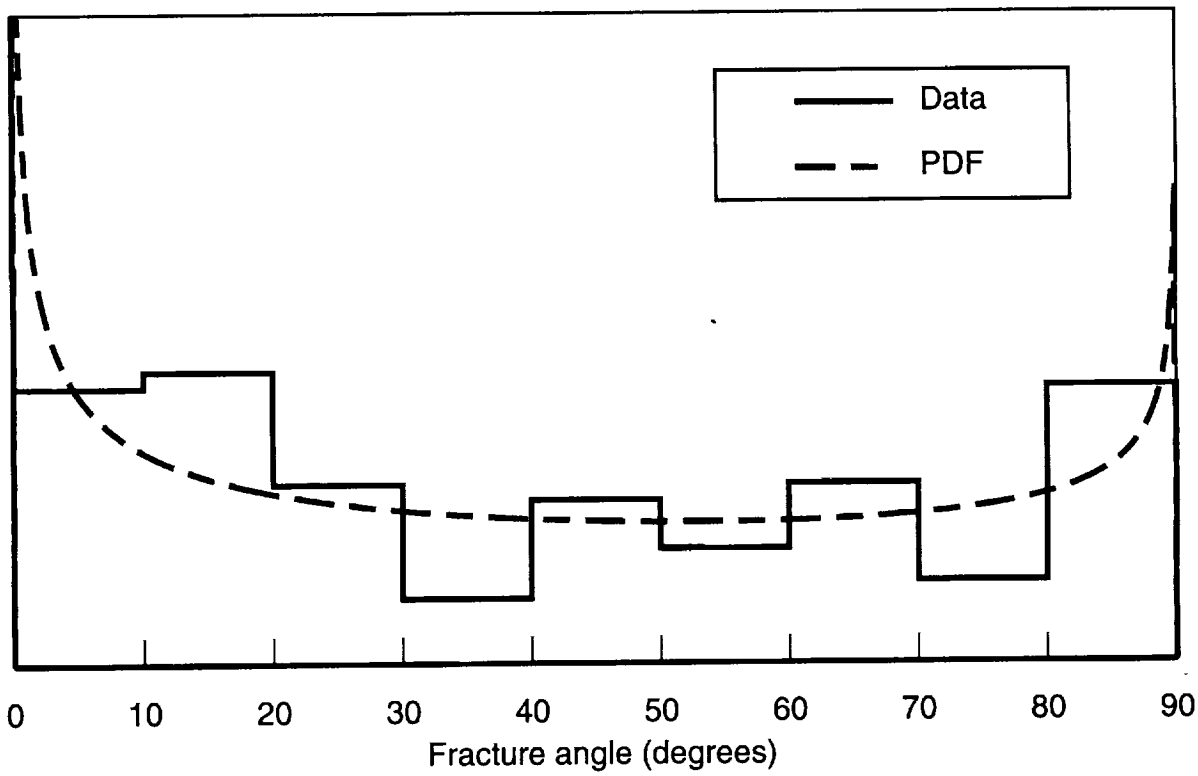

Figure 7-7. PDF for fracture orientations for unit 5 (Calico Hills nonwelded).

$$\phi_f = N_p b_f, \text{ and} \tag{7.4a}$$

$$k = N_p b_f^3/12, \tag{7.4b}$$

where b_f (m) is the hydraulic aperture, and N_p (m^{-1}) is number of fractures per unit distance (specified normal to the plane of the fractures). Freeze and Cherry state that "a permeability k, [calculated with Equation (7.4b)], can be considered as the permeability of an equivalent porous medium; one that acts hydraulically like the fractured rock."

It is important to note that this formula models parallel-plate fractures with N_p fractures per unit distance normal to the fractures. The fractures intersected by a drillhole may be oriented in any direction, so the number of fractures per unit distance measured along the borehole, N, differs from the number used in Equation 7.4b, N_p, whenever the fracture orientations are not horizontal. (The drillholes are assumed to be vertical for this analysis.) The number of fractures per unit distance normal to the plane of the fractures is therefore given by

$$N_p = N/cos(\theta_f), \tag{7.5}$$

where θ_f is the fracture orientation. Parallel-plate fracture spacing (a_f) is given by:

$$a_f = 1/N_p, \tag{7.6a}$$

or

$$a_f = cos(\theta_f)/N. \tag{7.6b}$$

The bulk permeability (k) is related to hydraulic conductivity (K_{bs}) by the viscosity and density of the fluid; at 20°C and sea level the conversion factor is K_{bs} (m/s) = k·1.022x10^{-7}(m^2) (Gerhart and Gross, 1985). Substituting for N_p and K_{bs}, the fracture hydraulic aperture can then be calculated by substitution in Equation 7.4:

$$b_f = \sqrt[3]{\frac{12K_{bs}\,cos(\theta_f)}{1.022x10^{-7}N}}. \tag{7.7}$$

Substituting Equation 7.6b into Equation 7.7 gives:

$$b_f = \sqrt[3]{1.226x10^{-6}K_{bs}a_f}. \tag{7.8}$$

Substituting Equation 7.5 into Equation 7.4a gives fracture porosity in terms of observed fracture frequency and hydraulic aperture:

$$\phi_f = \frac{Nb_f}{cos(\theta_f)}. \tag{7.9}$$

Lastly, fracture hydraulic conductivity, K_f, *is* calculated from

$$K_f = \frac{K_{bs}}{\phi_f}. \tag{7.10}$$

With these relations, the fracture parameters can be determined for use in the flow and transport models. To obtain distributions of the derived parameters, a computer routine developed at SNL randomly samples 100 values of K_{bs}, F_f, and θ_f from the PDFs for those properties, and then calculates 100 values of the derived parameters based on the above equations. The following subsections discuss the individual parameters.

7.4.3.1 Spacing (a_f)

Fracture spacings for the nine units are calculated from Equation 7.6b. A set of 100 values are computed from randomly sampled inputs, and the basic statistics are then derived. The statistical data and the beta-distribution parameters are presented in Table 7-17.

Table 7-17. Fracture spacing statistics and beta-distribution parameters.

Unit	Basic Statistics					Beta-Distribution Parameters	
	n	$E[x]$ (m)	$CV[x]$	Min (m)	Max (m)	Alpha	Beta
1	100	0.618	2.776	2.0×10^{-4}	13.444	-0.9222	0.6170
2	100	2.222	2.674	6.0×10^{-4}	43.907	-0.9178	0.5416
3	100	0.740	3.147	3.0×10^{-6}	19.878	-0.9400	0.5514
4	100	0.888	3.147	4.0×10^{-6}	23.854	-0.9400	0.5514
5	100	1.618	3.096	2.0×10^{-5}	42.465	-0.9378	0.5715
6	100	2.059	3.096	2.0×10^{-5}	54.046	-0.9377	0.5718
7	100	3.111	2.674	8.0×10^{-4}	61.469	-0.9178	0.5416
8	100	0.740	3.147	3.0×10^{-6}	19.878	-0.9400	0.5514
9	100	3.111	2.674	8.0×10^{-4}	61.469	-0.9182	0.5279

7.4.3.2 Hydraulic aperture (b_f)

Hydraulic apertures are calculated with Equation 7.8 for 100 randomly generated values for hydrogeologic units 1 thorough 9. Eight of the units exhibit similar sized mean apertures; their expected values range from approximately 100 to 200 microns.

Unit 9 is the exception; its value is somewhat smaller (60 microns), consistent with lithologic overburden compaction and slight healing of the fractures.

Hydraulic aperture is developed as a beta distribution function from the basic statistical data. Table 7-18 lists the basic statistics and the beta distribution parameters.

Table 7-18. Hydraulic aperture statistics and beta-distribution parameters.

	Basic Statistics					Beta Distribution Parameters	
Unit	n	$E[x]$ (μm)	$CV[x]$	Min (μm)	Max (μm)	Alpha	Beta
1	100	181	0.73	253	980	0.012	4.193
2	100	206	1.04	24.5	1640	-0.475	3.146
3	100	180	0.85	6.4	1190	-0.053	4.510
4	100	192	0.88	7.1	1320	-0.100	4.491
5	100	179	1.24	11.7	1760	-0.582	2.951
6	100	108	1.00	6.2	858	-0.338	3.881
7	100	203	1.66	11.8	2380	-0.785	1.450
8	100	103	1.00	4.3	800	-0.320	3.803
9	100	55.7	0.88	7.1	371	-0.285	3.644

7.4.3.3 Fracture porosity (ϕ_f)

Fracture porosity is a function of the fracture frequency and the hydraulic aperture. Starting with the 100 values for fracture apertures computed in the previous section, PDFs for fracture porosity are then calculated from Equation 7.9. Since Equation 7.9 has $cos(\theta_f)$ in the denominator, fracture angles near 90° (i.e., vertical) predict very large values for ϕ_f. To compensate for this, the highest of the 100 sampled values for θ_f have been eliminated from data. The porosities predicted by the omitted values include several above 1.0. (High fracture porosities are not necessarily physically unreasonable; the likelihood of a vertical drillhole intersecting a vertical fracture is small unless the fracture density—and thus the fracture porosity—is very high.) Some near-vertical fracture orientations are included in the data. Because the values calculated for ϕ_f span several orders of magnitude, the higher values skew the data; consequently, the data have been transformed to $\log_{10}$ space. The beta-distribution parameters for the log-transformed data are given in Table 7-19.

7.4.3.4 Fracture hydraulic conductivity (K_f)

Fracture hydraulic conductivity is calculated as a function of saturated bulk hydraulic conductivity and fracture frequency using Equation 7.10. From the 100 values sampled for K_{bs} and ϕ_f, fracture hydraulic conductivities for units 1 through 9 are com-

puted. Values have been transformed to log space; the beta-distribution parameters are given in Table 7-20.

Table 7-19. Fracture porosity statistics, $\log_{10}$ statistics and beta-distribution parameters.

	Basic Statistics					Log_{10} Statistics				Beta-Distribution Parameters	
Unit	n	$E[x]$	$CV[x]$	Min	Max	$E[x]$	$CV[x]$	Min	Max	Alpha	Beta
1	99	$1.38\text{x}10^{-3}$	1.20	$6.63\text{x}10^{-5}$	$1.08\text{x}10^{-2}$	-3.063	0.140	-4.179	-1.966	1.815	1.805
2	99	$4.12\text{x}10^{-4}$	1.47	$1.50\text{x}10^{-5}$	$4.43\text{x}10^{-3}$	-3.631	0.127	-4.825	-2.354	1.982	2.189
3	99	$2.75\text{x}10^{-3}$	2.18	$5.00\text{x}10^{-4}$	$4.25\text{x}10^{-2}$	-2.999	0.190	-4.301	-1.371	1.457	2.072
4	99	$2.44\text{x}10^{-3}$	2.18	$4.30\text{x}10^{-5}$	$3.74\text{x}10^{-2}$	-3.053	0.187	-4.367	-1.427	1.483	2.072
5	99	$9.98\text{x}10^{-4}$	2.18	$1.47\text{x}10^{-5}$	$1.38\text{x}10^{-2}$	-3.438	0.169	-4.834	-1.860	1.594	1.932
6	99	$4.84\text{x}10^{-4}$	2.07	$8.46\text{x}10^{-6}$	$6.69\text{x}10^{-3}$	-3.725	0.151	-5.073	-2.174	1.608	2.001
7	99	$2.78\text{x}10^{-4}$	2.06	$6.41\text{x}10^{-6}$	$4.91\text{x}10^{-3}$	-3.897	0.136	-5.193	-2.309	1.843	2.484
8	99	$1.55\text{x}10^{-3}$	2.31	$2.17\text{x}10^{-5}$	$2.54\text{x}10^{-2}$	-3.284	0.183	-4.664	-1.596	1.451	1.998
9	99	$8.06\text{x}10^{-5}$	1.35	$3.22\text{x}10^{-6}$	$6.92\text{x}10^{-4}$	-4.323	0.105	-5.493	-3.160	1.811	1.794

Table 7-20. Fracture hydraulic conductivity statistics, $\log_{10}$ statistics, and beta distribution parameters.

	Basic Statistics					Log_{10} Statistics				Beta-Distribution Parameters	
Unit	n	$E[x]$ (m/yr)	$CV[x]$	Min (m/yr)	Max (m/yr)	$E[x]$ (m/yr)	$CV[x]$	Min (m/yr)	Max (m/yr)	Alpha	Beta
1	100	$1.28\text{x}10^{6}$	2.20	$1.64\text{x}10^{4}$	$2.47\text{x}10^{7}$	5.766	0.090	4.216	7.394	3.082	3.289
2	100	$2.25\text{x}10^{6}$	3.38	$1.54\text{x}10^{4}$	$6.95\text{x}10^{7}$	5.774	0.113	4.188	7.842	1.910	2.794
3	100	$1.44\text{x}10^{6}$	2.73	$1.04\text{x}10^{3}$	$3.65\text{x}10^{7}$	5.694	0.117	3.018	7.563	5.046	3.223
4	100	$1.67\text{x}10^{6}$	2.86	$1.28\text{x}10^{3}$	$4.49\text{x}10^{7}$	5.745	0.116	3.108	7.652	4.991	3.332
5	100	$2.06\text{x}10^{6}$	4.13	$3.52\text{x}10^{3}$	$7.99\text{x}10^{7}$	5.567	0.138	3.547	7.903	2.244	2.751
6	100	$6.03\text{x}10^{5}$	3.33	$1.00\text{x}10^{3}$	$1.90\text{x}10^{7}$	5.200	0.137	3.002	7.278	3.112	2.888
7	100	$3.96\text{x}10^{6}$	4.65	$3.57\text{x}10^{3}$	$1.45\text{x}10^{8}$	5.537	0.155	3.552	8.163	1.616	2.461
8	100	$5.47\text{x}10^{5}$	3.19	$4.81\text{x}10^{2}$	$1.65\text{x}10^{7}$	5.126	0.153	2.682	7.217	2.939	2.370
9	100	$1.41\text{x}10^{5}$	2.77	$1.31\text{x}10^{3}$	$3.55\text{x}10^{6}$	4.680	0.132	3.118	6.550	2.028	2.626

7.4.3.5 Water retention air-entry (α_{vG_f}) parameter

The fracture air-entry parameter (α_{vG_f}) of the van Genuchten model is derived from the fracture aperture b_f by the method of Wang and Narasimhan (1985). This method assumes that we can apply capillary theory to model a set of parallel, smooth-wall fractures:

$$\alpha_{vG_f} = \frac{b_f}{(2\gamma \cos(\theta_{ls})/\rho g)}, \tag{7.11}$$

where γ is surface tension, ρ is fluid density, g is gravitational acceleration, and θ_{ls} is the contact angle between the liquid surface and solid surface. Values of $\theta_{ls} = 0°$, $\gamma = 0.072$ kg/sec^2, $\rho = 1000$ kg/m^3, and $g = 9.8$ m/sec^2 are used in Equation 7.11 to calculate α_{vGf} in units of m^{-1}. The denominator of the equation is a constant, (1.47×10^{-5} m^2), so the fracture aperture statistics given in Table 7-18 are divided by this value to compute α_{vGf}. Since the distribution being generated is essentially that of the fracture aperture, all other parameters (i.e., n, CV, and beta-distribution exponents) are identical. Table 7-21 gives the parameters.

7.5 Parameter correlations

Thus far, the PDFs of hydrogeologic properties have been discussed individually, but correlations among them could be important as well. For this reason, the data from the PADB are examined to determine whether correlations exist. For most of the parameters, data are not complete enough to calculate meaningful correlation coefficients, but a correlation analysis is conducted between matrix porosity and matrix saturated hydraulic conductivity. As more data become available, other correlations will be examined.

Table 7-21. Fracture air-entry parameter basic statistics and beta-distribution parameters.

Unit	Basic Statistics					Beta Distribution Parameters	
	n	$E[x]$ (m^{-1})	$CV[x]$	Min (m^{-1})	Max (m^{-1})	Alpha	Beta
1	100	12.3	0.73	1.7	66.7	0.012	4.193
2	100	14.0	1.04	1.7	111.6	-0.475	3.146
3	100	12.2	0.85	0.4	81.0	-0.053	4.510
4	100	13.1	0.88	0.5	89.8	-0.100	4.491
5	100	12.2	1.24	0.8	119.8	-0.582	2.951
6	100	7.3	1.00	0.4	58.4	-0.338	3.881
7	100	13.8	1.66	0.8	162.0	-0.785	1.450
8	100	7.0	1.00	0.3	54.4	-0.320	3.803
9	100	3.8	0.88	0.5	25.2	-0.285	3.644

The Latin Hypercube Sampler (LHS) program (Iman and Shortencarrier, 1984), which generates stochastic parameter realizations for the aqueous-transport simulations, accepts correlations among parameters being sampled. Spearman rank-correlation analyses provide the correlation constraints to the LHS. The correlation analyses are done separately for each hydrogeologic unit; correlations are significant if the

Spearman two-sided significance level is less than 0.05. As Table 7-22 shows, there is not a clear-cut pattern of either correlation or lack thereof.

Table 7-22. Spearman rank correlations for matrix porosity and saturated hydraulic conductivity.

Unit	Data Pairs (n)	Spearman Rank Correlation Coefficient	Two-Sided Significance Level	Correlation Significant?
1	10	-0.308	0.387	no
2	8	0.929	0.000	yes
3	25	0.467	0.019	yes
4	4	-0.400	0.600	no
5	16	0.744	0.000	yes
6	17	0.159	0.541	no
7	6	0.771	0.072	yes
8	5	-0.300	0.624	no
9	13	0.121	0.694	no
10	7	0.000	1.000	no

Although the significance level for unit 7 is greater than 0.05, the correlation coefficient implies a fairly high correlation among the data pairs; we assume that the correlation coefficient takes precedence. We therefore consider the parameters of the unit to be correlated.

7.6 Comparison of hydrogeologic parameters between TSPA-91 and TSPA-93

The five hydrogeologic units used in TSPA-91 modeled Yucca Mountain from the potential repository horizon down to the static water table. For TSPA-93, the domain is expanded above the repository horizon to the surface, and below the water table into the saturated formations. In this section we compare the basic statistics of the hydrogeologic parameters for the corresponding TSPA-93 and TSPA-91 hydrogeologic units. Identification of the correspondence between the two set of units is given in Table 7-23.

The units described in TSPA-91 as Welded Tuff, Vitrophyre, and Vitric tuff (1, 2, and 3) correspond directly to TSPA-93 units Topopah Spring welded, Topopah Spring vitrophyre, and Calico Hills/Prow Pass vitric (units (3R, 4, and 5). The Zeolitic tuff and Partially welded tuff units of TSPA-91 (units 4 and 5) cannot be directly compared with the Calico Hills/Prow Pass nonwelded zeolitic (TSPA-93 unit 6) or the Prow Pass welded (unit 7). In TSPA-91, the "partially welded" unit actually included both welded and nonwelded segments from the Prow Pass formation. For TSPA-93, the nonwelded segments from the Prow Pass have been included with the Calico Hills in unit 6.

Consequently, neither unit 4 nor unit 5 from TSPA-91 contain substantially the same rock types as unit 6 or unit 7 of TSPA-93.

Table 7-23. Corresponding hydrogeologic units in TSPA-91 and TSPA-93.

TSPA-93 Hydrogeologic Unit and Lithology		TSPA-91 Hydrostratigraphy and Lithology		Units Comparable?
1	Tiva Canyon welded	–	None	–
2	Paintbrush nonwelded	–	None	–
3C	Topopah Spring welded composite	–	None	–
3R	Topopah Spring welded repository	1	Welded tuff	Yes
4	Topopah Spring vitrophyre	2	Vitrophyre	Yes
5	Calico Hills/Prow Pass nonwelded vitric	3	Vitric tuff	Yes
6	Calico Hills/Prow Pass nonwelded zeolitic	4	Zeolitic tuff	No
7	Prow Pass welded	5	Partially welded tuff	No
8	Bullfrog welded	–	None	–
9	Bullfrog nonwelded	–	None	–
10	Tram welded	–	None	–

7.6.1 Matrix porosity

Both TSPA-9l and TSPA-93 model matrix porosity as beta distributions. The minima and maxima for both beta distributions are given by the theoretical limits of porosity (0.0 to 1.0). Consequently, differences in the PDFs arise because of differences in the means (arising from the different data sets) and differences in the coefficients of variation (arising from different assumptions about the variability of the data). Table 7-24 gives the means for the three comparable units.

Table 7-24. Comparison of expected values for matrix-porosity between TSPA-93 and TSPA-91.

Unit (TSPA-93/TSPA-91)	Porosity		Ratio: TSPA-93/TSPA-91
	TSPA-93	TSPA-91	
3R/1	0.139	0.11	1.26
4/2	0.065	0.04	1.68
5/3	0.331	0.21	1.58

Figure 7-8 compares the beta-function PDFs for the matrix porosity in the potential repository horizon (units 3R/1) for TSPA-93 and TSPA-91. The TSPA-93 distribution can be seen to have a considerably higher probability of yielding porosities above a porosity of 0.15 than does the TSPA-91 PDF. The different curve shapes result from a 26% larger expected value and 30% smaller CV. Differences of similar nature would be expected for the other two units.

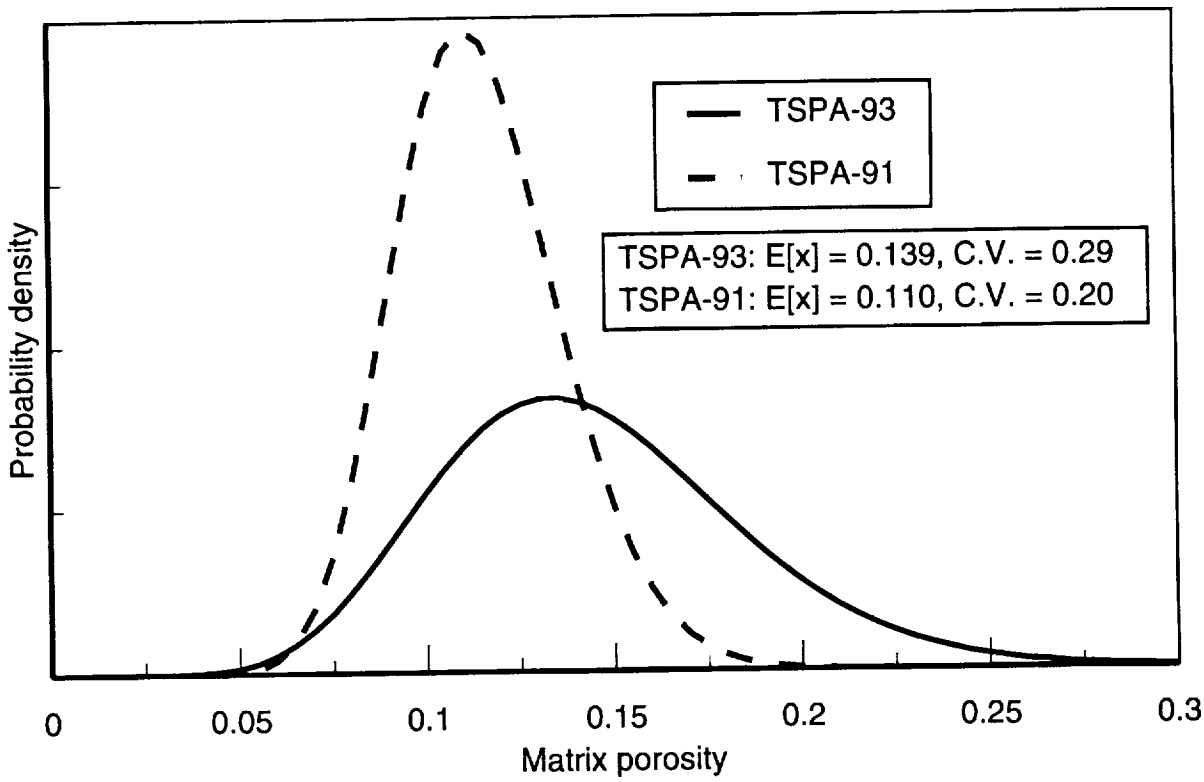

Figure 7-8. Comparison of PDFs for matrix porosity in potential repository horizon.

7.6.2 Matrix saturated hydraulic conductivity

The matrix saturated hydraulic-conductivity PDFs in TSPA-91 were beta-distribution approximations to an exponential, while the TSPA-93 PDFs are slightly skewed unimodal curves based on log-transformed data. Table 7-25 compares the means from the two analyses for the three comparable units, and Figure 7-9 shows two examples of the PDFs for the matrix hydraulic conductivity in the potential repository horizon.

Table 7-25. Comparison of expected values for matrix saturated hydraulic conductivity between TSPA-93 and TSPA-91.

Unit (TSPA-93/TSPA-91)	Saturated Hydraulic Conductivity (m/s)		Ratio: TSPA-93/TSPA-91
	TSPA-93	TSPA-91	
3R/1	2.37×10^{-10}	2.0×10^{-11}	12
4/2	2.26×10^{-11}	3.01×10^{-12}	7.5
5/3	1.82×10^{-8}	7.99×10^{-11}	228

As the table shows, the values for TSPA-93 range from about one order of magnitude to over 200 times larger than for TSPA-91. The range used in TSPA-91, differs from that used in TSPA-93, because in the former analysis the minimum was arbitrarily de-

fined as 0.0 for all units and the maximum to the value the data dictated. The data dictated the minimum and maximum values in TSPA-93.

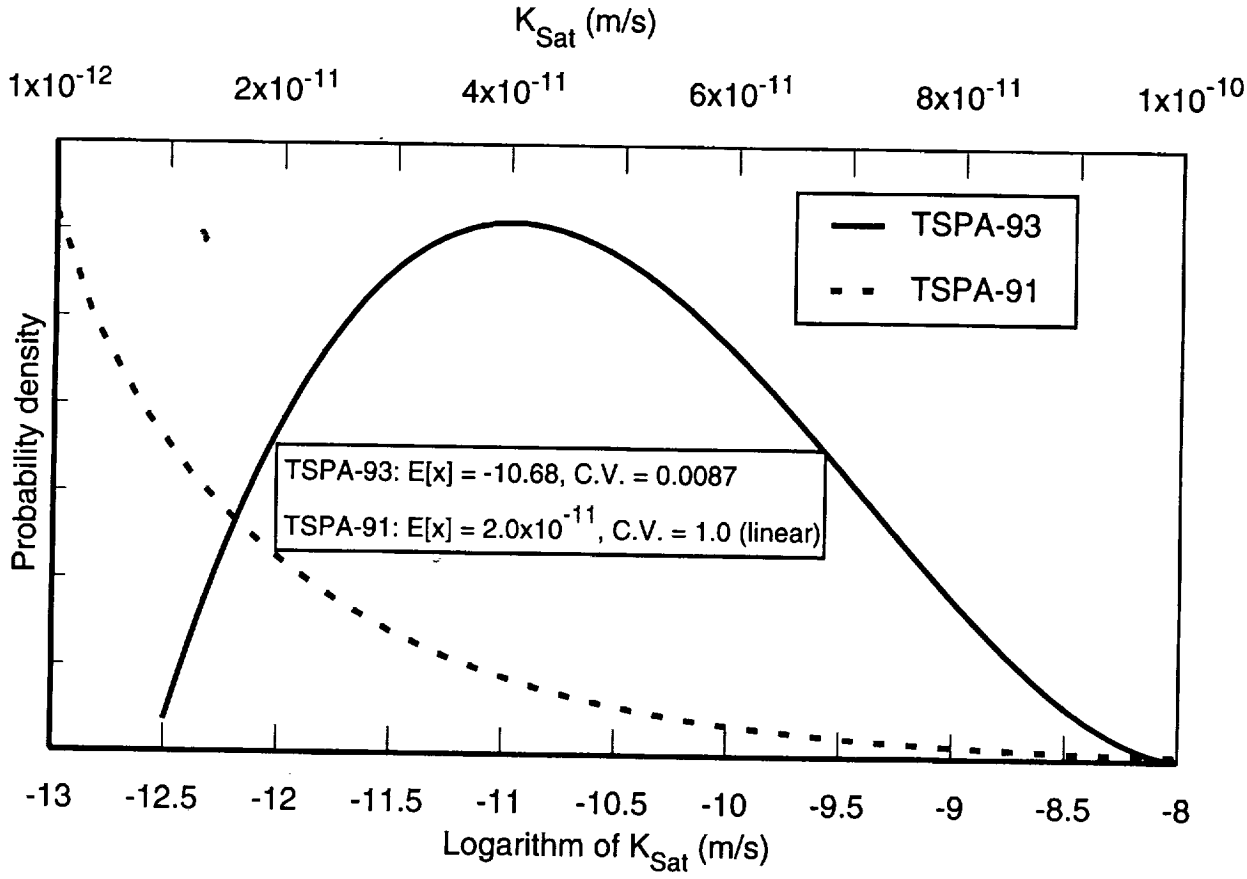

Figure 7-9. Comparison of PDFs for matrix saturated hydraulic conductivity in the potential repository horizon.

The difference between the two PDFs is quite striking. The distribution for K_{sat} for TSPA-91 is strongly weighted toward the lower values. (Note that the scale for the TSPA-91 K_{sat} runs from 10^{-12} to 10^{-10} m/s; had these values been plotted on the same scale as for TSPA-93, the curve would not have been visible.) Almost no realizations sampled from the TSPA-91 PDFs are even equal to the mean of the TSPA-93 PDF.

7.6.3 Water retention (van Genuchten) parameters

7.6.3.1 Matrix air-entry

The matrix air-entry PDFs for both TSPA-91 and TSPA-93 are beta functions. The values for TSPA-91 is range from 0.0004 m^{-1} to 137.0 m^{-1} for all units; the minimum is

within an order of magnitude of TSPA-93 values, but the maximum value is approximately four to six orders of magnitude greater. The coefficients of variation for the two studies vary approximately by factors of 2 to 6. Table 7-26 compares the parameters. The TSPA-93 values are all larger, by factors of 1.4 to over 5.

7.6.3.2 Matrix saturation/desaturation

Because the data sources for this parameter are similar to those used for the air-entry parameter, it is not surprising that the differences between the two analyses are also similar. Table 7-27 compares the two analyses.

Table 7-26. Comparison of expected values for matrix air-entry between TSPA-93 and TSPA-91.

Unit (TSPA-93/TSPA-91)	Matrix Air-Entry Parameter (m^{-1})		Ratio: TSPA-93/TSPA-91
	TSPA-93	TSPA-91	
3R/1	0.0299	0.0057	5.3
4/2	0.0023	0.0017	1.4
5/3	0.0531	0.0265	2.0

Table 7-27. Comparison of expected values for matrix saturation/desaturation between TSPA-93 and TSPA-91.

Unit (TSPA-93/TSPA-91)	Matrix Saturation/Desaturation		Ratio: TSPA-93/TSPA-91
	TSPA-93	TSPA-91	
3R/1	1.793	1.798	1.0
4/2	2.437	1.708	1.4
5/3	2.750	2.223	1.2

7.6.3.3 Matrix residual degree of saturation

The same sources of data are used in the residual degree of saturation analysis as are used in establishing the two water retention parameters described above. For both studies, the ranges are set to 0.0 and 1.0. The CV in TSPA-93 is approximately a factor of 6 higher for all the comparable units. Table 7-28 compares the parameters. The fact that some values of S_r are smaller for TSPA-93 is due to accepting zero values for Sr, which skews the mean toward the lower end of the PDF range. There are no zero values in the data set for TSPA-91 (Peters *et al.*, 1984, Table A.2).

7.6.4 Fracture parameter comparisons

Because fracture parameters were derived differently for TSPA-91, only two parameters can be compared with TSPA-93—fracture saturated hydraulic conductivity (K_f) and the van Genuchten fracture air-entry ($\alpha_v G_f$) parameter. In TSPA-91 both pa-

rameters are modeled as beta distributions; in TSPA-93, K_f is modeled as a beta distribution approximating an exponential, and the van Genuchten fracture air-entry parameter is modeled as a normal beta distribution.

Table 7-28. Comparison of matrix residual saturation expected values between TSPA-93 and TSPA-91.

Unit (TSPA-93/TSPA-91)	Matrix Residual Saturation		Ratio: TSPA-93/TSPA-91
	TSPA-93	TSPA-91	
3R/1	0.045	0.080	0.6
4/2	0.118	0.052	2.3
5/3	0.097	0.164	0.6

The fracture hydrogeologic properties for TSPA-93 are modeled by the parallel-plate approximation discussed in Section 7.4. The near-vertical fracture orientations in the TSPA-93 data set result in PDFs for fracture hydraulic conductivity that are weighted toward higher values. In TSPA-91 a composite-porosity model was used in which the fracture is assumed to have the hydraulic properties of sand. Fracture characteristics for all the TSPA-91 units were the same. Table 7-29 compares the fracture parameters. Note that the TSPA-93 values for K_f have been converted to m/s to allow comparison with the TSPA-91 values.

Table 7-29. Comparison of expected values for fracture parameters between TSPA-93 and TSPA-91.

Unit (TSPA-93/TSPA-91)	Fracture Hydraulic Conductivity (m/s)		Ratio: TSPA-93/TSPA-91
	TSPA-93	TSPA-91	
3R/1	4.57×10^{-2}	8.25×10^{-5}	550
4/2	5.30×10^{-2}	8.25×10^{-5}	640
5/3	6.54×10^{-2}	8.25×10^{-5}	790
	Fracture Air-Entry Parameter (m^{-1})		
3R/1	12.2	14.5	0.8
4/2	13.1	14.5	0.9
5/3	12.2	14.5	0.8

The significance of the differences between the TSPA-91 and TSPA-93 PDFs depends on the sensitivity of the hydrogeologic models to the parameters. This is discussed in Chapters 14 and 15.

Chapter 8
Infiltration and Percolation Rates

(Gauthier, Wilson)

Groundwater is expected to be one of the primary agents affecting the performance of a potential repository at Yucca Mountain. Groundwater can corrode the waste containers, can dissolve and transport the waste, and because of its probable value as an exploitable resource, can be the mechanism for spreading contamination to future inhabitants of the region. One of the reasons for choosing the unsaturated zone to locate a repository is that groundwater is thought to be of much more limited availability there than in the saturated zone.

A sensitivity study of parameters used in TSPA-91 indicates that the results were highly dependent on the value for the groundwater flux used in the analyses (Wilson, 1993). Thus, the assumptions made about percolation flux could have a profound effect on the results of this TSPA. In TSPA-91, an arbitrary distribution was chosen to describe groundwater flux because, for the most part, quantitative data did not exist.

Because of the importance of this parameter, it is disappointing that more quantitative data remain unavailable. As mentioned below, there is reason to believe that present day fluxes through the matrix at Yucca Mountain are extremely low, but almost nothing is known about flow through fractures or fault zones. Also, future groundwater fluxes will probably never be predicted with certainty. At each iteration of the TSPA process, we attempt to incorporate the best possible knowledge in this area, and if we err, we would like to err by overestimating our uncertainty in this parameter.

Thus, the goals relating to infiltration and percolation for TSPA-93 are twofold: first, to develop a basis for determining infiltration into and percolation through the unsaturated zone to produce reasonable values for use in this TSPA, and that can be built upon in future TSPAs; second, to begin explicitly considering climate change and, as discussed in later chapters, to develop TSPA models capable of handling it.

8.1 Definitions

Figure 8-1 illustrates some of the processes and terminology involved with groundwater flow through the unsaturated zone at Yucca Mountain. The term "infiltration" is used to describe the groundwater inflow near the surface. "Percolation" is used when discussing groundwater flow at depth through the unsaturated zone. The amount of "recharge" is the percolation rate over a given time period and region (Yucca Mountain or, typically, a larger region). The term "groundwater flux" is used interchangeably with percolation rate.

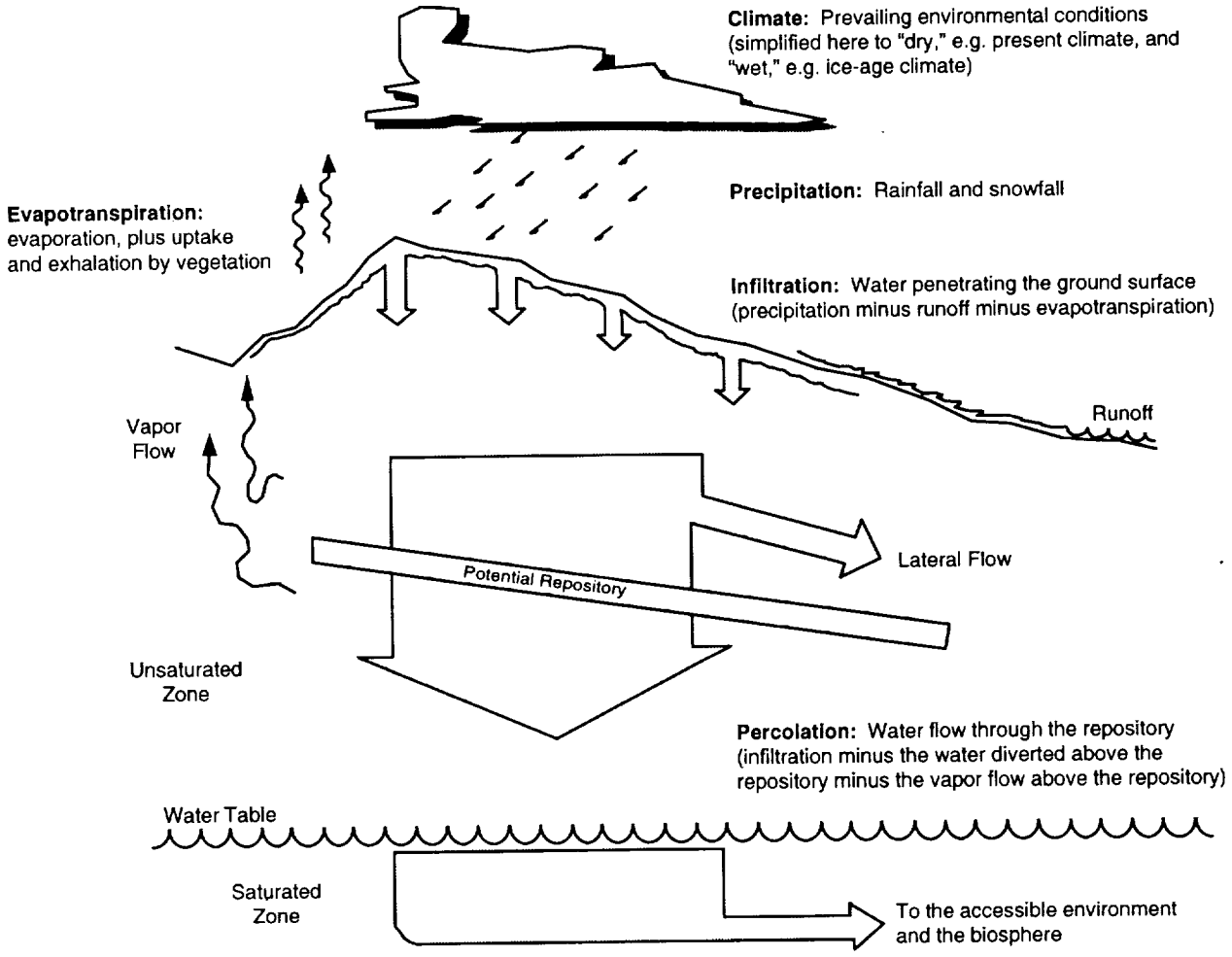

Figure 8-1. Overview of infiltration and percolation at Yucca Mountain, including definitions of terms used in Chapter 8.

In this TSPA, percolation rate is an input parameter. For a TSPA calculation, the processes that generate percolation cannot presently be handled—i.e., rainfall, evapotranspiration, etc. are not modeled. Typical parameters of climate modeling—precipitation and temperature—are extraneous to present TSPA models. It is not precipitation, per se, that can influence the performance of a repository, but that part of precipitation that eventually flows through the ground and reaches the repository. Although precipitation and temperature are of interest, this information is of very limited use—primarily to add confidence in the selected values for groundwater flux. This fact should not be lost sight of during the characterization of Yucca Mountain.

8.2 Strategy

Because of the lack of quantitative data and the inherent uncertainty in determining future groundwater flow rates, the strategy used is to determine likely past climates and percolation rates, then extrapolate them into the future. (1) From a number of sources in the scientific literature, a climate history for the Yucca Mountain region is estimated. At this time, only two different climate types—"wet" and "dry"—can be comfortably resolved. Wet climates correspond to periods of global glaciation, i.e., ice ages. Dry climates correspond to interglacial periods, e.g., the present climate. (2) The duration of each climate is estimated based on the apparent periodicity of the geologic record. Within the periodicity, the time of climate change is selected at random to maximize informational entropy. (3) The percolation rate during each climate type is approximated as follows. For each climate type, an estimate is made of the present day elevation at which a similar climate is in evidence. Then, a method devised by Nevada State hydrologists (Maxey and Eakin, 1949; Eakin *et al.*, 1951; Rush, 1971) is used to estimate recharge over a large area—essentially the needed parameter—at various elevations in Nevada. It is assumed that there is uncertainty in the estimated recharge (or infiltration); indeed, it is assumed that the estimated infiltration is only an average value. Future infiltration for a given climate is described as exponentially distributed with a mean specified as above. (When only a mean value is known, the probability distribution that produces the maximum information entropy is the exponential.) Under some conditions, percolation can vary from infiltration and, therefore, a method is devised for reducing percolation based on the possibility of upper strata at Yucca Mountain forming a capillary barrier to flow (only for the composite-porosity flow model; see Chapter 14). (4) For each climate type, water-table elevations are also estimated, based on ranges given in the scientific literature, and assuming a uniform distribution over those ranges. (When only minimum and maximum values are known, the uniform probability distribution produces maximum information entropy.) Finally, additional evidence is sought that supports the chosen values. It should be pointed out that much of this method is based on work of other researchers, and they are cited where possible in the following discussion.

Several limitations are recognized in this strategy. First, it is not at all certain that climate history will repeat itself, and thus, extrapolation from past climates might give erroneous results. Second, the state of knowledge about past climates is continually changing. The resolution into wet and dry climates with durations of tens of thousands of years is likely much too coarse. It is possible that uncertainty about past climates (and percolation) at Yucca Mountain might rival uncertainty about future climates. Third, possible anthropogenic effects on climate are ignored. A concern is that greenhouse gases will accumulate in the atmosphere, resulting in an overall global warming, and possibly a change in climate at

Yucca Mountain. Effects of such accumulation are not well understood; the climate change could be transient, lasting for perhaps 1000 years (Long and Childs, 1993), or it could set in motion an series of climate changes (White, 1993). Inclusion of this effect is warranted in future TSPAs. Fourth, expert opinion is, for the most part, discounted in favor of published analyses and field investigations. DeWispelare *et al.* (1993) describe predicting the future through the use of climate experts. But as mentioned above, climate is only of interest in terms of how it affects percolation rates and water-table fluctuations over time at one specific area. Climate and hydrology experts from the USGS and the WIPP project were consulted, but parameter probability distributions were not directly elicited from them.

8.3 Major differences with TSPA-91

There are two important qualitative differences between these new flux distributions and the TSPA-91 flux distribution. First, the time horizon is expanded. Because of the current uncertainty in what the EPA regulation might eventually be (see Chapter 2), release calculations were performed covering a million-year period. Such a time period is long enough to encompass many significant changes in climate (perhaps ten full glacial cycles). This time scale makes the role of climate change very different than in a 10,000-year calculation. Second, in TSPA-91, to simplify things, the same flux distribution was used for both conceptual models of flow (composite-porosity and weeps). In TSPA-93, different distributions are used, reflecting the different nature of flow in the two models and a difference in the uncertainties.

For TSPA-91, groundwater flux was described as an exponential probability distribution with mean of 1 mm/yr. The water-table elevation was held constant. The values for groundwater flux and water-table elevation used in TSPA-93 are shown in Table 8-1.

8.4 Climate-change timing

Fairly persuasive evidence has been documented that Pleistocene climate underwent a semi-regular progression of climate changes associated with glacial cycles (Imbrie and Imbrie, 1979; Imbrie, 1985). Based on these cycles, climate can be divided into two categories—glacial (or pluvial) and interglacial. Studies of pack-rat middens (e.g., Spaulding, 1985), ostracodes (e.g., Forester, 1987), lake levels (e.g., Benson *et al.*, 1990), and water-table levels (e.g., Paces *et al.*, 1993, and Marshall *et al.*, 1993), indicate that, in the southwestern United States as a whole, the glacial periods are typically reflected as "wet" climates, while the interglacials are typically "dry." The present climate is an interglacial, dry climate.

The glacial cycles are about 100,000 years long on average, and appear to correlate with various changes in the amount of solar radiation that reaches the Earth, known as

Table 8-1. Distributions used for climate/percolation parameters.

Parameter	"Dry" Conditions (interglacial)	"Wet" Conditions (ice age)
infiltration	exponentially distributed (mean = 0.5 mm/yr)	exponentially distributed (mean = 10 mm/yr)
duration	uniformly distributed from 0 to 100,000 yr (mean = 50,000 yr)	100,000 years minus "dry" duration (mean = 50,000 yr)
percolation (weeps model)	— same as infiltration —	
percolation (composite-porosity model)	— see Section 8.9 —	
water-table rise	uniformly distributed from 0 to 10 m (mean = 5 m)	uniformly distributed from 50 to 120 m (mean = 85 m)

the Milankovitch insolation cycles (Imbrie and Imbrie, 1979). These changes are caused by the eccentricity in the Earth's orbit around the Sun (a 100,000-year period), the tilt of the Earth's axis (a 41,000-year period), and the precession of the Earth's axis (19,000- and 23,000-year periods). Winograd *et al.* (1988) suggest a slightly different timescale, one not aligned with the Milankovitch insolation cycles; however, Imbrie *et al.* (1993) argue that the difference is not significant. Also, before 400,000 years ago, the primary period might have been 41,000 years rather than 100,000 years. A 41,000-year period actually aligns better with what should be a stronger insolation cycle; there are no reasonable explanations as to why a 100,000-year period is presently dominating. We cannot be sure if the 100,000-year period will persist for another million years, but it presently appears to be a reasonable working hypothesis.

Most of the information regarding glacial cycles comes from oxygen-isotope measurements of ocean-floor sediments (the relative abundance of ^{18}O is related to the size of the ice sheets). Figure 8-2 shows a climate history based on these data. These data have been interpretted to indicate that a typical glacial cycle consists of a 90,000-year glacial period followed by a 10,000-year interglacial period. If we were to go by this timing, we would have a 90,000-year wet period and a 10,000-year dry period each cycle. Furthermore, since the current dry period has already lasted for about 10,000 years, we would expect the next wet period to begin shortly. Indeed, Imbrie and Imbrie (1979) predict that within 23,000 years the earth will be in the throes of the next ice age.

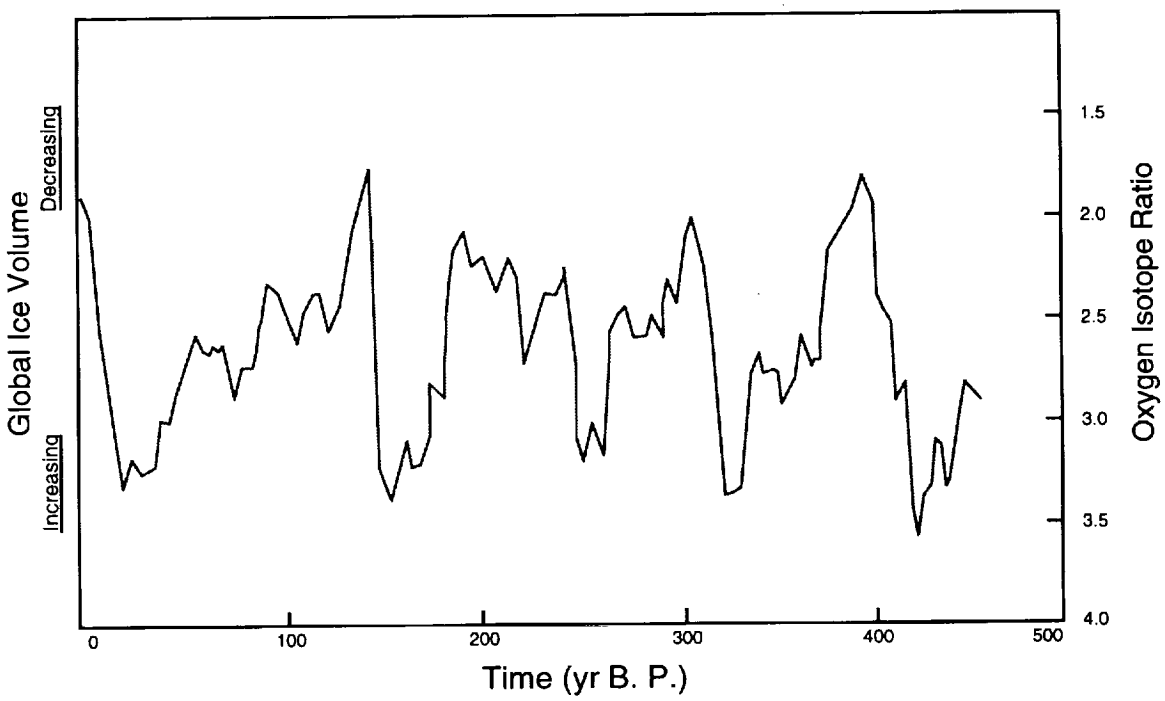

Figure 8-2. Oxygen isotope measurements made on two Indian Ocean cores by a CLIMAP research group showing size of the global ice sheets over the past half-million years. Figure based on Imbrie and Imbrie (1979) and Imbrie (1985).

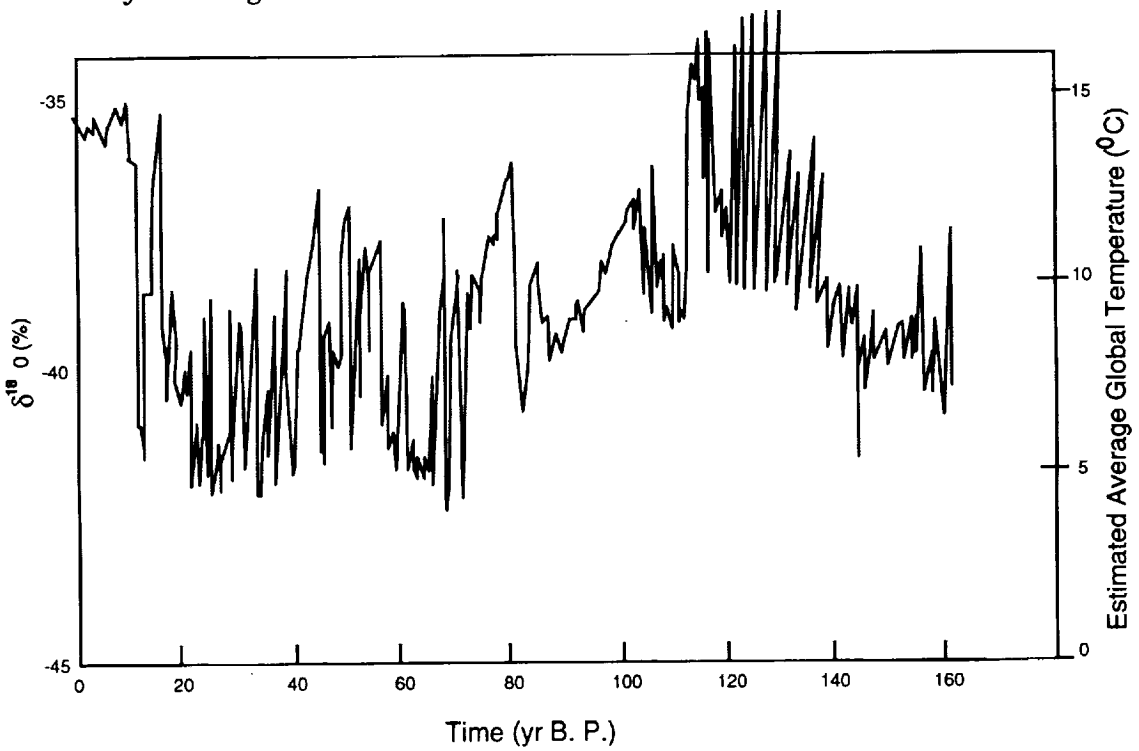

Figure 8-3. Oxygen isotope measurements made on ice core from central Greenland by a GRIP research group showing the average earth temperature over the past full glacial cycle. Figure based on GRIP (1993).

Actually, the climate history of the earth is probably not as simple as the ocean-floor sediments suggest. Recent ^{18}O data from Greenland ice cores (GRIP, 1993) shows the same general cooling and warming trends as the ocean-floor data, but with tremendous fluctuations superimposed on the general trends (Figure 8-3). The fluctuations appear to have a timescale of 1000 to 2000 years. It is not known if these fluctuations were reflected in the climate at Yucca Mountain—they do not appear so strikingly in the Devils Hole calcite data taken just a short distance from Yucca Mountain by Winograd *et al.* (1988) and by Winograd *et al.* (1992)—but future TSPAs should investigate the implications of this climate history. It is also important to note that the ice-core data show a unique stability of climate over the last 8000 years.

For TSPA-93, the short-term climate fluctuations are neglected, resulting in climate being divided into wet/dry pairs that last 100,000 years. And rather than divide the 100,000-year cycle into a long wet period and a short dry period, a more equal weighting has been chosen for the following reasons.

First, changes in local climates are driven by perturbations in weather patterns, not simply the size of the ice sheet. Swift (1992) reports that the ice-age climate at the WIPP site in southern New Mexico was probably dominated by the presence of the jet stream (i.e., the storm track) which, if modeling by COHMAP (1988) is correct, would be forced down to that region by the sheer physical bulk of the ice sheet further north. The COHMAP prediction, with approximate positions of the WIPP site and Yucca Mountain, is shown in Figure 8-4. Note that at full glacial maximum (18,000 years ago) the jet stream is south of Yucca Mountain. While the jet stream is traversing Yucca Mountain, the climate could be relatively mild and wet; while the jet stream is south of Yucca Mountain, the climate could be relatively cold and dry. Both situations could promote significant infiltration, which is what is really of interest, and thus, jet-stream movements would define the time period of interest (the wet period). This time period would only be indirectly related to the the size of the ice sheets.

Second, and lending some support to the jet-stream-location hypothesis, is evidence from the size of several pluvial lakes in the Great Basin (Lahontan, Bonneville, etc.). Benson *et al.* (1990) reported that the lakes were at relatively low levels approximately 35,000 years ago, expanding to maximum levels approximately 14,000 years ago (somewhat later than the height of the last ice age 18,000 years ago). Figure 8-5 shows the lake levels for a pluvial-lake that existed north of Yucca Mountain. Thus, if we base the climate time periods on pluvial-lake size, we would perhaps have a wet climate of 20,000 years, and a dry climate of 80,000 years for each glacial cycle. (Note however that the lake data do not go back 100,000 years, so there is no record of a complete glacial cycle.)

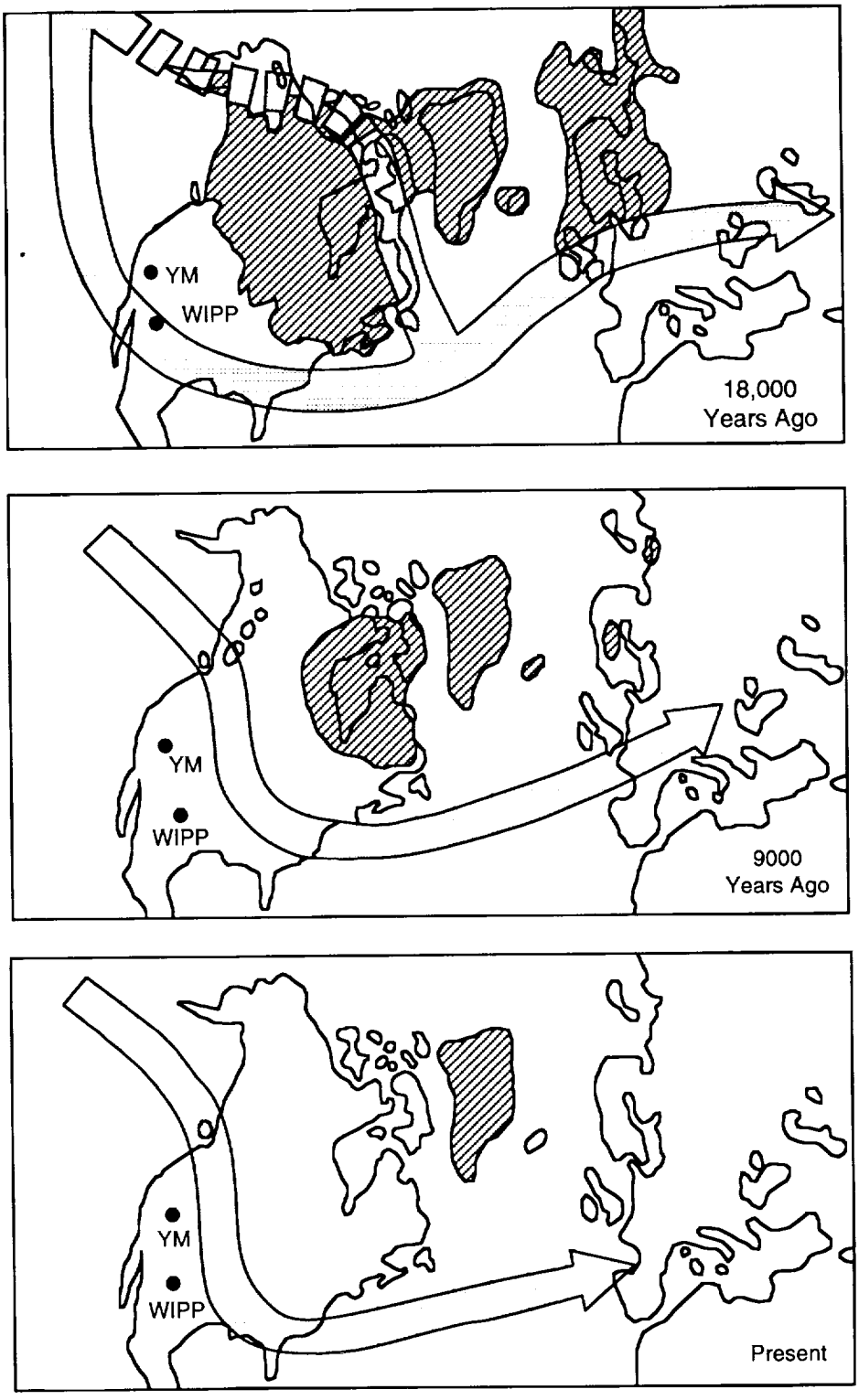

Figure 8-4. Distribution of northern-hemisphere ice sheets and modeled position of the jet stream. Ice shown with dark pattern, jet stream shown with arrow (broken where disrupted or weak). Figure taken from Swift (1992).

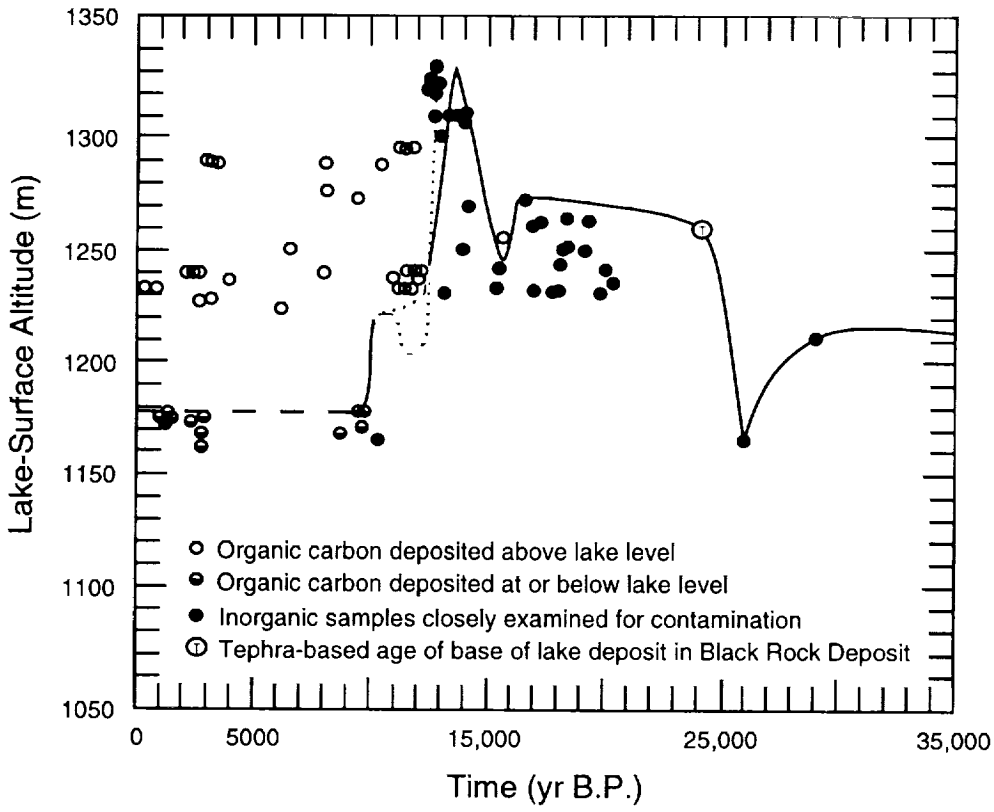

Figure 8-5. Chronology of lake levels for Lake Lahontan (presently divided into Pyramid Lake, Honey Lake, Walker Lake, and a number of dry basins), approximately 300 km northwest of Yucca Mountain. Figure taken from Benson *et al.* (1990).

The above information suggests that the times for climate changes at Yucca Mountain are uncertain, and that the time of the change from dry to wet climates might not coincide with the time the global climate goes from an interglacial to a glacial period. Therefore, the simplest assumption is made about these time periods—that, on average, the wet and dry periods are of equal length, but with variation about that mean. The variation about the mean is maximized, based on the maximum-entropy concept.

In summary, it is assumed that there exists a regular 100,000-year period for climate cycles, with each cycle including a dry and a wet period. Yucca Mountian is currently in a dry period, which started roughly 10,000 years ago. The next dry period is assumed to start 90,000 years from now, the one after that is assumed to start 190,000 years from now, etc. The starting times of the wet periods are treated as random variables, uniformly distributed over the available time. The start of the first wet period is between now and 90,000 years from now, with all choices equally likely. The start of the second wet period varies uniformly between 90,000 years from now and 190,000 years from now.

8.5 Infiltration rates for climate-change

Given that wet and dry climates have existed at Yucca Mountain, it is necessary to determine likely infiltration rates. For infiltration rate during dry periods, an exponential distribution with a mean of 0.5 mm/yr is chosen; for infiltration rate during wet periods, an exponential distribution with a mean of 10 mm/yr is chosen. These distributions are subjective, but not completely arbitrary, and in the following sections the reasoning that went into those choices is related. Periods of dryout or refluxing of condensate because of the repository thermal load are handled separately, as part of the hydrothermal model (Chapter 10).

8.6 Dry-climate infiltration

The infiltration distribution for the dry climate is thought of as being generally representative of current, interglacial conditions. Current evidence suggests a very low infiltration rate at present. For example, Gauthier (1993) found that a percolation rate of 0.01 mm/yr or lower was needed to match the measured in-situ matrix saturations for drillhole USW H-1. Weeks and Wilson (1984), using several simplifying assumptions, estimated a percolation rate of between 0.003 and 0.2 mm/yr for the Topopah Spring matrix at USW H-1; similarily, Montazer and Wilson (1984) estimated a percolation rate of between 10^{-7} and 10^{-4} mm/yr for the Topopah Spring matrix at USW G-1. Flint *et al.* (1993) show a relatively good match between matrix saturations observed at depth in USW UZ-16 and matrix saturations calculated using a percolation rate of approximately 0.005 mm/yr.

All of the above estimates are for single-phase flow through the matrix, although indirectly they could account for flow though fractures if matrix and fracture flow are coupled. Tsang and Pruess (1990) performed calculations to estimate the effects of vapor flow driven by the geothermal gradient and low-humidity boundary conditions. They found that vapor flow could be up to about 0.1 mm/yr upward; therefore, the downward groundwater flow through the matrix at about 0.1 mm/yr would result in negligible overall downward flux. They did not consider barometric pumping, which could increase net vapor flow (see Chapter 21).

Estimates of recharge to the saturated zone (which would include matrix, fracture, and vapor flow) have been made based on gross water balance—precipitation minus estimated runoff and evapotranspiration. Nevada State hydrologists have devised a method—the "Maxey-Eakin" method—for estimating recharge based on elevation and precipitation (Maxey and Eakin, 1949; Eakin *et al.*, 1951). Table 8-2 contains a summary of recharge for the Ash Meadows groundwater system based on the Maxey-Eakin method (Rush, 1971). The summit of Yucca Mountain is at an elevation somewhat higher than 1500 m. Additional

Table 8-2. Recharge for various precipitation zones in the Ash Meadows groundwater system as predicted by the Maxey-Eakin method (summarized from Rush, 1971).

Precipitation Zone (m)	Precipitation Range (mm/yr)	Recharge as Percentage of Precipitation	Infiltration Range (mm/yr)
> 2400	> 500	25	> 120
2100–2400	400–500	15	60–80
1800–2100	300–400	7	20–30
1500–1800	200–300	3	6–9
< 1500	< 200	Minor	—

elevations are included in the table because with a climate change, a region can effectively act as if it were at a different elevation.

For the present climate at the Yucca Mountain region, Rush estimated a recharge of less than 3% of precipitation, which is about 5 mm/yr (according to Flint *et al.*, 1993, average precipitation at Yucca Mountain is 170 mm/yr). Rice (1984) estimated a recharge from the Yucca Mountain region of less than 2.5 mm/yr. Basically, Rice and Rush both say that there is negligible recharge at Yucca Mountain, and the numbers above are upper limits to what is negligible. Long and Childs (1993) devised a fairly elaborate model of precipitation and infiltration for the EPRI performance assessment (McGuire *et al.*, 1992) and came up with an estimate of 0.9 ± 0.5 mm/yr.

An exponential probability distribution for infiltration was chosen because it is a simple functional form, gives greatest weight to low infiltrations, and requires only one parameter to be defined. The mean value of 0.5 mm/yr was chosen because it was thought that a very low value (near zero) was likely, but some weight to the possibility of higher values like those listed above was thought to be warranted (for example, with the chosen distribution there is a probability of 14% of an infiltration of 1 mm/yr or higher). The median value of the distribution is 0.35 mm/yr.

8.7 Wet-climate infiltration

The wet-climate infiltration distribution is thought of as representing conditions at a "full glacial maximum"—nominally the wettest period of a glacial cycle. (As shown in Figure 8-3, selection of a full glacial maximum is not straightfoward. Also, as mentioned in the discussion of Figure 8-4, and as shown in Figure 8-5, the full glacial maximum might not correspond to the wettest climate experienced in a given location.) Estimates of infiltration during a full glacial maximum come from modeling and field investigation, but data are sparse and extrapolations from the data are speculative.

In their model, Long and Childs (1993) found a rather modest increase in infiltration from current conditions to a full glacial maximum; they calculated an infiltration rate of 2.4 ± 1.4 mm/yr, only about $2\frac{1}{2}$ times their value for the current rate. However, they appear to have only increased precipitation for a full glacial maximum by 20%—from a rather low baseline of 150 mm/yr to an average of 180 mm/yr. Flint *et al.* (1993) are proponents of an even lower value; they used a maximum infiltration rate of 0.02 mm/yr for the wettest part of the glacial cycle in their prediction of in-situ saturations at Yucca Mountain.

Other than modeling, a method of estimating infiltration during a glacial maximum is to consider areas near Yucca Mountain that currently have greater precipitation and are somewhat cooler because of higher elevation, such as Pahute Mesa and Rainier Mesa. That is, another method is to consider Pahute Mesa and Rainier Mesa as possible analogs of Yucca Mountain during a global ice-age climate. As shown in Table 8-2, Rush (1971) estimated a recharge of about 7% of precipitation from elevations in the 1800- to 2100-m range. (Rainier Mesa is at about 2200-m elevation, and Pahute Mesa is a little lower). It has been estimated from actual observations that parts of Rainier Mesa have a recharge of about 8% of precipitation, or 24 mm/yr (Wang *et al.*, 1993). Based on a study of fossilized packrat middens, Spaulding (1985) estimated that annual precipitation at the last glacial maximum was about 30% to 40% higher than at present in the vicinity of the Nevada Test Site (60% to 70% higher in winter, when most infiltration is likely to occur). For comparison, 8% of 1.4×170 mm/yr is about 19 mm/yr. However, Flint and Flint (1993) point to the plugging of most fractures with calcite deposits near the surface of Yucca Mountain as evidence that infiltration at Yucca Mountain is very different from Rainier Mesa and has been for a long time.

For TSPA-93, the wet-climate infiltration is described using an exponential distribution with a mean of 10 mm/yr. The median value of this distribution is 7 mm/yr. This distribution is based on Spaulding's (1985) estimate of 40% higher precipitation during a glacial maximum. This increase would result in an annual precipitation of about 240 mm/yr (170 mm/yr $\times$ 1.4). Using Table 8-2, this value correlates with an effective elevation increase of several hundred meters at Yucca Mountain, and infiltration would be expected to be approximately 3% of this value, or 7 mm/yr (240 mm/yr $\times$ 0.03). Here it is useful to mention that evapotranspiration and other environmental effects are implicit in the Maxey-Eakin method, and thus, changes in vegetation, temperature, cloudiness, the amount of sunlight reaching the ground, etc., are taken into account.

The exponential distribution with mean of 10 mm/yr allows for the possibility of even greater infiltrations at Yucca Mountain during a full glacial maximum. This distribution has 14% of its probability above 20 mm/yr, and 1% of its probability above 46 mm/yr. We

feel that it is reasonable to include this probability tail out to very high infiltration values for three reasons. First, Spaulding (1985) found that some types of vegetation grew 1200 m lower than at present at the last glacial maximum, leading to a possible correspondence between Yucca Mountain at a full glacial maximum and areas 1200-m higher under present conditions. Using Table 8-2, an elevation of 1200-m higher than Yucca Mountain—2700 m—would have an infiltration of over 120 mm/yr. This effective elevation is even higher (and wetter) than Rainier Mesa. Second, based on an analysis of fossil ostracode species from deposits laid down approximately 15,000 years ago in southern Nevada, Forester and Smith (1992) predict an annual mean temperature of 9°C (as opposed to 17°C presently) and an annual precipitation of 341 mm/yr (as opposed to 112 mm/yr presently) for the region. This precipitation value is greater than the present value for Rainier Mesa. Third, Swift (1992) concluded that the evidence from a number of sources—packrat middens, lake levels, floral and faunal assemblages, isotopic data, etc.—suggest that the annual precipitation was a factor of 2 higher at the last glacial maximum in southern New Mexico. At Yucca Mountain, twice the present-day precipitation would be approximately 340 mm/yr. Using Table 8-2, this value correlates with an effective elevation of between 1800 and 2100 m, and a recharge of 7% of percolation; 7% of 2×170 mm/yr is about 24 mm/yr—coincidentally, the same as parts of Rainier Mesa. Again however, at the time the jet stream could have been directly over southern New Mexico, but south of Nevada, and the increase in precipitation in southern New Mexico might be an overestimate of the increase in precipitation in southern Nevada.

8.8 Water-table heights

Uranium isotopic dating of ancient spring deposits a few kilometers to the southwest of Yucca Mountain indicates that the water table in the region was between 80 and 115 m higher during the last full glacial maximum, approximately 18,000 years ago (Paces *et al.*, 1993). This finding is corroborated by strontium-isotope analyses of calcites taken from four drill holes in the immediate vicinity of Yucca Mountain (Marshall *et al.*, 1993). In itself, a large rise in the water table is evidence that recharge in the general region was probably significantly different in the past. Paces *et al.* also suggest that the water level might have fluctuated repeatedly in the past.

Based on this information, it was decided to use a uniform distribution of water-table rises from 50-m to 120-m. This distribution has an average rise of 85 m, which is the value given by Marshall *et al.*

For the dry periods, the range in water-table variations is unknown. Some information is available for water-table rises due to seismic events (Carrigan *et al.*, 1991; McGuire *et al.*, 1992, Section 6), but such water-table rises are probably transients with relatively short

time scales. For the TSPA-93 calculations, it was decided to specify a uniform distribution of water-table rises from 0 to 10 m during the dry periods. This distribution is arbitrary and it is not meant to imply that the present water table is at its lowest possible level and that the present climate is the driest possible climate. The distribution was specified primarily to see if the final results are sensitive to this parameter.

8.9 Infiltration vs. percolation for the composite-porosity model

The final topic to be covered in this chapter is the relationship between near-surface infiltration and deep percolation. For the weeps model (Chapter 15), they are assumed to be the same—all water that makes it past the zone of evapotranspiration flows through fractures all the way down to the water table. This is intended to be a conservative, bounding assumption. For the composite-porosity model (Chapter 14) however, with its assumption of matrix/fracture pressure equilibrium across columns that are intended to represent approximately a kilometer in lateral extent, such an assumption might not be reasonable. Modeling that has been done using the composite-porosity model (Ross, 1990; Prindle and Hopkins, 1990) has found significant lateral flow in the nonwelded Paintbrush (unit 2—PTn—in Table 6-3), above the repository, when infiltration is high. In fact, Ross showed that this unit might act as a capillary barrier because its pores are smaller than the fracture apertures in the Topapah Spring welded unit (unit 3—TSw). The capillary-barrier hypothesis is that water would avoid the TSw fractures, preferring to flow laterally in the PTn matrix. If this is the case, the TSw matrix might flow at capacity under wet conditions, but the fractures would not flow. The implication is that the saturated conductivity of the TSw matrix (K_{sm}) is the maximum attainable percolation rate. Thus, the distribution of values for K_{sm} is important to consider.

Before going on, it should be noted that there are some arguments against the capillary-barrier hypothesis. First, evaporation deposits are not in evidence in Abandoned Wash on down-dip faces where PTn is exposed. Second, at least part of PTn is composed of granular material, and although the pores within the grains are smaller than fractures, the voids between grains are comparable in size to fractures (Peters *et al.*, 1987). If the pores within the grains were to become saturated, flow into TSw fractures might be preferred over flow in the inter-grain pores in PTn (although, it might require considerable water flow to saturate the grains). Third, at Rainier Mesa, which is tilted more than Yucca Mountain and has a stratum that is more conductive than PTn, water is still found in fractures below the conductive stratum (note, however, that the potential repository block at Yucca Mountain is not as extensively faulted as Rainier Mesa, so they may not be comparable). Even without lateral diversion, though, it is unlikely that water would penetrate uniformly at high flow

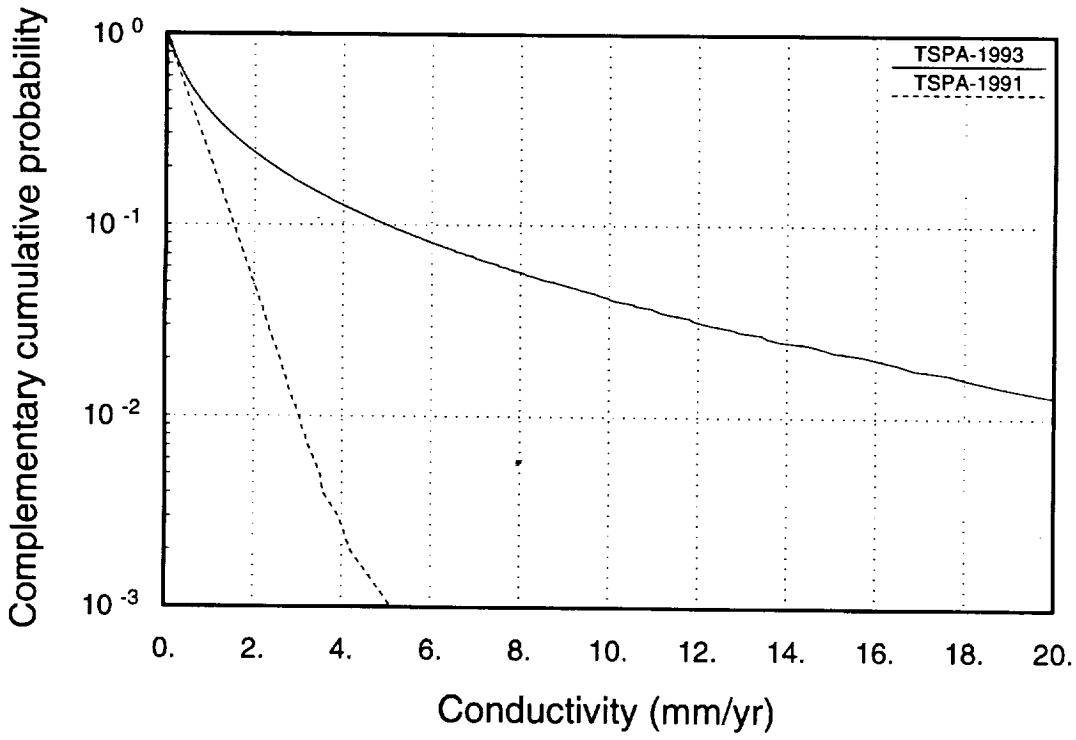

Figure 8-6. Probability distribution of K_{sm} for the TSw unit.

rates down to the potential repository horizon. And the weeps model was developed expressly to address the situation where water travels nonuniformly in saturated plumes.

The distribution of K_{sm} for the TSw unit, as developed for this TSPA (Table 7-5), is shown in Figure 8-6, along with the distribution used for TSPA-91. The large difference in the two curves is surprising. As mentioned in Section 7.2.3, an additional source of measurements was discovered, for drillhole UE25a-1 (Anderson, 1981). Those measurements go up to much higher conductivity values, which is why the new distribution in Figure 8-6 has values at such high conductivities. These higher conductivities could be an artifact of microfracturing, because UE25a-1 is in an imbricate fracture zone. However, all following discussion uses the new K_{sm} distribution, identified by "TSPA-1993" in Figure 8-6.

If the capillary-barrier hypothesis is believed, the infiltration distribution would be cut off above the matrix conductivity. Because there is some doubt about whether this process really happens, the percolation rate was allowed to be higher than K_{sm}, but with a reduced probability. The distribution decided upon is rather arbitrary in its details, but qualitatively produces the desired effect. The following procedure was used to obtain the distributions pictured in Figures 8-7 and 8-8. The distributions were generated using a simple Monte Carlo simulation in which infiltration rates q_i were sampled from the distributions described

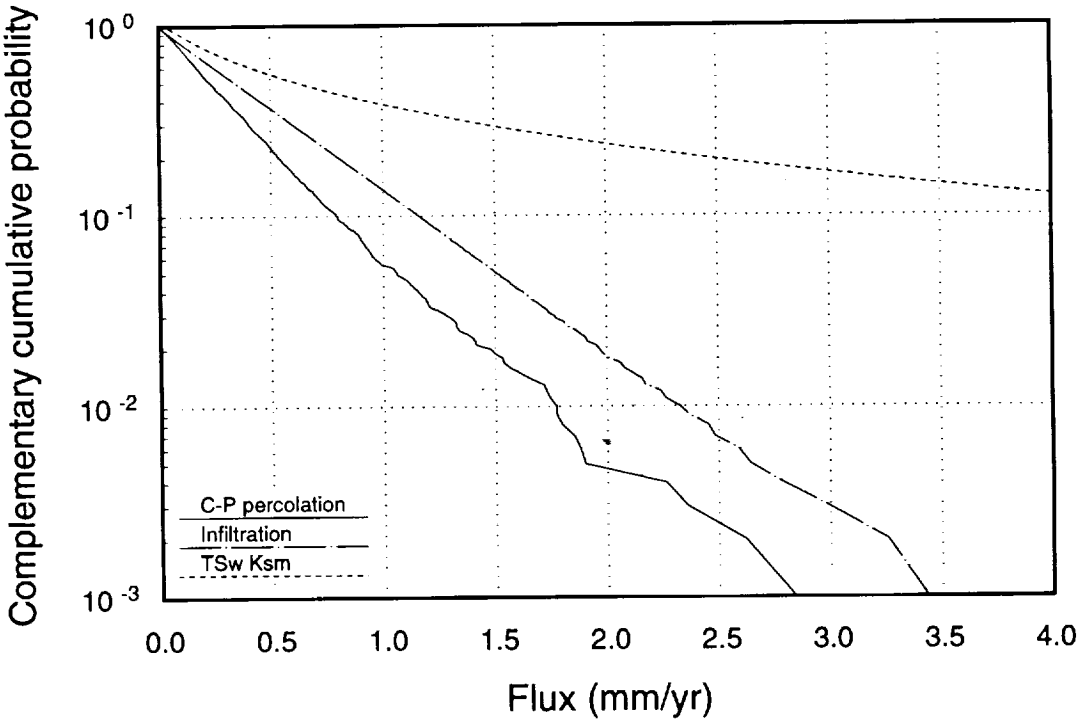

Figure 8-7. Infiltration and percolation flux under "dry" conditions.

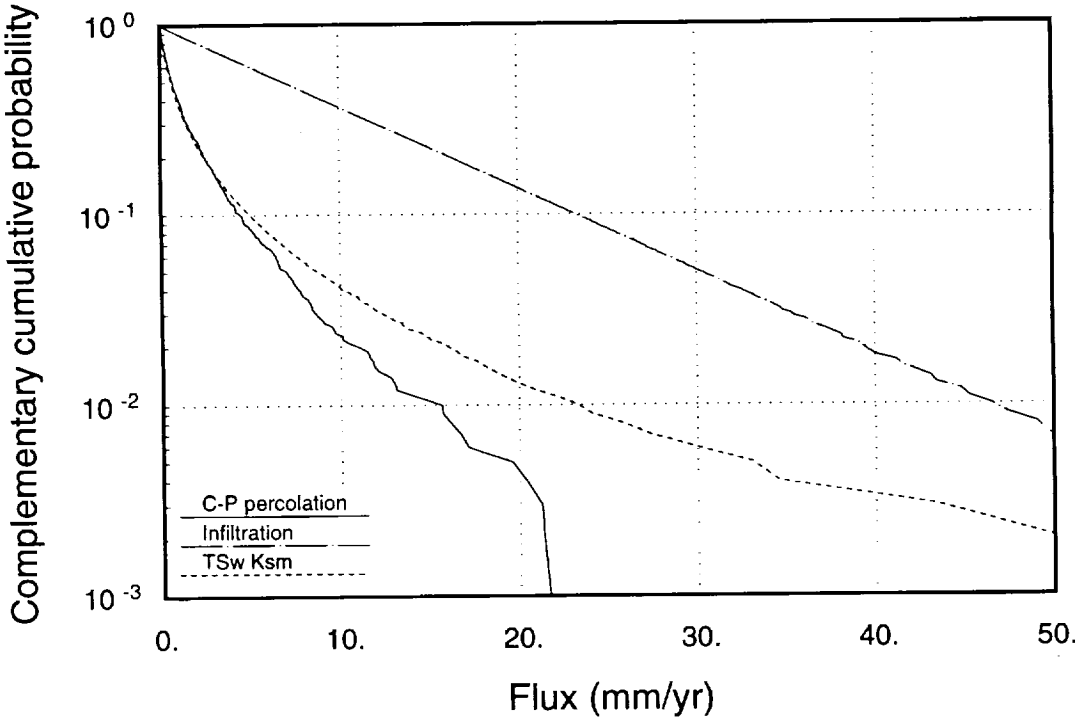

Figure 8-8. Infiltration and percolation flux under "wet" conditions.

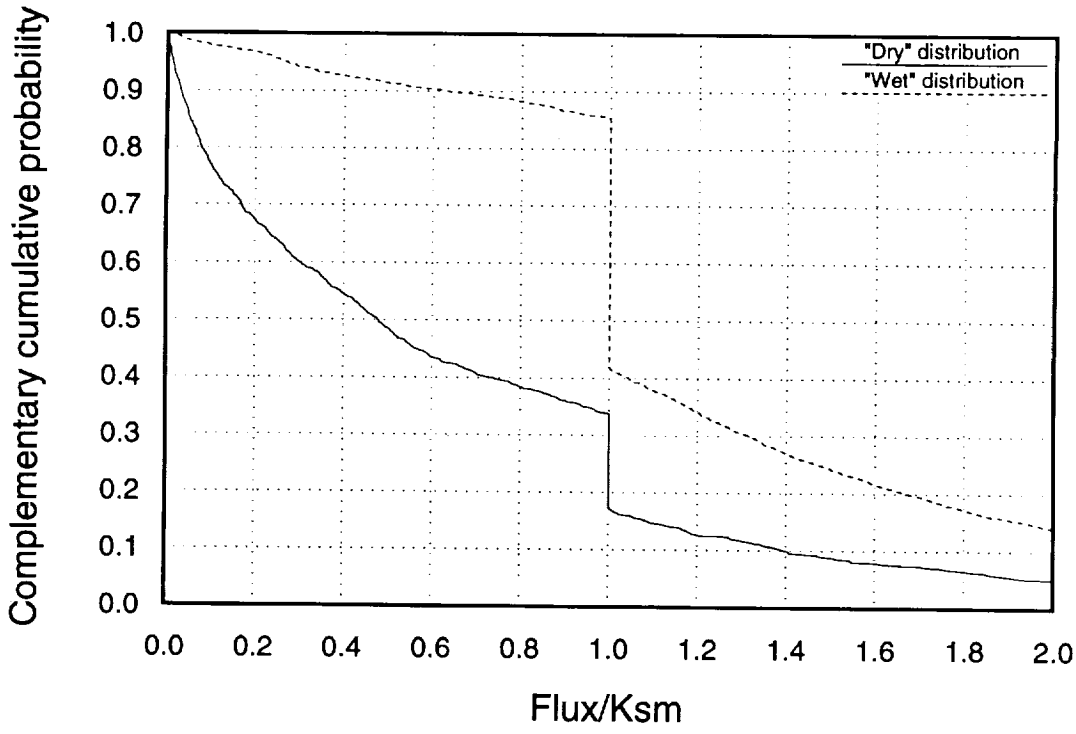

Figure 8-9. Distribution of the ratio of composite-porosity percolation to matrix conductivity (q/K_{sm}).

above and matrix conductivity K_{sm} was sampled from the TSPA-93 distribution pictured in Figure 8-6. If q_i was less than K_{sm}, percolation flux was simply set equal to infiltration: $q = q_i$. If q_i was greater than K_{sm}, the percolation flux was determined probabilistically, with $q = K_{sm}$ half of the time, and $q > K_{sm}$, distributed exponentially, the other half of the time (K_{sm} was used for the e-folding length of the exponential). The distributions of q/K_{sm} are shown in Figure 8-9. When this ratio is greater than 1, we have fracture-flow conditions in the composite-porosity model (for the TSw layer). Thus, it can be seen from Figure 8-9 that the assumptions give fracture flow at the repository horizon about 20% of the time under dry-climate conditions, and about 40% of the time under wet-climate conditions. Again, these percolation distributions are only intended for the composite-porosity model.

Chapter 9
Geochemistry: Solubility and Sorption Parameters

(Triay, Morris, Gauthier, Meijer, Dockery)

"Solubility" is the equilibrium concentration of a solute in a solution saturated with respect to that solute at a given temperature and pressure. In this case, the solute is a specified radionuclide contained in high-level waste, and the liquid into which it dissolves is groundwater occurring at Yucca Mountain. In addition to temperature and pressure, the solubility of a nuclide is dependent upon the groundwater geochemistry. This quantity is important because it provides an understanding of how quickly (or slowly) each nuclide will be dispersed once water comes in contact with the fuel pellets. The solubility distributions presented in this chapter are used by the source model in calculating releases from the waste package (Chapter 13).

"Sorption" is a general term that includes the processes of both adsorption (deposition of material on the surface of a solid) and absorption (entrance of a material into the interior of a solid). For this TSPA exercise, "sorption" is used to describe the amount of a nuclide that adsorbs onto a substrate (e.g., tuff), typically by surface complexation or ion exchange. Like solubility, sorption is dependent upon temperature, pressure, and groundwater geochemistry. In addition, there is a dependence upon the mineral phases present in the substrate. The sorption-coefficient distributions are used in TSPA-93 to calculate unsaturated-zone radionuclide transport using the composite-porosity model (Chapter 14). However, they are not used for the unsaturated-zone transport using the weeps model (Chapter 15). Sorption coefficients are used to calculate saturated-zone transport for both the composite-porosity and weeps models.

Parameter distributions for solubility and sorption have not been developed explicitly from available data as has been done for the hydrologic PDFs (Chapter 7). Because solubility and sorption properties depend strongly on the groundwater chemistry and the temperature, and because groundwater chemistry and temperature values at Yucca Mountain are expected to vary in both time and space, we have chosen to use expert judgment in the development of the PDFs. Opinions of experts have been elicited to define the distributions; their opinions are based on their knowledge of solubility and sorption data at Yucca Mountain, and of the possible influences of perturbing effects of the repository.

9.1 Elicitation method

The elicitation method used for obtaining values for sorption and solubility is essentially the same as that discussed in Chapter 3 of TSPA-91. In our method, an expert,

or group of experts, is elicited to extract information in the form of probability distribution functions (PDFs). The type and form of the information is determined by the requirements of the total-system analyses. The formalism used to generate the PDFs requires the expert to provide the range, mean, and variability for each parameter, along with data to support the determination. By using graphic interactive software, the experts then refine each PDF to best reflect their beliefs and uncertainty in the parameter. For a more detailed discussion of the elicitation method, refer to TSPA-91, Section 3.3.

SNL sponsored two elicitation sessions for TSPA-93—one for solubility and one for sorption. SNL analysts selected the set of elements to be considered during the elicitation process. The elements selected are based on significance of percentage in inventory and on the interpreted impact on performance (Barnard, 1993). The list has been further restricted for actual use in the TSPA-93 simulations, as discussed in Section 14.5.3. Experts contributing to the development of sorption-coefficient distributions were Ines Triay (LANL), Arend Meijer (Jacobs Engineering, Inc.) and Malcolm Siegel (SNL). Experts for development of solubility PDFs included those listed for sorption, as well as David Morris (LANL) and Michael Ebinger (LANL). In the elicitations all the distributions were specified by concurrence among the experts. The PDFs generated during the two elicitation exercises are shown in Appendix B.

9.2 Solubility

9.2.1 Assumptions

Solubility is a function of groundwater chemistry. The water chemistry at Yucca Mountain (summarized in Table 9-1) was reviewed by Meijer (1992). The groundwaters in the saturated volcanic units are dilute sodium bicarbonate waters (e.g., water from the well J-13). Sodium, calcium, potassium, and magnesium are the major cations present. The major anions, in order of decreasing concentration, are bicarbonate, sulfate, chloride, nitrate, and fluoride. The only other major constituent in these waters is silica. The water from the Paleozoic aquifer (UE-25p#1) has higher concentrations of virtually all constituents listed above. The composition of unsaturated zone (UZ) water given in Table 9-1 has been derived from core samples (Yang *et al.*, 1990). The ranges of values shown are based on observed sample variation. The concentration of the major cations and anions in unsaturated zone (UZ) groundwaters appears to be intermediate between the saturated-zone tuffaceous waters and waters from the carbonate aquifer. Consequently, the first assumption made is that the water from well J-13 and the Paleozoic aquifer bound the chemistry of the groundwaters at Yucca Mountain. The pH

of the waters at Yucca Mountain ranges from 6.5 to 9.4 (Ogard and Kerrisk, 1984; Yang *et al.*, 1990).

Most of the waters at Yucca Mountain are oxidizing. The large amounts of iron in the multi-purpose container would result in a reducing environment; although it is not clear for how long the reducing environment would last. The conservative approach is to assume that the groundwaters moving from the repository to the accessible environment are oxidizing, since radionuclides (such as the actinides and Tc) have higher solubilities in oxidizing than in reducing waters. Consequently, the second assumption is to consider solubility under oxidizing conditions only.

Table 9-1. Ground water chemistry at Yucca Mountain.

Component	Well J-13[a] (mg/l)	UZ[b] (mg/l)	Well UE-25p#1[a] (mg/l)
Ca	11.5	27–127	87.8
Mg	1.8	5–21	31.9
Na	45	26–70	171
K	5.3	5–16	13.4
Si	30.0	72–100	30.0
Cl^-	6.4	34–106	37.0
F^-	2.1	–	3.5
SO_4^{-2}	18.1	39–174	129
HCO_3^-	143	–	698
pH	6.9	6.5–7.5	6.7
Eh (mV)	340	–	360

[a] Ogard and Kerrisk (1984).
[b] Yang *et al.* (1990).

The third assumption is that the solubilities are best determined by the far-field environment. The increased temperature from the repository may cause more aggressive groundwater chemistries and increased solubilities for radionuclides in the near field; however, when the solute is transported out of the near field, the potentially lower solubilities in the far field would cause precipitation and thus would be the limiting factor. The experts have made this assumption primarily because the dearth of information about the near-field water chemistry makes accurate predictions of solubility impossible for this region. A potential concern must be mentioned with regard to this assumption. The high thermal loads being considered for the potential repository (e.g., 114 kW/acre) may cause near-field conditions to extend throughout the unsaturated zone.

The functional dependence of solubility with temperature can be expressed with thermodynamic rigor. However, using the functional dependence derived from thermodynamic considerations requires knowing the solubility products (K_{sp}) of the dominat-

ing dissolution reactions. The thermodynamic treatment to obtain the functional dependence of an equilibrium constant (such as K_{sp}) with temperature follows Daniels and Alberty (1975); this treatment is only valid when considering the same chemical reaction attaining equilibrium at different temperatures.

The symbols that are utilized in this derivation are defined as follows:

K_{sp} = Solubility product,

G = Gibbs free energy,

ΔG = $\sum_{products} G_i - \sum_{reactants} G_i$,

H = Enthalpy,

S = Entropy,

R = Gas constant,

T = Temperature,

C_p = Heat capacity at constant pressure,

a, b, and c = constants, and

° refers to reactants and products in their standard state (1 atm).

Equation 9.1 is a result of the Laws of Thermodynamics:

$$\Delta G = \Delta H - T\Delta S \text{ (at constant T).} \tag{9.1}$$

Equation 9.2 describes the functional dependence of the heat capacity of a substance with temperature:

$$C_p = a + bT + cT^{-2}. \tag{9.2}$$

Equation 9.3 describes the functional dependence of ΔC_p with temperature, where ΔC_p is the sum of the heat capacities of the products minus the corresponding sum for the reactants (it is the net change in heat capacity resulting from the reaction):

$$\Delta C_p = \Delta a + \Delta bT + \Delta cT^{-2}, \tag{9.3}$$

where Δa, Δb, and Δc denote the difference between the expansion of equation 9.2 for the product and the expansion of equation 9.2 for the reactant. Equation 9.4 is Kirchoff's formula:

$$\Delta C_p = \left[\frac{\partial(\Delta H)}{\partial T}\right]_P. \tag{9.4}$$

Substituting for ΔC_p using equation 9.3 and integrating equation 9.4 yields equation 9.5, where ΔH_i is an integration constant:

$$\Delta H = \Delta H_i + \Delta aT + \tfrac{1}{2}\Delta bT^2 - \Delta cT^{-1}. \tag{9.5}$$

Equation 9.6 is a result of taking the partial derivative of equation 9.1 with respect to temperature at constant pressure:

$$\left[\frac{\partial(\Delta G/T)}{\partial T}\right]_P = -\frac{\Delta H}{T^2} \text{ or } \left[\frac{\partial(\Delta G/T)}{\partial(1/T)}\right]_P = \Delta H. \tag{9.6}$$

Substituting for ΔH using equation 9.5 and integrating either form of equation 9.6, yields equation 9.7, where i is an integration constant:

$$\Delta G = \Delta H_i - \Delta aT\,ln\,T - \tfrac{1}{2}\Delta bT^2 - \tfrac{1}{2}\Delta cT^{-1} + iT. \tag{9.7}$$

Substituting for ΔG° in equation 9.8 (using equation 9.7), yields equation 9.9 after algebraic rearrangement:

$$\Delta G^\circ = -\,RT\,ln\,K_{sp}, \tag{9.8}$$

$$-R\,ln\,K_{sp} = \frac{\Delta H_i^0}{T} - \Delta a\,ln\,T - \frac{1}{2}\Delta bT - \frac{1}{2}\frac{\Delta c}{T^2} + i. \tag{9.9}$$

Equation 9.9 describes the functional dependence of the solubility product with respect to temperature.

It is important to make the following observations regarding LANL's empirical solubility data base for actinides (Nitsche *et al.*, 1993a): (1) Nitsche *et al.* only report solubility data obtained from oversaturation, (2) the solid phases reported at 25°C and 60°C for Np do not match the solid phases found at 90°C, (3) information on the Pu solid phases formed is not available, and (4) it is not clear that equilibrium is obtained in the time scale of the experiments. These observations are important for the following reasons: (1) Deriving a K_{sp} from the data of Nitsche *et al.* requires writing a dissolution reaction; being able to describe that K_{sp} as a function of temperature requires that the same dissolution reaction takes place within the desired temperature range. It is not clear that this is the case for either Np or Pu. (2) If equilibrium is not attained during the solubility experiments, the variability of the solubility data with temperature could be a result of kinetic effects. In particular, the apparent solubility measured by Nitsche *et al.* could increase with temperature as a result of faster dissolution rates at higher

temperatures. (3) In order to define a K_{sp}, equilibrium has to be attained from oversaturation and undersaturation. The same solubility for Am, Np, and Pu must be measured (regardless of whether the experimenter starts from an oversaturated solution or from an undersaturated solution using the solid phases formed during the oversaturation experiments). Data from undersaturation are not available yet although experiments are in progress (Nitsche *et al.*, 1993a and 1993b). Consequently, the experts decided not to apply the rigorous thermodynamic treatment derived above to extrapolate the empirical solubilities reported by Nitsche *et al.* (1993a and 1993b) as a function of temperature.

Two potentially important issues are neglected in the solubility data used: the potential impact of future climate changes as they relate to potential changes in the water chemistry at Yucca Mountain and the impact of colloid formation in facilitating radionuclide transport at Yucca Mountain. A strategy has been developed by the Yucca Mountain Site Characterization Project to address the latter issue (Triay *et al.*, 1994). The results of the work delineated by Triay *et al.* will be used in the next TSPA iteration.

9.2.2 Solubility values

Tables 9-2a and 9-2b show the parameters for the solubility probability models resulting from the expert elicitation. Appendix B, Figures B-1 through B-12, show the plots for these distributions. In all cases the experts attempted to base their opinions on empirical data, primarily from laboratory measurements. If empirical data are absent, the experts based their opinion on calculated or model results. Table 9-2a lists the parameters for elements whose distributions are given in linear space. Table 9-2b gives the distributions for U, Ra, Pd, Np, Pa, Ni, Sr, Zr, and Nb in logarithmic space. Solubilities for Cs, I, Tc, Se, C, and Cl are not listed; their solubilities are discussed in Section 9.2.2.8.

The parameters in Table 9-2 have been presented to the members of the Radionuclide Solubility Working Group (SolWOG) of the Yucca Mountain Site Characterization Project (David Morris, Michael Ebinger, Heino Nitsche, Robert Silva, James Johnson, David Clark, and Drew Tait). The SolWOG participants have reviewed the actinide solubilities presented in Table 9-2. Only two changes have been suggested by the SolWOG: (1) the minimum value for the solubility of Np should be 5×10^{-6} moles/l (rather than 10^{-8}), and (2) the minimum value for the solubility of Pu should be 10^{-8} moles/l (rather than 10^{-10}). These suggested changes are not incorporated into this version of the TSPA. Had they been included, the change in the final results would have been insignificant. Previous work has shown that Pu releases are minimal because of

its high sorption coefficient. A change in the solubility would not, therefore, cause a significant change in the overall releases. Also, for both Pu and Np, the suggested change only affects values on the tails of the distributions. In the course of the Monte Carlo sampling, values in those tails are selected only rarely.

Table 9-2a. Elicited solubilities for elements with linear PDFs (moles/l)[a].

Element	Minimum Value	Maximum Value	Distribution Type	Figure Number
Am	10^{-10}	10^{-6}	uniform	B-1
Pu	10^{-10}	10^{-6}	uniform	B-1
Ac	10^{-10}	10^{-6}	uniform	B-1
Sn	10^{-11}	10^{-7}	uniform	B-8
Sm	10^{-10}	10^{-6}	uniform	B-1

[a] Cs, I, Tc, Se, C, and Cl are given constant values of 1.0.

Table 9-2b. Elicited solubilities for elements with logarithmic PDFs (moles/l).

Element	Logarithm of Minimum Value	Logarithm of Maximum Value	E[x][a]	CV[b]	Distribution Type	Figure Number
U	-8	-2	-4.5	0.20	log beta	B-3
Th	-10	-7	–	–	log uniform	B-2
Ra	-9	-5	-7	0.10	log beta	B-4
Pb	-8	-5	-6.5	0.08	log beta	B-5
Np	-8	-2	-4	0.20	log beta	B-6
Pa	-10	-5	–	–	log uniform	B-7
Ni	-6	-1	-2.75	0.25	log beta	B-9
Sr	-6	-3	-4	0.12	log beta	B-10
Zr	-12	-7	–	–	log uniform	B-11
Nb	-9	-7	–	–	log uniform	B-12

[a] E[x] is the mean of the distribution in logarithmic space.
[b] Coefficient of variation CV = σ[x]/E[x], where σ[x] is standard deviation in log space.

9.2.2.1 Americium solubility distribution

The minimum and maximum values for the Am solubility distribution in Table 9-2a are based on the empirical solubility data reported by Nitsche *et al.* (1993a and 1993b). These values are consistent with other work on the solubilities of rare-earth elements in groundwaters (e.g., Choppin, 1986). The experts thought that any value within the range would be equally likely (a uniform distribution). A uniform distribution over the range implies that approximately 90% of samples from this distribution would lie between 10^{-7} and 10^{-6} moles/l, while approximately 0.1% of the samples would lie between 10^{-10} and 10^{-9} moles/l.

9.2.2.2 Plutonium solubility distribution

Plutonium is more soluble than Am (as the SolWOG members pointed out) based on the data of Nitsche *et al.* (1993a and 1993b). The experts chose a distribution for Pu solubility identical to the one chosen for Am. As mentioned above, a uniform distribution over the range in Table 9-2 implies that most of the samples from this distribution would lie between 10^{-7} and 10^{-6} moles/l. Kerrisk (1984) used the computer program EQ3/6 (Wolery, 1979) to calculate the solubility of Pu in Yucca Mountain groundwaters; he obtained a value of 10^{-5} moles/l for the solubility of Pu. The experts agreed that the laboratory data were more reliable for the TSPA calculations.

9.2.2.3 Uranium solubility distribution

No empirical data have been collected by the Yucca Mountain Site Characterization Project for U because the high U solubility is not expected to be the limiting factor for the U source term. The possible solubilities for U occur over a wide range, but the data support a central tendency between 10^{-4} and 10^{-5} moles/l with a spread of approximately one order of magnitude (Wanner and Forest, 1992). The experts thought that U solubility should be represented in logarithmic space. The resulting distribution is a skewed log-normal.

9.2.2.4 Thorium solubility distribution

Th is extremely insoluble (less soluble than Am and Pu). Such low solubilities make this element generally unimportant, except for the potential effects of the ^{229}Th daughter product of ^{237}Np. As with Am, the experts believed that the range of values was well defined and that the data might favor lower solubilities. However, for conservatism, the experts decided on a log-uniform distribution believing that it was equally likely to select the log of any value within the prescribed range.

9.2.2.5 Radium solubility distribution

Ra solubility is similar to Ba solubility. The distribution chosen is based on Kerrisk's calculation with EQ3/6 (Kerrisk, 1984). The solubility of Ra depends on the presence of sulfates. The experts chose a small relative standard deviation for Ra solubility because this element forms only one cation and is relatively insensitive to groundwater chemistry. Solubility values chosen are based on assumptions of sulfate content typical of groundwaters at Yucca Mountain.

9.2.2.6 Lead solubility distribution

The elicited Pb solubility distribution is based on the range published by Andersson (1988) and Pei-Lin *et al.* (1985). The Pb solubility depends on the amount of carbonate in the groundwater and variation in the Pb solubility is caused by carbonate concentration variations in the groundwaters (Table 9-1).

9.2.2.7 Neptunium solubility distribution

The Np solubility distributions were based on Nitsche's data (1993a and 1993b). The experts believed that the data supported a central tendency in log space with a spread of less than an order of magnitude. The Np solubilities used in TSPA-91 were very low (approximately five orders of magnitude below those suggested by the experts). The TSPA-91 solubilities were derived from spent-fuel tests (conducted by Wilson, 1990a and 1990b). The results from the spent-fuel tests are not necessarily representative of Np solubilities in the advecting groundwaters at Yucca Mountain. It is possible that the presence of the spent fuel could create a reducing environment; however, here we assume oxidizing conditions.

9.2.2.8 Cesium, iodine, technetium, selenium, carbon, and chlorine solubility distributions

All these elements are very soluble; however, suitable measured data are not currently available. Solubilities for these elements should be determined in the future from leaching tests. A solubility of 1 mole/l was considered by the experts to be a reasonable approximation for use in this TSPA.

9.2.2.9 Protactinium solubility distribution

The range for Pa solubilities was derived from SKI results (Andersson, 1988). The solubility distribution for Pa is expected to have a large variance, skewed towards smaller values. The experts believed that this radionuclide was less soluble than the range published by Andersson suggests. Therefore, a log-uniform distribution was chosen for Pa.

9.2.2.10 Actinium solubility distribution

The chosen solubility distribution for Ac is identical to the Am solubility distribution. Data for Ac solubility are not available, but the experts noted an expected similarity in chemistry to Am.

9.2.2.11 Tin solubility distribution

Sn is very insoluble. The distribution range was obtained from results published by SKI (Andersson, 1988); any value within this range was equally probable. A uniform solubility distribution was chosen for Sn.

9.2.2.12 Nickel solubility distribution

Ni solubility is a function of pH. The experts chose the same range as the one published by SKI (Andersson, 1988). The mean and standard deviation of the solubility distribution were approximated from data gathered in support of the caisson experiment conducted at LANL (Siegel *et al.*, 1993).

9.2.2.13 Samarium solubility distribution

The chosen solubility distribution for Sm is identical to the Am solubility distribution. As with Ac, data for Sm are not available, but the experts expect Sm to behave similarly to Am.

9.2.2.14 Strontium solubility distribution

The solubility distribution for Sr is based on the SKI values (Andersson, 1988) and the results published by Siegel *et al.* (1993).

9.2.2.15 Zirconium solubility distribution

Zr is very insoluble. The chosen distribution was based on SKI values (Andersson, 1988). A log-uniform distribution was chosen for Zr because the experts believed that lower values in the range should be given more weight than would occur with a uniform distribution.

9.2.2.16 Niobium solubility distribution

The Nb solubility distribution is based on SKI values (Andersson, 1988).

9.2.3 Correlations

Both the solubilities and sorption values developed in this chapter are used as stochastic inputs to the aqueous-transport analyses. That is, values are randomly drawn from probability distributions. Because some of the elements have similar chemical properties, the choices of stochastic values should be correlated among similar elements. This is done by a rank correlation of the distributions. When the distributions are sampled, the values from each PDF must maintain the same relationship to each other that the distributions do.

The experts suggested that the solubilities of many of the elements can be correlated based on their chemical properties (such as oxidation state and chemical speciation). Highly correlated element sets are: {U, Np}, {Th, Pa, Zr, Sn}, {Am, Sn, Ac}, {Ra, Sr}, and {Ni, Pb}. The experts suggested a high rank correlation coefficient in the range between 0.8 and 0.85. Elements that have a medium rank correlation are: Pu with the {Am, Sm, Ac} set. The experts suggested that a medium rank-correlation coefficient might be 0.6. Figures B-13 and B-14 show scatter plots of samples chosen from uniform and log-uniform distributions using ranked correlation of 60% and 80%, respectively.

9.3 Sorption

9.3.1 Assumptions

Sorption, like solubility, is a function of water chemistry. However, it is also dependent upon the rock type for which it is being analyzed. The assumptions concerning the water chemistry at Yucca Mountain for purposes of sorption are the same as described in Section 9.2.1 and in Table 9-1 above.

An assumption specific to sorption dealt with grouping all strata on the basis of rock type. K_d varies depending on the mineralogy of the substrate. The correspondence between geologic units used for the TSPA calculations and rock type for the purpose of sorption determination is shown in Table 9-3.

The containers to be utilized in the repository were added to the list after consideration of whether the corrosion by-products of the massive multi-purpose container could become a substrate for sorption. Actinides are sorbed strongly by iron oxides. Hematite is found in the tuffs at Yucca Mountain; however, the iron oxide minerals in the tuff appear to be "passivated"—i.e., all of the sorption sites could be occupied by other metals (Triay *et al.*, 1993a) and the sorption of the radionuclides onto tuff (containing iron oxides as trace minerals) is not as large as predicted on the basis of the sorption of radionuclides onto synthetic pure iron oxides. The sorption sites on the degraded container material would not necessarily be occupied by other metals. Therefore, the experts agreed to add the iron oxides (Fe) to the list of "rock" types.

This assumption reduced the number of sorption-coefficient distributions elicited to four per radionuclide: iron oxides (Fe), devitrified tuff (D), vitric tuff (V), and zeolitic tuff (Z). This grouping is based on the fact that sorption of radionuclides is the result of a chemical reaction between the radionuclide in the groundwater and the minerals in the tuff. The mineralogy of the different strata of the same rock group is very similar and the sorption coefficients can be grouped in terms of these rock types (Thomas, 1987).

Table 9-3. Stratigraphy *vs.* rock type.

Unit[a]	Stratum	Rock Type	Symbol
3	TSw	devitrified	D
4	.Vitrophyre	vitric	V
5	CH/PPnv	vitric	V
6	CH/PPnz	zeolitic	Z
7	PPw	devitrified	D
8	BFn	zeolitic	Z
9	BFw	devitrified	D
Container	–	Iron Oxides	Fe

[a] Unit numbers correspond to units and strata described in Chapter 6; units 1, 2, and 10 are not listed because they are not used in the TSPA calculations; see Section 14.5.1.

The effect of temperature on sorption coefficients was reviewed by Meijer (1990). Measured sorption coefficients onto tuffs were higher at elevated temperatures for all elements studied: Am, Ba, Ce, Cs, Eu, Pu, Sr, and U. Consequently, another assumption was that sorption coefficients measured at ambient temperatures should be applicable and generally conservative when applied to describing aqueous transport from a hot repository (provided that the high temperatures that will be sustained for long time periods due to potential high thermal loads do not result in changes in the mineralogy and the water chemistry at Yucca Mountain that are not predictable by short-term laboratory and field experiments).

9.3.2 Sorption coefficients

In this TSPA, sorption coefficients (K_ds) are used in a simple model of radionuclide retardation during transport in groundwater. Retardation expresses the reduction in advective transport velocity of solutes in groundwater. The model can be stated as follows:

$$R = 1 + \rho_b K_d / \theta, \tag{9.10}$$

where R is the retardation factor, ρ_b is the bulk density, and θ is the moisture content. Retardation by adsorption is presently assumed only to occur in the matrix, but because a strong matrix/fracture coupling is also assumed, radionuclides traveling in the fractures are eventually retarded in the matrix. (The weeps-model calculations, however, do not allow retardation in the unsaturated zone.)

Table 9-4 shows the parameters for the sorption coefficient probability models resulting from the elicitation. Plots of sorption-coefficient probability distributions are shown in Appendix B. In Table 9-4, the distribution parameters for Ni in iron oxides and Sr in zeolitic tuff are given in logarithmic space.

Table 9-4. Elicited sorption-coefficients (K_d) distributions (ml/g).

Element	Rock Type	Minimum Value	Maximum Value	E[x]	CV[a]	Distribution Type	Figure Number
Am, Sm,	D	100	2000	–	–	uniform	B-15
Zr, Nb,	V	100	1000	400	0.20	beta	B-16
Ac, Th	Z	100	1000	–	–	uniform	B-17
	Fe	1000	5000	–	–	uniform	B-18
Pu	D	50	200	100	0.25	beta	B-19
	V	50	200	100	0.25	beta	B-19
	Z	30	70	40	0.15	beta	B-20
	Fe	1000	5000	–	–	uniform	B-18
U, Se	D	0	5	–	–	uniform	B-21
	V	0	4	–	–	uniform	B-22
	Z	5	20	10	0.30	beta	B-23
	Fe	100	1000	–	–	uniform	B-17
Np, Pa	D	0	50	2	1	beta (exponential)	B-24
	V	0	12.5	0.5	1	beta (exponential)	B-25
	Z	0	100	4	1	beta (exponential)	B-26
	Fe	500	1000	–	–	uniform	B-27
Ra	D	100	500	–	–	uniform	B-28
	V	100	500	–	–	uniform	B-28
	Z	1000	5000	–	–	uniform	B-18
	Fe	0	750	30	1	beta (exponential)	B-29
Pb	D	0	500	–	–	uniform	B-28
	V	100	500	–	–	uniform	B-28
	Z	100	500	–	–	uniform	B-28
	Fe	100	1000	–	–	uniform	B-17
Cs	D	100	200	–	–	uniform	B-30
	V	100	200	–	–	uniform	B-30
	Z	500	3000	–	–	uniform	B-31
	Fe	0	250	10	1	beta (exponential)	B-32
Sn	D	20	200	–	–	uniform	B-33
	V	20	200	–	–	uniform	B-33
	Z	100	300	–	–	uniform	B-34
	Fe	0	5000	–	–	uniform	B-35
Ni	D	0	500	250	0.33	beta (normal)	B-36
	V	0	500	250	0.33	beta (normal)	B-36
	Z	0	500	250	0.33	beta (normal)	B-36
	Fe[b]	-0.1	3	2.4	0.20	log beta (log normal)	B-37
Sr	D	10	200	–	–	uniform	B-38
	V	20	50	–	–	uniform	B-39
	Z[b]	3.3	4.7	–	–	log uniform	B-40
	Fe	20	50	–	–	uniform	B-39
C	Fe	100	300	–	–	uniform	B-34
Cl, Tc, I	All	–	–	0	–	–	–

[a] Coefficient of variation CV = σ[x]/ E[x].

[b] Distribution parameters are defined in logarithmic space.

9.3.2.1 Americium sorption distributions

Americium sorbs strongly to most materials (Triay *et al.*; 1991a). The potential mechanisms for actinide sorption onto mineral surfaces have been reviewed by Meijer, 1992. The sorption-coefficient distributions for Am in Yucca Mountain tuffs and iron oxides (given in Table 9-4) were inferred from the data presented by Thomas (1987), Triay *et al.* (1991a), and Meijer (1992).

9.3.2.2 Plutonium sorption distributions

One of the problems of interpreting sorption data for Pu is that Pu can exist in multiple oxidation states under oxidizing conditions at near-neutral pH values (Nitsche *et al.*, 1993a). Plutonium can also exist as a polymer (Triay *et al.*, 1991b). The lack of information on the speciation of Pu in the groundwaters at Yucca Mountain makes it difficult to assess the sorption mechanism for Pu. However, the empirical data obtained in Yucca Mountain tuffs indicate that Pu sorbs strongly. The sorption-coefficient distributions for Pu in Yucca Mountain tuffs (Table 9-4) were inferred from the data presented by Thomas (1987) and Meijer (1992).

9.3.2.3 Uranium sorption distributions

No additional data for U have been collected for Yucca Mountain tuffs since the TSPA-91 effort. Consequently, no change was made for the sorption coefficient distributions used for this element. As is previously discussed (Meijer, 1992), U sorbs strongly to synthetic iron oxides.

9.3.2.4 Thorium sorption distributions

The information elicited for Am was also used for Th due to the lack of sorption information available for Th and the similarities exhibited by the sorption behavior of these two elements (Thomas, 1987).

9.3.2.5 Barium sorption distributions

Barium has been used in the experiments performed by LANL (Thomas, 1987) as an analog for Ra. These elements sorb to Yucca Mountain tuffs via an ion exchange mechanism and surface adsorption reactions (Meijer, 1992). The sorption-coefficient distributions for Ra in Yucca Mountain tuffs and iron oxides (Table 9-4) were inferred from the data presented by Thomas (1987), Meijer (1992), and Triay *et al.* (1991c).

9.3.2.6 Lead sorption distributions

Pb tends to complex with fulvic acids in the groundwaters and sorbs as a complex. The sorption coefficient distributions for Pb in Yucca Mountain tuffs and iron oxides

were inferred from the data presented by Meijer (1990). One of the experts believed that a value of zero was more appropriate for the sorption values, but the values shown in Table 9-4 reflects the group consensus.

9.3.2.7 Neptunium sorption distributions

Sorption-coefficient distributions for Np in tuff are the same as those used in TSPA-91. Recent data obtained (Triay *et al.*, 1993a) agree with previous observations. Np is a poorly sorbing radionuclide in tuff even when the tuffs are known to have iron oxides, because the iron oxides in the tuff appear to be passivated. The Np-sorption coefficient distribution onto iron oxides (in Table 9-4) was inferred from data presented by Meijer (1992) and Triay *et al.* (1993a) on synthetic iron oxides.

9.3.2.8 Protactinium sorption distributions

Very little information exists for Pa sorption onto tuffs (Thomas, 1987). The experts decided to use the same sorption coefficients elicited for Np for this element.

9.3.2.9 Tin sorption distributions

There is very little information for Sn sorption onto tuffs (Thomas, 1987). Based on the data available, Meijer (1992) suggested that Sn exhibited large K_ds in the devitrified tuffs (larger than 1000 ml/g). The sorption coefficient distribution in Table 9-4 was inferred from the SKI work (Andersson, 1988); the uniform distributions chosen were the result of the experts' uncertainty about the sorption of Sn.

9.3.2.10 Nickel sorption distributions

Ni sorption-coefficient distributions were inferred for devitrified, vitric, and zeolitic tuffs based on the data presented by Meijer (1992). The Ni sorption-coefficient distribution for iron oxides was inferred from the data presented by Siegel *et al.* (1992 and 1993.)

9.3.2.11 Cesium sorption distributions

Cs sorption-coefficient distributions for tuff and iron oxides were inferred from the data presented by Thomas (1987), Meijer (1992), and Triay *et al.* (1991c). Cs has one of the highest selectivity coefficients for zeolites among all chemical elements (Meijer, 1992). Cs sorption onto devitrified and vitric samples could be the result of ion exchange onto clays or feldspars in the tuff samples or surface adsorption reactions (Meijer, 1992).

9.3.2.12 Strontium sorption distributions

Sr sorption coefficient distributions for tuff and iron oxides were inferred from the data presented by Thomas (1987) and Triay *et al.* (1991c). Sr sorbs strongly to zeolites by ion exchange. Sr sorption onto other types of tuff may be dominated by the amount of clay in the tuff units. The values given in Table 9-4 are generally conservative.

9.3.2.13 Selenium sorption distributions

There are limited data on tuff for Se sorption (Thomas, 1987). The experts decided to use the same sorption-distribution coefficients for Se as the ones elicited for U. This is a conservative decision since U can be oxidized much more readily than Se in Yucca Mountain groundwaters.

9.3.2.14 Carbon sorption distributions

Carbon is a special case because transport is expected to occur primarily in the gaseous phase as CO_2. The major retardation mechanism is expected to be the exchange of ^{14}C with the C in the CO_2 dissolved in the groundwater (see Chapter 12). However, adsorption of CO_2 onto solid minerals in tuffs has not been measured. There is a possibility that it may be significant (Meijer, 1993). In Table 9-4, coefficients are given for sorption of carbon onto iron oxides; for conservatism, carbon is assumed not to sorb onto tuffs.

9.3.2.15 Actinium, samarium, niobium, and zirconium sorption distributions

All these elements are strongly sorbing (Meijer, 1992). The experts advised using the same sorption coefficient distributions elicited for Am for these elements.

9.3.2.16 Iodine, technetium, and chlorine sorption distributions

I and Cl are anions that do not sorb onto tuffs. Tc exists as pertechnetate under oxidizing conditions and does not sorb either (Triay *et al.*, 1993b).

9.3.3 Correlations

Most elements of interest sorb via one of two main mechanisms: surface complexation and ion exchange. Elements that sorb by surface complexation are Zr, Nb, Sn, Sm, Ac, Pa, Th, Am, and Cm. Sorption coefficients for these elements depend upon the same chemical parameters (e.g., Eh, pH, and ionic strength). Therefore, the experts expected these elements to be highly correlated. A rank correlation coefficient of 0.9 was suggested by the experts for these elements. Elements that sorb by ion-exchange are Cs, Sr, and Ra. These elements show significant sorption onto zeolitic materials. The experts suggested a rank correlation coefficient of 0.9 for these elements.

Ni and Pb were correlated (with a rank correlation of 0.9) because they are both transition metals and may be retarded in tuffs primarily by surface complexation onto available iron oxides. Se and U were correlated (with a rank correlation of 0.9) because under the expected oxidizing conditions at Yucca Mountain, the anion selenite (i.e., $SeO_3^=$) will probably be the dominant Se species, and it should behave similarly to uranyl (i.e., the $UO_2^=$ ion).

9.4 Major differences from TSPA-91

In TSPA-91, solubilities for radionuclides were based on nominal values from fuel-dissolution tests performed at Pacific Northwest Laboratory (Wilson, 1987; 1990a; 1990b). The nominal values were the highest steady-state values observed. Log uniform distributions were specified over a range with a maximum of a factor of three above and a minimum of a factor of 100 below the nominal value.

For TSPA-93, the elicited distributions contain more explicitly the uncertainty associated with temperature dependence and geochemistry. Correlations between the solubility of the various radionuclides were elicited and have been used in defining the source term and transport for the TSPA simulations. From a performance viewpoint, the major difference in the solubility distributions is that, in TSPA-93, we use a neptunium distribution that describes solubilities five orders of magnitude greater than those used in TSPA-91 (see Chapters 14 and 15.)

In both TSPA-91 and TSPA-93, radionuclide sorption coefficients were defined by an expert elicitation. In TSPA-91, one expert was involved; in this TSPA, three experts were interviewed. In TSPA-91, the "minimum K_d" approach was used, so that tin, plutonium, and americium were all assigned a constant-value K_d of 100 ml/g, indicating that the K_d was known to be at least that large; in TSPA-93, the experts provided distributions for even the highly sorbing radionuclides, in order to determine whether they might be important in sensitivity studies (Sections 14.6.3 and 15.5.4). For TSPA-93, an extra "rock type"—iron oxide—is considered as a sorption substrate (although this substrate was subsequently not included in the TSPA calculations). Finally, in the TSPA-93, correlations between the sorptivity of different radionuclides were elicited and have been included when defining the transport parameters for the TSPA simulations.

Part III

Detailed Modeling and Abstraction

Chapters 10 through 12 deal with three areas in which substantially new detailed process modeling was done for TSPA-93. These chapters also discuss how the detailed results were abstracted for use by the system models. (The role of abstraction in the performance-assessment process is discussed in Chapter 3.) The probabilistic system models and their results are presented in Part IV of the report.

Chapter 10 discusses thermal modeling and the abstracted hydrothermal model used to represent thermal effects. Chapter 11 discusses models of saturated-zone flow and transport, and the abstraction of effective flow parameters from them. Chapter 12 discusses models of gas flow and gaseous transport of ^{14}C, and the abstraction of ^{14}C travel-time distributions from them.

Below is a duplication of the document "road map" (Figure 1-1), with the items for this part highlighted.

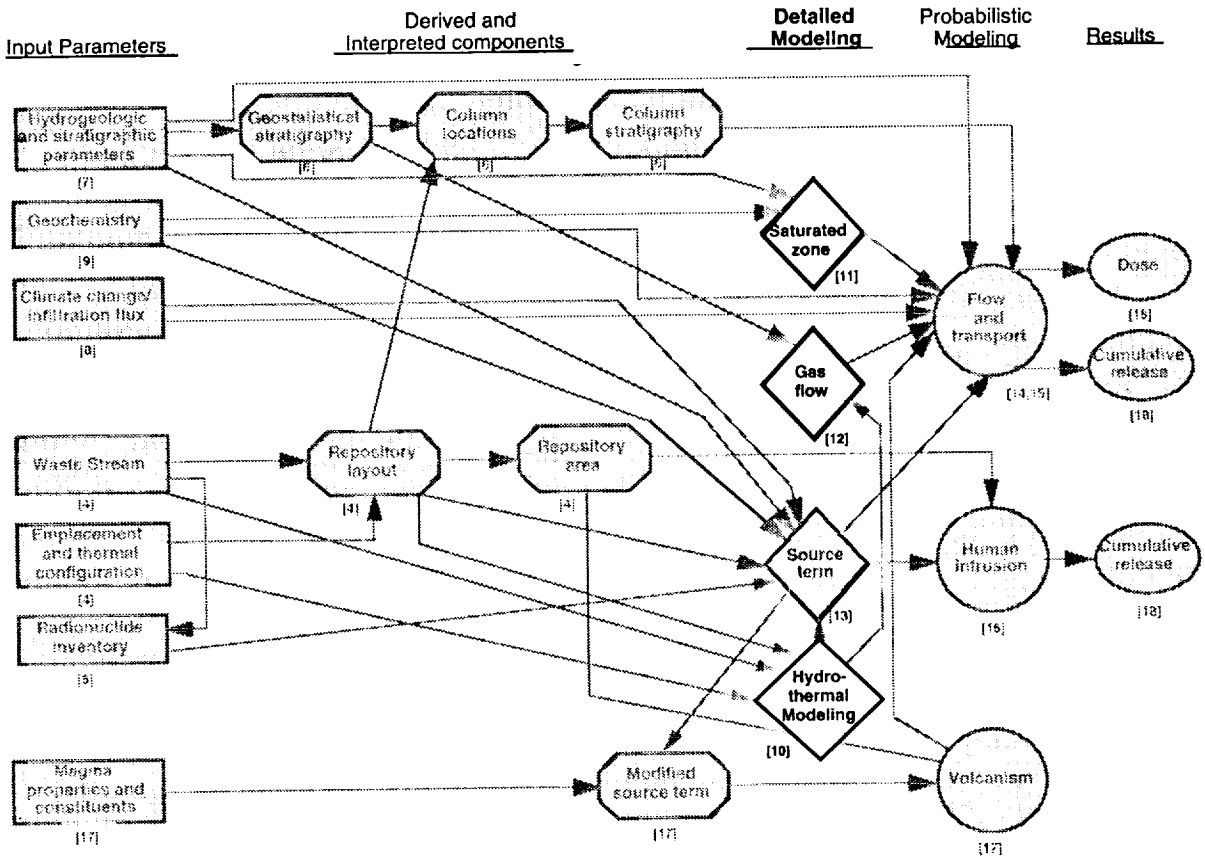

Chapter 10
Thermal Effects

(Ryder, Gauthier, Dunn)

In TSPA-91, transient thermal effects were not explicitly incorporated. The aqueous-release calculations in TSPA-91 accounted for thermal effects only as a simple delay time of 300 to 1,300 years before ambient conditions were assumed to return at Yucca Mountain. For gaseous-release calculations, centerline repository temperatures reported by Tsang and Pruess (1989) were used to identify the appropriate steady-state gas-flow calculation for gas-phase transport.

For TSPA-93, information from thermal design calculations at repository, panel, and drift scales have been abstracted into a conceptual hydrothermal model for use in both aqueous- and gaseous-release calculations. Included in this chapter are descriptions of thermally driven processes that are viewed as important to site performance, a description of the conceptual hydrothermal model formulated for this TSPA, details of the thermal design calculations carried out in support of this TSPA, and a discussion of how the conceptual hydrothermal model is implemented.

10.1 Important thermally driven processes

The emplacement of heat-generating waste at the potential repository site could perturb the ambient environment within Yucca Mountain in a number of ways. Figure 10-1 presents a visual overview of some of the thermal effects that have been hypothesized and forms the basis of the discussion in this section.

The heat generated by the waste is expected to enhance the vaporization of water within the tuff matrix, causing it to move upward because of buoyancy. A sizable volume of water could be displaced in this fashion resulting in a large *dryout* region. The dryout zone need not be completely dry, but should be a region of reduced saturation where any liquid water flow that could impact a repository has been significantly constrained. At the fringes of this dryout zone, condensation of the vapor could occur. Alternatively much of the water could exit the mountain, perhaps in noticeable fumaroles. If condensation occurs within the mountain, multiphase convection cells could form, where condensed liquid is pulled back into the hot rock by gravity and capillary forces, only to be revaporized and forced out again. Pruess *et al.* (1990) offered a description of physical processes involved in strongly heat-driven flow in partially saturated rocks, including heat pipes. Heat pipes forming within the repository, also called *refluxing*, could continually bathe containers in water and steam.

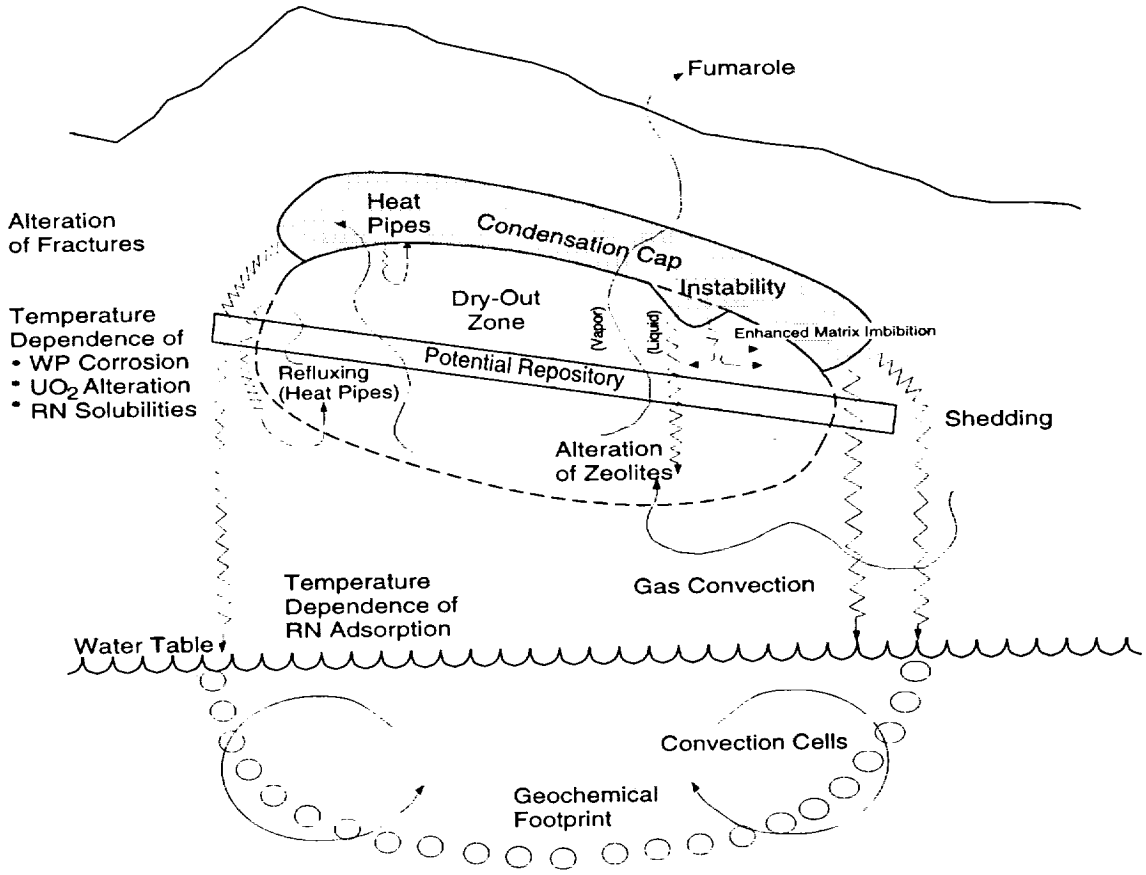

Figure 10-1. Possible thermally driven effects at a potential Yucca Mountain repository.

In addition to the possibility of aiding in the formation of multiphase convection cells, water condensing above the repository could be held in a *condensation cap*. Water within this condensation cap could be shed through cooler parts of the mountain or it could be held essentially immobile above the heated repository. If large volumes of water are held in a condensation cap, instabilities could occur, leading to pulses of water flowing back through the dryout zone or intruding into weakly coalesced boiling regions.

From a geochemical perspective, repository heat can cause alteration of minerals within the tuff. Alteration of the zeolites below the repository could diminish their ability to sorb radionuclides. Movement of hot water could also dissolve the faces of fractures, causing them to close under the pressure of the overburden. Coupled with these geochemical processes are thermomechanical effects that may cause expansion and movement of the matrix blocks. In some regions, these thermomechanical effects are likely to cause noticeable closure of the fractures. Additionally, precipitation of minerals could seal matrix voids and fractures alike, at least until the heat subsides and the matrix contracts.

It is further possible that large-scale convection cells could form in the saturated zone. Silica and other minerals dissolved in hot water could precipitate at the cooler extremes of these cells, producing a *geochemical footprint*. Large-scale gas convection cells could also form in the unsaturated zone. Large-scale gas buoyancy could move large amounts of water from below the repository, even from the saturated zone, to above the repository.

In the near-field environment, most of the waste-container corrosion processes are expected to be temperature dependent, including dry oxidation, steam corrosion, general aqueous corrosion, pitting corrosion, and stress-corrosion cracking. Once a container fails, the oxidation–alteration rate of the fuel and dissolution rates of the radionuclides are temperature dependent.

In a total-system performance assessment, the primary focus is on those thermally driven processes that could impact the performance of a repository.

10.2 Abstracted hydrothermal model

Identification of the thermally driven processes that are important to repository performance is problematic given the present state of knowledge. Although TSPA-91 did not explicitly consider hydrothermal effects, it does represent a starting point for the determination of what general processes and conditions are major contributors to radionuclide releases. The idea here is that thermal effects indirectly influence the performance of a repository by perturbing the aspects of the environment that directly influence performance. Wilson (1993) analyzed the results of TSPA-91 for sensitivity to input parameters. For aqueous releases, assuming the composite-porosity flow model, Wilson found that releases were almost totally dependent on the percolation flux through the repository. For aqueous releases, assuming the weeps model, releases were most dependent on the fracture aperture, followed by the groundwater flux and the duration of flow episodes (the *episodicity*). Releases were inversely proportional to the fracture aperture, indicating that the real sensitivity was to the number of containers that were contacted by flowing fractures, rather than the amount of water carried by the fractures.

For gaseous releases—assuming a composite-porosity flow model controlling the source term—the most important parameters were the bulk permeability and retardation capability of the tuffs, the container lifetime, and the oxidation–alteration rate of the uranium matrix of the spent fuel. Bulk permeability and retardation were considered as characteristics of the media in TSPA-91, although it was recognized that they are also functions of the amount of groundwater flow. Container lifetime and uranium

alteration rates were specified by rather arbitrary distributions; however, they should be dependent on temperature and groundwater flow. It is noted that groundwater indirectly affects uranium alteration because it is a major cause of container failure, and alteration cannot begin until the container has failed and allows oxygen to contact the uranium.

For TSPA-93, LLNL's source model, YMIM, is being used. In this model, uranium alteration is also directly dependent on groundwater. For gaseous releases, assuming that the weeps model controls the source term, the most important parameters are much the same as those for aqueous releases.

In general then, for the composite-porosity model, the most important factor was found to be the presence of significant groundwater flux. However, because of its influence on other parameters, temperature could also be a significant factor. For the weeps model, the most important factor was the number of containers subjected to flowing fractures. It is postulated that the hydrothermal effects that directly influence these factors are the most important to consider in TSPA-93. The quantities chosen to describe these hydrothermal effects are: (1) *dryout volume*, (2) *dryout fraction*, and (3) container-wall and fuel-rod temperatures (Figure 10-2).

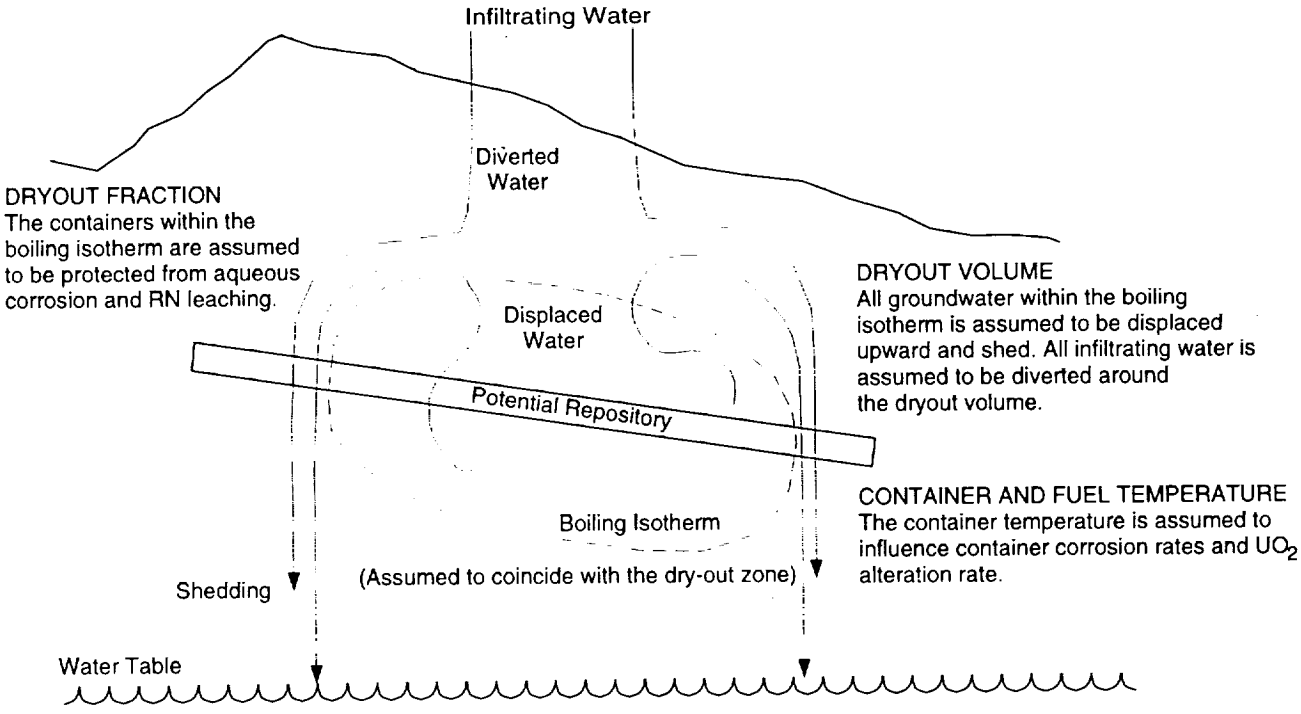

Figure 10-2. Conceptual hydrothermal model used in TSPA-93.

10.2.1 Dryout volume

At present, no consensus definition of dryout exists. For TSPA-93, a temperature-based definition has been adopted that assumes dryout occurs anywhere the host rock reaches or exceeds a temperature of 96°C, an approximation of the unconfined boiling point of water at the repository elevation. The volume of the dryout zone offers an estimate of the perturbation in groundwater flow caused by the repository thermal pulse. This perturbation includes water displaced from the dryout zone, and infiltrating water that is diverted around the dryout zone.

As the dryout zone expands, it is expected to displace some of the water held in the tuff matrix. This displacement phenomenon has been observed in several G-tunnel heater tests; however, what happens to the displaced water is not clear. Johnstone *et al.* (1985) collected significant amounts of liquid water flowing away from their heaters, with more water collected in regions connected by fractures than in nonfractured regions. Zimmerman *et al.* (1986) interpreted their results as vapor migration in fractures away from the boiling region, followed by condensation and liquid migration into the surrounding rock. Ramirez *et al.* (1991) also saw a *condensation halo*, although it was significantly smaller than expected and, based on temperature measurements, they surmised a runoff effect similar to that seen by Johnstone *et al.*

Using an equivalent continuum formulation, repository-scale modeling has shown behavior most consistent with that seen by Zimmerman *et al.* Buscheck and Nitao (1992 and 1993) predicted water accumulation primarily above the dryout zone in a *condensation zone*. The calculations of Pruess and Tsang (1993) show a similar effect. Both speculate, however, that a significant amount of water could move in fractures. This movement through fractures cannot be accurately tracked with their equivalent-continuum models. From the experimental data of Ramirez *et al.*, Buscheck and Nitao speculate that water is shed around the boundaries of the dryout zone, forming a *hydrothermal umbrella*. The couplings between thermal, mechanical, and hydrologic phenomena, however, make it unclear to what extent and over what scale shedding could occur. It has also been speculated, although not by the above researchers, that a significant amount of the water could exit the mountain as vapor, perhaps at one or more fumaroles.

In addition to the amount and behavior of thermally displaced water, another important aspect related to dryout volume is the diversion of any additional water influx. It is hypothesized that a dryout zone, as defined in TSPA-93, could divert any water influx that impinges on its boundaries. This assumption does not take into account the case where condensate or meteoric water sources may intrude, or penetrate, a boiling

envelope. Information on these phenomena is not available at present and could not be included.

10.2.2 Dryout fraction

The dryout fraction, or *fraction dry*, refers to the number of containers that would be protected from groundwater flow, and hence aqueous flow and transport processes. As discussed in the previous section, repository heat generation could reduce moisture content within some volume of rock around the repository. Although this dryout zone might not be completely dry, it is assumed that groundwater flow would be interrupted within this volume. In order to identify those packages that are encompassed within this boiling envelope, it is assumed that if a 96°C isotherm exists 5 m above the center of a given package, it is protected and considered part of the fraction dry.

It is expected that the dryout zone will grow for a period of time, then dissipate. Some investigators believe that the size and duration of the zone is primarily a function of the gross thermal load of the repository and is defined by heat conduction within the host rock (Buscheck and Nitao, 1992). It is noted, however, that Ross *et al.* (1993) speculated that convection could be an important process if the bulk permeability is large enough.

10.2.3 Container-wall and fuel-rod temperature

Along with the consideration of other factors, including whether containers are wet and whether containers have failed, container and fuel temperatures offer an estimate of EBS integrity. In YMIM, container temperature is used to calculate corrosion rates and to identify when different corrosion processes dominate. Fuel-rod temperature is used to calculate UO_2 alteration and radionuclide solubility. While it is impossible to account for each waste package's surface and fuel-rod temperatures, representative temperatures consistent with specific regions of a given repository layout are incorporated.

10.3 Detailed thermal modeling

The development of information consistent with the conceptual hydrothermal model discussed in Section 10.2 requires the complementary use of a number of thermal design models. Required are models that address issues related to the repository-scale couplings of heat and moisture transport, the impacts of specific waste characteristics and layouts, and the impact of various operational aspects (such as backfilling) on the host rock and waste-package thermal environments. In this section, background re-

garding repository thermal design will be presented followed by a discussion of specific thermal loading cases investigated for TSPA-93.

10.3.1 Background on repository thermal design

Underlying all repository thermal loading scenarios are assumptions regarding general repository layout, waste package design, waste stream characteristics, emplacement mode, and waste emplacement density. It is the specific combinations of these assumptions coupled with assumptions related to the physical models chosen to analyze a repository thermal loading case that define the resulting near- and far-field temperature responses. Since no single assumption uniquely defines a thermal profile, it is important to establish an understanding of the primary components of repository thermal design that contribute to host-rock thermal response.

10.3.1.1 General Repository Layout

With respect to general repository layout, the primary aspect that is most important to the prediction of host-rock thermal response is the overall continuity of the waste emplacement regions.

As introduced in Section 4.4.3, the repository design presented in the SCP–CDR (SNL, 1987) is composed of a series of emplacement panels (see Figure 4-5). Emplacement panels are typically 426 m (1,400 ft) wide and extend from the main accesses to the perimeter drift. The panels vary from 457 to 1,200 m (1,500 to 3,900 ft) in length and are approximately rectangular in shape. A total of 17 panels are designated in the SCP–CDR for waste emplacement, 14 full-width and 3 half-width. The principal access corridor to the emplacement panels is provided by a series of three main drifts that run the length of the developed region and combine to form a strip of unheated area 46 m (151 ft) in width. Associated with this main drift corridor is a thermal buffer zone between the outer main drift and the edge of what is considered the beginning of the actively heated region of a given panel. This buffer zone is defined to be 61 m (200 ft) wide. Combining the main drift width with its associated standoffs, a break of 168 m (551 ft) in the continuity of the major heated repository regions is defined.

On a smaller scale, there exists a similar break in continuity between adjacent panels. Access to an emplacement panel is via a dual set of panel access drifts that run perpendicular to the mains and intersect the perimeter drift. Panel access drifts are 6.4 m (21 ft) wide and, between adjacent panels, are separated by a 19.2 m (63 ft) wide barrier pillar. When this is combined with a 25.9 m (85 ft) standoff between the first container in an emplacement drift and the panel access drift, the actively heated drift length of an emplacement drift is reduced by 83.8 m (275 ft). As shown in Ryder (1993),

this lack of continuity at the repository and panel scales has a strong impact on the coalescence and duration of far-field isothermal surfaces.

With the move from a drill-and-blast repository construction method to an approach that relies on a tunnel boring machine (TBM) to construct the underground facility, several changes in repository layout have been proposed. First, the panel structure documented in the SCP–CDR has been abandoned in favor of a series of emplacement drifts that run approximately perpendicular to the main drift accesses. The concepts of access drifts and barrier pillars are no longer incorporated into the repository designs due to changes in operational approaches. These changes in design result in a stronger continuity in the heat source (see Figure 4-6). This continuity can be expected to provide larger scale coalescence and longer duration isothermal surfaces than the SCP–CDR design; however, the impact of the unheated main-drift corridor would still be evident.

10.3.1.2 Waste Package Design

In repository thermal design, the primary focus is on global changes in host-rock response. The internal environment of the waste package is not, therefore, of a scale that is typically modeled. Instead, the internal details are smeared and the heat-generating waste assumed to act uniformly throughout the package. Although the details are not modeled, waste package design impacts repository-scale calculations through its influence on waste steam characteristics.

10.3.1.3 Waste Stream

Waste package design (capacity) is one of many constraints that defines the thermal characteristics of a waste stream entering the repository. Given that the host rock thermal response is directly linked to the power output and decay characteristics of the waste emplaced, it is important to understand the variability that can be obtained through the application of different waste stream assumptions.

As an example of the variability that can be expected in a waste stream, output from the Waste Stream Analysis model (WSA; Andress and McLeod, 1988) will be presented for two cases. For both cases, it is assumed that the waste package design is capable of holding 21 PWR (or 40 BWR) assemblies. In addition, no alteration in pickup priorities is imposed and the MPA tonnage schedule is observed. Discussed in Section 4.4.1, the first case, known as the *double-blended* scenario, assumes complete freedom to select fuel at reactors and full blending capability at the MRS (i.e., a pool or vault storage technology). The resulting waste stream characteristics are shown in Figure 10-3.

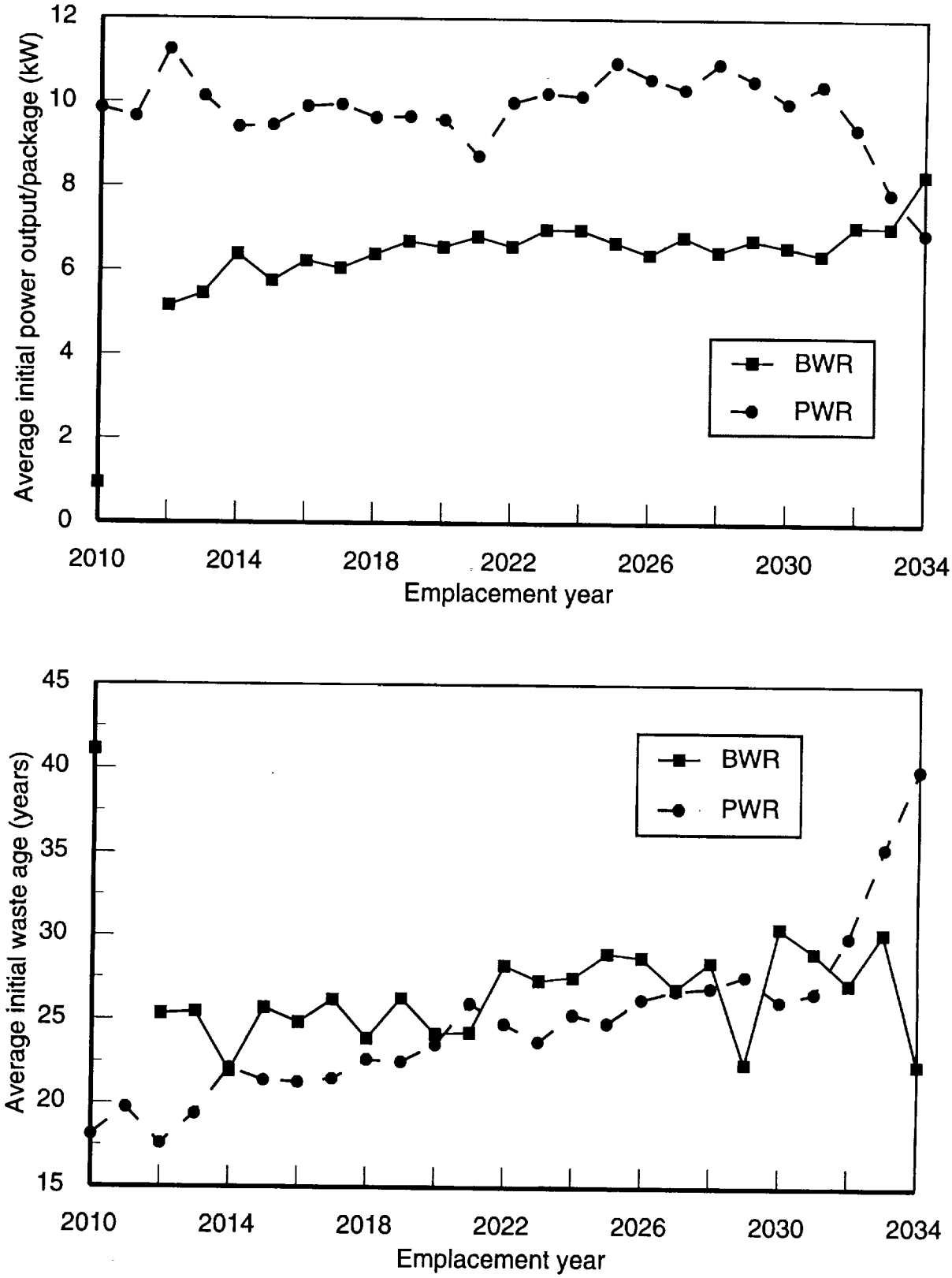

Figure 10-3. Characteristics of double-blended waste stream for 21/40 waste packages; average power per container (top) and average age (bottom).

For contrast, Figure 10-4 displays the waste stream characteristics for a *youngest-fuel-first* (YFF) scenario. For this particular YFF scenario, waste stream flowthrough is assumed at the MRS and no fuel younger than 10 years out-of-reactor is accepted for disposal at the repository.

Examining the yearly average power outputs and ages for the two waste streams, it is obvious that the near-field environment would exhibit different thermal responses depending on which waste stream is analyzed. On a larger scale, the total initial power deposited by each waste stream is also significantly different, approximately 63 MW for the double-blended case and over 80 MW for the YFF case. Such a difference in gross thermal power not only alters the area required for a given loading density, but also could impact the scale and magnitude of thermal-mechanical-hydrologic interactions.

10.3.1.4 Emplacement Mode

In addition to the waste package design and waste stream definition, host-rock thermal response—particularly in the near-field—is strongly dependent upon emplacement mode. As discussed in Section 4.3.1, the reference SCP emplacement mode is vertical borehole emplacement. Due to handling limitations, the waste package designs associated with this emplacement mode are limited in size and capacity. The thermal design implications of these limitations are that the number of spent-fuel waste packages that must be modeled for a vertical emplacement case is quite large, typically in excess of 30,000.

Beyond the modeling implications of 30,000 packages are issues related to transportation and handling that tend to favor a trend toward reducing the number of waste packages scheduled for permanent disposal. In order to decrease the number of packages while still meeting mandated MPA tonnage requirements, the capacity—and hence the size—of each waste package must be increased. If this approach is followed, there comes a point at which the waste packages can no longer be physically emplaced in a borehole. *In drift* emplacement is a concept that assumes that the waste will not be emplaced in boreholes, but instead will be placed horizontally on the emplacement drift floors (see Figure 4-4). With respect to thermal design calculations, the in-drift concept reduces the number of sources that must be modeled; however, the presence of the packages in the drifts makes near-field thermal calculations more sensitive to ventilation and backfill.

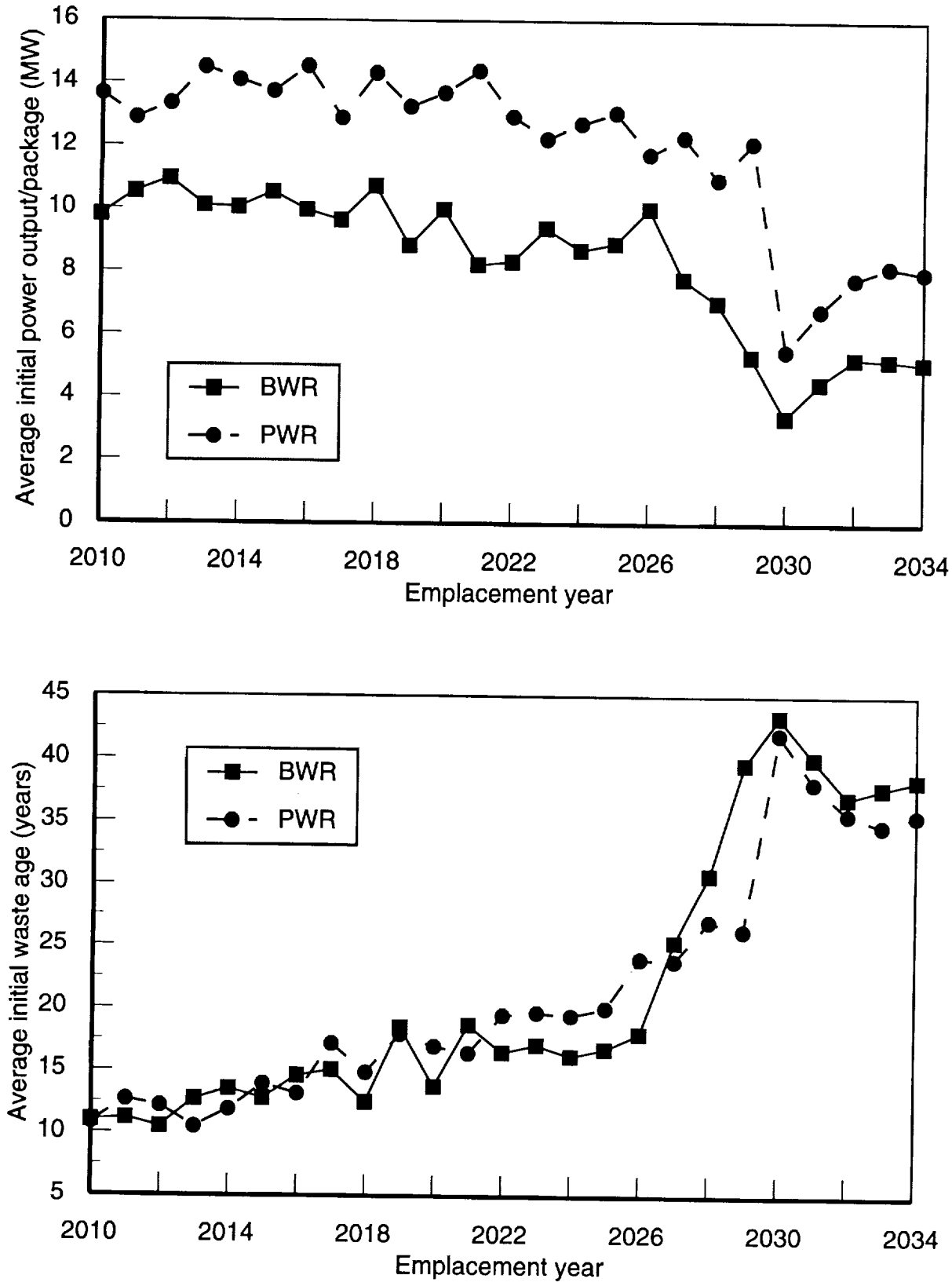

Figure 10-4. Youngest-fuel-first waste stream for 21/40 waste packages; average power per container (top) and average age (bottom).

10.3.1.5 Waste Emplacement Density

The density of waste emplacement at the repository is typically expressed in terms of an areal power density (APD), or alternatively as an areal mass loading (AML). The simplest definition is that for local areal power density (LAPD). Defined as the initial power output of a single container divided by the area of a unit cell, LAPD is not strongly dependent on overall repository layout (see Figure 10-5a). Using the product of the container and drift spacings directly adjacent to a container as the calculational base (unit cell), the value for LAPD is not affected by non-actively heated regions within a given design.

By contrast, the definition of design-basis areal power density is calculated on a larger physical scale than LAPD. Design-basis APD represents a reduction in LAPD equal to the ratio of heated drift length to total panel width, where heated drift length is defined as the distance from one half of a container spacing before the centerline of the first container in a drift to one half of a container spacing beyond the last container in a drift (see Figure 10-5b). Unlike LAPD, design-basis APD is strongly dependent upon general panel arrangement, and therefore, does not provide a good basis for comparison between conceptual layouts.

Regardless of the type of areal power density being discussed, however, APD does not maintain a constant value through time. Since it is calculated based on the instantaneous value of power output at emplacement, APD decreases at a rate consistent with the decay characteristics associated with the waste emplaced. Because of this, an alternate designation for waste emplacement density based on mass per unit area is often used, namely areal mass loading. AML has the primary appeal of staying constant through time, however, AML and APD can be directly related if information on waste package design and waste stream characteristics is known.

10.3.2 Thermal loading cases chosen for TSPA-93

Because of the wide range of variability and the competing nature of some of the assumptions that go into defining a repository thermal loading case, it is difficult to explicitly define bounding cases. With this in mind, it is the goal of this total-system performance assessment to examine a limited set of thermal loading cases that are considered representative, and that reflect current Project emphases.

10.3.2.1 Assumptions

For TSPA-93, it was decided that the TBM layout is most representative of current Project directions. Emplacement drifts are assumed to be 7.62 m (25 ft) in diameter and a constant drift spacing of 25.4 m (83.3 ft) is assumed, (consistent with a 30% extraction

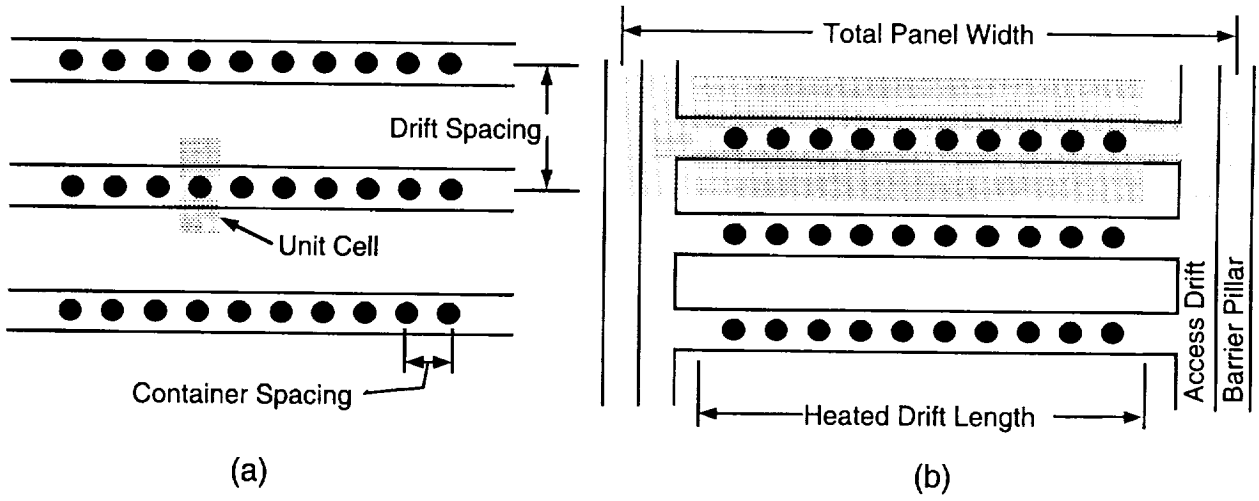

Figure 10-5. (a) Representation of unit cell used to calculate LAPD; (b) Heated drift length used to calculate design-basis areal power density.

ratio limit). For these calculations, it is assumed that waste emplacement would begin from the south end of the developed region and proceed to the north.

Two waste-package designs were identified for examination. The first is the thin-walled alternate design published in the SCP. By also assuming a vertical borehole emplacement scheme for this waste package, a direct link is provided in this TSPA to cases developed early in the evolution of thermal design within the Project. By virtue of its size, the second waste package chosen for consideration is predicated on an in-drift emplacement mode. This waste package provides an avenue for examining some of the performance implications of more recent work completed in the area of waste package and repository design.

For this iteration of TSPA, a double-blended or levelized waste stream was chosen. This assumption minimizes waste stream induced fluctuations in thermal profiles and, when taken in conjunction with the strong heat-source continuity exhibited by the assumed TBM layout, establishes a foundation for the direct application of model results that are based on globally smeared repository heat-source representations (e.g., Buscheck and Nitao, 1993).

Finally, two areal power densities were chosen for examination. Because of the structure and continuity of the TBM layout, LAPD and design-basis APD are assumed equal. The specific loadings chosen were 57 kW/acre and 114 kW/acre. The choice of 57 kW/acre is consistent with the design-basis APD specified for the layout published in the SCP (DOE, 1988a). This loading was originally identified in the Unit Evaluation Study (Johnstone *et al.*, 1985) as that which would not cause the floor of an emplace-

ment drift to exceed 100°C during the operational and retrieval lifetime of the repository. The 100°C limit used to define this loading is no longer considered a constraint in thermal design evaluations; however, the specific value of 57 kW/acre has been maintained by the Project as a baseline. Because of its historical significance and the large body of work that has been completed for this loading, 57 kW/acre was chosen for examination in this iteration of TSPA. The value of 114 kW/acre can be linked to recent work completed by LLNL on a concept known as *extended dry*. The reasoning behind this loading is one that bases the performance of the site in terms of containment and isolation on the establishment of a large dryout zone around the repository. It is noted that this approach to repository thermal design is different from that proposed in the SCP. The SCP approach is predicated on the evaluation of a given thermal loading case against a set of thermal goals aimed at limiting the degradation of multiple natural barriers. When evaluated with respect to the historical approach to repository thermal design, 114 kW/acre violates several of the established thermal goals. Because of recent interest in this alternate approach to thermal design, 114 kW/acre was adopted as the second loading for consideration in this iteration of TSPA. Table 4-4, as repeated in Table 10-1, documents the four analysis cases chosen for investigation.

Table 10-1. Summary of thermal loading cases examined in TSPA-93.

Analysis Case	Local Areal Power Density (kW/acre)	Emplacement Mode	Package Designs
1	114	In-Drift	21 PWR or 40 BWR
2	57	In-Drift	21 PWR or40 BWR
3	114	Vertical Borehole	4:3 Hybrid or 10 BWR or4 PWR
4	57	Vertical Borehole	4:3 Hybrid or 10 BWR or 4 PWR

The level of detail obtained from thermal design calculations of the above cases cannot be completely incorporated into currently available performance assessment tools. Therefore, output from the thermal modeling exercises completed for TSPA-93 had to be simplified into a limited set of information as defined by the abstracted hydrothermal model discussed in Section 10.2. The discussions that follow will use the abstracted hydrothermal model as a framework. Specifically, thermal modeling approaches and results will be presented for the categories of fraction dry, dryout volume, and representative container and waste-form temperatures.

10.3.2.2 Fraction Dry

The criterion used to quantify the fraction of waste packages that would be dry at any given time is founded on a temperature-based definition that assumes a waste package is protected from liquid water if a 96°C isotherm is predicted 5 m vertically above the waste-package center point. Two approaches for determining the fraction of waste packages encompassed by a 96°C isotherm were chosen for this TSPA. The first is based on calculations completed by Buscheck and Nitao (1993) using the hydrothermal V-TOUGH code (Nitao, 1989). Because it relies on a smeared axisymmetric definition of the heat-generating waste, Buscheck and Nitao's model formulation does not allow for the differentiation between cases that are defined with the same initial loading density (e.g., an in-drift case as compared to a vertical-borehole case). In order to account for such aspects as specific container locations, irregular repository geometry, and waste-stream variations, an analytical model has also been used to determine the fraction of containers protected by a 96°C isotherm. The results from both models are presented.

10.3.2.2.1 Axisymmetric hydrothermal model

Repository-scale thermal models have been run by LLNL using the strongly coupled hydrothermal code V-TOUGH. V-TOUGH can simulate the coupled transport of water, vapor, air, and heat in a porous medium. Fluid flow is described with a multiphase extension of Darcy's law and heat flow occurs by conduction and convection. The formulation of the V-TOUGH code is based on the combination of matrix and fracture properties into an equivalent continuum description.

The advantages of using V-TOUGH to predict host rock thermal responses are primarily centered on the model's strong hydrothermal coupling and the numerical nature of the code that allows for multiple functional material property designations. The V-TOUGH results used in this TSPA are amplifications of calculations reported in Buscheck and Nitao (1993). The calculations involve an axisymmetric geometry of layered media with a bulk permeability of 0.28 darcy (approximately 3×10^{-13} m^2) in the region of the repository. For the homogenized disk source, the entire waste inventory is assumed to be described by the characteristics of 26-year-old spent fuel with a burnup of 39,585 MWd/MTU.

Due to the smeared nature of this heat-source description, it is impossible to use this model to distinguish between layout concepts or emplacement modes. Results have therefore been obtained for two APDs: 57 and 114 kW/acre. For the 57-kW/acre case, the repository is defined as a disk with a radius of 1,200 m, translating to an area of 1,117 acres. For the 114-kW/acre case, the repository is defined with a radius of 848.5 m and

an area of 559 acres. These combinations translate into an initial thermal power deposition of 63,712 kW, consistent with the waste stream discussed in Section 4.4.1.

In order to calculate fraction dry using this model, the predicted time behavior of the 96°C isotherm has been monitored along a line parallel to the radius of the disk source at a distance of 5 m above the modeled repository. From this information, areas encompassed by the boiling isotherm have been calculated. By further assuming that the packages are uniformly distributed within the disk source, an approximation of the number of packages that would be protected can be calculated. Figures 10-10 and 10-11 (discussed below in Section 10.3.2.3—dryout volume) show the V-TOUGH approximations of fraction dry for the 114- and 57-kW/acre thermal loadings.

Although there are many benefits to using the V-TOUGH model for repository thermal calculations, there are limitations and assumptions incorporated into the model that impact predictions of repository thermal response. Inherent in the use of an axisymmetric heat source representation is the minimization of source perimeter length. For example, an axisymmetric disk source of 400 acres would have a perimeter of 4,510 m. A square plate source of the same acreage would have a perimeter of 5,089 m. The impact of an axisymmetric disk model's source perimeter minimization on the duration of isothermal surfaces was demonstrated by Ryder (Nelson and Bruch, 1993) as being an important factor in the evaluation of boiling-front duration. Along similar lines, the use of a single plate to represent the repository imposes an assumption of simultaneous emplacement that results in early and complete coalescence of isothermal surfaces. The impact of this imposed coalescence is apparent in Figures 10-10 and 10-11 (Section 10.3.2.3), which shows a fraction dry of approximately one immediately following the first year of the modeled time frame.

As indicated in Section 10.3.1, it is the combination of assumptions both external and internal to the models that define the host rock's thermal response. Since no single model can adequately capture the complexities of the physics, while also addressing all issues related to waste-package and repository designs, a complementary set of models is required. For this particular problem, an analytical solution has been chosen as a balance to the V-TOUGH calculations. While the analytical approach is not capable of modeling a layered stratigraphy or the direct coupling between thermal and hydrologic effects, it does capture the complexities of repository layout, waste stream, and emplacement mode.

10.3.2.2.2 Analytical model

Based on the closed-form analytical solutions to the heat conduction equation, the second method chosen to quantify the fraction of packages protected by a 96°C isotherm uses heat-generating points and cylinders to explicitly represent the waste packages, superposition, and the method of images to construct three-dimensional thermal profiles in a semi-infinite medium (see Appendix C). Because of the analytical nature of this model, the existence of open air spaces (drifts) and a complex layered stratigraphy is simplified into a single homogeneous isotropic material with constant properties.

Two of the primary benefits to choosing this method are the ability to capture the stepped nature of waste emplacement as dictated by the MPA (DOE, 1988b), as well as explicitly modeling each waste package and the irregular shape of the potential repository. A complete description of the model and inputs is included in Appendix C.

Figures 10-6 through 10-9 are representative isothermal plots for a plane defined 5 m above the waste package center points. Representing a time 50 years following waste emplacement, Figures 10-6 through 10-9 demonstrate the impact of concentrating the waste into 7,640 waste packages (for the in-drift options) versus 32,016 containers (for the vertical emplacement cases). Specifically, the vertical emplacement options result in a more uniform growth of the isotherms, whereas the in-drift options show a more mottled growth consistent with the concentrated nature of the in-drift heat sources. Using the temperatures predicted for this grid in conjunction with the defined locations of each waste package, the number of spent fuel containers protected by a 96°C isotherm was determined for each thermal loading case. Shown in Figures 10-10 and 10-11, the predictions of fraction dry for the analytical model are consistent with those predicted using the V-TOUGH model.

10.3.2.2.3 Comparison of results.

In comparing the results between the V-TOUGH and analytical approaches, the strengths and limitations associated with each approach must be kept firmly in mind. As illustrated by Figures 10-10 and 10-11, the differences between the V-TOUGH and the analytical model results are focused primarily in the early and late time periods.

At early times, the ability of the analytical model to capture the stepped nature of the waste emplacement results in a more realistic increase in the values for fraction dry than the V-TOUGH model's use of simultaneous emplacement. At late times, the limitations of the analytical model become apparent in terms of its representation of the mountain as a single material. This is likely to cause an earlier collapse of the boiling front than would be predicted by an equivalent layered or spatially heterogeneous

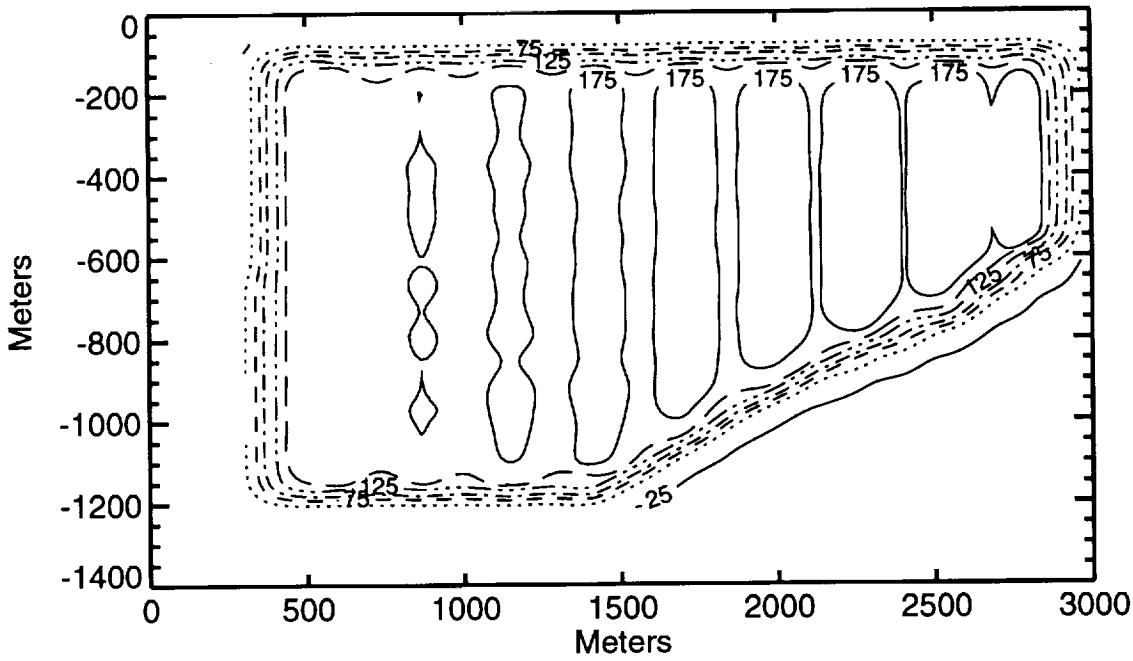

Figure 10-6. Isothermal plot for 5-m plane, 50 years following waste emplacement for the 114-kW/acre in-drift case.

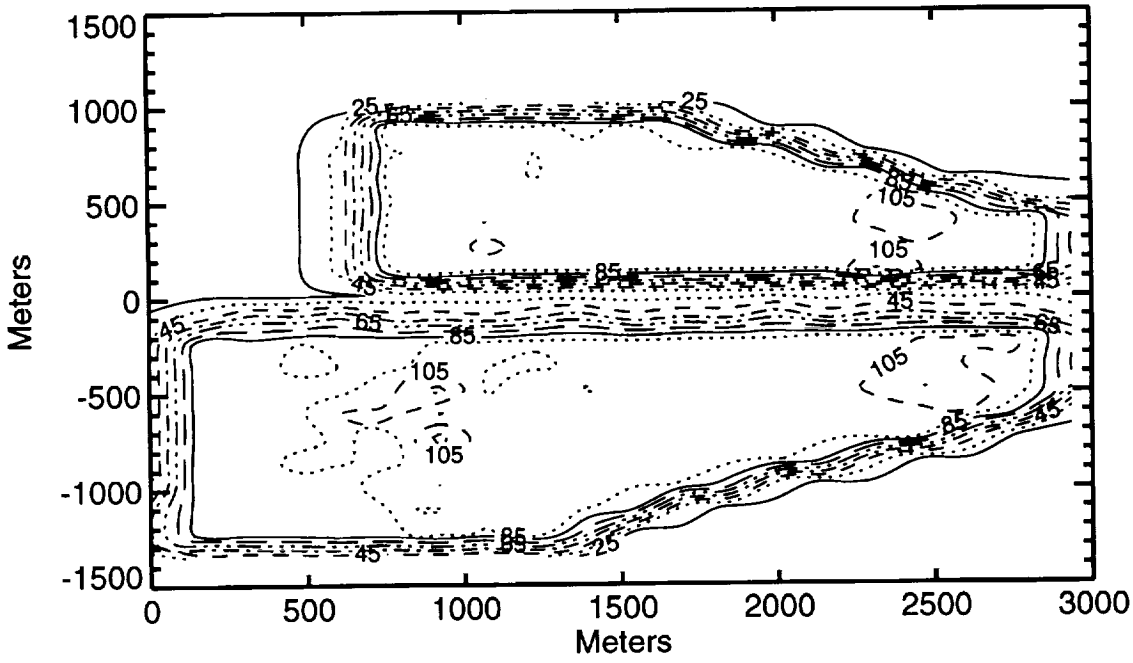

Figure 10-7. Isothermal plot for 5-m plane, 50 years following waste emplacement for the 57-kW/acre in-drift case.

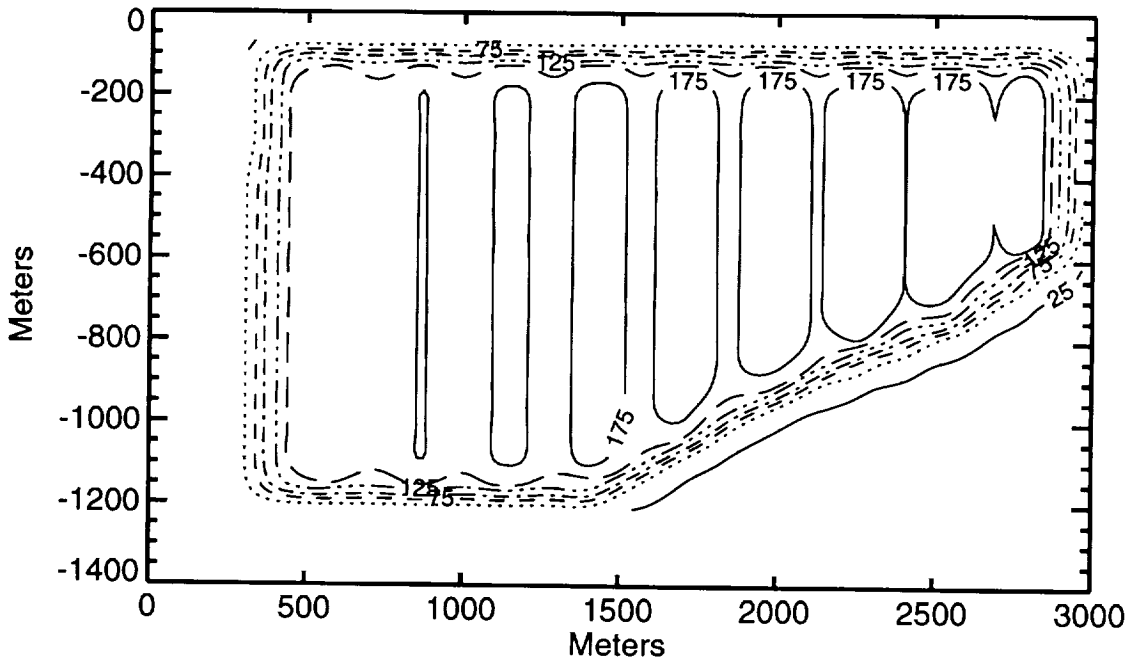

Figure 10-8. Isothermal plot for 5-m plane, 50 years following waste emplacement for the 114-kW/acre vertical-borehole case.

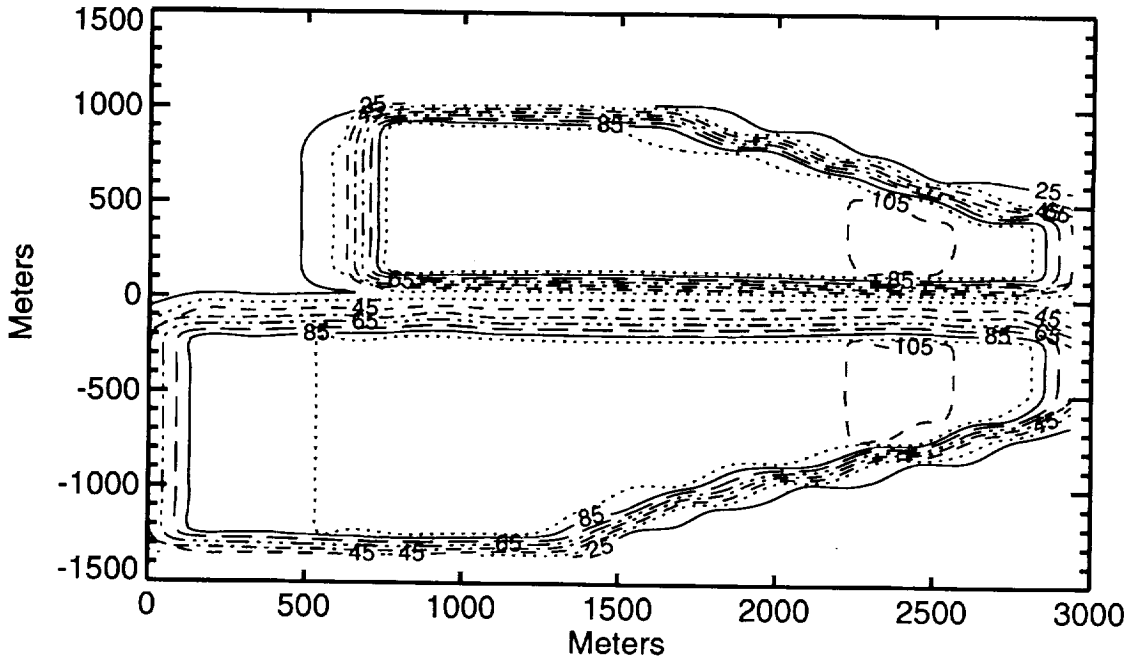

Figure 10-9. Isothermal plot for 5-m plane, 50 years following waste emplacement for the 57-kW/acre vertical-borehole case.

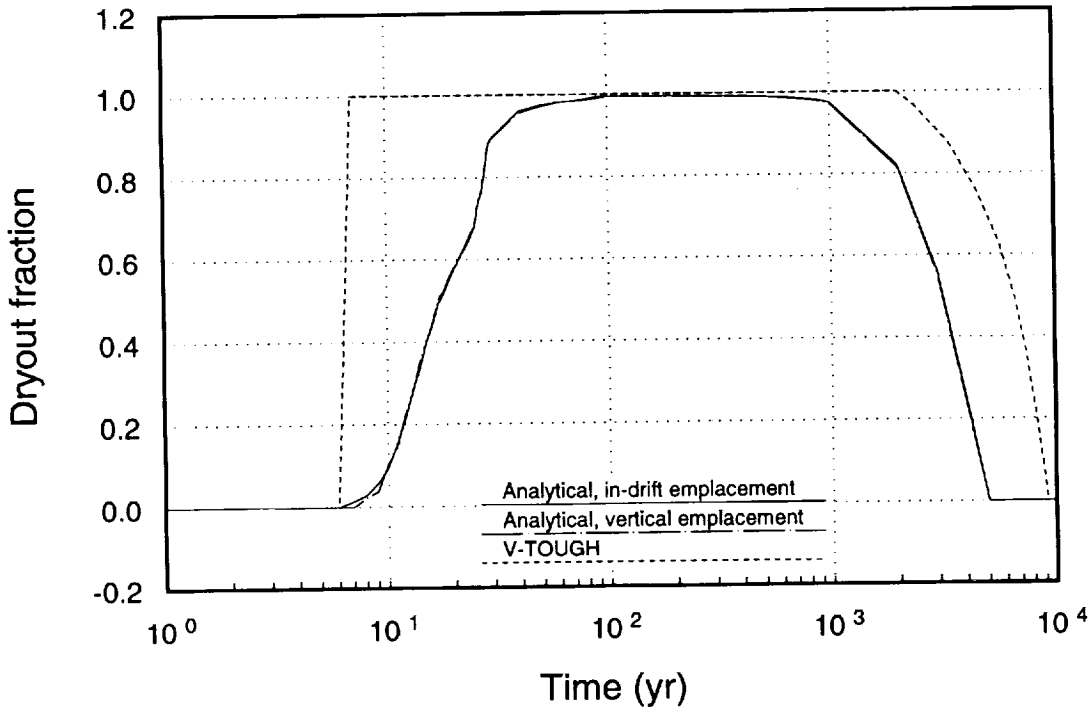

Figure 10-10. Fraction dry for 114-kW/acre cases.

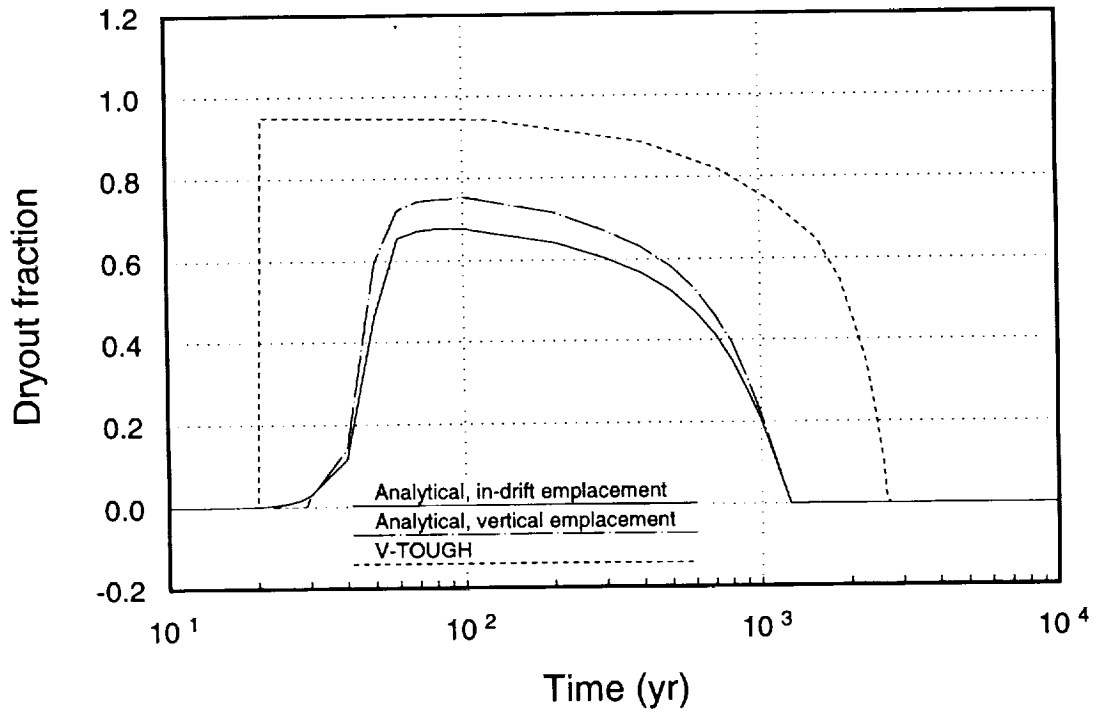

Figure 10-11. Fraction dry for 57-kW/acre cases.

model. It is noted that the V-TOUGH model does use a layered representation of the mountain; however, because of the major differences in heat source definitions between the two models, V-TOUGH results cannot be assumed to accurately model the late-time behavior. The most realistic late-time behavior of the fraction dry is therefore likely to fall somewhere between the V-TOUGH and analytical predictions.

10.3.2.3 Dryout volume

In order to estimate the volume of rock dryout for each TSPA thermal loading case, the same two methods used to determine fraction dry were used.

10.3.2.3.1 Axisymmetric hydrothermal model.

From the V-TOUGH calculations, information regarding the location of the 96°C isosurface above and below the repository has been obtained for two lines for the 57-kW/acre case and three lines for the 114-kW/acre case, sampled normal to the modeled repository plane (Figure 10-12). Calculation of the volume encompassed by the boiling front has been accomplished by assuming that a regular geometric shape connects the crossing points of the 96°C isotherm calculated for the three lines. For these calculations, the dryout zone is assumed symmetric about the repository centerline. Figures 10-13 and 10-14 show estimates of the dryout volumes obtained from the V-TOUGH calculations. It is noted that the oscillation in the 57-kW/acre case at 100 years results because the 96°C isotherm at the edge of the repository begins dissipating after only 80 years, and the rate of this dissipation is faster than the dryout volume near the center of the modeled repository is increasing.

10.3.2.3.2 Analytical model.

Using the same analytical approach chosen to determine the fraction of waste packages protected by a 96°C isosurface (see Appendix C), temperatures along lines normal to the repository plane have been monitored. The resulting profiles provide information regarding the vertical extent of the 96°C isotherm that, when coupled with the detailed information from the 5-m grid defined parallel to the repository plane, allow for rough estimations of the volume encompassed by the boiling isotherm. Figures 10-13 and 10-14 show approximations of the volume encompassed by the 96°C isotherm for each of the four thermal loading cases.

10.3.2.3.3 Comparison of results.

The same limitations of the V-TOUGH and analytical models discussed in Section 10.3.2.2.3 are also applicable to the calculation of dryout volume. Early-time behavior is

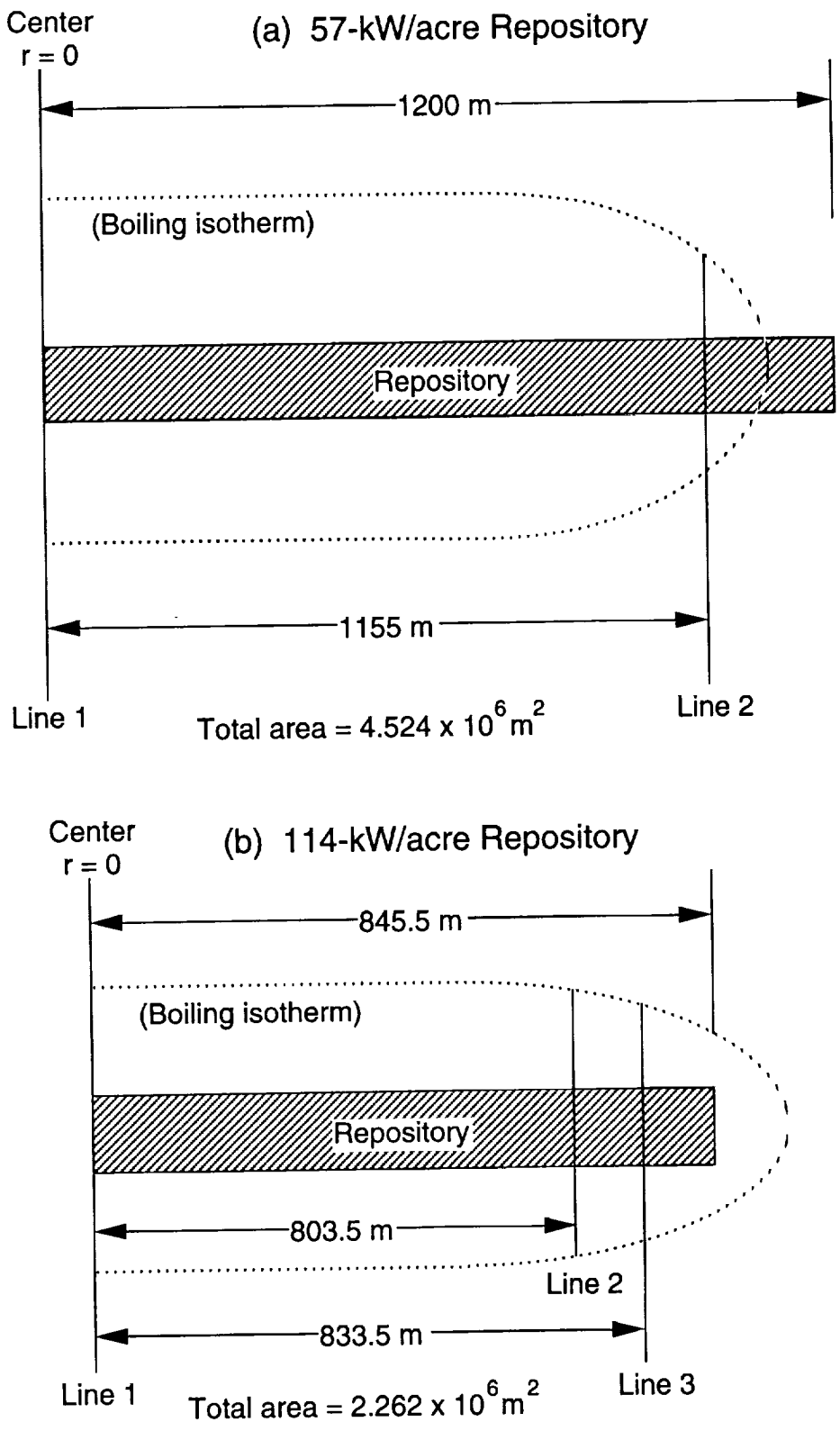

Figure 10-12. Sampling lines used in V-TOUGH estimations of volume dry.

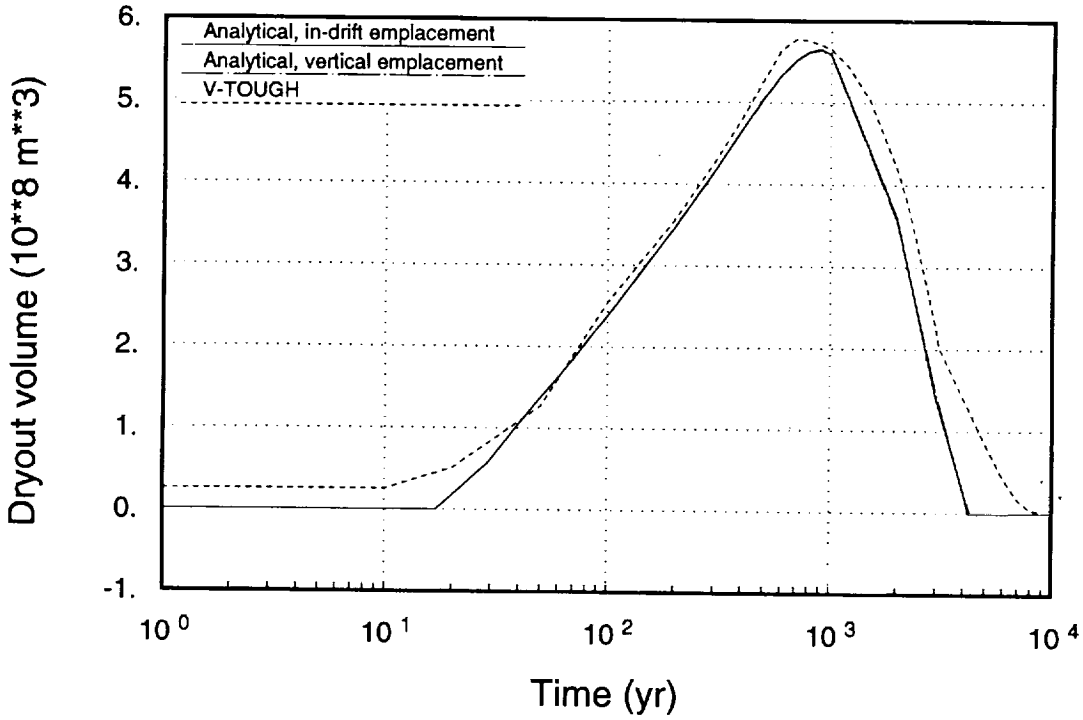

Figure 10-13. Dryout volume for 114-kW/acre cases.

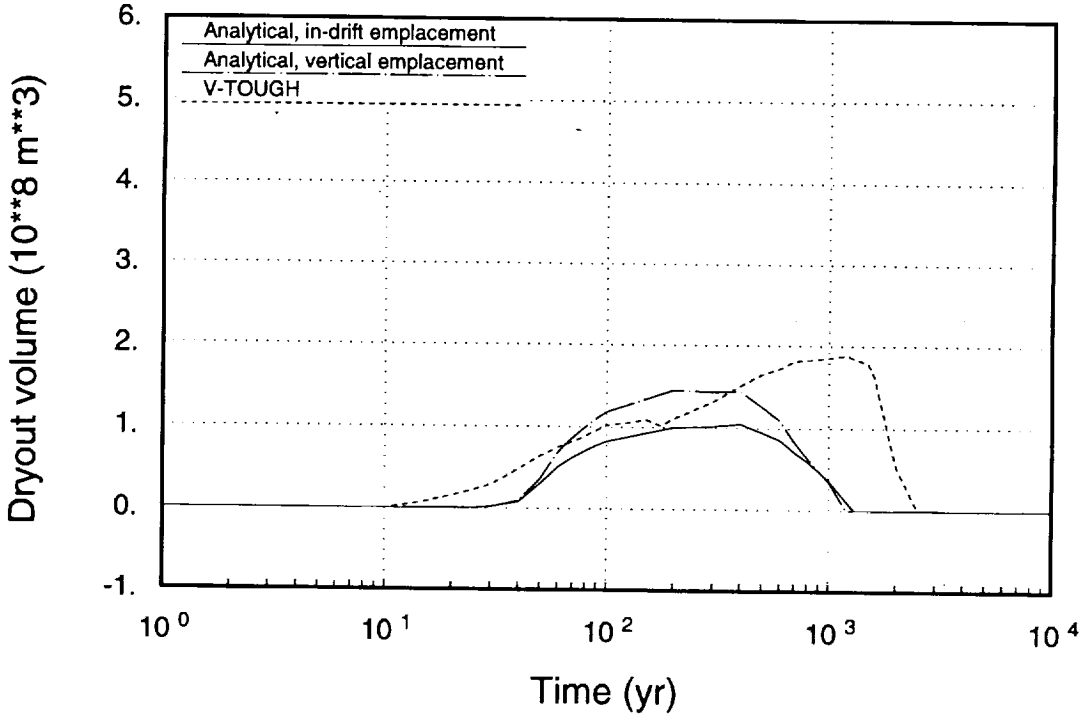

Figure 10-14. Dryout volume for 57-kW/acre cases.

primarily a function of the 25-year waste emplacement schedule and the irregular repository layout; therefore, the analytical model is probably the more realistic representation. At later times, neither approach is ideally suited to determining the duration of the dryout zone. Again it is speculated that the late-time behavior is likely to fall somewhere between the two predictions.

10.3.2.4 Waste-package and fuel-rod temperatures

While it is understood that each waste package is likely to have a unique surface and internal temperature signature, thermal design and performance assessment modeling at this resolution is impractical. For TSPA-93, two regions are chosen as representative; center and edge. Center refers to a package best described as being emplaced within the thermal core of the repository. More specifically, it refers to the thermal behavior that a central package within a central section of a given layout would experience. Such a package would be subjected to the strongest thermal communication with its nearest neighbors and would remain at elevated temperatures for the longest period of time. As a balance to this definition, an edge container would be one that is located within a region that experiences high temperatures early in time, but because of its closer proximity to the unheated rock-mass adjacent to the total waste emplacement area, it would cool faster than one that is centrally located.

In order to define representative temperature profiles for center and edge containers, a combination of models is required. The approach taken matches the early-time behavior of a three-dimensional nonlinear heat conduction model with the late-time predictions of the analytical model discussed previously. These composite container surface temperatures were then post-processed through detailed waste-package models to obtain characteristic fuel-rod responses.

10.3.2.4.1 Waste-package temperatures.

For the early-time behavior of the waste-package surface, results from a three-dimensional nonlinear heat-conduction model developed as an extension of the COYOTE code (Gartling, 1982) are used. By virtue of the finite-element formulation, the calculations are able to employ a layered stratigraphy to define the mountain and to explicitly model the effects of the open (and later backfilled) drifts. A complete description of the geometry analyzed and model inputs used in the COYOTE simulations is presented in Appendix C.

Since the COYOTE models are formulated based on boundary conditions that imply an infinite repository extent, the late-time temperature predictions from these models are overestimates of expected thermal response. It is therefore necessary to match

the early solutions of the COYOTE model with the late solutions for waste-package temperatures that are based on a finite-extent repository layout.

For TSPA-93, the analytical model for calculating fraction- and volume-dry is used. Specifically, since the analytical model is based on heat-generating right-circular cylinders consistent with waste-package dimensions, container temperatures for a number of center and edge waste packages were extracted from the model. From the analytical model's results, two representative profiles were chosen for each thermal loading case. Thermal profiles, obtained from the COYOTE, and analytical simulations, were then combined to create composite temperature histories. It is noted that for both the center and the edge containers, the COYOTE results are used to represent the early-time behavior.

As an example, Figure 10-15 shows the COYOTE temperature history and the analytical model's temperature history for a central waste package as predicted for the 57-kW/acre, in-drift case. It is apparent that the analytical model is incapable of capturing the impact of radiation-dominated heat transfer across the drift prior to backfill or the spike in surface temperature following backfill. Similarly, at late times, the infinite-extent formulation of the COYOTE model makes it incapable of capturing a drop in temperature consistent with the dissipation of the deposited energy into the surrounding rock mass. The time-steps chosen to transfer from the COYOTE to the analytical solution are presented in Table 10-2 for each case. Figures 10-16 through 10-19 document the composite temperature histories generated for the center and edge containers defined for each thermal loading case.

10.3.2.4.2 Fuel-rod temperatures.

In order to get fuel-rod temperatures, the composite container wall temperature profiles defined in the previous section are used as boundary conditions in detailed models of the internal waste-package environment.

Table 10-2. Time at which the composite container surface temperatures change from the COYOTE to the analytical predictions.

Case	Time (years)	
	Center	Edge
In-Drift:		
114 kW/acre	1000	200
57 kW/acre	1000	200
Vertical Borehole:		
114 kW/acre	1000	150
57 kW/acre	400	100

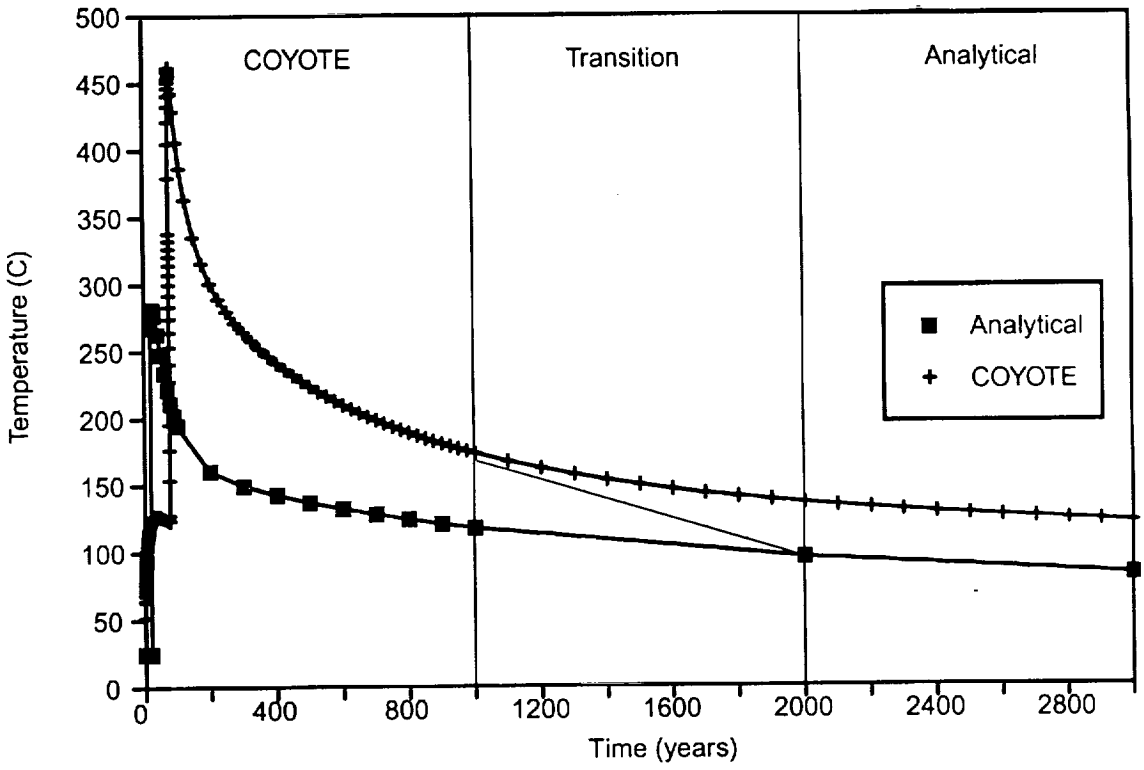

Figure 10-15. COYOTE and analytical waste-package surface temperatures for the 57-kW/acre, in-drift case.

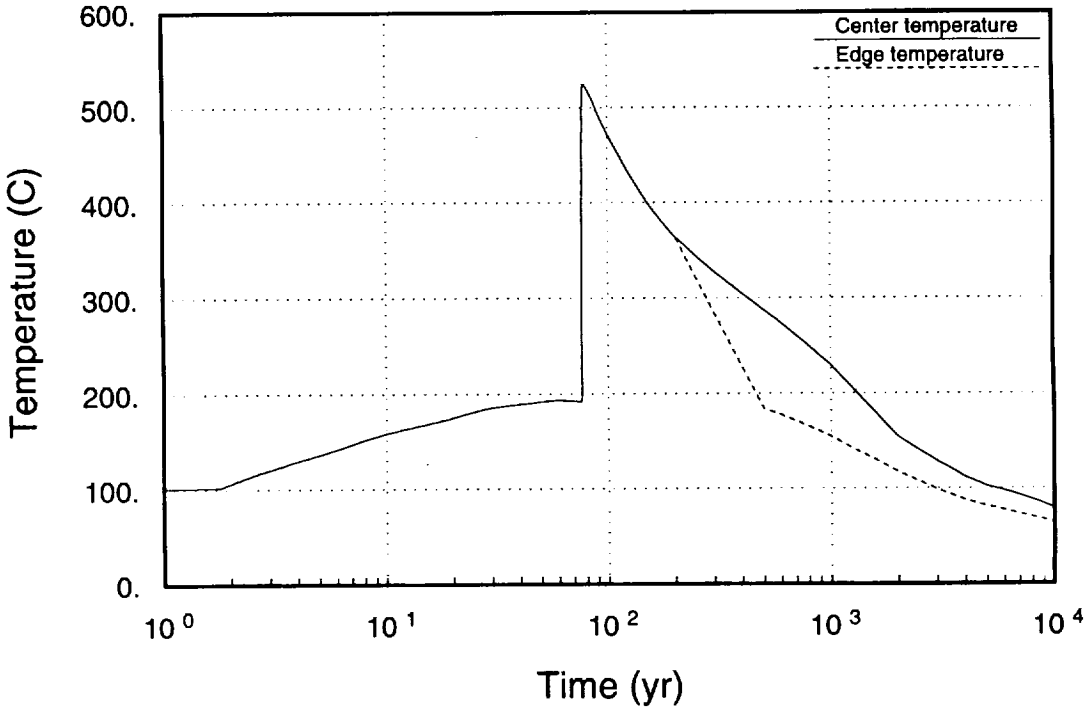

Figure 10-16. Composite container surface temperature for the 114-kW/acre, in-drift case.

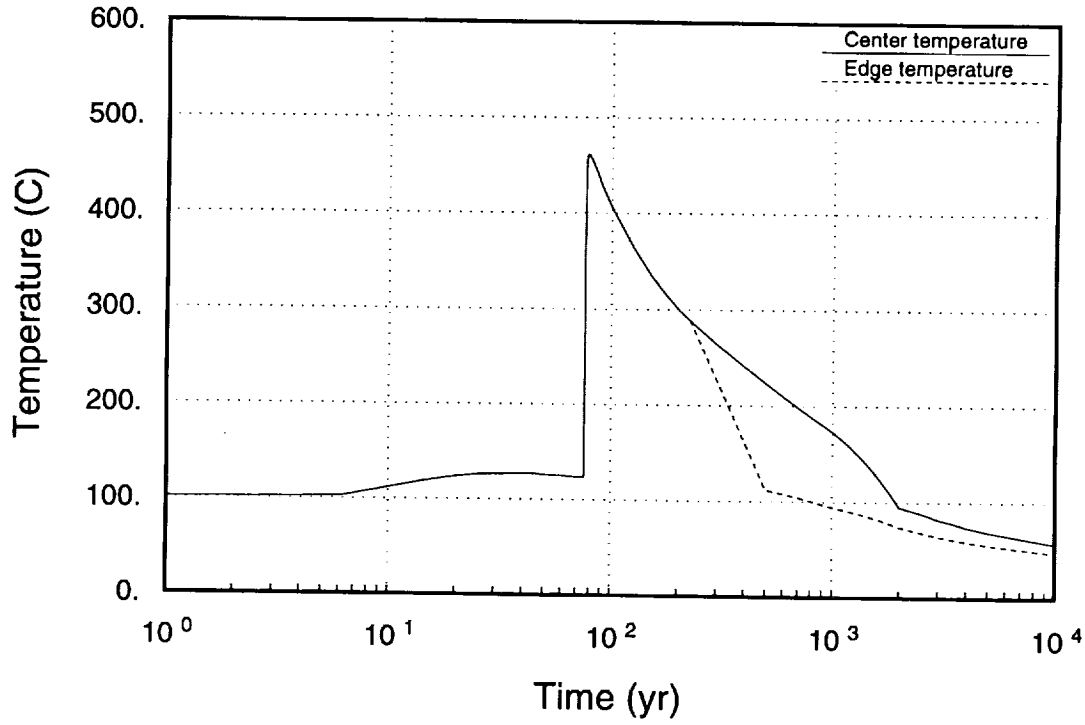

Figure 10-17. Composite container surface temperature for the 57-kW/acre, in-drift case.

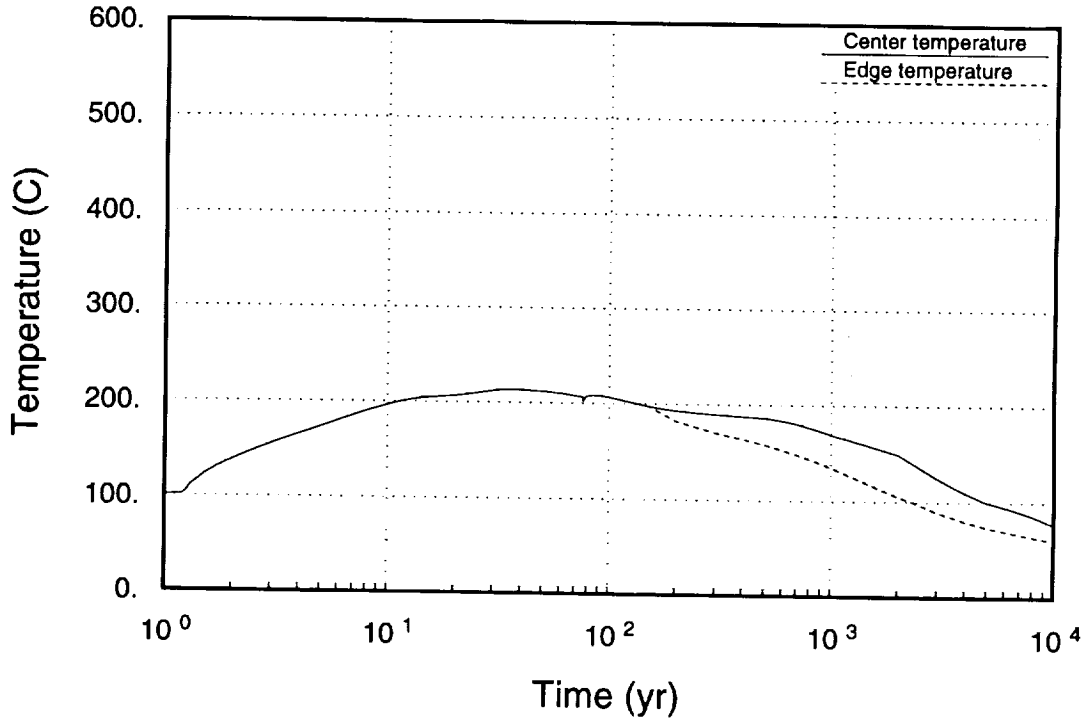

Figure 10-18. Composite container surface temperature for the 114-kW/acre, vertical-borehole case.

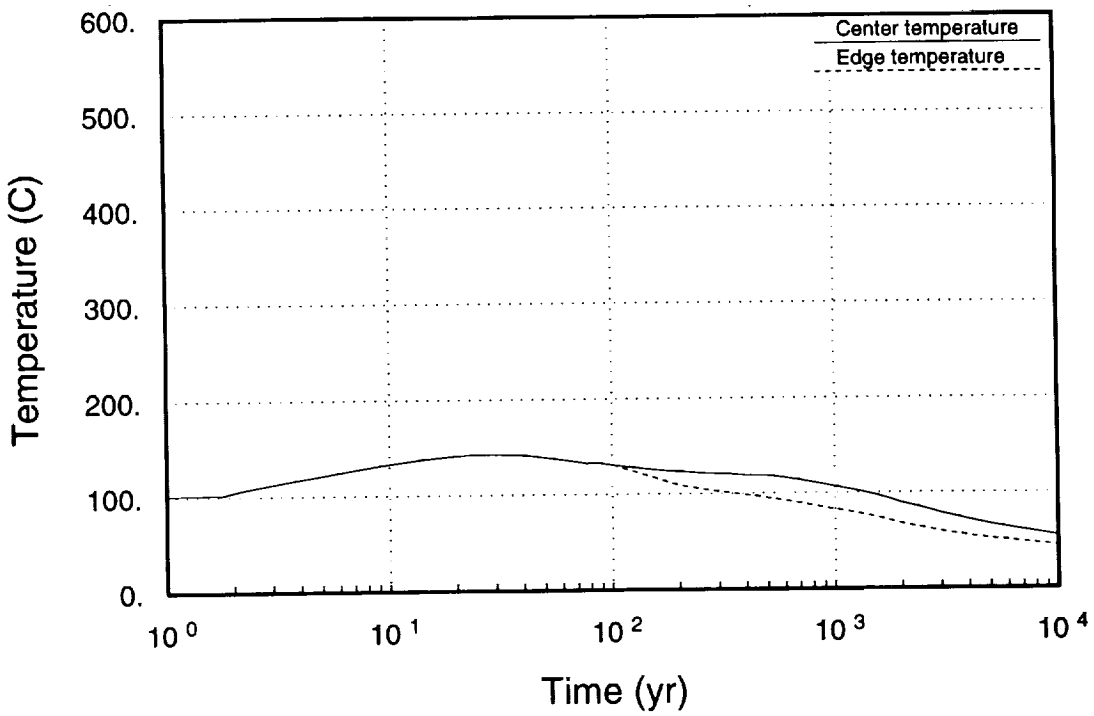

Figure 10-19. Composite container surface temperature for the 57-kW/acre, vertical-borehole case.

For the vertical emplacement option, fuel-rod temperature histories were estimated by establishing a time-varying offset between the container-wall and fuel-rod temperature histories. Performed at LLNL, this offset was calculated as a function of fuel-rod volumetric heat generation using the TOPAZ (Shapiro and Edwards, 1990) code, assuming an internal waste-package geometry consistent with the alternate SCP design containing three intact PWR and four intact BWR assemblies. It was assumed that the waste packages contain 26-year-old spent fuel with a burnup of 39,585 MWd/MTU for both vertical-borehole cases. Figures 10-20 and 10-21 show the estimated fuel-rod temperatures for both vertical emplacement cases.

An evaluation of the error that is introduced by using this offset method was carried out by LLNL and indicates that at its peak, the fuel-rod temperatures may be overestimated by as much as 30°C for the 114-kW/acre case and underestimated by as much as 50°C for the 57-kW/acre case. These errors decrease with time as fuel-rod heat generation decreases. Methods used to generate the fuel-rod histories for the vertical-borehole cases should be refined in future TSPAs.

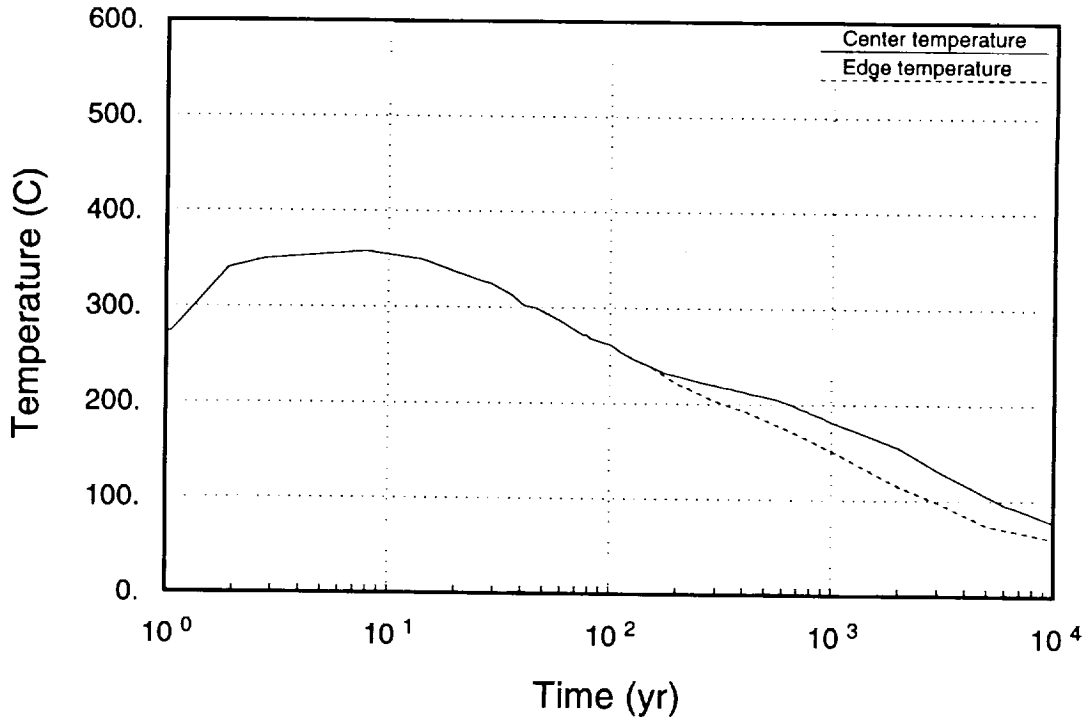

Figure 10-20. Fuel-rod temperatures for the 114-kW/acre, vertical-borehole case.

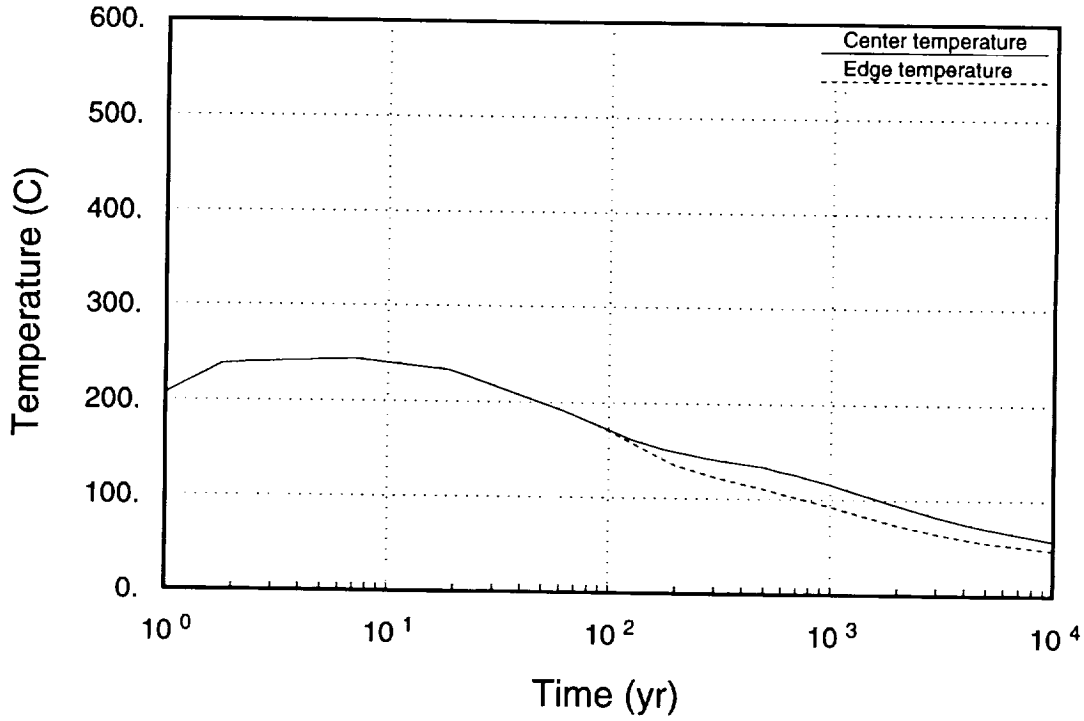

Figure 10-21. Fuel-rod temperatures for the 57-kW/acre, vertical-borehole case.

For the in-drift emplacement options, finite-element analyses of a 21 PWR waste package were conducted by personnel from the YMP management and operating contractor's waste-package design team. For times out to 75 years, the model uses rock wall temperatures obtained from the COYOTE simulations as boundary conditions. Beyond 75 years, a second model has been employed that uses the composite container histories generated above as boundary conditions. It is noted that these analyses were not run as transient analyses, but instead as steady-state approximations. While transient analyses would be more appropriate, particularly during times of sharp gradients, the steady-state analyses should be conservative first-order estimates. As with the estimates of fuel-rod temperatures completed for the vertical emplacement cases, the in-drift estimates should be refined in future TSPAs. Figures 10-22 and 10-23 document the fuel-rod temperatures calculated for the two in-drift cases.

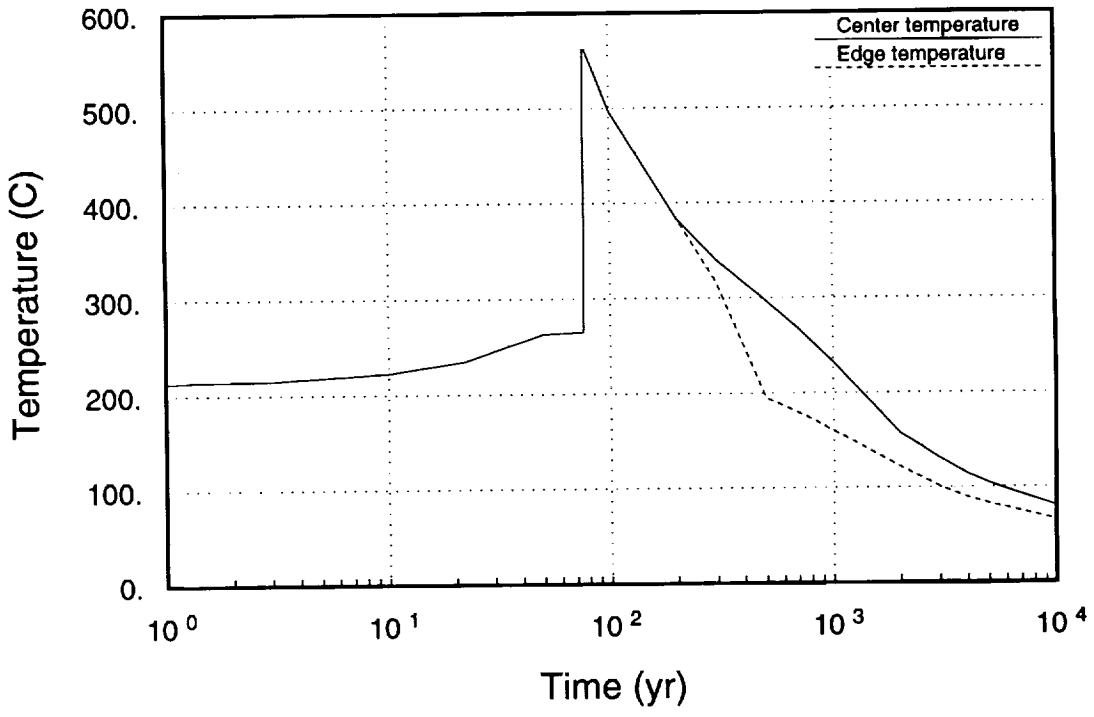

Figure 10-22. Fuel-rod temperatures for the 114-kW/acre, in-drift case.

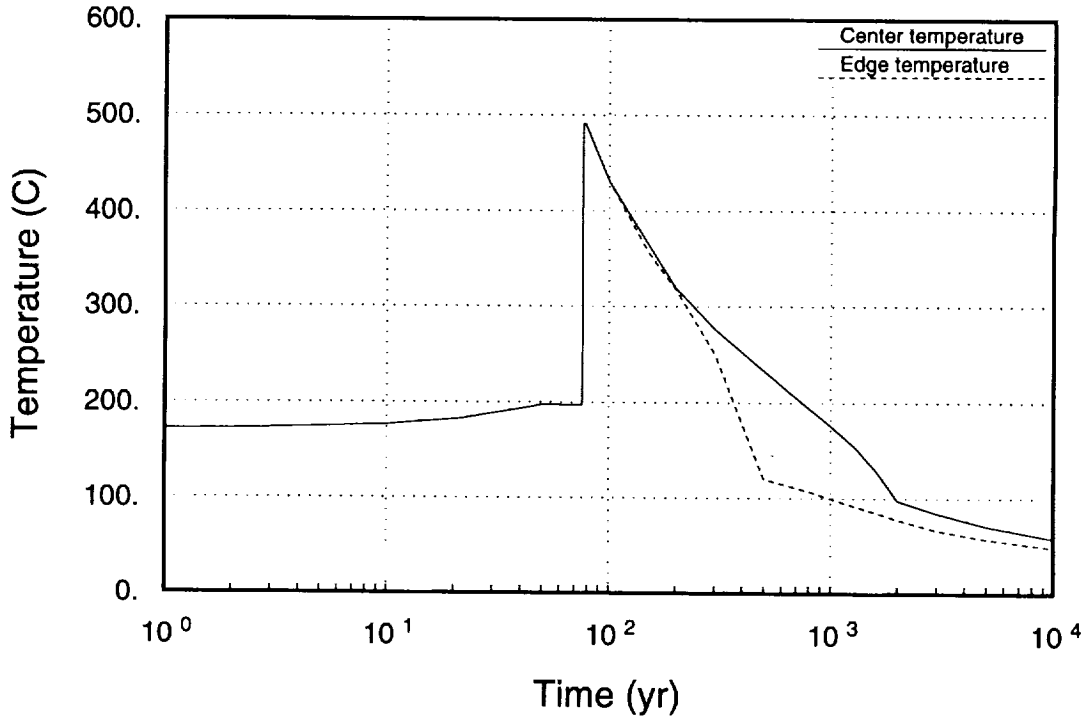

Figure 10-23. Fuel-rod temperatures for the 57-kW/acre, in-drift case.

10.4 Implementation of conceptual hydrothermal model

The abstracted hydrothermal model in TSPA-93 is based on using the information obtained from the detailed thermal design calculations as adjustments in the composite-porosity and weeps models.

10.4.1 Dryout volume and fraction dry

Dryout volume and fraction dry have impacts on performance assessment calculations in terms of both the amount and behavior of displaced and diverted water. For TSPA-93, flow from displaced and diverted water is modeled as follows: For a given time step, the rate at which water is displaced (Q_d) is determined using the predicted rate of increase in dryout volume. This quantity is estimated as the product of the volumetric water content of the affected region (θ) and the change in the volume encompassed by the boiling isotherm (V_{dry}):

$$Q_d = \theta \frac{\Delta V_{dry}}{\Delta t}, \tag{10.1}$$

where t is the time step. The volumetric water content is the product of the porosity (n) and the ambient liquid saturation (S): $\theta = nS$. For the composite-porosity model, θ is calculated from the porosity sampled for Topopah Spring welded (unit 3, TSw) tuff and from the matrix saturation calculated for TSw as the initial condition. θ is only calculated at the beginning of a TSPA run, and is not changed if a climate change occurs during the thermal perturbation. For the weeps model, where flow in the matrix is not considered, no calculated or sampled matrix properties are available. Therefore, values of $n = 0.1$ and $S = 0.65$, with $\theta = 0.065$ are used. In the future, sampling from distributions of measured values of n and S may be possible.

For TSPA-93, it is assumed that the displaced water is either removed from the problem when the entire repository is within the dryout zone (i.e., shed when fraction dry = 1), or it is added to the groundwater flowing through parts of the repository that are outside the dryout zone. The groundwater flux through the unprotected part of the repository (q_{eff}) is thus calculated as the influx over the entire repository (q_{in}) concentrated in the unprotected part, plus the displaced water moved through the unprotected part:

$$q_{eff} = q_{in} \frac{A_{rep}}{A_{wet}} + \frac{Q_d}{A_{wet}}, \tag{10.2}$$

where A_{rep} is the area of the entire repository, and A_{wet} is the area of the unprotected part of the repository—the area of the repository outside the boiling isotherm ($A_{wet} = A_{rep}\text{-}A_{dry}$, where A_{dry} is the area of the repository within the boiling isotherm, and thus, the fraction dry is $f_{dry} = A_{dry}/A_{wet}$).

The composite-porosity model and the weeps model use the flux through the unprotected part of the repository to determine the hydrologic parameters for the source term and the transport model. As the boiling isotherm expands and contracts over time, both the effective area of the repository (A_{wet}) and the flux (q_{eff}) change. For the weeps model, a complicated scheme is implemented that allows some of the weeps to remain constant, based on an area-weighted average of the new flux, while adding or subtracting weeps to newly unprotected or protected areas. A similar scheme has been devised for the composite-porosity model.

The above model implementation rests on several major assumptions. A statement and description of these assumptions is presented below.

1. **The volume encompassed by the 96°C isotherm defines the dryout zone.**
This assumption has a number of corollaries. First, pressures must remain fairly constant and near atmospheric in the boiling region. Ramirez *et al.* (1991) did not see a significant increase in pressure during their G-tunnel heater test. They speculated that as long as the rock was well fractured, boiling pressures would not build. Pressures could build within matrix blocks, leaving pockets of liquid water, but this water is not expected to be mobile. Second, heat pipes are not significant. Heat pipe structures (Pruess *et al.*, 1990) can extend far into the boiling region and are probably responsible for much of the elevated saturations that intrude within the boiling isotherm in calculations performed by Buscheck and Nitao (1993). Heat pipes or refluxing could significantly increase the amount of water contacting containers, especially at temperatures around boiling. However, it is not certain that heat pipes will develop in welded tuffs, except perhaps where liquid water is mobile in fractures. Results of the G-tunnel heater test conducted by Zimmerman *et al.* (1986) could not be explained entirely by heat pipes, specifically the dryout zone near the heater could not be explained. For TSPA-93, heat pipes are neglected, although it is acknowledged that future work may need to address this issue.

2. **A localized temperature above boiling around individual containers outside the 5-m boiling isotherm is not a barrier to flow.**
In its simplest form, this assumption questions whether the local heat capacity of a small volume of rock is capable of sufficiently overcoming the heat of vaporization of inflowing water. In reality, this question is not limited to containers outside the 5-m boiling isotherm; flow instabilities may develop anywhere over the repository and could potentially penetrate the boiling isotherm. For TSPA-93, it has been arbitrarily decided to allow flow to containers outside the 5-m boiling isotherm regardless of local environment. Flow is assumed to be effectively halted within the dryout volume, and the encompassed containers are considered protected from contact with liquid water.

3. **The 5-m boiling isotherm is the defining boundary between protected and unprotected containers.**
For protected containers, temperature-dependent dry-oxidation corrosion and juvenile failures are recognized. Steam corrosion has not been implemented in the source term. For unprotected containers, all aqueous-corrosion processes, temperature-dependent and flux-dependent, are recognized. For failed containers, temperature-dependent uranium alteration takes place (temperature-dependence of radionuclide solubility, although implemented in the YMIM source model, is not being used in this

TSPA—see Chapter 13). Only gaseous releases are allowed from failed, protected containers; aqueous and gaseous releases are allowed from failed, unprotected containers.

4. **All the water vapor within the dryout zone is displaced upward.**
   This assumption is contradicted somewhat by Pruess and Tsang (1993), who indicated that the vapor moves away from the repository both upward and downward. There is a possibility, however, that a more concentrated thermal loading and greater bulk permeability could enhance the thermal buoyancy of the vapor and cause more of it to ascend. Furthermore, allowing all the water to condense above the repository should eventually cause increased liquid flux through the repository, and thus should be conservative.

5. **All of the displaced water condenses above the repository; none of it escapes the mountain to the atmosphere.**

6. **The rate at which water is displaced matches the rate that the dryout zone grows.**
   When the dryout zone reaches its maximum extent, it is assumed that no more water is displaced. No allowance is made for the continual refluxing of steam for the entire duration of the thermal perturbation. That is, water drawn up as steam from below the repository is not modeled for the entire duration of the thermal perturbation, only during the expansion of the dryout zone. The way in which thermal buoyancy is curtailed is not conservative. It is possible to estimate the additional vapor movement, but it might not be necessary. Pruess and Tsang show that this assumption could be reasonable, because in their simulations the water vapor below the repository moves downward.

7. **All of the displaced water is immediately shed (i.e., within a time step).**
   No condensation cap is allowed to form. The displaced water is assumed to flow through parts of the repository that are outside the boiling isotherm predicted at 5 m above the modeled repository.

8. **As the boiling isotherm contracts, the groundwater flux immediately returns to normal.**
   That is, we are assuming that there is no enhanced matrix imbibition occurring to create an extended-dry scenario. It is argued that the extended-dry concept could be an artifact of the equivalent-continuum model (composite-porosity model) that is be-

ing used by Buscheck and Nitao (1992 and 1993). The equivalent continuum model does not allow flow in the fractures until the matrix is saturated, and therefore the water can only return to the dryout zone through the matrix (i.e., much slower than the receding boiling isotherm would allow). Buscheck and Nitao (1992 and 1993) offered justification of the extended-dry scenario through the argument that water flowing in fractures would show an exaggerated propensity to be in the matrix, presumably because the matrix is so dry. However, no evidence is offered for this effect, and unpublished calculations performed by Gauthier at SNL indicate that the imbibition rate into the tuff matrix is relatively independent of the degree of saturation of the matrix. Pruess and Tsang (1993) argued similarly that matrix/fracture disequilibrium will exist in the condensation zone. Indeed, Buscheck and Nitao (1993) indicated that the equivalent-continuum model might not be appropriate when it predicts *hydrothermal perching*. Thus, in the interests of conservatism, TSPA-93 allows flow to return to the dryout zone at the same rate that the boiling isotherm retreats. For consistency, the amount of water that reaches the repository should be reduced by the amount of water that does imbibe into the matrix. One estimate of this equilibration flux is as follows:

$$q_{eff} = q_{in}\frac{A_{rep}}{A_{wet}} + \frac{1}{2}\frac{Q_d}{A_{wet}}, \tag{10.3}$$

where the term $\frac{1}{2}\frac{Q_d}{A_{wet}}$ indicates that only the upper half of the dryout zone is reducing the flux before it contacts the repository. TSPA-93 was unable to implement this rewetting adjustment; however, it is recommended for consideration in the next iteration.

10.4.2 Container wall and fuel-rod temperatures

For TSPA-93, container wall and fuel rod temperatures are used explicitly only in the source calculations. The YMIM source-term model uses temperature in the calculation of container corrosion, uranium alteration, and radionuclide dissolution (Chapter 13). Note that container corrosion and uranium alteration are parameters that were found by Wilson (1993) to be significant to radionuclide releases. It is not practical to calculate temperature histories for all containers. Therefore, TSPA-93 uses the temperature histories of center and edge containers and interpolates for histories of containers that lie between these representative packages.

10.5 Conclusions

Detailed thermal calculations performed in support of TSPA-93 are presented in terms of a simplified model of hydrothermal effects based on an abstraction of expected processes at Yucca Mountain. The abstract model is primarily based on the location of, and the volume encompassed by, the boiling isotherm. The model uses this information to determine the following: (1) the containers that are protected from groundwater flow and how long they are protected, (2) how much water is displaced and diverted around the repository or to the parts of the repository that are not protected. The model also uses container-temperature and rod-temperature information in the calculation of the source term.

The abstracted model is not a process model. A number of hydrothermal effects are being neglected: the potential instabilities in the system, the refluxing of large amounts of water through the repository, loss of water as vapor from the system, etc. However, the model does address much of the supportable, anticipated behavior that is relevant to the performance of a thermally active repository, and it does so in a manner considered to be conservative.

From the standpoint of the cases chosen for detailed thermal modeling, it must be recognized that these are only four of many representative cases. The layout and waste stream chosen are ideal in the sense that they homogenize many important features of the potential repository. For example, a waste stream that has a wider variation in characteristics could result in a boiling surface that is not predominantly convex everywhere above the potential repository. If depressions in the boiling surface were to exist, there is a possibility that displaced water or episodic events could concentrate in these areas and establish a self-supporting intrusion into the boiling surface. Similarly, since the repository resides in a natural geologic setting, it is unrealistic to assume that all the identified area will be acceptable for waste emplacement. Some regions may need to be abandoned, resulting in a divided heat source that may exhibit weak or no coalescence of the boiling isosurfaces. These two examples point out that the thermal design calculations completed in support of TSPA-93 represent only a starting point in the integration of thermal design efforts into total-system performance assessment. Additional calculations addressing the primary issues of repository thermal design must be assessed prior to making any definitive conclusions regarding the impact of thermal loading on total-system performance assessment.

Chapter 11
Saturated-Zone Models

(Barr, Shannon, Wilson)

The saturated zone underlying Yucca Mountain is a significant part of the pathway for radionuclides traveling from the repository horizon out to the boundaries of the regulated area. Understanding of the saturated zone has increased since models were developed for prior performance assessment analyses. The TSPA-91 exercise used a 2-D representation of the saturated flow system built on models of Czarnecki (1985) and Czarnecki and Waddell (1984). New interpretations of the cause of the large hydraulic gradient in the saturated zone northwest of the site (Fridrich *et al.*, 1991; Sinton, 1989; Czarnecki, 1989) suggest that the saturated flow system may only be adequately represented locally in three dimensions.

These new interpretations are based on two models, called the non-diversionary model and the diversionary model, that best fit the available information concerning the existence of the large hydraulic gradient region in that area. For the non-diversionary models, all fluid flowing within the tuffaceous units northwest of the large hydraulic gradient region continue flowing in the tuffs as the fluid moves to the southeast. In the diversionary model, some portion of the fluid flowing in the saturated tuffs flows abruptly downward, in the area coincident with the high gradient region, and then continues to flow to the southeast within the Paleozoic carbonate aquifer that underlies the tuffs. Both model types are examined in this report, however, more emphasis is placed on the non-diversionary models.

The purpose of this analysis is to provide two calibrated models that represent two alternate conceptual models of the saturated flow system, consistent with current site data. Numerical experiments are used to determine the effects on the flow system induced by the introduction of four geologic features. The exact values of the hydraulic properties associated with these four features are currently unknown, however, values thought to be appropriate are inserted for the purpose of the exercise. If, indeed, the introduction of the features produces a better fit to current data, subsequent guidance to site characterization will be to test the validity of the assumptions associated with the features.

Although a 3-D geological representation of the potential site is being developed (e.g., Wittwer *et al.*, 1993, for the unsaturated zone), it is not yet available for use in TSPA-style analyses. Even if the model were available, the scale would be too large for this exercise. For the purposes of this analysis, we construct a 3-D model for the region

which preserves most of the geologic features expected to be important to the model and allows some exploration of the effects of modeling in three dimensions. It should be noted that this model is not directly related to the unsaturated zone model developed in Chapter 6.

11.1 Three-dimensional geological model

The saturated zone is modeled here as an approximately 8 km x 8 km x 200 m confined system. The modeled region extends far enough laterally to include the region of the high hydraulic gradient to the northwest and the 5-km limit for the accessible environment down gradient.

11.1.1 Model Thickness

The three-dimensional block is divided into four layers, each 50 m thick. There are several technical arguments indicating that the mixing depth can be represented using a block thickness on the order of 200 to 300 m for this model. USGS tracer injection tests (e.g., Lobmeyer *et al.*, 1983) show considerable inhomogeneity over the tested depths, i.e. in excess of 1,000 m. In each well, evidence of one or more zones with significant differences in hydraulic properties is encountered within the first 200 meters below the water table. These zones might then be expected to divert flow at different levels in different locations, thus inducing mixing within that 200 m layer. In addition, data from well P-1 shows an aquitard at about 1100 m depth, sufficiently nontransmissive to support a 20-m head difference across the aquitard (Craig and Robison, 1984). This implies that, if the aquitard is continuous, the problem can be truncated vertically by a horizontal plane above the aquitard. This would argue that 400 meters is a maximum thickness for the block. However, it should be noted that there are very few wells that sample to this depth, so the continuity of the aquitard is not known.

Another argument for the 200 meter thickness of the block can be based on the proposed effect of the thermal output of the potential repository. As the repository heats the surrounding rock, it is possible that a thermally driven convective circulation pattern may develop. Preliminary studies indicate that the thermal effects will probably be limited to a few hundred meters below the repository. When the convection cells form, it is probable that the cells will be confined to individual layers, as opposed to maintaining a cell across layers with differing hydrogeologic properties. Thus, the cell height would be about the same as the thickness of the geohydrologic units, also on the order of 100 to 300 meters.

Superimposed on the thermal effects may be geochemical effects. Because of the temperature-dependent solubility of various rock components, the warm water circula-

tion may cause dissolution and redeposition of certain mineral phases in the saturated rock units. Investigation of the effects of this phenomenon would require a model thick enough to include the entire zone of thermal disturbance.

Finally, computational time becomes excessive for a much thicker model. However all of these arguments for the 200-m mixing depth must be tested using additional numerical and experimental investigations.

11.1.2 Model Stratigraphy

This model uses work done at the USGS on the potential causes of the large hydraulic gradient in the saturated zone. Fridrich *et al.* (1991) has constructed a bent cross section from wells G-2 to P-1 and has provided a plan view of units intersected by the water table (Figure 11-1). This information allows us to superimpose on the block a representation of where the geologic units are expected to intersect the water table. Due to the 5° to 6° east-southeasterly dip of the Cenozoic units underlying Yucca Mountain, five stratigraphic units are known to intersect the water table at various locations within the block. These five units are the Topopah Spring Member of the Paintbrush Tuff, the Calico Hills Tuff, and the Prow Pass, Bullfrog, and Tram Members of the Crater Flat Tuff. Each successive vertical layer of the block is generated by translating a gridded version of the locations of these five units at the water table about 591 m eastward for each additional 50 m in depth. In effect, the sloping units are constructed of sets of contiguous blocks 80 to 200 m x 80 to 200 m x 50 m. Individual units constructed in this fashion are plotted in three dimensions to check continuity. Figure 11-2 shows the distribution of the Topopah Spring unit in the model. The absence of this unit from some portions of the modeled volume may be inferred from Figure 11-1.

This translation scheme to construct a 3-D representation of this region has several difficulties. It may introduce artificial geologic features. It ignores changes that occur across faults and propagates other changes that make it appear as if units pinched out or suddenly appeared. As a result, this is a first-order approximation of the more sophisticated 3-D geological model that the USGS will eventually provide, however, it is probably a reasonable representation between the Solitario Canyon fault and the Bow Ridge fault (Figure 11-3) for the thickness of this model. The repository and major faults are located as indicated in Figure 11-4.

11.2 Calibration of the non-diversionary model

The STAFF3D (version 2.5) computer code is the tool used in this calibration exercise (Huyakorn *et al.*, 1992). It is a finite-element code that simulates flow and transport in fractured porous media. The 3-D modeled region consists of four layers, each contain-

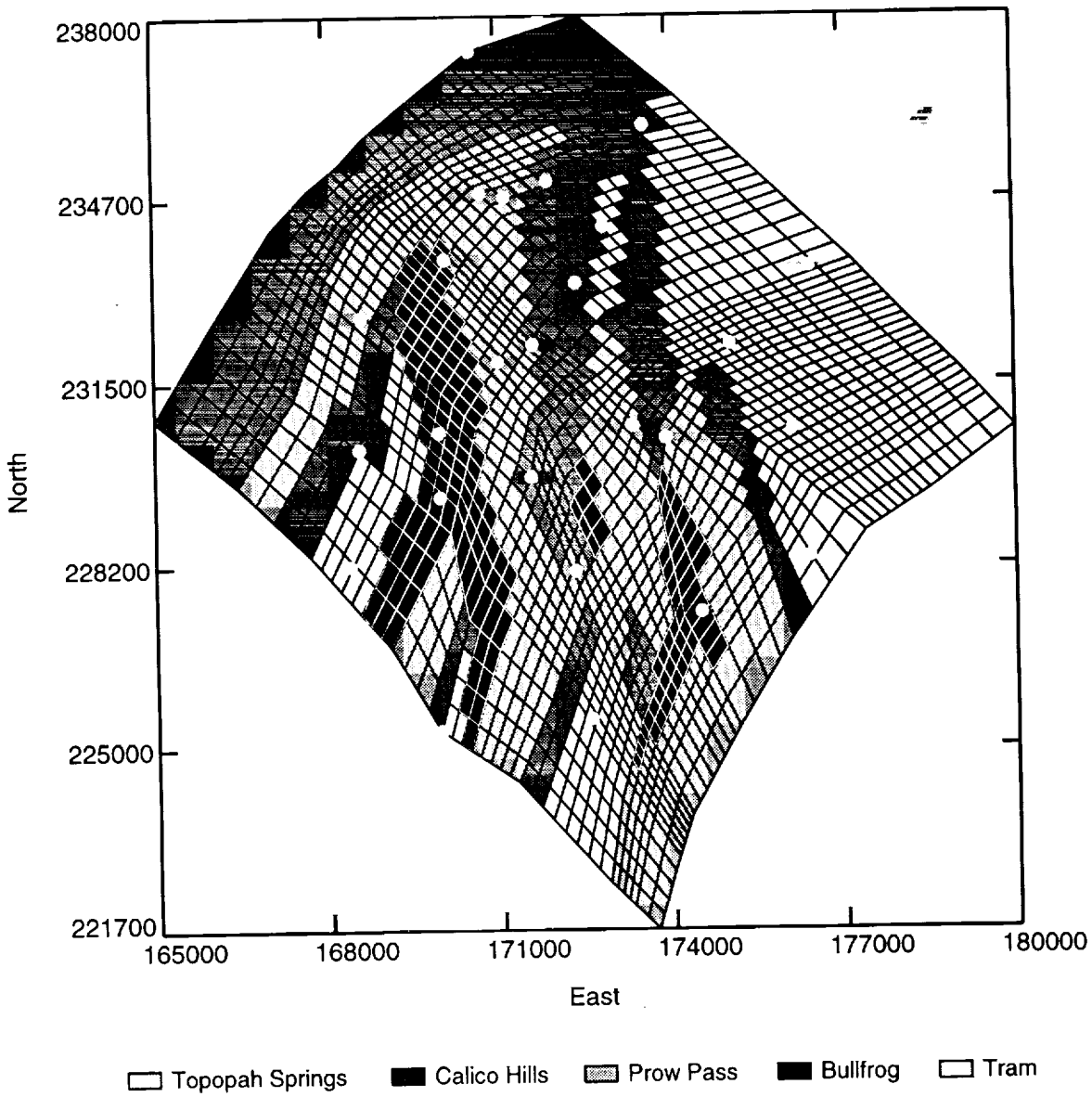

Figure 11-1. Geologic units intercepted by the water table (interpreted from Fridrich *et al.*, 1991). Stars indicate well locations. Ordinate and abscissa values are Nevada state plane coordinates in meters.

ing 1,804 elements, and five planes, each with 1,890 nodes bounding the elements, for a total of 9,450 nodes and 7,216 elements. For the region modeled, there are 28 wells that provide data on water-table elevations (Ervin *et al.*, 1993a; Robison, 1984). Three of the wells occur on the boundary of the grid. Two wells drilled in the area, WT-18 and G-1, provide questionable data and, therefore, are not used in the calibration. In addition to the well data, regional modeling (Czarnecki, 1985; Czarnecki and Waddell, 1984) establishes the general potentiometric framework into which this more localized model fits.

Constant head boundary conditions for the entire boundary are assigned consistent with the three boundary wells, the regional potentiometric surface (Czarnecki and Waddell, 1984) and the local potentiometric surface (Ervin *et al.*, 1993a) (Figure 11-5). Experimental heads are generally compound values (vertical head distributions are not established), so the same head assignments are made for boundary nodes differing only by elevation.

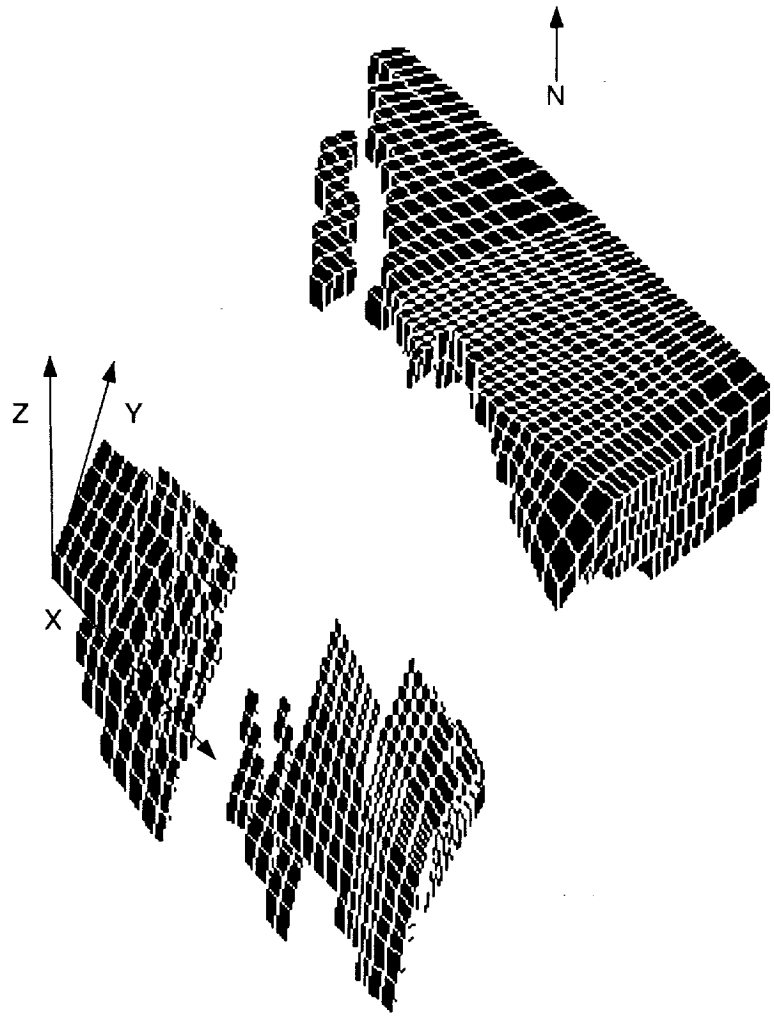

Figure 11-2. A three-dimensional view of the Topopah Spring unit below the water table, as constructed by translation.

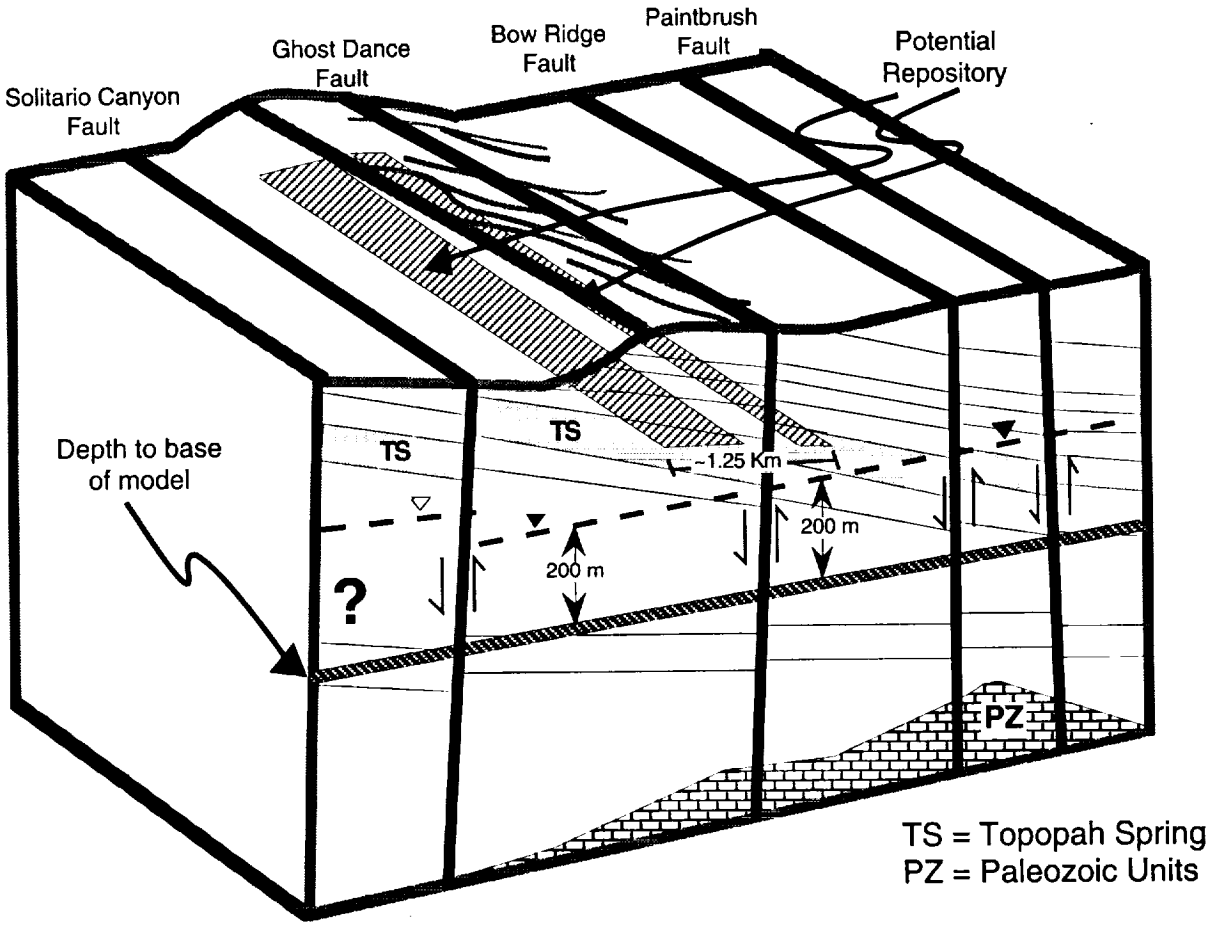

Figure 11-3. A schematic diagram showing the three-dimensional relationship among the potential repository, the stratigraphic units, and the major faults. Also shown is the depth of the base of the saturated-zone model developed for TSPA-93.

For the non-diversionary model simulations, calibration was first attempted without including any faults. Values for hydraulic conductivities, K, are systematically varied in the five geologic units over the known range of values provided in Schenker *et al.* (1994). Calibration (i.e., match to measured heads) is for a steady-state flow system, with each geologic unit assumed to be isotropic. No fracture data are available so each unit is treated as an effective porous medium.

Neither altering K over a large scale nor making any small-scale changes of the boundary conditions provided a reasonable calibration. We limit ourselves to large-scale manipulation of K (generally more than 200 elements) because the scale of deposition of the units is larger than this and smaller-scale alteration suggests more data are

used than actually exist. Basically, there are a number of Wells: H-1, WT-4, WT-10, and WT-7 (along Drill Hole Wash) and well H-5, that have head values which are difficult to match.

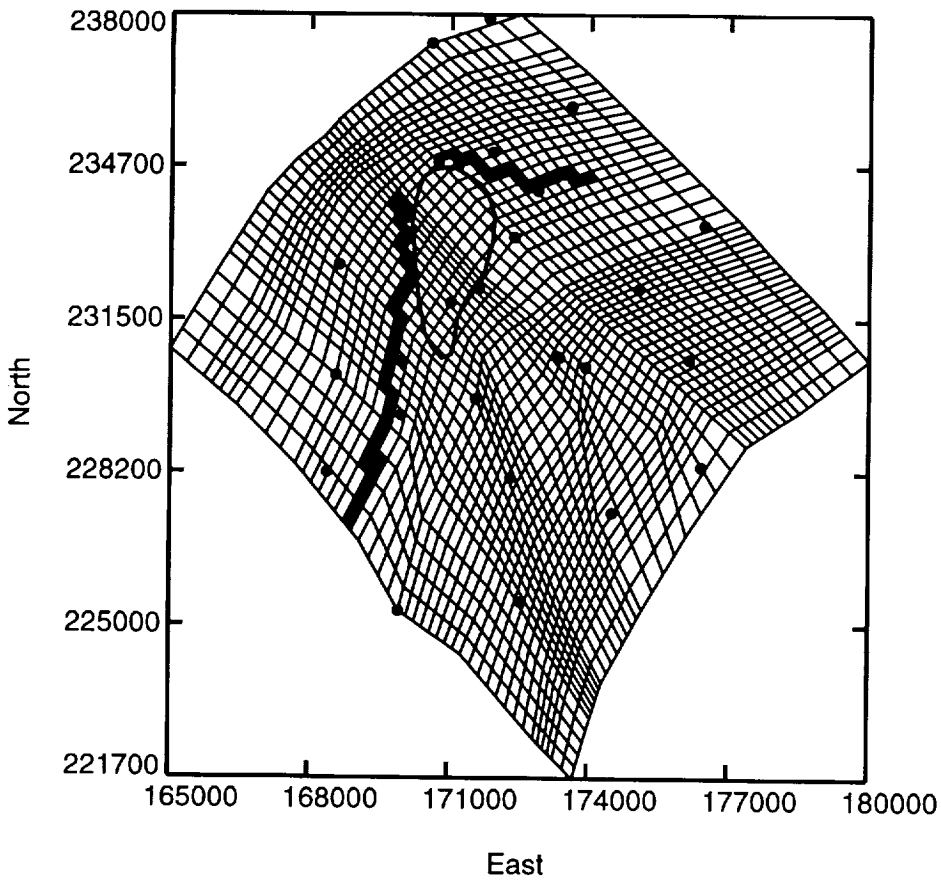

Figure 11-4. The approximate location of the potential repository, Solitario Canyon Fault Zone, and Drill Hole Wash Fault Zone on the calculational grid of Figure 11-1. Coordinates are Nevada state plane coordinates (in meters).

To improve the fit to the well data, we introduce two geologic features known to exist, but with unknown hydraulic properties; the fault zone along Solitario Canyon (SCF) and the fault presumed to be present along Drill Hole Wash (DHWF) (Scott and Bonk, 1984) (Figure 11-4). Addition of either feature causes a partial correction to the calibration. The SCF affects primarily those head values west of the SCF zone and the DHWF affects those values to the east and north of the DHWF zone.

Experiments have been performed assigning K values to each feature that are either more conductive or less conductive than the surrounding rock. Making the fault zones less transmissive by two or more orders of magnitude than the surrounding rock produces a much better fit to data, except at well H-5. All attempts at calibration to well

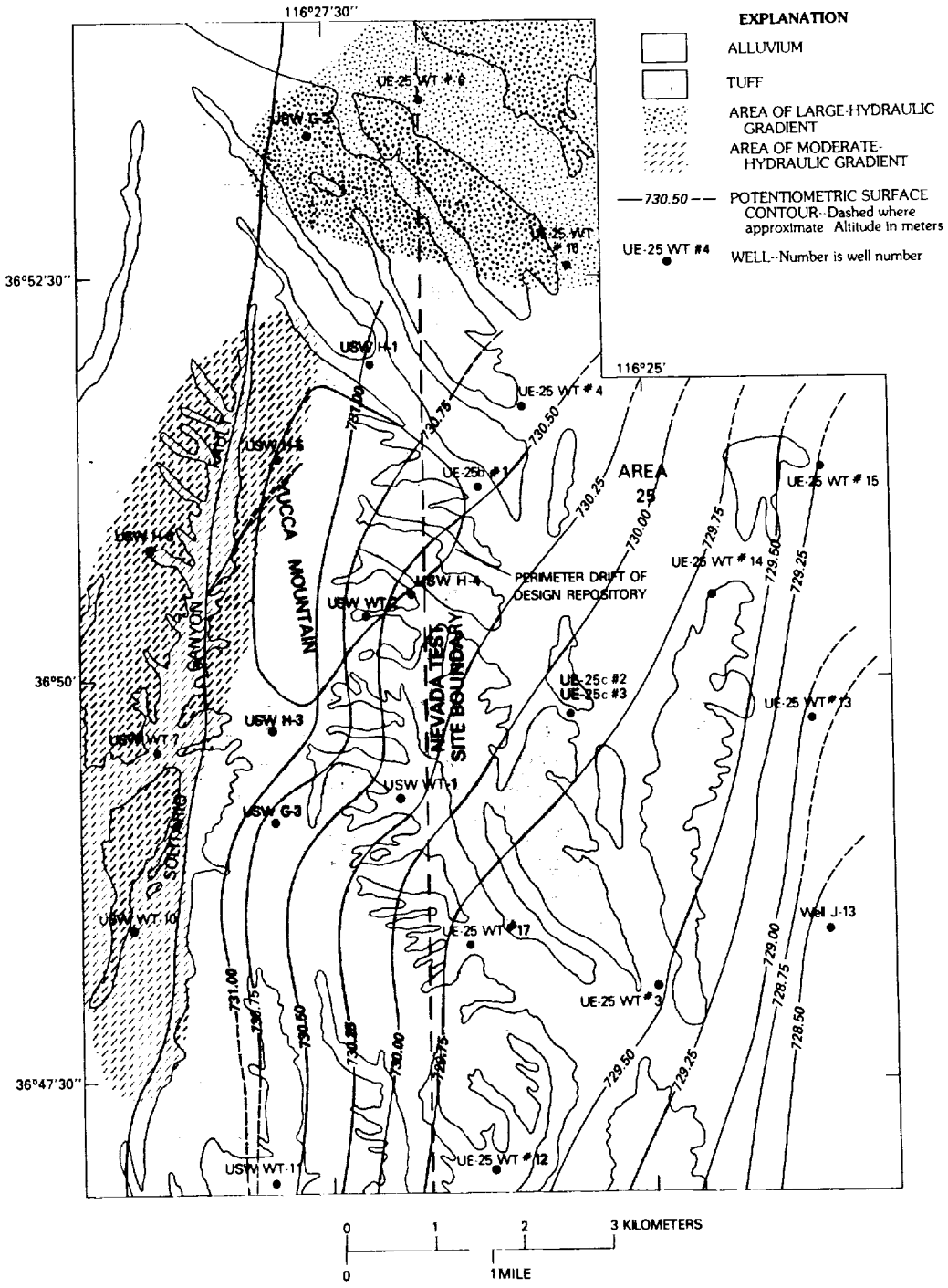

Figure 11-5. The revised potentiometric surface map from Ervin *et al.* (1993a).

H-5 values results in head values that are too low. Upwelling was added at the bottom of the model at nodes below H-5 to compensate for low calculated values. This is done by fixing a value of 820 m for the head at the bottom boundary (200 m below the water table) at four nodes below H-5. Although there is no specific information concerning upwelling at this location, the presence of elevated temperature measurements at the water table along the southern portion of the SCF have been interpreted as resulting from upwelling (Sass *et al.*, 1987). H-5 is believed to located along a splay of the SCF (Ervin *et al.*, 1993b); therefore, there is some justification for including the effect of upwelling in this area. The actual values of K used in calibration are listed in Table 11-1. The calibration itself, along with well locations and Nevada state plane coordinates (in meters) are shown in Table 11-2.

The potentiometric surface associated with this calculation is shown in Figure 11-6. The result is a self-consistent 3-D model which attempts to honor geologic information in order to produce a velocity field for further calculations.

Table 11-1. Parameters and boundary conditions used for calibration, non-diversionary model.

	Hydraulic Parameters			
Unit (subunit)[a]	Porosity[b]	K_x (m/sec)	K_y (m/sec)	K_z (m/sec)
Topopah Spring (1)	0.20	6.00×10^{-5}	6.00×10^{-5}	6.00×10^{-5}
Topopah Spring (2)	0.20	2.00×10^{-5}	2.00×10^{-5}	2.00×10^{-5}
Calico Hills (1)	0.20	1.25×10^{-6}	1.25×10^{-6}	1.25×10^{-6}
Calico Hill (2)	0.20	5.00×10^{-6}	5.00×10^{-6}	5.00×10^{-6}
Calico Hills (3)	0.20	2.50×10^{-8}	2.50×10^{-8}	2.50×10^{-8}
Prow Pass (1)	0.20	5.00×10^{-5}	5.00×10^{-5}	5.00×10^{-5}
Prow Pass (2)	0.20	5.00×10^{-5}	5.00×10^{-5}	5.00×10^{-5}
Bullfrog (1)	0.20	5.00×10^{-4}	5.00×10^{-4}	5.00×10^{-4}
Bullfrog (2)	0.20	5.00×10^{-4}	5.00×10^{-4}	5.00×10^{-4}
Tram	0.20	2.00×10^{-7}	2.00×10^{-7}	2.00×10^{-7}
Solitario Canyon fault	0.20	6.00×10^{-7}	6.00×10^{-7}	6.00×10^{-7}
Drill Hole Wash fault	0.20	3.00×10^{-11}	3.00×10^{-11}	3.00×10^{-11}
Element below H-5	0.20	1.00×10^{-11}	1.00×10^{-11}	1.00×10^{-11}

[a] Units are broken up into large subunits consistent with the expected scale of depositional changes. Hydraulic conductivities K_i are specified in three orthogonal directions and are assumed to be isotropic.

[b] Porosity is the mean of values for the water-table units in Table 7-11.

11.3 Transport calculations using the non-diversionary model

STAFF3D, the code used for flow field calibration, is also capable of performing transport calculations. Accordingly, in order to provide some insight for more extensive transport calculations, contaminant movement from sources located at the water table

are calculated. Use of this code to perform a complete suite of transport calculations is prohibitive because of the run long times required for each calculation. The abstracted calculations are discussed in the last section of this chapter.

Table 11-2. Comparison of calculated heads to data for heads measured in various wells.

Well	Node Number	Node at Water Table	Measured Head (m)	Calculated Head (m)	Residual
WT-11	23	7583	730.72	730.70	-0.02
WT-10	59	7619	775.92	773.13	-2.79
WT-7	191	7751	775.70	774.50	-1.2
G-3	243	7803	730.56	731.76	+1.2
WT-12	305	7865	729.52	730.99	+1.47
H-3	376	7936	731.72	732.35	+0.63
H-6	504	8064	775.96	777.19	+1.23
WT-1	518	8078	730.4	731.25	+0.85
WT-17	524	8084	729.64	730.92	+1.28
WT-2	738	8298	730.71	732.54	+1.83
H-5	912	8472	775.47	774.30	-1.17
WT-3	940	8500	729.57	730.05	+0.48
H-4	964	8524	730.33	732.68	+2.35
C-3	1018	8578	730.10	730.91	+0.81
C-2	1018	8578	729.95	–	–
P-1	1066	8626	730.00	730.47	+0.47
J-13	1169	8729	728.45	729.17	+0.72
G-1	1226	8786	754.20[a]	738.62	–
B-1	1234	8794	730.66	733.61	+2.95
H-1	1272	8832	730.95	737.01	+6.91
WT-18	1407	8967	730.80[a]	737.86	–
WT-13	1387	8947	728.98	729.13	+0.15
WT-4	1456	9016	730.70	734.07	+3.37
WT-14	1512	9072	729.71	728.84	-0.87
G-2	1576	9136	1029.00	1029.00	0.0
WT-16	1765	9325	738.32	734.92	-3.4
WT-6	1801	9361	1035.10	1035.10	0.0
WT-15	1822	9382	729.24	729.46	+0.22

[a] These measured heads are questionable; comparisons to calculated heads were not made.

The problem setup for the STAFF3D calcuations is a follows. Since the water table intersects three different units below the potential repository, trial sources are located at four adjacent nodes in the Prow Pass, Bullfrog, and Calico Hills in each of three separate calculations for transport in these effective porous media. A "fence" of selected nodes ~5 km from the repository boundary (representing the boundary to the accessible environment) is monitored for the first arrival of contaminants. This information is then used to calculate breakthrough curves (Figure 11-7). These calculations assume unit concentration sources located at the four nodes throughout the calculation (4,700 years). The transport retardation factor is set to 1, and longitudinal and transverse

dispersivities are set to 10^3 and 10^2, respectively. (Since STAFF3D uses Darcy fluxes, the dispersivities cited here are related to those used elsewhere in the text by division by the porosity, 0.2). In the absence of experimental measure, dispersivity values are chosen to ensure convergence. The retardation factor equal to 1 describes a conservative tracer—one that travels with the water and describes the fastest arrival of tracer. Locations of the sources (in the Calico Hills, the Prow Pass, and the Bullfrog) are shown in Figure 11-8. The resulting breakthrough curves are displayed in a series of plots in Figure 11-9 for the source in the Prow Pass, in Figure 11-10 for the Bullfrog, and in Figure 11-11 for the Calico Hills. These figures plot breakthrough along the fence line for each plane of nodes. Generally, steady state is reached in 1,000 to ~5,000 years; however, not all nodes reach a steady state by the end of the calculation. Time to reach steady state is not the same for different layers and some layers exhibit considerable structure along the fence line.

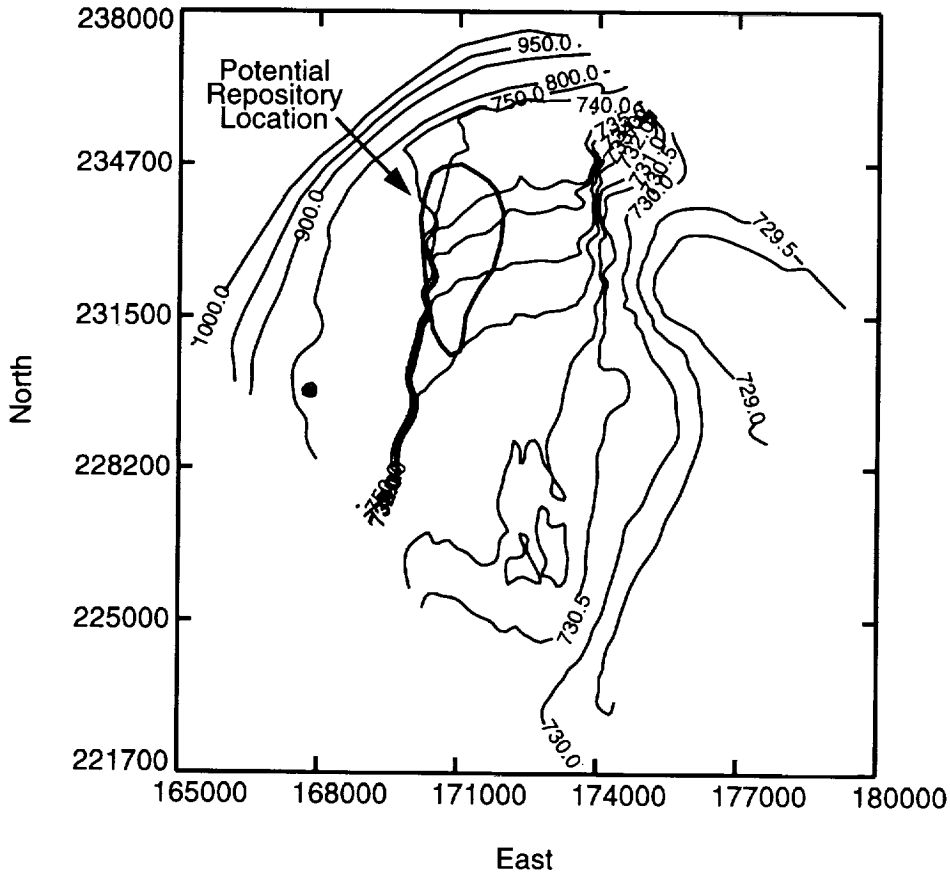

Figure 11-6. The potentiometric surface map based on calculated values of head for the case described in Table 11-2. Contour labels are meters above mean sea level. Coordinates are Nevada state plane coordinates (in meters).

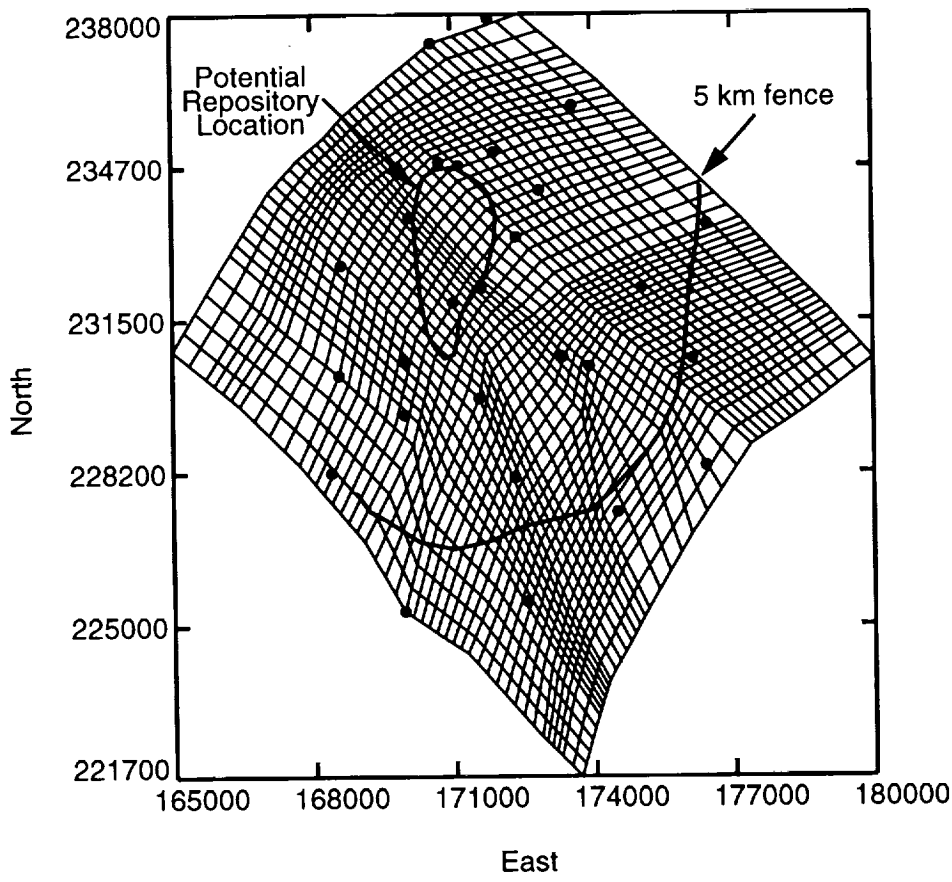

Figure 11-7. Approximate location of the 5-km fence at which breakthroughs are calculated. Coordinates are Nevada state plane coordinates (in meters)..

The various locations of the source generate somewhat different structures of breakthrough curves. However, backwater nodes, that is those nodes with little contaminant, are preserved for all three source locations. It appears that this model generates a multi-lobed contaminant plume different for different depths below the water table because of the heterogeneous geologic structure. Plume development is shown more explicitly in the series of Figures 11-12 through 11-14, for the Prow Pass, Bullfrog, and Calico Hills units, respectively. The first figure in each series (11-12a, 11-13a, and 11-14a) display the plume at the water table. The second (11-12b, 11-13b,and 11-14b) and the third (11-12c, 11-13c, and 11-4c) show the plume 100 m and 200 m below the water table, respectively. The structure of the plume is smoothed because of the choice of plot intervals.

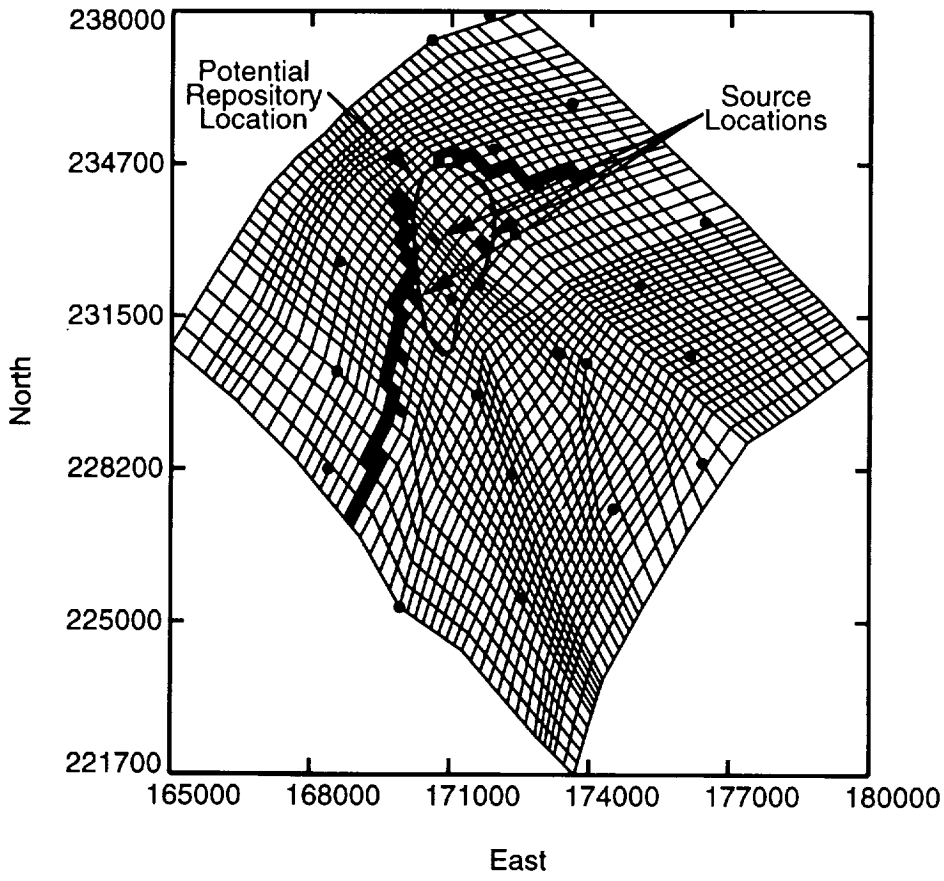

Figure 11-8. Locations of the three contaminant sources for transport calculations, shown as filled elements. Coordinates are Nevada state plane coordinates (in meters).

11.4 Calibration of the diversionary model

The 3-D non-diversionary model used in the previous analysis depended on mapping and interpretation of one alternative conceptual model of the saturated-zone flow system (Fridrich *et al.*, 1991). A different conceptual model is discussed in this section.

This alternative model assumes that the large hydraulic gradient region is controlled by a drain which diverts fluid from the tuff aquifers down to the carbonate aquifers in a region just north of the potential site (roughly E-W at the level of wells G-2 and WT-6). Unpublished 2D calculations done on a cross section selected from Fridrich *et al.* (1991) established that the drain model is a feasible alternative. This 2-D cross section was 2,500 m in thickness, considerably thicker than the 3-D models presented here. To simulate the flow field in the presence of the drain, the 3-D model is truncated (vertically) at 200 m below the water table and approximates the drain by specifying

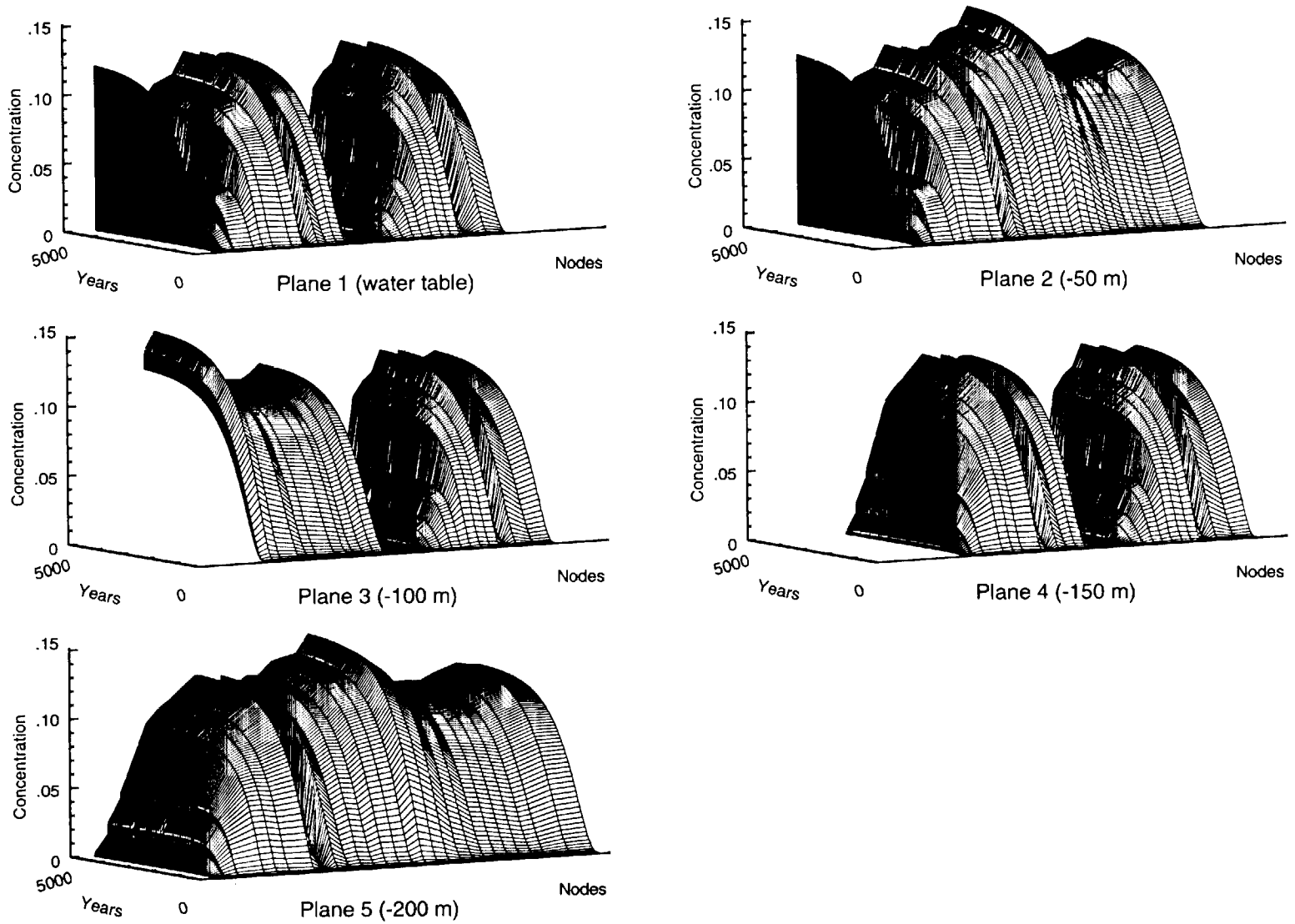

Figure 11-9. Breakthrough curves along the 5-km fence for a source of unit concentration located at the water table in the Prow Pass. Each set of curves is for a different depth below the water table.

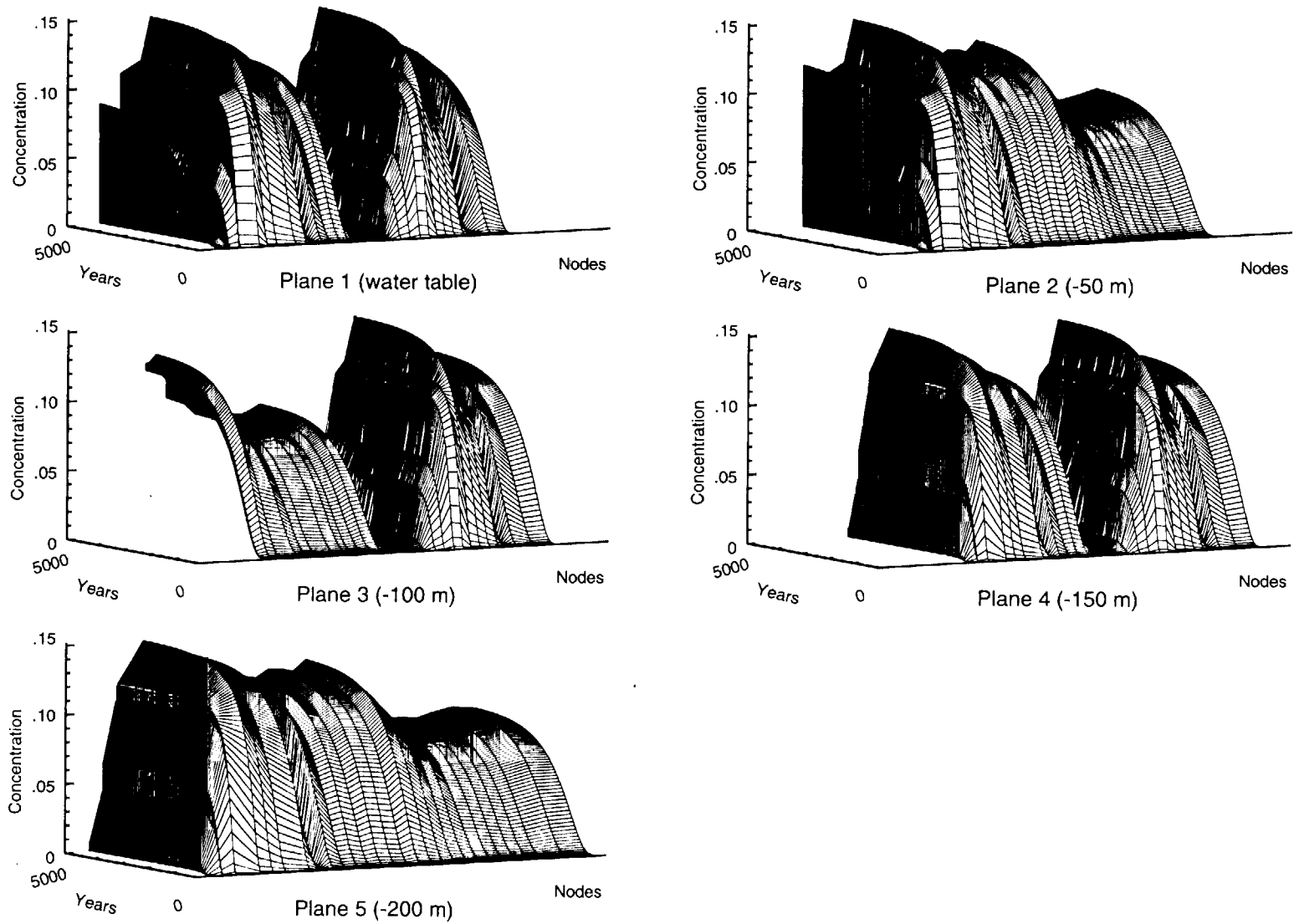

Figure 11-10. Breakthrough curves along the 5-km fence for a source of unit concentration located at the water table in the Bullfrog. Each set of curves is for a different depth below the water table.

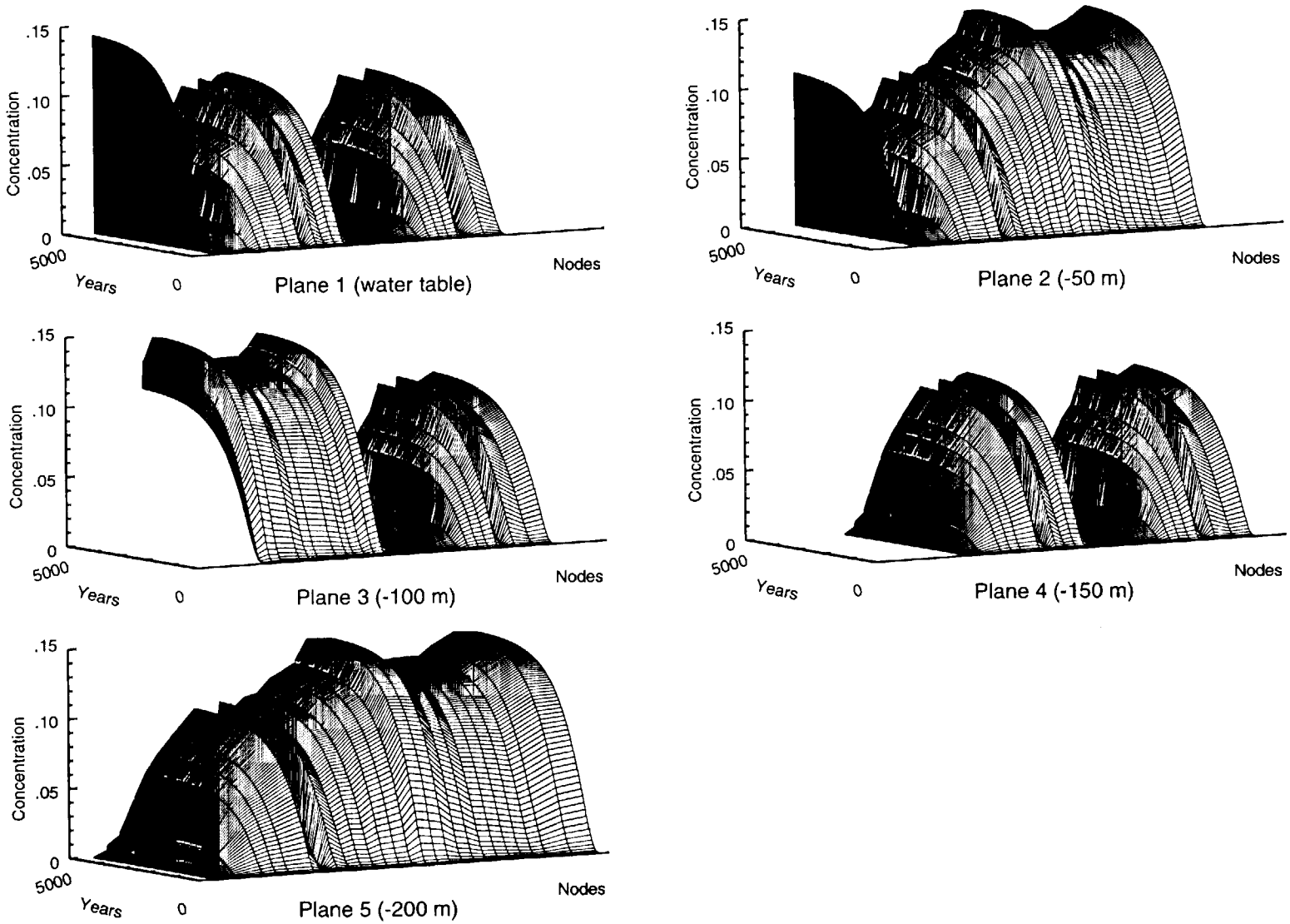

Figure 11-11. Breakthrough curves along the 5-km fence for a source of unit concentration located at the water table in the Calico Hills. Each set of curves is for a different depth below the water table.

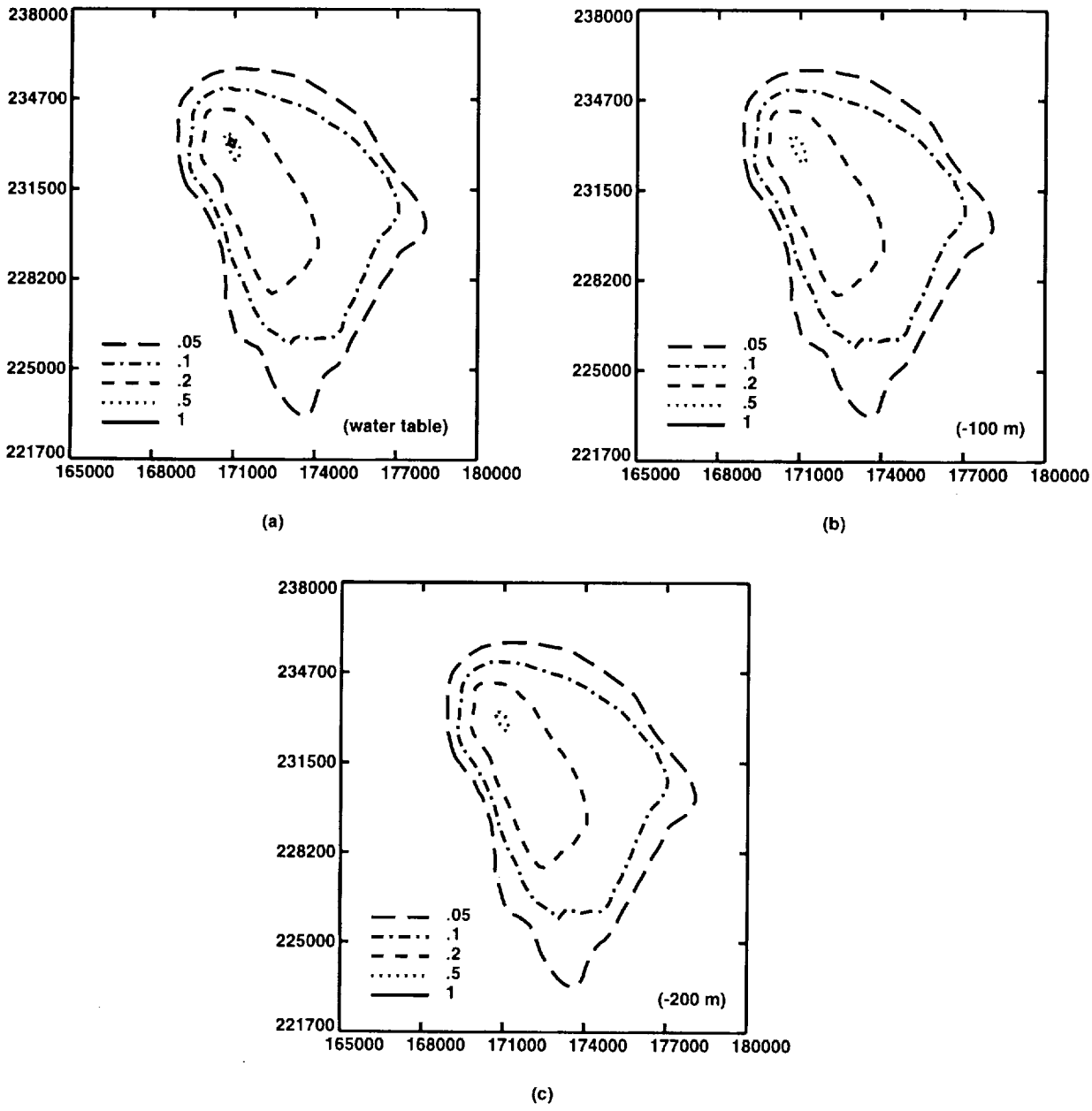

Figure 11-12. Concentration contours at the water table at 4,700 years for a continuous source of unit concentration, with retardation = 1, located in the Prow Pass at the water table. Coordinates are Nevada state plane coordinates (in meters).

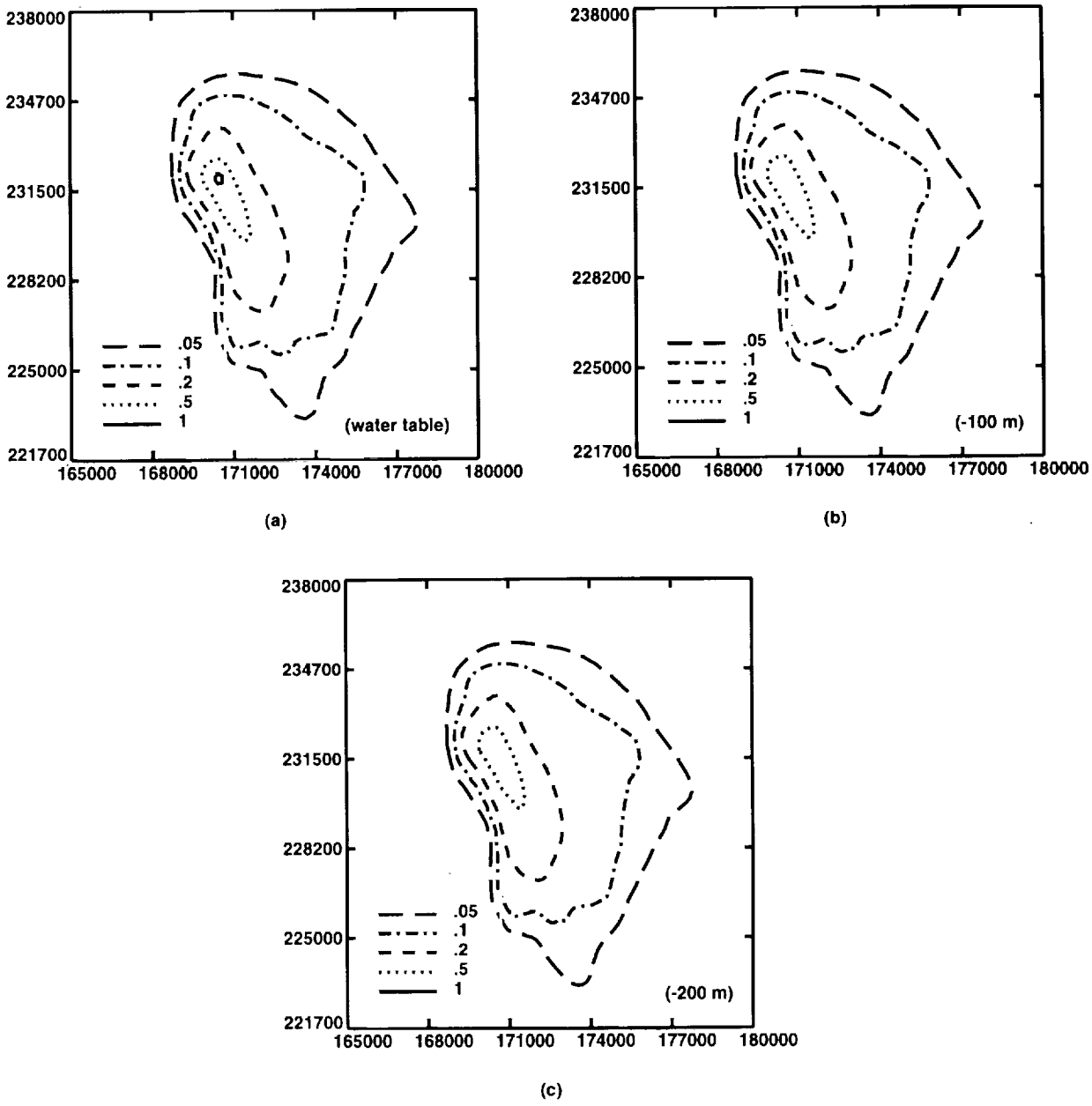

Figure 11-13. Concentration contours at the water table at 4,700 years for a continuous source of unit concentration, with retardation = 1, located in the Bullfrog at the water table. Coordinates are Nevada state plane coordinates (in meters).

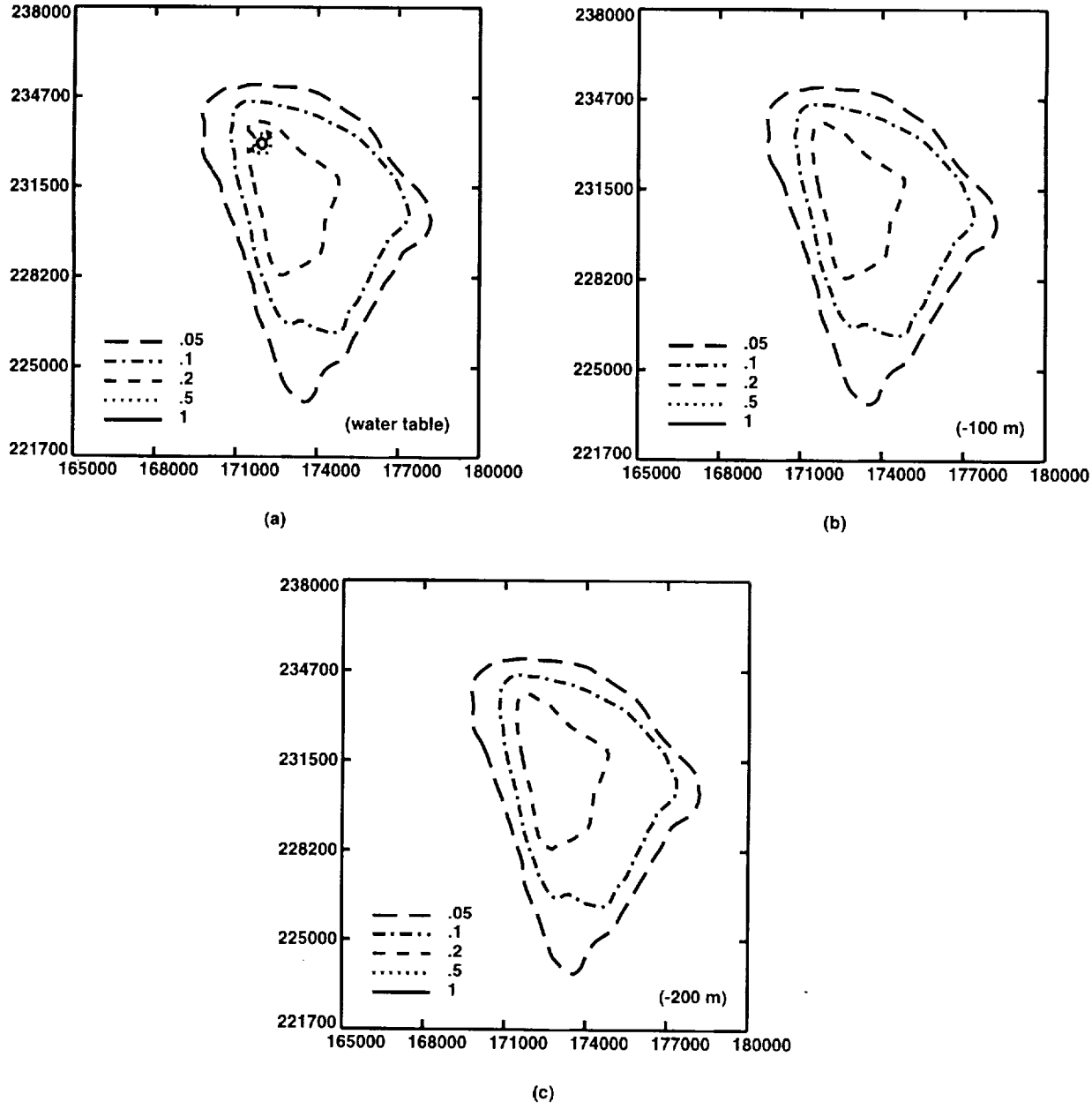

Figure 11-14. Concentration contours at the water table at 4,700 years for a continuous source of unit concentration, with retardation = 1, located in the Calico Hills at the water table. Coordinates are Nevada state plane coordinates (in meters).

heads (and separately, fluxes) along a strip at -200 m in roughly the location suggested by Fridrich *et al.* Neither head nor flux data are available to support such boundary conditions, since the only head datum in the carbonates in this vicinity is at P-1. However, numerical experiments are used to explore possible effects of the drain.

A series of calculations, varying hydraulic conductivities throughout the region and head assignments along the drain, produces a best fit (Table 11-3). This fit is hardly satisfactory, so flux boundary conditions are introduced along the drain. Substitution of flux boundary conditions improves the fit slightly, except for wells along Drill Hole Wash and Solitario Canyon.

Table 11-3. The fit of calculated heads to data for the diversionary model without Solitario Canyon and Drill Hole Wash faults.

Well	Node	Calculated Head	Residual
WT-11	7583	730.70	-0.02
WT-10	7619	768.63	-7.
WT-7	7751	767.40	-8.
G-3	7803	742.34	+12.
WT-12	7865	732.02	+2.5
H-3	7936	745.76	+14.
H-6	8064	777.12	+1.1
WT-1	8078	738.33	+8.
WT-17	8084	735.37	+5.7
WT-2	8298	743.72	+13.
H-5	8472	751.95	-23.5
WT-3	8500	731.10	+1.6
H-4	8524	743.05	+12.8
C-3	8578	736.48	+6.8
P-1	8626	733.65	+3.6
J-13	8729	729.46	+1.
G-1	8786	748.91	–
B-1	8794	743.53	+12.9
H-1	8832	747.77	+16.8
WT-18	8967	746.71	–
WT-13	8947	731.11	+2.1
WT-4	9016	744.32	+13.6
WT-14	9072	732.13	+2.6
G-2	9136	1029.00	–
WT-16	9325	737.91	-.4
WT-6	9361	1035.10	–
WT-15	9382	730.42	+1.2

Therefore, as before, zones with properties representing the SCF and DHWF are introduced. The fit, that is, the calibration, is then as good as for the non-diversionary model. It is possible to vary the hydraulic conductivity of the fault zones, in particular the DHWF, over a wide range while still preserving a reasonable fit to well data. One such fit, with the hydraulic conductivity for DHWF increased by several orders of mag-

nitude from the non-diversionary model and constant head at the drain, appears in Table 11-4. Values used in this fit are in Table 11-5.

Table 11-4. The fit of calculated heads to data for the diversionary model with Solitario Canyon and Drill Hole Wash faults.

Well	Node	Calculated Head	Residual
WT-11	7583	730.70	0.
WT-10	7619	772.66	-3.3
WT-7	7751	772.85	-2.9
G-3	7803	732.12	+1.5
WT-12	7865	730.40	+0.9
H-3	7936	732.50	+0.83
H-6	8064	773.46	-2.5
WT-1	8078	731.76	+1.3
WT-17	8084	731.34	+1.7
WT-2	8298	732.92	+2.7
H-5	8472	773.48	-2.0
WT-3	8500	729.85	+0.3
H-4	8524	733.15	+2.85
C-3	8578	731.40	+1.3
P-1	8626	730.42	+0.47
J-13	8729	729.17	+0.72
G-1	8786	738.20	–
B-1	8794	733.68	+4.2
H-1	8832	736.83	+5.9
WT-18	8967	737.01	–
WT-13	8947	729.29	+0.3
WT-4	9016	734.34	+3.6
WT-14	9072	729.69	0.
G-2	9136	1029.00	0.
WT-16	9325	734.96	-3.4
WT-6	9361	1035.10	0.
WT-15	9382	729.72	+0.5

The associated potentiometric surface appears in Figure 11-15. While this fit is relatively good, it is not a guarantee that the drain model requires the fault zones to properly represent the flow system. An alternative, self-consistent, truncated model is constructed using fault zones to supplement controls of the drain. Truncation and replacement of the absent structure in a flow-system model so strongly three dimensional should be viewed with skepticism.

11.5 Transport calculations using the diversionary model

Breakthrough curves are calculated for the three different locations of a unit concentration source (in the Prow Pass, Bullfrog, and Calico Hills, respectively) for selected nodes along the 5-km fence discussed in section 11.3. The results (Figures 11-16, 11-17,and 11-18) display quite different structure than seen earlier (Figures 11-9, 11-10,

Table 11-5. Parameters and boundary conditions used for calibration of the diversionary model.

Unit	Porosity[a]	Hydraulic Parameters K_x[b] (m/sec)	K_y (m/sec)	K_z (m/sec)
Topopah Spring (1)	0.20	6.00×10^{-5}	6.00×10^{-5}	6.00×10^{-5}
Topopah Spring (2)	0.20	2.00×10^{-5}	2.00×10^{-5}	2.00×10^{-5}
Calico Hills (1)	0.20	1.25×10^{-6}	1.25×10^{-6}	1.25×10^{-6}
Calico Hill (2)	0.20	5.00×10^{-6}	5.00×10^{-6}	5.00×10^{-6}
Calico Hills (3)	0.20	2.50×10^{-8}	2.50×10^{-8}	2.50×10^{-8}
Prow Pass (1)	0.20	5.00×10^{-5}	5.00×10^{-5}	5.00×10^{-5}
Prow Pass (2)	0.20	5.00×10^{-5}	5.00×10^{-5}	5.00×10^{-5}
Bullfrog (1)	0.20	5.00×10^{-4}	5.00×10^{-4}	5.00×10^{-4}
Bullfrog (2)	0.20	5.00×10^{-4}	5.00×10^{-4}	5.00×10^{-4}
Tram	0.20	2.00×10^{-7}	2.00×10^{-7}	2.00×10^{-7}
Drain	0.20	1.00×10^{-3}	1.00×10^{-3}	1.00×10^{-3}
Solitario Canyon fault	0.20	6.00×10^{-7}	6.00×10^{-7}	6.00×10^{-7}
Drill Hole Wash fault	0.20	3.00×10^{-11}	3.00×10^{-11}	3.00×10^{-11}
Element below H-5	0.20	1.00×10^{-11}	1.00×10^{-11}	1.00×10^{-11}

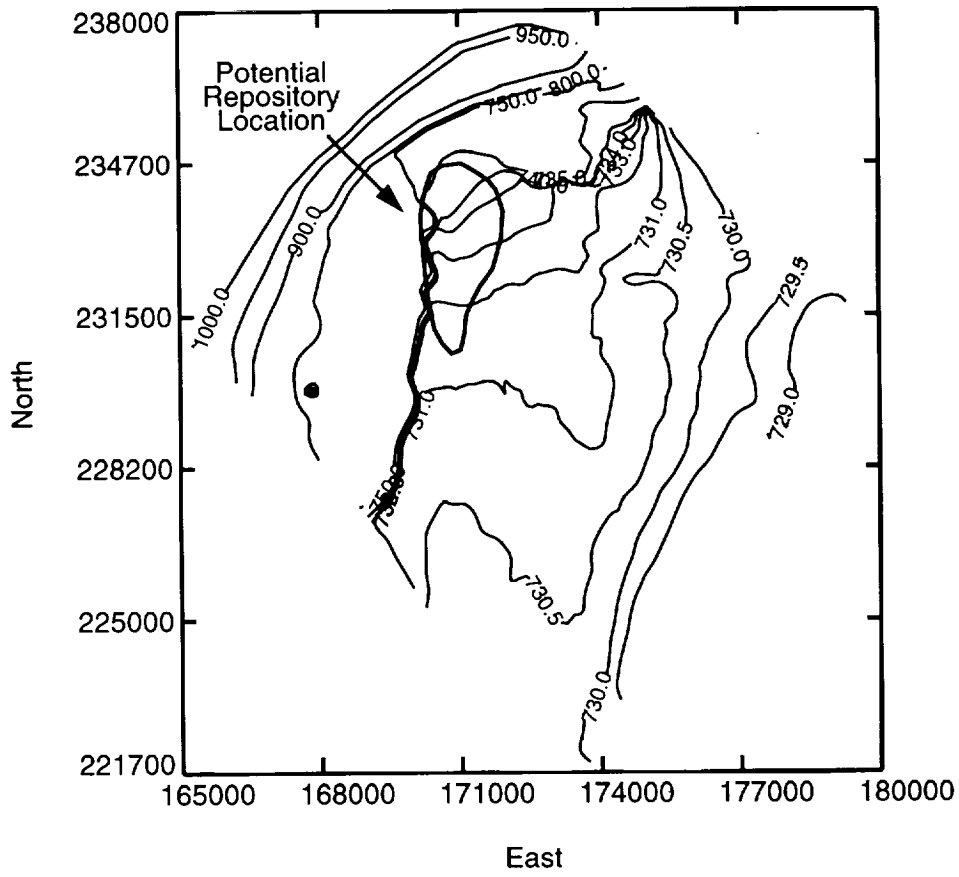

Figure 11-15. The potentiometric surface map based on calculated values of head for the case described in Table 11-4. Contours are altitude in meters. Coordinates are Nevada state plane coordinates (in meters).

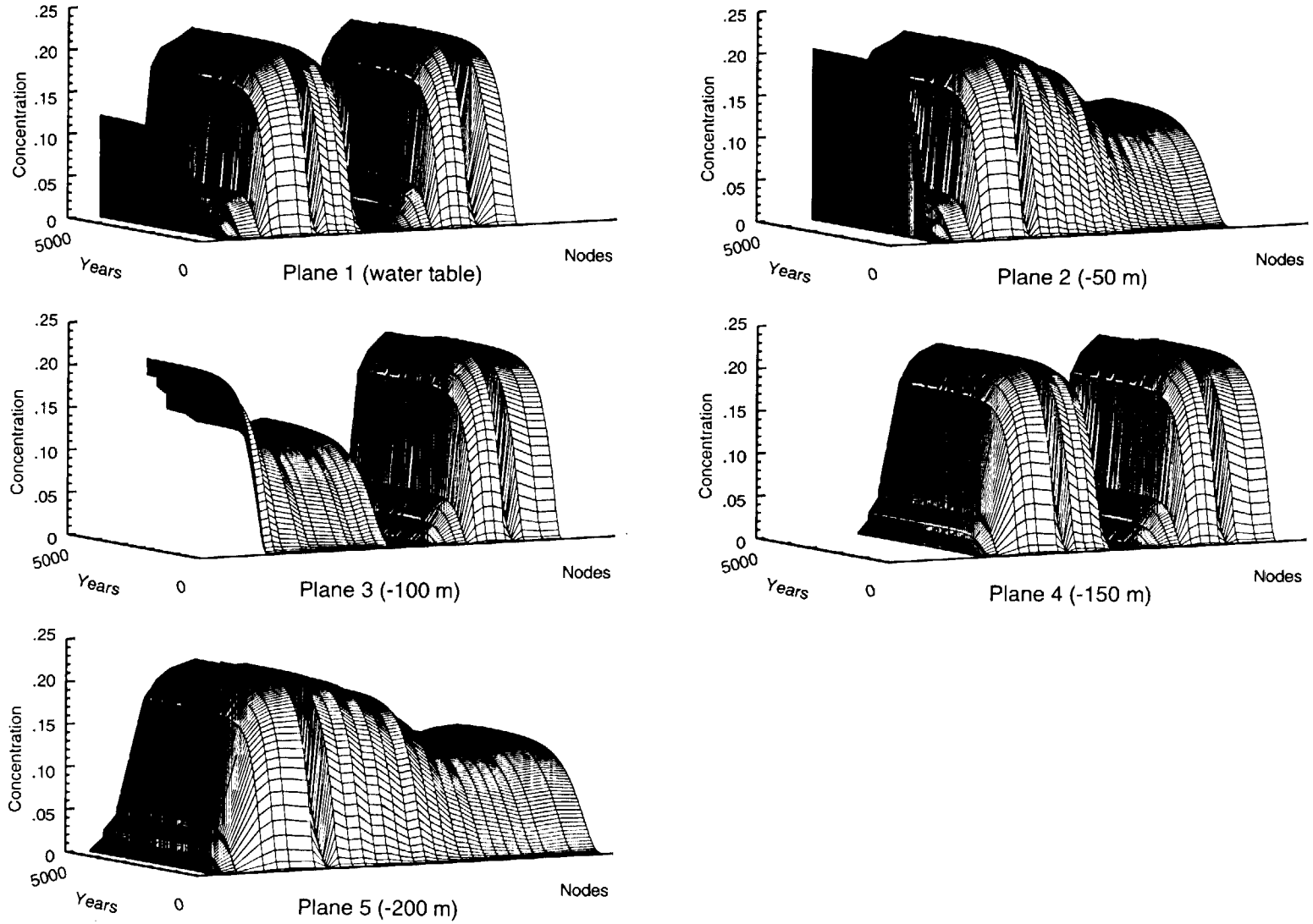

Figure 11-16. Breakthrough curves along the 5-km fence for a source of unit concentration located at the water table in the Prow Pass. Each set of curves is for a different depth below the water table. (Vertical axis values as shown; time and nodes as in Figure 11-9.)

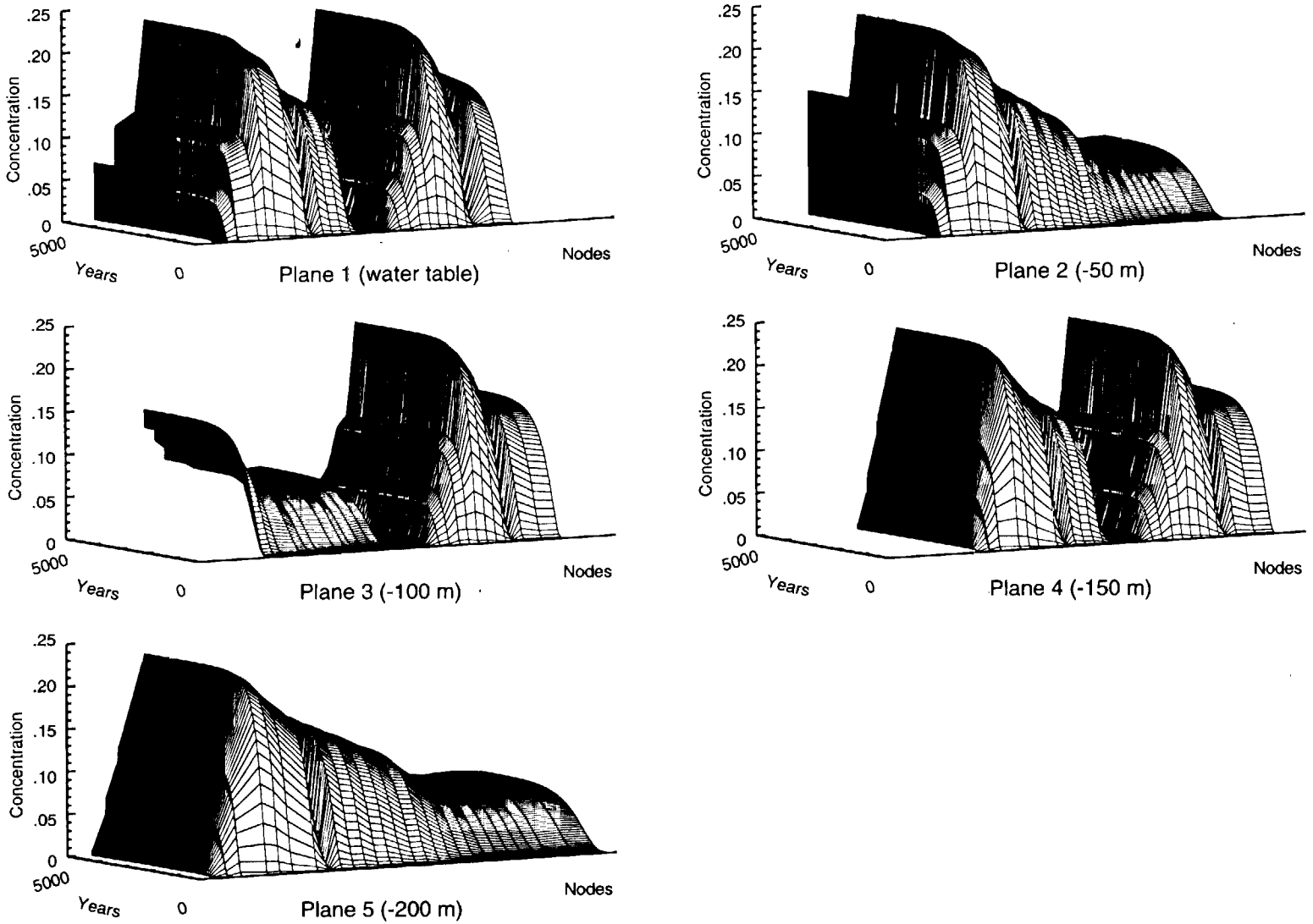

Figure 11-17. Breakthrough curves along the 5-km fence for a source of unit concentration located at the water table in the Bullfrog. Each set of curves is for a different depth below the water table.

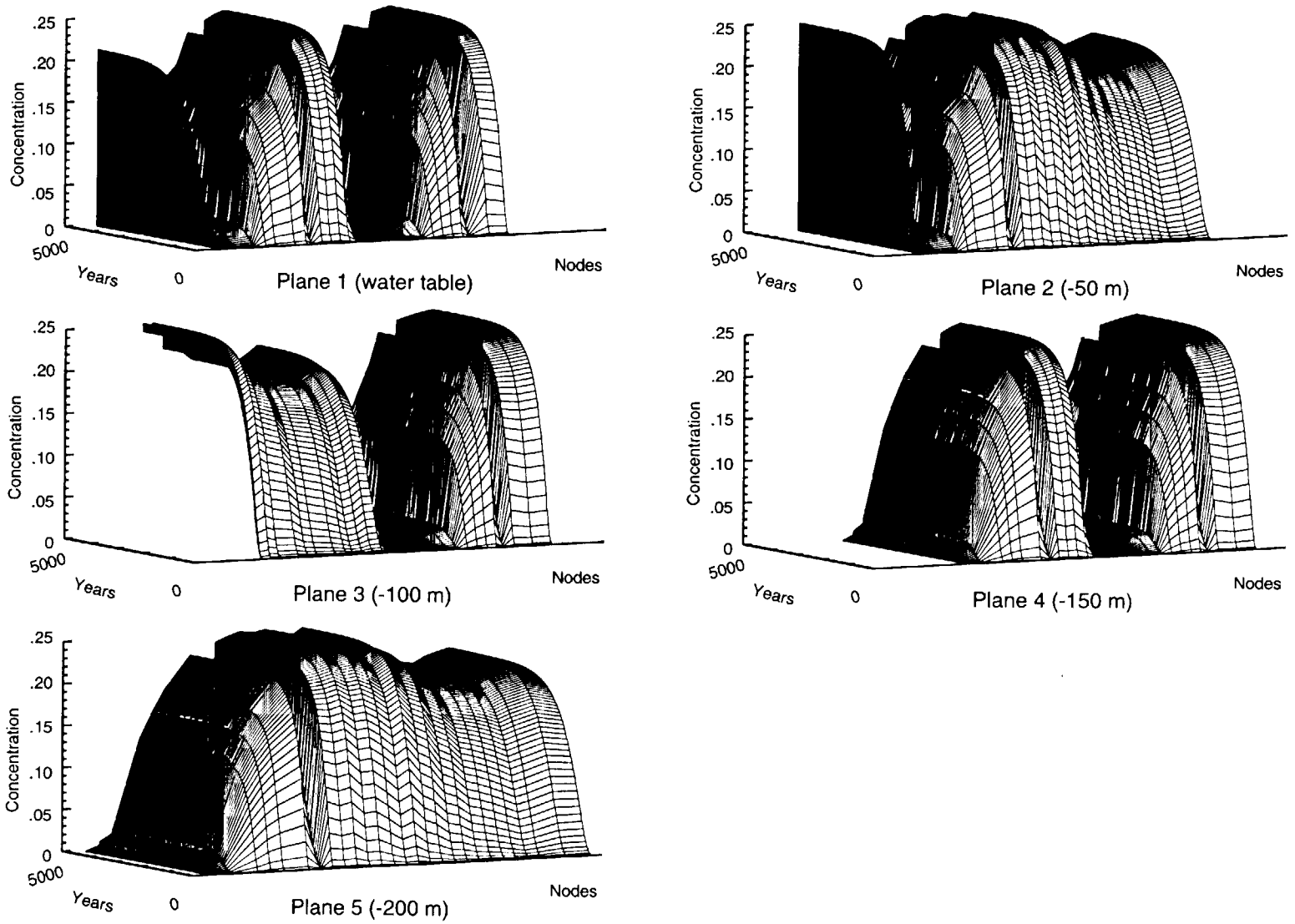

Figure 11-18. Breakthrough curves along the 5-km fence for a source of unit concentration located at the water table in the Calico Hills. Each set of curves is for a different depth below the water table.

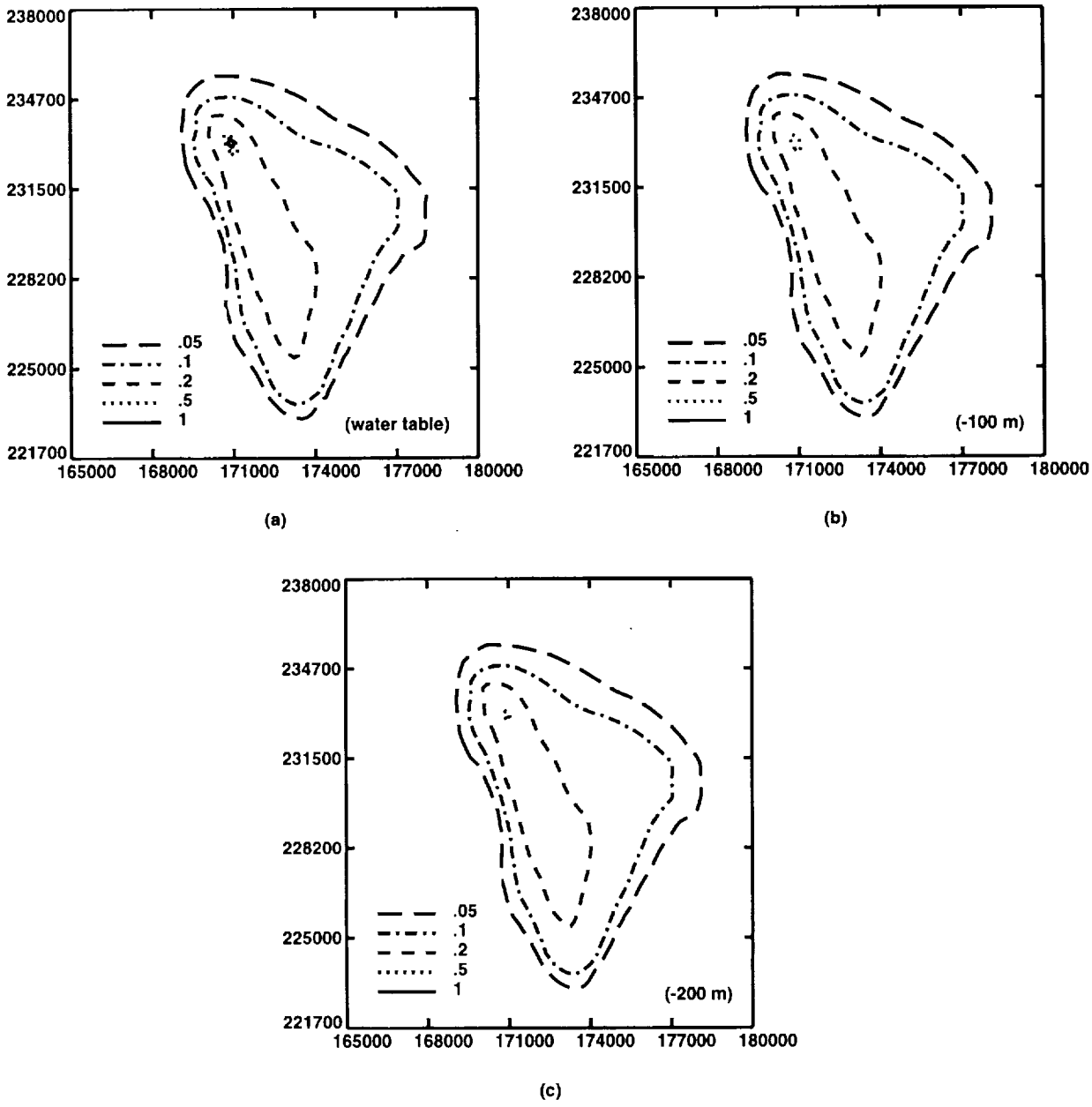

Figure 11-19. Concentration contours at 4,700 years for a continuous source of unit concentration, with retardation = 1, located in the Prow Pass at the water table. Coordinates are Nevada state plane coordinates (in meters).

and 11-11). The drain and increased hydraulic conductivity of the DHWF have redirected some flow. Plume development is shown more explicitly in Figure 11-19 for the source located in the Prow Pass unit. The figures in this series of contour plots display the plume at the water table and at two lower horizontal slices. The plume shape and extent are rather different from the plume for the source in the Prow Pass in the non-diversionary model (Figure 11-12). Since there are open questions about the diversionary model, the remaining plumes corresponding to the other source locations are not displayed here.

11.6 Abstraction of results for the TSA

Because of constraints on computer time, disk space, etc., it is not practical to incorporate the three-dimensional saturated-zone model directly into the Monte Carlo simulations of aqueous release. Instead, it is necessary to "abstract" the important elements of the complex model into a simplified model that can be used within the total-system analyzer (TSA; see Wilson *et al.*, 1991). For this TSPA, we continue to use the same simplification as was used in TSPA-91 for the saturated-zone calculations, but with the detailed results described in the preceding sections substituted for the results based on Czarnecki's model that were used for TSPA-91.

For the Monte Carlo simulations, we simplify the calculation of saturated-zone transport of radionuclides by using only one spatial dimension, but with water velocity and hydrodynamic dispersivity chosen in such a way as to mimic the three-dimensional results.

Radionuclide releases from an unsaturated-zone calculation are used as the source for a transport calculation in a one-dimensional flow tube that follows the radionuclides out to the accessible environment, five kilometers from the repository.

The TSPA-91 method could have been extended by feeding the releases from all eight unsaturated-zone columns into a common saturated-zone calculation involving one or more saturated-zone flow tubes, but we did not do so because of the complicated logistics of coupling the column calculations and because of potential computer problems. It may be worthwhile to explore such extensions of the method in the future. The TSPA-91 method is improved slightly in the composite-porosity calculations by defining a saturated-zone (SZ) flow tube individually for each unsaturated-zone (UZ) column rather than using a single flow tube for all columns. A single SZ flow tube is used for weeps-model calculations, both for TSPA-91 and TSPA-93.

The remainder of this chapter describes the simplifications and assumptions made for the saturated-zone-transport calculations within the total-system analyzer.

11.6.1 Velocity and dispersivity

The abstraction of the detailed three-dimensional transport results is based on the final concentration and the amount of time to reach one-half of that concentration for each of the observation nodes along the 5-km-radius "fence" described in Section 11.3. Both the nondiversionary ("no drain") and diversionary ("drain") models are considered. In the three-dimensional breakthrough plots, most of the nodes have apparently reached their steady-state concentration by the end of the 4700-yr calculation period, so the final concentration represents a steady-state value. The time to reach a given breakthrough concentration is sensitive to the dispersivity chosen for the calculation, and the proper value to use for dispersivity is quite uncertain. The following reasoning, however, indicates that the time to reach the 50% breakthrough may be relatively independent of the dispersivity.

Dispersion spreads out the concentration from the position it would have if transport were purely by advection. The amount of spread of a contaminant packet depends on hydrodynamic dispersion (and on numerical dispersion and other numerical artifacts), but the central point of the packet should be reasonably representative of the underlying advective part of the solution. As an example, consider the solution to the advection/dispersion equation in one dimension with constant coefficients (i.e., a homogeneous medium) and a step source:

$$C = \frac{C_0}{2}\left\{\operatorname{erfc}\left(\frac{x - vt}{2\sqrt{D_L t}}\right) + \exp\left(\frac{vx}{D_L}\right)\operatorname{erfc}\left(\frac{x + vt}{2\sqrt{D_L t}}\right)\right\} \tag{11.1}$$

(see, e.g., Freeze and Cherry, 1979, p. 391). In this equation, C is solute concentration at distance x and time t, C_0 is the source concentration after time 0, v is water velocity, and D_L is the coefficient of longitudinal dispersion. The function erfc is the complementary error function. The midpoint, where $C = C_0/2$, occurs at $x \simeq vt$. Thus, if $t_{1/2}$ is the breakthrough time for 50% concentration, then $x/t_{1/2}$ is a good estimate of v for this simple case. It is not certain that this conclusion remains valid for a three-dimensional heterogeneous problem, but it appears to be a reasonable assumption.

For each observation node, then, the distance from the source, x, is divided by the 50% breakthrough time $t_{1/2}$ to get an effective transport velocity v for unretarded contaminant arriving at that node. The velocities are weighted by the associated concentration flux from the three-dimensional results, so that the velocity distribution obtained represents the quantity of contaminant being transported at each velocity. The concentration flux is $F = Cq$, where C is the concentration (the final, or steady-state, concentration) and q is the Darcy velocity. The Darcy velocities at the observation nodes are predominantly radially outward from the source (the particlar observation nodes were chosen because they were expected to be close to the flow path, after all), so the magnitude of the Darcy velocity is

used in the flux calculation, though ideally the component of velocity normal to the release surface would be used.

The first four observation nodes were eliminated (actually, 20 observation nodes—five layers at each of four locations), because they were receiving spuriously high weightings by the above procedure. The reason, apparently, is that they are not close enough to the actual flow path, and the contaminant reaching those nodes is transported primarily by lateral dispersion and not by advection. The formula $F = Cq$ does not include the dispersive flux, which is proportional to concentration gradient rather than concentration, and so the formula is not appropriate for those nodes where transport is dispersive rather than advective.

The resulting distributions of effective velocity for the six transport calculations (three source locations for each of two flow models) are shown in Figures 11-20 through 11-25. The distributions are not simple—they appear to be bimodal or even trimodal. Using the concept of one-dimensional flow tubes, such velocity distributions could be approximated with two or three flow tubes, with each flow tube having a different velocity and representing a different apparent mode. However, to reduce the amount of computer time needed, we represent each case with a single flow tube.

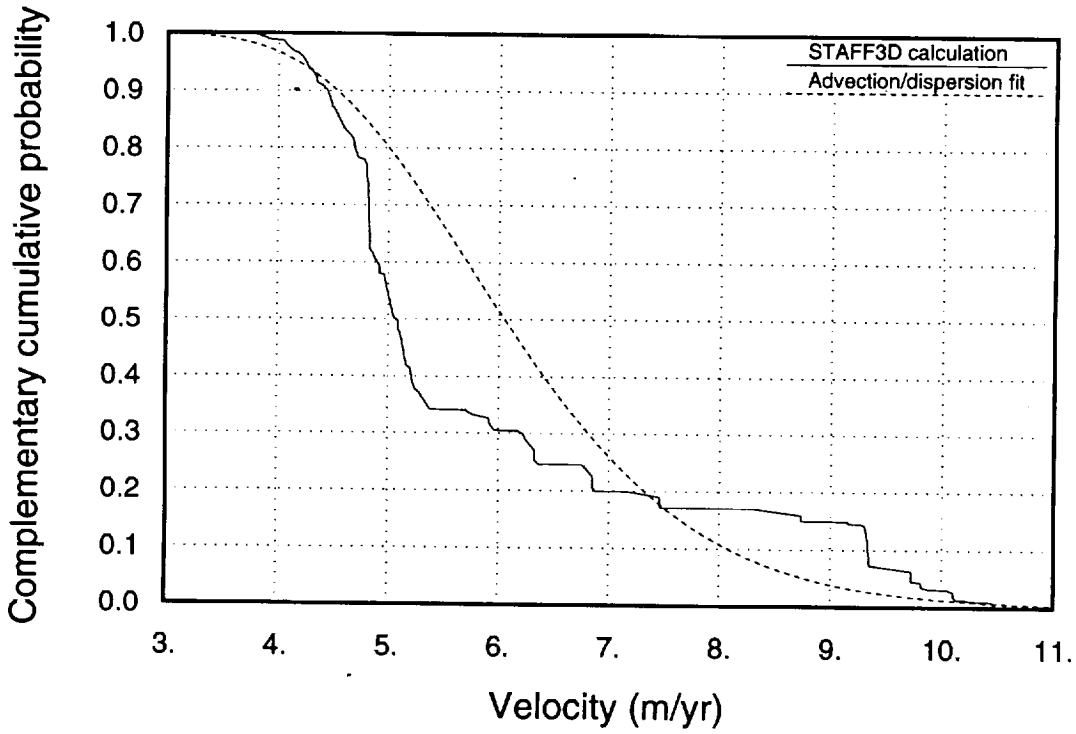

Figure 11-20. Distribution of effective velocities for Prow Pass source, no drain.

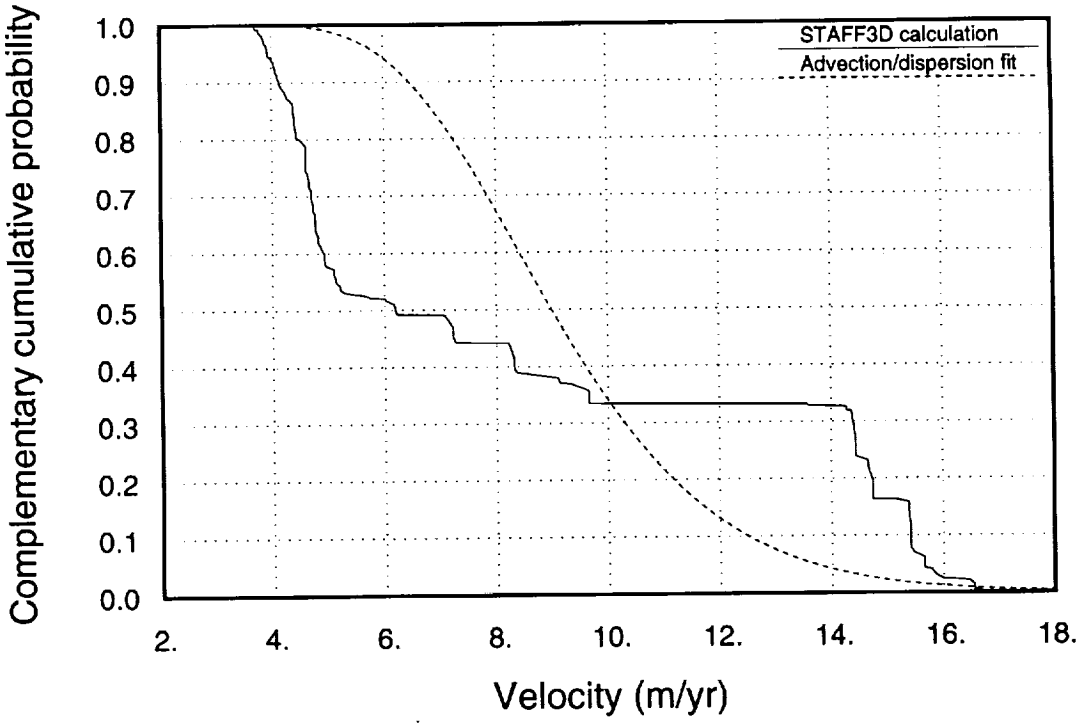

Figure 11-21. Distribution of effective velocities for Bullfrog source, no drain.

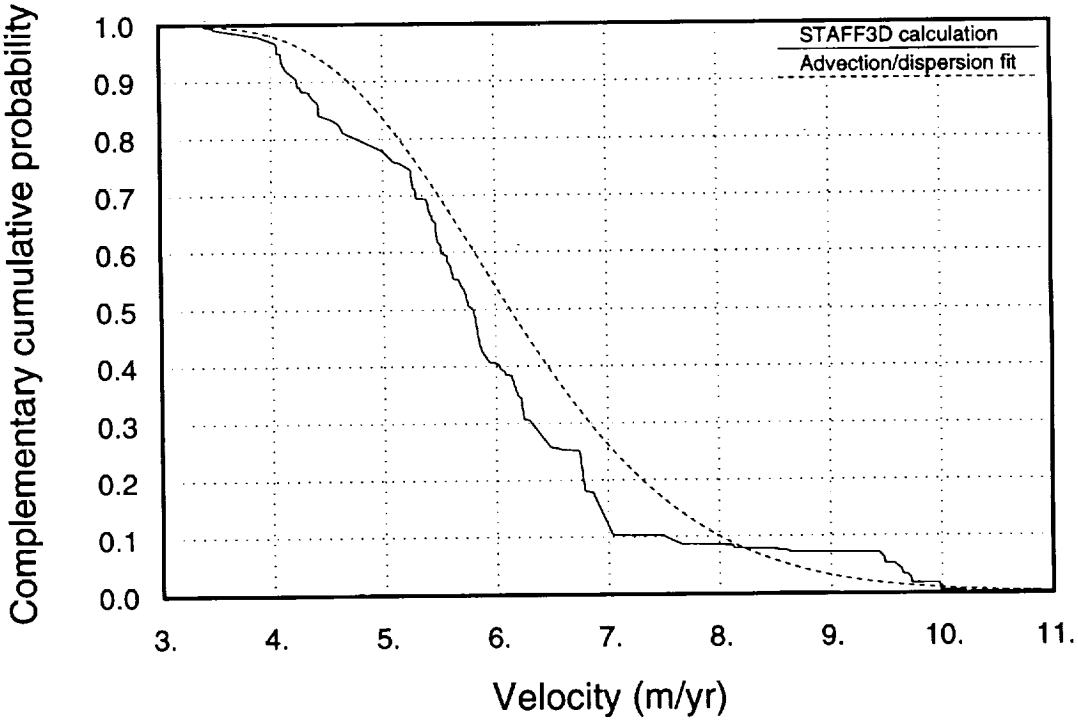

Figure 11-22. Distribution of effective velocities for Calico Hills source, no drain.

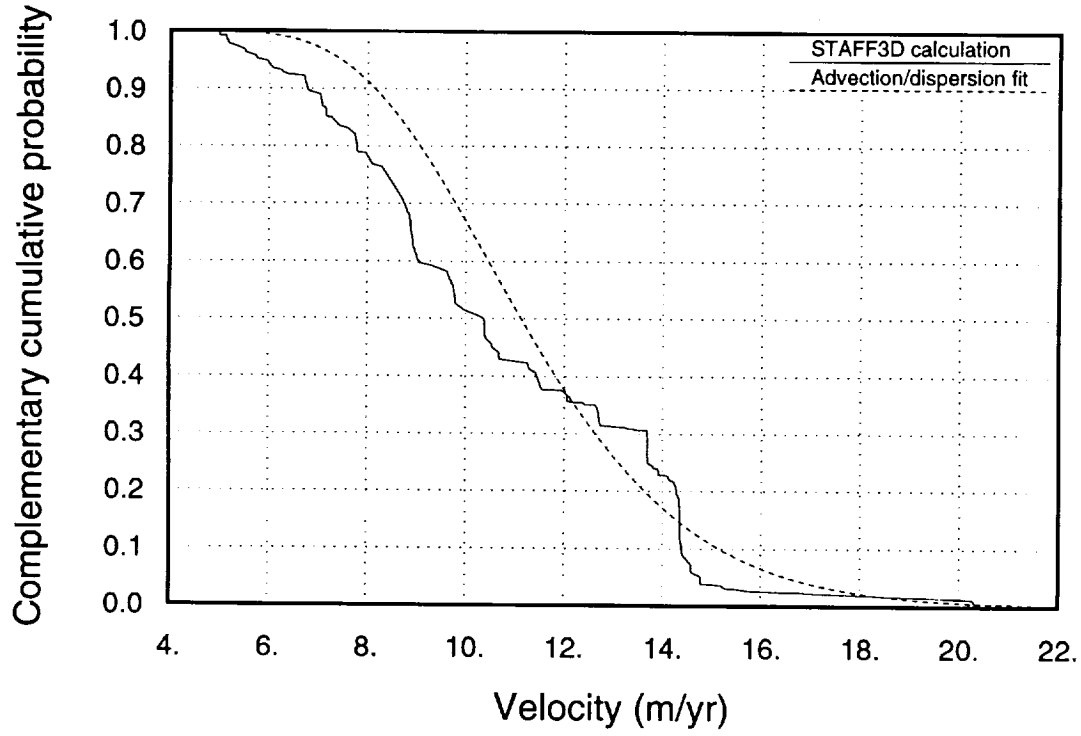

Figure 11-23. Distribution of effective velocities for Prow Pass source, with drain.

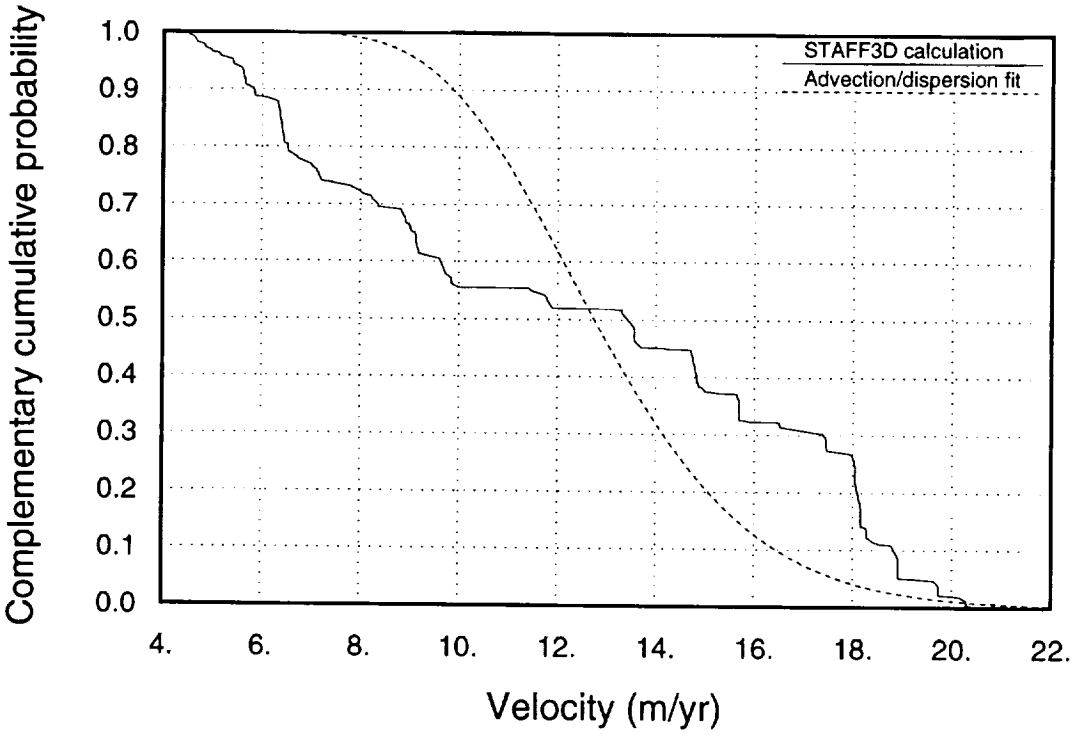

Figure 11-24. Distribution of effective velocities for Bullfrog source, with drain.

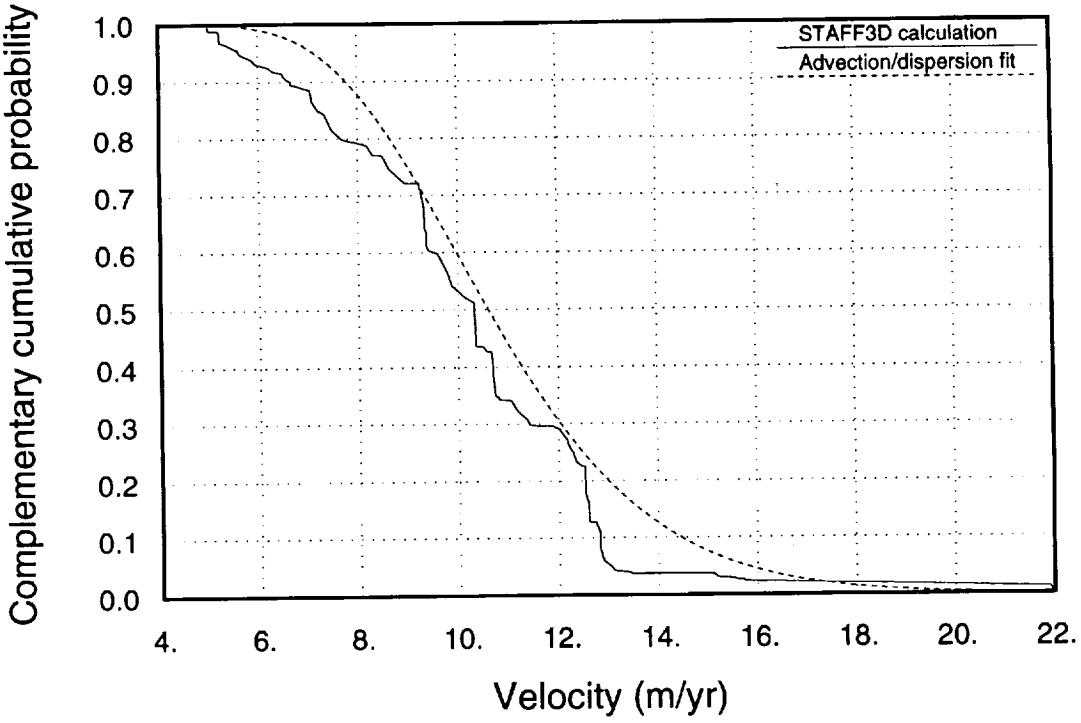

Figure 11-25. Distribution of effective velocities for Calico Hills source, with drain.

In the one-dimensional SZ transport calculations, the only parameters available to vary are the velocity and the dispersivity (the dispersion coefficient D_L is given by $D_L = \alpha_L|v|$, where α_L is the longitudinal dispersivity). Thus, each of the six velocity distributions is fit to a one-dimensional advection/dispersion solution, with values of v and α_L chosen so as to obtain a reasonable fit. Using the solution in Equation 11.1 for C as a function of x and t, an expression for the distribution of effective velocity can be developed as follows. If the velocity parameter in the solution is renamed to v_0, and D_L is eliminated in favor of α_L, then C is given as a function of x, t, v_0, and α_L. The distance x is known—it is the 5-km distance to the accessible environment. The concentration-breakthrough curve can then be thought of as a cumulative distribution of breakthrough times. The time t can be eliminated in favor of effective velocity by defining $v = x/t$, to obtain a complementary cumulative distribution of effective velocity:

$$G(v) = \frac{1}{2}\left\{\operatorname{erfc}\left(\sqrt{\frac{x}{4\alpha_L v_0 v}}(v - v_0)\right) + \exp\left(\frac{x}{\alpha_L}\right)\operatorname{erfc}\left(\sqrt{\frac{x}{4\alpha_L v_0 v}}(v + v_0)\right)\right\}, \qquad (11.2)$$

where v_0 and α_L are parameters that can be varied.

Such a curve is plotted along with each of the six velocity distributions from the STAFF3D calculations in Figures 11-20 through 11-25. The fits are made by using the

mean of the STAFF3D distribution for the v_0 parameter and adjusting the α_L parameter until a reasonable fit is achieved. The α_L choice is made subjectively, not by least squares or other formal fitting procedure.

The fitted values of v_0 and α_L for the six cases are shown in Table 11-6. The results for the Calico Hills source and the Prow Pass source are quite similar, so they are lumped together for purposes of the TSPA. The results for the Bullfrog source are significantly different, though, so two velocity distributions were developed. One distribution, based on the Calico Hills and Prow Pass cases, is used for UZ columns 3, 4, 5, 7, and 8. The other distribution, based on the Bullfrog cases, is used for UZ columns 1, 2, and 6 (see Figures 6-8 and 6-9).

For the Calico Hills/Prow Pass sources, velocities of 5.9 and 6.0 m/yr are obtained with no drain, and velocities of 10.8 and 10.3 m/yr are obtained with the drain. The corresponding dispersivities are 130 m/110 m and 150 m/150 m. The numbers are rounded slightly to arrive at a velocity distribution from 5.5 to 11.0 m/yr. Not having any information on relative likelihood, we assume a uniform distribution between those limits.

The spread of effective velocities in Figures 11-20 through 11-25 results from the large-scale heterogeneity in the saturated-zone models, not from hydrodynamic dispersion; there should be additional spread because of hydrodynamic dispersion. A rule of thumb quoted by de Marsily (1986, p. 247) is that hydrodynamic dispersivity is typically one tenth of the traveled distance, which would be 500 m in our situation. Based on this rule of thumb and on the dispersivity values listed in Table 11-6, we assume a uniform distribution from 100 m to 500 m for dispersivity. In TSPA-91, a log-uniform distribution of dispersivity from 50 to 500 m was used. We use a uniform distribution rather than log-uniform for TSPA-93 in order to give equal weight to all values within the range.

For the Bullfrog source, velocities of 8.7 m/yr (no drain) and 12.5 m/yr (drain) were obtained. Dispersivities of 170 m (no drain) and 100 m (drain) were obtained. Rounding

Table 11-6. Effective velocity and dispersivity for the six SZ cases.

Case	Velocity (m/yr)	Dispersivity (m)
Prow Pass source, no drain	5.9	130
Bullfrog source, no drain	8.7	170
Calico Hills source, no drain	6.0	110
Prow Pass source, drain	10.8	150
Bullfrog source, drain	12.5	100
Calico Hills source, drain	10.3	150

slightly, we use a uniform distribution between 8.5 and 12.5 m/yr for velocity. For dispersivity, we once again use a uniform distribution from 100 to 500 m.

The saturated-zone velocity and dispersivity distributions for the aqueous-release calculations in this TSPA are summarized in Table 11-7. It must be emphasized that these distributions are based on only two possible models of the saturated-zone system in the vicinity of Yucca Mountain, so they do not represent the full uncertainty about the parameter values. Additional work is needed to explore the possibilities for saturated-zone flow.

A comparison of the two SZ velocity distributions for TSPA-93 with the SZ velocity distribution for TSPA-91 is shown in Figure 11-26. Plotted in the figure are cumulative probability distributions for the transport time through the saturated zone of an unretarded tracer. It can be seen that the SZ transport times for this TSPA are significantly lower than those assumed for TSPA-91. The mean transport times are 600 yr for the Bullfrog source, 800 yr for the Calico Hills/Prow Pass source, and 1300 yr for TSPA-91. The shorter SZ transport times have some effect on the results for the weeps model but not for the composite-porosity model, because UZ transport times are much longer than SZ transport times for the composite-porosity model (see Chapters 14 and 15).

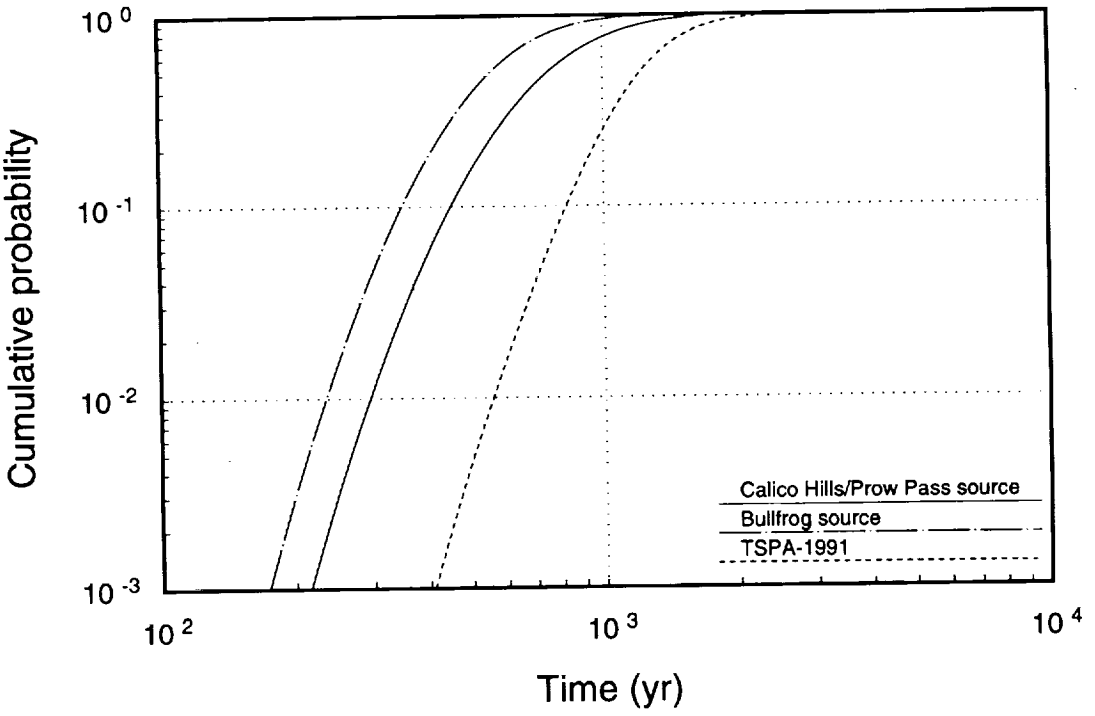

Figure 11-26. Comparison of SZ transport times for TSPA-91 and TSPA-93.

Table 11-7. Velocity and dispersivity distributions for TSA simulations.

Model parameter	Distribution
CH/PP* velocity (Cols. 3–5, 7, 8)	uniform from 5.5 to 11 m/yr
BF† velocity (Cols. 1, 2, 6)	uniform from 8.5 to 12.5 m/yr
Dispersivity	uniform from 100 to 500 m

*Calico Hills/Prow Pass source.
†Bullfrog source.

11.6.2 Transport area

To calculate cumulative release of radioactivity as specified in 40 CFR 191.13 (EPA, 1985), the cross-sectional area of the SZ flow tubes does not matter because releases are integrated over the area. However, because realistic estimates of individual drinking-water doses are desired for this TSPA, the flow-tube area is very important because it determines the magnitude of the concentrations in the contaminated plume. Thus, estimates of the vertical and horizontal mixing lengths are needed.

The horizontal width of the contaminated plume can be estimated by taking the width of the repository and adding on an estimate of the transverse dispersion. The width of the repository normal to the water-flow direction is approximately 3000 m. Transverse dispersion on each side of that is given by $W \approx \sqrt{2D_T t} \approx \sqrt{2\alpha_T x}$, where α_T is the transverse dispersivity and x is the observation distance (5 km). (The quantity $\sqrt{2D_T t}$ is the standard deviation of the Gaussian that a pulse release spreads out to after a time t, in a homogeneous medium.) Assuming a range of 5 to 50 m for α_T (about one tenth of the longitudinal dispersivity), we get a range of about 200 to 700 m for W, so that the total width of the contaminated plume is between 3400 and 4400 m.

We have almost no information regarding the vertical mixing depth. It could be quite small if saturated-zone flow is highly channelized, or it could be comparable to the estimates above for horizontal spread. The three-dimensional models used for the detailed calculations of saturated-zone flow and transport make the latter assumption. Arbitrarily assuming a range of 10 to 500 m for the vertical mixing depth gives a range of transverse areas from 3.4×10^4 m^2 (3400 m $\times$ 10 m) to 2.2×10^6 m^2 (4400 m $\times$ 500 m). For the TSA simulations, we round the numbers and use a range of 2×10^4 to 2×10^6 m^2. Because the range spans orders of magnitude, we assume a log-uniform distribution.

This simple conceptual picture is complicated somewhat by the fact that, for the composite-porosity model, transport is separated into several flow tubes. The best, most consistent, way to handle the SZ transport would be to feed the releases from all UZ columns into a single SZ calculation, so that interactions between the nuclides from different UZ

columns would be represented properly. However, to simplify the logistics of the calculations, this is not done, and separate flow tubes are used. The concentrations would not be right if the total effective transport area were used for each of the flow tubes, because each flow tube has only a portion of the radionuclides. To make the concentrations approximately correct, the total SZ transport area, discussed above, is divided among the SZ flow tubes in proportion to the UZ column area (which is approximately in proportion to the number of waste containers). As an example, for the 57-kW/acre cases Column 1 has an area of 5.99×10^5 m^2 and the total for all columns is 4.63×10^6 m^2. Thus, Column 1 has 13% of the area (and, we are assuming, 13% of the radionuclide releases), so SZ flow tube #1 is given 13% of the SZ transport area, leading to a distribution from 2.6×10^3 m^2 to 2.6×10^5 m^2 for its area.

11.6.3 Porosity, bulk density, and sorption coefficients

The distributions of effective saturated-zone water velocity derived above (Table 11-7) are based on detailed calculations of transport of an unretarded tracer. In the TSA simulations, transport of multiple radionuclides is calculated, including ones that have significant adsorption retardation. Therefore, in the TSA saturated-zone calculations, the transport velocity for each nuclide is defined as water velocity divided by a retardation factor given by

$$R = 1 + \rho_b K_d / n \ . \tag{11.3}$$

R is the retardation factor, ρ_b is bulk rock density, K_d is the sorption coefficient, and n is porosity.

In addition to its role in the calculation of retardation factors, porosity enters into the definition of the effective water velocity, because water velocity is Darcy velocity divided by porosity. The velocity distributions could be adjusted to add the uncertainty in porosity (the STAFF3D calculations simply set $n = 0.2$ everywhere), but this was not done for two reasons. The first is that it would take a great deal of additional effort to determine which units the contaminant plumes go through along their entire flow paths. Each saturated-zone flow tube would have to be broken into multiple units instead of treating it as a single unit. Second, the appropriate effective porosity for transport is related to the issue of matrix diffusion and matrix/fracture coupling (if coupling is weak, the effective porosity might be more like the fracture porosity rather than the matrix porosity). There was not time for a consideration of matrix/fracture coupling in this TSPA, so we simply use 0.2 for the porosity in the TSA simulations, as in the detailed calculations discussed earlier in this chapter.

Similarly, for bulk density we assign a value of 2000 kg/m^3 (2 g/cm^3). This value is in the middle of the expected values reported in Table 7-4, which range from about 1700 to 2300 kg/m^3.

Sorption coefficients are discussed in detail in Chapter 9, but it is not clear which of the three rock types—devitrified, vitric, or zeolitic—should be used for the one-dimensional SZ flow tubes. As noted above, the single saturated-zone "unit" for a TSA simulation represents a combination of several rock types. The "devitrified" rock type is used for the SZ flow tubes because that choice is conservative for the low-retardation elements: neptunium, uranium, protactinium, and selenium (see Table 9-4). That choice is also consistent with TSPA-91.

Chapter 12
Gaseous Flow and Transport

(Ross, Lu, Wilson)

In this chapter, results of detailed gas-flow modeling are presented and discussed, and then the abstraction of those results for use in the Monte Carlo simulation of nominal gaseous release to the accessible environment is discussed.

The detailed calculations of gaseous flow and transport are two-dimensional, and use three parallel east-west cross sections. The latest information about mountain topography and stratigraphy is incorporated into the calculations. The system is modeled with fixed temperature at a lower boundary far below the repository level and with the repository heated by a full load of waste packages, with the heat input varying as a function of time.

For each two-dimensional calculation, travel paths are determined for a large number of particles traveling from points evenly distributed throughout the potential repository area to the surface. The travel times are calculated along each path line for a particle of ^{14}C retarded by isotopic exchange with bicarbonate dissolved in the aqueous phase. The concentration of dissolved bicarbonate is determined by assuming thermodynamic equilibrium with solid calcite and the measured rock-gas composition.

The results of the detailed calculations are used to define distributions of ^{14}C travel time throughout the repository (combining all three cross sections). The travel-time distributions are then combined with a model of ^{14}C release from the repository to obtain estimates of ^{14}C release to the accessible environment (see Chapters 14 and 15).

12.1 The models

^{14}C travel times at Yucca Mountain are analyzed in two steps. First, transient, coupled gas flow and heat transfer are solved by an explicit finite-difference method. Then, transient particle-tracking analysis is performed using the calculated velocity and temperature fields to obtain ^{14}C particle travel times.

Because gas flows are driven by heat and in turn affect temperatures, accurate calculations require a transient coupled model of heat transfer and gas flow. Until recently, the only models that had been used for such calculations of Yucca Mountain were various versions of TOUGH (Pruess, 1987), which solves fully coupled equations for multi-phase flow of air, water, and heat both above and below the boiling point. By including so much physics, this model requires intensive use of computer resources and limits the size of feasible grids.

To model the migration paths of ^{14}C with reasonable accuracy, a relatively fine grid is needed. We have developed a model that, by simplifying the physics, allows finer grids

to be used. The principal simplification in this model, called TGIF2, is the assumption that relative humidity is always near 100%. This allows the numerically challenging problem of unsaturated water movement to be omitted entirely from the model.

The TGIF2 model analyzes a gas whose humidity is maintained at 100% by evaporation or condensation of water when the gas flows through pressure and temperature gradients. Flow of liquid water is not modeled explicitly, but water is assumed to flow toward areas of evaporation readily enough to keep the medium partially saturated. This humidity constraint is physically realistic; unsaturated soils and rocks almost always contain some liquid water except very near the ground surface, and this water keeps the humidity close to 100% (Hillel, 1980).

Because we assume that the relative humidity is always kept at 100%, vapor pressure can be treated as a function of temperature only. This assumption can be well justified as long as temperature is below or around the boiling point (about 96°C at the repository elevation), but is not true if temperature is above the boiling point. As temperature enters that regime, 100% humidity will not be present and the heat-pipe phenomenon might occur. To deal with high temperatures at the repository, two techniques are employed in this study. First, we spread the heat over several rows of mesh blocks. This allows emplacement of the actual amount of spent fuel, but loses some accuracy in predicting the exact temperatures at or around the repository. Second, we redefine a smooth relationship between vapor pressure and temperature near and above the boiling point so that vapor pressure changes slowly and approaches a constant value when passing the boiling point. Because the current focus is on mountain-scale gas flow and heat transfer, these assumptions still allow satisfactory predictions of temperature and gas flow in the far field. Furthermore, because ^{14}C particles spend most of their time in the far field, travel-time errors due to the heat-source assumption are small. Future work will be directed toward developing a better approach to eliminate this limitation.

With the above assumptions, the governing equations consist of four equations (Amter *et al.*, 1991): a constitutive relation, Darcy's Law, a volume balance, and an energy balance. They are given by

$$\rho = \frac{1}{RT}(P_v\Omega_v + P_a\Omega_a) \ , \tag{12.1}$$

$$\mathbf{q} = -\frac{k}{\mu}(\nabla P - g\rho\mathbf{z}) \ , \tag{12.2}$$

$$\nabla\cdot\mathbf{q} - \mathbf{q}\cdot\left[\left(\frac{1}{T} + \frac{1}{P_a}\frac{dP_v}{dT}\right)\nabla T - \frac{1}{P_a}\nabla P\right] = 0 \ , \tag{12.3}$$

$$K_t \nabla^2 T - c_p^{gas} \rho \mathbf{q} \cdot \nabla T + \frac{1}{c}\left(1 + \frac{P_v}{P_a}\right)\mathbf{q} \cdot \nabla P_a$$

$$-\frac{H_v \Omega_v}{RT}\mathbf{q} \cdot \left[\left(1 + \frac{P_v}{P_a}\right)\frac{dP_v}{dT}\nabla T - \frac{P_v}{P_a}\nabla P\right] = c_p^{rock}\rho_{rock}(1-n)\frac{\partial T}{\partial t}\,, \qquad (12.4)$$

where ρ is the gas density, R is the gas constant, T is temperature, Ω_v and Ω_a are the molar weights of water and dry air, g is the acceleration of gravity, k is the intrinsic permeability of the porous medium, μ is the gas viscosity, and $\mathbf{z}$ is a downward-pointing unit vector. The variable P_v is the vapor pressure of water, which depends only on temperature, as discussed above. The variable P_a is the partial pressure of air; by assumption, we have $P_a = P - P_v$. In the energy equation (Equation 12.4), K_t is the thermal conductivity of the porous medium, c is a conversion factor equal to 4.18 J cal^{-1}, c_p^{gas} is the specific heat of gas at constant pressure, c_p^{rock} and ρ_{rock} are the specific heat and density of rock (including liquid water in the pores), H_v is the heat of vaporization of water, and n is the drained porosity. Note that fractures are not included explicitly in the formulation, but an equivalent porous medium is assumed (see Appendix B of Ross *et al.*, 1992).

For given initial and boundary conditions at Yucca Mountain, Equations 12.1 through 12.4 can be solved for fields of density ρ, pressure P, temperature T, and gas flux $\mathbf{q}$. The solution is obtained by an explicit transient finite-difference technique.

^{14}C moves more slowly than the uncondensible components of the gas, because it spends most of its time in the relatively immobile liquid phase as dissolved bicarbonate. The slowing is incorporated into the travel-time calculations by dividing the gas velocity at each point along a flow path by a retardation factor to obtain the effective ^{14}C transport velocity. The retardation factor is calculated by using the reaction-path model PHREEQE (Parkhurst *et al.*, 1980) to model the geochemical system. The conceptual model adopted here for the geochemical system has three principal features (Ross *et al.*, 1992; Doctor *et al.*, 1992):

- Sufficient calcium carbonate is present in the unsaturated zone to determine the aqueous chemistry, and to buffer the pH of the water.
- A relatively minor amount of calcium is derived from silicate weathering reactions; calcium concentrations are the result of equilibration with calcium carbonate.
- Fractionation plays a negligible role in removing ^{14}C from the gas phase, and concentrations of ^{14}C are proportional to those of ^{12}C. The relative concentrations of carbonate species in liquid and gas phases at equilibrium are used to calculate retardation factors for ^{14}C transport in the gas phase.

The modeled retardation factors are shown in Figure 12-1. The possibility of sorption onto solids is neglected in these calculations. There could be significant sorption onto iron oxides (see Section 9.3.2.14).

The particle tracking is done using a newly developed transient semianalytical theory. The theory has been implemented in a particle-tracking program TRACK that can accurately compute a ^{14}C particle's travel time and trajectory. To permit accurate particle tracking in transient flows, the particle velocity is interpolated linearly in both space and time within each finite-difference cell and time step. Using this interpolation scheme, the particle-velocity field is approximated and then integrated analytically to obtain the particle's trajectory within each cell and time step. Errors are much smaller than in simple numerical-integration schemes.

The TGIF2 model recently has been verified against an analytical solution for an instability problem of an infinite horizontal layer of rock gas heated from below (Ross *et al.*, 1993). The numerical results match very well with the analytical solution.

12.2 Inputs and assumptions

The TGIF2 and TRACK models are used to simulate transient gas flow, heat transfer, and ^{14}C migration in Yucca Mountain. The objective of the work is to obtain ^{14}C travel times, with a simulation time of 20,000 years. To represent the entire repository area, three east-west cross sections through Yucca Mountain are simulated using the TGIF2 model and

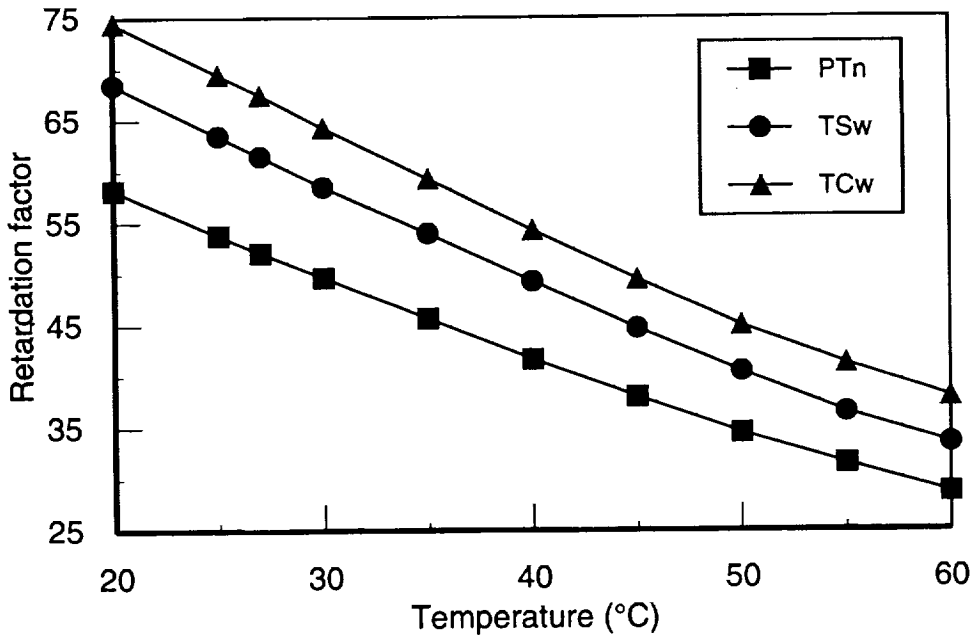

Figure 12-1. Retardation factor as a function of temperature for the modeled units.

the particle-tracking technique. Two critical variables—bulk permeability and ^{14}C release time—are varied to test the sensitivity of the system performance.

Figure 12-2 shows a map view of the potential repository and its location on the State of Nevada coordinate system. The three cross sections used in this study, shown in Figure 12-2 for locations and Figure 12-3 for geometries, are aligned along the east-west direction. These figures were generated from Sandia's Interactive Graphics Information System (IGIS), which is based on Ortiz *et al.* (1985).

The repository layout shown in Figure 12-2 is different from the layouts shown in Chapter 4 because of a change in our information regarding average spent-fuel age between the time the gas-flow calculations were started and the time the final thermal and release calculations were made. The difference probably does not have a significant effect on the results. Note that gas-flow calculations were made only for a thermal load of 57 kW/acre.

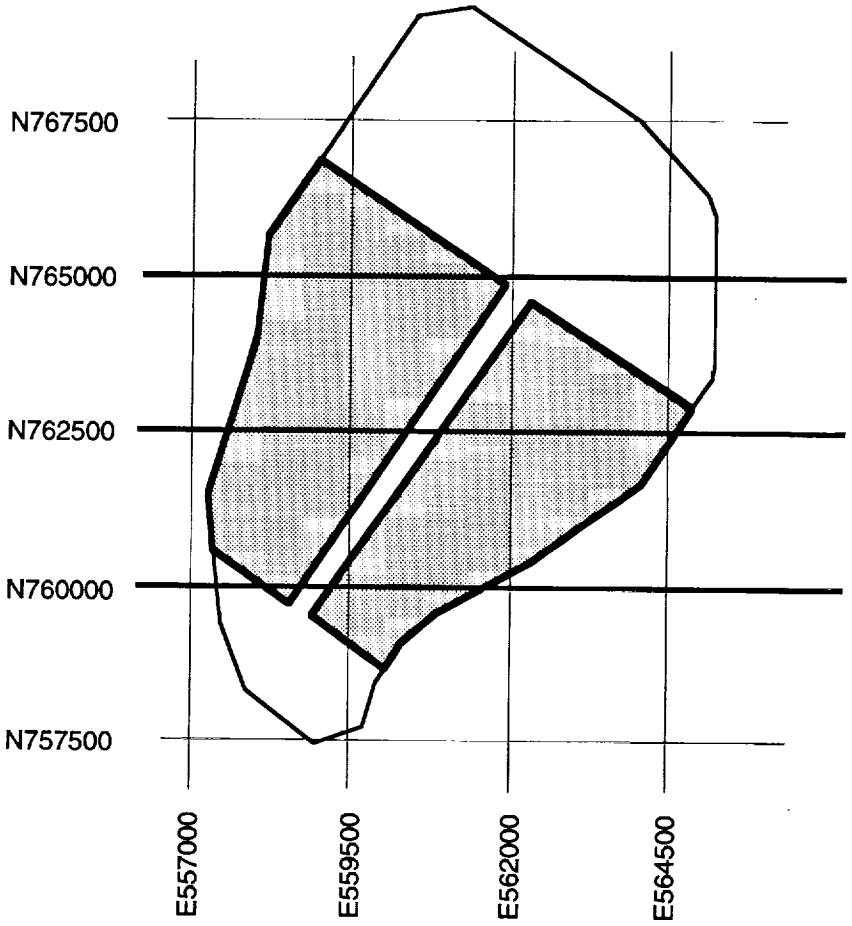

Figure 12-2. Repository layout used for gas-flow calculations (shaded). Cross sections modeled are shown with dark lines. The larger outline shows the area assumed for the repository in TSPA-91. Coordinates are in the State of Nevada coordinate system, in feet.

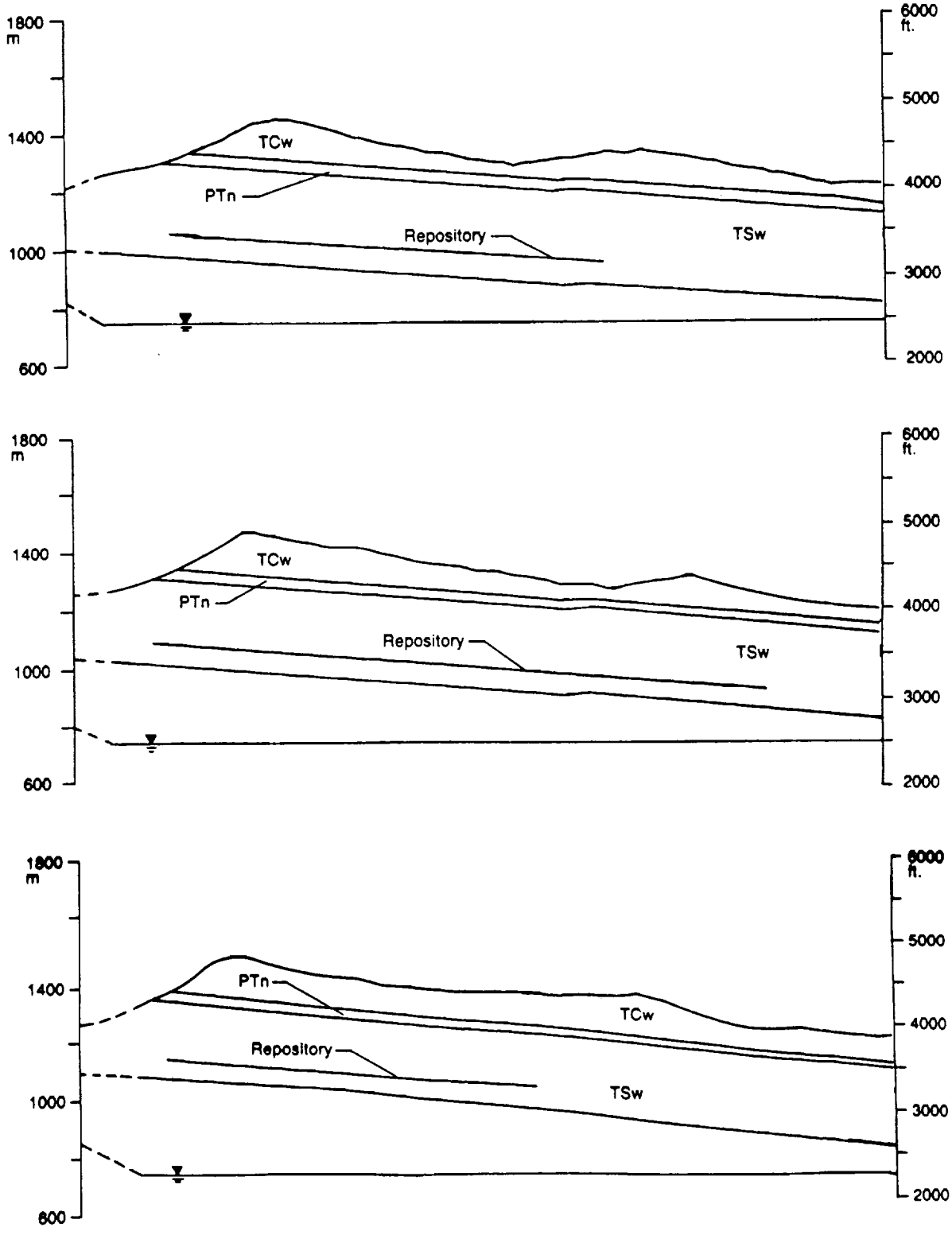

Figure 12-3. Geometry of the three modeled cross sections. Top: N765000; middle: N762500; Bottom: N760000.

Time constraints and concerns about performance of the TGIF2 model under the higher thermal load prevented us from calculating the gas flow with 114-kW/acre thermal load. The Ortiz *et al.* stratigraphy is used, as shown in Figure 12-3, rather than the geostatistical stratigraphy discussed in Chapter 6, but the geostatistical stratigraphy is not significantly different from the Ortiz *et al.* stratigraphy (on the length scales of interest) in the upper part of the mountain. Note also that the region modeled in the gas-flow calculations is considerably larger than the region modeled in Chapter 6.

There are three distinct hydrogeologic subdivisions in the Paintbrush Tuff Formation. These dip approximately six degrees to the east and differ in permeability. The upper and lower layers represent the Tiva Canyon welded unit (TCw) and the Topopah Spring welded unit (TSw). These layers are thick, welded, densely fractured, and relatively permeable. The middle layer is the Paintbrush nonwelded unit (PTn), a thin, nonwelded tuff that includes all or part of several stratigraphic subdivisions of the Paintbrush Tuff.

The hydrogeologic stratigraphy just described is represented in the simulations by defining three material types. The upper and lower welded layers are assumed to have identical material properties. Two cases were run for all three cross sections, with welded-tuff bulk permeability of 10^{-11} m^2 and 10^{-12} m^2 (the range for the Topopah Spring welded bulk-conductivity distribution reported in Table 7-13 equates to a bulk-permeability distribution approximately from 5×10^{-13} m^2 to 10^{-11} m^2). The middle layer, because it is nonwelded tuff, is expected to be less permeable than the welded units (see Table 7-13); nonwelded bulk permeability ten times smaller than the welded bulk permeability is assumed in both cases.

Each cross section is discretized into a finite-difference mesh. All meshes contain 33 rows and 99 columns of blocks. Figure 12-4 shows the mesh that represents the top cross section in Figure 12-3. Meshes for other cross sections are similar. The mesh contains various sizes of blocks. Finer mesh cells are used in and around the Paintbrush nonwelded unit and the potential repository area. Coarser mesh cells are used in the lower zone where there is no gas advection and only heat conduction is accounted for. The remaining area is discretized by square mesh cells of 30 m by 30 m.

The simulated region is surrounded by two types of boundary conditions for both gas flow and heat flow:

- fixed head along the mountain's atmospheric contact,
- no-flow conditions along the sides and along the interface between the Topopah Spring welded unit and the Calico Hills nonwelded unit (the lowest slanted line in each cross section of Figure 12-3),
- fixed elevation-dependent temperature along the mountain's atmospheric contact,

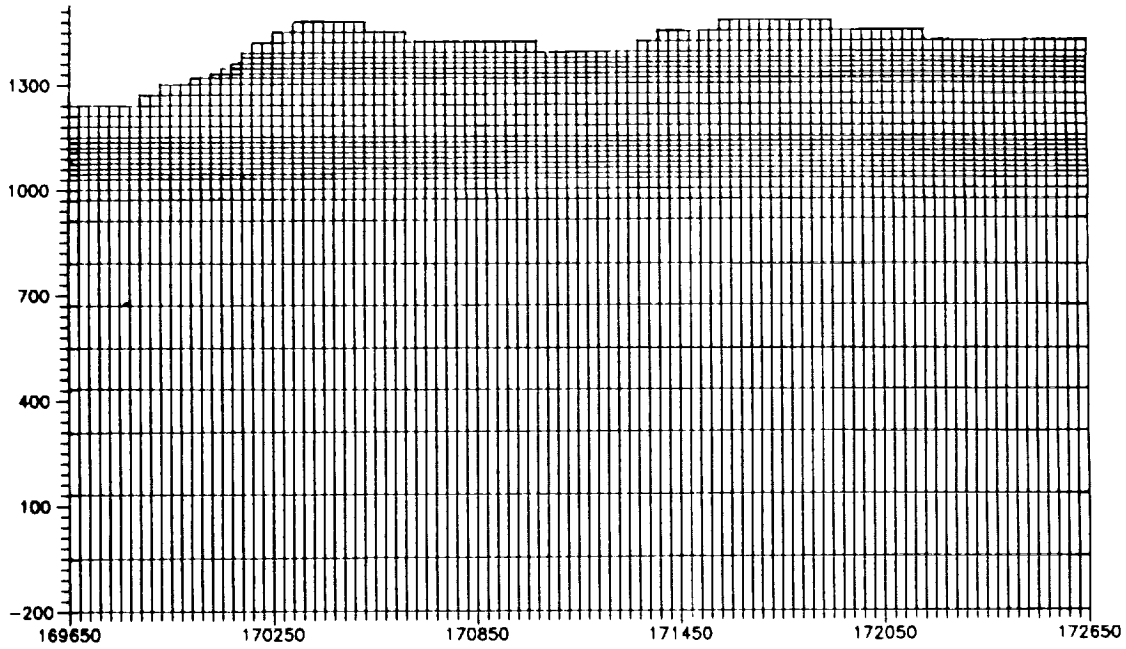

Figure 12-4. Finite-difference mesh for cross section N765000. Only heat conduction is modeled in the lower part of the mesh; heat and gas flow are modeled in the upper part of the mesh.

- fixed temperature at the far bottom boundary according to a geothermal-gradient calculation, and
- heat source treated as an internal boundary with given time-dependent heat flux at the repository location.

The numerical formulation of the external boundary conditions is described in detail by Ross *et al.* (1992). The no-flow boundary assigned at the interface between the Topopah Spring welded unit and the Calico Hills nonwelded unit is due to the low-permeability tuffaceous beds of the Calico Hills unit, which would impede downward gas flow. The boundary to the west is located in the trough of Solitario Canyon, which is a natural flow divide. The boundary to the east is located far to the east of the repository, so that it should have little effect on gas flow and heat transfer near the repository (Ross *et al.*, 1992). The repository heat source is described as follows.

A time-dependent heat source is used in this study. The heat is assumed to come from radioactive decay of PWR spent fuel. In order to incorporate the heat source into the TGIF2 model efficiently, a curve-fitting equation is used (originally developed by A. J. Mansure of Sandia National Laboratories), which has the following form:

$$P(t) = \sum_{n=1}^{6} A_n e^{-B_n t} , \qquad (12.5)$$

where $P(t)$ is the repository power output at time t, and A_n and B_n are coefficients defined by Table 12-1. The maximum fitting error is less than 2.7%. The advantage of using Equation 12.5 is that it allows an analytical evaluation of the source term in the temporal finite-differencing scheme.

The total amount of spent fuel is assumed to be 63,020 metric tons (MTU); see Chapter 5. We further assume that the spent fuel is 30 years old ($t = 30$ in Equation 12.5) at the beginning of the calculation and that the waste is emplaced at a constant rate evenly over a 25-year period. The heat source is spread uniformly over the repository, with initial density of 57 kW/acre. Because the waste is 30 years old when emplacement begins, the repository area is less than the area used in previous studies (Ross *et al.*, 1992; Barnard *et al.*, 1992), which assumed emplacement of 57 kW/acre of 10-year-old waste. (The area is also less than that used for 57-kW/acre calculations in the other components of this TSPA, as mentioned previously.)

Fixed parameter values used in the simulations are given in Table 12-2.

^{14}C particle travel times are calculated for a mathematical particle that is not affected by diffusion or dispersion. A transient semianalytical method is used to calculate advective travel times. Theoretically, diffusion and dispersion processes would affect a particle of

Table 12-1. Coefficients used in Equation 12.5.

n	A_n (W/MTU)	B_n (yr^{-1})
1	11.226	0.000028283
2	16.852	0.00012949
3	155.78	0.0017590
4	844.97	0.019999
5	224.14	0.062594
6	4567.4	0.44460

Table 12-2. Fixed parameter values used in the simulations.

Parameter	Symbol	Value	Source
Reference atmospheric temperature	T_a	296.44 K	—
Reference fluid density	ρ_0	1.007 kg m^{-3}	—
Reference internal temperature	T_0	300 K	—
Reference elevation	z_0	1275 m	—
Reference pressure	P_0	88,052.1 Pa	—
Viscosity at T_0	$\mu(T_0)$	1.86×10^{-5} kg m^{-1} s^{-1}	Lide (1990)
Atmospheric relative humidity at z_0	η	20%	—
Lapse rate	λ	6.5×10^{-3} K m^{-1}	Donn (1975)
Geothermal gradient	γ	2.0×10^{-2} K m^{-1}	Montazer *et al.* (1986)
Permeability of the welded tuff	k'	$10^{-11}/10^{-12}$ m^2	Montazer *et al.* (1986)
Permeability of the nonwelded tuff	k	$0.1 \times k'$	Montazer *et al.* (1986)

^{14}C or any other contaminant and cause some spreading in the distribution of travel times. However, the spreading of travel times caused by the geometry of the mountain and the gas-flow field is so large that diffusion and dispersion can safely be ignored (unless permeability is very small). The calculated transient gas-flow and temperature fields are used for particle trajectory and travel-time calculation by the TRACK model.

To obtain ^{14}C travel-time distributions, particles are emplaced at numerous locations throughout the repository horizon for each run in the three cross sections. In order to prevent the results from being biased by a non-random selection of particle origins, particle starting locations are selected using a simple analog of the Latin-hypercube method (Doctor *et al.*, 1992). In each of the three cross sections, the repository is divided into 30-meter intervals and one particle origin is chosen randomly within each interval. In all, travel times from the repository to the surface are calculated for a total of 260 starting points. These travel times are then used to obtain the travel-time distributions. This method gives less statistical noise and avoids clustering of starting points compared to having the same number of particles randomly and independently located.

In this study, all 260 particles are assumed to be released at the same time. Because the travel times vary with particle release time, and at present the time dependency of release of ^{14}C from spent fuel is not well known, particle-tracking analysis is performed for nineteen different release times ranging from 1000 to 18,000 years in increments of 1000 years. Once a transient ^{14}C release model is established, ^{14}C release distributions can be obtained directly by a simple numerical-integration technique (see Section 12.4).

12.3 Simulation results

Figures 12-5a through 12-5d show travel-time histograms that combine the results of all three cross sections, for a bulk permeability of 10^{-11} m^2 for the welded tuff. Figures 12-6a through 12-6d illustrate calculated temperature fields at 1,000, 5,000, 10,000, and 15,000 years for one of the three cross sections.

Figure 12-5a shows travel times for release of the ^{14}C particles at 1000 years after waste emplacement. At this early time, temperatures near the repository are high (Figure 12-6a) due to the large heat output. Gas velocities near the repository are larger than in the far field. The calculated ^{14}C travel times range from 200 to 600 years.

At 5000 years, the heat has spread outward and temperature gradients have become smaller within the mountain (Figure 12-6b). Note that the hottest area moves upward from the repository toward the mountain surface as a result of advective heat flow. Particles released at this time travel through the mountain in 300 to 900 years (Figure 12-5b). The

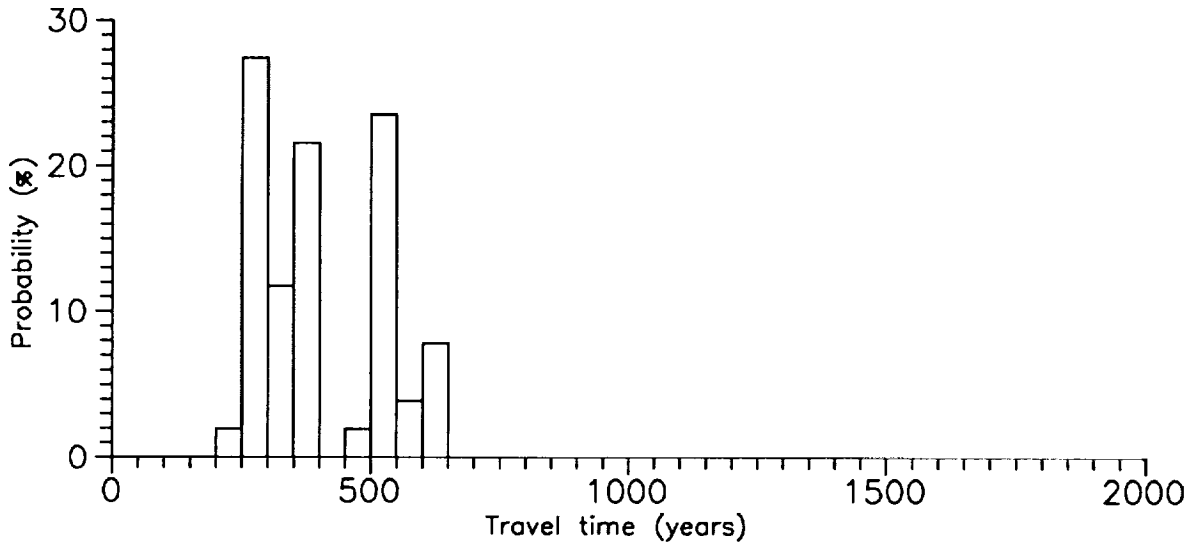

Figure 12-5a. Retarded travel times of ^{14}C particles from the repository to the atmosphere for particles released at 1000 years. Welded-tuff bulk permeability of 10^{-11} m^2.

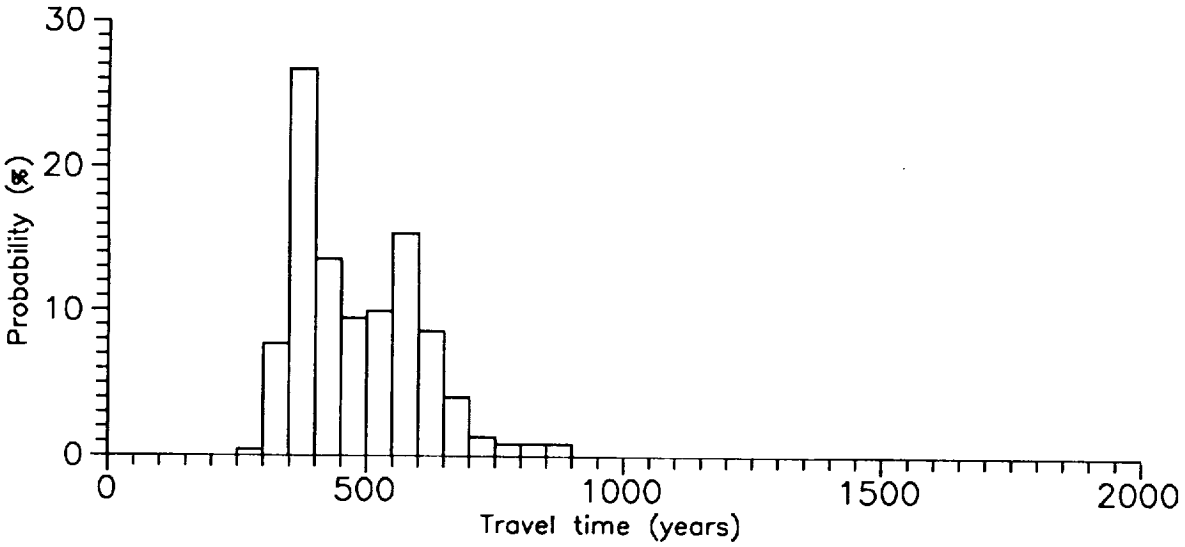

Figure 12-5b. Retarded travel times of ^{14}C particles from the repository to the atmosphere for particles released at 5000 years. Welded-tuff bulk permeability of 10^{-11} m^2.

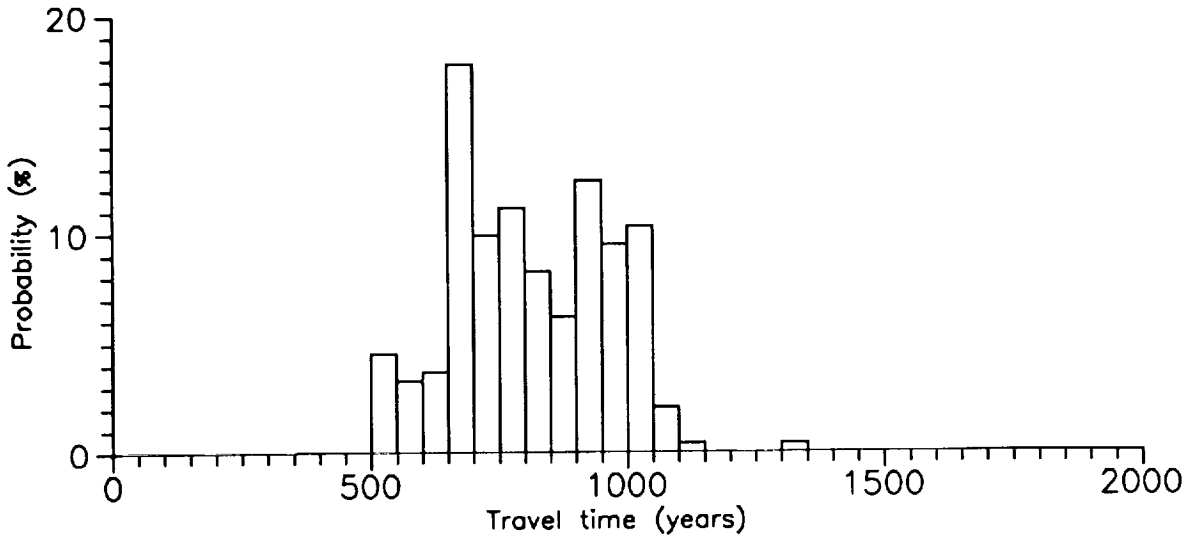

Figure 12-5c. Retarded travel times of ^{14}C particles from the repository to the atmosphere for particles released at 10,000 years. Welded-tuff bulk permeability of 10^{-11} m^2.

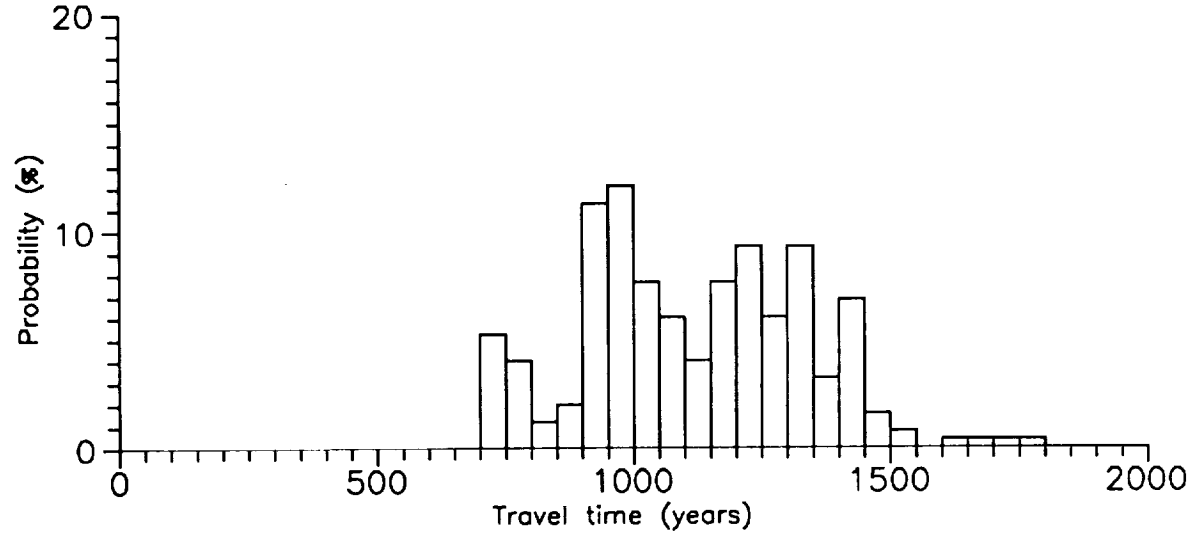

Figure 12-5d. Retarded travel times of ^{14}C particles from the repository to the atmosphere for particles released at 15,000 years. Welded-tuff bulk permeability of 10^{-11} m^2.

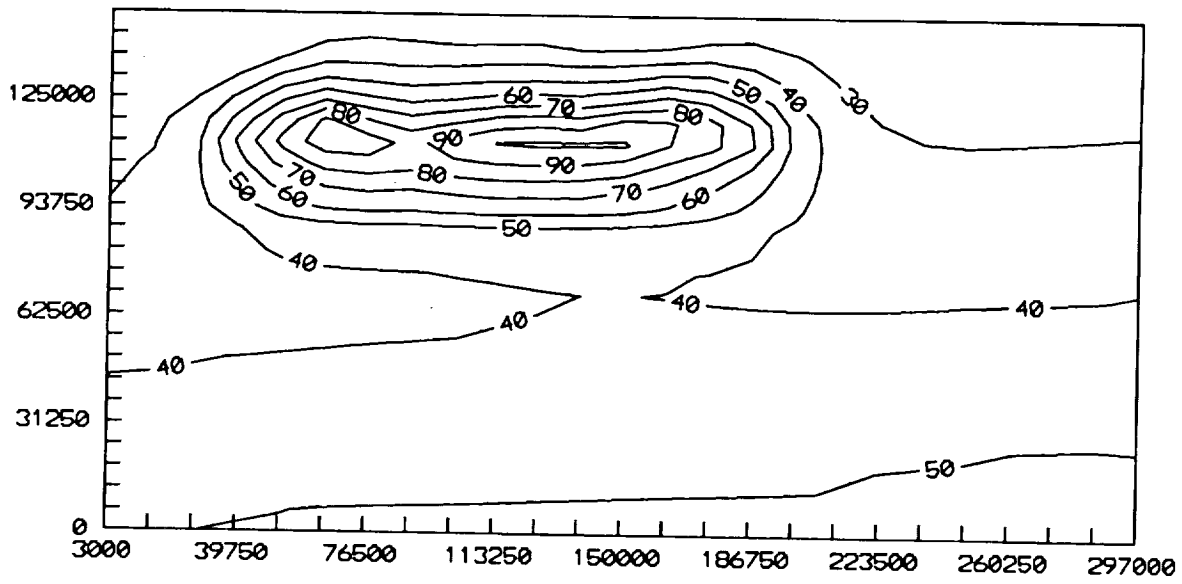

Figure 12-6a. Calculated temperature field (°C) at 1000 years for cross section N765000. Welded-tuff bulk permeability of 10^{-11} m^2.

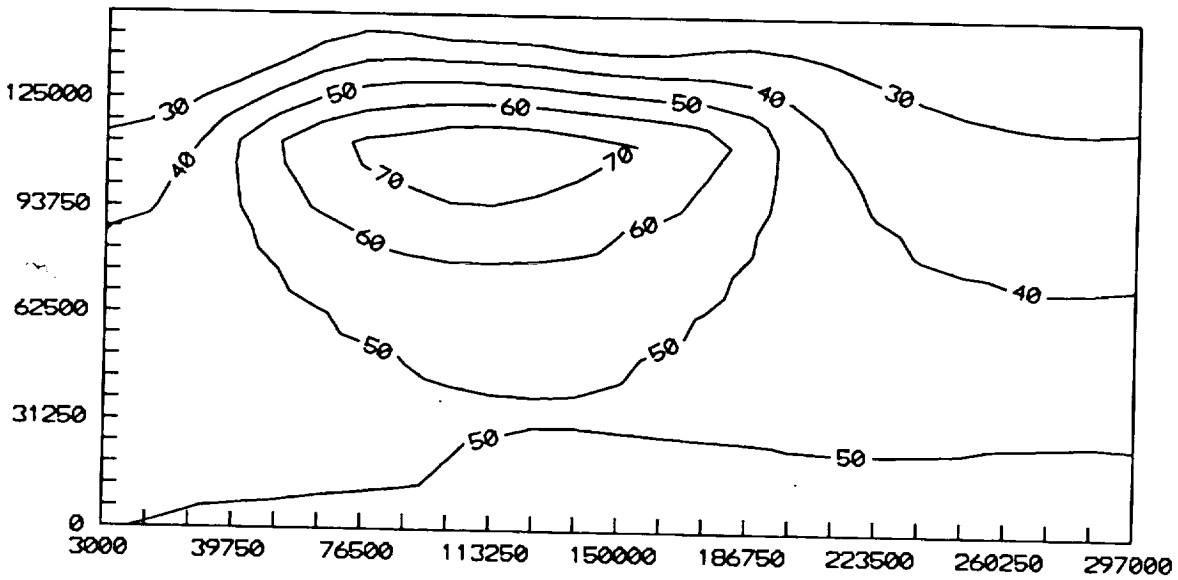

Figure 12-6b. Calculated temperature field (°C) at 5000 years for cross section N765000. Welded-tuff bulk permeability of 10^{-11} m^2.

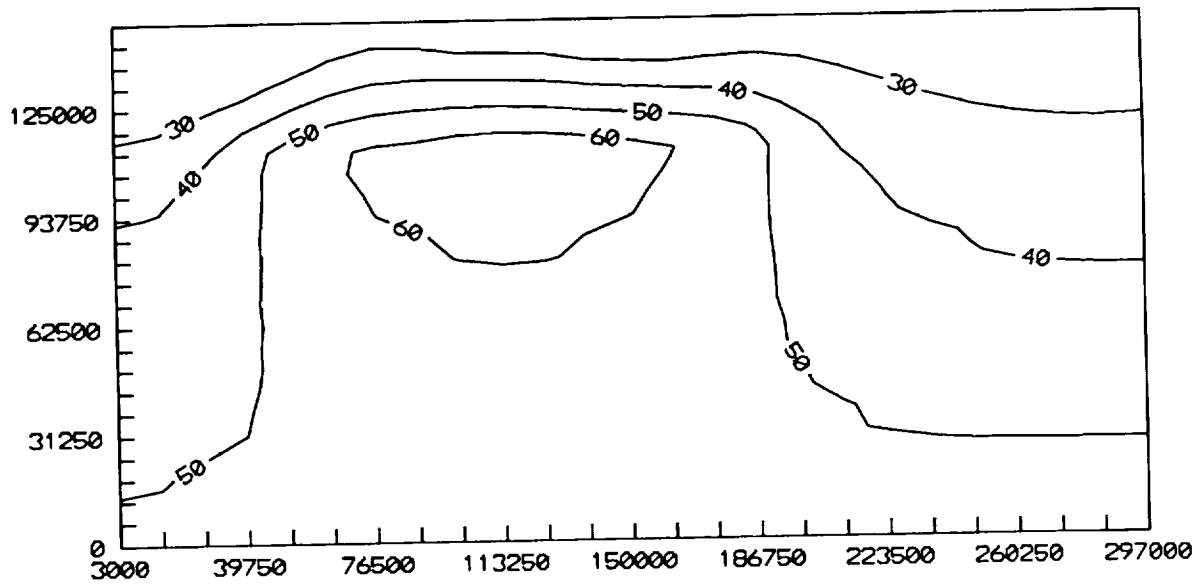

Figure 12-6c. Calculated temperature field (°C) at 10,000 years for cross section N765000. Welded-tuff bulk permeability of 10^{-11} m^2.

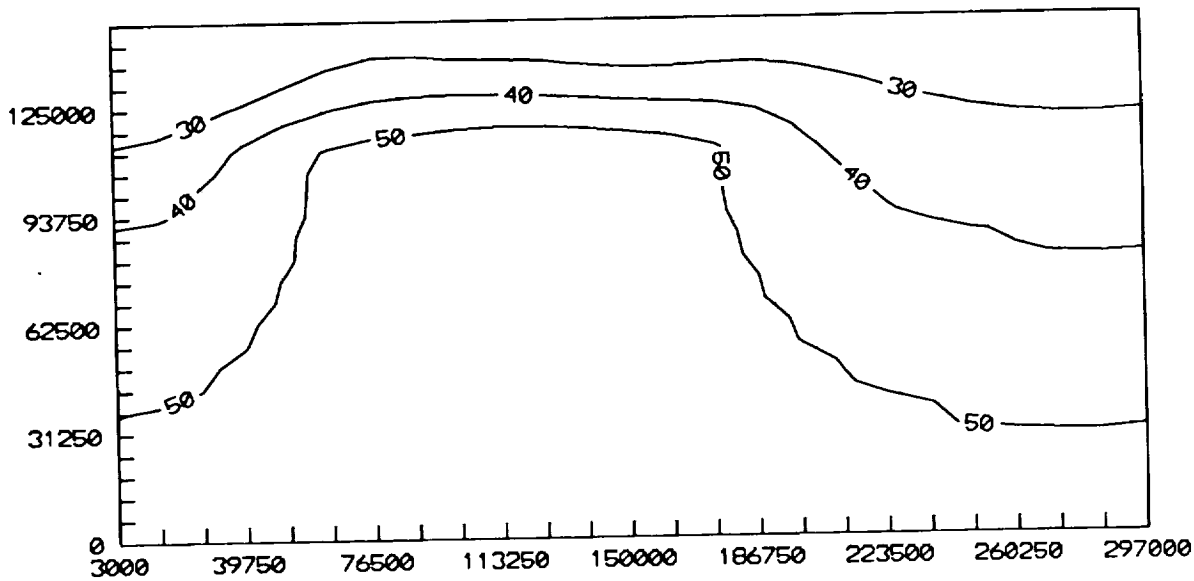

Figure 12-6d. Calculated temperature field (°C) at 15,000 years for cross section N765000. Welded-tuff bulk permeability of 10^{-11} m^2.

calculated gas-flow field at 5000 years is illustrated in Figure 12-7a. At this time, the maximum velocity is 3.9×10^{-7} m/s.

As the time reaches 10,000 years, the temperature and gas-flow fields within the mountain become smoother (Figure 12-6c and Figure 12-7b) and temperature gradients are smaller than at earlier times. ^{14}C particles released at this time travel slower than particles released earlier. Travel times range from 500 to 1200 years (Figure 12-5c).

Finally, we present the results when the waste has been emplaced 15,000 years. Less heat is being released from the repository, and the temperature and gas-flow fields become more linearly distributed (Figure 12-6d and Figure 12-7c). As time passes, gas velocity and temperature decrease and their magnitudes are much smaller than at earlier times. Particle travel times are slower and some of the particles can travel as long as 1800 years before they escape from the mountain (Figure 12-5d).

The travel times calculated for later times are faster than those previously calculated for TSPA-91. This is due to the assumed emplacement of older waste at the same initial power density, leading to a larger mass density of waste in the repository. The heat output at late times depends on the mass density of the waste; thus, heat output and temperatures at these times are greater than in the TSPA-91 calculations.

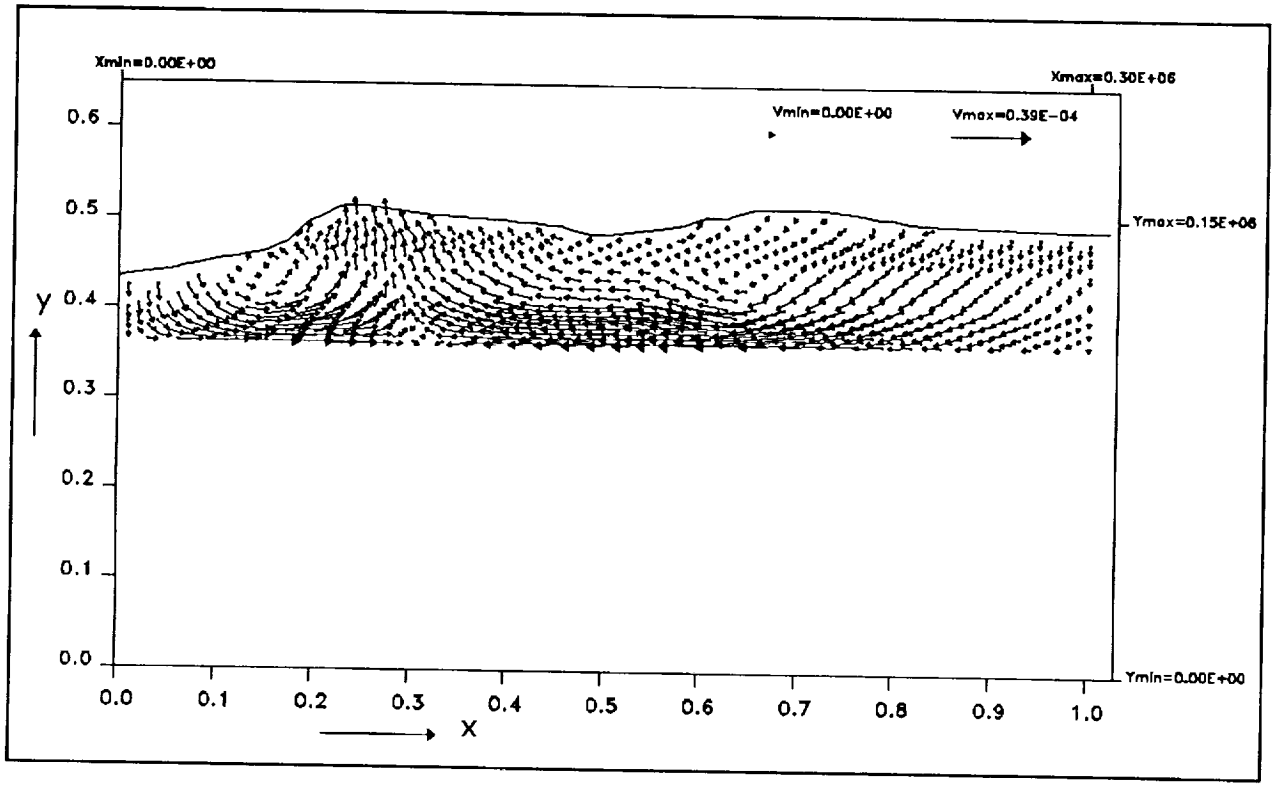

Figure 12-7a. Calculated gas-flow field at 5000 years for cross section N765000. Welded-tuff bulk permeability of 10^{-11} m^2.

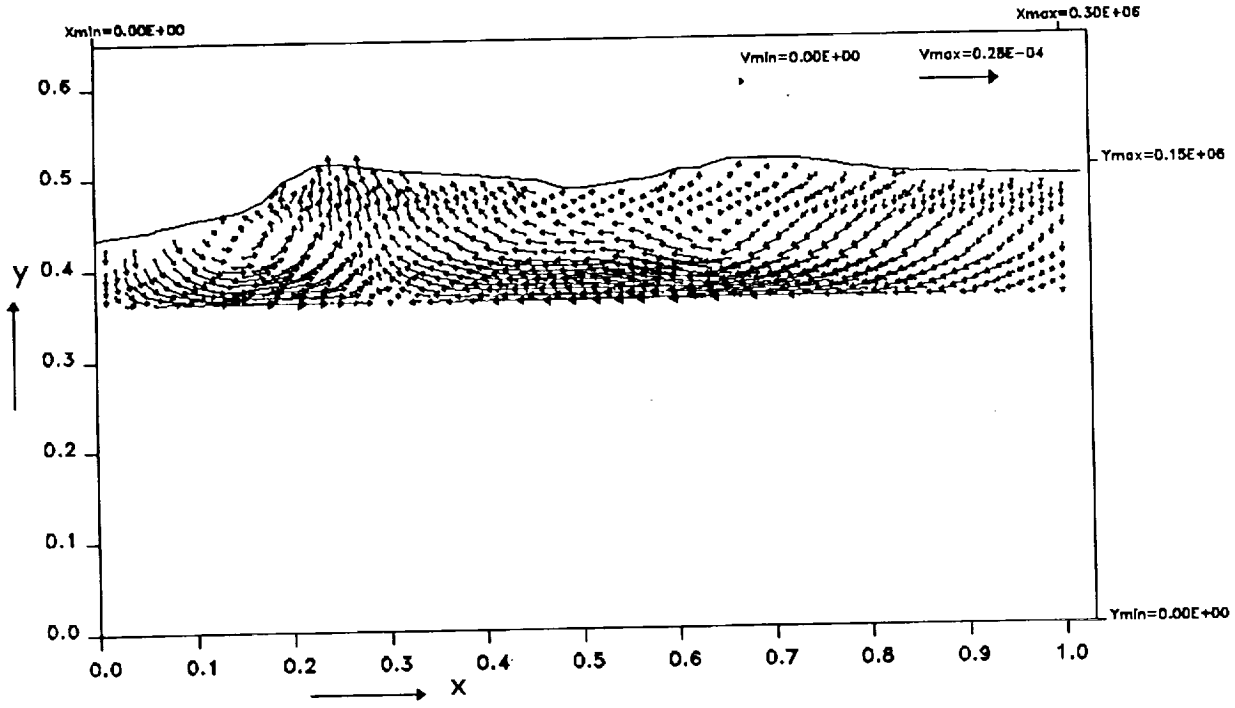

Figure 12-7b. Calculated gas-flow field at 10,000 years for cross section N765000. Welded-tuff bulk permeability of 10^{-11} m^2.

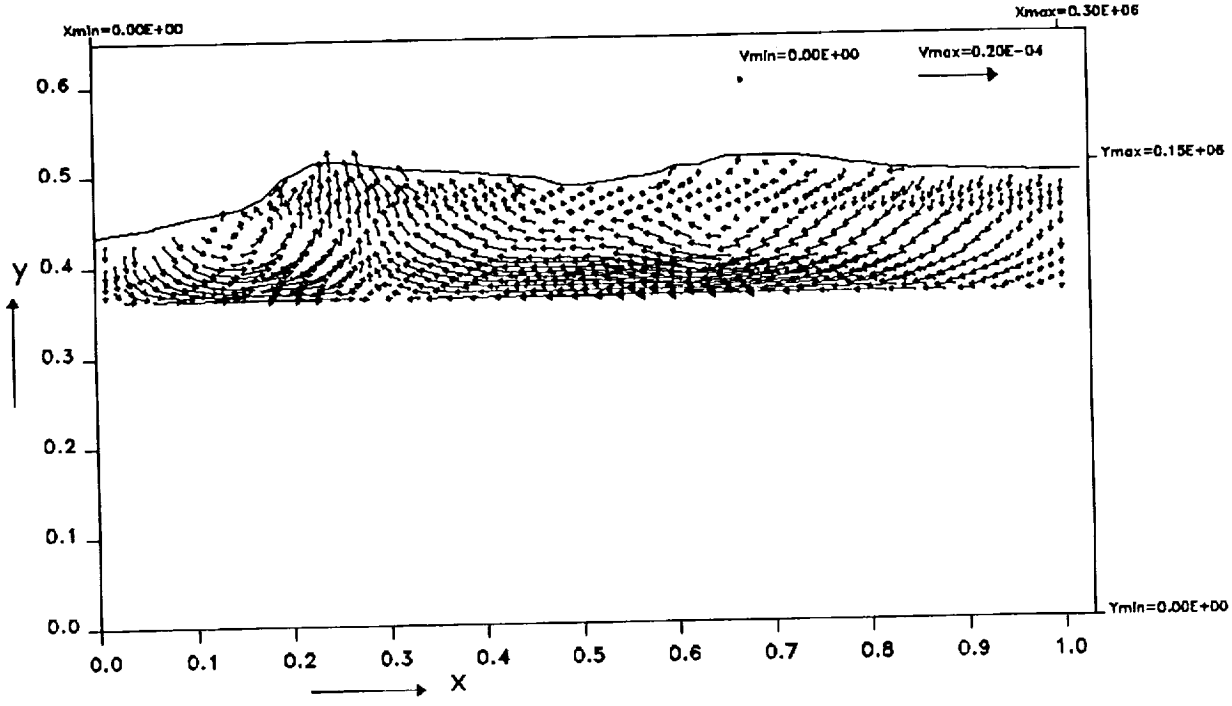

Figure 12-7c. Calculated gas-flow field at 15,000 years for cross section N765000. Welded-tuff bulk permeability of 10^{-11} m^2.

To examine the sensitivity of ^{14}C particle travel time to the bulk permeability, simulation runs with a welded-tuff bulk permeability of 10^{-12} m^2 were also conducted. Figures 12-8a through 12-8c show travel-time histograms that combine the results of all three cross sections at 2,000, 5,000, and 10,000 years. Travel times range from 3,000 to 15,000 years. Figures 12-8b and 12-8c can be compared to Figures 12-5b and 12-5c to see that a decrease of bulk permeability by a factor of 10 increases travel times by more than a factor of 10. The comparison is presented more directly in Figure 12-9 for starting times of 2,000 years and 10,000 years. Plotted in Figure 12-9 are cumulative ^{14}C travel-time distributions for welded-tuff bulk permeability of 10^{-12} m^2, and the corresponding distributions for welded-tuff bulk permeability of 10^{-11} m^2 with the travel times scaled by a factor of 10. If the travel time were inversely proportional to bulk permeability the two distributions would be the same, but the figure shows that during the early hot period (e.g., the 2000-yr curves in the figure) the distributions are quite different. The effect can be explained as follows. With lower permeability, the ^{14}C particles travel slower and take longer to reach the surface. During that longer time period temperatures decline substantially, thereby reducing the driving force and reducing the velocities further. The effect is less pronounced for later start times (e.g., the 10,000-yr curves in the figure) because the temperature decline is slower.

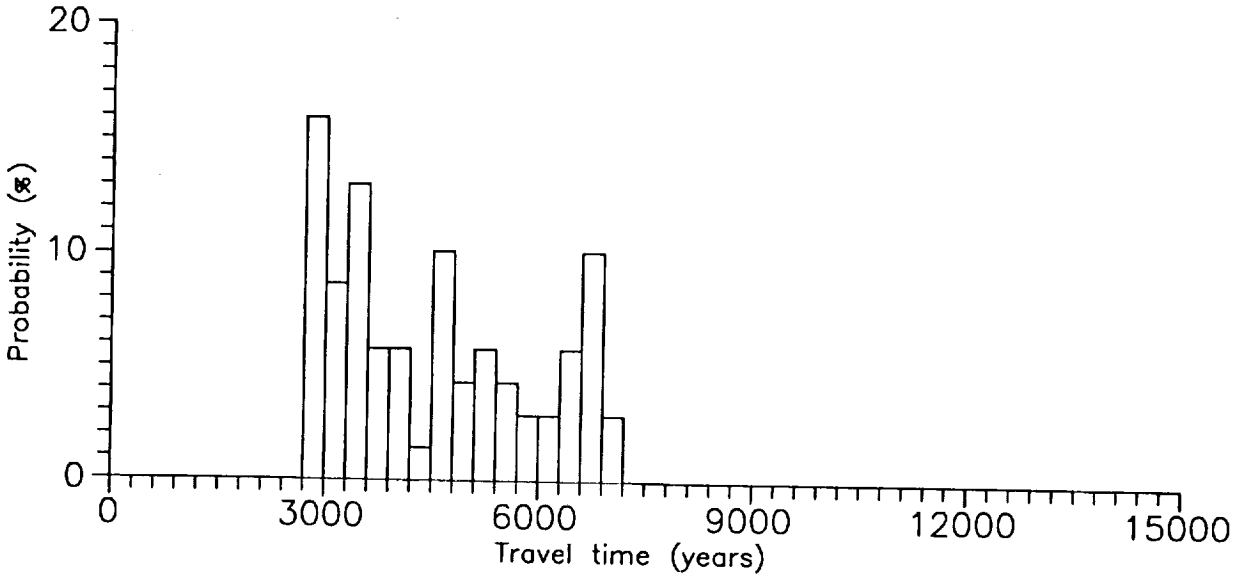

Figure 12-8a. Retarded travel times of ^{14}C particles from the repository to the atmosphere for particles released at 2000 years. Welded-tuff bulk permeability of 10^{-12} m^2.

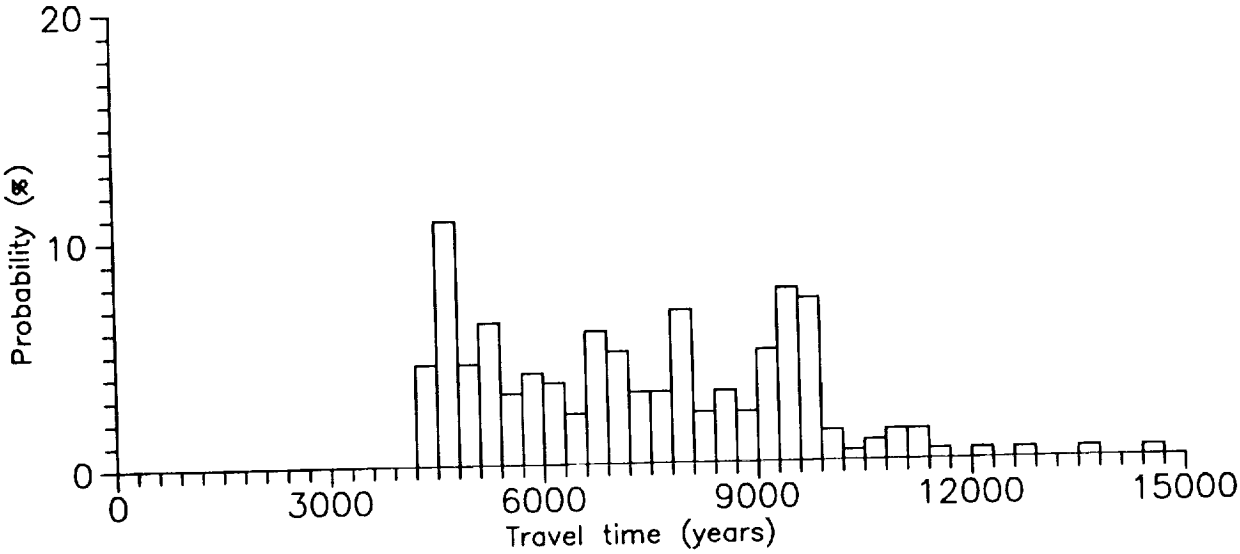

Figure 12-8b. Retarded travel times of ^{14}C particles from the repository to the atmosphere for particles released at 5000 years. Welded-tuff bulk permeability of 10^{-12} m^2.

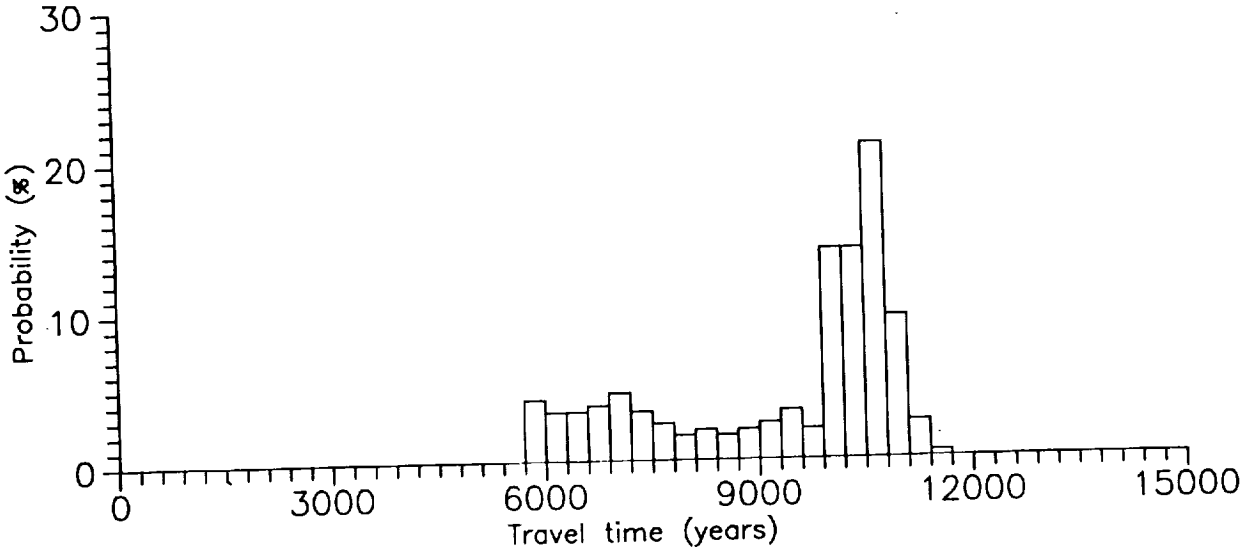

Figure 12-8c. Retarded travel times of ^{14}C particles from the repository to the atmosphere for particles released at 10,000 years. Welded-tuff bulk permeability of 10^{-12} m^2.

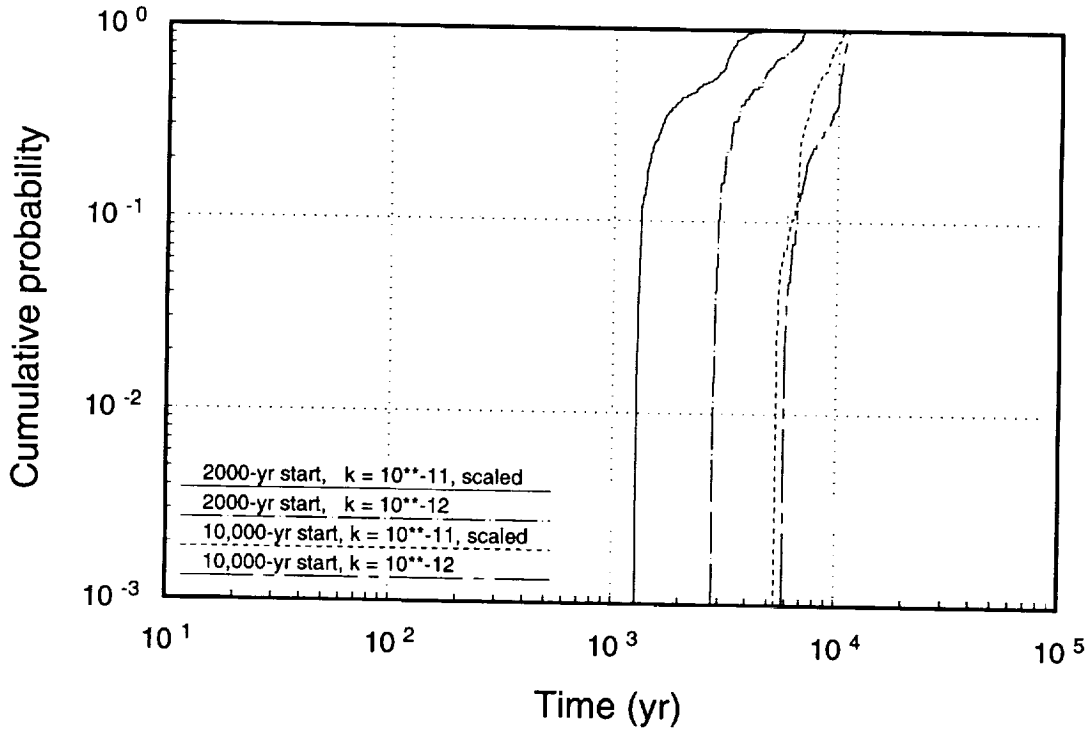

Figure 12-9. ^{14}C travel times for welded-tuff permeability of 10^{-12} m^2 compared to ^{14}C travel times for welded-tuff permeability of 10^{-11} m^2. The travel times for 10^{-11} m^2 are increased by a factor of 10 in this figure.

12.4 Abstraction of results for the TSA

The abstraction of results from detailed calculations of gas flow and ^{14}C gaseous transport is made in exactly the same way as for TSPA-91. It is not possible, at least at this time, to incorporate the TGIF2 and TRACK models directly into the Monte Carlo release simulations. Thus, as described in Section 5.4 of the TSPA-91 report, gaseous releases are calculated in total-system analyzer (TSA) simulations by a simple convolution integral of the ^{14}C source-release function with the ^{14}C travel-time distributions, as follows:

$$E = \int_0^T d\tau\, \Sigma(\tau) \int_0^{T-\tau} dt\, P(t;\tau) e^{-\lambda t}\ , \tag{12.6}$$

where E is the cumulative release to the accessible environment, $\Sigma(\tau)$ is the source release rate at time τ, $P(t;\tau)$ is the travel-time distribution, with t being the time to reach the surface, T is the EPA time period (10,000 yr; EPA, 1985), and λ is the decay rate of ^{14}C. As indicated, the travel-time distribution P depends on the release time τ; P is normalized so that $\int_0^\infty P(t;\tau)\, dt = 1$.

The application of Equation 12.6 is actually easier this time than it was in TSPA-91 because we are explicitly given $P(t;\tau)$ for several release times τ. For TSPA-91 the travel-time distributions were calculated with a steady-state model (TGIF), based on a given

repository temperature. It was necessary to estimate the time τ to which the distribution applied. With the transient solutions from TGIF2, that step is unnecessary.

The source term $\Sigma(\tau)$ is discussed in general in Chapter 13, and application to the two conceptual groundwater-flow models is discussed in Chapters 14 and 15. In this section, some issues related to the travel-time distribution $P(t;\tau)$ are discussed.

At the time the gaseous-release calculations were made, only one set of the travel-time distributions—those for welded-tuff bulk permeability $k = 10^{-11}$ m^2—was available. For the Monte Carlo simulations, we need to be able to represent as much of the uncertainty in the models and parameters as possible. Since the appropriate value of bulk permeability is uncertain, and the travel times are sensitive to bulk permeability (compare Figures 12-5 and 12-8), we need to be able to vary k in the gaseous-release simulations.

For TSPA-91, a parameter called the "retardation/permeability factor" was defined, which was used to scale the travel-time distributions. The idea behind the factor was that, if we were to change all the retardations throughout the mountain by a factor x, then the travel times would all be multipled by x ($t \rightarrow tx$). Similarly, in the TGIF model if all the permeabilities were changed by a factor x, then the travel times would all be divided by x ($t \rightarrow t/x$). Thus, F was defined as $(R/R_b)(k_b/k)$, where k_b is the "base" permeability and R_b is the base retardation. A probability distribution was defined for F and the sampled values of F were used to scale the travel-time distributions. This procedure does not represent the full uncertainty, of course, because permeability and retardation can change in ways other than uniformly by a single factor everywhere. In fact, since R is a function of temperature, scaling R by the same factor everywhere may be unrealistic.

Because of the coupling between gas flow and heat flow, TGIF2 travel times no longer scale inversely with bulk permeability; there is a more complicated, nonlinear relationship. As discussed in the previous section, when k is decreased by a factor of 10, the travel times increase by more than a factor of 10 (see Figure 12-9). This being the case, scaling the travel times inversely with bulk permeability is conservative. Rather than rolling retardation and permeability up into a single factor, for this TSPA values are sampled for bulk permeability and for a "retardation multiplication factor" R', and the travel times are scaled by the factor $F = R'(k_b/k)$. This scaling allows us to include some, at least, of the uncertainty in ^{14}C gaseous transport.

The distribution used for sampling k is the Topopah Spring welded bulk conductivity from Table 7-13 (unit 3); conductivity is converted to permeability by multiplying by 1.02×10^{-7} m^2/(m/s). The base welded bulk permeability is $k_b = 10^{-11}$ m^2.

The distribution chosen for the retardation multiplication factor R' is subjective, with little actual information to base it on. We use a uniform distribution from 0.75 to 2. The

reasoning for the upper limit is as follows. Possible sorption of carbon dioxide onto solid minerals is neglected in the retardation derivation, and sorption onto solids could be significant (see, e.g., Table 9-4). Meijer (1993) states that retardation for CO_2 could be as much as a factor of three higher if surface adsorption is included. Because higher values of retardation are non-conservative, we use only 2 rather than 3 for the upper limit. The reasoning for the lower limit is simply that we think higher retardations are more likely than lower ones because a significantly lower retardation requires both negligible solid adsorption and water chemistry significantly different than that calculated by PHREEQE. The value 0.75 is used to allow some possibility that retardations are lower, but to make the probability of lower retardations less than the probability of higher ones.

The effective retardation/permeability distribution for this TSPA ($R'k_b/k$) is compared with the retardation/permeability distribution F for TSPA-91 in Figure 12-10. The new distribution is about a factor of three higher than the old one. However, as will be seen, the new travel times are lower than the old ones by more than a factor of three, so the net effect is still faster ^{14}C transport for this TSPA.

We close out this section with a comparison of the ^{14}C travel-time distributions for this TSPA and for TSPA-91. The base-case travel-time distributions for TSPA-91 are shown

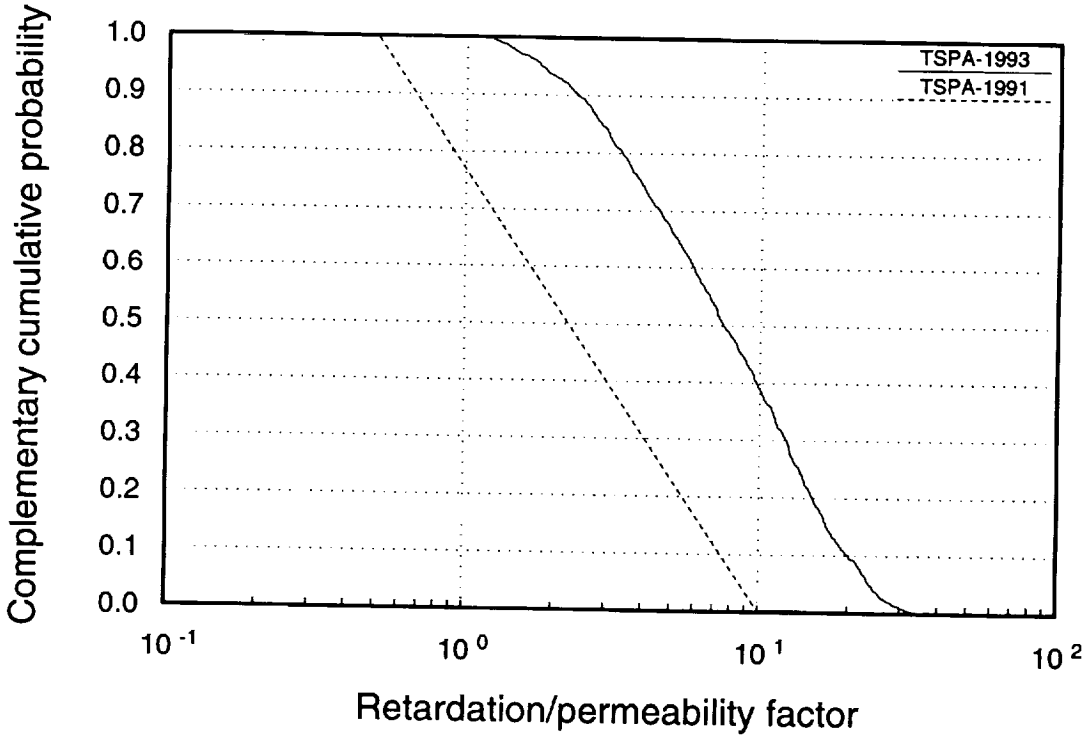

Figure 12-10. Comparison of retardation/permeability factor for TSPA-91 and TSPA-93.

in Figure 12-11. The curve for ambient conditions is not included in the plot because that travel-time distribution was not used for 10,000-year calculations. The approximate starting time is shown for each of the distributions, taken from Figure 5-13 of the TSPA-91 report. The base-case travel-time distributions for TSPA-93 are shown in Figure 12-12; only the ones used in a 10,000-year calculation are shown; i.e., starting times from 1000 yr to 9000 yr.

The curves in the two figures are very different—in shape as well as in mean travel time. Part of the difference between the two, and most of the difference in the shapes, is because different assumptions were made about the bulk permeability of the nonwelded layer. The base case for TSPA-91 assumed a bulk permeability of 10^{-11} m^2 for the welded tuff and a bulk permeability of 10^{-13} m^2 for the nonwelded tuff. The base case for TSPA-93 assumes the same value as before for the welded tuff and a bulk permeability of 10^{-12} m^2 for the nonwelded tuff. The choice of 10^{-12} m^2 rather than 10^{-13} m^2 makes the results more conservative because the lower nonwelded bulk permeability for TSPA-91 made the nonwelded layer much more of a confining layer, forcing longer path lengths for most of the ^{14}C. A fraction of the ^{14}C was able to avoid the confining layer by exiting along the side of Solitario Canyon; this explains the bimodal shape of the TSPA-91 travel-time curves.

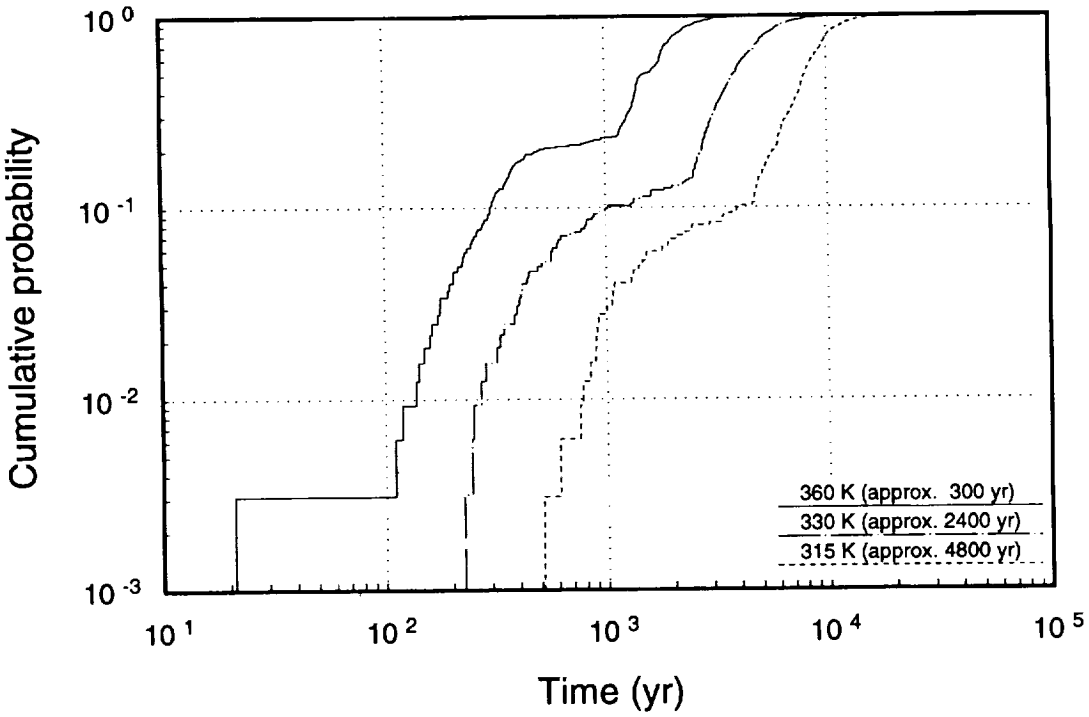

Figure 12-11. ^{14}C travel-time distributions for TSPA-91.

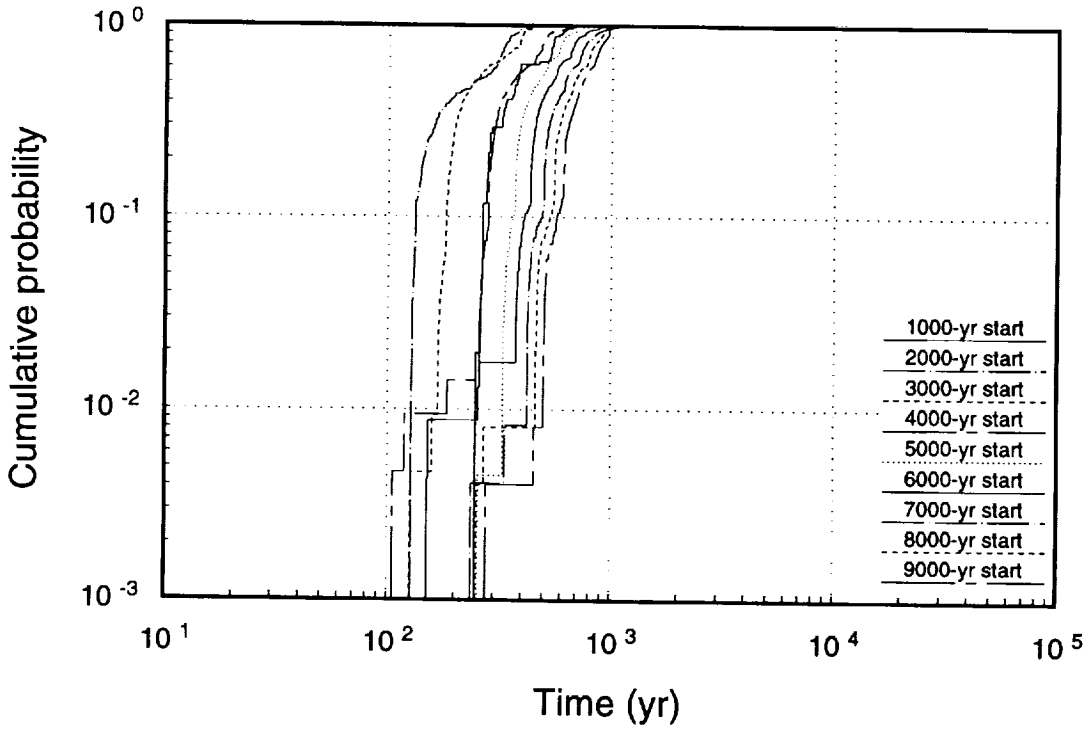

Figure 12-12. ^{14}C travel-time distributions for TSPA-93.

A more direct comparison of TGIF and TGIF2 results is available, because Ross *et al.* (1992) analyzed both cases: nonwelded bulk permeability of 10^{-13} m^2 and 10^{-12} m^2. The travel-time curves for the latter case are shown in Figure 12-13. Those curves are much more similar to the TGIF2 travel-time curves, except for the first one. The differences in a steady-state vs. a transient calculation are expected to be greatest at early times, when the temperature gradients are large.

Comparison of Figures 12-12 and 12-13 indicates that, as was mentioned in the previous section, temperatures decline much more slowly in the new calculations than they were assumed to do in the old ones (travel times remain small for a longer time). The TGIF travel-time distribution for a repository temperature of 330 K is close to the TGIF2 10,000-yr distribution (not shown in the figure), whereas in TSPA-91 the 330-K distribution was used for transport starting at 2400 yr.

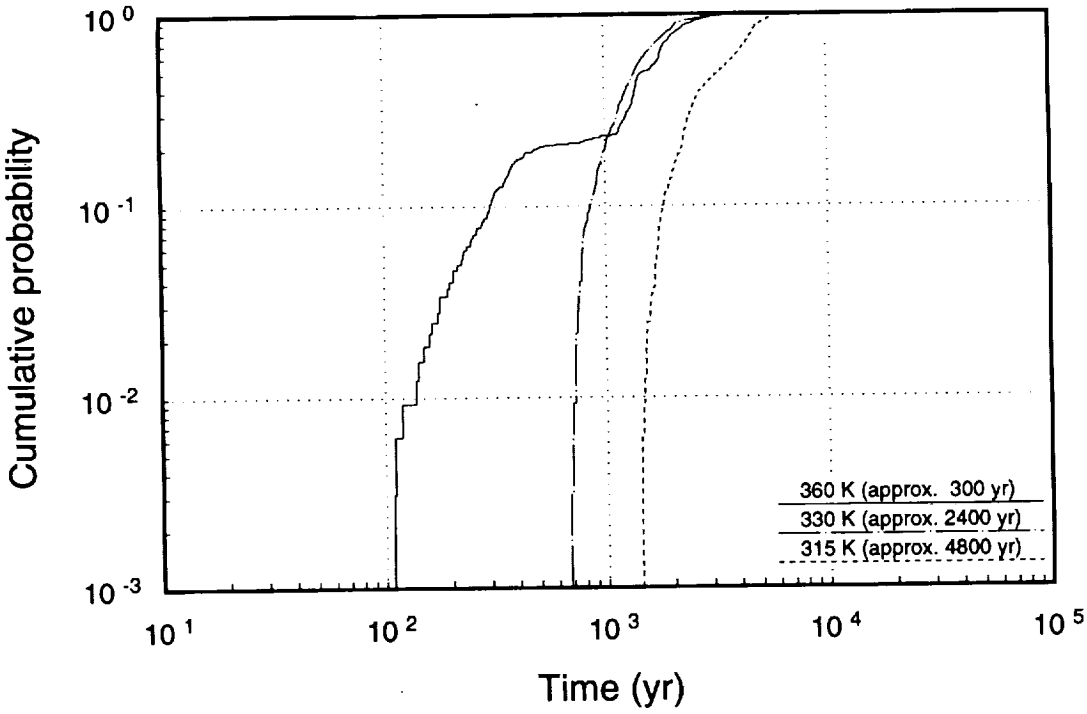

Figure 12-13. ^{14}C travel-time distributions for steady-state gas flow, with welded-tuff permeability of 10^{-11} m^2 and nonwelded-tuff permeability of 10^{-12} m^2.

YUCCA MOUNTAIN SITE CHARACTERIZATION PROJECT
DISTRIBUTION LIST

1 D.A. Dreyfus (RW-1)
Director
OCRWM
US Department of Energy
1000 Independence Avenue SW
Washington, DC 20585

1 L.H. Barrett (RW-2)
Acting Deputy Director
OCRWM
US Department of Energy
1000 Independence Avenue SW
Washington, DC 20585

1 J.D. Saltzman (RW-4)
Office of Strategic Planning and International Programs
OCRWM
US Department of Energy
1000 Independence Avenue SW
Washington, DC 20585

1 J.D. Saltzman (RW-5)
Office of External Relations
OCRWM
US Department of Energy
1000 Independence Avenue SW
Washington, DC 20585

1 Samuel Rousso (RW-10)
Office of Program and Resource Mgt.
OCRWM
US Department of Energy
1000 Independence Avenue SW
Washington, DC 20585

1 J. C. Bresee (RW-10)
OCRWM
US Department of Energy
1000 Independence Avenue SW
Washington, DC 20585

1 R.M. Nelson (RW-20)
Office of Geologic Disposal
OCRWM
US Department of Energy
1000 Independence Avenue, SW
Washington, DC 20585

1 S. J. Brocoum (RW-22)
Analysis and Verification Division
OCRWM
US Department of Energy
1000 Independence Avenue SW
Washington, DC 2585

1 D. Shelor (RW-30)
Office of Systems and Compliance
OCRWM
US Department of Energy
1000 Independence Avenue, SW
Washington, DC 20585

1 J. Roberts (RW-33)
Director, Regulatory Compliance Division
OCRWM
US Department of Energy
1000 Independence Avenue, SW
Washington, DC 20585

1 G. J. Parker (RW-332)
Reg. Policy/Requirements Branch
OCRWM
US Department of Energy
1000 Independence Avenue, SW
Washington, DC 20585

1 R. A. Milner (RW-40)
Office of Storage and Transporation
OCRWM
US Department of Energy
1000 Independence Avenue, SW
Washington, DC 20585

1 S. Rousso (RW-50)
Office of Contract Business Management
OCRWM
US Department of Energy
1000 Independence Avenue, SW
Washington, DC 20585

1 T. Wood (RW-52)
Director, M&O Management Division
OCRWM
US Department of Energy
1000 Independence Avenue, SW
Washington, DC 20585

4 Victoria F. Reich, Librarian
Nuclear Waste Technical Review Board
1100 Wilson Blvd, Suite 910
Arlington, VA 22209

5 R.M. Nelson Jr, Acting Project Manager
Yucca Mountain Site Characterization Office
US Department of Energy
P.O. Box 98608--MS 523
Las Vegas, NV 89193-8608

1 C. L. West, Director
Office of External Affairs
DOE Nevada Field Office
US Department of Energy
P.O. Box 98518
Las Vegas, NV 89193-8518

8 Technical Information Officer
DOE Nevada Field Office
US Department of Energy
P.O. Box 98518
Las Vegas, NV 89193-8518

1 P. K. Fitzsimmons, Technical Advisor
Office of Assistant Manager for Environmental Safety and Health
DOE Nevada Field Office
US Department of Energy
P.O. Box 98518
Las Vegas, NV 89193-8518

1 D. R. Elle, Director
Environmental Protection and Division
DOE Nevada Field Office
US Department of Energy
P.O. Box 98518
Las Vegas, NV 89193-8518

1 Repository Licensing & Quality Assurance
Project Directorate
Division of Waste Management
US NRC
Washington, DC 20555

1 Senior Project Manager for Yucca Mountain
Repository Project Branch
Division of Waste Management
US NRC
Washington, DC 20555

1 NRC Document Control Desk
Division of Waste Management
US NRC
Washington, DC 20555

1 Philip S. Justus
NRC Site Representive
301 E Stewart Avenue, Room 203
Las Vegas, NV 89101

1 E. P. Binnall
Field Systems Group Leader
Building 50B/4235
Lawrence Berkeley Laboratory
Berkeley, CA 94720

1 Center for Nuclear Waste Regulatory Analyses
6220 Culebra Road
Drawer 28510
San Antonio, TX 78284

3 W. L. Clarke
Technical Project Officer - YMP
Attn: YMP/LRC
Lawrence Livermore National Laboratory
P.O. Box 5514
Livermore, CA 94551

1 J. A. Blink
Deputy Project Leader
Lawrence Livermore National Laboratory
101 Convention Center Drive
Suite 820, MS 527
Las Vegas, NV 89109

4 J. A. Canepa
Technical Project Officer - YMP
N-5, Mail Stop J521
Los Alamos National Laboratory
P.O. Box 1663
Los Alamos, NM 87545

1 H. N. Kalia
Exploratory Shaft Test Manager
Los Alamos National Laboratory
Mail Stop 527
101 Convention Center Dr., #820
Las Vegas, NV 89101

1 N. Z. Elkins
Deputy Technical Project Officer
Los Alamos National Laboratory
Mail Stop 527
101 Convention Center Dr., #820
Las Vegas, NV 89101

5 L. E. Shephard
Technical Project Officer - YMP
Sandia National Laboratories
Organization 6302, M/S 1333
P.O. Box 5800
Albuquerque, NM 87185

1 J. F. Devine
Asst Director of Engineering Geology
US Geological Survey
106 National Center
12201 Sunrise Valley Drive
Reston, VA 22092

1 L. R. Hayes
Technical Project Officer
Yucca Mountain Project Branch
MS 425
US Geological Survey
P.O. Box 25046
Denver, CO 80225

1 V. R. Schneider
Asst. Chief Hydrologist--MS 414
Office of Program Coordination and Technical Support
US Geological Survey
12201 Sunrise Valley Drive
Reston, VA 22092

1 J. S. Stuckless
Geologic Division Coordinator
MS 913
Yucca Mountain Project
US Geological Survey
P.O. Box 25046
Denver, CO 80225

1 D. H. Appel, Chief
Hydrologic Investigations Program
MS 421
US Geological Survey
P.O. Box 25046
Denver, CO 80225

1 E. J. Helley
Branch of Western Regional Geology
MS 427
US Geological Survey
345 Middlefield Road
Menlo Park, CA 94025

1 R. W. Craig, Chief
Nevada Operations Office
US Geological Survey
101 Convention Center Drive
Suite 860, MS 509
Las Vegas, NV 89109

1 D. Zesiger
US Geological Survey
101 Conventional Center Drive
Suite 860, MS 509
Las Vegas, NV 89109

1 G. L. Ducret, Associate Chief
Yucca Mountain Project Division
US Geological Survey
P.O. Box 25046
421 Federal Center
Denver, CO 80225

1 A. L. Flint
US Geological Survey
MS 721
P.O. Box 327
Mercury, NV 89023

1 D. A. Beck
Water Resources Division, USGS
6770 S Paradise Road
Las Vegas, NV 89119

1 P. A. Glancy
US Geological Survey
Federal Building, Room 224
Carson City, NV 89701

1 Sherman S.C. Wu
US Geological Survey
2255 N. Gemini Drive
Flagstaff, AZ 86001

1 J. H. Sass - USGS
Branch of Tectonophysics
2255 N Gemini Drive
Flagstaff, AZ 86001

1 DeWayne Campbell
Technical Project Officer - YMP
US Bureau of Reclamation
Code D-3790
P.O. Box 25007
Denver, CO 80225

1 J. M. LaMonaca
Records Specialist
US Geological Survey
421 Federal Center
P.O. Box 25046
Denver, CO 80225

1 W. R. Keefer - USGS
913 Federal Center
P.O. Box 25046
Denver, CO 80225

1 M. D. Voegele
Technical Project Officer - YMP
SAIC
101 Convention Center Drive
Suite 407
Las Vegas, NV 89109

2 L. D. Foust
Nevada Site Manager
TRW Environmental Safety Systems
101 Convention Center Drive
Suite 540, MS 423
Las Vegas, NV 89109

1 C. E. Ezra
YMP Support Office Manager
EG&G Energy Measurements Inc
MS V-02
P.O. Box 1912
Las Vegas, NV 89125

1 E. L. Snow, Program Manager
Roy F. Weston Inc
955 L'Enfant Plaza SW
Washington, DC 20024

1 Technical Information Center
Roy F. Weston Inc
955 L'Enfant Plaza SW
Washington, DC 20024

1 D. Hedges, Vice President, QA
Roy F. Weston Inc
4425 Spring Mountain Road
Suite 300
Las Vegas, NV 89102

1 D. L. Fraser, General Manager
Reynolds Electrical & Engineering Co, Inc
MS 555
P.O. Box 98521
Las Vegas, NV 89193-8521

1 B. W. Colston, President and General Manager
Las Vegas Branch
Raytheon Services Nevada
MS 416
P.O. Box 95487
Las Vegas, NV 89193-5487

1 R. L. Bullock
Technical Project Officer - YMP
Raytheon Services Nevada
Suite P-250, MS 403
101 Convention Center Drive
Las Vegas, NV 89109

1 Paul Eslinger, Manager
PASS Program
Pacific Northwest Laboratory
P.O. Box 999
Richland, WA 99352

1 A. T. Tamura
Science and Technology Division
OSTI
US Department of Energy
P.O. Box 62
Oak Ridge, TN 37831

1 Carlos G. Bell Jr
Professor of Civil Engineering
Civil and Mechanical Engineering Dept.
University of Nevada, Las Vegas
4505 S Maryland Parkway
Las Vegas, NV 89154

1 P. J. Weeden, Acting Director
Nuclear Radiation Assessment Div.
US EPA
Environmental Monitoring Systems Lab
P.O. Box 93478
Las Vegas, NV 89193-3478

1 ONWI Library
Battelle Columbus Laboratory
Office of Nuclear Waste Isolation
505 King Avenue
Columbus, OH 43201

1 T. Hay, Executive Assistant
Office of the Governor
State of Nevada
Capitol Complex
Carson City, NV 89710

3 R. R. Loux
Executive Director
Agency for Nuclear Projects
State of Nevada
Evergreen Center, Suite 252
1802 N. Carson Street
Carson City, NV 89710

1 C.H. Johnson
Technical Program Manager
Agency for Nuclear Projects
State of Nevada
Evergreen Center, Suite 252
1802 N. Carson Street
Carson City, NV 89710

1 John Fordham
Water Resources Center
Desert Research Institute
P.O. Box 60220
Reno, NV 89506

1 David Rhode
Desert Research Institute
P.O. Box 60220
Reno, NV 89506

1 Eric Anderson
Mountain West Research-
Southwest Inc
2901 N Central Avenue #1000
Phoenix, AZ 85012-2730

1 The Honorable Cyril Schank
Chairman
Churchill County Board of
Commissioners
190 W First Street
Fallon, NV 89406

1 Dennis Bechtel, Coordinator
Nuclear Waste Division
Clark County Department of
Comprehensive Planning
301 E Clark Avenue, Suite 570
Las Vegas, NV 89101

1 Juanita D. Hoffman
Nuclear Waste Repository
Oversight Program
Esmeralda County
P.O. Box 490
Goldfield, NV 89013

1 Eureka County Board of
Commissioners
Yucca Mountain Information
Office
P.O. Box 714
Eureka, NV 89316

1 Brad Mettam
Inyo County Yucca Mountain
Repository Assessment Office
Drawer L
Independence, CA 93526

1 Lander County Board of
Commissioners
315 South Humbolt
Battle Mountain, NV 89820

1 Vernon E. Poe
Office of Nuclear Projects
Mineral County
P.O. Box 1026
Hawthorne, NV 89415

1 Les W. Bradshaw
Program Manager
Nye County Nuclear Waste
Repository Program
P.O. Box 153
Tonopah, NV 89049

1 Florindo Mariani
White Pine County Nuclear
Waste Project Office
457 Fifth Street
Ely, NV 89301

1 Judy Foremaster
City of Caliente Nuclear Waste
Project Office
P.O. Box 158
Caliente, NV 89008

1 Phillip A. Niedzielski-Eichner
Nye County Nuclear Waste
Repository Project Office
P.O. Box 221274
Chantilly, VA 22022-1274

1 Jason Pitts
Lincoln County Nuclear Waste
Project Office
Lincoln County Courthouse
Pioche, NV 89043

1 Economic Development Dept.
City of Las Vegas
400 E. Stewart Avenue
Las Vegas, NV 89101

1 Commmunity Planning and Development
City of North Las Vegas
P.O. Box 4086
North Las Vegas, NV 89030

1 Community Development and Planning
City of Boulder City
P.O. Box 61350
Boulder City, NV 89006

1 Commission of the European Communities
200 Rue de la Loi
B-1049 Brussells
BELGIUM

2 M. J. Dorsey, Librarian
YMP Research and Study Center
Reynolds Electrical & Engineering Co Inc
MS 407
P.O. Box 98521
Las Vegas, NV 89193-8521

1 Amy Anderson
Argonne National Laboratory
Building 362
9700 S Cass Avenue
Argonne, IL 60439

1 Steve Bradhurst
P.O. Box 1510
Reno, NV 89505

1 Michael L. Baughman
35 Clark Road
Fiskdale, MA 01518

1 Glenn Van Roekel
Director of Community Development
City of Caliente
P.O. Box 158
Caliente, NV 89008

1 Ray Williams, Jr
P.O. Box 10
Austin, NV 89310

1 Nye County District Attorney
P.O. Box 593
Tonopah, NV 89049

1 William Offutt
Nye County Manager
Tonopah, NV 89049

1 Charles Thistlethwaite, AICP
Inyo County Planning Department
Drawer L
Independence, CA 93526

1 R. F. Pritchett
Technical Project Officer - YMP
Reynolds Electrical & Engineering Company Inc
MS 408
P.O. Box 98521
Las Vegas, NV 89193-8521

1 Dr. Moses Karakouzian
1751 E Reno #125
Las Vegas, NV 89119

3 Brenda Bailey White
CCS
5301 Central NE
Suite 1520
Albuquerque, NM 87108

1 Clarence R. Allen
NWTRB
1000 E. California Blvd.
Pasadena, CA 91106

1 Johan Andersson
SKI
Division of Nuclear Waste
Sehlstedtgatan II
Box 27106
S-102 52 Stockholm
SWEDEN

1 Michael J. Apted
Intera Sciences
3609 S. Wadsworth Blvd
Denver, CO 80235

1 Dwayne Chesnut
Lawrence Livermore National Laboratory
P.O. Box 808
M/S L202
Livermore, CA 94551

1 Richard Codell
US Nuclear Regulatory Commission
M/S 4-H-3
Washinton, DC 20555

1 Seth M. Coplan
US Nuclear Regulatory Commission
M/S 4-H-3
Washington, DC 20555

1 Kevin Coppersmith
Geomatrix Consultants
100 Pine Street, 10th Floor
San Francisco, CA 94111

1 C.F. Costa
Nuclear Radiation Assessment Division
US EPA
Environmental Monitoring Systems Laboratory
P.O. Box 93478
Las Vegas, NV 89193-3478

1 Allen G. Croff
Chemical Technology Division
Oak Ridge National Laboratory
4500N, MS-6235
P.O. Box 2008
Oak Ridge, TN 37831-6235

1 Bruce M. Crowe
Los Alamos National Laboratory
101 Convention Center Drive
Suite 820
Las Vegas, NV 89109

1 Department of Comprehensive Planning
Clark County
225 Bridger Avenue, 7th Floor
Las Vegas, NV 89155

1 D.W. Engel
Pacific Northwest Laboratory
P.O. Box 999
M/S K7-34
Richland, WA 99352

1 Leonard J. Fiorenzi
P.O. Box 257
Eureka, NV 89316

1 A.B. Gureghian
CNWRA
6220 Culebra Road
San Antonio, TX 78228-0510

5 William G. Halsey
Lawrence Livermore National Laboratory
P.O. Box 808
M/S L-204
Livermore, CA 94551

1 M.E. Harr
School of Civil Engineering
Purdue University
1284 Civil Engineering Building
West Lafayette, IN 47907-1284

1 Dwight Hoxie
US Geological Survey
101 Convention Center Drive
Suite 860
Las Vegas, NV 89109

1 Edwin E. Kinter
Bradley Hill Road
P.O. Box 682
Nortwich, VT 05055

1 Donald Langmuir
Nuclear Waste Technical Review Board
109 So. Lookout Mountain Cr.
Golden, CO 80401

1 Lincoln County Commission
Lincoln County
P.O. Box 90
Pioche, NV 89043

1 Ian Miller
Golder Associates Inc
4104 148 Avenue NE
Redmond, WA 98052

1 R.W. Nelson
INTERA-M&O
101 Convention Center Drive
Suite P110
Las Vegas, NV 89109

1 Claudia Newbury
Yucca Mountain Project Office
US Department of Energy
P.O. Box 98608
M/S 523
Las Vegas, NV 89193-8518

1 D. Warner North
NWTRB
Decision Focus Inc
4984 El Camino Real
Los Altos, CA 94062

2 William J. O'Connell
Lawrence Livermore National Laboratory
P.O. Box 808, M/S L-195
Livermore, CA 94551

1 Michael Revelli
Lawrence Livermore National Laboratory
P.O. Box 808
M/S L-206
Livermore, CA 94551

1 Benjamin Ross
Disposal Safety Inc
1660 L STreet NW, Suite 314
Washington, DC 20036

2 SAIC-T & MSS Library
101 Convention Center Drive
Suite 407
Las Vegas, NV 89109

1 Frank W. Schwartz
195 Thornbury Lane
Powell, OH 43065

1 Bjorn Selinder
190 W. First Street
Fallon, NV 89406

1 Ardyth Simmons
Yucca Mountain Project
US DOE
P.O. Box 98608
M/S 523
Las Vegas, NV 89193-8518

1 Scott Sinnock
TRW
101 Convention Center Drive
Suite P110
Las Vegas, NV 89109

1 Ellis D. Verink
Nuclear Waste Technical Review Board
4401 NW 18th Place
Gainesville, FL 32605

1 Joseph Wang
Lawrence Berkeley Laboratory
Earth Sciences Division
1 Cyclotron Road
Berkeley, CA 94720

1 R.V. Watkins, Chief
Project Planning and Management
USGS
P.O. Box 25046
421 Federal Center
Denver, CO 80225

1 Ed Weeks -USGS
P.O. Box 25046
Federal Center M/S 413
Lakewood, CO 80225

1 C.L. West, Director
Office of External Affairs
DOE Field Office, Nevada
US DOE
P.O. Box 98518
Las Vegas, NV 89193-8518

1 Robert F. Williams
EPRI Nuclear Power Division
P.O. Box 10412
Palo Alto, CA 94303

1 George Zyvoloski
Geoanalysis Group
Los Alamos National Lab
M/S F665
Los Alamos, NM 87545

1 Jean Younker
TRW
101 Convention Center Drive
Suite P110
Las Vegas, NV 89109

1 Dr. June Fabryka-Martin
Los Alamos National Lab
MS J-514
Los Alamos, NM 87545

1 Dr. F. Owen Hoffman
Oak Ridge National Lab
P.O. Box 2008
Oak Ridge, TN 37831-6036

1 Dr. Arjun Makhijani
Institute for Energy and Environmental Research
6935 Laurel Avenue
Takoma Park, MD 20912

1 Dr. James E. Martin
Assistant Professor of
Radiological Health
University of Michigan
School of Public Health
Ann Arbor, MI 48109

1 Dr. H. Robert Meyer
C.N.S.I.
750 East Park Drive
Suite 200
Harrisburg, PA 17111

1 Jess Riley
Heinman Research Labs
P.O. Box 35457
Charlotte, NC 28207

1 James E. Watson Jr
Environ. Science and Engineering
Campus Box 7400
University of North Carolina
Chapel Hill, NC 27599-7400

1 Dr. William M. Murphy
Center for Nuclear Waste
Regulatory Analyses
Southwest Research Institute
6220 Culebra Road
San Antonio, TX 78238-5166

1 Miroslav Kucerka, Consultant
Radioactive Waste Management
Botevova 3104
143 00 Praha 4
Czech Republic

1 Dr. John Kessler
Nuclear Power Division
EPRI
P.O. Box 10412
Palo Alto, CA 94303-0813

1 Per-Eric Ahlstrom
Research Director
Swedish Nuclear Fuel and
Waste Management Co
Box 5864 S-102 48
Stockholm, Sweden

1 W.A. Seddon
AECL Technologies
9210 Corporate Boulevard
Suite 410
Rockville, MD 20850

1 Dr. Wilfried Albert
NAGRA
Hardstrasse 73
CH-5430 Wettingen
Switzerland

1 Runo Barrdahl
Swedish Radiation Protection
Institute
P.O. Box 60204
S-104 01 Stockholm
Sweden

1 Dr. John E. Gale
Fracflow Consultants Inc
36 Pearson Street
St. John's, Newfoundland
Canada A1A 3R1

1 Dr. Furruccio Gera
ISMES S.P.S.
Via dei Crociferi 44
00187 Rome, Italy

1 Dr. Gunnar Gustafson
Department of Geology
Chalmers University of Technology
and University of Goteborb
S-412 96 Goteborg
Sweden

1 Dr. Alan W. Herbert
AEA Technology
Theoretical Studies Department
Harwell Laboratory B424.4
Oxfordshire OX11 ORA
United Kingdom

1 David Hodgkinson
INTERA
Chiltern House
45 Station Road
Henley-on-Thames, Oxon
RG9 1AT
United Kingdom

1 Dr. Yong Soo Hwang
Korea Atomic Energy
Research Institute
P.O. Box 7
Daeduk-Danji
Taejeon, Korea

1 Dr. Katsumi Kamemura
Shinozuka Research Institute
5F Maguna Kogyo Building 1-31-13
Yoyogi, Shibuya-ku
Tokyo, 151, Japan

1 Dr. Bill Lanyon
Geo-Science Limited
Falmouth Business Park
Bickland Water Road
Falmouth, Cornwall
TR11 4SZ, United Kingdom

1 Dr. Jussi Palmu
Imatran Voima Oy
Rajatorpantie 8
P.O. Box 112
SF-01601 Vantaa, Finland

1 Dr. Carmen Bajos Parada
ENRESA
Emilio Vargas 7
28043 Madrid, Spain

1 Dr. Gunnar Ramqvist
ELTEKNO AB
Gruvvagen 1
S-714 00 Kopparberg
Sweden

1 Dr. Robert Rundberg
Los Alamos National Lab
Mail Stop J-514
Los Alamos, NM 87545

1 James A. Steadman
Building Research Establishment
Structural Performance Division
Garston, Watford WD2 7JR
United Kingdom

1 Dr. Ove Stephansson
Department of Engineering Geology
Royal Institute of Technology
S-100 44 Stockholm, Sweden

1 Dr. Juhani Vira
Teollisuuden Voiman Oy
Annankatu 42 C
SF-00100 Helsinki
Finland

1 Peter Wallman
Golder Associates
4104 148 Avenue NE
Redmond WA 98052

1 Minoro Yamakuma
Geoscience Research Project
PNC Tokyo, Japan

1 David Leaver
Polestar
Four Main Street
Los Altos, CA 94022

1 James Gansemer
Lawrence Livermore National Laboratory
P.O. Box 808
Livermore, CA 94551

1 Lynn C. Lewis
Lawrence Livermore National Laboratory
P.O. Box 808
Livermore, CA 94551

1 Alan D. Lamont
Lawrence Livermore National Laboratory
P.O. Box 808
Livermore, CA 94551

1 Ines Triay
Los Alamos National Laboratory
P.O. Box 1663
Los Alamos, NM 87545

1 David Morris
Los Alamos National Laboratory
P.O. Box 1663
Los Alamos, NM 87545

1 Ning Lu
USGS
P.O. Box 25046, MS 421
Denver Federal Center
Lakewood, CO 80225

1 Gary LeCain
USGS
P.O. Box 25046
Denver Federal Center
Lakewood, CO 80225

1 Edward Kwicklis
USGS
P.O. Box 25046
Denver Federal Center
Lakewood, CO 80225

1 Jerry McNeish
INTERA
M/S 423
101 Convention Center Drive
Las Vegas, NV 89109

1 April V. Gil
Yucca Mountain Project
M/S 523
101 Convention Center Drive
Las Vegas, NV 89109

1 Joseph J. Dlugosz
Yucca Mountain Project
M/S 523
101 Convention Center Drive
Las Vegas, NV 89109

1 Wendy R. Dixon
Yucca Mountain Project
M/S 523
101 Convention Center Drive
Las Vegas, NV 89109

1 Jeanne C. Nesbit
Yucca Mountain Project
M/S 523
101 Convention Center Drive
Las Vegas, NV 89109

1 Susan B. Jones
Yucca Mountain Project
M/S 523
101 Convention Center Drive
Las Vegas, NV 89109

1 William B. Simecka
Yucca Mountain Project
M/S 523
101 Convention Center Drive
Las Vegas, NV 89109

1 Dennis R. Williams
Yucca Mountain Project
M/S 523
101 Convention Center Drive
Las Vegas, NV 89109

1 C. Thomas Statton
Yucca Mountain Project
M&O/WCFS
M/S 423
101 Convention Center Drive
Las Vegas, NV 89109

1 Yvonne Tsang
Lawrence Berkeley Laboratory
Earth Sciences Division
1 Cyclotron Road
Berkeley, CA 94720

1 Tom Bjerstedt
Yucca Mountain Project
US DOE
P.O. Box 98608
M/S 523
Las Vegas, NV 89193-8518

1 Maxwell Blanchard
Yucca Mountain Project
P.O. Box 98608
M/S 523
Las Vegas, NV 89193-8518

2 Jeremy Boak
Yucca Mountain Project
US DOE
P.O. Box 98608
M/S 523
Las Vegas, NV 89193-8518

1 Garry D. Brewer
Nuclear Waste Technical Review Board
University of Michigan
Dana Bldg, Room 3516
Ann Arbor, MI 48109-1115

1 Daniel B. Bullen
Iowa State University
P.O. Box 1768
Ames, IA 50010

1 Thomas A. Buscheck
Lawrence Livermore National Laboratory
P.O. Box 808
M/S L206
Livermore, CA 94550

1 John E. Cantlon, Chairman
Nuclear Waste Technical Review Board
1795 Bramble Drive
East Lansing, MI 48823

1 K.W. Causseaux
NHP Reports Chief
U.S. Geological Survey
421 Federal Center
P.O. Box 25046
Denver, CO 80225

1 Pat Domenico
NWTRB
1100 Wilson Boulevard, Suite 910
Arlington, VA 22209

2 A.L. Dudley
SPECTRA Research Institute
1603 University NE
Albuquerque, NM 87102

1 William Dudley
US Geological Survey
P.O. Box 25046
M/S 425
Denver, CO 80225

1 J. Russell Dyer
Yucca Mountain Project Office
US DOE
P.O. Box 98608
M/S 425
Las Vegas, NV 89193-8518

1 Norman A. Eisenberg
US Nuclear Regulatory Commission
M/S 4-H-3
Washington, DC 20555

1 W.W.-L. Lee
Environmental Evaluation Group
7007 Wyoming NE
Suite F-2
Albuquerque, NM 87109

1 R.E. Lowder
MAC Tec
101 Conventional Center Drive
Suite 1100
Las Vegas, NV 89109

1 R.R. Luckey
USGS
Building 53
Denver Federal Center
Room H2314/MS 5421
Denver, CO 80225

1 Annette MacIntyre
Lawrence Livermore National Laboratory
P.O. Box 808
M/S L-194
Livermore, CA 94551

1 Edward A. Mason
Amoco Resource Center
P.O. Box 451
46 Admirals Lane
Osterville, MA 02655-0451

1 Russell McFarland
NWTRB
100 Wilson Blvd, Suite 910
Arlington, VA 22209

1 Robin McGuire
Risk Engineering Inc
5255 Pine Ridge Road
Golden, CO 80403

1 John J. McKetta
NWTRB
Department of Chemical Engineering
CRE Building 1450
Austin, TX 78712-1062

1 Ian McKinley
NAGRA
Hardstrasse 73
Wettingen, CH-5430
SWITZERLAND

1 Fred W. McLafferty
Department of Chemistry
Cornell University
2600 Baker Laboratory
Ithaca, NY 14853-1301

1 Arend Meijer
GCX Inc
P.O. Box 87198-2427
Albuquerque, NM 87198

1 Dr. Martin Mifflin
Water Resources Center
Desert Research Center
2505 Chandler Avenue, Suite 1
Las Vegas, NV 89120

1 Suresh Pahwa
INTERA
6850 Austin Center Blvd
Suite 300
Austin, TX 78731

1 Planning Department
Nye County
P.O. Box 153
Tonopah, NV 89049

1 F. Joseph Pearson Jr
1304 Walnut Hill Lane
Suite 210
Irving, TX 75038

1 Chris Pflum
SAIC
101 Conventional Center Drive
Las Vegas, NV 89109

1 T.H. Pigford
University of California
Department of Nuclear Engineering
Berkeley, CA 94720

1 P.T. Prestholt
NRC Site Representative
301 E. Stewart Avenue, Room 203
Las Vegas, NV 89101

1 Dennis L. Price
NWTRB
1011 Evergreen Way
Blackburg, VA 24060

1 Karsten Pruess
Lawrence Berkeley Laboratory
Earth Sciences Division
1 Cyclotron Road
Berkeley, CA 94720

1 Norman C. Rasmussen
MIT
Department of Nuclear Engineering
Bldg 24-205
Cambridge, MA 02139

1 Leon Reiter
NWTRB
1100 Wilson Blvd, Suite 910
Arlington, VA 22209-2297

1 Everett Springer
Los Alamos National Laboratory
P.O. Box 1663
M/S J495
Los Alamos, NM 87545

1 Roger Staehle
University of Minnesota
Department of Chemical Engineering
and Materials Science
22 Red Fox Road
North Oaks, MN 55127

1 Jane Summerson
US DOE
Forrestal RW-22, 7F-091/FORS
Washington, DC 20555

1 Aaron Thode
Los Alamos National Lab
M/S F607
P.O. Box 1663
Los Alamos, NM 87545

1 K.T. Thomas
National Academy of Sciences
2001 Wisconsin Ave NW
Harris Bldg, Room 456
Washington, DC 20007

1 C.F. Tsang
Lawrence Berkeley Laboratory
Earth Sciences Division
1 Cyclotron Road
Berkeley, CA 94720

1 Greg Valentine
Los Alamos National Lab
P.O. Box 1663
M/S F665
Los Alamos, NM 87545

1 Richard Van Konynenburg
Lawrence Livermore National Lab
P.O. Box 808
Livermore, CA 94551

1 Abraham Van Luik
Intera-M&O
101 Convention Center Drive
Suite #P110
Las Vegas, NV 89109

1 C. John Mann
Department of Geology
245 Natural History Building
1301 West Green Street
Urbana, Illinois 61801

1 Henry Loo
Westinghouse Idaho Nuclear Co.
P.O. Box 4000
M/S 5219
Idaho Falls, ID 83415

1 Kjell Andersson
Karinta-Konsult
P.O. Box 6048
S-183 06
Taby, Sweden

1 Dr. G. Ross Heath
College - Ocean/Fishery Sciences
583 Henderson Hall
University of Washington
Seattle, WA 98195

1 Carl Anderson
National Academy of Sciences
2101 Constitution Ave NW
Harris Building, Room 456
Washington, DC 20418

1 Dorothy M. Clark
Secretary, Science Advisory Board
US EPA
401 M Street SW, A-101F
Washington, DC 20460

1 Kathleen W. Conway
Science Advisory Board - EPA
401 M Street SW, A-101F
Washington, DC 20460

1 Dr. Chris Whipple
Clement International
160 Spear Street
Suite 1380
San Francisco, CA 94105-1535

13 Priscilla Bunton
US DOE, OCRWM (RW-331)
1000 Independence Ave SW
Washington, DC 20585

1 Linda Desell
US DOE, OCRWM (RW-331)
Suite 200
1000 Independence Ave SE
Washington, DC 20585

1 Robert J. Budnitz, President
Future Resources Associates Inc
2000 Center Street, Suite 418
Berkeley, CA 94704

1 Thomas A. Cotton
JK Research Associates Inc
4429 Butterworth Place, NW
Washington, DC 20016

1 Srikanta Mishra
M&O/ INTERA
M/S 423
101 Convention Center Drive
Las Vegas, NV 89109

120 Eric Smistad
Yucca Mountain Project
M/S 523
101 Convention Center Drive
Las Vegas, NV 89109

1 Margaret Federline
Nuclear Regulatory Commission
Washington, DC 20555-0001

1 Dr. Alan Hooper
United Kingdom Nirex Limited
Curie Avenue, Harwell
Didcot, Oxfordshire OX11 0RH
United Kingdom

1 Dr. Michael J. Bell
IAEA
Wagramerstrasse 5
P.O. Box 100
A-1400 Vienna
Austria

1 Dr. Neil Chapman
INTERA
Park View House
14B Burton Street
Melton Mowbray, Leicestershire
United Kingdom LE13 1AE

1 Dr. James G.T. Chyr
Taiwan Power Company
AF 2 Alley 15
Lane 196 Sec 4
Roosevelt Road
Taipei, Taiwan
Republic of China

1 Dr. Nestor R. Correa
NAGRA
Hardstrasse 73
CH-5430 Wettingen
Switzerland

1 Kenneth W. Dormuth, AECL
Whiteshell Laboratories
Pinawa, Manitoba
Canada ROE 1L0

1 Dr. Esko Eloranta
Finnish Centre for Radiation
P.O. Box 268
SF-00101 Helsinki
Finland

1 Dr. Helmut D. Fuchs
Gesellschaft fur Nuklear-
Service mbH
Lange Laube 7
D-3000 Hannover 1
Germany

1 Ito Fumio
c/o Prof. Swoboda
University of Innsbruck
Technikerstr 13
A-6020 Innsbruck
Austria

1 Dr. Hilkka Leino-Forsman
VTT, Technical Research
Centre of Finland
Otakaari 3 A
P.O. Box 200
SF-02151 Espoo, Finland

1 Dr. Robert W. Lieb
NAGRA
Hardstrasse 73
CH-5430 Wettingen
Switzerland

1 Dr. J.W. Lloyd
School of Earth Sciences
Edgbaston, Birmingham
B 15 2TT, United Kingdom

1 D. Ganpat S. Lodha, AECL
Whiteshell Laboratories
Pinawa, Manitoba
Canada ROE 1L0

1 Douglas E. Metcalfe
Waste Management Division
P.O. Box 1046, Station B
270 Albert Street
Ottawa, Canada K1P 5S9

1 Dr. Ivars Neretnieks
Department of Chemical
Engineering
Royal Institute of Technology
Teknikringen 26
S-100 44 Stockholm
Sweden

1 Dr. Jean-Pierre Olivier
OECD/NEA
12 Boulevard des Iles
92130 Issy Les Molineaux
France

1 Dr. Olle Olsson
Conterra AB
P.O. Box 493
S-751 06 Uppsala, Sweden

1 Maria Onofrei, AECL
Whiteshell Laboratories
Pinawa, Manitoba
Canada ROE 1L0

1 Dr. Liu Wen-Chung
Radwaste Adminstration
Atomic Energy Council
6F 65 Lane 144 Keeling Load
Section 4 Taipei
Taiwan

1 Dr. Sidney H. Whitaker
AECL
Whiteshell Laboratories
Pinawa, Manitoba
Canada ROE 1L0

1 Dr. Roger Yearsley
Inspectorate of Pollution
Room A5.02
Romney House
43 Marsham Street
London SW1P 3Py
United Kingdom

1 Dr. Piet Zuidema
NAGRA
Hardstrasse 73
CH-543o Wettingen
Switzerland

1 Dr. Arthur Motta
Nuclear Engineering Department
Pennsylvania State University
231 Sackett Building
University Park, PA 16802

1 Dr. M.R. Chandratillake
Capcis March Limited
Bainbridge House, Granby Row
Manchester M1 2PW
United Kingdom

1 Serge Runge
Eurisys Consultants S.A.
14 rue du Printemps
74017 Paris, France

1 Peter Suci
Montana State University
Bozeman, MT

1 Dr. David Kreamer
Geoscience Department - UNLV
4505 South Maryland Parkway
Las Vegas, NV 89159

1 Richard Forester
USGS
P.O. Box 25046
Denver Federal Center
Lakewood, CO 80225

1 Zell Peterman
USGS
P.O. Box 25046
Denver Federal Center
Lakewood, CO 80225

1 Kevin McCoy
B&W Fuel Company
101 Convention Center Drive
Suite P110
Las Vegas, NV 89109

1 John Nitao
Lawrence Livermore National Laboratory
P.O. Box 808
Livermore, CA 94551

1 Anne-Marie Meike
Lawrence Livermore National Laboratory
P.O. Box 808
Livermore, CA 94551

1 G.S. Bodvarsson
Lawrence Berkeley Laboratory
1 Cyclotron Road
Berkeley, CA 94720

1 Jiamin Wan
Lawrence Berkeley Laboratory
1 Cyclotron Road
Berkeley, CA 94720

1 Robert Andrews
INTERA
M/S 423
101 Convention Center Drive
Las Vegas, NV 89109

1 Tim Dale
INTERA
M/S 423
101 Convention Center Drive
Las Vegas, NV 89109

1 Dan McCright
Lawrence Livermore National Laboratory
P.O. Box 808
M/S L-204
Livermore, CA 94551

1 Ray Stout
Lawrence Livermore National Laboratory
P.O. Box 808
M/S L-204
Livermore, CA 94551

INTERNAL DISTRIBUTION

	MS	
4	1330	G. M. Gerstner-Miller, 6352 100/12541/SAND93-2675/QA
20	1330	WMT Library, 6352
1	0827	P. J. Hommert, 1502
1	1375	D. A. Dahlgren, 4400
5	0899	Technical Library, 7141
1	0619	Technical Publications, 7151
10	1119	Document Processing for DOE/OSTI, 7613-2
1	9018	Central Technical Files, 8523-2
1	0827	J. C. Cummings, 1502
1	0827	J. S. Rottler, 1511
1	0827	P. L. Hopkins, 1511
1	0827	M. J. Martinez, 1511
1	0835	R. R. Eaton, 1513
1	0835	R. D. Skocypec, 1513
1	1324	P. D. Davies, 6115
1	1324	R. J. Glass, 6115
1	1324	C. A. Rautman, 6115
1	1324	V. C. Tidwell, 6115
1	1324	C. Ho, 6115
1	1320	M. D. Siegel, 6119
1	1333	F. J. Schelling, 6302
10	1326	H. A. Dockery, 6312
5	1326	R. W. Barnard, 6312
1	1326	G. E. Barr, 6312
1	1326	J. H. Gauthier, 6312
1	1326	P. G. Kaplan, 6312
1	1326	T. H. Robey, 6312
1	1326	L. H. Skinner, 6312
1	1326	W. G. Perkins, 6312
1	1326	A. R. Schenker, 6312
1	1326	S. A. Shannon, 6312
60	1326	M. L. Wilson, 6312
1	1325	L. S. Costin, 6313
1	1325	R. E. Finley, 6313
1	1325	E. Dunn, 6313
1	1325	J. F. Holland, 6313
1	1325	J. Pott, 6313
1	1325	C. S. Chocas, 6313
1	1325	E. E. Ryder, 6313
1	1325	S. R. Sobolik, 6313
1	1330	M. C. Brady, 6314
1	1345	T. Brown, 6331

1	1328	M. E. Fewell, 6342
1	1328	C. T. Stockman, 6342
1	1328	R. P. Rechard, 6342
1	1328	M. G. Marietta, 6342
1	0755	B. D. Zak, 6612
1	1315	T. E. Blejwas, 7500
1	9043	R. Nilson, 8745

*U.S. GOVERNMENT PRINTING OFFICE 1994-0-573-026/00002

SAND93-2675

The number in the lower right-hand corner is an accession number used for Office of Civilian Radioactive Waste Management purposes only. It should not be used when ordering this publication.

Org.	Bldg.	Name	Rec'd by	Org.	Bldg.	Name	Rec'd by

Sandia National Laboratories

SANDIA REPORT

SAND93—2675
Unlimited Release
Printed April 1994

Yucca Mountain Site Characterization Project

Total-System Performance Assessment for Yucca Mountain – SNL Second Iteration (TSPA-1993)

Volume 2

Michael L. Wilson, John H. Gauthier, Ralston W. Barnard, George E. Barr, Holly A. Dockery, Ellen Dunn, Roger R. Eaton, David C. Guerin, Ning Lu, Mario J. Martinez, Robert Nilson, Christopher A. Rautman, Thomas H. Robey, Benjamin Ross, Eric E. Ryder, Albert R. Schenker, Sharon A. Shannon, Lee H. Skinner, William G. Halsey, James D. Gansemer, Lynn C. Lewis, Alan D. Lamont, Inés R. Triay, Arend Meijer, David E. Morris

Prepared by
Sandia National Laboratories
Albuquerque, New Mexico 87185 and Livermore, California 94550
for the United States Department of Energy
under Contract DE-AC04-94AL85000

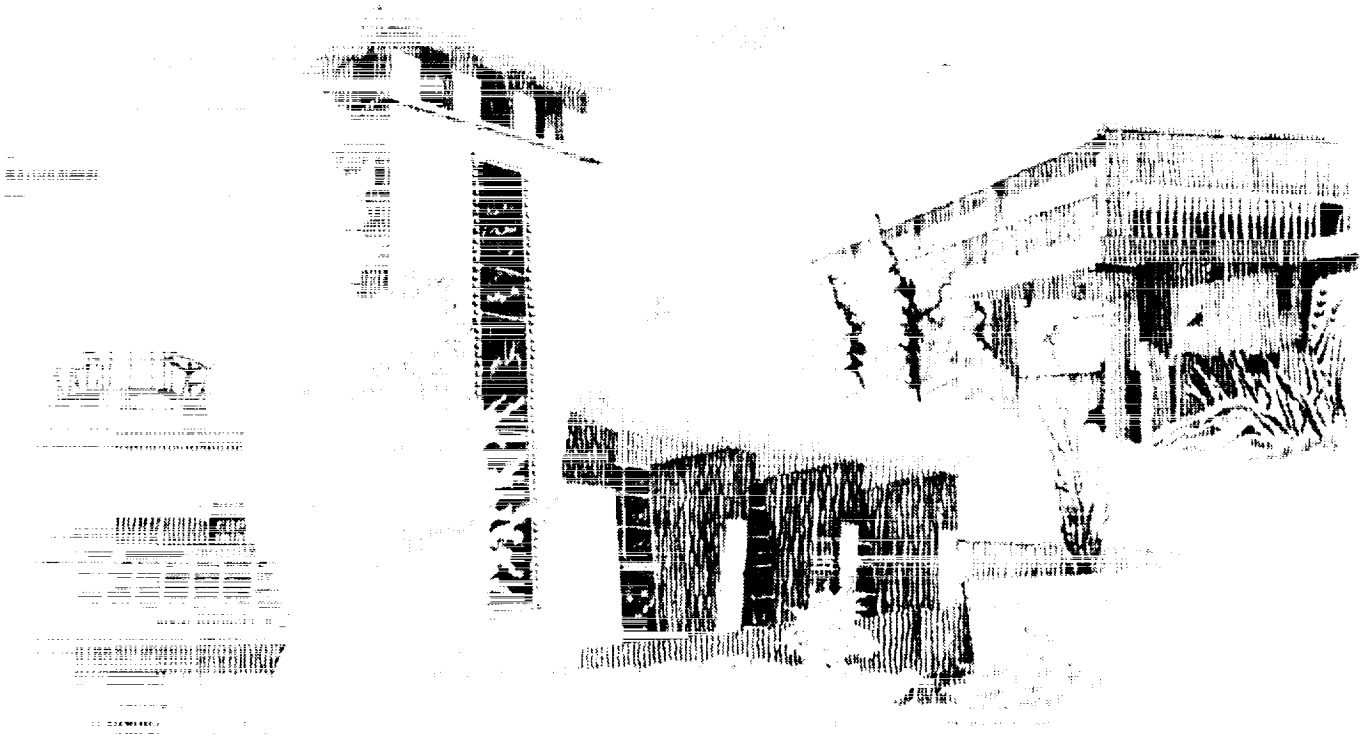

"Prepared by Yucca Mountain Site Characterization Project (YMSCP) participants as part of the Civilian Radioactive Waste Management Program (CRWM). The YMSCP is managed by the Yucca Mountain Project Office of the U.S. Department of Energy, DOE Field Office, Nevada (DOE/NV). YMSCP work is sponsored by the Office of Geologic Repositories (OGR) of the DOE Office of Civilian Radioactive Waste Management (OCRWM)."

Issued by Sandia National Laboratories, operated for the United States Department of Energy by Sandia Corporation.

Printed in the United States of America. This report has been reproduced directly from the best available copy.

Available to DOE and DOE contractors from
Office of Scientific and Technical Information
PO Box 62
Oak Ridge, TN 37831

Prices available from (615) 576-8401, FTS 626-8401

Available to the public from
National Technical Information Service
US Department of Commerce
5285 Port Royal Rd
Springfield, VA 22161

NTIS price codes
Printed copy: A21
Microfiche copy: A01

Distribution Category
UC-814

SAND93-2675
Unlimited Release
Printed April, 1994

Total-System Performance Assessment for Yucca Mountain — SNL Second Iteration (TSPA-1993)

Volume 2

Michael L. Wilson, John H. Gauthier†, Ralston W. Barnard, George E. Barr, Holly A. Dockery, Ellen Dunn, Roger R. Eaton, David C. Guerin‡, Ning Lu*, Mario J. Martinez, Robert Nilson, Christopher A. Rautman, Thomas H. Robey†, Benjamin Ross*, Eric E. Ryder, Albert R. Schenker‡, Sharon A. Shannon, Lee H. Skinner†
(Sandia National Laboratories)

William G. Halsey, James D. Gansemer, Lynn C. Lewis, Alan D. Lamont
(Lawrence Livermore National Laboratory)

Inés R. Triay, Arend Meijer§, David E. Morris
(Los Alamos National Laboratory)

† Spectra Research, Inc.
‡ Los Alamos Technical Associates, Inc.
* Disposal Safety, Inc.
§ Jacobs Engineering, Inc.

The Executive Summary
is in a separate volume

Volume 1
contains the Abstract, Acknowledgments,
complete Table of Contents, Lists of Figures and Tables,
and Chapters 1 through 12

Volume 2
contains Chapters 13 through 25,
References,
and the Appendices

Contents of Volume 2

Figures
(in Volume 2)

Tables

(in Volume 2)

Part IV

Probabilistic Modeling and Results

Chapters 13 through 17 deal with the system modeling that was done forTSPA-93, and the results obtained for the performance measures considered—normalized cumulative release, as specified in 40 CFR 191.13, and radiation-dose rate to individuals from drinking contaminated saturated-zone water. All the information discussed in previous parts of the report feeds into the system simulations. Simulations of nominal flow and transport are performed using two different conceptual models of unsaturated-zone groundwater flow and transport.

Chapter 13 discusses the models and inputs for radionuclide releases from waste containers. Chapter 14 discusses nominal flow and transport for the composite-porosity conceptual model. Chapter 15 discusses nominal flow and transport for the weeps conceptual model. Chapter 16 discusses human intrusion (exploratory drilling). Chapter 17 discusses magmatic activity (intrusion of a basaltic dike).

Below is a duplication of the document "road map" (Figure 1-1), with the items for this part highlighted.

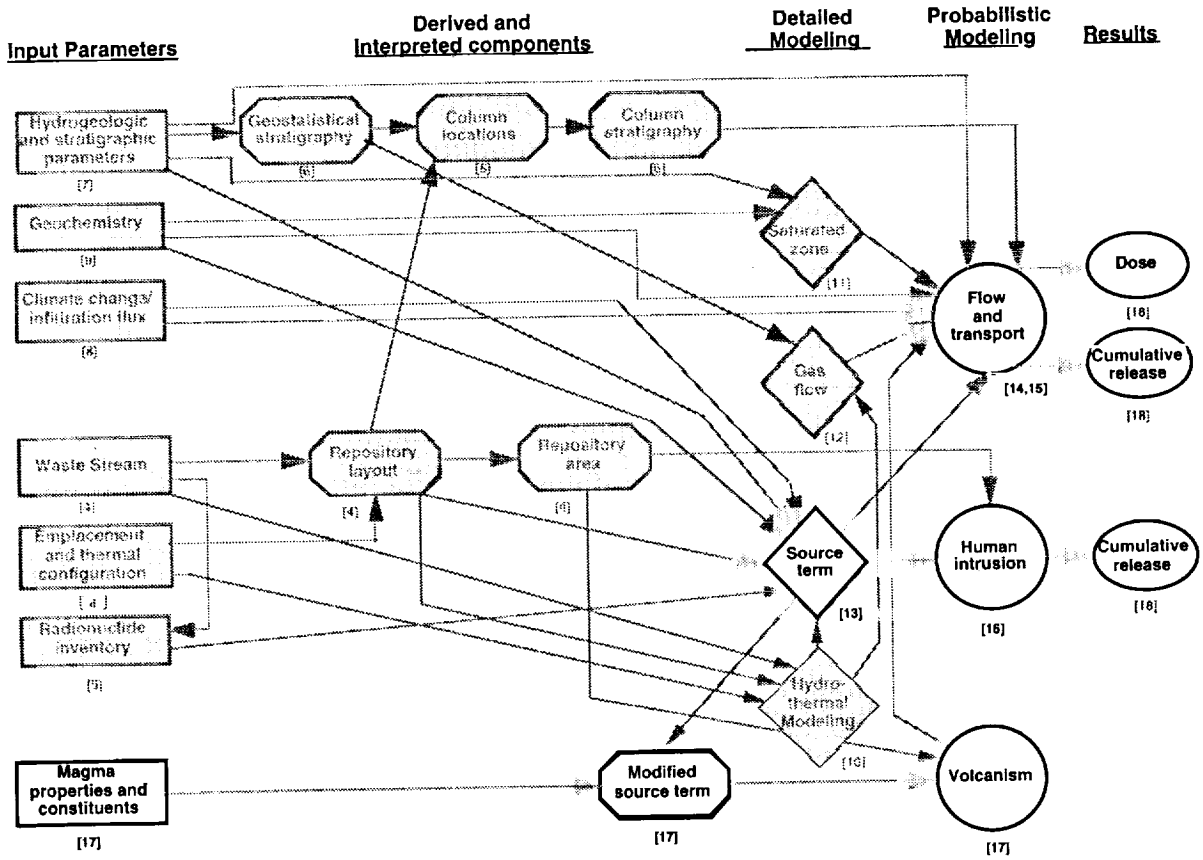

Chapter 13
Source-Term Model

(Lamont, Gansemer, Barnard)

The Yucca Mountain Integrating Model (YMIM) is a computer model developed by Lawrence Livermore National Laboratories to calculate radionuclide releases from repository waste packages and the engineered barrier system (EBS). YMIM uses a number of inputs descriptive of the EBS and near-field processes and calculates failure of a waste container due to corrosion, and the time-varying releases of radionuclides from the failed waste package. The model considers the interactions among the processes to make the container-lifetime and release estimates. Table 13-1 summarizes the mechanisms included in the YMIM model. Note, however, that not all mechanisms have been implemented for TSPA-93. For the purposes of description in YMIM, the near field is considered to be that portion of the natural system that is needed to define the operating environment for the EBS.

Table 13-1. Principal mechanisms included in YMIM.

Component	Principal Mechanisms
Near-field hydrology	Time history of fractional time waste packages are wet; time history of matrix and fracture flow past package.
Near-field chemistry	Time history of pH, Eh, chloride concentration, carbonate concentration, and fluorine concentration.
Temperature	Time history of container-wall temperature; time history of fuel-rod temperature.
Container failure	Air oxidation; general aqueous corrosion; pitting corrosion; early failure of defective containers.
Cladding failure	Creep rupture of cladding; cladding hydride reorientation; fluorine attack of cladding.
Fuel-matrix dissolution	Temperature-dependent fuel-matrix aqueous alteration; temperature-dependent fuel-matrix oxidation; aqueous and gaseous release modes; pulse release from fuel-cladding gap; release of gaseous nuclides from surface of fuel cladding; temperature-dependent solubilities.

13.1 Functional description of the YMIM code

The performance of the potential Yucca Mountain nuclear-waste repository is partially determined by the interaction of the hydrologic, thermal and chemical regimes within the near-field environment and the engineered barrier system (EBS) of the repository. Evaluating the overall performance of the repository requires the integra-

tion of models of each of these components. YMIM is a modular framework for integrating these models.

YMIM models the processes in the mobilization and release of radionuclides from the repository. It is designed to allow a user to predict the time history of the releases from the waste packages. YMIM models radionuclide release as occurring when the waste-container walls and the fuel-rod cladding have failed. The model also allows for user-defined failures of the containers, and for defective containers. The radionuclides specified in the YMIM inventory module can then be transported out of the EBS either by gas or advective groundwater transport through the corroded container and the ruptured fuel rods. The mechanisms listed in Table 13-1 all contribute to these processes.

Each of the modules in YMIM is a model of one of the physical processes required for the mobilization and release of nuclides from the repository. Although each module has a well defined scope limited to a single physical process, they are designed to work together as a single model. To do this the interfaces between modules have been carefully defined. Since each module is responsible for a specific process, it can provide to any other module certain specific data about the status of that process during each time step of the model run. The data provided by any module are intended to provide a complete description of the status of that process. Thus the Hydrology module provides fluxes each period, the Temperature module provides rod and container temperatures, the Container Failure module provides the number of containers failing each period, the Waste-Form Dissolution module provides the amount of each nuclide mobilized during each time step and the amount remaining, and so forth.

Each of the modules updates its relevant state variables each time step of the model run. For example the Container-Failure module updates the progress of corrosion and the numbers of containers that have actually failed, the Waste-Form Dissolution module updates that amount of material altered, decayed, and dissolved. To make its update, most modules require information from other modules. This is obtained by calling the other modules and requesting the needed information. The called module may need to call other modules to make whatever calculations it requires.

Through this separation into modules, and through the clear definition of the information that each module is responsible for providing, YMIM is highly flexible and can easily be adapted to use alternate models in its modules. As long as a module can provide the information that is required, it will work within the YMIM framework.

The basic YMIM model is a stand-alone application that runs on a Macintosh or Sun computer. It estimates the history of releases from a group of containers that represent a region of the repository. It is assumed that all of the containers in the group

are subjected to the same near-field conditions of temperature, hydrology, and geochemistry. Therefore, in order to model the performance of the entire repository, several YMIM runs, each representing a different repository region, are made and the radionuclide releases are added.

A second, FORTRAN-callable, version of YMIM has been developed to provide the source-term modeling for groundwater-transport codes TOSPAC and WEEPTSA. The FORTRAN-callable version of YMIM groups together several YMIM runs representing different regions of the repository (see Chapter 14 for details). Each group shares the same system parameters and geochemistry scenarios, while the temperature and hydrology scenarios are allowed to vary from region to region. The FORTRAN-callable version of YMIM is queried by the transport codes once during each period of the simulation. It calculates the release from each repository region during the period and returns the summed mass release rate for each nuclide to the calling program. In WEEPTSA, each container is considered individually and YMIM is called for each container that is contacted by a flowing fracture for long enough to have a chance of failing (Chapter 15).

13.1.1 Comparison with TSPA-91 source term

The YMIM model is a functional improvement in many respects over the source-term models used in TSPA-91 (Barnard *et al.*, 1992). Improvements include

- Mechanistic thermal dependencies,
- Container and cladding failure mechanisms,
- Dependence on geochemical properties and episodic near-field hydrology, and
- More detail in time histories of input properties.

To limit complexity and running time, less detail is modeled in other topics. For example, diffusive release is not modeled. The threshold for local seepage flow based on global parameters is not modeled, but groundwater flow time history is an input. Local spatial variability is not modeled in the basic YMIM, but is handled by multiple calls to YMIM with different parameter sets.

The thermal effects in the TSPA-91 source term were represented by a delay and an interval of re-wetting times of the waste packages. For TSPA-93, YMIM implements an input groundwater flux time history and temperature-dependent container corrosion, cladding failure, and waste-form oxidation and alteration rates. YMIM has time-dependent input geochemistry and temperature-dependent radionuclide solubility rates, although these were taken as constant for the TSPA-93 inputs.

Container breach in the TSPA-91 source term was represented by input delay and duration of breach times subsequent to the wetting time for the different containers, generated by expert judgment or prior analysis. YMIM has a model for one- or two-walled containers and several corrosion processes. The YMIM pitting corrosion model gives a stochastic distribution of breach times for a given environmental history. YMIM has a cladding model giving a distribution of cladding breach times.

In hydrology and hydrology-related effects the TSPA-91 and YMIM models are different, and YMIM has in some respects less detail.

- At the container level, the TSPA-91 model distinguished a fraction of containers that remained dry in the presence of matrix groundwater flux because of a maintained air gap. This applied to vertical borehole-emplacement cases. YMIM models the containers as undergoing aqueous corrosion if there is any matrix or fracture flux in the near field.

- At the waste release level, TSPA-91 had a diffusive release process, operating without or in parallel to seepage advective flux into the container. The diffusive release is most important when there is water contact but low flux. YMIM has no diffusive release, but has advective release whenever there is groundwater flux and a breached container and cladding. YMIM has input time histories for fracture and matrix flux, and input areal weighting factors for each. The advective flux into the container is the weighted sum of these two fluxes. YMIM's release of solubility-limited radionuclides, limited by water flux, may be slower than in TSPA-91's diffusion process. Release of highly soluble radionuclides such as ^{135}Cs may be faster than in TSPA-91's diffusion process with retardation.

- The TSPA-91 source-term model had a computed threshold for fracture seepage flux based on the global percolation flux, matrix hydraulic conductivity, and local variability. This was applied to the advective and diffusive release-enabling conditions. YMIM, as noted, has input time histories for fracture and matrix flux, and multiples of both are treated as seepage flux into the container. These inputs can be correlated with other variables of the total system analysis before input. YMIM has episodic flux which the TSPA-91 model did not.

- The TSPA-91 model had local variability in hydrology, represented by a distribution about the mean hydrology, and arising in principle from stochastic or spatially dependent effects. Release rate was a non-linear function of the local inputs. The TSPA-

91 model aggregated the net release rate. This was done analytically, and hence is only applicable when using the underlying simple bounding models. YMIM handles spatial variability by a YMIM superstructure which does multiple calls with different parameter sets to the core YMIM model.

13.2 Description of YMIM modules and model inputs

YMIM consists of nine modules that model the fundamental mechanisms leading to nuclide release. Each module requires information from and provides information to other modules. Figure 13-1 shows the modules and the information passed between them.

When parameter values are listed in this section for a module, they are constants used for all analyses. In other cases, the parameter values and ranges are applicable to specific analyses, and are discussed in subsequent chapters. The following sections describe the application of the modules to the TSPA-93 analyses.

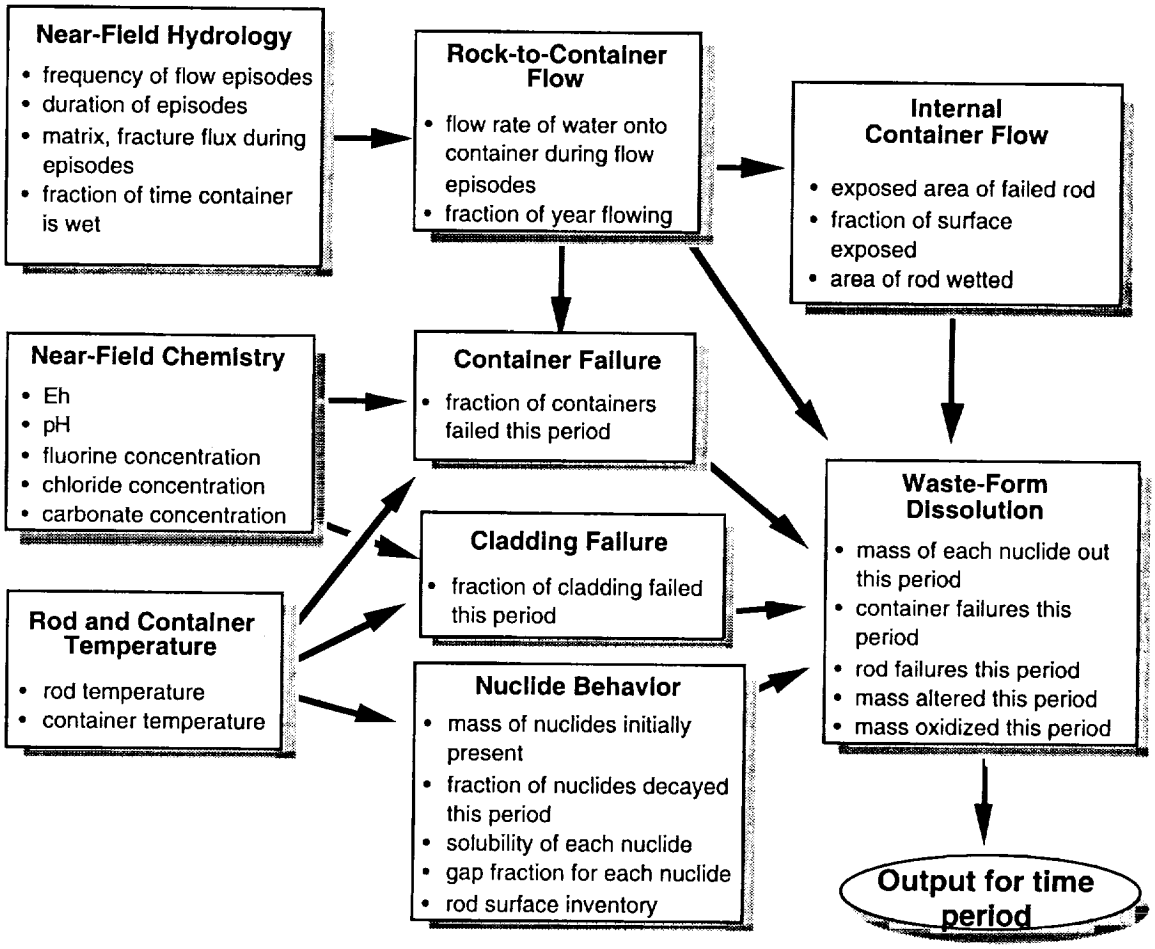

Figure 13-1. Functional structure of the YMIM model.

13.2.1 Near-field hydrology

This module provides information about the flux in the near-field rock and the fraction of the year that containers are wet. The amount of water present is used in two ways. First, the waste-package lifetime is dependent upon the amount of time the container is wet, and second, the transport of released radionuclides is dependent upon the matrix and fracture fluxes. All water-flow parameters permit episodic contact, expressed as fractions of the time that water is flowing or in contact with the waste package. The parameter values for this module are dependent upon the analysis, and are discussed in Chapters 14 and 15, and in Section 16.2.

Container degradation is assumed to occur by aqueous corrosion, and other processes. The amount and timing of the wetting of containers is a factor in the corrosion processes. These parameters must be consistent with the thermal history of the waste packages; thus, at temperatures above boiling, water contact is assumed to be insignificant. Below boiling, water availability depends on assumptions about the groundwater percolation flux, and the degree of dryout of the repository rock surrounding the container. The YMIM corrosion model only differentiates between wet containers and dry containers; the model does not consider the amount of water involved in wetting the container.

The matrix and fracture fluxes can be specified independently. This implies that the YMIM model can accommodate fracture and matrix fluxes characteristic of both the composite-porosity (TOSPAC) and the fracture-flow (WEEPTSA) codes used in TSPA-93. The flux used by YMIM is the sum of the matrix and fracture components.

13.2.1.1 Rock-to-container flow

The fluxes in the rock near the waste package are specified in the near-field hydrology module, as described in Section 13.2.1. This module calculates the fraction of near-field flux that contacts a waste package. The output of the module is the input to the Waste-Form Dissolution, Container-Failure, and Internal Container Flow modules.

The volume of water flowing onto a container is defined to be the amount of matrix and fracture flux passing through a collection area. The module provides for the specification of matrix- and fracture-flux collection areas that may be larger or smaller than the cross-sectional area of the container. The total flow into the container is given by the following equation:

$$\text{Total Flow (vol/time)} = C_f \cdot f_f + C_m \cdot f_m, \qquad (13.1)$$

where C_f and C_m are the fracture and matrix flux collection areas, respectively, and f_f and f_m are the fluxes in the fractures and matrix, respectively. For example, for a vertically placed container, the collection area would be roughly the size of the cross-sectional area of the container, if it is assumed that there is no concentration or dispersal of flux at the container. Different values for matrix and fracture collection areas can be specified, as would be consistent with the two flow models used in TSPA-93.

13.2.2 Near-field geochemistry

This module specifies the geochemistry parameters used in the Container-Failure, Cladding-Failure, and Waste-Form Dissolution modules. The input parameters are pH and Eh, and chlorine, carbonate, and fluorine concentrations of the groundwater. (In the current version of YMIM, Eh, and chlorine concentrations are not used.) The information is used to estimate the rate of container corrosion, cladding-failure rates due to fluorine, and the alteration rate of the fuel matrix. For time-varying geochemical parameters, values can be specified for different intervals of the model run.

For the TSPA-93 analyses, the geochemistry values listed in Table 13-2 were held constant for the entire simulation time, due to the current lack of site-specific near-field geochemical information. The data are taken from Meijer (1992). (See also Table 9-1 in this report.) Groundwater chemistry data from two wells (J-13 and UE25p#1), and water extracted from unsaturated-zone rocks are cited. (It must be noted that the data are for far-field conditions, and are being applied to the near field, where the conditions may be considerably different.) These data are our best estimates for ambient geochemical conditions. It is not clear which direction the values may change for descriptions of the near field, so the ranges are fairly broad.

Table 13-2. Geochemistry parameters used in YMIM.

	Well Data			
Component	J-13	UZ	UE25p#1	Analysis Parameter Values/Ranges
HCO_3	143 mg/l	–	698 mg/l	$2x10^{-3}$ – $1x10^{-2}$ mole/l
F	2.1 mg/l	–	3.5 mg/l	2.8 ppm
pH	6.9	6.5 – 7.5	6.7	6.5 – 7.5

13.2.3 Temperature

This module provides information about the temperature at the container wall and at the fuel rods. Container temperature is used to determine the temperature-dependent corrosion rates. Fuel rod temperature is used to calculate cladding failures, fuel alteration and oxidation, and nuclide solubilities. Waste-package and fuel-rod tempera-

ture profiles are discussed in detail in Chapter 10. They are dependent upon the emplacement configuration and repository heat-load assumptions.

13.2.4 Container failure

The Waste-Package-Failure module contains mechanisms for waste-package failure due to corrosion as well as defective containers. The following sections describe the processes modeled in the corrosion and defective-container models.

13.2.4.1 Container corrosion

This model can calculate the time to corrode both single-wall (borehole-emplacement configurations) and double-wall (in-drift configurations) containers. It considers air oxidation, generalized aqueous corrosion, and localized pitting corrosion. The air-oxidation and generalized aqueous corrosion rates are functions of temperature. Pitting corrosion is modeled as a stochastic process with parameters that are also temperature-dependent.

Two materials have been considered for the waste containers: a corrosion-resistant high-nickel alloy (Alloy 825) for the borehole-emplaced container and for the inner container of the in-drift package, and mild carbon steel for the in-drift overpack. The Alloy 825 is assumed to be 0.95 cm thick for both containers, while the mild steel is assumed to be 10 cm thick; these values are based on the SCP design for the thin-walled waste package (DOE, 1988a), and YMP system studies for the in-drift configuration (DOE, 1993a).

Air oxidation of the waste package materials is a temperature-dependent deterministic process that follows an Arrhenius relationship and is assumed to occur whenever there is no water present. The Arrhenius equation is:

$$\text{Rate} = Ke^{-k/T}, \tag{13.2}$$

where K and k are rate constants and T is temperature (K). In order to determine the parameters of the oxidation rate equation, corrosion rates are specified at two temperatures, and the program calculates the parameter values from this information. Air oxidation rates are listed in Table 13-3.

Generalized aqueous corrosion requires the presence of liquid water to proceed. This is the dominant mode of corrosion for mild steel. The corrosion rate is a temperature-dependent parabolic function with a maximum rate occurring at a temperature below boiling. It is assumed that no general aqueous corrosion occurs above 100°C. The corrosion rate decreases as the temperature approaches the boiling point of water be-

cause the corrosion process requires the presence of oxygen, which decreases as the temperature approaches boiling. Figure 13-2 shows the shape of the aqueous-corrosion curve. The model also includes a pitting-enhancement factor, which increases the depth of generalized corrosion to account for pits in the mild steel overpack on double-walled containers. Pits in mild steel tend to be broad and shallow, unlike those in Alloy 825, which have a high aspect ratio. Thus, the pitting process in mild steel tends to decrease the thickness of the container wall rather than creating small pinhole failures.

Table 13-3. Air-oxidation rates used for TSPA-1993.

Temperature (°C)	Oxidation Rate (mm/yr)
Alloy 825[a]	
253	2.4×10^{-7}
20	5.5×10^{-16}
Carbon Steel[b]	
540	10.08
25	6.35×10^{-6}

[a] Data from Brasunas *et al.*, 1946.
[b] Data from Uhlig, 1946.

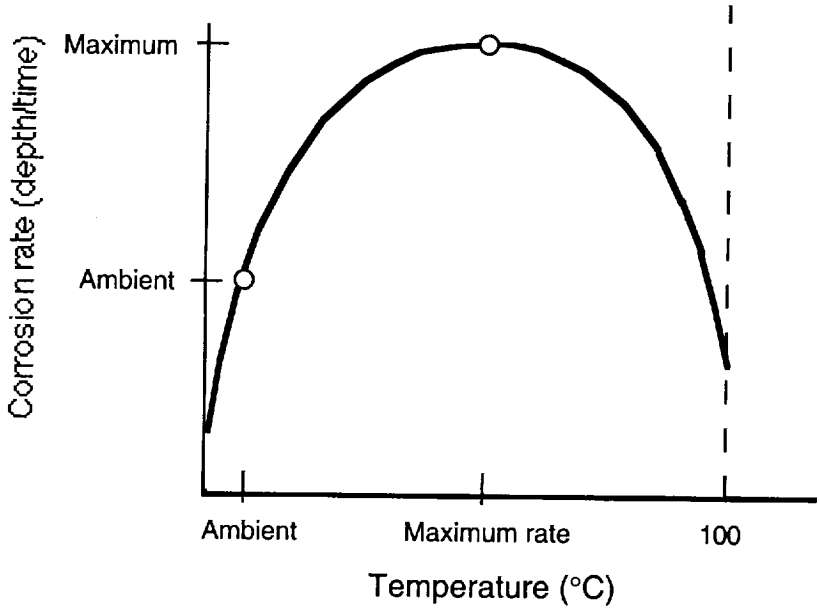

Figure 13-2. Generalized aqueous corrosion rate as a function of temperature.

In order to specify the parameters for the general aqueous corrosion relationship, the corrosion rate is specified at two temperatures, and the module calculates the neces-

sary parameter values. The temperatures at which the rates are specified are the temperature where the maximum pitting rate occurs, and 20°C. Table 13-4 lists the parameters elicited from experts by LLNL (R. D. McCright and G. A. Henshall) that are used for this study. A pitting enhancement factor of 1 is used for the TOSPAC and WEEPTSA analyses, and a value of 4 is used for the container-lifetime studies. The actual pitting factor is not known, so the two choices reflect this uncertainty. Additionally, the experts feel that the corrosion process is so rapid that the difference in the values may be insignificant.

Table 13-4. Generalized aqueous corrosion rates for mild steel.

Temperature (°C)	Rate (mm/yr)
80	0.38 (maximum)
20	0.12

Localized pitting corrosion of Alloy 825 is based on a probabilistic model of pit growth (Henshall *et al.*, 1993). As with generalized aqueous corrosion, it is assumed to occur only for temperatures less than 100°C. Under this model, it is assumed that pits will randomly form on the waste-package surface. During each period of time (e.g., one year) there is a probability, r, that the pit will grow. If it grows, it grows by a fixed increment, g. The depth of a pit at any period is given by the sum of the incremental amounts that it grew in prior periods. Pits randomly grow deeper until one pit on the container has a depth equal to the wall thickness. At that time the container is considered to have failed.

Estimates of long-term pitting corrosion rates for Alloy 825 were elicited from experts by LLNL (R. D. McCright and G. A. Henshall). The experts were asked to estimate the probability distribution over the long term of the growth rates of pits on waste packages in the repository. However, because the true conditions at the repository are unknown at this time, the true distribution of growth rates is uncertain. To account for this, three sets of pitting-rate distributions have been elicited. The Median growth rate represents the median estimate of LLNL experts. It is considered equally likely that the true mean rate of growth could be greater than or less than this. The Low and High growth rates define the limits within which the growth rates are most likely to be observed, (depending on environmental conditions). In the experts' judgment there is only about a 5% chance that the true growth-rate distribution will have a mean higher than

that of the High growth-rate distribution and about a 5% chance that it will be lower than the mean of the Low growth-rate distribution.

The values elicited from the experts are shown in Table 13-5. Figure 13-3 illustrates the way that the elicitations should be interpreted. The figure shows three different probability distributions over growth rate at 70°C. It is uncertain which of these will be the true distribution at the repository, however, it is unlikely that the true distribution over growth rate will be less than the mean of the Low growth-rate case, or larger than the mean of the High growth-rate case.

Table 13-5. Estimates of corrosion rates for high-nickel alloy.

	Temperature = 70°C		Temperature = 100°C	
Growth Condition	Mean Growth (mm/yr)	95th Percentile (mm/yr)	Mean Growth (mm/yr)	95th Percentile (mm/yr)
Low Growth Rate	0.0001	0.001	0.01	0.1
Median Growth Rate	0.001	0.01	0.1	1.0
High Growth Rate	0.01	0.1	1.0	10.0

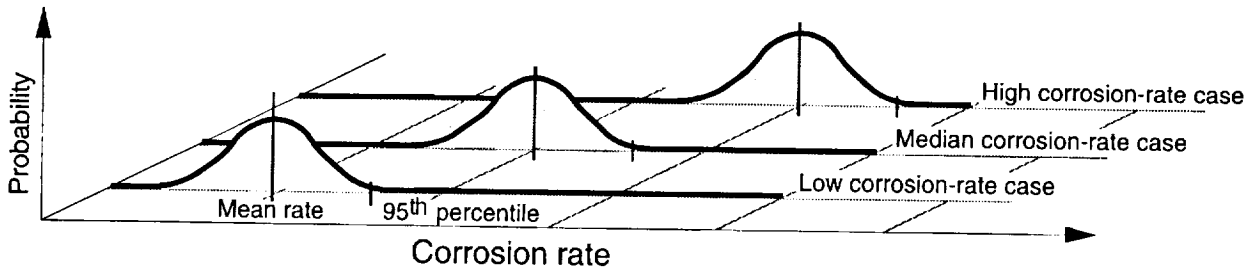

Figure 13-3. Illustration of pitting growth rates for three growth conditions.

The pitting corrosion program assumes an Arrhenius relationship between these parameters and temperature in order to compute values for g and r at other temperatures. Additional calculations are needed to determine the values of g and r needed by the model. The actual values are shown in Table 13-6. The discussion below illustrates the derivation of the model parameters using the Median distribution at a temperature of 100°C.

Finding the values of r and g for this case requires a two-step process. First we recognize that the underlying pit growth model is a Poisson process (a random number of growths in a period, each of equal size). Given the mean and variance of this process, the values of r and g can be computed (equations are shown below). Second, the Poisson process converges to a normal distribution in the long run. Thus, the long-term distribution over the pit depths will be normally distributed. However, the mean and vari-

ance of this distribution are equal to the mean and variance of the Poisson distribution that gave rise to it. Thus, by calculating the mean and variance of the distribution over long-term pit growth, we can determine the mean and variance of the underlying Poisson process and estimate the values of r and g.

To calibrate the parameters of the corrosion model it is necessary to estimate the mean and variance of the distribution of pit depths using the elicited data. The means are given in Table 13-5. The underlying model of pit growth assumes that the pits grow randomly in increments and that the probability that a pit will grow by an increment is independent of its current depth. Consequently, the actual depth is a sum of independent variables and it can be assumed that in the long term, the pit depths (and the long-term growth rates) will have approximately a normal probability distribution. Given the mean and the 95th percentile of the distribution, the variance can be calculated as follows: For the normal distribution, the difference between the mean value and the 95th percentile value is equal to 1.645 times the standard deviation. In the Median growth-rate case at 100°C the difference is equal to (1.0 - 0.1) mm/yr, so the standard deviation equals (0.9 / 1.645) or 0.547 mm/yr. The variance of the annual growth for this case equals 0.299 mm^2.

Since we assume in the underlying model of pit growth that the pits grow randomly in increments, a Poisson model can be applied to estimate the distribution over total growth in a relatively short period of time (note that in the long term, the Poisson process converges to a normal distribution). The Poisson model of pit growth is parameterized by the expected rate of growth increments, r (i.e., the probability of a growth increment in a time period), and size of the increment of growth, g, given that a growth increment occurs. From the Poisson growth model we have the following relationships between the mean and variance of growth during a time period, and g and r:

$$E(G) = g \cdot r \cdot t, \tag{13.3}$$

and

$$Var(G) = g^2 \cdot r \cdot t, \tag{13.4}$$

where G is total growth in a period of time, r is expected number of growth increments per unit time, g is the incremental growth, when a pit grows, and t is the length of the period under consideration. In this case, the time period is one year so t=1, since the data are given in terms of annual growth rates.

The above relationships lead to the following equations for g and r based on the mean and variance of the total growth:

$$r = E^2(G)/Var(G), \tag{13.5}$$

and

$$g = E(G)/r. \tag{13.6}$$

Given the values for the mean and variance of annual growth, the values of g and r for the Median case at 100°C case are:

$$r = 0.033,\ g = 2.99 \text{ mm}.$$

The parameters for all the combinations of growth rate and temperature age shown in Table 13-6.

Table 13-6. Parameters used in YMIM Alloy 825 pitting model.

Growth Condition	Temperature = 70°C		Temperature = 100°C	
	g (mm)	r	g (mm)	r
Low Growth Rate	0.003	0.033	0.299	0.033
Median Growth Rate	0.030	0.033	2.99	0.033
High Growth Rate	0.299	0.033	29.9	0.033

During each period of a model run, the pitting rate parameters are used to determine the mean and variance of the distribution on pit growth. This distribution follows a Poisson distribution. The cumulative pit-depth distribution is built up of these Poisson distributions, which in the limit approaches a normal distribution.

The normal distribution of cumulative pit depths is the distribution of depths of *all* pits on the surface of a container. It is conservatively assumed that a container wall fails once the deepest pit reaches a depth equal to the wall thickness; therefore, it is not the distribution of all pit depths that is of interest, but the distribution of the deepest pits. This distribution is the extreme-value distribution. YMIM calculates the extreme-value distribution from the underlying normal distribution of all pits on a container's surface. The fraction of containers that fail in a given period is the fraction of pits in the extreme-value distribution whose depth exceeds the wall thickness.

The extreme-value analysis assumes that each container has a fixed number of pits on its surface. Letting the number of pits on a single container be n, the extreme-value distribution is the probability distribution over the deepest pit in a sample of n

pits. It is assumed in this analysis that the number of pits on a container would be in the order of hundreds. The results of the corrosion model are relatively insensitive to the assumed number once the number is larger than tens.

This reason for the insensitivity is illustrated in Figure 13-4, which shows the complementary cumulative distribution over the depth of the deepest pit for the cases of 2, 10, 100, and 1000 pits per container. This analysis assumes the Median corrosion case at 100°C for 100 years. The value of the complementary cumulative distribution at a depth of D is the probability that the deepest pit on container is deeper than D.

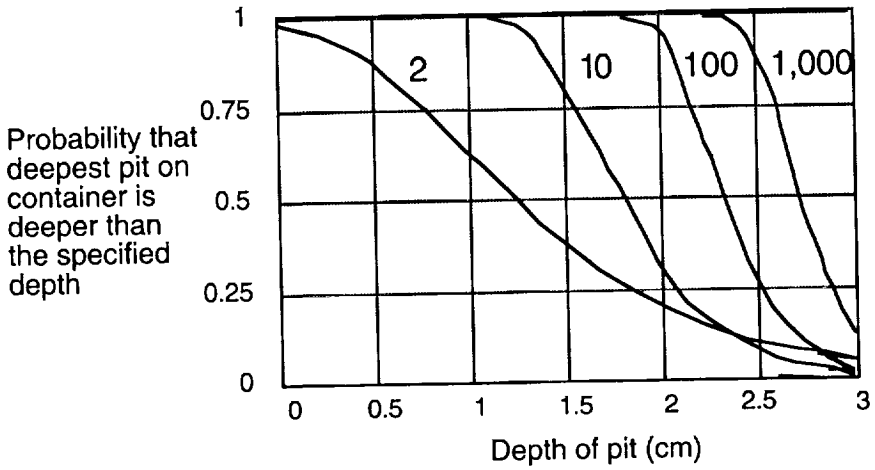

Figure 13-4. Probability of failure as a function of number of pits.

From Figure 13-4 we see that if there are only two pits per container, there is approximately a 0.65 probability that the deepest pit is deeper than 1 cm. Thus, out of a collection of containers all having a wall thickness of 1 cm, about 65% will have been penetrated by at least one pit after 100 years under the assumed conditions. If however, there are 10 or more pits per container the probability that one pit will be deeper than 1 cm is essentially 1.0. This result arises from the observation that the more pits there are on a container, the greater the chance that at least one of them will be deep.

From this illustration, we find that essentially all the containers fail in a relatively short time even when there are only tens of pits on a container. Increasing the number of pits shortens the time until most of the containers fail. But because most containers fail in a short period of time anyway, it makes no appreciable impact on the analytic results.

For double-walled containers with mild steel overpack and Alloy 825 lining, the corrosion model provides a probability distribution over the time of container failures. Corrosion of the outer wall is a deterministic process involving only air oxidation and

general aqueous corrosion. Pitting corrosion of the inner wall is a stochastic process and therefore produces a distribution over the time of inner-wall failure. The electrochemistry of the interaction between the two components could influence the corrosion of the metals, but the tendency would be to reduce the corrosion of the high-nickel alloy. For the single-walled vertical-emplacement container, the container corrosion module provides a failure-time distribution due to the pitting process. In both cases, the failure-time distribution is used to determine the fraction of containers that fail in each time period of a model run.

13.2.4.2 Failure of defective containers

The failure of defective containers is assumed to follow an exponential distribution with defective failures beginning immediately after emplacement. The parameters specified for this model are the fraction of containers that are defective, and the mean failure rate for a defective container. The fraction of containers failing in period i is given by:

$$Failures\ in\ period\ i = F_0 \cdot \left[e^{-\lambda t_{i-1}} - e^{-\lambda t_i}\right], \tag{13.7}$$

where F_0 is the fraction of containers that are defective, t_{i-1} and t_i are the times at the start and end of the ith period, and λ is the mean failure rate. This process was used for the TOSPAC calculations; the parameters are given in Chapter 14.

13.2.4.3 User-specified failures of containers

The user can specify a uniform rate of failures over a specified time period. Although this is not intended to model specific failure processes (such as corrosion), it allows the user the flexibility to specify failures for any process desired. This failure mode was used for the WEEPTSA calculations; the parameters used are given in Chapter 15.

This module models failure mechanisms for fuel-rod cladding—creep rupture of the Zircaloy cladding, hydride reorientation of the Zircaloy, and fluorine-contact failure. All three processes occur in different temperature ranges. The cladding-failure model assumes that only one failure mechanism can be active at any given time, and the times at which a mechanism may be active are defined by the temperature profiles. Given that the conditions for a particular mechanism to be active are met, cladding fails at a constant rate.

It is assumed that after emplacement, the fuel-rod and waste-package temperatures will rise. During the initial temperature rise and cool-down, the fuel rods are assumed to be dry. Only when the temperature drops below boiling would it be possible for

water to come into contact with fuel rods (after the waste package has failed). The model assumes creep can occur only if the temperature is above 350°C. Hydride reorientation occurs for temperatures between 100°C and 350°C. Fluorine-contact failure occurs at temperatures below 100°C (all these temperatures are user-definable). This latter process only occurs for groundwater with fluorine concentrations greater than 200 parts per million (ppm). For TSPA-93, the fluorine content of the groundwater is considered to be well below the 200-ppm threshold (see Table 13-2).

The parameters used to calculate the failure rate are the fractions of rods that would fail by the two high-temperature processes, the failure periods for these processes, and the fluorine-failure period. The fluorine-failure fraction is assumed to be the fraction of fuel rods that do not fail by other mechanisms. The rate at which failures occur is the failure fraction divided by the failure period. The fraction of rods failing in a period by one of these mechanisms between times t_1 and t_2 is:

$$Fraction\ failing = (t_2 - t_1) \cdot F_t / T, \tag{13.8}$$

where t_1 and t_2 are the times at the start and end of the period, F_t is the total fraction that can fail by the mechanism, and T is the time required to fail F_t of the rods by this mechanism. These parameters were obtained by expert elicitation (R. B. Stout, LLNL), and are listed in Table 13-7.

Table 13-7. Parameters of YMIM fuel-rod cladding failure model.

Process	Temperature (°C)	Fraction	Period (years)
Creep Rupture	>350	0.1–0.25	300
Hydride Reorientation	100–350	0.075–0.09	100
Fluorine	<100	balance	10,000

As is discussed in Chapter 14, cladding has not been considered as a barrier to releases for aqueous processes for the TSPA; the hydride reorientation process has been artificially set to 1 (i.e., 100% failures by this mechanism) to model this. The values listed in Table 13-7 are used for the container lifetime studies.

13.2.5 Radionuclide properties

This module specifies the radionuclide inventory in a fuel rod being modeled, as well as solubility and release properties of the inventory components. Solubility can be temperature dependent, although temperature-dependence is not specified in the TSPA-93 analyses.

This module calculates the amount of each nuclide specified in the initial rod inventory, adjusted for decay. In addition to the radionuclide inventory in the fuel matrix, the amounts located in the gap between the fuel pellets and the cladding are also calculated for highly soluble nuclides. Pulse-release fractions (from matrix grain boundaries and from the matrix-cladding gap), and cladding-surface fractions can be specified for appropriate radionuclides. The YMIM model does not include ingrowth of decay-chain daughter products, so inventories must be modified accordingly. The choice of radionuclides and associated properties are dependent upon the analysis, and is discussed in Chapter 5.

13.2.6 Internal-container flow

This module computes the exposed and wetted areas of a failed fuel rod. The internal-container-flow module takes as inputs the volumetric expansion of the waste form due to oxidation and the initial cross-sectional area and length of a fuel rod. It calculates the exposed area by assuming that a fuel rod with failed cladding undergoes a transition which results in complete oxidation to U_3O_8. The amount by which the UO_2 matrix expands due to oxidation is an input parameter. The module computes the change in circumference of the fuel rod and multiplies this value by the length of a fuel rod to compute the exposed area. The wetted area of a failed fuel rod is assumed to be the exposed area. Table 13-8 lists these parameters.

Table 13-8. Parameters for YMIM fuel-oxidation model.

Parameter	Value
Volumetric Expansion	0.33
Initial Cross-sectional Area of Fuel Rod (m^2)	9.6×10^{-5} [a]
Length of Fuel Rod (m)	3.71[a]

[a] Data from *Characteristics Data Base* (DOE, 1992b).

13.2.7 Waste-form dissolution

The dissolution module models a number of mechanisms that determine the dissolution rate of fuel in rods with failed cladding in failed waste packages. These include: fuel-matrix oxidation, fuel-matrix alteration, aqueous release, gaseous release of nuclides from the internal structures of the container, and pulse release from the fuel-rod surface. Each of these mechanisms is discussed in the following sections. The waste-form dissolution module keeps track of mass balances to ensure that amounts dissolved are consistent with amounts altered and with the initial radionuclide inventory and decay.

13.2.7.1 Fuel oxidation

After the container and cladding fail, the availability of oxygen will allow the waste form to begin to oxidize. As oxidation progresses, the UO_2 matrix is altered, and nuclides are released from the matrix; they become available to be mobilized. Radionuclides with gaseous release modes (e.g., ^{14}C) are also released. The rate of fuel oxidation is assumed to obey an Arrhenius relationship (Figure 13-5). Estimates of oxidation rates are based on expert judgment (R. B. Stout, LLNL) of the time required to oxidize a fuel rod at various temperatures. Although these estimates do not follow an Arrhenius relation perfectly, the general trend is roughly consistent with the Arrhenius model. The discrepancy between the data and an Arrhenius relationship is allowed to occur at the high temperatures (i.e., 300°C), where an oxidation rate of 30 years or 0.3 years is essentially the same on the scale of the TSPA analyses. Table 13-9 lists the fuel-oxidation parameters.

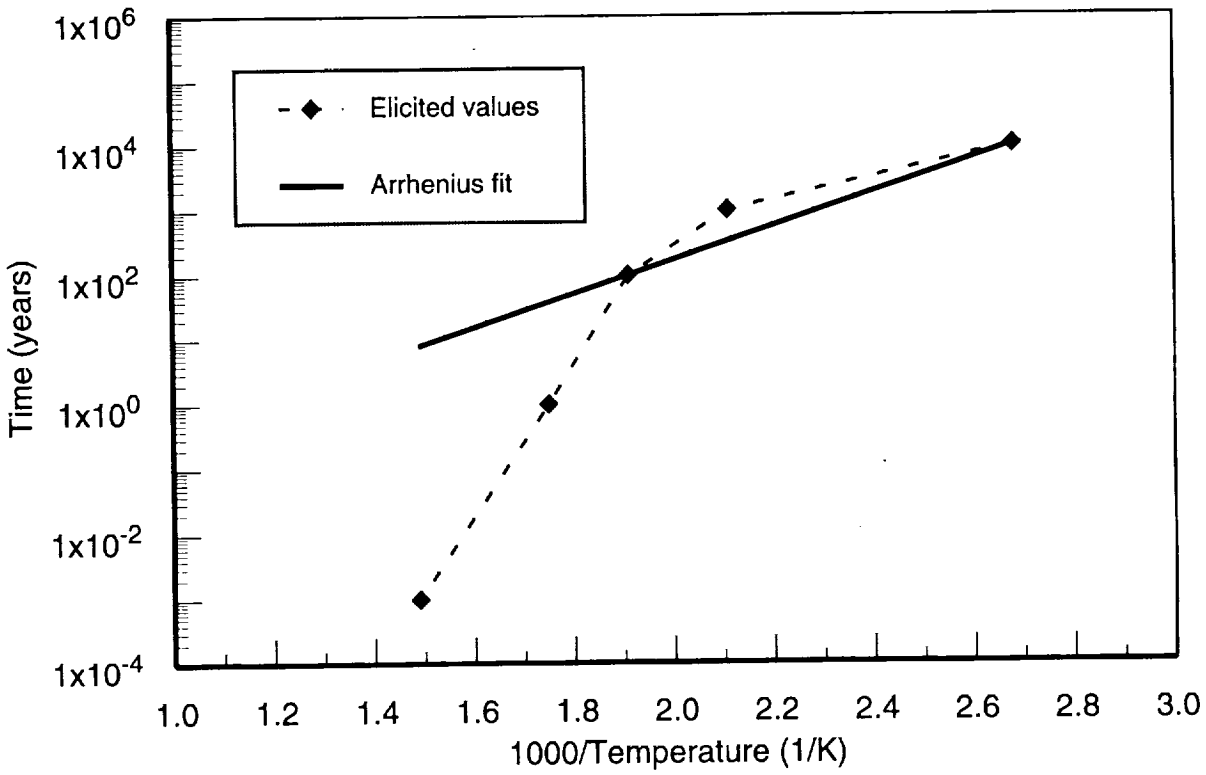

Figure 13-5. Fuel oxidation rates.

13.2.7.2 Fuel-matrix alteration

The dissolution module used includes a model of matrix alteration resulting from dissolution upon contact with water. As the UO_2 in the matrix alters, the elements em-

bedded in the fuel matrix become available for transport. The altered nuclide mass can then be transported away, be released as gas, or reprecipitate. (The mechanisms for transport are described below.) The alteration rate of the UO_2 matrix is modeled as a function of temperature, water pH, and water carbonate concentration, and has the form:

$$Rate = A \cdot 10^{[B+C \cdot log(carbonate)-D \cdot pH-E/T]}, \tag{13.6}$$

where the rate is given in g/m^2-year, carbonate concentration in mole/l, and temperature, T, in K. Parameter values are given in Table 13-10, and were obtained from Gray *et al.* (1992), and by expert elicitation (R. B. Stout, LLNL).

Table 13-9. Fuel-oxidation parameters used in TSPA-93.

Parameter	Time (years)
Fuel oxidation at 250°C	100
Fuel oxidation at 100°C	10,000

Table 13-10. Parameters for YMIM fuel-matrix alteration model.

Parameter	Value
A	0.414
B	7.45
C	0.258
D	0.142
E	1550.

13.2.7.3 Gaseous release from fuel cladding

The fuel-cladding gaseous release model assumes that ^{14}C is present on the surface of the cladding. Upon container failure, this mass will be released from the container as a gas. The amount of ^{14}C released upon container failure is computed assuming that there is a mass per unit area of ^{14}C on the surface of all fuel cladding. Therefore, the total gaseous release upon container failure is the total surface area of all fuel rods in a container multiplied by the mass per unit area. The mass per unit area for each nuclide is an input parameter to the nuclide behavior model.

13.2.7.4 Pulse releases from fuel-cladding gap

The pulse-release model assumes that a fraction of the radionuclide inventory in the waste form migrates to the surface of the fuel rod and is available for release once cladding and container failure have occurred. The pulse-release fraction for each nu-

clide is specified in the Nuclide-Behavior module. For each simulation time step, the pulse amount released from a newly failed container is the product of the pulse-release fraction, the cumulative number of fuel rods with failed cladding, and the mass of that nuclide in a single fuel rod. For containers that failed in previous time steps, the pulse release amount is the product of the pulse release fraction, the number of fuel rods whose cladding has failed in the current time step, and the mass of the nuclide in a single fuel rod. The amount of each nuclide that is actually released is the pulse-release amount times the fraction of the rod surface area that is wetted.

13.2.7.5 Aqueous release

Once radionuclides have been freed from the fuel matrix, they are available for aqueous transport out of the failed waste package. The aqueous-release model defines releases from the container to be a function of the amount of a radionuclide that has been mobilized from the fuel matrix and the amount that is soluble in the volume of water passing over fuel rods with failed cladding. The radionuclide inventory available for transport is the sum of the inventory that has been mobilized from the fuel matrix by oxidation, aqueous alteration, and gap-release processes. The amount of a nuclide that can be transported by water flowing through a container is the product of the volume of water encountering fuel rods with failed cladding and the solubility limit of that nuclide. Aqueous release from the waste package is the minimum of these two values.

Chapter 14
Nominal-Case Releases: Composite-Porosity Model

(Wilson)

The "nominal case" concerns aqueous and gaseous releases to the accessible environment under undisturbed conditions—that is, undisturbed by human intrusion or effects of volcanism or tectonism. Our nominal case includes processes, notably climate change, that are sometimes separated out and treated as disruptive events or processes (e.g., Codell *et al.*, 1992).

As in TSPA-91 (Barnard *et al.*, 1992), we calculate nominal aqueous and gaseous releases using two different conceptual models for unsaturated-zone groundwater flow at Yucca Mountain: the composite-porosity model and the weeps model. The composite-porosity model assumes that flow is shared between the rock matrix and the fractures because of capillary forces (pressure equilibrium between matrix and fracture flows), whereas the weeps model assumes that water flows in locally saturated fractures with no matrix/fracture interaction. Both of these conceptualizations are idealized, and reality is probably somewhere in between. Currently, not enough evidence exists to be able to rule out either type of behavior. As was seen in TSPA-91, and as will be shown below for TSPA-93, releases to the accessible environment are significantly different for the two models, so it is important to study both models and to look for field evidence that may determine which model (if either) is a better representation of reality.

In this chapter, the composite-porosity model and its computational implementation will be discussed briefly, followed by a detailed discussion of release results obtained for the model, parameter sensitivities of the model, and implications of the results for site characterization and repository design. The weeps model and its results and implications will be discussed in the following chapter.

14.1 Similarities to and differences from TSPA-91

The release calculations for the composite-porosity model are the same as those for TSPA-91 in most respects, but they have been improved in several key areas. As in TSPA-91, the release calculations are done using the Monte Carlo method to generate probability distributions for various measures of performance. The Monte Carlo simulations are done using the total-system analyzer (Wilson *et al.*, 1991; Wilson, 1992). The TSA is simply a shell to run a sequence of stand-alone programs many times. Sampling of parameter values from the input probability distributions is done using the LHS program (Iman and Shortencarier,

1984), which is an implementation of the Latin-hypercube sampling method. Aqueous flow and transport are calculated using the TOSPAC program (Dudley *et al.*, 1988; Gauthier *et al.*, 1992). Gaseous releases are calculated using the GASTSA program, as described in Section 5.4 of the TSPA-91 report, though the ^{14}C transport times and source releases that go into the calculation are different, as described in Chapters 12 and 13 of this report.

14.1.1 Similarities

Realistic calculations of groundwater flow and aqueous transport in three-dimensional, heterogeneous systems, including all significant physical processes, are difficult, if not impossible, at the present time. The situation is made all the more difficult by the need to calculate many realizations in order to characterize the system probabilistically. Therefore, many simplifications were made in TSPA-91 to reduce the computational requirements to tractable levels. We are well aware that the appropriateness of these simplifications must be studied, but because of time and resource constraints we had to focus on improvements in a few areas for TSPA-93.

Important simplifications that are unchanged from TSPA-91 include the following.

- Unsaturated-zone groundwater flow and aqueous transport are modeled as one-dimensional (vertical).
- Gas flow and gaseous transport are modeled as two-dimensional.
- Groundwater flow and aqueous transport are modeled as isothermal and single-phase. Flow is represented by Darcy's Law, and transport is represented by generalized advection/dispersion equations (see Dudley *et al.*, 1988).
- Gas flow is modeled using the assumption that relative humidity is always 100% (see Chapter 12).
- Gaseous transport is modeled as being purely advective, with no diffusion (see Chapter 12).
- Percolation flux at the repository is applied as a boundary condition rather than by calculating infiltration and diversion in upper layers.
- Hydrogeologic properties within stratigraphic layers are modeled as homogeneous and isotropic.
- Radionuclide retardation during transport is modeled by a simple distribution coefficient (K_d).

- Matrix/fracture coupling is assumed to be strong for transport and for water flow.
- Aqueous and gaseous releases are calculated independently and combined afterward in an *ad hoc* manner (as described in Chapter 8 of the TSPA-91 report).
- Radionuclide releases from waste containers are calculated taking no credit for the fuel-rod cladding and no credit for the waste container as a barrier after container failure.
- All waste, including vitrified high-level waste, is treated as spent fuel in the source calculation; a model for releases from glass waste has not yet been incorporated.

14.1.2 Differences

The choice of where to focus our limited resources was driven by three main considerations. (1) The YMP is currently reconsidering some of the choices that were made during the development of the Site Characterization Plan (SCP; DOE, 1988a). In particular, a change in the reference thermal loading is being considered and changes in the container design and emplacement mode are being considered. Many of the reasons for these considerations have to do with interim storage and transportation of waste, economics, and other areas outside the scope of this effort, but it is important to study the effect of the various options on repository performance. The desire to evaluate relative merits of various thermal loadings and container types drove us to give priority to improving our modeling of thermal effects and container failure. (2) In late 1992, Congress declared that 40 CFR Part 191 (EPA, 1985) no longer applies to the Yucca Mountain site, and directed the EPA to develop a new regulation based on individual radiation doses (Public Law 102-486, 1992). Thus, it was clearly important for us to begin looking at dose calculations and to try to evaluate different possible regulatory performance measures. One significant effect is that the saturated zone plays a much more important role in dose calculations than in cumulative-release calculations of the type specified in 40 CFR 191.13. Thus, we wanted to improve our saturated-zone modeling. (3) From qualitative analysis of the models and from results of a sensitivity study of the TSPA-91 aqueous- and gaseous-release results (Wilson, 1993), we knew that composite-porosity aqueous releases are extremely sensitive to the percolation flux. Composite-porosity gaseous releases are sensitive to bulk permeability, ^{14}C retardation, container-failure time, and fuel-matrix-alteration rate. Thus, we tried to improve our models or data sets in each of those areas.

Important differences from TSPA-91 include the following.

- Four repository cases are considered, as discussed in Chapter 4.

- Many changes have been made to the source-release model (Chapter 13), especially the inclusion of additional thermal effects, inclusion of a phenomenological container-failure model, inclusion of juvenile container failures, and non-inclusion of diffusive releases (only advective releases are modeled). Some dependence on chemistry (pH, carbonate concentration) is included in the source model, though ambient-condition values are used for the geochemical parameters because realistic waste-package and near-field values are not available.

- The gas-flow calculations are transient and coupled with the heat flow (Chapter 12). The TSPA-91 gas-flow calculations were steady-state, and the steady-state temperature field was calculated assuming that heat flow was purely by conduction, with the repository being held at a given fixed temperature.

- Peak radiation-dose rates from drinking water are calculated in addition to the EPA's performance measure from 40 CFR 191.13.

- A longer time period is modeled: one million years rather than 10,000 years. The main reason for the longer time period is so that the calculations include the projected time of peak drinking-water dose rate. The gaseous-release calculations are still only 10,000 years.

- The saturated-zone transport velocities are based on new work described in Chapter 11 of this report.

- A model for climate changes is included (Chapter 8). Climate changes are important both because of the longer time period under consideration and because of the importance of percolation flux to aqueous releases.

- There are many differences in the stratigraphy and parameter distributions used (Chapters 6 and 7).

- A different set of radionuclides is used for the aqueous-release calculations.

Most of the important differences listed above are discussed in previous chapters of this report. However, our method for calculating doses has not yet been described, and some aspects of the climate-change and source models are specific to the composite-porosity calculations. Those three subjects will be discussed in the following sections.

14.2 Dose calculation

We did not perform any dose calculations for TSPA-91, though Pacific Northwest Laboratory performed some dose calculations using our release results (Eslinger *et al.*, 1993). As

a first step toward modeling radiation doses, for TSPA-93 we calculate drinking-water doses, but do not perform full biosphere dose calculations. A calculation of dose from drinking water is relatively straightforward and not so speculative as calculations that require more detailed assumptions about future human behavior (such as, for example the possibility of doses related to a farm in the Amargosa Desert).

We take as our dose-based performance measure the maximum annual dose that could be incurred by a person who drinks water from the saturated zone, within the region defined by the EPA in 40 CFR Part 191 as the "accessible environment." That is, the dose is based on the maximum radionuclide concentration in the saturated zone at a distance of 5 km from the potential repository. The concentration is taken directly from the saturated-zone transport calculation, with no mixing or dilution assumed for the well-withdrawal process. The standard assumption is made that water is drunk at a rate of 2 liters per day, which makes 730 ℓ/yr. The calculated annual dose is then obtained by multiplying the radioactivity contained in that amount of water by a dose-conversion factor:

$$D_i = d_i a_i C_i V_w \ , \tag{14.1}$$

where D_i is the dose rate from radionuclide i (mrem/yr), d_i is the dose-conversion factor for nuclide i (mrem/Ci), a_i is the specific activity of nuclide i (Ci/g), C_i is the concentration of nuclide i (g/m^3), and V_w is the volume of water consumed (m^3/yr). From the above, we have $V_w = 0.73$ m^3/yr. Dose-conversion factors for ingestion were taken from Barnard (1993, Table 7), who in turn took them from DOE (1988c); dose-conversion factors for the seven radionuclides included in the aqueous-release calculations are given in Table 14-1. Specific activities are given later in Table 14-5.

The total dose is the sum over all nuclides:

$$D = \sum_i D_i \ . \tag{14.2}$$

Table 14-1. Total-body dose-conversion factors for ingestion.

Species	Dose-conversion factor (mrem/Ci)
^{239}Pu	4.3×10^9
^{237}Np	3.9×10^9
^{234}U	2.6×10^8
^{231}Pa	1.1×10^{10}
^{129}I	2.8×10^8
^{99}Tc	1.3×10^6
^{79}Se	8.3×10^6

Because only a subset of radionuclides is included in our calculations, the doses may be low. We have attempted to include the most important nuclides, but there could be significant doses from some daughter products that are not included. (Because of radioactive generation, it is possible for a radionuclide to be present in non-negligible quantities even though it may be short-lived or highly retarded.) Evaluation of additional nuclides with a more complete dose model is left for future work.

It is important to keep in mind that for an individual to receive the magnitude of dose that we use for our performance measure, he must drill and extract water from the contaminated region at the time of peak dose. If the water-extraction takes place earlier or later, or outside the contaminated region, the dose is smaller. As discussed in Section 11.6.2, we assume in the saturated-zone (SZ) transport calculation that the plume of contaminated water is about 3- to 4-km wide by the time it reaches the accessible-environment boundary. Drilling for water must be within this band to get the maximum dose. We also assume that the contaminated water is in a zone 10- to 500-m thick (vertically), within the tuff saturated zone. Water extraction must be from this zone to get the calculated dose. The width of the dose peak in time is quite variable, but the maximum dose is probably near the peak dose for thousands of years, typically; the time of peak dose varies from about 10,000 years up to about a million years.

14.3 Climate change

Our basic climate-change model is described in Chapter 8. In this section, some details of its implementation within the composite-porosity model are given.

As discussed in Chapter 8, we divide the calculational period into "dry" and "wet" periods. During wet-climate intervals, the percolation flux is increased and the water table is higher. As described by Dudley *et al.* (1988), TOSPAC could calculate aqueous contaminant transport only for steady-state groundwater flow. Thus, it was necessary to modify TOSPAC to be able to include changing flow conditions. Rather than going to fully transient water flow, TOSPAC was modified to allow transport with a series of steady-state water flows. This choice was made primarily because transient water-flow calculations would take too much computer time (see, for example, the drastic difference in computer times reported for steady-state solutions and transient solutions by Dudley *et al.*).

Also to save on computer time, each composite-porosity realization switches back and forth between the same two steady-state flows rather than sampling percolation flux and water-table height separately for each climate period. This simplification also has the advantage of reducing the number of input variables.

Representing the water flow by a series of steady states creates some difficulties in the transport calculation. First is that when a flow change occurs, the pore-water saturations change abruptly. It is necessary to adjust the radionuclide concentrations so that mass is conserved. The mass of a nuclide in a mesh cell before a flow change is given by

$$M = (\theta_m R_m C_m + \theta_f R_f C_f) V \ , \tag{14.3}$$

where M is nuclide mass (g), θ is moisture content (dimensionless), R is the retardation factor due to adsorption (dimensionless), C is nuclide concentration (g/m^3), and V is the volume of the mesh cell (m^3). An m subscript refers to rock-matrix quantities and an f subscript refers to fracture quantities. After the flow change, the nuclide mass in the cell is given by

$$M' = (\theta'_m R'_m C'_m + \theta'_f R'_f C'_f) V \ . \tag{14.4}$$

Primed quantities are values after the flow change; note that volume does not change. To conserve mass, we must have $M' = M$. This is not, however, enough of a constraint to determine C'_m and C'_f uniquely. The condition used to complete the system of equations is $C'_m = C'_f$; that is, matrix and fracture concentrations are set equal to each other after a flow change. Thus,

$$C'_m = C'_f = \frac{\theta_m R_m C_m + \theta_f R_f C_f}{\theta'_m R'_m + \theta'_f R'_f} \ . \tag{14.5}$$

If matrix/fracture coupling is strong this condition is quite reasonable. If matrix/fracture coupling is weak another condition might be preferable, but it would be difficult to specify a single condition that would work better under all possible conditions, given the arbitrary nature of instantaneous flow changes. Furthermore, some choices can lead to quite unpleasant consequences. For example, if matrix and fracture radionuclide masses are conserved separately, a climate change to a dry condition with fractures that are nearly dry can result in a very large spike in the fracture concentration.

Another difficulty caused by instantaneous flow changes relates to the fact that the water table can be higher or lower after a change. If the water table is higher, that means that some of the contaminant mass has abruptly left the computational domain. Under this circumstance, that mass is assumed to have been released to the saturated zone. This method can result in a large spike in releases to the saturated zone. It can also produce a spike in the drinking-water dose rate calculated at the accessible environment. Such spikes may not be wholly unrealistic: A climate change that causes the water table to rise 100 m in a short period of time could well lead to significantly higher drinking-water doses temporarily. To explore such effects would require an integrated model of flow and transport in the unsaturated zone (UZ) and the saturated zone, which we do not have at present. Note

that the saturated-zone flow is not modified at climate changes; a single steady-state water flow is used for the saturated zone over the whole calculational period. It is left to future work to try to integrate the UZ and SZ climate fluctuations better. If the water table is lower after a flow change, there is the problem of what the nuclide concentrations should be in the interval between the two water-table levels. We simply set the concentrations to zero in that interval. Once again, the only way to improve on this assumption is with an integrated UZ/SZ model.

An additional problem with decoupling the UZ and SZ flow calculations and assigning their properties randomly from probability distributions is that some of the resulting realizations may not be realistic. In particular, the total amount of water flow in the unsaturated zone (UZ percolation flux times repository area) may turn out to be higher than the total flow in the saturated zone (SZ percolation flux times SZ flow-tube area). Such a situation is unacceptable in that, when contaminants were transferred from the UZ calculation to the SZ calculation, their concentration would increase, which is unphysical. Presumably, such a high UZ water flux would, in reality, result in a significant perturbation of the SZ flow. In the composite-porosity aqueous-release calculations, a check is made for this condition (UZ flow greater than SZ flow), and if it exists the SZ flow-tube area is increased enough so that the concentrations do not increase. With the parameter distributions used in this TSPA, such an adjustment is needed less than one-half percent of the time.

There is a similar problem with the release spikes associated with jumps in the water table. When all of the radionuclides swept out of an interval as large as 120 m are injected into the saturated zone in a single pulse, SZ concentrations rise to unrealistic levels temporarily. It would be possible to ameliorate this behavior by spreading out the release to the saturated zone over a period of time, but this was not done for TSPA-93. More information is needed on the way climate changes really affect groundwater flow in the vicinity of Yucca Mountain. Fortunately, the saturated-zone concentration spikes attenuate considerably by the time they travel 5 km to the accessible environment, so the effect on our calculated peak dose rates is probably no more than about a factor of two.

The importance of the climate changes is illustrated in Figure 14-1, which shows distributions of unsaturated-zone transport time for an unretarded tracer. Separate dry-climate and wet-climate distributions are shown, and it can be seen that transport through the unsaturated zone takes considerably longer under dry-climate conditions. Also shown is a composite curve that includes the effects of switching between the two flow regimes. For short times (i.e., faster transport), the composite curve is closer to the "dry" curve because our model climate always starts out in the "dry" condition. For longer times, the composite curve approaches the "wet" curve because both "dry" and "wet" periods have been experi-

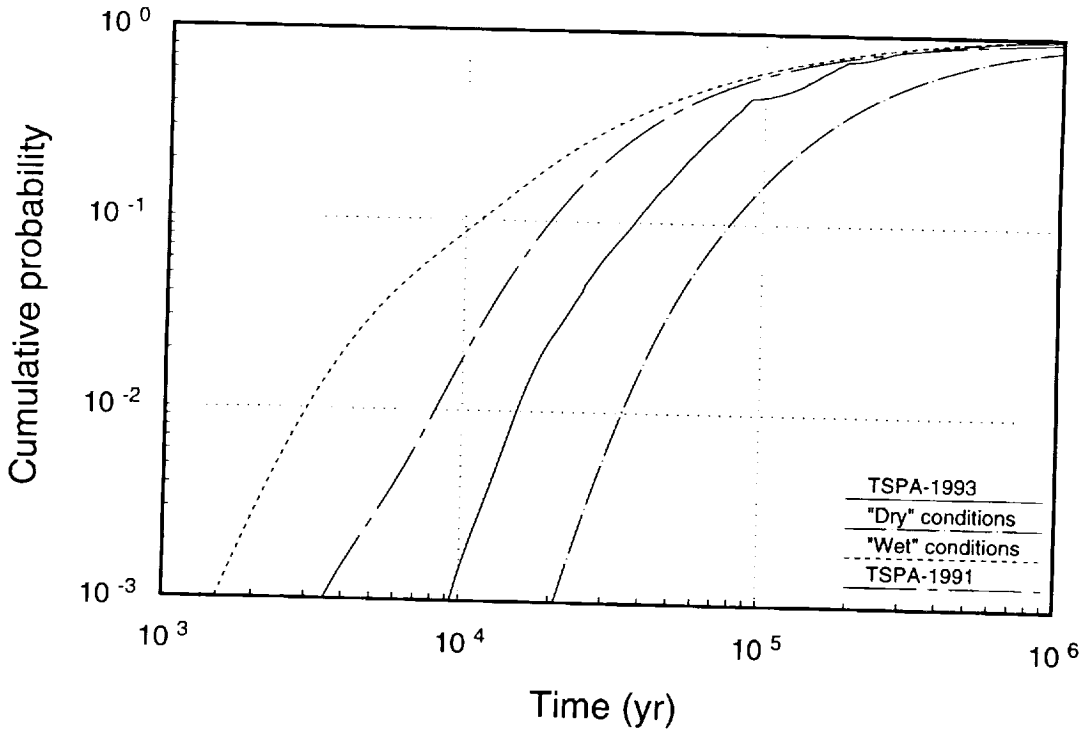

Figure 14-1. Mean distributions of UZ transport time for an unretarded tracer, for TSPA-91 and TSPA-93. Also shown are distributions for "dry" and "wet" conditions with no climate changes.

enced, and typically most transport takes place during the wet-climate periods. Also included in the figure, for comparison, is the unsaturated-zone transport-time curve from TSPA-91. It can be seen that calculated UZ transport times were shorter in TSPA-91 than they are for TSPA-93, primarily because the dry-climate periods have lower percolation flux than in TSPA-91. Note, however, that the TSPA-91 curve has a longer tail (out to longer transport times); the wet-climate periods reduce the long-time tail of the TSPA-93 curve.

14.4 Radionuclide source term

This subsection describes the adaptation of the abstracted hydrothermal model of Chapter 10 and the YMIM source-release model of Chapter 13 for use with the composite-porosity model. For aqueous-release calculations, the source model is incorporated directly into TOSPAC. It is also incorporated into a subset of TOSPAC called SRCTSA, which is used for running source calculations only (without flow or transport). SRCTSA is used for some of the special calculations discussed below, such as calculations to determine the distribution of container-failure time. It is also used to calculate the source releases for GASTSA, for gaseous-release calculations.

14.4.1 YMIM capabilities not used

Before going on to the specifics of the adaptation, let us first note that YMIM has some capabilities that were not used for this TSPA, including:

- Because of uncertainty in the performance of the fuel-rod cladding, especially uncertainty about how long the fuel assemblies may be subjected to high temperatures during interim storage and transportation, we neglect the cladding as a barrier for the TSPA-93 calculations. The cladding barrier is removed by artificially specifying to YMIM that all the fuel rods fail by hydride reorientation, with a hydride-failure time of 1 yr. Thus, after year one, all rods have failed and radionuclides can be released as soon as containers fail. Neglecting the cladding may be a quite conservative assumption. Experts at Lawrence Livermore National Laboratory, when asked about cladding failure, estimated that somewhere between 17.5% and 34% of the fuel rods would fail due to creep rupture or hydride reorientation (see Table 13-7). This estimate implies that 66% to 82.5% of the fuel rods would *not* fail, providing a significant reduction in releases. It is probably worth examining the cladding barrier in detail in a future study, but we did not do so for this TSPA. Fuel temperatures are much higher for the in-drift containers than for the borehole-emplaced containers, and temperatures are somewhat higher for 114 kW/acre than for 57 kW/acre (see Figures 10-20 through 10-23), so there may be differences in cladding performance for the four repository cases that we are considering.

- YMIM allows for a linear temperature dependence of nuclide solubilities, but on the advice of our solubilty experts from Los Alamos National Laboratory we did not try to include temperature-dependence of solubility in our calculations (see Section 9.2.1). Their feeling was that the uncertainty in geochemistry is a bigger factor than temperature in determining solubilities. It still may be worthwhile to include temperature-dependent solubilities in the future, however.

- A pitting factor, or pitting-enhancement factor, can be used in the general aqueous corrosion model of YMIM to allow the deepest pits to advance faster than the general corrosion front. In this TSPA, general aqueous corrosion is only used for the mild-steel outer container of the in-drift multipurpose containers. Mild steel is not expected to have strong pitting, though it could have a pitting factor as high as 4 (see Section 13.2.4.1). For a 10-cm overpack, the calculated lifetimes are generally rather short anyway, so there would be little difference if a pitting factor were included. For a thicker mild-steel overpack, inclusion of a pitting factor might be important.

14.4.2 Container groups

One of the most important features of the composite-porosity adaptation of YMIM is that releases are represented by a limited number of distinct groups. The use of such groups allows the incorporation of variation of container environments within the repository. Each group's releases are calculated using a single representative container, so effectively each group is treated as a set of containers with identical conditions. However, from one group to the next, temperature and hydrologic conditions can vary. (In principle, other properties, such as geochemistry and even container properties, could vary from group to group, but the current version of YMIM does not allow such variations. Adding such variations is primarily a matter of setting up the input in such a way that all the desired information can be entered and passed to the appropriate YMIM module.)

Unfortunately, computer memory and processing-time requirements increase rapidly with the number of container groups. For this reason, it is necessary to set the number of groups relatively low. All composite-porosity-model computer runs use ten container groups. (Note, however, that a 57-kW/acre simulation with eight unsaturated-zone columns has a total of 80 container groups—10 × 8.) The number of containers in each group is chosen so that seven of the groups have the same number of containers, one group has approximately one tenth as many, one group has approximately one hundredth as many, and the last group has approximately one thousandth as many. The small groups are included so as to have small numbers of containers to better resolve releases under conditions when only a small fraction of containers is wet. For example, suppose in a particular simulation that 1% of containers is calculated to be contacted by water. With ten equal container groups, 1% would have to be approximated by 0 or 10%—neither of which is very satisfactory. With the scheme described above, 1% of the containers can be approximated much more closely.

Container and fuel temperatures are interpolated between the "center" and "edge" temperature curves given in Figures 10-16 through 10-23 as follows. A fraction of containers equal to the "dryout" fraction (see Figures 10-10 and 10-11) is assumed to have the "center" temperature. A number of groups as close to that number of containers as possible is set to the "center" temperature. Temperatures for the other groups are interpolated linearly between the "center" and "edge" temperatures. The groups with small numbers of containers are always chosen to be at the "edge" end of the interpolation (because cooler containers are more likely to be wet).

The most importance difference among the container groups is in assumptions about wetting. Using algorithms to be described below, three wetting states are defined: wet, moist, and dry. Wet containers are assumed to be contacted by flowing water, so they can be attacked by aqueous corrosion processes (if the temperature is low enough) and they can have

advective aqueous releases and/or gaseous releases. Moist containers are assumed to have no flowing water, but they are contacted by rubble and so are moist because of contact with pore water. We assume that aqueous-corrosion processes can take place on moist containers (if the temperature is below 100°C), and they can have gaseous releases if they fail, but no aqueous releases. (Note that moist containers could potentially have diffusive releases, but YMIM has no diffusive-release model at present.) Dry containers have no flowing water and either have no contact with rubble or are within the dryout fraction of the repository. Only dry oxidation can take place on dry containers, and they can have only gaseous releases if they fail.

The current version of YMIM has a switch in the aqueous-corrosion module so that, if container temperature is defined to be over 100°C, aqueous corrosion does not occur. There is no similar switch in the aqueous-dissolution module, so aqueous releases are allowed even when fuel temperatures are high. In the future, it would be desirable to develop models of interaction of water with container and fuel at high temperature. It may be possible, for example, if enough water contacts a hot container, for the container temperature to be reduced because of heat loss to the water or steam. The rate of aqueous corrosion, then, would depend on the quantity of water present as well as the temperature and the wetting state. (It should also be noted that YMIM does not currently have a steam-corrosion model.) Similarly, aqueous releases would depend on temperature as well as quantity of water and wetting state.

The division of containers into the three wetting states is not fixed, but varies with time. At some times, in some of the simulations, all of the containers are dry because the dryout fraction is 1. During a wet-climate period, most of the containers may be wet, while during a dry-climate period they are mostly dry. Because the flow conditions switch between the same two steady states at climate changes, the same number of containers are wet during each wet period and the same (different) number are wet during each dry period (except during the thermal period, which is the first few thousand years). However, we do not assume that the *same* containers are wet or dry during similar climate periods. During a single climate period (except for the thermal period), container groups remain wet, moist, or dry, but when climate changes the groups are shuffled so that the wetting state of a group can change (actually, only the seven equal-size container groups are shuffled; the three small groups have the same wetting state during similar climate periods).

This shuffling of flow among the containers is a change from previous work. In TSPA-91, we assumed that flow paths were persistent, so that the same containers were always wet or dry. (Note, though, that container shuffling for this study is not allowed until the second climate change, at 90,000 yr, so there would be no difference for a 10,000-yr calculation.) The

change was made in order to be more conservative (additional containers can be contacted by water and release their waste if shuffling is allowed). Examination of evidence regarding persistence of flow paths is left to future work; wetting from one climate period to the next should perhaps be correlated so that wet containers tend to remain wet.

14.4.3 Container wetting

Container wetting is determined with the same basic algorithm as was used for TSPA-91 (see Section 4.3.2 of the TSPA-91 report), but with three new features. (1) A dryout fraction is now defined explicitly. As discussed in Chapter 10, the containers in the dryout fraction are assumed to be protected from flowing water and are considered to be dry. (2) Percolation flux that would have fallen on the dryout fraction is diverted around it instead, and falls on the parts of the repository outside the dryout fraction, if any. Furthermore, when the "dryout volume" is expanding, we assume that additional water is shed onto the parts of the repository outside the dryout fraction, as explained in Section 10.4.1. Note that the shedding flux is only accounted for in the source calculation, and is not included in the calculation of flow and transport after release. (3) The fractions that are derived for wet, moist, and dry must be approximated by fractions available within the container-group structure.

The basic equations are as follows. If q is the input percolation flux, f_d is the dryout fraction, and q_{sh} is the shedding flux (if any), then the effective flux through the "wet" part of the repository (the part outside the dryout fraction) is

$$q_{eff} = q/(1 - f_d) + q_{sh} \tag{14.6}$$

(assuming that $f_d < 1$). This equation is the same as Equation 10.2, with the correspondence $q_{in} = q$, $A_{wet}/A_{rep} = 1 - f_d$, and $Q_d/A_{wet} = q_{sh}$.

The fraction of the wet area that actually has flowing fractures (seepage flow) is calculated using W. J. O'Connell's algorithm from TSPA-91, which assumes a log-normal distribution of groundwater flux, spatially:

$$f_s = P[q_{eff} > q_0] = \tfrac{1}{2}\mathrm{erfc}\left(\frac{\ln q_0 - \mu}{\sqrt{2}\sigma}\right), \tag{14.7}$$

where f_s is the fraction of the area with seepage flow, q_0 is the fracture-flow threshold flux (the matrix saturated conductivity), erfc is the complementary error function, μ is the mean of the spatial flux distribution in log space, and σ is the standard deviation of the spatial flux distribution in log space. The mean and standard deviation in log space are related to other parameters by

$$\mu = \ln q_{eff} - \tfrac{1}{2}\ln(\upsilon^2 + 1), \tag{14.8}$$

$$\sigma = \sqrt{\ln(\upsilon^2 + 1)}\,, \tag{14.9}$$

where υ is the coefficient of variation of the spatial flux distribution, an input parameter.

The average flux for those containers subjected to seepage flow is given by

$$q' = q_{eff} \cdot f_s^{-1} \cdot \tfrac{1}{2}\mathrm{erfc}\left(\frac{\ln q_0 - \mu - \sigma^2}{\sqrt{2}\sigma}\right). \tag{14.10}$$

It is assumed that q_0 of that flux is carried by the porous matrix, so that the average flux available for seepage flow is given by

$$q_s = q' - q_0\,. \tag{14.11}$$

This quantity is the amount of water flux that is used in calculating advective releases for those containers that have advective releases.

Now, f_s is the fraction of the "wet" part of the repository having seepage flow. The fraction of the repository as a whole is

$$f_{wet} = f_s(1 - f_d)\,. \tag{14.12}$$

The fraction of the repository that is moist is given by

$$f_{moist} = (1 - f_s) f_r (1 - f_d)\,, \tag{14.13}$$

where f_r is the fraction of containers that have rubble contact, an input parameter. The fraction of the repository that is dry is then everything else:

$$f_{dry} = f_d + (1 - f_s)(1 - f_r)(1 - f_d)\,. \tag{14.14}$$

The above fractions are matched to the container groups by first finding a set of groups that has a fraction of containers as close as possible to f_{wet}; those groups are designated as wet, and the containers in them are subjected to flux q_s. Next, additional groups are added to increase the total fraction as close as possible to $f_{wet} + f_{moist}$; the additional groups are moist. Any remaining groups are dry.

For illustration, Figures 14-2 through 14-4 show distributions for fraction of containers wet, moist, and dry. The distributions shown are for f_{wet}, f_{moist}, and f_{dry} after the thermal period (i.e., with $f_d = 0$ and $q_{sh} = 0$). The effective distributions in a simulation are slightly different because of the discretization into ten groups. Distributions are shown for "dry" conditions, "wet" conditions, and for the values used in TSPA-91. Vertical-borehole containers are assumed for these plots (results are different for in-drift containers, because for them we assume that rubble always contacts the containers; i.e., $f_r = 1$).

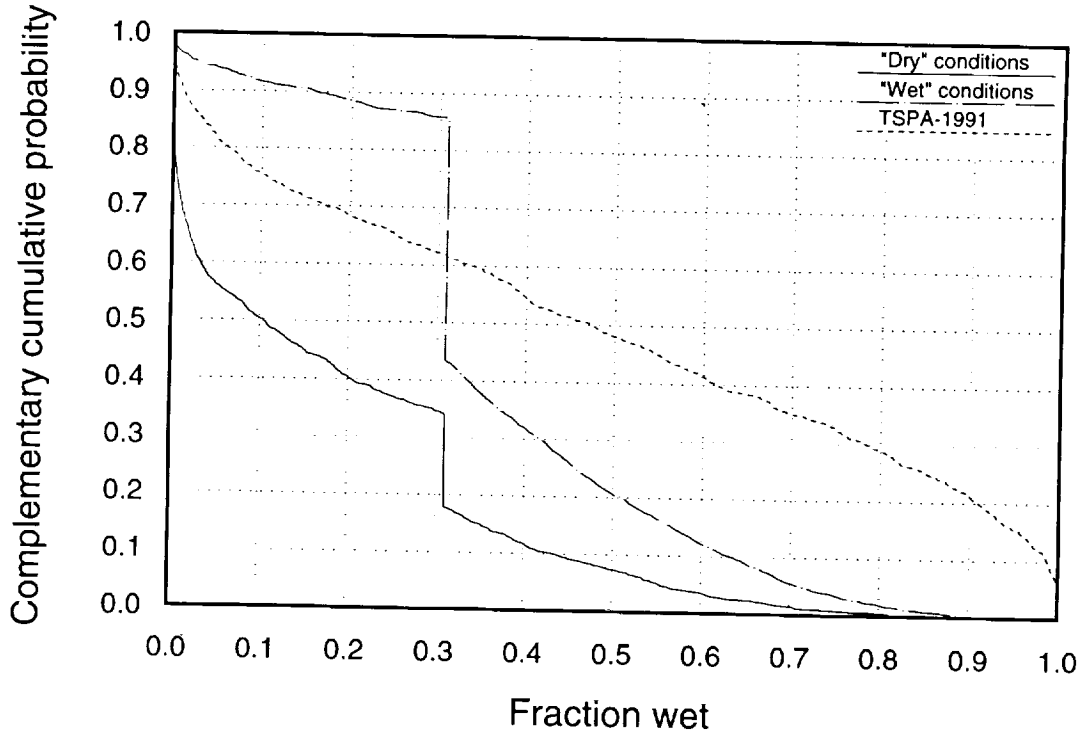

Figure 14-2. Fraction of containers wet, for vertical-borehole containers (valid after the thermal period).

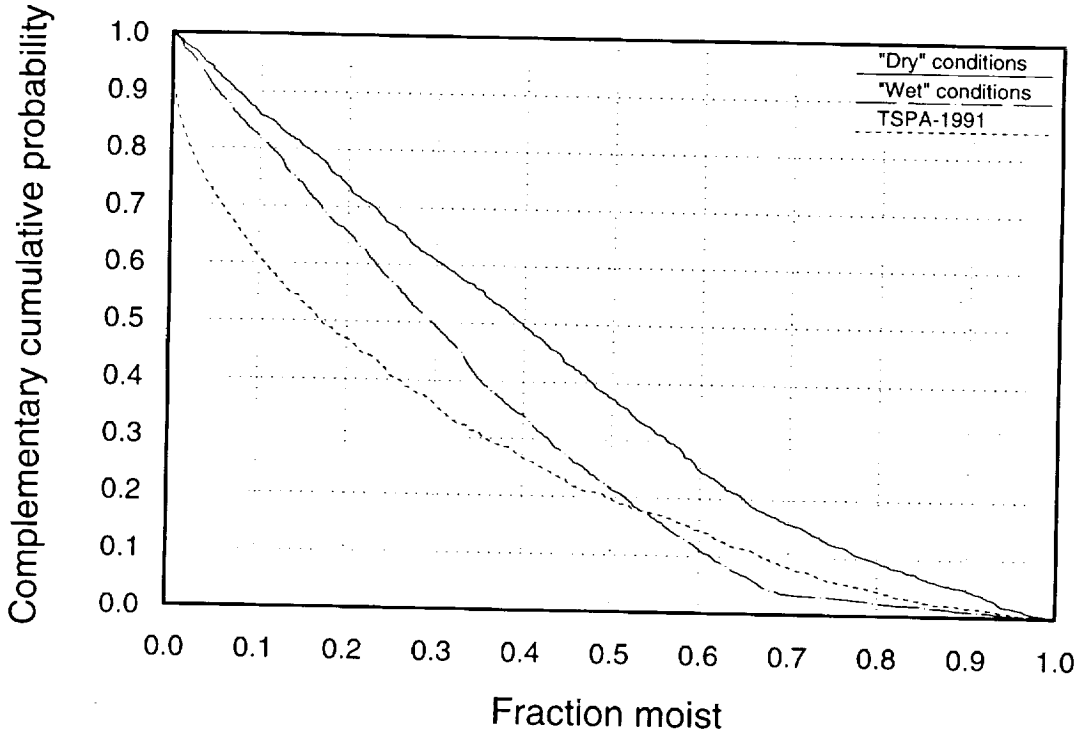

Figure 14-3. Fraction of containers moist, for vertical-borehole containers (valid after the thermal period).

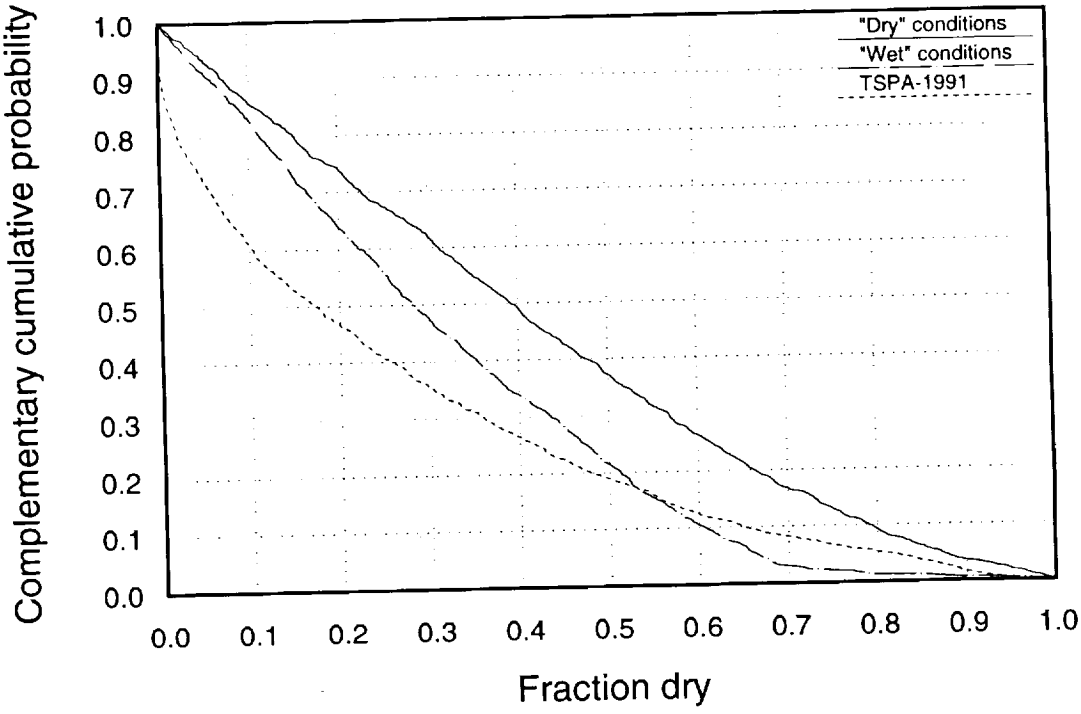

Figure 14-4. Fraction of containers dry, for vertical-borehole containers (valid after the thermal period).

The jumps in the wet-climate and dry-climate curves in Figure 14-2 are a result of the algorithm used for converting infiltration to percolation for the composite-porosity model (see Section 8.9). It can be seen that fewer containers are wet in this TSPA, even under wet-climate conditions, than in TSPA-91. This reduction in the wet fraction is caused by two changes: the inclusion of the infiltration/percolation reduction, and a significant increase in the matrix saturated conductivity (see Sections 7.6.2 and 8.9).

The required wetting inputs for YMIM are, for each time period and for each container group, water flux and episodity (fraction of time that water is flowing) and moisture episodity (fraction of time that container is moist). The moisture episodity is set to 1 for any group that is wet or moist, and to 0 for any group that is dry. The water flux is set to q_s and the episodity is set to 1 for any group that is wet; they are both set to zero for moist and dry groups.

14.5 Problem setup and parameter values

There is a great proliferation of input data (and output results) for this TSPA as compared to TSPA-91 because four repository cases are examined instead of one, and because a

great deal of thermal and hydrothermal information is required that had no analog in the previous TSPA.

In this section, the problem setup and parameter values for the composite-porosity-model simulations will be summarized. Most of the information is presented in earlier chapters, so most parameter distributions will not be presented here, but only a notation giving their location in the report. Additional discussion will be presented here on some of the more important parameters.

14.5.1 Repository layout, column stratigraphies, and SZ flow tubes

Repository layout and subdivision into one-dimensional columns for unsaturated-zone modeling are discussed in detail in Chapters 4 and 6. The repository and column areas are shown in Figures 6-8 and 6-9. The repository is subdivided into eight columns of approximately equal area for the 57-kW/acre cases and into five columns for the 114-kW/acre cases. The actual areas used and numbers of containers for each column are listed in Tables 14-2 and 14-3.

A word of explanation is needed regarding the numbers of containers. The waste-stream figures that were used to define the number of containers and the inventory give a total of 32,022 spent-fuel containers for the vertical-emplacement cases and a total of 7,640 spent-fuel containers for the in-drift-emplacement cases (Table 5-1). However, the spent fuel accounts for only 63,000 MTU of the waste, there being 7,000 MTU of glass waste. The source model does not include a model for releases from glass waste, so we treat all of the waste as spent fuel in the release calculations. We include the full 70,000-MTU radionuclide inventory, but it does not make sense to put it all into the above number of containers (32,022 or 7,640). It also does not make sense to use the total number of spent-fuel containers plus glass containers, because the glass containers hold much less waste than

Table 14-2. Areas (in m^2) for the UZ columns.

Column	57 kW/acre	114 kW/acre
1	5.99×10^5	5.46×10^5
2	5.26×10^5	5.26×10^5
3	6.03×10^5	6.03×10^5
4	6.19×10^5	3.48×10^5
5	5.42×10^5	3.08×10^5
6	5.38×10^5	—
7	6.23×10^5	—
8	5.75×10^5	—
Total	4.63×10^6	2.33×10^6

Table 14-3. Number of containers in each column.

Column	57 kW/acre vertical	57 kW/acre in-drift	114 kW/acre vertical	114 kW/acre in-drift
1	4,631	1,114	8,463	2,016
2	4,076	976	8,118	1,931
3	4,418	1,071	8,784	2,131
4	4,920	1,144	5,410	1,291
5	4,412	1,022	4,805	1,120
6	4,203	1,006	—	—
7	4,646	1,124	—	—
8	4,274	1,032	—	—
Total	35,580	8,489	35,580	8,489

spent-fuel containers do. Thus, we arbitrarily increase the number of spent-fuel containers by the factor 70/63, leading to 35,580 vertical containers or 8,489 in-drift containers. This assumption is as good as any, short of modeling both spent fuel and glass waste in the release calculations.

For gaseous-release calculations, the repository is treated as a whole in calculating the source releases, with no subdivision into columns. Thus, for gaseous-release calculations the "Total" values from Tables 14-2 and 14-3 are used.

The stratigraphy used for the composite-porosity aqueous-release calculations is described in detail in Chapter 6. The base case is the stratigraphy taken from the first geostatistical simulation. Elevations of the unit interfaces are given in Table A-1. Only one of the geostatistical stratigraphies was modeled, because of time constraints. It is important to note that, as discussed in Chapter 6, the stratigraphy used is not intended to represent the "most likely" stratigraphy in any sense. It is only one of a set of simulated stratigraphies that are considered equally likely. Additional stratigraphies from the set of geostatistical simulations will be modeled in the future so that sensitivity of releases to variations in stratigraphy can be evaluated.

We restrict our UZ aqueous-transport modeling to the region from the repository down to the water table, so the stratigraphies actually used for the calculations only go up to 12 m above the position listed as "Repository base" in Table A-1. The eight UZ columns are shown in Figure 14-5. The vertical position assumed for the repository is slightly different for the vertical and in-drift cases; Figure 14-5 shows the source location for the vertical-emplacement case. For the vertical cases, the source location is taken to be a 4-m interval with its top 4 m below "Repository base" (the vertical containers are in boreholes below the drift floors). For the in-drift cases, the source location is taken to be a 2-m interval with "Repository base" at its base (the in-drift containers sit on the floor of the drift). The choice of distances that are multiples of 2 m is strictly for convenience: the computational meshes have 2-m cells in the vicinity of the source. The water-table elevations shown in Figure 14-5 are for present conditions. In the simulations, water-table elevation for dry-climate periods can vary from the elevation shown in the figure to 10 m higher, and water-table elevation for wet-climate periods varies from 50 m higher than in the figure to 120 m higher (see Chapter 8). During wet-climate periods, the water table may rise above the zeolitic unit in Columns 3, 4, 5, and 8.

The one-dimensional saturated-zone flow tubes are shown in Figures 14-6 and 14-7 for 57-kW/acre cases and 114-kW/acre cases, respectively. Each flow tube is associated with one of the unsaturated-zone columns, with releases from the bottom of the UZ column being transported through the SZ flow tube. As shown in the figures, transport through Columns

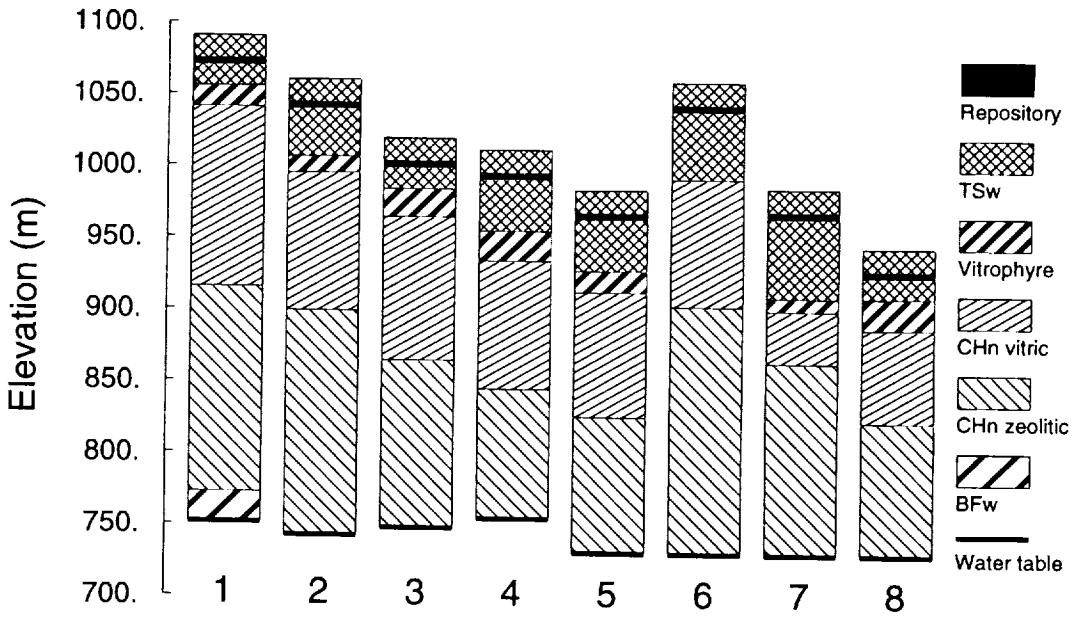

Figure 14-5. Column stratigraphies for the composite-porosity calculations. Repository location assumes vertically emplaced containers.

1, 2, and 6 is calculated using the Bullfrog velocity distribution, and transport through the rest of the columns is calculated using the Calico Hills/Prow Pass velocity distribution (see Section 11.6.1). Releases from the UZ are spread out over a source region that is approximately the width of the UZ column, and the distance from the source region to the accessible environment varies for different columns. The widths and distances are given in Table 14-4.

Table 14-4. Flow-tube dimensions (in m) for saturated-zone transport.

Flow tube (57 kW/acre)	Distance to accessible environment	Source-region width	Flow tube (114 kW/acre)	Distance to accessible environment	Source-region width
1	5550	1050	1	5000	1000
2	5550	500	2	5000	500
3	6050	1000	3	5000	1000
4	6400	750	4	5500	550
5	5500	600	5	5000	500
6	5000	550			
7	5000	750			
8	5000	750			

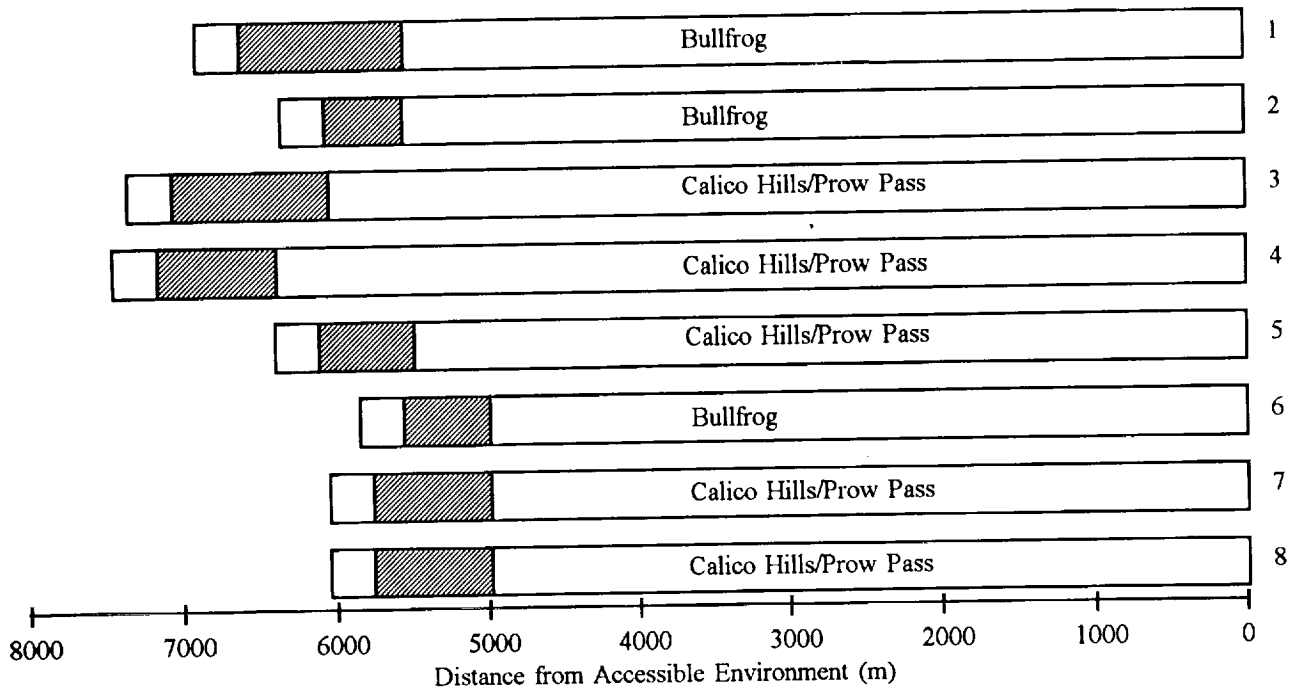

Figure 14-6. Saturated-zone flow tubes for 57-kW/acre cases. Unsaturated-zone releases are injected in the cross-hatched regions.

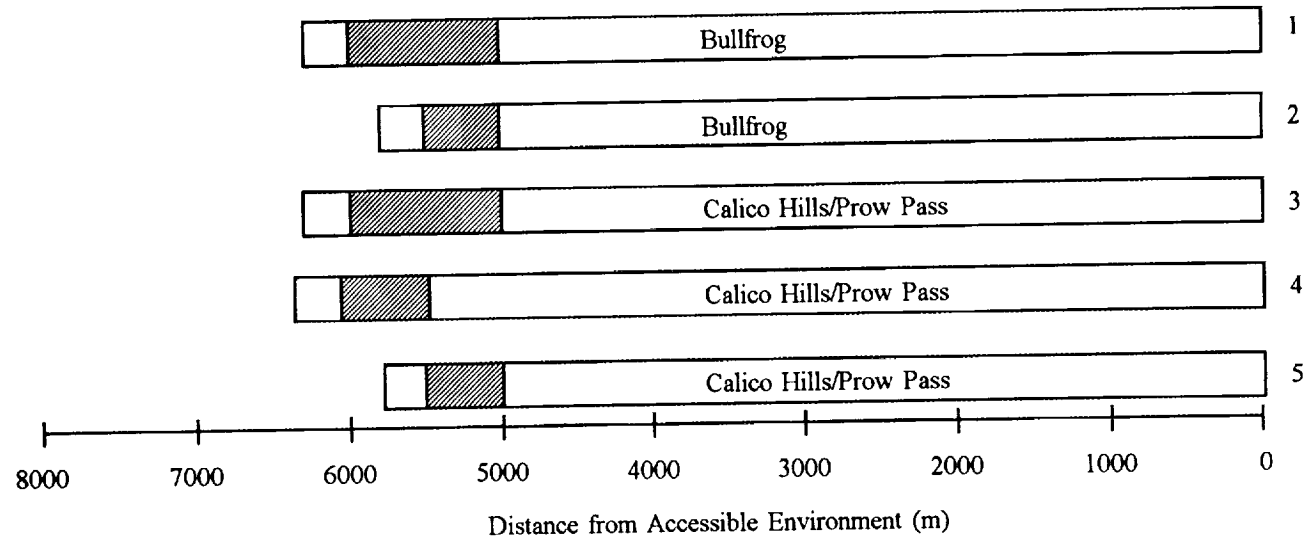

Figure 14-7. Saturated-zone flow tubes for 114-kW/acre cases. Unsaturated-zone releases are injected in the cross-hatched regions.

14.5.2 Dryout fraction and shedding volume

As was mentioned above, for the gaseous-release composite-porosity calculations, the repository is not subdivided into columns. Thus, the overall dryout-fraction and dryout-volume curves can be used (see Figures 10-10, 10-11, 10-13, and 10-14). For the aqueous-release calculations, though, we need those quantities defined individually for each column; an interior column like Column 3 (see Figure 6-8) is expected to have quite different dryout behavior than an edge column like Column 8. Note that all composite-porosity-model calculations use dryout fraction and dryout volume calculated using the "analytical model" of Chapter 10; the "axisymmetric hydrothermal model" results are not used.

To calculate the dryout quantities for individual columns, the same procedure is used as described in Section 10.3.2.2.2, but with attention restricted to the containers in a given column rather than looking at all containers. The resulting dryout-fraction curves are shown in Figures 14-8 through 14-11. Some points of interest are:

- Column 3 dries out significantly more than the other columns, and stays dry longer.
- The columns in the southern part of the repository (especially Columns 1 and 6) dry out somewhat earlier than the other columns, and also rewet earlier. This behavior results from the assumption that emplacement of waste begins in the south.
- All five columns are almost completely dry for nearly a thousand years when thermal loading is 114 kW/acre. None of the columns dries out completely when thermal loading is 57 kW/acre, and some of them never even get above 50%. Recall that "dry," for purposes of calculating the dryout fraction, is defined to mean that temperature is 96°C or higher 5 m above waste-package center.

Dryout volume is not calculated for the individual columns using the procedures in Section 10.3.2.3.2. Recall, though, that the dryout volume is used to estimate the amount of displaced water that could be shed onto the cooler parts of the repository. Thus, the dryout volume within a column's boundaries is not really the desired quantity, because water could be shed from one column onto another. What is desired is an estimate of the volume of water shed on each column.

To get effective shedding volumes for the individual columns, we assume that, when shedding takes place, the shedding flux is distributed uniformly over the available repository area (the part of the repository outside the dryout fraction). Thus, the total dryout volume is apportioned to the individual columns in proportion to their available area.

In the 57-kW/acre thermal calculations detailed in Chapter 10, the boiling isotherms for the two parts of the repository (Columns 1 through 5 and Columns 6 through 8) never

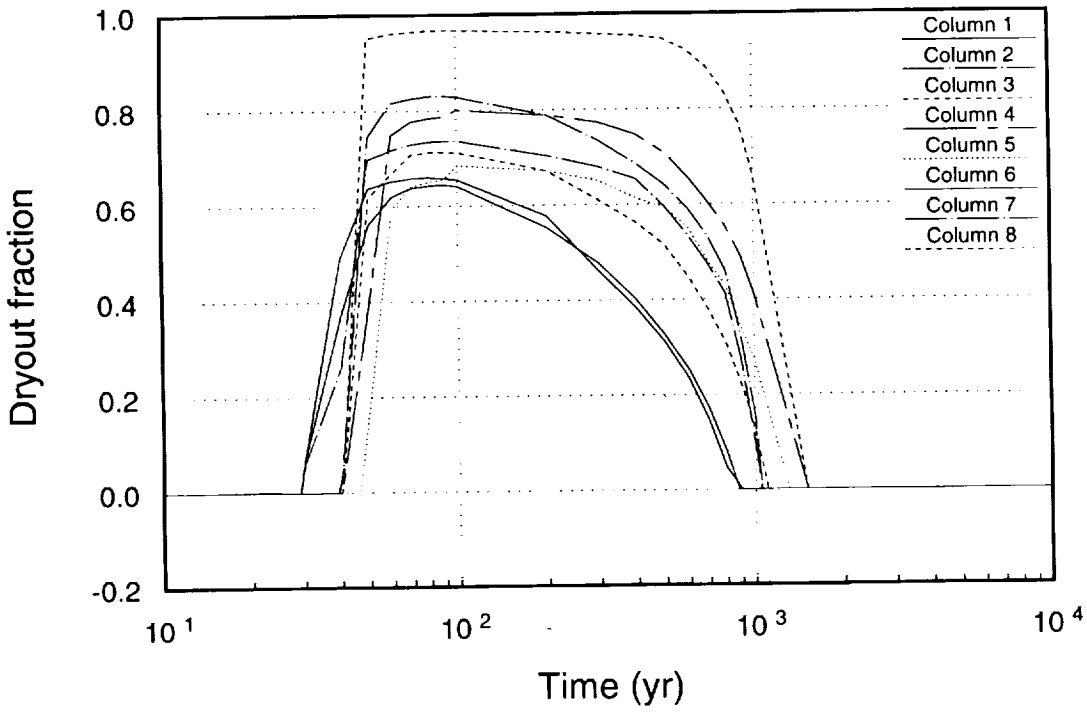

Figure 14-8. Dryout-fraction curves for 57 kW/acre, vertical emplacement.

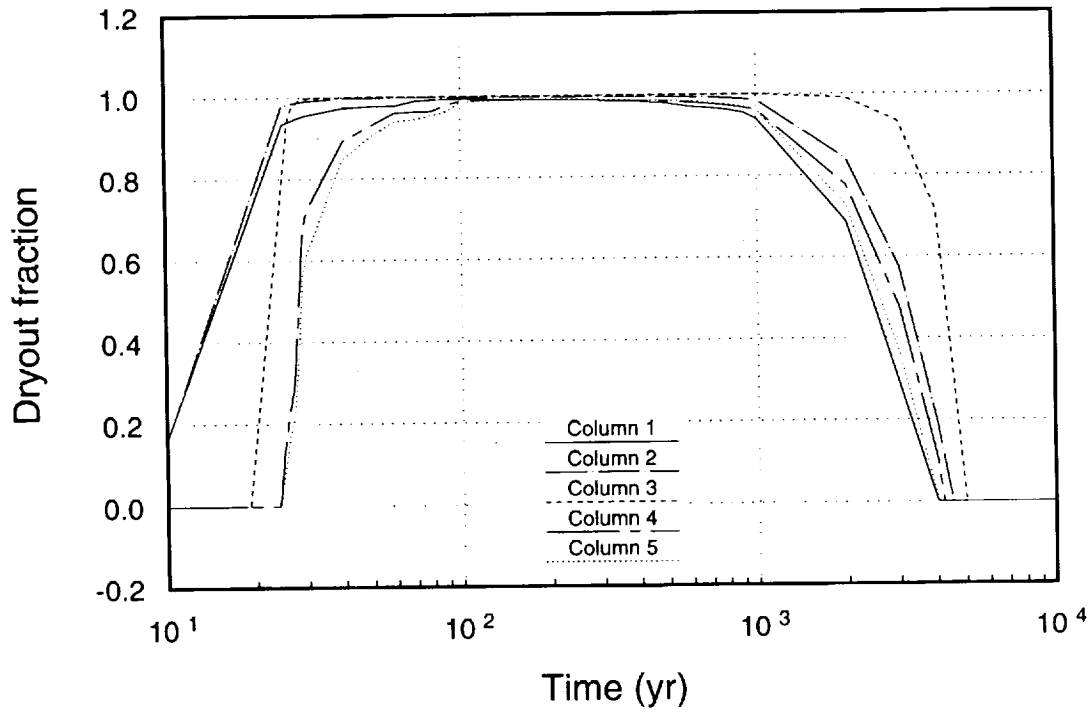

Figure 14-9. Dryout-fraction curves for 114 kW/acre, vertical emplacement.

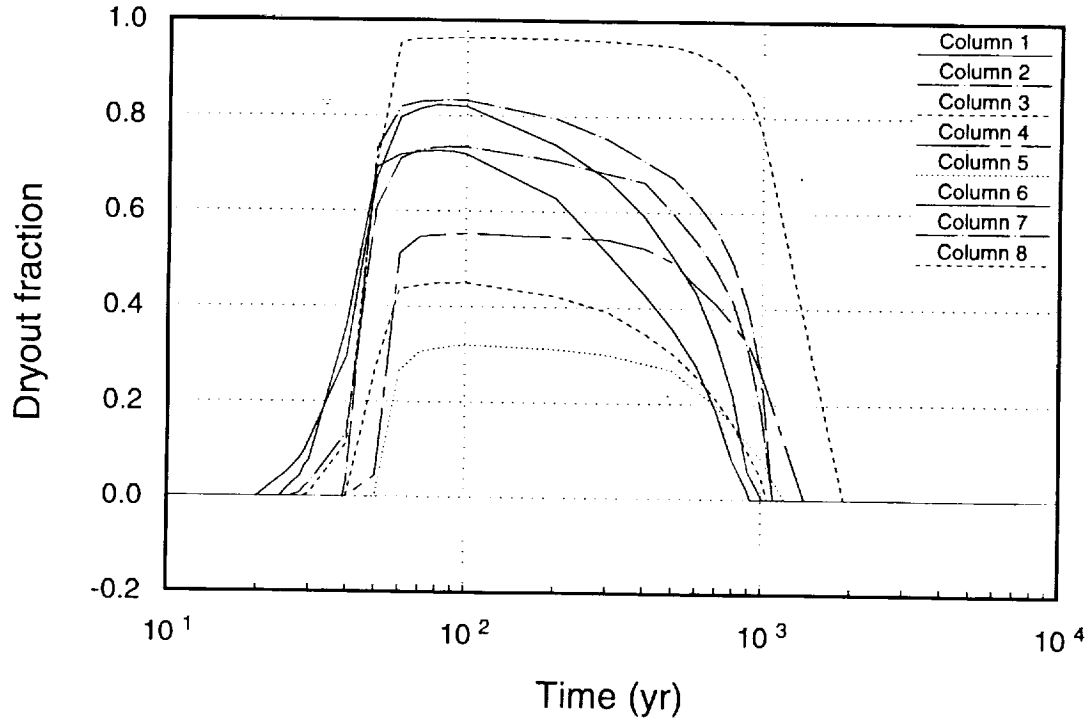

Figure 14-10. Dryout-fraction curves for 57 kW/acre, in-drift emplacement.

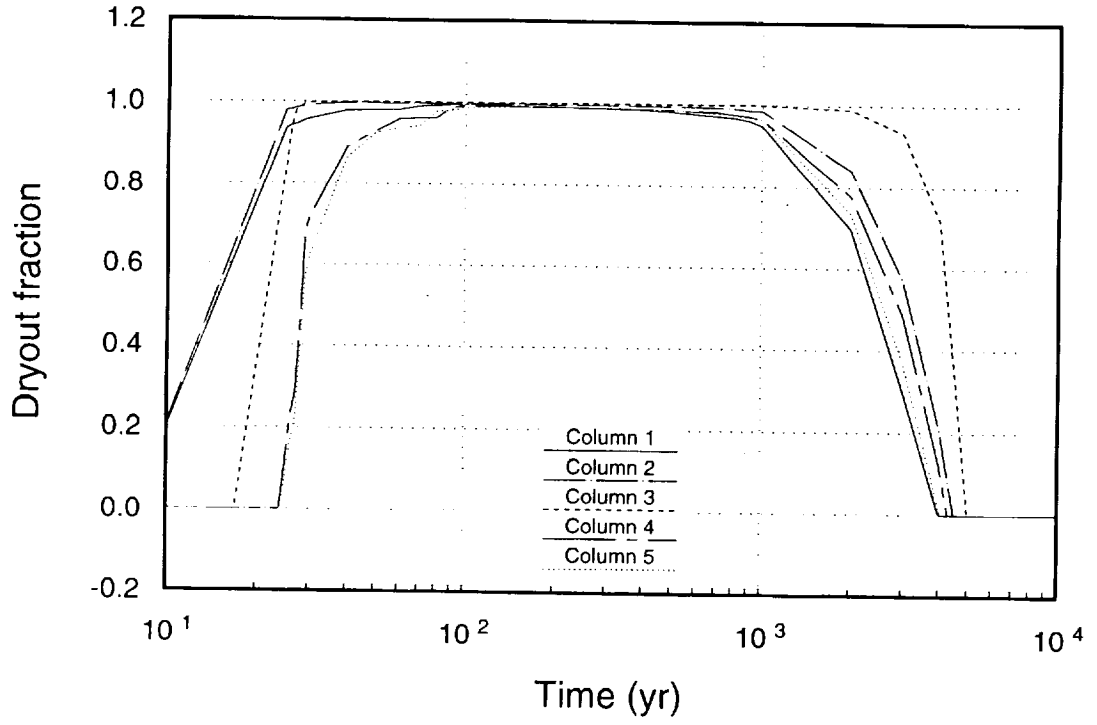

Figure 14-11. Dryout-fraction curves for 114 kW/acre, in-drift emplacement.

merge, so we calculate shedding volumes for the two parts separately, on the assumption that water from one side of the main drifts will not be shed onto waste packages on the other side of the main drifts.

At a given time, the total available area for the two parts of the repository is given by

$$A_u = \sum_{i=1}^{5} A_i(1 - f_{di}) \ , \tag{14.15}$$

$$A_\ell = \sum_{i=6}^{8} A_i(1 - f_{di}) \ , \tag{14.16}$$

where A_i is the area of Column i and f_{di} is the dryout fraction for Column i. A_u is the available area for the upper part of the repository (Columns 1 through 5) and A_ℓ is the available area for the lower part of the repository (Columns 6 through 8). For a 114-kW/acre case, there is only the upper part. If the two dryout volumes at the given time are V_u and V_ℓ, then the individual-column shedding volumes are given by

$$V_i = V_u \frac{A_i(1 - f_{di})}{A_u} \ , \tag{14.17}$$

for Columns 1 through 5, and

$$V_i = V_\ell \frac{A_i(1 - f_{di})}{A_\ell} \ , \tag{14.18}$$

for Columns 6 through 8.

Note that the shedding volume for an individual column is not the actual volume of water shed on the column. The rate of shedding is calculated by taking the difference in shedding volume from one time step to the next, multiplying by moisture content, and dividing by the time increment, as in Equation 10.1.

Shedding-volume curves for all columns and all cases, calculated as just outlined, are presented in Figures 14-12 through 14-15. Note that the vertical scales for 57 kW/acre and 114 kW/acre are different. Points of interest are:

- The highest curves represent the wettest columns. They are the columns that have the greatest amount of available area (i.e., the lowest dryout fraction). Column 1 is the wettest in most cases, and Column 3 is the driest in all cases.

- The "blips" in some of the curves result from the relative time histories of the dryout fractions for the columns. It is doubtful that the blips represent any real behavior; they are most likely artifacts of the way the individual-column shedding volumes are calculated. In the future the method should be improved, but the blips probably do not have a significant effect on the final results.

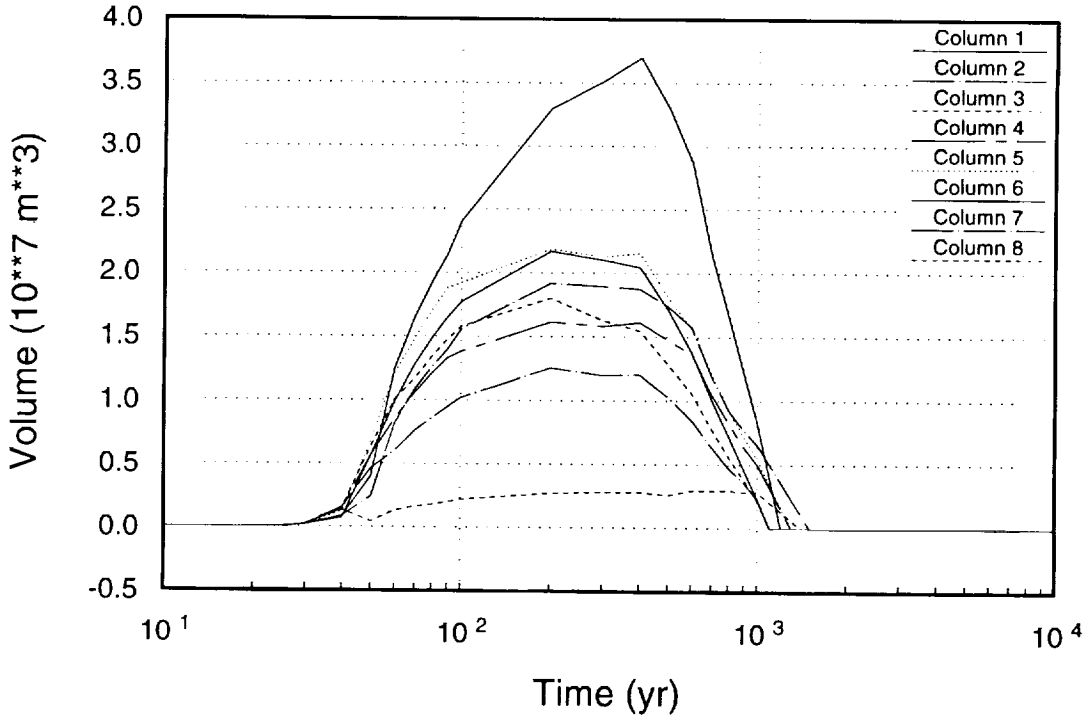

Figure 14-12. Shedding-volume curves for 57 kW/acre, vertical emplacement.

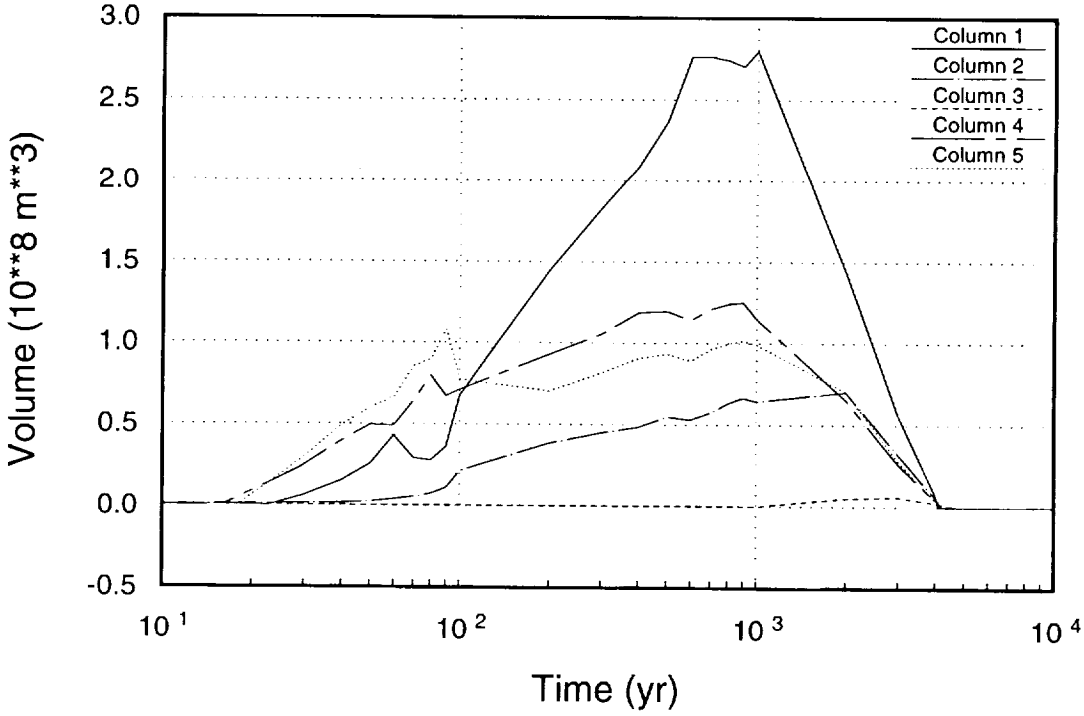

Figure 14-13. Shedding-volume curves for 114 kW/acre, vertical emplacement.

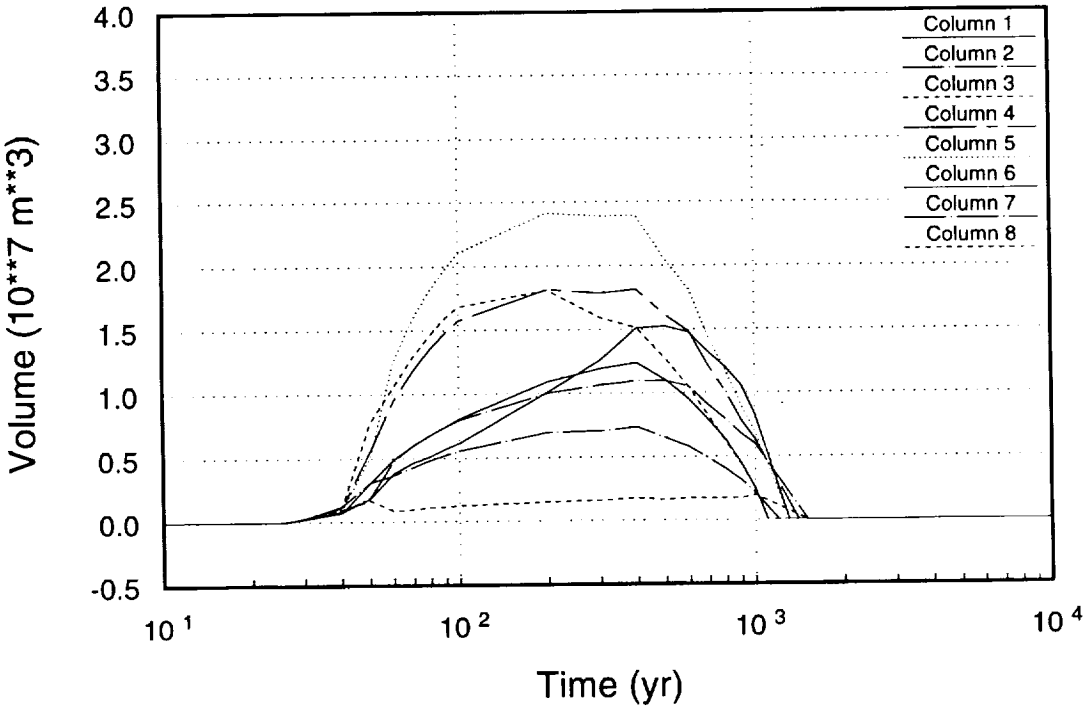

Figure 14-14. Shedding-volume curves for 57 kW/acre, in-drift emplacement.

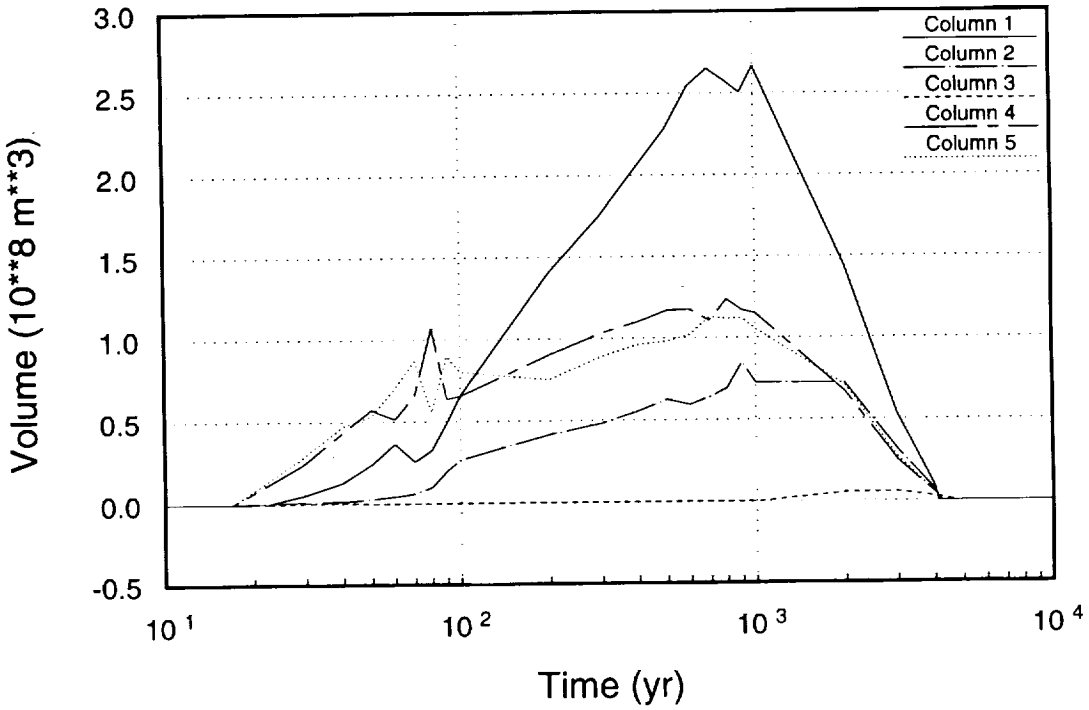

Figure 14-15. Shedding-volume curves for 114 kW/acre, in-drift emplacement.

14.5.3 Inputs for YMIM

This subsection lists all source-related parameters, including ones for YMIM and ones that are used for preliminary calculations to generate input for YMIM. Parameters such as q_0 and υ (see Section 14.4.3) are not used directly by YMIM, but are used by TOSPAC or SRCTSA to generate fluxes and episodities that are then used by YMIM.

As discussed in Section 5.4, seven radionuclides (^{239}Pu, ^{237}Np, ^{234}U, ^{231}Pa, ^{129}I, ^{99}Tc, and ^{79}Se) are included in the aqueous-release calculations, and one (^{14}C) is included in the gaseous-release calculations (we assume that ^{14}C is transported in the gaseous phase, as $^{14}CO_2$, because the gaseous transport time is much less than the aqueous transport time). TSPA-91 results and many preliminary calculations for TSPA-93 have shown that the highly retarded nuclides do not make a significant contribution either to 10,000-year cumulative EPA releases or to drinking-water doses over one million years. (This conclusion is not general, and must be revisited when additional processes, such as colloid formation and transport or reduced matrix/fracture coupling are considered.) We continue to include ^{239}Pu in our aqueous-release calculations as a check, to see if significant quantities of it are released in a simulation. Other isotopes of uranium (notably ^{235}U) could be included, but their releases are much lower than releases of ^{234}U, and nothing new would be learned by their inclusion.

Basic radionuclide properties, inventories, and solubilities are summarized in Table 14-5. As shown, most of the information may be found in Chapters 5 and 9. The only new items of information presented in the table are the specific activities, the solubilities used for the high-solubility elements, and solubility partitioning factors for the isotopes used. Specific activities were calculated from the molar activities listed in Table 5-2 by multiplying by molecular weight. We did not attempt to determine true solubility values for iodine, technetium, and selenium, but simply adopted the arbitrary value 1 mol/ℓ for their solubilities. The particular value does not matter as long as it is high enough that release of those elements is alteration-rate-limited rather than solubility-limited. Note that the uranium and neptunium solubilities are assumed to be correlated, with an 80% rank correlation (see Section 9.2.3). These rank correlations and ones to be mentioned in following discussion are used as input to the LHS program. In addition to probability distributions for input parameters, a rank correlation matrix can be defined, so that known correlations among parameters can be preserved during the sampling process.

The solubility partitioning factor is the factor by which elemental solubility is multiplied to obtain effective solubility for a particular isotope. For example, most of the uranium is in the form of ^{238}U, and the amount of ^{234}U in solution is proportional to its abundance relative to ^{238}U. The partitioning factor varies with time, as different isotopes decay at dif-

Table 14-5. Summary of radionuclide properties.

Species	Half-life (yr) (Table 5-2)	EPA limit (Ci/MTU) (Table 5-2)	Specific activity (Ci/g)	Initial inventory (Ci/MTU) (Table 5-12)	Elemental solubility (mol/ℓ)	Solubility partitioning factor
^{239}Pu	2.406×10^4	0.1	6.22×10^{-2}	3.04×10^2	Table 9-2	0.77
^{237}Np	2.140×10^6	0.1	7.06×10^{-4}	1.21	Table 9-2	1.
^{234}U	2.445×10^5	0.1	6.26×10^{-3}	2.19	Table 9-2	4.1×10^{-4}
^{231}Pa	7.038×10^{8}*	0.1	4.73×10^{-2}	3.10×10^{-2}	Table 9-2	1.
^{129}I	1.570×10^7	0.1	1.77×10^{-4}	3.05×10^{-2}	1.	1.
^{99}Tc	2.130×10^5	10.	1.70×10^{-2}	1.35×10^1	1.	1.
^{79}Se	6.496×10^4	1.	6.98×10^{-2}	4.26×10^{-1}	1.	1.
^{14}C	5.729×10^3	0.1	4.46	9.09×10^{-1}	N/A	N/A

*Value listed is for ^{235}U. See text.

ferent rates. Because we are not carrying all isotopes in our transport calculations (and even if we were, YMIM does not at present include capabilities for chain decay or partitioning of solubility among isotopes), the partitioning factor must be approximated. We approximate it by taking the largest value attained over the time period of interest. To estimate the maximum ^{234}U partitioning factor, the abundances of all significant isotopes of uranium were taken from the Characteristics Data Base (DOE, 1992) for 20 yr, 10^4 yr, 10^5 yr, and 10^6 yr. The fraction of the total uranium in ^{234}U at each time was determined, and the greatest one (at 10^4 yr for this example) was used for the partitioning factor. A similar procedure was followed for ^{239}Pu; none of the other nuclides has significant competing isotopes.

The half-life listed for ^{231}Pa in Table 14-5 is really the half-life of ^{235}U. As explained in Section 5.4, ^{231}Pa is treated as though it is in secular equilibrium with ^{235}U, so that its inventory changes according to ^{235}U's half-life.

The solubility parameters for ^{14}C are listed as N/A (not applicable) in the table because YMIM does not use solubilities in calculating releases of gaseous nuclides. ^{14}C is always released at the rate at which it is mobilized by alteration of the fuel.

In Table 14-5, the most important difference from TSPA-91 is the neptunium solubility. The assumed neptunium solubility is approximately five orders of magnitude higher than that assumed for TSPA-91 (see Figure 14-16). The difference apparently is related to assumptions about oxidizing vs. reducing chemistry (see Section 9.2.2.7).

Source parameters relating to temperature and container wetting are summarized in Table 14-6. It should be noted that there is an inconsistency between the release calculations and the thermal calculations described in Chapter 10. The thermal calculations assume that

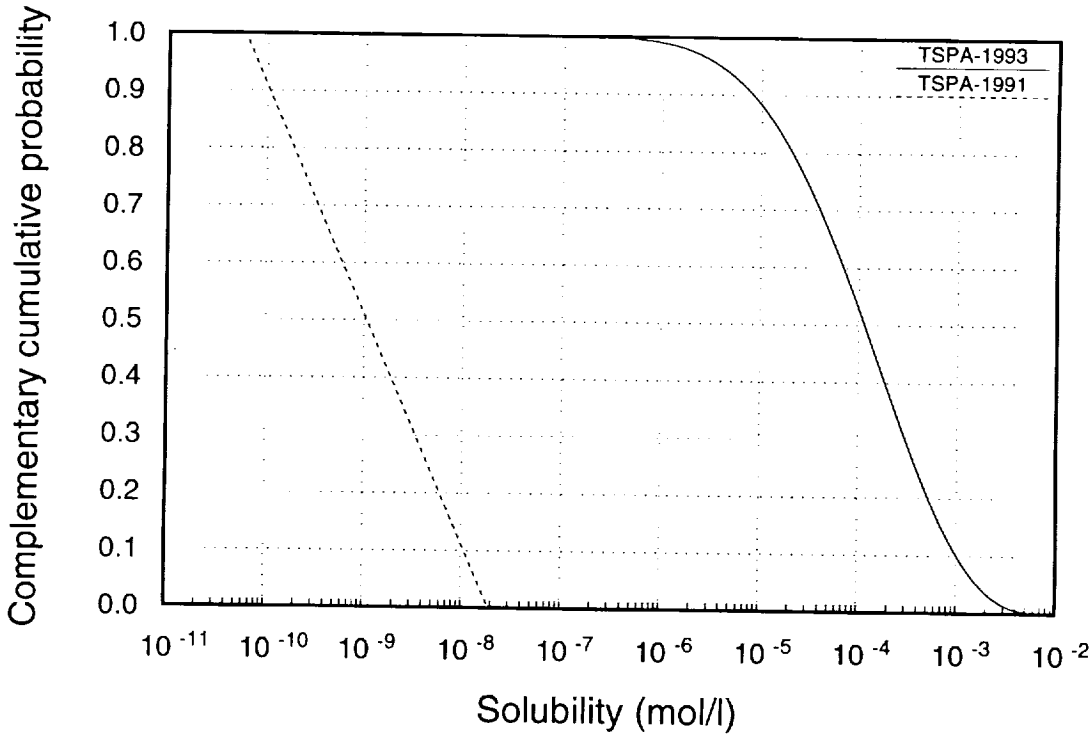

Figure 14-16. Neptunium-solubility distributions for TSPA-91 and TSPA-93.

waste is emplaced over a 25-yr period, starting at the southern end of the repository and proceeding north. The release calculations do not include that level of detail; they assume that all waste is emplaced at time 0. Thus, the temperature and dryout parameters are inconsistent with the release calculation for the first 25 years. This inconsistency has no significant effect on the results.

The flux coefficient of variation (υ) is unchanged from TSPA-91, and we still have no information on what its value might be. Aside from υ, almost everything in Table 14-6 is a significant change from TSPA-91. The only way that thermal effects entered into the TSPA-91 calculations was by the inclusion of a dryout period that lasted from 300 to 1300 years. In terms of performance, the most important changes seem to be in percolation flux and fracture-flow threshold. These changes and their effects are discussed in Sections 8.9 and 14.4.3.

The moisture content used to calculate the shedding flux (Equation 10.1) is calculated self-consistently within TOSPAC for the aqueous-release simulations, but water flow is not calculated within the gaseous-release simulations so moisture content must be specified directly. For simplicity, we set the moisture content equal to the matrix porosity in the gaseous-release simulations (i.e., we assume a liquid saturation of 1 in calculating the shed-

Table 14-6. Summary of hydrothermal parameters.

Model parameter	Distribution or value
"Edge" container temperature	see Sections 10.3.2.4.1 and 14.4.2
"Center" container temperature	see Sections 10.3.2.4.1 and 14.4.2
"Edge" fuel temperature	see Sections 10.3.2.4.2 and 14.4.2
"Center" fuel temperature	see Sections 10.3.2.4.2 and 14.4.2
Dryout fraction	see Sections 10.3.2.2.2 and 14.5.2
Shedding volume	see Sections 10.3.2.3.2 and 14.5.2
Moisture content	
aqueous-release simulations	calculated by TOSPAC
gaseous-release simulations	TSw matrix porosity (Table 7-3, unit 3R)
Percolation flux	see Section 8.9
Flux coefficient of variation	1.3
Fracture-flow threshold	see Table 7-5, unit 3R
Fraction of containers with rubble	
vertical emplacement	uniform from 0 to 1
in-drift emplacement	1
Flow episodity	see Section 14.4.3
Moisture episodity	see Section 14.4.3
Water-collection area	
vertical emplacement	log-uniform from 0.13 to 1.3 m^2
in-drift emplacement	log-uniform from 2.7 to 27 m^2

ding flux). This approximation should be conservative, as it maximizes the amount of shed water.

The fraction of containers contacted by rubble (f_r) is different for vertical or in-drift containers because in-drift-emplaced containers are always contacted by backfill, whereas borehole-emplaced containers may be protected from contact with moist rock by the borehole airgap. We have not investigated borehole stability and the probability of rubble infill, though the Electric Power Research Institute, in its performance assessments, has considered the subject (McGuire *et al.*, 1990, 1992). In TSPA-91 we simply took $f_r = \frac{1}{2}$; this time we represent the potential range of values by taking a uniform distribution. The difference in assumptions about f_r for vertical and in-drift containers has important consequences in our model predictions of container wetting and failure. This subject will be discussed further in the Results section.

Water-collection area (A_{cross}) is another parameter that is different for vertical and in-drift containers. A_{cross} is used to calculate the amount of water flowing through a container by multiplying it by the flux q_s (see Section 14.4.3). We have no real idea what the effective water-collection area should be. Water could tend to avoid the excavated, backfilled tunnels or it could be focused by the stress-relief fractures. The subject has not been studied in detail, so we are forced to make assumptions about it. In TSPA-91, we arbitrarily used 2 m^2 for the water-collection area. For this TSPA, we tied the value of A_{cross} to the horizontal cross-

sectional area of the waste containers. We use a log-uniform distribution with a one-order-of-magnitude range, centered on the physical container cross-sectional area. The uncertainty in this parameter is probably greater than one order of magnitude, but by including this distribution, at least we obtain information about sensitivity of the results to the parameter.

Source parameters giving physical dimensions of containers and fuel rods, numbers of containers, and geochemistry are summarized in Table 14-7. Except for the number of containers, none of these quantities was used in TSPA-91.

The only items in Table 14-7 that require some explanation are fuel-rod mass and number of fuel rods per container. Data on fuel assemblies are given in Section 5.1.2. There, it is shown that the average fuel-rod mass for PWR fuel assemblies is 1.87×10^{-3} MTU/rod and the average for BWR fuel assemblies is 2.99×10^{-3}. Table 5-1 shows that the spent fuel for the repository is expected to be 64.7% PWR and 35.3% BWR (in terms of MTU). Weigthing the above fuel-rod masses by those fractions gives 2.27×10^{-3} MTU/rod for the overall average, or 2270 g/rod. Next, 63,000 MTU of spent fuel divided by 32,022 containers for vertical emplacement gives 1.97 MTU/container. Dividing by 2.27×10^{-3} MTU/rod then gives 867 rods/container. For in-drift emplacement there are 7640 containers, leading to 8.25 MTU/container and 3630 rods/container.

Source parameters relating to container and fuel-rod failure are summarized in Table 14-8. There was no analog to any of these parameters in TSPA-91, which used a single parameter to represent container lifetime.

As stated in Section 13.2.4.2, defective, or juvenile, container failures are assumed to be exponentially distributed in time. The failure rate used implies a mean time-to-fail of

Table 14-7. Summary of physical dimensions and geochemistry.

Model parameter	Distribution or value
Fuel-rod cross-sectional area	9.7×10^{-5} m^2 (see Table 13-8)
Fuel-rod length	3.71 m (see Table 13-8)
Fuel-rod mass	2270 g
Number fuel rods per container	
vertical emplacement	867
in-drift emplacement	3630
Alloy-825 wall thickness	9.5 mm (see Section 13.2.4.1)
Mild-steel wall thickness (in-drift emplacement only)	100 mm (see Section 13.2.4.1)
Number of container groups	10 (see Section 14.4.2)
Number of containers	see Table 14-3-
pH	uniform distribution (see Table 13-2)
Carbonate concentration	uniform distribution (see Table 13-2)
Fluorine concentration	2.8 ppm (see Table 13-2)

Table 14-8. Summary of parameters for container and fuel-rod failure.

Model parameter	Distribution or value
Defective-container fraction	
vertical emplacement	uniform from 0.1% to 0.5%
in-drift emplacement	uniform from 0.05% to 0.25%
Defective-failure rate	0.00333/yr
Creep-failure fraction of rods	0 (see Section 14.4.1)
Creep-failure temperature	N/A (see Section 14.4.1)
Hydride-failure fraction	1 (see Section 14.4.1)
Hydride-failure period	1 yr (see Section 14.4.1)
Hydride-failure temperature	N/A (see Section 14.4.1)
Fluorine-failure period	N/A (see Section 14.4.1)
Alloy 825	
dry-oxidation rate	see Table 13-3
pit increment in mm (70°C)	log-beta distribution:* −3.523, 0.477, −1.523, 0.606
pit increment in mm (100°C)	log-beta distribution:* −1.523, 2.477, 0.477, 0.606
pit growths/yr	0.033 (see Table 13-6)
number of pits modeled	500
Mild steel (in-drift emplacement only)	
dry-oxidation rate	see Table 13-3
aqueous-corrosion rate	see Table 13-4
pitting factor	1 (see Section 14.4.1)

*Parameters for the log-beta distribution are minimum, maximum, mean, standard deviation (in log space).

300 yr for the defective containers; 300 yr is an arbitrary small time period. The range chosen for the fraction of containers that is defective is also quite subjective. Note that the defective fraction for the single-walled vertical containers is chosen to be twice as large as the defective fraction for the double-walled in-drift containers. The ratio is subjective, but two walls should provide more protection against defects than one wall.

The distributions shown for the pitting-increment parameters are based on the information in Table 13-6. The distributions are intended to be log-normal-type distributions, with the 5, 50, and 95 percentiles given. The log-beta distributions listed in Table 14-8 reproduce those percentiles. A rank correlation of 0.99 was assumed between the two pitting-increment parameters, so that the 100°C increment would always be approximately 100 times the 70°C increment, as desired.

The number of pits modeled is fairly arbitrary, but it is based on estimates of the number of growing pits on a container. As discussed in Section 13.2.4.1, the modeled time of container failure is not sensitive to the number of pits used.

Finally, parameters relating to UO_2 dissolution and oxidation and pulse releases are summarized in Table 14-9. The dissolution and oxidation parameters go into a model for fuel-matrix alteration. In TSPA-91, fuel-matrix alteration was represented by a single parameter,

Table 14-9. Summary of parameters for UO_2 alteration and pulse releases.

Model parameter	Distribution or value
UO_2 dissolution parameters	see Table 13-10
UO_2 oxidation time	see Table 13-9
Volumetric expansion factor	0.33 (see Table 13-8)
Pulse fraction for ^{129}I, ^{99}Tc, ^{79}Se	15%
Pulse fraction for ^{14}C	1.2%
Rod-surface inventory for ^{14}C	9.80×10^{-5} g/m^2

the alteration rate. We have not made a comparison of the calculated TSPA-93 alteration rates with the assumed TSPA-91 alteration rates, but they seem to be comparable in effect. In both TSPAs the fuel matrix was usually altered completely within a few thousand years after container failure.

The pulse-release fractions were chosen to be the same as were used in TSPA-91, though they do not look the same in the table. YMIM contains a simple model to calculate the fraction of the spent fuel that is wetted, and the specified pulse releases (15%) are reduced by that fraction. The wetted-area calculation is based on the following conceptual model (see also Section 13.2.6): After exposure to oxygen (i.e., after container failure and fuel-rod failure), the UO_2 expands volumetrically, splitting the cladding and exposing a portion of the fuel. With the assumed fuel-rod dimensions (radius 0.546 mm, length 3.71 m) and volumetric expansion (33%), the exposed fraction is calculated to be 13.3%. Thus, for aqueous releases, the actual pulse release is $0.133 \times 15\% \simeq 2\%$, which is the same as was used in TSPA-91. YMIM does not make this same reduction for gaseous releases, so it is not necessary to apply the exposure fraction to the ^{14}C pulse fraction. The pulse-release fraction is less than 2% for ^{14}C, as it was in TSPA-91, because we assume that the pulse release is 2% of the fraction of ^{14}C in the fuel matrix, but a substantial fraction of the ^{14}C is outside of the matrix. From Van Konynenburg (1991), the fraction of ^{14}C in the fuel matrix is 0.58/1.01 = 57% (assuming 65% PWR and 35% BWR spent fuel). Thus, the ^{14}C pulse-release fraction is only 1.2%.

In TSPA-91, the ^{14}C quick-release fraction was varied between 0.5% and 5%. (As we are using the terms here, the pulse-release fraction comes from the pellet/cladding gap and the grain boundaries within the fuel matrix; the quick-release fraction comes from the outside surface of the fuel-rod cladding.) Currently, this parameter is not allowed to vary, so the mean of the old distribution (2.75%) is used. With the fuel-rod dimensions given above, the fuel-rod area is 0.13 m^2. If 2.75% of the ^{14}C inventory is spread out over the fuel-rod surface, the rod-surface inventory comes out to 9.8×10^{-5} g/m^2, as listed in the table.

14.5.4 Inputs for TOSPAC

The TOSPAC input for a composite-porosity-model simulation has three parts: unsaturated-zone-flow input, saturated-zone-flow input, and transport input. (In addition, many of the source-term parameters are input to TOSPAC and then passed on to YMIM.) The unsaturated-zone part of the calculation is much more detailed and complicated than the saturated-zone part, because the unsaturated zone is considered to be the primary barrier. Saturated-zone flow is handled quite differently from unsaturated-zone flow; the flow is not calculated by TOSPAC, but simply taken from detailed calculations (Chapter 11). See Section 11.6 for a description of how the abstraction is done.

The first ingredient of the setup for a TOSPAC unsaturated-zone calculation is definition of the locations of the one-dimensional columns and the stratigraphic representation of each column. These are presented in Sections 6.5.1 and 14.5.1.

Unsaturated-zone-flow parameters are summarized in Table 14-10. The detailed data are primarily in Chapter 7. Only a subset of the information in Chapter 7 is used. Typically, the tables there list values for 10 hydrogeologic units (sometimes 11, with two values listed for the Topopah Spring unit). Our base-case stratigraphy (Figure 14-5) includes only five of the units (only four units in most of the columns). The units used are

- unit 3 or 3R, Topopah Spring welded unit, abbreviated TSw;
- unit 4, Topopah Spring vitrophyre;
- unit 5, Calico Hills/Prow Pass nonwelded-vitric, abbreviated CHnv;
- unit 6, Calico Hills/Prow Pass nonwelded-zeolitic, abbreviated CHnz; and
- unit 8, Bullfrog welded, abbreviated BFw.

The footnotes to Table 14-10 indicate that a few of the distributions are modified slightly from those presented in Chapter 7. The reason is pragmatic—the LHS sampling program does not accept a beta distribution with α or β parameter less than $\frac{1}{2}$ (such distributions diverge rather strongly at one of the end points). By reducing the stated coefficient of variation (CV) slightly to 1, a distribution is obtained that is acceptable to LHS. The existence of these strong divergences may be an indication that it would be better to represent these distributions in log space.

The only other item in the table that needs explanation is the distribution for the fracture van Genuchten saturation/desaturation parameter β_{vG}. This parameter is not discussed in Chapter 7 because we know of no data on which to base a distribution; we are forced to

Table 14-10. Summary of parameters for unsaturated-zone flow.

Model parameter	Distribution or value
Water density	1000 kg/m^3
Water compressibility	4.3×10^{-6} m^{-1}
Bulk-rock compressibility	0
Matrix porosity	see Table 7-3
Matrix full saturation	1
Matrix residual saturation	see Table 7-8*
Matrix van Genuchten α_{vG}	see Table 7-6
Matrix van Genuchten β_{vG}	see Table 7-7
Matrix saturated conductivity	see Table 7-5
Fracture compressibility	0
Fracture porosity	see Table 7-19
Fracture full saturation	1
Fracture residual saturation	0
Fracture van Genuchten α_{vG}	see Table 7-21†
Fracture van Genuchten β_{vG}	uniform from 1.8 to 4.23
Fracture saturated conductivity	see Table 7-20
Percolation flux	see Section 8.9
Climate-change times	see Table 8-1
Water-table rise above nominal	see Table 8-1
Water-table pressure head	0 m

*Distributions for unit 4 (vitrophyre) and unit 8 (BFw) modified by setting coefficient of variation to 1.
†Distribution for unit 5 (CHnv) modified by setting coefficient of variation to 1.

estimate the distribution using models and analogs. The choice of uniform for the distribution type is made simply because we have no information to warrant doing otherwise (a uniform distribution maximizes the uncertainty).

The lower bound is based on a model for fracture saturation/desaturation developed by Wang and Narasimhan (1985). They represent the distribution of fracture apertures in a rough fracture by a gamma distribution and calculate the relative conductivity by integrating the cubic law over the aperture distribution, with a cutoff aperture depending on saturation. They develop an analytical formula for fracture conductivity that approaches $K \propto |\psi|^{-4}$ asymptotically for large negative pressure head. (See, for example, in their Figure 7, the two curves labelled "without phase-separation constriction factor." The curves "with phase-separation constriction factor" approach vertical slopes asymptotically.) The relative-conductivity formula used in the TOSPAC flow calculations (see Equation 2.1-21 in Dudley *et al.*, 1988) asymptotically approaches $K \propto |\psi|^{-(5\beta_{vG}-1)/2}$ for large $|\psi|$. Thus, asymptotically, Wang and Narasimhan's formula behaves as though $\beta_{vG} = \frac{9}{5} = 1.8$. This asymptotic value is used for the lower limit because almost all other estimates of β_{vG} are

higher than 1.8 and, if β_{vG} is much lower, the saturation/desaturation is spread out over an inordinate range of pressure heads.

The upper bound of the β_{vG} distribution is a value that was used extensively in past years (see, for example, Dudley *et al.*, 1988, Table 2.1-2), which was based on analogy of fracture saturation/desaturation to that of a coarse sand. The choice of 4.23 for the upper bound has the additional advantage that it makes the mean of the distribution approximately 3. Fits of the fracture-saturation curves of Wang and Narasimhan with van Genuchten parameters tend to give values of about 3 for β_{vG}.

As discussed in Section 7.5, a study was made of correlations between matrix porosity and matrix saturated conductivity in the data available. Rank correlation was found to be significant for only two of the five units in our simulations, TSw and CHnv. Rounding off the values in Table 7-22, we assign a rank correlation of 0.5 between matrix porosity and matrix conductivity for TSw and a rank correlation of 0.75 between matrix porosity and matrix conductivity for CHnv.

In addition, we assign subjective rank correlations to some of the fracture parameters. Based on the fracture-property model described in Section 7.4.3, we expect fracture porosity (b_f/a_f), fracture saturated conductivity ($\propto b_f^2$), and fracture air-entry parameter ($\propto b_f$) to be correlated. (In these expressions, b_f is fracture aperture and a_f is fracture spacing.) According to the model, K_s and α_{vG} both depend only on b_f, so they should be strongly correlated. We assign them a rank correlation of 0.9 for each unit. Correlation between fracture porosity and the other two is not expected to be as strong since it depends on a_f as well. We impose a rank correlation of 0.5 between fracture porosity and fracture saturated conductivity and between fracture porosity and fracture air-entry parameter. The high correlation between K_s and α_{vG} could be an artifact of the simple fracture model used (Section 7.4.3); in the future we would like to try fitting the data with a more realistic fracture-network model.

Many of the parameters in Table 14-10 have changed significantly from TSPA-91. The changes are discussed in Sections 7.6 and 8.9. Repository performance is most affected by changes in the percolation flux.

Saturated-zone-flow parameters are summarized in Table 14-11. The table is very brief because saturated-zone flow is not calculated, but is simply taken from the detailed results described in Chapter 11. The one-dimensional saturated-zone flow tubes are presented in Section 14.5.1. Differences between the saturated-zone parameters and their TSPA-91 counterparts are discussed in Section 11.6.

Transport parameters (both UZ and SZ) are summarized in Table 14-12. The correspondence between our hydrogeolic units and the rock types used to define sorption coefficients in Chapter 9 is given in Table 9-3.

For the most part, these parameters have little change from TSPA-91. The one big change is in fracture spacing, which is significantly higher for all units, but especially for TSw and the vitrophyre. The spacing this time reflects the distance between the largest fractures, whereas previously the spacing was more reflective of distance between the smallest fractures. The mean fracture spacings are used rather than including distributions because the derived distributions are poorly behaved, with very strong divergence at zero spacing. With the strong matrix/fracture coupling assumed, the fracture spacing matters little, anyway. In the future we would like to examine the issue of matrix/fracture spacing more closely, and for that examination better information on fracture spacing will be needed.

Two other changes from TSPA-91 of possible significance have to do with dispersivity. In TSPA-91, dispersivities were sampled independently for each unit; this time, a single dispersivity is sampled for matrix transport and a single one for fracture transport, and they are applied to all units. This change has the effect of making the sampled dispersivity a little

Table 14-11. Summary of parameters for saturated-zone flow.

Model parameter	Distribution or value
Water velocity	see Table 11-7
Porosity	0.2 (see Section 11.6.3)

Table 14-12. Summary of transport parameters.

Model parameter	Distribution or value
UZ transport area	see Table 14-2
SZ transport area	see Section 11.6.2
Diffusion coefficient	3.16×10^{-2} m^2/yr
Matrix tortuosity factor	10
Fracture tortuosity factor	1
UZ dispersivity	uniform from 10 to 25 m
SZ dispersivity	see Table 11-7
Fracture sorption coefficient	0
Matrix sorption coefficient	see Table 9-4
UZ bulk density	see Table 7-4
SZ bulk density	2000 kg/m^3 (see Section 11.6.3)
UZ fracture spacing	mean values from Table 7-17
SZ fracture spacing	none
Matrix/fracture coupling factor	1
Matrix velocity correlation length	0
Fracture velocity correlation length	0

more important since it applies over a larger region. The lower limit for the saturated-zone dispersivity is higher this time than in TSPA-91 (see Section 11.6.1), and the distribution type was changed from log-uniform to uniform. Both changes lead to higher dispersivities.

14.5.5 Inputs for GASTSA

Detailed discussion of the gaseous flow and transport modeling is in Chapter 12. As with saturated-zone water flow, for TSA calculations gas flow and transport are not calculated—the results of detailed calculations described in Chapter 12 are used. The method of abstraction is described in Section 12.4. A summary of the parameters for gaseous-release calculations (aside from source parameters) is given in Table 14-13. Differences from TSPA-91 are discussed in Section 12.4.

"Base" in Table 14-13 refers to the values used for the detailed calculations of gas flow and ^{14}C transport. As discussed in Section 12.4, the base ^{14}C transport times are scaled by the retardation multiplication factor and by the ratio of base permeability to welded-tuff bulk permeability.

As noted in Chapter 12, gas flow was only calculated for a thermal loading of 57 kW/acre. Since we have no other information, we use the 57-kW/acre ^{14}C transport times for all four of our cases, including the 114-kW/acre cases. This procedure probably underestimates slightly the releases to the accessible environment within 10,000 years for the 114-kW/acre cases, since gas velocities are expected to be higher for the higher thermal loading (because temperatures are higher). However, even for 57 kW/acre, the ^{14}C transport times are well below 10,000 years (see Figure 12-12), so an additional reduction is not expected to make a big difference.

Calculation of individual radiation doses is not made for gaseous releases of ^{14}C, because they are known to be negligible (Park and Pflum, 1990; Van Konynenburg, 1991). Population doses, on the other hand, may not be negligible for ^{14}C. The "EPA ratio" made by dividing the cumulative release of radioactivity over 10,000 years by the EPA's limit from

Table 14-13. Summary of parameters for gaseous flow and transport.

Model parameter	Distribution or value
Base permeability for nonwelded	10^{-12} m^2 (see Section 12.4)
Base permeability for welded tuff	10^{-11} m^2 (see Section 12.4)
Bulk permeability for welded tuff	see Table 7-13, unit 3*
Base retardation factors	see Figure 12-1
Retardation multiplication factor	see Section 12.4
^{14}C transport times (base values)	see Figure 12-12

*Values in Table 7-13 are multiplied by 1.02×10^{-7} to convert from m/s to m^2.

40 CFR 191.13 (EPA, 1985) is a surrogate for population dose, and the fact that calculated ^{14}C EPA ratios are high (see, e.g., Chapter 5 in the TSPA-91 report) is an indication that population doses for ^{14}C may be significant.

Unlike the aqueous-release calculations, the ^{14}C gaseous-release calculations are carried out only to 10,000 years. Because the half-life of ^{14}C is only 5730 yr, releases after 10,000 years are unlikely to be significant.

14.6 Results

In this section, results of the composite-porosity-model Monte Carlo simulations are presented. As discussed in Section 2.3, the results are presented in terms of two measures of repository performance: the "EPA sum," or normalized cumulative release of radioactivity to the accessible environment, and the maximum radiation-dose rate to an individual received by drinking contaminated water from the saturated zone in the accessible environment. The accessible environment is defined as in 40 CFR Part 191; for aqueous releases the accessible environment is 5 km away from the repository, and for gaseous releases (and other types of surface release such as from drilling) the accessible environment is the ground surface above the repository. Cumulative release is normalized as specified by the EPA in 40 CFR 191.13. Even though 40 CFR Part 191 no longer applies to Yucca Mountain, the EPA sum is still a useful quantity to calculate, for three reasons: (1) A new regulation for the Yucca Mountain site has not yet been specified; (2) EPA sums are a surrogate for total dose to the population, but are easier to calculate; and (3) EPA sums can be compared with those from past calculations (TSPA-91 and several others), whereas past estimates of doses are less common (Doctor *et al.*, 1992; Eslinger *et al.*, 1993).

Results are reported for three time periods: 10,000 years, 100,000 years, and 1,000,000 years. For EPA sums, the 10,000-year period is most relevant, because the EPA has only specified limits on the EPA sum for 10,000 years. For doses, the million-year period is most relevant, because the time of peak dose rate is usually greater than 100,000 years. Note that million-year calculations are included as illustration of how results can change when longer time periods are considered, but there may be additional processes that should be included for such a long time period.

Aqueous releases are reported for all the above combinations (two performance measures times three time periods), but gaseous releases are reported only in terms of 10,000-yr EPA sum. For each applicable combination, aqueous and gaseous releases are reported for four repository cases: vertically emplaced thin-walled containers for thermal loading of 57 kW/acre or 114 kW/acre and in-drift-emplaced double-walled multipurpose containers for thermal loading of 57 kW/acre or 114 kW/acre.

14.6.1 Aqueous releases

For each aqueous-release simulation, 300 realizations are computed for each of the unsaturated-zone columns. For each realization of a column, unsaturated-zone flow is calculated for both "dry" and "wet" climatic conditions; releases from the engineered barrier system (EBS) and unsaturated-zone transport are calculated, switching between the "dry" and "wet" flows at climate-change times; and then saturated-zone transport is calculated for the SZ flow tube corresponding to the UZ column. Cumulative releases from the EBS, from the unsaturated zone, and to the accessible environment are saved at each of three times—10^4 yr, 10^5 yr, and 10^6 yr. Highest dose rate so far at the accessible environment is also saved at the same three times. There is a total of 26 UZ columns (eight each for the 57-kW/acre cases, five each for the 114-kW/acre cases), each with 300 realizations computed (a total of 7800 realizations), and with 12 performance measures saved for each realization (EBS release, UZ release, release to accessible environment, and dose rate at three times). In addition, subsidiary simulations are performed to better understand transport time, container failure, and the effect of percolation flux and water-table fluctuations on the results.

Most model parameters are sampled independently for the columns contributing to a given simulation because the correlation lengths for hydrogeologic properties are expected to be much smaller than the distance between columns (for example, Rautman and Robey, 1993, use 150 m for the major-axis porosity correlation length). The only model parameters that are correlated among columns are the climate parameters (infiltration, water-table rise, and climate-change times), and they are chosen to be the same for all columns in a given simulation. Note that water-table elevation varies from column to column, but the change from nominal is taken to be the same for all columns. Also note that percolation flux varies from column to column because it depends on matrix saturated conductivity, and has a random aspect as well (see Section 8.9).

Because of the climate parameters, the release calculations for the columns are not completely independent, as they were in TSPA-91. Thus, it is no longer appropriate to combine the cumulative releases from different columns in the way it was done for TSPA-91 (see Chapter 8 of the TSPA-91 report). The combination is actually simpler this time, with releases from all the columns for a given realization simply added together, since the realization represents the same climate scenario for each column.

Doses are not additive as cumulative releases are, so they must be treated differently. As discussed in Section 11.6.2, the areas of the SZ flow tubes are chosen so that the radionuclide concentrations in each flow tube are approximately correct. The dose rates from all the flow tubes cannot be combined because they represent different spatial locations. However,

each flow tube has a valid dose calculation. Thus, to get a single representative dose rate, the largest of the flow-tube dose rates is taken.

An example of the combination of releases and dose rates for one of the cases is shown in Figure 14-17. The figure shows probability distributions of release and dose rate, generated from the 300 realizations in the Monte Carlo simulations. The realizations are all weighted equally, so the lowest probability shown on the curves is 1/300. The probability distributions are displayed in the form of complementary cumulative distribution functions (CCDFs), which show the probability that release (or dose rate) is greater than a given value. There is a much greater range of computed 10,000-yr cumulative releases than of computed peak dose rates over 10^6 yr. There is a range of only three orders of magnitude in the maximum dose rate for a realization, but seven orders of magnitude variation in EPA sum is shown, and over 70% of the EPA sums are not even on the plot because they are less than 10^{-8}.

Ten thousand years is a relatively small time compared to most of the unsaturated-zone transport times (see Figure 14-1), which explains the large number of zero and near-zero 10,000-yr releases. Also, releases that do come through are on a very nonlinear part of the breakthrough curve, which explains the large range of 10,000-yr releases. One million years, on the other hand, is a relatively large time, and behavior is more linear. In fact, much of the variation in the dose curves comes from variations in the saturated-zone transport area, which enters the dose calculation simply as a divisor, but which varies over two orders of magnitude.

A comparison of the composite-porosity aqueous-release results with the EPA standard (40 CFR 191.13) is given in Figure 14-18. Results for all four repository cases are shown, as well as the composite-porosity aqueous-release CCDF from TSPA-91. The limits set by the EPA (no longer applicable to Yucca Mountain) are indicated by the shading: Under the EPA standard, the CCDF curve must stay outside the shaded region. Note, however, that the EPA limits are applicable to a CCDF that includes all significant processes, whereas the CCDFs in Figure 14-18 include only nominal groundwater flow and transport (and those with many simplifications).

Two things are striking about Figure 14-18. First, although the calculated 10,000-yr releases are lower for the 114-kW/acre cases than for the 57-kW/acre cases, and releases are slightly lower for the in-drift cases than for the vertical cases, the CCDFs for the four cases really are not very different. The differences among the cases in Figure 14-18 are explainable in terms of the temperature curves (see Figures 10-16 through 10-19): The 114-kW/acre cases stay above 100°C longer than the 57-kW/acre cases, and to a lesser extent the in-drift cases stay above 100°C longer than the vertical cases (as noted in Chapter 13, the YMIM corrosion models allow aqueous corrosion only when temperature is 100°C or

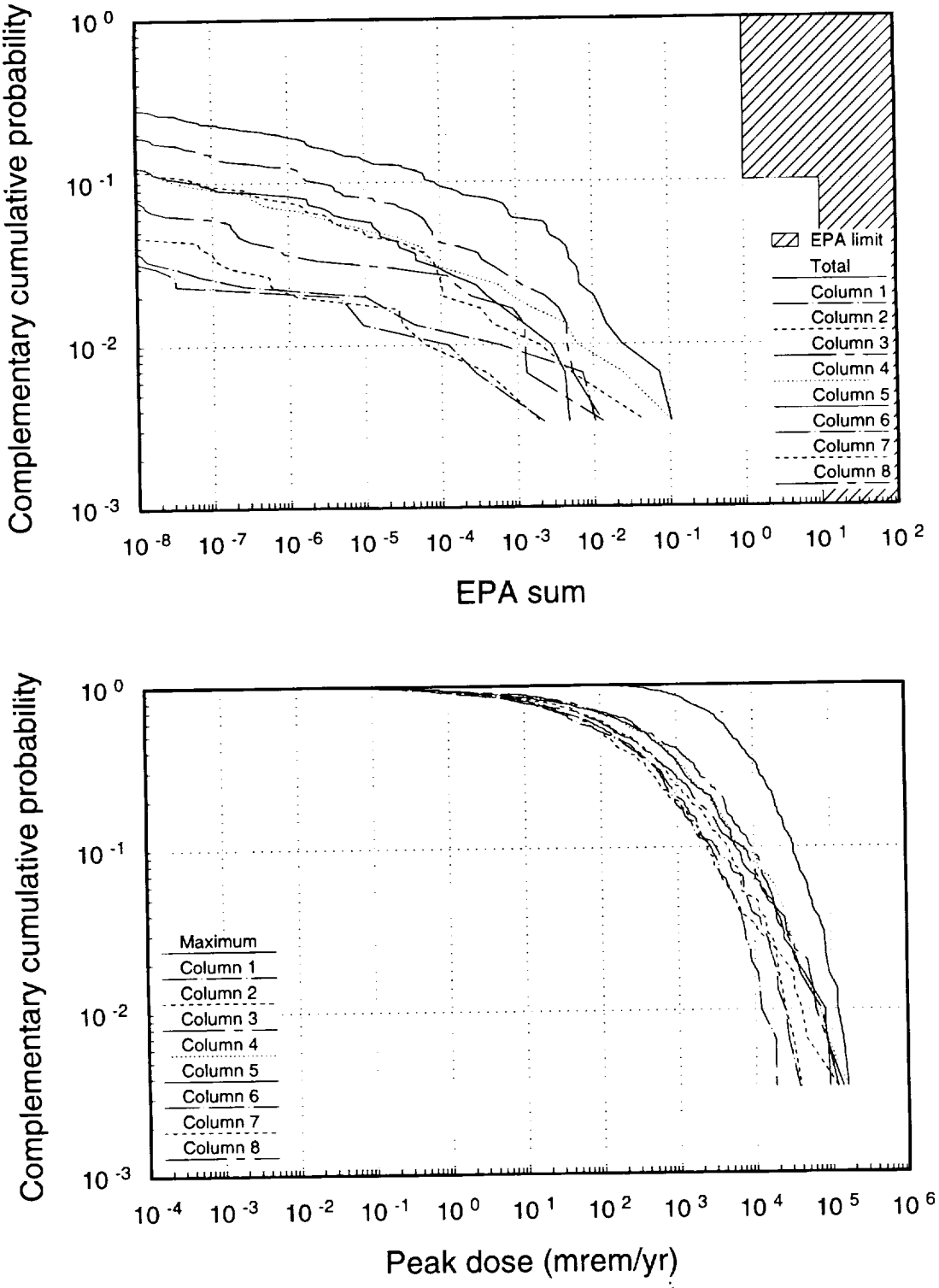

Figure 14-17. CCDFs for individual columns, plus the combination CCDF (57 kW/acre, vertical emplacement). Top: normalized cumulative aqueous release over 10,000 years. Bottom: peak individual drinking-water dose rate over 1,000,000 years.

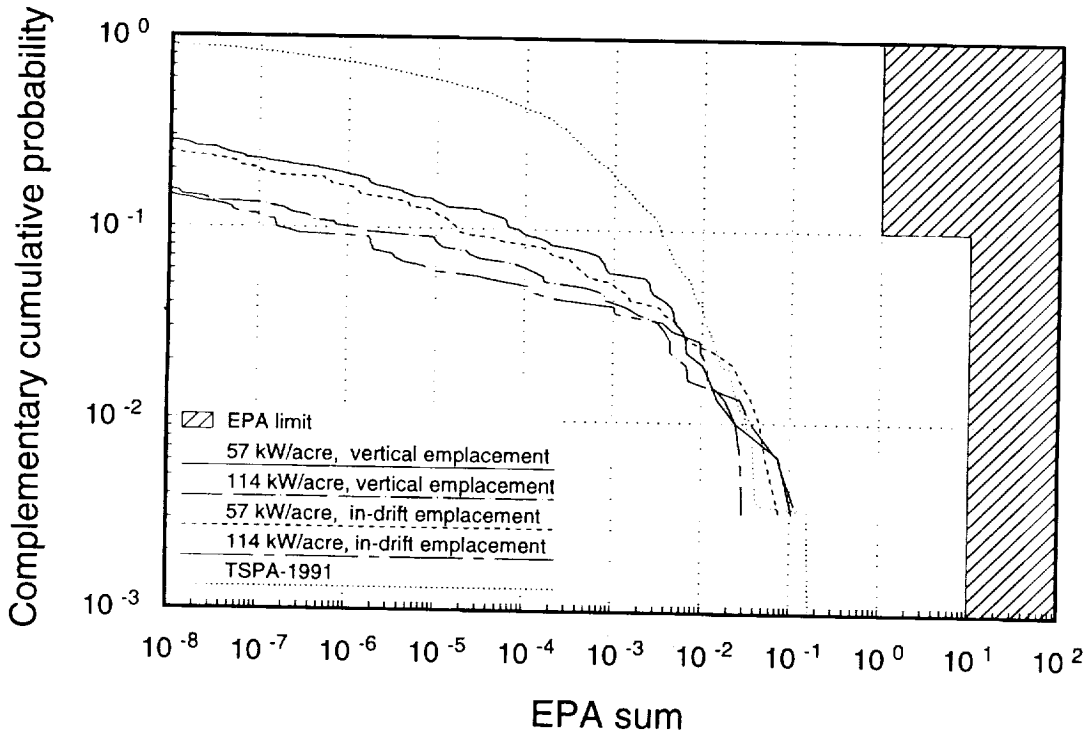

Figure 14-18. CCDFs of normalized cumulative aqueous release over 10,000 years for the four cases and for TSPA-91.

lower). Second, the CCDFs are significantly lower than the TSPA-91 CCDF (the TSPA-91 distribution has 90% of its normalized releases greater than 10^{-8}, whereas the TSPA-93 distributions have only about 15% to 30% of their normalized releases greater than 10^{-8}, depending on the case).

The reduction in releases compared to TSPA-91 is primarily because the initial percolation-flux distribution is lower—for TSPA-91, the percolation flux was exponentially distributed with a mean of 1 mm/yr. This time, the "dry" infiltration distribution is exponentially distributed with mean of 0.5 mm/yr, and the percolation distribution is a little lower, averaging 0.35 mm/yr (see Figure 8-7; the dry-climate distribution is discussed rather than the wet-climate distribution because, with our assumptions, the climate is usually "dry" for the first 10,000 years—see Chapter 8). Sensitivity analysis of the TSPA-91 results (Wilson, 1993) showed that the composite-porosity aqueous-release results were extremely sensitive to percolation flux, with flux accounting for 90% of the variability in the results. The change in the release CCDF from TSPA-91 to TSPA-93 is another demonstration of that sensitivity.

To show the effect of the percolation distribution, the aqueous-release simulation was re-run for one of the cases (57 kW/acre, vertical emplacement) using the TSPA-91 percolation distribution with no climate changes, but keeping everything else the same. The

resulting CCDF (see Figure 14-19) is very similar to the TSPA-91 CCDF, confirming that the percolation-flux distribution determines 10,000-yr composite-porosity aqueous releases to a great extent.

Another demonstration of the importance of percolation flux and climate change is shown in Figure 14-20, where the CCDF for the 57-kW/acre, vertical-emplacement case is separated into realizations that have a climate change within the first 10,000 years and realizations that have dry-climate conditions for the whole 10,000 years. It can be seen that realizations including a climate change account for all of the highest releases, though only about 10% of the realizations have a climate change before 10,000 yr.

Distributions of peak drinking-water radiation-dose rate over a period of a million years are shown in Figure 14-21. Once again, there is little difference among the four cases, though the vertical cases are lower than the in-drift cases and the 114-kW/acre cases are lower than the 57-kW/acre cases. (Note that cases with better 10,000-yr performance are not necessarily better over longer time periods.)

The most striking thing about Figure 14-21 is that the maximum dose numbers are so high. The means of the distributions shown in the figure range from 11,000 to 20,000

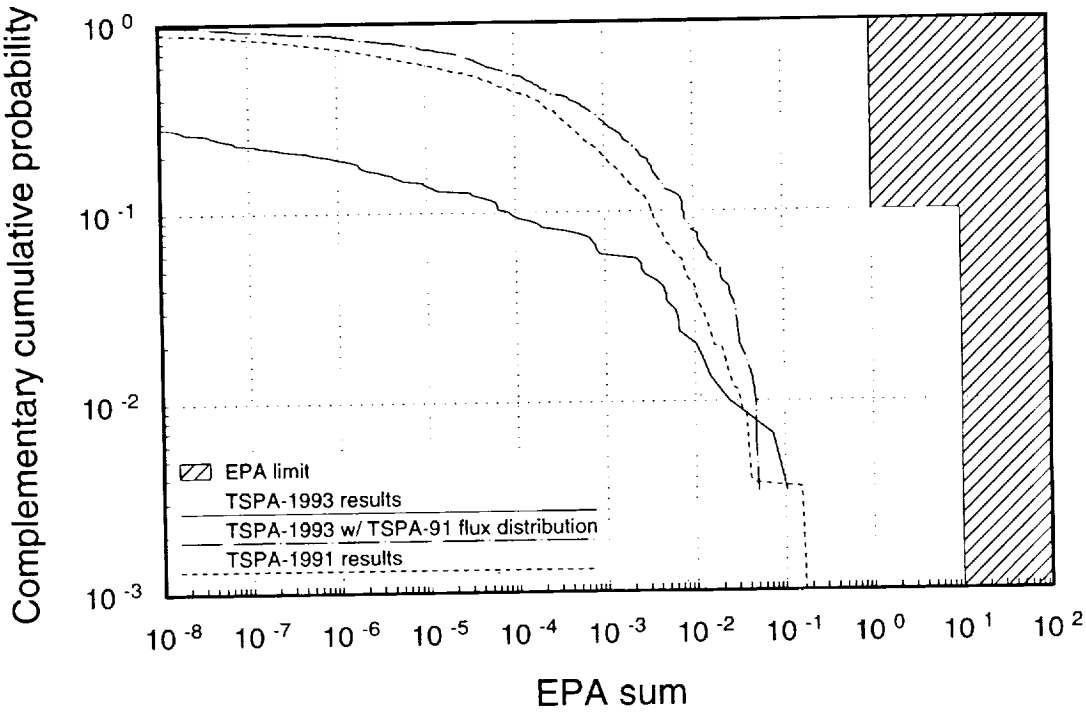

Figure 14-19. Comparison of normalized cumulative aqueous release over 10,000 years for TSPA-91, TSPA-93, and a test case in which percolation flux is the same as for TSPA-91 but everything else is the same as for TSPA-93 (57 kW/acre, vertical emplacement).

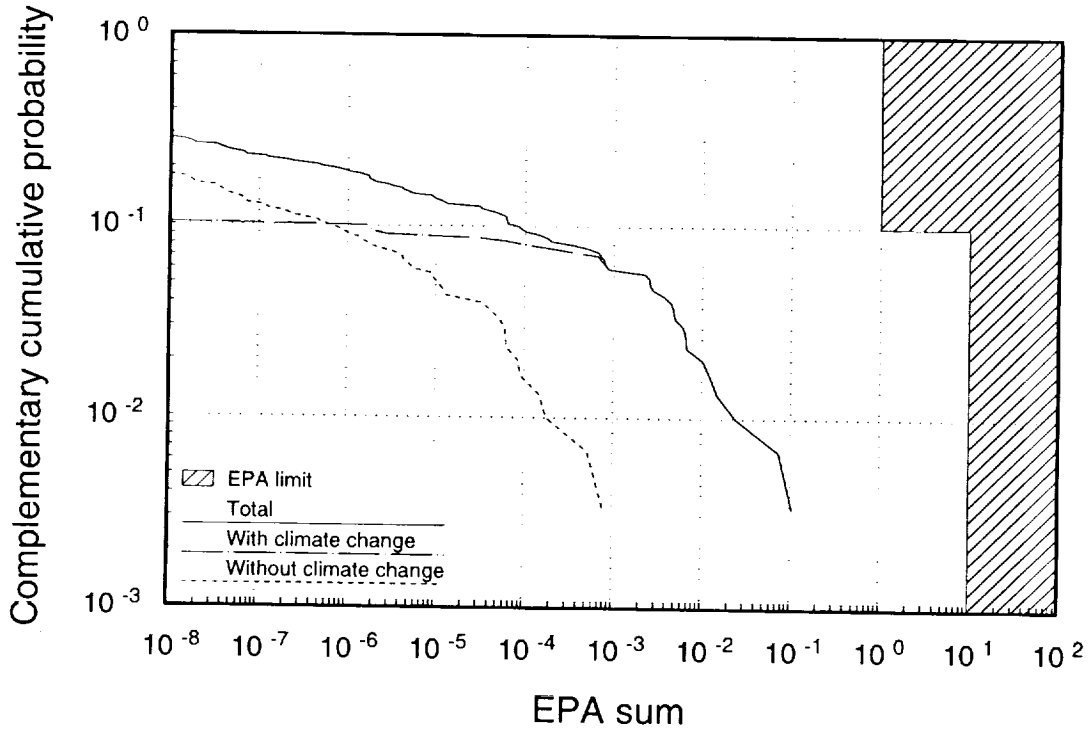

Figure 14-20. CCDF of normalized cumulative aqueous release over 10,000 years, divided into two parts: one part with a climate change within the period and the other part with no climate change within the period (57 kW/acre, vertical emplacement).

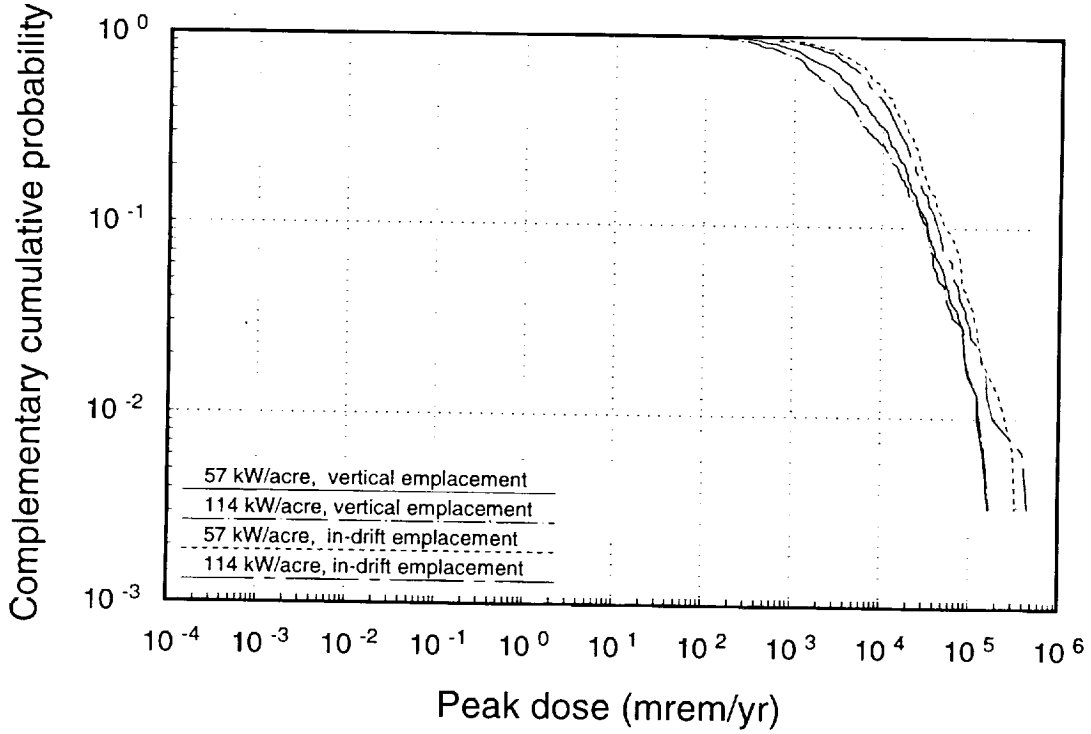

Figure 14-21. CCDFs of peak individual drinking-water dose rate over 1,000,000 years for the four cases.

mrem/yr; for comparison, the National Council on Radiation Protection and Measurements estimates the average dose rate to individuals in the U. S. from natural background radiation to be about 300 mrem/yr, with a broad distribution going up to a few thousand mrem/yr (NCRP, 1987).

The dose numbers in Figure 14-21 are preliminary and so should not be given too much weight, but the high calculated values are an indication of a fact about the Yucca Mountain site: it is arid. As a result, Yucca Mountain is a good site in terms of time delay. Geosphere transport times are much longer than they would be at many sites (according to the composite-porosity model, at least); however, Yucca Mountain is not a particulary good site in terms of dilution. If waste does escape from the repository, little water is available to dilute it, and the peak dose rates really depend on only two things—release rate from the source and amount of dilution afterward.

If a dose regulation has no time limit, long transport times are not enough to guarantee low dose rates—low release rates from the repository are necessary, and the amount of dilution after release determines how low they must be. Low water velocity or high sorption can push the peak dose rate far into the future without lowering its magnitude. To obtain low peak dose rates from transport time alone, it is necessary for the transport time to be greater than the half-life for all important radionuclides. As discussed below, the calculated doses are dominated by ^{237}Np, which has a half-life of about two million years, so a ^{237}Np transport time greater than two million years would be needed to reduce the peak dose rates significantly.

The saturated zone in the vicinity of Yucca Mountain is not well characterized at the present time, so it is certainly possible that the amount of dilution is underestimated. However, we are unlikely to underestimate by several orders of magnitude. Thus, to lower the calculated dose rates significantly, the calculated EBS release rates would have to be significantly lower. Our source model has a number of conservatisms, so there are several possibilities for lowering the EBS release rates. Some important areas to investigate are container wetting, mechanisms for water flow into a partially failed container, mechanisms for transporting radionuclides out of a partially failed container, and cladding failure. Some aspects of repository design can affect dose rates also. For example, it may be possible to design the container/emplacement system in such a way as to spread out container failures more (to reduce peak dose *rates*, what is needed is not necessarily a longer-lived container, but rather containers that do not all fail at once), and the waste packages could perhaps be designed to maintain long-term reducing conditions (which would lower many of the solubilities, notably neptunium's).

To understand why the simulated doses are lower for the vertical-emplacement cases than for the in-drift cases, it is useful to consider the distributions of container-failure times in Figure 14-22. Three features stand out in the distributions: (1) The four cases are differentiated in time: according to the calculations, containers fail earlier for 57 kW/acre than for 114 kW/acre, and the vertically-emplaced containers fail earlier than the in-drift-emplaced containers. (2) The cases are also differentiated in probability: fewer containers fail for vertical emplacement than for in-drift emplacement, and fewer containers fail for 57 kW/acre than for 114 kW/acre. (3) The exponentially distributed juvenile container failures are clearly visible at the bottom of the plot. Note that we assume more juvenile failures for the vertically-emplaced containers than for the in-drift containers (see Table 14-8). Point (2) explains the dose differentiation between vertical and in-drift containers—if fewer containers fail, releases are lower and doses are lower, in the long run.

The first two points above can be explained as follows. For the container-failure model and input parameters used (discussed in Chapter 13), containers above 100°C are protected, but they fail very quickly after their temperature falls below 100°C *if they are wet or moist.* As mentioned earlier, container temperature stays above 100°C longer for 114 kW/acre than for 57 kW/acre and, secondarily, container temperature stays above 100°C longer for in-

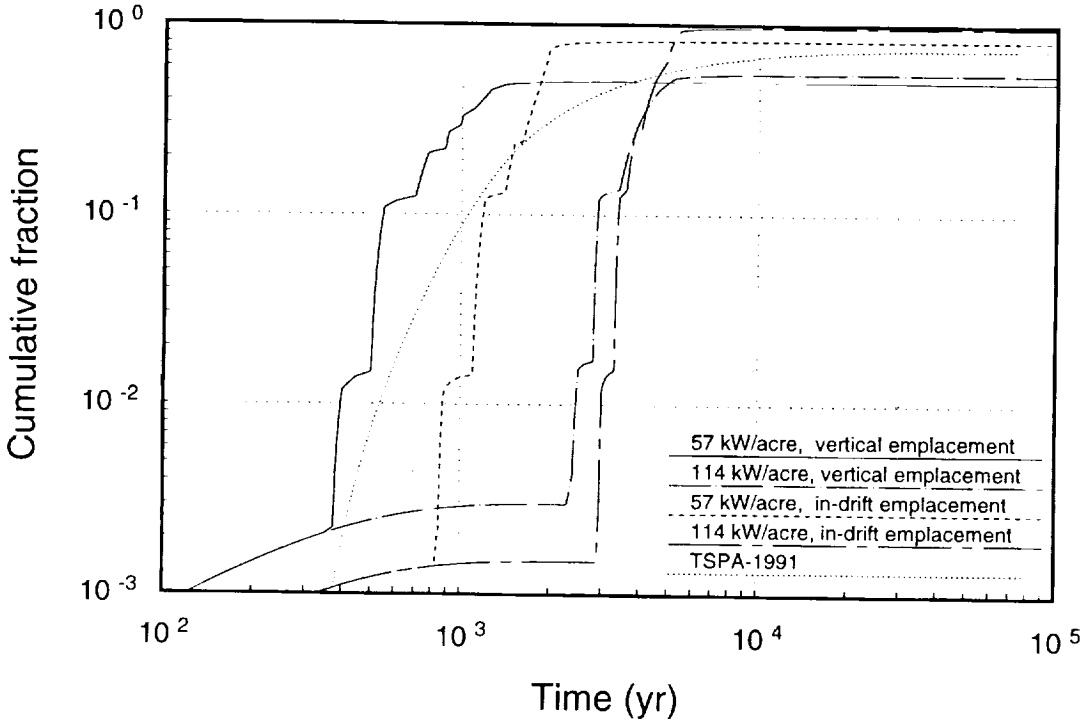

Figure 14-22. Mean distributions of container-failure time for the four repository cases and for TSPA-91.

drift containers than for vertical containers. The times when most of the containers fail in Figure 14-22 can be matched with the times (see Figures 10-16 through 10-19) when container temperature falls below 100°C. (The "stair step" effect in Figure 14-22 is caused by having all containers in the repository represented by only ten container groups; see Section 14.4.2.) The failure of fewer vertically emplaced containers can be traced to the assumptions about container wetting and rubble contact (see Section 14.4.3 and Table 14-6). We assume that the borehole airgap protects some of the vertically emplaced containers from contact with moist rubble. Hence, some of the vertically emplaced containers are dry at the time container temperature falls below 100°C, and as a result they do not fail. (Some of them may be wetted at a later time, but at lower temperatures the corrosion rates are much lower, and so containers usually do not fail at late times, according to our model.) On the other hand, in-drift containers are always assumed to have contact with moist rubble after the dryout period is past, so they almost all fail when the temperature falls below 100°C. The fact that some of the in-drift containers do not fail is related to the assumed distributions for pitting increment (see Table 14-8). The pitting rates at the low end of the distribution are slow enough that there is not time for failure while the containers are still warm. The small difference in total failure probability between the 57-kW/acre cases and the 114-kW/acre cases is because the container temperatures fall off more rapidly for 57 kW/acre (and so the period when the containers are warm enough to pit through is shorter).

Also shown in Figure 14-22 is a curve for container-failure time in TSPA-91. The source model in TSPA-91 did not have a container-failure distribution as such, because several time scales were rolled up together. The curve in Figure 14-22 is the closest thing to a container-failure distribution: it is a distribution of release time for a hypothetical nuclide that has 100% prompt releases. While rather different in shape (the failures are spread out over a longer time than any of the TSPA-93 curves), the TSPA-91 curve is in the middle of the other curves. Thus, the container-failure model for this TSPA is not really very different in effect from the assumed distribution of container-failure times in TSPA-91.

Dilution is an important component of a dose estimate, so it is of interest to know the amount of dilution in the model system. We can approximate the dilution by the "potential dilution factor," a term we use to mean the amount of dilution that there could be if the flow and transport were in steady state (i.e., neglecting all transient effects).

The potential dilution factor is calculated by considering the following three quantities. The amount of water that could be flowing through waste containers, according to the wetting model being used (see Section 14.4.3), is

$$Q_c = N_{cans} f_s A_{cross} q_s \ , \tag{14.19}$$

where Q_c is the amount of water per unit time contacting waste, N_{cans} is the number of waste containers, f_s is the fraction of the containers contacted by flowing water (seepage flow), A_{cross} is the water-collection area, and q_s is the average seepage flux through a container that has seepage flow. The total amount of water flowing through the potential repository area is given by

$$Q_{uz} = A_{rep} q \ , \tag{14.20}$$

where Q_{uz} is the water flow per unit time through the repository, A_{rep} is the repository area, and q is the percolation flux. The amount of water flowing through the corresponding saturated-zone flow tube is given by

$$Q_{sz} = A_{sz} q_{sz} = A_{sz} v_{sz} n_{sz} \ , \tag{14.21}$$

where Q_{sz} is the amount of contaminated water flowing through the saturated zone per unit time, A_{sz} is the effective SZ transport area (see Section 11.6.2), q_{sz} is the SZ water flux (Darcy velocity), v_{sz} is the SZ water velocity, and n_{sz} is the SZ porosity.

We assume that radionuclides released from the EBS are fully mixed with the UZ flow before they reach the water table, so the potential amount of dilution in the unsaturated zone is given by Q_c/Q_{uz}. Similarly, the radionuclides are assumed to be fully mixed within the SZ flow tube, so the additional potential dilution in the saturated zone is given by Q_{uz}/Q_{sz}. The total potential dilution is then Q_c/Q_{sz}. The water flow, and therefore the dilution, varies with changes in climate. Figure 14-23 shows distributions of potential dilution factor for dry and wet climates (for 57 kW/acre, vertical emplacement, Column 8). The UZ, SZ, and total dilution factors are shown. The potential dilution factor is the factor by which concentration would change; since concentration decreases at each stage of transport, the dilution factors are always less than 1.

From the figure, it can be seen that there is more dilution (i.e., a lower potential dilution factor) during dry-climate periods than during wet-climate periods. This result may seem surprising at first, because UZ water flow increases during wet-climate periods. However, the saturated-zone flow does not change with climate in our simulations, so that the radionuclides are assumed to be dissolved in the same amount of SZ water independent of climate conditions. This assumption should be examined in future TSPAs. Secondarily, along with the increase in UZ flux when going from dry climate to wet climate comes an increase in the amount of water contacting a wet waste container and an increase in the number of containers contributing to release. The net result is that both UZ and SZ dilutions are greater for dry-climate conditions than for wet-climate conditions. Figure 14-23 also shows that in the extreme cases dilution in the unsaturated zone is almost as great as the total dilution, but at higher probabilities the UZ dilution is much less than the total dilution.

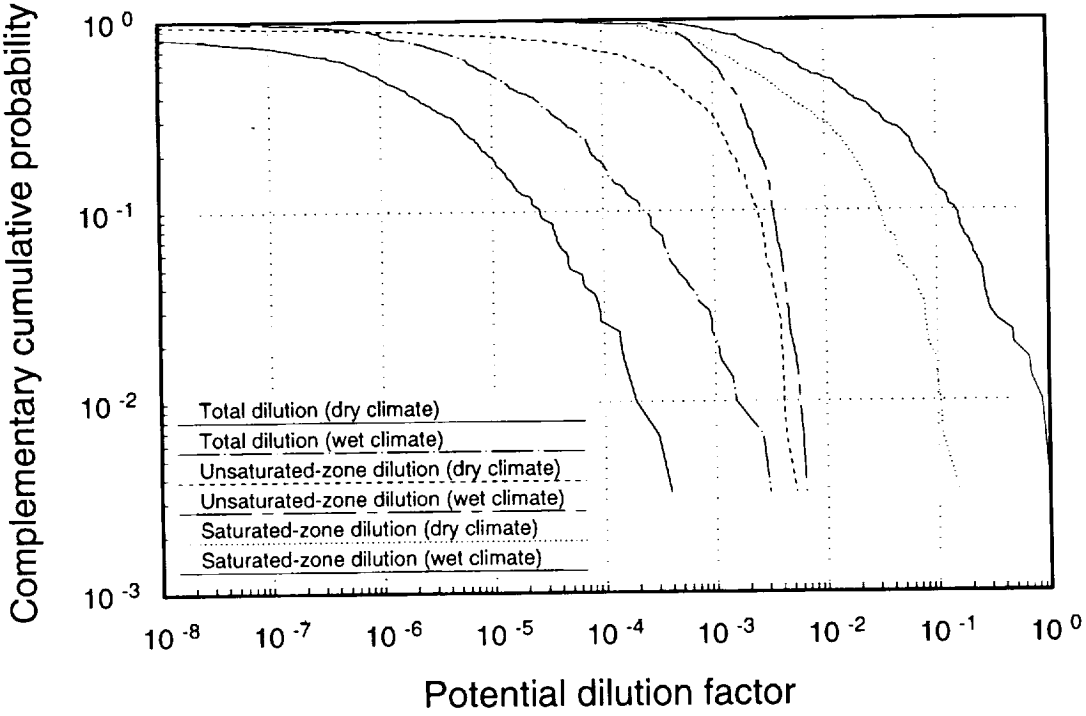

Figure 14-23. Distributions of potential dilution factor for dry and wet climates (57 kW/acre, vertical emplacement). Potential dilution factors for the unsaturated zone and the saturated zone are shown in addition to the total dilution factor.

Another factor contributing to high dose estimates is the abrupt change in water-table height at climate-change times. A water-table rise associated with a change from "dry" to "wet" conditions can result in a pulse release of radionuclides to the saturated zone, which in turn can result in a spike in the calculated drinking-water dose 5 km downstream at the accessible environment. To determine the magnitude of this effect, one of the simulations was re-run with fixed water table. Figure 14-24 shows calculated peak-dose distributions for 57 kW/acre, vertical emplacement, Column 8. Distributions for fixed water table and for fluctuating water table are shown. It can be seen that the peak dose rates with fluctuating water table are about a factor of three to ten higher than those with fixed water table. Thus, the dose-rate spikes caused by sudden rises in the water table are typically about a factor of three to ten higher than the maximum dose rates obtained with no change in water-table height. Note that percolation flux still varies with climate in the fixed-water-table simulation, so the variation in dilution illustrated above is included. As discussed in Section 14.3, the dose spikes caused by water-table rises may be higher than they should be because of the assumption of instantaneous changes in water-table height. However, at present we have no estimate for the amount of time over which rises in water table should

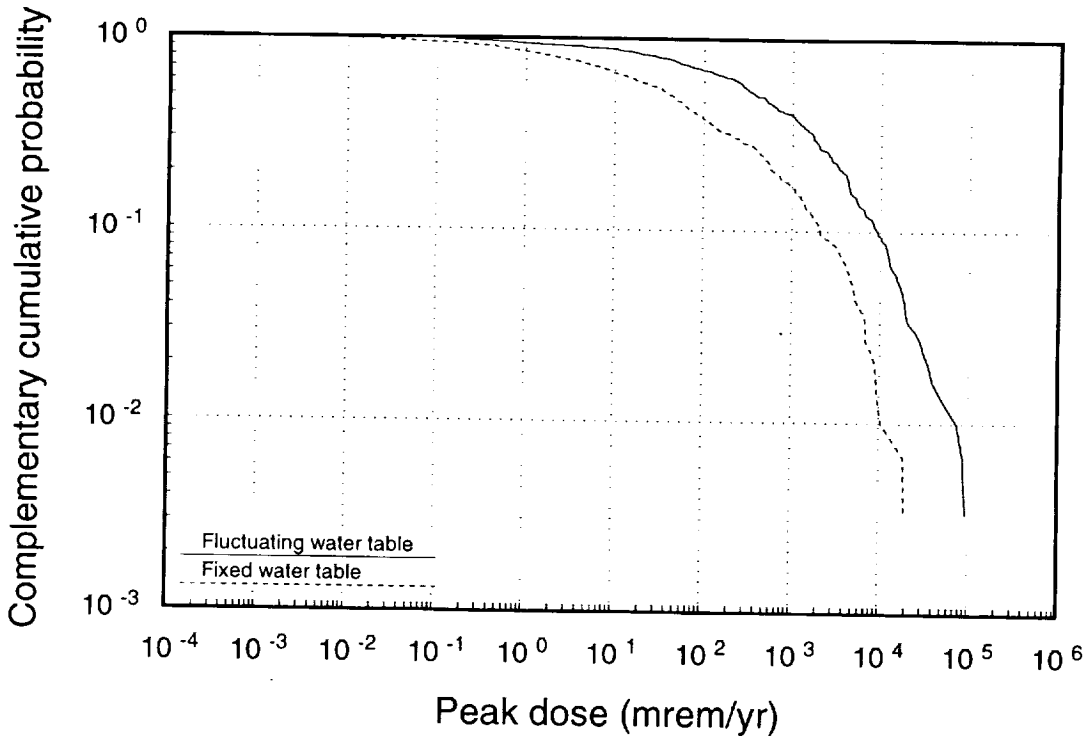

Figure 14-24. CCDFs of peak individual drinking-water dose rate over 1,000,000 years with fluctuating water table (TSPA-93 base case) and with fixed water table (57 kW/acre, vertical emplacement, Column 8).

take place. As shown in Figure 14-25, cumulative releases to the accessible environment are also affected significantly by the assumed water-table fluctuations.

Figure 14-26 shows distributions of the time of peak dose rate for the four repository cases. The steps in the curves result from the climate-change model—as discussed above, high dose rates are more likely during wet-climate periods, both because of decreased dilution and because of abrupt water-table rises. The calculated times of peak dose rate are a little higher for the in-drift cases than for the vertical cases; this is probably because many of the in-drift containers fail at 1000 to 3000 years because of contact with moist rubble (see Figure 14-22), but do not have water contact leading to releases until later, during a wet-climate period. This delay between container failure and releases can happen in the vertical-emplacement cases also, but it happens for a lower fraction of the containers (see Figure 14-22). The most important point to make about Figure 14-26 is that the peak-dose times are spread out (almost log-uniformly) from several tens of thousands of years up to about a million years. It appears that 10^6-yr calculations are sufficient to see most of the dose peaks, though extending the simulation time to 2×10^6 yr may account for the last few percent.

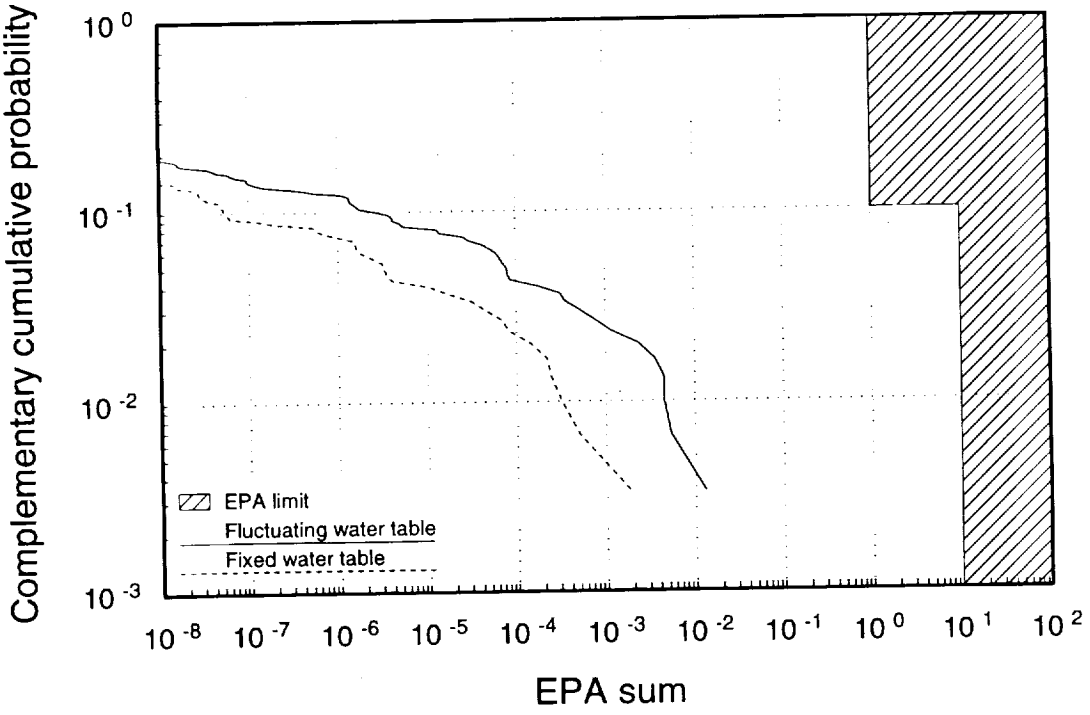

Figure 14-25. CCDFs of normalized cumulative aqueous release over 10,000 years with fluctuating water table (TSPA-93 base case) and with fixed water table (57 kW/acre, vertical emplacement, Column 8).

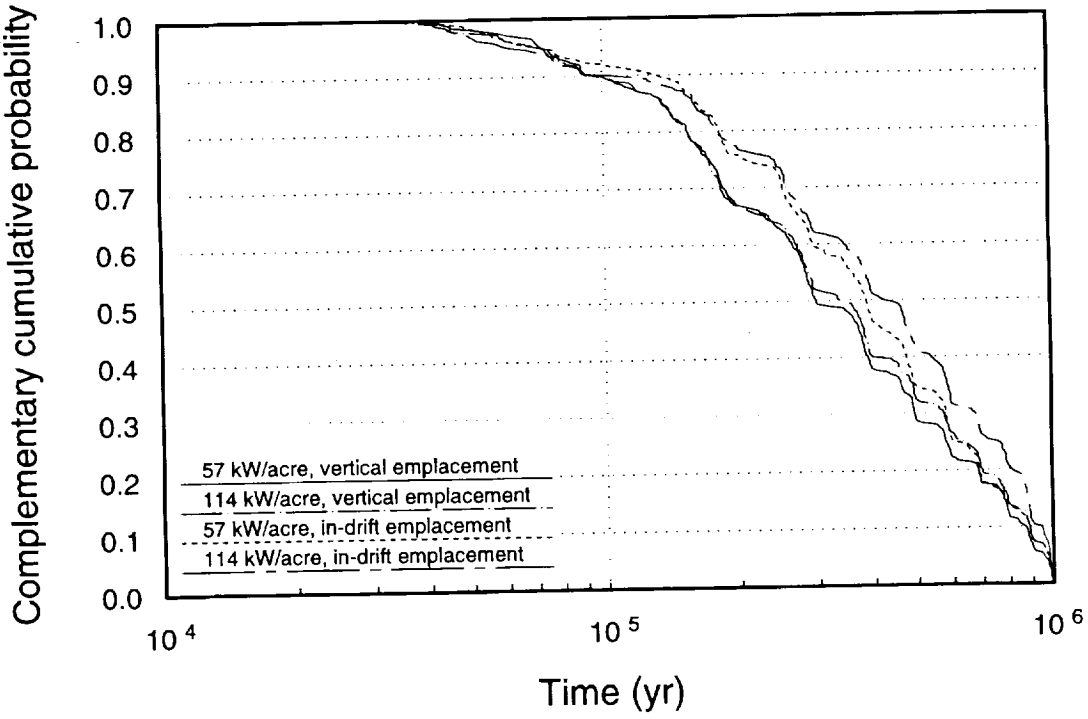

Figure 14-26. Distributions of time of peak individual drinking-water dose rate for the four cases.

The variation of EPA releases and dose rates with time period is shown in Figure 14-27 for 57-kW/acre thermal load and vertically emplaced containers. The corresponding figures for the other cases are similar. Keep in mind that the shaded "EPA limit" region in Figure 14-27a applies only to the 10,000-yr curve. Both for EPA sum and for peak dose rate, two things happen as time increases: the release or dose rate increases and the spread decreases. The 10^6-yr EPA-sum curve has less than an order of magnitude spread. Basically, almost all of the low-retardation radionuclides released from the EBS make it to the accessible environment by 10^6 years, and almost none of the high-retardation nuclides do. The total amount of low-retardation radionuclides released from the EBS depends only on the total number of containers that fail and release their radionuclides. Apparently, the number of containers that fail does not vary greatly from one realization to the next. The 10^6-yr dose curve has more variation—about three orders of magnitude. As already mentioned, much of that variation is due to variation in the SZ-transport-area parameter (i.e., variation in the amount of dilution in the saturated zone), a parameter that does not affect the cumulative release to the accessible environment.

CCDFs for 10,000-yr normalized cumulative releases and 10^6-yr peak dose rates for the individual radionuclides modeled are shown in Figure 14-28 for one of the cases (57 kW/acre, vertical emplacement). At 10,000 years, the calculated releases are dominated by the nonsorbing species ^{99}Tc and ^{129}I. The 10^6-yr peak dose rates are dominated by ^{237}Np. Three other nuclides have dose rates about an order of magnitude below that of ^{237}Np: ^{231}Pa, ^{99}Tc, and ^{129}I. The mean releases and dose rates for individual nuclides, divided by the mean totals at three times are given in Table 14-14. The dose columns add up to more than 100% because the peak dose rates for different nuclides occur at different times (the peak nuclide dose rate divided by peak total dose rate is listed, not the contribution of the nuclide to the peak total dose rate).

Table 14-14 shows that ^{99}Tc dominates both EPA release and dose at early times and ^{237}Np dominates both at late times. At 100,000 years, ^{99}Tc has the highest calculated EPA release but ^{237}Np has the highest calculated peak dose rate.

The roles of the engineered-barrier system, unsaturated zone, and saturated zone are illustrated in Figure 14-29. The figure shows the CCDFs for EPA releases from the EBS, from the UZ, and to the accessible environment at three times. The latter two curves are always well below the EBS-release curve, indicating that the unsaturated zone is containing a significant fraction of the radionuclides. Much of the difference between EBS release and UZ release at 10^5 years and 10^6 years is because ^{239}Pu released from the EBS has such a high retardation that it does not reach the saturated zone. Many other highly retarded nuclides, including several isotopes of plutonium and americium, are also released from the EBS in

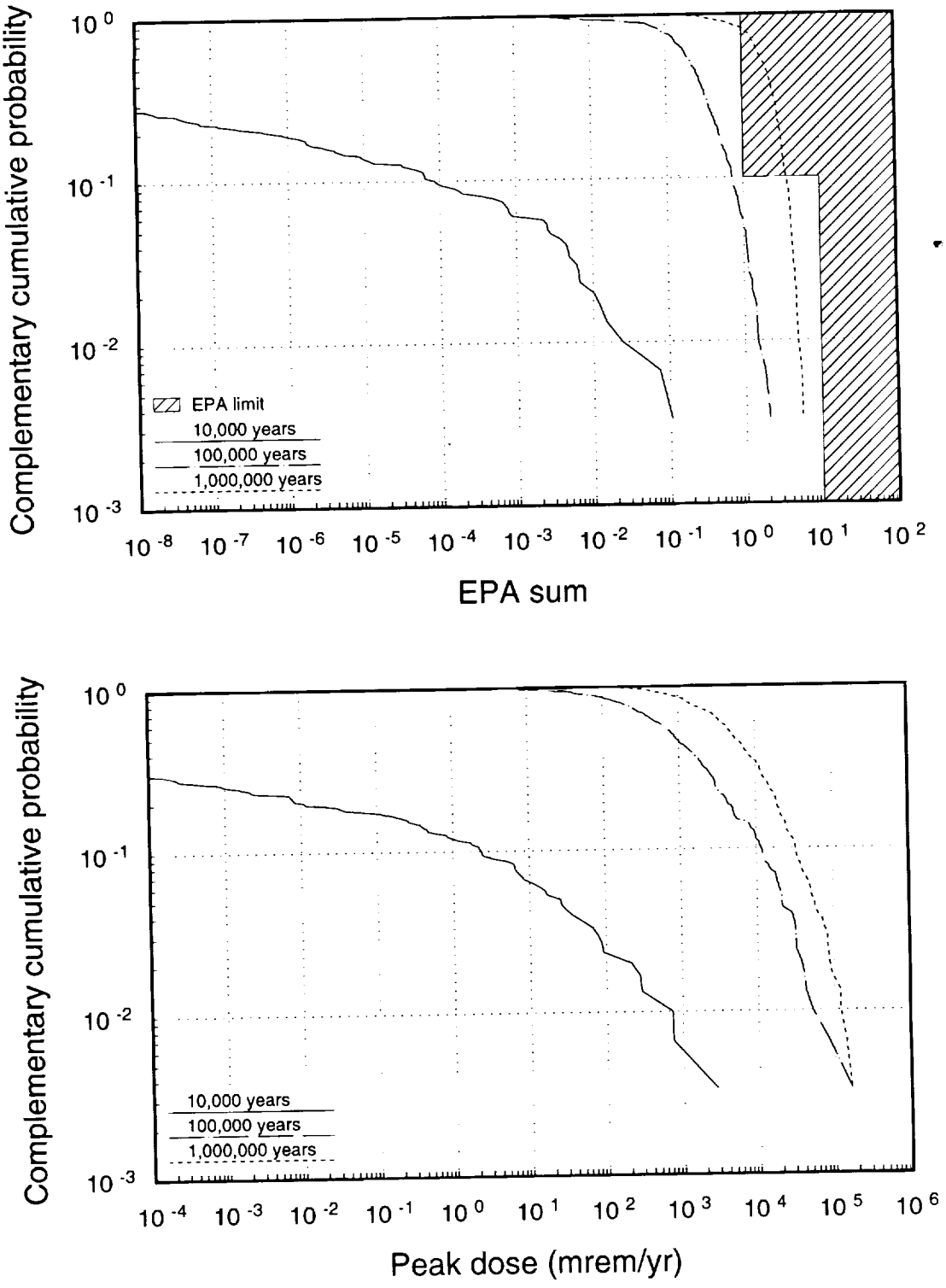

Figure 14-27. CCDFs for three time periods (57 kW/acre, vertical emplacement). Top: normalized cumulative aqueous release. Bottom: peak individual drinking-water dose rate.

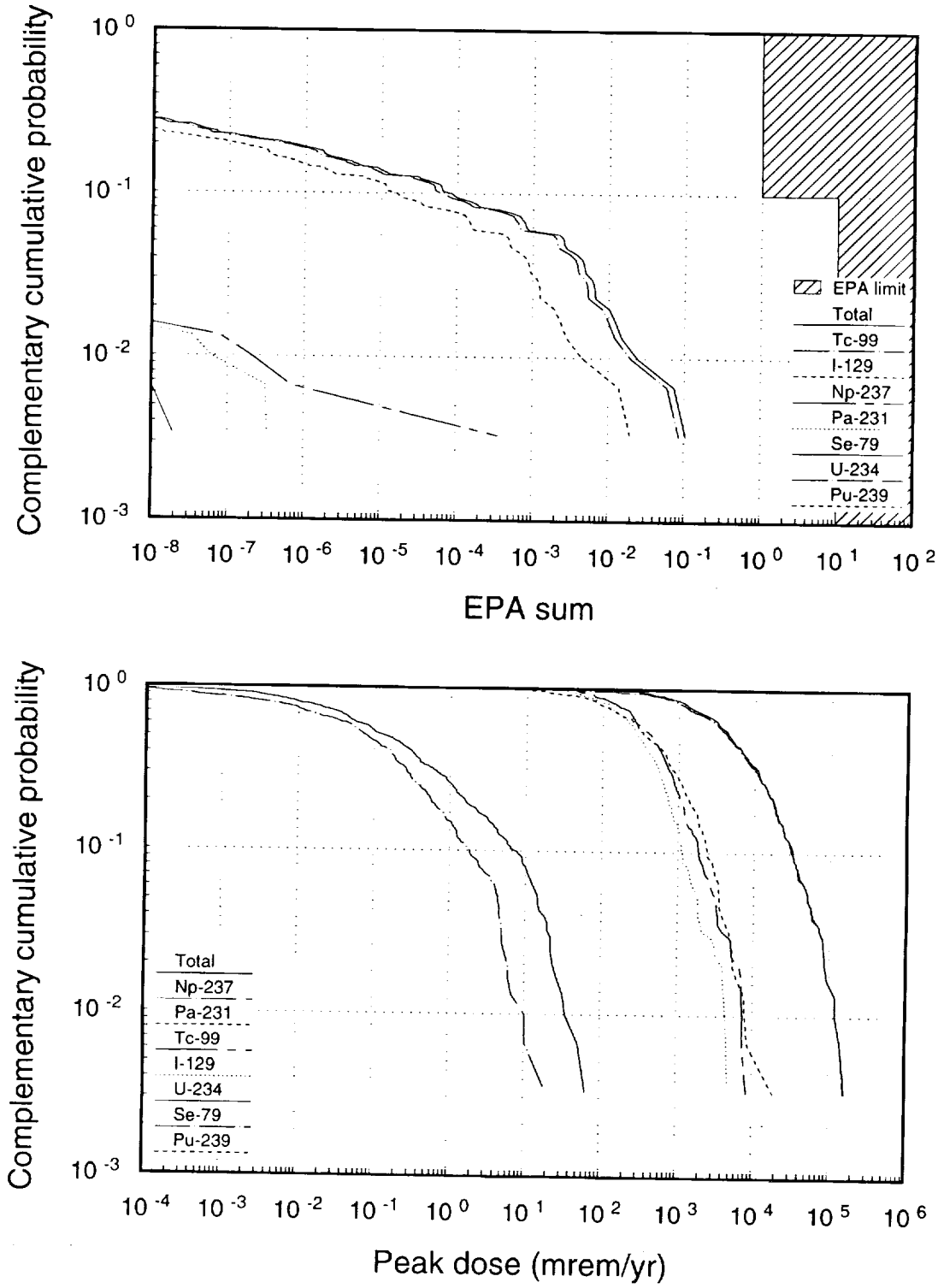

Figure 14-28. CCDFs for individual radionuclides (57 kW/acre, vertical emplacement). Top: normalized cumulative aqueous release over 10,000 years. Bottom: peak individual drinking-water dose rate over 1,000,000 years.

Table 14-14. Nuclide mean releases and dose rates in relation to total. (57 kW/acre, vertical emplacement)

Normalized cumulative release		
10^4 years	10^5 years	10^6 years
^{99}Tc (81.2%)	^{99}Tc (52.6%)	^{237}Np (74.4%)
^{129}I (18.7%)	^{237}Np (32.1%)	^{99}Tc (16.3%)
^{237}Np (0.1%)	^{129}I (14.1%)	^{129}I (6.6%)
	^{231}Pa (0.8%)	^{231}Pa (1.9%)
	^{79}Se (0.2%)	^{234}U (0.5%)
	^{234}U (0.1%)	^{79}Se (0.1%)
Peak individual dose rate		
10^4 years	10^5 years	10^6 years
^{99}Tc (66.7%)	^{237}Np (81.5%)	^{237}Np (96.9%)
^{129}I (33.1%)	^{99}Tc (15.8%)	^{231}Pa (7.6%)
^{237}Np (1.2%)	^{129}I (9.1%)	^{99}Tc (6.5%)
	^{231}Pa (6.2%)	^{129}I (4.2%)

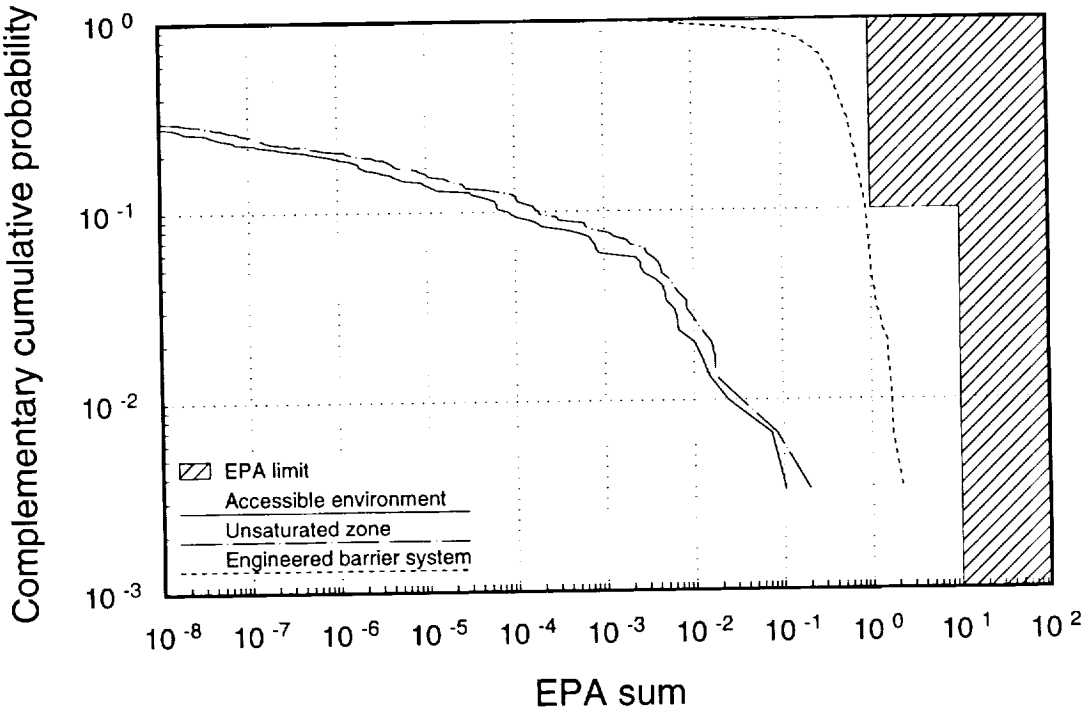

Figure 14-29a. CCDFs for normalized cumulative aqueous release over 10,000 years from the EBS, from the unsaturated zone, and to the accessible environment (57 kW/acre, vertical emplacement).

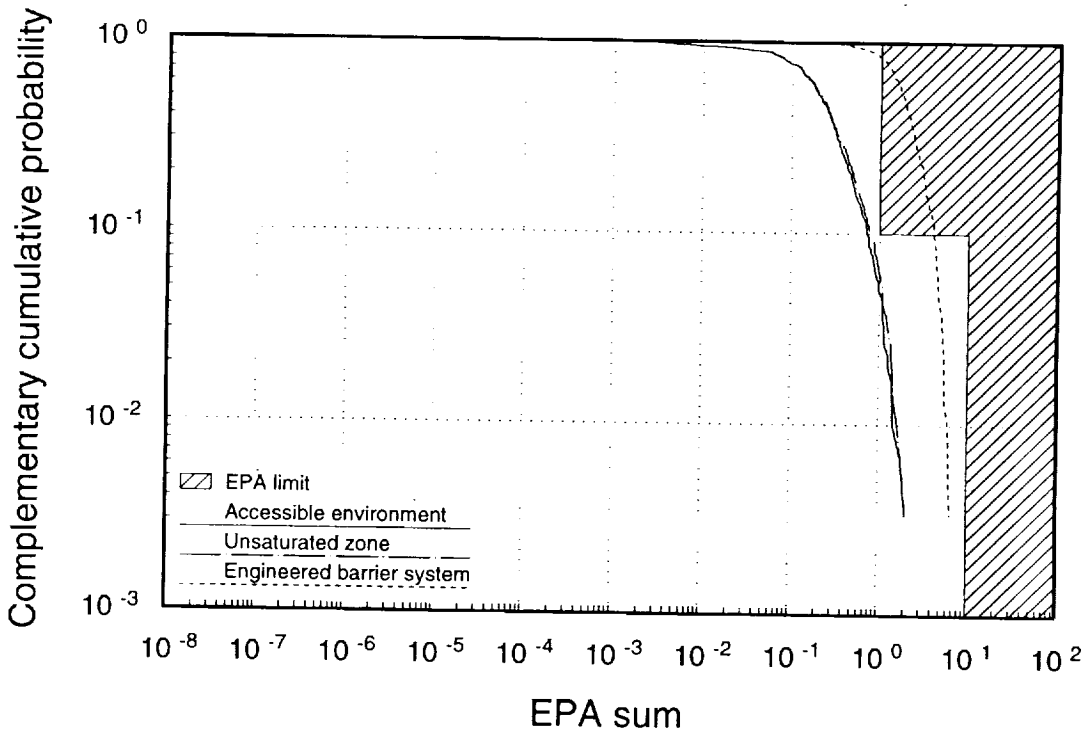

Figure 14-29b. CCDFs for normalized cumulative aqueous release over 100,000 years from the EBS, from the unsaturated zone, and to the accessible environment (57 kW/acre, vertical emplacement).

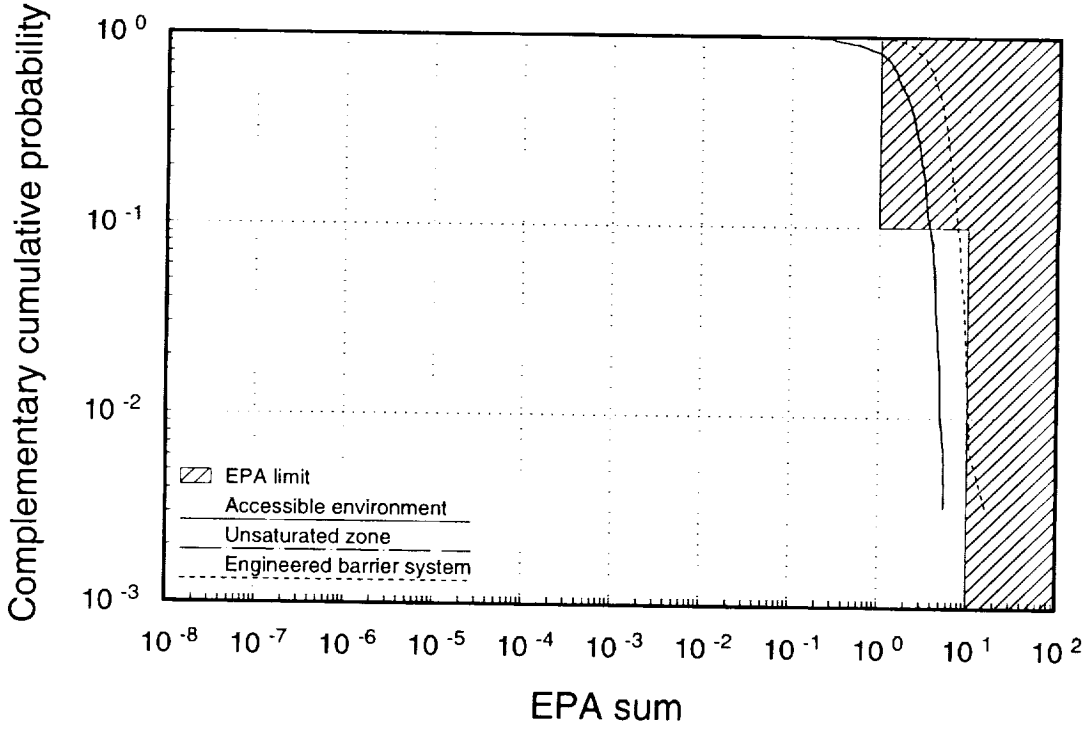

Figure 14-29c. CCDFs for normalized cumulative aqueous release over 1,000,000 years from the EBS, from the unsaturated zone, and to the accessible environment (57 kW/acre, vertical emplacement).

significant quantity and contained by the UZ, so the difference between the curves should be even larger. The small separation between the curves for releases from the unsaturated zone and releases to the accessible environment is because the calculated SZ transport times are much shorter than the calculated UZ transport times (see Figures 11-26 and 14-1).

14.6.2 Gaseous releases

For each gaseous-release simulation, 1000 realizations are computed. The repository is not subdivided into columns for these calculations, but is treated as a whole. For each realization, releases from the EBS are calculated and then convolved with ^{14}C transport-time distributions, as shown in Equation 12.6. Cumulative releases from the EBS and to the accessible environment over 10,000 years are saved for each realization. Radiation doses are not calculated for gaseous releases. Calculated gaseous releases are different for the two models of unsaturated-zone groundwater flow (composite-porosity and weeps) because water flow and distribution are intimately involved in the radionuclide source term (see Chapter 13 and Section 14.4). Thus, gaseous-release results are reported both in this chapter and in the next, which deals with the weeps model.

A comparison of the composite-porosity gaseous-release results with the EPA standard is given in Figure 14-30. Results for all four repository cases are shown, as well as the composite-porosity gaseous-release CCDF from TSPA-91. All four cases have higher releases than TSPA-91 at low probability and lower releases at high probability. Since the high releases are of most concern, even if they do have low probability, we would say that all four of the TSPA-93 cases are worse than TSPA-91 (they go farther into the shaded region). The higher releases to the surface are primarily because of the faster ^{14}C transport this time (see Section 12.4). There is very little difference among the four cases, but it can be seen that 57-kW/acre thermal load with vertically emplaced containers has the highest releases and 114 kW/acre with in-drift emplacement has the lowest releases (but reversed at high probability). All four cases were calculated using ^{14}C transport-time distributions based on a thermal load of 57 kW/acre, so the 114-kW/acre releases are probably a little lower than they should be, because gas velocities should be higher for higher thermal loads.

As in TSPA-91, calculated ^{14}C releases exceed the limits specified by the EPA in 40 CFR 191.13. Also as in TSPA-91, we believe that there are enough conservatisms built into the calculations that this exceedence should not be cause for alarm. For example, as mentioned in Section 14.4.1, inclusion of the fuel-rod cladding in the source-release calculations could reduce releases by a factor of 3 to 5.

Normalized releases from the EBS for all four cases are shown in Figure 14-31. The four new cases and TSPA-91 are all clustered very tightly for probability below about 0.3. For

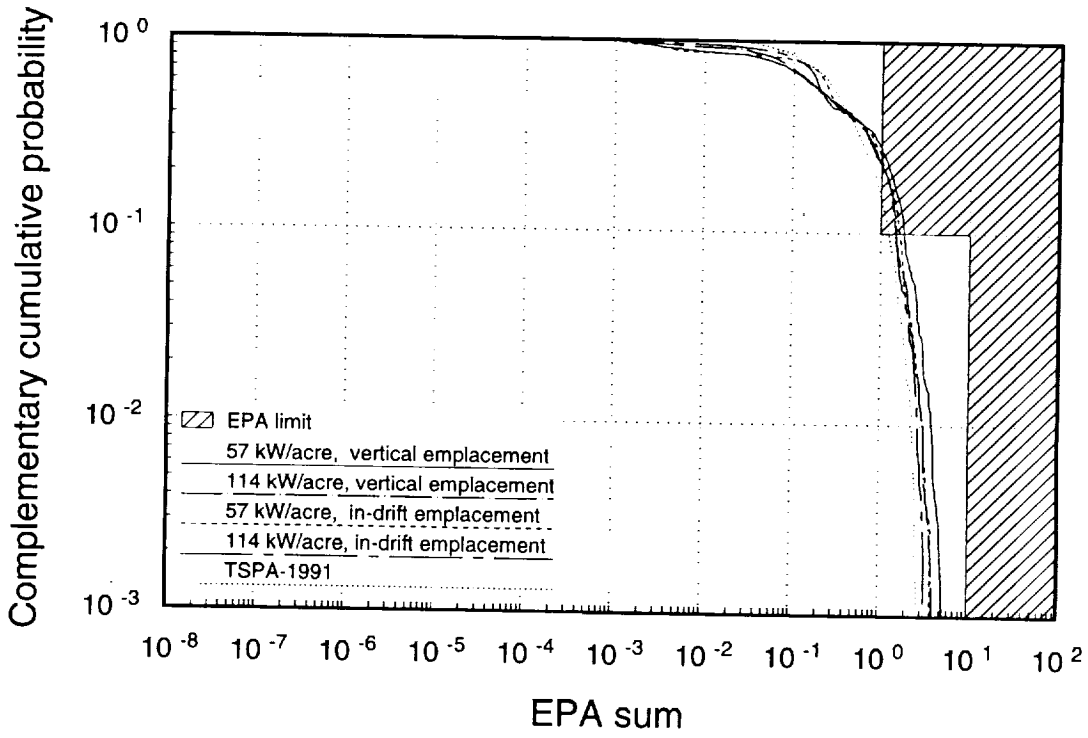

Figure 14-30. CCDFs of normalized cumulative gaseous release over 10,000 years for the four cases and for TSPA-91.

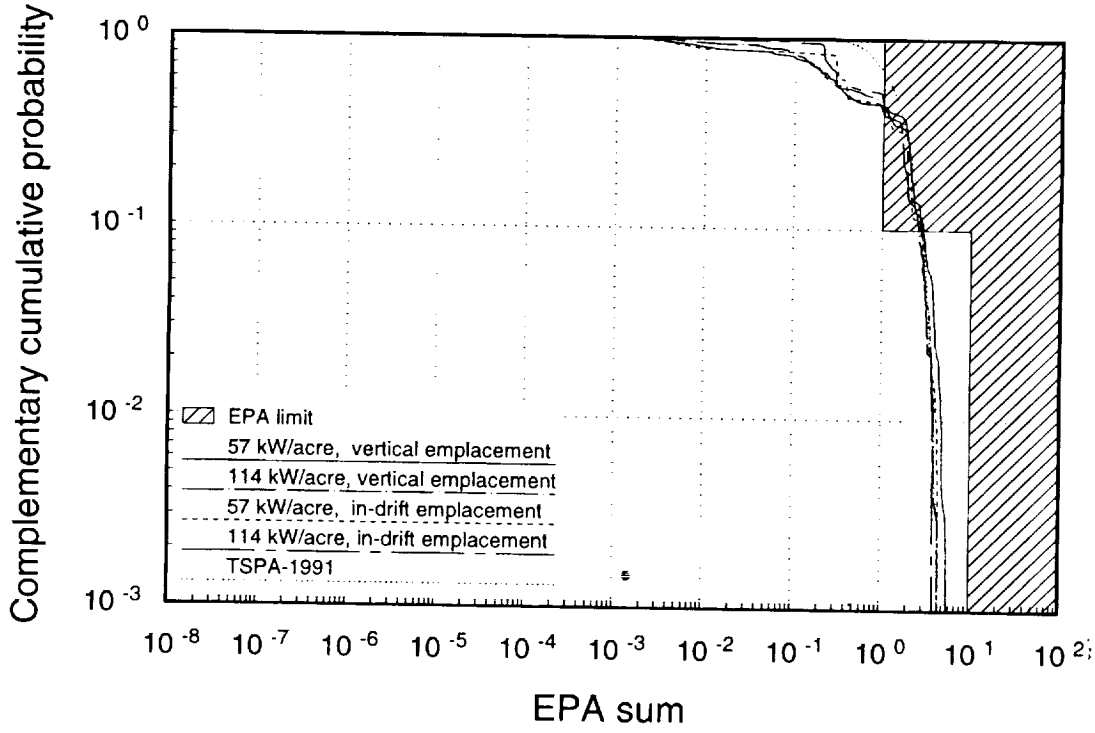

Figure 14-31. CCDFs of normalized cumulative gaseous release from the EBS over 10,000 years for the four cases and for TSPA-91.

higher probability (i.e., what might be considered normal conditions), the new calculations have lower releases than TSPA-91. The reduction is caused by the changes in the way thermal dryout and container failure are handled. In the 114-kW/acre cases most containers do not fail until roughly 3000 years, and in the 57-kW/acre cases many containers never fail (see Figure 14-22).

The final topic under gaseous releases is the combination of gaseous and aqueous releases to obtain the distribution of releases for nominal conditions assuming the composite-porosity model. We only make such a combination for cumulative releases since doses were not calculated for gaseous releases. The cumulative gaseous and aqueous releases are combined in the same way as described in Chapter 8 of the TSPA-91 report, by adding gaseous and aqueous partial EPA sums at the same probability level. This procedure is followed because the aqueous and gaseous releases are calculated independently. It would be preferable to calculate them in parallel, using the same values for shared variables (climate variables, source variables, and bulk conductivity), in which case the aqueous and gaseous releases for each realization would be additive. Because the dependencies between the two are not preserved, it is necessary to follow some *ad hoc* procedure to combine them, and the one mentioned above appears to be the best choice. Because the 10,000-yr normalized gaseous releases are much greater than the normalized aqueous releases (compare Figures 14-18 and 14-30), the combined CCDFs (Figure 14-32) are nearly identical to the gaseous-release CCDFs.

14.6.3 Parameter sensitivities

In this subsection, we discuss the parameters to which the results are most sensitive. Knowing which model parameters affect the results most strongly indicates where to concentrate modeling, site-characterization, and design resources.

It must be emphasized that the sensitivity results are only indications of what may be important. Our models and datasets are still very preliminary, so great confidence cannot be placed in the results. However, when viewed appropriately, the results can be useful. For example, a parameter that appears in our sensitivity analysis as possibly important is the fraction of containers contacted by rubble, or rubble fraction. The proper way to view this finding is not necessarily to conclude that rubble is important to repository performance. We must consider how the rubble fraction fits into the models. It is used as part of a simple model to predict wetting of containers (see Section 14.4.3). Therefore, a more general conclusion is that container-wetting mechanisms and near-field water flow are important, and should be understood better. We must also be aware of the dependencies that exist in the models. Part of the reason that container wetting is important to the results is that the model used

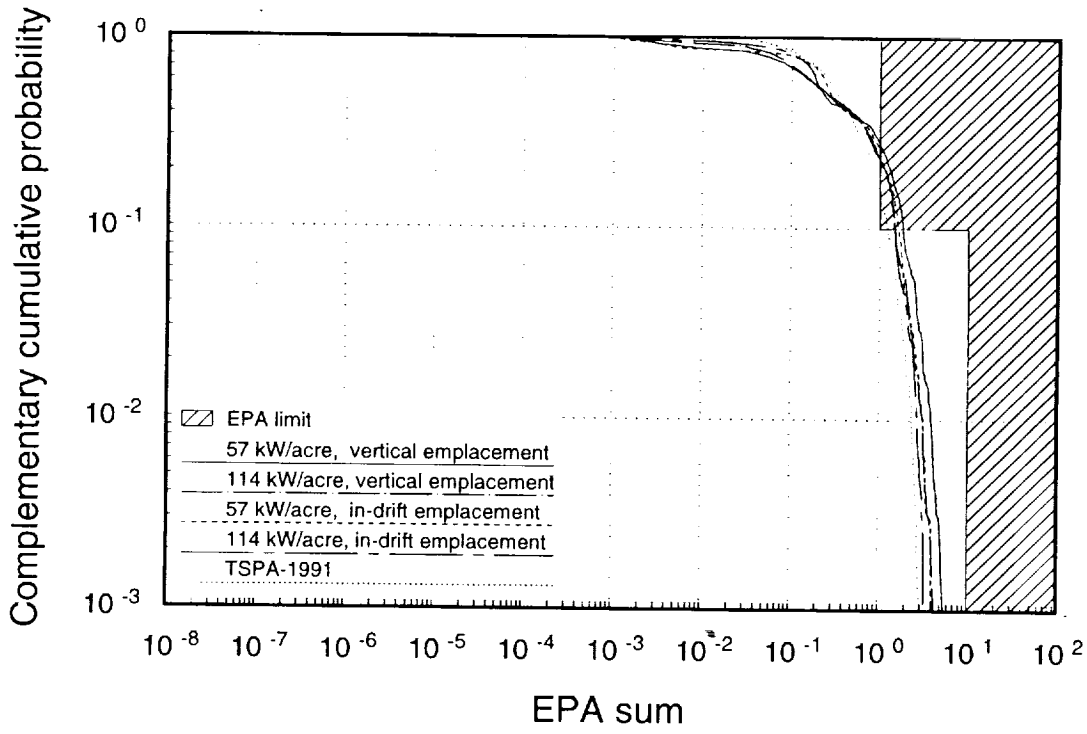

Figure 14-32. CCDFs of normalized cumulative nominal release (aqueous + gaseous) over 10,000 years for the four cases and for TSPA-91.

for container corrosion is strongly temperature-dependent and moisture-dependent, and the two are linked. If the temperature-dependence of the pitting rate for Alloy 825 were reduced, it could also reduce the importance of the container-wetting model—such connections should be investigated.

It is necessary always to keep in mind the limitations of modeling...the models are limited by what we put into them, both in terms of processes modeled and in terms of input data. If the input data are incorrect, we could be misled into drawing false conclusions. If significant processes are left out of the models, they will not tell us so; it is up to us to continue to evaluate processes that have heretofore been neglected in order to determine whether or not they are significant.

With the appropriate caution, then, let us proceed with an examination of the results and their sensitivities. The primary tool used is rank linear regression—linear regression performed upon the ranks rather than upon actual data values. (By ranks, we mean that the values are put in order and the ranks are the order numbers—lowest is 1, second lowest is 2, etc.) A good discussion of the subject, including some of the theory, is given by Helton *et al.* (1991). An application of regression analysis to TSPA-91 results is given by Wilson (1993). A secondary tool, useful for visualization, is the scatter plot (plots of one variable

against another; usually plots of output—EPA release or peak dose rate—against one of the inputs).

First, in Table 14-15, we present results of rank linear regression for 10,000-yr cumulative aqueous releases with 57-kW/acre thermal load and vertically emplaced containers. Results for Column 8 are used for the analysis. The other cases/columns are similar.

The ΔR^2 value is a measure of the relative importance of a parameter (see Helton *et al.*). All parameters with $\Delta R^2 \geq 0.01$ are listed in the table, and in similar tables to come. Note that correlations between input variables complicates the interpretation of ΔR^2 somewhat; some of the importance attributed to a given variable could actually be due to another variable that is correlated with it. Great significance should not be attached to the actual ΔR^2 values listed in Table 14-15 and succeeding tables, but they should be viewed as qualitative indicators of importance. The sum of the ΔR^2s, or R^2 is a measure of goodness of fit of the linear regression (see Helton *et al.*). R^2 near 1 indicates a good fit, meaning that the variation in releases is well accounted for by the parameters used in the regression model. (R^2 is the square of the correlation coefficient between the actual release values and the release values predicted by the regression model.) In this case, $R^2 \simeq 0.77$, which is only a fair fit.

Scatter plots of the most important parameters, shown in Figures 14-33 and 14-34, show why a linear fit is not particularly good: there are two populations, realizations with a climate change within 10,000 years and realizations that have "dry" climate for the whole 10,000 years. This fact is also illustrated in Figure 14-20. If the two populations were separated and linear regression run on each separately, regression fits would probably be much better. The importance of percolation flux and climate change to 10,000-yr releases has already been discussed.

Next, results of rank linear regression for 10^6-yr peak dose rates are given in Table 14-16 for the same case (57 kW/acre, vertical emplacement, Column 8). The R^2 for the regression model is 0.71; once again, only a fair fit. The inclusion of a plutonium sorption coefficient in the regression model is clearly spurious since plutonium does not make a significant contribution to the doses (see Figure 14-28).

Table 14-15. Parameters important to composite-porosity aqueous EPA releases. (57 kW/acre, vertical emplacement, Column 8)

No.	Variable	Units	ΔR^2
1	"dry" percolation flux	m/yr	0.69
2	1st climate-change time	yr	0.07
3	UZ matrix dispersivity	m	0.02

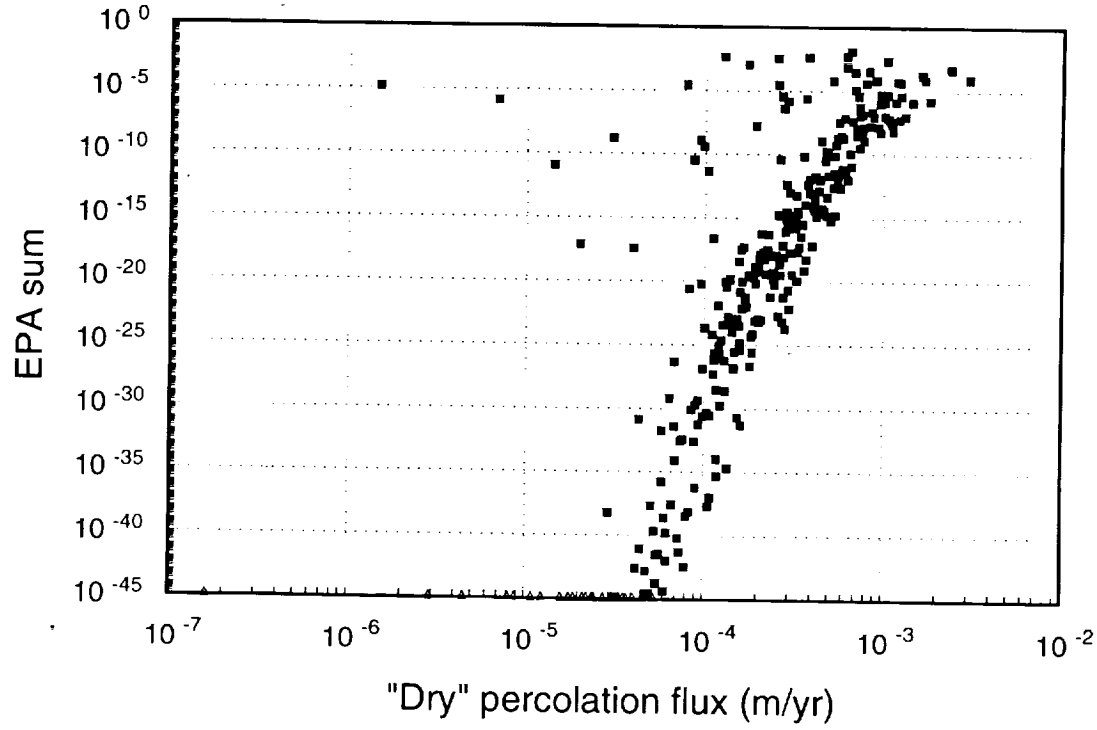

Figure 14-33. Scatter plot of normalized cumulative aqueous release over 10,000 years vs. "dry" percolation flux (57 kW/acre, vertical emplacement, Column 8).

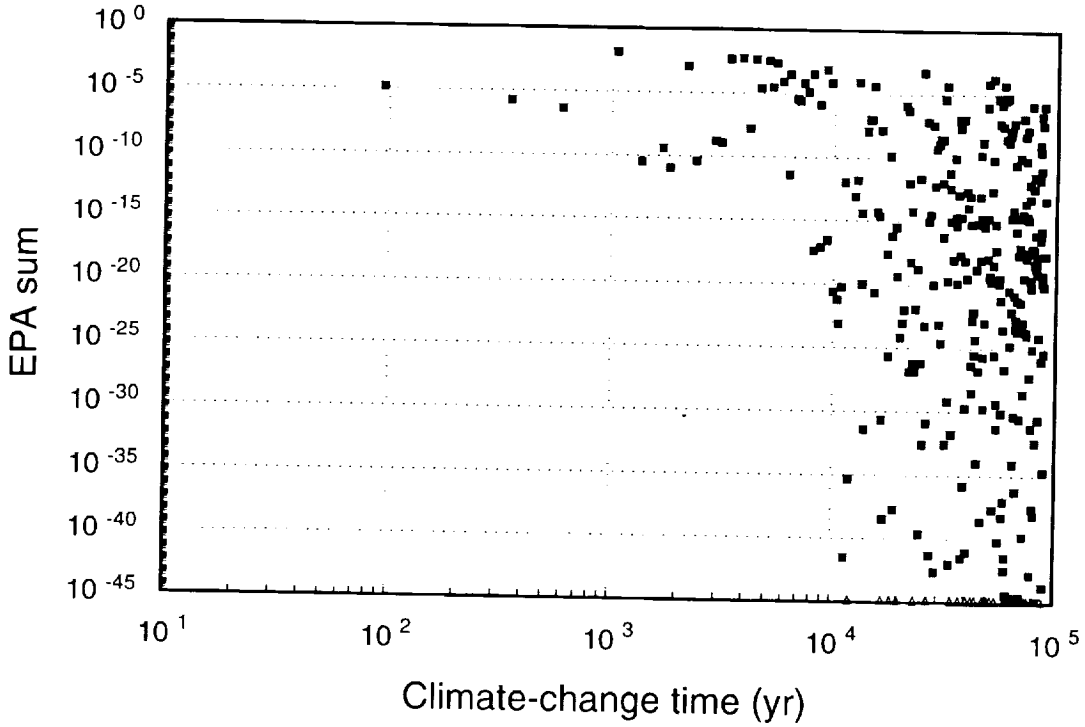

Figure 14-34. Scatter plot of normalized cumulative aqueous release over 10,000 years vs. first climate-change time (57 kW/acre, vertical emplacement, Column 8).

Table 14-16. Parameters important to composite-porosity aqueous peak dose rates. (57 kW/acre, vertical emplacement, Column 8)

No.	Variable	Units	ΔR^2
1	SZ transport area	m^2	0.34
2	"dry" percolation flux	m/yr	0.11
3	TSw matrix conductivity	m/yr	0.07
4	100°C pitting increment	mm	0.06
5	Np solubility	g/m^3	0.05
6	rubble fraction	none	0.05
7	"wet" percolation flux	m/yr	0.02
8	Pu K_d for vitrophyre	m^3/kg	0.01
9	Np K_d for SZ	m^3/kg	0.01

Scatter plots for some of the parameters listed in Table 14-16 are shown in Figures 14-35 through 14-39. The importance of SZ transport area to dose values has already been discussed. "Dry" percolation flux, TSw matrix saturated conductivity, and pitting increment all appear in the list of parameters to which dose rates are sensitive because of their roles in determining how many containers fail. "Dry" percolation flux is more important than "wet" percolation flux because dry-climate conditions usually prevail when container temperatures fall below 100°C, at which time containers that are wet or moist will fail unless the pitting increment is too low (see Figure 14-22 and the accompanying discussion). No trend is readily apparent in Figure 14-37, showing peak dose rate plotted against TSw matrix conductivity, so it is unclear why it appears in the regression model. However, matrix conductivity does enter into the model for determining how many containers are wetted. Neptunium solubility is important because ^{237}Np doses dominate the dose calculation. Only a weak trend is visible in Figure 14-39 because the release rate of ^{237}Np from the EBS depends on neptunium solubility only when the fuel-matrix-alteration rate is low enough. ^{237}Np releases are alteration-limited much of the time.

Lastly, results of rank linear regression for 10,000-yr cumulative gaseous EPA releases are given in Table 14-17, once again for the 57-kW/acre, vertical-emplacement case. The R^2 for the regression model is only 0.59, a rather poor fit.

Scatter plots for TSw matrix conductivity, pitting increment, "dry" percolation flux, and TSw bulk permeability are shown in Figures 14-40 through 14-43. Once again, TSw matrix conductivity, "dry" percolation flux, and pitting increment appear because of their roles in container failure. Figure 14-41 is a very clear demonstration that, when pitting increment is low enough in the model used, containers do not fail. The releases for the low values of pitting increment are all from juvenile-failure containers. TSw bulk permeability appears as an important parameter because of its role in scaling the ^{14}C transport-time curves (see

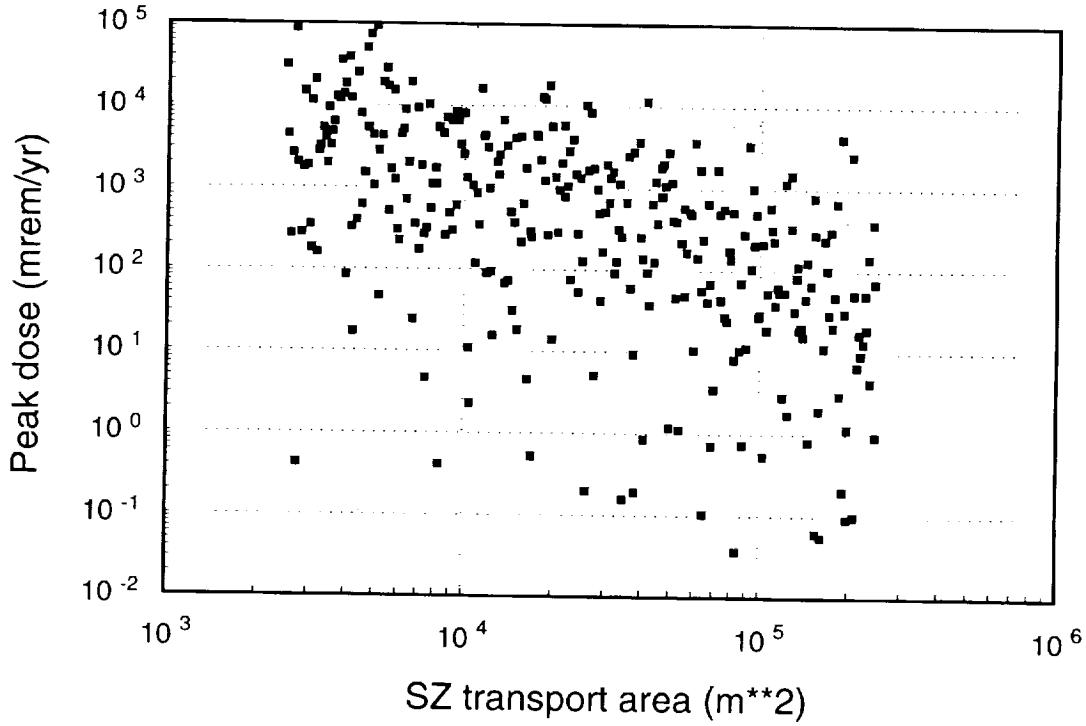

Figure 14-35. Scatter plot of peak individual drinking-water dose rate over 1,000,000 years vs. saturated-zone transport area (57 kW/acre, vertical emplacement, Column 8).

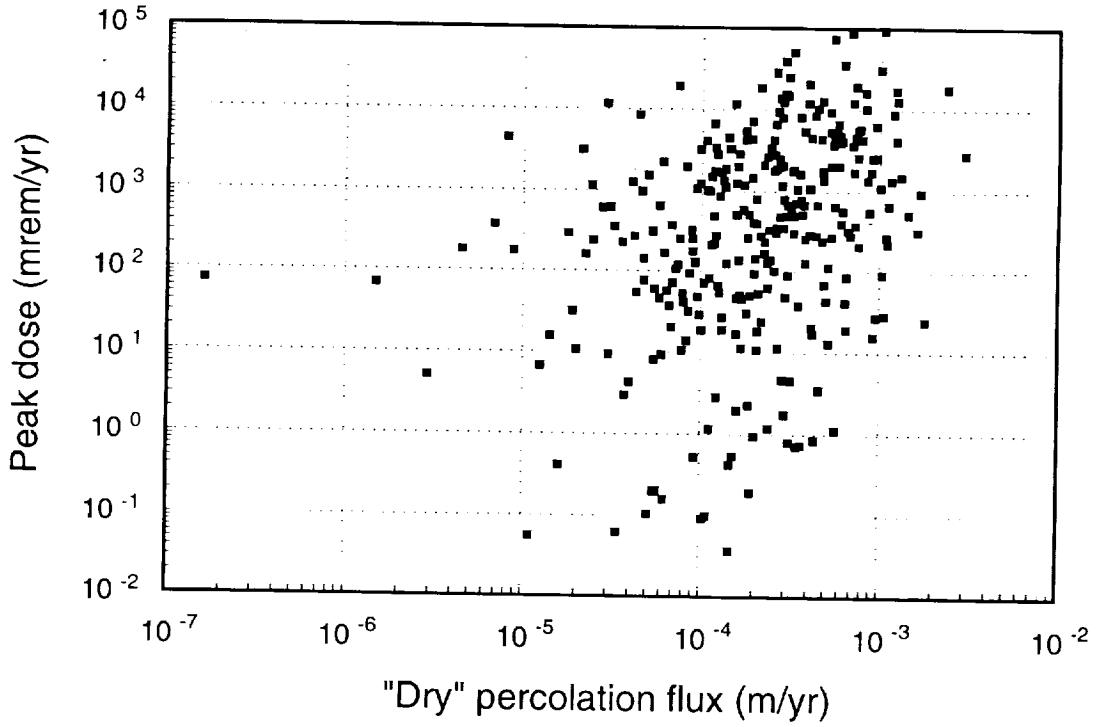

Figure 14-36. Scatter plot of peak individual drinking-water dose rate over 1,000,000 years vs. "dry" percolation flux (57 kW/acre, vertical emplacement, Column 8).

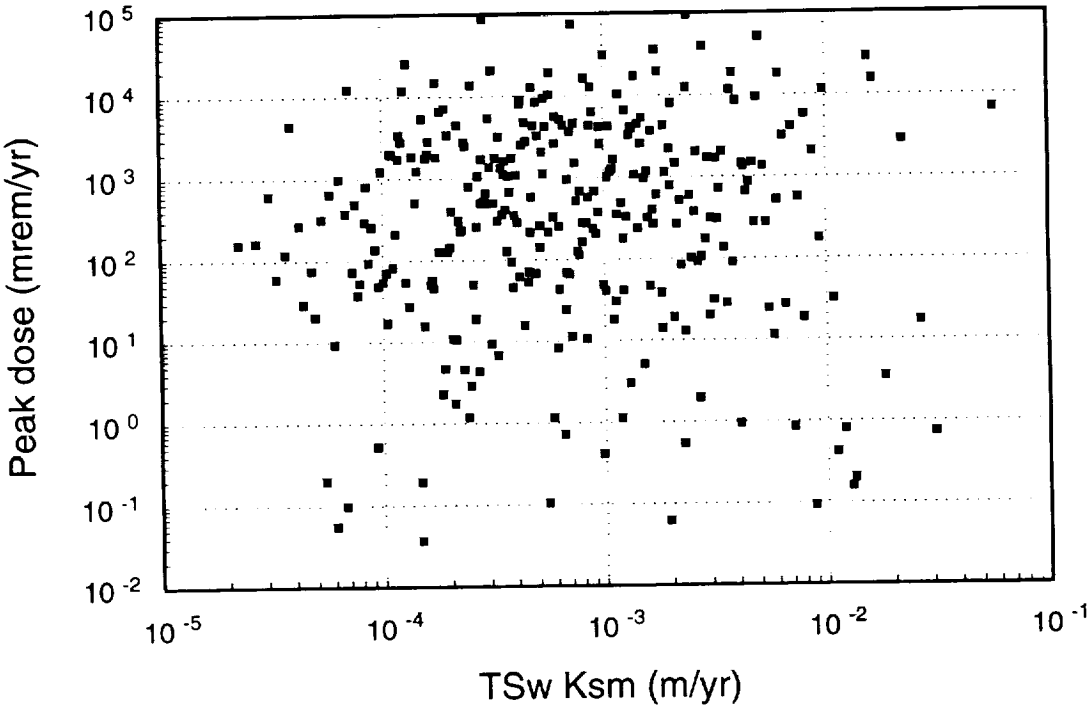

Figure 14-37. Scatter plot of peak individual drinking-water dose rate over 1,000,000 years vs. TSw matrix saturated conductivity (57 kW/acre, vertical emplacement, Column 8).

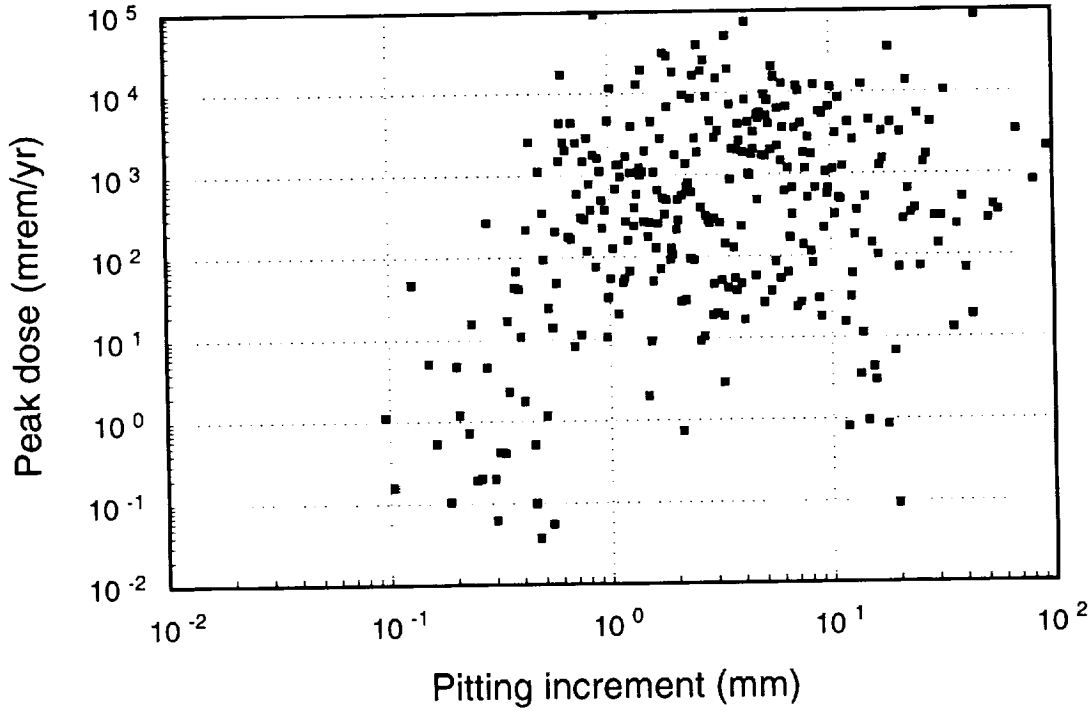

Figure 14-38. Scatter plot of peak individual drinking-water dose rate over 1,000,000 years vs. 100°C pitting increment (57 kW/acre, vertical emplacement, Column 8).

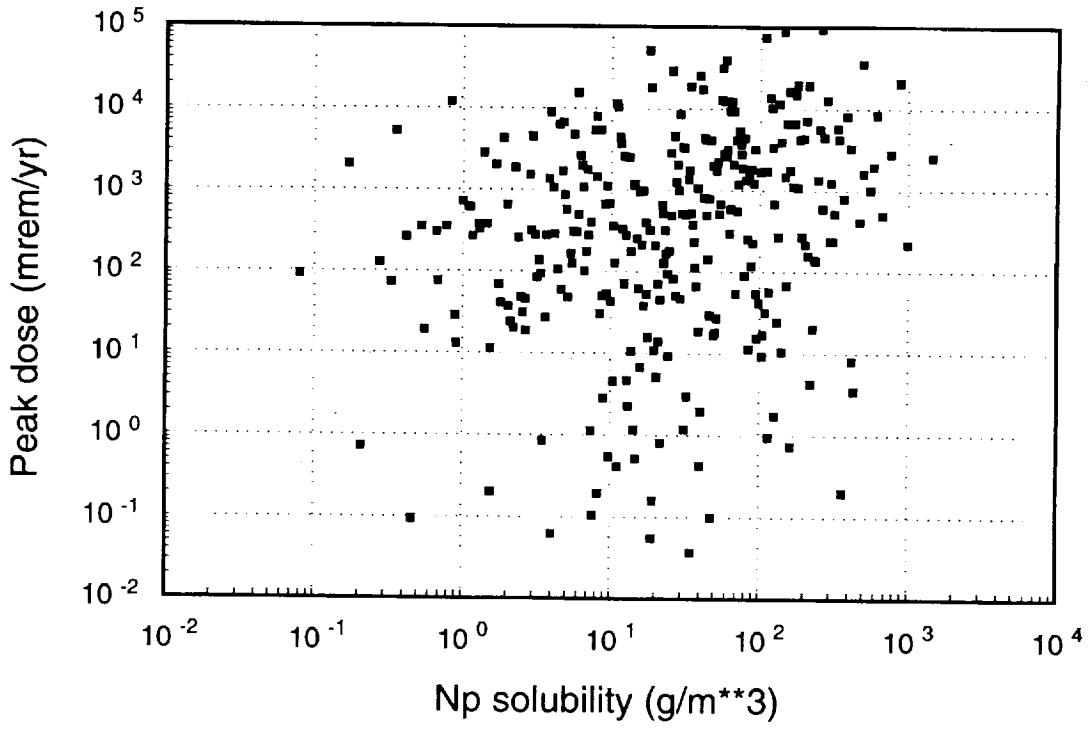

Figure 14-39. Scatter plot of peak individual drinking-water dose rate over 1,000,000 years vs. neptunium solubility (57 kW/acre, vertical emplacement, Column 8).

Table 14-17. Parameters important to composite-porosity gaseous EPA releases. (57 kW/acre, vertical emplacement)

No.	Variable	Units	ΔR^2
1	TSw matrix conductivity	m/yr	0.23
2	100°C pitting increment	mm	0.14
3	"dry" percolation flux	m/yr	0.13
4	TSw bulk permeability	m^2	0.05
5	rubble fraction	none	0.02
6	retardation multiplication factor	none	0.01

Section 12.4). The dependence of releases on permeability would be stronger except that the base transport times are so short. If most of the transport times are small, then they can be scaled by quite a bit and still remain well below 10,000 years.

The above-listed parameters to which the results are sensitive fall into a few categories that appear to be important. First, "dry" percolation flux, "wet" percolation flux, and the first climate-change time all concern percolation and climate change. There is little doubt that percolation and climate change are extremely important if the composite-porosity model has any validity, especially for short times (like 10,000 years).

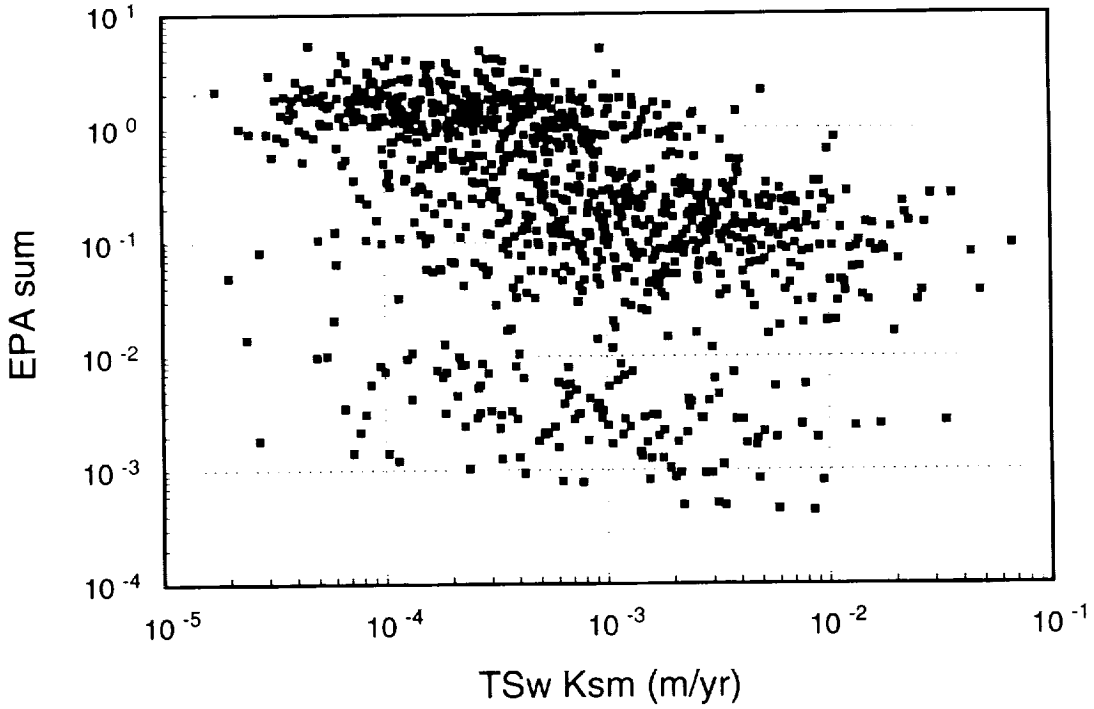

Figure 14-40. Scatter plot of normalized cumulative gaseous release over 10,000 years vs. TSw matrix saturated conductivity (57 kW/acre, vertical emplacement, Column 8).

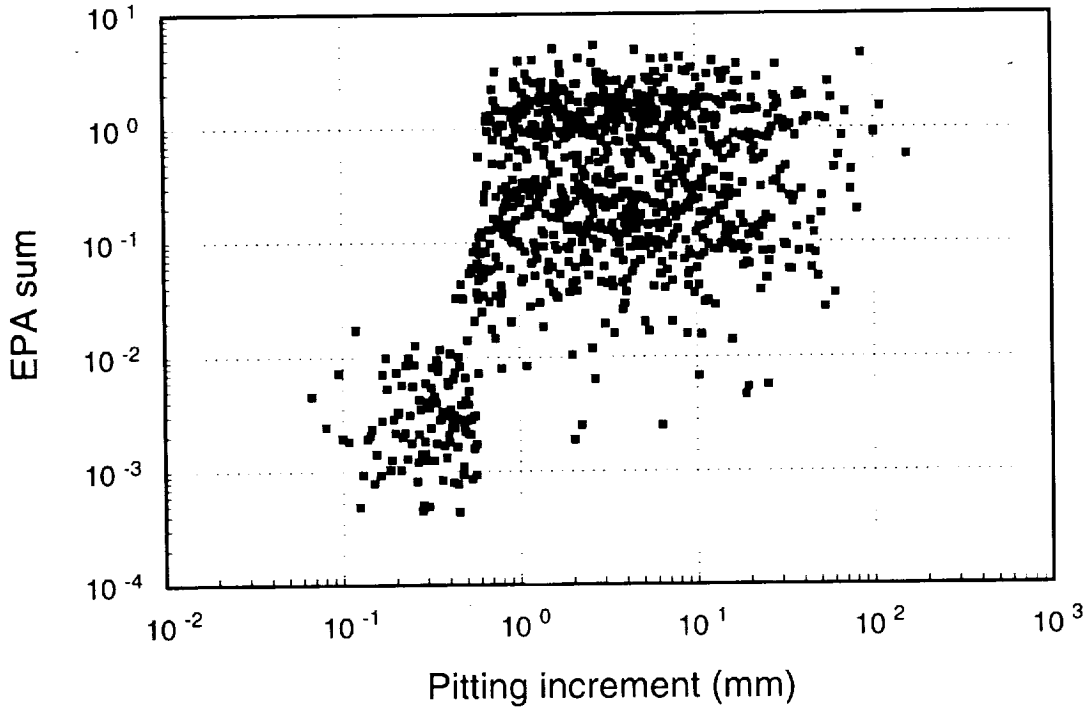

Figure 14-41. Scatter plot of normalized cumulative gaseous release over 10,000 years vs. 100°C pitting increment (57 kW/acre, vertical emplacement, Column 8).

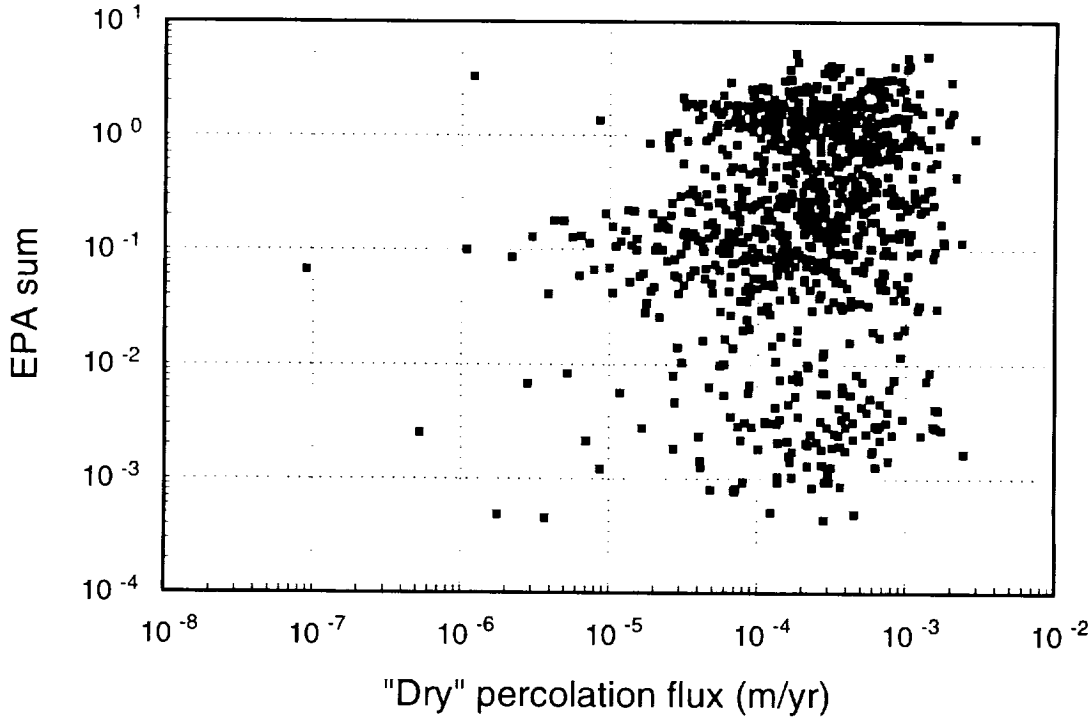

Figure 14-42. Scatter plot of normalized cumulative gaseous release over 10,000 years vs. "dry" percolation flux (57 kW/acre, vertical emplacement, Column 8).

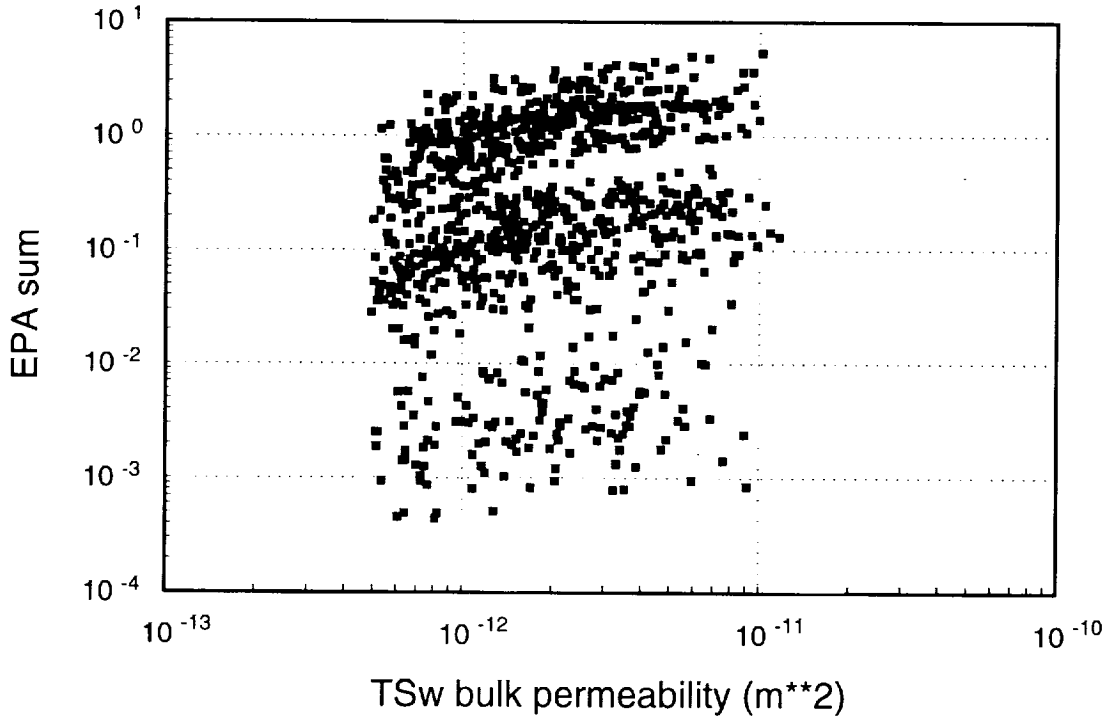

Figure 14-43. Scatter plot of normalized cumulative gaseous release over 10,000 years vs. TSw bulk permeability (57 kW/acre, vertical emplacement, Column 8).

Second, the SZ transport area represents the more general topic of dilution in the saturated zone. For dose-rate calculations, characterization of the saturated zone, and especially its dilution capability, is very important.

Third, the presence of TSw matrix saturated conductivity and rubble fraction (as well as percolation flux) on the list are indicators of the importance of container wetting and near-field water flow to container failure and releases. These processes are not well understood, and it is clearly important to understand container failure as well as possible so that the repository can be designed appropriately.

Fourth, the Alloy-825 pitting increment appears on the list representing the more general category of corrosion processes. For Alloy 825, pitting may be the most important form of corrosion, but other materials corrode differently. Once again, the importance of understanding container failure should be self-evident. We might also add at this point the importance of cladding failure. We included no cladding-failure variability in this TSPA, so it produced no "important parameters," but there is a large potential for reduction of releases by the cladding, the big question being whether we can have confidence in any model or assumptions we make about cladding failure.

Fifth, neptunium solubility represents solubility in general and, even more generally, the topics of waste-package and near-field chemistry and release rates. (Near-field chemistry also affects container corrosion, of course.) There are no variables in the simulations representing fuel-matrix alteration—it is calculated with a deterministic model—but the matrix-alteration rate is certainly important as well.

Sixth and last, TSw bulk permeability and retardation multiplication factor are important for the old EPA measure of cumulative release for ^{14}C (40 CFR 191.13), because they affect how much of the ^{14}C can be transported to the surface in 10,000 years. Their importance is fairly closely linked to the performance measure used, so when the EPA promulgates a new regulation for Yucca Mountain, the importance of these gaseous-transport parameters may change. The two parameters represent the more general areas of characterization of bulk permeability and ^{14}C retardation factor for the whole mountain.

14.7 Conclusions/recommendations

The quantities mentioned in the previous section, on parameter sensitivities, are the ones that appear to be most important, according to our current models. Therefore, these are areas that we recommend be given priority in the site-characterization program:

- Characterize percolation flux—at present and how it may change in the future.
- Characterize saturated-zone flow, especially its dilution capability (horizontal and vertical mixing). This item is very important to dose-rate calculations.

- Characterize bulk permeability and ^{14}C retardation factor. These items are very important to EPA-type gaseous-release calculations.
- Study container-wetting processes and near-field water flow under realistic conditions (e.g., in heater tests).
- Study container corrosion under realistic conditions.
- Study fuel-rod-cladding failure.
- Study waste-package and near-field chemistry; in particular, determine solubilities and fuel-matrix-alteration rates under realistic conditions. With our current models, neptunium, technetium, and iodine appear to be the most important elements.

In addition, it is important to examine our modeling assumptions and determine their validity. Some of the most important are:

- The results and conclusions in this chapter depend on the assumption of the composite-porosity flow model. Site characterization should search for evidence of nonequilibrium fracture flow (weeps) at present and in the past. The possibility of reduced matrix/fracture coupling due to fracture coatings, large effective fracture spacings, etc. should be investigated.
- Our calculations are made with one spatial dimension. As shown in Chapter 23, one-dimensional calculations are appropriate under some circumstances, but evidence of more complicated flow patterns, perhaps associated with fault zones, should be sought.
- Our calculations use very simplified assumptions about thermal effects. Processes such as formation and shedding of condensation caps, thermal and chemical alteration of flow properties, and rewetting after the thermal period should be studied.
- Our calculations do not include any possible effects of colloids. Colloid formation and transport should be studied.
- Our hydrogeologic input dataset is primarily based on measurements of properties using drill core, whereas the block sizes in a typical numerical calculation are meters to hundreds of meters in size. Scaling of properties from small to large should be studied.

Finally, based on the results and parameter sensitivities, we have the following comments and recommendations for repository/waste-package design.

- There is no substantive difference in our results for the four repository cases, so we have no strong recommendation on which one to choose, but we do have lesser recommendations.
- According to the models that we use, the mild-steel outer container of the multipurpose containers does not increase container lifetime significantly. For reference, some additional container-failure results are shown in Figure 14-44. The figure shows that, with our current container-failure models, much thicker container walls are necessary to achieve better performance. However, cathodic protection resulting from having two walls of different metals has not yet been investigated.
- Methods to reduce container corrosion should be sought. If possible, the repository system should be designed so that containers fail over a long period of time, rather than all tending to fail near the same time.
- Container emplacement should be engineered to reduce moisture contact with containers—for example, by borehole emplacement or by capillary-barrier backfill techniques for in-drift emplacement.

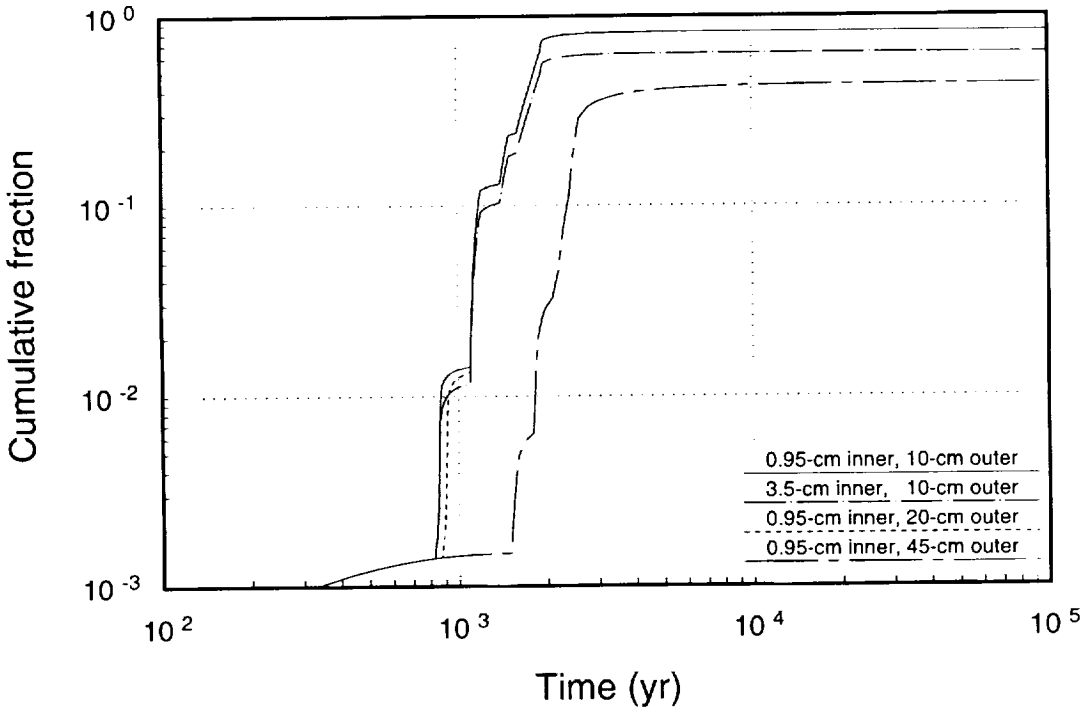

Figure 14-44. Mean distributions of container-failure time for some alternative two-walled containers (57 kW/acre, in-drift emplacement).

- Projected internal waste-package temperatures should not be so high as to cause the fuel-rod claddings to rupture. Even if we are not certain that the cladding will contain radionuclides, it makes sense to promote its effectiveness. The SCP listed thermal goals that were intended to protect the effectiveness of cladding and other barriers; those goals should not be eliminated lightly.

- If possible, the waste packages should be designed to maintain long-term reducing conditions (not for just a few hundred or thousand years).

Chapter 15
Nominal-Case Releases: Weeps Model

(Gauthier)

One concern about locating a high-level radioactive waste repository at Yucca Mountain is that groundwater might not percolate slowly and uniformly through the mountain; rather, it might flow in episodic pulses through the fractures. In this conceptual model of groundwater flow, Yucca Mountain is a sieve, offering waste containers little or no protection from fast moving streams of water. Some evidence exists for this flow mechanism, but the evidence is inconclusive. Locally perched water has been observed at Yucca Mountain (at USW UZ-1, Whitfield *et al.*, 1990, and at USW UZ-14, Dyer, 1993), and approximately 20 km southeast of Yucca Mountain at Skull Mountain (Ingraham *et al.*, 1991). At Rainier Mesa, some 50 km northeast of Yucca Mountain with a tuff stratigraphy similar to Yucca Mountain, substantial flow has been observed through faults and fractures in the unsaturated zone (Wang *et al.*, 1993).

The weeps model was designed to investigate this alternative flow concept. A complete description of the weeps model can be found in Gauthier *et al.* (1992) and TSPA-91.

15.1 Brief description of the weeps model

The weeps model is not a process model; rather it is a mathematical construct based on several postulates or axioms, upon which mathematical transformations are performed. Thus, if the postulates hold, and if the transformations are appropriate and properly parameterized, the results should describe the basic flow conditions at Yucca Mountain.

The most important postulate is that flow within Yucca Mountain occurs vertically downward in locally saturated zones, as suggested in Figure 15-1. That is, flow is gravity driven; capillary effects are negligible. Flowing groundwater therefore does not interact with the bulk of the tuff matrix (if it does, something similar to the composite-porosity model results). Notice that we use the more general term, "locally saturated zones," or more briefly, "weeps." The weeps model need not be restricted to investigate flow only in fractures; it could be used to examine flow in saturated plumes, e.g., fingers, through matrix materials.

Another important postulate is that the weeps only contact the repository at discrete points, and degradation of the repository only occurs at those points of contact (Figure 15-2). If a weep passes through the repository without contacting a container, there is no effect. We assume that containers not contacted by weeps do not corrode. This assumption is not necessarily conservative, because the containers at least undergo dry oxidation, and could be

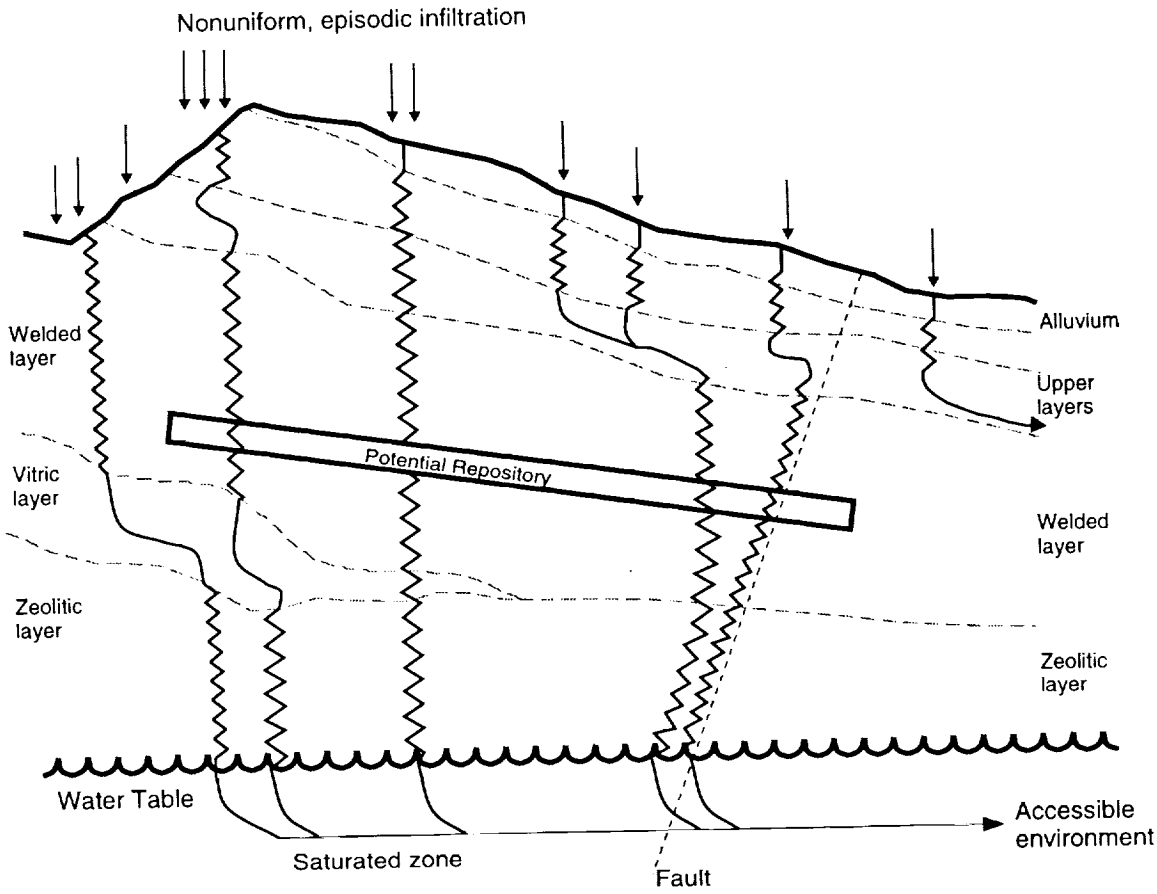

Figure 15-1. Overview of potential weep flow through the unsaturated zone at Yucca Mountain; locally saturated water flow through fractures is indicated by zig-zag lines, flow in saturated plumes through nonwelded matrix is indicated by curved lines.

subject to aqueous corrosion from nonflowing water held in the tuff matrix. In general, we would expect corrosion to be minor in these cases. If containers fail, releases are most likely limited to gaseous radionuclides or diffusion of dissolved radionuclides unless the container is subsequently contacted by a weep. This situation should be addressed in future TSPAs. In TSPA-93, failed containers that are not contacted by weeps are assumed to only release gaseous radionuclides.

The weeps model is parameterized based on descriptions of the weeps and the geometric layout of the repository. Figure 15-3 presents an overview of this parameterization. Weeps are described according to their size, the amount of water they carry, and their flow episodity—which can occur on different timescales. For example, a weep might only flow during pluvial climates, and then only one month out of the year. The repository is parameterized by its overall planar area and the cross-sectional area, i.e., contact area, that the waste containers present to the weeps.

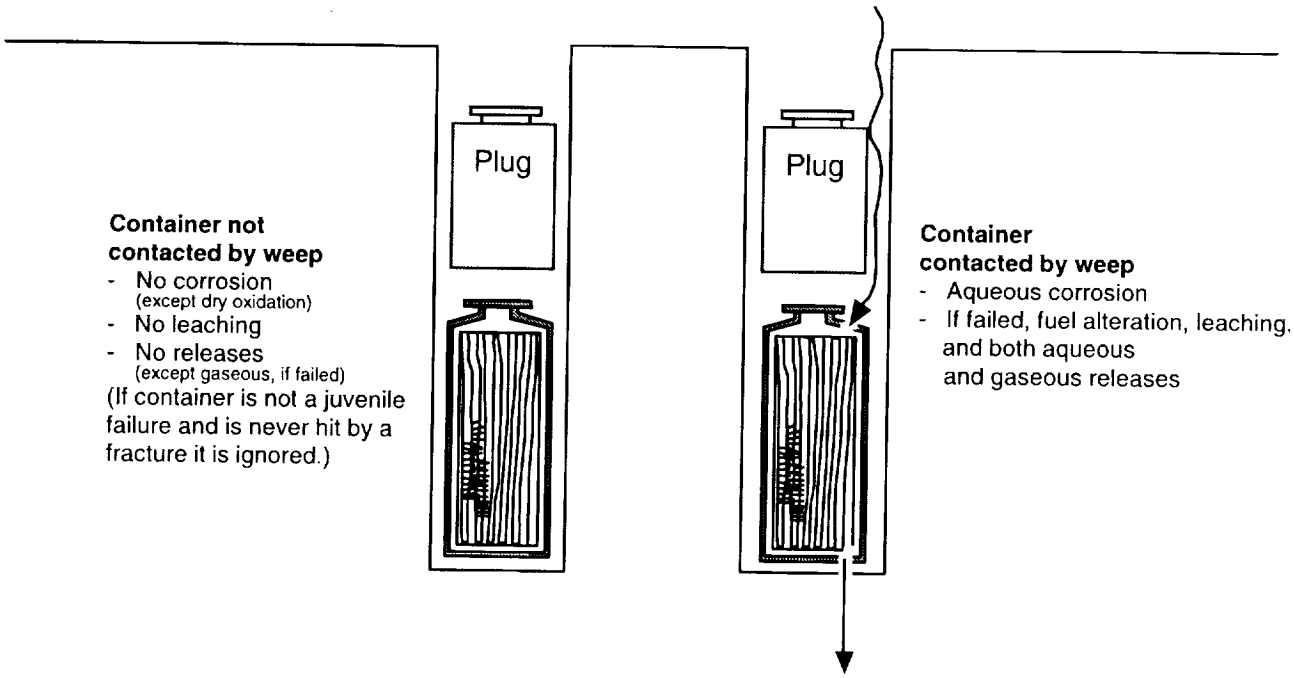

Figure 15-2. Illustration of adjacent containers, one contacted by a weep and suffering degradation, the other not contacted and remaining intact.

Descibing weeps is difficult because we have no reliable data on weeps at Yucca Mountain. We use a surrogate—Rainier Mesa—in our description. At Rainier Mesa, flow is concentrated in several large fractures/faults that are typically most active several months after the spring thaw (Wang *et al.*, 1993). We therefore describe weep flow at Yucca Mountain as flow through fractures. This assumption appears appropriate, at least in the repository block where the highly fractured, low permeability matrix of the Topopah Spring unit could be conducive to fracture flow. However, the porous, permeable matrix of the overlying Paintbrush unit could allow weep flow through the matrix.

Weep size is parameterized by an aperture and a width (a horizontal length). Wilson (1993) showed that results of the weeps model are very sensitive to the aperture and hence to the size of the weeps. Gauthier *et al.* (1992) showed that a large number of small weeps are worse for repository performance than a small number of large weeps. Thus, we believe it is conservative to underestimate weep size. Again, we have no site data concerning weeps, but if weeps tend to flow in faults or larger fractures and fracture zones (as at Rainier Mesa, Wang *et al.*, 1993, and as observed at the STRIPA mine in Sweden, Olsson, 1992), then using general fracture data to describe weeps might be conservative. Therefore, we assume that weeps at Yucca Mountain flow in fractures of any size, and that the distribution of weep sizes is the same as that of fracture sizes.

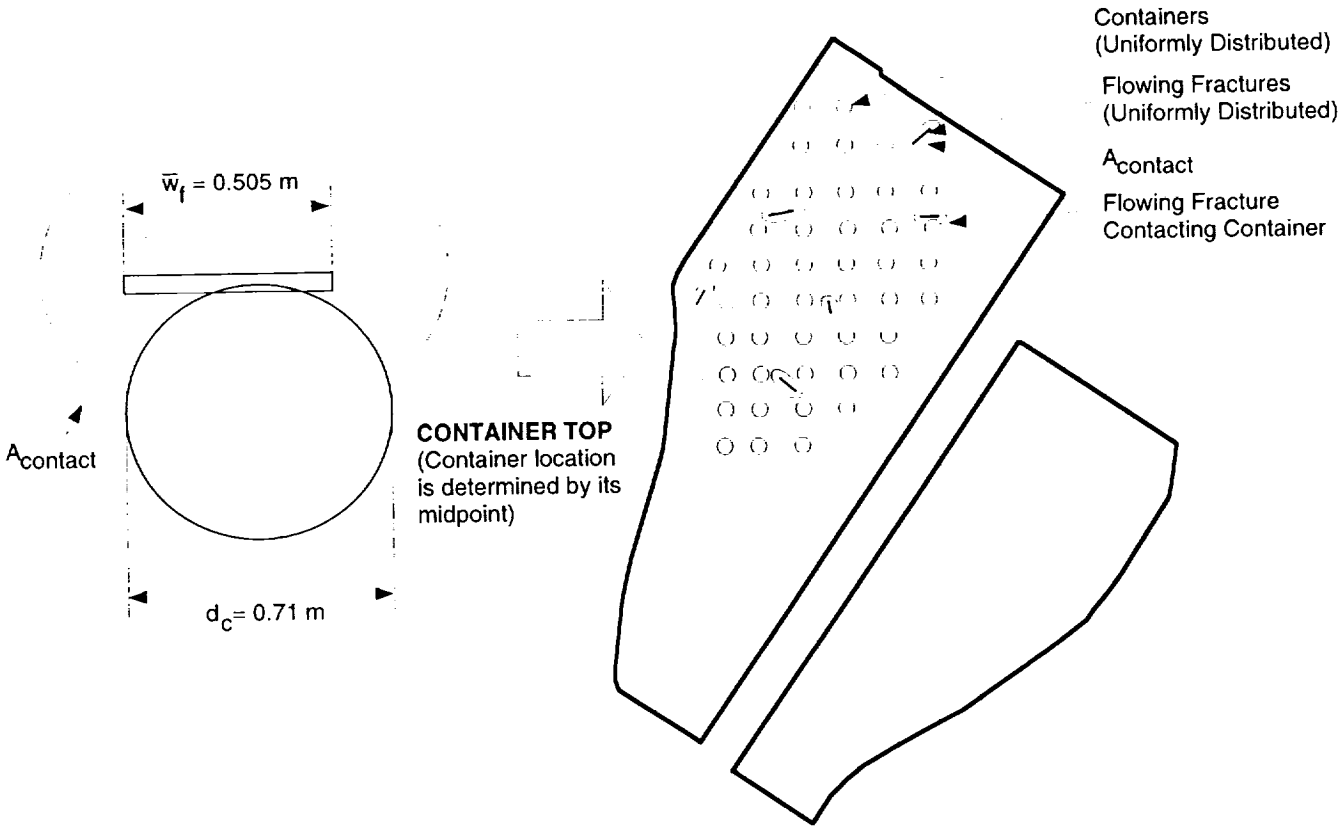

Figure 15-3. Overview of the method used by the weeps model to calculated probability of a weep contacting a container. For uniformly distributed weeps and containers, the probability is the quotient of the area of contact and the area of the repository ($A_{contact}/A_{rep}$).

We further assume that, during a flow episode, a given weep is flowing at the capacity of the fracture it occupies. This assumption allows us to distribute infiltrating water among fractures and compute the number of flowing fractures. Conductivity of the fracture is calculated using the parallel-plate approximation. Flow through the fracture is calculated using Darcy's law, enhanced to take into account nonlaminar flow. The enhancement is based on an empirical model defined by Ward (1964).

The amount of water flowing through the fracture over a given time is dependent on flow episodity, as is evidenced to a certain extent at Rainier Mesa. In this TSPA, the episode factor is constant for all weeps of a given weep pattern. This episode factor is also carried through the calculation involving transient weeps formed during the repository thermal pulse. The number of flowing fractures in a particular flow pattern can then be calculated by generating weeps, and subtracting the amount of water flowing through the weeps from the total infiltrating water, until the infiltrating water is totally distributed.

The results of this weep-flow calculation are the amount of water flowing through each weep, the area contacted by each weep, and the total number of weeps. The amount of flowing water is used by the source term (YMIM) to determine container lifetime (actually only the presence of water below 100°C is used in the corrosion calculation) and wasteform dissolution. The weep area and the contact area of a container are used to calculate the probability of this weep hitting a container.

The velocity of water flowing in weeps can also be calculated, and the travel time from the repository to the water table is typically on the order of days to years. These times are so short that we neglect travel time in the analysis; i.e., the groundwater travel time in the unsaturated zone is assumed to be zero.

Because the weeps model treats each weep and container as a discrete entity, it is necessary to keep track each weep, each container, and each change in flow pattern, whether caused by repository thermal effects or the vagaries of climate. Tracking each weep was considered prohibitive in terms of the needed computer memory, so all weeps are produced, but only weeps contacting containers are tracked.

For TSPA-93, the weeps model was used to produce 1000 realizations in a Monte Carlo simulation of repository performance for each of the four repository designs being examined. Each realization spans one million years. During this time, new weep patterns form, intersecting new sets of containers. These new flow patterns and container sets are calculated at each climate change (Chapter 8) and at each time step during the time period of the repository thermal pulse (Chapter 10). In the model, no memory is maintained of old weep patterns after a climate change; however, changes in weep patterns caused by the repository thermal pulse take into account previously flowing weeps (Section 15.3). The saturated zone is not changed in response to these perturbations for two reasons: first, the assumption that travel time through the unsaturated zone is negligible makes the water-table rise immaterial to the problem; and second, we have no data concerning differences in water velocity in the saturated zone when the water table is elevated.

In our implementation of the weeps model, no interaction is allowed between the tuff matrix and the flow in the fractures. In the composite-porosity model (Chapter 14), flow is allowed in both the matrix and the fractures and the flow is completely coupled. Thus, the weeps model is a bound for matrix-fracture interaction. But the weeps model is *not* a bound for repository performance—i.e., we cannot say that it represents either a best-case or worst-case scenario for releases from the repository. Indeed, when we first developed the weeps model, we thought it might depict the worst-case groundwater flow that a repository might experience; however, Gauthier *et al.* (1992) and TSPA-91 have shown that our intuition was

faulty. We simply offer the weeps model a tool for investigating how a repository might perform if flow is limited to discrete, locally saturated zones through Yucca Mountain.

15.2 Major differences with TSPA-91

Although the basic concept remains the same, several significant changes were made to the weeps model for TSPA-93. The changes were intended to eliminate some of the assumptions made in the previous model, to incorporate new data, and to add some new effects.

A major assumption made in TSPA-91 was that weep-flow could be characterized by considering a single size for all the weeps. The weep size was held constant during a realization, but different realizations considered different weep sizes. This assumption was based on the parallel-plate-fracture approximation that showed flow increasing as a cubic function of the aperture; thus, the largest weeps would pass a disproportionate amount of water and could be used to characterize the entire system. Results of TSPA-91 (Wilson, 1993) proved to be sensitive to the aperture, however, and indicated that the smaller the weeps, the greater the releases, primarily because they contacted more containers. The implication is that small weeps are important. For TSPA-93, weeps of varied sizes are allowed during each realization.

To determine the aperture of a weep in TSPA-91, values were selected from a lognormal distribution with a minimum of 10 μm and a maximum of 1 mm, giving a mean of 214 μm. This distribution was arbitrary, justified only because it seemed to include the values for apertures of fractures typically seen at Yucca Mountain. The aperture for a weep—for any large-scale, connected channel—probably cannot be characterized by observations at a few discrete locations, however. The flow is probably constrained by a few necks or constrictions that appear somewhere in the path. For TSPA-93, we devised a method for determining aperture based on bulk permeability measurements, which should have path constrictions built-in (Chapter 7). The weep apertures are exponentially distributed, with the mean of the distribution chosen at random between a minimum of 100 μm and a maximum of 260 μm for each realization, giving a mean of the mean aperture of 180 μm, the value calculated for the TSw unit (Section 15.4). Because of the lack of data, we still assume that weep sizes are directly related to fracture sizes.

In TSPA-91, weep flow was held constant for the 10,000-year duration of a realization. At the time, we believed that there would be no significant changes, over the next 10,000 years, in infiltration rate or in topology at Yucca Mountain to cause weeps to change location. For TSPA-93, we have added two factors that could cause changes in flux and in the location of weeps: hydrothermal effects and climate change. Inclusion of hydrothermal effects is

discussed in Chapter 10 and Section 15.3. Hydrothermal effects in general and an analysis of the relationship between fracture size and dryout extent are discussed in Chapter 24. Inclusion of climate change is discussed in Chapter 8 and Section 15.1.

In TSPA-91, a "connectivity" factor and an "absorption" factor were included in the weeps model. The connectivity factor defined the fraction of weeps that actually flowed continuously from the surface to the repository. The absorption factor defined the fraction of the aqueous releases from the EBS that was absorbed into the tuff matrix, by matrix diffusion, during transport. Both factors were assigned uniform distributions ranging between 0 and 1, so that in an average realization releases were reduced approximately by 75% for aqueous releases, and 50% for gaseous releases. These reductions were mostly insignificant. The factors were not included in the TSPA-93 weeps model.

For TSPA-91, the source term provided by W. J. O'Connell (LLNL) was modified for implementation in the weeps model. The source term was designed to consider both advective and diffusive releases and to consider the repository as a whole. For the weeps model, only advective releases were considered, and the fraction of the repository considered in the calculation was scaled according to the number of containers contacted by weeps. Juvenile failures were not considered.

For TSPA-93, LLNL's YMIM was added to the weeps model. YMIM is described in Chapter 13. The incorporation of YMIM into WEEPTSA is similar to the incorporation into TOSPAC (Section 14.4), except that each container is considered individually. Juvenile failures are now considered. Further discussion of the implementation of YMIM in the weeps model is offered in Section 15.3.

To evaluate the performace of a Yucca Mountain repository with respect to a possible new criterion, TSPA-93 includes a radiation-dose calculation. The calculation involves only doses accrued from drinking water, and is described in Section 14.2.

15.3 Incorporation of the hydrothermal model and YMIM

The weeps model used in TSPA-91 described all weeps as being of a single size and each flow pattern to be constant for a given realization of weep flow. Thus, all containers contacted by weeps were contacted by the same amount of water for the same duration (the entire 10,000-year performance period). This abstraction allowed a repository-scale source term to be used by simply reducing the size of the repository to the number of containers that were contacted by weeps.

In this TSPA, we allow weeps of varied sizes in every weep-flow realization; therefore, containers can be contacted by different amounts of water. Further, we allow the weep pattern to change in response to thermal effects and climate changes, and therefore the du-

ration of contact can be different for different containers. To track these evolving conditions, the weeps model used in this TSPA accounts for each container individually.

15.3.1 YMIM implementation

Although the LLNL source term, YMIM (Chapter 13), was developed to calculate the failures of and releases from a group of similar containers, it can be used to investigate a single container. To utilize this capability in the weeps model, the entire future water-contact and thermal history of every container is calculated and saved. Then, each container history is examined. If the container is a juvenile failure, or if it is ever contacted by a weep long enough to fail, then YMIM is used to calculate the releases from this container. In the interests of efficiency, the YMIM calculation is terminated when releases stop and the container has no future contact with a weep.

Not all containers contacted by weeps are simulated by YMIM. A simplified corrosion calculation is performed on each container contacted by a weep to determine if it can eventually fail; only a container that can fail is then considered for a YMIM calculation. The simplified corrosion calculation is similar to that used by YMIM, except as follows. For corrosion-resistant materials, i.e., the thin-walled SCP-type container and the inner liner of the multipurpose container, only localized aqueous corrosion is considered and the corrosion is confined to only one pit. For corrosion-allowance materials, i.e., the overpack of the multipurpose container, only generalized aqueous corrosion is considered, and the corrosion parameters are overestimated—0.4 mm/yr at 70°C and 0.8 mm/yr at 100°C. Dry oxidation is not considered in the simplified calculation; the overestimate of generalized aqueous corrosion typically causes the overpack life to be insignificant.

To model temperature-dependent processes, YMIM requires wall and fuel temperatures for a container. For the TSPA calculations, temperature-over-time functions are available for a representative "hot," centrally located container and a "cold," edge container. To determine the temperatures for a given container, the following algorithm was used. If the container was calculated to be within the dryout zone, the hot temperatures were used. If the container was outside the dryout zone, the temperatures were linearly interpolated between the hot and cold temperature functions based on the distance between a container on the edge of the dryout zone and one on the edge of the repository. We estimate these distances by numbering (ordering) the containers according to temperature-distance. We define temperature-distance as an ordering that corresponds to when containers enter and leave the expanding and contracting dryout zone. If a group of containers is never encompassed by the dryout zone, then the temperature-distance is the ordering according to their distance from the dryout zone. Figure 15-4 illustrates this ordering.

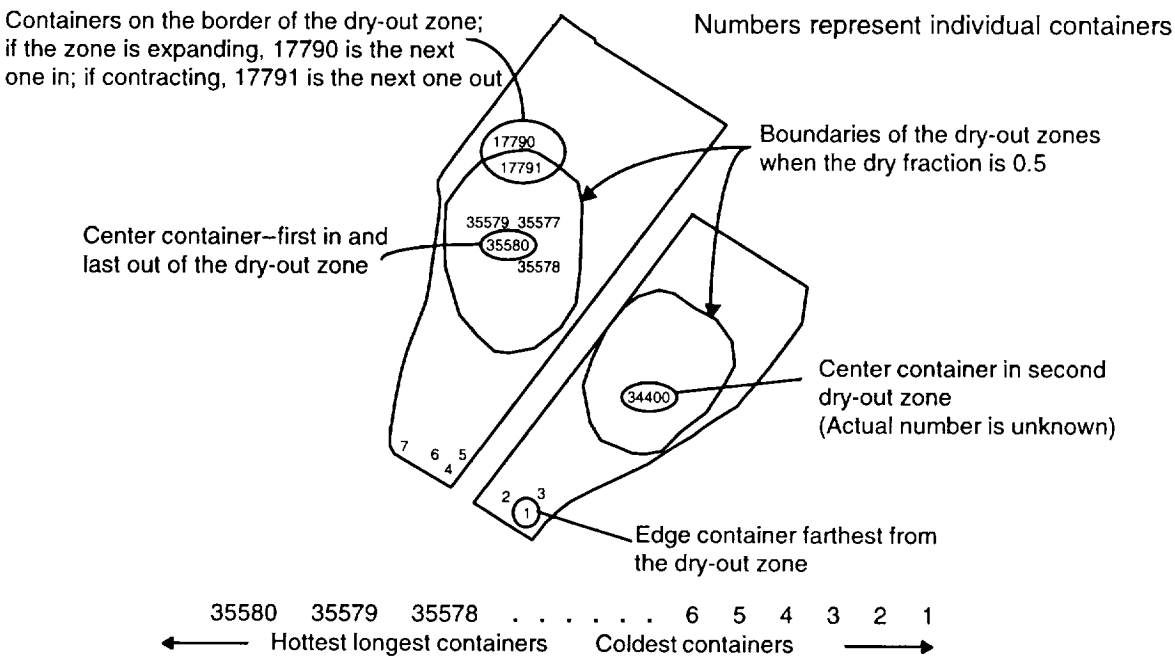

Figure 15-4. Container numbering scheme used by the weeps model for determining container-wall and fuel-rod temperatures. Actual physical locations are unimportant; of significance is how the containers are ordered with respect to distance from the dryout zone or, if a container is ever encompassed by the dryout zone, then the order of entry/exit from the dryout zone.

For example, consider the 57-kW/acre repository, which in our simulations includes containers that are never within the dryout zone. The container located the farthest from the dryout zone—i.e., the representative edge container—is numbered 1; the container located in the center is numbered 35,580 (8489 for multipurpose containers). So if the dryout fraction is 0.5, then containers 1 to 17,790 (multipurpose containers 1 to 4,244) would be outside the dryout zone, while containers 17,791 to 35,580 (multipurpose containers 4,245 to 8,489) would be within. And if container number 1000 was being contacted by a weep, we would determine its wall temperature as follows:

$$T_{wall} = T_{wall,cold} + a_c(T_{wall,hot} - T_{wall,cold}) \ , \qquad (15.1)$$

where a_c is the linear interpolation factor (in this example, $a_c = \frac{1000}{17,791}$), $T_{wall,cold}$ is the surface temperature of a representative container on the edge of the repository, and $T_{wall,hot}$ is the surface temperature of a representative container near the center of the repository. $T_{wall,cold}$ and $T_{wall,hot}$ would be taken from the temperature functions presented in Figure 10-19. The fuel-rod temperature for container 1000 would be calculated similarly.

Behind this numbering scheme are two assumptions: first, that the container distance from the dryout zone and the order in which containers enter and leave the dryout zone can be approximated by a linear function; and second, that as time progresses the temperature-distance relationship remains constant (e.g., the center of the dryout zone does not move and the containers do not reorder with respect to the center). We anticipate that these assumptions are not perfect, because of heterogeneities, edge effects, and irregular placements of containers. However, this ordering is probably reasonable at this stage in the TSPA process because the actual design of a repository is undecided, and further, variations in dryout-zone distance might not be significant.

Modeling of juvenile failures is handled differently for the weeps model and the composite-porosity model (Sections 14.4 and 14.5). For the weeps model, juvenile failures are assigned at random to individual containers. For the composite-porosity model, they are assigned to a population of containers. For the weeps model, the time of failure for each juvenile-failure container is specified by a uniform distribution between 0 and 100 years. For the composite-porosity model, juvenile-failure times are exponentially distributed in time with a mean of 300 years. The weeps model specifies failure time using YMIM's mechanical-failure input variables; the composite-porosity model uses the defective-container input variable. For the weeps model, the intent is that failures occur at an instant within this 100-year period; however, YMIM distributes the "failure" over the entire period. Thus, all juvenile failures fail during the first time step of a weeps calculations (0 to 0.25 years), but the prompt releases are spread over the 100-year failure period. The same fraction of juvenile failures is specified for both models in each of the repository cases.

15.3.2 Hydrothermal model implementation

As the dryout zone expands and contracts, changes are expected to occur in the flow pattern. As implemented in the weeps model, these changes take into account previously flowing weeps, thus providing some memory in the process. (As mentioned in Section 15.1, when a climate change occurs the weeps model produces an entirely new pattern, without memory of previously flowing weeps.)

When the dryout zone is expanding, weeps that fall within the growing protected area of the repository are eliminated. Then, an effective flux over the new unprotected part of the repository is calculated from both the water displaced by the dryout zone and the diverted infiltrating water (Equation 10.2). The difference between the new flux and the old flux over the new unprotected area is used to calculate how much water should be added to the weep flow. This amount of water, as modified by an episodity factor, is used to generate weeps in the new unprotected area until the water is depleted. (The assumption of episodic flow in

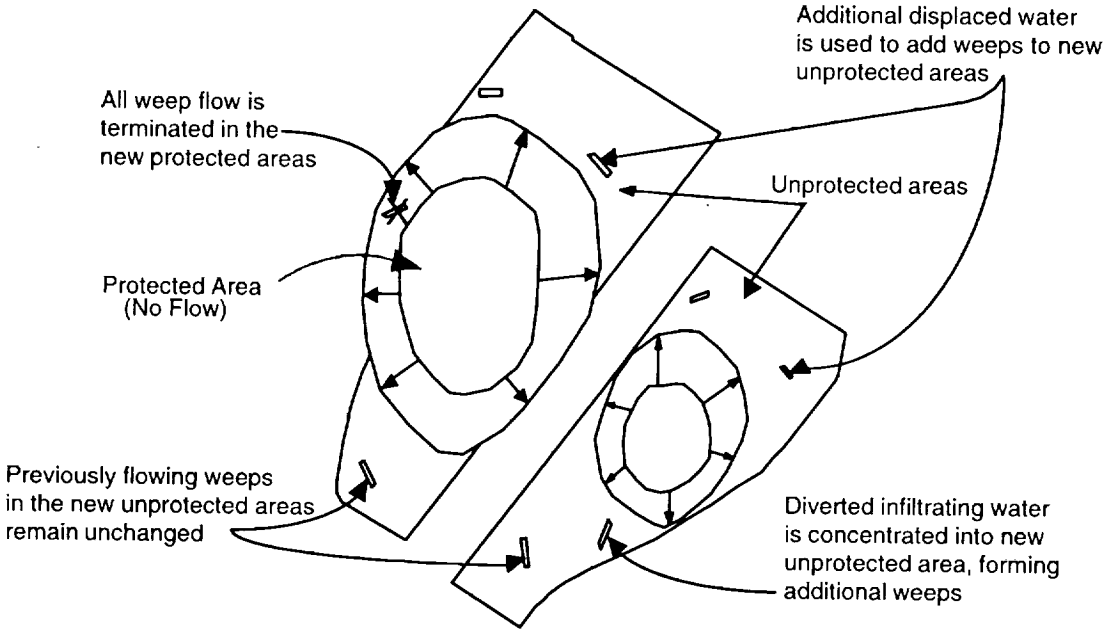

Figure 15-5. Illustration of flow-pattern changes calculated by the weeps model when the dryout zone is expanding.

these weeps should be reexamined, because these weeps might be fed by a fairly constant recharge.) The weeps that had been flowing in the new unprotected area continue unabated. Figure 15-5 illustrates flow-pattern changes during dryout-zone expansion.

The numbering scheme shown in Figure 15-4 is used to determine what containers and what repository area are affected by the dryout expansion. For example, if the dryout fraction increases from 0.5 to 0.6, then SCP-type containers 17,790 down to 14,232 (multipurpose containers 4,244 down to 3,396) become protected, and any weeps contacting containers within that range are terminated. The additional flux from the displaced water and the increased focusing of the diverted water is then used to create additional weeps in the unprotected 40% of the repository. Thus, for our example, containers within the range of 1 to 14,231 (multipurpose containers 1 to 3395) could be contacted by these new weeps.

When the dryout zone is contracting, displacement of water ceases, and infiltrating water is spread over an ever increasing area of the repository. New weeps are formed in the formerly protected areas, and some weeps are eliminated in the unprotected areas. Figure 15-6 illustrates flow-pattern changes during dryout-zone contraction.

During the design of the weeps model used in this TSPA, it appeared impractical to remember the characteristics of every weep generated for a given flow pattern, and therefore, only weeps that contact containers are saved at any particular time during a computer simulation. This decision leads to a problem when eliminating some, but not all, weeps from

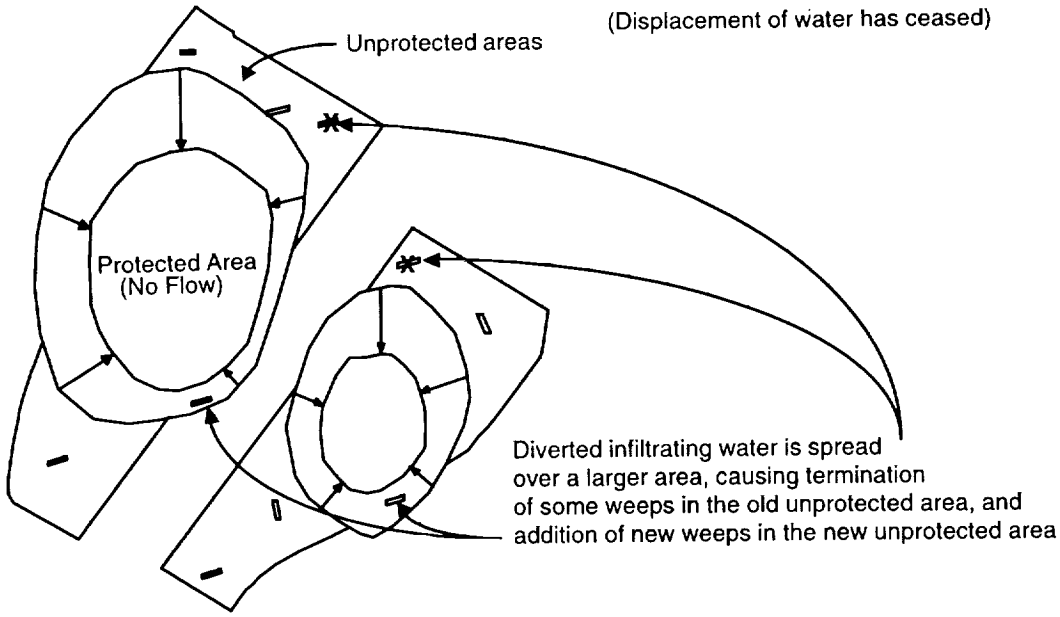

Figure 15-6. Illustration of flow-pattern changes calculated by the weeps model when the dryout zone is contracting.

an area, because the eliminated weeps should be selected randomly (we have no information on how to eliminate them, therefore random selection should preserve our uncertainty), but the weeps that have not contacted containers have been forgotten. Thus, we subtract water from weeps that contact containers in proportion to the amount of water that should be subtracted from all the weeps in the area. To calculate the amount of water subtracted only from weeps that contact containers, we first calculate the total reduction in flow (Q_{less}) over the old unprotected area (A_{old}):

$$Q_{less} = Q_{total} \frac{A_{new} - A_{old}}{A_{new}} , \tag{15.2}$$

where Q_{total} is the flow rate over the entire repository, and and A_{new} is the new, larger, unprotected area. (In WEEPTSA, this equation is written in a more general form that allows for changes in flow rates from one time step to the next. Typically, however, the flow rate with respect to the entire repository does not change when the dryout zone is contracting.) Then we reduce the weep water that is contacting containers by the following amount:

$$Q_{sub} = \frac{Q_{less}}{Q_{total}} \sum Q_i , \tag{15.3}$$

where Q_{sub} is the amount of water (flow rate) to be subtracted, and $\sum Q_i$ is the sum of all water (flow rates) contacting containers. Once the amount of water to be subtracted is known, a weep that contacts a container in the area is selected at random. If the amount of

water to be subtracted is less than the amount of water in the weep, then the weep water is reduced by the appropriate amount and the process is terminated. If more water is to be subtracted than is flowing in the weep, the weep is eliminated, the amount of water to be subtracted is reduced, another container-contacting weep is selected at random, and the process is repeated until all the water to be subtracted is removed from the area.

Once the flow through the old unprotected area is reduced, new weeps are generated with the amount of water Q_{less}. These weeps are distributed over the entire new unprotected area.

For example, if the dryout fraction decreases from 0.6 to 0.5, the number of unprotected containers increases from 14,232 to 17,790 (multipurpose containers 3,396 to 4,244). The flow rate in the former unprotected area is reduced by 20% ((0.5-0.4)/0.5 = 0.2) and this 20% is spread over the 50% of the repository that constitutes the new unprotected area. Cans numbered 1 to 17,790 (multipurpose containers 1 to 4,244) are then subject to the possibility of new contacts with weeps.

Because some container-contacting weeps typically remain from the previous flow pattern, the new pattern can have less weep-population density in the formerly protected area. This effect is compounded when, during the dryout expansion, weeps are concentrated into an ever decreasing area, thus causing very high weep-population density around the fringes of the repository. If the hydrothermal model used in this TSPA sees continued use in future TSPAs, this situation should be examined. Two alternatives are to make either the weep-population density more uniform, or to force the displaced and diverted water into a band around the dryout zone. At this time, we have no data to suggest that either of these alternatives is more realistic.

15.4 Parameters

Weep-flow parameters used by the weeps model are presented in Table 15-1. A footnote to Table 15-1 indicates that the weep-aperture distribution presented in Chapter 7 was modified. The reason was pragmatic: solving the inverse incomplete beta function for tens of thousands of weeps each time a flow pattern changed required excessive computer time. The change is justified because the coefficients of variation for the fracture-aperture distributions of the units in the unsaturated zone (Table 7-18) are approximately 1, indicating approximately exponential distributions (the average of these coefficients is very close to 1).

The distribution for the mean weep aperture is based on the 180 μm mean fracture aperture for unit TSw given in Table 7-18, with a spread large enough to encompass the mean apertures for the other units. Distributing this parameter allows its involvement in the sensitivity study described in Section 15.6. (In the sensitivity study performed by Wilson,

Table 15-1. Weeps-model parameters used for flow calculation.

Model Parameter	Distribution or Value
Weep aperture	exponential—see Table 7-18[a]
Mean weep aperture	uniform from 100 to 260 μm[a]
Weep width	uniform from 0.01 to 1 m
Flow episode factor	loguniform from 1 to 100
Hydraulic gradient	1
Density of water	1000 kg/m^3
Dynamic viscosity of water	31,621 kg/m-yr
Gravitational acceleration	9.77×10^{15} m/yr^2
Dry-climate percolation rate	see Table 8-1
Wet-climate percolation rate	see Table 8-1
Climate-change times	see Table 8-1
Flow-pattern-change times	same as climate-change times[b]
TSw moisture content	0.065

[a]Chapter 7 distribution modified; see text.
[b]Flow patterns also change with changes in hydrothermal environment, see Chapter 10 and Section 15.3.

1993, for TSPA-91, the weep aperture was indicated as a critical parameter; however, for TSPA-91 the weep-aperture distribution had a much greater variance and the weep aperture was handled much differently in the calculations.) The distribution for the weep width is arbitrary because of the lack of data, and it is the same as that used for TSPA-91.

The weeps model requires several repository-related dimensions to solve for the probability of a weep contacting a container. These parameters are given in Table 15-2. As discussed below, most source-term parameters for YMIM in the weeps model are the same as those used in the composite-porosity model. Exceptions are the juvenile-failure times, which are given in Table 15-2.

Table 15-2. Repository-related parameters required by the weeps model.

Model Parameter	Distribution or Value
Number of containers (vertical)	35,580
Number of containers (in-drift)	8489
Container diameter (vertical)	0.71 m
Container diameter (in-drift)	1.75 m
Container length (in-drift)	4.91 m
Juvenile-failure fraction (in-drift)	uniform from 0.0005 to 0.0025
Juvenile-failure fraction (vertical)	uniform from 0.001 to 0.005
Juvenile-failure times	uniform from 0 to 100 yr[a]
Area of repository (57 kW/acre)	4.63×10^6 m^2
Area of repository (114 kW/acre)	2.33×10^6 m^2
Contact area	see Figure 15-7

[a]See Section 15.3.1.

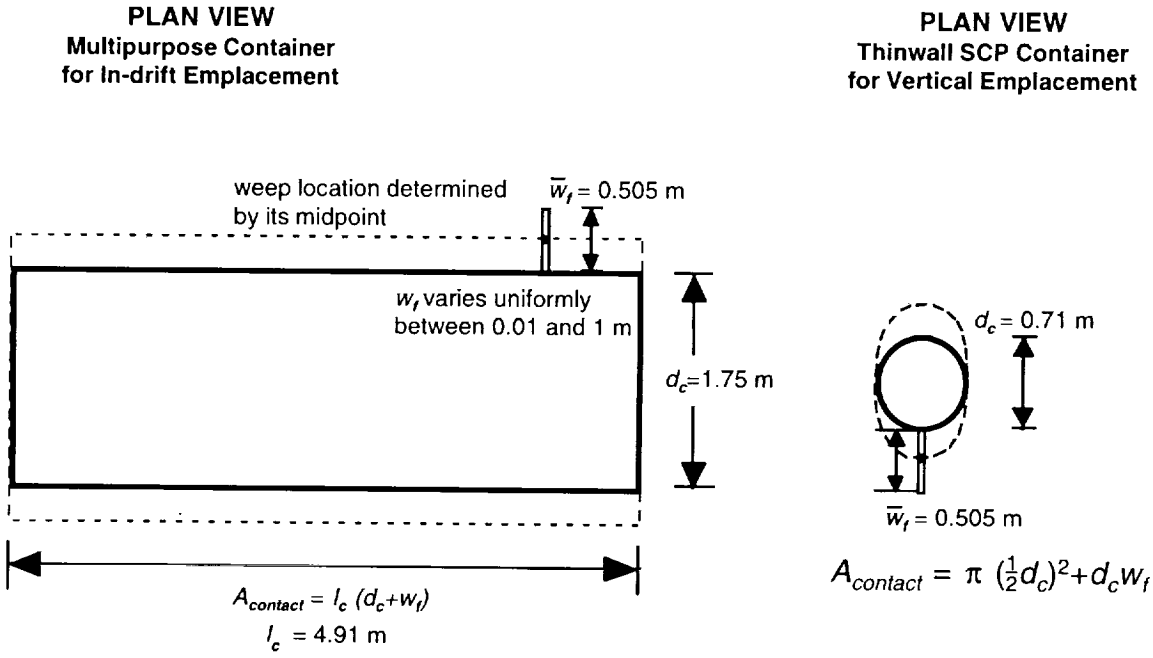

Figure 15-7. Calculation of the area in which a weep can intercept a container ($A_{contact}$).

Figure 15-7 illustrates how the contact area is calculated for the two different container sizes. The contact area shown for the in-drift, multi-purpose container is a worst-case estimate because it only considers the weep orientation that produces the greatest area. Considering all orientations results in a 10% decrease in the contact area. However, fractures and faults at Yucca Mountain appear to have a preferred orientation. Carr (1992) reports faults with a north-northeast strike. Lin *et al.* (1993) report fracture strikes in the Topopah Spring member of N10°W, N25°E, and N45°E for drillhole USW GU-3, and N12°W and N-N40°E for drillhole USW G-4. These orientations are close to right angles to the in-drift emplacement. Because the vertically-emplaced container presents a circular profile, all angles of orientation result in the same contact area.

Because of the assumption of negligible groundwater travel time in the unsaturated zone with the weeps model, only the saturated zone was considered for radionuclide transport. Saturated-zone hydrology parameters are given in Table 15-3.

The water velocity differs from those used with the composite-porosity model (Table 11-7), because there is no discrimination between flow in underlying units. With the composite-porosity model, columns were connected to the saturated zone at locations that correponded to specific geologic units—i.e., radionuclides from column 1 were released into

Table 15-3. Parameters used by the weeps model for calculating saturated-zone flow.

Model Parameter	Distribution or Value
Water velocity	uniform from 5.5 to 12.5 m/yr
Dispersivity	uniform from 100 to 500 m
Porosity	0.2[a]
Flow-tube length (57 kW/acre)	7800 m[b]
SZ source region (57 kW/acre)	2500 m[b]
Flow-tube length (114 kW/acre)	6400 m[b]
SZ source region (114 kW/acre)	1100 m[b]

[a]See Section 11.6.3.
[b]See Figure 15-8.

the BFw unit at the water table. The weeps model presently considers the repository as a whole, and therefore radionuclides are released to all the units underlying the repository in the saturated zone. The water velocity distribution in Table 15-3 encompasses the velocity distributions for the individual columns in Table 11-7.

The weeps model also only used a single flow tube to represent the entire saturated zone; the composite-porosity model used a different flow tube for each column. Figure 15-8 illustrates the flow-tube layouts used for the two different repository thermal configurations.

Saturated-zone transport parameters used by the weeps model are the same as those used for the composite-porosity model and are given in Table 14-12. In the TSPA-93 weeps model, sorption is only modeled in the saturated zone. Sorption coefficients are given in Table 9-4. The substrate for sorption in the saturated zone is assumed to be devitrified tuff.

A number of other parameters used in the weeps model are also the same as those used in the composite-porosity model. The list of radionuclides and their properties are given in Table 14-5. Hydrothermal parameters are given in Table 14-6. Physical parameters and geochemical parameters associated with the source term are given in Table 14-7. Parameters for container and fuel-rod failure are listed in Table 14-8. Table 14-9 contains fuel-alteration and pulse-release parameters.

Parameters used in defining gas flow and transport are the same as those used in the composite-porosity model and are listed in Table 14-13. Properties of ^{14}C are given in Table 14-5. Weeps-model parameters for calculating the ^{14}C source are the same as those for calculating aqueous releases (Tables 15-1 and 15-2). YMIM source-term parameters governing ^{14}C releases are given in Tables 14-7, 14-8, and 14-9.

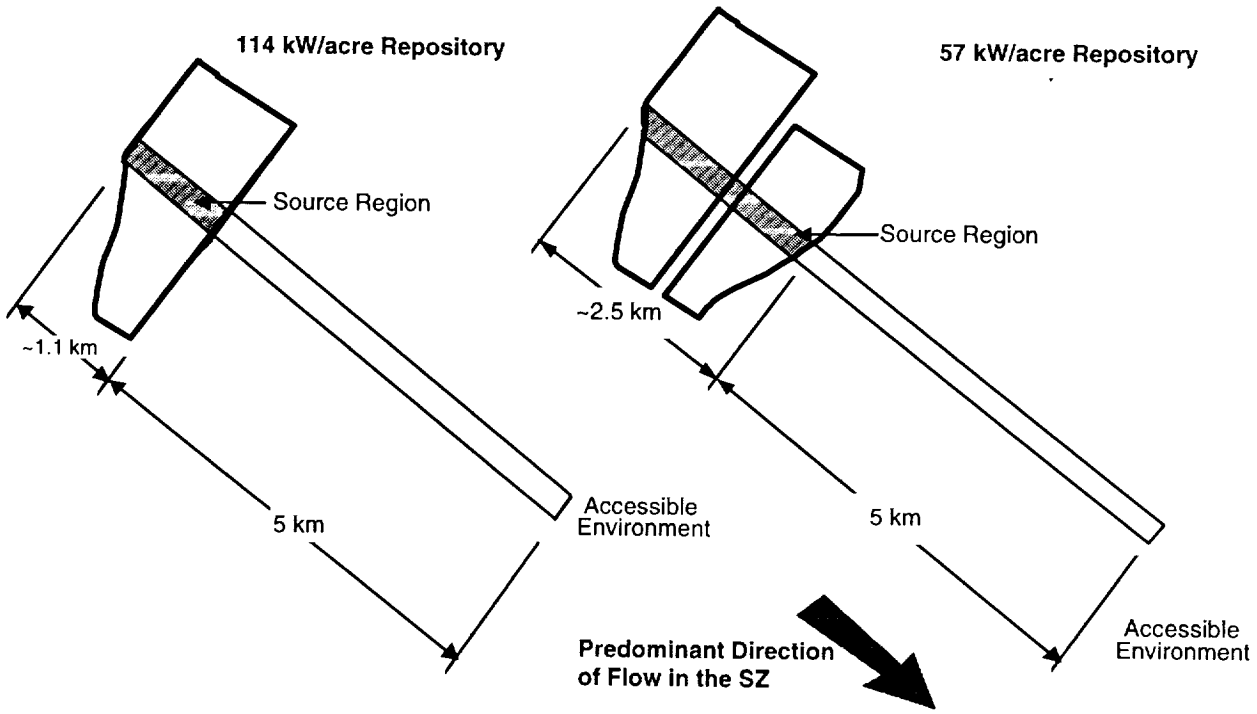

Figure 15-8. Layout of the one-dimensional flow tube used to describe the saturated zone for a weeps-model calculation.

15.5 Results

Weeps-model results are primarily based on two performance measures: (1) the U. S. Environmental Protection Agency (EPA) standard from 40 CFR Part 191 (EPA, 1985), which is loosely based on radiation dose to a population, and (2) a possible dose standard involving radiation dose to a maximally exposed individual. However, the weeps model is inherently a probabilistic representation of the future performance of a repository (even a single realization involves flow fields selected probabilistically). Thus, it is useful to examine statistics associated with the behavior of the weeps model to allow us to understand the predictions related to the performance measures.

In this section, we first examine the general behavior of the weeps model by looking in some detail at the results for the 57-kW/acre repository with vertically emplaced containers—the base case for this TSPA (and the only case considered in TSPA-91). Of interest is how the model predicts the response of this repository to hydrothermal effects, climate change, etc. Once we know how the model acts for the base case, we compare all four cases. Both aqueous releases and gaseous releases are discussed, but results for gaseous releases are

only compared to the EPA standard because the individual dose from gaseous releases is expected to be negligible. We then report on several sensitivity studies that investigate which of the input parameters cause the greatest variation in releases—i.e., the parameters on which the results are most dependent. The section concludes with a discussion of the assumptions and limitations inherent in the results.

15.5.1 Base case

15.5.1.1 Typical realization

The weeps model was used to perform 1000 realizations in a Monte Carlo simulation of the 57-kW/acre repository with vertically-emplaced containers. Each realization simulates 1,000,000 years of repository life, beginning with a thermal perturbation of the environment and including 21 climate changes that alternated between dry and wet periods. In the EBS, different containers at different temperatures are contacted by weeps for varying durations. Figure 15-9 presents a overview of the general behavior of the weeps model.

A weeps-model calculation begins by determining which containers are juvenile failures. For the base case, between 0.1 and 0.5% of the containers are specifed to fail within the first 100 years of the repository life; with 35,580 containers, the average is approximately 100 containers. Immediately upon failure, these containers begin releasing ^{14}C (the only gaseous radionuclide under consideration) and their UO_2 fuel begins oxidation alteration.

The initial flow calculation determines the weep-flow pattern through a repository for a given time period as follows. A dry-climate infiltration rate (to simulate the current climate) is selected and multiplied by the area of the repository to produce a volumetric flow rate. The amount of water displaced by the expanding dryout zone over this time period is then calculated and added to the flow rate. This flow is then distributed in episodically flowing weeps over the unprotected region of the repository. Typically, only a few hundred weeps are required to handle the flux during a dry climate, and only a few containers are contacted by weeps. If a contacted container is not a juvenile failure, nothing happens because the container wall is too hot to undergo aqueous corrosion. If one of the contacted containers is a juvenile failure (and it almost never is this early in a simulation), then radionuclide dissolution—i.e., release from the EBS—begins, even though the container could be well above boiling (this effect is a problem with the YMIM model, but it is inconsequential in the final results, as shown by the lack of sensitivity to juvenile failures for aqueous releases, see Section 15.6).

As time passes, the dryout zone increases in size and the amount of displaced water increases. Using the results shown in Figure 10-14, we calculate that the flux of the displaced water is approximately 1 to 2 mm/yr. Simultaneously, the size of the unprotected part of the

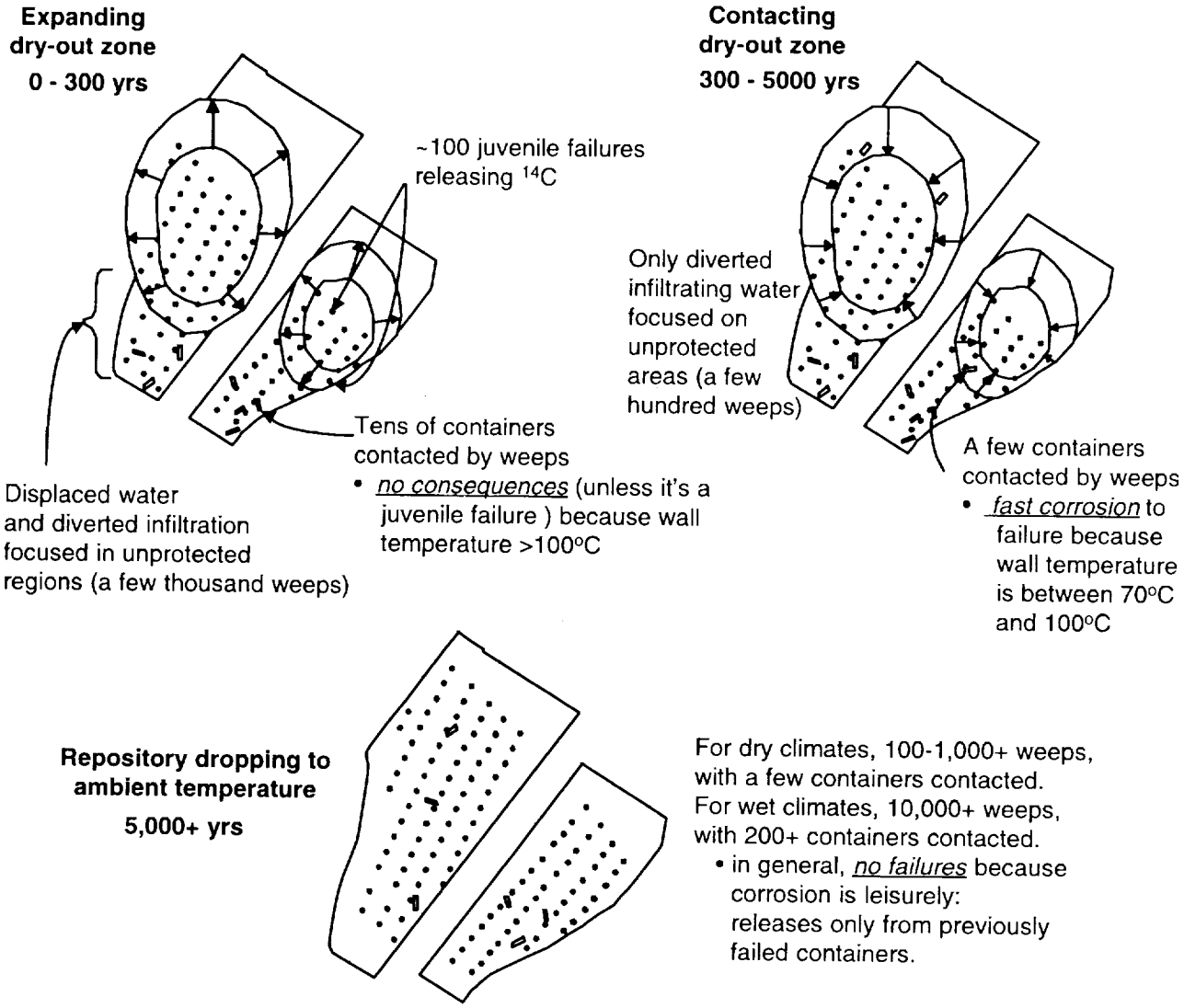

Figure 15-9. Overview of a typical realization of the weeps model for a 57-kW/acre repository with vertically emplaced containers.

repository decreases. The downward flow is funnelled into a smaller and smaller region. The combined displaced water and diverted infiltration can typically result in a downward flux of up to 8 mm/yr through unprotected parts of the repository for time periods on the order of a hundred years. Containers near the edge of the repository can get drenched, although the ramifications are minimal—these containers are rarely juvenile failures and they are still too hot to undergo corrosion. For the base case, the dryout zone never encompasses more than about 75% of the repository, but for the 114-kW/acre cases, a point is reached where the entire repository is protected and groundwater is completely shed outside the repository boundaries.

The size of the dryout zone peaks at approximately 300 years. At this time, water displacement by the dryout zone ceases; however, infiltrating water continues to be diverted around the dryout zone. Also, wall temperatures of the containers located on the edge of the repository begin to drop below boiling. This is the critical time for the repository. Between 300 and 1,500 years, the container walls are falling below 100°C. Containers subject to weep flow fail within a few hundred years when the wall temperature is between 70° and 100°C. Typically, only one or two containers fail by corrosion, and they fail between 370 and 36,000 years, although typically within 3,000 years. For corrosion-failed containers, oxidation alteration of the UO_2 fuel and aqueous and gaseous release of radionuclides begin immediately upon failure.

Only one or two containers fail by corrosion because there is very little groundwater flux during a dry climate. Occassionally (approximately 2% of the time), a climate change occurs when many containers in the repository are still near 100°C (i.e., before 2000 years). In these instances, container failures number in the hundreds, or even the thousands.

After 2000 years, the hydrothermal effects have ceased and a stable, dry-climate flow pattern exists. Approximately 1000 weeps are spread over the repository, contacting at most a few containers. After 5000 years, the container walls have all dropped below 70°C. For the typical realization, no more corrosion failures occur; all the damage has been done. (If the temperature never rises above approximately 70°C, our source term typically does not produce any corrosion failures, and the only container failures are juvenile failures. This result requires further examination.)

The first climate change—change in percolation—occurs at 45,000 years for the typical realization. At this time, the repository is very close to ambient temperature. A new flow pattern is established, typically consisting of more than 10,000 weeps and more than 200 containers contacted by weeps. By now, all the ^{14}C has either been released or has effectively decayed. Because of the low temperature, there are no more corrosion-induced failures. Aqueous releases are limited to containers that have previously failed (typically they are juvenile failures) and are now being contacted anew by weeps. New dry-climate and wet-climate flow patterns are repeated on 100,000-year cycles into the future, but releases are from previously failed containers contacted or recontacted by weeps.

15.5.1.2 Aqueous releases

In general, over a million years, thousands of containers are contacted by weeps, as shown in Figure 15-10. The plot shows the total number of containers contacted by weeps for every realization, and thus, the probability axis is also the fraction of realizations. The

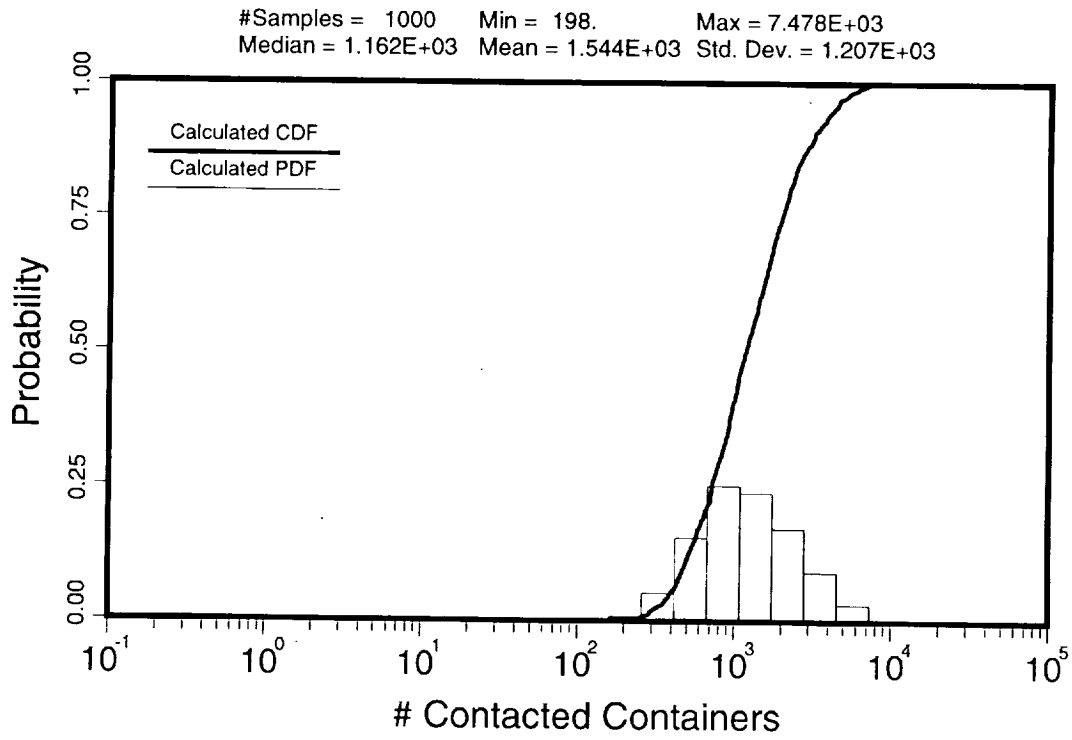

Figure 15-10. Distribution of containers contacted by weeps over a 1,000,000-year period (57 kW/acre, vertical emplacement).

mimimum number of contacted containers is around 200; the maximum is around 7500. Thus, even in the worst case, almost 80% of the containers are never contacted by weeps.

Of the containers that are contacted by weeps, those that exhibit aqueous releases of radionuclides into the groundwater are presented in Figure 15-11. The plot shows the total number of releasing containers for every realization, and thus, as above, the probability axis corresponds to the fraction of realizations. Juvenile failures are omitted from this distribution, unless they have also been contacted by a weep sometime during the million-year period. Approximately 3% of the realizations have no aqueous releases. Approximately 10% have aqueous releases from only one container. On average, less than 10 containers have aqueous releases, but the maximum number of releasing containers is 500.

The distribution of times at which containers begin aqueous releases is shown in Figure 15-12, which was created by plotting the initial release time of every container that released radionuclides in all the realizations; thus, the probability axis represents the fracture of releasing containers. Because the YMIM source term does not return the time of container failure, these initial release times are estimates (they are actually the beginning of the WEEPTSA time step when releases first occur). All of the time-related distributions presented in this chapter are estimates.

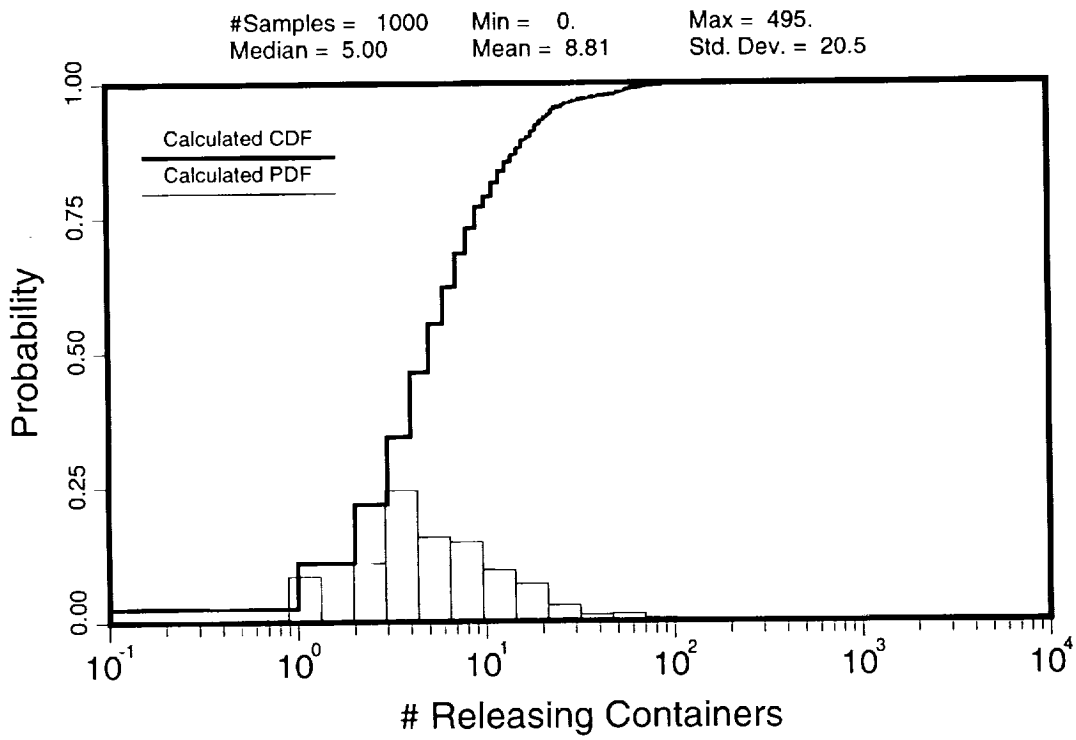

Figure 15-11. Distribution of containers that have aqueous releases of radionuclides over a 1,000,000-year period (57 kW/acre, vertical emplacement).

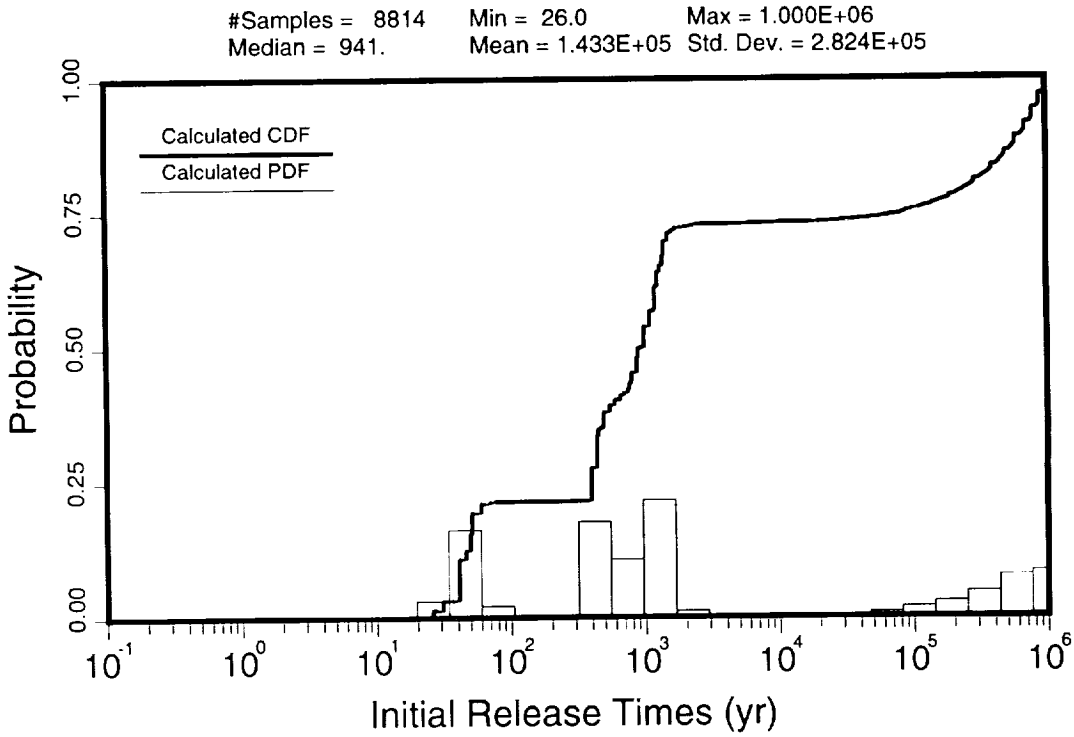

Figure 15-12. Distribution of initial times at which containers have aqueous releases of radionuclides (57 kW/acre, vertical emplacement).

The initial-release-time distribution is trimodal, and the modes correspond to the expansion of the dryout zone, the contraction of the dryout zone, and the changes in flow patterns associated with climate changes. Approximately 20% of the containers that release radionuclides begin releasing them within 100 years. These releases are entirely from juvenile failures and occur during the expansion of the dryout zone when rapidly changing flow patterns occasionally and briefly contact these previously failed containers. Approximately 50% of the releasing containers experience releases during the contraction of the dryout zone. During this time period corrosion failures take place. Also during this time, flow patterns are changing, but not as rapidly as during the dryout expansion—thus, the large spread in initial release times. Approximately 30% of the releasing containers do not begin releasing until tens of thousands of years into the future. These containers are primarily juvenile failures that have not been contacted by weeps before (in the average case, only a few containers ever release). Most of these containers are contacted during wet climates.

Of interest is the number of containers that suffer corrosion failures and the lifetimes of these containers. Figure 15-13 presents the distribution of containers that fail by corrosion: 25% of the time no corrosion failures occur; most of the time only one container fails by corrosion. At the extreme case, however, almost 500 containers fail by corrosion. Comparing Figure 15-11 with Figure 15-13, we see that juvenile failures play a large part in determining aqueous releases from the repository in the most probable cases. The distribution of juvenile failures, which is determined by input parameters to the YMIM source term, is shown in Figure 15-14. Indeed, in the average case, only one third of the aqueously releasing containers are corrosion failures, as shown in Figure 15-15. But in the worst case, performance is dominated by corrosion failures.

Because a container is only occasionally contacted by a weep, there are two ways to consider container lifetime: (1) the time between emplacement and failure, and (2) the accumulated time that a container is contacted by a weep before failure. Figure 15-16 presents the distribution of estimated times from emplacement to when corrosion-induced failures occur. (The times are estimates because the YMIM model used in the probabilitic calculations only indicated the time step when containers failed and not the exact time of failure.) The failures typically occur before 1000 years, but the distribution extends from a minimum of 370 years to a maximum of 36000 years. The distribution of estimated times that containers have been contacted by weeps before they fail by corrosion is shown in Figure 15-17. Most corrosion-failed containers were contacted for less than 400 years before failure.

By far the vast majority of corrosion failures coincide with the rewetting of the repository after the passing of the thermal pulse. When the containers are between 70° and

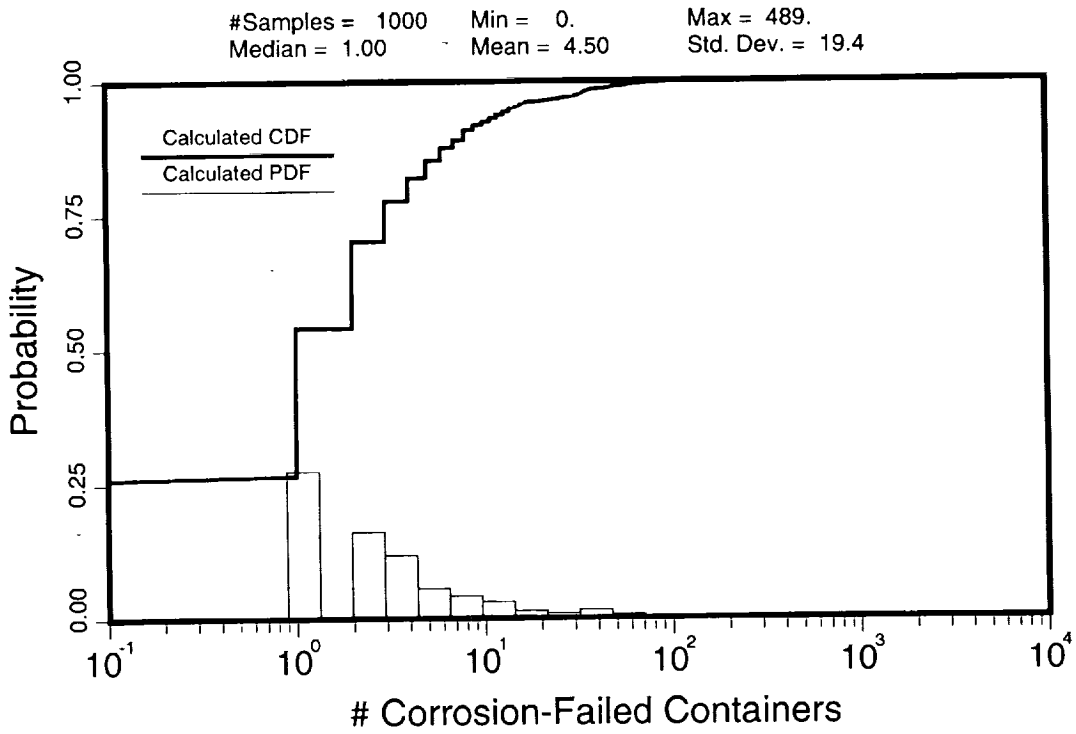

Figure 15-13. Distribution of containers that experience corrosion-induced failure over a 1,000,000-year period (57 kW/acre, vertical emplacement).

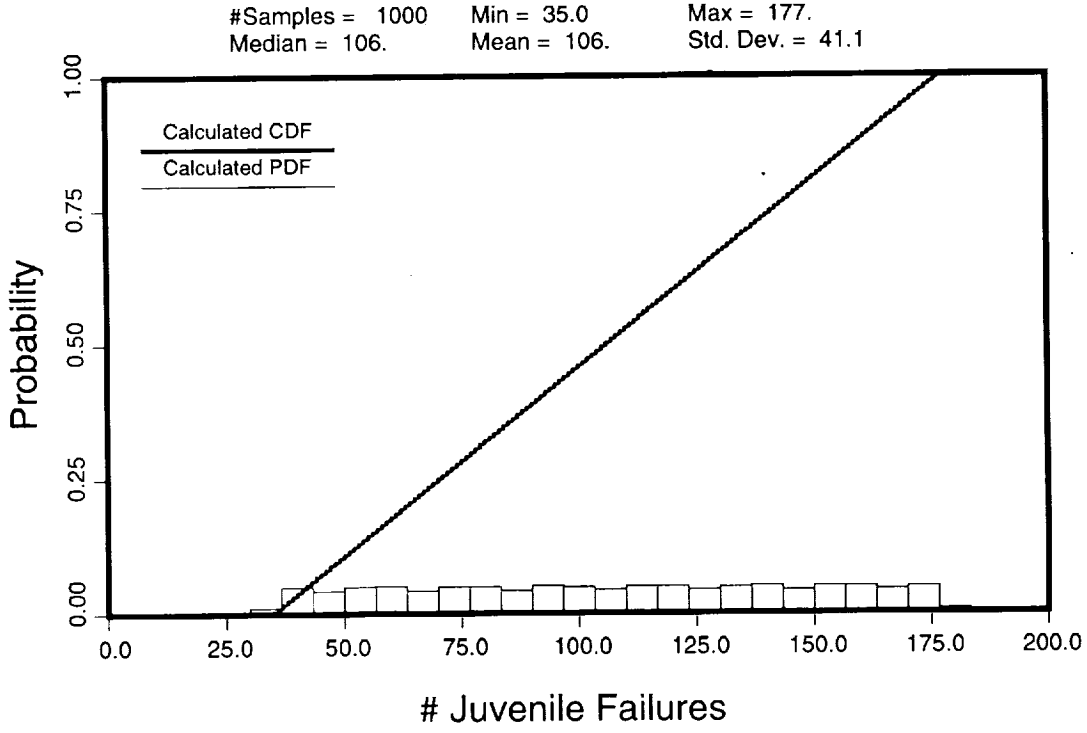

Figure 15-14. Distribution of juvenile failures specified as an input parameter (57 kW/acre, vertical emplacement).

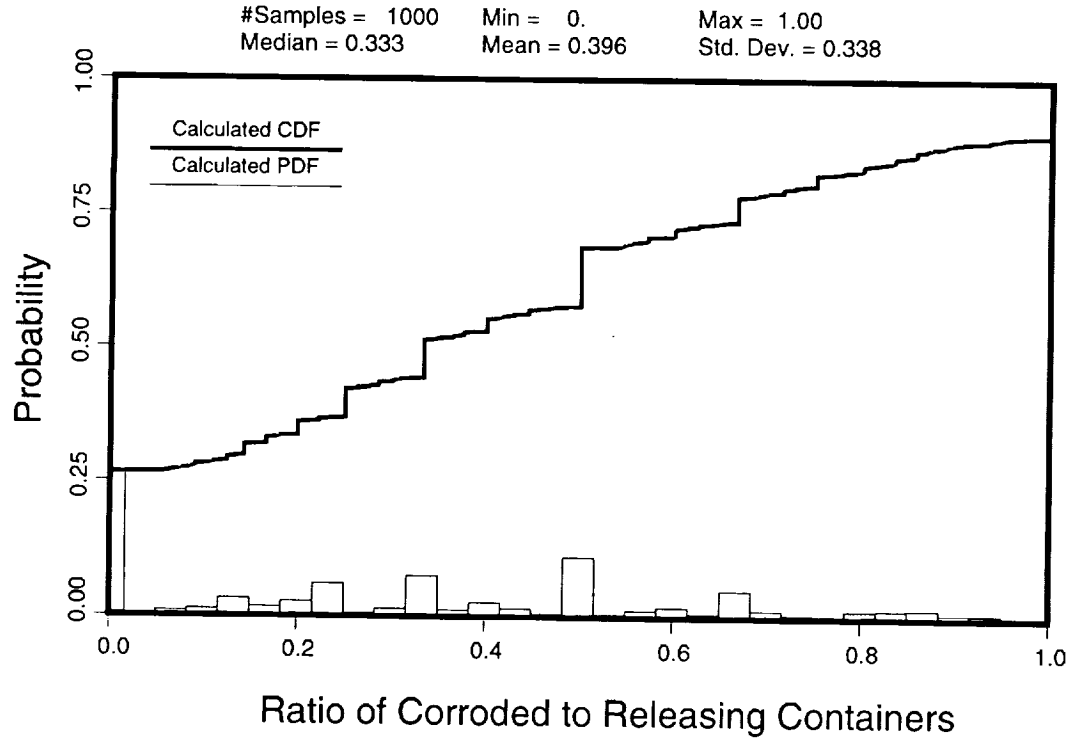

Figure 15-15. Distribution of the ratio of aqueous-releasing containers that experience corrosion-induced failures to all aqueous-releasing containers over a 1,000,000-year period (57 kW/acre, vertical emplacement).

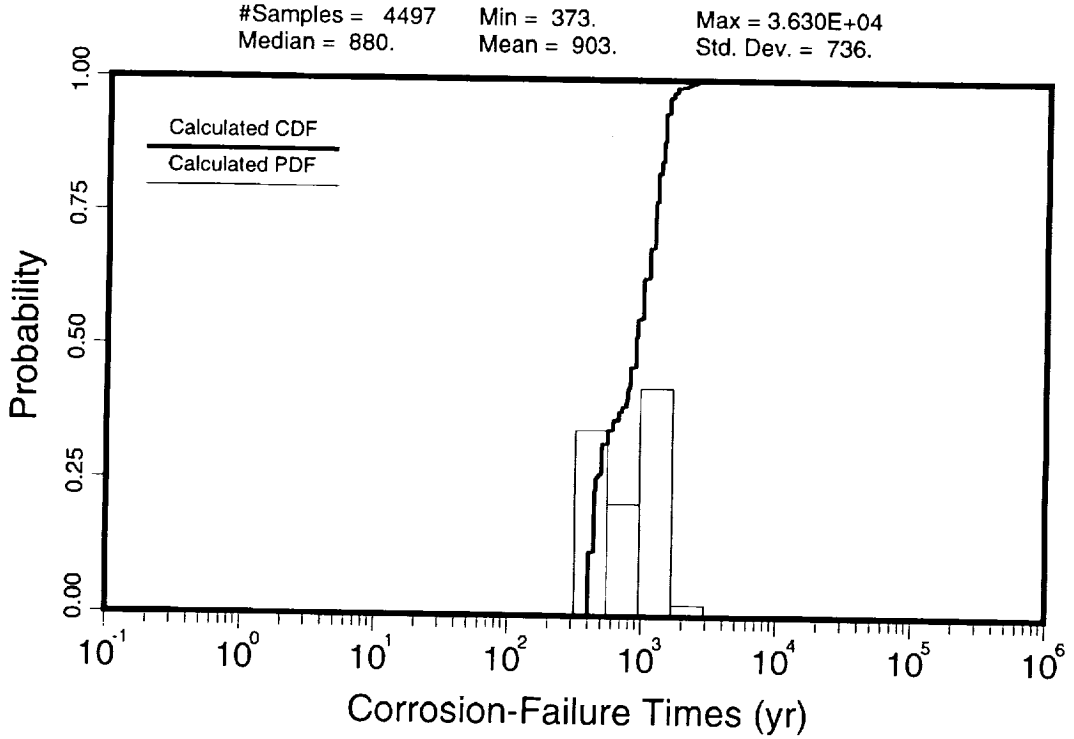

Figure 15-16. Distribution of the times of corrosion-induced failures (57 kW/acre, vertical emplacement).

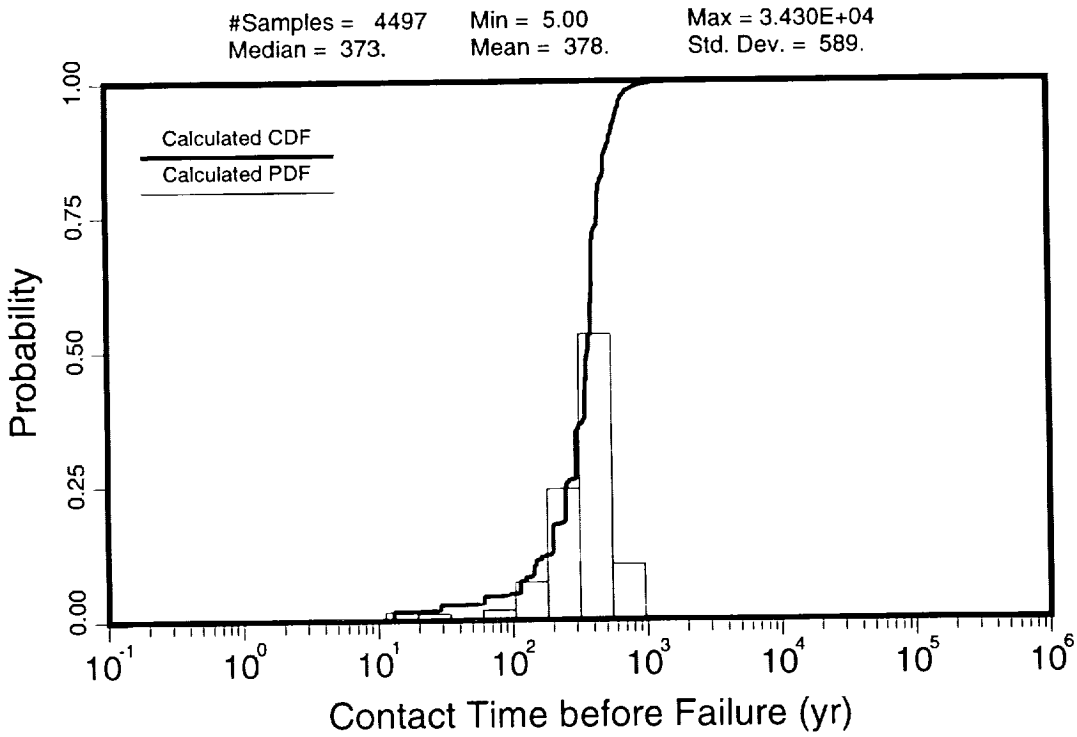

Figure 15-17. Distribution of the durations that weeps contact containers before corrosion-induced failure occurs (57 kW/acre, vertical emplacement).

100°C and contacted by water, corrosion proceeds rapidly. In general, only a few containers are contacted by weeps during this time period; however, in some cases, especially when an early climate change occurs, a large number of containers can be contacted (Figure 15-13). Of course, whether or not containers can be contacted by weeps during the collapse of the boiling isotherm is open to debate; an "extended-dry" period could allow containers to fall to much lower temperatures before they are rewetted (see discussion in Section 15.5.3). However, an extended-dry concept was not modeled because it is inconsistent with a basic premise of the weeps model—decoupling of the matrix and fractures does not allow the "enhanced matrix imbibition" of the rewetting water that is proposed to account for the extended-dry period.

The duration of aqueous releases of radionuclides from containers is shown in Figure 15-18. This distribution also corresponds to the durations that corrosion-failed containers are contacted by weeps. The release durations of juvenile failures are not included in the figure. The distribution is bimodal: the short-duration mode reflects releases caused by the relatively short-duration weeps produced during the thermal pulse; the long-duration mode reflects contact by long-duration weeps created by a climate change. The modes contain approximately the same number of releasing containers.

The first performance measure considered is the the regulatory standard for a high-level radioactive waste repository that formerly applied to Yucca Mountain, as promulgated

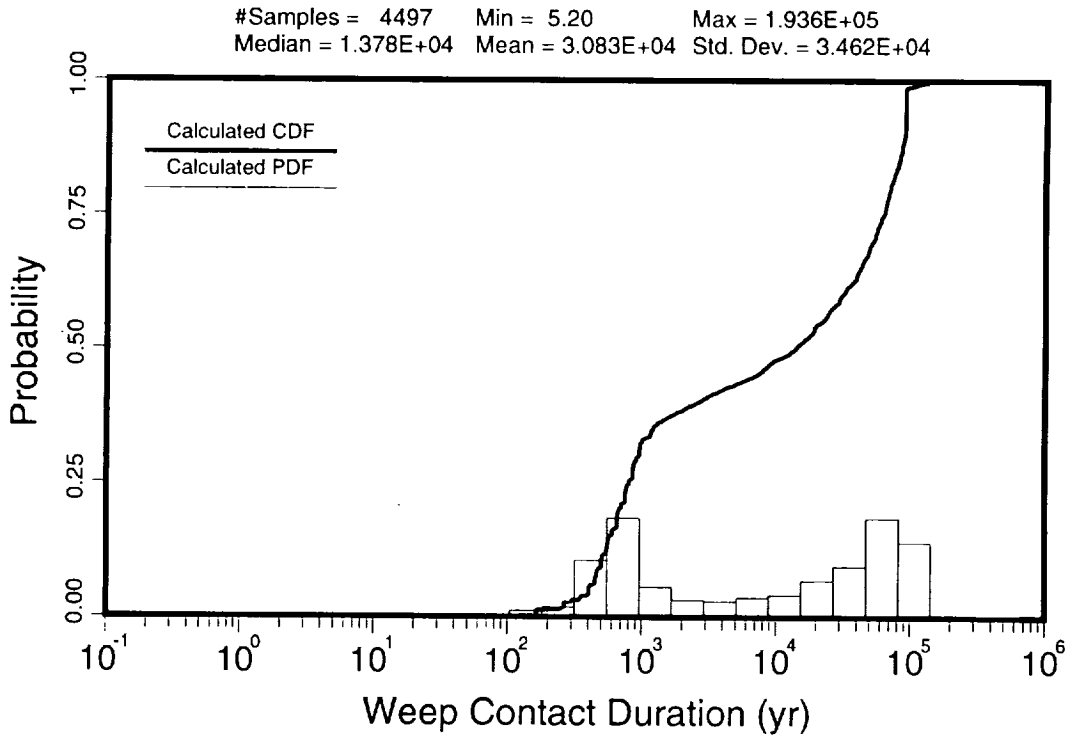

Figure 15-18. Distribution of the total durations that weeps contact containers (57 kW/acre, vertical emplacement). Juvenile-failed containers are not included in the figure.

by the EPA in 40 CFR Part 191. The conditional complementary cumulative distribution functions (CCDFs) based on this standard are shown in Figure 15-19. The CCDFs are conditional for a number of reasons: one reason is that the CCDFs only represent aqueous releases and not all possible releases; another reason is that the CCDFs are based on only a single conceptual model of flow.

The CCDFs show the cumulative releases of radionuclides as normalized by the release limits given in 40 CFR Part 191; e.g., the release limits for most actinides is 0.1 Curies per metric ton of heavy metal (Ci/MTHM). The EPA standard is based only on the releases for the first 10,000 years. The curves labeled "10,000 years" and "TSPA-91" directly address the EPA standard. The other two curves show predictions for releases as if the EPA standard applied to cumulative releases over longer times; they are provided for information only.

Considering only the 10,000-year and the TSPA-91 curves, it is apparent that the releases predicted by TSPA-91 are similar to those predicted by TSPA-93, with both TPSAs showing releases an order of magnitude or more below the EPA limit. In general, however, the TSPA-93 prediction shows greater releases for the most likely cases, while TSPA-91 shows greater releases for the extreme cases. The median value of the EPA sum for TSPA-91 is approximately 5×10^{-5}, while for TSPA-93 it is approximately 10^{-3}. At a probability of

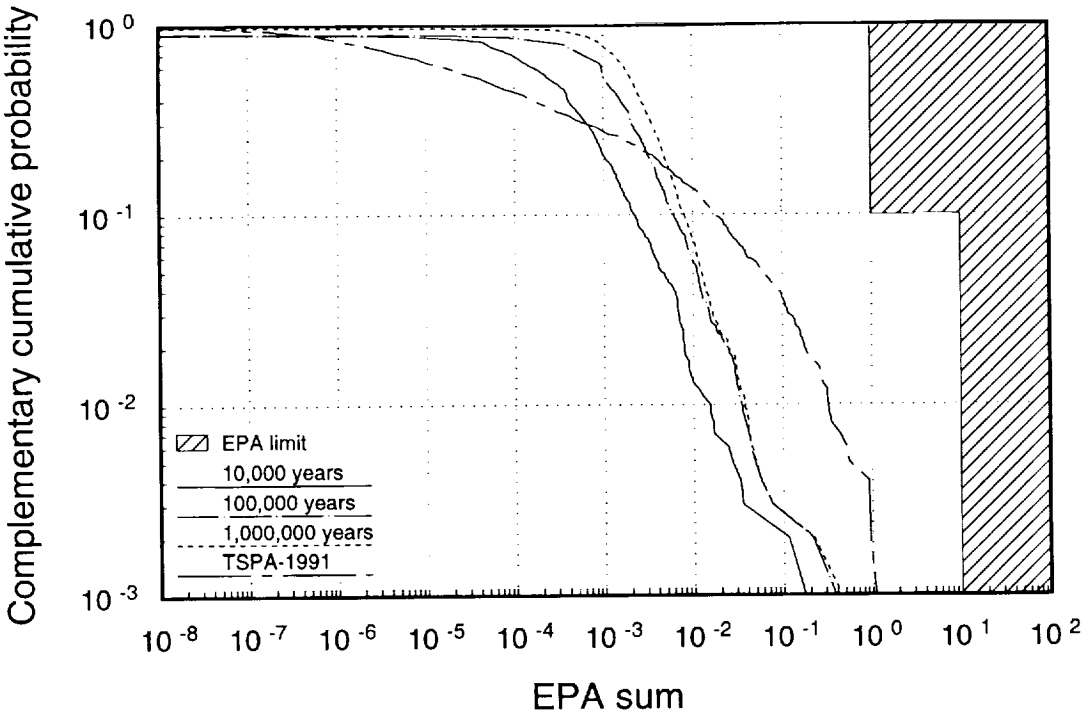

Figure 15-19. Conditional CCDFs of cumulative aqueous releases to the accessible environment, normalized by the EPA limits (57 kW/acre, vertical emplacement). Cross-hatching denotes area of noncompliance with the EPA standard, but only for the 10,000-year cumulative releases.

0.001, TSPA-91 has an EPA sum of near 1, while TSPA-93 has a sum of around 0.2. These two discrepancies can be both explained primarily by the different number of weeps generated in the two TSPAs. TSPA-91 used a very broad distribution of aperture sizes, plus only one aperture size was used for all the weeps in a given realization. Thus, TSPA-91 generated some realizations with only a few hundred weeps, which produced very minor releases, and some realizations with millions of weeps, which contacted almost all the containers and produced the extreme values shown in the plot. TSPA-93, on the other hand, generated only a few thousand weeps (during the initial dry climate) every realization. The small variance in the number of weeps is caused somewhat paradoxically by allowing varied weep sizes in every realization. Varied weep sizes allow some big weeps every realization; the big weeps take a disproportional share of the flow, and hence, deny creation of large numbers of small weeps.

The spread in a CCDF can be taken for the amount of uncertainty in the results. The reduction in spread from TSPA-91 to TSPA-93 suggests that, by using less uncertain weep properties, overall uncertainty can be reduced. In this case, however, the overriding uncertainty is whether the model represents reality.

Although the number of weeps is the most important factor explaining the differences between TSPA-91 and TSPA-93, several other factors play a role. The groundwater-flux distributions used in the two TSPAs are different but, for the dry climate at least, only by a factor of 2; however, because the number of weeps varies linearly with the groundwater flux, flux is not the dominant parameter in the weeps model that it is in the composite-porosity model. Also, in the most probable cases, TSPA-93 predicts releases from both juvenile-failed and corrosion-failed containers. Juvenile failures were not included in TSPA-91. In TSPA-93, low releases can be dominated by juvenile failures, which are a relatively constant contributor to releases. Therefore, these releases can be expected to be higher than those predicted by TSPA-91.

Figure 15-19 also shows that approximately 10% of the TSPA-93 realizations result in no releases. All of the TSPA-91 realizations showed releases because the source was handled as a continuum; i.e., what was essentially a fraction of a container could be contacted by a weep. After a million years, only about 1% of the TSPA-93 realizations resulted in no releases.

The CCDFs at 100,000 and 1,000,000 years indicate that releases do not increase significantly at these longer times. The 100,000-year curve shows approximately a factor of 2 increase in releases over the 10,000-year curve. The 1,000,000-year curve shows only a slight increase over the 100,000-year curve. In other words, the weeps model predicts that most of the damage to the repository occurs within the first 10,000 years.

The radionuclides that contribute to the 10,000-year EPA sum for this TSPA are shown in Figure 15-20. The major contributor when releases are low—the most likely releases—is ^{99}Tc, followed by ^{129}I. These radionuclides transport without sorbing to tuff and they were by far the dominant radionuclides in the releases predicted by TSPA-91. The major contributor when releases are high is ^{237}Np, followed by ^{234}U. Neptunium releases are significant because of the high solubility assigned in TSPA-93 (Chapter 9).

Neptunium and uranium adsorb poorly to tuff, but more strongly than ^{99}Tc and ^{129}I. In the extreme cases, more ^{234}U and ^{237}Np are being released from the EBS than ^{99}Tc and ^{129}I. Large amounts of water are contacting the containers, and dissolution is being controlled by availability rather than solubility. Plutonium is one of the most abundant radionuclides in the source, but ^{239}Pu releases at the accessible environment are insignificant—the ^{239}Pu curve is not in evidence on the plot—because ^{239}Pu is being significantly retarded in the saturated zone.

Figure 15-21 shows cumulative releases from the EBS, as normalized by the EPA limits, even though the EPA standard only applies at the accessible environment. This plot

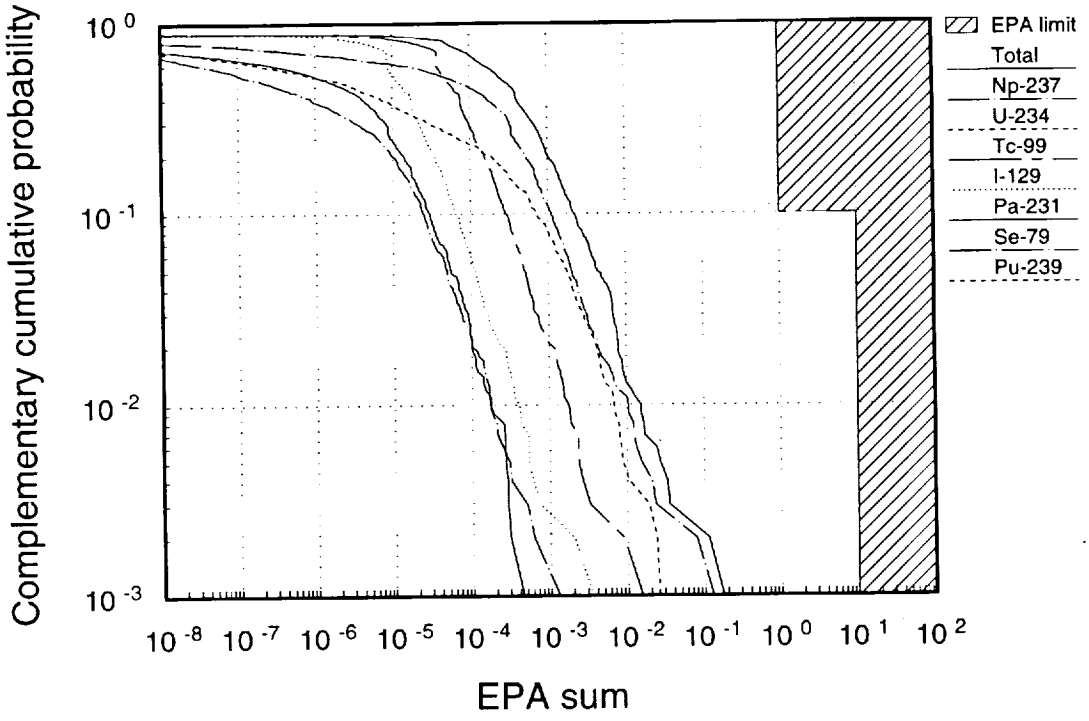

Figure 15-20. Conditional CCDFs of cumulative aqueous releases to the accessible environment, at 10,000 years, normalized by the EPA limits, for specified radionuclides and their combination (57 kW/acre, vertical emplacement). Cross-hatching denotes area of noncompliance with the EPA standard.

indicates the impact of the natural barrier system on mitigating releases from the EBS. For the weeps model, natural-barrier-system mitigation is limited to the saturated zone.

Figure 15-21 indicates that releases from the EBS are below the EPA limit in all but the most extreme cases. Thus, the low probability of being contacted by a weep offers substantial protection for the repository. The figure also indicates that almost all of the releases from the EBS occur within the first 10,000 years. In the next million years, only a few more containers contribute to releases, and the main effect is that the 10% of realizations that produce no releases is reduced to 1%.

Comparison of Figures 15-19 and 15-21 shows that the saturated zone reduces releases by about two orders of magnitude. Figure 15-22 shows why this reduction occurs. The major contributor to releases from the EBS is ^{239}Pu—by two orders of magnitude. As mentioned, ^{239}Pu is being retained in the saturated zone by adsorption. Releases of ^{237}Np and ^{234}U are greater than shown in Figure 15-20 for two reasons: (1) they are sorbed somewhat in the saturated zone; and (2) the approximately thousand-year travel time in the saturated zone has kept some of their mass from the accessible environment at 10,000 years. Releases of ^{99}Tc and ^{129}I are slightly greater than shown in Figure 15-20 because of the travel time.

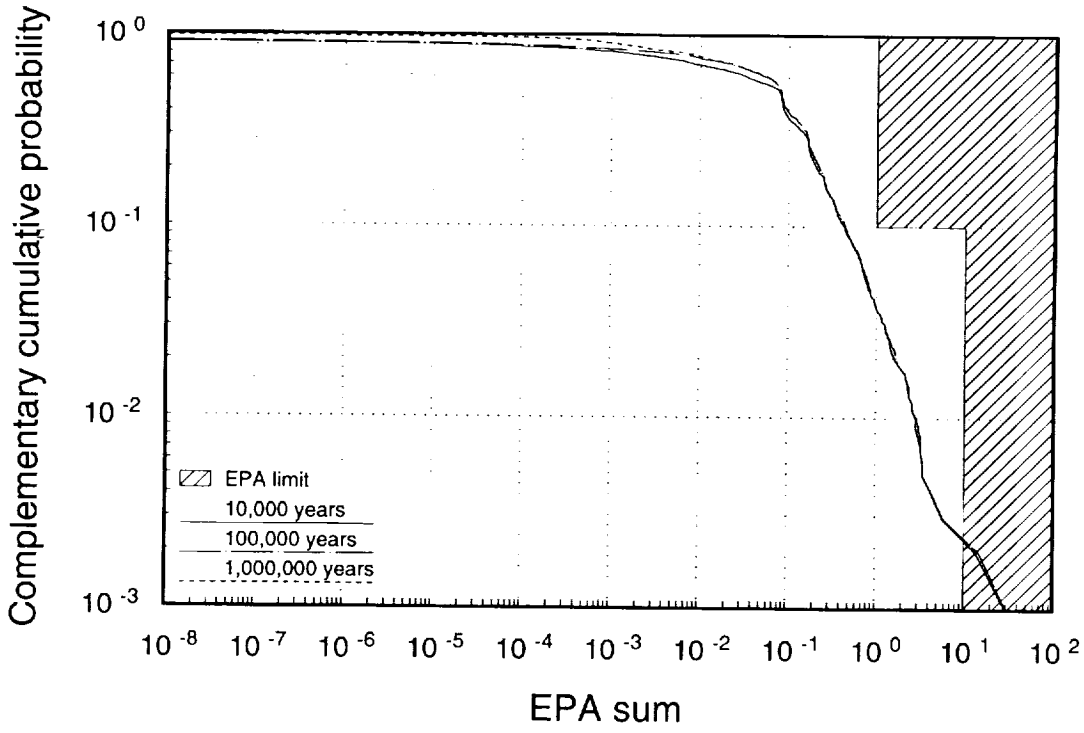

Figure 15-21. Conditional CCDFs of cumulative aqueous releases from the EBS, normalized by the EPA limits (57 kW/acre, vertical emplacement). Cross-hatching denotes area of noncompliance with the EPA standard, and is included for informational purposes only, because the standard does not apply to releases from the EBS.

Plutonium was included in the analysis for two reasons: (1) to see if releases of a highly retarded radionuclide could be significant (if so, other highly retarded radionuclides should be added to the analysis); and (2) to estimate the effect that significant colloid formation and transport could have on the releases. Based on Figure 15-22, highly retarded radionuclides need not be included in an EPA-sum calculation as long as colloid formation and transport can be ruled out as significant. If colloids are important, they could have an important—albeit low probability—effect on repository performance as predicted by the weeps model. Colloid formation and transport are not considered in TSPA-93.

The other performance measure we consider is the the radiation dose to the maximally exposed individual (hereafter called "dose"). As discussed in Chapter 2, and again in Chapter 14, this measure has been offered by the NCRP and the ICRP as a means of judging the hazards of radiation, and has been suggested as a replacement to the essentially population-dose standard given in 40 CFR Part 191 (EPA, 1985). Regulatory dose limits have yet to be suggested.

An explanation of the dose model used with both the composity-porosity model and the weeps model is given in Section 14.2. Only whole-body doses to adults from drinking

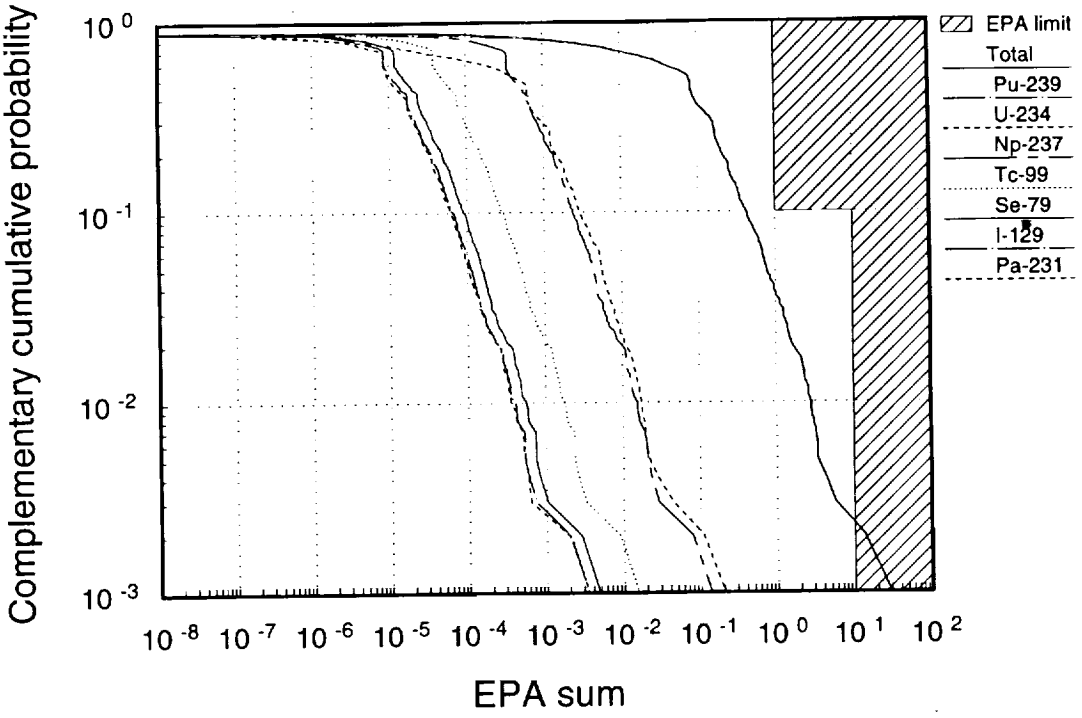

Figure 15-22. Conditional CCDFs of cumulative aqueous releases from the EBS, at 10,000 years, normalized by the EPA limits, for specified radionuclides and their combination (57 kW/acre, vertical emplacement). Cross-hatching denotes area of noncompliance with the EPA standard, and is included for informational purposes only, because the standard does not apply to releases from the EBS.

water are considered. Caveats concerning the dose calculation are stated in Section 14.6; these caveats also apply to the weeps-model dose calculation. The dose calculations made by Pacific Northwest Laboratory for TSPA-91 are not directly comparable to the TSPA-93 dose calculations and are omitted from this discussion.

The conditional CCDFs for drinking-water dose are presented in Figure 15-23. The dose is the peak dose that occurs at any time up to the time given for each curve. The median dose shown in the figure is between 2 and 4 mrem/yr; in the extreme cases, the dose is up to 2000 mrem/yr (2 rem/yr). In contrast to the doses given for the composite-porosity model in Chapter 14, the peak dose predicted by the weeps model does not increase much after 10,000 years, especially for the extreme cases. In approximately 10% of the realizations before 100,000 years, there is no dose. This finding is consistent with the cumulative-releases plot (Figure 15-19). Also, the weeps model predicts substantially lower doses overall than the composite-porosity model.

The doses shown in Figure 15-23 appear to be higher than would be expected given the relatively low cumulative releases shown in Figure 15-19. The EPA standard for cumulative

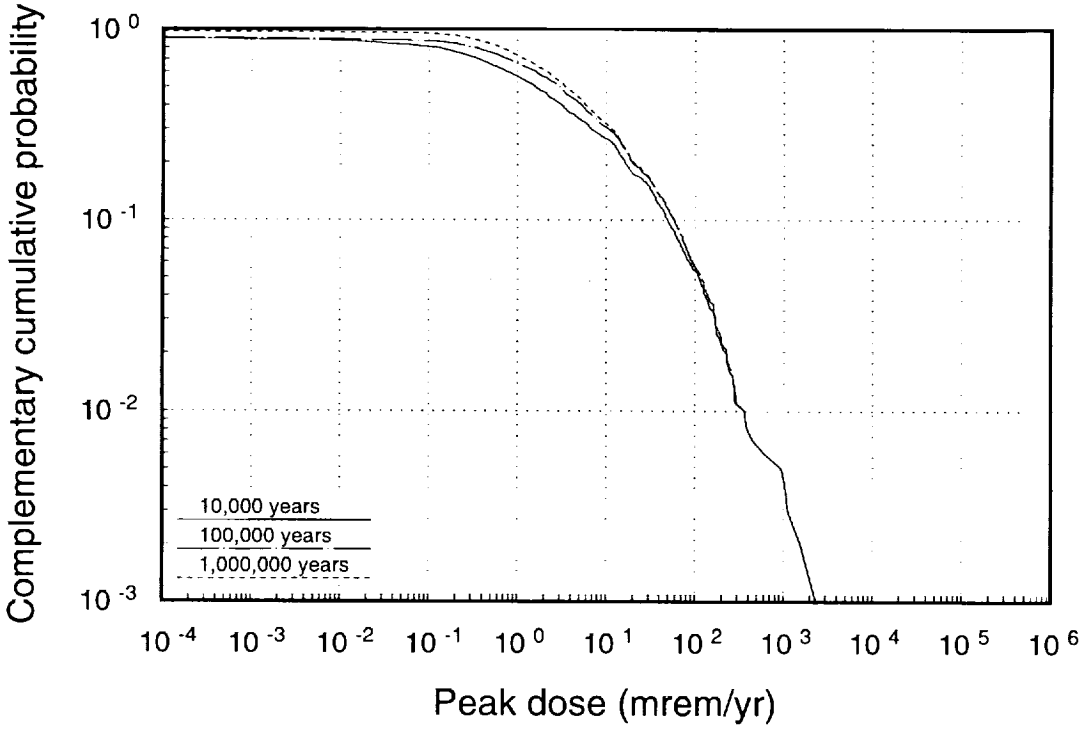

Figure 15-23. Conditional CCDFs of peak radiation doses from drinking water to a maximally exposed individual (57 kW/acre, vertical emplacement).

releases was based on a population dose; hence, the magnitude of an individual dose does not necessarily indicate the number of health effects expected from the accompanying population dose. As discussed in Chapter 14, individual dose is basically a function of release rate of radionuclides from the repository and dilution of these radionuclides in the environment. Release rate can be poorly related to cumulative releases, especially when there are spikes in the releases, e.g., when a number of containers fail—perhaps coincidentally—at the same time. Dilution in the groundwaters of the Yucca Mountain vicinity is an unknown, and we have input a distribution with a wide variance for the saturated-zone transport area (the cross-sectional area of the flow path through the saturated zone), to reflect this uncertainty. Also, when examining these doses it should be remembered that, at this point in the TSPA process, the models are extremely simple and incorporate a number of what we believe to be conservative assumptions.

Figure 15-24 presents the radionuclides that contribute to the dose. The most important radionuclide, responsible for approximately an order of magnitude greater dose than the other radionuclides, is ^{237}Np. Neptunium is significant because (1) it will have a large inventory in a repository, (2) under oxidizing conditions it is relatively soluble (Section 9.2), (3) it has a long half-life (2.6 million years), (4) it is relatively unretarded during transport and, (5) like most actinides, it has a high dose conversion factor. The dose conversion factor

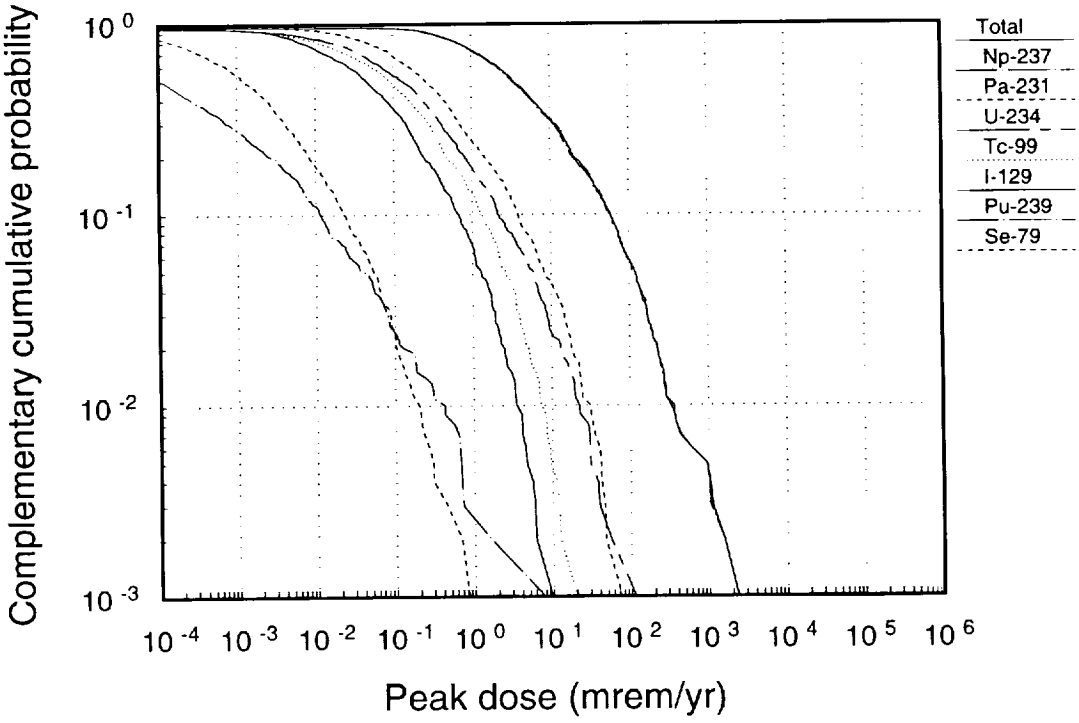

Figure 15-24. Conditional CCDFs of peak radiation doses from drinking water to a maximally exposed individual, for specified radionuclides and their combination (57 kW/acre, vertical emplacement).

transforms radiation exposure (in our case, given the mass ingested) to dose. Neptunium's dose conversion factor is high because it is retained in the body, thus exposing it to radiation, for a long period of time. The other radionuclides shown in Figure 15-24 are deficient in one or more of these areas, and contribute less to the total dose. Note that ^{239}Pu is a minor contributor because of its high retardation during transport; the saturated zone delays ^{239}Pu long enough for most of it to decay away before it reaches the assumed well location at the accessible environment.

The times at which the peak doses (Figure 15-23) occur are presented in Figure 15-25. As suggested by the proximity of the curves in Figure 15-23, many of the peak doses occur before 10,000 years. Examination of Figure 15-25 shows that 40% of the realizations produce the peak dose before 10,000 years; 60% of the realizations produce the peak dose before 20,000 years; and 80% of the realizations produce the peak dose before 100,000 years. At 1,000,000 years, approximately 99% of the realizations have produced a peak dose, indicating that only about 1% of the realizations have not yet reached their peak dose during the time period of the simulations.

The bimodal nature of the curve in Figure 15-25 suggests that most of the maximum doses are the result of releases during the contraction of the dryout zone. The second mode

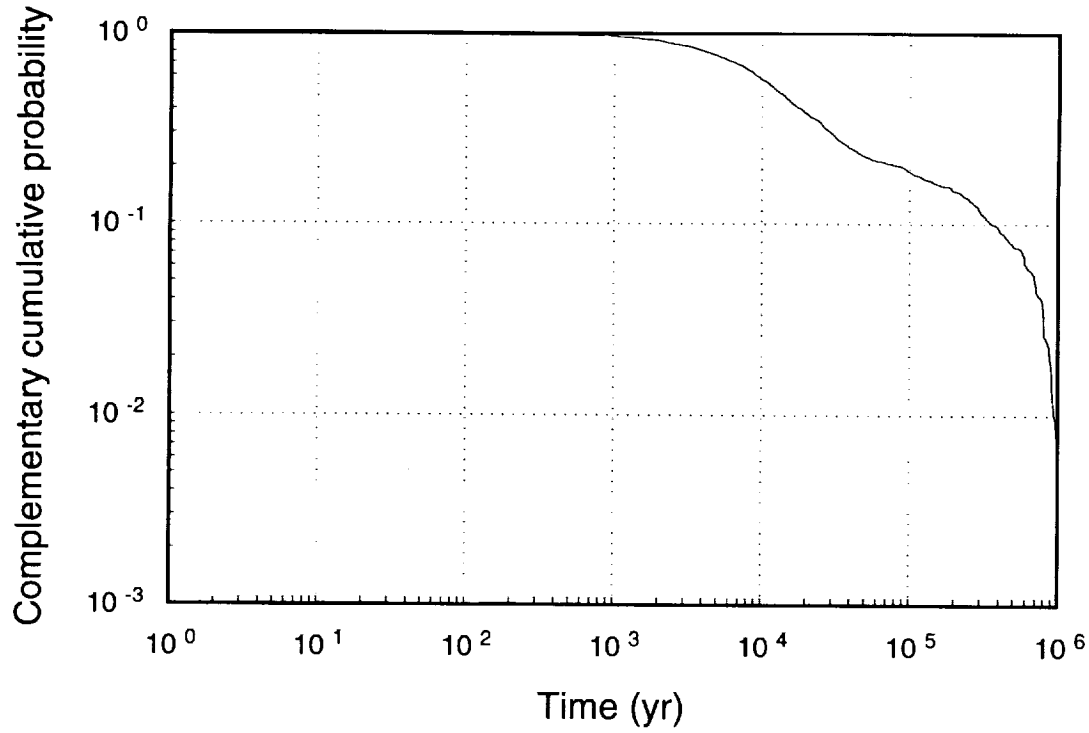

Figure 15-25. Conditional CCDFs of the times of peak radiation doses (57 kW/acre, vertical emplacement).

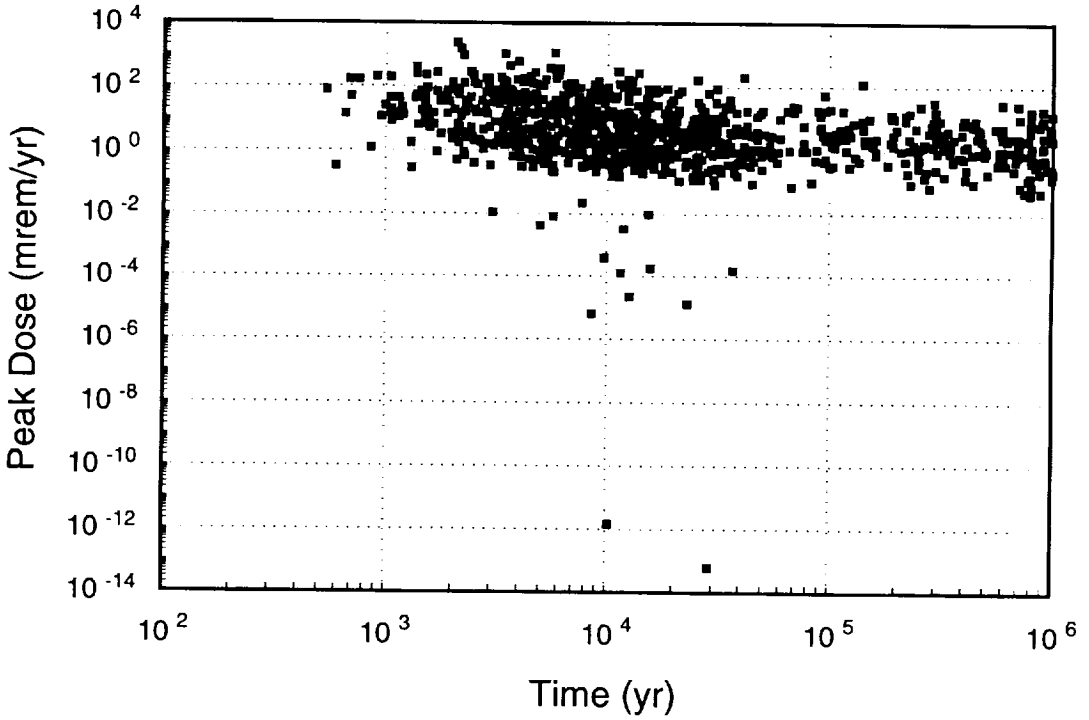

Figure 15-26. Scatter plot of peak dose vs. time of occurrence (57 kW/acre, vertical emplacement).

Table 15-4. Weeps-model mean releases and doses in relation to total.

Normalized Cumulative Release

10^4 years	10^5 years	10^6 years
^{237}Np (55.2%)	^{234}U (50.5%)	^{234}U (45.7%)
^{234}U (28.2%)	^{237}Np (41.1%)	^{237}Np (45.0%)
^{99}Tc (12.1%)	^{99}Tc (4.9%)	^{99}Tc (4.1%)
^{129}I (2.8%)	^{79}Se (1.2%)	^{239}Pu (1.8%)
^{231}Pa (1.0%)	^{129}I (1.1%)	^{129}I (1.2%)
	^{231}Pa (1.0%)	^{231}Pa (1.2%)
		^{79}Se (1.0%)

Peak Individual Dose

10^4 years	10^5 years	10^6 years
^{237}Np (94.7%)	^{237}Np (97.0%)	^{237}Np (97.1%)
^{231}Pa (6.0%)	^{231}Pa (6.4%)	^{231}Pa (6.5%)
^{234}U (3.8%)	^{234}U (4.5%)	^{234}U (4.6%)
^{99}Tc (2.1%)	^{99}Tc (2.0%)	^{99}Tc (1.9%)
^{129}I (1.0%)	^{129}I (1.0%)	

could be from releases occuring when previously failed containers are contacted by weeps during subsequent climate changes. Figure 15-26 presents a scatter plot of the peak dose and the time at which it occurs. In the figure, each square is the result of a realization. The figure indicates that greater peak doses tend to occur at earlier times. These earlier times correspond to when the dryout zone is contracting (plus the thousand-year travel time through the saturated zone). During the contraction of the dryout zone, weep-flow is focused into unprotected parts of the repository, containers are more likely to be contacted by weeps, and containers are warm and more subject to corrosion. At these earlier times, these containers also have an inventory that is generally more radioactive, because as time progresses radioactive decay tends to eventually produce stable isotopes. Thus, in most cases, these early failures produce the greatest doses. Late-time peak doses are less likely to be realized. They occur primarily in realizations where containers fail during the contraction of the dryout, but the failed containers are not contacted by weeps of sufficient size or duration to produce large doses; then at a climate change, these failed containers are recontacted by larger, more durable weeps resulting in greater releases and the peak doses.

Table 15-4 summarizes the contribution of the individual radionuclides to the performance measures for the 57-kW/acre repository with vertically emplaced containers. ^{234}U and ^{237}Np dominate the EPA releases. (Cumulative ^{14}C gaseous releases are approximately the same magnitude as ^{234}U and ^{237}Np—see below.) ^{237}Np alone dominates the doses. The dose columns add up to more than 100% because the peak doses for different nuclides oc-

cur at different times (the peak nuclide dose divided by peak total dose is listed, not the contribution of the nuclide to the peak total dose).

15.5.1.3 Gaseous releases

Only ^{14}C was considered for gaseous releases in both TSPA-91 and TSPA-93. Calculations of releases were restricted to 10,000 years in both TSPAs, because ^{14}C decays relatively rapidly—its half-life is 5,730 years—and only about 30% of the initial inventory remains at 10,000 years. Individual dose from gaseous releases is expected to be inconsequential given the large dilution offered by the atmosphere (Park and Pflum, 1990; Van Konynenburg, 1991), and therefore individual dose was not calculated for ^{14}C. The weeps model was used to calculate the interaction of groundwater with the EBS, and thus supply the source term for the gaseous-release model described in Chapter 12.

The distribution of containers contacted by weeps during the 10,000-year calculational period is presented in Figure 15-27. The figure shows fewer contacted containers than Figure 15-10 shows for the aqueous-release calculations because the aqueous releases were calculated over a million-year period. Somewhat surprisingly, although the time period was decreased by a factor of 100, the number of containers contacted by weeps typically

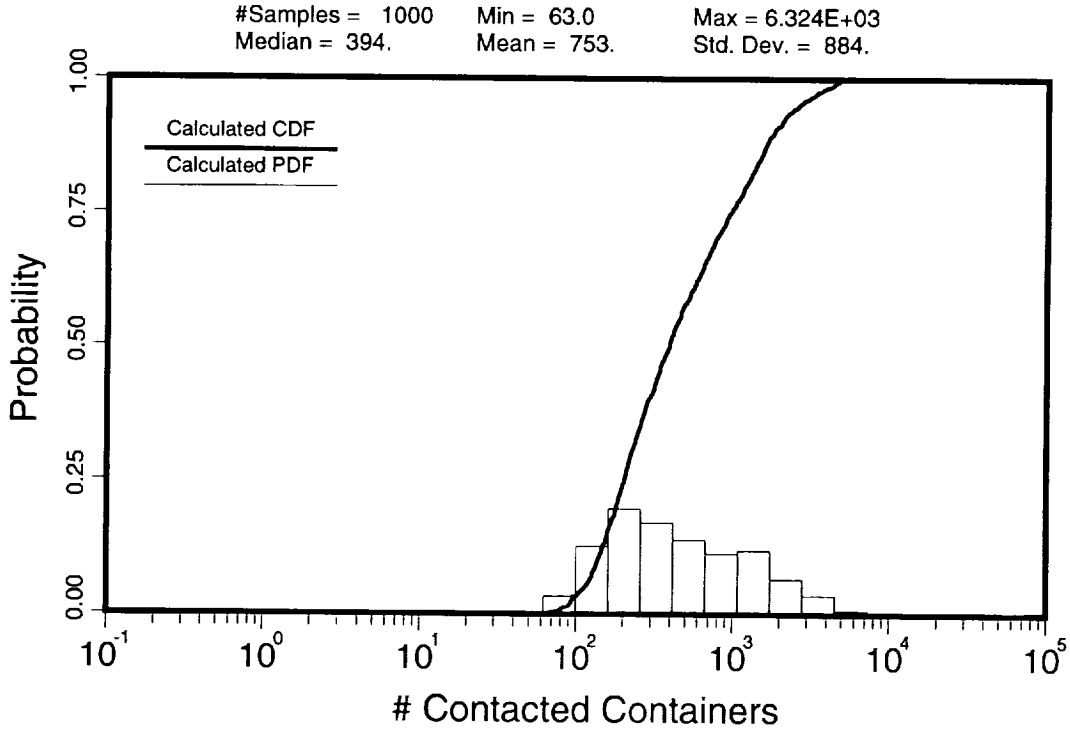

Figure 15-27. Distribution of containers contacted by weeps over a 10,000-year period (57 kW/acre, vertical emplacement).

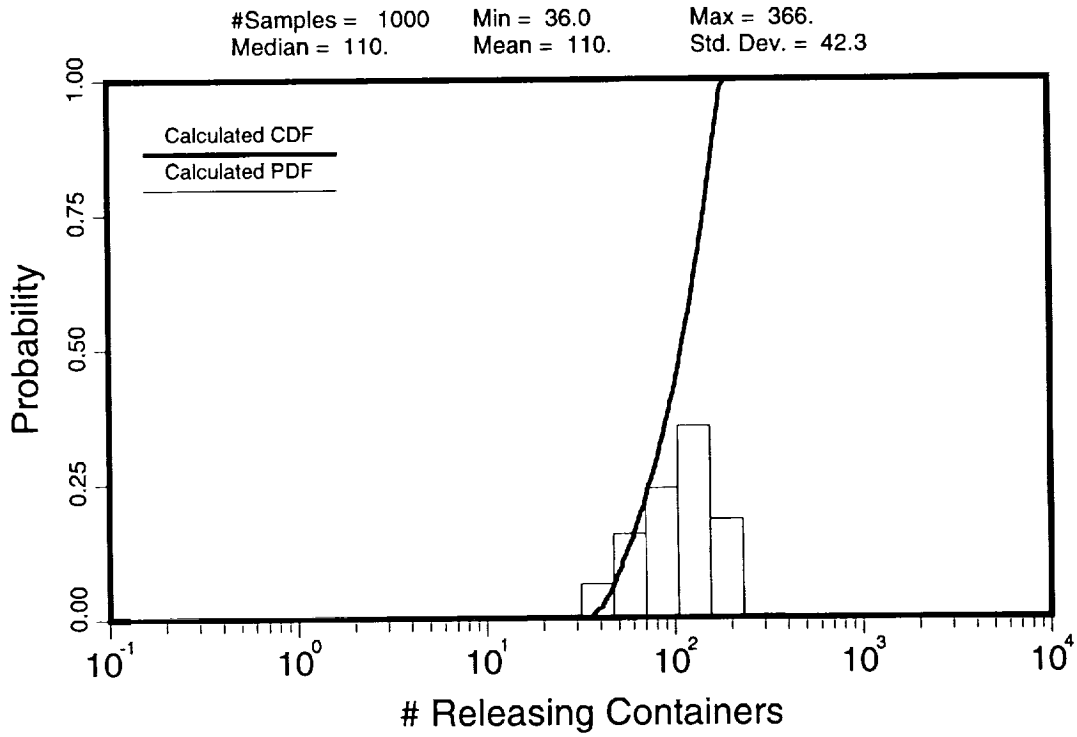

Figure 15-28. Distribution of containers that have gaseous releases of radionuclides over a 10,000-year period (57 kW/acre, vertical emplacement).

only decreased by a factor of 2 to 4. The implication is that the thermal perturbation is responsible for a significant number of weep/container contacts.

Figure 15-28 presents the distribution of containers that release ^{14}C. Compared with Figure 15-11, approximately 100 times as many containers release gaseous radionuclides as aqueous radionuclides. The discrepancy is due to juvenile failures, which are more important to gaseous releases than to aqueous releases because the containers release ^{14}C immediately upon failure and do not require contact by a weep. The distribution of juvenile failures is shown in Figure 15-14, and it is the same distribution as used in the weeps aqueous-release calculations.

The distribution of times at which containers start gaseous releases is presented in Figure 15-29. The distribution shows the predominant contribution—over 95%—of juvenile failures to the calculations. The initial time step for the calculation was 0.25 years, and thus the releases begin at this time. The releases that occur at later times emanate from corrosion-failed containers. In the worst case, approximately as many corrosion-induced failures occur as juvenile failures (see below).

Figure 15-30 presents the number of containers that suffer corrosion failures over the 10,000-year calculational period. The distribution is similar to that shown in Figure 15-13 for the aqueous-release calculations, execpt for a few extreme cases (which could have been

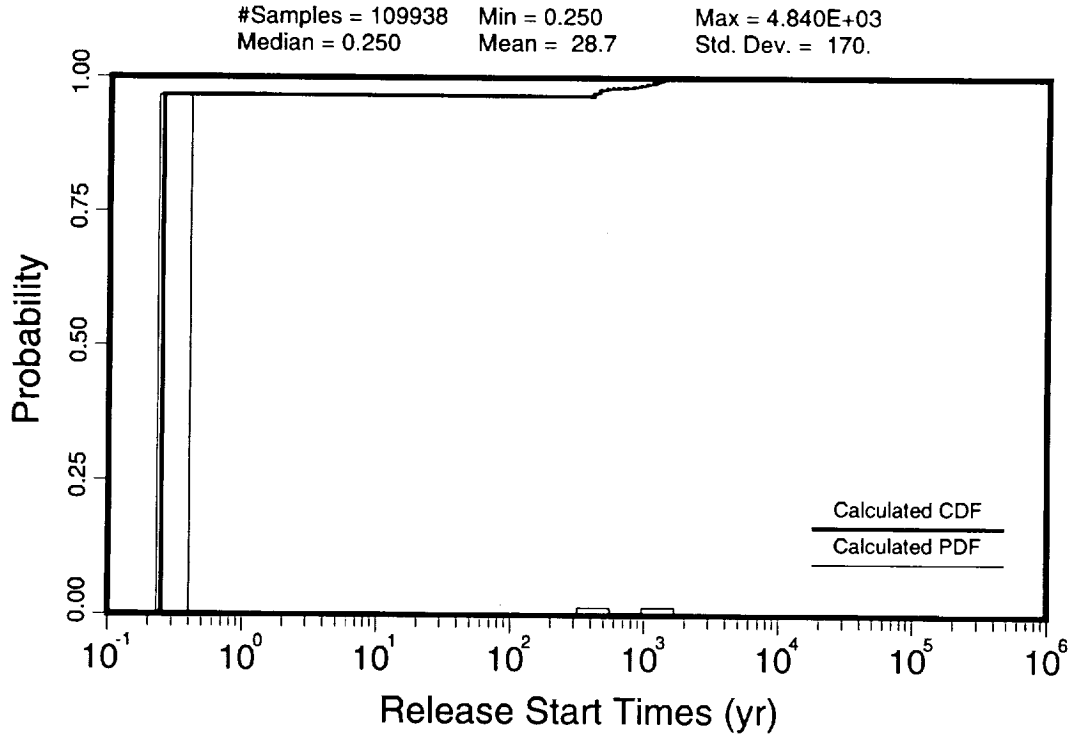

Figure 15-29. Distribution of initial times at which containers have gaseous releases of radionuclides (57 kW/acre, vertical emplacement).

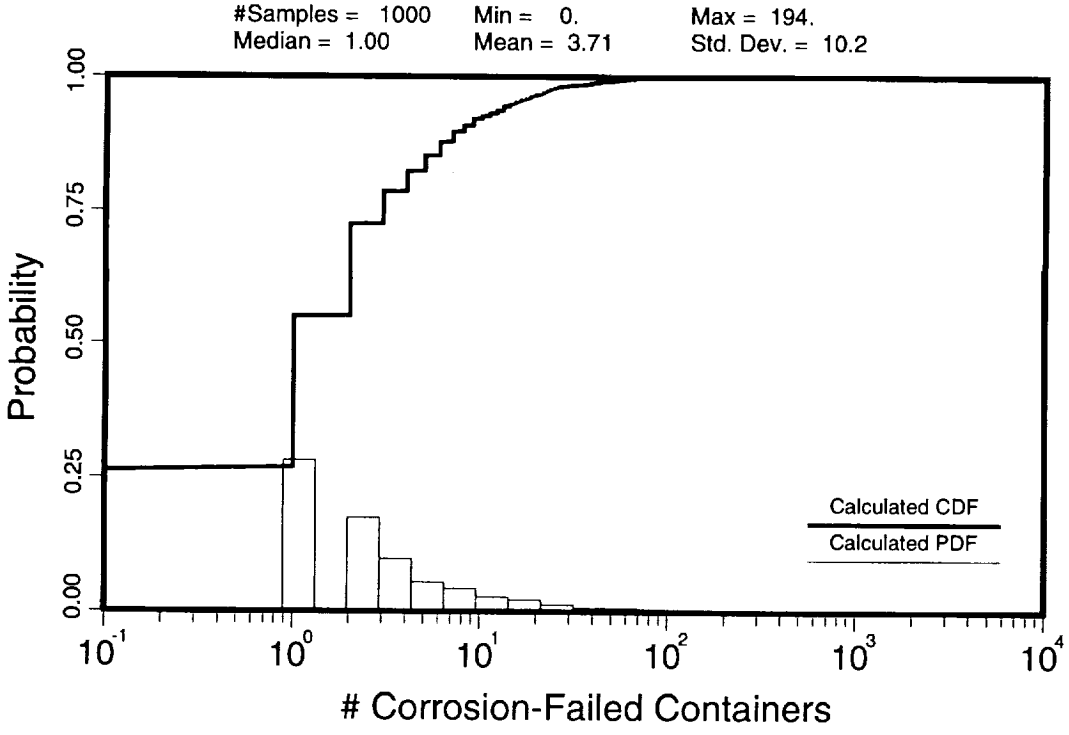

Figure 15-30. Distribution of containers that experience corrosion-induced failure over a 10,000-year period (57 kW/acre, vertical emplacement).

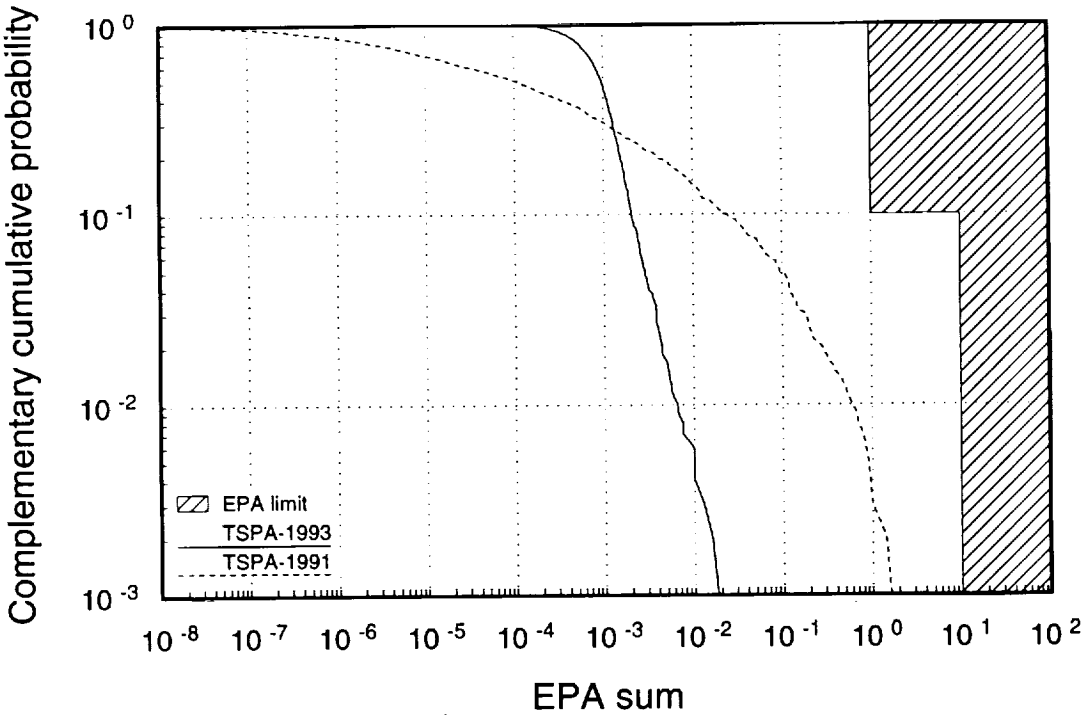

Figure 15-31. Conditional CCDFs of cumulative gaseous releases to the accessible environment, at 10,000 years, normalized by the EPA limits (57 kW/acre, vertical emplacement). Cross-hatching denotes area of noncompliance with the EPA standard.

caused simply by random selection). The similarity in the distributions is another indication that, given the source term used in this TSPA, corrosion only occurs in concert with the collapse of the thermal pulse. The distributions of corrosion-failure times (absolute corrosion-failure times), times of weep contact before failure (relative corrosion-failure times), and duration of weep contact are similar to those presented for the aqueous-release calculations—Figures 15-16, 15-17, and 15-18, respectively—with the major difference being the trunction of times at 10,000 years.

The conditional CCDF for cumulative gaseous releases, as normalized to the EPA limits, is shown in Figure 15-31. The figure shows results from both TSPA-91 and TSPA-93. The curves exhibit the same general shape as the curves for aqueous releases given in Figure 15-19, and the similarity in shape follows because the same mechanisms apply; although, for TSPA-93, juvenile failures are more important for gaseous releases than for aqueous releases. For TSPA-91, releases were primarily a function of the number of containers contacted by weeps which, because of the wide variation allowed in weep aperture, ranged from less than one container up to all the containers in the repository. The number of container failures varied from a fraction of one container (an artifact of the modeling) up

to several thousand containers. This wide variation in failed containers is reflected in the spread of the TSPA-91 curve. For TSPA-93, releases are a function of the number of juvenile failures and the number of containers contacted by weeps during the contraction of the dryout zone when they are susceptible to corrosion failure. The sum of juvenile failures and corrosion-induced failures vary from 36 to 366; thus, the TSPA-93 curve shows less spread than the TSPA-91 curve. As with TSPA-91, transport times are of secondary importance because they are very short (Section 14.6.2).

In both TSPA-91 and TSPA-93, the weeps model predicts fewer releases of ^{14}C than are predicted by the composite-porosity model. The reason is because we assume that, in the weeps model, failures (other than juvenile failures) only occur when containers are contacted by weeps. The composite-porosity model allows any container in contact with moisture to fail. This assumption is more realistic for the containers that are vertically emplaced in boreholes, where the air gap between the rock wall and the container could keep a substantial number of containers dry. If we relax this assumption in the weeps model, and allow corrosion of containers in a moist environment whether or not contacted by weeps, then the weeps-model gaseous releases might approach those predicted by the composite-porosity model.

15.5.1.4 Combined aqueous and gaseous releases

The conditional CCDF for combined cumulative aqueous and gaseous releases at 10,000 years, as normalized to the EPA limits, is shown in Figure 15-32. The figure also allows comparison of the magnitude of the aqueous and gaseous releases. With the parameter distributions selected for TSPA-93, the weeps model produces cumulative aqueous and gaseous releases that are of similar magnitude. (Individual dose calculations were not performed for gaseous releases, and therefore no combination of doses is offered.)

For the most likely cases—those expected 90% of the time—gaseous releases are the major contributor to total releases. As mentioned in the previous subsection, gaseous releases at these magnitudes are primarily a function of the number of juvenile failures. For the cases where the most releases occur, aqueous releases dominate. These cases are expected 10% of the time. In these extreme cases, corrosion-induced failures can approach and even outnumber juvenile failures.

15.5.2 Comparison of the four repository cases

In this section, the four different repository cases considered in this TSPA are compared with each other based on their general behavior as predicted by the weeps model, as well as their performance with respect to EPA and possible dose criteria.

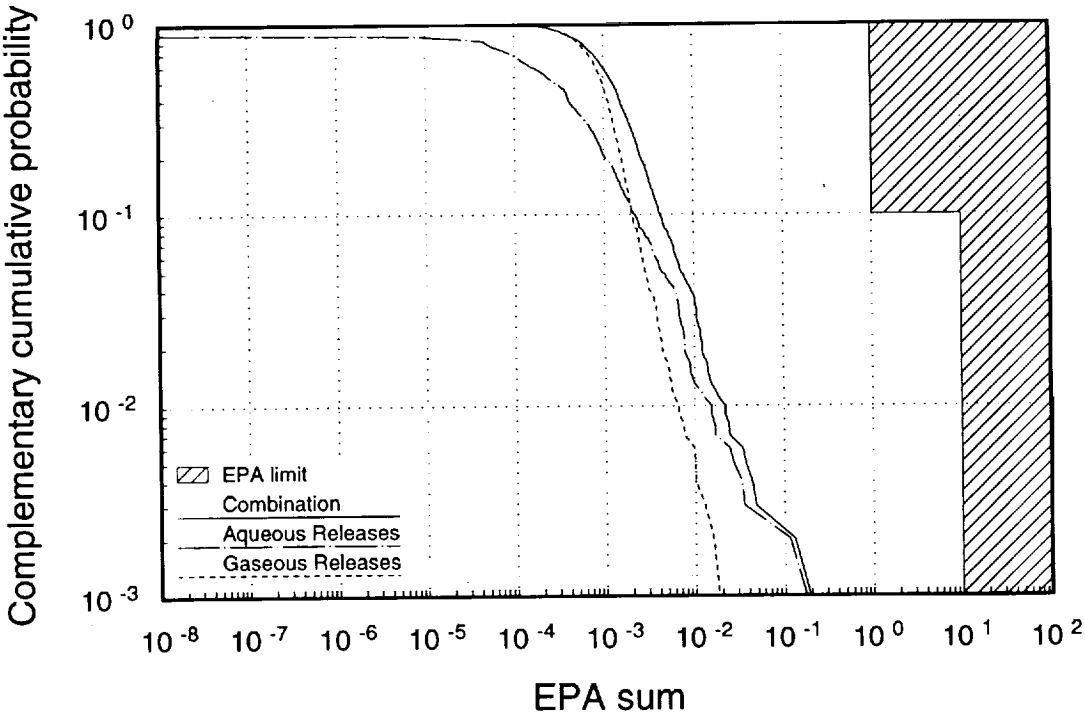

Figure 15-32. Combined conditional CCDFs of cumulative aqueous and gaseous releases to the accessible environment, at 10,000 years, normalized by the EPA limits (57 kW/acre, vertical emplacement). Cross-hatching denotes area of noncompliance with the EPA standard.

15.5.2.1 Aqueous releases

The weeps model predicts that different repository designs lead to different numbers of containers being contacted by weeps. Figure 15-33 presents the cumulative probability distributions of the numbers of containers contacted by weeps (compare this figure with Figure 15-10). The probability axis in the plot corresponds to the fraction of realizations that a given number of contacts occur.

Examination of the median values in the figure (those with a probability of 50%) shows that the 114-kW/acre, vertical-emplacement case has about 1100 more containers contacted by weeps than does the 57-kW/acre, vertical-emplacement case—approximately twice as many contacts. The 114-kW/acre, in-drift-emplacement case has about 1300 more containers contacted by weeps than does the 57-kW/acre, in-drift-emplacement case—approximately a factor of 1.5 more contacts. Comparing the different emplacements, the figure shows that the in-drift-emplacement cases have more than a factor of 2 more contacts than the corresponding vertical-emplacement cases. For the 57-kW/acre repositories, the difference is about 1500 containers. For the 114-kW/acre repositories, the difference is about 1800 con-

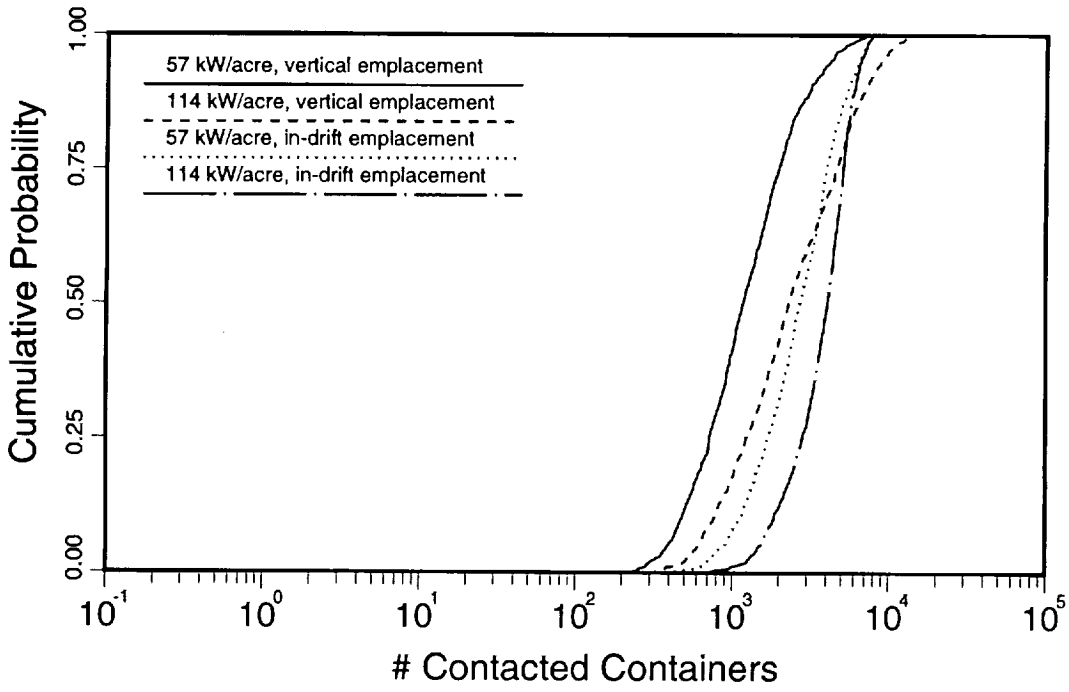

Figure 15-33. Comparison of the distributions of containers contacted by weeps over a 1,000,000-year period, for the four repository cases.

tainers; although, at the upper extreme of the distributions, the vertical-emplacement case has substantially more containers contacted by weeps than does the in-drift emplacement.

In general, Figure 15-33 illustrates two points. First, a greater number of the larger, in-drift containers is contacted by weeps than the number of the smaller, vertically emplaced containers. The reason is that the larger containers lying on their sides offer a greater cross-sectional area to weeps—i.e., they are easier to hit. Second, the 57-kW/acre cases result in fewer containers contacted by weeps than the corresponding 114-kW/acre cases. Here, the reason is that the hotter repository displaces more water than the cooler repository, creating more weeps. Increasing the number of weeps increases the probability of contacting a container. Also, as modeled, the hotter repositories shed the displaced water into a smaller area of the repository at the times when the dryout volumes are largest. Concentrating weeps in a smaller area increases the chance of hitting containers in that area; although, this effect is important only when few containers are contacted.

As is shown in the preceeding section, with the YMIM source model, very few containers contacted by weeps ever release radionuclides. The number of containers that are predicted to have aqueous releases of radionuclides is presented in Figure 15-34. The probability axis in the plot corresponds to the fraction of realizations that a given number of containers eventually release radionuclides to the groundwater. Releasing containers that were juvenile

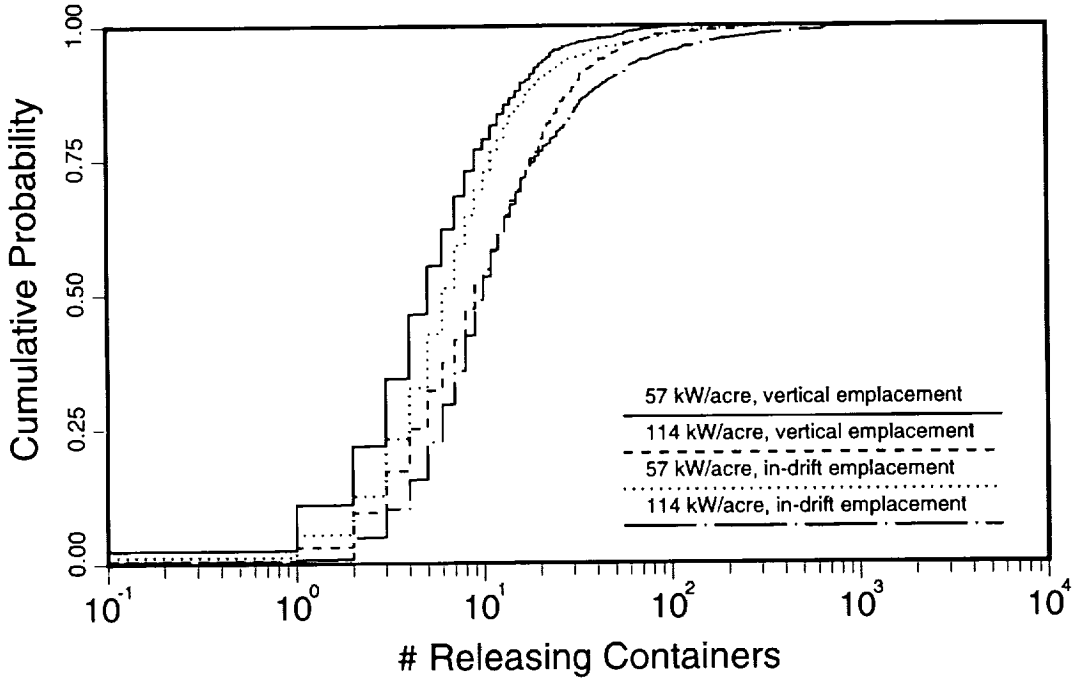

Figure 15-34. Comparison of the distributions of containers that have aqueous releases of radionuclides over a 1,000,000-year period, for the four repository cases.

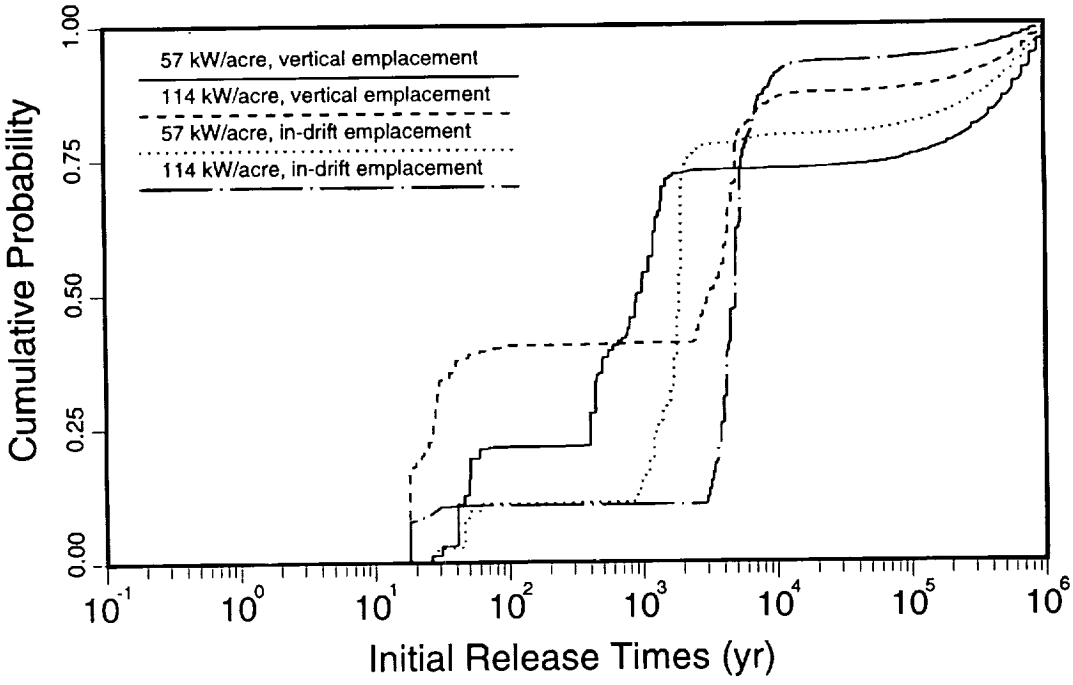

Figure 15-35. Comparison of the distributions of initial times at which containers have aqueous releases of radionuclides, for the four repository cases.

failures (and were eventually contacted by weeps) and those that failed by corrosion are both included in the figure.

Examination of the median values in this figure shows that the 114-kW/acre, vertical-emplacement case has 9 containers contacted by weeps, while the 57-kW/acre, vertical-emplacement case has 5. The differences are relatively linear—at the upper extreme it still approaches a factor of 2. The in-drift-emplacement cases show a similar pattern of weep contact. Comparing the different emplacements, the figure shows that the in-drift-emplacement cases have only a few more contacts than the corresponding vertical-emplacement cases, although the upper extreme values show more divergence. The in-drift containers hold approximately 4 times the waste that the vertically-emplaced containers hold. Thus, a factor of 2 increase in releasing containers is effectively a factor of 8 increase in releases of mass. The figure also shows the same general pattern seen in Figure 15-33: the number of releasing containers is greater with larger containers and in a hotter repository.

Figure 15-35 presents the initial release times for failed containers. Release times for both corrosion-failed containers and juvenile failures are included in the figure. The data in the figure are every initial release time for every releasing container for all realizations; thus, the probability axis corresponds to the fraction of releasing containers. As mentioned in the previous section, all time-related distributions are estimates based on the WEEPTSA time step during which releases occur.

The release times in Figure 15-35 exhibit the trimodal distributions seen in Figure 15-12. Early-time releases are caused primarily during expansion of the dryout zone which sheds water onto juvenile failures. Releases commencing between several hundred and several thousand years are primarily the end result of containers failed by corrosion during the collapse of the dryout zone. Most of the releases begin at these intermediate times for all four repository cases. The late-time releases are caused by changing flow patterns from changing climates contacting juvenile failures. As is to be expected, the in-drift emplacements show fewer early-time and late-time initial releases because they are modeled with fewer juvenile failures.

To compare the four repository cases according to the initial release times, the time periods must be examined separately. At early times, the differences are insignificant because releases begin from all four repository cases within a few decades of eachother. (Actually, the containers are all above boiling temperature, there should probably be no releases at all, but the YMIM source term does not screen out these instances.) At intermediate times, the cooler repositories begin releasing waste sooner than the hotter repositories, because the dryout zone collapses faster and water contacts the containers sooner. Also during this interval, the thin-wall, SCP containers tend to fail before the multipurpose containers. At

late times, the juvenile failures of the cooler and less robust containers have more releases, primarily because fewer of them failed at earier times.

Isolating the container failures that occur because of corrosion provides a more accurate view of container lifetime. Figure 15-36 presents the distributions of the number of corrosion-induced failures for all realizations, and thus the probability axis corresponds to the fraction of realizations. At the lower extreme, all cases have realizations where there are no corrosion-induced failures: for the 57-kW/acre cases, over 25% of the realizations have no corrosion failures; for the 114-kW/acre cases, about 15% of the time there are no corrosion failures. At the medians of the distributions, only a few containers experience corrosion-induced failure, although a pattern is developing that carries through to the upper extreme. The vertically emplaced containers undergo fewer corrosion-induced failures than the in-drift containers, and the cooler repository has few corrosion-induced failures than the hotter repository. The reasons are the same as those given in the discussion of Figure 15-34: bigger containers present a larger target for weeps; and hotter repositories move more water creating more weeps. The upper extremes of the failure distributions are very similar to the upper extremes of the containers-releasing distributions, indicating that in the worst case most failures are caused by corrosion.

The times at which containers undergo corrosion-induced failures are presented in Figure 15-37; these times correspond to the container lifetimes. The figure shows that containers in a 114-kW/acre repository can generally be expected to last longer than containers in a 57-kW/acre repository (although not in the extreme cases—see below). At the median values, the difference in lifetimes between the hotter repositories and the cooler repositories is over 3000 years. The longer lifetimes occur because the thermal load protects more of the hotter repositories for longer periods of time. The figure also shows a performace advantage of the multipurpose containers: at the median values, the larger containers last almost 1000 years longer than smaller SCP-type containers. However, these increased lifetimes are caused by the additional heat generated within the larger containers and not by the extra steel overpack (see below).

The weeps model predicts that virtually all corrosion-failed containers fail within 10,000 years. Although not apparent in Figure 15-37, the times of the last corrosion-induced failures is of interest. For the vertically emplaced containers, the last failures are at 36,000 years for the 57-kW/acre case, and at 33,000 years for the 114-kW/acre case; for the in-drift containers, the last failures are at 820,000 years for the 57-kW/acre case, and at 590,000 years for the 114-kW/acre case. These containers underwent significant corrosion while warm, but not enough to fail; when they cooled, corrosion rates were very low, but they experienced enough corrosion to cause the final breach.

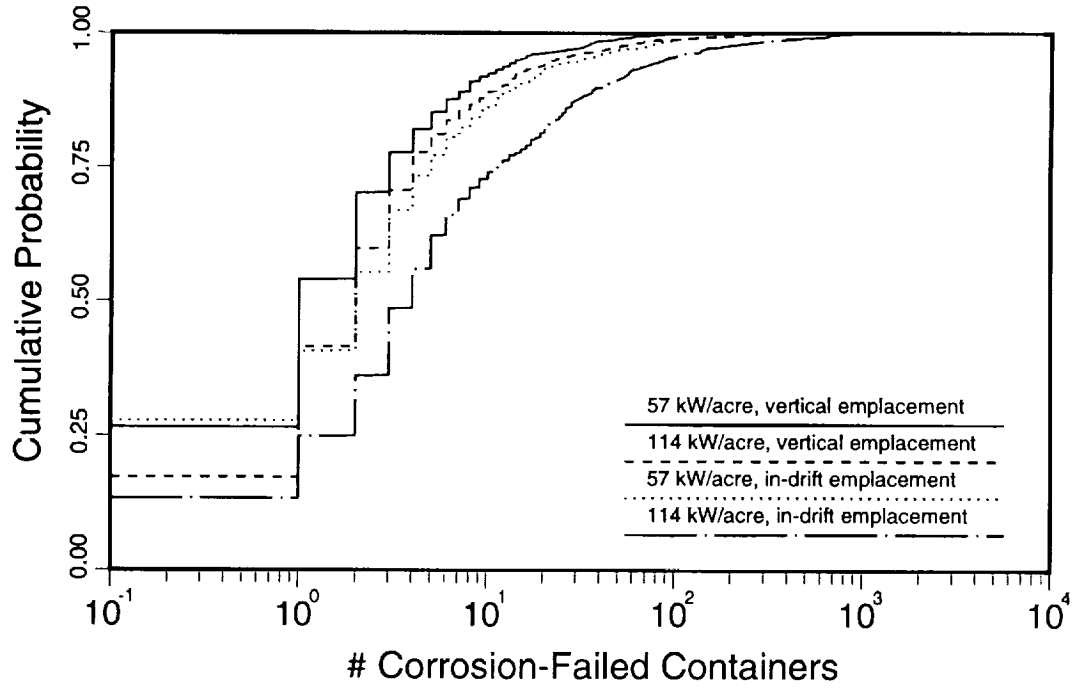

Figure 15-36. Comparison of the distributions of containers that experience corrosion-induced failure over a 1,000,000-year period, for the four repository cases.

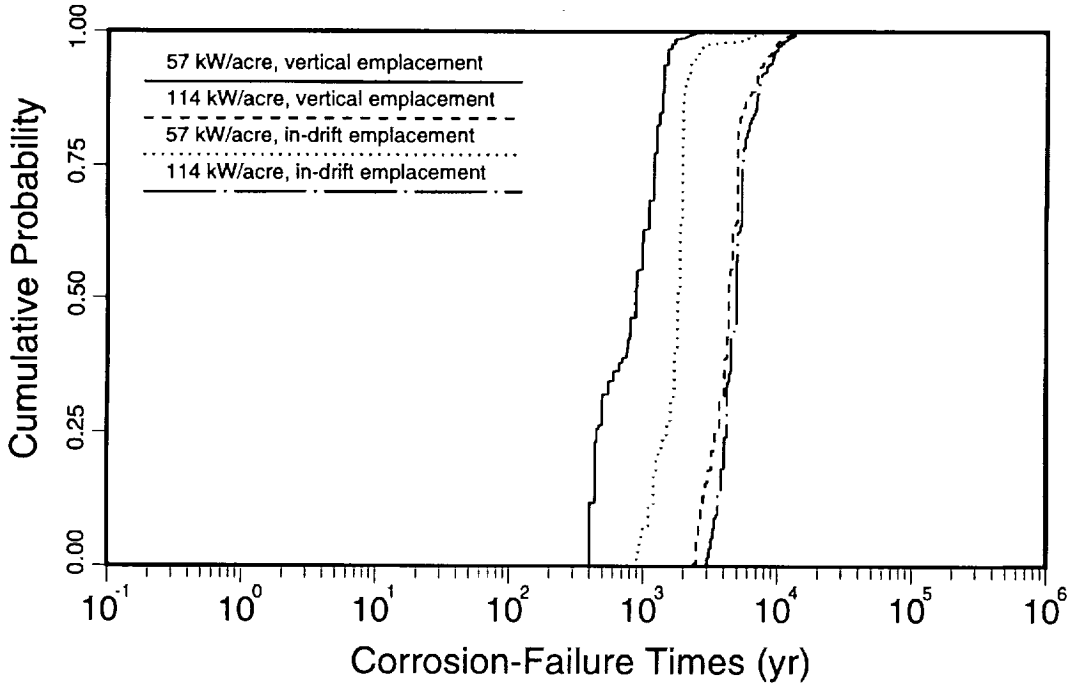

Figure 15-37. Comparison of the distributions of the times of corrosion-induced failures for the four repository cases.

For containers that fail by corrosion, the amount of time that they are contacted by weeps before failure offers a more accurate picture of the time scale of the corrosion process. Figure 15-38 presents the estimated time of water contact before corrosion failure for containers from the four repository cases. For containers that fail by corrosion, approximately 20% undergo extremely rapid corrosion. These containers have been sampled with high corrosion rates and they are contacted by weeps when they are at high temperatures. Approximately 5% of the corrosion-failed containers undergo relatively slow corrosion; these containers are contacted by weeps when they are at sub-optimal temperatures for corrosion. Most of the water-contact times, however, are close to the median times. For the 57-kW/acre repository with vertically emplaced containers, the median water-contact time before failure is about 400 years; for the other repositories, the median times are near 1100 years. These containers are contacted at high temperatures, but they have been selected with average corrosion rates.

Figure 15-38 shows that the larger, multipurpose containers offer an increased lifetime that averages 700 years, but only for the cooler repositories. In the hotter repositories, the multipurpose containers last only as long as the thin-wall, SCP-type containers. Actually, in both 57-kW/acre and 114-kW/acre repositories, dry oxidation significantly corrodes the mild steel overpack of the multipurpose containers while the containers are above boiling. The difference in container lifetime in the cooler repository is primarily due to differences in the duration of the dryout zone (see Figure 10-11) and the higher surface temperature of the multi-pupose container, which delays aqueous corrosion when containers are outside the dryout zone (see Figures 10-17 and 10-19). In the hotter repository, the dryout zone collapses at approximately the same time, independent of container type (see Figure 10-10), and aqueous corrosion begins at the same time on the thin-wall, SCP-type container and the inner liner of the multipurpose container. Thus, with the YMIM source model, the weeps model predicts effectively no performance advantage from the overpack of more robust, multipurpose container (although even thicker overpacks could afford a performace advantage, see Section 14.7).

The amount of time that containers are contacted by weeps offers an estimate of how long waste is being released from these containers. Figure 15-39 shows the total time of water contact for containers from the four repository cases. In general, the distributions are bimodal, with the short-duration mode caused by contact with the more transient weeps formed during the contraction of the dryout zone, and the long-duration mode caused by contact with weeps formed at a climate change (see discussion of Figure 15-18 in Section 15.5.1.2). In general, the vertically emplaced containers, with their smaller cross-section, are contacted for shorter durations than the larger cross-section, in-drift containers. The in-drift

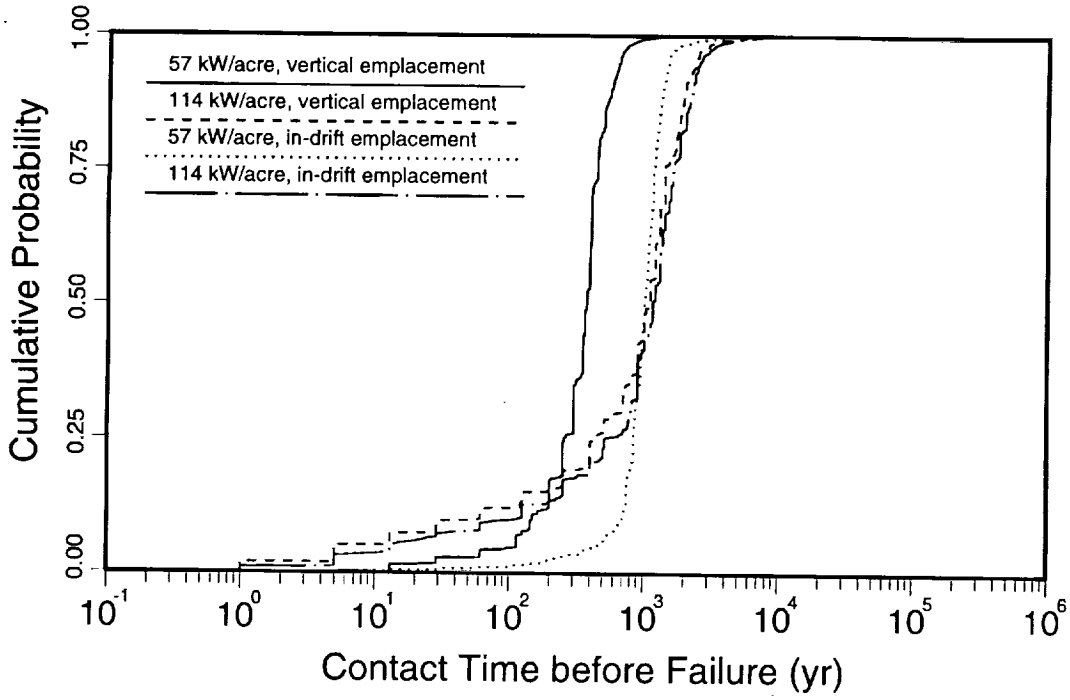

Figure 15-38. Comparison of the distributions of the durations that weeps contact containers before corrosion-induced failure occurs, for the four repository cases.

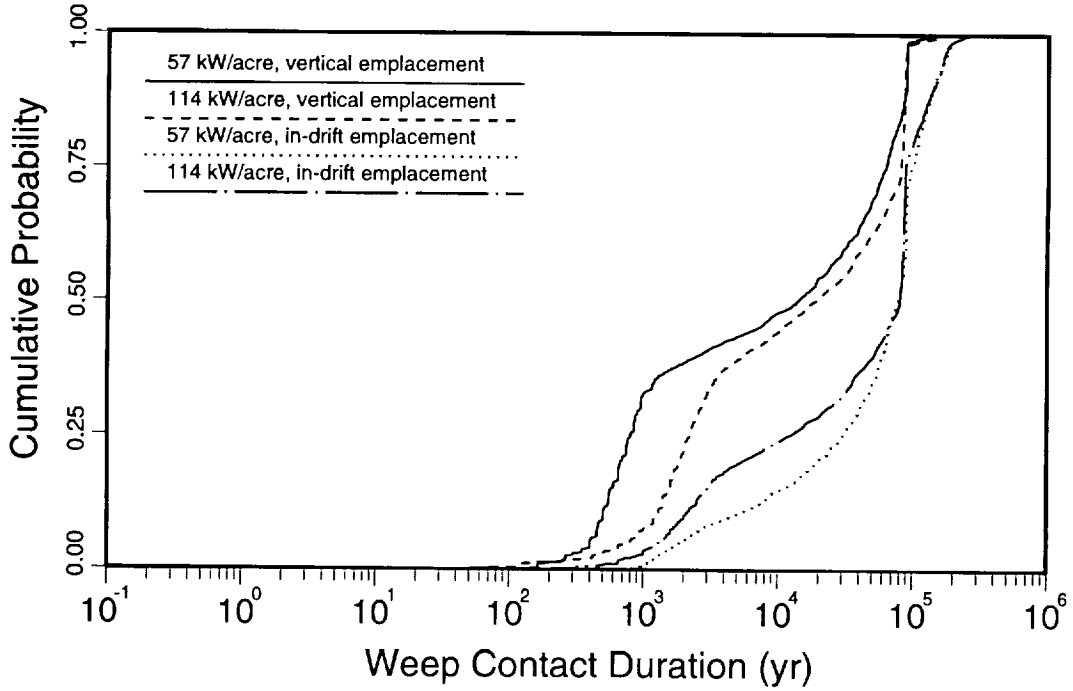

Figure 15-39. Comparison of the distributions of the total durations that weeps contact containers, for the four repository cases.

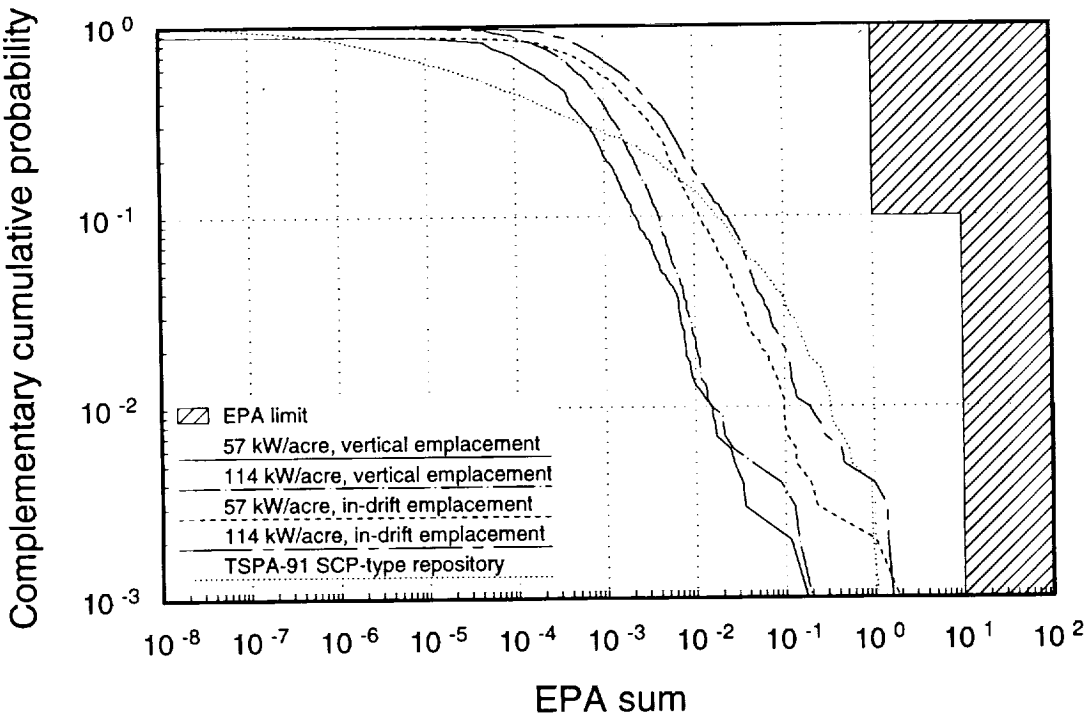

Figure 15-40. Comparison of the conditional CCDFs of cumulative aqueous releases to the accessible environment, at 10,000 years, normalized by the EPA limits, for the four repository cases. Cross-hatching denotes area of noncompliance with the EPA standard.

containers have proportionally fewer short-duration contacts, primarily because many of the containers contacted at short-duration are also contacted by the longer-duration weeps. The picture is more complicated when the different repository thermal loads are compared (for the vertically emplaced containers, the hotter repository typically has longer contact durations; for the in-drift containers, the hotter repository typically has shorter contact durations), but the differences in duration are relatively insignificant.

The cumulative aqueous releases to the accessible environment, normalized to the EPA limits, are presented for the four cases in Figure 15-40. Releases are calculated over a 10,000-year period. All four cases are below the EPA limit. Further, none of the cases is drastically different. Releases for the four cases are within an order of magnitude of each other, except when releases are very low. The 114-kW/acre repositories both always have some releases, while 10% of the 57-kW/acre repositories have no releases. The 114-kW/acre repositories produce large dryout zones—in fact, their dryout zones completely encompass the repositories for a time. Near the outside boundaries of the dryout zones, a large amount of water is being displaced and diverted—focused—into a small fringe of the repository. In

every realization some releases result from failed containers, either juvenile or corrosion-induced, that are contacted by weeps at the edges of these repositories.

Examination of Figure 15-40 reveals a trend in the results. In general, the in-drift containers produce greater releases than the vertically emplaced containers. A secondary effect is that the 114-kW/acre thermal load produces greater releases than the 57-kW/acre thermal load.

The in-drift containers present a substantially larger target for weeps. As alluded to in Section 15.4, the area of contact for a weep with a multipurpose, in-drift container averages over 11 m^2, while the area of contact for a weep with a thin-walled, vertically emplaced container averages about 0.75 m^2. Thus, the in-drift containers present a cross-section approximately 15 times larger than that of vertically emplaced containers. However, approximately 4 of the vertically emplaced containers are required to hold as much waste as 1 in-drift container. Therefore, in a repository designed for multipurpose, in-drift containers, waste is about 5 times more likely to be contacted by weeps than in a repository designed for thin-wall, vertically emplaced containers. The releases shown in Figure 15-40 are typically between 4 and 10 times higher for the larger containers. Releases can be greater than a factor of 4 for two reasons: (1) the in-drift containers are specified to have only half the fraction of juvenile failures as the vertically-emplaced containers, but this number of failures translates into 2 times as much waste potentially being exposed to weeps, and (2) in the extreme cases, when juvenile failures are inconsequential to the results, only a few realizations are involved, and random chance can lead to presented differences.

The somewhat poorer performance of the hot repositories is caused by greater displacement and focusing of water by their larger dryout zones. This effect is mitigated, but not completely abated, by the generally longer container lifetimes provided by the protection of the larger dryout zones.

The cumulative aqueous releases from the EBS, normalized to the EPA limits, are presented for the four cases in Figure 15-41. The difference between these curves and those shown in Figure 15-40 suggests that a large amount of ^{239}Pu released from the EBS is subsequently trapped before it reaches the accessible environment. The adsorption of ^{239}Pu in the saturated zone is a deciding factor for meeting the EPA standard, especially for the in-drift containers.

The radiation dose to a maximally exposed individual, as predicted by the weeps model, is presented in Figure 15-42. The curves represent the peak dose that is realized within a million-year period. The median values shown range from approximately 4 mrem/yr for the 57-kW/acre repository with vertical containers, to approximately 80 mrem/yr for the 114-kW/acre repository with in-drift containers. At the extreme values of the distri-

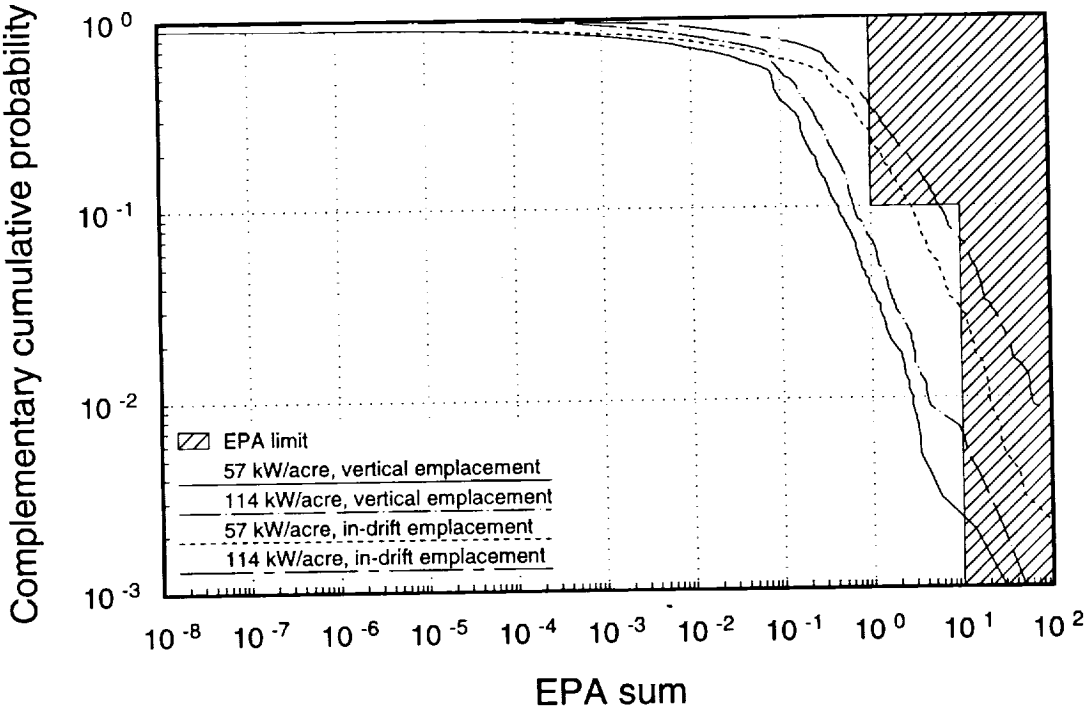

Figure 15-41. Comparison of the conditional CCDFs of cumulative aqueous releases from the EBS, at 10,000 years, normalized by the EPA limits, for the four repository cases. Cross-hatching is offered for informational purposes only.

butions, the 57-kW/acre repository with vertical containers produces a dose that exceeds 2,000 mrem/yr, while the dose for the 114-kW/acre repository with in-drift containers exceeds 80,000 mrem/yr. These predicted doses are high, although not as high as those predicted with the composite-porosity model, and are probably overestimates of releases and doses, because of assumptions that we believe to be generally conservative.

The same pattern implied in the plot of cumulative releases at 10,000 years (Figure 15-40) is implied here. Large cross-section containers produce greater doses than those with small cross-sections because they are more likely to be contacted by weeps. Repositories with greater thermal loads, and hence greater perturbation of the groundwater flow, produce greater doses than repositories with lower thermal loads, because more weeps are generated and focused on a smaller area of the repository.

Figure 15-43 shows the times when the peak doses occur. The median times range from approximately 10,000 years for the 114-kW/acre repository with vertical containers to approximately 20,000 years for the 57-kW/acre repository with in-drift containers. The difference in times is not especially significant, given that somewhat greater magnitude doses are predicted for the latter of these cases. The fact that the thin-wall containers do not last as long as the multipurpose containers is compensated for by the fact that they

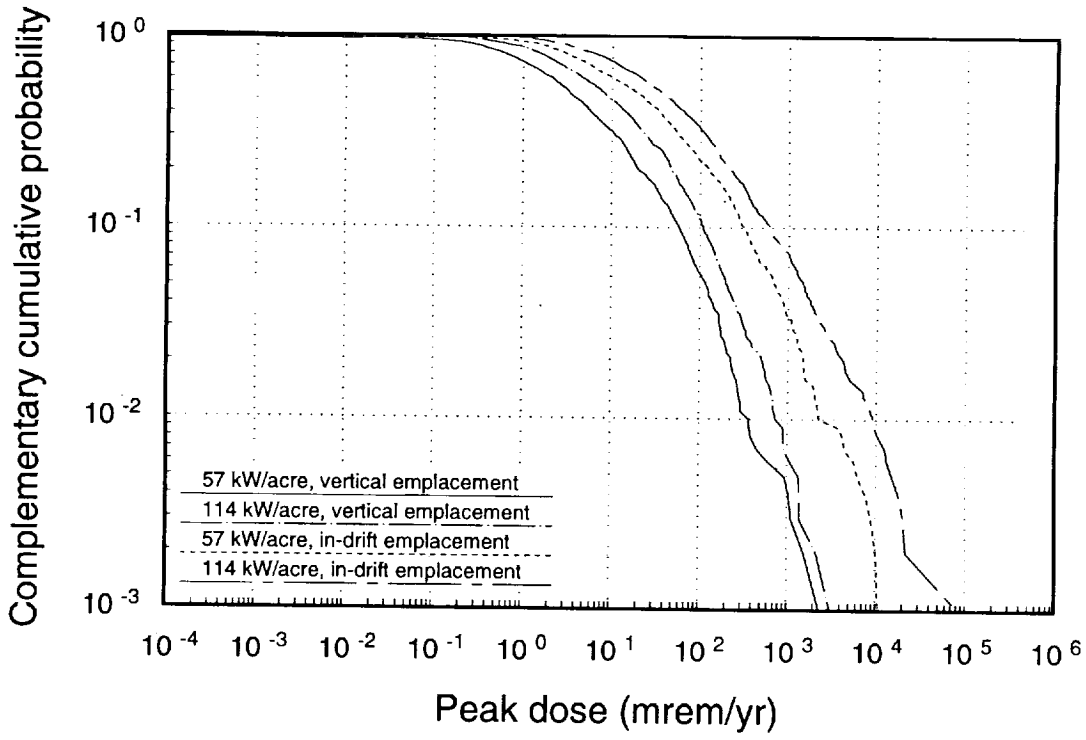

Figure 15-42. Comparison of the conditional CCDFs of peak radiation doses from drinking water to a maximally exposed individual, for the four repository cases.

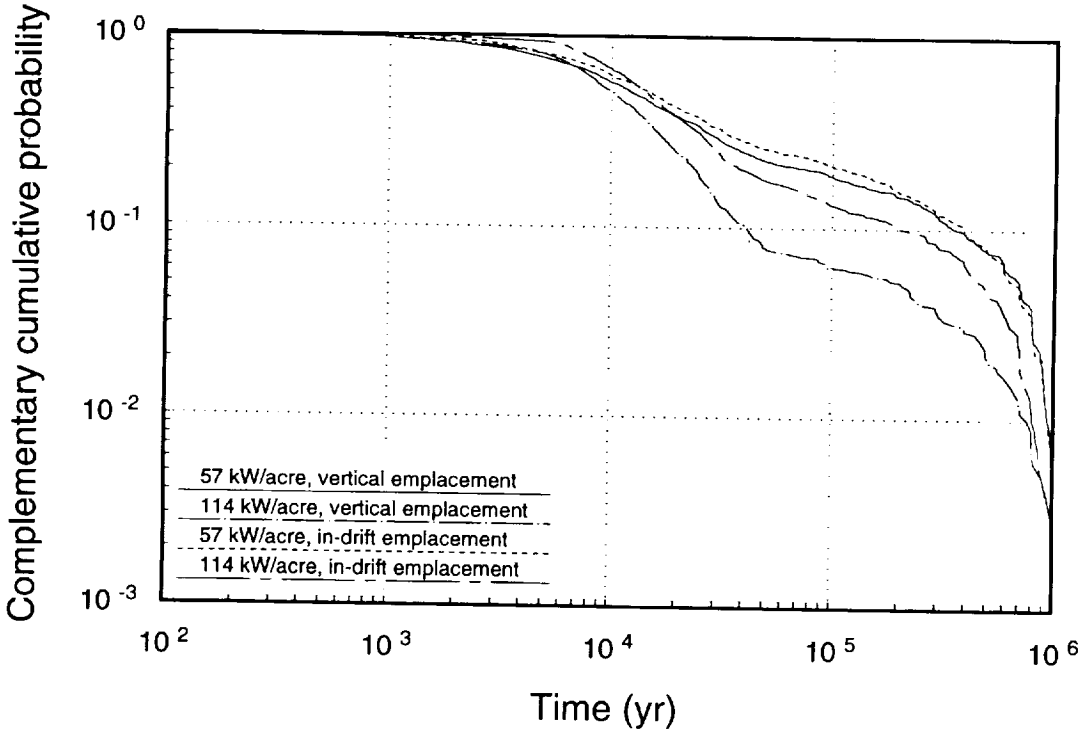

Figure 15-43. Comparison of the conditional CCDFs of the times of peak radiation doses for the four repository cases.

are less likely to be contacted by weeps. Also, the waste in the in-drift containers takes longer to leach, which can delay the peak dose. Of some interest is that less than 1% of all realizations have not reached the peak dose at a million years.

15.5.2.2 Gaseous releases

With respect to gaseous releases, the comparison of performance of the four repository cases is resticted to the EPA standard. As discussed in Chapter 2 and Section 14.6.2, individual dose from gaseous releases is expected to be inconsequential given the large dilution offered by the atmosphere, and dose was not calculated for ^{14}C. Thus, the weeps-model calculations were limited to a 10,000-year period.

Only ^{14}C was considered for gaseous releases. In TSPA-93, the weeps model is primarily used to determine the interaction of groundwater with the EBS. The source term YMIM (Chapter 13 and Section 14.5.3) is used to determine container failures and the releases of ^{14}C from the EBS. The gaseous-transport model that is described in Chapter 12 is used to determine releases at the ground surface (the accessible environment).

The distribution of containers contacted by weeps during the 10,000-year calculational period is presented in Figure 15-44. Fewer containers are contacted than for the aqueous-release calculations because of the shorter time period. In general, the cooler repositories suffer fewer container/weep contacts than the hotter repositories because the cooler repositories create less perturbation in the flow field. The repositories with vertically emplaced containers suffer fewer contacts than the repositories with in-drift containers because the vertically emplaced containers present a smaller target for the weeps. As shown in the figure, the 114 kW-acre repository with in-drift containers is an exception approximately 25% of the time. The fewer number of containers and the longer duration of the hot-repository dryout zone combine to limit the total number of container/weep contacts.

Figure 15-45 presents the distribution of containers that release gaseous ^{14}C. Containers with gaseous releases far out number those with aqueous releases (Figure 15-34) because juvenile failures begin gaseous releases immediately and do not require contact by a weep. The distributions shown in the figure follow closely the juvenile-failure distributions assigned as input. Only between 0.05% and 0.25% of the 8489 in-drift containers are specified as juvenile failures (the median is 13); between 0.1% and 0.5% of the 35,580 vertically emplaced containers are juvenile failures (the median is 107). The multipurpose, in-drift containers carry approximately 4 times the mass of the thin-wall, SCP-type containers: thus, in terms of mass, a median value of 104 metric tons of waste is immediately exposed in in-drift containers that are juvenile failures, and a median value of 214 metric tons is immediately exposed in vertically emplaced containers.

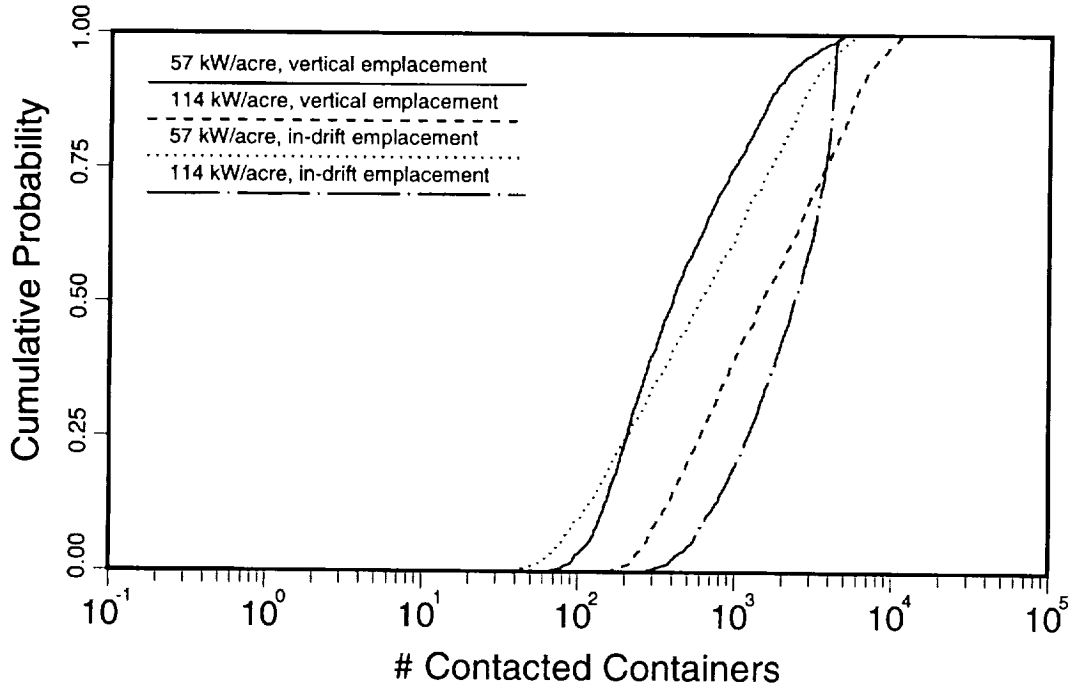

Figure 15-44. Comparison of the distributions of containers contacted by weeps over a 10,000-year period, for the four repository cases.

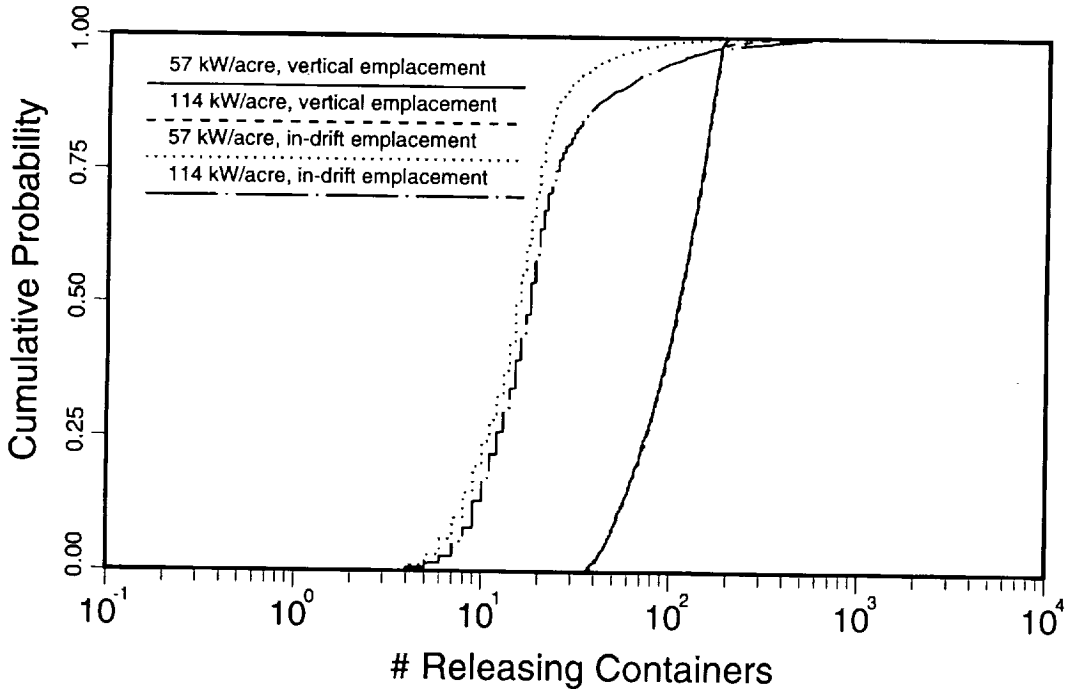

Figure 15-45. Comparison of the distributions of containers that have gaseous releases of radionuclides over a 10,000-year period, for the four repository cases.

The times of initial releases are presented in Figure 15-46. For the 57-kW/acre repository with vertically emplaced containers, 96% of the releasing containers are juvenile failures with immediate releases, and virtually all the other 4% of releasing containers begin releasing within 1500 years. For the 114-kW/acre repository with vertically emplaced containers, 94% of the releasing containers are juvenile failures, and virtually all the other releasing containers begin releasing within 6000 years. For the 57-kW/acre repository with in-drift containers, 64% of the releasing containers are juvenile failures, and virtually all the other releasing containers begin releasing within 3000 years. For the 114-kW/acre repository with in-drift containers, 36% of the releasing containers are juvenile failures, and the other 64% of releasing containers begin releasing at times between 2,000 and 10,000 years.

Corrosion-induced failures are generally an insignificant part of the releasing vertically emplaced containers, as shown in Figure 15-47. The number of corrosion failures exceeds the median number of juvenile failures only about 1% of the time. However, for in-drift containers, corrosion failures rival juvenile failures, and in the 114-kW/acre case, can far outnumber juvenile failures. (Separate calculations were performed for gaseous and aqueous releases; by chance, the gaseous-release calculations produced a larger corrosion-failure realization than did the aqueous-release calculations.) The times of corrosion-induced failures are virtually identical for the gaseous-release and the aqueous-release calculations (although the times are truncated slightly because of the reduction in time periods), and therefore a plot of the corrosion-failure times is not offered.

Based on the number of failures and how the failures are distributed in time, the multipurpose containers and the hotter repositories could offer a performance advantage, at least in terms of average behavior. Figure 15-48 presents the cumulative gaseous releases of ^{14}C over 10,000 years, as normalized by the EPA limits, for the four repository cases. The four repositories produce cumulative releases below the limits set in the EPA standard. Also, the weeps model predicts less gaseous releases than does the composite-porosity model (compare with Figure 14-29).

Figure 15-48 does not confirm the expected performance advantage of the hotter repositories and larger containers. Rather, Figure 15-48 is similar to Figure 15-40, and tends to confirm that large containers are predicted by the weeps model to lead to more releases. As a secondary effect, high thermal loads are generally predicted to cause greater releases. When releases are predicted to be low—a sizeable percentage of the time—the expected performance advantage is found. However, the in-drift containers suffer a disproportionate number of corrosion-induced failures, especially in terms of waste mass that is exposed. Also, the hotter repositories tend to produce shorter travel times for gases. Thus, despite the fact that fewer of the large in-drift containers fail (primarily because of the juvenile-failure

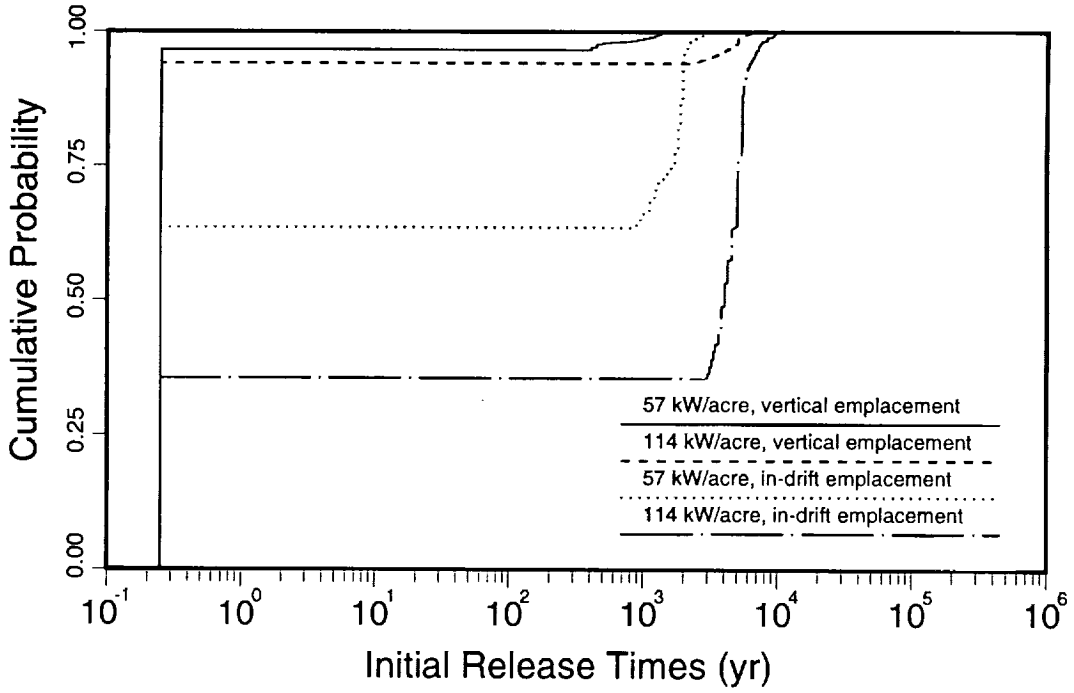

Figure 15-46. Comparison of the distributions of initial times at which containers have gaseous releases of radionuclides, for the four repository cases.

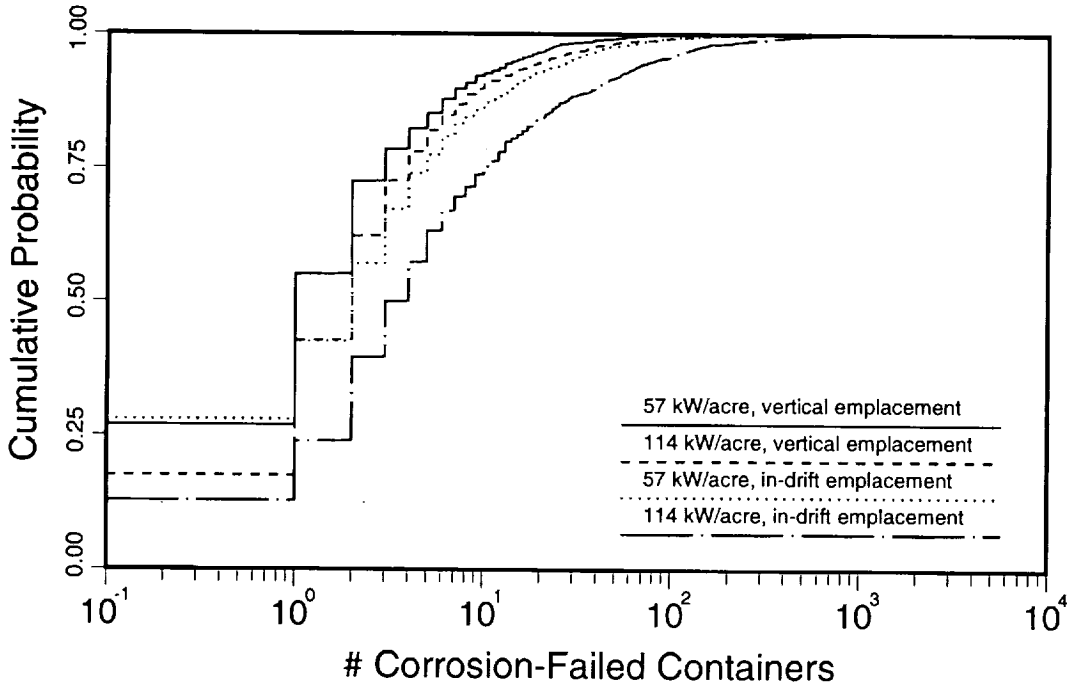

Figure 15-47. Comparison of the distributions of containers that experience corrosion-induced failure over a 10,000-year period, for the four repository cases.

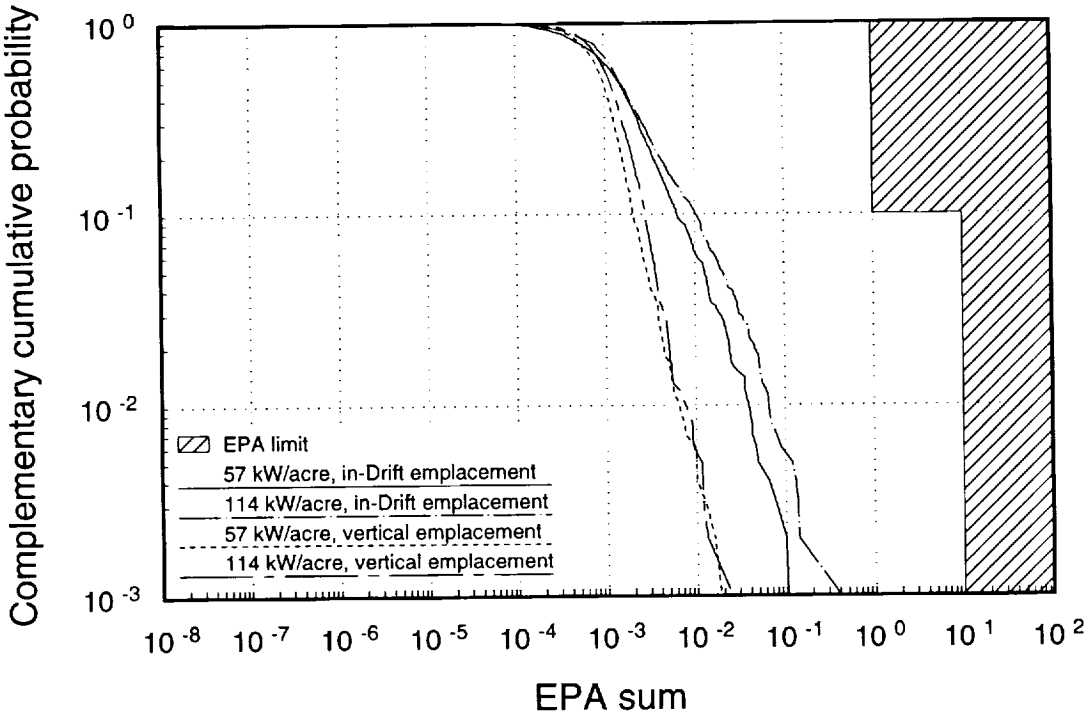

Figure 15-48. Comparison of the conditional CCDFs of cumulative gaseous releases to the accessible environment, at 10,000 years, normalized by the EPA limits, for the four repository cases. Cross-hatching denotes area of noncompliance with the EPA standard.

distributions assumed as input), and generally the ones that fail by corrosion fail at later times, the performance advantage is not realized.

15.5.2.3 Combined aqueous and gaseous releases

Figure 15-49 presents the combined cumulative aqueous and gaseous releases to the accessible environment, normalized to the EPA limits. (The dose calculations involved only drinking water doses, and thus no combination of aqueous and gaseous doses is offered.) Releases are calculated over a 10,000-year period.

As with the results shown in Figure 15-32, gaseous releases are most important most of the time (i.e., for most of the realizations); however, at the extremes of the CCDFs, aqueous releases dominate. In any event, all four cases are below the EPA limits. The same general pattern shown in all of the performance calculations is shown here: large containers result in more releases than small containers, and secondarily, a 114-kW/acre repository results in more releases than a 57-kW/acre repository.

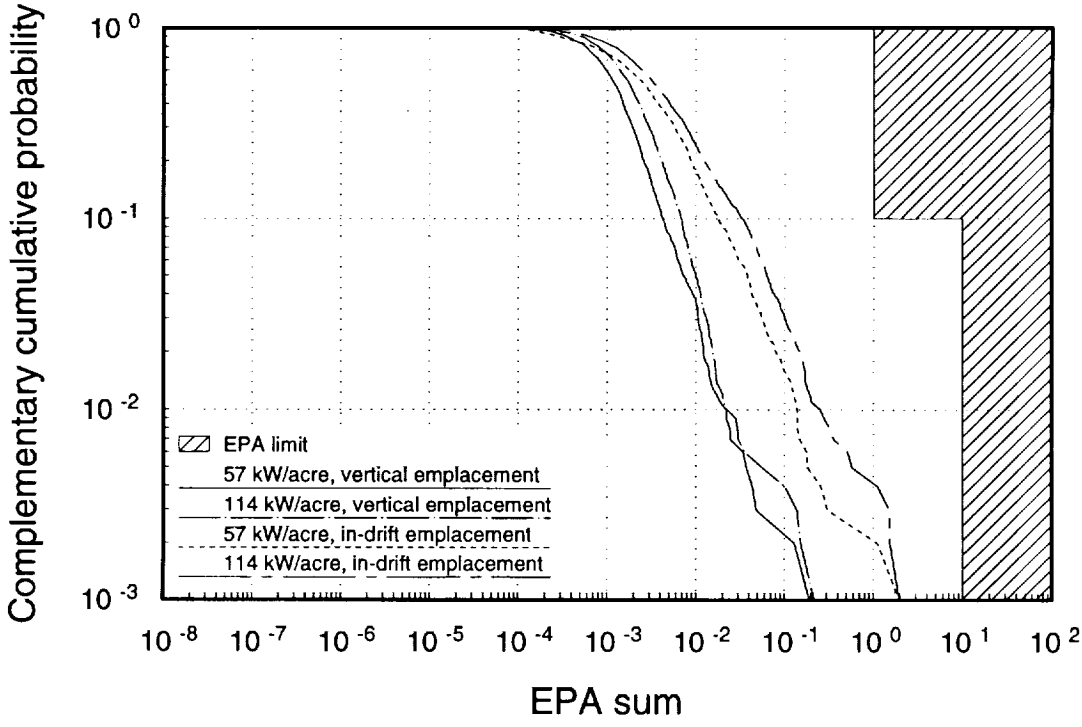

Figure 15-49. Comparison of the combined conditional CCDFs of cumulative aqueous and gaseous releases to the accessible environment, at 10,000 years, normalized by the EPA limits, for the four repository cases. Cross-hatching denotes area of noncompliance with the EPA standard.

15.5.3 Thermal modeling sensitivities

Deterministic thermal calculations, essentially one for each of the four repository cases, were used as the basis of the hydrothermal model in this TSPA (Chapter 10). Although heat conduction is a well-understood phenomenon, and heat-conduction effects could be expected to dominate the hydrothermal regime within Yucca Mountain, there are still many uncertainties in predicting the future performance of a repository in this environment. Uncertainties exist in several areas, including in our description of the mountain (e.g., bulk permeabilities, heterogeneities in thermal conductivities), in our neglecting of various possible hydrothermal effects, (e.g., extended dry, and bouyant water vapor being pumped from the water table to above the repository), and in our foretelling of future infiltration and percolation rates.

One additional series of TSPA calculations was performed to estimate the sensitivity of weeps-model predictions to the parameters used in the hydrothermal model. The calculations were the same as the calculations reported above, except that the dry-fraction and dryout-volume curves used as parameters to the hydrothermal model were changed. Rather than using the curves defined by E. E. Ryder and coworkers, the curves used were those produced

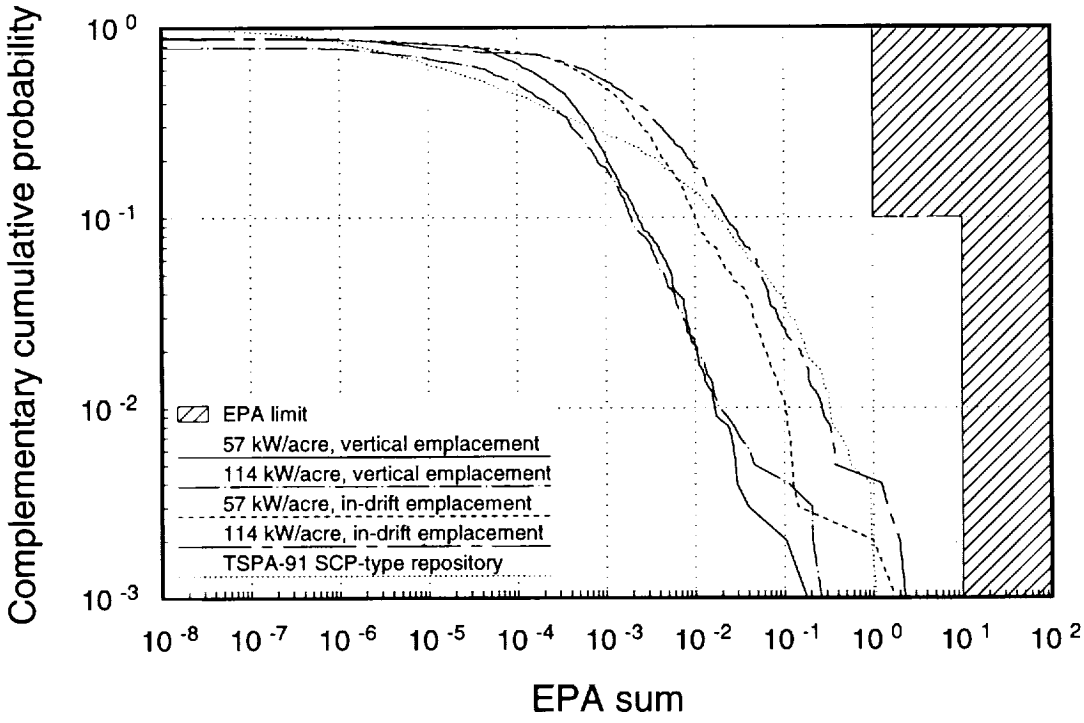

Figure 15-50. Comparison of the conditional CCDFs of cumulative aqueous releases to the accessible environment, at 10,000 years, normalized by the EPA limits, for the four repository cases. Calculations to produce the CCDFs used thermal effects from V-TOUGH calculations (provided by T. A. Buscheck, LLNL). Cross-hatching denotes area of noncompliance with the EPA standard.

by T. A. Buscheck of Lawrence Livermore National Laboratory (Chapter 10). The Ryder curves are based on calculations that considered only thermal conduction, but from discrete containers. The Buscheck curves are based on calculations that included hydrothermal effects, but with a smeared heat source. The major difference in the two sets of curves is that the Ryder curves show the dryout zone collapsing at the center of the repository at around 5000 years; the Buscheck curves show the dryout zone existing for slightly over 9000 years. (As discussed in Chapter 24, Eaton examined dryout extent and duration and shows that they are also a strong function of fracture size.) The same container-wall and fuel-rod temperatures were used in the additional TSPA calculations.

Figure 15-50 presents the cumulative aqueous releases to the accessible environment over 10,000 years, as normalized by the EPA limits, for the four repository cases, using Buscheck's results. Figure 15-50 should be contrasted with Figure 15-40. The major difference between the two figures is not in the extreme releases, but rather in the lowest releases. In Figure 15-40, up to 10% of the realizations have no releases. In Figure 15-50, between 10% and 20% of the realizations have no releases.

We do not show the results of the dose calculations performed with the Buscheck curves because they are virtually identical to the results shown in Figure 15-42. A 4000-year increase in thermal-pulse duration has little effect on doses because 4000 years is a small fraction of a million-year calculation and because the repository rewets while it is still relatively hot. To noticeably impact releases, the containers must remain dry until they are below the temperature at which they are susceptible to corrosion.

The results shown in Figure 15-50 offer insight into what could occur if the extended-dry concept were modeled. In some realizations, parts of a repository could still be inundated with water and high releases could result. However, in the most probable realizations, all or almost all of the repository would be protected by flow until long after the thermal pulse dissipates and repository temperatures fall to near ambient. In this situation, few or no corrosion-induced failures would occur because the containers would be below the temperature where they are susceptible to corrosion. Therefore, there would be few or no releases of radionuclides. We suspect that this result would also hold for doses.

Thus, extended-dry conditions could have a significant impact on repository performance. We excluded the extended-dry concept from consideration in TSPA-93 because it is supported only by the composite-porosity model, and the assumptions behind this model are known to be physically inaccurate in describing rapidly changing flows (Peters and Klavetter, 1988). Physical models that describe hydrothermal phenomena must be improved.

In concluding this section, we examine hydrothermal effects to determine whether the thermal pulse of a repository can dominate the natural groundwater flow at Yucca Mountain, and thus to determine whether the creation of a significant thermal perturbation can add confidence to performance predictions. One way to determine this dominance is by examining the magnitude of the water displaced by the thermal pulse compared to percolation values associated with Yucca Mountain. Based on expansion of the dryout volume used in our hydrothermal model, we can estimate a displaced water flux as follows:

$$q_d = \frac{\Delta V}{\Delta t}\frac{\theta}{A_{rep}}, \tag{15.4}$$

where q_d is the displaced water flux, $\Delta V/\Delta t$ is the change in dryout volume with respect to time, θ is the moisture content of the tuff being dried, and A_{rep} is the area of the repository. From Figure 10-13, the dryout volume expands for approximately 800 yr, with a change in volume of approximately 5.7×10^8 m^3; thus, $\Delta V/\Delta t$ for a 114-kW/acre repository averages to approximately 7×10^5 m^3/yr. The moisture content of TSw is estimated as 0.065 and the area of a hot repository is about 2.33×10^6 m^2. Therefore, an estimate of the flux from water displaced by a thermal pulse is $7 \times 10^5 \times 0.065 / 2.33 \times 10^6 \approx 0.02$ m/yr, or about 20 mm/yr. This value compares well with estimates of wet-climate infiltration given in Chapter 8. It

follows that, from a performance perspective, thermal effects cannot be expected to dominate potential hydrologic effects with any degree of confidence.

15.5.4 Parameter sensitivities

As in the sensitivity analysis for the parameters associated with the composite-porosity model (Section 14.6.3), rank linear regression is used to determine which weeps-model parameters most strongly influence the repository-performance measures. Table 15-5 presents results of rank linear regression for 10,000-yr cumulative aqueous releases for the four repository cases being considered in this TSPA.

As discussed in Section 14.6.3, the ΔR^2 value is a measure of the relative importance of a parameter. All parameters with $\Delta R^2 \geq 0.01$ are listed in the tables in this section. R^2 is a measure of goodness of fit of the linear regression, and R^2 near 1 indicates a good fit, meaning that the variation in releases is well accounted for by the parameters used in the regression model. In this case, R^2 ranges between 0.60 and 0.66 (listed on the line labeled "Total"), which are all relatively poor fits.

The results shown in Table 15-5 require interpretation. Generally, the parameter to which the EPA performance measure is shown most sensitive is the 100°C pitting increment. This parameter is one of two that determines the corrosion rate for the corrosion-resistant thin-wall container and the inner liner for the multipurpose container—essentially it describes the container lifetime. As has been shown, the calculated container lifetimes approach the same time span as the performance measure—10,000 years—and therefore, this sensitivity is expected. However, as is shown in the comparison of the four repository cases (Section 15.5.2.1), the hotter repositories have the longest container lifetimes but also the

Table 15-5. Parameters important to weeps-model aqueous EPA releases.

No.	Variable	Units	57 kW/acre Vertical ΔR^2	114 kW/acre Vertical ΔR^2	57 kW/acre In-Drift ΔR^2	114 kW/acre In-Drift ΔR^2
1	100°C pitting increment	mm	0.26	0.06	0.32	0.22
2	Initial flow-episode factor	—	0.13	0.29	0.12	0.13
3	Np K_d for SZ	m^3/kg	0.10	0.17	0.08	0.14
4	U K_d for SZ	m^3/kg	0.04	0.04	0.02	0.02
5	Initial "dry" percolation flux	m/yr	0.03	0.01	0.04	0.05
6	Mean weep aperture	m	0.02	0.03	0.02	0.01
7	SZ water velocity	m/yr	0.01	0.02	0.01	0.01
8	Juvenile failures	—	0.01	0.02	0.01	0.01
9	Time of first climate change	yr	<0.01	<0.01	<0.01	0.01
10	Np solubility	kg/m^3	<0.01	0.01	<0.01	<0.01
	Total		0.60	0.66	0.61	0.60

greatest releases. This parameter is important, primarily when considered within a single repository-design context.

Next most important parameter is the flow-episode factor for the present climate. The flow-episode factor determines how often and for what length of time weeps flow. A basic assumption behind the weeps model is that a finite amount of water infiltrates Yucca Mountain; if this water is confined to weeps, then short episodic pulses would require more weeps than long pulses in order to handle a given amount of infiltration. Thus, the episode factor is a measure of the number of weeps. Other parameters also reflect the number of weeps generated during a calculation: the percolation flux, the mean weep aperture, and parameters associated with the hydrothermal perturbation—dryout fraction and dryout volume (these do not appear in Table 15-5 because they were not handled probabilistically). Considering both sensitivity to the results of a single repository design and different repository designs, the calculations are probably most sensitive to the number of weeps, hence, the combination of these parameters. The relative insignificance of the timing of the first climate change is probably due more to the rare occurrence of a climate change during the period when the containers are susceptible to corrosion, than to any resistance of the repository to increased flow.

The sorption coefficients (K_ds) for neptunium and uranium appear as important parameters because they slow the transport of these elements to the accessible environment enough to cause different releases for different realizations. We know that the K_d for plutonium is also important, but it does not appear on the list because virtually no Pu reaches the accessible environment in the calculations. If the K_d distribution for Pu should include lower values, of if colloid formation and transport is important for Pu (something not modeled in this TSPA), then a significant amount of Pu could possibly reach the accessible environment.

Another parameter that does not appear in the table, but one that we know is important, is the solubility of neptunium. The solubilities for Np used in TSPA-93 are generally 5 orders of magnitude greater than those used in TSPA-91 (Sections 9.2 and 14.5.3). In TSPA-93, Np is the major radionuclide being released; in TSPA-91, Np releases were relatively insignificant.

In Table 15-6, we present results of rank linear regression for drinking-water doses caused by aqueous releases, from all four repository cases being considered in this TSPA. The R^2 for the regression models range from 0.74 to 0.81—all reasonable fits.

Generally, the parameter to which drinking water doses are most sensitive is the saturated zone transport area—effectively the amount of dilution afforded by the saturated zone. More dilution implies reduced concentration of radionuclides in the drinking water. In the calculations, this parameter was described with a log-uniform distribution ranging over two

Table 15-6. Parameters important to weeps-model aqueous peak doses.

No.	Variable	Units	57 kW/acre Vertical ΔR^2	114 kW/acre Vertical ΔR^2	57 kW/acre In-Drift ΔR^2	114 kW/acre In-Drift ΔR^2
1	SZ transport area	m^2	0.41	0.48	0.41	0.41
2	Np K_d for SZ	m^3/kg	0.12	0.15	0.13	0.12
3	100°C pitting increment	mm	0.10	0.04	0.00	0.12
4	Initial flow-episode factor	—	0.06	0.09	0.03	0.04
6	Mean weep aperture	m	0.03	0.02	0.03	0.02
7	Initial "dry" percolation flux	m/yr	0.01	0.01	0.02	0.03
8	Juvenile failures	—	0.01	0.01	0.01	<0.01
9	70°C pitting increment	mm	<0.01	<0.01	0.12	<0.01
	Total		0.74	0.81	0.74	0.76

orders of magnitude. The nonlinear distribution and the obvious connection with dose is responsible for the importance of this parameter.

The next most important parameter is the K_d for Np. Theoretically, this parameter should have no influence on doses because it cannot cause retardation of Np in the saturated zone on time scales approaching the half-life of Np. It is possible that Np can be retarded in varying degrees so that its appearance does or does not coincide with the prompt release fraction of other radionucides (Tc and I). Probably, however, the appearance of this parameter in the list is an indication that no other parameters are dominant.

The list is completed with the parameters that define container corrosion, the parameters that define the number of weeps, and the parameter defining the number of juvenile failures. As mentioned above, we suspect that the the parameters defining the number of weeps have a synergistic effect, and that the number of weeps is a significant parameter. Climate-change parameters are not indicated as significant for two reasons. Primarily, it is very rare for a climate change to occur during the period when the containers are susceptible to corrosion. Secondarily, climate-change parameters do not vary enough from one realization to the next to produce much variance in the results.

Results of rank linear regression for 10,000-yr cumulative gaseous EPA releases are given in Table 15-7 for the four repository cases. The R^2 for the regression models ranges from 0.58 to 0.77, or from a poor fit to a reasonable fit.

For gaseous releases, the container design has an impact on which parameters are most important. Considering the thin-wall, SCP-type container, the two most important parameters are the number of juvenile failures and the bulk permeability of the TSw unit. The importance of juvenile failures to gaseous releases should be obvious from the discussion in Section 15.5.1.3. The bulk permeability of TSw determines to a large extent the travel

Table 15-7. Parameters important to weeps-model gaseous EPA releases.

No.	Variable	Units	57 kW/acre Vertical ΔR^2	114 kW/acre Vertical ΔR^2	57 kW/acre In-Drift ΔR^2	114 kW/acre In-Drift ΔR^2
1	Juvenile failures	—	0.24	0.25	0.04	0.03
2	TSw bulk permeability	m^2	0.23	0.22	0.08	0.16
3	Initial flow-episode factor	—	0.09	0.18	0.19	0.09
4	100°C pitting increment	mm	0.09	0.03	0.32	0.22
5	Retardation multiplication factor	—	0.04	0.04	0.01	0.02
6	Mean weep aperture	m	0.02	0.03	0.03	0.02
7	Initial "dry" percolation flux	m/yr	0.02	0.01	0.03	0.04
9	Time of first climate change	yr	<0.01	<0.01	<0.01	0.01
	Total		0.73	0.77	0.61	0.58

time of carbon dioxide from the repository to the surface. Lengthening the travel time allows ^{14}C to decay, plus extends the release of some of the mass to beyond the 10,000-year regulatory period. Parameters that determine the number of weeps again appear in the list, as does the corrosion-rate factor for the container.

Considering the multipurpose container, the most important parameter is the 100°C pitting increment—essentially the inner-container lifetime. As discussed in Section 15.5.2, the multipurpose container holds more waste and generates a surface temperature above 100°C longer than the thin-wall container, thus more of the repository performance is shifted to this barrier. The other parameters of importance are the same as those discussed for the thin-wall containers; however, the degree of importance varies with the repository thermal load. In general, the parameters describing the number of weeps and the retardation-multiplication factor could be underrated in the list.

15.5.5 Assumptions and limitations

Weeps-model predictions are dependent on the assumptions that form the bases for the weeps flow model, the hydrothermal model, the source-term model (YMIM), the transport models, and the dose model. This subsection contains a brief discussion of some of the major assumptions that could limit applicability of the weeps-model results. These assumptions must be analyzed in the future.

The primary caveat to the weeps-model results is that the weeps model has not been validated; i.e., it is unknown whether or not the weeps model represents reality. Perched water has only been observed infrequently at Yucca Mountain and its presence might not indicate widespread weep flow. Even if weeps are an important flow mechanism at Yucca

Mountain, the weeps model could be improperly parameterized. Gauthier *et al.* (1992) discuss in detail assumptions behind and limitations to the weeps flow model.

Application of the weeps model to total-system calculations requires an additional set of assumptions. For TSPA-93, we assume that the thermal pulse does not produce an extended-dry period. Diversion of water around the dryout zone and rapid rewetting of the dryout zone are major assumptions that have not been tested.

Also we have assumed in this TSPA that, when a weep contacts a container, all the waste is available for dissolution and transport. Indeed, for the large containers, only a fraction of the waste might be contacted by running water, and thus releases could be lower than indicated. It is also assumed that when a container is not contacted by a weep, no aqueous corrosion occurs, although moisture in the backfill could allow aqueous corrosion. (Vertically emplaced containers are designed with an air gap between the container and the borehole wall, and would probably not be susceptible to aqueous corrosion by unflowing water unless rubble bridges the gap.) Further, we only consider vertical flow in this weeps model; flow from different angles would see different cross-sectional areas of the different containers.

The in-drift containers are surrounded by backfill. The backfill is assumed to be crushed welded tuff, compacted to approximately 40% void space. Thus, the backfill should have the consistency of a gravel. A major assumption presently used in the weeps model is that the backfill does not interfere with weep flow. Further, it is assumed that increased fracturing caused by construction of the drifts and the redistribution of stress in the vicinity of the drifts does not interfere with weep flow. That is, axial fractures are assumed to not divert water from the drifts, and radial fractures are assumed to not concentrate water toward the drifts. (The assumption that increased fracturing does not influence weep flow also holds for the vertically emplaced containers.) Engineering measures to divert flow could also be designed into the EBS, but no such measures were considered in TSPA-93.

The source-term model, YMIM, contains a number of simplifications and omissions that are germane to performance. For instance, steam corrosion and the consequences of liquid water contacting container walls over 100°C are two factors that are not considered. And the Arrhenius relationship that is used to determine the temperature dependence of corrosion might be inaccurate when determining corrosion failures at nominal temperatures over million-year time spans. No credit is taken for the fuel cladding in TSPA-93, but it could form a significant barrier to the release of radionuclides from containers, especially if the fuel assemblies are not allowed to reach temperatures that would degrade the cladding. No credit is taken for any galvanic protection that might occur with the dissimilar metals that might be used in the multipurpose container.

Formation and transport of colloids are not considered in TSPA-93, and could significantly alter the results. Retardation of radionuclides by the iron oxides that would remain from corroded containers is not considered. Indeed, no credit is taken for transport time through the unsaturated zone. Diffusion of radionuclides from the fractures into the rock matrix could impact the cumulative releases over 10,000 years; whether predictions of peak individual doses could be significantly changed is not certain. The possibility of fast paths through the saturated zone, potentially combined with weak matrix diffusion, is not investigated in TSPA-93.

15.6 Conclusions/recommendations

Using the YMIM source term, the weeps model predicts that a repository at Yucca Mountain is subject to degradation primarily during the decay of the thermal pulse. During the buildup of the thermal pulse, containers are too hot to experience corrosion, even though a large amount of water is being displaced by the expanding dryout zone and subsequently being shed onto unprotected parts of the repository. But as the thermal pulse decays and container temperatures drop, two conditions conspire to cause container failures and potentially high release rates. First, when container walls are between 70° and 100°C, they are predicted to be extremely susceptible to corrosion. Second, although the contracting dryout zone is no longer displacing water, the presence of the dryout zone is still enough to focus—concentrate—infiltrating water onto unprotected, and at this time, cooling but warm parts of the repository.

In the typical weeps-model realization, only a few containers corrode to failure during the life of a repository—less than the number assumed to be juvenile failures. But in the extreme cases, especially when an early climate change provides a large amount of infiltrating water, hundreds of containers fail by corrosion. And because containers are contacted by water when they fail by corrosion, dissolution and release of radionuclides begins immediately. The result is often a temporarily high release rate. The cumulative releases as measured by the EPA standard are predicted by the weeps model to be inconsequential; however, the high release rate, although brief, combines with the low environmental dilution to potentially result in high radiation doses to exposed individuals. At late time, after approximately 20,000 years, the containers have cooled enough to be relatively impervious to corrosion. Releases after this time are caused by changing flow patterns that contact or recontact previously failed containers. Because a failed container being contacted by a weep is a relatively rare event, releases are low. After the degradation incurred during the thermal disruption, the repository remains largely intact.

General conclusions drawn from the results of the weeps model in TSPA-93 are as follows.

1) *Container type*. The weeps model predicts that the greater the cross-sectional area that a container presents to a weep, the greater the probability of interaction. Weeps are discrete, localized features; containers are localized objects. Performance is improved when there is no contact. Vertical containers offer a smaller target than in-drift containers (assuming vertical flow), by approximately a factor of 15, or a factor of 4 if the amount of mass is included in the ratio. Thus, a weep is 4 times as likely to contact a given mass of spent fuel if it is contained in a multipurpose, in-drift container as opposed to an SCP-type, vertically emplaced container. And the difference in performance can be up to an order of magnitude when measured by either the EPA standard or the possible dose standard. Whether or not an order of magnitude is significant remains to be seen, but this conclusion still holds. Also, the YMIM source model in the weeps model predicts that a multipurpose container offers a performance advantage over a thin-wall container only in a 57-kW/acre repository—and then only because of the higher surface temperature of the larger container, not because of the additional steel overpack. In both the 57-kW/acre and the 114-kW/acre repositories, dry oxidation consumes virtually the entire mild steel overpack of the multipurpose containers before weep contact occurs.

2) *Thermal load*. The weeps model predicts that higher thermal loads result in more displaced (vaporized) water that causes more weeps. More weeps contact more containers, causing more failures (when the containers are between 70° and 100°C), resulting in more releases. This effect is of secondary importance to the container cross-section. Performance deteriorates only by about a factor of 2 with the higher thermal load, again when measured by either the EPA standard or a dose standard. Consideration of steam corrosion, which should affect a 114-kW/acre repository more than a 57-kW/acre repository, could make this performance difference more significant. If the extended-dry concept is correct, the 114-kW/acre repostory could perform much better than the 57-kW/acre repository because it would keep water away from the containers during the critcal corrosion period.

3) *Regulatory compliance*. The weeps model predicts that cumulative releases from a repository at Yucca Mountain should be relatively low, even in the extreme cases. This prediction holds true for gaseous and aqueous releases, for 57-kW/acre and 114-kW/acre repositories, for thin-wall, SCP-type, vertically emplaced containers and large, multipurpose, in-drift-emplaced containers. However, the low cumulative releases can

contain brief periods of high release rates, and high release rates combined with relatively low dilution in the environment can cause high individual doses. While not as high as those predicted by the composite-porosity model, the doses predicted by the weeps model are still notable. All four repository cases considered in this TSPA result in doses above background: the 57-kW/acre repository with vertical containers exceeds doses from background approximately 1% of the time; and the 114-kW/acre repository with in-drift containers exceeds background doses approximately 20% of the time. Despite the unsophisticated dose model and the caveats associated with the weeps model, a major conclusion of this TSPA is that the factors associated with high dose should be addressed in the characterization of the site and the design of a repository.

In the following subsections, we offer recommendations concerning site characterization and repository design considering only what is important to the results of the weeps model. Chapters 19 and 20 present recommendations taken with a broader perspective.

15.6.1 Site characterization

Concerning weep flow, site characterization should be directed in two efforts. First, it must be determined when (temporally) and where (spatially) weeps are a valid flow mechanism.

- Determine whether weep flow is a valid flow mechanism at Yucca Mountain. We suspect that this validation can be accomplished in one of three ways. (1) The preferable method is direct observation—take measurements of weeps encountered in drillholes and the Exploratory Studies Facility. Unfortunately, finding weeps might prove problematic given the present climate. (2) A proxy method is to investigate the geologic record for the signature of previous weep flow. For example, examine fracture coatings for evidence of precipitates left by flowing water. It would be useful to keep a record of such observations and attempt a population study to determine the likelihood of weep flow. Although not as convincing as direct observation, this method has the advantage that it could provide information on paleoclimates and rates of percolation (see below). (3) Finally, the least preferable method is to perform field tests to track the movements of large amounts of water. This method might be impractical at Yucca Mountain.

- Determine what conditions support (or obviate) weep flow. Examine how much water is necessary to cause weep flow. Determine how matrix imbibition is curtailed—by fracture coatings, by the presence of parallel fractures forming a capillary barrier, or by episodic flow where the timescale is short enough to make matrix imbibition

insignificant. Some of this work can be performed in the laboratory, but preferably should be done in the field in order to have confidence in the results.

Second, if weep flow is found to be a valid flow mechanism at some time and location within Yucca Mountain, site characterization should be directed to measure properties (weeps-model parameters) related to high individual doses. The weeps model predicts that individual dose is the most important aspect of repository performance. The most important properties are those associated with parameters to which the dose results are most sensitive (Section 15.5.4).

- Characterize SZ transport area. The saturated zone must be defined in terms of mixing volume (i.e., dilution factor), dispersivity, and matrix diffusion (i.e., the degree of matrix/fracture coupling). These measurements are in addition to the characterization required to calibrate saturated-zone flow models (Chapter 11). Although difficult, we also need to determine whether these properties change when the water table rises.

- Measure bulk permeability. In this TSPA we used fracture properties as a surrogate for weep properties. In the long run, knowledge of weep properties is essential (see next item); however, because there will always be uncertainty in flow paths, we must have data on the fracture network. The methodology we developed to determine fracture-flow properties (Chapter 7) relies heavily on bulk permeability. Only a few bulk-permeability data are presently available for the unsaturated zone and more are needed. (Bulk permeability is also important to gas flow and hydrothermal problems.)

- Characterize weeps. Determine population statistics for weeps, including size (i.e., amount of water flow), location, orientation (dip and strike), and short-term flow periods (episode factor), long-term flow periods (flow patterns), and overall percolation rate. The obstacle here is that these data are needed for *future* weeps. We believe that a reasonable strategy is to extrapolate from present and previously flowing weeps (although studies of both past and future climates must continue in order to reasonably apply paleoflow data.) We recommend that a study be immediately initiated involving the isotopic analysis and dating of fracture coatings and other groundwater precipitates. This study would probably have to be supplemented with chemical and geochemical studies to achieve what is needed for performance assessment—basically a temporal and spatial map of weep flow at Yucca Mountain.

- Better characterize the source term. Container corrosion rates are an important parameter to the weeps-model results and they must be better specified. However, the weeps-model results also suggest that several factors not explicity considered could also

be very important to the performance of a repository at Yucca Mountain. (1) Significant colloid formation and transport could allow large amounts of plutonium to reach the accessible environment. Plutonium is the major element predicted by the weeps model to be released from the EBS. (2) Hydrothermal effects, especially shedding and the rewetting behavior of the mountain, are poorly understood but could impact performance significantly. Large-scale heater tests should be performed to examine hydrothermal processes. These heater tests should be performed at percolation rates suspected for future climates (e.g., the tests should be performed in a location similar to Rainier Mesa). (3) Steam corrosion could significantly degrade containers, at a rate that some suggest could be similar to the rate of aqueous corrosion. Steam-corrosion processes and rates must be studied. (4) Near-field chemistry, especially at elevated temperatures, could impact flow patterns, container lifetime, waste dissolution, etc. Thermally induced geochemical alterations to the matrix and fractures should be anticipated and investigated. Grout and concrete being planned for use in repository construction must be considered as a significant perturbation to the geochemistry of the mountain.

15.6.2 Repository design

Recommendations to repository design are contingent on two factors. First is the validity of the weeps flow mechanism. Second is other Project requirements, such as cost. In this TSPA, the four repository designs that are analyzed varied little in terms of performance. In general, design elements related to reduced container area and lower thermal loads produced the lowest releases. However, the differences might not prove significant, i.e., with the EPA standard, all four repositories perform well, while with a possible dose standard, all are questionable (although some are more questionable than others). Therefore, we offer the following recommendations with the caveat that other requirements might override them.

- Minimize target cross section, i.e., design containers and emplace them such that they offer a minimum area of contact for weeps. (This recommendation also follows from human-intrusion results, Chapter 16.)

- If rapid rewetting occurs after the thermal pulse, the containers can be wet when still warm and susceptible to corrosion. In this case, design a low-thermal-load repository. If steam corrosion is found to be significant, then design a low-thermal-load repository.

- For multipurpose containers, a 10-cm mild-steel overpack adds nothing to performance; either specify a significantly thicker overpack or no overpack.

- Investigate possible methods for suppressing dissolution of neptunium over long periods of time, e.g., maintaining a local reducing environment.

Chapter 16
Human Intrusion

(Barnard, Skinner)

The analysis of human intrusion is based on the scenario that as a result of drilling into the potential Yucca Mountain repository, radionuclides are entrained in the drilling fluid and carried to the surface. The analysis assumes that at various times in the future, drillholes are bored into Yucca Mountain. If a drill bit intersects a waste package, it is assumed that it can break the container open and transport the contents directly to the surface in the circulating drilling mud. If the drill passes near a container that has previously corroded, then the drilling operation can bring to the surface rock cuttings contaminated with radioactivity.

The drilling operation is assumed to be trying to reach the carbonate formations beneath the potential repository. The analysis assumes that present-day drilling technology is used (i.e., a rotary drill bit, liquid drilling fluid to lubricate the bit and carry away cuttings, and well-bore casing to stabilize the drillhole), as stated in guidelines given in 40 CFR Part 191 (EPA, 1985). Fragments of waste or contaminated rock cuttings are carried to the surface in the circulating drilling mud. They will accumulate in the drilling-mud pit at the drill site at the surface.

The analysis assumes that at randomly selected times after closure of the repository, drilling operations occur above the repository. The probability that a drilling operation intersects waste is another random function: if the function has a value equal to the probability of hitting a container, a direct hit is assumed to occur; if the function has a value equal to the probability of hitting only contaminated rock, a near miss occurs. Otherwise, there is no hit. Both the direct-hit and near-miss probabilities are proportional to the areas of the targets—the container, or the amount of contaminated rock. Finally, if a direct hit occurs, a random amount of waste (ranging from 0% to 100% of the contents of the waste package) is assumed to be brought to the surface. The amount of radioactivity released therefore is dependent upon the activity of the radionuclide inventory (which is dependent upon the time of occurrence of the hit), whether it was a direct hit or near miss, and the amount of waste brought to the surface.

For TSPA-93, the calculations have been made more sophisticated than previously, and the data more realistically describe the repository inventory. Cumulative releases are now estimated not only for 10,000 years, but also for 1,000,000 years into the future. It should be noted that estimates of human behavior and technological capabilities so far in the future are highly speculative. Consequently, there is even greater uncertainty in the

interpretation of the human-intrusion results than there are for those of the aqueous and gaseous analyses.

16.1 Parameter definition

The factors needed to perform an analysis are the number of boreholes expected to be drilled into the repository, the probability of a drill bit intersecting a container, the amount and type of waste that can be carried to the surface ("exhumed") by the drilling, the amount of waste that can be brought to the surface by near misses, and several additional parameters related to the determination of these factors. For a repository containing radionuclides from several different sources (e.g., spent fuel and vitrified high-level waste—HLW), the probability of releasing radionuclides from a specific source is dependent upon the probability of a drill bit intersecting a container and the probability that the released radionuclides are from that source. Using this concept of separate sources, the human-intrusion analyses have been enhanced to account for different inventories of the waste packages (e.g., spent fuel from pressurized water reactors—PWRs and boiling water reactors—BWRs, and HLW), different package sizes, and different inventories available for near-miss releases.

16.1.1 Probability of hitting a container

The probability of a drill bit intersecting a container is proportional to the "enhanced area" of the drill and the container(i.e., the maximum area obtainable from the dimensions of the drill and the container). The four thermal loading and emplacement cases that are analyzed in TSPA-93 differ from TSPA-91 because of different container sizes, spacings, and numbers. Thus, there are different probabilities of hits for each case. The formula for P_{hit}, the probability that a drill will hit any package in the repository is

$$P_{hit} = \frac{N_1 f(d_1)}{A_{Repos}} + \frac{N_2 f(d_2)}{A_{Repos}} + \ldots, \tag{16.1}$$

where the N_i are the numbers of packages for the ith type of waste, A_{Repos} is the area of the repository, and the $f(d_i)$ are the enhanced areas of intersection of the drill bit and the packages for each type of waste. For borehole emplacement of cylindrical packages, $f(d_i)$ is the horizontal projection of the area of the drill and the ith type of container:

$$\pi\left(r_{Pkg_i} + r_{Drill}\right)^2, \tag{16.2}$$

while for horizontal in-drift emplacement of packages with rectangular cross sections, $f(d_i)$ is the horizontal projection of the area of the drill and the cross section of the ith type of container:

$$(l_{Pkg_i} + d_{Drill})(w_{Pkg_i} + d_{Drill}) \quad . \tag{16.3}$$

For this analysis, the enhanced area has been redefined slightly to specify that the *inside* dimensions of the container be used to determine the waste-package projected area. Since the in-drift container is assumed to have a 10-cm-thick wall, this change results in a more realistic estimate of P_{hit}. The inside diameter of the thin-walled vertically emplaced container is also used for consistency. The diameter of the drill is 0.61 m, as in TSPA-91.

The probability that a certain type of waste is exhumed can be represented in several ways. If all the containers are identical, then the probabilities can be expressed by the fractional amounts of the different inventories. If the containers are of different sizes, or contain different amounts or types of waste, then the probabilities can be proportional to the number of each type of package. For this analysis, the numbers of packages are used to determine inventory fractions. Table 16-1 lists the values of P_{hit} and the fractions of the repository represented by the various container types.

Table 16-1. Drilling analysis probabilities and parameters.

Package Type	Container Dimension(s)[a]	A_{Repos} (km^2)	N_{Pkg}[b]	P_{hit}[b]	Repository Fraction
Borehole, 57 kW/acre		**4.61**	**(45,979)**	**(0.0128)**	
Hybrid Package	0.69 m I.D.		28,057	0.0081	0.610
BWR-Fuel Package	0.69 m I.D.		1,215	0.0004	0.026
PWR-Fuel Package	0.64 m I.D.		2,750	0.0008	0.060
HLW Package	0.61 m I.D.		13,957	0.0035	0.304
Borehole, 114 kW/acre		**3.14**	**(45,979)**	**(0.0186)**	
Hybrid Package	0.69 m I.D.		28,057	0.0118	0.610
BWR-Fuel Package	0.69 m I.D.		1,215	0.0005	0.026
PWR-Fuel Package	0.64 m I.D.		2,750	0.0011	0.060
HLW Package	0.61 m I.D.		13,957	0.0052	0.304
In-Drift, 57 kW/acre		**4.63**	**(11,130)**	**(0.0283)**	
BWR-Fuel Package	1.52 m I.D. x 4.91 m L.		3,109	0.0079	0.279
PWR-Fuel Package	1.52 m I.D. x 4.91 m L.		4,531	0.0115	0.407
HLW Package	1.52 m I.D. x 4.91 m L.		3,490	0.0089	0.314
In-Drift, 114 kW/acre		**2.33**	**(11,130)**	**(0.0562)**	
BWR-Fuel Package	1.52 m I.D. x 4.91 m L.		3,109	0.0157	0.279
PWR-Fuel Package	1.52 m I.D. x 4.91 m L.		4,531	0.0229	0.407
HLW Package	1.52 m I.D. x 4.91 m L.		3,490	0.0176	0.314

[a] I.D. = inside diameter; L = length.
[b] Totals given in parentheses.

16.1.2 Analysis parameters

The number of boreholes expected to be drilled at Yucca Mountain is based on the guidance given by the EPA in 40 CFR Part 191. The EPA provides guidelines for the maximum number of drillholes at repositories located in sedimentary and non-sedimentary geologic formations. For non-sedimentary locations such as Yucca Mountain, 3 boreholes per square kilometer are assumed to be drilled over 10,000 years. The number of boreholes drilled into the repository over 10,000 years therefore is dependent upon the size of the repository. These values are listed in Table 16-2.

Table 16-2. Repository-related parameters for drilling analyses.

Emplacement Configuration	Repository Area (km^2)	Maximum Number of Boreholes/ 10,000 years
Borehole, 57 kW/acre	4.61	14
Borehole, 114 kW/acre	3.14	10
In-Drift, 57 kW/acre	4.63	14
In-Drift, 114 kW/acre	2.33	7

The amount of waste available to be exhumed is expressed as a fraction of the entire inventory of the repository. The containers for the two emplacement configurations all contain different amounts of waste. They are listed in Table 16-3. For this analysis we assume the borehole vitrified-waste canisters each contain the equivalent of 0.5 metric tons of heavy-metal waste (MTHM). The in-drift packages holding vitrified HLW are overpacks containing four HLW canisters.

The near-miss component of the drilling analyses is based on the same diffusive processes as in TSPA-91. Waste packages emplaced in the drift are considered an instantaneous source for the purpose of calculating the diffusion of contaminants into the rock surrounding the containers. For this problem, the fractional concentration C, at a point x at time t is given by

$$C(x,t)/C_0 = 1/4\pi Dt\, e^{-x^2/4Dt}, \tag{16.4}$$

where C_0 is the initial concentration, and D is the diffusion constant. The same value is used for D as was used in TSPA-91: 3.65×10^{-4} m^2/yr. The area defined by the 10^{-3} concentration surrounding the waste package is used in the calculation of the near-miss probability.

Initially, the probability is given by a circular area surrounding the container. For sufficiently large times, equation 16.4 predicts that even for large values of the distance, x, the fractional concentration $C(x,t)$ approaches C_0. However, the diffusional concentration

in the direction between containers in a drift would eventually be influenced by the adjacent waste packages. To account for this, the circular near-miss area is modified to become an ellipse with the minor axis equal to the container half-spacing. The container-spacing values are dependent upon the emplacement configuration. For all but the 114-kW/acre, borehole configuration, the HLW canisters or overpacks can be interspersed among the spent-fuel packages without changing the repository area or heat load. In these cases, the spacings between HLW canisters and spent-fuel packages are different than the spent-fuel package emplacement pitch. We assume that the HLW canisters are located halfway between the spent-fuel packages, so the spacing to the nearest neighbor is half of the distance between the spent-fuel packages minus the radii of the waste-package and HLW canister. For the case where HLW must be segregated, the additional area necessary to accommodate the canisters is based on the same emplacement pitch as for spent fuel. The 13,957 HLW canisters require 31,906 m of linear emplacement drifts; for 25.4-m drift spacing, this is 0.81 km^2, or 200 acres. Table 16-3 summarizes the source-term parameters for the drilling analyses.

Table 16-3. Source-term parameters for drilling analyses.

Emplacement Configuration/ Package Type	Container Capacity (MTHM)	Inventory Fraction	Near-Miss Fraction	Container Spacing (m)	Container Lifetime (years)
Borehole, 57 kW/acre					475 – 5,000
Hybrid Package	2.0	2.86×10^{-5}	1.15×10^{-5}	5.6	
BWR-Fuel Package	1.7	2.43×10^{-5}	8.01×10^{-6}	5.6	
PWR-Fuel Package	1.7	2.43×10^{-5}	1.08×10^{-5}	5.6	
HLW Package	0.5	7.14×10^{-6}	3.43×10^{-6}	2.5	
Borehole, 114 kW/acre					2,450 – 7,500
Hybrid Package	2.0	2.86×10^{-5}	1.15×10^{-5}	2.3	
BWR-Fuel Package	1.7	2.43×10^{-5}	8.01×10^{-6}	2.3	
PWR-Fuel Package	1.7	2.43×10^{-5}	1.08×10^{-5}	2.3	
HLW Package	0.5	7.14×10^{-6}	3.43×10^{-6}	2.3[a]	
In-Drift, 57 kW/acre					950 – 10,000
BWR-Fuel Package	7.0	1.00×10^{-4}	3.30×10^{-5}	17.0	
PWR-Fuel Package	9.0	1.29×10^{-4}	5.70×10^{-5}	27.5	
HLW Package	2.0	2.86×10^{-5}	1.37×10^{-5}	9.1[b]	
In-Drift, 114 kW/acre					3,050 – 8,000
BWR-Fuel Package	7.0	1.00×10^{-4}	3.30×10^{-5}	8.5	
PWR-Fuel Package	9.0	1.29×10^{-4}	5.70×10^{-5}	13.7	
HLW Package	2.0	2.86×10^{-5}	1.37×10^{-5}	4.4[c]	

[a] HLW is segregated; additional area is necessary, based on spacing for spent-fuel packages.
[b] Based on weighted-average emplacement pitch for PWR and BWR packages.
[c] Assumes HLW is located between adjacent PWR packages only.

The radionuclides available to diffuse from the waste packages into the surrounding rock are assumed to be composed of the mobile species in the inventory. The near-miss fraction values listed in Table 16-3 are expressed as fractions of the inventory-fraction entries. The percentage of mobile species in the entire inventory is in the range of 33% to 48%. In TSPA-91, the near-miss fraction was limited to ^{129}I and ^{99}Tc, which have high solubility and low far-field retardation. For this TSPA analysis, other elements that have high solubilities but not necessarily low retardations have been added. They are Cs, Se, C, and Cl.

Container lifetimes are another factor in the near-miss calculations. During the times that the containers are intact, there is no diffusion. Details of the container lifetime calculations are given in Section 16.2.

16.1.2.1 High-level waste parameters

Since HLW canisters in an in-drift overpack are essentially self-contained, the amount of waste exhumed would be dependent upon the number of canisters ruptured by the drill. Four canisters can be fit into each overpack with the following cross sections (Figure 16-1).

In either configuration, a drill bit of the diameter that is used in the baseline calculations (i.e., 0.61 m) striking the overpack from above could pass through 1, 2, 3, or 4 of the canisters. Thus, the amount of waste that can be exhumed from this package is modeled as a uniform random variable with a range of 0% to 100% of the contents of the overpack. Because there is a HLW canister inside the in-drift container, there is a third steel wall surrounding the waste. This is assumed to increase the time before the containers degenerate enough to permit the escape of radionuclides, implying a longer period before the HLW can contaminate the surrounding rock. Because HLW containers are not modeled by YMIM, the lifetime for HLW in-drift packages is assumed to be 15,000 to 20,000 years.

16.1.3 Measurements of performance

The previous TSPA measured releases against the EPA standards set forth in 40 CFR Part 191, despite the standards having been adjudged to be inapplicable to Yucca Mountain. For this analysis, we continue to use the concepts of release limits (i.e., the EPA limits) and exclusion of short-lived radionuclides from contribution to the releases, but we do not limit releases to 10,000 years. This can produce inconsistencies, however, since the EPA limits are specified for 10,000-year periods, and releases that are inconsequential over 10,000 years can be quite substantial over 1,000,000 years.

For the human-intrusion analyses, simulations have been run for 10,000-year periods. To estimate the cumulative releases for 1,000,000 years, it is necessary to calculate the releases for all the 10,000-year periods in this time. Running the 100 simulations necessary

to account for every 10,000-year time period is impractical, so about a dozen runs have been made at different starting times from 0 years to 999,990 years. Because not every 10,000-year period in the 1,000,000-year range has been modeled, releases are interpolated for those time periods not done. The simulations and the interpolated estimates have been combined to give a cumulative normalized release over the 1,000,000-year period. The releases are normalized to EPA limits for the various radionuclides.

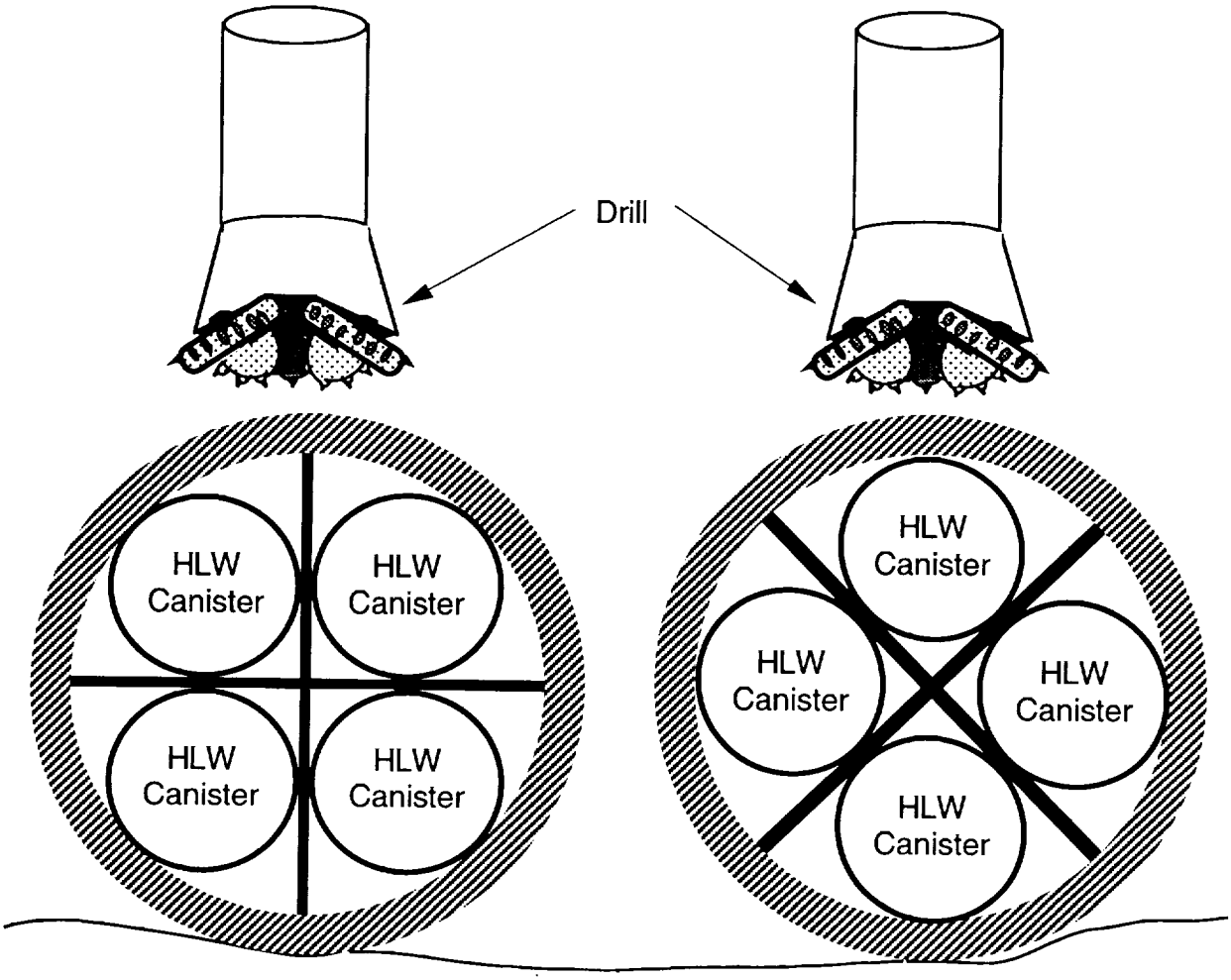

Figure 16-1. Possible orientations of drill and in-drift HLW containers.

16.2 Waste-container lifetime studies

The time that a waste container remains intact is important for determining the amount of contamination that a near-miss drilling incident can exhume. Radionuclide release from waste packages is considered to start when the walls of the waste containers fail. Using the stand-alone version of YMIM, container failure times for the four analysis cases

have been calculated. These analyses are limited to a determination of the times at which containers would fail as a result of the corrosion processes modeled in YMIM. Only a limited number of parameters have been varied to do these studies.

16.2.1 Analysis setup

The factors that affect container lifetime the most are the temperatures to which the container is exposed, the near-field hydrology, and the corrosion rates of the container-wall materials. The other factors used by YMIM, as discussed in Section 13.2, mostly affect the release of radionuclides. The lifetime studies investigate two temperature conditions for each of the four analysis cases and three or four near-field hydrology conditions.

16.2.1.1 Temperature profiles

As is discussed in Chapter 10, the repository-driven hydrothermal effects may produce hotter, dryer areas at the center of the repository and cooler, wetter areas at the periphery. Time-temperature profiles are generated at the surface of containers representing both "hot" and "cold" conditions for each analysis case. Figures 10-16 through 10-19 show the profiles for the four analysis cases. Cold conditions differ from hot conditions by the extent that repository edge effects can reduce rock temperatures, and thus influence the container surface temperature.

The 100°C-temperature value is indicated on each graph. The time at which the temperature decreases below 100°C is an important factor in the YMIM model. These times range from ~350 years at the repository edge for the borehole, 57-kW/acre, conditions to ~5000 years for the in-drift, 114-kW/acre, center condition.

The temperature profiles assume that the repository remains open and is ventilated for the first 75 years. At that time, the drifts are backfilled and the repository is closed. The rapid temperature increase for the two in-drift cases reflects the reduction in cooling when ventilation is removed and the reduced conductivity of the backfill material.

As is discussed in the next sections, the time period during which the containers cool from 100°C to ~70°C is critical to the corrosion mechanism. Table 16-4 lists the times at which these temperatures are reached for the four analysis cases.

As would be expected, the 57-kW/acre cases cool to 100°C faster than the 114-kW/acre cases, and edge locations cool faster than center locations. The duration that the containers are between 100°C and 70°C is primarily dependent upon the thermal power density and less on the emplacement configurations.

Table 16-4. Times to cool to 100°C and 70°C for various analysis cases.

Configuration	Edge of Repository			Center of Repository		
	Time to Cool to Temperature: (years)			Time to Cool to Temperature: (years)		
	100°C	70°C	Duration	100°C	70°C	Duration
Borehole, 57 kW/acre	350	1,200	850	1,400	2,700	1,300
Borehole, 114 kW/acre	2,300	4,000	1,700	5,000	9,000	4,000
In-drift, 57 kW/acre	820	1,700	880	1,940	3,200	1,260
In-drift, 114 kW/acre	2,900	5,200	2,300	5,400	9,700	4,300

16.2.1.2 Near-field hydrology

Near-field hydrology conditions are modeled in a standardized fashion for the container lifetime studies. Only the container-wetting component of the near-field hydrologic conditions is varied in the studies, since it is this factor that controls the water contact (and thus the corrosion).

A temperature profile and the associated container-wetting values are shown in Figure 16-2. The figure shows a portion of the temperature curve for the 57-kW/acre, in-drift case. The critical temperatures are from ~100°C to ~70 °C.

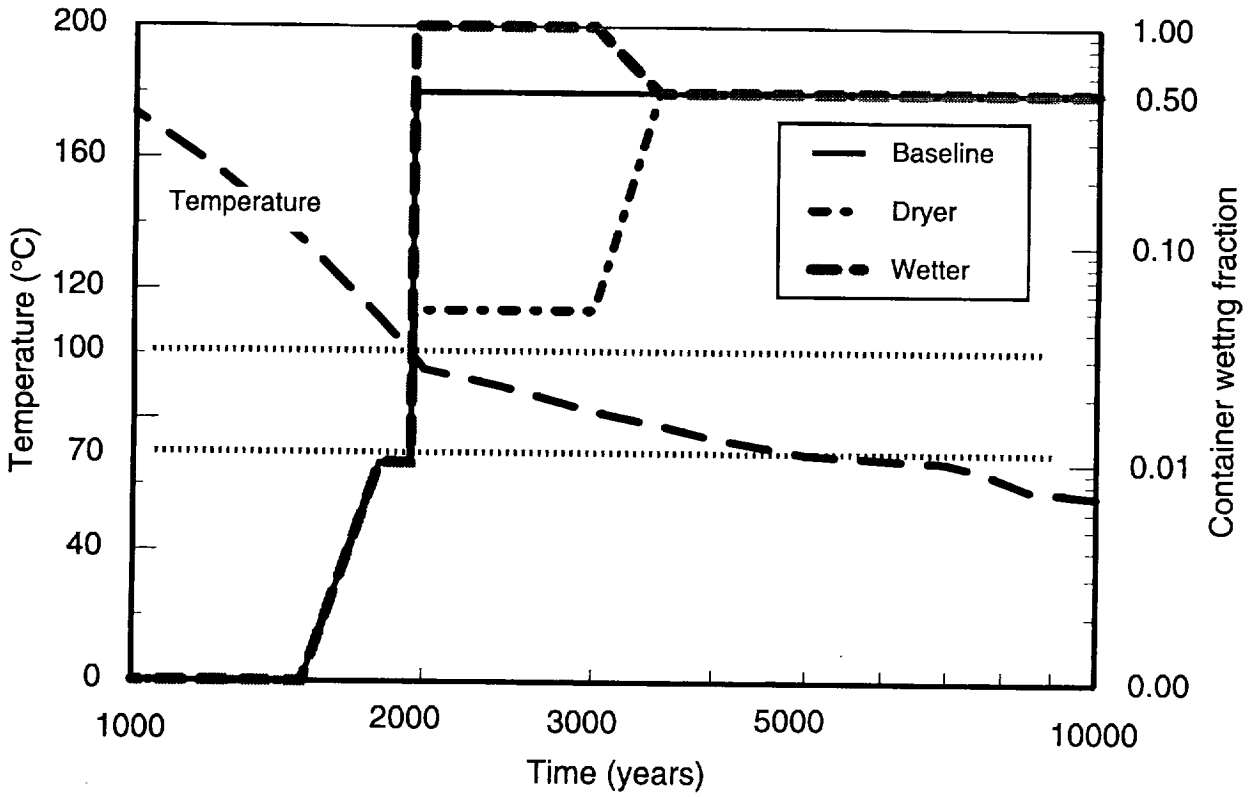

Figure 16-2. Standardized container-wetting conditions used for lifetime studies (time scale shown for 114-kW/acre thermal loading).

For these analyses, it is assumed that the containers would remain completely dry until the temperature dropped toward 100°C. Starting at temperatures of ~110°C, water could reach the containers for approximately 1% of the year. Such a process is consistent with some analyses of water penetration through hot rock, although YMIM does not model aqueous corrosion at temperatures above 100°C. From 100°C to ~70°C, the maximum corrosion is assumed to occur. Generalized aqueous corrosion has a maximum rate at 80°C, while localized pitting corrosion has an Arrhenius dependence on temperature. In the time period for the temperature to drop from 100°C to 70°C, the fraction of the year that water could contact the container is varied. The baseline assumption is that the container would be wet for 50% of the year. For the hot, dry conditions, wetting fractions of 10% and 5% of the year are also modeled. For cold, wet conditions, wetting fractions of 100% and 20% are used. For later time periods, it is assumed that the containers would be wet for 50% of the year. The extent of corrosion is assumed to be directly proportional to the amount of water present at the containers.

16.2.1.3 Corrosion rates

The air-oxidation rates given in Section 13.2.4.1 are used for the nickel alloy and the carbon steel. As Figure 16-3 shows, the oxidation rate for Alloy 825 near 100°C implies that it would take ~10^{12} years to consume the container wall. Even at the highest temperatures experienced by the containers (~500°C), oxidation of nickel alloy is not a factor. At 100°C, the 100-mm-thick carbon-steel wall would require ~10^5 years to oxidize through. However, the oxidation rate is ~1 mm/yr at 400°C; the 100-mm-thick outer container wall could oxidize in 100 years at that temperature. As Figures 10-16 and 10-17 show, the container may remain above that temperature for ~100 years for the in-drift cases.

The generalized aqueous corrosion parameters given in Section 13.2.4.1 are also used. This process applies to the carbon steel only. General aqueous corrosion has a maximum rate of 0.38 mm/yr at 80°C, so the 100-mm wall could corrode away in ~260 years at this temperature.

For the container lifetime studies, the Median Growth-Rate conditions described in Section 13.2.4.1 for pitting corrosion of the Alloy 825 are used. These conditions predict a mean pit growth rate of 0.1 mm/yr, and a 95th-percentile growth rate of 1.0 mm/yr at 100°C. The corrosion-resistant high-nickel alloy would have a lifetime of between 10 and 100 years at this temperature.

16.2.2 Lifetime predictions

The stand-alone YMIM code models the probability of failure of a single container under the conditions provided as inputs. The results can also be interpreted as the failure dis-

tribution of a number of containers all exposed to identical conditions. By combining the failure distributions for containers exposed to different conditions (such as the different temperatures and wetting fractions discussed above), a container failure distribution for all the containers in the repository can be generated.

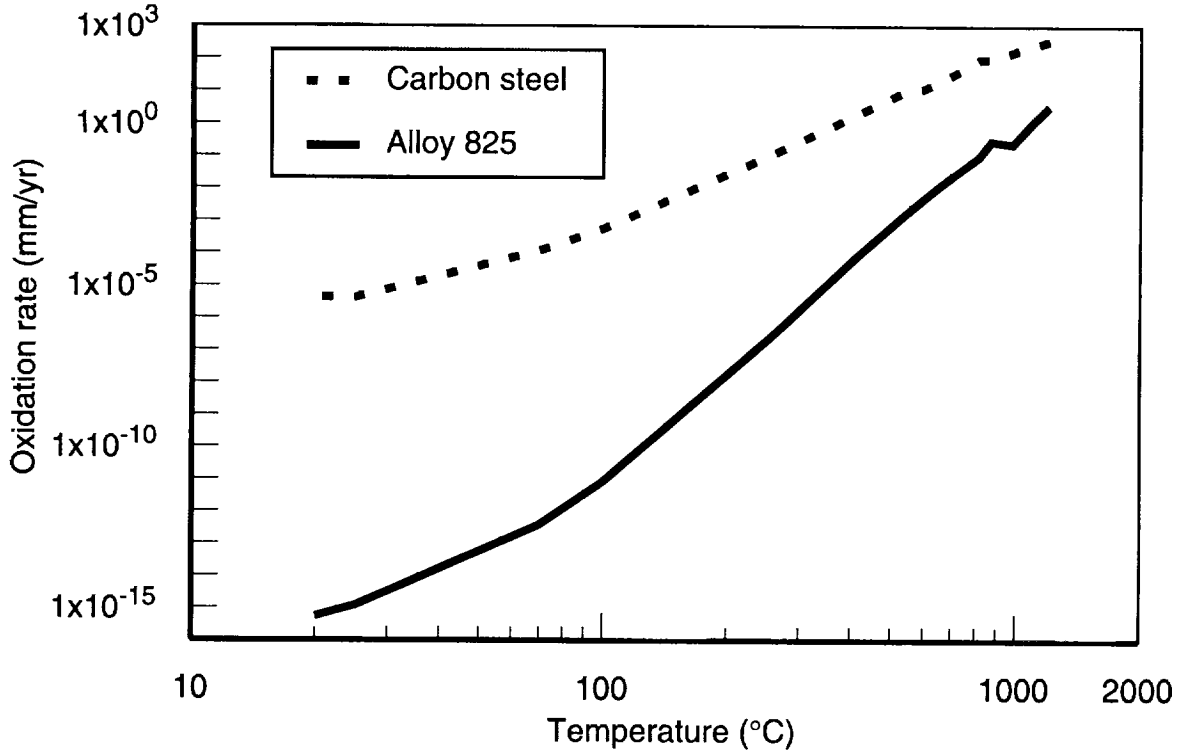

Figure 16-3. Air-oxidation rates for alloy 825 and carbon steel.

16.2.2.1 Waste-package failures for specific conditions

Using the parameters discussed in Section 13.2, the YMIM model predicts that when sufficient water is present, the container will corrode in a few hundred years. This applies to both the single-wall borehole package and the double-wall in-drift package. Figure 16-4 illustrates the failure-rate profile for a borehole package at the edge of the repository exposed to 50% yearly wetting.

As is shown in Table 16-4, the container temperature drops to 100°C at ~350 years after emplacement for the edge locations. This corresponds closely with the onset of failure shown in Figure 16-4. It takes ~1,200 years before the temperature reaches 70°C. During the time from 350 to 1,200 years, 50% container wetting is a sufficiently large fraction of the year that the container corrodes in ~200 years.

The failure profile for the double-walled, in-drift container is similar when sufficient water is present. Figure 16-5 shows the failure of a single container for the 114-kW/acre,

center case. From Table 16-4, we see that the temperature drops to 100°C at ~5,600 years. The container fails over the period from 5,550 to 5,800 years—approximately the same 250-year length of time as for the borehole container.

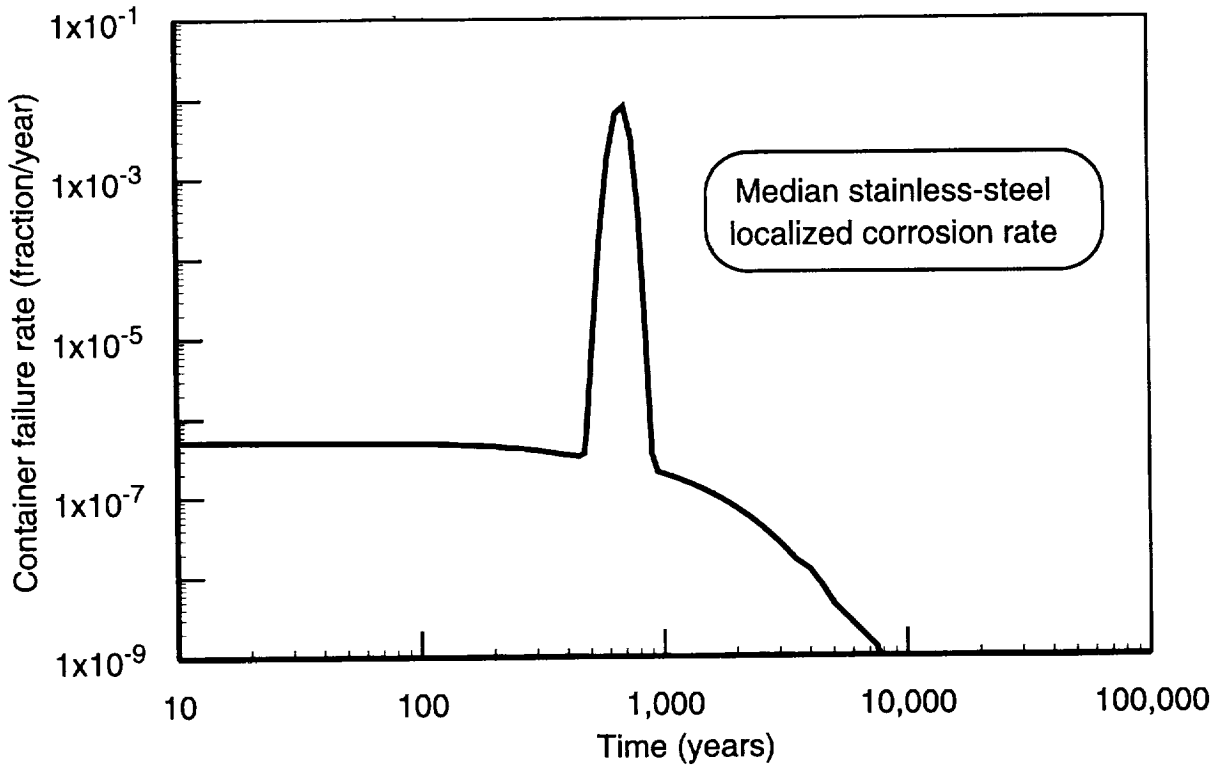

Figure 16-4. Container failure profile for 50% container wetting conditions (borehole, 57-kW/acre, edge of repository).

If water is present for less time, the container lifetime is extended considerably. Figure 16-6 shows the failure profile when water is present only 20% of the year during the time the container is in the temperature range from 100°C to 70°C. In this case, package corrosion can take tens of thousands of years. The peak failure rate in Figure 16-6 is about 3 orders of magnitude lower than those shown in Figures 16-4 or 16-5.

16.2.2.2 Distributions of container lifetimes for the four analysis cases

For any analysis case, one would expect both hot and cold conditions and a range of container wetting durations. The range of container lifetimes for that case can be approximated by the combining the lifetimes of the specific conditions modeled. Figures 16-7 through 16-10 show the ranges of lifetimes that are calculated for the four cases. In these figures, the failure rates for specific conditions have been integrated and normalized to

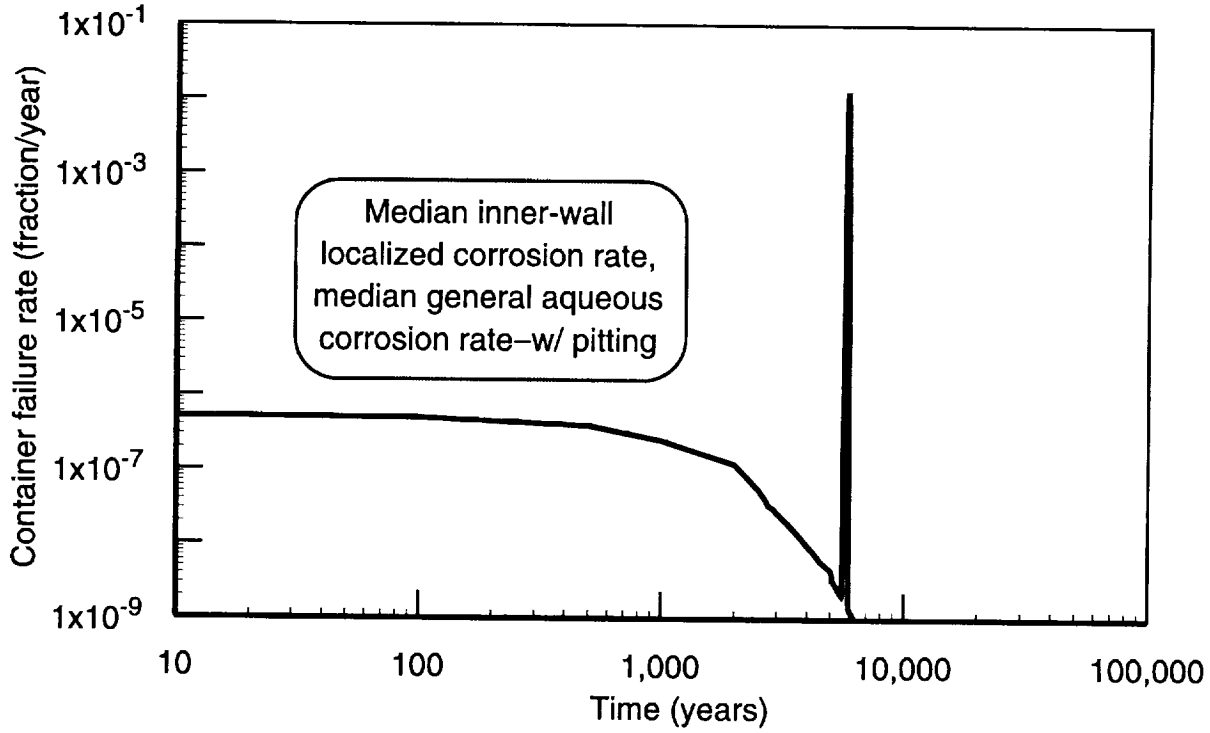

Figure 16-5. Container failure profile for 50% container wetting conditions (in-drift, 114 kW/acre, center of repository).

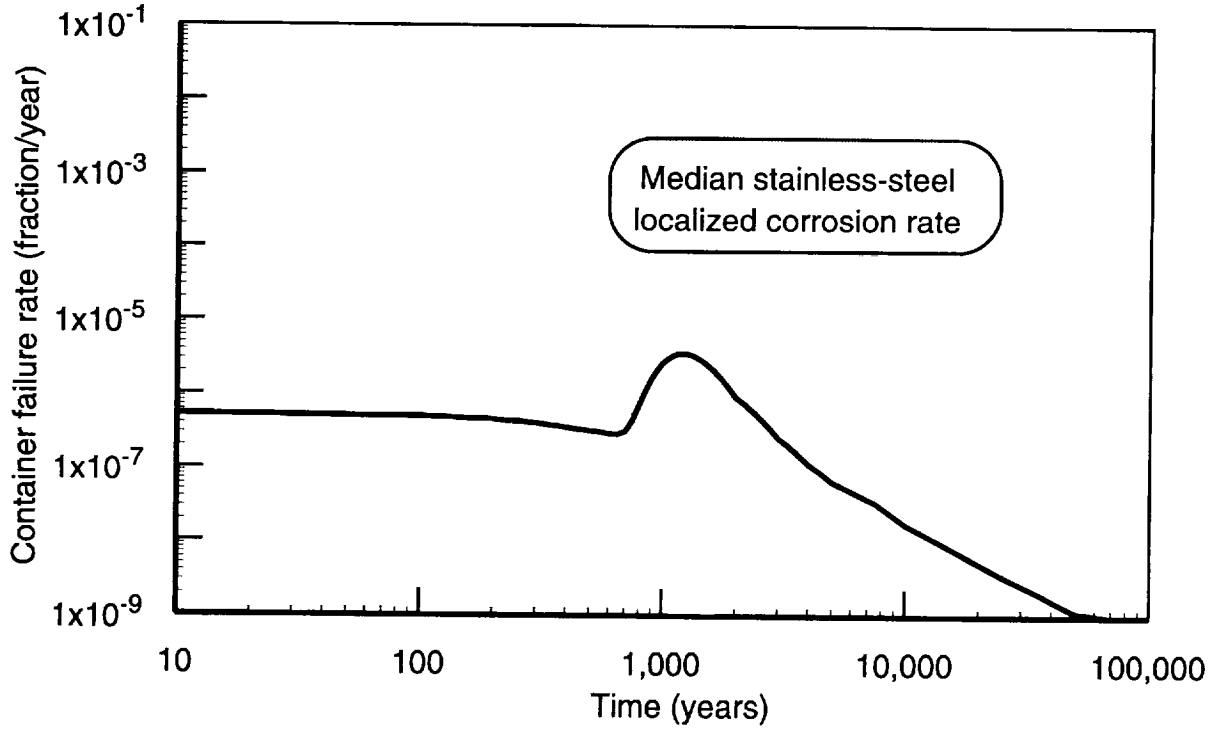

Figure 16-6. Container failure profile for 20% container wetting conditions (borehole, 57 kW/acre, edge of repository).

100% of containers in the repository. Thus, each curve in Figures 16-7 through 16-10 assumes every container is exposed to the same conditions.

As Figure 16-7 shows, all the containers that are exposed to 100% wetting under cold conditions fail over the period from 475 to 550 years. As the amount of time that the containers are exposed to water decreases, the onset of failures is later and the time necessary for the containers to fail increases. For hot conditions at the center of the repository, the wetter conditions again produce rapid failures and the dryer conditions are again more distributed. For the human-intrusion calculations, the range of container lifetimes for the 57-kW/acre, borehole emplacement case is taken to be from the onset of the earliest failure to the time when approximately 85% of the containers have failed under the longest failure scenario, and is from 475 to 5,000 years, as indicated by the solid lines in Figure 16-7.

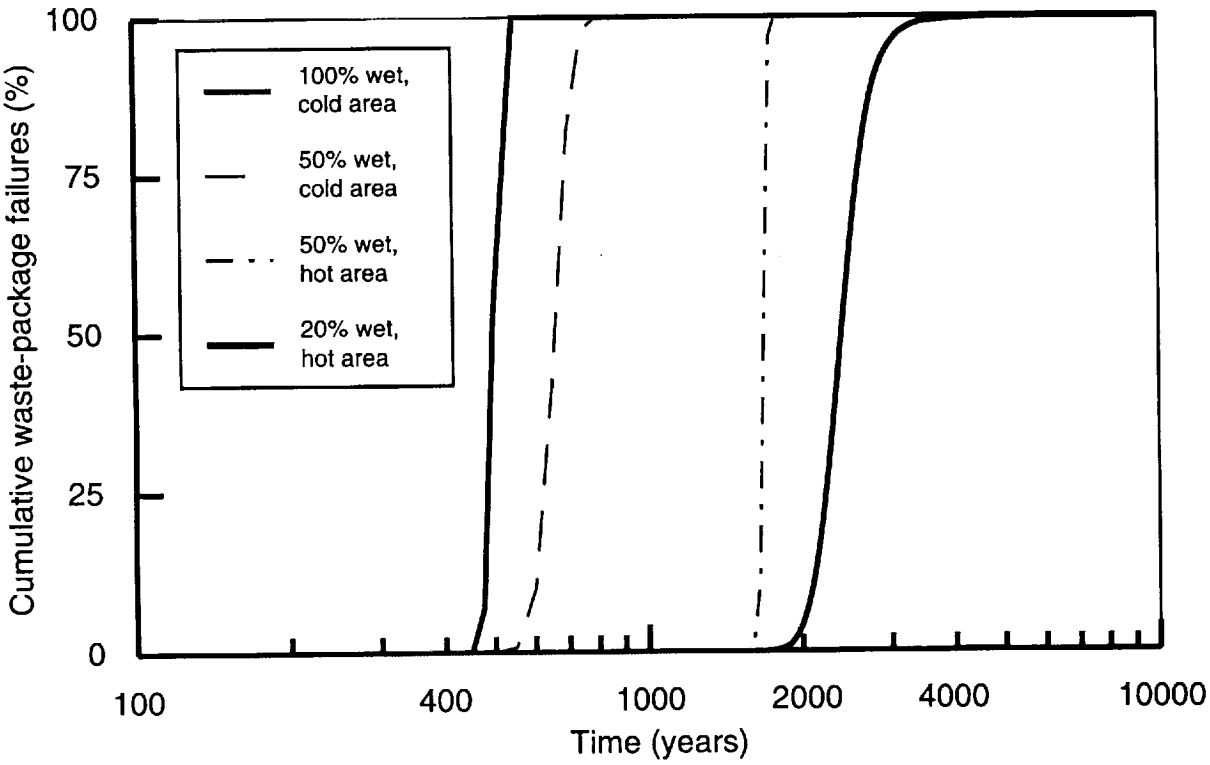

Figure 16-7. Range of container failures for 57-kW/acre, borehole case.

Figure 16-8 shows the range of container lifetimes for the 114-kW/acre, vertical emplacement case. The range (indicated by the solid lines in the figure) is ~2,450 to 7,500 years. Note that there are more wetting conditions plotted for the 114-kW/acre case because, at lower wetting conditions for the 57-kW/acre case, no failures are predicted. In Figures 16-6 through 16-10, the lowest water conditions shown are those for which there are significant (i.e., greater than 5%) failures.

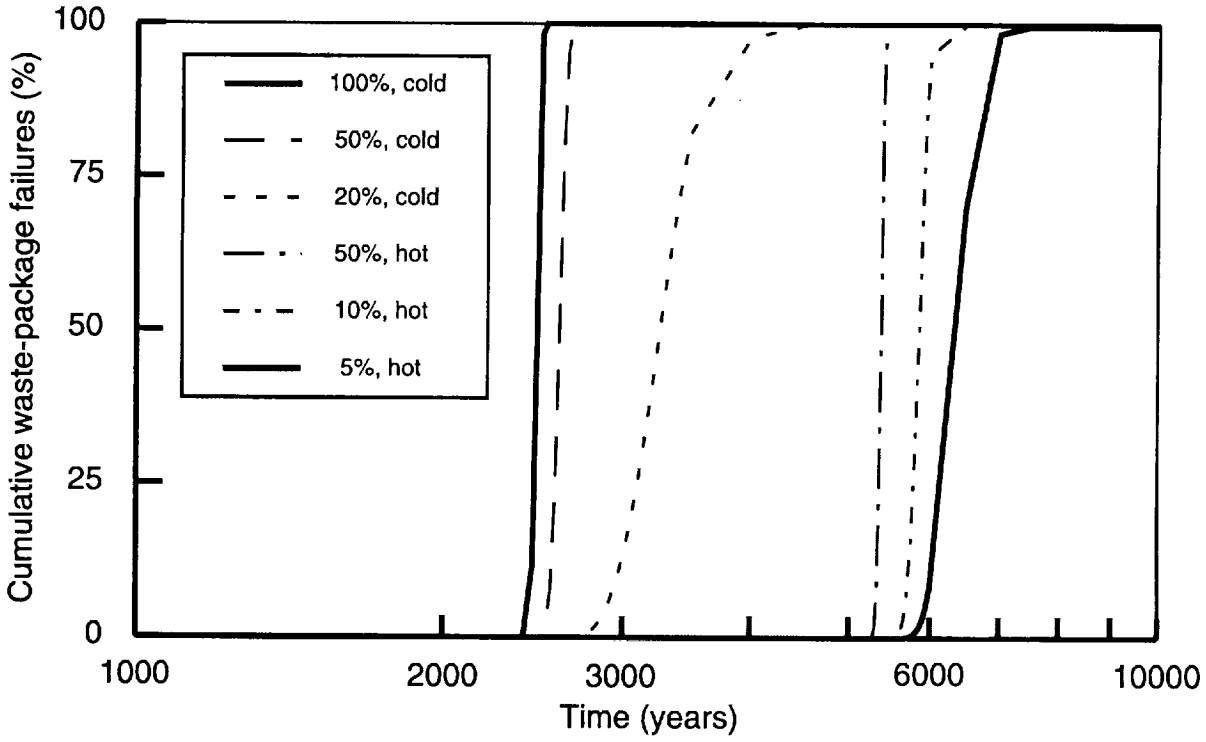

Figure 16-8. Range of container failures for 114-kW/acre, borehole case.

For the in-drift cases, the results are similar. For the lower power-density case, the containers fail over a period of ~950 to 10,000 years (Figure 16-9). For the 114-kW/acre case, failures occur from ~3,050 years to ~8,000 years (Figure 16-10).

Figure 16-10 also shows an example of the effects of having limited water available for corrosion. Very few containers fail within 10,000 years for the cold, 10% wet conditions. This is because during the critical time while the temperature is between 100°C and 70°C, there is insufficient water to cause complete corrosion. Below 70°C, the corrosion rates decrease sufficiently that the containers can last for a long time.

The range of failure times for human intrusion is taken to be from the earliest onset of failure to the latest **complete** failure (i.e., conditions that produce less than complete failure in 10,000 years have not been considered). For all four analysis cases, the ranges of failure times are at least 4,000 years. The values are listed in Table 16-5.

Table 16-5. Range of container failure times.

Configuration	Start of Earliest Failure (years)	End of Latest Failure (years)	Range (years)
Borehole, 57 kW/acre	475	5,000	4,525
Borehole, 114 kW/acre	2,450	7,500	5,050
In-Drift, 57 kW/acre	950	10,000	9,050
In-Drift, 114 kW/acre	3,050	8,000	4,950

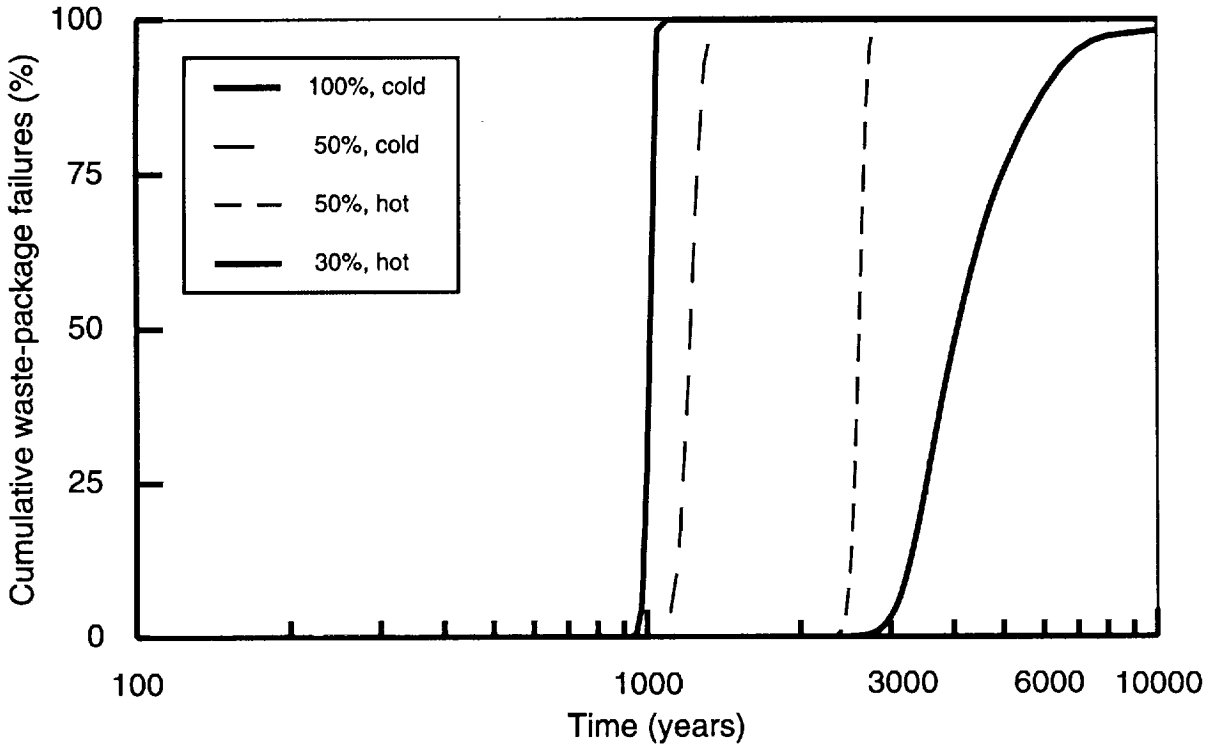

Figure 16-9. Range of container failures for 57-kW/acre, in-drift case.

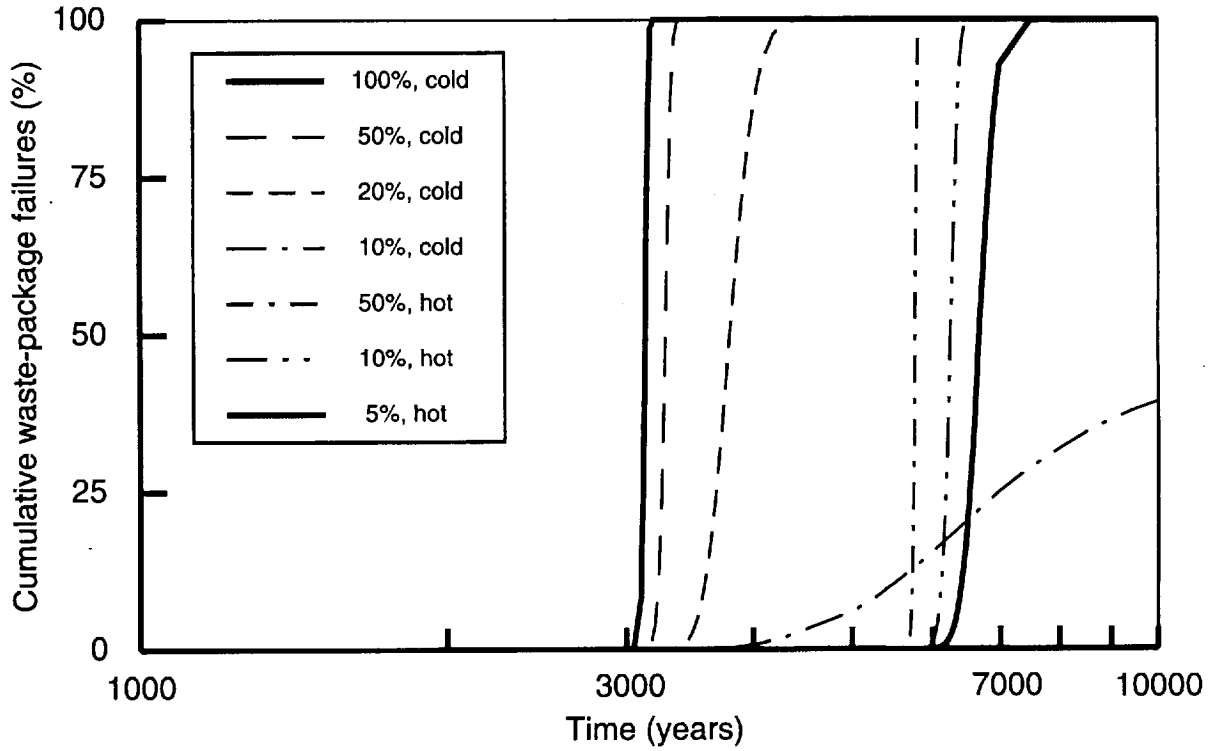

Figure 16-10. Range of container failures for 114-kW/acre, in-drift case.

16.3 Release results

The baseline human-intrusion analysis consists of calculations to model the radionuclide releases over several 10,000-year periods (with starting times from 0 years through 999,990 years) for the four analysis cases: 57 kW/acre repository thermal loading, borehole emplacement; 114 kW/acre, borehole; 57 kW/acre, in-drift emplacement; and 114 kW/acre, in-drift.

Each simulation models 20,000 realizations of a 10,000-year time period. During the 10,000-year period, the number of boreholes listed in Table 16-2 are drilled into the repository. This results in some direct hits, some near misses, and some complete misses, each with characteristic releases. Accumulating the 20,000 outcomes produces a histogram of releases. Figure 16-11 is an example histogram, showing the distribution of releases from direct hits and near misses.

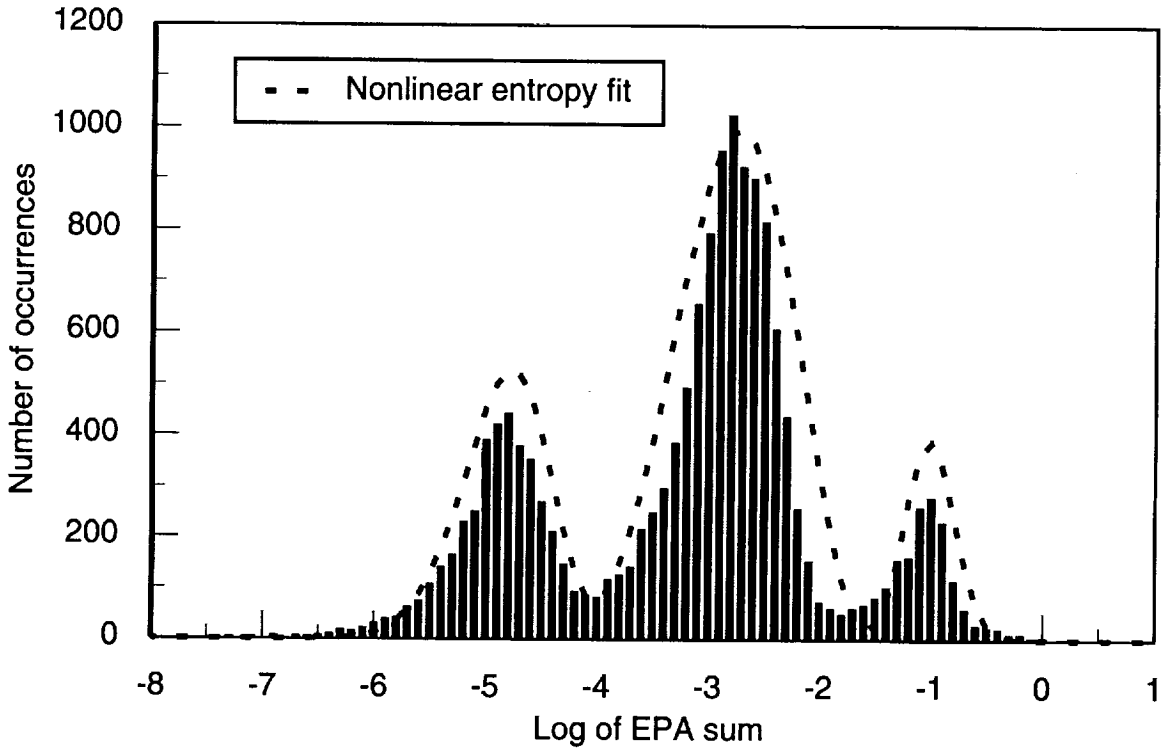

Figure 16-11. Nonlinear entropy fit to histogram of releases.

To calculate the cumulative 1,000,000-year releases, it is necessary to sum the releases for every 10,000-year sub-period in the 1,000,000-year time span. Since not all subperiods have been simulated, the releases for the missing periods are estimated. For each analysis that has been run, the peaks of the release histograms are fitted by a nonlinear entropy fit (described in Schenker *et al.*, 1994) to get the mean values, standard deviations,

and areas under the peaks. Figure 16-11 shows an example of the fit to the histogram peaks.

From the fits to the histograms that have been run at various starting times, a spline-fit interpolation is made for each peak for the time periods that have not been analyzed. Figure 16-12 shows an example of the data and the interpolations. Note that although the logarithms of the releases are interpolated, Figure 16-12 shows the actual releases. To estimate the cumulative releases in time periods that have not been analyzed (for example, from 110,000years through190,000 years), the interpolated releases from each peak are summed and used as a multiplicative factor for the nearest release value that has been run (e.g., 100,000 years for the example given above). Table 16-6 gives means and the interpolation scale factors for the three peaks for the four analysis cases. The weighted-average scale factor is weighted by the peak areas calculated by the entropy fit.

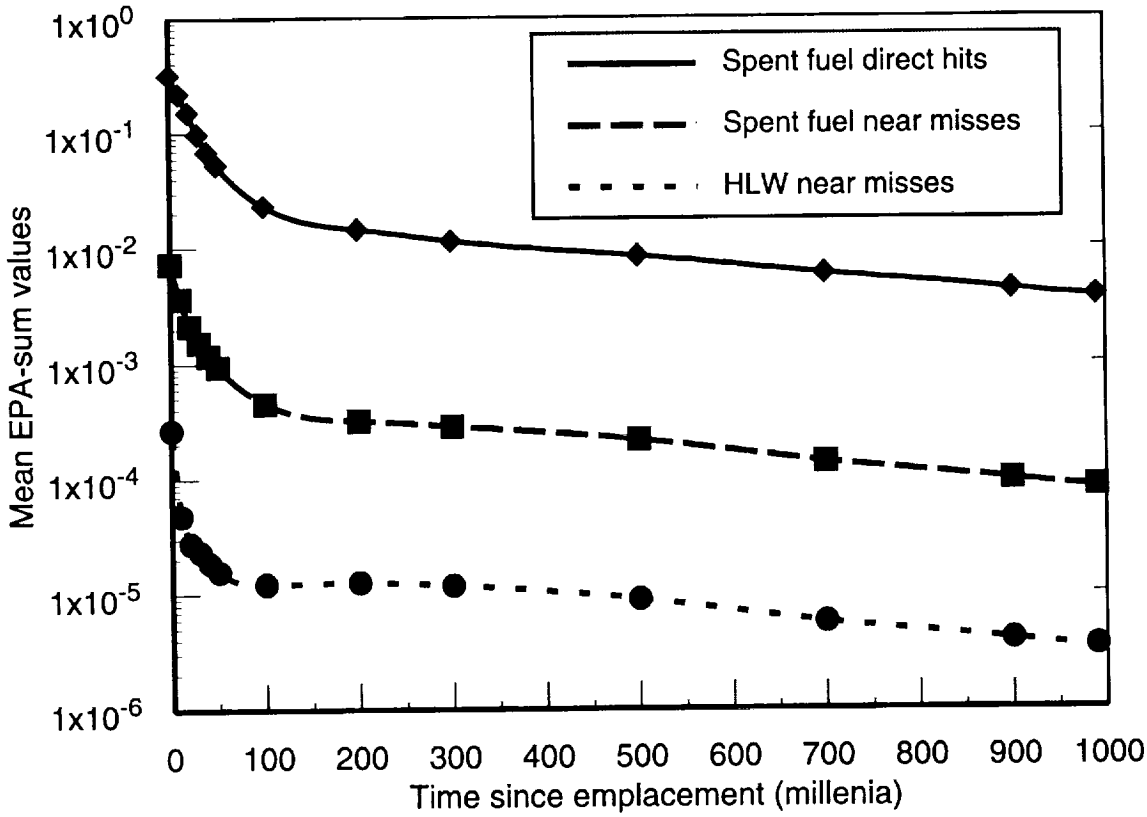

Figure 16-12. Mean values of release peaks for times to 1,000,000 years (in-drift, 114-kW/acre case).

Table 16-6. Scaling factors for 1,000,000-year releases.

Time Period	Spent-Fuel Direct Hits	Interpolation Scale Factor	Spent-Fuel Near Misses	Interpolation Scale Factor	HLW Near Misses	Interpolation Scale Factor	Weighted Scale Factor
			Borehole Emplacement, 57 kW/acre				
0	9.84×10^{-2}		1.60×10^{-3}		1.39×10^{-5}		
10,000	4.86×10^{-2}		1.07×10^{-3}		1.18×10^{-5}		
20,000	3.63×10^{-2}		7.47×10^{-4}		9.44×10^{-6}		
30,000	2.53×10^{-2}		5.52×10^{-4}		7.09×10^{-6}		
40,000	1.41×10^{-2}		3.96×10^{-4}		6.41×10^{-6}		
50,000	1.49×10^{-2}		3.21×10^{-4}		5.80×10^{-6}		
60,000–90,000		3.36		3.60		4.64	3.83
100,000	5.13×10^{-3}		1.52×10^{-4}		4.81×10^{-6}		
110,000–190,000		6.89		7.85		9.48	8.14
200,000	2.87×10^{-3}		1.00×10^{-4}		4.51×10^{-6}		
210,000–290,000		9.12		9.51		9.76	9.53
300,000	2.29×10^{-3}		8.96×10^{-5}		4.16×10^{-6}		
310,000–490,000		17.11		16.36		16.68	16.53
500,000	1.58×10^{-3}		5.48×10^{-5}		2.70×10^{-6}		
510,000–690,000		14.39		15.87		16.14	15.77
700,000	8.08×10^{-4}		3.41×10^{-5}		1.73×10^{-6}		
710,000–890,000		19.85		17.12		17.10	17.48
900,000	7.07×10^{-4}		2.40×10^{-5}		1.21×10^{-6}		
910,000–980,000		7.42		8.29		8.29	8.18
990,000	4.84×10^{-4}		2.06×10^{-5}		1.04×10^{-6}		
			Borehole Emplacement, 114 kW/acre				
0	7.76×10^{-2}		1.26×10^{-3}		1.17×10^{-5}		
10,000	4.20×10^{-2}		9.76×10^{-4}		1.02×10^{-5}		
20,000	2.62×10^{-2}		6.18×10^{-4}		8.07×10^{-6}		
30,000	1.86×10^{-2}		4.72×10^{-4}		6.43×10^{-6}		
40,000	1.44×10^{-2}		3.78×10^{-4}		5.74×10^{-6}		
50,000	1.07×10^{-2}		2.90×10^{-4}		5.18×10^{-6}		
60,000–90,000		3.44		3.58		4.53	3.81
100,000	4.28×10^{-3}		1.34×10^{-4}		4.19×10^{-6}		
110,000–190,000		7.55		7.79		9.59	8.24
200,000	2.76×10^{-3}		8.62×10^{-5}		3.89×10^{-6}		
210,000–290,000		9.36		8.92		9.03	9.00
300,000	2.31×10^{-3}		6.57×10^{-5}		2.98×10^{-6}		
310,000–490,000		15.51		15.50		15.62	15.53
500,000	1.30×10^{-3}		3.73×10^{-5}		1.77×10^{-6}		

Table 16-6. Scaling factors for 1,000,000-year releases (continued).

Time Period	Spent-Fuel Direct Hits	Interpolation Scale Factor	Spent-Fuel Near Misses	Interpolation Scale Factor	HLW Near Misses	Interpolation Scale Factor	Weighted Scale Factor
510,000–690,000		17.17		15.63		15.94	15.91
700,000	1.12×10^{-3}		2.30×10^{-5}		1.10×10^{-6}		
710,000–890,000		23.98		18.21		17.09	18.71
900,000	1.06×10^{-3}		1.74×10^{-5}		7.72×10^{-7}		
910,000–980,000		6.06		7.84		8.30	7.75
990,000	4.74×10^{-4}		1.34×10^{-5}		6.65×10^{-7}		
In-Drift Emplacement, 57 kW/acre							
0	3.59×10^{-1}		9.48×10^{-3}		2.44×10^{-4}		
10,000	2.66×10^{-1}		1.14×10^{-2}		6.36×10^{-5}		
20,000	1.64×10^{-1}		7.96×10^{-3}		8.98×10^{-5}		
30,000	1.14×10^{-1}		5.35×10^{-3}		9.65×10^{-5}		
40,000	8.04×10^{-2}		4.26×10^{-3}		8.30×10^{-5}		
50,000	6.05×10^{-2}		3.40×10^{-3}		7.24×10^{-5}		
60,000–90,000		3.41		3.75		4.44	3.83
100,000	2.54×10^{-2}		1.69×10^{-3}		5.91×10^{-5}		
110,000–190,000		7.62		7.79		9.76	8.17
200,000	1.59×10^{-2}		1.13×10^{-3}		5.63×10^{-5}		
210,000–290,000		9.54		9.59		9.84	9.63
300,000	1.44×10^{-2}		1.02×10^{-3}		5.39×10^{-5}		
310,000–490,000		17.05		16.93		17.67	17.11
500,000	9.78×10^{-3}		6.81×10^{-4}		3.90×10^{-5}		
510,000–690,000		16.87		16.24		16.15	16.35
700,000	6.89×10^{-3}		4.36×10^{-4}		2.48×10^{-5}		
710,000–890,000		17.18		16.80		17.07	16.94
900,000	4.82×10^{-3}		3.03×10^{-4}		1.70×10^{-5}		
910,000–980,000		8.29		8.52		8.11	8.38
990,000	4.16×10^{-3}		2.74×10^{-4}		1.41×10^{-5}		
In-Drift Emplacement, 114 kW/acre							
0	3.16×10^{-1}		7.28×10^{-3}		2.65×10^{-4}		
10,000	2.18×10^{-1}		3.64×10^{-3}		4.76×10^{-5}		
20,000	1.50×10^{-1}		2.12×10^{-3}		2.75×10^{-5}		
30,000	9.73×10^{-2}		1.54×10^{-3}		2.32×10^{-5}		
40,000	5.42×10^{-2}		1.10×10^{-3}		1.79×10^{-5}		
50,000	5.31×10^{-2}		9.43×10^{-4}		1.57×10^{-5}		
60,000–90,000		3.53		3.65		4.27	3.75
100,000	2.31×10^{-2}		4.52×10^{-4}		1.22×10^{-5}		

Table 16-6. Scaling factors for 1,000,000-year releases (continued).

Time Period	Spent-Fuel Direct Hits	Interpolation Scale Factor	Spent-Fuel Near Misses	Interpolation Scale Factor	HLW Near Misses	Interpolation Scale Factor	Weighted Scale Factor
110,000–190,000		7.59		8.02		10.17	8.41
200,000	1.44×10^{-2}		3.18×10^{-4}		1.26×10^{-5}		
210,000–290,000		9.01		9.53		9.78	9.47
300,000	1.14×10^{-2}		2.84×10^{-4}		1.18×10^{-5}		
310,000–490,000		17.09		17.74		17.87	17.62
500,000	8.30×10^{-3}		2.14×10^{-4}		8.90×10^{-6}		
510,000–690,000		17.06		16.40		16.24	16.51
700,000	5.84×10^{-3}		1.38×10^{-4}		5.63×10^{-6}		
710,000–890,000		17.33		16.98		17.00	17.06
900,000	4.23×10^{-3}		9.65×10^{-5}		3.96×10^{-6}		
910,000–980,000		8.38		8.35		8.37	8.36
990,000	3.72×10^{-3}		8.42×10^{-5}		3.46×10^{-6}		

16.3.1 Results for borehole-emplacement, 57-kW/acre case

The releases for the 57-kW/acre, borehole case include contributions from both direct hits and near misses. Direct-hit releases fall into two major groups—those from the spent fuel, and those from the HLW. Releases from spent fuel vary slightly depending on whether the drill strikes a hybrid, PWR, or BWR container. Direct hits on HLW canisters have the same magnitude of releases as the near misses for spent-fuel wastes. Figure 16-13 shows a histogram with the contributions to releases (for the first 10,000 years) of the source-term components.

Figure 16-14 shows several CCDFs for releases occurring after various start-time periods for the 57-kW/acre, borehole case. The analysis for the 10,000-year starting time shows the largest releases are about an order of magnitude lower than for the analysis with a 0-year starting time. For start times later than 50,000 years, the releases at similar probabilities on the CCDF plots are at least one order of magnitude below the 0-year case. Consequently, contributions to cumulative releases are controlled by the releases occurring during approximately the first 50,000 years.

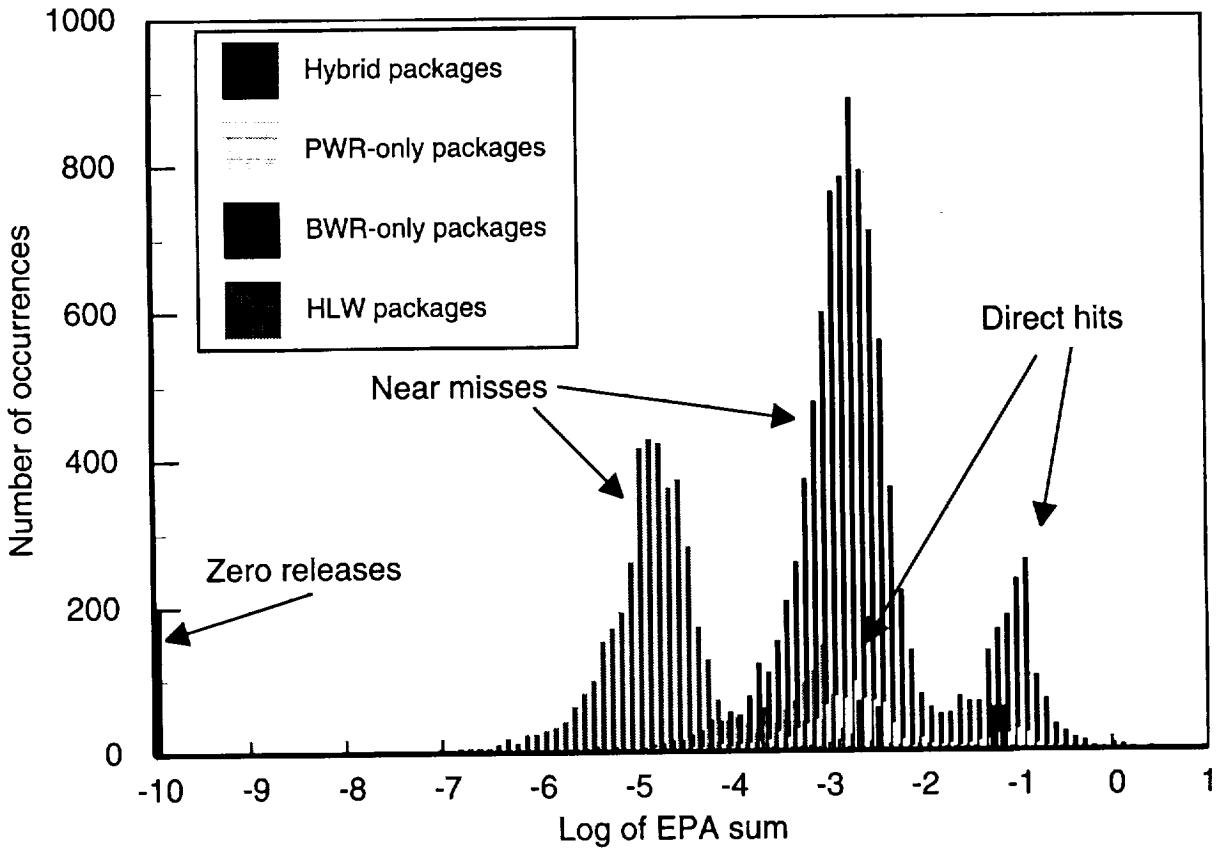

Figure 16-13. Contributions to releases from components of source term for 57-kW/acre borehole case.

The "structure" shown in a CCDF curve can be related to a histogram. Sloping sections of the CCDF (e.g., A, B, or C in Figure 16-14) correspond to releases (i.e., peaks in Figure 16-13). The steepness of the CCDF slope indicates the narrowness of the histogram peak. The flat sections of a CCDF curve indicate values of the EPA sum for which there are no releases. Section A of the CCDF in Figure 16-14 corresponds to the direct-hit releases from spent fuel; section B of the CCDF corresponds to spent-fuel near misses (and HLW direct hits), while section C is the HLW near misses.

Figure 16-15 shows the estimates for the conditional CCDF for releases over 1,000,000 years for the 57-kW/acre, borehole case. Shown for comparison is the CCDF for the releases during the first 10,000-year period. Note that the maximum releases over 1,000,000 years do not increase appreciably from those of the first 10,000-year analysis. This is because to get a large maximum release requires a combination of events—multiple direct hits, hits occurring early in the life of the repository when the radioactivity is high, and exhumation of most of the contents of the waste packages. The first and third of these conditions are random, so the maximum releases are effectively controlled by the starting times.

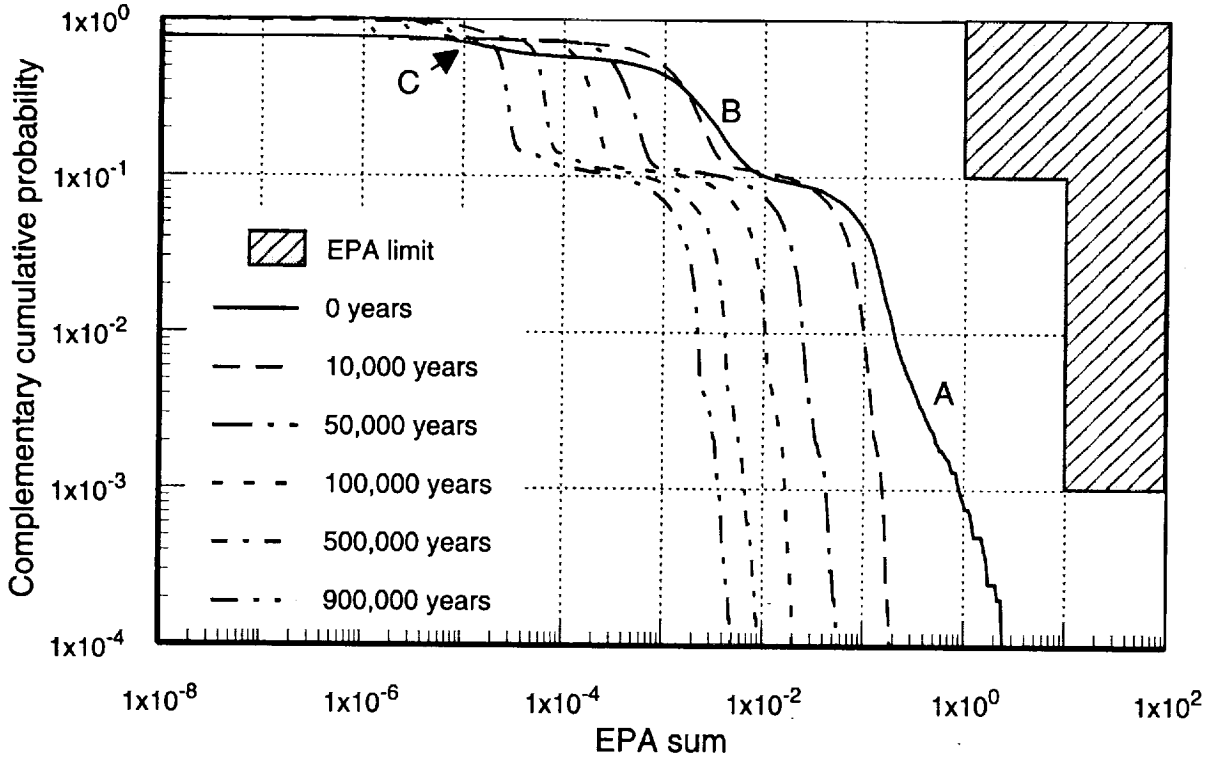

Figure 16-14. Conditional CCDFs for 10,000-year cumulative releases after various starting times for 57-kW/acre borehole case.

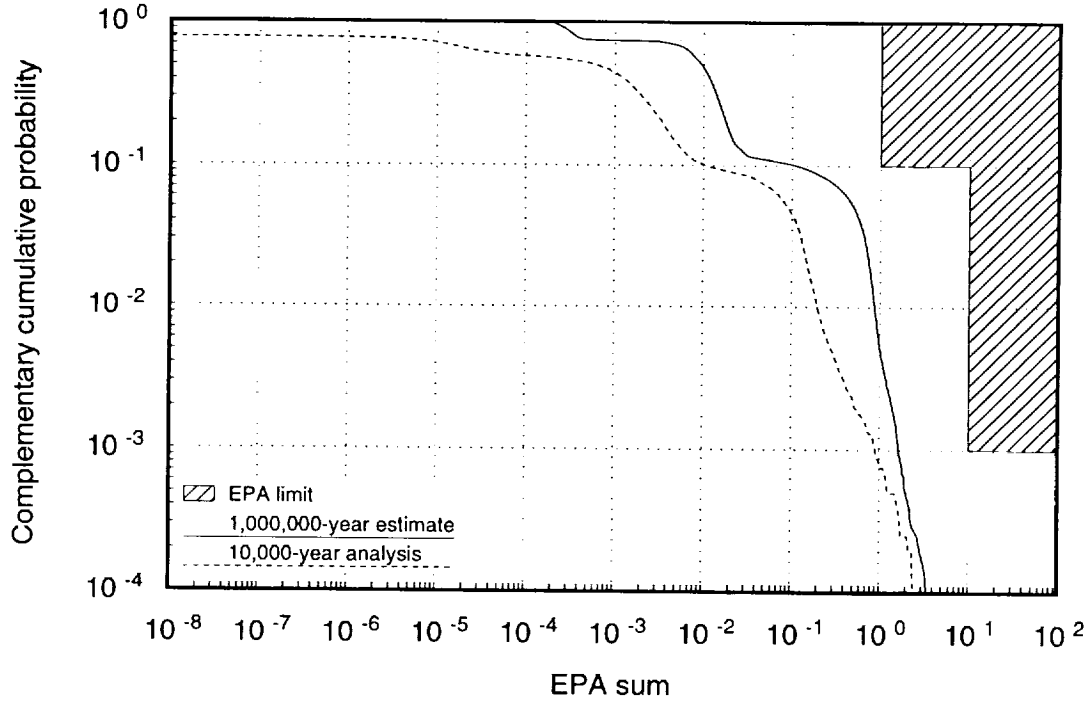

Figure 16-15. Conditional CCDFs for cumulative releases over 1,000,000 years for 57-kW/acre borehole case.

The releases shown in the 1,000,000-year CCDF of about 10^{-2} of the EPA sum are from both direct hits on HLW and spent-fuel near misses; those around $4x10^{-4}$ are from near misses on HLW. Near misses contribute proportionally more to the 1,000,000-year releases because the contamination of rock surrounding the waste package increases with time. The EPA limits have been included in the plot as a reference, however they do not apply for releases beyond 10,000 years.

The 57-kW/acre, borehole case is most closely comparable to the TSPA-91 analysis. Figure 16-16 compares the CCDF for the TSPA-91 with that for the first 10,000-year period of the current analysis. The maximum releases are quite similar, but the contributions from the several components of the source give the TSPA-93 CCDF more structure. Because of the multiple sources in TSPA-93, the range of direct-hit releases is broader than for TSPA-91. Because the TSPA-91 analysis only used a single value for waste-package lifetime (the factor that controls the time that diffusion of radionuclides into the surrounding rock starts), those near-miss releases were fairly tightly bunched; the current analysis assumes that waste-package failures can occur over a 4,500-year period, thus greatly increasing the variability of the amount of diffusion that can occur. Consequently, the near misses are not so pronounced on the current CCDF.

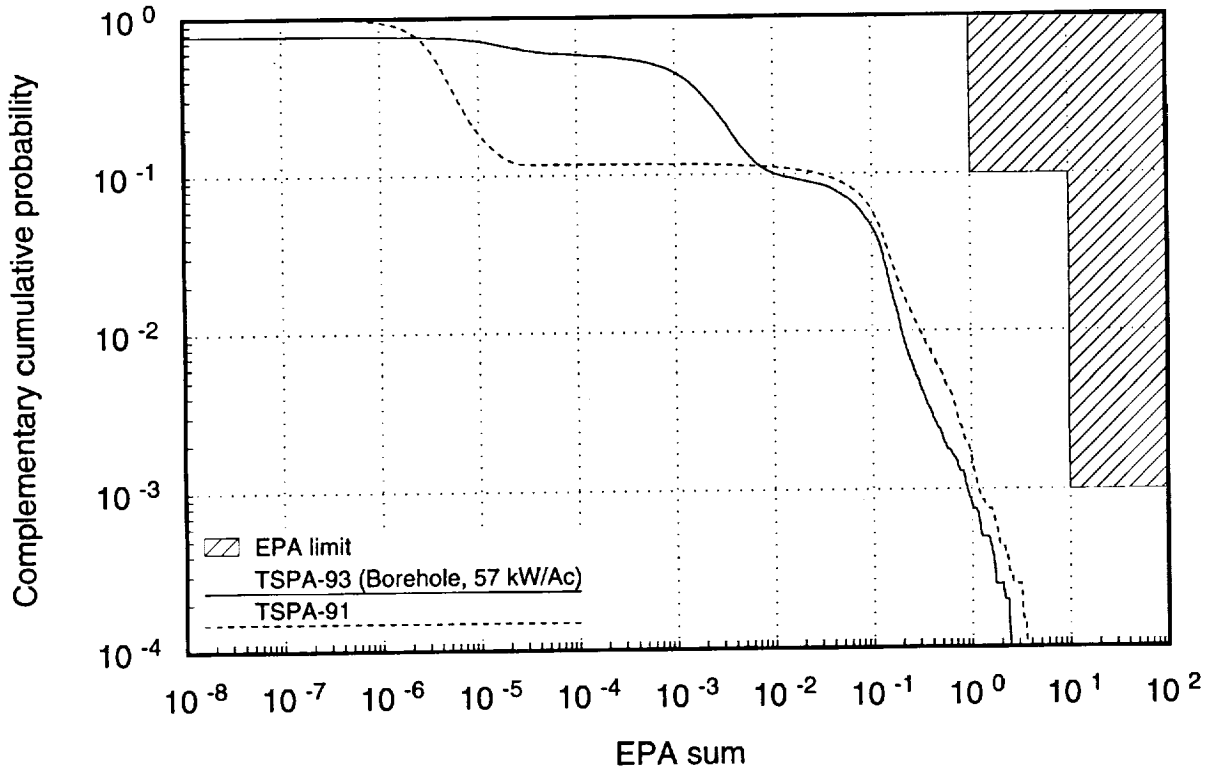

Figure 16-16. Comparison of CCDFs for similar TSPA-91 and TSPA-93 analyses.

16.3.2 Results for borehole-emplacement, 114-kW/acre case

Releases for the 114-kW/acre, borehole case over 10,000 years (Figure 16-17) are quite similar to those for the 57-kW/acre, borehole case (also shown in the figure). The greater probability of a hit per drilling operation (i.e., 0.0186 *vs.* 0.0128) is offset by the fewer holes drilled (i.e., 10 *vs.* 14) because of the smaller repository area in the 114-kW/acre case. As Figure 16-17 shows, the maximum releases are almost the same, and the curve shapes are quite similar. The near-miss releases from spent fuel (occurring for the range of EPA sums from 10^{-3} to about 10^{-2}) are lower for the 114-kW/acre case than for the 57-kW/acre case because the container lifetime is considerably longer for the former. Consequently, there is less time for the contamination to accumulate in the surrounding rock. Figure 16-18 shows the 1,000,000-year cumulative CCDF and the first 10,000-year run for comparison. As with the 57-kW/acre case, the peak releases do not increase as much for the 1,000,000-year estimate as do the lesser releases.

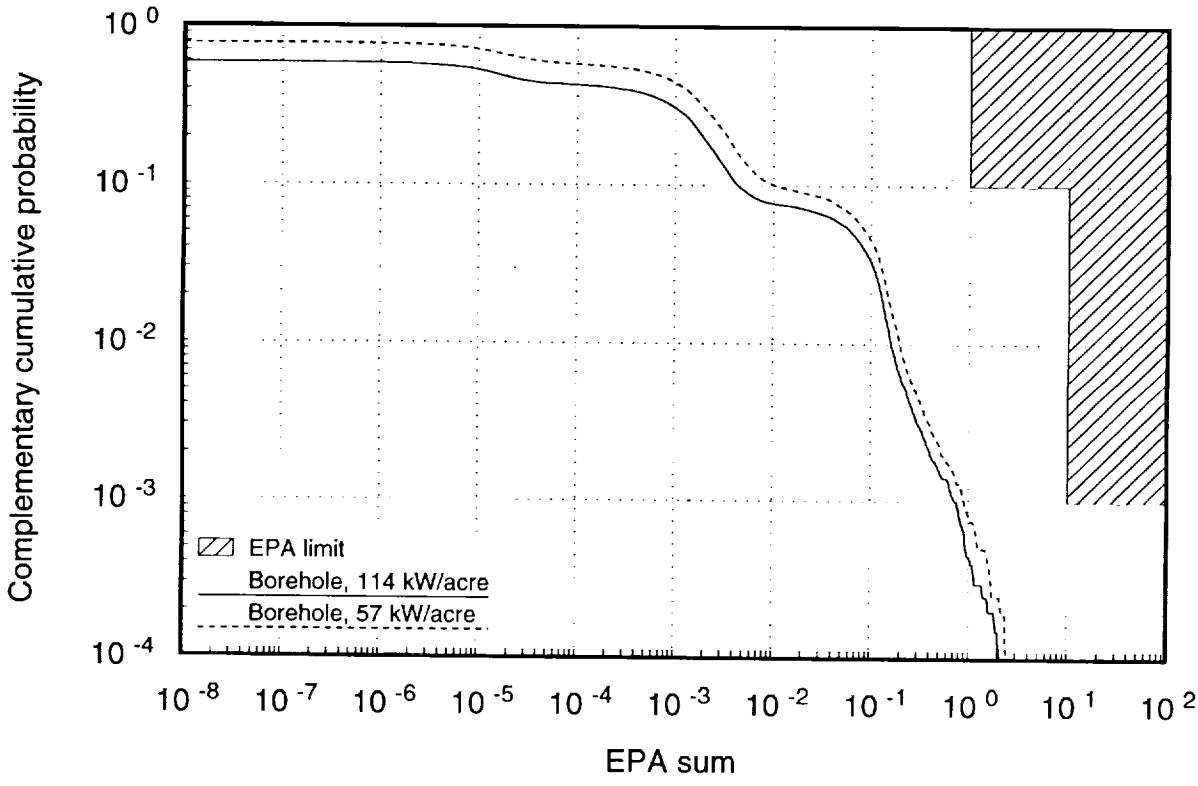

Figure 16-17. Conditional CCDF for releases for 114-kW/acre, borehole case.

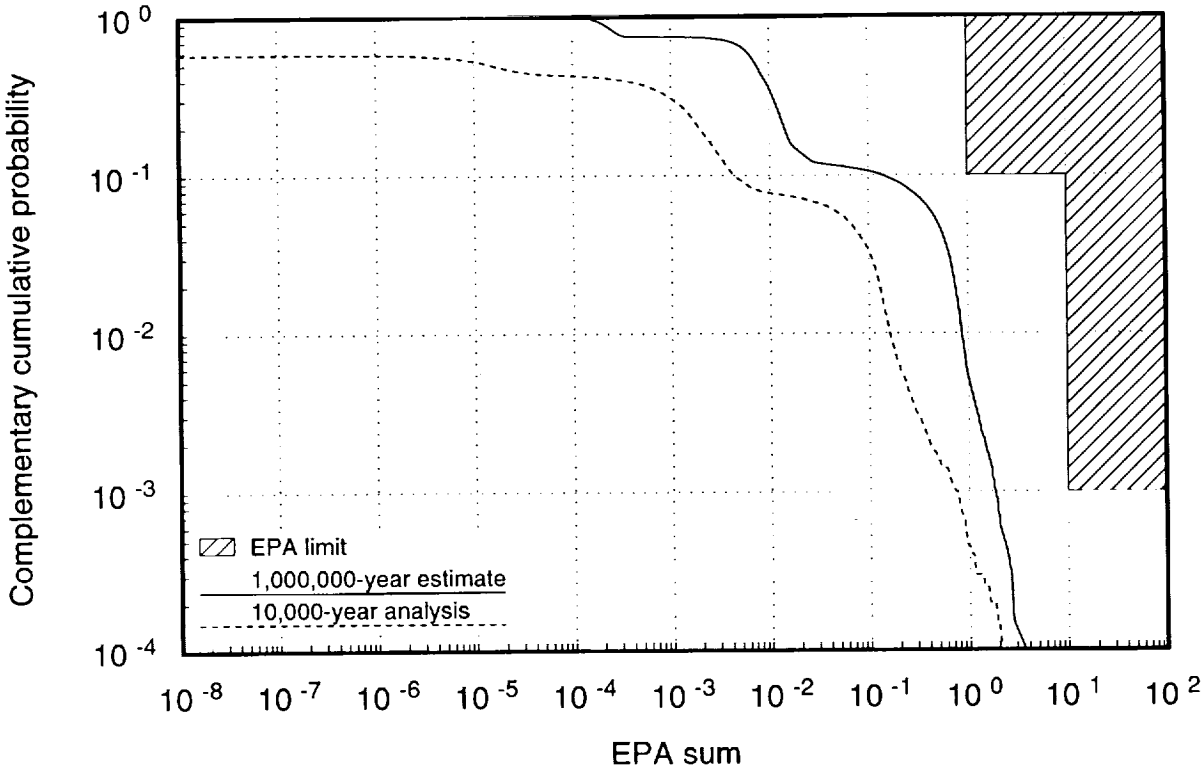

Figure 16-18. Conditional CCDF for cumulative releases over 1,000,000 years for 114-kW/acre, borehole case.

16.3.3 Results for in-drift-emplacement cases

Figure 16-19 shows the histogram of releases for in-drift waste-package emplacement for the 0-year starting time run. It has been assumed for these analyses that the lifetime of the HLW containers is greater than 10,000 years because their construction consists of the two steel layers of the container described previously, plus the steel HLW canister. There are therefore no HLW near misses for the first 10,000-year simulation.

Figure 16-20 shows the CCDFs for the two in-drift cases for the 0-year starting time. Both have maximum releases several times higher than the borehole, 57-kW/acre case (also shown in the figure). The maximum for the 114-kW/acre, in-drift case is about three times larger than that for the 57-kW/acre, borehole case, because of the larger amount of waste in the container available to be exhumed.

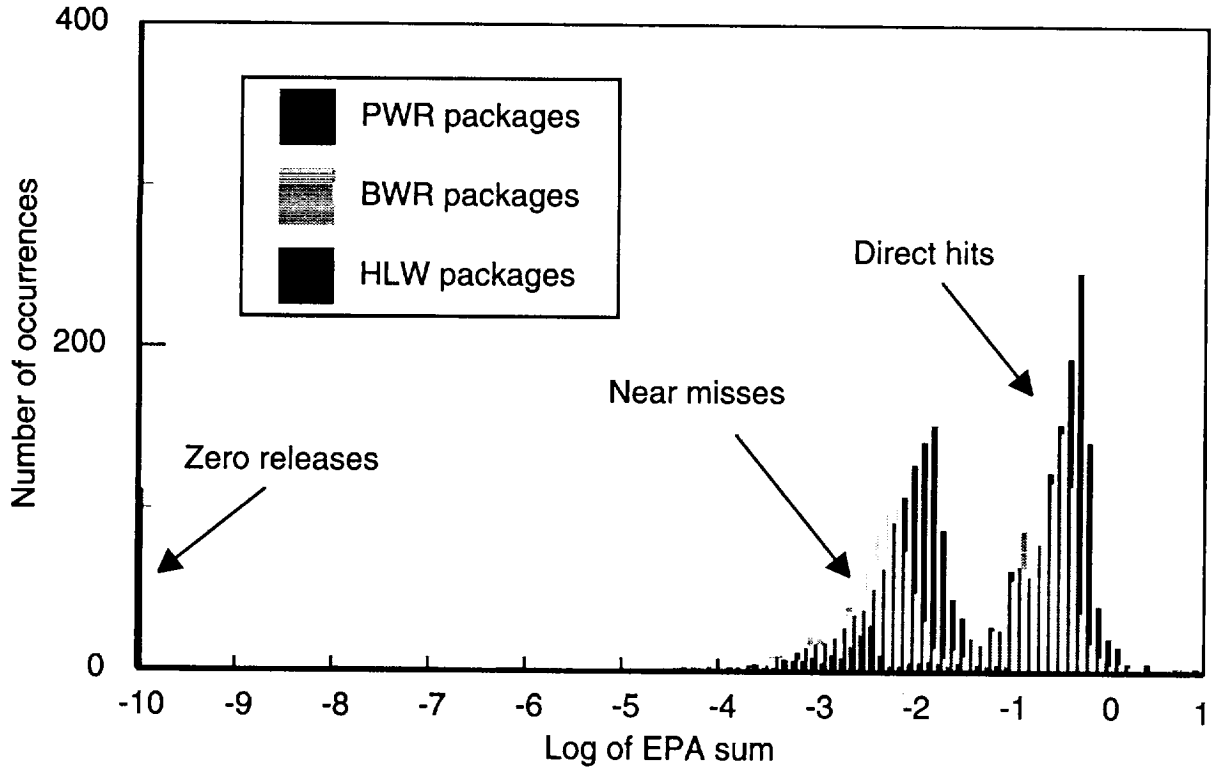

Figure 16-19. Contributions to releases from components of source term for 114-kW/acre in-drift case.

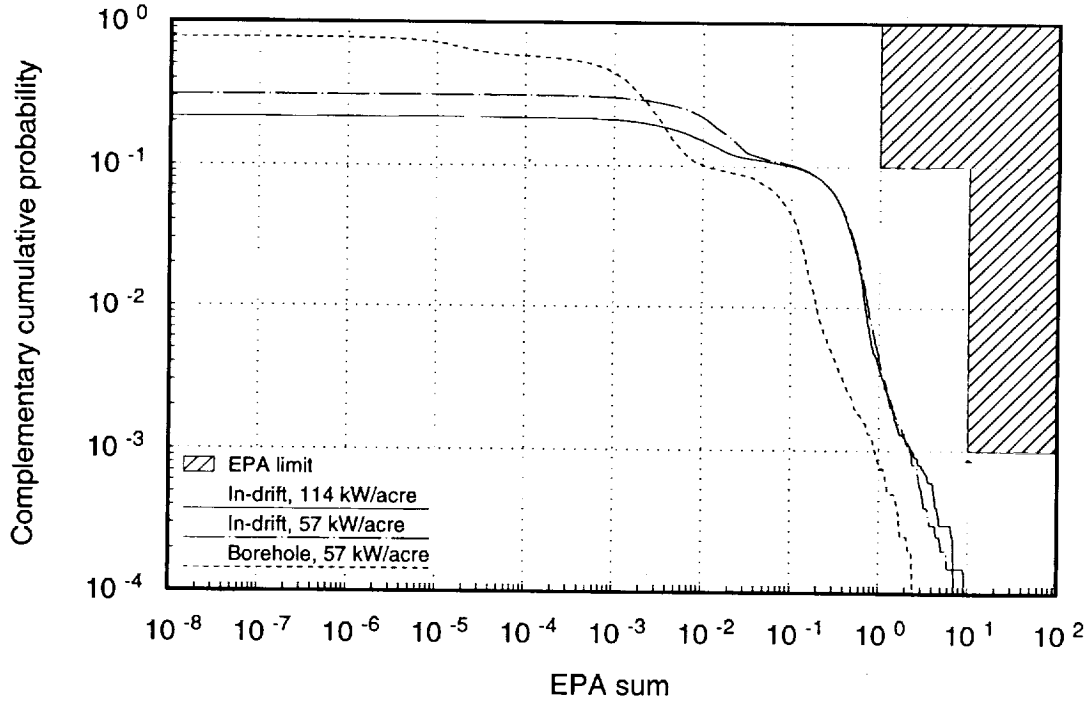

Figure 16-20. Conditional CCDF for 10,000-year releases for the two in-drift cases.

The CCDFs for the in-drift cases show that about 70% to 80% of the time there are zero releases (the CCDFs have a maximum probability of occurrence at the 10^{-8} release level of about 20% to 30%, therefore 70% to 80% of the time releases are effectively zero). The lifetimes of the in-drift container range from 1,000 to 10,000 years for the 57-kW/acre case and from 3,000 to 8,000 years for the 114-kW/acre case. We would therefore not expect many near misses during the first 10,000 year period from any source—spent fuel or HLW.

The extrapolations to 1,000,000-year releases for the in-drift emplacement cases are shown in Figure 16-21 for 57 kW/acre and Figure 16-22 for 114 kW/acre. In both cases, the 1,000,000-year releases exceed the EPA limits set for 10,000-year performance. Whereas the borehole cases have shown an increase in releases of less than an order of magnitude at the 0.1 probability level and above, for the in-drift cases the increases are at least an order of magnitude greater at these probabilities. The primary factor in the increase is the contributions from near misses. These are not important during the first 10,000-year period because the containers are largely intact. As with the borehole cases, after a million years, there is a 100% probability that there will be surface releases due to human intrusion of at least 10^{-4} of the EPA sum.

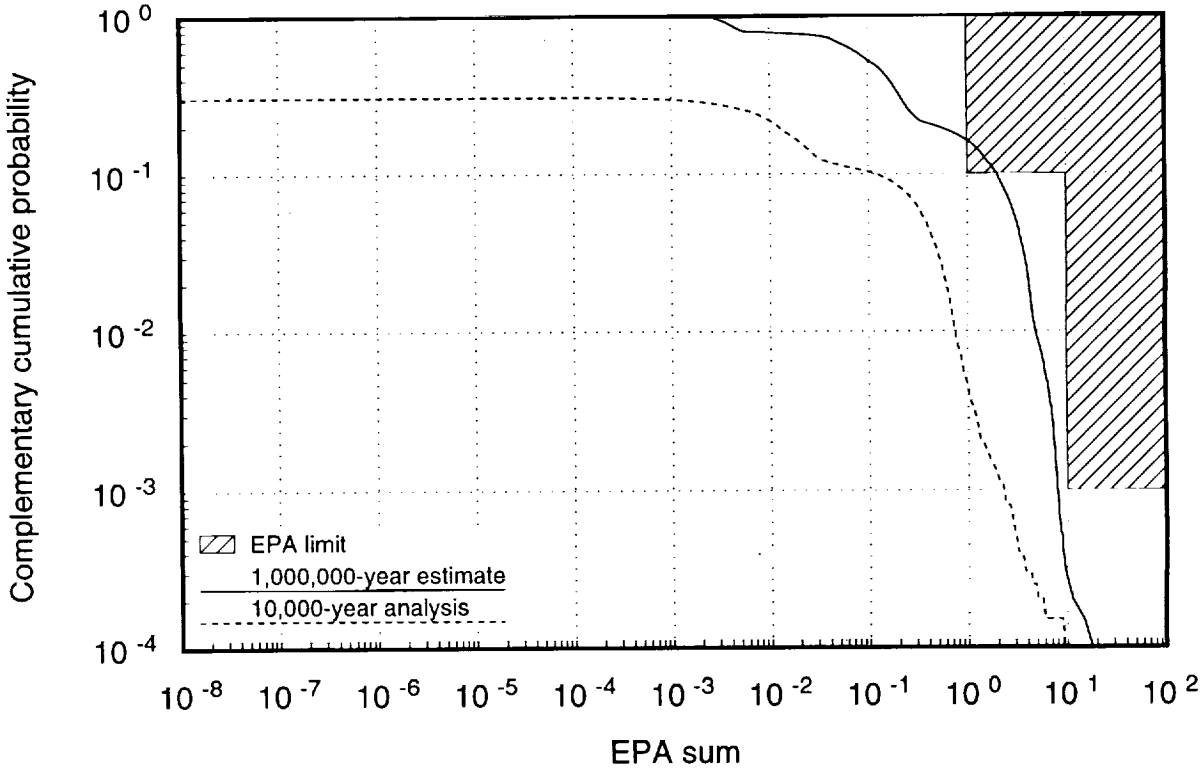

Figure 16-21. Conditional CCDFs for cumulative releases over 1,000,000 years for 57 kW/acre, in-drift case.

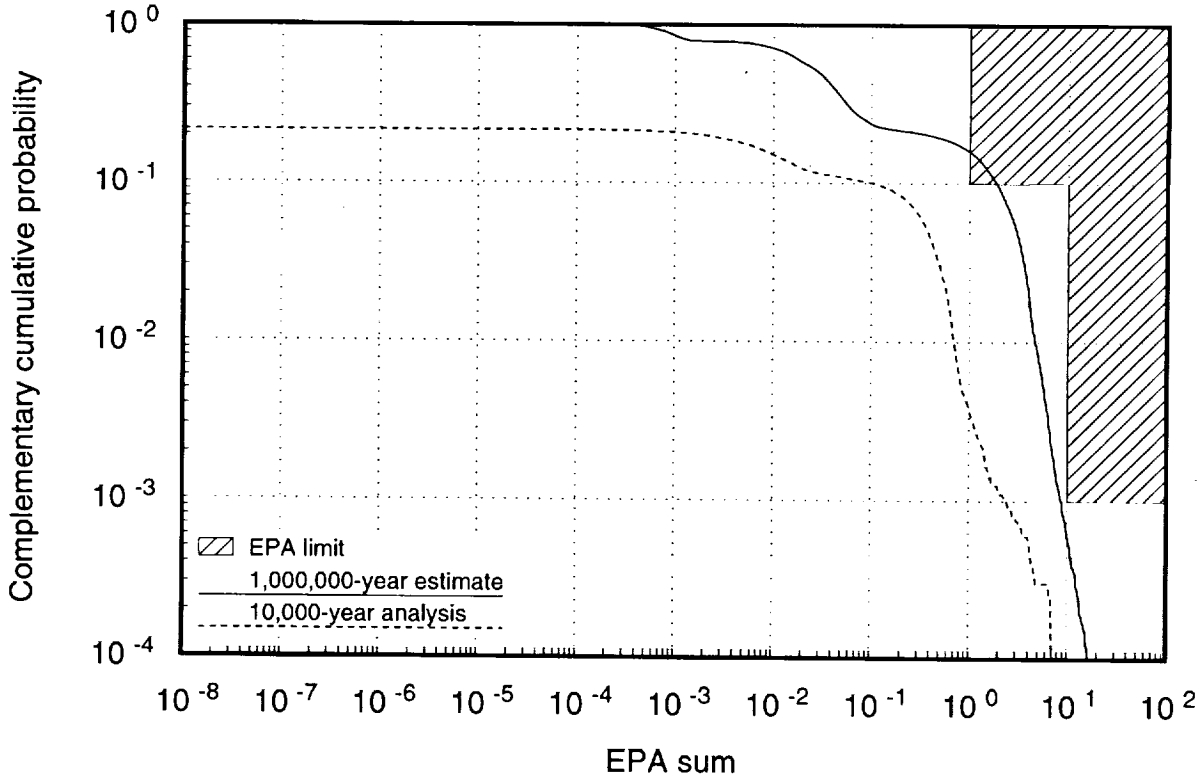

Figure 16-22. Conditional CCDF for cumulative releases over 1,000,000 years for 114 kW/acre, in-drift case.

16.4 Sensitivity studies

16.4.1 Amount of waste released by a drilling hit

There is conceptual uncertainty regarding how much waste would be exhumed in a drilling incident. For the borehole-configuration containers and canisters, we assume that the amount of waste that can be brought up is a random value uniformly distributed from 0% to 100% of the waste in the package. The drill bit and the container have approximately the same diameters, so a direct hit on a waste package could grind up its entire contents. For the in-drift spent-fuel packages, we also assume a uniform distribution for the amount of waste that can be exhumed for the four baseline analyses. However, a non-uniform distribution may be more realistic because of the large amount of waste in the package. If the drill intersects the waste package along a diameter, it cuts a hole representing approximately 5% of the waste-package volume. After the drill passes through the waste package, there is much less waste entrainment caused by the flowing drilling mud. If we assume that the mean amount of waste that can be exhumed is 5%, and the standard deviation of

that number is 13% (arrived at by assuming that the diameter of the hole through the waste is about 50% larger than the drill diameter), then we can describe the probability distribution with a beta function. Figure 16-23 illustrates a beta-function distribution based on the parameters given above.

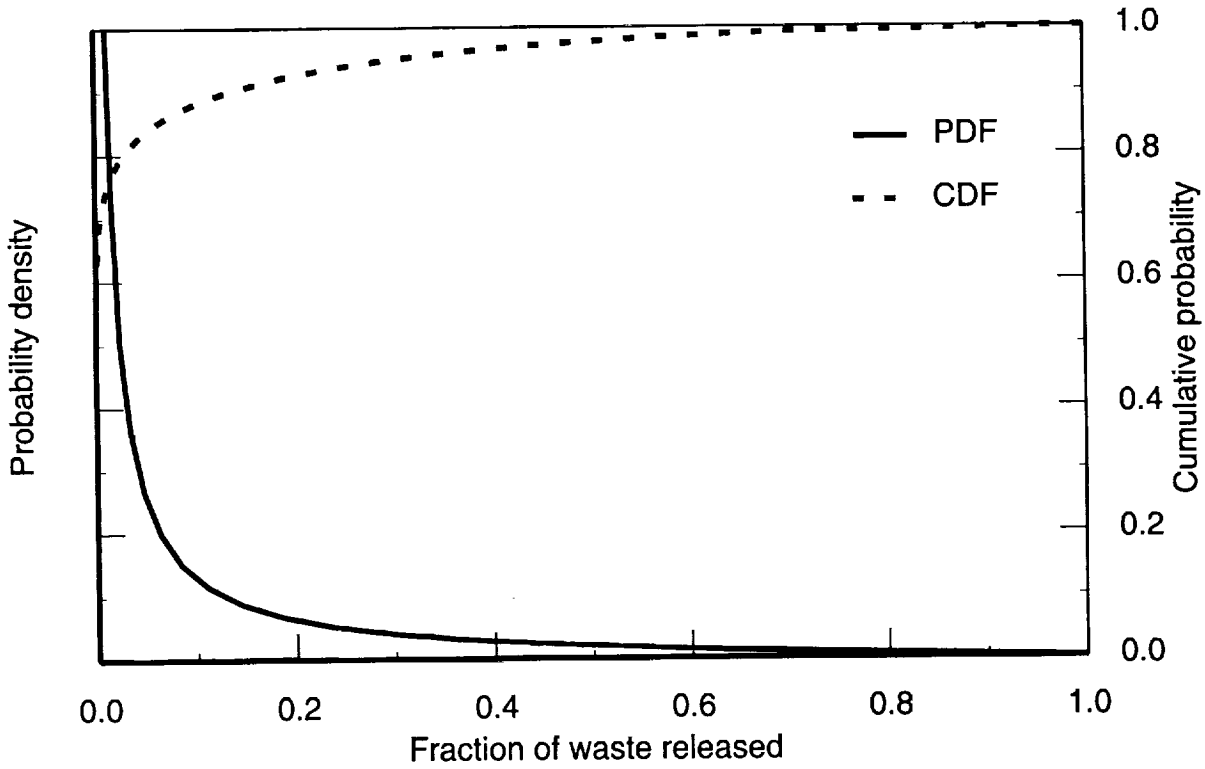

Figure 16-23. Alternative distribution of waste released from in-drift waste package.

The distribution shows that there is an ~90% chance that the fraction of waste released is less than 10%. Comparing this case with the baseline case run for the first 10,000 years shows that maximum releases are about 2 orders of magnitude smaller (Figure 16-24). Furthermore, the range of direct-hit releases is smaller than for the baseline. The 1,000,000-year estimates show a similar difference (Figure 16-25), with the maximum releases being two orders of magnitude lower and the HLW releases about one order of magnitude smaller. As would be expected, the near-miss component does not differ between the two studies.

16.4.2 Size of drill bit

For both TSPA-91 and TSPA-93, the drill-bit diameter has been fixed at 0.61 m (24 inches). This size drill is one of the largest sizes that is used in oil production. Generally, exploration drilling is done with bits ranging from 6.5 in. (0.16 m) to 8.5 in. (0.21 m) in di-

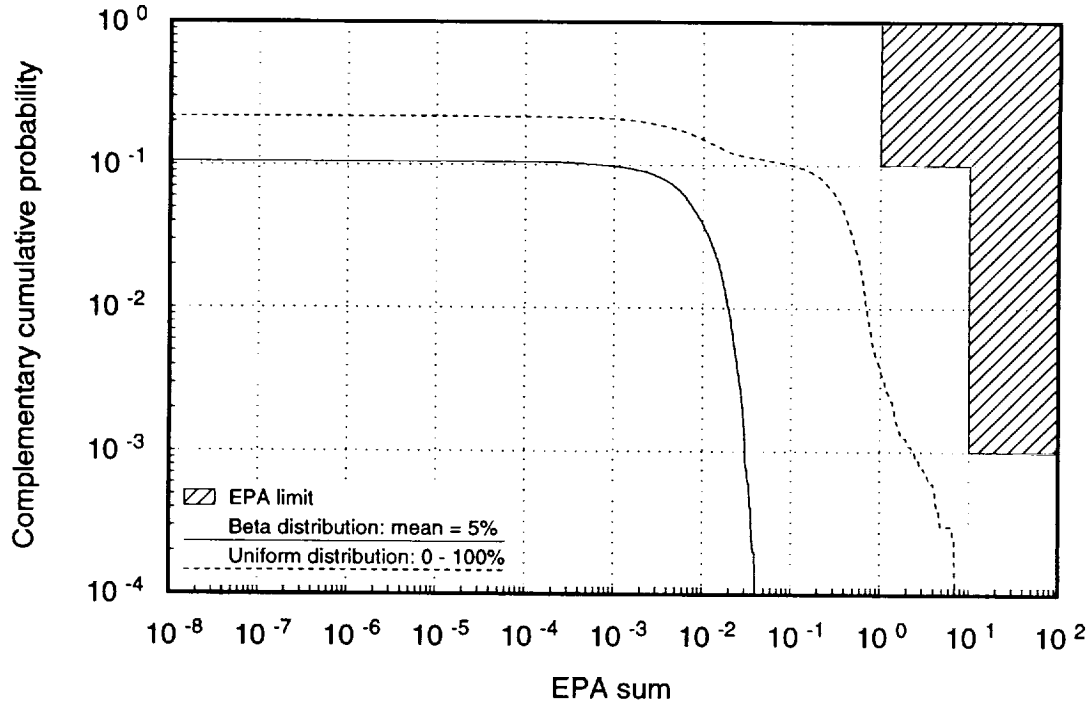

Figure 16-24. Comparison of 10,000-year CCDFs for two assumptions for distributions of waste-package releases.

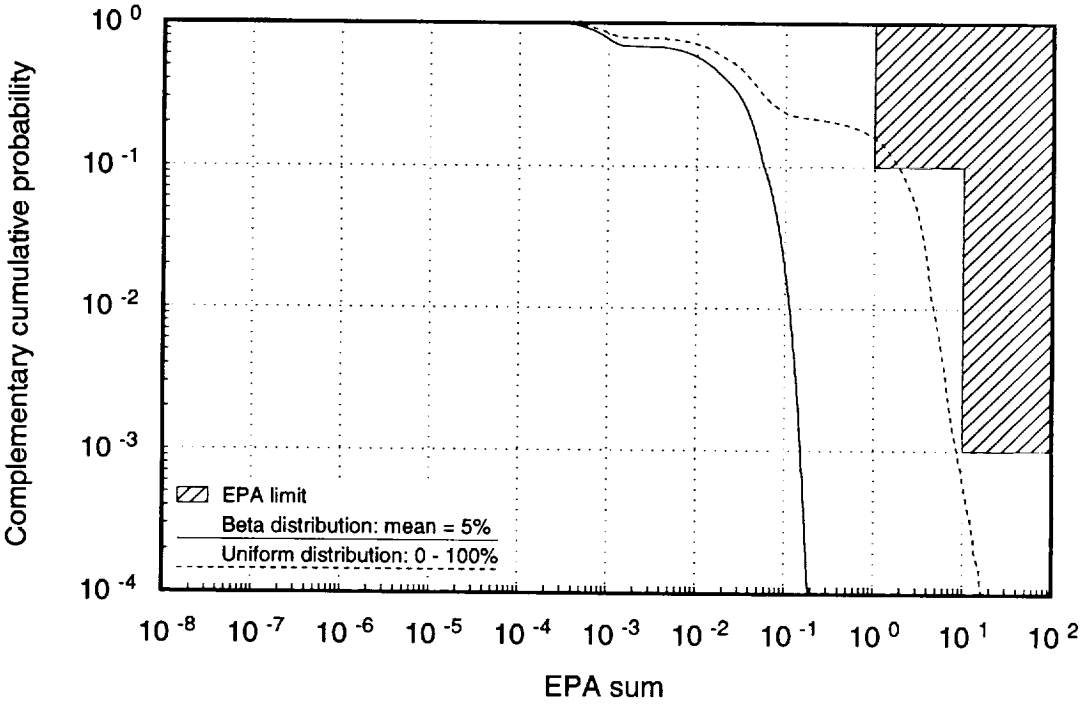

Figure 16-25. Comparison of 1,000,000-year CCDFs for two assumptions for distributions of waste-package releases.

ameter. A parameter-variation study has been done to determine whether using a 0.21-m drill size makes a significant difference in the surface releases.

The drill size is a factor in the probability of the drill hitting a waste package. For a 0.21-m drill, the probabilities of hitting a waste package (P_{hit}) for the four analysis cases are given in Table 16-7. Drill size also influences the amount of contaminated rock that can be exhumed in near-miss incidents. Near-miss releases are a function of the area of the drill and the area of the contaminated zone (the latter being a time-dependent function of diffusion). The difference in areas for the two drill diameters is approximately a factor of 8.

Table 16-7. Probabilities of hits for 0.21-m drill-bit diameter.

Emplacement Configuration	P_{hit}
Borehole, 57 kW/acre	0.0060
Borehole, 114 kW/acre	0.0088
In-Drift, 57 kW/acre	0.0213
In-Drift, 114 kW/acre	0.0524

For the borehole cases, the probabilities of a hit are about half those of the baseline case (Table 16-1), since the probability varies as the square of the drill diameter. For the in-drift cases, the probabilities are about 75% of the baseline. Figure 16-26 shows the releases for the two drill-bit sizes for the borehole, 57-kW/acre cases. There is approximately a one order-of-magnitude reduction in the releases from the near-miss component (indicated by the arrow on the figure), because of the smaller amount of contaminated rock that is intercepted by the smaller drill.

The releases for the in-drift cases are shown in Figure 16-27. As with the borehole case, the largest change in releases occurs for the near misses. There is a very small difference for the direct hits, because the analysis assumes that if a waste package is hit, a random amount of waste is exhumed, regardless of the size of the hole that is drilled into it.

In summary, assuming that the amount of waste that can be brought up from a container is not a uniformly-distributed parameter, but can be described by a beta distribution with a mean of ~5% of the volume, then there is a marked reduction of the releases from the in-drift packages. The choice of a smaller drill-bit diameter does not produce significant changes in the maximum releases.

16.5 Discussion

This section summarizes the results of the lifetime studies that were needed to parameterize the near-miss releases, and of the total human-intrusion releases.

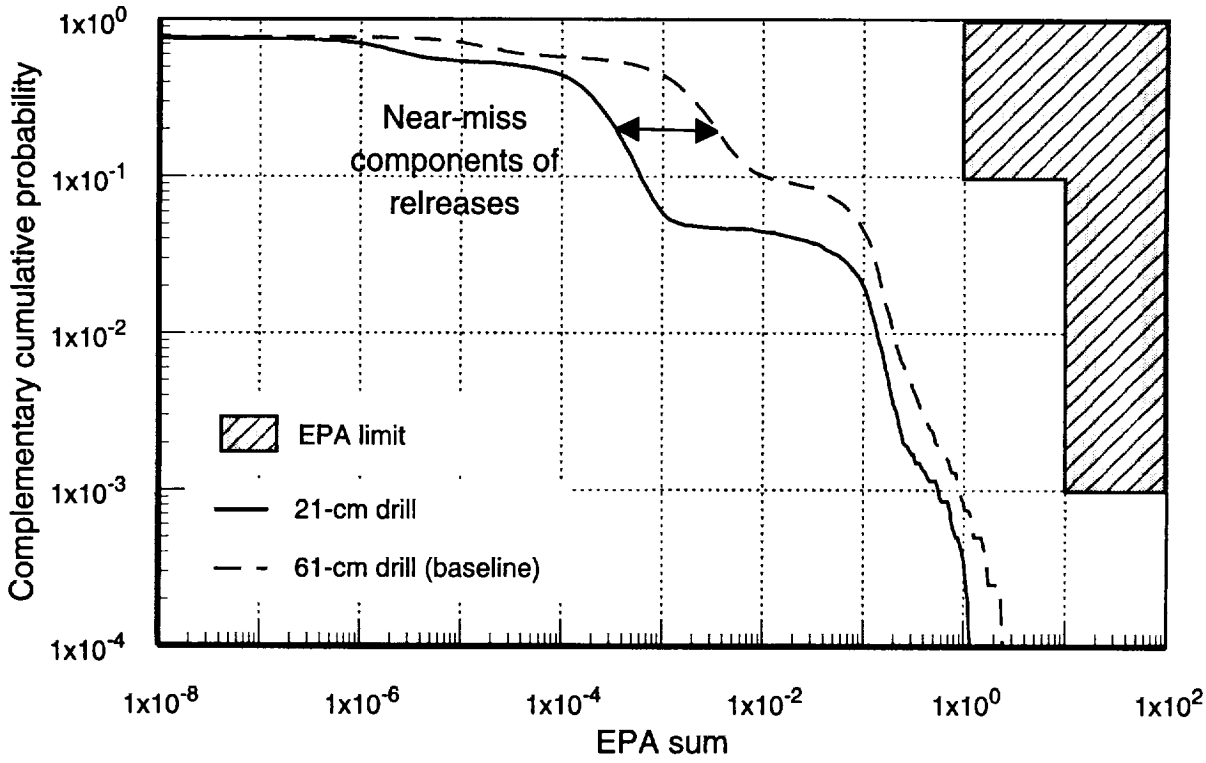

Figure 16-26. Comparison of CCDFs for two drill-bit diameters (borehole, 57-kW/acre).

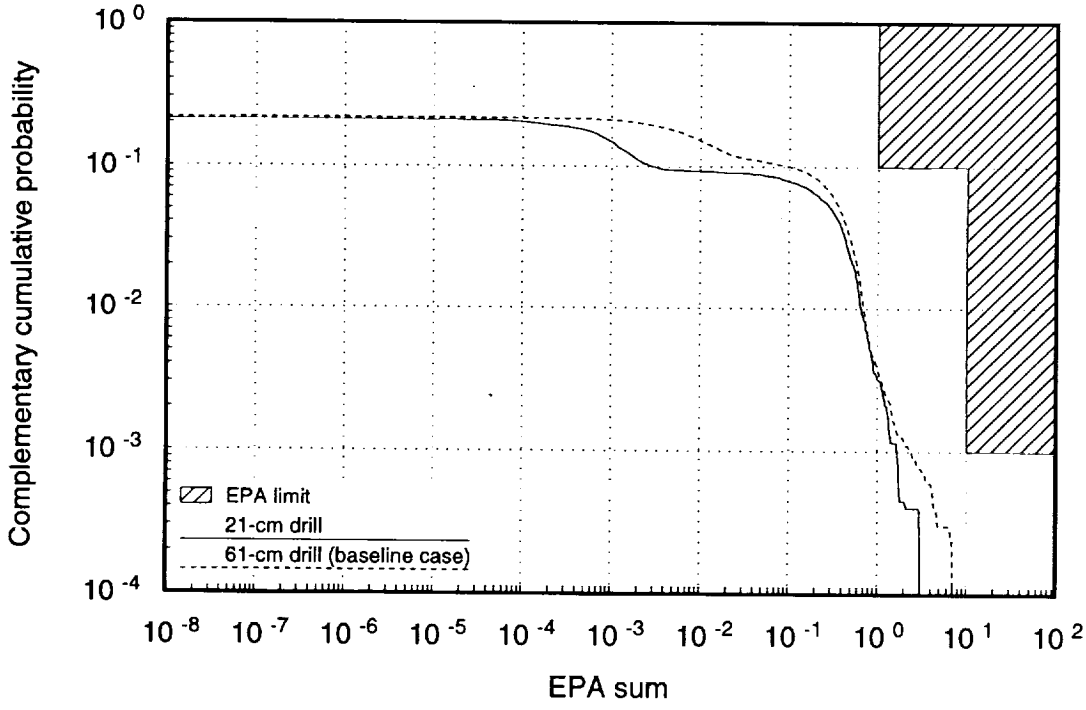

Figure 16-27. Comparison of CCDFs for different drill-bit diameters (in-drift, 114-kW/acre case).

16.5.1 Lifetime studies

Container lifetime (i.e., the time to failure of the container) is an important factor in determining the magnitude of releases from drilling near misses. The delay from the time that the container reaches 100°C to onset of failure and the time that it takes to completely fail are measures of the degradation resistance of the container. Table 16-8 lists the times to onset of failure and the additional times to complete failure.

Table 16-8. Waste-package failure times for various analysis cases.

	Edge of Repository				Center of Repository			
	Moist Conditions		Dry Conditions		Moist Conditions		Dry Conditions	
Configuration	Time to Onset (years)	Time to Failure (years)	Time to Onset (years)	Time to Failure (years)	Time to Onset (years)	Time to Failure (years)	Time to Onset (years)	Time to Failure (years)
Borehole, 57 kW/acre	125	75	650	>9000	200	200	900	>7700
Borehole, 114 kW/acre	150	75	1050	>6650	300	125	850	1650
In-Drift, 57 kW/acre	155	125	780	>8400	410	550	1460	>6600
In-Drift, 114 kW/acre	200	100	750	>6350	300	175	650	1950

Under "moist" conditions (i.e., the highest wetting conditions that are modeled), the time to onset of failure is less than 200 years at the edge of the repository, and 200 to 400 years at the center of the repository. Under "dry" conditions, the time to onset of failure is more than 600 years at both the edge and center. The times to complete failure are strongly dependent upon the amount of moisture present. Under moist conditions, complete failure ranges from 75 years for borehole packages at the edge of the repository to several hundred years for other emplacement configurations. As Table 16-8 shows, the dual-wall, in-drift containers do not have substantially greater degradation resistance than the borehole containers.

As modeled by YMIM, failures start when the temperature drops below 100°C, and proceed at rates dependent upon the amount of water present. The range of failure times is not significantly greater for the double-walled in-drift containers than for the borehole containers. The container lifetimes are strongly dependent upon the assumed corrosion rates. For these lifetime studies, a "median" corrosion rate is assumed for the Alloy 825 wall. If the "low" rates are assumed (i.e., one order of magnitude lower than the median rates), container lifetimes would increase greatly. As Figure 16-28 shows, there is no significant container failure out to 1,000,000 years. (In order to get any failures predicted for times after 50,000 years, a 100% wetting fraction has been assumed for the critical time period from 100°C to 70°C.)

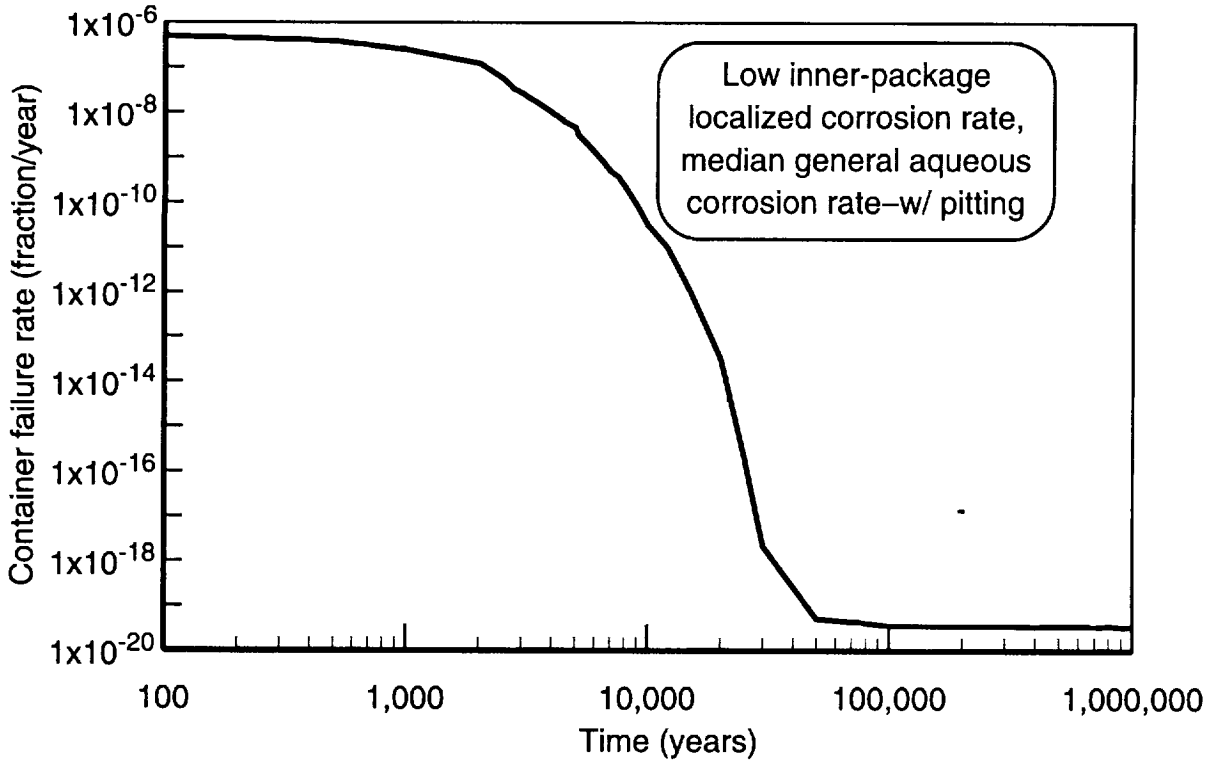

Figure 16-28. Container lifetime profile for low corrosion rate assumption (in-drift, 114-kW/acre, center of repository).

In view of the relatively large contribution of near misses over time periods longer than 10,000 years, container lifetime becomes an important issue. Significantly longer periods during which the containers are intact (such as would occur with the conditions illustrated in Figure 16-28), would reduce the releases over 1,000,000 years.

16.5.2 Drilling releases

Surface releases due to human-intrusion drilling do not exceed the EPA standards (if these standards were applied to Yucca Mountain) for 10,000 years. As modeled in TSPA-93, releases are not particularly sensitive to site characteristics, although they do depend on some of the design choices, such as type of waste package used. The overall magnitude of releases is quite dependent on the number of boreholes drilled into the repository over 10,000 years, as is illustrated by the sensitivity studies done for TSPA-91. The EPA guidance on the number of boreholes drilled at the Yucca Mountain site does not consider possible increases in the drilling frequency due to exploitation of attractive minerals. There are ongoing YMP activities to assess the potential for economically attractive minerals or other geologic properties that could require modification of the drilling frequency.

Results reported for 1,000,000 years should be considered highly suspect. Predicting human behavior or technology even a few years in the future has not been successful in the past, so there is little confidence that it will be accurate for the future. The assumption that twentieth-century drilling techniques will continue to be used for 10,000 years is certainly unlikely, but it is specified in the EPA regulations for calculating human-intrusion releases. It is even more unlikely that these techniques will be used for 1,000,000 years, and regulatory specification of these techniques may be even harder to justify.

Chapter 17
Magmatic Activity

(Barnard, Wilson, Skinner, Barr)

The performance of the potential Yucca Mountain repository under certain magmatic-activity disruptive events has been evaluated in TSPA-93. This analysis is a continuation of that done for TSPA-91 (Barnard *et al.*, 1992). In the previous assessment, direct releases from the repository subjected to magma–waste interactions was investigated. This analysis looks at indirect releases due to the magma–waste interactions. Specifically, this analysis treats the change to the aqueous-transport source term arising because of accelerated waste-package degradation due to the heat and aggressive volatiles emitted from a magmatic intrusion near a waste package. The analysis assumes the waste package lifetime is drastically shortened by the presence of the magmatic intrusion. Figure 17-1 illustrates the scenario for the interaction. The magmatic-interaction scenarios are discussed in detail in Barr *et al.* (1993).

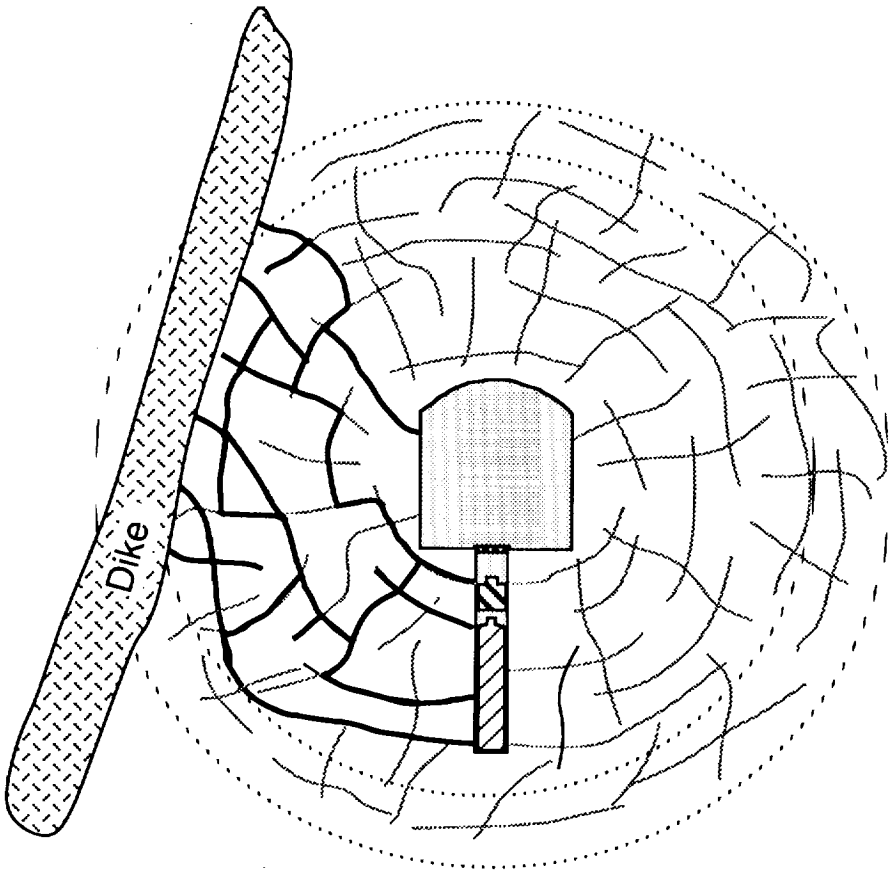

Figure 17-1. Interaction between waste packages and magmatic intrusion.

The TSPA-93 analysis is an attempt to bound the range of consequences of interactions between magma and repository waste. TSPA-91 looked at direct surface releases due to volcanism, while this analysis considers only indirect effects where there is no waste-magma contact. Actual volcanic events would naturally be expected to have a range of interactions—from entrainment of waste, to encapsulation of waste, to attack by volatiles. It must be emphasized that this analysis is restricted to investigating the effects of heat and aggressive volatiles only (i.e., no direct waste–magma contact). As will be seen in this chapter, this requires several restrictive assumptions regarding the nature of the interactions. Because of the low probability of occurrence for volcanism, the consequences are calculated separately, and the probability of occurrence is then applied to produce the CCDF.

17.1 Probability estimates

The probability of occurrence used for TSPA-93 is calculated using the same formalism as that used for the TSPA-91 analysis; a discussion of the factors in the probability calculation is given in Section 7.3 of that document (Barnard *et al.*, 1992). The overall probability of exceeding a given release value from a potential Yucca Mountain repository is given by

$$P[E_1E_2E_3] = P[E_1] \bullet P[E_2|E_1] \bullet P[E_3|E_1E_2], \tag{17.1}$$

where E_1 is the volcanic recurrence rate in the region of Yucca Mountain, E_2 is the probability of eruption in the repository itself, and E_3 is the probability that the releases (i.e., the consequences of the volcanism) exceed a given release value. In Crowe *et al.* (1992) are given several estimates of the volcanic recurrence rate published since the TSPA-91 work was done. The values of E_1 range from 6.0×10^{-7}/yr to 2.8×10^{-5}/yr, with the most geologically reasonable values clustered in the range 1×10^{-6}/yr to 6×10^{-6}/yr. The mean value of this range is 4.0×10^{-6}/yr. Crowe *et al.* do not report new values for the probability of an event occurring in the repository. E_2 was originally calculated using the assumption that the repository area was 6 km^2. For these analyses, the repository areas are different (4.6 km^2 for the 57-kW/acre layouts and 2.3 km^2 for the 114-kW/acre cases). Scaling the previous value of E_2 by the two areas gives the probability of occurrence for a magmatic intrusion over 10,000 years as 1.8×10^{-4} for the 57-kW/acre case and 1.0×10^{-4} for the 114-kW/acre case. E_3 is given by the conditional CCDF produced by the analysis.

To extrapolate this probability to 1,000,000 years requires assumptions about whether the 10,000-year rate of volcanism will be constant, increasing, decreasing, or chaotic over the 1,000,000-year period. Crowe *et al.* (1992) argue that using a constant rate will not underestimate the recurrence rate with acceptable assurance. With the assumption of a con-

stant million-year rate, the probabilities for the two cases become 1.8×10^{-2} and 1.0×10^{-2} for 57 kW/acre and 114 kW/acre, respectively, over this period. Table 17-1 lists the probabilities that 0, 1, or 2 magmatic events will occur over the 10,000- and 1,000,000-year periods using the 57 kW/acre probability of occurrence. From the table it can be seen that a magmatic event is quite unlikely over both periods—there is an almost 100% probability of having no events over 10,000 years; there is about a 98% chance of having no events over 1,000,000 years. The probabilities of having 1 event occur are in the range 10^{-4} to 10^{-2} for the two time periods, and multiple magmatic events are even more unlikely. Therefore, it will be assumed that the releases for both 10,000 and 1,000,000 years are due to the occurrence of a single event.

Table 17-1. Probabilities of occurrence for magmatic events (57-kW/acre repository).

Number of Events	10,000 Years	1,000,000 Years
0	9.998×10^{-1}	9.8×10^{-1}
1	2.4×10^{-4}	2.3×10^{-2}
2	2.9×10^{-8}	2.8×10^{-4}

17.2 Analysis setup

The analysis calculates the temperature in rock adjacent to a dike as a function of dike temperature, dike thickness, distance into the rock, and time. Rather than simply assuming that all the waste packages "near" the dike are affected, this analysis attempts to calculate time and distance bounds for the temperature effects. The temperature excursion as calculated is superimposed onto the nominal-case waste package temperature profile (discussed in Chapters 10 and 13) and the modified time-temperature curve is used by YMIM to calculate waste-package lifetimes. In addition, the waste-package corrosion rates are modified to account for the aggressive magmatic volatiles.

The previous TSPA analysis assumed that waste packages were homogeneously distributed throughout the repository area. The number of packages intersected by the dike was simply a function of the dike length and width. For this analysis, the repository layout has been incorporated, so the number of waste packages affected by an intrusion is a function of the number of drifts intersected.

Because this analysis specifically investigates waste-magma interactions where there is no contact, dike widths are limited to be less than the spacing between waste packages.

17.2.1 Calculation of temperature excursion

The temperature in rock adjacent to a dike has been calculated by an analytical formula for heat conduction in a semi-infinite composite medium (Churchill, 1944). The medium consists of a slab of half-thickness a with thermal conductivity and diffusivity values K_A and k_A, respectively. The balance of the medium has thermal conductivity and diffusivity values K_B and k_B, respectively. Diffusivity is defined as

$$k = K/\rho_b C_v, \tag{17.2}$$

where ρ_b is the bulk density and C_v is the specific heat of the material.

For the two-component medium, with the slab initially at temperature T_A, and the remainder at temperature T_B, the time-dependent temperature for distances $x > a$ is given by equation 17.3. The slab is assumed to cool as time progresses. This is equivalent to assuming that the dike has intruded and begins cooling. If it were assumed that the magma continued to flow along the path of the dike, a different analytical solution would be used.

$$T(x,t) = T_B + (T_A - T_B)\frac{K_A}{K_B}\sqrt{\frac{k_B}{k_A}}\frac{1}{\gamma_B}\sum_{n=0}^{\infty}\left(\frac{\gamma_A}{\gamma_B}\right)^2 \cdot \left\{ Erfc\left(\frac{2na\sqrt{\frac{k_B}{k_A}} + x - a}{2\sqrt{k_B t}}\right) - Erfc\left(\frac{2a(1+n) + (x-a)\sqrt{\frac{k_A}{k_B}}}{2\sqrt{k_A t}}\right)\right\} \tag{17.3}$$

where $Erfc$ is the complementary error function, and γ_A and γ_B are given by

$$\gamma_A = \frac{K_A\sqrt{k_B} - K_B\sqrt{k_A}}{K_B\sqrt{k_A}}, \quad \text{and} \quad \gamma_B = \frac{K_A\sqrt{k_B} + K_B\sqrt{k_A}}{K_B\sqrt{k_A}}. \tag{17.4}$$

Because the value of the complementary error function goes to zero rapidly with increasing arguments, the series converges rapidly. The formula predicts that the temperature excursion in the rock will be proportional to the difference between the dike temperature and the ambient rock temperature, and will decrease with increasing time or distance.

Figures 17-2 and 17-3 illustrate the behavior of the rock-temperature excursion for two values of dike thickness, a. The probability distribution of dike widths used for the TSPA-93 analysis is the same as that used for TSPA-91—a beta distribution with a mean of 1.5 m and a range of 0.01 m to 4.5 m (Figure 17-4). The temperature excursion shown in Figure 17-2 assumes a dike half-width of 0.75 m; this illustrates the impact of a mean-

thickness dike, while Figure 17-3 shows the effect of the thickest possible dike (half-width of 2.25 m). In each case, the temperature immediately adjacent to the dike reaches ~700°C (i.e., an increase of ~650°C over ambient rock temperature) after a few days. The temperature returns to ambient after ~100 years. One of the most noticeable differences between the two plots is the length of time that the temperature stays at the maximum close to the dike. For the narrower dike, the peak temperature lasts for only about 0.01 year; for the thicker dike, the temperature stays at the maximum for about one month.

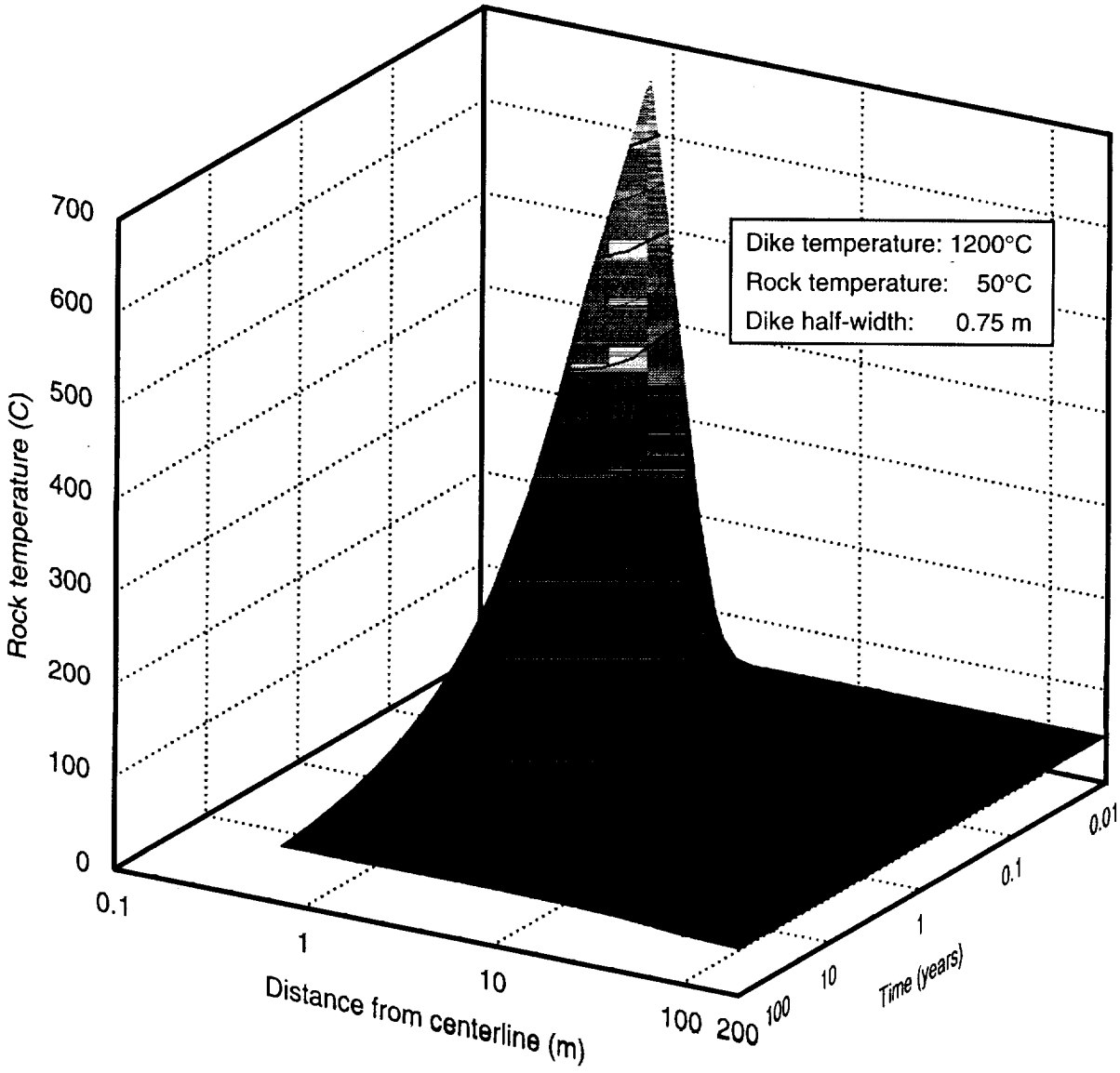

Figure 17-2. Time-temperature surface for rock temperatures adjacent to a 0.75-m (half-width) dike.

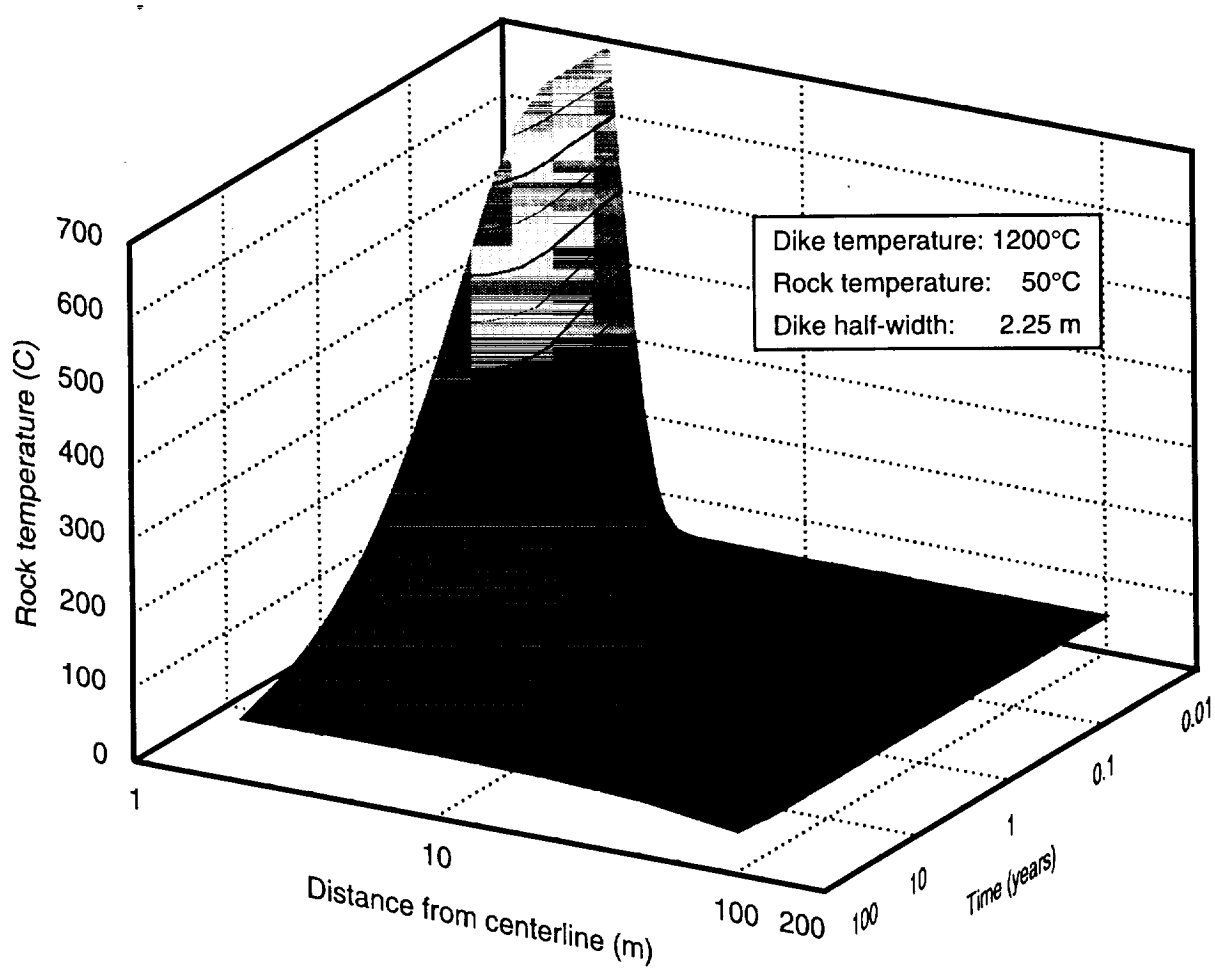

Figure 17-3. Time-temperature surface for rock temperatures adjacent to a 2.25-m (half-width) dike.

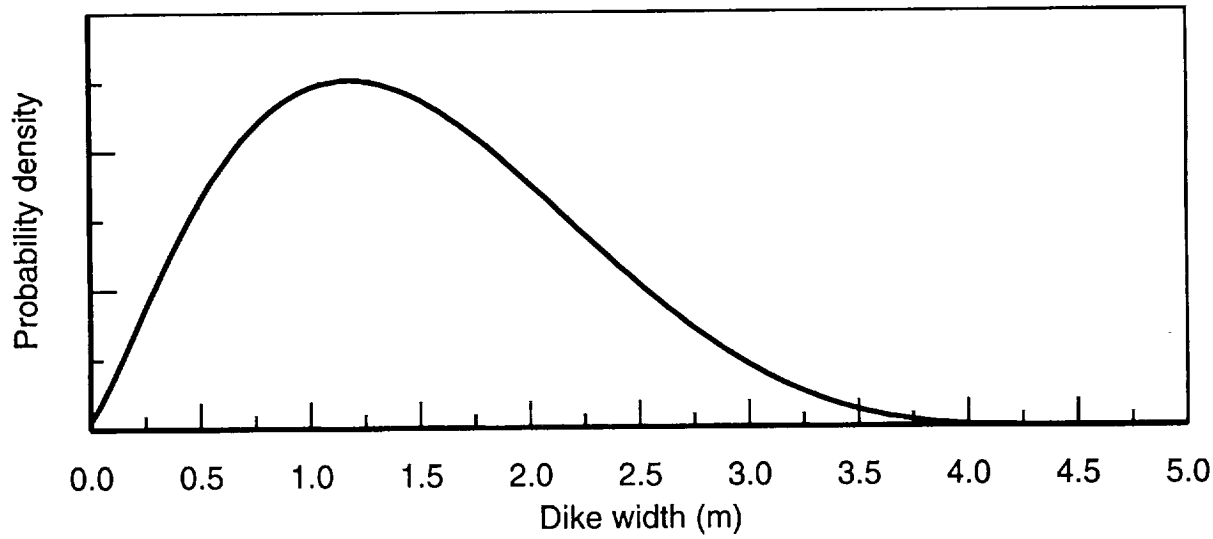

Figure 17-4. Distribution of dike widths.

17.2.1.1 Thermal parameters

The values for thermal conductivity and diffusivity in this analysis were sampled from the probability distributions discussed below. Values for dikes are not as well known as for the tuff host rock, so a range of values found in the literature has been used for the former (Clark, 1966; Mossop and Gafner, 1951). For tuff, values from the YMP Reference Information Base (RIB) were used. Thermal conductivities for the dike and the host rock are given in Table 17-2. The probability distributions are assumed to be uniform over the ranges. A value of thermal conductivity was sampled, and the diffusivity then calculated using independently sampled values of density and specific heat.

Table 17-2. Thermal properties of tuff and dike.

Thermal Property	Tuff	Dike
Thermal Conductivity (cal/cm sec °C)	0.00410 – 0.00660	0.00281 – 0.00329
Bulk Density (g/cm^3)	2.4 – 2.8	1.89 – 2.91
Specific Heat (cm^2/sec)	0.20 – 0.23	0.215 – 0.263

17.2.2 Dike–waste-package interactions

The number of waste packages intersected by a dike depends on the location of the dike in the repository and the size of the repository. The extent that the waste packages are disturbed by the dike, and the amount of waste mobilized from them depends on the proximity of the dike to the container.

17.2.2.1 Number of containers passed by a dike

Both TSPA-91 and TSPA-93 analyses assume that dikes start at the southern boundary of the repository and have the distribution of orientations as shown in Figure 17-5. For a sampled dike orientation and length, the number of waste packages available to interact with the dike is two times the number of drifts crossed by the dike. (The dike is assumed to pass at the midpoint between waste packages in an emplacement drift.) Figure 17-6 shows examples of dikes crossing emplacement drifts for a 57-kW/acre repository. The modification to the nominal aqueous source terms can be calculated from the number of waste packages that the dike passes.

Given a periodic two-dimensional array of waste packages, there are actually a very limited number of dike orientations for which a straight-line dike can pass through the array and not intersect any containers. This reduction in the number of allowable dike orientations and lengths can be expressed as a reduction in the probability that this scenario can occur. Such a reduction in probability has not been calculated, so the CCDFs shown later in this chapter may overestimate the probability of this scenario. It should be reiterated that this

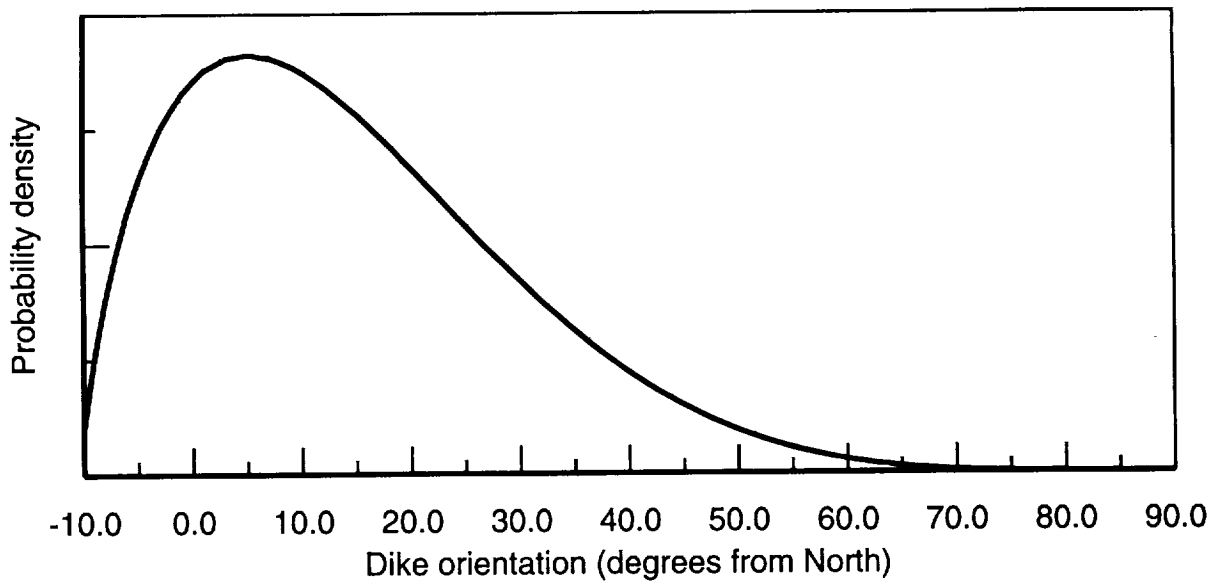

Figure 17-5. Distribution of dike orientations.

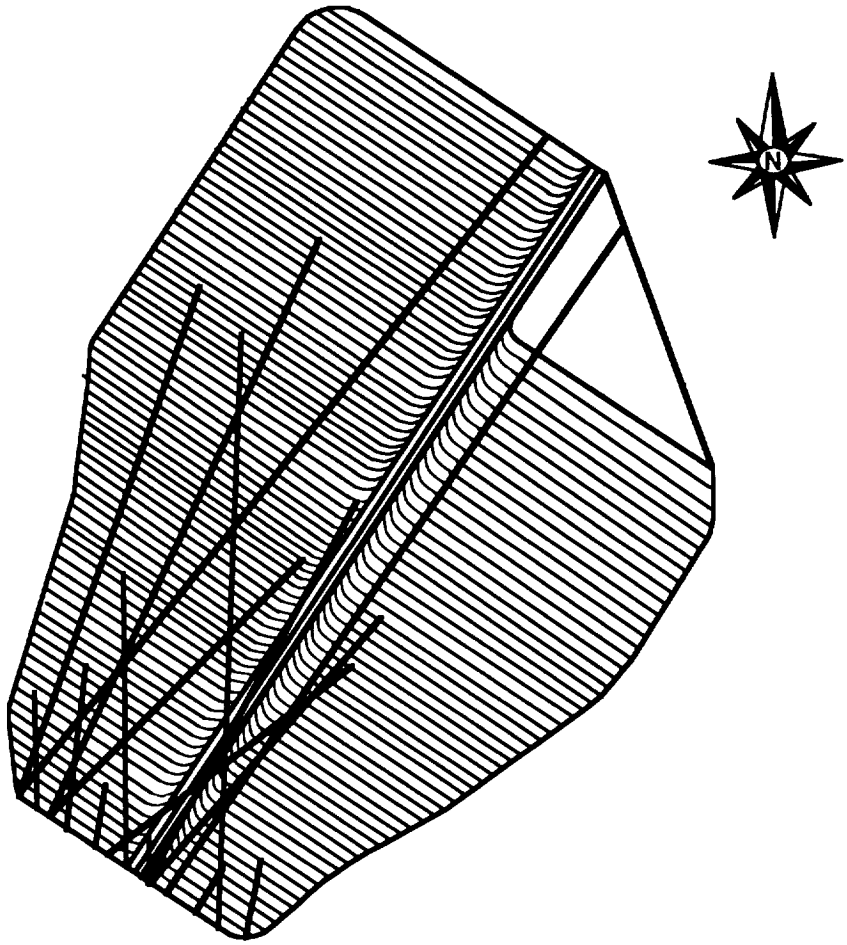

Figure 17-6. Examples of dikes crossing drifts for 57 kW/acre repository area.

calculation estimates the maximum number of containers that are exposed to magmatic volatiles *only*. The scenario is an end member of the range of interactions with the magma, with direct transport being the other extreme. As such, it may represent a lower bound on the range of releases from this class of magmatic interactions.

17.2.2.2 Temperatures at a container

The temperature excursions discussed in Section 17.2.1 can occur at any time in the life of the repository. Therefore, the ambient rock temperature is dependent upon the repository thermal history, as discussed in Chapter 10. Depending on when the intrusion occurs, the ambient rock temperature may be above or below the boiling point of water. Further, thermal effects on the waste package may differ depending on whether the container is hot, or has cooled (and possibly already corroded). Figures 17-7 and 17-8 illustrate two temperature excursions starting at randomly selected times superimposed on 57-kW/acre and 114-kW/acre temperature histories, respectively. Figure 17-9 compares the temperature excursion at 1 m distant from a 1,200°C dike of 2.25-m half-width in rock that is at 50°C and at 500°C. The temperature increases by ~400°C in the cooler rock, and only increases by ~250°C in the hotter rock.

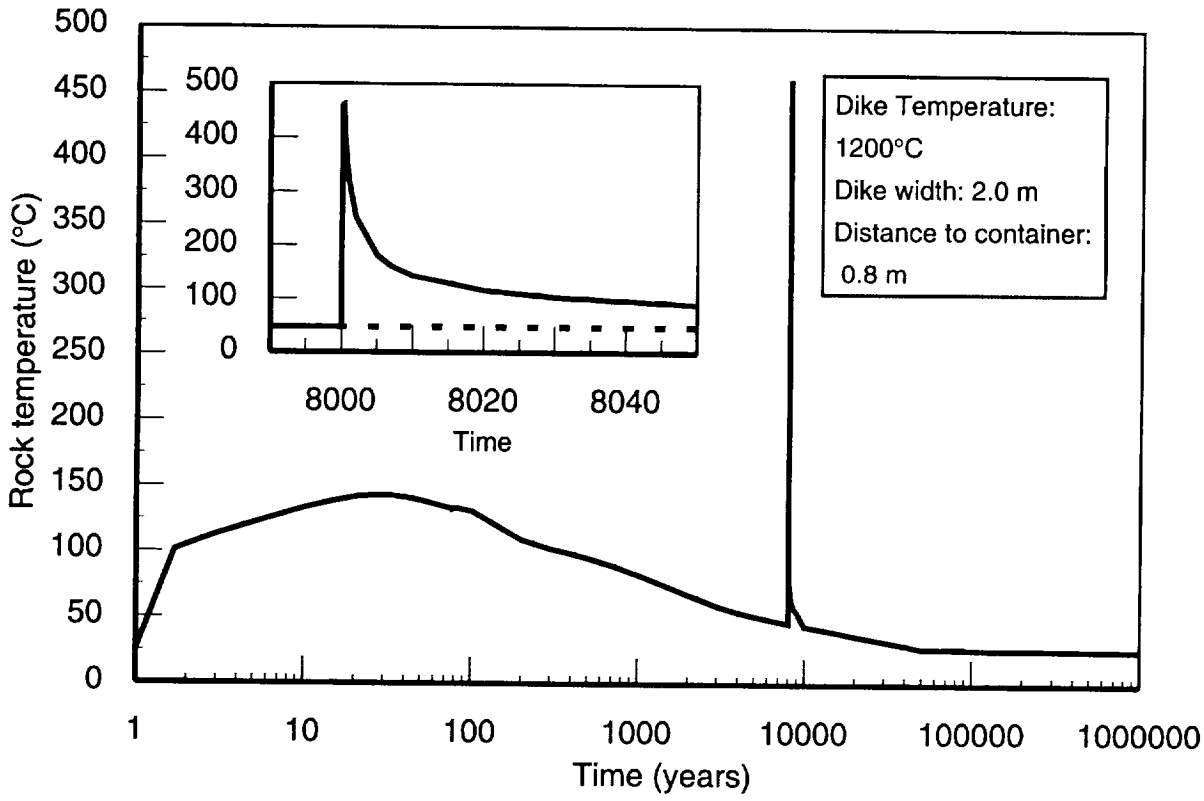

Figure 17-7. Dike-induced temperature excursion for 57-kW/acre repository.

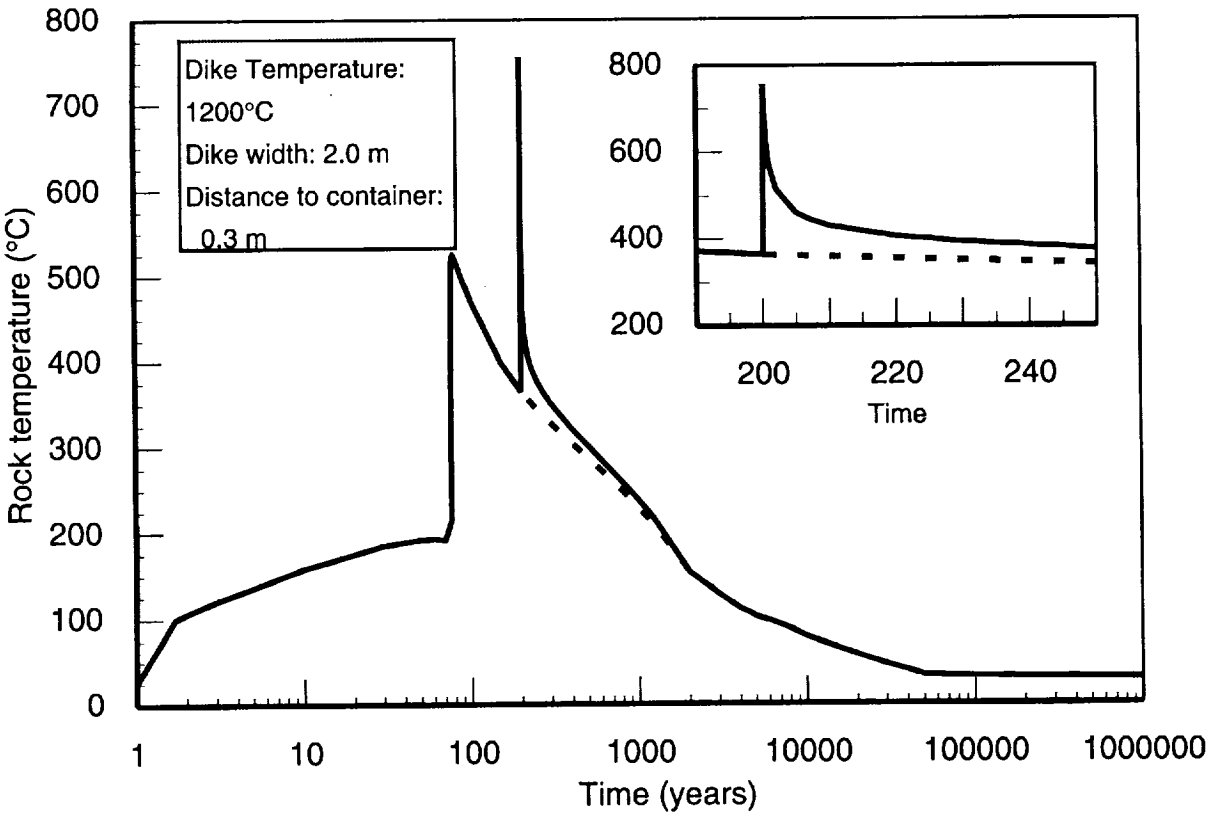

Figure 17-8. Dike-induced temperature excursion for 114-kW/acre repository.

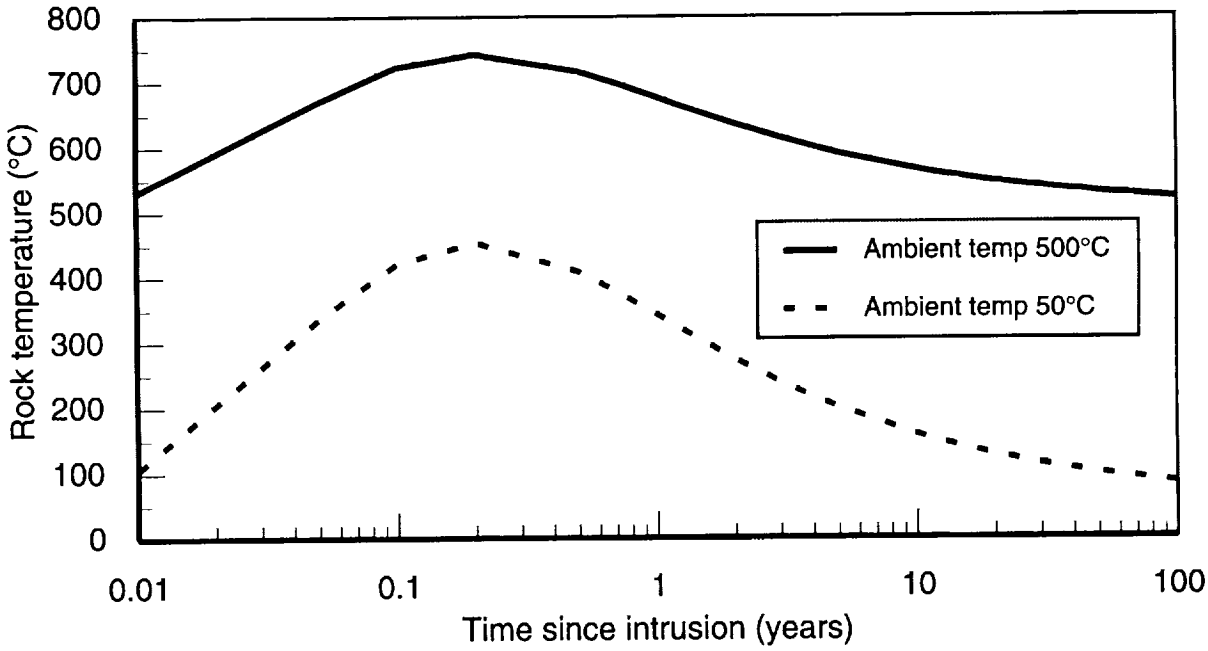

Figure 17-9. Comparison of rock-temperature excursions from a dike in host rock at 50°C and 500°C ambient temperatures.

Because the dike is assumed to pass at the midpoint of the spacing between waste packages, the distances from dike to container are dependent upon the choice of dike thickness. Table 17-3 lists the half-spacings between spent-fuel containers for the four analysis cases (HLW containers are not considered in this model), the maximum half-widths of dikes consistent with the waste-package spacing, and the ranges of distances from dike to waste package. We assume a minimum distance of 0.01 m to assure that there is no waste–magma contact. Close passage of the dike to the container does not necessarily mean that the container is mechanically disturbed; other investigations show that the mineralogy of the country rock adjacent to a dike is only perturbed thermally (i.e., not mechanically) by the intrusion (Buchan *et al.*, 1980). Therefore this analysis is restricted to those waste packages that are not physically disturbed. Minimum dike width is also considered to be 0.01 m.

Table 17-3 shows that the dike can pass quite close to the borehole-emplaced waste packages; from Figures 17-2 or 17-3, it can be seen that for separation distances less than ~5 m, the temperature rise is several hundred degrees. The only emplacement configuration for which the effects of a passing dike are calculated to be minimal is the 57-kW/acre, in-drift case.

Fuel-rod temperatures are assumed to experience the same temperature excursion as the container (which in turn is the same as the surrounding rock). Because fuel rods are hotter than the container, the temperature excursion should be less, as Figure 17-9 implies; generally, the rod–container temperature difference is at about 20°C to 50°C, so assuming they have the same temperature excursions is not a major inaccuracy.

Table 17-3. Container half-spacings and range of distances from dikes.

Emplacement Configuration/ Package Type	Waste-Package Half-Spacing (m)	Maximum Dike Half-Width (m)	Range of Dike–Container Distances (m)
Borehole, 57 kW/acre			
All spent-fuel waste packages	2.8	2.25	0.55–2.79
Borehole, 114 kW/acre			
All spent-fuel waste packages	1.4	1.39	0.01–1.39
In-Drift, 57 kW/acre			
BWR-Fuel Package	8.5	2.25	6.25–8.49
PWR-Fuel Package	13.75	2.25	11.50–13.74
In-Drift, 114 kW/acre			
BWR-Fuel Package	4.25	2.25	2.00–4.24
PWR-Fuel Package	6.85	2.25	4.60–6.84

17.2.2.3 Effects of magma on waste package

The effects of a nearby magmatic intrusion are expected to include both thermal degradation and attack by aggressive magmatic volatiles. Both the waste-package components (container and cladding) and the waste itself will be affected.

While it is difficult to anticipate the actual amount of magmatic volatiles for a given event, they can be qualitatively estimated for plausibility discussions. General values of the weight percent of water and gases from basaltic systems (MacDonald, 1972) suggest the range 0.5% to 1%. This translates to 10 to 25 kg of gas per cubic meter of dike. If the depth of the dike from which magmatic gas is exsolved is the order of 100 m below the waste, then a non-flowing dike of 2 m thickness supplies 2000 to 5000 kg per meter of dike length of magmatic volatiles. For a flowing dike the estimate has to be adjusted to reflect the flow rate. The dike tends to produce an adjacent, narrow fracture zone during emplacement. As a first-order approximation it is reasonable to assume that gas flow is primarily along this zone—a zone that reaches containers close to the dike but not their next nearest neighbors. When the dike stops flowing it begins to cool. Almost all the magmatic volatiles that will reach the waste after the dike has stopped flowing are produced during the solidification period—2 months or less for the size dikes being considered here. This limits the exposure time of the waste to the time for solidification except for one, presumably less important, mechanism. That mechanism for adding more magmatic volatiles is the case in which the cooling dike produces a local hydrothermal system that leaches any residual volatiles from the dike.

The waste container, made of Alloy 825 and/or mild steel, is subject to sulfidation by the magmatic volatiles (Colp *et al.*, 1976). Sulfidation rates are three to six orders of magnitude greater than oxidation rates, and the metals form low-melting eutectics with their sulfides (Douglass and Healey, 1979). These conditions cause catastrophic corrosion of the iron-based materials. The Zircaloy reacts with the constituents of magma, such as oxygen and aluminum. The result of these reactions is severe embrittlement (Douglass and Healey, 1979).

Using the constituents of magmatic gas given in Gerlach (1980), 2,000 to 5,000 kg of magmatic gas would contain enough sulfur to form about 50 to 150 kg of FeS. The SCP-design thin-walled waste container is constructed from about 500 kg of iron, while the in-drift container contains about 17,000 kg of iron. The amount of sulfur available would be insufficient to completely convert all the iron to iron sulfides, but would probably cause localized degradation of the container wall, resulting in penetration of the container. For modeling purposes, it is assumed that sulfidation occurs at a rate 4 orders of magnitude faster than the oxidation rates discussed in Chapter 13. These processes are assumed to

occur for any waste package in the vicinity of a dike, since the active agents are the magmatic volatiles. Table 17-4 adapts the rates of Table 13-3 for this analysis.

Table 17-4. Magma-induced sulfidation rates used for TSPA-93.

Temperature (°C)	Sulfidation Rate (mm/yr)
Alloy 825	
253	2.4×10^{-3}
20	5.5×10^{-13}
Carbon Steel	
540	1.0×10^{5}
25	6.35×10^{-2}

These sulfidation rates are applied in the YMIM model during the time that a temperature excursion occurs. During the remaining time of the temperature history of the container, the oxidation conditions described in Section 13.2.4.1 apply.

UO_2 has been shown to be soluble in basaltic melts at temperatures above 1,200°C (Westrich, 1982). The solubility ranges from 20 wt.% at 1,200°C to 40 wt.% at 1,550°C. The liquidus for the basalt used in the experiments by Westrich was ~1,250°C. Although magma temperatures are assumed to be somewhat below the range studied by Westrich (i.e., 1,100°C to 1,200°C), using the relationship observed for the higher temperatures predicts a UO_2 solubility between 7 wt.% and 20 wt.%. Dissolution of UO_2 is applicable to the magma-encapsulation scenario.

Not much is known about the effects of magmatic volatiles on oxides, particularly UO_2. The oxides of which the spent fuel is composed are quite refractory. Thus, simply exposing the spent fuel to high temperatures may not accelerate its degradation. Magmatic volatiles consist of SO_2, H_2S, HCl, H_2, CO_2, CO, and other agents; further, the oxygen fugacity is about 10^{-9} bars (Gerlach, 1980). It would therefore be expected that the UO_2 would oxidize rapidly to U_3O_8, and that sulfides and sulfates would form in the presence of such volatiles. UO_2 forms several oxide-sulfide and sulfate compounds (e.g., UOS, UO_2S, $UO_2 \cdot 2US_2$, $U(SO_4)_{2,3} \cdot nH_2O$, $UO_2SO_4 \cdot nH_2O$). The oxide-sulfide compounds can be formed by H_2S reacting with UO_2 in the presence of carbon at temperatures of 600°C and above. The uranyl sulfate, UO_2SO_4, can be formed from UO_3 and SO_3, or from UOS and oxygen saturated with water vapor at temperatures typical of those produced by a nearby dike (Brown and Wedemeyer, 1984).

The UOS compound is very slightly soluble in water, but is attacked by oxidizing compounds. The uranium and uranyl sulfates are soluble in water (Brown and Wedemeyer, 1984). The more rapid oxidation of UO_2 to U_3O_8 will accelerate the rupture of any Zircaloy

cladding that has pinholes or other defects. These modifications to the spent fuel can be represented in the YMIM model by an enhanced rate of oxidation, increased solubility limits for the UO_2, and greater fuel-rod volume change during the time that the temperature excursion occurs. These effects have not yet been incorporated into the YMIM model.

17.2.2.4 Location of the magma-altered source

As a result of heating by the dike and interaction of magmatic volatiles with the waste, the contaminants are effectively partitioned into two different sources, one source distributed away from the container and another at the container. Contaminants with low enough vaporization temperatures are cooked out of the corroded containers. These volatiles plate out in the rock along fractures and preferential flow channels wherever the temperature is cool enough. These contaminant volatiles, driven by dike and container heat, form a partial halo away from the dike and container. The isotopes deposited are those with low boiling temperatures (e.g., Cs). The total mass of such contaminants is expected to be quite small and will not be considered further here.

The second source is produced by interaction of waste with magmatic volatiles and represents a much larger mass of potentially mobile contaminants than the first source—possibly the entire contents. In this case, chemical reaction (i.e., sulfidation, oxidation and hydration), occurs throughout the waste mass (spent fuel). The altered contaminants remain in the vicinity of the emplacement site but in much more soluble forms. They can be mobilized from the emplacement hole and surrounding rock by condensing magmatic fluids, or from the waste package and surrounding backfill by introduction of water from the flow field (e.g., condensation-cap return).

17.2.2.5 Modeling of releases from magma-altered source

Cumulative releases and doses at the accessible environment resulting in aqueous flow and transport of contaminants from the magma-altered source are modeled in the same fashion as that described in Chapter 14. Only the composite-porosity model (i.e., TOSPAC) was used for calculating the aqueous releases. It is assumed that the same flow and transport processes as those used for the nominal-flow analyses can be applied to a magma-altered source used in the TOSPAC code.

The stochastic calculations of the number of drifts crossed by dikes (shown in Figure 17-6) predict that from 2 to 232 waste packages can be affected. All dikes are modeled to start in the southern end of the repository; most trend north-northeast. The affected packages are modeled by assuming they all lie in the repository segment described by column 2 (see Figure 6-7 for column locations). All magma-affected packages are included in container group 3 (see Section 14.4.2 for a discussion of container groups). TOSPAC simula-

tions use independently calculated thermal spikes added to the normal thermal profiles, with the time of the spike distributed uniformly between 100 and 1,000,000 years. During the time of the spike, the sulfidation rate is increased. The borehole, 57-kW/acre and in-drift, 114-kW/acre cases are modeled. Three hundred release simulations for column 2 are modeled for each analysis case. The column-2 results are used with the results calculated in Chapter 14 for the other columns to calculate releases from the entire repository.

17.3 Results

The cumulative releases to the accessible environment from the interaction of one dike with waste packages in the repository over 10,000, 100,000, and 1,000,000 years have been calculated. Figure 17-10 shows the conditional CCDFs for magma-altered releases for the borehole, 57 kW/acre case. (The CCDFs do not include the probability of occurrence of a magmatic intrusion, so they are conditional on that factor.) The results are quite similar to those for the undisturbed case (see Figure 14-25a). Because of the close similarity of results, the incremental releases due to the magmatic interaction are shown in Figure 17-11. Note that the releases shown in Figure 17-11 do not represent the **amount** of release caused by the intrusion event, but rather the **difference** between releases with the event and releases without the event. Some of the normalized releases below 10^{-4} are higher than they should be, caused by round-off error in the subtraction of releases with and without the intrusion event. Some realizations that should have zero difference have a small non-zero difference because of the round-off error. In many cases, the radionuclides released by the intrusion event would have been released within 1,000,000 years anyway.

For a uniform random distribution of intrusion times over 1,000,000 years, we would expect that approximately 1% of the events would occur in the first 10,000 years, and 10% of the events would occur in the first 100,000 years. As Figure 17-11 shows, there are no releases due to magmatism for 10,000 years greater than 10^{-8} of the EPA sum; in 100,000 years, the probability of releases greater than 10^{-8} is about 5%. For 1,000,000 years, the probability of releases greater than about 10^{-4} of the EPA sum is about 60%. This implies that if the expected numbers of events do indeed occur, some of the releases from them are less than 10^{-8} of the EPA sum. The reason that many releases are less than 10^{-8} is because variations in the dike width (affecting extent of container degradation), dike orientation (affecting number of waste packages influenced), and time of intrusion (affecting activity of released waste) all can reduce the availability of contaminants to be transported. Furthermore, there is considerable variability inherent in the aqueous flow and transport calculations. If a dike intrudes and causes a container to fail, but percolation flux is low in

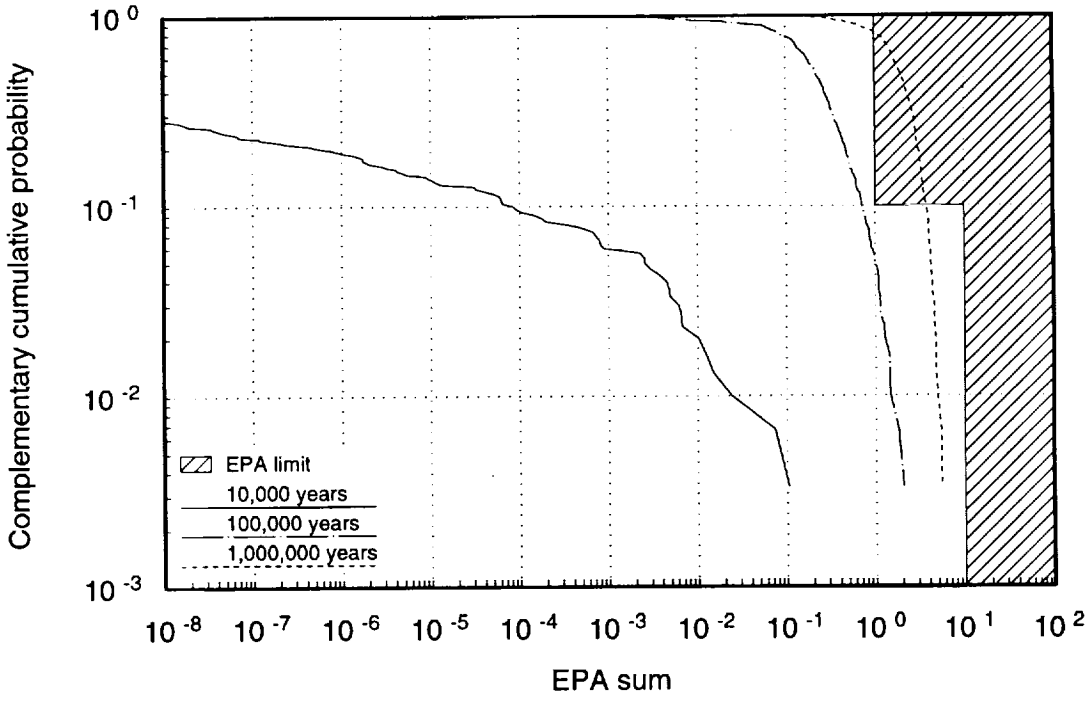

Figure 17-10. Cumulative releases to the accessible environment, with magmatic intrusion (57 kW/acre, borehole emplacement).

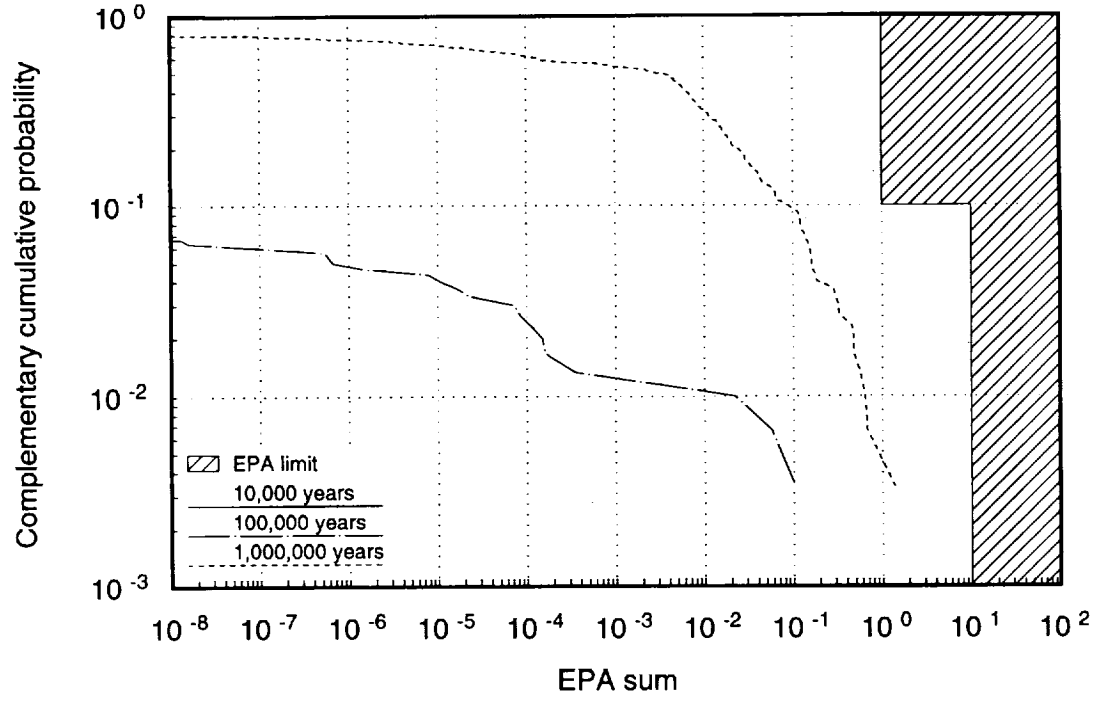

Figure 17-11. Releases due to magmatic intrusion (borehole, 57 kW/acre),

that particular realization, then releases to the accessible environment will probably be low despite the magmatic intrusion.

Table 17-5 gives the fractions of the undisturbed releases that the magma-altered releases represent, for the maximum releases and at several probability levels. Releases from volcanism in this scenario can be seen to represent very small fractions of the overall aqueous releases.

Table 17-5. Fractions of undisturbed releases at various probability levels (borehole, 57 kW/acre).

	Fraction of Undisturbed Releases due to Volcanism				
Period (years)	At Maximum	At 1% Probability	At 6% Probability	At 10% Probability	At 70% Probability
100,000	5.1E-02	1.5E-02	1.1E-07	–	–
1,000,000	2.5E-01	1.3E-01	3.7E-02	2.3E-02	7.1E-06

Figure 17-12 shows the incremental releases due to volcanism for the in-drift, 114-kW/acre case (the cumulative releases including volcanism differ so little from the nominal releases that the differences in the plots are indistinguishable). As noted for the borehole, 57-kW/acre case above, there are no releases greater than 10^{-8} of the EPA sum in 10,000 years. For this case, only about 15% of the waste packages have releases greater than 10^{-8} at 1,000,000 years. Releases for both the 100,000-year and 1,000,000-year periods have lower probabilities than the corresponding releases for the borehole, 57-kW/acre periods. This arises primarily because the dike-container distances for the in-drift analysis case can range from 2.0 m to 4.24 m, compared to a much smaller 0.55 m to 2.79 m for the other case (see Table 17-3). The greater spacing for the in-drift waste packages results in the waste package being exposed to lower temperatures and thus reduced degradation of the container.

The fraction of undisturbed releases that the magma-altered releases represent for the two time periods are given in Table 17-6. For the 1,000,000-year period, the maximum incremental releases are a much larger fraction of the undisturbed releases (about 15%).

Table 17-6. Fractions of undisturbed releases at various probability levels (in-drift, 114 kW/acre).

	Fraction of Undisturbed Releases due to Volcanism				
Period (years)	At Maximum	At 1% Probability	At 5% Probability	At 10% Probability	At 40% Probability
100,000	3.2E-04	1.3E-04	4.3E-07	–	–
1,000,000	1.0E-01	3.8E-02	7.4E-04	7.0E-05	1.3E-06

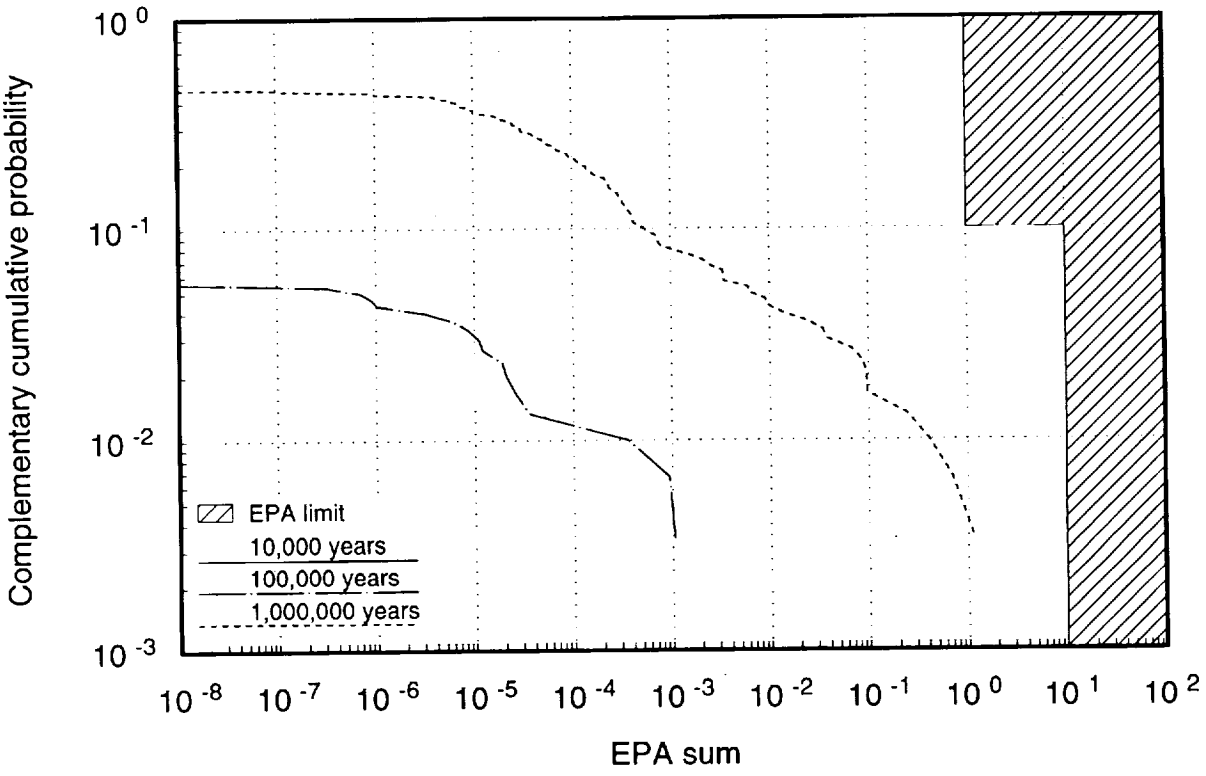

Figure 17-12. Releases due to magmatic intrusion (in-drift, 114 kW/acre).

Figure 17-13 compares the indirect effects of volcanism modeled in TSPA-93 with the direct releases investigated in TSPA-91. Only releases for 10,000 years are compared, since this time period was used for TSPA-91 analyses. Because there are no significant 10,000-year releases in the 1,000,000-year simulations described above, the simulations were re-done for this comparison. Three hundred realizations were computed for a 10,000-year time period, with time of magmatic intrusion distributed uniformly from 100 years to 10,000 years. The indirect effects can be seen to be much smaller (and less probable) than direct effects, for the assumptions used.

Figures 17-14 and 17-15 show the CCDFs for the two analysis cases discussed above with the probability of occurrence applied. The probabilities in Figures 17-11 and 17-12 are multiplied by the probabilities of occurrence given in Section 17.1 to obtain Figures 17-14 and 17-15. For both cases, the consideration of the probability of occurrence moves the CCDFs considerably away from the remanded EPA limits.

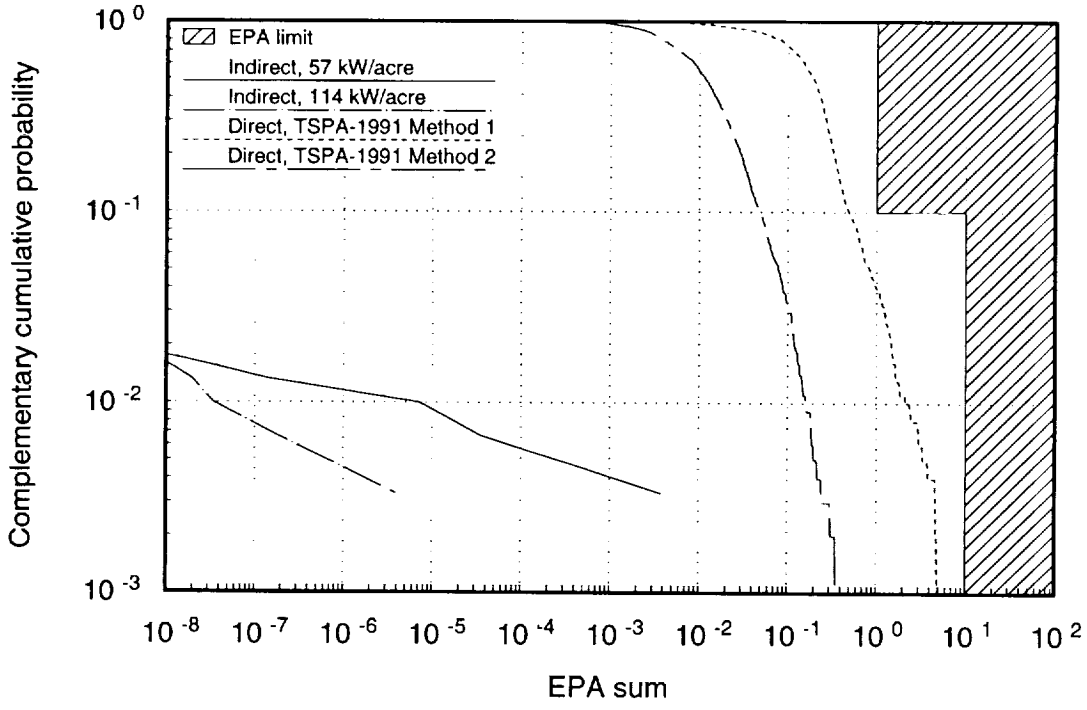

Figure 17-13. Comparison of direct and indirect releases over 10,000 years.

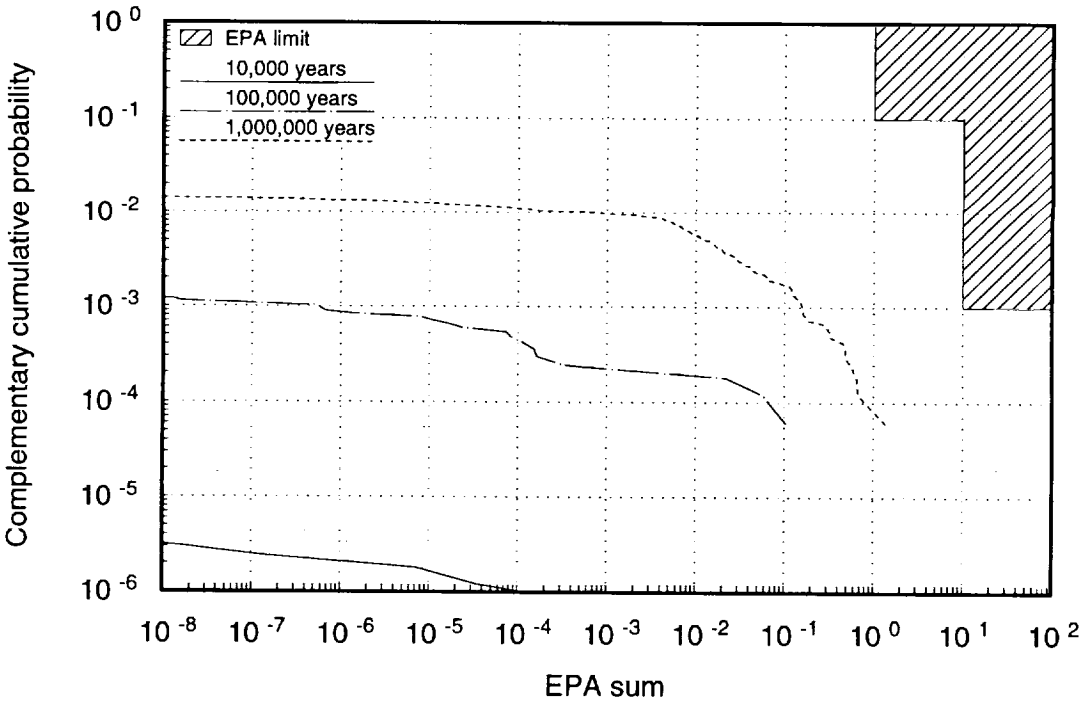

Figure 17-14. Releases due to magmatic intrusion, scaled by probability of occurrence (57 kW/acre).

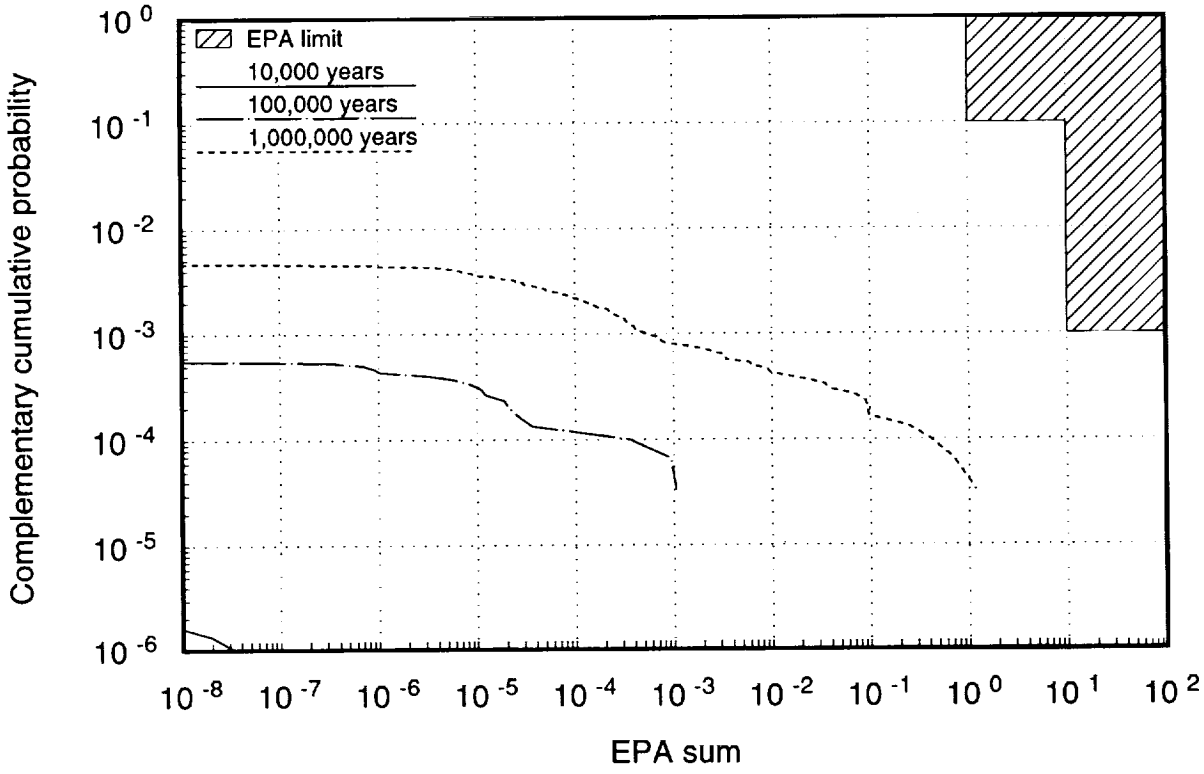

Figure 17-15. Releases due to magmatic intrusion, scaled by probability of occurrence (114 kW/acre).

Peak drinking-water doses, including the contribution from the magma-altered source, are shown in Figure 17-16. Only doses from column 2 for the borehole, 57-kW/acre case are compared. It can be seen that the altered source term makes very little change in the doses.

17.4 Discussion

If a magma intruded a repository, it would be expected that the magma would interact with the waste in a variety of ways—ranging from entrainment by flowing magma (modeled in TSPA-91) to contact only by the volatiles (modeled here). The TSPA-93 results imply that, for the scenarios modeled, the consequences of thermal effects and aggressive volatiles from a magmatic intrusion that does not contact the waste are not great. Furthermore, the restrictive assumptions necessary to model the scenario make its occurrence quite unlikely.

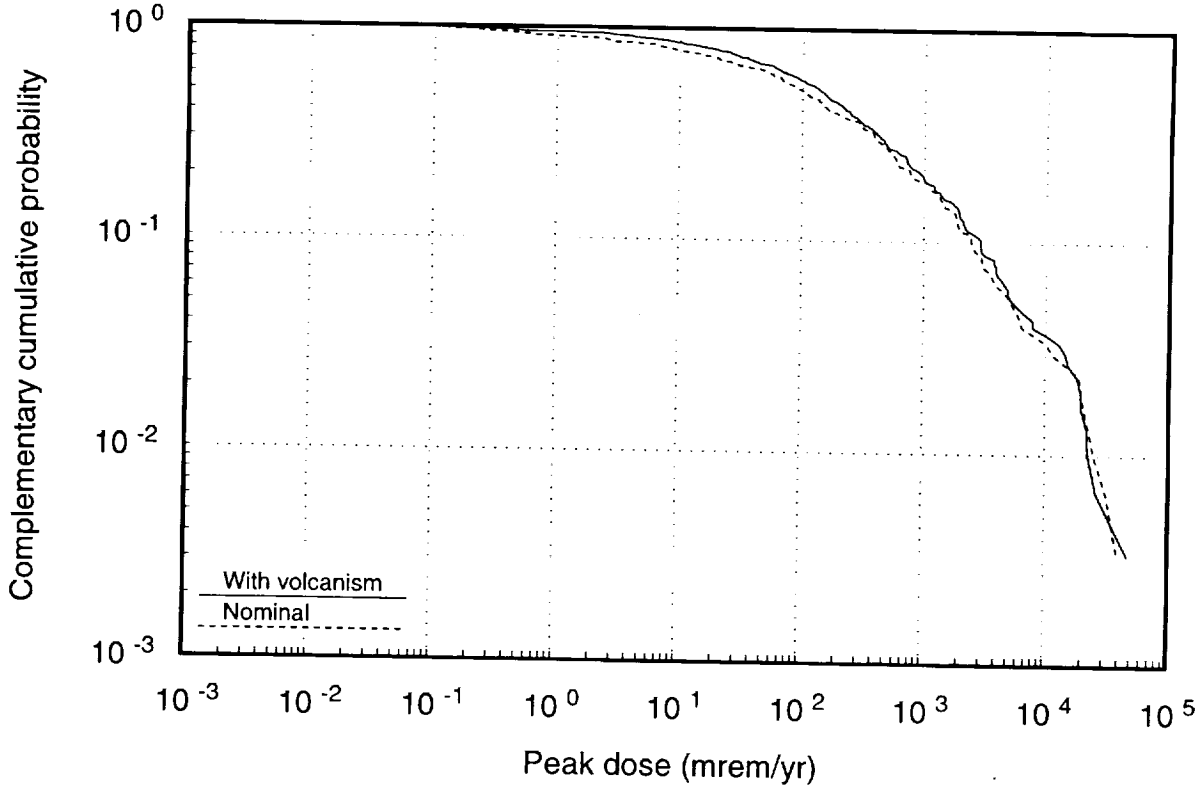

Figure 17-16. Comparison of peak doses with and without magmatic intrusion (borehole, 57 kW/acre).

There is not much difference in releases for the two cases analyzed. There are larger effects for the borehole-emplacement case because the distances from the dike to the waste packages are generally less. Releases would most likely be greater if the model included the accelerated degradation of the fuel itself due to magmatic interactions.

Part V

Summary and Conclusions

Chapters 18 through 20 summarize the results of the previous parts of the report, and provide recommendations for future work, based on the simulation results, as well as insights gained during the completion ofTSPA-93.

Chapter 18 contains a discussion of the results and the major conclusions drawn. Chapter 19 contains recommendations for the site-characterization and design programs, and some observations regarding possible impacts of regulation changes on performance assessment. Chapter 20 contains a discussion of work that needs to be done to improve performance-assessment models so that future TSPAs will be closer to the ultimate goal of a determination of compliance of the potential repository with applicable regulations.

Chapter 18
Discussion and Conclusions

(Barnard, Wilson, Halsey, Gauthier)

18.1 Discussion of results

A summary of the results for the TSPA-93 scenarios analyzed follow—nominal aqueous and gaseous release based on the composite-porosity model; nominal releases from the weeps model; releases from human intrusion; and aqueous releases resulting from magmatic activity.

18.1.1 Aqueous and gaseous releases based on composite-porosity model

This section summarizes the work described in Chapters 12 and 14. Cumulative releases by aqueous transport to the accessible environment over 10,000 years are all quite similar for the four emplacement/thermal-loading analysis cases: borehole emplacement, 57 kW/acre; borehole, 114 kW/acre; in-drift emplacement, 57 kW/acre; and in-drift, 57 kW/acre. Furthermore, none of the releases exceed the EPA limits originally specified in 40 CFR Part 191 (EPA, 1985) for sites like Yucca Mountain.

The current estimates of aqueous releases are significantly lower than those of TSPA-91. The reduction is primarily due to the different assumptions regarding percolation flux. In TSPA-91, the percolation flux was exponentially distributed with a mean of 1 mm/yr. In TSPA-93, most of the simulations started with "dry" conditions during the first 10,000 years, with an exponentially distributed flux of 0.5 mm/yr. This again illustrates the sensitivity of the composite-porosity model to the groundwater percolation flux. Although the difference in percolation flux is the major contributor to the difference in releases, another factor is the difference in waste-package lifetimes; TSPA-93 uses explicit thermal-history curves in place of the delays used in TSPA-91.

Gaseous releases were calculated for 10,000 years only, since the half-life of ^{14}C is sufficiently short that releases beyond that time would not be expected to be important. The releases for the four analysis cases are again quite similar. As occurred in the TSPA-91 simulations, releases exceed the EPA limit. The TSPA-93 releases occurring with probabilities less than about 50% are greater than those of TSPA-91. The larger releases are primarily due to the faster $^{14}CO_2$ transport times calculated with the current gas-flow model.

The drinking-water dose estimates are again quite similar among the four analysis cases. The differences among the cases are probably as insignificant as they were for cumulative releases. The mean estimated peak doses for the four analysis cases exceed by 10 to 50 times the NCRP estimates for natural background doses to individuals in the United States. The large doses arise primarily because of the limited amount of dilution of the re-

leased radionuclides that occurs in the groundwater at Yucca Mountain. Despite the long transport times predicted by the composite-porosity model for radionuclides to reach the accessible environment, high doses still occur at some point in the future.

Reduction of the dose estimates requires either a lower radionuclide release rate from the source or greater dilution. Given the uncertainties in the model, neither option is foreclosed. Because the saturated zone at Yucca Mountain is not well characterized, our estimates of water available for dilution are uncertain; however, it is unlikely that a more favorable determination of the water available will be sufficient to reduce the dose estimates significantly. A better understanding of the waste-package degradation processes and transport in the near field will give us more confidence in the dose calculations.

The parameters to which the composite-porosity model is sensitive fall into a few categories. Of paramount importance is the unsaturated-zone percolation flux. This parameter significantly affects aqueous doses and releases, and gaseous releases. The saturated-zone transport area is quite important to dose calculations because of its effect on reducing concentration by dilution. Results are also sensitive to parameters related to releases from the waste package, which include container wetting, near-field water flow, and corrosion rates. These factors are especially important to dose estimates.

18.1.2 Aqueous and gaseous releases based on weeps model

This section summarizes the work described in Chapter 15. Cumulative aqueous releases to the accessible environment from the weeps model over 10,000 years are well below the EPA limits originally specified in 40 CFR Part 191, as in TSPA-91. In contrast to the composite-porosity results, the results are sensitive to container type. In most cases, the in-drift waste packages release about 10 times as much contaminants as do the vertical-borehole-emplaced packages. This result occurs primarily because the weeps are discrete entities that have a probability of impinging on a waste package that is proportional to the size of the container. The weeps model also predicts a sensitivity to thermal loading; higher thermal loadings lead to greater releases, primarily because higher thermal loads perturb the environment more and cause more weeps to be formed, especially around the edges of the repository. This sensitivity to thermal loading is much less pronounced than the sensitivity to container size.

Gaseous releases over 10,000 years do not exceed the now-inapplicable EPA standard, in contrast to the comparable results for the composite-porosity model. Gaseous releases are much more narrowly distributed for TSPA-93, compared with TSPA-91, primarily because of the assumptions made about the failures and the release mechanism from the waste packages. In the prior TSPA analysis, releases were strongly controlled by the num-

ber of containers contacted by weeps, and by the assumption that once a container was contacted, it rapidly degraded. The number of containers contacted had a wide range in TSPA-91. This time, the assumptions about repository dryout and groundwater shedding, and the mechanistic source-term model resulted in a different (smaller) number of waste packages available to release ^{14}C.

Although cumulative releases over 10,000 and 1,000,000 years do not exceed the old EPA standard, the model predicts that release rates are relatively high at certain times. This situation occurs if containers are contacted by water while their temperatures range from 70°C to 100°C. The YMIM source-term model predicts that corrosion is rapid under these conditions, resulting in a temporarily high release rate. Because of the limited amount of water available to dilute the contaminants, relatively high dose rates (in some cases above the NCRP estimates for natural background doses) are a consequence.

The weeps-model results are sensitive to several parameters; the parameters are different for different performance measures. For the EPA standard, the container lifetime, the number of weeps, which is a function of the groundwater flux, the size of the weeps, and how often they flow, and the retardation of the actinides in the saturated zone are most important for aqueous releases. For gaseous releases, the number of juvenile waste-package failures and the bulk permeability of the host rock are most important. Dose results are most sensitive to the amount of dilution in the saturated zone, container lifetime, and the number of weeps.

18.1.3 Releases due to human intrusion

This section summarizes the work described in Chapter 16. Results from the four baseline analysis cases show that the EPA release limits are not exceeded in 10,000 years. The CCDFs are quite similar to those produced for TSPA-91, although the TSPA-93 CCDFs show releases from more components (i.e., direct hits on spent fuel, near misses, and high-level waste) as a result of a more complex source term.

Because the drilling probability model has a linear relationship between the probability of hitting a single container and the density of placement of containers in the repository, there is very little difference between releases from a repository with 57-kW/acre thermal load and one with 114-kW/acre loading.

The baseline analyses assume that the amount of waste released from a breached waste package is a uniform distribution ranging from 0 to 100%. With this assumption, releases from the in-drift waste packages are 5 to 10 times greater than those from vertical-borehole packages.

Releases resulting from contaminated rock being brought to the surface by drilling ("near misses") are a larger contributor to releases in TSPA-93 than in TSPA-91, because the near-miss component of the source term inventory is larger. The TSPA-93 near-miss inventory included all the radionuclides likely to be easily mobilized from a degraded waste package. The use of probability distributions for container lifetimes also produced differences in the near-miss releases.

Releases estimated over 1,000,000 years did exceed the 10,000-year EPA standards for the in-drift waste packages. The highest releases for the 1,000,000-year simulations (occurring with the lowest probabilities) did not increase significantly over those of the 10,000-year simulations; slightly lesser releases, with probabilities of occurrence in the range 10% to 30% increased more than an order of magnitude between 10,000 and 1,000,000 years, and exceeded the EPA guidelines. Because of the significant uncertainties associated with estimating human behavior and technology for 1,000,000 years, these results should be interpreted with caution.

If we assume that the most likely amount of waste released from an in-drift waste package by a drilling hit is about 5% of the contents (based on the volume of waste cut out of a waste package by a drill bit), releases from in-drift waste packages are about 2 orders of magnitude lower. Consequently, the EPA standards are not exceeded for either the 10,000-year or 1,000,000-year simulations.

18.1.4 Releases due to magmatic activity

This section summarizes the work described in Chapter 17. Releases from magmatic activity assumed that a limited region of the potential Yucca Mountain repository would experience a dike intrusion. As a modeling assumption, the dike does not directly make contact with the waste packages; instead they are subjected to a thermal excursion and attack by aggressive volatiles. The containers exposed to the dike are assumed to degrade at a rate 10^4 times greater than nominal oxidation rates. Aqueous releases from the entire repository, using a source term modified by the effects of the dike on the affected waste packages have been calculated. Because of the improbability of a magmatic event at the potential repository, releases for each simulation were assumed to occur from a single dike for the 1,000,000 years modeled.

The analyses only modeled accelerated degradation of the waste containers; other processes, such as enhanced degradation of the fuel cladding, accelerated alteration of the waste form, and increased solubility of the UO_2 fuel and the other components contained in the fuel were not modeled. These latter factors may increase the releases from magmatic interactions.

Releases attributable to the alteration of the aqueous source term by the magmatic intrusion are not significant. When the probability of occurrence of magmatic activity is considered, this scenario does not cause any discernible increase in the overall total-system releases. Over 10,000 years there were no increase in releases of as much as 10^{-8} of the EPA sum. The increases in cumulative releases compared with the corresponding undisturbed cases range from about 10^{-2} over 100,000 years to 25% after 1,000,000 years. Releases from the borehole, 57-kW/acre case were higher than those from the in-drift, 114-kW/acre case, because, on average, the closer distance between the intruding dike and the containers resulted in greater attack by magmatic volatiles.

The scenario analyzed represents the opposite extreme in the range of magma–waste interactions. TSPA-91 investigated direct contact; this analysis was restricted to only thermal and volatile interactions. Actual magma–waste interactions would fall somewhere between these two conditions.

18.1.5 Supporting analyses

18.1.5.1 Source term

Central to the TSPA-93 results is the inclusion of a mechanistic source-term model (embodied in YMIM—see Chapter 13). This model predicts waste-package releases and container lifetimes—factors that are important to all the TSPA-93 analyses.

The source term incorporated a variety of new detailed models. Temperature dependencies were included for container corrosion, waste-form degradation and water contact. Including temperature allowed alternative thermal loadings to be considered. Because many potentially important thermal effects were not incorporated, and because of the simplifications made, the results should not be interpreted as a direct quantitative correlation between thermal loading and repository performance. Rather, the contribution of thermal effects relative to other mechanisms should be examined for indications of performance sensitivity.

Mechanistic corrosion models were incorporated to begin evaluating which corrosion modes are significant and under what conditions. These models supplant the TSPA-91 source-term model, whose container-failure distribution was entirely based on expert judgment. The corrosion models are a first-step improvement; they are still limited in that several modes are combined into one abstraction, and the rates and environmental dependencies are primarily from expert judgment based on general corrosion experience rather than tied directly to appropriate data. Compared to the arbitrary container failure distributions used previously, these mechanistic models do not cause large changes in repository perfor-

mance over 10,000 years. However, they do indicate the importance of water contact on the waste package performance.

Water contact was modeled with both matrix flow and fracture flow, with total water availability controlled by both infiltration processes and near-field hydrothermal processes. There are a number of limitations on these models as they were used in this TSPA. The assumption that resaturation is coincident with the boiling point isotherm eliminates the concept of extended dryout of the host rock. Percolation diversion into the backfill was not modeled, and water contact is independent of the volume of water present near the waste package. Under these conditions, water contact is important to waste package performance. Waste packages that remain dry, in general are not expected to fail.

The temperature dependence of corrosion and the modeling of corrosion solely by aqueous processes points to the importance of the temperature at which aqueous processes begin. Containers that are wet and hot corrode to failure rapidly, containers that are cool and wet corrode to failure very slowly. With the caveat that the temperature dependence and the water contact are still preliminary and fairly simple, these results direct our attention to the coupled processes of temperature-dependent water contact. That is, the temperature-dependent onset of aqueous processes may be more important to container lifetime than the details of the corrosion mechanisms. The importance of such coupled processes (temperature, water contact, corrosion) is an important observation from the results.

The YMIM container-lifetime studies predict a wide range of container-failure times, strongly driven by the choices for corrosion and container-wetting parameters. Under certain conditions, the lifetime of the 0.95-cm corrosion-resistant-alloy wall for both styles of container is only about 100 years. The 114-kW/acre thermal loadings result in somewhat longer container lifetimes, primarily because of the longer time for the container wall to cool to 100°C, where aqueous-corrosion processes proceed rapidly. Compared with the vertical-borehole containers, the double-walled in-drift containers have only marginally longer lifetimes. In-drift waste packages reach much higher temperatures, where the air-oxidation rate of the 10-cm-thick mild-steel overpack is sufficiently high to degrade it within about 100 years. When these packages then cool to 100°C, the inner corrosion-resistant alloy wall is subjected to the same corrosion processes as is the vertical-borehole containers.

18.1.5.2 Thermal effects

This section summarizes the work described in Chapter 10. For TSPA-93, information from thermal-design calculations was used to develop a conceptual hydrothermal model for use by the aqueous- and gaseous-release analyses. The model assumes that the heat from radioactive-waste decay will drive water from the surrounding rock away from the reposi-

tory until the temperature is again low enough that the water can accumulate in the rock. As a consequence of this process, a "dryout" zone and a "condensation" zone may form at the repository. The extent that the repository dries out is dependent on, among other things, the amount of heat available to drive the water. In addition to determining the dryout volume, the thermal effects described the thermal dependence of container corrosion and fuel-matrix alteration.

Detailed thermal models were used to calculate the location of the boiling isotherm as a function of time for the four analysis cases. Both an axisymmetric numerical model, that accounted for the layered rock stratigraphy near the repository, and an analytical model, that captured the details of repository layout, waste stream and emplacement mode, were used.

Waste-package and fuel-rod temperatures were also calculated. Two representative repository areas—"hot" (for waste packages surrounded by other hot packages) and "cold" (for waste packages near the edge of the repository)—were modeled. By using the rock temperatures near the container wall as an initial condition, fuel-rod temperatures consistent with the thermal loading, waste-package emplacement configuration, and repository area (hot or cold) were determined.

The hydrothermal conditions predicted by the detailed modeling were abstracted for use in the TSPA analyses. Some of the most important abstractions for the analyses are: (1) the dryout volume is assumed to coincide with the boiling isotherm, and the rock immediately resaturates as the boiling front contracts (this obviates the "extended-dry" concept); and (2) water displaced by the boiling isotherm condenses above the repository; it may be diverted, and is therefore available to interact with waste packages unprotected by the dryout zone.

18.1.5.3 Gaseous flow and transport

Using a coupled gas-flow/heat transfer model and a transient particle tracker, travel times for $^{14}CO_2$ flow from the potential Yucca Mountain repository to the surface were calculated. Gas flow is assumed to be driven by repository heat, and varies with time, as the waste decays. $^{14}CO_2$ is assumed to be retarded by exchange with bicarbonate in the pore water.

Travel times for the CO_2 particles range from as short as 200 years early in the life of the repository to about 1800 years when the thermal gradient from the repository to the surface is small. The results are sensitive to the choice of welded-tuff permeability. A decrease of a factor of 10 in the permeability increases the travel time by more than one order of magnitude.

18.1.5.4 Saturated zone

This section summarizes the work described in Chapter 11. The saturated zone in the vicinity of the potential Yucca Mountain repository was modeled using a three-dimensional representation. An area extending about 8 km on a side and including the Solitario Canyon and Bow Ridge faults was modeled to a depth of 200 m below the water table.

Two alternative conceptual models for the flow system were developed—a non-diversionary model and a diversionary one. To calibrate the models to existing saturated-zone data required the inclusion of unobserved properties in two known geologic features at the site. In addition, the area near one data point was adjusted by adding upwelling. A vertical gradient is not observed at the well corresponding to this datum, but is observed elsewhere. In the diversionary model, a drain to divert fluid from the upper aquifers down to the lower aquifers was included. Such a structure is postulated for the Yucca Mountain region. With either of these interpretations of the saturated zone, the computer models adequately describe the observed data.

Transport calculations were done for contaminants introduced at various locations at the water table below the repository. Concentrations at points 5 km from the sources at various depths were calculated. Concentrations reached approximate steady state in about 2,000 to 5,000 years, but the concentrations varied considerably depending on the depth and location of the measurement at the 5-km boundary. The considerable horizontal and vertical structure to the contaminant plume implies that where the contaminants are introduced makes a difference for travel time, mixing and dilution.

18.2 Comparison of results from the two flow models

As in TSPA-1991, two separate performance assessments were completed in this TSPA, for different conceptual models of groundwater flow through the unsaturated zone at Yucca Mountain. We considered this necessary since unsaturated-zone water flow at Yucca Mountain is not well understood, and it is crucial to considerations of repository performance, both in its effect on radionuclide transport time and in its effect on container corrosion and radionuclide releases from the waste packages. Assumptions and results are presented in detail in Chapters 14 and 15; in this section, we present a brief comparison of the results of the two models and some discussion of the implications.

For 10,000-year normalized cumulative release to the accessible environment, as specified in 40 CFR Part 191 (EPA, 1985), results are similar to those for TSPA-91—calculated aqueous releases are higher for the weeps model than for the composite-porosity model, but calculated gaseous releases are lower for the weeps model than for the composite-porosity model. Comparison of the aqueous and gaseous releases predicted for both

models for one of the repository cases—57-kW/acre thermal load with vertically emplaced containers—is shown in Figures 18-1 and 18-2. Two effects are largely responsible for the differences in the results for the two models (as explained in the TSPA-91 report). The distribution of water is quite different in the two models, resulting in many more wet or moist containers in the composite-porosity model than in the weeps model. This, in turn, results in many more container failures in the composite-porosity model and thus greater gaseous releases. The aqueous releases from the EBS are also higher for the composite-porosity model than for the weeps model, but aqueous transport times are much longer for the composite-porosity model and the net result is lower releases to the accessible environment within 10,000 years.

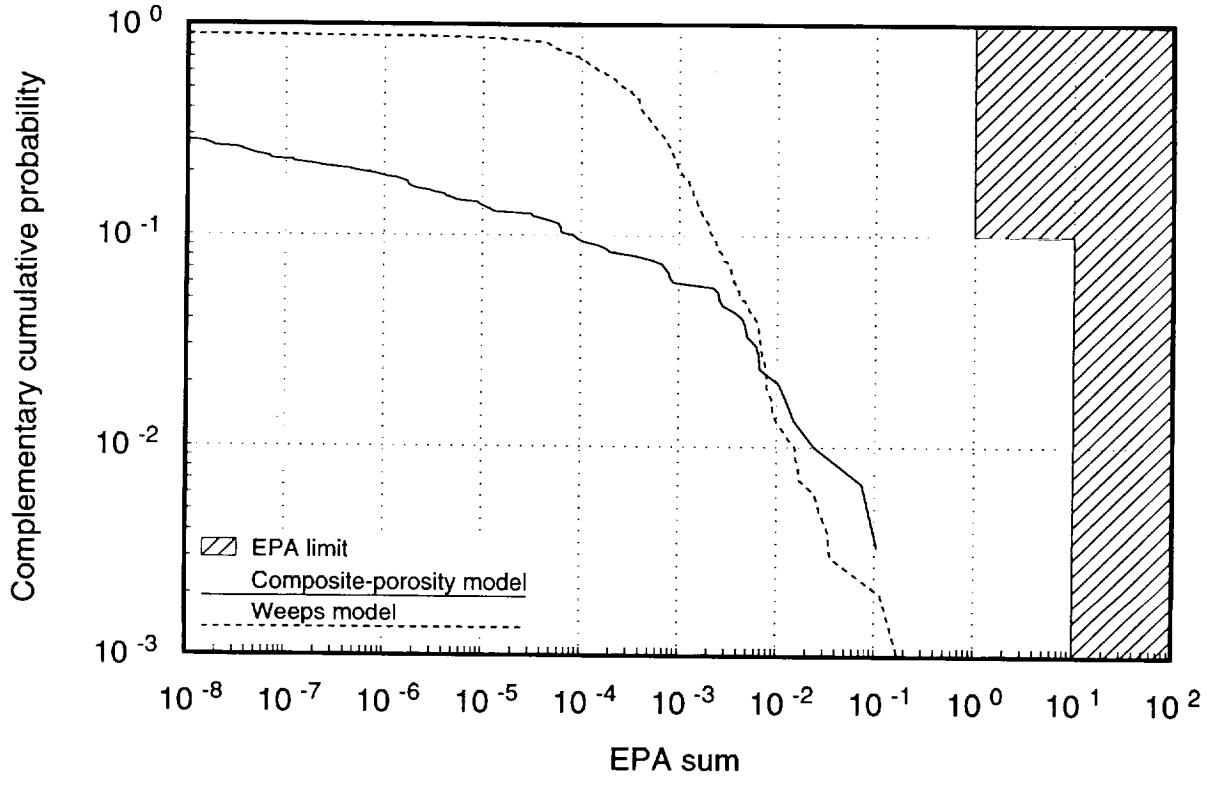

Figure 18-1. CCDFs of normalized cumulative release over 10,000 years for nominal aqueous releases (57-kW/acre, vertical-emplacement case).

The weeps/composite-porosity comparison depends somewhat on the repository configuration. For example, the aqueous-release CCDFs for the 114-kW/acre, in-drift case are shown in Figure 18-3. For that case, the weeps aqueous-release CCDF is entirely to the right of the composite-porosity CCDF, whereas for the 57-kW/acre, vertical case the composite-porosity curve is higher only for probabilities below about 2%.

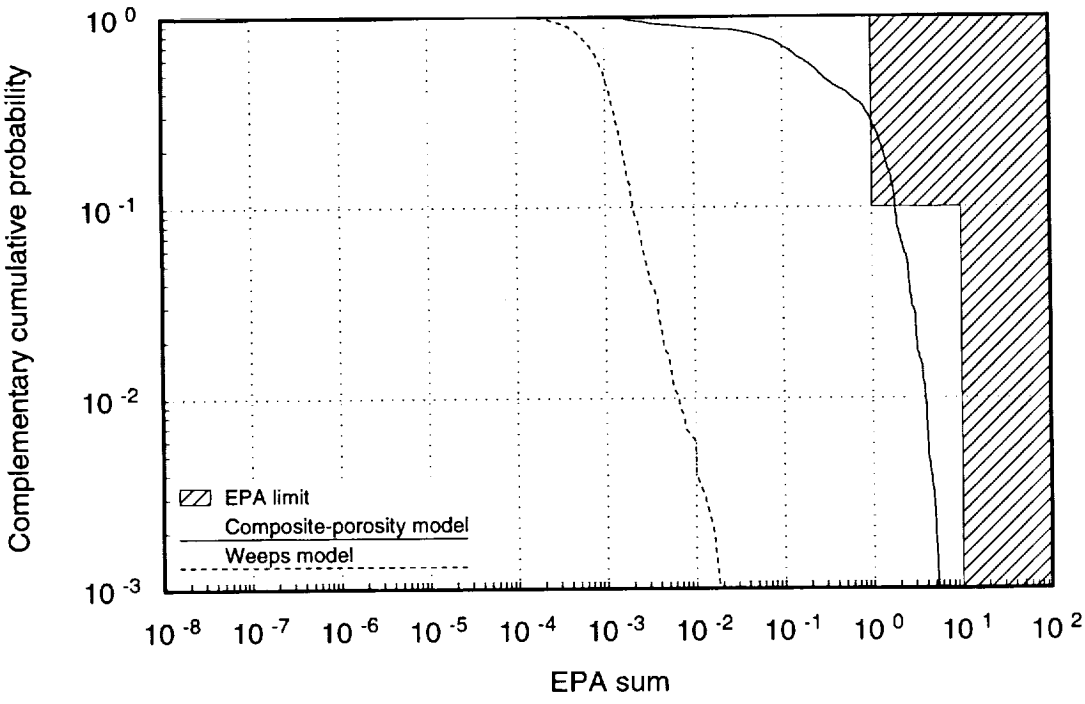

Figure 18-2. CCDFs of normalized cumulative release over 10,000 years for nominal gaseous releases (57-kW/acre, vertical-emplacement case).

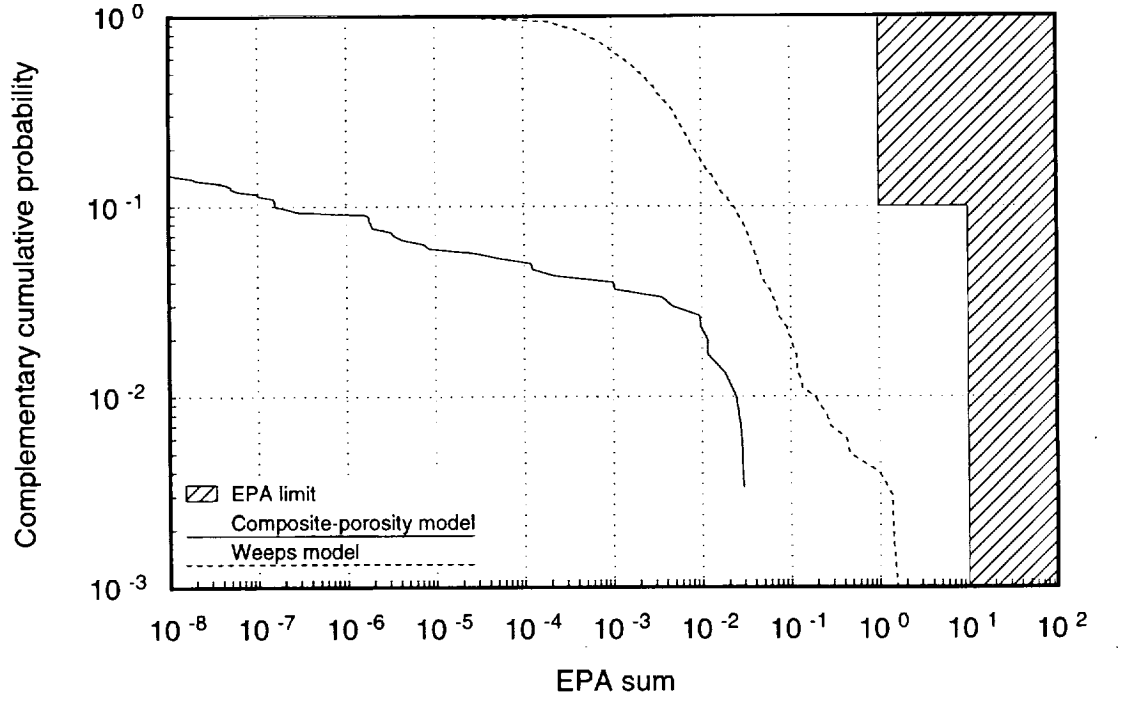

Figure 18-3. CCDFs of normalized cumulative release over 10,000 years for nominal aqueous releases (114-kW/acre, in-drift-emplacement case).

A comparison of the peak individual drinking-water doses over a 1,000,000-year period for the two models is shown in Figure 18-4 (for 57 kW/acre, vertical emplacement). The calculated composite-porosity doses are significantly higher than the weeps doses. The reason is the same as for higher 10,000-year gaseous releases: more containers fail and release their radionuclides in the composite-porosity calculations, and there is sufficient time in a million years for the low-retardation nuclides to reach the accessible environment. The distributions of peak-dose time for the 57-kW/acre, vertical-emplacement case are shown in Figure 18-5. Note that the peak doses occur earlier for the weeps model because the unsaturated-zone transport time is assumed to be zero, whereas the unsaturated-zone transport time is quite large for the composite-porosity model. For both models, the doses are dominated by ^{237}Np. The peak-dose times for the weeps model reflect the transport time through the saturated zone of ^{237}Np, while the peak-dose times for the composite-porosity model include the same saturated-zone transport time plus a large unsaturated-zone transport time. (Of course, the distribution of release times from the EBS affects the peak-dose time as well.)

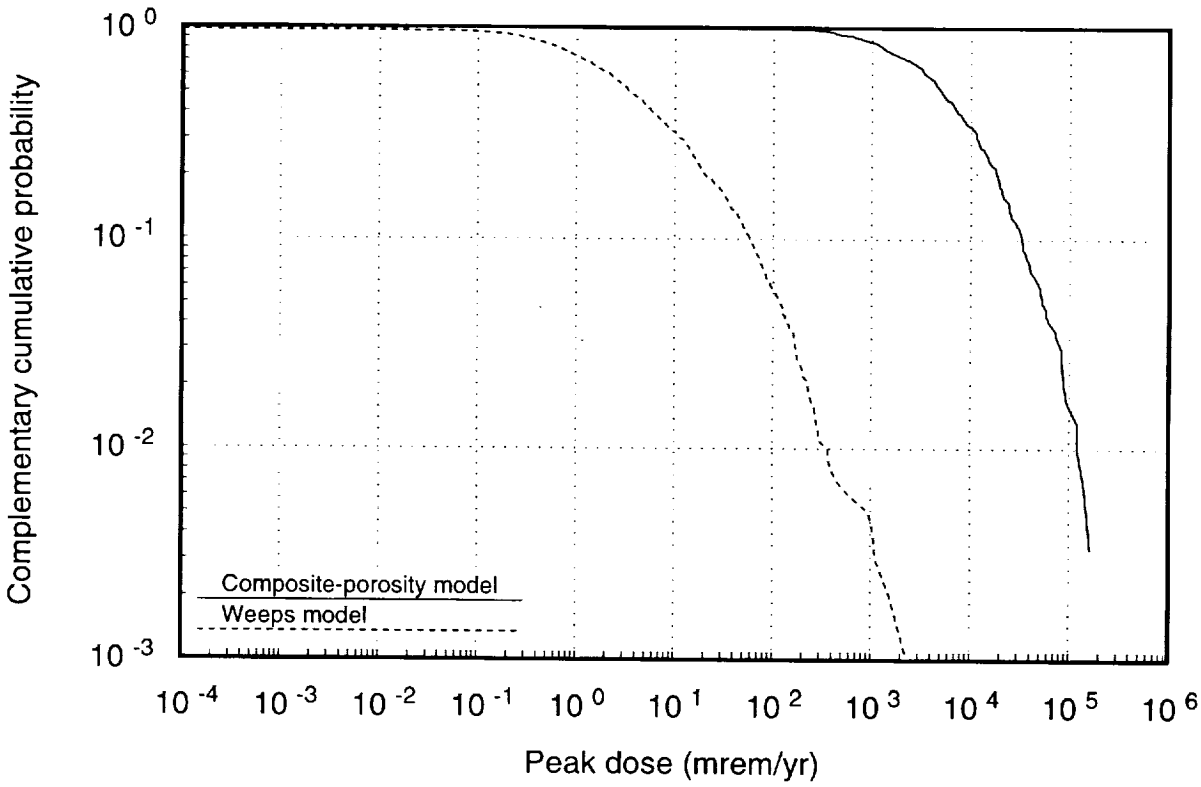

Figure 18-4. CCDFs of peak individual drinking-water dose over 1,000,000 years for nominal aqueous releases (57 kW/acre, vertical emplacement).

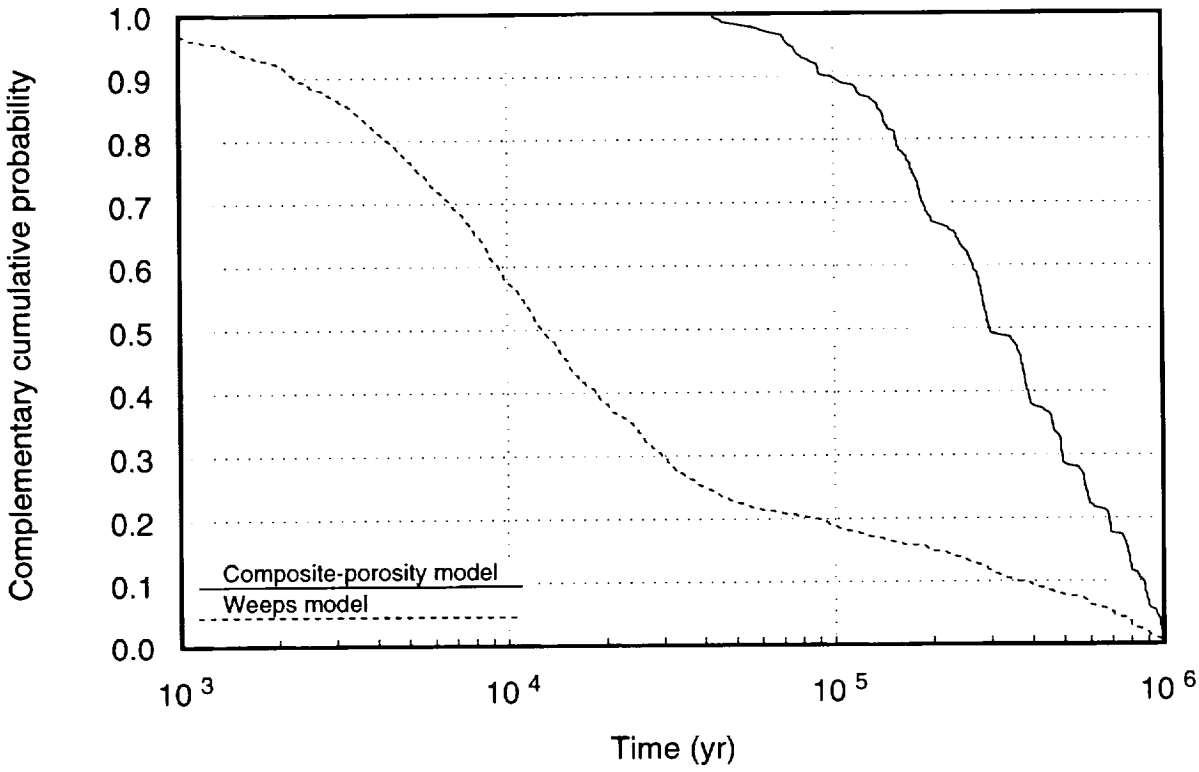

Figure 18-5. Distribution of time of peak dose for nominal aqueous releases (57 kW/acre, vertical emplacement).

18.3 Combination of CCDFs

In previous chapters of this report, releases of radioactivity to the accessible environment by several mechanisms are discussed. In this section we consider the combination of those separate releases to obtain the distribution of total release. Combination of doses is not considered. Dose rates are not additive as cumulative releases are, because location and time of release enter in, whereas cumulative release is a simple sum over locations and times. In addition, only drinking-water doses were calculated, so we have no dose information on gaseous or direct releases.

Methods of combining CCDFs for different scenarios analyzed are discussed in Chapter 8 of the TSPA-1991 report, and will not be repeated here. The relationship among releases from different scenarios can be considered to fall into three categories: independent, mutually exclusive, and correlated. The combination of aqueous and gaseous releases (considered to be correlated) is described in Chapters 14 and 15 of this report. We describe the combination of nominal-condition releases (nominal aqueous and gaseous releases) with releases due to human intrusion and magmatic intrusion (Chapters 16 and 17) in the following paragraphs.

We treat the nominal releases and direct releases as being independent (i.e., having no effect on each other). This approximation is made to simplify the calculations—so that we can make the calculations separately. It would be preferable if the near-miss drilling releases and indirect volcanic releases were coupled to the nominal releases properly, and if the direct and indirect volcanic releases were coupled properly, but those releases are small; the coupling is expected to have little effect on the results. With the assumption of independence, the correct way to combine the releases is called "probabilistic sum." In this method, we perform a secondary Monte Carlo simulation in which partial EPA sums are drawn from each of the distributions to be combined, and the partial EPA sums are added to produce the combined EPA sum. Chapter 8 of the TSPA-1991 report discussed this in detail.

The distribution of "total-system" releases formed by combining the partial releases, is illustrated in Figures 18-6 and 18-7, for nominal releases calculated by the composite-porosity model and the weeps model, respectively (for 57 kW/acre, vertical emplacement). The combination is for normalized cumulative release over 10,000 years, as specified in 40 CFR Part 191. The figures show that for the composite-porosity model, nominal releases (mostly gaseous ^{14}C releases) are much larger than drilling or volcanic releases, so the resultant conditional CCDF curve is essentially the same as the nominal-condition curve (which is essentially the same as the gaseous-release curve). For the weeps model, human-intrusion releases are higher at low probabilities and nominal releases are higher at high probabilities; nominal and human-intrusion releases are both much larger than volcanism releases.

The curve for direct volcanism releases was taken from TSPA-1991 (Method 1); the curve would be somewhat different if it were redone, because of the slightly different inventory used for TSPA-1993 and because of the slightly different repository area used for TSPA-1993. There is no curve for indirect-volcanism releases in Figure 18-7 because the indirect-volcanism releases were only calculated for the composite-porosity model. Note that the two volcanism scenario classes should be sharing the volcanism probability, since the two scenario classes are mutually exclusive as defined. Because the probability is so low and volcanism makes negligible contribution to the combination CCDF, we have not attempted to define relative probabilities for the two volcanism scenario classes, but have conservatively assigned the full volcanism probability to each.

The relative magnitudes of the releases vary among the different repository cases. For the composite-porosity model, calculated nominal releases are always much greater than calculated drilling releases. The weeps model produces greater variations, as shown in Figure 18-8 for the 114-kW/acre, in-drift-emplacement case. The probability of a mag-

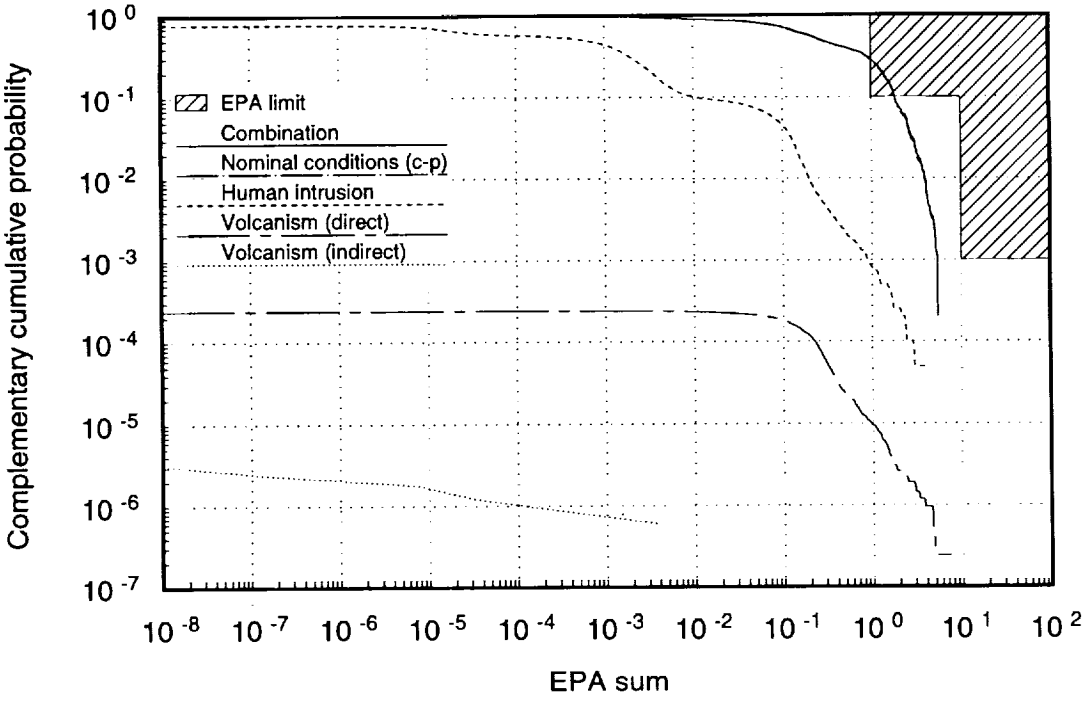

Figure 18-6. Combination of nominal, human-intrusion, and volcanic CCDFs (cumulative release over 10,000 years; 57-kW/acre, vertical emplacement). Composite-porosity model used for UZ flow and transport.

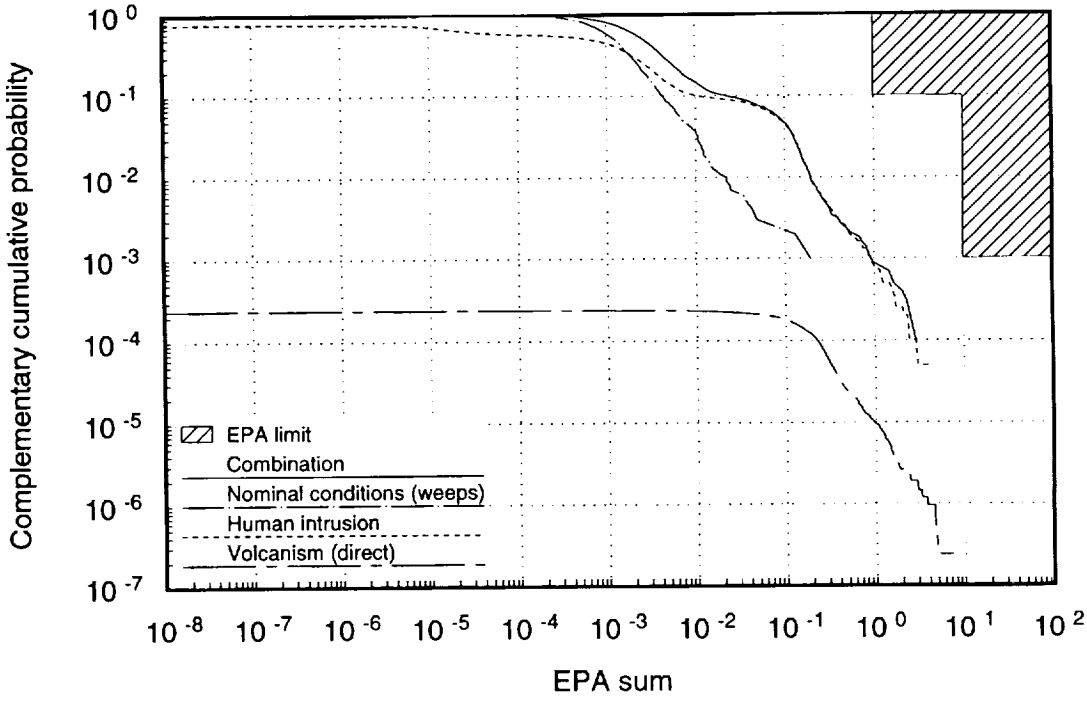

Figure 18-7. Combined (nominal, human-intrusion, and volcanic) CCDFs (cumulative releases for 10,000 years; 57-kW/acre, vertical emplacement, weeps model).

matic intrusion should be significantly lower for the smaller area of the 114-kW/acre cases (see Chapter 17), but that lower probability is not reflected in the volcanism curve in Figure 18-8; it is taken directly from TSPA-1991, which assumed a larger repository area.

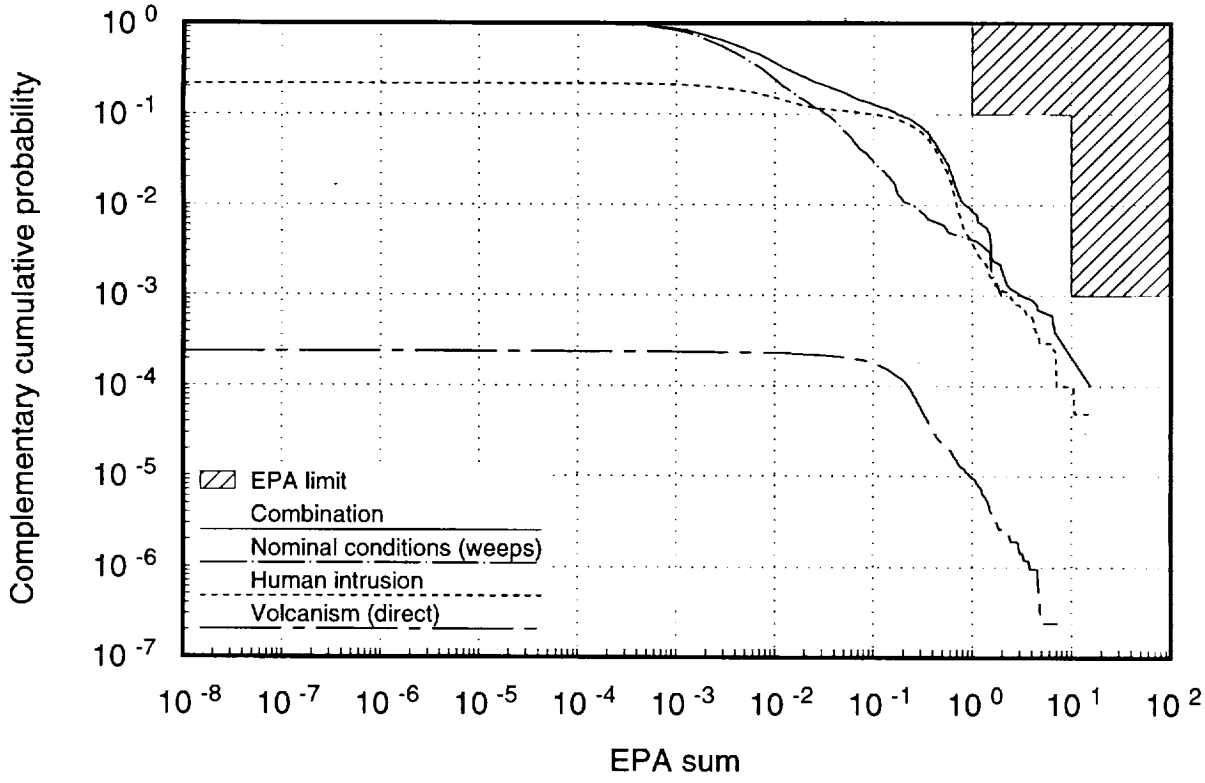

Figure 18-8. Combined (nominal, human-intrusion, and volcanic) CCDFs (cumulative releases for 10,000 years; 114-kW/acre, in-drift emplacement, weeps model).

Gaseous releases were only calculated for 10,000 years, so, in generating Figures 18-9 and 18-10, the 10,000-year gaseous releases were added to 1,000,000-year aqueous releases to obtain the nominal-condition releases. This approximation should be reasonable because most gaseous ^{14}C releases occur within the first 10,000 years (the half-life of ^{14}C is only 5730 years). Note that at 1,000,000 years, the composite-porosity nominal-condition releases are dominated by aqueous releases of ^{237}Np rather than by gaseous releases of ^{14}C.

We close this section by presenting the total system CCDFs for all four analysis cases at 10,000 years in Figures 18-11 and 18-12. The corresponding TSPA-1991 curves are also shown. Figure 18-11 shows very little variation among the four analysis cases for 10,000-year composite-porosity releases. The releases are also very similar to those calculated for TSPA-1991. Figure 18-12, for 10,000-year weeps releases, shows some dependence on repository configuration. For both weeps nominal releases and human-intrusion releases, the calculated releases are higher for the in-drift cases; thus, the same is true for their

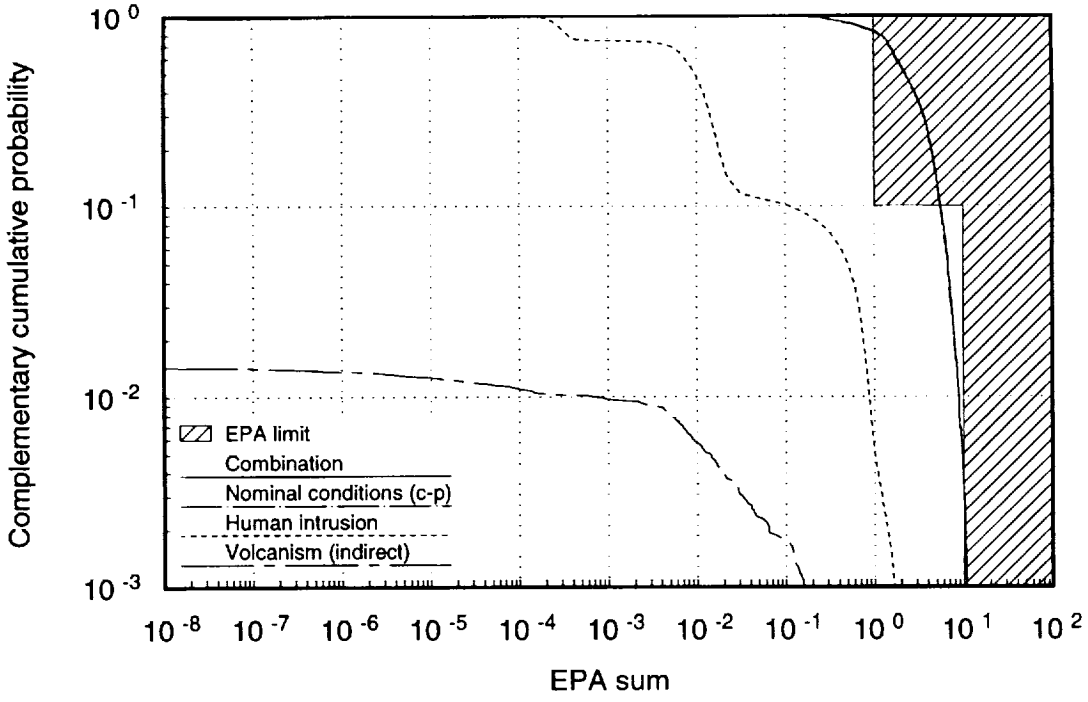

Figure 18-9. Combination of nominal, human-intrusion, and indirect volcanic CCDFs (cumulative release over 1,000,000 years; 57-kW/acre, vertical emplacement, composite-porosity model).

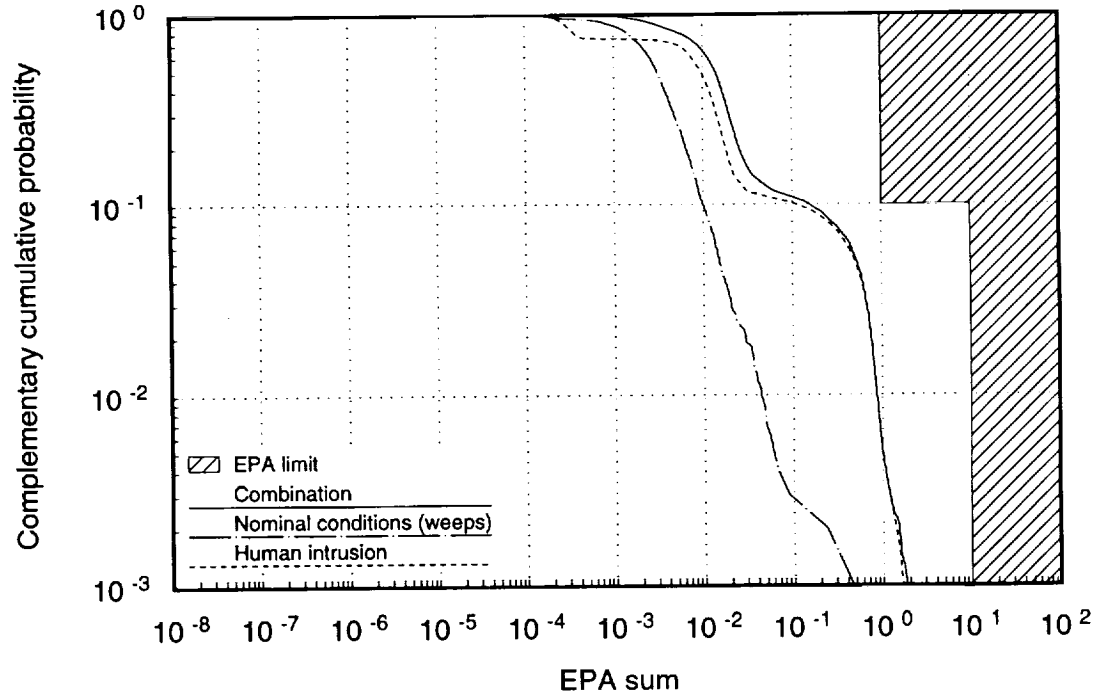

Figure 18-10. Combination of nominal and human-intrusion CCDFs (cumulative releases over 1,000,000 years; 57-kW/acre, vertical emplacement, weeps model).

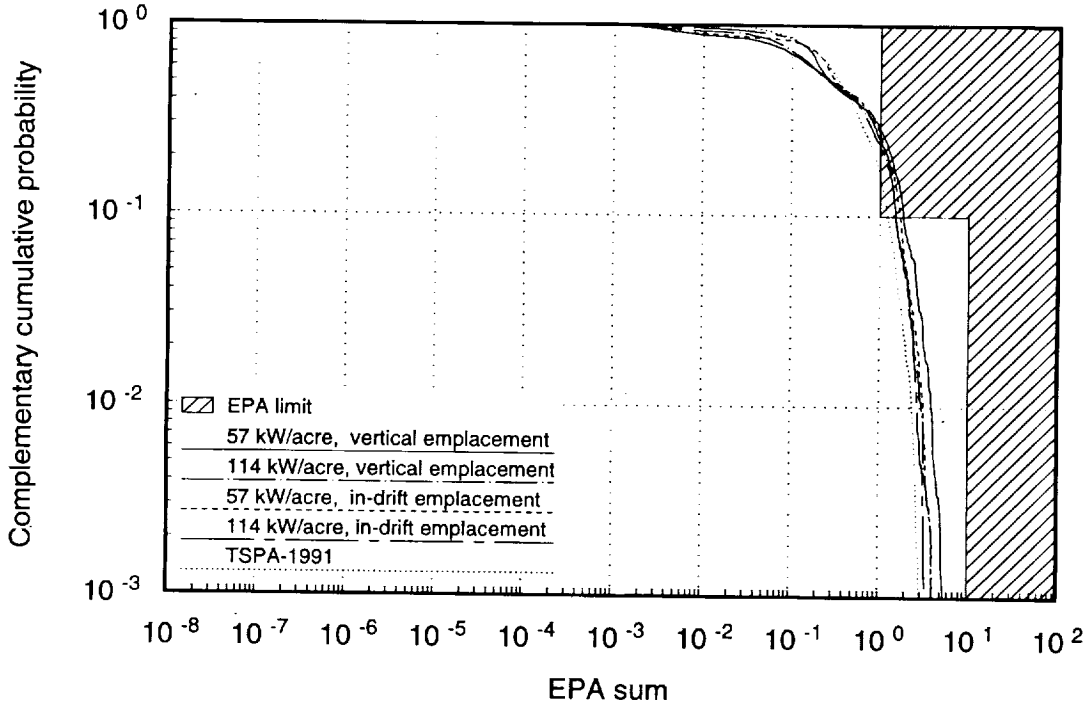

Figure 18-11. CCDFs of normalized cumulative release over 10,000 years. Composite-porosity model used for UZ flow and transport.

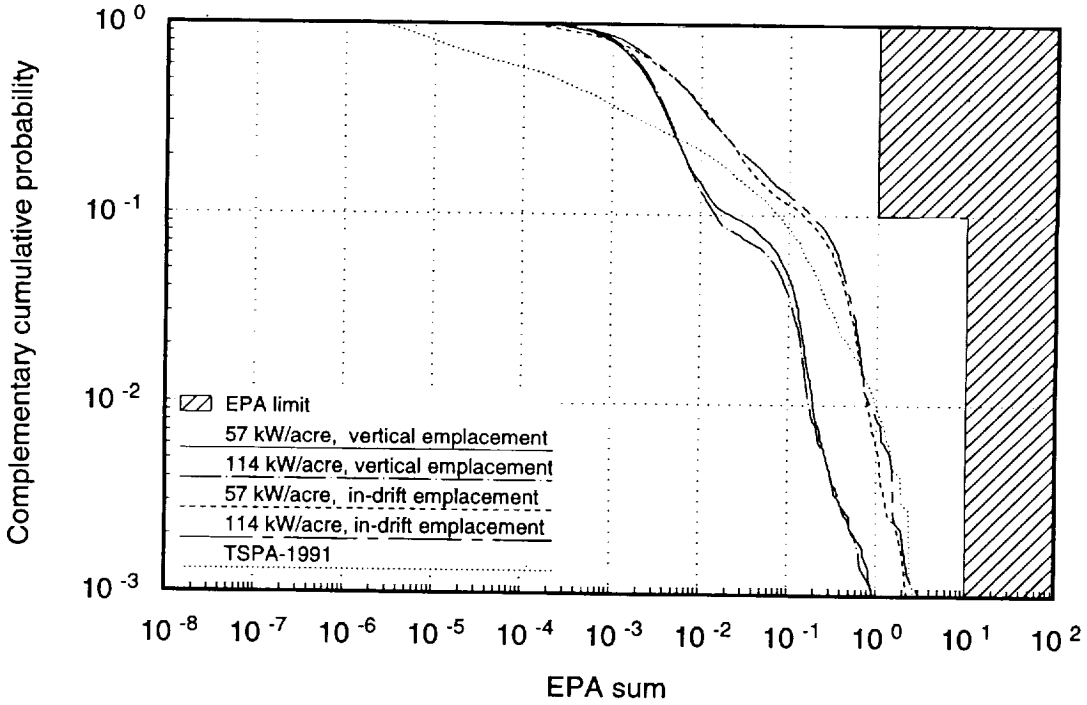

Figure 18-12. CCDFs of normalized cumulative release over 10,000 years. Weeps model used for UZ flow and transport.

combination. The TSPA-1991 curve is rather different from any of the TSPA-1993 curves, but the probability of higher releases is comparable to that shown by the new curves.

18.4 Conclusions from the TSPA-93 study

Gaseous releases are still the dominant component for nominal-condition composite-porosity releases over 10,000 years. However, in 1,000,000 years there can be significant releases from both gas and groundwater transport. Over 1,000,000 years, releases and doses are less dependent on the transport barriers provided by the geologic isolation of the repository than they are on water-flow patterns through Yucca Mountain contacting the source and on the release rate of radionuclides from the source.

Human-intrusion activities are not a major contributor to overall releases. Until a better evaluation of future human activities can be made, these results should only be used as relative indicators of repository design issues. Aqueous releases from interaction between the waste and a magmatic intrusion are also not significant. When the probability of occurrence is considered, the contribution to total-system performance is even less important.

Waste-package failure is dependent on the combination of temperature and water contact. Based on the parameters used in the corrosion model, little differentiation can be made between the waste-package designs, from the standpoint of corrosion resistance. From the standpoint of the weeps aqueous-flow and human-intrusion performance, the larger in-drift waste packages provide a larger "target area" for the respective interactions (weeps or drilling impinging on the waste package).

The different effects of the alternative thermal-loading configurations were controlled by the simplifications and limiting assumptions. The combination of thermal effects and water contact dominated, and the result is that responses were largely the same for both thermal loadings, and differed only by the timing of their occurrence. The performance effects of alternative thermal loadings may not be significant.

Inclusion of the results of a detailed 3-d model of the saturated zone near Yucca Mountain represents a distinct improvement over prior TSPA analyses. The structure of the breakthrough curves and the structure of the contaminant plumes, which vary markedly with depth below the water table, imply that 3-D analyses give a much different picture of flow (and transport) than would have been anticipated from past 2-D models.

Interpretation of the results of TSPA-93 must recognize some of the limitations:

- Excluding the barrier effects of the cladding from the source term may be overly conservative; further, inclusion of the properties of cladding might discriminate among some of the thermal profiles used in the analyses.

- The geochemical conditions inside a waste package were not explicitly modeled; far-field geochemical values were used because of the lack of more applicable numbers.

- Diffusive releases from the waste package were not included in the YMIM model; for many near-field environmental conditions, this process may be important.

- Abstractions of the hydrothermal models may have prevented us from testing some important issues, such as potential improvements to repository performance that may be gained by relying on repository heat release to produce an extensive and long-lived dry-out zone surrounding the repository.

- Some waste-alteration mechanisms from volcanic processes were not included in the source term.

- In view of the uncertainties in the calculations, the releases should not be used as discriminators among the thermal/emplacement alternatives.

This iteration of the Yucca Mountain TSPA has produced a number of enhancements of capabilities and models over TSPA-91:

- A mechanistic model to approximate waste-package degradation has been included. Results are sensitive to the parameters of the model.

- Approximations for coupled thermal–hydrologic processes have been included. Both aqueous and gaseous transport models include these coupled processes.

- A systematic database of stratigraphic and hydrologic rock properties has been established; geostatistical realizations of one-dimensional stratigraphic rock-column representations are now available for use in analyses.

- Climate-change effects have been added to the flow and transport models.

- Drinking-water doses are now estimated.

- The saturated zone is abstracted from three-dimensional models.

- The radionuclide inventory reflects current assumptions regarding fuel burnup and decay, and waste-receipt schedule; both spent-fuel and high-level waste have been included in the inventory.

Chapter 19
Recommendations

The need for additional data should be obvious from the preceding chapters. What is not necessarily obvious is which data are most important—what priorities should be given to data collection. In this chapter we discuss recommendations for data gatherers, experimenters, and repository designers. We also present some observations concerning impacts of possible regulation changes on performance assessment. In the next chapter we discuss recommendations for future work on total-system performance assessment (including the detailed modeling that feeds into it). The recommendations are based on our release results and sensitivity studies; it is important to keep in mind that the results are preliminary. Some of the recommendations are contingent upon which of our UZ flow models is used or upon the nature of expected regulation changes (see Public Law 102-486, 1992); those contingencies will be noted.

An initial comment on the site-characterization program is that, if the radioactive-release standard changes to a standard based on individual dose rates over a time period much longer than 10,000 years, significant changes in the priorities of the site-characterization program may be needed. With releases regulated by 40 CFR Part 191 (EPA, 1985), the emphasis of the program has been on the natural barriers. Radionuclide transport times greater than 10,000 years would enable the site to meet 40 CFR Part 191. With a regulation based on peak individual dose rates, there would have to be more emphasis on radionuclide release rates. This does not mean that the natural barriers are unimportant, but they are important in different ways. Peak dose rates are basically affected by two things—the source release rate and the amount of dilution after release. The amount of dilution is a property of the natural system that would have to be characterized, and the natural system has important interactions with the engineered system to produce the radionuclide release rates. For example, the amount of water available for container corrosion and releases, the distribution of water among the containers, and the geochemistry of the near field are all crucial to prediction of release rates. Radionuclide transport time is not particularly important to a calculation of peak dose rate unless the transport time is greater than the radionuclide half-life (two million years for ^{237}Np). If the standard is changed to an individual-dose standard but the regulated time period remains at 10,000 years, there would be less impact on the site-characterization needs.

19.1 Site data

Our recommendations regarding site-data needs come from our nominal-condition results (Chapters 14 and 15). The human-intrusion results (Chapter 16) are largely site-independent and the volcanism results (Chapter 17) appear to be insignificant compared to the others.

An important caveat in identifying parameters of importance is that the sensitivity analyses we have performed are not comprehensive. Nonlinear systems can behave in complicated, unexpected ways, and our sampling (300 or 1000 samples distributed throughout the parameter space) could be too coarse to discover some types of behavior. Also, important behaviors could be left out of our models. A simple example is the separate investigation of the composite-porosity and weeps models. It is entirely possible that the Yucca Mountain flow system could behave like the composite-porosity model under some conditions (perhaps low infiltration) and like the weeps model under other conditions (perhaps high infiltration). If this were the case, then the system parameters that control the switching between the two flow regimes would be vitally important but we would not know that from our analysis. Thus, it is important to gather data that could shed light on flow regimes at Yucca Mountain (past and present), in addition to measuring parameter values for input into existing models.

The most important feature of our nominal-condition results is the substantial difference between the results of the two flow models, composite-porosity and weeps. Thus, we believe that the number one priority is to determine the model that best describes unsaturated-zone flow at Yucca Mountain.

- Look for evidence of weeps (flowing fractures) at present and in the past.
- If weeps or paleoweeps are found, characterize their size (amount of water carried), connectivity, orientation, and frequency and duration of flow. Isotopic dating of fracture coatings and fillings would be very useful.

The largest 10,000-year releases in our calculations continue to be (as in TSPA-91) gaseous releases of ^{14}C for the composite-porosity model. Thus, with 40 CFR Part 191 as the controlling regulation, it is important to characterize gas flow and ^{14}C retardation better.

- Characterize gas flow and ^{14}C retardation. More data are needed on the spatial distribution of bulk permeability throughout Yucca Mountain, and on adsorption of carbon dioxide to tuff. Rock layers with high moisture saturation should be investigated to determine whether or not they block gas flow. Pore-gas-composition data are needed to evaluate the degree of connectivity of the Topopah Spring welded unit with the atmosphere. These recommendations are contingent upon the governing regulations. With

40 CFR Part 191 or a regulation based on population doses, ^{14}C releases are important; with a regulation based only on individual dose rates, ^{14}C releases would not be important. It should also be noted that improvements in EBS modeling, or additional engineered features to retain ^{14}C, could reduce the importance of ^{14}C transport time.

- The usefulness of bulk-permeability measurements goes beyond their application to ^{14}C transport time. Bulk permeability is useful in characterizing the fractures for water flow, and it is potentially an important parameter to thermal modeling if advective heat transfer is significant (Ross *et al.*, 1993; see also Chapter 24 of this report). In addition to on-site measurements of large-scale gas permeability (for example, by measurements of barometric-pressure fluctuation), pump tests at wells where Yucca Mountain's unsaturated-zone units are in the saturated zone would be useful in establishing large-scale fracture permeability.

The most important quantity for composite-porosity-model aqueous releases is the percolation flux. Thus, we put it high on our priority list.

- Characterize percolation flux, both now and in the future. Characterization of future climates is important, but the quantities usually studied—precipitation and surface temperature—are only of interest to us insofar as they affect percolation. Variations in water-table height caused by climate changes are also important. These recommendations are most important if the composite-porosity model is correct. In the weeps model and the composite-porosity gaseous-release model, percolation flux is important, but less so.

The other quantity identified as high-priority is the amount of dilution in the saturated zone.

- Characterize saturated-zone flow, and especially its dilution capability (horizontal and vertical dispersion). This item is very important for calculations of individual dose rate. For calculations of cumulative release, as in 40 CFR 191.13, or for calculations of total population dose, saturated-zone characterization is less important.

- Two alternative models of the saturated zone were developed for this TSPA (see Chapter 11). Calibration required introduction of reduced permeability for Solitario Canyon fault and Drill Hole Wash fault for both models. The diversionary model required an estimate of coupling between the tuff and carbonate aquifers as well. None of these hydraulic properties is known. It is suggested, therefore, that priority be given to acquisition of these properties.

- We need to know the effect of climate changes on saturated-zone flow and dilution. Information on ancient water-table heights and flow can be obtained by isotopic dating and evidence of geochemical alteration. A systematic search for paleosprings in the vicinity of Yucca Mountain should be undertaken.

- We need to understand the UZ/SZ coupling. At present it appears likely that recharge at Yucca Mountain is negligible and the water-table height and flow volume are determined by processes at a distance rather than by processes local to Yucca Mountain. Is the same true under wet-climate conditions, or would there be sufficient recharge at Yucca Mountain to affect the local saturated zone?

Many simplifying assumptions were made for our models and, in many cases, their effect on the results is unknown. Areas that may be important include

- colloid formation and transport,
- matrix/fracture coupling,
- multidimensional flow effects, and
- persistence of flow paths through time.

To close out this section, we would like to emphasize the importance of the performance-assessment data base (see Chapter 7). The data base should be maintained and, as new data become available, they should be analyzed (not a simple task) and put into a form that is usable for PA calculations. Some issues related to data completeness and analysis are:

- Additional drillholes (with associated measurement of hydrogeologic properties) are needed, especially in the western and southern parts of the repository area.
- Research is needed on scaling of properties from the scale of measurement (usually small core samples) to the scale appropriate for any given computation (typically mesh blocks with dimensions of tens of meters).
- Additional information is needed on heterogeneity and spatial correlation for geostatistical modeling of properties.
- Additional information is needed on cross-correlations among parameters.
- The rock-matrix saturated hydraulic conductivities reported for drillhole UE25a-1 (Anderson, 1981) had a significant effect on our distributions of matrix saturated conductivity, which, in turn, had important effect on our results for percolation and container

wetting in the composite-porosity model. The UE25a-1 conductivities should be examined to determine whether they are reasonable values, are unrepresentative of values within the repository block, or are flawed in some way. In addition, alternative methods for averaging the data (e.g., harmonic averaging) should be investigated to determine whether outlying data are dominating the derived distributions unrealistically.

- Assumptions about backfill are important to our results, especially for the in-drift cases. Thermal and hydrologic properties of crushed-tuff rubble (and any other proposed backfill material) should be characterized.

- Research is needed on hydraulic characterization of unsaturated fractures. For this TSPA, we used a simple model based on bulk permeability, fracture frequency, and fracture orientation. Additional data are needed on these quantities, but we also need to know the appropriate model for fracture saturation, desaturation, and conductivity.

- Research is also needed on hydraulic characterization of the rock matrix. Is the van Genuchten/Mualem model that we are currently using a good choice, or would another model (such as a gamma-function model) be better?

- Characterization of fault-zone hydrogeologic properties is needed.

19.2 Waste-package data and near-field processes

Container wetting and corrosion and releases from waste packages are very important to the aqueous- and gaseous-release results (and the near-miss human-intrusion results). Many of the near-field processes are poorly understood and require testing so that we can improve our models and parameter values.

Near-field interactions involve complex coupled processes. To develop reliable models of such processes and the parameters that would go into the models, integrated testing is needed in the following areas:

- waste-package water contact including host rock, backfill, and heated container material under both saturated and unsaturated conditions;

- radionuclide transport out of a degraded container, through backfill, and into host rock;

- near-field coupled thermal-mechanical-hydrologic-chemical processes, including

  - formation and shedding of condensation caps,

  - penetration of water into a "boiling" zone,

- thermal, mechanical, and chemical alteration of flow properties, and
- rewetting after the thermal period; and

- interaction of "man-made" materials (especially grout, concrete, and steel) with natural and engineered system components.

Heater tests should be performed under wetter conditions representative of possible future climates (e.g., at Rainier Mesa) in addition to tests at Yucca Mountain itself.

A better understanding of container corrosion and waste-form alteration is needed. We recommend further work in the following areas.

- Study container corrosion under realistic conditions. Temperature dependence and the transition from non-aqueous (including steam) to aqueous processes need to be understood better.
- Study the possible reduction of corrosion by galvanic effects.
- Study waste-package internal chemistry. In particular, determine solubilities and fuel-alteration rates under realistic conditions.
- Study cladding degradation, particularly temperature-dependent processes.

19.3 Repository and waste-package design

Recommendations for repository and waste-package design come from our human-intrusion results in addition to the nominal-condition results. It is important to note that there is no substantive difference in our results for the four repository cases studied; however, all four cases are highly idealized. There is up to an order of magnitude difference in the results, but in comparison with 40 CFR 191.13, either all four cases are below the EPA limits or all four cases exceed the EPA limits, depending on the release mechanism. The calculated peak dose rates are all relatively high.

- The SCP thermal goals should be re-examined to determine if they should be kept. (Note that three of the four analysis cases considered exceed one or more of the thermal goals.)
- The biggest difference in the performance measures for the repository cases is a result of the difference in container "target size." Vertical container emplacement presents a smaller target for drilling or for vertical flowing fractures. Therefore, our results suggest that vertical emplacement is preferable.

- According to the models we used, there is no significant increase in container lifetime provided by a 10-cm mild-steel outer container. However, the temperature dependence of the corrosion processes is not well known and should be reviewed. Also, the possibility of cathodic protection resulting from two walls of different metals has not been examined.

- If possible, the repository system should be designed so that containers fail over a long period of time, rather than all tending to fail near the same time. The assumptions made for this study lead to predictions of large numbers of containers failing over a relatively short period of time when temperatures fall below 100°C.

- Container emplacement should be designed to reduce moisture contact with containers—for example, by borehole emplacement. For in-drift emplacement, backfill could possibly be engineered to control water contact.

- Projected internal waste-package temperatures should not be so high as to cause the fuel-rod claddings to rupture. Even if we are not certain that the cladding will contain radionuclides, it makes sense to promote its effectiveness. In our calculations, the thermal insulation of the backfill causes a severe rise in waste-package temperatures for the in-drift cases. Could the backfill be engineered to increase its thermal conductivity (without unacceptable alteration of the near-field geochemistry)?

- If possible, the waste packages should be designed to maintain long-term local reducing conditions (not for just a few hundred or thousand years).

19.4 Regulation

Based on our results and our experience in performance assessment, we have the following comments regarding impacts that regulatory changes could have on performance assessment for radioactive-waste disposal.

- Calculations of radiation dose require more information than calculations of cumulative release to the accessible environment. (1) For the latter, it is possible to neglect (i.e., not take credit for) the saturated zone, but for dose calculations saturated-zone flow must be well characterized. (2) Depending on how a dose standard is written, characterization of a much larger region may be needed. For 40 CFR Part 191, detailed characterization is only needed for the "controlled area" (though for many purposes a larger surrounding region must be considered). (3) Dose calculations may require additional characterization of the biosphere in the vicinity of Yucca Mountain (and biosphere characterization introduces additional uncertainty into the calculations).

- The calculated peak dose rates for Yucca Mountain are high because of relatively little dilution, but at the same time there is relatively low probability of someone being exposed to those high doses because of the aridity. The whole issue of individual vs. population doses enters at this point. Peak individual dose rates may be high while population doses are low. (Keep in mind, though, that the dose calculations are very preliminary, and the high individual doses calculated in this study could decrease upon further examination.) A reasonable approach might be a dual standard, having relatively high limits on individual dose rates coupled with limits on total population dose (or some surrogate, such as the EPA sum) to ensure that the population as a whole is protected.

- There are good reasons to consider time periods longer than 10,000 years in building a safety case since (1) a large portion of the first 10,000 years is dominated by transient thermal conditions not representative of "normal" conditions, and (2) the greatest environmental effects are often predicted to occur at times greater than 10,000 years. However, there is a tremendous increase in uncertainty as the time period increases, suggesting that quantitative calculations beyond 10,000 years should only be used as indicators of long-term performance, not as compliance measures. Also, a much greater effort is required to simulate longer time periods. Additional characterization work is required and, for this study, using a one-million-year period rather than a 10,000-year period increased the amount of computer time required for the composite-porosity calculations by a factor of four to five.

- Several processes with significant impact on repository performance will always be uncertain, and this fact should be reflected in the regulations. Specifically, future climates and percolation rates will always be uncertain. The time of container failures and the accompanying release pulses will always be uncertain, even if designed to fail at a given time. Chance simultaneous failure of a number of containers can produce a temporary spike in the release rate that results in high dose rates.

- Regulations should be written in a way that does not require predictions of future human behavior or technology, since humans are unpredictable. Where information about humans is necessary (such as population density or drilling rate, for example), the information, or a method for determining it, should be specified in the regulation.

Chapter 20
Future TSPA Work

Much work remains to be done on total-system performance assessment for Yucca Mountain. Many potentially important features, processes, and events have yet to be included in our models, and many model simplifications have not yet been evaluated to determine whether they cause us to underestimate releases.

In Chapter 11 of the TSPA-91 report, we discussed some of the limitations of that study and listed several areas where we wanted to improve our models and data. For TSPA-93, we made improvements in some areas, but many of the issues listed in Chapter 11 are still valid and are discussed either in this chapter or the previous one.

Following is a list of areas where more TSPA work is needed. We list improvements that need to be made to our computer models and simplifications that need to be reconsidered. Items related to data or design are listed in Chapter 19; here the discussion is limited to models. (The distinction is between work that the performance-assessment group would do vs. work that site-characterization or design groups would do.) We do not restrict the list to discussion of "total-system" simplified models, but also discuss the detailed modeling work that feeds into TSPA. The list is not exhaustive, but it does contain the areas that we think are most important and areas that we think should be worked on next.

20.1 General

- We need to work toward an exhaustive set of scenarios and eventually perform the calculations within one of the formal methods discussed in Chapter 8 of the TSPA-91 report. One potentially important scenario category that has not yet been considered at all is seismic events (tectonism).

- We should maintain an ongoing effort to validate the abstractions used in the TSPA.

- Parameter distributions and models should be updated as new information becomes available.

- We need to include other exposure pathways in our dose calculations. In particular, doses should be evaluated for human-intrusion scenarios.

- The effects of disturbing conditions such as volcanism, tectonism, and human intrusion on nominal-flow conditions should be investigated.

- Further study of the effects of heterogeneity is needed in all areas—effects on thermal modeling, source-term modeling, flow modeling, and transport modeling.

20.2 Thermal modeling

- The effect of different waste-stream, repository-layout, and emplacement assumptions on temperature and dryout should be investigated.
- The effect of different backfill assumptions should be investigated.
- A more consistent approach to predicting fuel-rod temperature is needed.
- A method of including uncertainty in the hydrothermal parameters is needed. (In this TSPA, temperature, dryout fraction, and dryout volume were treated deterministically.)
- Additional detailed modeling and improved abstaction are needed for hydrothermal effects:
  - What is the effect of thermal-mechanical-hydrologic-chemical couplings?
  - How does water penetrate into a "boiling" zone, and how far can it penetrate? (How large must the "dryout" region around a container be for the container to be "protected"?)
  - What is the relationship between the location of the boiling isotherm and the location of the dryout zone? In the "extended dry" concept, rewetting lags considerably behind cooling; in this study, we assumed no lag.

20.3 Source term

- We must develop models for the coupled thermal, mechanical, hydrologic, and chemical processes in the near field so that we can evaluate their effect on EBS releases and near-field flow and transport.
- Detailed modeling of near-field water flow and container wetting should be done.
- The use of phenomenological corrosion models in this study is a big improvement over past work, but additional improvements are needed:
  - a model for steam corrosion,
  - improved modeling of the transition from non-aqueous to aqueous processes,
  - models for interaction of water with a hot waste package, and
  - inclusion of galvanic effects.

In addition, the current corrosion models and input parameters should be reviewed for appropriateness, particularly the temperature dependence.

- The evolution of container condition after initial failure should be investigated. The waste container could be a barrier to transport of radionuclides out of a waste package and a barrier to transport of water into a waste package. A simple way to include some of the effects of the container would be to include transport through a layer of iron oxide in the source model (iron oxides sorb most radionuclides strongly—see Section 9.3.1—so such a layer could provide considerable retardation).

- Models for cladding degradation should be improved, particularly temperature-dependent processes. Reduction of releases by inclusion of cladding should be studied.

- Modeling of fuel alteration should be improved, especially the temperature dependence.

- Additional chemical effects should be included in the source models (e.g., effect of chlorine concentration on corrosion).

- Additional source submodels are needed for those nuclides that are present in the cladding and the fuel-assembly hardware. A source submodel for releases from glass waste is needed.

- A more complete radionuclide-behavior module should be incorporated into YMIM to account for decay chains properly.

- A model for diffusive releases should be incorporated into YMIM.

20.4 Aqueous flow and transport

- Additional study of climate change and its effects on percolation flux is needed.

- Hydrothermal effects should be incorporated into the flow and transport calculations in a consistent manner. In this study, hydrothermal effects are assumed to increase the water flux seen by waste containers in the source model, but the water flow in the composite-porosity model is not adjusted to include that extra flux. (In the weeps model, since transport time through the unsaturated zone is taken to be zero, the only possible effect of the extra flux would be on saturated-zone flow.)

- The effects of colloids—especially of plutonium and americium—must be studied. This requires a source model for formation of colloids and a model for transport of colloids. Because of the large inventory of these elements, even a small fraction that could be transported rapidly because of colloid formation could be important.

- Additional methods of parameter scaling should be studied.
- It may be useful to investigate methods for modeling radionuclide transport in addition to the use of K_d values.
- The effects on system performance of altered initial conditions due to repository construction and operation should be considered (for example, the effects of changes in saturation because of underground water usage or ventilation).
- Additional work should be done on incorporating cross-correlations into the TSA simulations. The sensitivity of the results to cross-correlations has yet to be evaluated.
- The geostatistical modeling of stratigraphy should be refined. Areas for improvement include using outcrop information to condition the simulations and addition of a zeolitic-material indicator. Geostatistical modeling of other properties should be investigated as well.
- Composite-porosity aqueous releases should be simulated using additional geostatistical realizations of the stratigraphy. Comparison of the results for several geostatistical realizations would give a first estimate of the amount of uncertainty in releases because of uncertainty in the stratigraphy.
- The effect of varying properties for the unsaturated-zone columns (for example, using different fracture properties in the column(s) representing the Ghost Dance fault or applying different amounts of percolation in different columns, depending on their topographic characterization) should be explored.
- The feasibility of incorporating multidimensional effects into composite-porosity TSA simulations should be investigated, perhaps using the method outlined in Section 23.2.1.
- The effect of fracture orientation on the probability of water contact with a container should be considered in the weeps model.
- Also in the weeps model, the possibility of aqueous corrosion and failure of containers not contacted by weeps should be considered.
- It may be worthwhile to investigate the performance consequences of combining the composite-porosity and weeps models in various ways. A combination could possibly have higher releases than either one does separately.

- Additional study of the saturated-zone models presented in Chapter 11 of this report is needed, and additional calibrated models should be developed to try to quantify the amount of uncertainty in effective saturated-zone velocity. The detailed three-dimensional models should also be used to study saturated-zone dilution and effects of climate change on saturated-zone flow (for example, higher water table).

- Effects of matrix/fracture coupling in the saturated zone must be investigated. If flow in the tuff aquifer is primarily in a few fracture zones, there may not be time for the matrix and fracture concentrations to equilibrate before the accessible environment is reached. Matrix/fracture coupling in unsaturated-zone flow should also be studied, but the weeps model is at least an attempt at exploring this issue.

- Methods for better integration of unsaturated-zone transport and saturated-zone transport in the aqueous-release simulations should be investigated.

- Effects on saturated-zone flow due to seismic, tectonic, and volcanic activity should be investigated. The direction and magnitude of regional groundwater flow could change significantly because of such events. These events are likely to be of low probability, but the probability has not been quantified.

20.5 Gaseous flow and transport

- The aqueous- and gaseous-release calculations should be linked by running them with equal values of common parameters, to avoid the inaccuracy of combining the releases without the proper dependencies.

- Additional detailed calculations are needed to determine the variation of ^{14}C transport time with variations in permeability of the different layers. In addition to variations in intrinsic permeability, gas permeability could be affected significantly by variations in saturation—a nearly saturated layer could impede gas flow, for example.

- It would be useful to have ^{14}C transport-time distributions for 114 kW/acre (and perhaps other thermal loads) in addition to 57 kW/acre.

- Incorporation of barometric-pumping effects (see Chapters 21 and 22) into the TSA simulations should be investigated.

20.6 Human intrusion

- Further effort should be made to determine the likelihood that commercially attractive natural resources are present at the site. The presence of attractive natural resources would imply that extensive drilling might occur. Since releases are strongly influenced

by the number of holes drilled, resource exploration could increase the likelihood of releases. On the other hand, if no attractive resources are present, the probability that drilling might occur should decrease, thus reducing the importance of human intrusion. As shown in Chapter 16, predicted 10,000-yr releases are well below the EPA limits in 40 CFR 191.13 if the EPA's drilling-frequency guidance is followed, so drilling frequency is only important if it is greater than the 3 boreholes per km^2 per 10,000 yr assumed by the EPA.

- It would be desirable to couple the near-miss part of the human-intrusion calculations with the nominal-release calculations, especially for long time periods (drilling releases from contaminated rock near degraded waste packages make a bigger relative contribution over 10^6 years than over 10^4 years).

- Drilling scenarios in which waste is introduced directly into the saturated zone should be reconsidered. Their consequences may be more important in terms of dose than in terms of cumulative release.

20.7 Basaltic volcanism

- The processes by which waste can be entrained by flowing magma should be investigated; these processes include sidewall erosion and thermal and mechanical stresses produced on waste containers by a propagating dike. Ranges of waste-particle sizes that can be transported in magma need to be determined.

- The kinetics of dissolution of UO_2, Zircaloy, and structural materials (e.g., stainless steel) in magma should be investigated.

- The interaction of dikes with openings and stress-altered regions of the repository should be investigated.

- Other scenarios, such as encapsulation of waste packages by magma, and the subsequent production of volatiles from the waste and dissemination of contaminants into the host rock, should be investigated.

Part VI

Ancillary Calculations

Chapters 21 through 24 discuss additional detailed modeling that was done as part of TSPA-93, but that was not incorporated directly into the system study. Some of this work supports the system study (for example, the discussion in Chapter 23 of the validity of one-dimensional modeling), but the work is primarily exploratory. It is part of the process, discussed in Chapter 3, of determining the important features, events, and processes. FEPs found to be significant will be incorporated into future system studies.

Chapter 21 contains a discussion of barometric pumping as a mechanism to facilitate transport of gaseous radionuclides to the surface. Chapter 22 contains a discussion of barometric pumping as a mechanism to transport moisture out of the mountain. Chapter 23 contains a discussion of the validity of representing two-dimensional unsaturated groundwater flow by one-dimensional calculations under several conditions. Chapter 24 contains a discussion of hydrothermal calculations exploring the effects of fracture conductivity on predicted dryout caused by repository-generated heat.

Chapter 21
Barometric Pumping of Contaminated Gases Through Unsaturated Fractured Rock

(Nilson, Martinez)

Barometric pressure variations cause oscillatory gas motions in permeable rock formations. During falling barometric pressure, gases are drawn out of the ground, whereas rising barometric pressure forces atmospheric air into the formation. The associated subsurface pressure variations have been monitored at a number of sites, with the data used to infer the pneumatic diffusivity and permeability of the intervening medium (Snoeberger *et al.*, 1974; Weeks, 1978 and 1987; Burkhard *et al.*, 1987). Such measurements have indicated that the bulk permeability of the volcanic rocks at the proposed Yucca Mountain Repository is as great as 10-100 darcies even though the permeability of core samples is no greater than 10^{-6}-10^{-3} darcies. This disparity between large- and small-scale permeability suggests that fractures are responsible for nearly all of the large-scale permeability.

The presence of fractures greatly increases the amplitude of gas motions driven by barometric pressure variations. This is because fractures serve as the breathing passages for all of the subsurface air volume which, in general, exceeds the fracture volume by one or two orders of magnitude. Thus, even though a barometric pressure decrease is typically no greater than 10-20 millibars (i.e., 1-2%), the associated volumetric expansion of all the subsurface gases is sufficient to sweep upward a large fraction of the gas residing within the fractures. Accordingly, parcels of gas within a fracture may be displaced a significant fraction of the formation depth during a single barometric cycle lasting only 1-5 days. These gas displacements carry with them contaminant species in the manner depicted schematically in Figure 21-1.

Successive cycles of barometric pumping will have a cumulative effect when fractures or preferential pathways are present. During an upstroke of motion, some of the contaminant which travels rapidly up a fracture will diffuse into the surrounding porous matrix and remain there, at a relatively high elevation, throughout the next downstroke of motion. Reverse diffusion of this contaminant from the wall back into the fracture will then occur during the next upstroke, and the vertical flow will carry it higher. In essence the porous walls of the formation provide a temporary storage location where contaminants can reside between successive cycles of upward motion.

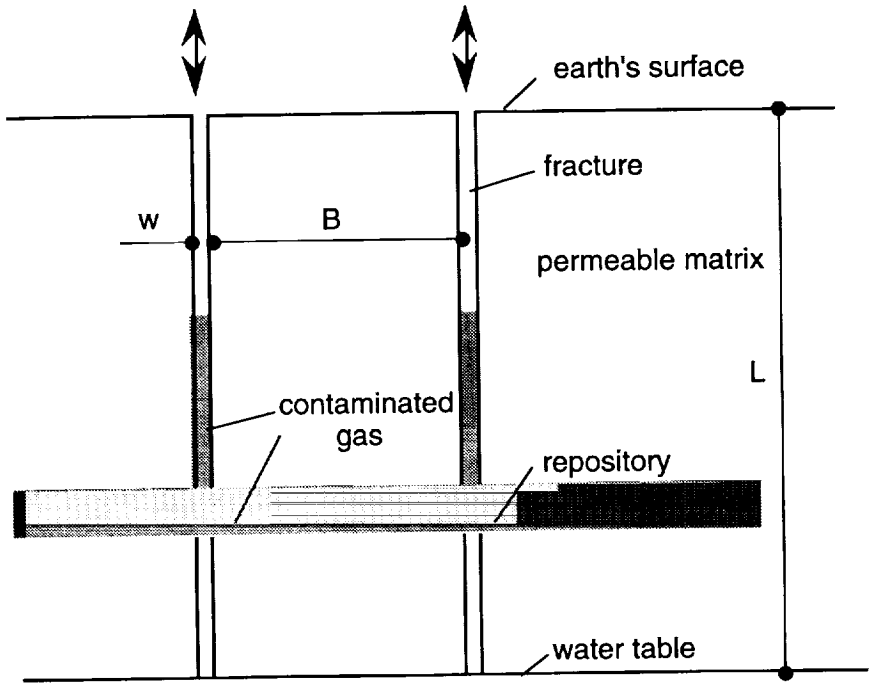

Figure 21-1. Schematic of barometric pumping in a fractured permeable medium. Cyclical changes in barometric pressure induce oscillatory gas flow along fractures. The fracture spacing, B, is actually small compared to breadth of repository, and the fracture aperture, w, is small compared to the fracture spacing.

Contaminated gases may be transported through hundreds of meters of fractured rock in a few months time as a result of this barometric pumping process (Nilson *et al.*, 1991). Such rapid transport has been experimentally observed at the Nevada Test Site in volcanic rock formations which are similar to those at Yucca Mountain (Nilson *et al.*, 1992). Thus, there is reason to believe that the same processes will be operative at Yucca Mountain.

A quantitative assessment of the barometric pumping process will contribute in three ways to the analysis of Yucca Mountain Repository.

- Subsurface pressure measurements provide a passive means of learning the large-scale permeability which is of critical importance in predicting the probable consequences of any transport process, barometrically driven or otherwise. Such measurements are currently being conducted by the U.S. Geological Survey.

- Barometric pressure variations may be important in the transport of hazardous gases released from the repository. The remainder of this chapter will provide

estimates of the rate of release of contaminated gases to the atmosphere in the absence of repository-induced thermal effects. These results can then be compared with those obtained for other transport processes (e.g., Ross *et al.*, 1992) to determine which considerations are likely to dominate during different periods of the repository life.

- Barometric transport of water vapor will influence the overall water balance of the mountain. This is important because a net downflow of moisture could carry radionuclides from the repository down to the water table. In the next chapter we will estimate the vertical flux of moisture which results from barometric pumping. Those results are intended to provide guidance in assessing the current state of the mountain and in judging the relative importance of the various physical processes which may influence the repository performance.

All of these issues are directly relevant to estimating the probable rate of release of radioactive materials from the repository to the surrounding environment.

21.1 Repository geometry and rock properties

A schematic diagram of Yucca Mountain is shown in Figure 21-2 (Ross *et al.*, 1992). The proposed repository depth is roughly 400 m which places it about 200 m above the static water level. Although the stratigraphy includes a number of distinct subunits, it is reasonable for present purposes to only distinguish between the three major units shown in Figure 21-2. Moreover, there is considerable similarity between the upper Tiva Canyon unit and the lower Topopah Spring unit. Both are welded tuffs which are heavily fractured and thought to have a bulk permeability on the order of 10-100 darcies (Montazer *et al.*, 1986; Ross *et al.*, 1992).

By contrast, the intervening Nonwelded Paintbrush unit is more sparsely fractured and is believed to have a permeability of 0.01-1.0 darcy (Montazer *et al.*, 1986). Subsurface measurements of barometric pressure response reported by Montazer *et al.* (1986) clearly indicate the ability of this unit to impede the vertical flow of gas. However, the available measurements are too sparse to rule out the possibility of much greater vertical permeability in other locations, particularly since borehole measurements may not provide a reliable indication of the large-scale vertical permeability associated with vertical fractures. Also, the nonwelded unit is only ~30 m thick, suggesting that it may be a somewhat tenuous barrier when viewed in a geologic framework.

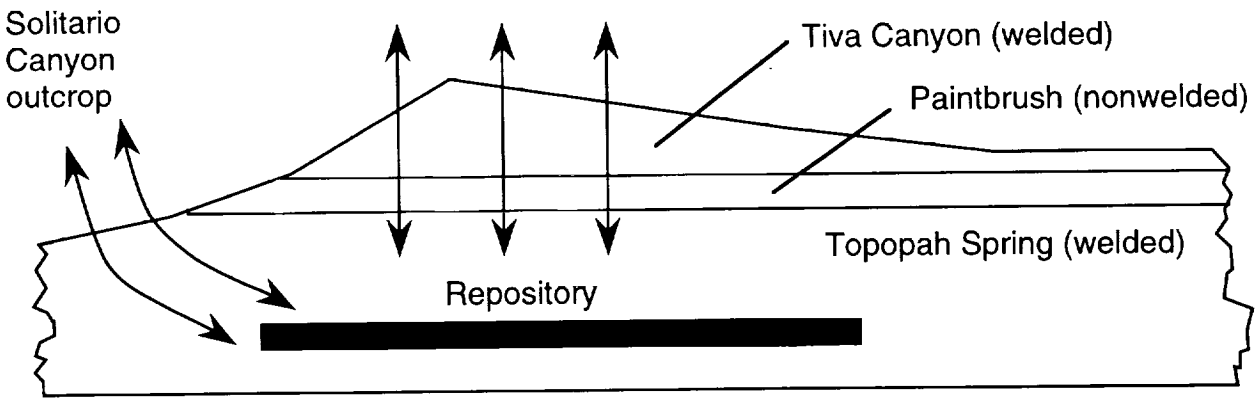

Figure 21-2. Schematic of proposed Yucca Mountain repository. Repository may breathe vertically through the paintbrush or horizontally through the Solitario Canyon outcrop.

Even if the nonwelded barrier near the mountain's top was entirely impermeable, the deeper layers may still breathe horizontally through the Solitario Canyon outcrop shown in Figure 21-2. Under this scenario of a nearly impermeable caprock, the barometrically driven gas flow within the repository region would be nearly horizontal. The streamlines would converge as the flow approached the outcrop owing to a reduction in the cross-sectional flow area by roughly 50%.

Thus, two alternative scenarios are of interest. Vertical breathing should dominate if the Nonwelded Paintbrush has a large enough permeability (>1 darcy). Otherwise, the primary flow direction will probably be horizontal. Since gravity plays no role in barometric transport, either situation can be approximated by a model which assumes that the breathing process is basically one dimensional in either the vertical or horizontal direction. The features of such a model are described immediately below.

21.2 Conceptual model

Our analysis is based on the dual-porosity, dual-permeability model shown earlier in Figure 21-1. Since the bulk permeability of the formation exceeds the matrix permeability by a few orders of magnitude, it is clear that fractures are the dominant pathways of the long range flow from the interior of the mountain to the surface. However, most (>90%) of the air-filled porosity resides within the matrix blocks, so the matrix will supply most of the gas which breathes in and out of the mountain. Moreover, it is the matrix permeability which controls the flow of that gas from the matrix blocks into the fractures. Thus, all of these features must be taken into account.

The simplest conceptual model which includes these basic features is that of identical, equally spaced fractures which separate slabs of matrix material having uniform permeability and porosity. Under this idealization, it is sufficient to focus attention upon a single representative fracture and the matrix material immediately adjacent to it. Flow and transport occur one-dimensionally (here, either vertically or horizontally) along the fractures and one-dimensionally in and out of the matrix material. We neglect the flow which moves through the matrix parallel to the fractures since the associated mass flow is smaller by the ratio of matrix permeability to bulk formation permeability ($<10^{-5}$).

Although the formation is ~70% saturated, water should have little influence on the bulk air flow in the formation except for the associated reduction of the gas-filled porosity and gas permeability of the matrix, here denoted as k_m and ϕ_m. Further, since the matrix is only partly saturated, the fractures are expected to be relatively dry, except during short periods after heavy rains. Thus, we will ignore the presence of water in calculating the air flow and contaminant transport induced by barometric pumping. Moisture transport will be addressed in the next chapter.

21.3 Governing equations

The gas flow along a fracture is governed by the following one-dimensional statement of mass conservation

$$\frac{\partial \rho_g}{\partial t} + \frac{\partial}{\partial y}\left(\rho_g q_{gy}\right) = -\frac{2}{w} F_{gx} \tag{21.1}$$

in which t is time and y is a position coordinate measured upward along the fracture. ρ_g and q_{gy} are the density and longitudinal velocity averaged over the cross-sectional area of the fracture, F_{gx} is the instantaneous mass flux from the fracture to the adjacent porous matrix, and w is the aperture of the fracture. The longitudinal flow velocity is determined by the well-known laminar-flow relationship

$$q_{gy} = -\left(\frac{w^2}{12\mu}\right)\frac{\partial P}{\partial y} \tag{21.2}$$

in which μ is the gas viscosity and P is the deviation of the gas pressure from the mean static head, $\rho_g g y$. No distinction is made between the geometric aperture in Equation (21.1) and the hydraulic aperture in (21.2). Also, a departure from laminar flow is not expected at the very modest velocities (<10 cm/sec) which are typically induced by barometric pumping.

The transport of a trace contaminant species along the fracture is controlled by a conservation equation which resembles the bulk continuity equation but is written in terms of the partial density, ρ_c of the contaminant gas.

$$\frac{\partial \rho_c}{\partial t} + \frac{\partial}{\partial y}\left(\rho_c q_{gy} + J_c\right) = -\frac{2}{w} F_c - \lambda \rho_c \tag{21.3}$$

Here, J_c is the diffusive flux of contaminant which depends upon the binary diffusion coefficient, D_0, the bulk density of the gas, ρ_g, and the gradient of the mass fraction, C, of contaminant

$$J_c = -\rho_g D_0 \frac{\partial C}{\partial y} \qquad \text{where} \qquad C = \frac{\rho_c}{\rho_g} \tag{21.4}$$

Although Equation (21.3) may generally include a radioactive decay process, that effect will be suppressed in the present calculations (i.e. $\lambda = 0$) with the understanding that the results so obtained can be post processed to incorporate the decay rate of any radioactive species. The remaining term in Equation (21.3) represents the flux, F_c, of contaminant from the fracture into the wall. It is controlled by the transport processes occurring within the matrix.

The governing equations which apply to the permeable matrix are similar to the fracture equations except that the mass exchange terms do not appear:

$$\phi_m \frac{\partial \rho_g}{\partial t} + \frac{\partial}{\partial x}\left(\rho_g q_{gx}\right) = 0 \quad \text{where} \quad q_{gx} = -\frac{k_m}{\mu}\frac{\partial P}{\partial x} \tag{21.5}$$

$$(1+R)\phi_m \frac{\partial \rho_c}{\partial t} + \frac{\partial}{\partial x}\left(\rho_c q_{gx} + J_{cx}\right) = -(1+R)\phi_m \lambda \rho_c \tag{21.6}$$

$$J_{cx} = -\rho_g \beta D_0 \frac{\partial C}{\partial x} \quad \text{where} \quad \beta = \frac{\phi_m}{\tau} \tag{21.7}$$

Here, x is measured into the matrix, q_{gx} is the gas velocity in that direction, and β is a correction factor which accounts for the fact that the diffusive flux J_{cx} is reduced because the porosity ϕ_m is less than unity and the tortuosity τ is greater than unity. Finally, R is a retardation factor which accounts for the fact that a contaminant gas may be stored in the liquid phase (e.g., dissolved $C^{14}O_2$) or adsorbed on solid surfaces. Retardation is not included in the equations for fracture transport because the fractures are dry and their

surface area is negligible compared to that of the matrix. However, transport along the fracture will be appropriately retarded by an increase in the exchange fluxes between fracture and matrix.

The flow rates of mass and contaminant from the fracture into the matrix can be written either as surface fluxes or as volume integrals of time derivatives.

$$F_{gx} = \left(\rho_g q_{gx}\right)_0 = \phi_m \int_0^{B/2} \frac{\partial \rho_g}{\partial t}\, dx \tag{21.8}$$

$$F_{cx} = \left(\rho_c q_{gx} + J_{cx}\right)_0 = (1+R)\phi_m \int_0^{B/2} \left(\frac{\partial \rho_c}{\partial t} + \lambda \rho_c \right) dx \tag{21.9}$$

These relationships can be readily derived by integration of Equations (21.5) and (21.6) from the fracture surface, denoted by subscript "0", to the centerplane of the matrix, $x = B/2$, where the fluxes must vanish because of symmetry. The integral form is advantageous in formulating a numerical scheme which is capable of treating the exchange terms in an implicit noniterative fashion.

The systems of equations is completed by assuming that the gas is ideal

$$P = \rho_g \Re T \tag{21.10}$$

and that the temperature T is constant. Since the contaminant gas is presumed to be a trace constituent, the gas constant in Equation (21.10) may be taken as that of air. We will further require that the pressure, P, and contaminant mass fraction, C, both be continuous across the fracture/matrix interface. This is equivalent to assuming that, at any elevation, the variations in these quantities across the fracture are small compared to the variation across the matrix, which should hold true in the problem of interest.

To facilitate an efficient numerical solution, the continuity equations for the fracture and matrix are each combined with their respective momentum equations to obtain the following pair of diffusion equations for the gas pressure.

$$\frac{\partial P}{\partial t} = \frac{\partial}{\partial y}\left(\frac{w^2}{12\mu} P \frac{\partial P}{\partial y} \right) - \frac{2\phi_m}{w} \int_0^{B/2} \frac{\partial P}{\partial t}\, dx \tag{21.11}$$

$$\frac{\partial P}{\partial t} = \frac{\partial}{\partial x}\left(\frac{k_m}{\mu\phi_m} P \frac{\partial P}{\partial x}\right) \tag{21.12}$$

These equations determine the pressure and velocity of the gas. In addition, the continuity equations for gas flow (21.1) and contaminant transport (21.3, 21.4) along the fracture can be combined to obtain the following equation for the concentration or mass fraction of contaminant

$$\rho_g \frac{\partial C}{\partial t} + \rho_g q_{gy} \frac{\partial C}{\partial y} = \frac{\partial}{\partial y}\left(\rho_g D_0 \frac{\partial C}{\partial y}\right) + \frac{2\rho_g}{w}\left(q_{gx}\left(C_f - C_w\right) + D_0 \beta \frac{\partial C}{\partial x}\right)_{x=0} \tag{21.13}$$

Here we use C_f and C_w to respectively denote the concentrations in the fracture and in the wall at the interface where $x = 0$. Since these concentrations are presumed identical, it is only the lateral diffusive flux which can directly alter the concentration in the channel. Equations (21.6) and (21.7) are combined in a similar fashion to obtain a partial differential equation for the contaminant concentration in the matrix.

In solving the preceding equations and presenting numerical results, we will use the symbol C to represent a scaled concentration which has been normalized by the maximum concentration appearing in the initial/boundary conditions. This rescaling does not alter the governing equations since the contaminant transport Equations (21.6, 21.7, and 21.13) are linear in C and the trace amounts of interest have a negligible influence on the total gas pressure and velocity.

21.4 Numerical procedure

The finite difference procedure described by Nilson and Lie (1990) is used to solve the foregoing equations. Extreme care was taken in formulation and testing of the method to ensure that the artificial diffusion in the numerical procedure would be small compared to the actual transport processes. This is particularly important in the present application because the net transport produced by many cycles of motion results from a relatively small difference between the upward and downward fluxes occurring on each of thousands of cycles of motion.

To guard against numerical diffusion errors, the advective fluxes in the fracture and the matrix are evaluated using the FRAM filtering remedy and methodology developed by Chapman (1981). Like the FCT (flux corrected transport) algorithms of Boris and Book (Rood, 1987), FRAM uses a second-order nondissipative explicit finite-difference scheme in regions where the concentration profile is smooth, and introduces a minimal amount of

dissipation only in those regions where the higher-order algorithm would produce unphysical oscillations.

Since the speed of pressure waves is generally much greater than the particle velocity of the gas, the pressure equations are solved by a time-centered Crank-Nicholson algorithm which remains stable and sufficiently accurate even when the time step is large compared to the time required for pressure waves to traverse a calculational cell. This, together with an integral evaluation of the transfer terms allows the present calculations to be completed with a reasonable expenditure of computing resources.

In the simulations reported here, the computational domain includes just one fracture and one adjacent half-slab of matrix material. This region is covered by rectangular mesh which usually has 120 cells along the fracture and 40 cells into the matrix for a total of 4800 cells. Exceptions to this gridding will be noted. Typically 150-300 time steps must be taken for each daily barometric cycle, such that 1-10 million time steps must be executed for a simulation covering 10-100 years. These runs require 5-50 hours of computing on a Silicon Graphics Indigo workstation.

21.5 Numerical simulations

Breathing simulations are now presented for a number of examples which are relevant to Yucca Mountain. In most examples, the medium has uniform properties and a depth of 600 m. At the onset of each calculation, a contaminant gas is presumed present at unit concentration within the repository region which is modeled as a porous horizontal layer 20 m thick at a depth of 400 m. This contaminant gas could represent any trace species which might be released from the repository.

The object of each calculation is to predict the rate of release of a representative "puff" of contaminant to the atmosphere. Since the transport equations are linear in concentration, this fundamental solution for a "unit" release can be used to predict the time history of contaminant release to the atmosphere for any prescribed sequence of release into the repository. Also, since the volume of contaminant species is expected to be very small (compared to the pore volume of the overburden), it is assumed that the release of the gas produces no local overpressure or, equivalently, that there is no upward displacement associated with the initial release into the repository. Thus, the upward transport is solely a consequence of barometric pressure fluctuations.

To drive the calculations, the barometric pressure is varied sinusoidally at the earth's surface, causing a vertical oscillatory flow along the fractures. In accordance with the Yucca Mountain measurements reviewed by Tsang and Pruess (1989), the period and peak-to-peak amplitude of the pressure variation are taken as 24 hours and 8 millibars,

respectively. Table 21-1 includes these configuration parameters as well as a set of material properties which are believed to be representative of the welded tuffs which comprise most of Yucca Mountain. Here we introduce a bulk permeability k_b which represents an area weighted average of the matrix permeability, k_m, and the apparent fracture permeability, $k_f = w^2/12$.

$$k_b = k_f \frac{w}{B} + k_m \frac{B-w}{B} \cong \frac{w^3}{12B} \tag{21.14}$$

After presenting the results for the "baseline" case of Table 21-1, consideration will be given to the influence of variable or uncertain parameters such as the bulk permeability and the fracture spacing of the medium.

Table 21-1. Parameters used in base case calculation of contaminant transport at Yucca Mountain.

Parameter	Symbol	Value
Formation depth	L	600 m
Fracture aperture	w	0.783 mm
Fracture spacing	B	4 m
Bulk permeability	k_b	10 D
Matrix permeability to air	k_m	0.1 mD
Air-filled porosity	ϕ_m	0.04
Binary diffusion coefficient	D_o	$2 \cdot 10^{-5}$ m^2/s
Diffusion strength	$\beta = \phi_m/\tau$	0.004
Retardation factor	R	0.0
Pressure amplitude (mean to peak)	ΔP	4 millibars
Mean pressure	P_o	800 mbars
Period of pressure oscillation	T	1 day

21.5.1 The baseline case

Concentration profiles for the baseline case are shown in Figure 21-3. The initial profile has unit amplitude within the repository region from 400-420 m. After 40 years of barometric pumping, the contaminant has reached about half way to the earth's surface. At 120 years the contaminant has spread all the way across the medium and the peak concentration has fallen to roughly 10% of the initial unit value. By comparison, if all of the initial contaminant were uniformly distributed across the medium the concentration would be roughly 3%. The concentration profiles displayed in Figure 21-3 indicate the conditions along the vertical centerline of the porous slabs. These concentrations vary only

slowly in time, even though there are daily perturbations of the concentration in the fractures owing to the daily barometric cycles.

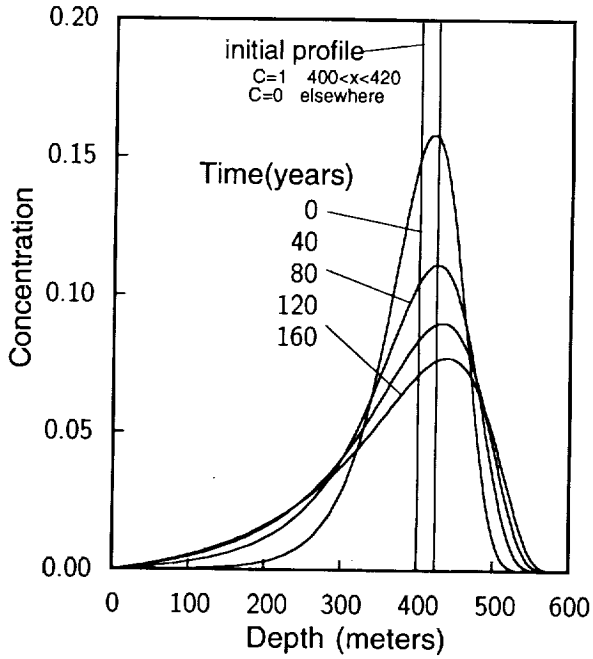

Figure 21-3. Concentration profiles for typical Yucca Mountain parameters.

The time history of gas exchange and contaminant release to the atmosphere is presented in Figure 21-4. The uppermost solid line, labeled $\dot{V}^*$, indicates the rate of exchange of gas between the porous formation and the atmosphere. It is calculated by integrating the outflow velocity from a typical fracture over the most recent barometric cycle of period T, thereafter normalizing by the total gas volume within the corresponding unit cell ($V_0 = L(w + \phi_m B)$) and, finally, multiplying by the number N of barometric cycles occurring over 1 year.

$$\dot{V}^* = \text{fractional outflow of gas per year} = \frac{Nw}{V_0} \int_{t-T}^{t} \max(q_{gy}, 0)\, dt \qquad (21.15)$$

The calculated value of $\dot{V}^* = 0.3$ in Figure 21-4 indicates that the volume of gas which breathes out to the atmosphere and back into the medium over a year's time is 30% of the gas-filled pore volume. The constancy of $\dot{V}^*$ indicates that each cycle has essentially the same gas flow, since the trace gas has a negligible influence on the bulk density and velocity of the gas. Note that the above integration only includes the incremental outflows of gas ($q_{gy} \geq 0$) which occur when the barometer is falling. Since equal amounts of gas are

inhaled during periods of rising barometer, there is actually no net exchange of gas between the medium and the atmosphere over any sequence of complete barometric cycles. Even so, the magnitude of the oscillatory gas flow is important because it serves as the carrier of a net outward flux of contaminant.

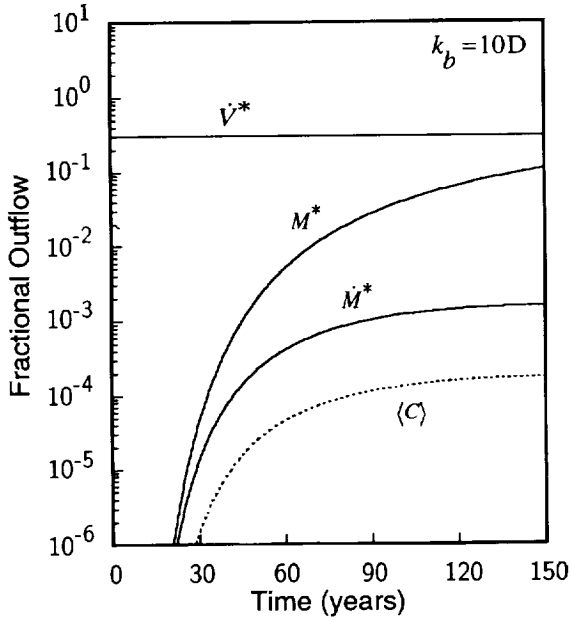

Figure 21-4. Normalized outflows for typical Yucca Mountain parameters.

The rate of contaminant release to the atmosphere is also presented in Figure 21-4. It is calculated by integration of the instantaneous advective outflow at the earth's surface, $C\rho_g q_{gy}$, over the most recent barometric cycle.

$$\dot{M}^* = \text{ fractional outflow of contaminant per year } = \frac{Nw}{M_0}\int_{t-T}^{T} C\rho_g q_{gy}\,dt \qquad (21.16)$$

In analogy with the earlier normalization of volumetric outflow, N is the number of cycles per year and $M_0 = C_0\rho_{g_0}\delta L_r(w+\phi_m B)$ is the amount of contaminant initially present in the repository layer having thickness $\delta L_r \approx 20m$ and initial concentration of unity.

Unlike the bulk flow of gas which produces no net flux over a full cycle, there is a net flux of contaminant into the atmosphere. During periods of rising barometer, $q_{gy} < 0$ and $C = 0$ since the incoming gas contains only a negligible amount of contaminant. During a falling barometer, $q_{gy} > 0$ and $C > 0$ since the gas at the surface is coming up from below

where the concentration is nonzero. Thus, the integral increases monotonically. It is seen that contaminant outflow approaches a constant rate of ~10^{-3}, indicating that 0.1% of the initial contaminant inventory is being released each year.

Within 100 years, the amount of contaminant released is ~10%, as indicated by the integrated outflow shown in Figure 21-4.

$$M^* = \text{cumulative contaminant outflow} = \frac{w}{M_0}\int_0^t C\rho_g q_{gy}\, dt \tag{21.17}$$

Although the numerical simulation ends at 150 years, it is possible to extrapolate into the future based on the expectation that the process will remain quasi-steady. The yearly contaminant outflow should then remain a nearly constant fraction, $\dot{M}^*$, of the current inventory, $(1-M^*)$. Accordingly, $d(1-M^*)/dt = -(1-M^*)\dot{M}^*$ which implies that the inventory decreases exponentially as $\exp(-\dot{M}^* t)$ and that

$$M^* = 1-\exp\left(-\dot{M}^* t\right) \tag{21.18}$$

Here we have taken the liberty of applying this quasi-steady solution for the entire time period, rather than beginning the integration at the time (~150 years) when steady state is achieved and about 10% of the contaminant has already left the medium. This adjustment is easy to make or, alternatively, the exponential solution may be viewed as a late-time complement to the early-time numerical solution. This exponential approximation avoids the need for running computations several times longer than the 40 hour runs presented here. The accuracy of the approximation is further addressed in a later section of the paper.

Finally, the dotted line shown in Figure 21-4 indicates the average concentration of contaminant in the effluent stream.

$$\langle C\rangle = \frac{1}{\rho_{g_0}}\frac{\int_{t-T}^{t}\rho_g q_{gy} C\, dt}{\int_{t-T}^{t}\max(q_{gy},0)\, dt} = \left(\frac{\dot{M}^*}{\dot{V}^*}\right)\left(\frac{M_0}{\rho_{g_0}V_0}\right) \tag{21.19}$$

It is seen to approach a nearly constant value of ~10^{-4} which is 300 times smaller than the average subsurface concentration of ~3%. This is to be expected because the contaminant concentration of the gases rising slowly through fractures cannot differ greatly from the

local concentration in the adjacent rock. Furthermore, the time-mean concentration in the wall rock must approach zero near the surface, as seen earlier in the profiles of Figure 21-3. Thus, it is only the slight disequilibrium between the instantaneous fracture concentration and the time-mean wall concentration which permits a net outflow of contaminant. That is why any prediction of barometric transport requires a double porosity model which accurately accounts for the disequilibrium between fracture and wall concentrations.

21.5.2 Comparison with Nevada Test Site experience

A comparative calculation is now presented which is identical to the preceding baseline case except that the bulk permeabiliy is increased from 10 to 50 darcies. This corresponds a 70% increase in the fracture aperture, since the bulk permeability increases as the cube of the hydraulic aperture. The fracture spacing and matrix properties are the same as before.

The selected bulk permeability of 50 darcies is typical of measurements made in large-scale experiments conducted at the Nevada Test Site (Burkhard *et al.*, 1987; Nilson *et al.*, 1992). This permeability was deduced by comparing surface pressure histories with corresponding subsurface pressure histories measured at a depth of 400 m within the rubblized regions produced by underground nuclear explosions. Since these rubblized regions, called chimneys, are greater than 100 m across, their pressure response is controlled by the bulk permeability of a very large column of overburden rock. This scale of measurement, which is comparable to the repository scale of interest, generally provides a larger estimate of the bulk permeability than do smaller scale borehole or laboratory experiments. Although there is some concern that the fracture-related permeability may have been enhanced by the underground explosion, there is one set of measurements which suggests that an explosion at 600 m causes only a modest alteration of the permeability in the uppermost 400 m rock which are sampled by the breathing experiments. Moreover, some of the borehole measurements at Yucca Mountain have indicated permeabilities as large as 50 Darcies and, presumably, greater permeabilities will be measured when larger scales are sampled by future experiments.

Figures 21-5 and 21-6 show the concentration profiles and ouflow histories for a medium having a bulk permeability of 50 darcies. The qualitative character of these results is very similar to those for the base case having a 10 darcy bulk permeability, but it is important to note that the time scale of the contaminant transport process has been altered by roughly a factor of ten. In recognition of this, the concentration profiles in Figure 21.5 are given at 4-year intervals, rather than the 40-year intervals of Figure 21-3.

Similarly, only 15 years is now required to release 10-20% of the contaminant to the atmosphere, as opposed to 150 years in Figure 21-4.

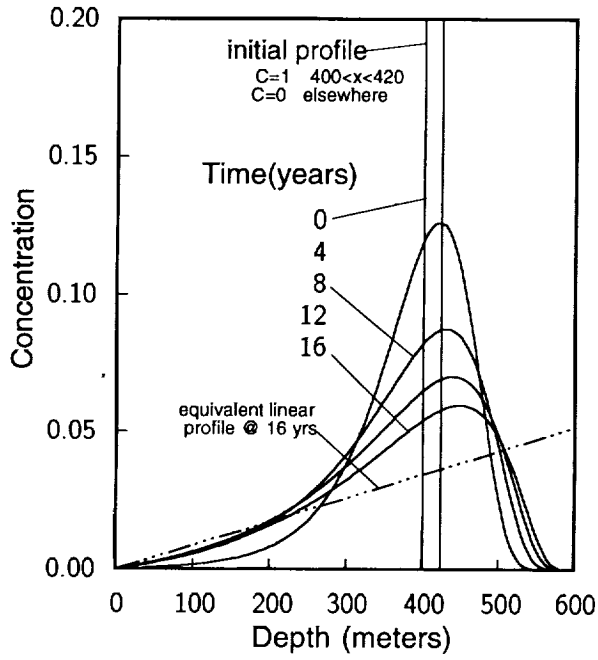

Figure 21-5. Concentration profiles for typical Nevada Test Site parameters.

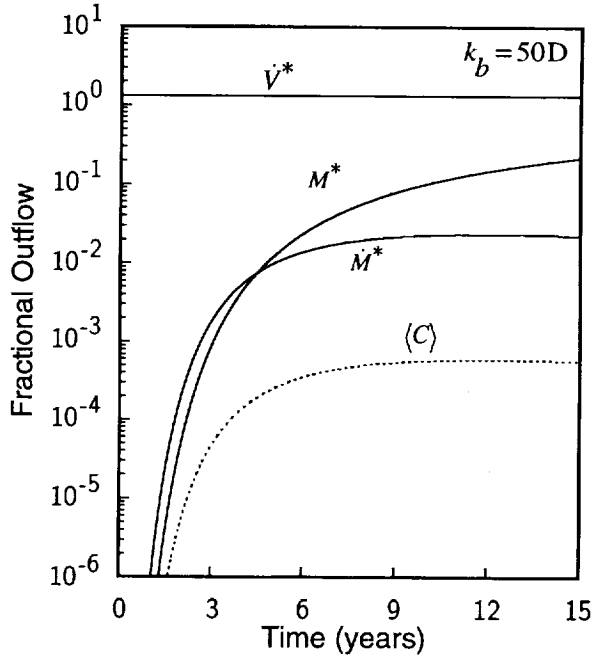

Figure 21-6. Normalized outflows for typical Nevada Test Site parameters.

The primary reason for the increased rate of transport is that the volumetric flow of carrier gas has increased by more than a factor of 3 for the prescribed five-fold increase of the bulk permeability, as seen by comparing $\dot{V}^*$ in Figures 21-4 and 21-6. Thus, the gas displacements along the fracture are increased by roughly a factor of three, which causes an order of magnitude increase in the rate of transport. This calculational outcome is consistent with a simple analytical model, presented later, in which the rate of contaminant transport increases as the square of the vertical displacement. The maximum attainable value of $\dot{V}^*$, corresponding to very large bulk and matrix permeabilities, is approximately 3.65, since there are 365 daily barometric cycles each having a pressure change of ~1% (ie. 8 millibar changes about a mean pressure of ~800 millibars). Thus, the value of $\dot{V}^*$~1.2 shown in Figure 21-6 is almost a third of the maximum. This suggests that further increases in permeability, bulk and/or matrix, could not increase the transport by more that one additional order of magnitude.

A maximum effluent concentration of $\langle C \rangle \sim 6 \cdot 10^{-4}$ now reaches the earth's surface within 5 years as indicated by the dotted line in Figure 21-6. This is about 3 times greater

than the maximum effluent concentration seen earlier for k_b=10D. Since the maximum subsurface concentration is on the order of $6 \cdot 10^{-2}$ at this time (Figure 21-5), there is roughly a 100 fold dilution associated with the transport process. This result is in keeping with earlier numerical calculations (Nilson *et al.*, 1991) and experimental observations (Nilson *et al.* 1992) of barometric transport at the Nevada Test Site.

21.5.3 Retardation effects

Both of the preceding calculations presume that there is no retardation of contaminant species, as appropriate for inert radioactive gases such as Krypton and Radon and for conservative tracer gases like those used in the previous barometric pumping experiments at NTS. However, other gases, most notably $C^{14}O_2$, are expected to be significantly retarded because they are soluble in the water which occupies 70% of the porosity. Ross *et al.* (1992) estimate that the equilibrium concentration (mass/total pore volume) of $C0_2$ in the pore water is roughly 30-70 times greater than that in the vapor phase. This effect is incorporated in the matrix transport equations (21.6 and 21.9) through the retardation factor, R, which increases the apparent capacitance of the medium.

To explore the influence of retardation, a simulation was run with R=10 and all other parameters the same as in the preceding calculation. Results are presented in Figures 21-7 and 21-8. As expected, the time scale of the transient is slowed by roughly a factor of 10 when R=10, as apparent in comparing Figures 21-6 and 21-8. However, it appears that the quasi-steady rate of contaminant transport is not as sensitive to retardation, since $\dot{M}^*$ and $\langle C \rangle$ in Figure 21-8 seem to be approaching asymptotes which are not far below those of the preceding case shown in Figure 21-6. This conjecture is further supported by the quasi-steady parameter studies which follow.

It is noted that the profiles in Figure 21-7 are not as smooth as those shown previously in Figures 21-3 and 21-5. This is because the number of zones along the fracture was reduced from 121 to 61 to gain a factor of four savings of computer time (the time step can also be doubled when the zones are twice as wide). To verify that this would not significantly degrade the solution accuracy, quasi-steady test calculations were run with 31, 61, 121, and 241 zones along the fracture, using the methodology explained in the next section.

21.6 Quasi-steady transport calculations

The simulations reported in the preceding section demonstrate that the barometric pumping process approaches a quasi-steady regime in which the fractional amount of contaminant released to the atmosphere is nearly the same for each successive barometric

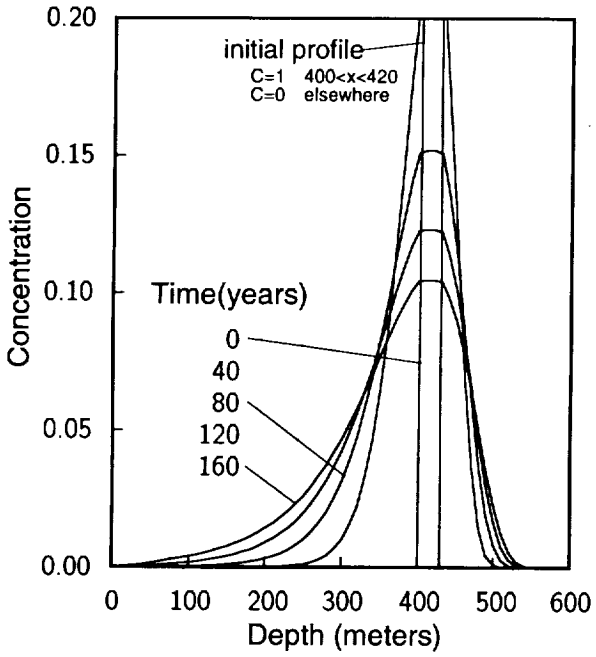

Figure 21-7. Concentration profiles for typical Nevada Test Site parameters with retardation (R=10).

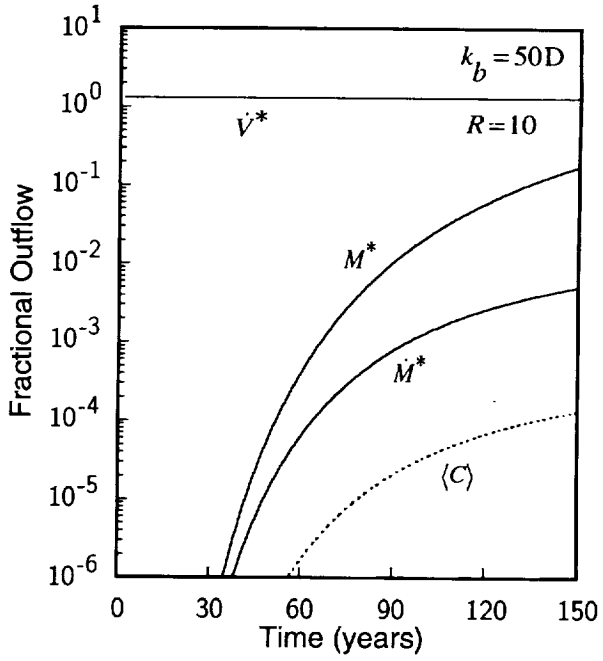

Figure 21-8. Normalized outflows for typical Nevada Test Site parameters with retardation (R=10).

cycle. This generally occurs by the time 10% of the contaminant inventory has been expelled to the atmosphere, suggesting that roughly 90% of the outflow can be predicted from a knowledge of the quasi-steady outflow parameter, $\dot{M}^*$, which has been identified as the reciprocal of the time constant for the exponential decay process of Equation (21.18).

A linear vertical gradient of the concentration is used as the initial condition for the quasi-steady analyses which follow. The initial concentration is presumed uniform across each horizon, since the time mean concentration in the matrix is, at any elevation, nearly the same as that in the fracture. This choice of initial conditions is based on the preceding simulations and others like them (Nilson *et al.*, 1991) which all appear to tend toward a relatively linear gradient as time progresses. For example, the concentration profiles in Figure 21-5 become nearly steady in the upper 200 meters of the medium, and the overall profile appears to be moving toward the linear distribution (shown dotted in Figure 21-5) which properly incorporates the remaining inventory of contaminant.

Figure 21-9 shows a comparison between the initial and final profiles of a 20-day simulation for the base case parameters of Table 21-1. This calculation was run with the same model as the earlier calculation in Figures 21-3 and 21-4 except that: (1) the initial profile is now linear and, (2) the concentration at the floor of the medium is now held fixed

at unity rather than prescribing that there be no vertical contaminant flux through the floor. By fixing the concentration at the floor we prevent the gradual drift of the linear profile which would otherwise occur during depletion of the subsurface inventory. Throughout the calculational period of 20 barometric cycles there is only a negligible change in the linear concentration profile, demonstrating the connection between linear profiles and quasi-steady behavior. Much longer runs confirm the same behavior.

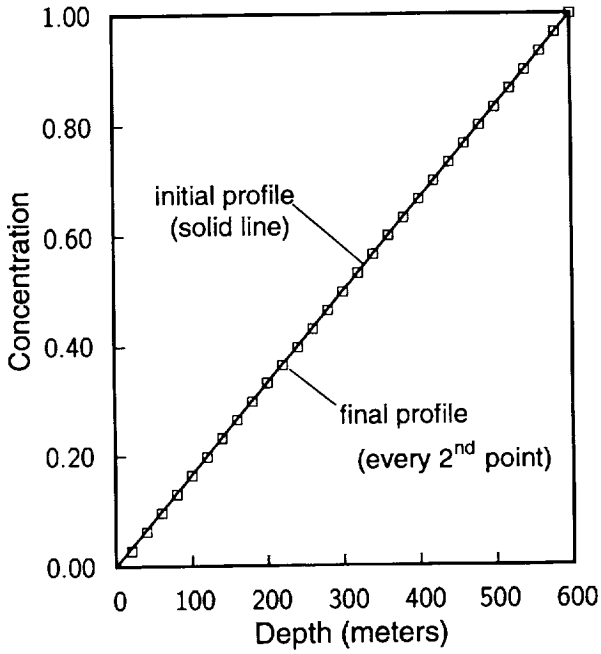

Figure 21-9. Concentration profiles for quasi-steady analysis with typical Yucca Mountain parameters.

The corresponding history of contaminant outflow in Figure 21-10 shows that the effluent flux, $\dot{M}^*$, becomes quasi-steady within just a few days when a calculation is begun with a linear profile. Moreover, the predicted value of $\dot{M}^* \approx .003$ in Figure 21-10 is quite consistent with the corresponding quasi-steady value of $\dot{M}^* \approx .002$ for the full simulation in Figure 21-4. The difference is attributed to the fact that linearity was never fully established in the complete simulation. In this context it is noted that the $\dot{M}^*$ associated with a linear profile is insensitive to the choice of unit concentration at the floor of the medium, since the outflow, $\dot{M}^*$, is normalized by the total amount of contaminant present and the transport equations are linear in concentration. However, the mean concentration in the medium is reflected in the average concentration of the effluent $\langle C \rangle$ which differs by more than an order of magnitude between Figures 21-4 and 21-10 because the ratio of mean concentrations is 0.5/0.03~170.

The primary advantage of performing quasi-steady calculations for linear initial profiles is that parameter studies can be performed with a huge savings of computer time since the required calculations span 15-150 days rather than 15-150 years. This approach is particularly beneficial in cases with weak transport and large retardation factors which would otherwise require 10-100 times more computation than the 50-hour runs which generated Figures 21-4 and 21-8. The same savings cannot be realized by simply increasing the magnitude of the calculational time step, because it is constrained by the time scale of barometric cycles and by the Courant limitation imposed by virtually all nondiffusive advection algorithms. The only shortcoming of the quasi-steady simulations is that they do not explicitly reveal the time required for the profile to spread across the medium. However, this can be estimated after the fact since the quasi-steady calculations do indicate the strength of the transport and this, together with a knowledge of the capacitance, can be used to estimate the time required to reach quasi-steady state.

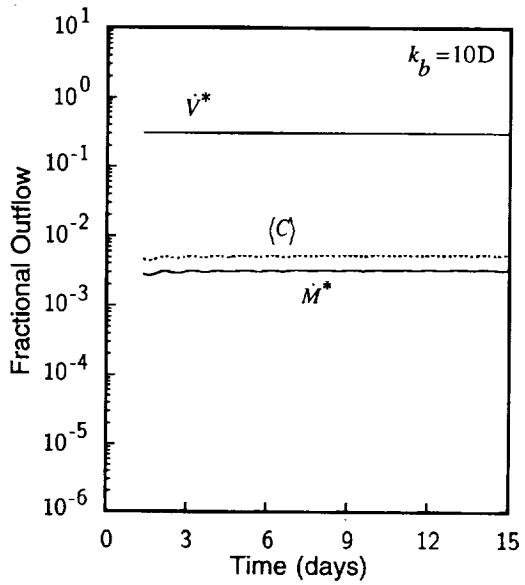

Figure 21-10. Normalized outflows for quasi-steady analysis with typical Yucca Mountain parameters.

Parameter studies presented in Figures 21-11 through 21-15 depict the influence of retardation factor, matrix permeability, fracture spacing, and binary diffusion strength. Aside from the parameter varied in the plots, all other parameters are set at the base case values in given in Table 21-1; any exceptions to this are noted on the plots. In every case, the result of primary interest is the normalized rate of contaminant outflow, $\dot{M}^*$. The volumetric outflow $\dot{V}^*$ is also included in cases where it varies, as is the mean concentration of the outflow <C> with the understanding that the last of these must always be

interpreted relative to the mean concentration in the medium. The values of $\dot{M}^*$ can, however, be taken at face value since they already indicate the yearly outflow relative to the total amount present in the medium.

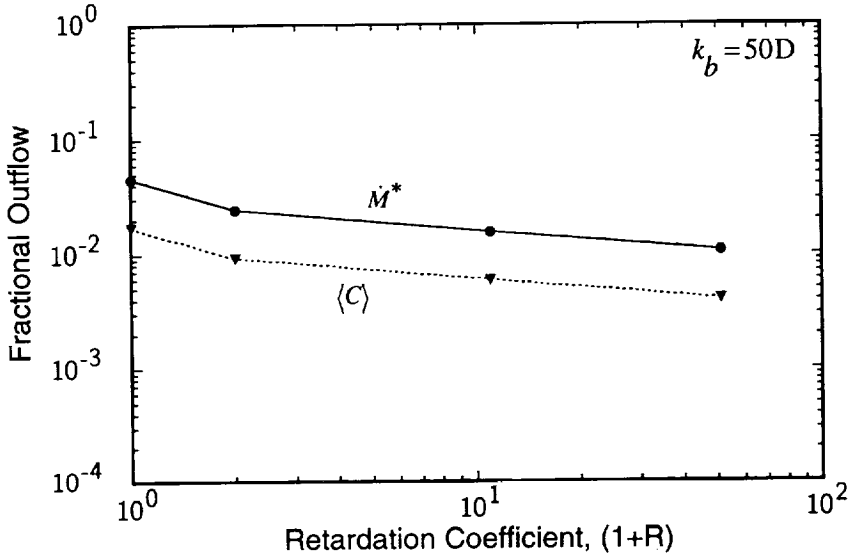

Figure 21-11. Influence of retardation factor on quasi-steady outflow of contaminant.

An increase of the retardation coefficient, 1+R, from 1 to 51 causes a factor of four reduction in the rate of contaminant outflow, as illustrated in Figure 21-11. This is roughly the amount of retardation expected for $C^{14}O_2$, according to Ross *et al.* (1992). Moreover, it appears that further increases in the retardation factor would be of less benefit, since the dependance becomes weaker for values of R beyond 10.

A reduction of the matrix permeability from 10^{-2} darcies to 10^{-6} darcies produces a 100-fold reduction in outflow of contaminant. Examination of Figure 21-12 shows that this is due to a ten-fold decrease in volumetric flow coupled with a 10-fold decrease in the mean concentration of the contaminant outflow. The microdarcy permeabilities at the lower end of this permeability range are typical of tuff cores. Conversely, the upper end of the range, corresponding to millidarcies, is probably more representative of the bulk permeability of the meter-scale blocks of material which breathe into the interconnected fractures which carry contaminated gases to the surface. Ideally, it would be desirable to model the permeability existing over a broader range of length scales than can be accommodated by the double-porosity model used here, perhaps using a more complex network model. However, given present constraints, meter-scale blocks combined with millidarcy permeabilities seems an appropriate choice for reasonable upper-bound calculations of

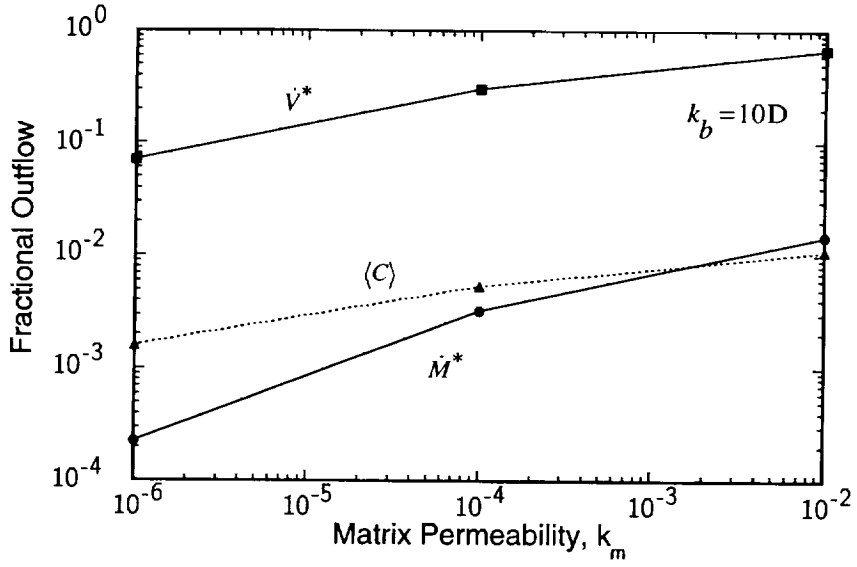

Figure 21-12. Influence of matrix permeability on quasi-steady outflow of contaminant.

contaminant transport. Those were the parameters used in the present base-case calculations and they are in reasonable agreement with values inferred from previous field experiments conducted at Nevada Test Site (Nilson *et al.*, 1992) and at Yucca Mountain (Weeks, 1987).

A fracture spacing of a few meters produces a maximum outflow of contaminated gases, as illustrated in Figure 21-13. Wider fracture spacings causes a reduction in the volumetric flow, since the pore space in the interior of larger blocks cannot participate in the breathing process, given the 0.1 matrix permeability used in these calculations. Narrower spacing caused a reduction in the concentration of the outflowing gas, as also seen in Figure 21-13. This occurs because narrow spacing leads to a closer equilibrium between concentrations in the matrix and in the fracture, as will be later explained in the context of Figure 21-15. Coincidentally, the 5-meter fracture spacing which produces maximum transport is comparable to the spacing of significant well-connected cooling cracks in volcanic rocks.

A diffusion strength of $\beta \approx 10^{-4}$ corresponds to the maximum outflow of contaminant for the 4-meter fracture spacing used to construct Figure 21-14. Recall from Equation (21.7) that $\beta = \phi_m / \tau$ which is likely to be in the range 10^{-2}-10^{-3}. Thus, as with the fracture spacing, the transport is likely to be near its maximum for the parameter range appropriate to Yucca Mountain. An explanation for this peaking behavior is contained in the discussion of the next figure.

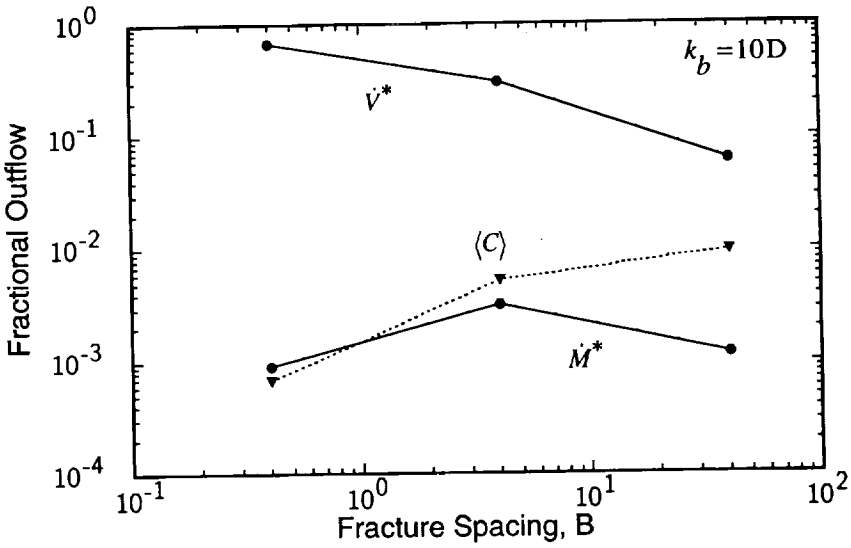

Figure 21-13. Influence of fracture spacing on quasi-steady contaminant outflow.

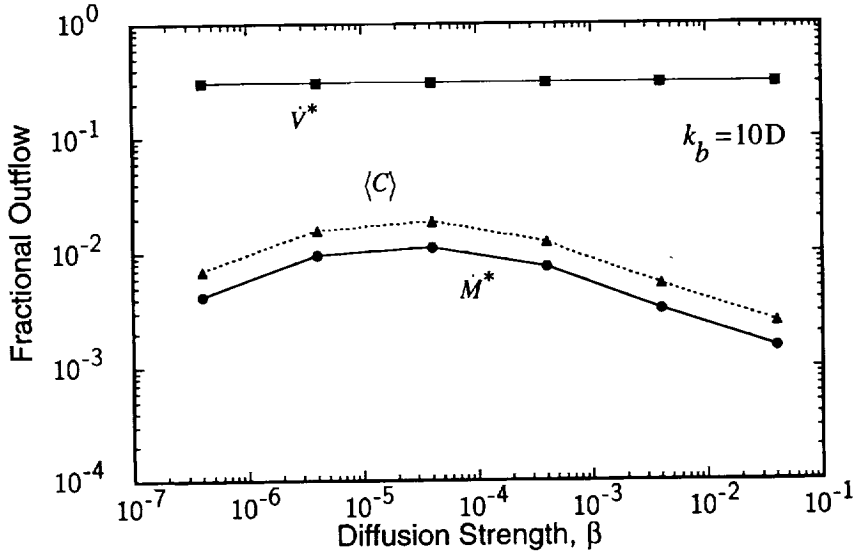

Figure 21-14. Influence of diffusion strength on quasi-steady contaminant outflow.

21.7 Single-horizon models

In the preceding sections it was shown that the barometric pumping process evolves toward quasi-steady transport through a linear gradient. In the paragraphs which follow we will briefly explore the use of analytical and numerical models which seek to evaluate the rate of quasi-steady transport by solving the time dependent transport equations in a single typical horizontal plane. The key supposition is that the vertical gradients appearing in the differential equations can be replaced by their time-mean values. This reduces the dimensionality of the problem from two to one. The associated reduction in computational effort will be particularly beneficial in the next chapter which addresses the more complex multiphase flow processes that control barometric respiration of water vapor. The single-horizon model also helps to illuminate the physical mechanisms which determine the strength of the transport process as well as the somewhat unusual parametric dependencies which were encountered in the preceding section.

To illustrate the nature and the validity of a single-horizon model, we will first consider a simplified version of the barometric pumping process. It will be assumed that the fracture walls are porous ($\phi_m \neq 0$) but impermeable ($k_m = 0$) so that the horizontal transport of contaminant in the matrix occurs purely by molecular diffusion; there is no bulk flow in the horizontal direction. Conversely, the vertical transport in the fracture is presumed to be advection dominated, as expected in most applications. Under these simplifications, the transport equations given earlier reduce to the following pair of equations which respectively apply to the fracture and the matrix. Here we introduce a modified diffusivity $D^* = D_0\beta / \phi_m$ which helps to simplify subsequent equations.

$$\frac{\partial C}{\partial t} + q_{gy}\frac{\partial C}{\partial y} = \phi_m D^* \frac{2}{w}\frac{\partial C}{\partial x} \tag{21.20}$$

$$\phi_m \frac{\partial C}{\partial t} = \phi_m D^* \frac{\partial^2 C}{\partial x^2} \tag{21.21}$$

These can be solved analytically if it is further assumed that the vertical velocity in the fracture is harmonic, i.e., $q_{gy} = q_0 \Re e(\exp(i\omega t))$, and that the vertical concentration gradient is uniform. Both of these suppositions are consistent with the behavior observed in the earlier numerical simulations.

The exact solution to this prototype problem is the real part of the following complex function (Kurzweg, 1985; Nilson *et al.*, 1991)

$$C = \gamma\left[y + b\,g(x^*)e^{i\alpha t}\right] \tag{21.22}$$

in which $\gamma = dC/dy$ is the vertical concentration gradient, b is half the fracture spacing, and g is a complex function of the normalized depth into the wall $x^*=x/b$.

$$g = \frac{iq_0}{b\omega}\left[\frac{W\sqrt{i}}{W\sqrt{i}+\alpha\tanh\left(W\sqrt{i}\right)}\right]\frac{\cosh\left[W\sqrt{i}\left(1-x^*\right)\right]}{\cosh\left(W\sqrt{i}\right)} \tag{21.23}$$

The two dimensionless parameters appearing here are the Womersley number, $W = b\sqrt{\omega/D^*}$, and the ratio of pore volume to fracture volume, $\alpha = B\phi_m/w$. From Equation (21.22) it is seen that the time mean concentration varies linearly with height, y, but is independent of depth into the wall, x. Further, the variation of concentration is sinusoidal at all locations with the amplitude and phase modulated by the depth into the wall, as embodied through the complex function $g(x^*)$.

The volume of fluid, ΔV, and corresponding mass of contaminant, ΔM, which pass through any horizontal plane during a single cycle of motion are given by the following integrals

$$\Delta V = w\int_0^{T/2}\Re e(q_{gx})\,dt = \frac{wq_0T}{4\pi} \tag{21.24}$$

$$\Delta M = w\int_0^{T}\Re e(q_{gx})\,\Re e(C)\,dt = -\frac{w\gamma q_0^2T^2}{4\pi}\Re e\left[\frac{W\sqrt{i}}{W\sqrt{i}+\alpha\tanh\left(W\sqrt{i}\right)}\right] \tag{21.25}$$

These are analogous to the integrals used earlier to summarize the numerical simulations except that the present expressions have not been normalized by the subsurface inventories of gas and contaminant since there is no depth dimension in the single-horizon model.

As before, the ratio of these two integrals is used to define an effective mean concentration $\langle C\rangle$ which characterizes the net throughput of contaminant.

$$\langle C\rangle = \frac{\Delta M}{\Delta V} = \gamma\Delta L\Psi(W_a,\alpha) \tag{21.26}$$

This mean concentration depends upon the vertical gradient, $\gamma = dC/dy$, the amplitude of the vertical motion, $\Delta L = \Delta V/w = q_0T/4\pi$, and a dimensionless function $\Psi(W_a,\alpha)$ of a modified Womersley number, $W_a = W/\alpha$, and the volume ratio α.

$$\Psi(W_a,\alpha) = -\frac{\pi}{4}\Re e\left[\frac{W_a\sqrt{i}}{W_a\sqrt{i} + \tanh(\alpha W_a\sqrt{i})}\right] \tag{21.27}$$

$$W_a = \frac{w}{\phi_m}\sqrt{\frac{2\pi}{D^* T}} \quad \text{and} \quad \alpha = \frac{B\phi_m}{w} \tag{21.28}$$

It is seen in Figure 21-15 that for any choice of α there is a maximum rate of transport which occurs for W_a near unity. For $W_a >> 1$, the period T is too short to allow a significant diffusive interaction between the channel and the wall. Conversely, for $W_a << 1$, the period is so long that the fracture and the wall are always nearly equilibrated in concentration; this also leads to a minimal net transport over a full cycle of motion. Thus, the transport is greatest when the period T is comparable to the time required for molecular diffusion to access a pore volume which is comparable to the fracture volume.

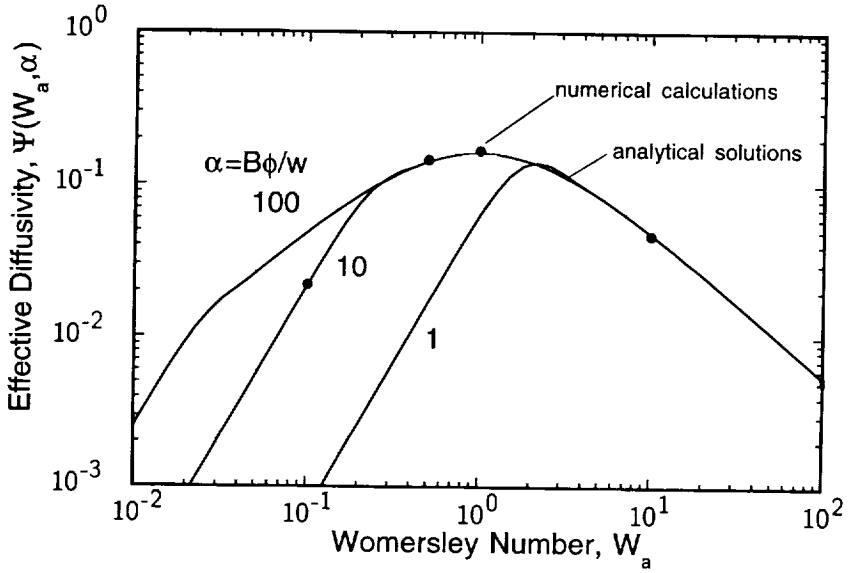

Figure 21-15. Comparison of analytical and numerical solutions for quasi-steady contaminant transport through a uniform gradient in a semi-infinite medium.

A fundamental assumption of any such single-horizon model is that the vertical concentration gradient, $\gamma = dC/dy$, can be taken as a constant. One might, however, expect that the flow along the channel would perturb the gradient in an oscillatory fashion. Furthermore, it is implicitly presumed that the domain is of infinite extent in the direction of the concentration gradient. In the present application this implies infinite depth, so there is no opportunity to apply boundary conditions at the floor and the surface of the

medium. This precludes the specification that there be no contaminant in the fresh air which flows into the fracture at the earth's surface. Instead, the concentration at every elevation, including the surface, oscillates sinusoidally about a mean value which increases linearly with depth. Although these simplifications of the model would appear to be well justified if the amplitude, ΔL, of the vertical motion were small compared to the depth, L, of the medium, they become questionable in the present application where $\Delta L / L$ sometimes exceeds unity.

The validity of the single-horizon model was evaluated by comparing the above analytical solutions with two-dimensional numerical solutions which were posed on a domain of finite depth. In conformance with the analytical solutions, the vertical velocity was prescribed as sinusoidal in time and of equal amplitude at all elevations. However, in contrast to the analytical solutions, the numerical solutions satisfied more realistic boundary conditions with $C = 0$ for downflows from the upper surface and $C = 1$ for upflows from the bottom of the medium. Thus, the boundary condition at the earth's surface is identical to that used in the Yucca Mountain simulations where the atmosphere is idealized as an infinite reservoir of fresh air. For symmetry, the lower boundary is now idealized as an infinite reservoir of fully contaminated gas. Our goal is to determine whether the single-horizon model remains valid in cases where the vertical gradient is substantially perturbed from linearity and the gas displacements are as large as the vertical extent of the medium.

A series of numerical solutions were calculated for different values of the parameter $\Delta L / L$ with the other parameters held fixed at $W_a = 1.0$, $\alpha = 1.0$ and $\Delta C = 1.0$. Using these choices and the fact that $\gamma = \Delta C / L$, Equation (26) can be rewritten as

$$\langle C \rangle = \frac{\Delta M}{\Delta V} = \gamma \Delta L \Psi(W_a, \alpha) = \Psi(1,1) \frac{\Delta L}{L} \tag{21.29}$$

This analytical expression is plotted in Figure 21-16 along with the numerical results obtained in five different simulations. In each, the value of $\langle C \rangle$ was determined by time integration of the defining equation (i.e., first equality in [21.25]). It is seen that the numerical results are extremely close to the analytical solutions for $\Delta L / L \leq 2$. Even for displacements twice that large, the error in the single-horizon model is still less than 20% which is small compared to a number of other uncertainties involved in defining the problem of interest and the associated geologic parameters.

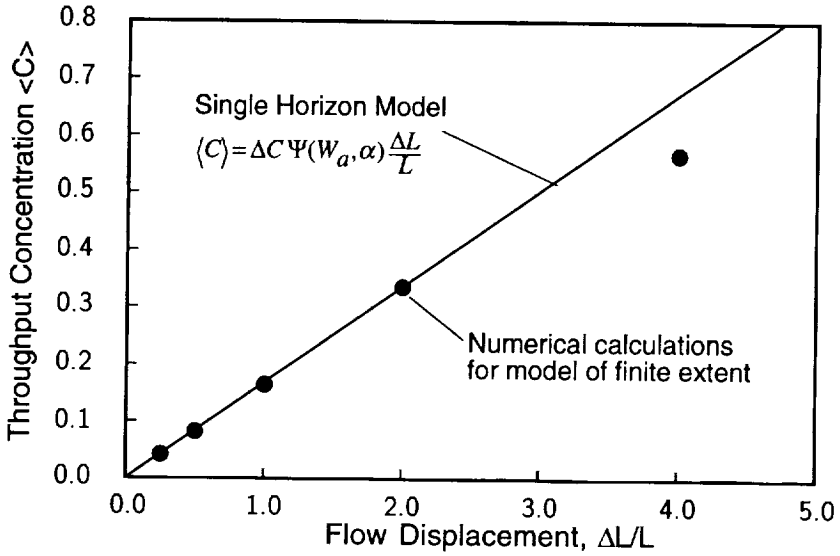

Figure 21-16. Comparison of single-horizon model with numerical calculations which take account of finite height and nonuniform gradients.

To better understand the success of the single horizon model it is useful to further explore the details of the numerical solutions. Figures 21-17 and 21-18 show the numerical results for $\Delta L / L = 1/2$. The first of these indicates that the time variation at midheight follows a smooth sinusoidal path, in keeping with the analytical solution for an infinite domain. However, as expected, the time histories of concentration at the ends of the domain are far from sinusoidal, owing to the application of boundary conditions. In spite of this, the net flux is the same through all three elevations and it is nearly identical to the analytical prediction of Equation (21.29). Part of the explanation for this agreement is apparent in Figure 21-18 which shows that the slope of the concentration profile remains nearly constant despite significant displacements to the right and the left. If this slope were always to remain uniform and constant, we would be fully justified in replacing the vertical derivatives in the transport equations with their time mean values, as assumed in the single-horizon model. Thus, the results for moderate displacements are, in all respects, quite consistent with the analytical solutions, as expected.

What is somewhat suprising, however, is that the single-horizon model closely predicts the numerical results shown in Figures 21-19 and 21-20 for $\Delta L / L = 2$. Here, there are very significant departures from the mean gradient of $\gamma = \Delta C / L = 1$ which is presumed applicable in the analytical model. In spite of this, the single-horizon model provides an excellent prediction. Since the displacements of interest rarely exceed twice the layer depth, we have gained considerable confidence in the use of this approach in modeling the

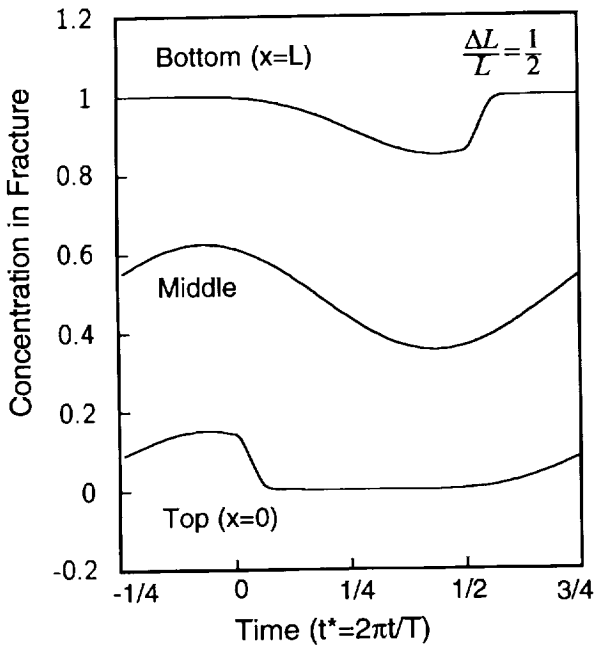

Figure 21-17. Concentration histories at three elevations for ΔL/L=1/2.

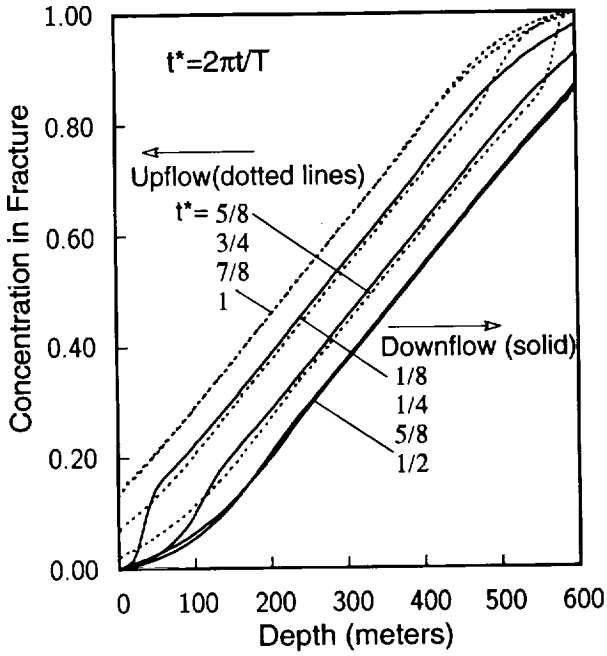

Figure 21-18. Concentration profiles at various times during typical cycle with ΔL/L=1/2.

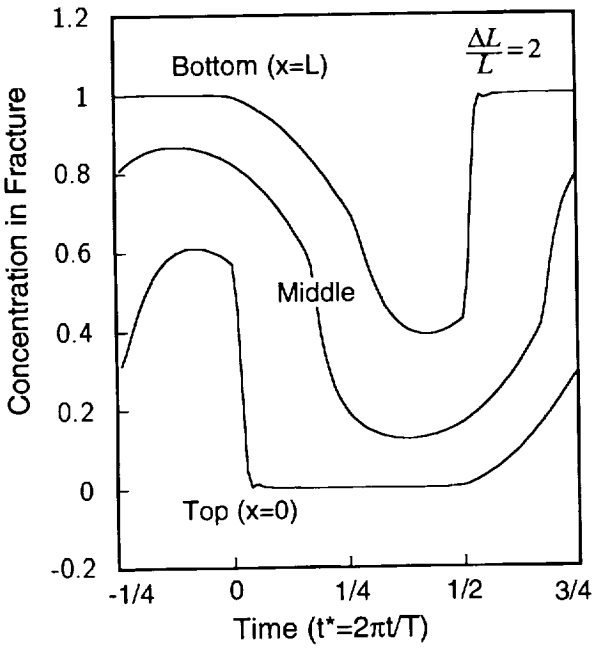

Figure 21-19. Concentration histories at three elevations for ΔL/L=2.

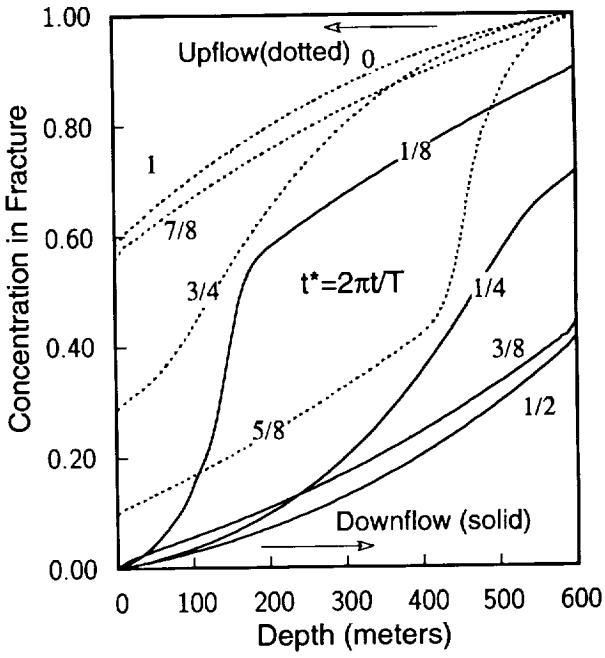

Figure 21-20. Concentration profiles at various times during typical cycle with ΔL/L=2.

more complex problem of moisture transport by barometric pumping, as discussed in the next chapter of this volume. In this context it is further noted that the symbols shown in the Womersley plot of Figure 21-15 were obtained by the mathematical solution procedure described in the next chapter. Here again, the agreement was excellent.

21.8 Summary

Transport of contaminated gases by barometric pumping has been estimated using a dual-permeability model in which identical equally spaced fractures are separated by slabs of permeable matrix material. The fractures were assumed to be vertically continuous from the water table at 600 m to the earth's surface. The material properties used are representative of the welded tuff units which comprise most of Yucca Mountain. The model was driven at the surface by daily pressure variations of 1%, in keeping with measurements made at the site. At the onset of each simulation a fixed quantity of contaminated gases was emplaced at the repository level. The primary output of the calculations was the rate of contaminant release to the atmosphere, $\dot{M}^*$, expressed as a fraction of the amount initially present.

Simulations spanning 150 years were presented for three primary cases. The first two were unretarded by adsorption and should be representative of noble radioactive gases and inert tracers. The third simulation included a retardation process of the type expected to occur for $C^{14}O_2$.

1. For parameters currently believed typical of Yucca Mountain (k_{bulk}=10 darcies) the release rate became quasi-steady at $\dot{M}^* \cong 0.1\%$ per year after a time of 100 years.

2. For parameters derived from experience at Nevada Test Site (k_{bulk}=50 darcies) the release rate became quasi-steady at $\dot{M}^* \cong 1.0\%$ per year after a time of 10 years.

3. A retardation factor of R=10 causes a three-fold reduction in the quasi-steady rate of contaminant outflow but the time required to reach quasi-steady state was increased by 10. R is on the order of 70 for $C^{14}O_2$.

The contaminant outflow can be projected beyond the time of these simulations, based on the observation that the subsurface inventory of contaminated gas decreases exponentially in time as $\exp(-\dot{M}^* t)$, where $\dot{M}^*$ is stated in fractional rather than percentage units.

Parameter studies were performed to learn the dependence of the quasi-steady release rate, $\dot{M}^* \approx \dot{V}^* \langle C \rangle$, on the bulk permeability, matrix permeability, fracture spacing,

binary diffusion coefficient, and retardation factor. The results can be understood by noting the influence of each of these variables on the volumetric air flow, $\dot{V}^*$, and the average concentration $\langle C \rangle$ of the gas released to the atmosphere. The volumetric flow increases monotonically with the bulk permeability, matrix permeability, and porosity. When the subsurface pressure closely follows the surface pressure variations, $\dot{V}^*$ attains a maximum value of $\dot{V}^* = 3.65$ (i.e., 365%) since there are 365 daily cycles in which may each exchange a maximum of 1% of the subsurface gas volume.

The average concentration of the effluent $\langle C \rangle$ is typically on the order of 10^{-4}, relative to the initial concentration of the repository gas. Of this, a dilution of 30:1 is attributed to spreading of the contaminant across the medium while the remaining dilution of 100:1-1000:1 is associated with the quasi-steady transport process. This latter component of the dilution is minimized (i.e., $\langle C \rangle$ maximized) when the time scale for molecular diffusion into the matrix is comparable to the time period of barometric pressure changes. Because of this the transport is optimal for particular combinations of the binary diffusion coefficient, retardation coefficient, and fracture aperture and spacing.

The occurrence of optimal transport was explained using a simplified single-horizon model which couples horizontal transport occurring at a typical horizon with vertical transport through a uniform concentration gradient of infinite extent. Furthermore, by comparison with numerical simulations of the complete problem, it was demonstrated that single-horizon models of this type provide remarkably good estimates of quasi-steady transport through a medium of finite height even for cases in which the vertical gas displacement exceeds the vertical height of the medium and the vertical gradient is substantially perturbed. Thus, confidence was gained in the use of a single-horizon model to analyze the closely related process of moisture transport by barometric pumping, as reported in the next chapter of this volume.

Chapter 22
Barometric Pumping of Moisture Through Unsaturated Fractured Rock

(Martinez, Nilson)

In this work, we present a theory of the motion of water vapor in a fractured permeable medium induced by atmospheric barometric pressure fluctuations, or "barometric pumping." This mechanism may be of some importance to subsurface water vapor transport in fractured rock situated in arid regions where annual moisture infiltration is exceedingly low owing to very low permeability of the intact country rock. This study, though motivated by the Yucca Mountain Project, is applicable to other similar sites involving fractured rock.

In such material, the fracture system is presumed to provide the primary permeability. However, the capacity of the system lies with the intact matrix. Because capillary forces will be stronger in the smaller pores of the matrix, resident liquid moisture will prefer to reside in the matrix, with the exception perhaps, of asperities or other small features of the fracture system. On the other hand, the gas, a mixture of air and water vapor, will prefer the fracture system and shares the void space of the matrix with liquid water. The idea behind barometric pumping, hereafter referred to as BP, is that rising barometric pressure will force ambient gas into the matrix which is drier than the resident soil gas. The latter is in thermodynamic equilibrium with resident liquid water, and is probably nearly saturated (in the thermodynamic sense) with water vapor at the prevailing temperature. The incoming dry gas will come to thermodynamic equilibrium with the soil gas, thereby humidifying the former. When the barometric pressure decreases, gas will be respired from the fractured medium, thereby discharging gas with a higher humidity than the ambient. There are two such barometric cycles of interest, the diurnal cycle and that associated with weather patterns. Typically, a weather-related barometric cycle has an average period of roughly five days (Nilson *et al.*, 1991).

22.1 Maximum moisture transport

An estimate of the amount of moisture extracted by the diurnal cycle was given by Tsang and Pruess (1989) for Yucca Mountain. During a diurnal cycle, the barometric pressure undergoes a fluctuation of magnitude ΔP_g. This induces a compression and rarefaction of the gas in a column of porous material of length L, and unit plan area. The rising pressure induces a compression ΔV of the resident gas, which is replaced with drier ambient gas. This volume is humidified while in the subsurface and discharged when the barometric pressure drops. Thus, over each cycle, this process extracts an amount of water vapor equal to

$L(\Delta P_g/P_g)\theta_g\rho_g(X_{v,out}-X_{v,in})$, where θ_g is the volumetric gas content in the porous material, ρ_g is the gas density, and X_v is the mass fraction of water vapor. Summing all such contributions over a year, Tsang and Pruess estimated a net discharge of 0.3 mm/yr, expressed in an equivalent liquid water flux.

While this calculation ought to provide an upper bound on the amount of moisture that could be extracted via BP, it also raises the question of how realistic this bound is. Clearly, the estimate contains no information about how the transport occurs, or where the water is extracted from. For example, one might imagine the incoming dry gas would humidify after only a short travel distance along the fracture, as happens for example when dry air passes over a wetted surface in evaporative cooling equipment or humidifiers. This may imply that all the moisture is extracted from the surface layer of the medium, tending to dry out that near surface region. On the other hand, if this layer is dry, respired moist gas may condense out in this region before exhausting into the ambient, thereby reducing the effectiveness of BP for moisture extraction. This argument does suggest a mechanism for establishment of a vertical gradient in moisture content.

In this work, we consider a somewhat more detailed model of the BP mechanism in the hopes of providing a tighter bound on moisture respiration. The ground work for the processes considered was laid in the models discussed by Nilson *et al.* (1992, 1991) who considered the parallel problem of BP of contaminant-laden gases. The idea is that a periodic fluctuation in a potential is able to transport a conserved quantity through an average background gradient of said quantity. A net transport takes place even though, as happens in the contaminant transport problem, at any horizon, there is no net transport into or out of the matrix during a cycle. This rather remarkable process was considered by Kurzweg (1985), and Nilson *et al.* (1991) for the case of transport by diffusion only along an infinitely long channel embedded in a porous matrix. Transport via advection and diffusion was also considered by Nilson *et al.* (1991) and in the previous chapter, as specifically applied to Yucca Mountain.

22.2 Vertical background gradients

The most notable background gradient that is known to exist is the geothermal gradient, which itself induces a vapor pressure gradient with depth. In order to establish a "nominal" state of the fractured medium in the presence of the geothermal gradient, we reconsider a problem discussed by Tsang and Pruess (1989, 1990) in a study of gas flow at Yucca Mountain. Our objective in reconsidering this problem was two-fold, 1) it establishes the vertical background gradients that, on the scale of the considered domain, assist the transport of water vapor via BP, and 2) it serves as a benchmark for the numerical algorithm to be discussed

in the following by allowing a comparison with the results of Tsang and Pruess (1989, 1990) who used the code TOUGH (Pruess, 1987) for their simulations.

In the simplest version, we consider a 600 m depth of fractured medium over which a temperature gradient is imposed. This corresponds to the depth to the water table at Yucca Mountain, and material properties thought to be representative of the Topopah Springs unit, which is being considered for placement of a high-level nuclear waste repository, are specified over the entire depth. The lower boundary is assumed saturated with liquid water, and at a temperature of 30.85 °C and pressure of 1 bar. The upper boundary, which represents the top of Yucca Mountain and therefore the interface with the ambient, is at 12.85°C and 0.9334 bar, see Tsang and Pruess (1989). Tsang and Pruess go on to consider the effects of a reduced saturation at the top boundary, presumably induced by low ambient humidities, on water vapor movement in the subsurface.

Specifying a no-flow boundary condition at the top for the moisture, we compute liquid saturation and mass flux profiles that agree well with those given by Tsang and Pruess (1989, 1990). Our simulation establishes an average vapor mass fraction gradient, $\langle dX_v/dy \rangle = -3.24x10^{-5}\text{m}^{-1}$ owing to the imposed background geothermal gradient $\langle dT/dy \rangle = -0.03$ °C/m. The flux of water vapor implied by these gradients is on the order of $0.5\text{x}10^{-4}$ mm/yr, quite a bit smaller than the theoretical upper bound discussed above.

22.3 Problem formulation

Our mathematical description of the fractured medium is best described as a multicontinuum theory, wherein we write equations governing the transport in the fractures and matrix separately. However, the equations contain terms which describe the transfer of material and energy between the fracture and matrix system. We assume that the horizontal gradients in the matrix are much larger than vertical gradients, and invoke the approximation that variables in the matrix are uncoupled along the vertical direction.

The fracture model consists of a specification at the considered horizon of the gas pressure fluctuation, which drives a mass flux comprising moisture and air into and out of the matrix block. The gas flow in the fracture is derived from a balance of this mass with the vertical transport up and down the fracture. The statement of this balance allows evaporation and condensation of moisture at the fracture/matrix interface to convert liquid into vapor or vice versa, if required to satisfy the imposed conditions. A balance equation for water vapor in the fracture also balances the net moisture flux at the fracture/matrix interface with the transport of water vapor up and down the fracture. There is also an energy balance to account for energy transported between the matrix and fracture. The vapor pressure is assumed continuous at the fracture/matrix interface. Finally, the capillary pressure in the

matrix at the fracture/matrix interface is specified from the Kelvin equation, a thermodynamic relation for modifying vapor pressures across a curved interface. This latter relation couples the vapor pressure, temperature and vapor mass fraction together.

The bulk permeability for the two-dimensional fractured porous material model depicted in Figure 22-1 is expressed as

$$k_b = k_f \frac{w}{B} + k_m \frac{B - w}{B} , \tag{22.1}$$

where k_f is the fracture permeability, w is the fracture aperture, B is the fracture spacing, and k_m is the matrix permeability. The fracture permeability is related to the effective hydraulic aperture by the formula for flow in a slot (planar Hagen-Poiseuille flow),

$$k_f = \frac{w^2}{12} . \tag{22.2}$$

For material properties typical of Yucca Mountain (and other fractured rock systems), $k_f \gg k_m$ and $w \ll B$, so that the bulk permeability is effectively

$$k_b = \frac{w^3}{12B} . \tag{22.3}$$

22.3.1 Fracture model

In the fractures, we assume that only gas is mobile. Furthermore, the equations are averaged over the width of the fractures and so variables vary only along the path of the fracture. In this particular case, the fractures are assumed vertical, and the coordinate y (positive upward) measures distance along the fracture. A balance equation for the gas is

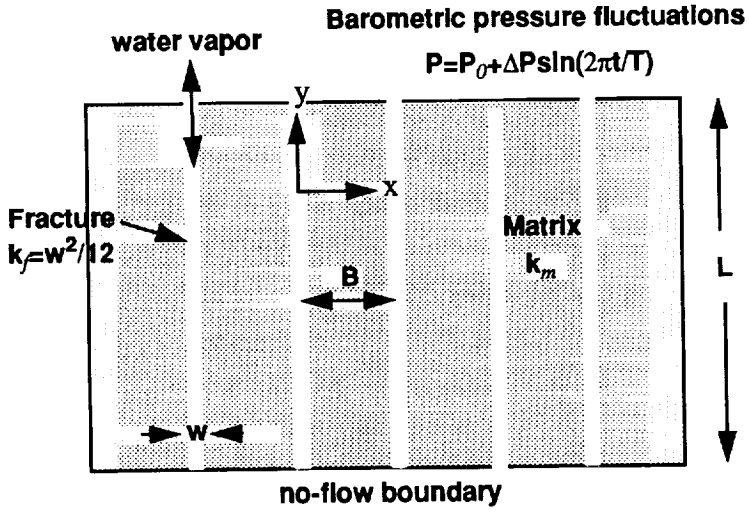

Figure 22-1. Conceptual model of the fractured permeable medium.

$$\frac{\partial \rho_g}{\partial t} + \frac{\partial}{\partial y}(\rho_g q_{gy}) = -\frac{2}{w}[F_l + F_g] \tag{22.4}$$

where ρ_g is the density of the gaseous mixture composed of air and water vapor, q_{gy} is the (vertical) flux of gas, and F_l and F_g denote the mass fluxes of liquid and gas entering (or leaving) the fracture from the matrix. In the remainder of this work, subscript g refers to gas, v to water vapor, a to air, l to liquid and m to moisture (e.g. liquid and vapor). Because only gas is allowed to exist in the fracture, any liquid that may cross the fracture/matrix interface must be evaporated (condensed) upon entering (leaving) the fracture. A balance equation for the water vapor is also specified:

$$\rho_g \frac{\partial X_v}{\partial t} + \rho_g q_{gy} \frac{\partial X_v}{\partial y} = -\frac{2}{w}[F_l(1 - X_v) + J_v], \tag{22.5}$$

where

$$X_v = \frac{\rho_v}{\rho_v + \rho_a} \tag{22.6}$$

is the mass fraction of water vapor in the gas, and J_v denotes the horizontal diffusive flux of water vapor through air in the matrix. In arriving at this form, the over-all gas balance equation (22.4) has been used, and continuity between the mass fraction of water vapor in the fracture and matrix was imposed. Again, the terms on the RHS represent mass fluxes of water from the matrix, and any net liquid flux is evaporated or condensed at the fracture/matrix interface.

An energy balance is also specified:

$$\frac{\partial}{\partial t}[\rho_g(X_a u_a + X_v u_v)] + \frac{\partial}{\partial y}[\rho_g(X_a h_a + X_v h_v) q_{gy}] = -\frac{2}{w}[q_h] \tag{22.7}$$

where u denotes internal energy and h enthalpy, and q_h is the net heat flux from the matrix.

In order to determine the exchange terms in these equations, the matrix model must be specified.

22.3.2 Matrix model

A balance equation for matrix water, including liquid and vapor phases is given by

$$\frac{\partial}{\partial t}(\rho_l \theta_l + \rho_v \theta_g) + \nabla \bullet \boldsymbol{F}_m = 0 \tag{22.8}$$

where θ_l is the volumetric liquid moisture content, θ_g the volumetric gas content, and $\theta_l + \theta_g = \phi$, where ϕ is the porosity. The flux of moisture is

$$\boldsymbol{F}_m = \rho_l \boldsymbol{q}_l + X_v \rho_g \boldsymbol{q}_g + \boldsymbol{J}_v \tag{22.9}$$

Starting from the left, the terms on the RHS represent the mass flux of liquid, the advective mass flux of water vapor and the diffusive flux of water vapor, respectively. A balance equation for air reads

$$\frac{\partial}{\partial t}(\rho_a \theta_g) + \nabla \bullet \boldsymbol{F}_a = 0, \tag{22.10}$$

where

$$\boldsymbol{F}_a = X_a \rho_g \boldsymbol{q}_g + \boldsymbol{J}_a. \tag{22.11}$$

An energy balance takes the form

$$\frac{\partial}{\partial t}[[(1-\phi)\rho_s C_s + \rho_l C_l \theta_l + \rho_g C_g \theta_g](T - T_0)] + \nabla \bullet \boldsymbol{q}_h = Q\ , \tag{22.12}$$

where

$$C_g = C_{va} X_a + C_{vv} X_v\ , \tag{22.13}$$

$C_{v\alpha}$ is the constant volume specific heat of component α, T_0 is a reference temperature, and Q is an extraneous heat source.

22.3.3 Constitutive relations

The advective fluxes are assumed to be adequately described by the extended Darcy law, in which relative permeabilities are introduced to account for the multiphase motion of fluids. Thus the mass flux of liquid is

$$\rho_l \boldsymbol{q}_l = \boldsymbol{F}_l = -\frac{\rho_l k_m k_{rl}}{\mu_l}(\nabla P_l + \rho_l g \nabla y)\ , \tag{22.14}$$

and the mass flux of gas is

$$\rho_g \boldsymbol{q}_g = \boldsymbol{F}_g = -\frac{\rho_g k_m k_{rg}}{\mu_g}(\nabla P_g + \rho_g g \nabla y)\ , \tag{22.15}$$

where P is pressure, g is the gravitational acceleration, and μ is dynamic viscosity. The diffusive flux of water vapor in air is given by

$$\boldsymbol{J}_v = -\rho_g D_{va} \nabla X_v\ , \tag{22.16}$$

and the diffusion coefficient is (Pruess, 1987),

$$D_{va} = \frac{\theta_g}{\tau} D^0_{va} \frac{P_{ref}}{P_g} \left(\frac{T}{T_{ref}}\right)^{\nu}\ , \tag{22.17}$$

where τ is tortuosity and D_{va}^0 is the diffusivity in free space at temperature T_{ref} and pressure P_{ref}. In accordance with mass conservation for the binary mixture, $\boldsymbol{J}_a = -\boldsymbol{J}_v$. The heat flux includes conduction and convective contributions,

$$\boldsymbol{q}_h = -\lambda \nabla T + h_v \boldsymbol{F}_v + h_a \boldsymbol{F}_a + h_l \boldsymbol{F}_l \,, \tag{22.18}$$

where λ is an effective thermal conductivity and we have introduced the shorthand notation for mass fluxes: $\boldsymbol{F}_v = X_v \boldsymbol{F}_g + \boldsymbol{J}_v$, and $\boldsymbol{F}_a = X_a \boldsymbol{F}_g + \boldsymbol{J}_a$. The enthalpies are defined by $h_\alpha = C_{p\alpha}(T - T_0)$, with $\alpha = a$ or l, and $h_v = \Delta h_{fg} + C_{pl}(T - T_0)$, where Δh_{fg} is the latent heat of water vapor at reference temperature T_0.

22.3.4 Mixture relations and thermodynamics

Ideal gas equations of state and mixing rules are used to approximate the thermodynamics of the system. Thus,

$$P_v = \rho_v R_v T, \qquad P_a = \rho_a R_a T \,, \tag{22.19}$$

with $R_\alpha = \Re / M_\alpha$, for $\alpha = v$ or a, $\Re$ is the gas constant and M_α denotes the molecular weight. Also

$$\rho_g = \rho_v + \rho_a \qquad P_g = P_v + P_a \,. \tag{22.20}$$

The vapor pressure is specified according to Kelvin's equation of vapor pressure lowering (Edlefsen and Anderson, 1943),

$$P_v = P_{vs}(T) \exp\left(-\frac{P_c}{\rho_l R_v T}\right) \tag{22.21}$$

where P_{vs} denotes the flat-interface saturation vapor pressure. We will assume that the system remains a two-phase mixture, otherwise the vapor pressure is independent of temperature in the superheated regime. Kelvin's equation introduces the capillary pressure,

$$P_c \equiv P_g - P_l = \hat{P}_c(\theta_l) \tag{22.22}$$

which, as indicated, is assumed to be empirically specified as a function of liquid moisture content.

22.3.5 The single-horizon approximation

A basic tenet of our conceptual model is the transport of water vapor via barometric pressure fluctuations through a background vertical (uniform) gradient of temperature, and therefore vapor pressure. The lower boundary of the model is the water table, the spatial limit of moist gas. There are two motivations for appealing to a single-horizon approxima-

tion in the present work. First, the analysis in the previous chapter clearly showed the efficacy of the single-horizon approximation for periodic or quasi-steady transport of contaminated gas, the analog to water vapor in this discussion. Secondly, the gross flow of gas in the fracture/matrix system due to a sinusoidal variation in barometric pressure should be well-described by an analytical solution given by Nilson *et al.* (1991, Appendix A). This solution could be used to provide a good estimation of the ratio of matrix to fracture gas flow at any horizon. We in fact compared the variations in phase and amplitudes for problem parameters relevant to the present work and found only modest deviations from the model we present in the following.

In the present work, for barometric pumping of water vapor, we motivate the single-horizon model by casting the gas balance equation in the fracture in an integral representation, and by approximating vertical gradients in the fracture by their average over the depth of the medium considered. Accordingly, integrating the balance of gas in the fracture (Eqn. 22.4) over the depth L, the flux of gas in the fracture at the elevation L is related to the matrix fluxes according to,

$$\rho_g q_{gy} = -\frac{2L}{w}\left[F_l + F_g\right]_{x=0^+}, \tag{22.23}$$

which, according to the foregoing discussion, represents a balance of material (air and water) from the matrix into the fracture. The "+" superscript denotes the interface as approached from the matrix. In this form, the matrix fluxes of liquid and gas now represent depth-averaged quantities. In addition, we have neglected the temporal change in gas density over the length of the fracture, $d\left(\int \rho_g dy\right)/dt$, and its effect in modulating the flux at elevation L above the lower boundary. Note that this statement of gas balance includes the possibility of evaporation/condensation of water at the fracture/matrix interface to satisfy the balance. The balance of water vapor in the fracture is stated as

$$\frac{\partial X_v}{\partial t} + q_{gy}\langle\frac{\partial X_v}{\partial y}\rangle = -\frac{2}{\rho_g w}\left[F_l(1-X_v) + J_v\right]_{x=0^+}, \tag{22.24}$$

where the average vertical gradient of water vapor has replaced the local gradient in the advective term. Additionally, the balance of gas in the fracture has been used to arrive at the form given above. The energy equation is given by

$$\begin{aligned}\rho_g C_{pg}\frac{\partial T}{\partial t} + \rho_g q_{gy}\left[C_{pg}\langle\frac{\partial T}{\partial y}\rangle + (C_{pv}-C_{pa})(T-T_0)\langle\frac{\partial X_v}{\partial y}\rangle\right] - \frac{\partial P_g}{\partial t} + \\ \rho_g (C_{pv}-C_{pa})(T-T_0)\frac{\partial X_v}{\partial t} = -\frac{2}{w}\left[-\lambda\frac{\partial T}{\partial x} - F_l(h_g-h_l) + J_v(h_v-h_a)\right]_{x=0^+}\end{aligned} \tag{22.25}$$

where $h_g = X_v h_v + X_a h_a$. Here again we approximate the vertical gradients in the fracture by the average background gradients discussed earlier. The time derivative of the vapor pressure is related to time derivatives of the state variables according to

$$\dot{P}_v = \frac{\left[(X_v \dot{P}_g + \dot{X}_v P_g - \dot{X}_v P_v) \frac{M_a}{M_v} + \dot{X}_v P_v \right]}{1 + X_v \left(\frac{M_a}{M_v} \right)}, \tag{22.26}$$

derived from the definition of the vapor mass fraction. Using the Kelvin equation, the time rate of change of the capillary pressure is given by

$$\dot{P}_c = \frac{\rho_l}{\rho_v} \dot{P}_v + \left[\frac{\rho_l R_v T}{P_{vs}} \frac{dP_{vs}}{dT} + \frac{P_c}{T} \right] \dot{T} . \tag{22.27}$$

This set of equations (Eqns. 22.23 through 22.27) describe the transport of gas, water vapor and energy in the fracture and are coupled to the mass fluxes of air, water and energy in the matrix.

22.4 Numerical treatment

The foregoing governing equations constitute a coupled set of highly nonlinear partial differential equations (PDEs). The numerical method applied for solving the coupled system of parabolic PDEs is the so-called Method-of-Lines (MOL) (Hyman, 1979). The MOL technique is a semi-discretization method wherein the spatial derivatives are first approximated by some appropriate method (in this case, finite differences), resulting in a system of coupled ordinary differential equations (ODEs) describing the temporal variation of the state variables at a number of discrete points or nodes. The effective treatment of the highly nonlinear system considered here is made possible by the availability of highly optimized ODE solvers (Shampine and Watts, 1980). In the present work, the spatial derivatives are approximated by a centered difference approximation. The resulting system of ODEs is integrated forward in time by the variable-order, variable-step backward-difference code DEBDF (Shampine and Watts, 1980). The backward-difference formulae result in systems of nonlinear algebraic equations to be solved for nodal quantities. These equations are solved as part of the DEBDF package via a Newton-type algorithm.

In this model, we will assume the system remains in the two-phase regime in the matrix. Hence, we choose as primary variables the capillary pressure, the gas pressure and temperature. Approximating the spatial divergences by central differences, the system of discrete ODEs describing the temporal variation of primary variables at node points takes the form

$$\begin{bmatrix} C_\psi & 0 & C_{\psi T} \\ C_{p\psi} & C_P & C_{PT} \\ C_{T\psi} & C_{TP} & C_T \end{bmatrix}_i \begin{bmatrix} \dot{P}_c \\ \dot{P}_g \\ \dot{T} \end{bmatrix}_i = \frac{1}{x_{i+1/2} - x_{i-1/2}} \begin{bmatrix} F_{m,i+1/2} - F_{m,i-1/2} \\ F_{a,i+1/2} - F_{a,i-1/2} \\ q_{h,i+1/2} - q_{h,i-1/2} \end{bmatrix} + \begin{bmatrix} 0 \\ 0 \\ Q \end{bmatrix}_i \tag{22.28}$$

for a mesh of nodes with node points at x_i. The net moisture flux appearing in this equation is defined by $F_m = F_l + F_v$. Each flux is also expressed as a central difference (on a staggered mesh), for example,

$$F_{l,i+1/2} = -\left(\frac{\rho_l k_m k_{rl}}{\mu_l}\right)_{i+1/2} \frac{P_{l,i+1} - P_{l,i}}{x_{i+1} - x_i} \,. \tag{22.29}$$

The definition of each entry in the capacitance matrix can be determined by considering the differential equation from which it was derived. For example, from Eqn. (22.8),

$$C_\psi = \frac{\partial}{\partial P_c} (\rho_l \theta_l + \rho_v \theta_g) \,. \tag{22.30}$$

For the BP simulations, no-flow boundary conditions are imposed for moisture, air and energy at the center of the blocks. Boundary conditions at the fracture are provided by the fracture equations given in Section 22.3.5 above.

22.4.1 Test problems

The two-phase code was tested as discussed in the introduction for establishing the vertical background gradients. This problem involved computing the steady distribution with elevation of water and air fluxes due to a geothermal gradient. The code was also tested by computing the heat pipe problem discussed by Udell and Fitch (1985). The heat pipe effect is established by applying a heat flux to one end of a porous column which results in a flow of water vapor towards the cold end and wicking of liquid water towards the hot end of the column. This problem exercises features of evaporation/condensation and vapor and liquid flows in the code. Excellent agreement with the numerical solution given in by Udell and Fitch was found.

Finally, in order to test the method of coupling the fracture and matrix used in the barometric pumping problem, the fracture/matrix diffusive transport problem discussed by Nilson *et al.* (1991) was also computed. This problem considers diffusive transport in a system of evenly spaced fractures separating slabs of porous matrix. The flow in this system is driven by an oscillating potential. Results for the net transport of conserved quantity computed with the present numerical model compared very well with the analytic solution given by Nilson *et al.* The results of this calculation were reported in the previous chapter (see Figure 21-15) on contaminant transport via barometric pumping.

22.5 Barometric pumping of water vapor

22.5.1 Figures of merit and characteristic material functions

In order to quantify the transport of water vapor by barometric pumping, we define here several quantities characterizing the motion. The travel distance, or displacement of gas in the fracture, is defined by (Nilson *et al.*, 1991):

$$\Delta L = \int_{t}^{t+T} max\,(q_{gy}, 0)\,dt\ , \tag{22.31}$$

where T denotes the time period of the barometric pressure fluctuation. The respired mass flux of moisture per fracture per barometric cycle is computed according to

$$\Delta M_v = \int_{t}^{t+T} \rho_v q_{gy} dt\ . \tag{22.32}$$

The amount of moisture mass removed during a cycle is $\Delta M_v w$ per fracture. The average concentration of effluent vapor is then defined as

$$\langle C \rangle = \frac{\langle \rho_v \rangle}{\bar{\rho}_v}\ , \tag{22.33}$$

where

$$\langle \rho_v \rangle = \frac{\Delta M_v}{\Delta L} \tag{22.34}$$

is a time-average of water vapor density and $\bar{\rho}_v$ is the (initial) average vapor density. This ratio is a normalized concentration and can be thought of as a ratio of the amount of water vapor transported via barometric pumping to the maximum possible amount that could be available for transport. Finally, the annual net moisture respired per unit surface area by the periodic barometric pumping is

$$q_0 = \Delta M_v N_T \frac{w}{B}\ , \tag{22.35}$$

where N_T is the number of cycles per year. In the following, this bulk moisture flux will be reported as an equivalent liquid water flux to facilitate comparisons with estimates of average annual infiltration for Yucca Mountain.

In order to apply the barometric pumping model to Yucca Mountain in particular, the appropriate material functions must be specified. The relation between capillary pressure

and liquid moisture content is described by the so-called van Genuchten equation (van Genuchten, 1978),

$$\frac{\theta_l - \theta_{lr}}{\phi - \theta_{lr}} = (1 + p^{\beta_v})^{-\lambda_v}, \tag{22.36}$$

where $p = \alpha_v P_c / \rho_l g$ and $\lambda_v = (\beta_v - 1)/\beta_v$. The corresponding relative permeability to the liquid is given by (van Genuchten, 1978),

$$k_{rl} = (1 + p^{\beta_v})^{-\lambda_v/2} \left[1 - \left(\frac{p^{\beta_v}}{1 + p^{\beta_v}} \right)^{\lambda_v} \right]^2 . \tag{22.37}$$

The relative permeability to the gas is approximated by the relation, (Bixler, 1985, Pruess, 1987)

$$k_{rl} + k_{rg} = 1. \tag{22.38}$$

The saturation-dependent effective heat conductivity was specified according to (Pruess, 1987),

$$\lambda = \lambda_0 + \frac{\theta_l}{\phi} (\lambda_1 - \lambda_0) . \tag{22.39}$$

Over the range of temperatures considered in the barometric pumping problem, a Clapyron equation adequately describes the flat-interface vapor pressure as a function of temperature,

$$\rho_{vs} = \rho_{v,ref} exp\left(\frac{\Delta h_{fg}}{R_v} (T_{ref}^{-1} - T^{-1}) \right) = A e^{-B/T} , \tag{22.40}$$

with $A = 7.055 \times 10^5$ kg/m^3, $B = 5137.46$ K, and $P_{vs} = \rho_{vs} R_v T$.

22.5.2 General features of the motion

It is instructive to consider the general features of the motion induced by the periodic variation in barometric pressure. We discuss the solution of a "base case" for which the parameters are specified as in Table 22-1. Included in this table are the parameters which enter into the characteristic matrix material functions representative of the Topopah Springs unit of Yucca Mountain. The values of aperture and fracture spacing in Table 22-1 correspond to a bulk permeability of $k_b = 10$D. The binary diffusion coefficient takes the form given in Eq. (22.17). Parameter variations about this base set will be discussed below.

The magnitude of the barometric pressure fluctuations, ΔP in Table 22-1, was determined by Tsang and Pruess (1989) by analysis of the data collected at Yucca Mountain by Church *et al.* (1985, 1986). The initial state of the system is taken from the steady solution

Table 22-1: Standard problem parameters, k_b=10D.

Parameter	Symbol	Value
Formation depth	L	600 m
Fracture aperture	w	621 μm
Fracture spacing	B	2 m
Matrix permeability	k_m	10 μD
Tortuosity	τ	2
Barometric time period	T	5 days
Pressure amplitude	ΔP	1 kPa
Temperature gradient	$\langle dT/dy \rangle$	-0.03 °C/m
Mass fraction gradient	$\langle dX_v/dy \rangle$	-3.24×10^{-5} m^{-1}
Binary diffusion coefficient	D^0_{va}	2.14×10^{-5} m^2/s
Diffusion parameter, Eqn. (22.17)	υ	2.334
Rock density	ρ_s	2580 kg/m^3
Rock heat capacity	C_s	840 J/kg°C
Effective conductivity (dry)	λ_0	1.74 W/m°C
Effective conductivity (wet)	λ_1	2.34 W/m°C
Porosity	ϕ	0.11
Residual moisture content	θ_{lr}	0.0088
van-Genuchten parameter	α_v	0.0057 m^{-1}
van-Genuchten parameter	β_v	1.798

for the background gradients (discussed in Section 22.2) at the mid-height of the 600 m model. Specifically, the initial gas pressure is, P_g=0.955x10^5 Pa, the initial temperature is, T_0 = 22.2°C, and the initial moisture content is θ_l = 0.066 (60% liquid-saturated) corresponding to an initial capillary pressure, P_c=2.93x10^7 Pa.

Figure 22-2 shows the profiles of gas pressure, relative to the initial (and average) value, in the matrix at 1-day intervals during the 5-day cycle. The fracture pressure driving the motion varies over ±1 kPa and the damped pressure wave extends fully into the centerline of the matrix block for this value of B and k_m. By contrast, the capillary pressure wave (also relative to the initial capillary pressure), shown in Figure 22-3, extends to about 20 cm into the block and its variation is only about ±0.02 kPa at the fracture/matrix interface. The tem-

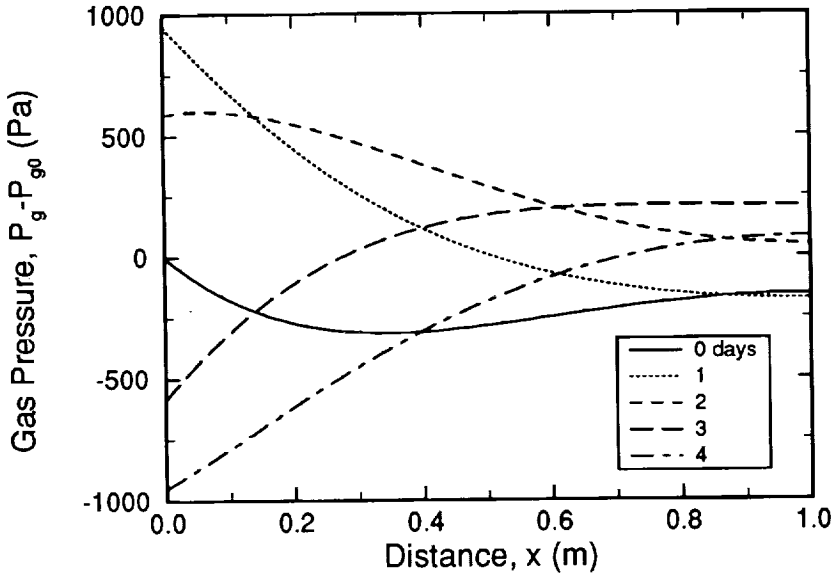

Figure 22-2. Profiles of gas pressure in the matrix during a 5-day barometric cycle.

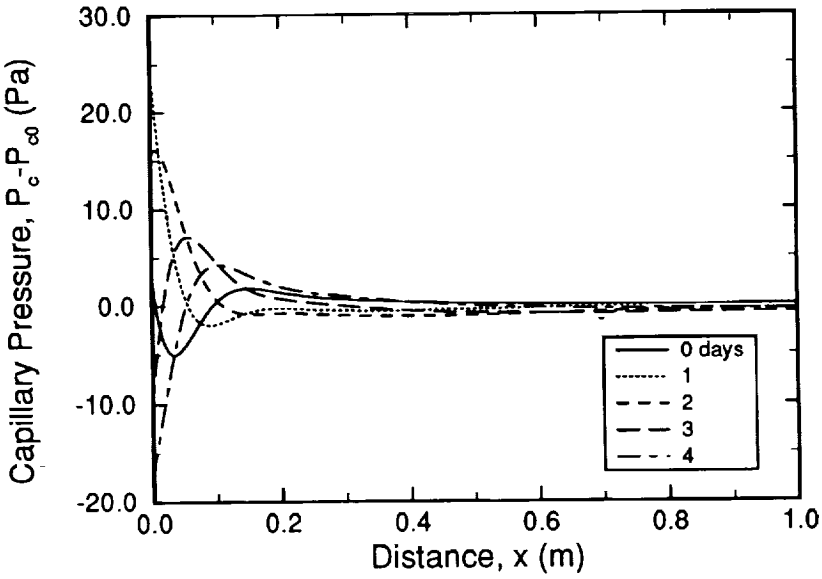

Figure 22-3. Profiles of capillary pressure in the matrix during a 5-day barometric cycle.

perature in the matrix undergoes very minute fluctuations and is not shown. The BP process for this magnitude of barometric pressure fluctuations is essentially isothermal.

Profiles of the vapor mass fraction are shown in Figure 22-4. They resemble a "mirror image" of the gas pressure profiles, i.e., high gas pressure at the fracture corresponds to low vapor mass fraction at the same location, etc. The vapor mass fraction can be expressed as

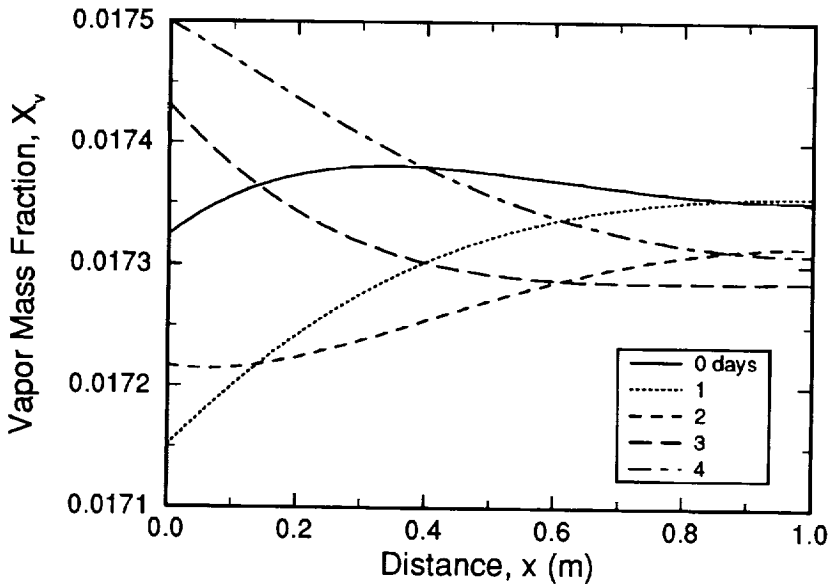

Figure 22-4. Profiles of vapor mass fraction in the matrix during a 5-day barometric cycle.

$$X_v = \frac{P_v M_v}{P_v M_v + (P_g - P_v) M_a}, \tag{22.41}$$

therefore, increasing the gas pressure at the fracture decreases the mass fraction of water vapor for constant vapor pressure. The vapor pressure depends on temperature and capillary pressure, both of which exhibit only small fluctuations, and the fluctuations in vapor pressure are correspondingly small. When the gas pressure rises, it dilutes the concentration of water vapor in the fracture gas as well as in the adjacent matrix gas. This sets up a diffusive flux of water vapor towards the fracture, to equilibrate the water vapor gradient. Thus, the rarefaction and compression of fracture gas allows the mixture to take on more or less water vapor, respectively, for the same temperature and vapor pressure. These fluctuations in water vapor density provide the mechanism for binary diffusion of water vapor through air. This effect is important in understanding the role of binary diffusion between water vapor and air in the gas transport.

Profiles of the mass flux of gas and liquid are shown in Figures 22-5 and 22-6. The average mass flux of the gaseous mixture is driven only by the gas pressure gradient, and the flux profiles are readily understood by comparing with Figure 22-2. Note that the flux of gas can be in both directions at the same time owing to the time lag of points deeper into the block with respect to locations closer to the fracture wall. Beyond about 20 cm into the block, the liquid flux profiles resemble the gas flux profiles. In this region, the liquid pressure gradient is set up solely due to the gas pressure gradient, since

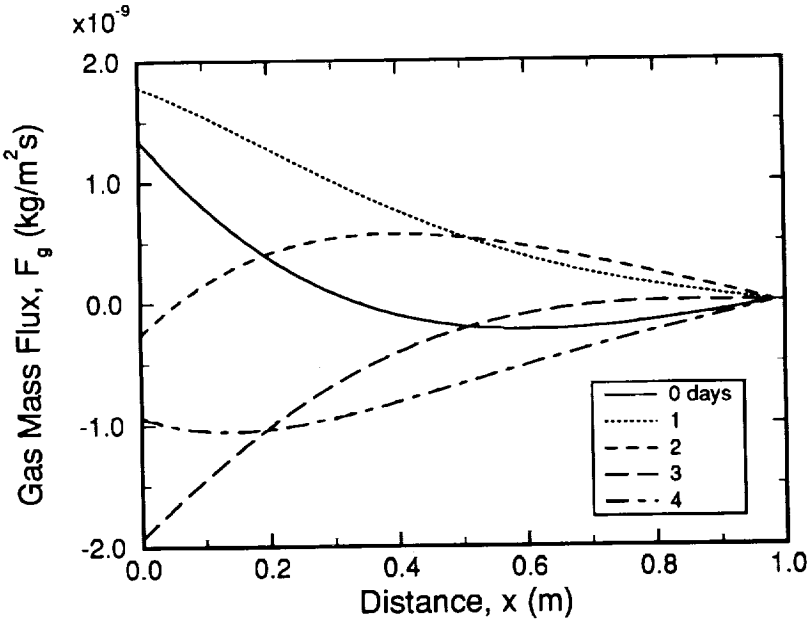

Figure 22-5. Profiles of gas mass flux in the matrix during a 5-day barometric cycle.

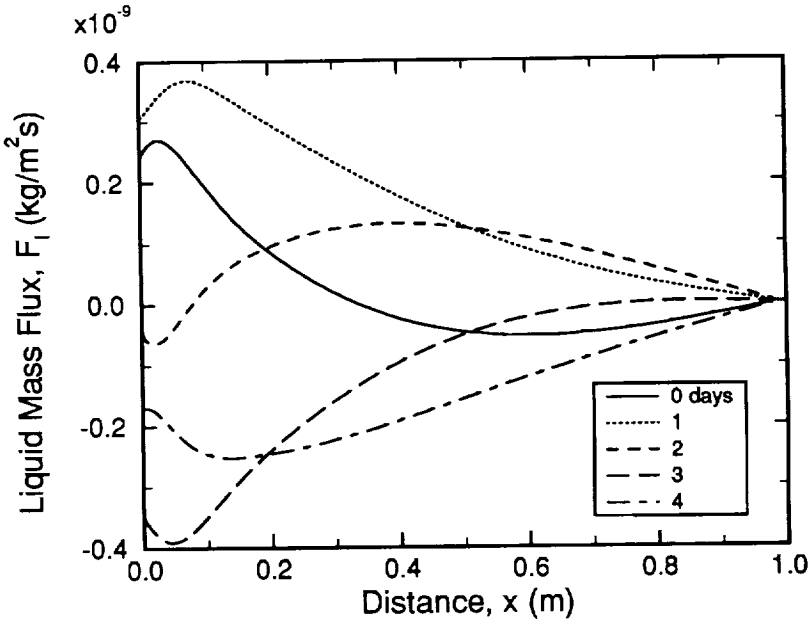

Figure 22-6. Profiles of liquid mass flux in the matrix during a 5-day barometric cycle.

$$\frac{\partial P_l}{\partial x} = \frac{\partial P_g}{\partial x} - \frac{\partial P_c}{\partial x}, \tag{22.42}$$

and the capillary pressure gradient is negligible in this region. Near the fracture, the interaction of the capillary pressure and gas pressure both act to modify the liquid flux profiles.

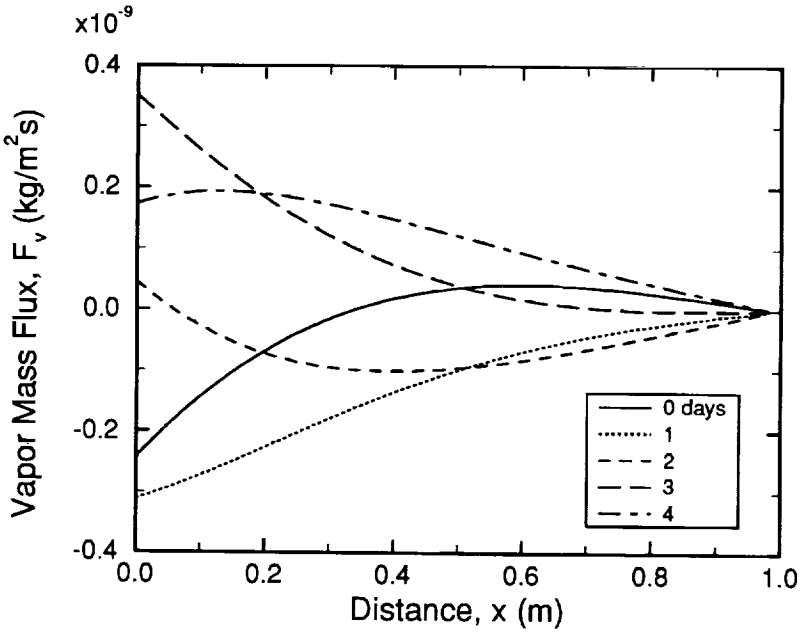

Figure 22-7. Profiles of vapor mass flux in the matrix during a 5-day barometric cycle.

The mass fluxes of liquid are about an order-of-magnitude less than the gas fluxes. The flux of water vapor is shown in Figure 22-7. Note that the flux is in a direction *opposite* to the average gas flux. The mass flux of water vapor is a sum of advective and diffusive components, and under present conditions, the diffusive component overwhelms the advective contribution, and water vapor flows in a direction opposite to the average gas flux. At any horizon, as the gas pressure in the fracture rises the flow of gas via pressure gradients is into the matrix (at least in the vicinity of the fracture). However, the compression of gas near the fracture results in dilution (rarefaction) of the vapor mass fraction relative to locations deeper in the matrix where the increased pressure has not penetrated. This mechanism gives rise to a diffusive flux of vapor in a direction opposite to the gross flow of gas. In fact, this mechanism is required to allow transport of water vapor from the matrix to the fracture (and vice versa) in the presence of pressure driven flows. By this mechanism, incoming drier gas is humidified by the opposing diffusive flux.

The net flux of air is very similar to the average gas flux, indicating that the air flows mostly due to the gas pressure gradient, with the diffusive contribution playing a smaller role. The flux of air does exceed the average gas flux since the diffusive flux component aids (is in the same direction as) the advective component. The net mass flux of air is about an order of magnitude larger than the mass flux of water vapor. The net mass flux of moisture (including liquid water and water vapor), which includes advective and diffusive contributions,

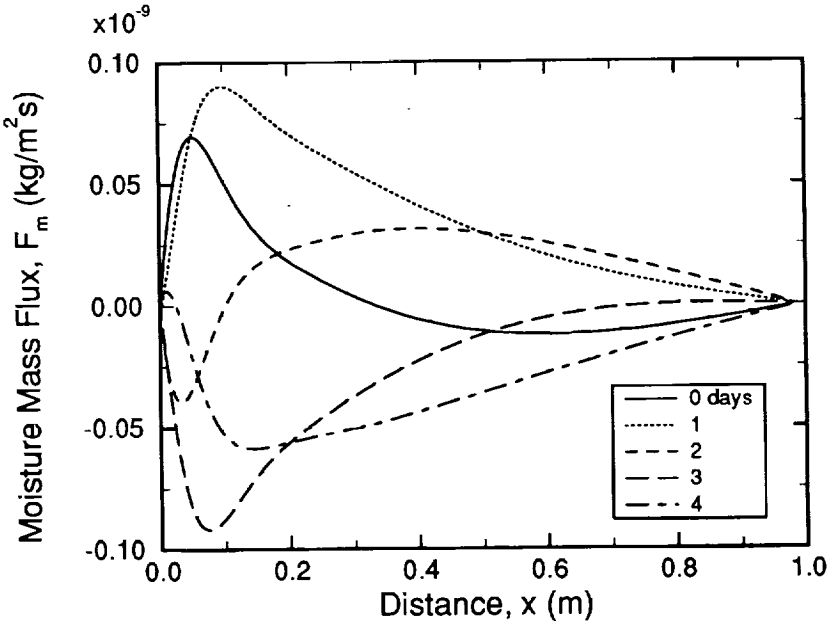

Figure 22-8. Profiles of moisture (liquid and vapor) mass flux in the matrix during a 5-day barometric cycle.

is shown in Figure 22-8. The net flux of water is in the same direction as the average gas flux and the liquid flux. That is, the liquid and vapor fluxes flow in opposing directions, but their sum results in a net flux in the same direction as the liquid mass flux. Thus, the liquid mass flux is larger in magnitude than the water vapor mass flux, although the Darcy velocity of the liquid is roughly 1/1000th of the water vapor velocity. The net moisture flux is about 1/10th the flux of water vapor and liquid; in this case, the mass flux of water vapor and liquid water are nearly the same magnitude.

The net moisture flux decreases rapidly in magnitude as it approaches the fracture. That is, near the fracture is a region undergoing large rates of condensing and evaporating flow such that the net moisture flux is reduced to a value consistent with the fracture transport. This phenomena, which is a recurring feature of this transport mechanism, is related to the net amount of moisture that can be extracted from the matrix and transported out the fracture. Because the fracture model balances the mass flux of material flowing out of the matrix with the transport up and down the fracture, it acts as a throttle to control the amount of moisture which can be carried by the channel. Thus, the combination of rates of gas pressure, temperature and capillary pressure specified by the fracture model, which are strongly coupled with the matrix fluxes, determine the net amount of moisture that can flow into and out of the matrix. Although the matrix liquid and vapor fluxes are of comparable magnitude to the air flux at the fracture, they sum to yield a much smaller net flux of mois-

ture transport into or out of the fracture, the latter being determined by the amount the fracture can transport with the prevailing gas flux and thermodynamic conditions consistent with the adjoining matrix conditions (the fracture and matrix equations require that the vapor mass fraction be continuous at the fracture/matrix interface).

For the base case problem just described, the gas displacement was determined to be ΔL = 556.5 m, while the net efflux of water vapor was ΔM_v = 0.130 kg/m^2/cycle per fracture. For this case, the net moisture respired is q_0 = 0.0029 mm/yr, expressed as an equivalent annual liquid flux of water. This flux can be compared to the net infiltration estimated by Montazer and Wilson (1984), who suggested a nominal value of 0.01 mm/yr. Thus, about 30% of the infiltration estimated by Montazer and Wilson could be extracted back to the ambient by barometric pumping, for the present parameter values. Furthermore, this estimate for barometric pumping represents only about 1% of the theoretical maximum estimated earlier, 0.3 mm/yr. The average normalized concentration of effluent water vapor is $\langle C \rangle$ = 0.0135. Thus, the cyclic average water vapor density, $\langle \rho_v \rangle$, is also about 1% of the average water vapor concentration, $\bar{\rho}_v$ = 0.01732. This suggests the assumptions made in Section 22.1 to compute the theoretical maximum moisture extraction via barometric pumping may not be achievable.

22.5.3 Factors controlling the net moisture respired

Insight into the mechanisms controlling the vapor transport can be attained by consideration of the equations representing the fracture, which serve both to model the fracture and to set boundary conditions on the multiphase flow problem for the matrix block. In order to determine whether there is a net flux of mass into or out of the matrix blocks during each barometric cycle, the various fluxes are integrated over a cycle once the solution is deemed to attain a time-periodic variation. This latter flux determines how much moisture, in the form of water vapor, is transported out of the system by the barometric pumping mechanism.

Because X_v at the interface depends mostly on P_g, while its dependence on T and P_c is negligible, X_v at this location is specified by the gas pressure and is essentially determined by P_g. This means that in the balance equation for water vapor in the fracture, Eqn (22.24), the net moisture flux and air flux must combine in such a way to meet this specification of $\partial X_v/\partial t$. This balance equation, which is coupled with the remaining variables in the problem, controls the net amount of moisture transported into the fracture. This relation couples F_m, F_a, and q_{gy}, i.e., it couples all the conserved fluxes in the model.

Since we solve for time-periodic solutions of the barometric pumping process, the time-phase lag between the gas pressure wave in the fracture and mass fluxes in the matrix plays an important role in determining the net water vapor transport. Consider the expression for the net moisture flux respired per cycle,

$$\Delta M_v = \int_t^{t+T} \rho_v q_{gy} dt = \int_t^{t+T} X_v (F_m + F_a)\, dt \ , \tag{22.43}$$

where the latter form is found using the definition of q_{gy}. This can further be expressed as

$$\Delta M_v = \overline{X}_v \int_t^{t+T} (F_m + F_a)\, dt + \int_t^{t+T} \delta X_v (F_m + F_a)\, dt \ , \tag{22.44}$$

where the mass fraction of vapor has been written as an average value ($\overline{X}_v$=0.01732) plus a deviation. This form is useful to illustrate the role of the phase lag between the net mass flux, $F_m + F_a$, and the vapor mass fraction. The respiration of water vapor per cycle depends on whether the integral per cycle of the net mass flux is non-zero (this effect is embodied in the first term on the right-hand-side) and on the phase difference between the deviation in vapor mass fraction and the net mass flux over a cycle (determined by the second term on the right-hand-side). For example, if the integral over a cycle of the net mass flux were zero, the first term on the right-hand-side would be zero. In this case the second term supplies the entire contribution to the respiration. Because both the net mass flux and the deviation of vapor mass fraction are periodic functions, the value of this integral depends strongly on their phase difference. The integral is maximized or minimized for certain values of the phase lag. In the simulations performed, the net flux of material over a cycle was finite, but often it was the second term on the RHS that contributed to the resulting variations of moisture transport with parameter variations. Hence, it appears that phase shifts of the various conserved quantities are important in determining the net vapor transport in this problem as it was in the contaminant transport problem discussed in the preceding chapter.

22.5.4 Effect of binary diffusion

There has been some discussion in the literature (Philip and de Vries, 1957, Ross, 1984) about enhanced diffusion in multiphase systems. The observations are that the apparent diffusion of water vapor in air is substantially greater than would be expected based on multicomponent diffusion theory modified for porous media, thus the introduction of a vapor diffusion enhancement factor, β. Given this uncertainty in the value of effective diffusivity of binary systems in permeable media, we considered a parameter study to determine its effect on the net respiration, with remaining parameters as specified for the base case problem.

In the contaminant transport problem discussed in the previous chapter, the net transport is maximized for a certain ratio of matrix diffusion distance to matrix width and fracture-to-matrix capacitance ratios. We demonstrate that the respired moisture in the current

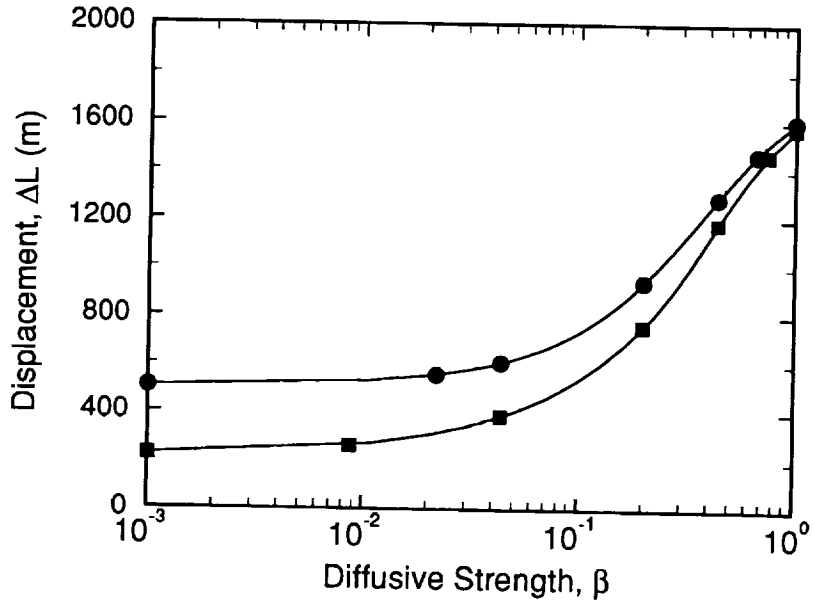

Figure 22-9. Gas displacement in the fracture as a function of diffusive strength and matrix permeability (10μD, circles; 1.9μD, squares).

problem is also maximized for a certain value of diffusion strength, β, here defined as in Tsang and Pruess (1990)

$$J_v = -\beta \rho_g D_{va} \nabla X_v \qquad \beta = \frac{\phi - \theta_l}{\tau} . \tag{22.45}$$

Figure 22-9 shows the displacement of gas in the fracture as a function of β, and for two values of matrix permeability. The maximum value of β=1 completely eliminates the effect of the porous matrix; the formula for the diffusive flux is then the same as for molecular diffusion in an open system. The figure shows a monotonic increase of displacement with increasing β, although the rate decreases as $\beta \rightarrow 1$. The figure suggests diffusion-enhanced gas flow in the fracture/matrix system. Figure 22-10 shows the net outflow of water vapor, expressed as an equivalent flux of liquid water, from the fracture/matrix system as a function of β. This figure shows a maximum efflux for β in the range of 0.4 to 0.6. Notice also that the curves for different matrix permeabilities begin to coalesce with increasing β as diffusion becomes the dominant transport mechanism. For large β, the gas flow becomes nearly independent of matrix permeability (β=1 completely ignores the presence of the porous matrix.). The maximum in q_0 can be explained in terms of the time phase lag between the barometric pressure fluctuations driving the motion and the matrix fluxes. As β increases, the rate of transport of the gaseous mixture increases. Hence, the response time of the matrix fluxes decreases such

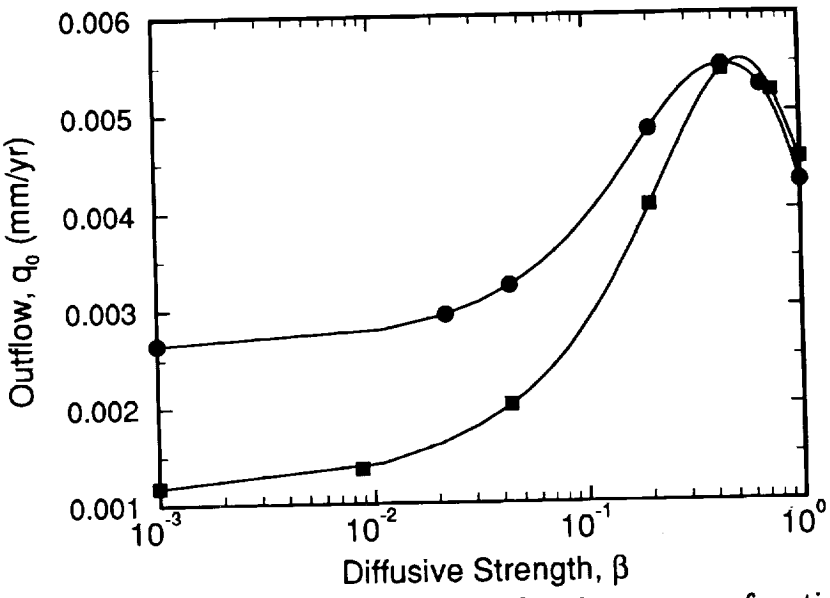

Figure 22-10. Net annual outflow of moisture as a function of diffusive strength and matrix permeability (10μD, circles; 1.9μD, squares).

that the time-phase of the fluxes approaches that of the barometric pressure. Because the vapor mass fraction is 180° out of phase with the barometric pressure, the vapor fraction also approaches a 180° phase lag with the matrix fluxes. Consequently, the net transport, i.e., the value of the integral shown in Eqn. (22.44), decreases. In fact, in earlier work (Nilson *et al.*, 1991) on similarly driven problems it has been shown that a phase lag is critical to achieve a net transport in such systems.

This effect is illustrated in Figure 22-11 which shows the integrand of the second term in Eqn. (22.44) for various values of β. The middle value corresponds closely to the maximum in q_0 and the remaining values correspond to lower values of moisture transport. The amplitudes increase with β for the same reason the displacement does; more gas is transported as the diffusion increases. However, the moisture transport is given by the integral under the curves over a time period. As β increases and the phase angle between δX_v and $F_m + F_a$ decreases, the functions become more symmetric about the ordinate and the integral under the curves decrease. In the figure, the integral for β=1 is less than that for β=0.44 due to the higher positive excursions caused by phase shifts with β, even though β=1 results in larger amplitudes.

22.5.5 Effect of matrix permeability

In this section we consider the effects of variation in the effective matrix permeability, an uncertain quantity for geologic media. Data available for Yucca Mountain (Barnard *et al.*,

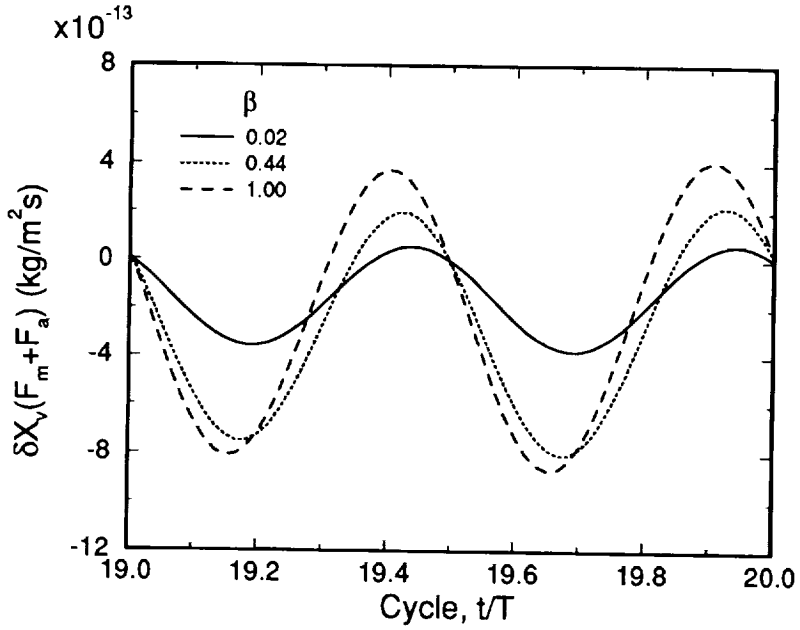

Figure 22-11. Illustration of time-phase shifts and optimal moisture respiration with respect to diffusive strength.

1992) suggests values in the range of a few microdarcies for the welded units. In order to illustrate the role of matrix permeability in this work, we consider matrix permeabilities in the range of micro- to millidarcies.

Figure 22-12 shows the displacement of gas in the fracture and the net efflux of moisture as a function of matrix permeability, with all other parameters as specified for the standard case. The displacement initially increases with matrix permeability, however, an asymptote is eventually attained, roughly for k_m greater than about 0.5 mD. As the matrix permeability increases, the pressure wave is able to more easily penetrate the full extent of the matrix, resulting in increased movement of gases back and forth into the fractures. However, as the matrix becomes even more permeable, the gas pressure gradient within the blocks diminishes, i.e., the response time within the blocks becomes similar to the timescale for gas pressure fluctuations in the fracture. When this happens, the amount of gas transported approaches an asymptotic value. The diffusive component of gas flow decreases as k_m increases, owing to a flatter gradient of X_v with increasing k_m.

The moisture transport has a maximum for a matrix permeability of about 50 μD (for present parameters). Increasing k_m from the low values initially results in an increase in the moisture transport for the same reason the entire gas flow increases. As k_m increases further

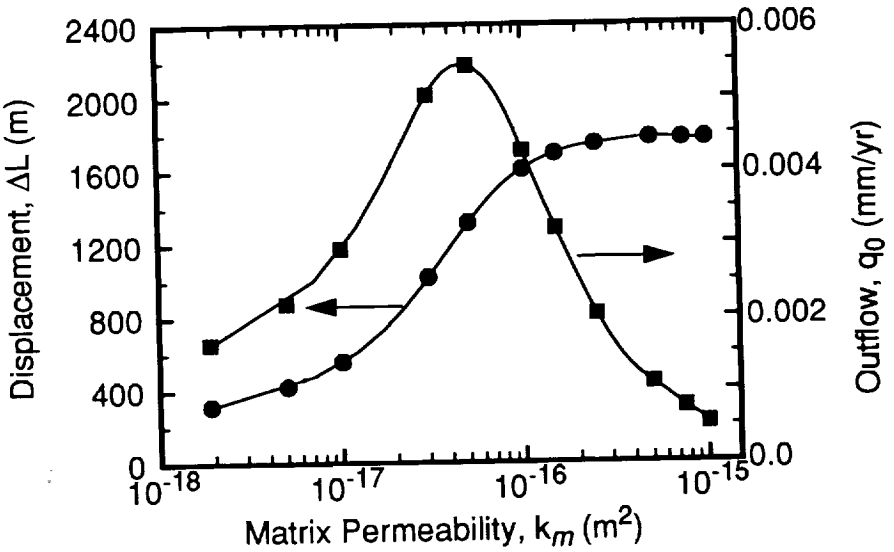

Figure 22-12. Gas displacement and net annual outflow as function of matrix permeability. Symbols indicate numerical values.

the response time of matrix fluxes within the blocks decreases. Therefore, the time phase lag between matrix fluxes at the fracture/matrix interface and the barometric pressure decrease, causing a decrease in the net water vapor extracted per cycle. This is the same effect discussed earlier with large values of diffusion. In between these limits lies a value of k_m which results in a maximum efflux of moisture. Note that this maximum will depend on the other problem parameters as well.

22.5.6 Effect of bulk permeability

The bulk permeability depends on the ratio of aperture cubed over the fracture spacing. However, the simulations indicated that the more fundamental variable is B and not w. For fixed B, variation of w changes the displacement, ΔL, and the amount of moisture extracted per unit area, per fracture, per cycle, (ΔM_v), but the net outflow of moisture is independent of w. This also implies that the net outflow of water vapor is independent of bulk permeability, *with respect to changes in aperture*. Implicit in our model is that the gas flow in the fracture is unaffected by w, assuming w is larger than some threshold value where the resistance to gas flow becomes important. In other words, the imposed amplitude of gas pressure fluctuation is independent of w in this simple model. Under these conditions, the displacement depends on aperture according to, $\Delta L \sim w^{-1}$, and a similar relation holds for ΔM_v. The net efflux, q_0, is proportional to $\Delta M_v w$ and is therefore independent of variations in aperture.

The dependence of respiration with B is more complicated. Figure 22-13 shows the displacement of gas and the bulk transport of water as a function of fracture spacing. The apertures for these variations were chosen to keep the bulk permeability constant at 10 Darcies. In order to maintain uniform k_b, the aperture was increased according to

$$w \sim B^{1/3}, \tag{22.46}$$

as the fracture spacing is increased. The figure shows that both the displacement and outflow are maximized for a fracture spacing near 1 m. As the block thickness becomes large, the amount of water vapor that is extracted per fracture approaches an asymptotic value, $\Delta M_v w \rightarrow$ constant; for spacings greater than about 3 m and for a 5 day time period of the barometric fluctuations, the blocks act as though they were semi-infinite in extent (perpendicular to the fractures), and the water vapor extracted per fracture is independent of B. Therefore, the displacement decreases because the aperture must be increased to maintain constant bulk permeability. The bulk moisture extracted also decreases as B becomes large because q_0 is inversely proportional to B. The displacement, the respiration flux per fracture and the net efflux of water vapor also decrease as the spacing becomes small. Clearly, the displacement will decrease as the blocks become thin simply because there is less gas to move back and forth in the matrix blocks. Less gas also means less water vapor. However, the time-phase shifts between the mass fraction of water vapor in the fracture and the matrix fluxes also influences the transport of water vapor. The smaller the spacing, the more accessible is the resident moisture to be extracted. Also, the pressure wave in the matrix

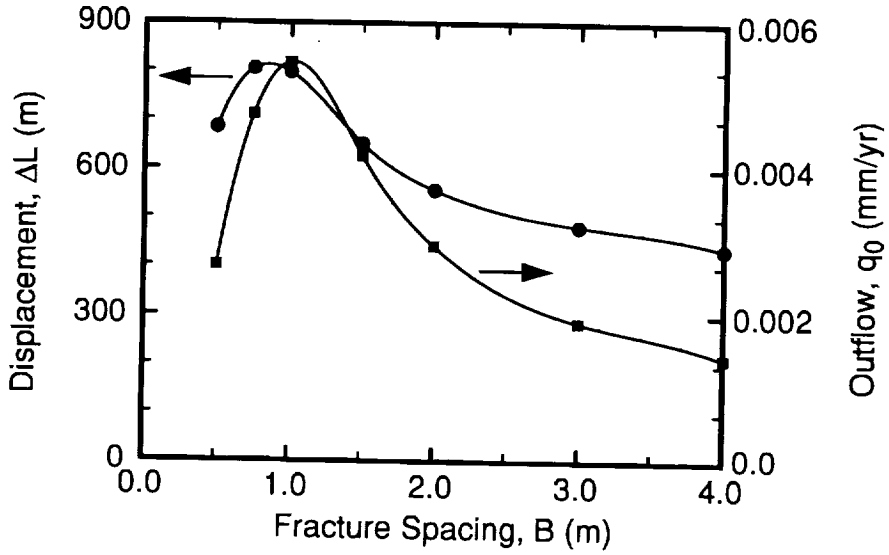

Figure 22-13. Gas displacement and annual net outflow as a function of fracture spacing.

becomes closer in phase with the barometric pressure, causing cancellation in the integral per cycle of water vapor extracted from the matrix blocks. This same effect reduced the moisture transport when the diffusion strength approached unity, and when the matrix permeability became relatively large, $k_m > 100\mu D$. Each of these conditions reduces the phase difference between $X_v(t)$, and $F_a(t) + F_m(t)$ at the fracture/matrix interface.

22.5.7 Other parameter effects

Reducing the active depth, L, of the fracture/matrix system from 600 to 100 m reduces the gas displacement and respired moisture in a linear fashion. The 100 m depth corresponds to the depth of the nonwelded Paintbrush unit. If this unit is substantially less fractured than the welded units and consequently has a much smaller bulk permeability, it could attenuate barometric pressure fluctuations down the fractures.

The barometric pressure fluctuation used in the foregoing, ΔP = 1kPa, was doubled to determine the model sensitivity. Doubling ΔP quadruples the gas displacement and the efflux of water vapor per fracture, i.e,

$$\Delta L \sim \Delta P^2 \ . \tag{22.47}$$

A similar relation holds for ΔM_v and q_0 with respect to ΔP.

In the foregoing analysis, we have only considered the 5-day barometric cycle. The simulations indicate that this cycle is more effective in extracting moisture than the diurnal cycle, for which measured variations in barometric pressure are about 8 millibars peak-to-peak. This is less than half the 20 millibars (peak-to-peak) used for the 5-day cycle, and the preceding shows the respiration varies quadratically with the pressure amplitude. Indeed, we simulated the base case for the diurnal cycle and computed a net outflow, q_0=0.001 mm/yr, which is about one-third the outflow for the 5-day cycle (the reduction is not simply $(8/20)^2$ because we've also shortened the period of the fluctuation by one-fifth). The displacement for the one-day cycle was, ΔL = 98.24m, and the average concentration, $\langle C \rangle$ = 0.0054. The former is about one-fifth the displacement of the 5-day cycle, and the latter about four-tenths.

22.6 Conclusions

We have presented a theory for the motion of air and water in an unsaturated fractured permeable medium driven by fluctuations in barometric pressure. The model is of the multiple-continuum type where separate equations represent the fracture and matrix. The separate continua are coupled by transfer terms involving exchange of mass and energy between the fractures and matrix. The barometric pumping process is simulated numerically by a method-of-lines procedure using finite-difference approximations for spatial gradients.

The barometric fluctuations are approximated by a sine wave in time, with an amplitude corresponding to measured barometric fluctuations at Yucca Mountain, and with a period of five days, typical of weather-induced barometric cycles. Time-periodic solutions to the governing equations are computed in order to estimate the moisture extraction per cycle.

Estimates of the annual net outflow of moisture by barometric pumping range between 0.001 and 0.006 mm/yr, expressed as an equivalent liquid flux. This represents at most about 2% of the theoretical maximum of 0.3 mm/yr, discussed in the introduction. This also represents about 50% of some estimates of net infiltration into Yucca Mountain (Montazer and Wilson, 1984), i.e., half the estimated infiltration could be respired back into the atmosphere by barometric pumping. Owing to the uncertainty in material properties for Yucca Mountain, parameter variations of the diffusion strength, matrix permeability, and fracture spacing were conducted. Maxima in the estimated outflow of moisture was found for variations of each of these parameters. The maxima are related to the time-phase lag between matrix fluxes and the barometric fluctuations driving the motion.

The motion of the various components and phases is a complex function of parameters. However, several general features were determined. 1) The rarefaction and compression of gas in the fractures gives rise to a diffusion-driven flux of water vapor opposing the gross flow of the gaseous mixture. 2) Even with evaporation/condensation of water, particularly near the fracture/matrix interface, the barometric pumping process is essentially isothermal. 3) Because the moisture being extracted by barometric pumping mostly resides in the matrix, the block size (fracture spacing) plays an important role in determining the net transport achievable by this mechanism. However, beyond a certain block size, no additional net outflow is attainable for a given characteristic barometric time period, i.e., the blocks act as though they were semi-infinite in extent.

Chapter 23
Appropriateness of One-Dimensional Calculations

(Eaton)

Total-system performance analysis typically requires hundreds of discrete calculations to statistically account for the uncertainties in the parameters, such as material properties, which define the problem. The material parameter variability within the layered-tuff stratigraphy at Yucca Mountain is greatest in the vertical direction as a result of differences in depositional, cooling, and alteration histories of the individual units. These same differences occur in a lateral sense; however, they generally do not vary as rapidly as in the vertical sense. In addition, the layered rock mass itself is cut by faults that cause offset of the layers and by fractures that introduce discontinuities. Therefore, stochastic simulations that can sample from a range of parameter values are required to represent the uncertainty and variability of those values. Including the details of all these heterogeneities in numerical models of the mountain results in computer calculations which are computationally intensive. One practical alternative is to perform a series of one-dimensional analyses. When the dimensionality of a problem is reduced to a single dimension for computational purposes, the applicability of the results obtained using the simplified model may be of questionable value. This chapter investigates the validity of one-dimensional calculations in modeling the multidimensional waste repository problem.

The following sections outline numerous issues which help define the regimes in which one-dimensional modeling is applicable. The two primary issues addressed are: (1) When is it appropriate to use effective material characteristics to incorporate small-scale geologic heterogeneities into large-scale modeling and (2) Can appropriate numerical boundary conditions, such as unit-gradient, be developed to make it computationally expedient to obtain lateral-flow estimates resulting from geologic dip using one-dimensional calculations? The material in this chapter is presented in greater detail by Eaton (1993).

The results of these studies demonstrate that the use of one-dimensional modeling to analyze a multidimensional problem may be less restrictive than previously assumed. In most cases, the effect of small-scale, low-conductivity heterogeneities can be accounted for through the use of effective hydraulic conductivity. This occurs, in part, because of the highly nonlinear nature of unsaturated flows. It is also shown that when the media are assumed to be homogeneous along dipping geologic units, a minor extension to one-dimensional calculations (the unit gradient approach) can be used to obtain reasonable estimates of two-dimensional flow path lines without additional computational complexity. Considering the two-dimensional effect of lateral flow on path lines can be beneficial when calculating solute transport because the geometry of the two-dimensional path lines can vary considerably from

their one-dimensional counterpart. It is important to note that only the relationships between one- and two-dimensional flow are considered in this study. The extension of these equivalent material concepts to three-dimensional geometries will be considered in future work.

23.1 Effect of material heterogeneity

One approach to reducing the number of dimensions required in numerical computations is to include the effect of small-scale material heterogeneities by lumping them into larger-scale equivalent properties, such as effective hydraulic conductivity. The simplest type of material heterogeneities is that of a perfectly layered system. For perfectly layered systems, one can analytically derive the effective hydraulic conductivity for flow parallel to and perpendicular to the layering (Freeze and Cherry, 1979). For materials which are not perfectly layered, approximating the effective material properties can be considerably more complex. Several studies have been made (Eaton and Dykhuizen, 1988; Martinez *et al.*, 1992) which attempt to identify the flow regimes in which the concept of effective material properties is appropriate. These studies are outlined below.

23.1.1 Effect of low-hydraulic-conductivity obstructions on effective properties

The effect of material heterogeneities on two-dimensional deterministic calculations of water flow and particle travel times has been investigated numerically by Eaton and Dykhuizen (1988). Upper and lower bounds on the infiltration rates for Dirichlet boundary conditions were defined as a function of the degree of material heterogeneity. The parallel/series concept for predicting flow limits was previously documented by Crane *et al.* (1977) for materials with constant-material properties. Crane assumed that materials with different conductivities were arranged in either a parallel or series configuration and that the materials were saturated. Because of the nonlinear nature of flow in partially saturated media, Crane's techniques for determining the bounds for saturated flows were found to be too stringent. A new, less stringent set of limits was proposed by Eaton and Dykhuizen.

23.1.1.1 Problem definition and results

For simplicity, it was assumed that the region considered consists of a two-dimensional array of material units having small and large hydraulic conductivities (Figure 23-1a). This arrangement is idealized as a uniform array of high and low hydraulic conductivity materials (Figure 23-1b). The flow through a single unit cell (Figure 23-1b) was investigated. The mesh shown in Figure 23-1c was used for the two-dimensional calculations. The size of the flow obstruction was varied by stretching the mesh horizontally. The hydraulic conductivity for the highly permeable material is chosen to be the composite conductivity of the hydrogeologic

Tiva Canyon unit (Klavetter and Peters, 1986) (Figure 23-2). The hydraulic conductivity of the low- conductivity obstruction into the unit cell is assumed to be zero, which is the limiting case.

Steady-state numerical solutions of the Richards' equation (Richards, 1931) for a wide range of obstruction sizes and water-flow rates were obtained. A bottom boundary pressure condition of -100 m was specified for all cases. Three different flow rate regimes were investigated by fixing the top boundary pressure at -17.86 m to give flow rates of ~0.2 mm/yr, Case A; -1.225 m to give ~1.0 mm/yr, Case B; and -0.6 m to give ~64 mm/yr, Case C. The hydraulic conductivity range for these cases is shown in Figure 23-2.

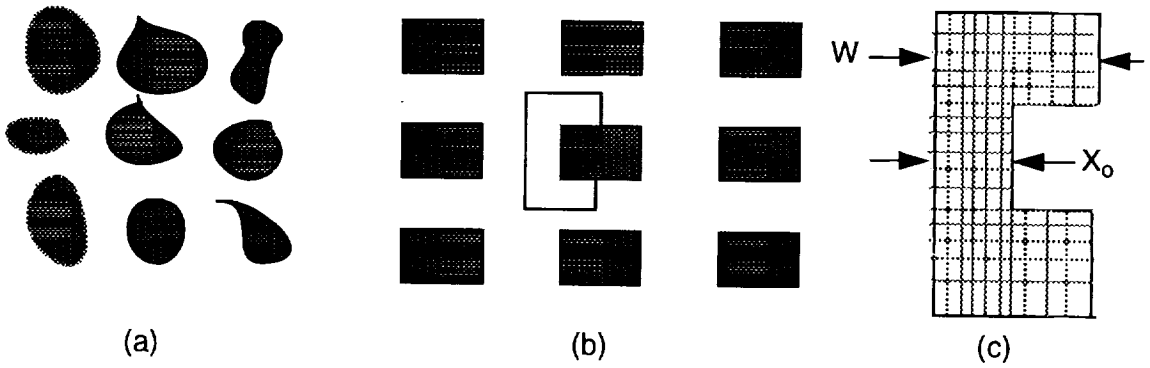

Figure 23-1. (a) Nonhomogeneous material concept, (b) assumed idealized symmetric array and (c) numerical mesh.

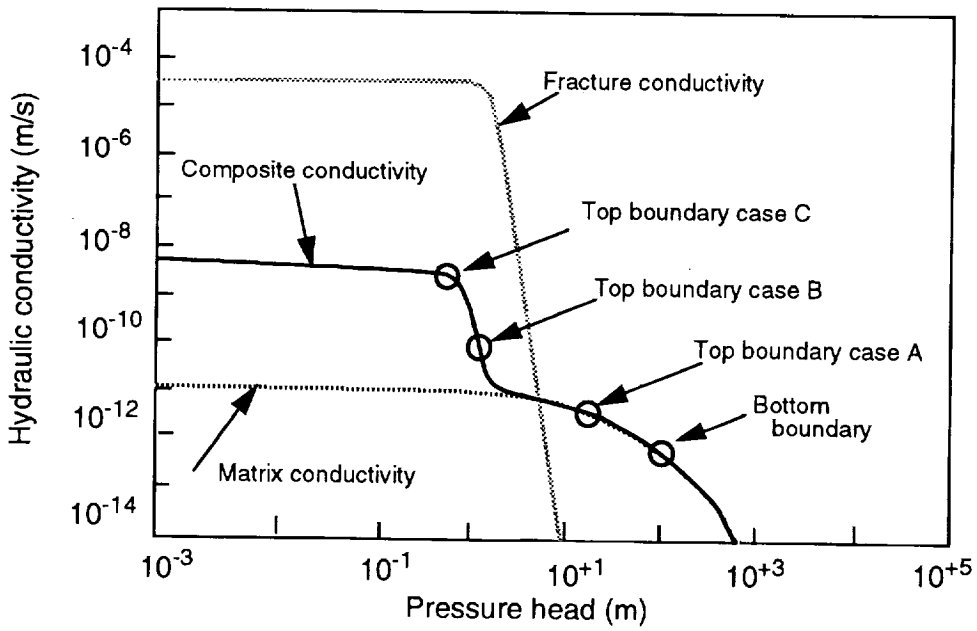

Figure 23-2. Material hydraulic conductivity.

Case A spans a relatively constant portion of the conductivity curve, while Cases B and C span the nonconstant portion of the conductivity curve. Solutions were obtained for the three different pressure boundary conditions for reduced-flow areas (X_o/W) varying from 0.0125 m to 0.95 m. Additionally, a one-dimensional solution ($X_o/W = 1.0$) was computed for each case. The average nondimensional flux, as a function of reduced flow area, is given for all three cases in Figure 23-3. This figure also shows the flow rates that result when the low- and high-permeability materials in the region are arranged in parallel and series configurations. For Case A, the flux through the region gradually decreases as the obstruction size is increased and it is always bounded by the parallel and series cases. Intuitively, this is reasonable because the material hydraulic conductivity in the resulting pressure range is relatively constant. However, it still changes by an order of magnitude. Some of the water undergoes a more tortuous path around the obstruction, thus increasing the total resistance to flow.

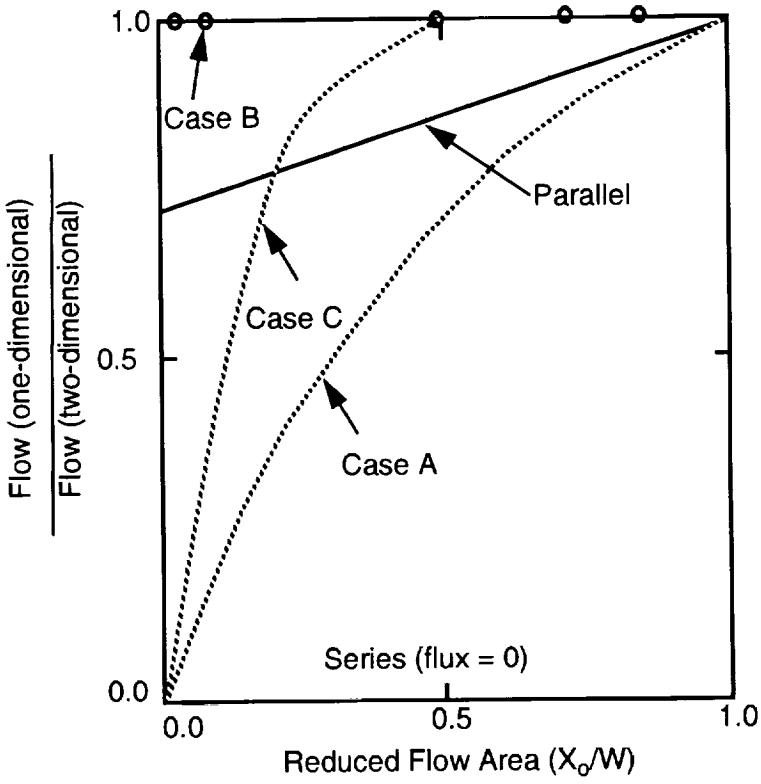

Figure 23-3. Nondimensional fluxes for three geometric configurations (Eaton and Dykhuizen, 1988).

Case B is more interesting in that the average flux through the region is nearly independent of the obstruction size. The flow is independent of the obstruction size because

of the highly nonlinear nature of the unsaturated material conductivity in this pressure range. This is a pronounced departure from the parallel limit for fixed-conductivity material.

For the high-flux condition, Case C, the calculated flux is less sensitive to obstruction size than in Case A, but more sensitive than in Case B. The level of sensitivity is a function of material nonlinearities and the zone of influence of the obstruction on pressure gradients. A detailed explanation of these results is given by Eaton and Dykhuizen (1988).

The effect of the geometry change, resulting from the nonhomogeneous properties, on particle travel times was investigated for Case B. The ratio of fastest to slowest travel times varied from one to four with increase in obstruction size. As the obstruction increases in size, saturation increases and water previously flowing through the matrix now experiences less resistance to flow in the fractures. The result is an increase in fracture flow and a decrease in particle travel time because of the small-fracture porosity.

23.1.1.2 Conclusions regarding low-hydraulic-conductivity obstructions

The effect of obstruction size on average flux through the heterogeneous-flow region is a strong function of nonlinearities in the material characteristic curves. When conditions are such that the highly nonlinear portion of the hydraulic conductivity curve is not involved, the average flux through the region decreases monotonically with obstruction size and the flow rates are bounded by the parallel and series equivalents. When conditions are such that the flow involves the highly nonlinear portion of the curves (corresponding to the onset of fracture flow), the average flux is a weaker function of the obstruction size and flow rates are not bounded by the parallel and series equivalents.

23.1.2 Effects of unsaturated fractures on effective material properties

The influence of horizontal fractures on the steady seepage of moisture in variably saturated porous media was analyzed by analytical and numerical means (Martinez *et al.*, 1992). In their work, the fractures were assumed to contain many open (dry) regions and assumed to be distributed periodically in two dimensions.

23.1.2.1 Problem description

A schematic of the periodic global fracture/matrix system is given in Figure 23-4a. A unit cell of the region and boundary conditions are shown in Figure 23-4b. The dry region of the fracture forms a barrier to moisture flow through the geologic medium. An idealized two-dimensional model that maximizes the effect of the fractures was analyzed. The results of the analysis quantified the effect of the dry regions of the fractures on global-water flow through the fractured medium. An apparent hydraulic conductivity is determined such that the fractured system can be replaced by a homogeneous medium for describing steady-unsaturated flow. An asymptotic analysis yields an analytic expression for the apparent

hydraulic conductivity through such a system in the limit of a small sorptive number (fracture spacing divided by a characteristic capillary suction) for the intact matrix material. The apparent hydraulic conductivity for arbitrary spacing and the sorptive number is determined by numerical means. The numerical model accounts for variable hydraulic conductivity as a function of the local pressure head, whereas the asymptotic solution represents the limit of constant conductivity. The numerical results confirm the analytical solution as a lower bound on the apparent hydraulic conductivity.

23.1.2.2 Conclusions regarding unsaturated fractures

It was concluded from this study that the flow is relatively unimpeded by the fracture system except for the cases where the blockage ratio of the unit cell (b/w) approaches one.

23.1.3 Effective hydraulic conductivities for random material mixtures

A conceptual understanding of the effect of material heterogeneities on the flow of water through low permeability rock was obtained by Dykhuizen and Eaton (1991) through solving the Richards' equation for multiple realizations of materials randomly located within a meter-scale region, Figure 23-5. The object of this study was to determine a procedure for determining the effective hydraulic conductivity of the material mix as function of material mix and conductivity ratios.

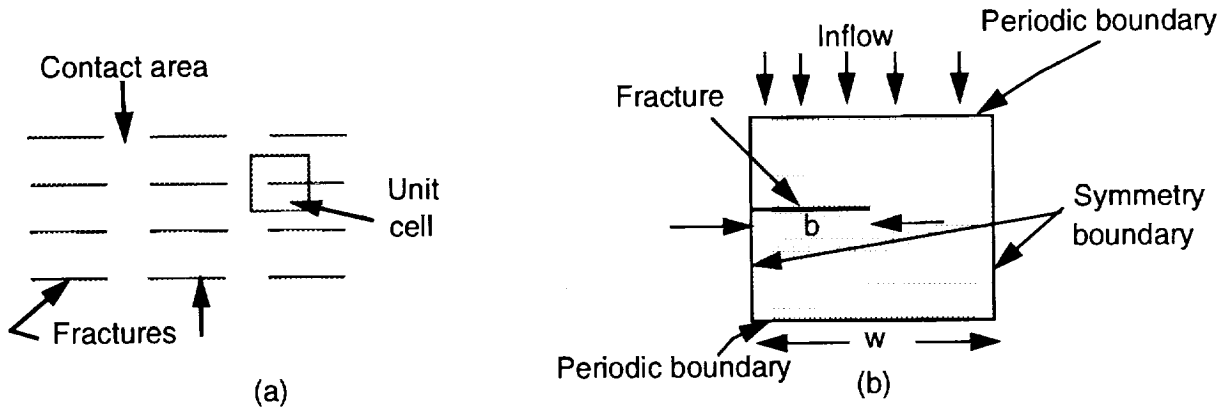

Figure 23-4. (a) Schematic of the periodic global fracture/matrix system, (b) representative unit cell of the periodic fracture model.

23.1.3.1 Problem description and results

Figure 23-5 shows three randomly arranged spatial mixes of the low and high hydraulic conductivity materials considered in this study. The percentages given are the percent of low conductivity material. The material property values for this study were taken from the PACE-90 study repository unit (Barnard and Dockery, 1991). The value of saturated

hydraulic conductivity, equal to 2×10^{-11} m/s, was assigned to the high-conductivity material. The value of hydraulic conductivity for the low-conductivity material was varied between two and six orders of magnitude smaller than the high-conductivity material.

Figure 23-5 also shows the calculated flow path lines for these three geometric mixes of high- and low-permeability materials. The results of these material variations on flow resistance, mechanical dispersion, and channeling were addressed using multiple realizations of random geometric hydraulic conductivity mixes. The 50% mix tends to result in noticeable flow channeling and the largest mechanical dispersion based on maximum and minimum particle-path-line travel times. The variation of path line travel times for the 50% mix was as high as a ratio of eight.

23.1.3.2 Conclusions regarding random mixtures

For the types of geometries and material mixes considered in this study, two-dimensional flow can be reasonably approximated using one-dimensional calculations and the effective hydraulic conductivity obtained from Kirkpatrick's theory (Kirkpatrick, 1973). Many formulations have been proposed such as arithmetic and harmonic averaging to obtain effective properties. Kirkpatrick's equation provides a power averaging for random geometric mixtures of material that fall between the arithmetic and harmonic extremes.

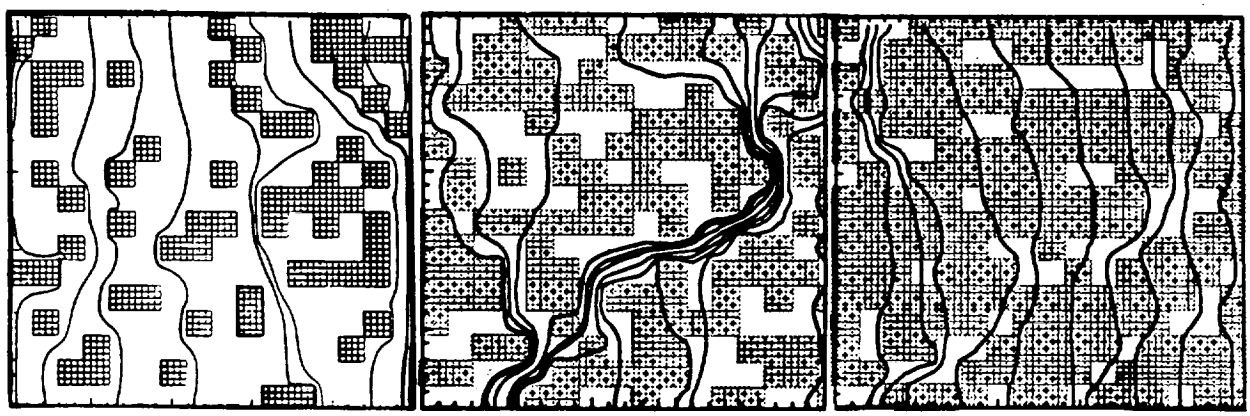

Figure 23-5. Flow path lines for material mixes: (a) 25%, (b) 50%, and (c) 75% (precentages based on the low conductivity material).

23.2 Effect of boundary conditions on global-scale modeling

Section 23.1 of this report deals with small-scale heterogeneities on the order of 0.1 to 10 m. We shall now consider the difficulties associated with global-scale modeling. This scale has not received as much attention as smaller scales because it is computationally intensive.

The results of numerical calculations are often strongly influenced by the flow conditions applied at the boundaries. In a comprehensive study by Prindle and Hopkins (1990), they give the results of a set of numerical calculations of water infiltration through a two-dimensional model of Yucca Mountain.

Computational parameters which were varied include: the rate of infiltration (0.01 mm/yr to 3.0 mm/yr), the width of the fault (0.5 m to 5.0 m), anisotropy hydraulic conductivity ratios (1v:1h to 1v:500h), and material characteristics. However, no variation was done at the vertical and bottom geometric boundaries. All calculations were made using fixed pressure along the bottom (water table) and no flow on both vertical boundaries. The results of Prindle and Hopkins (1990) indicated that the application of this no-flow condition has a strong influence on the overall flow patterns. Simply by the nature of the no-flow condition, all flow approaching the fault at the dip boundary of the region is forced to flow vertically down through the flow domain. All of the extensive variation of fault width and fault material properties affected the exact width of the region with considerable downflow. However, the results for each case were essentially the same. The water was forced to flow down through a small region in the vicinity of the applied no-flow boundary condition.

The unit-gradient boundary condition shows promise for relaxing this potentially unrealistic no-flow boundary restraint. The application of this condition assumes that the component of flow exiting the boundary is driven by a unit-pressure gradient. The following section will show that this concept may be useful in significantly reducing the computational effort required to simulate two-dimensional flow. The use of one-dimensional calculations in conjunction with the unit-gradient boundary concept and dip information to generate two-dimensional flow path lines will be discussed.

23.2.1 Unit-gradient boundary conditions

Application of the unit-gradient boundary condition results in constant flow parallel to the geologic-unit interfaces and path lines that are similar when the material is assumed homogeneous along these units. This implies that, under these ideal conditions, two-dimensional flow path lines can be generated using an extremely simplified one-dimensional computational mesh. This approximation can reduce computational times required to generate two-dimensional path lines by one to two orders of magnitude. Application of the unit-gradient condition will be demonstrated below to illustrate the concept and its usefulness.

23.2.1.1 Problem description

The problem domain is a rectangular grid (Figure 23-6) with the dip of the geologic units approximated by rotating the gravitational force vector by 6.25 degrees. The 500-m wide

domain considered started ~500 m east of drillhole H-5 at Yucca Mountain. The material properties for the four geologic regions are shown in Table 23-1. Unsaturated hydraulic conductivity values are generated using the van Genuchten (1978) formulation. The fractures properties for all layers are: K_s=4x10^{-5}, m/s α=1.2851, 1/m, β=4.23, and S_r=0.395.

Steady-state solutions were obtained using evenly distributed steady-state infiltration rates of 0.01, 0.1, and 1.0 mm/yr across the top boundary. Unit-gradient boundary conditions were specified at the left, right, and bottom boundaries. These conditions are similar to the second type boundaries discussed by McCord (1991). A second set of solutions was obtained by replacing the side unit-gradient conditions with no-flow conditions while maintaining the unit-gradient condition along the bottom.

23.2.1.2 Description of the unit-gradient boundary condition

The unit-gradient condition specifies that the flux component exiting the boundary be computed by assuming that the head gradient in the direction of the gravity vector at the boundary is unity. Consequently, at boundaries where the unit-gradient condition is specified, the flux components leaving the region, are defined by

$$q_x = -K_x \sin\theta \tag{23.1}$$

and

$$q_z = -K_z \cos\theta \quad , \tag{23.2}$$

where

q_x is the Darcy flux along the x-coordinate direction (m/s), q_z is the Darcy flux along the z-coordinate direction (m/s), K_x and K_z are the prevailing hydraulic conductivity as a function of capillary pressure (m/s), and θ is the dip of strata. The x and z coordinates are parallel and perpendicular to the geologic unit interfaces.

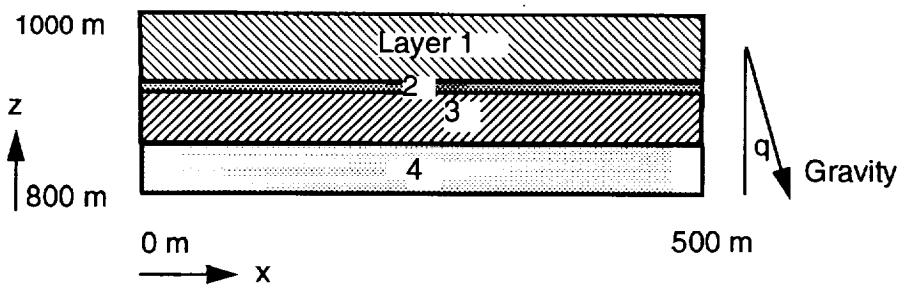

Figure 23-6. Two-dimensional computational domain.

Table 23-1. Material properties

Layer	Porosity Total	K_s (m/s)	α (1/m)	β	S_r	Fractures ($1/m^3$)
1	0.11	$2x10^{-11}$	0.00567	1.798	0.080	28.3
2	0.09	$3x10^{-12}$	0.0033	1.798	0.052	35.6
3	0.21	$8x10^{-11}$	0.0265	2.223	0.164	2.0
4	0.41	$3x10^{-12}$	0.0220	1.236	0.010	1.6

The flux components at the boundaries, parallel to the domain boundaries, are computed using the pressure gradients computed by the code. This is essentially the same method as is used at all internal mesh points. It is important to note that for computational geometries that are not parallel and perpendicular to the unit boundaries, a coordinate rotation must be applied.

23.2.1.3 Results of varying applied boundary conditions

Figure 23-7 shows steady-state Darcy velocity vectors for an infiltration rate of 0.01 mm/yr. For the purpose of comparison, the Darcy velocity vectors using the no-flow conditions are given in Figure 23-8. The flow near the middle of the mesh is not significantly affected. This implies that, if the region were considerably longer, the side boundary conditions may not significantly affect the results in regions adequately removed from these boundaries. Particle path lines for the 0.01 mm/yr case are given in Figure 23-9 for the no-flow and unit-gradient conditions. Comparison of these path lines show that considerably more relative lateral particle movement is calculated using the unit-gradient boundary conditions.

23.2.1.4 Implications for simplified two-dimensional flows

There is an interesting aspect regarding the use of the unit-gradient boundary condition that may be extremely useful for reducing computational times required to approximate two-dimensional flows. That is, the flow of water is constant along each geologic unit if each geologic layer is assumed to be homogeneous. Under these assumptions the fluid particle path lines are similar to each other.

Thus using information regarding the average dip of each geologic unit, a minor extension may be made to any one-dimensional code which allows the calculation of a single path line. Because of the mathematically similar nature of scenarios with these constraints, this path-line configuration is applicable at all horizontal locations along the geologic unit. Significant savings in computer execution times can be realized by approximating two-

dimensional flow using this concept. Our current plan is to demonstrate this concept by making the appropriate modifications to the one-dimensional code TOSPAC (Dudley *et al.*, 1988).

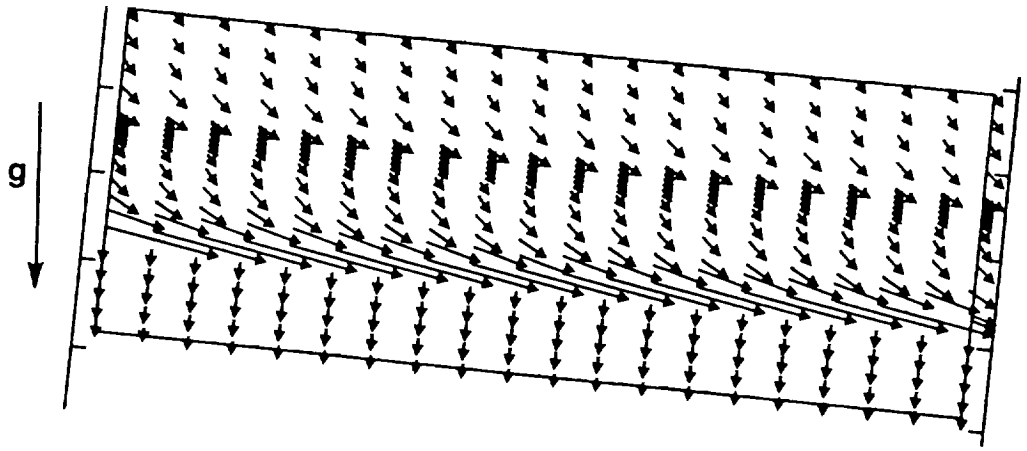

Figure 23-7. Darcy velocity vectors, using unit-gradient boundary conditions, q=0.01 mm/yr.

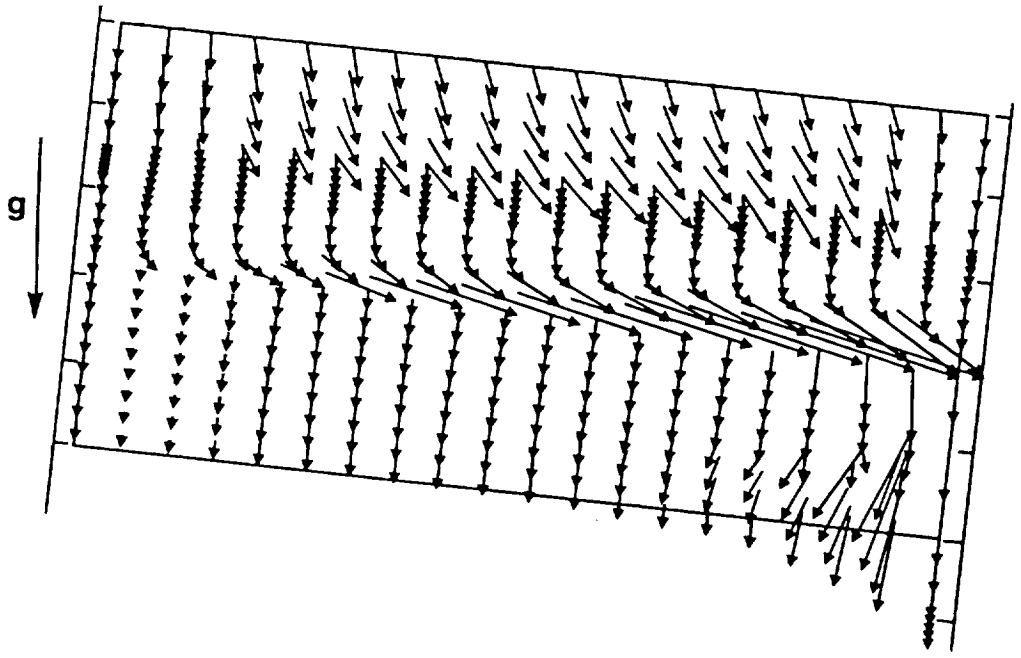

Figure 23-8. Darcy velocity vectors, using no-flow boundary conditions, q=0.01 mm/yr.

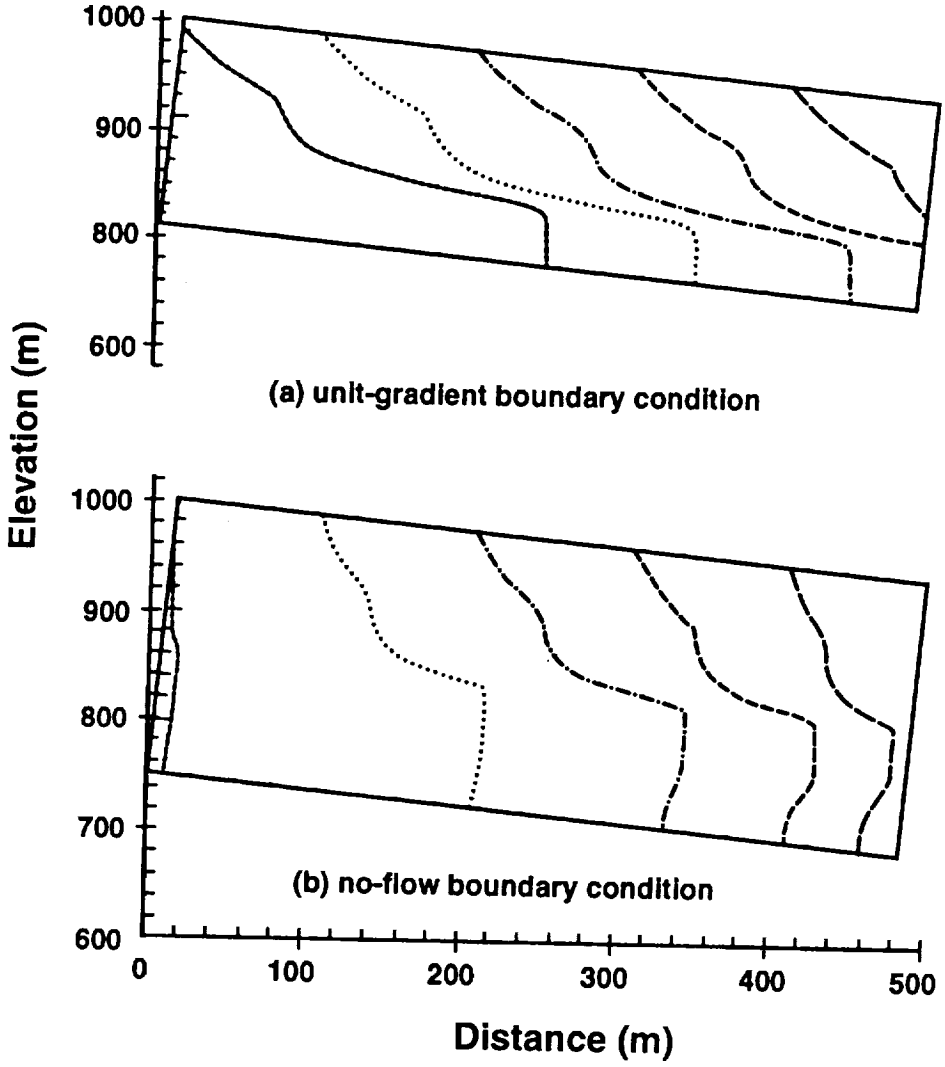

Figure 23-9. Particle path lines, 0.01 mm/yr.

23.3 Nonisotropic hydraulic conductivity effects

In all numerical calculations of the flow through Yucca Mountain to date, the ratio of hydraulic conductivity parallel and normal to layering is assumed constant within a geologic unit. Most calculations have assumed the ratio equal to one. Values as large as 500 were considered by Prindle and Hopkins (1990). Considerable experimental data exist which imply that the hydraulic conductivity ratio is a strong function of saturation and dip of the geologic strata (Yeh *et al.*, 1985). LLUVIA-II (Eaton and Hopkins, 1992) has been used to predict the nonisotropic nature of equivalent hydraulic conductivities as a function of capillary pressure (saturation) and geologic dip (Eaton and McCord, 1992). The numerical results for layered regions are compared with semianalytical expressions presented by Yeh *et al.* (1985). Good agreement was obtained for hydraulic conductivity ratios $K_{parallel}/K_{normal}$ for wet and moderately dry conditions.

The use of analytical expressions for these hydraulic conductivity ratios would simplify the implementation of layered effects in global calculations where it is impractical to include detailed geologic structure.

23.3.1 Analytic model

The Yeh *et al.* (1985) expression for the equivalent effective hydraulic conductivity of an arbitrarily oriented layered medium is given by

$$K_p = K_m exp\left(\frac{\sigma_f^2 + \sigma_\alpha^2 \Psi^2}{2\,[1 + A\lambda\cos(\beta)]}\right), \tag{23.3}$$

where K_p is the effective hydraulic conductivity in the direction parallel to the material layering, and

$$K_n = K_m exp\left(-\frac{\sigma_f^2 + \sigma_\alpha^2 \Psi^2}{2\,[1 + A\lambda\cos(\beta)]}\right), \tag{23.4}$$

where K_n is the effective hydraulic conductivity in the direction normal to the layering. The parameters in the above equations are defined by: K_m is the geometric-mean of the saturated hydraulic conductivity, σ_f^2 is the variance of the $ln\,(K_{sat})$ field, σ_α^2 is the variance of the slope of the $ln\,(K)$ versus ψ random field, Ψ is the mean pressure head, A is the mean of α (see conductivity equation below for definition of α; λ is the correlation length normal to layering, and β is the dip of the soil layering). The form of unsaturated conductivity used in the Yeh *et al.* (1985) analysis is given by

$$K(\psi) = K_{sat} e^{-\alpha\psi}. \tag{23.5}$$

One important aspect of these effective conductivity expressions is that they indicate that the anisotropy of layered media can vary (by orders of magnitude) as the hydraulic state (capillary pressure) changes. This behavior could have a significant impact on flow and transport predictions.

23.3.2 Numerical approach

The problem geometry and applied boundary conditions used in the LLUVIA-II numerical calculations are given in Figure 23-10. Geologic dip is approximated by rotation of the gravitational vector with respect to the z axis. In all calculations, the top boundary (maximum z) was set to a fixed capillary pressure. The unit-gradient boundary condition was applied at the remaining three boundaries. A 31- by 31-node grid was used. Steady-state solutions were obtained for capillary pressures varying from -2 m to -6 m and dips ranging from 10 degrees to 70 degrees. These capillary pressures represent dry to very dry saturation

conditions. Hydraulic conductivities vary by up to four orders of magnitude over this pressure range. For capillary pressures of -6 m, the hydraulic conductivity values are as much as 7 orders of magnitude lower than their corresponding values at saturated conditions.

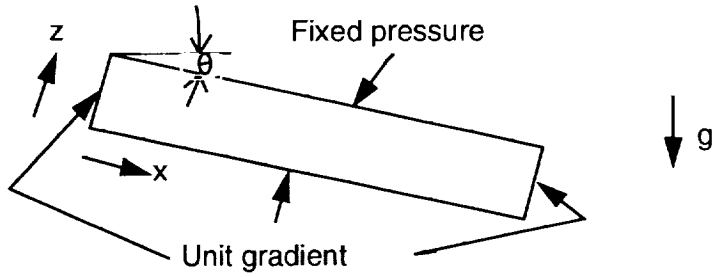

Figure 23-10. Problem geometry and numerical boundary conditions.

The randomly generated saturated-hydraulic-conductivity fields used in this study were typical of layered soil since considerable soil data are available. Typical values of the quantities required by the Yeh *et al.* (1985) equation are: mean of $\ln K_{sat}$ = $-1.1\text{x}10^{+1}$, variance of $\ln K_{sat}$ = 1.5, A = mean of α = 3.0, and geometric mean K_{sat} = $1.291\text{x}10^{-6}$. The effective hydraulic conductivity result was calculated using two different methods. In the first, the effective hydraulic conductivity was calculated by the following equation using the numerically calculated fluxes

$$K_{eff_x} = \frac{flux_x \Delta x}{\Delta P_x} \quad , \tag{23.6}$$

where $flux_x$ is the mass flux in the x direction, Δx is the width of region, ΔP_x is the average change in effective pressure head across the region in the x direction. The K_{eff_z} value is calculated by interchanging x and z values in the above equation.

In the second method, effective conductivities were approximated using the calculated conductivities along a single column at $x = x_{max}/2.0$ while assuming one-dimensional series flow in the z-direction and one-dimensional parallel flow in the x-direction. These equations give

$$\frac{\Sigma(\Delta z)}{K_n} = \frac{\Delta z_1}{K_1} + \frac{\Delta z_2}{K_2} + \ldots = \Sigma \frac{(\Delta z_i)}{K_i} \quad , \tag{23.7}$$

and

$$K_p = \frac{\Delta z_1 K_1 + \Delta z_2 K_2 + \ldots}{\Sigma \Delta z} = \frac{\Sigma(\Delta z_i K_i)}{\Sigma(\Delta z_i)} \quad , \tag{23.8}$$

23.3.3 Results of nonisotropic-hydraulic conductivity effects

Effective hydraulic conductivity ratios as a function of capillary pressure are given for an average of eleven calculations in Figures 23-11 and 23-12 for dips of 10 degrees and 70 degrees. Each calculation used a different set of randomly generated values of K_{sat} and α data typical of soil material. The three curves represent results from the three calculation methods: (1) mass balance and Darcy's equation, (2) parallel and series analogy, and (3) the Yeh *et al.* analytical relations. Good agreement is obtained for $-4 < \psi < -2$ m. At the

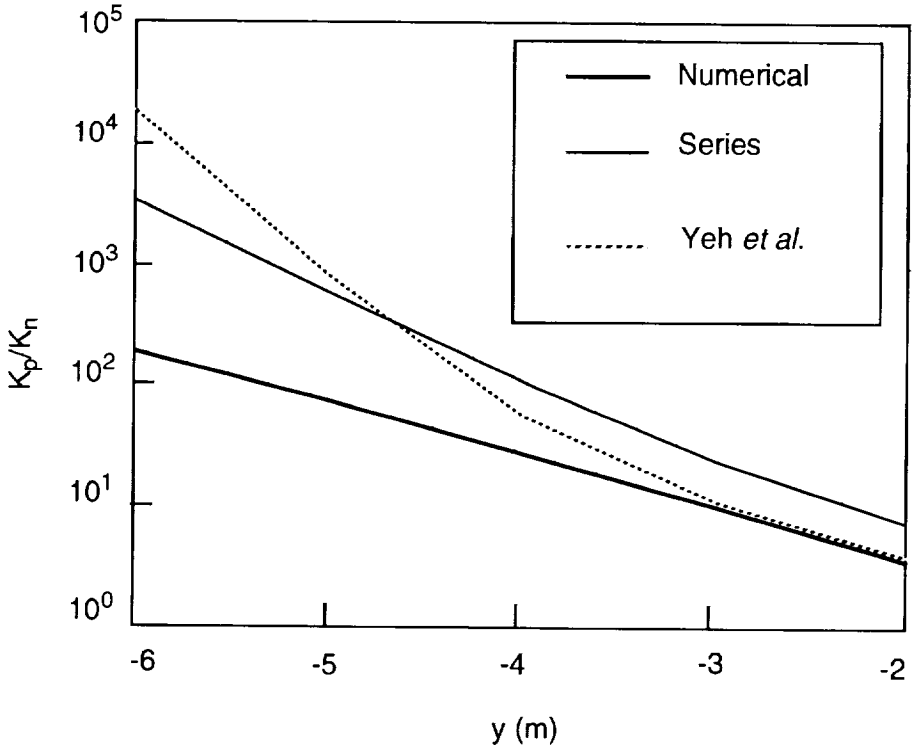

Figure 23-11. Hydraulic conductivity ratio as a function of boundary capillary pressure for an average of eleven realizations, dip = 10 degrees

pressure level of -4 m, the ratio of saturated hydraulic conductivity to hydraulic conductivity is on the order of 10^5, indicating dry conditions. For the extremely dry conditions, $\psi < -4$ m, agreement between the numerical and analytical results is not good.

The conductivity ratio $K_{parallel}/K_{normal}$ was also determined as a function of dip. These results show that the hydraulic conductivity ratio is relatively insensitive to the dip. The series and parallel equations show no dependence on the angle. The LLUVIA-II and Yeh *et al.* results are in reasonable agreement for a capillary pressure of -2.0 m and poor agreement at a capillary pressure of -6.0 m. This disagreement is not critical because the hydraulic conductivity ratio is reasonably insensitive to the dip for all cases. Additionally, in most situations the dip is fairly well known and does not vary appreciably between layers. In

order to evaluate the applicability of concept to Yucca Mountain, this study should be repeated using the best available Yucca Mountain material characteristics.

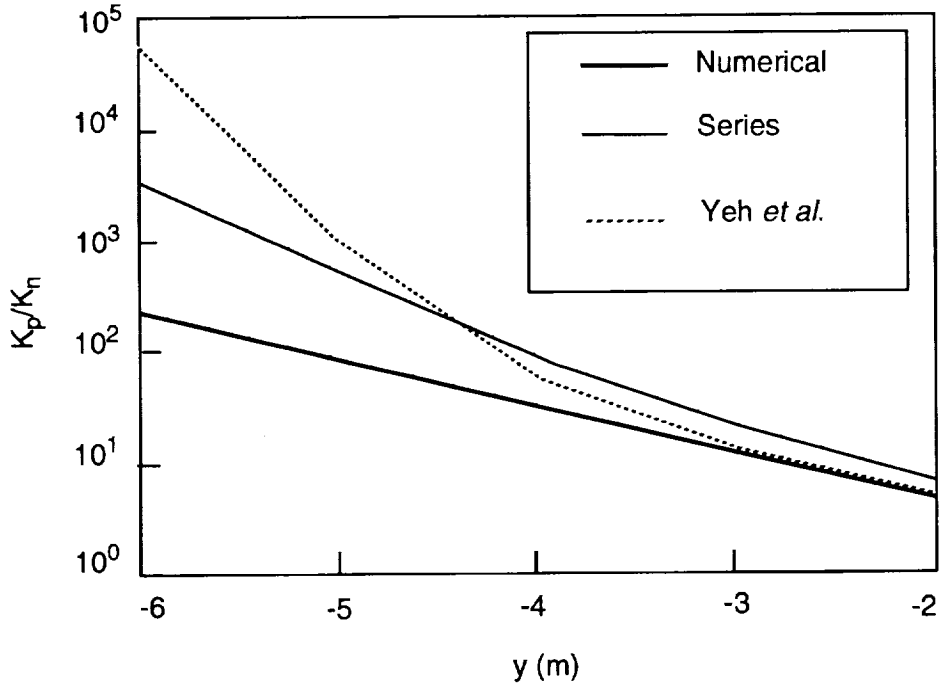

Figure 23-12. Hydraulic conductivity ratio as a function of capillary pressure for an average of eleven realizations, dip = 70 degrees.

23.4 Summary of one-dimensional appropriateness studies

Presented in this report are various aspects of numerical modeling that help define the bounds of applicability of using one-dimensional numerical calculations for approximating the water flow through two-dimensional, nonhomogeneous, partially saturated porous regions. This information can be particularly helpful when making abstractions in support of the one-dimensional calculations in the total-system performance analysis study. The results of the studies described in this chapter are itemized below.

1. It is demonstrated that the effect of low-hydraulic-conductivity meter-scale obstructions can, in many cases, be accounted for by the use of effective conductivities. In unsaturated flows where the material characteristics are extremely nonlinear, the presence of low-hydraulic-conductivity obstructions (Figure 23-1) provide little flow resistance over and above that resulting from the high-conductivity background material (Eaton and Dykhuizen, 1988).

2. For most fracture/matrix material combinations, the presence of unconnected unsaturated

fracture arrays (Figure 23-4) generate little resistance to infiltrating water (Martinez *et al.*, 1992).

3. Effective conductivities for materials comprised of meter-scale random binary mixtures of high and low conductivities can be represented using the analytical model of Kirkpatrick (Figure 23-5) (Dykhuizen and Eaton, 1991).

4. The unit-gradient boundary concept can be used in conjunction with one-dimensional modeling to effectively approximate two-dimensional flow path lines (Figure 23-9) on a mountain scale in layered geologic media when the media are homogeneous in the direction normal to the layering (Eaton and McCord, 1992).

5. The effect of nonisotropic hydraulic conductivity can possibly be included through the use of analytical expressions which provide $K_{parallel}/K_{normal}$ as a function of material saturation and dip. This was shown to be true for soils on meter-scale problems. It remains to be determined for Yucca Mountain materials (Eaton and McCord, 1992).

In summary, with the incorporation of the above concepts, it is possible to use one-dimensional modeling to approximate two-dimensional flow path lines in layered systems while accounting for, to some extent, low-hydraulic conductivity obstructions, unsaturated fractures, random mixes of material conductivities, and nonisotropic conductivities. These phenomena are accounted for without explicitly including them in the geometry of the numerical model. Additionally, the effect of lateral flow, resulting from geologic dip, can be accounted for by the use of the unit-gradient boundary conditions.

Chapter 24
Effect of Fractures on Repository Dryout

(Eaton)

Historically the majority of the calculations in support of total-system performance analysis were completed using isothermal single-phase flow conditions. Typical codes used for TSPA investigations, such as TOSPAC, calculate the flow of single-phase water through porous media and do not address the effect of vapor transport. Numerous multiphase two-dimensional calculations for buried waste have been made by Buscheck and Nitao (1993) using the code V-TOUGH (1989). These calculations predicted considerable dryout in the region of the buried waste and a perched water region above the repository. This calculated dryout-perched condition existed for thousands of years, implying that the multiphase aspect of the repository problem should be considered in TSPA calculations.

Because of the complexity of multiphase calculations they do not readily adapt themselves to Monte Carlo type calculations, where hundreds of realizations may be required to adequately account for the uncertainties in: (1) material properties, (2) environmental considerations, (3) waste-canister properties, and (4) the geometry of the geologic media.

An additional potential problem when calculating multiphase flow is that the flow characteristics of the vapor in the fractures must be accurately modeled. For most materials, liquid water only travels through the fractures when the flow is nearly liquid saturated. However, water in vapor phase will flow in the fractures even at low values of liquid saturation. Because of this sensitivity to the computational model a study has been made using the multiphase code TOUGH2 (Pruess, 1991) to determine the sensitivity of computed dryout and water perching to the model used for flow through fractures. Based on material characteristics for a highly fractured media, calculations predict considerable dryout in the vicinity of buried waste and a large perched water region above the repository for times exceeding 10,000 yr after waste burial. When the apertures of the fractures are reduced by a factor of 10 (from 100 μm to 10 μm), the size of the dryout and perched regions are significantly reduced. When the aperture of the fractures is reduced to less than 10 μm, the dryout and perched regions are essentially nonexistent. Additionally, it was observed that the extent of the calculated dryout is sensitive to the material characteristic model used to define saturation and permeability as a function of capillary pressure.

24.1 Problem description

The TOUGH2 code has been used to simulate an axisymmetric repository with an aerial power density of 114 kW/acre and 30-yr-old spent nuclear fuel (SNF). To obtain a benchmark

for the Sandia version of the TOUGH2 code, the results of one-dimensional calculations along the center of the repository (r = 0.0, Figures 24-1 and 24-2), were compared with the two-dimensional results of Buscheck and Nitao (1993) (Figures 24-3 and 24-4). Their results were obtained using V-TOUGH (Nitao, 1989), Lawrence Livermore National Laboratory's

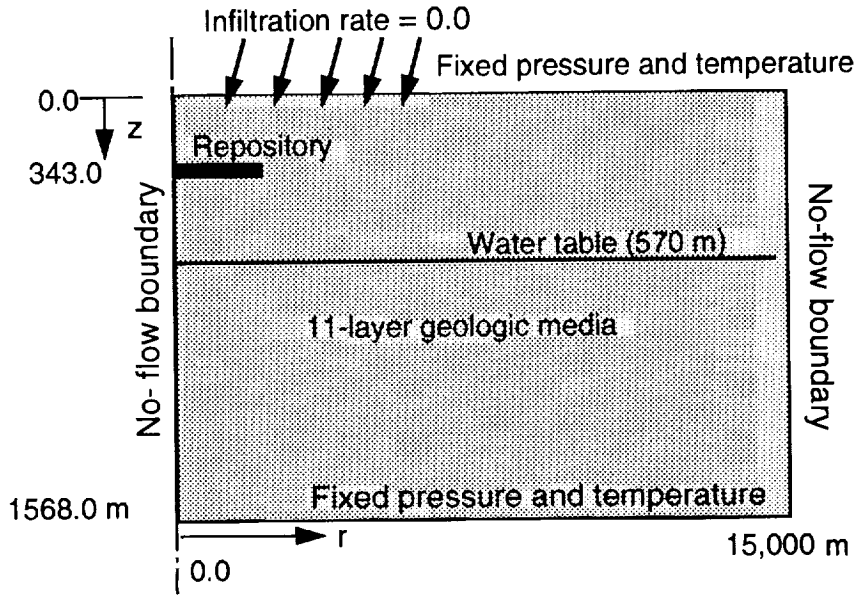

Figure 24-1. Two-dimensional axisymmetric geometry of repository and surrounding geologic media for 114-kW/acre, 30-yr-old fuel (Buscheck and Nitao, 1993). The TOUGH2 calculations were made along the r = 0 vertical axis.

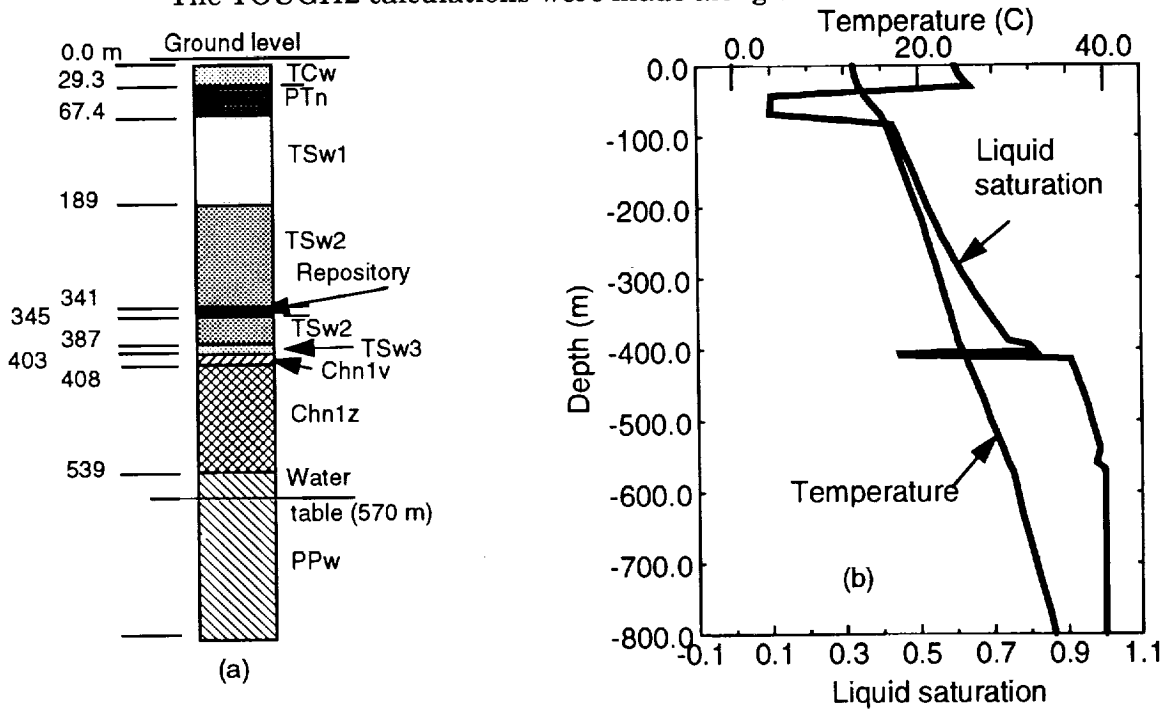

Figure 24-2. (a) One-dimensional approximation to repository and surrounding layered geologic media, and (b) Initial temperature and saturation profiles.

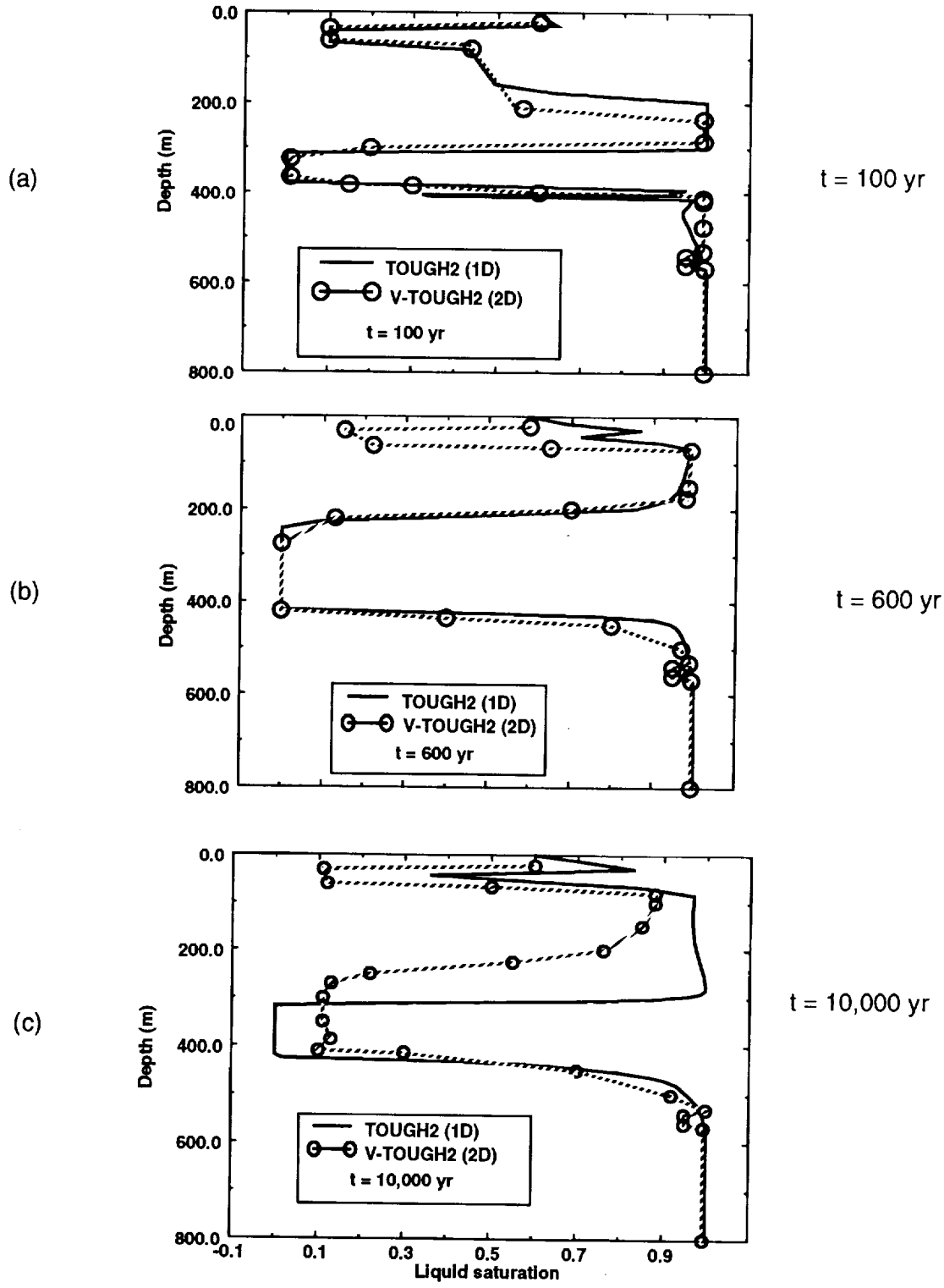

Figure 24-3. Vertical liquid saturation profiles along the repository centerline, 30-yr-old SNF, 114 kW/acre. Comparison of TOUGH2 and V-TOUGH results, t = 100, 600, and 10,000 yr.

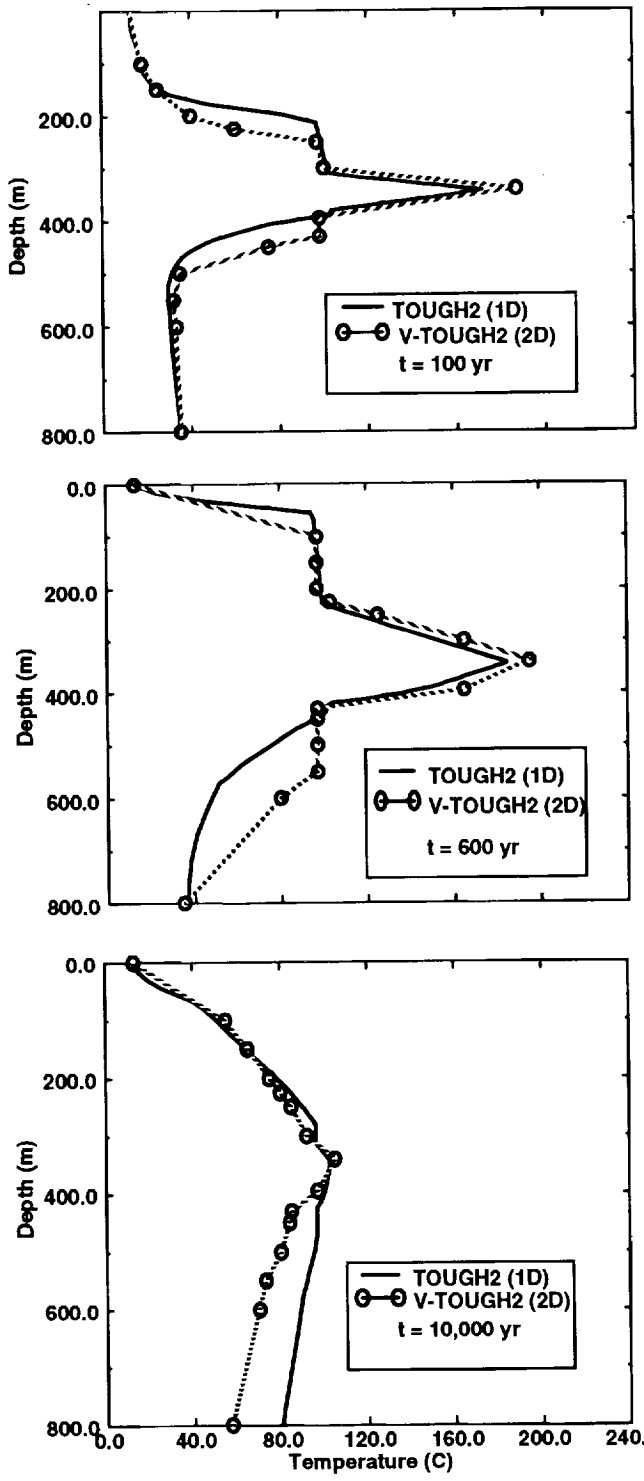

Figure 24-4. Vertical temperature profiles along the repository centerline, 30-yr-old SNF, 114 kW/acre. Comparison of TOUGH2 and V-TOUGH results, t = 100, 600, and 10,000 yr.

vectorized version of the TOUGH code (Pruess, 1987). Matrix and fracture material properties for the layered geologic media are given in Tables 24-1 and 24-2 (Klavetter and Peters, 1986). Initial saturation and temperature profiles are given in Figure 24-2. It should be noted that the initial dry state of the PTn unit results from the large value of β (6.873) given by Klavetter and Peters (1986). Even though this value does not correspond to recently obtained values it will be used in this study to be consistent with the work of Buscheck and Nitao (1993). Fracture porosity and permeability for the nominal case addressed in this paper is based on 3.33, 100 μm fractures per meter. The equivalent continuum model of Peters and Klavetter (1988) and the relative permeability model of van Genuchten (1978) were used to obtain saturation and permeability values for the variably-saturated highly-fractured geologic media. A composite material option using the van Genuchten theory has been added to the SNL version of the TOUGH2 code. It allows for area-weighted matrix and fracture materials. Solutions were also obtained by neglecting fractures. Large differences in repository dryout and water perching were observed.

To obtain a better understanding of the sensitivity of the amount of perched water and dryout to fracture characteristics, additional calculations were made. The same basic configuration was used as shown in Figure 24-1 and the material properties given in Tables 24-1 and -2. A parametric study was performed by varying the fracture aperture (b), given in Table 24-3, from 1 μm to 1000 μm. Fracture permeability is defined by $b^2/12\ m^2$.

Table 24-1. Material matrix properties.

Unit	$k_m\ (m^2)$	α (1/Pa)	β	ϕ_m	S_r
TCw	9.70×10^{-19}	8.40×10^{-7}	1.558	0.08	0.0020
PTn	3.90×10^{-14}	1.53×10^{-6}	6.873	0.40	0.100
TSw1	1.90×10^{-18}	5.80×10^{-7}	1.798	0.11	0.080
TSw2	1.90×10^{-18}	5.80×10^{-7}	1.798	0.11	0.080
TSw3	1.50×10^{-19}	4.51×10^{-7}	2.058	0.07	0.080
CHn1v	2.70×10^{-14}	1.64×10^{-6}	3.872	0.46	0.041
CHn1z	2.00×10^{-18}	3.15×10^{-7}	1.602	0.28	0.110
PPw	4.5×10^{-16}	1.44×10^{-6}	2.639	0.24	0.066

Table 24-2. Fracture properties for all units.

$k_f\ (m^2)$	α (1/Pa)	β	ϕ_f	S_r
8.33×10^{-10}	1.315×10^{-3}	4.23	3.33×10^{-4}	0.0395

Table 24-3. Parametric variation in material properties.

Case	b (μm)	k_f (m^2)	ϕ
1	1,000	8.33×10^{-8}	3.33×10^{-3}
2 (base case)	100	8.33×10^{-10}	3.33×10^{-4}
3	10	8.33×10^{-12}	3.33×10^{-5}
4	1	8.33×10^{-14}	3.33×10^{-6}

24.2 Results

Vertical profiles of liquid saturation and temperature are given for times of 100, 600, and 10,000 yr after waste emplacement in Figures 24-5 and 24-6. The extent of calculated water perching above the repository and dryout in the vicinity of the repository is gradually reduced by decreasing the assumed fracture aperture from 1000 μm to 10 μm. When the aperture of the fractures is reduced to 10 μm the size of the dryout and perched regions are significantly reduced. When the fracture aperture is reduced to 1 μm, the dryout and perched regions are nonexistent.

The calculated temperatures are less sensitive to the existence of fractures than are the liquid saturations, Figure 24-6. The most noticeable difference is the disappearance of the heat pipe (constant temperature) region as the fracture aperture is reduced. Reducing the fracture aperture to 10 μm or less increased the maximum calculated temperatures by approximately 30 c. Temperature profiles for the base case (100 μm) and 1000 μm case are essentially the same.

Figures 24-7 and 24-8 give a summary of these water-perching and dryout calculations as a function of fracture aperture. The extent of water perching and dryout increase appreciably with fracture size up to 100 μm. Increasing the fracture aperture greater than 100 μm does not appreciably increase the dryout and perched regions.

These calculated liquid saturation and temperature results show that the choice of the fracture properties used in the calculations has a strong influence on predicted water perching and dryout. This results primarily from vapor transport and the way it is calculated in the TOUGH2 code. Permeability and liquid saturation are given as a function of capillary pressure in Figures 24-9 and 24-10 for the matrix, fractures, and composite model for the TSw2 material. It can be seen from these figures that matrix and composite permeability are the same unless saturation is in excess of 0.99 ($\psi > -0.1$). Therefore, the flow of liquid is

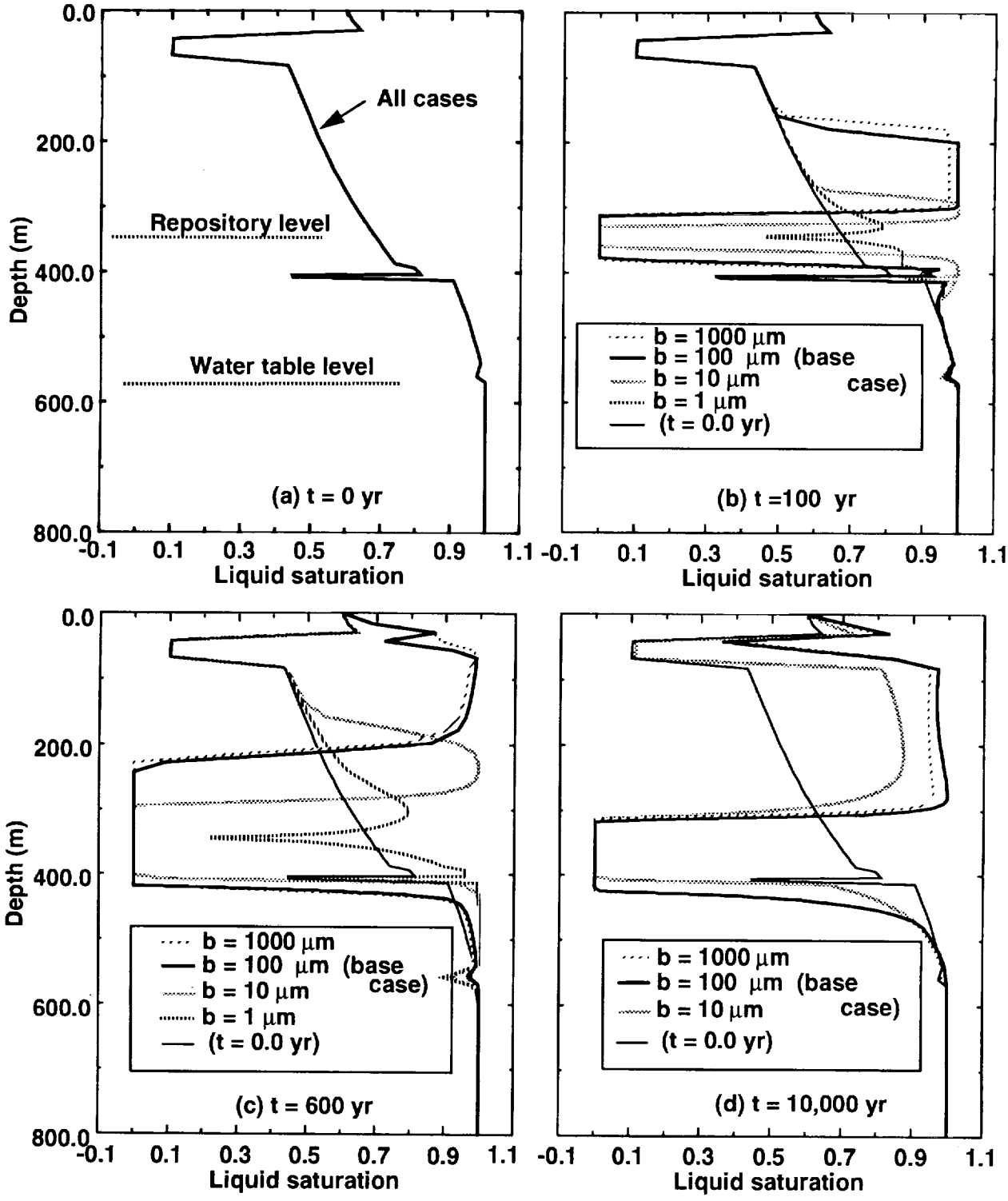

Figure 24-5. Vertical liquid saturation profiles along the repository centerline for 30-yr-old SNF, 114 kW/acre, t = 0, 100, 600, and 10,000 yr.

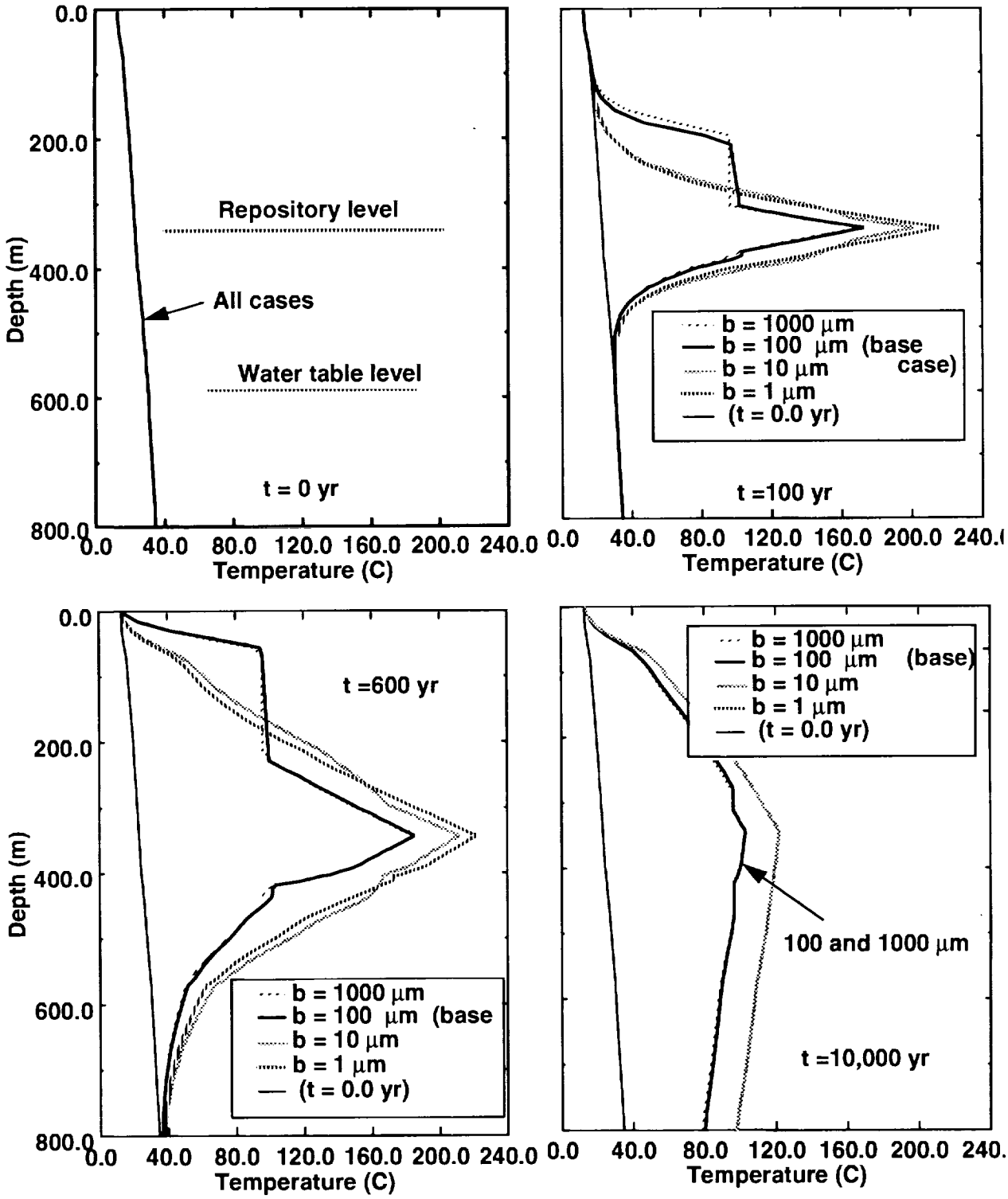

Figure 24-6. Vertical temperature profiles along the repository centerline for 30-yr-old SNF, 114 kW/acre, t = 0, 100, 600, and 10,000 yr.

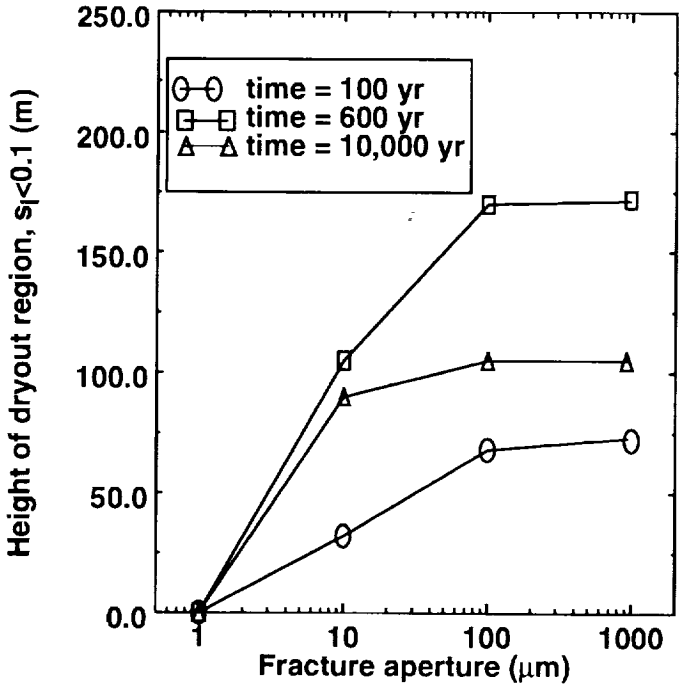

Figure 24-7. Vertical extent of dryout as a function of fracture permeability.

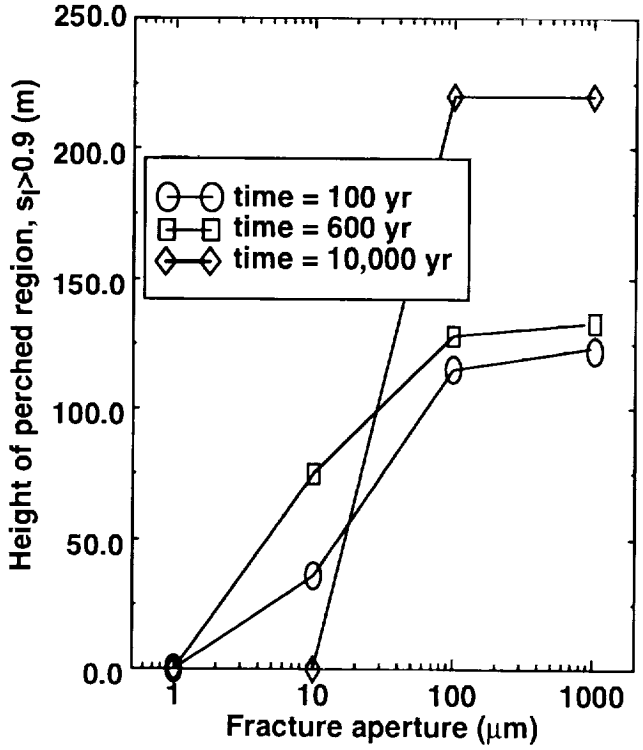

Figure 24-8. Vertical extent of perched water above the repository as a function of permeability.

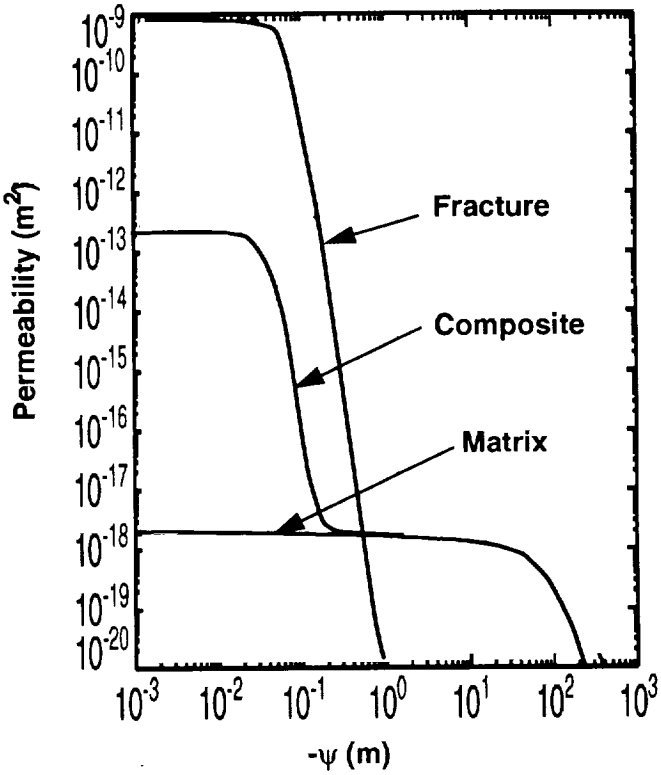

Figure 24-9. Permeability as a function of capillary pressure, TSw2.

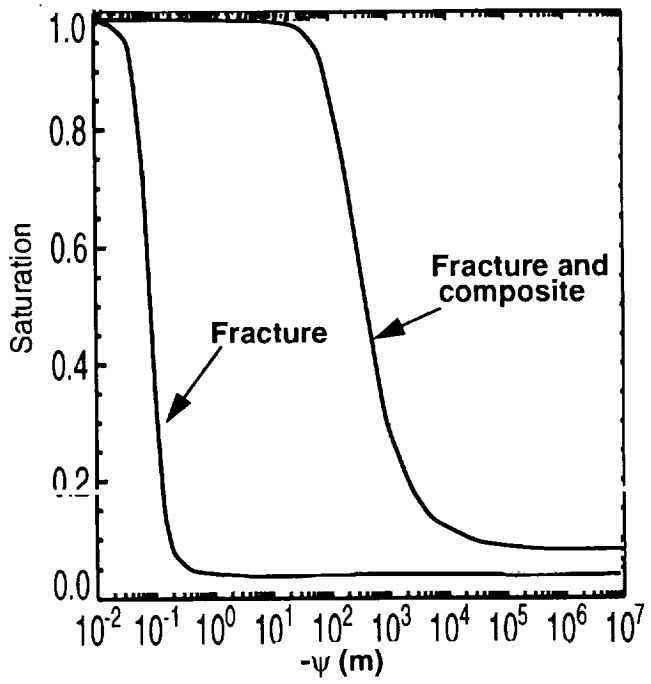

Figure 24-10. Liquid saturation as a function of capillary pressure, TSw2.

independent of the fractures unless saturated conditions are approached and liquid water begins to flow in the fractures. This is not true for vapor transport. The composite permeability for vapor transport is calculated as follows:

$$K_{vapor} = (1.0 - K_{relative-liquid}) \times K_{saturated-composite} \quad (24.1)$$

The vapor permeability is a direct function of the saturated composite permeability. For the TSw2 material shown in Figure 24-9, the inclusion of the composite model increases the vapor permeability by 5 orders of magnitude. Thus for a given pressure field, the vapor transport is significantly enhanced by the addition of the composite model while liquid transport is unaffected, except at liquid saturation levels greater than approximately 0.99.

Typically the van Genuchten formulation, (OPTION 7) in TOUGH2, is used to model flow through tuff rock. In this model, a cutoff value of capillary pressure must be given by the user. The magnitude of this value is left to the discretion of the user. If it is chosen to be too small, the code is forced to choose time step sizes which are too small to be practical and code execution times are excessive. If it is chosen too large, then the liquid saturation is truncated at a value which eliminates the calculation of any dryout. It was for this reason that OPTION 9, which eliminates the no-dryout problem and allows for considerably larger time step sizes, was added to the code. The calculated results for all regions except the near repository region are the same. However, in the flow in the near region of the potential repository, both water perching and repository dryout are reduced by the use of OPTION 7.

24.3 Conclusions regarding repository dryout

The results of the repository simulations presented above are outlined below:

- The temperature profiles calculated using TOUGH2, with a one-dimensional model compare favorably with those calculated by Buscheck and Nitao (1993) using V-TOUGH and a two-dimensional model.
- Liquid saturation results obtained with the one-dimensional approximation compare favorably with the two-dimensional results for times up to 600 yr. At a calculated time of 10,000 yr, the two-dimensional model begins to rewet in the vicinity of the repository. Rewetting for the one-dimensional case does not begin until t > 30,000 yr.
- The magnitude of the dryout and perched regions increases monotonically with fracture aperture in the range of 1 μm to 100 μm.
- Dryout and perched regions are nonexistent when the fracture apertures are reduced to 1 μm.

- The magnitude of the dryout and perched regions is insensitivity to aperture size in the range of 100 μm to 1000 μm.
- The maximum calculated repository temperature increases as the fracture apertures are decreased.
- The algebraic model used to define the material properties can significantly affect calculated values of water perching and dryout in the vicinity of the repository.

Chapter 25
References

Abramowitz, M., and I. A. Stegun, 1972, *Handbook of Mathematical Functions with Formulas, Graphs, and Mathematical Tables, National Bureau of Standards*, U.S. Government Printing Office, Washington, DC, December. (NNA.891106.0179)

Amter, S., N. Lu, and B. Ross, 1991, "Thermally Driven Gas Flow Beneath Yucca Mountain, Nevada," in *Multiphase Transport in Porous Media—1991,* edited by R. R. Eaton, M. Kaviany, M. P. Sharma, K. Vafai, and K. S. Udell, American Society of Mechanical Engineers, New York, NY. (NNA.920428.0026)

Anderson, L. A., 1981, "Rock Property Analysis of Core Samples from the Yucca Mountain UE25a-1 Borehole, Nevada Test Site, Nevada," *USGS/OFR-81-1338*, U.S. Geological Survey, Denver, CO. (NNA.870406.0031)

Anderson, L. A., 1984, "Rock Property Measurements on Large-Volume Core Samples from Yucca Mountain USW GU-3/G-3 and USW G-4 Boreholes, Nevada Test Site, Nevada," *USGS/OFR-84-552,* U.S. Geological Survey, Denver, CO. (NNA.870323.0195)

Anderson, L. A., 1991, "Results of Rock Property Measurements Made On Core Samples from Yucca Mountain Boreholes, Nevada Test Site, Nevada—Part 1: Boreholes UE25a-4, -5, -6, and -7, Part 2: Borehole UE25p#1," *USGS/OFR-90-474,* U.S. Geological Survey, Denver, CO. (NNA.910411.0081)

Andersson, K., 1988, "SKI Project-90: CHEMICAL DATA," *SKI TR 91:21*, Swedish Nuclear Power Inspectorate, Stockholm, Sweden. (NNA.940303.0040)

Andress, D., and N. B. McLeod, 1988, "Waste Stream Analysis Model," prepared for Oak Ridge National Laboratory, Oakridge, TN, and Sandia National Laboratories, Albuquerque, NM. (NNA.890309.0187)

Barnard, R. W., 1993, "Review of Radionuclide Source Terms Used for Performance-Assessment Analyses," *SAND92-2431*, Sandia National Laboratories, Albuquerque, NM. (NNA.930614.0030)

Barnard, R. W., and H. A. Dockery, editors, 1991, "Technical Summary of the Performance Assessment Calculational Exercises for 1990 (PACE-90)," Volume 1: Nominal Configuration Hydrogeologic Parameters and Calculational Results, *SAND90-2726*, Sandia National Laboratories, Albuquerque, NM. (NNA.910523.0001)

Barnard, R. W., M. L. Wilson, H. A. Dockery, J. H. Gauthier, P. G. Kaplan, R. R. Eaton, F. W. Bingham, and T. H. Robey, 1992, "TSPA 1991: An Initial Total-System Performance Assessment for Yucca Mountain," *SAND91-2795*, Sandia National Laboratories, Albuquerque, NM. (NNA.920630.0033)

Barr, G. E., 1984, "Reduction of the Well Test Data for Test Well USW H-1, Adjacent to Nevada Test Site, Nye County, Nevada," *SAND84-0637*, Sandia National Laboratories, Albuquerque, NM. (NNA.870407.0324)

Barr, G. E., E. Dunn, H. Dockery, R. Barnard, G. Valentine, and B. Crowe, 1993, "Scenarios Constructed for Basaltic Igneous Activity at Yucca Mountain and Vicinity," *SAND91-1653*, Sandia National Laboratories, Albuquerque, NM. (NNA.930811.0013)

Benson, L. V., D. R. Currey, R. I. Dorn, K. R. Lajoie, C. G. Oviatt, S. W. Robinson, G. I. Smith, and S. Stine, 1990, "Chronology of Expansion and Contraction of Four Great Basin Lake Systems During the Past 35,000 Years," *Palaeogeography, Palaeoclimatology, Palaeoecology*, **78**:241-286. (NNA.920131.0261)

Bentley, C. B., 1984, "Geohydrologic Data for Test Well USW G-4, Yucca Mountain Area, Nye County, Nevada," *USGS/OFR-84-063*, U.S. Geological Survey, Denver, CO. (NNA.870519.0100)

Bentley, C. B., J. H. Robison, and R. W. Spengler, 1983, "Geohydrologic Data for Test Well USW H-5, Yucca Mountain Area, Nye County, Nevada," *USGS/OFR-83-853*, U.S. Geological Survey, Denver, CO. (NNA.870519.0098)

Beyerlein, S. W., and H. C. Claiborne, 1982, "The Possibility of Multiple Temperature Maxima in Geologic Repositories for Spent Fuel from Nuclear Reactors," *Transactions of the ASME, Journal of Heat Transfer*, **104**:180. (NNA.890713.0178)

Bixler, N. E., 1985, "NORIA - A Finite Element Computer Program for Analyzing Water, Vapor, Air, and Energy Transport In Porous Media, *SAND84-2057*, Sandia National Laboratories, Albuquerque, NM. (NNA.870721.0002)

Brasunas, A. DeS., J. T. Gow, and O. E. Harder, 1946, "Resistance of Iron-Nickel-Chromium Alloys to Corrosion in Air at 1600° to 2200°F," *American Society for Testing and Materials Proceedings*, **46**:870 ff. (NNA.940301.0021)

Brown, D., and H. Wedemeyer, 1984, *Gmelin Handbook of Inorganic Chemistry, 8th Edition: Uranium, Supplement Volume C10 (Compound with Sulfur),* Springer Verlag, New York, NY. (NNA.940323.0006)

Broxton, D. E., R. G. Warren, R. C. Hagan, and G. Luedemann, 1986, "Chemistry of Diagenetically Altered Tuffs at a Potential Nuclear Waste Repository, Yucca Mountain, Nye County, Nevada, *LA-10802-MS*, Los Alamos National Laboratory, Los Alamos, NM. (NNA.890327.0036)

Buchan, K. L., E. M. Schwartz, D. T. A. Symons, and M. Stupavsky, 1980, "Remnant Magnetization in the Contact Zone Between Columbia Plateau Flows and Feeder Dikes: Evidence for Groundwater Layer at Time of Intrusion," *Journal of Geophysical Research*, **85**(B4):1888-1898. (NNA.930330.0058)

Buesch, D. C., J. E. Nelson, R. P. Dickerson, and R. W. Spengler, 1993, "Development of 3-D Lithostratigraphic and Confidence Models at Yucca Mountain, Nevada," in *High Level Radioactive Waste Management, Proceedings of the Fourth Annual International Conference, Las Vegas, Nevada, April 26-30, 1993*, pp. 943-948, American Nuclear Society, La Grange Park, IL. (NNA.931214.0104)

Burkhard, N. R., J. R. Hearst, and J. M. Hanson, 1987, "Estimation of the Bulk Diffusivity of Chimneys Using Post Shot Holes," *Proceedings of the Fourth Symposium on Containment of Underground Nuclear Explosions, LLNL-CONF-870961*, Lawrence Livermore National Laboratory, Livermore, CA, pp. 288-351. (NNA.940303.0041)

Buscheck, T. A., and J. J. Nitao, 1991, "Modeling Hydrothermal Flow in Variably Saturated, Fractured, Welded Tuff During the Prototype Engineered Barrier System Field Test of the Yucca Mountain Project," *Proceedings of the Fifth NRC Workshop on Flow and Transport through Unsaturated Fractured Rock*, University of Arizona, Tucson, AZ; also *UCRL-ID-106521*, Lawrence Livermore National Laboratory, Livermore, CA. (NNA.911212.0238)

Buscheck, T. A., and J. J. Nitao, 1992, "The Impact of Thermal Loading on Repository Performance at Yucca Mountain," in *High Level Radioactive Waste Management, Proceedings of the Third Annual International Conference, Las Vegas Nevada, April 12-16, 1992,* American Nuclear Society, La Grange Park, IL. (NNA.920408.0008)

Buscheck, T. A., and J. J. Nitao, 1993, "Repository-Heat-Driven Hydrothermal Flow at Yucca Mountain, Part I: Modeling and Analysis," *Nuclear Technology*, **104**(3):418-448. (NNA.940427.0095)

Byers, F. M., W. J. Carr, P. Orkild, W. D. Quinlivan, and K. A. Sargent, 1976, "Volcanic Suites and Related Cauldrons of Timber Mountain–Oasis Valley Caldera Complex, Southern Nevada, U.S. Geological Survey Professional Paper 919, U.S. Geological Survey, 70 pp. (NNA.870406.0239)

Canepa, J. A., editor, 1992, *Proceedings of the DOE/Yucca Mountain Site Characterization Project Radionuclide Adsorption Workshop at Los Alamos National Laboratory, September 11-12, 1990, LA-12325-C*, Los Alamos National Laboratory, Los Alamos, NM. (NNA.920421.0117)

Carr, W. J., 1988, "Volcano-Tectonic Setting of Yucca Mountain and Crater Flat, Southwestern Nevada," *U.S. Geological Survey Bulletin*, **1790**:35-49. (NNA.891114.0346)

Carr, W. J., 1992, "Structures in Continuously Cored, Deep Drill Holes at Yucca Mountain, Nevada, with Notes on Calcite Occurrence," *SAND91-7037*, Sandia National Laboratories, Albuquerque, NM. (NNA.921204.0014)

Carr, M. D., S. J. Wadell, G. S. Vick, J. M. Stock, S. A. Monsen, A. G. Harris, B. W. Cork, and F. M. Byers, Jr., 1986, "Geology of Drill Hole UE-25p#1: A Test Hole Into Pre-Tertiary Rocks Near Yucca Mountain, Southern Nevada," *USGS/OFR-86-175*, U.S. Geological Survey, Menlo Park, CA. (HQS.880517.2633)

Carrigan, C. R., G. C. P. King, G. E. Barr, and N. E. Bixler, 1991, "Potential for Water-Table Excursions Induced by Seismic Events at Yucca Mountain, Nevada," *Geology*, **19**:1157-1160. (NNA.920427.0050)

Carslaw, H. S., and J. C. Jaeger, 1967, "Conduction of Heat in Solids,"Oxford, London, UK. (NNA.900522.0259)

Chapman, M., 1981, "FRAM (Filtering Methodology and Remedy): A Nonlinear Algorithm for Continuity Equations," *Journal of Computational Physics*, **44**(1):84-103. (NNA.940301.0022)

Choppin, G. R., 1986, "Speciation of Trivalent *f* Elements in Natural Waters," *Journal of the Less-Common Metals*, **126**(1986):307-313. (NNA.940427.0094)

Christiansen, R. L., P. W. Lipman, W. J. Carr, F. M. Byers, P. P. Orkild, and K. A. Sargent, 1977, "Timber Mountain–Oasis Valley Caldera Complex of Southern Nevada," *The Geological Society of America Bulletin*, **88:**943-959. (NNA.870406.0166)

Church, H. W., D. L. Freeman, K. Boro, and R. T. Egami, 1985, "Meteorological Tower Data Yucca Ridge (YR) Site," *SAND85-1053*, Sandia National Laboratories, Albuquerque, NM. (NNA.931012.0005)

Church, H. W., D. L. Freeman, K. Boro, and R. T. Egami, 1986, "Meteorological Tower Data for the Yucca Alluvial (YA) Site," *SAND86-2533*, Sandia National Laboratories, Albuquerque, NM. (NNA.871229.0045)

Churchill, R. V., 1944, *Modern Operational Mathematics in Engineering*, McGraw-Hill Book Co., Inc., New York, NY. (NNA.940414.0110)

Clark, L., 1979, *Practical Geostatistics,* Elsevier Applied Scientific Publishers, New York, NY. (NNA.890906.0194)

Clark, S. P., 1966, *Handbook of Physical Constants—Revised Edition*, Section 21, The Geological Society of America Memoir 97. (NNA.890327.0070)

Codell, R., N. Eisenberg, D. Fehringer, W. Ford, T. Margulies, T. McCartin, J. Park, and J. Randall, 1992, "Initial Demonstration of the NRC's Capability to Conduct a Performance Assessment for a High-Level Waste Repository," *NUREG-1327*, U.S. Nuclear Regulatory Commission, Washington, DC. (NNA.940301.0023)

Colp, J. L., M. J. Davis, E. J. Graber, and H. C. Hardee, 1976, "Magma Energy Research Project," *SAND75-0451*, Sandia National Laboratories, Albuquerque, NM. (NNA.940303.0044)

Cooperative Holocene Mapping Project (COHMAP), 1988, "Climatic Changes of the Last 18,000 Years: Observations and Model Simulations," *Science*, **241**:1043-1052. (NNA.920131.0444)

Craig, R. W., and K. A. Johnson, 1984, "Geohydrologic Data for Test Well UE-25p#1, Yucca Mountain Area, Nye County, Nevada," *USGS/OFR-84-450*, U.S. Geological Survey, Lakewood, CO and Fenix and Scisson, Inc., Mercury, NV. (NNA.890905.0207)

Craig, R. W., and J. H. Robison, 1984, "Geohydrology of Rocks Penetrated by Test Well UE-25p#1, Yucca Mountain Area, Nye County, Nevada," *USGS/WRI-84-4248,* U.S. Geological Survey, Denver, CO. (NNA.890905.0209)

Craig, R. W., R. L. Reed, and R. W. Spengler, 1983, "Geohydrologic Data for Test Well USW H-6, Yucca Mountain Area, Nye County, Nevada," *USGS/OFR-83-856*, U.S. Geological Survey, Denver, CO and Fenix and Scisson, Inc., Mercury, NV. (NNA.870406.0058)

Crane, R. A., R. I. Vouching, and M. S. Khader, 1977, "Thermal Conductivity of Granular Materials—A Review," in *Proceedings of the 7th Symposium on Thermophysical Properties*, pp. 109-123, American Society of Mechanical Engineers, New York, NY. (NNA.910123.0030)

Crowe, B. M., 1990, "Basaltic Volcanic Episodes of the Yucca Mountain Region," in *High Level Radioactive Waste Management, Proceedings of the International Topical Meeting, April 8-12, 1990, Las Vegas, Nevada*, 1:65-73, American Nuclear Society, La Grange Park, IL. (NNA.920131.0236)

Crowe, B. M., R. Picard, G. Valentine, and F. V. Perry, 1992, "Recurrence Models of Volcanic Events: Applications to Volcanic Risk Assessment," *High Level Radioactive Waste Management, Proceedings of the Third Annual International Conference, Las Vegas, Nevada, April 12-16, 1992,* pp. 2344-2355, American Nuclear Society, La Grange Park, IL. (NNA.920505.0067)

Czarnecki, J. B., 1985, "Simulated Effects of Increased Recharge on the Ground-Water Flow System of Yucca Mountain and Vicinity, Nevada-California," *USGS/WRI-84-4344*, U.S. Geological Survey, Denver, CO. (NNA.870407.0008)

Czarnecki, J. B., 1989, "Preliminary Simulations Related to a Large Horizontal Hydraulic Gradient at the North End of Yucca Mountain, Nevada," *EOS, Transactions of the American Geophysical Union*, **70**(15):321. (NNA.891218.0142)

Czarnecki, J. B., and R. K. Waddell, 1984, "Finite-Element Simulation of Ground-Water Flow in the Vicinity of Yucca Mountain, Nevada-California," *USGS/WRI-84-4349*, U.S. Geological Survey, Denver, CO. (NNA.870407.0173)

Dagan, G., 1989, *Flow and Transport in Porous Formations*, Springer-Verlag, New York, NY. (NNA.940303.0052)

Daily, W., and W. Lin, 1991, "Laboratory Determined Suction Potential of Topopah Spring Tuff at High Temperatures," *UCRL-102127,* Lawrence Livermore National Laboratory, Livermore, CA. (NNA.910128.0047)

Daniels, F., and A. Alberty, 1975, *Physical Chemistry, 4th Edition*, Part 1, John Wiley and Sons, Inc., New York, NY. (NNA.940421.0046)

de Marsily, G., 1986, *Quantitative Hydrogeology: Groundwater Hydrology for Engineers*, Academic Press, Orlando, FL. (NNA.910207.0116)

Department of Energy (DOE), 1984, "Nuclear Waste Policy Act of 1982; General Guidelines for the Recommendation of Sites for the Nuclear Waste Repositories; Final Siting Guidelines," *Code of Federal Regulations,* Title 10, Part 960, U.S. Department of Energy, Washington, DC. (NNA.870506.0140)

Department of Energy (DOE), 1988a, "Site Characterization Plan, Yucca Mountain Site, Nevada Research and Development Area, Nevada," *DOE/RW-0199*, U.S. Department of Energy, Washington, DC. (HQO.881201.0002)

Department of Energy (DOE), 1988b, "Draft 1988 Mission Plan Amendment," *DOE/RW-0187*, Office of Civilian Radioactive Waste Management, Washington, DC. (HQO.880620.0022)

Department of Energy (DOE), 1988c, "Internal Dose Conversion Factors for Calculation of Dose to the Public," *DOE/EH-0071*, U.S. Department of Energy, Washington, DC. (HQX.880826.0043)

Department of Energy (DOE), 1991, "Integrated Data Base for 1991: U.S. Spent Fuel and Radioactive Waste Inventories, Projections, and Characteristics," *DOE/RW-0006*, Rev. 7, Office of Civilian Radioactive Waste Management, Washington, DC. (HQX.910711.0004)

Department of Energy (DOE), 1992a, "Integrated Data Base for 1992: Spent Fuel and Radioactive Waste Inventories, Projections, and Characteristics," *DOE/RW-0006*, Washington, DC, September. (HQX.921106.0023)

Department of Energy (DOE), 1992b, "Characteristics of Potential Repository Wastes," *DOE/RW-0184-R1*, Office of Civilian Radioactive Waste Management, Washington, DC. (Includes computer database program for IBM-compatible PCs.) (NNA.921218.0013)

Department of Energy (DOE), 1993a, "Waste Package Design Status Report Fiscal Year 1993," *B00000000-01717-570500007-00*, prepared by TRW for the DOE Yucca Mountain Site Characterization Project Office, Las Vegas, NV. (HQV.931202.0005)

Department of Energy (DOE), 1993b, "The Yucca Mountain Site Characterization Project–Reference Information Base, Version 4, Revision 7," *YMP/CC-0002*, U.S. Department of Energy, Las Vegas, NV. (NNA.930517.0092)

Deutsch, C. V., and A. G. Journel, 1992, *GSLIB Geostatistical Software Library and User's Guide,* Oxford University Press, New York, NY. (NNA.930507.0081)

DeWispelare, A., L. T. Herren, M. Miklas, and R. Clemen, 1993, "Expert Elicitation of Future Climate in the Yucca Mountain Vicinity—Iterative Performance Assessment Phase 2.5," *CNWRA 93-016*, Center for Nuclear Waste Regulatory Analyses, San Antonio, TX. (NNA.940427.0098)

Diehl, S. F., and M. P. Chornack, 1990, "Stratigraphic Correlation and Petrology of the Bedded Tuffs, Yucca Mountain, Nye County, Nevada," *USGS/OFR-89-3,* U.S. Geological Survey, Denver, CO. (NNA.901102.0006)

Dockery, H. A., 1984, "Rotating Late Cenozoic Extensional Stresses, Yucca Flat Region, Nevada Test Site, Nevada," Ph.D. thesis, Rice University, Houston, TX. (HQS.880517.1165)

Doctor, P. G., P. W. Eslinger, D. M. Elwood, D. W. Engel, M. D. Freshley, A. M. Liebetrau, P. W. Reimus, D. L. Strenge, J. E. Tanner, and A. E. Van Luik, 1992, "An Example Post-Closure Risk Assessment Using the Potential Yucca Mountain Site," *PNL-8081*, Pacific Northwest Laboratory, Richland, WA. (NNA.930414.0031)

Donn, W. L., 1975, *Meteorology, 4th Edition*, Chapter 3, McGraw-Hill, New York, NY. (NNA.911024.0074)

Douglass, D. L., and J. T. Healey, 1979, "The Corrosion of Some Pure Metals in Basaltic Lava and Simulated Magmatic Gas at 1150°C," *SAND79-1981*, Sandia National Laboratories, Albuquerque, NM. (NNA.890626.0386)

Dudley, A. L., R. R. Peters, J. H. Gauthier, M. L. Wilson, M. S. Tierney, and E. A. Kavetter, 1988, "Total System Performance Assessment Code (TOSPAC) Volume 1: Physical and Mathematical Bases," *SAND85-0002*, Sandia National Laboratories, Albuquerque, NM. (NNA.881202.0211)

Dyer, J. R., 1993 letter, "Perched Water Encountered in Borehole UZ-14 and Notification of U.S. Nuclear Regulatory Commission (NRC) On-Site Representatives (OR)," dated 20 August. (NNA.940113.0032)

Dykhuizen, R. C., and R. W. Barnard, 1992, "Groundwater Flow Code Verification 'Benchmarking' Activity (COVE-2A): Analysis of Participants' Work," *SAND89-2558*, Sandia National Laboratories, Albuquerque, NM. (NNA.920130.0016)

Dykhuizen, R. C., and R. R. Eaton, 1991, "Effect of Material Heterogeneities on Flow Through Porous Media," in *High Level Radioactive Waste Management, Proceedings of the Second Annual International Conference, Las Vegas, Nevada, April 28-May 3, 1991,* pp. 529, American Nuclear Society, La Grange Park, IL. (NNA.920131.0203)

Eakin, T. E., G. B. Maxey, T. W. Robinson, J. C. Fredericks, and O. J. Loeltz, 1951, "Contributions to the Hydrology of Eastern Nevada," *Water Resources Bulletin No. 12*, Nevada Department of Conservation and Natural Resources, Carson City, NV. (NNA.870406.0382)

Eaton, R. R., 1993, "The Appropriateness of One-Dimensional Yucca Mountain Hydrologic Calculations," *SAND93-0852*, Sandia National Laboratories, Albuquerque, NM. (NNA.930930.0068)

Eaton, R. R., and R. C. Dykhuizen, 1988, "Effect of Material Nonhomogeneities on Equivalent Conductivities in Unsaturated Porous Media Flow, "*International Conference and Workshop on the Validation of Flow and Transport Models for the Unsaturated Zone, Ruidoso, New Mexico, May 22-25.* (NNA.900403.0278)

Eaton, R. R., and P. L. Hopkins, 1992, "LLUVIA-II: A Program for Two-Dimensional, Transient Flow Through Partially Saturated Porous Media," *SAND91-2416*, Sandia National Laboratories, Albuquerque, NM. (NNA.920630.0034)

Eaton, R. R., and J. T. McCord, 1992, "Comparison of Numerical and Analytical Estimates for Effective Unsaturated Conductivities for Stratified, Heterogeneous Media," *EOS, Transactions of the American Geophysical Union*, **73**(43), October 27. (NNA.930526.0001)

Edlefsen, N. E., and Anderson, B. C., 1943, "Thermodynamics of Soil Moisture," *Hilgardia*, **15**(2):31-298. (NNA.900312.0151)

Eckel, E. B., 1968, "Geologic Setting of the Nevada Test Site and Nellis Air Force Range," Geological Society of America Memoir 110, pp. 5-10. (HQS.880517.1178)

Ellis, W. L., and H. S. Swolfs, 1983, "Preliminary Assessment of In-Situ Geomechanical Characteristics in Drill Hole USW G-1, Yucca Mountain, Nevada," *USGS/OFR-83-401*, U.S. Geological Survey, Las Vegas, NV. (HQS.880517.1188)

Environmental Protection Agency (EPA), 1975, "National Primary Drinking Water Regulations," *Code of Federal Regulations*, Title 40, Part 141. (HQS.880517.2369)

Environmental Protection Agency (EPA), 1985, "Environmental Radiation Protection Standards for Management and Disposal of Spent Nuclear Fuel, High-Level, and Transuranic Radioactive Wastes," *Code of Federal Regulations*, Title 40, Part 191. (HQS.880517.3264)

Erickson, J. R., and R. K. Wadell, 1985, "Identification and Characterization of Hydrologic Properties of Fractured Tuff Using Hydraulic and Tracer Tests, Test Well USW H-4, Yucca Mountain, Nye County, Nevada," *USGS/WRI-85-4066*, U.S. Geological Survey, Denver, CO. (NNA.890713.0211)

Ervin, E. M., R. R. Luckey, and D. J. Burkhardt, 1993a, "Summary of Revised Potentiometric-Surface Map for Yucca Mountain and Vicinity, Nevada," *High Level Radioactive Waste Management, Proceedings of the Fourth Annual International Conference, Las Vegas, Nevada, April 26-30, 1993*, **2**:1554-1558, American Nuclear Society, La Grange Park, IL. (NNA.931129.0086)

Ervin, E. M., R. R. Luckey, and D. J. Burkhardt, 1993b, "Revised Potentiometric-Surface Map, Yucca Mountain and Vicinity," *USGS/WRI-93-4000,* U.S. Geological Survey. (NNA.931129.0086)

Eslinger, P. W., L. A. Doremus, D. W. Engel, T. B. Miley, M. T. Murphy, W. E. Nichols, M. D. White, D. W. Langford, and S. J. Ouderkirk, 1993, "Preliminary Total-System Analysis of a Potential High-Level Nuclear Waste Repository at Yucca Mountain," *PNL-8444*, Pacific Northwest Laboratory, Richland, WA. (HQO.930219.0001)

Evans, D. D., T. C. Rasmussen, and T. J. Nicholson, 1987, "Fracture System Characterization for Unsaturated Rock," in *Proceedings of the Symposium on Waste Management at Tucson, Arizona, March 1-5, 1987, High-Level Waste*, **2**:209-212. (NNA.920923.0052)

Flint, A., 1989, "Characterization of Infiltration," in transcript of public meeting of Hydrology and Geochemistry Panel of the U.S. Nuclear Waste Technical Review Board, Denver, Colorado, December 11-12, 1989, U.S. Nuclear Waste Technical Review Board, Arlington, VA. (NNA.920218.0021)

Flint, A. L., L. E. Flint, and J. A. Hevesi, 1993, "The Influence of Long Term Climate Change on Net Infiltration at Yucca Mountain, Nevada," in *High Level Radioactive Waste Management, Proceedings of the Fourth Annual International Conference, Las Vegas, Nevada, April 26-30, 1993,* American Nuclear Society, La Grange Park, IL. (NNA.930615.0054)

Flint, L., and A. Flint, USGS/YMP, 1993, Memo to M. L. Wilson and J. H. Gauthier, SNL/YMP, Subject: TSPA Modeling Plans, July 15, 1993. (NNA.940113.0030)

Flint , L. E., and A. L. Flint, 1990, "Preliminary Permeability and Water-Retention Data for Nonwelded and Bedded Tuff Samples, Yucca Mountain Area, Nye County, Nevada," *USGS/OFR-90-569,* U.S. Geological Survey, Denver, CO. ~~(NNA.920225.0002)~~ (NNA.901015.0200) 9/28/94

Forester, R., USGS, 1993, Memo to M. L. Wilson and J. H. Gauthier, SNL/YMP, Subject: Groundwater Flux Distributions for TSPA-Comment, July 16, 1993. (NNA.940113.0031)

Forester, R. M., 1987, 'Late Quaternary Paleoclimate Records from Lacustrine Ostracodes,' "North America and Adjacent Oceans During the Last Deglaciation," editors W. F. Ruddiman and H. E. Wright, Jr., *The Geology of North America*, **K-3**:261-276, Geological Society of America, Inc., Boulder, CO. (HQS.880517.2130)

Forester, R. M., and A. J. Smith, 1992, 'Microfossils as Indicators of Paleohydrology and Paleoclimate,' in "Disposal of Radioactive Waste by Paleohydrological Methods and Their Applications," *Proceedings of an NEA Workshop,* November 9-10, pp. 39-57, Paris, France. (NNA.940421.0045)

Freeze, R. A., and J. A. Cherry, 1979, *Groundwater*, Prentice-Hall, Englewood Cliffs, NJ. (NNA.870406.0444)

Fridrich, C. J., D. C. Dobson, and W. W. Dudley, 1991, "A Geologic Hypothesis for the Large Hydraulic Gradient Under Yucca Mountain, Nevada," *EOS, Transactions of the American Geophysical Union*, **72**:121. (NNA.910919.0013)

Gartling, D. K., 1982, "COYOTE—A Finite Element Computer Program for Nonlinear Heat Conduction Problems," *SAND77-1332 (Rev.)*, Sandia National Laboratories, Albuquerque, NM. (HQS.880517.2294)

Gartling, D. K., R. R. Eaton, and R. K. Thomas, 1981, "Preliminary Thermal Analyses for a Nuclear Waste Repository in Tuff," *SAND80-2813*, Sandia National Laboratories, NM. (HQS.880517.2295)

Gauthier, J. H., 1993, "The Most Likely Groundwater Flux Through the Unsaturated Tuff Matrix at USW H-1," in *High Level Radioactive Waste Management, Proceedings of the Fourth Annual International Conference, Las Vegas, Nevada, April 26-30, 1993*, American Nuclear Society, La Grange Park, IL. (NNA.930702.0025)

Gauthier, J. H., M. L. Wilson, R. R. Peters, A. L. Dudley, and L. H. Skinner, 1992, "Total System Performance Assessment Code (TOSPAC) Volume 2: User's Guide," *SAND85-0004*, Sandia National Laboratories, Albuquerque, NM. (NNA.920623.0013)

Gerhart, P. M., and R. J. Gross, 1985, *Fundamentals of Fluid Mechanics*, Addison-Wesley Publishing Co., Reading, MA. (NNA.940303.0056)

Gerlach, T. M., 1980, "Evaluation of Volcanic Gas Analyses From Kilauea Volcano," *Journal of Volcanology and Geothermal Research,* **7**:295-317. (NNA.930330.0037)

Gram, H. F., L. W. Scully, R. I. Braiser, and M. L. Wheeler, 1985, "Comparative Study of Radioactive Waste Emplacement Configurations," *SAND83-1884*, Sandia National Laboratories, NM. (NNA.870903.0092)

Gray, W., Leider, H., and Steward, S., 1992, "Parametric Study of LWR Spent Fuel Dissolution Kinetics," *UCRL-JC-110160,* Battelle Pacific Northwest Laboratory, Richland, WA. (NNA.940301.0024)

Greenland Ice-Core Project Members (GRIP), 1993, "Climate Instability During the Last Interglacial Period Recorded in the GRIP Ice Core," *Nature*, **364**:203-207. (NNA.940301.0025)

Hagstrum, J. T., J. J. Daniels, and J. H. Scott, 1980, "Interpretation of Geophysical Well-Log Measurements in Drill Hole UE25a-1, Nevada Test Site, Radioactive Waste Program," *USGS/OFR-80-941*, U.S. Geological Survey, Las Vegas, NV. (HQS.880517.1245)

Harr, M. E., 1987, *Reliability-Based Design in Civil Engineering*, McGraw-Hill, Inc., New York, NY. (NNA.890713.0149)

Healy, J. H., S. H. Hickman, M. D. Zoback, and W. L. Ellis, 1984, "Report on Televiewer Log and Stress Measurements in Core Hole USW-G1, Nevada Test Site, December 13-22, 1981," *USGS/OFR-84-15*, U.S. Geological Survey, Menlo Park, CA and Denver, CO. (NNA.870406.0374)

Helton, J. C., J. W. Garner, R. D. McCurley, and D. K. Rudeen, 1991, "Sensitivity Analysis Techniques and Results for Performance Assessment at the Waste Isolation Pilot Plant," *SAND90-7103*, Sandia National Laboratories, Albuquerque, NM. (NNA.930104.0089)

Henshall, G., W. Halsey, W. Clarke, and R. McCright, 1993, "Modeling Pitting Corrosion Damage of High-Level Radioactive-Waste Containers, With Emphasis on the Stochastic Approach," *UCRL-ID-111624*, Lawrence Livermore National Laboratory, Livermore, CA. (NNA.921222.0001)

Hillel, D., 1980, *Fundamentals of Soil Physics*, Academic Press, Orlando, FL, p. 269. (HQS.880517.1776)

Hopkins, P. L., R. R. Eaton, and N. E. Bixler, 1991, "NORIA-SP—A Finite Element Computer Program for Analyzing Liquid Water Transport in Porous Media," *SAND90-2542*, Sandia National Laboratories, Albuquerque, NM. (NNA.911202.0031)

Huyakorn, P. S., S. Panday, and A. Sinha, 1992, "STAFF3D—A Three-Dimensional Finite Element Code for Simulating Fluid Flow and Transport of Radionuclides in Fractured Porous Media with Water Table Boundary Conditions, Version 2.0" HydroGeoLogic, Inc., Herndon, VA. (NNA.940427.0093)

Hyman, J. M., 1979, "A Method Of Lines Approach to the Numerical Solution of Conservation Laws," in *Advances in Computer Methods for Partial Differential Equations III*, R. Vichnevetsky and R. S. Stepleman, editors, IMACS publications. (NNA.910405.0040)

Iman, R. L., and M. J. Shortencarier, 1984, "A FORTRAN 77 Program and User's Guide for the Generation of Latin Hypercube and Random Samples for Use with Computer Models," *SAND83-2365*, Sandia National Laboratories, Albuquerque, NM. (NNA.900117.0157)

Imbrie, J., 1985, "A Theoretical Framework for the Pleistocene Ice Ages," *Journal of the Geological Society of London*, **142**:417-432. (HQS.880517.2147)

Imbrie, J., and K. P. Imbrie, 1979, *Ice Ages: Solving the Mystery*, Enslow Publishers, Short Hills, NJ. (NNA.940427.0092)

Imbrie, J., A. C. Mix, and D. G. Martinson, 1993, "Milankovitch Theory Viewed from Devils Hole," *Nature*, **363**:531-533. (NNA.940301.0026)

Ingraham, N. L., B. F. Lyles, R. L. Jacobson, and J. W. Hess, 1991, "Stable Isotopic Study of Precipitation and Spring Discharge in Southern Nevada," *Journal of Hydrology*, **125**:243-258. (NNA.920413.0145)

INTERA, 1993, "A Comparative Application of the Repository Integration Program (RIP) to Total System Performance Assessment - 1991," Document No. *B00000000-01717-2200-00010-00*, INTERA Inc., Las Vegas, NV. (HQV.930408.0003)

International Commission on Radiological Protection (ICRP), 1985, "ICRP Publication 46: Radiation Protection Principles for the Disposal of Solid Radioactive Waste," *Annals of the ICRP*, **15**(4). (NNA.940421.0047)

International Commission on Radiological Protection (ICRP), 1991, "ICRP Publication 60: 1990 Recommendations of the International Commission on Radiological Protection," *Annals of the ICRP,* **21**(1-3). (NNA.940414.0111)

Isaaks, E. H., and R. M. Srivastava, 1989, *Applied Geostatistics,* Oxford University Press, New York, NY. (NNA.900420.0087)

Iwai, K., 1976, "Fundamental Studies of Fluid Flow Through a Single Fracture," Ph.D. dissertation, University of California, Berkeley, CA. (NNA.900501.0238)

Jaynes, E. T., 1957, "Information Theory and Statistical Mechanics, II," *Physics Review*, **108**, October 15. (NNA.910306.0127)

Johnstone, J. R., G. R. Hadley, and D. R. Waymire, 1985, "In-Situ Tuff Water Migration/ Heater Experiment: Final Report," *SAND81-1819*, Sandia National Laboratories, Albuquerque, NM. (HQS.880517.1655)

Journel, A. G., 1983, "Nonparametric Estimation of Spatial Distributions, " *Math. Geol.,* **15**:445-468. (NNA.891114.0349)

Journel, A. G., 1989, "Fundamentals of Geostatistics in Five Lessons," *Short Course in Geology,* **8**, American Geophysical Union, Washington, DC. (NNA.910405.0057)

Journel, A. G., and Ch. J. Huijbregts, 1978, *Mining Geostatistics,* Academic Press, New York, NY. (NNA.900919.0192)

Journel, A. G., and F. Alabert, 1989, "Non-Gaussian Data Expansion in the Earth Sciences," *Terra Nova,* **1**:123-134. (NNA.891208.0051)

Kerr, R. A., 1993, "How Ice Age Climate Got the Shakes," *Science*, **260**:890-892. (NNA.940301.0027)

Kerrisk, J., 1984, "Solubility Limits on Radionuclide Dissolution at a Yucca Mountain Repository," *LA-9995-MS*, Los Alamos National Laboratory, Los Alamos, NM. (NNA.870519.0049)

Kilbury, R. K., T. C. Rasmussen, D. D. Evans, and A. W. Warrick, 1986, "Water and Air Intake of Surface-Exposed Rock Fractures In Situ," *Water Resources Research*, **22**(10):1431-1443. (NNA.920923.0053)

Kipp, K. L., 1987, "Effect of Topography on Gas Flow in Unsaturated Fractured Rock," Flow and Transport Through Unsaturated Fractured Rock, Geophysical Monograph 42, pp. 171-176. (HQS.880517.3117)

Kirkpatrick, S., 1973, "Percolation and Conduction," *Reviews of Modern Physics*, **45**(4):574-588. (NNA.910128.0133)

Klavetter, E. A., and R. R. Peters, 1986, "Estimation of Hydrologic Properties of an Unsaturated, Fractured Rock Mass," *SAND84-2642*, Sandia National Laboratories, Albuquerque, NM. (NNA.870317.0738)

Knauss, K. G., and D. W. Peifer, 1986, "Reaction of Vitric Topopah Spring Tuff and J-13 Ground Water Under Hydrothermal Conditions Using Dickson-Type, Gold-Bag Rocking Autoclaves," *UCRL-53795,* Lawrence Livermore National Laboratory, Livermore, CA. (NNA.891102.0117)

Knauss, K. G., W. J. Beiriger, D. W. Peifer, and A. J. Piwinskii, 1985, "Hydrothermal Interaction of Solid Wafers of Topopah Spring Tuff with J-13 Water and Distilled Water at 90, 150, and 250°C, Using Dickson-Type, Gold-Bag Rocking Autoclave," *UCRL-53645,* Lawrence Livermore National Laboratory, Livermore, CA. (NNA.900207.0282)

Krumbein, W. C., and F. A. Graybill, 1974, *An Introduction to Statistical Models in Geology, Second Edition*, McGraw-Hill, New York, NY. (HQZ.870301.7475)

Kume, J., and D. P. Hammermeister, 1990, "Geohydrologic Data from Test Hole USW UZ-7, Yucca Mountain Area, Nye County, Nevada, *USGS/OFR-88-465*, U.S. Geological Survey, Denver, CO. (NNA.900312.0300)

Kume, J., and D. P. Hammermeister, 1991, "Geohydrologic Data from Drill-Bit Cuttings and Rotary Cores from Test Hole USW UZ-13, Yucca Mountain Area, Nye County, Nevada," *USGS/OFR-90-362,* U.S. Geological Survey, Denver, CO. (NNA.901015.0196)

Kurzweg, U. H., 1985, "Enhanced Heat Conduction in Oscillating Flow Within Parallel Plate Channels," *Journal of Fluid Mechanics*, **156**:291-300. (NNA.940301.0028)

Lahoud, R. G., D. H. Lobmeyer, and M. S. Whitfield, Jr., 1984, "Geohydrology of Volcanic Tuff Penetrated by Test Well UE-25b#1, Yucca Mountain, Nye County, Nevada," *USGS/WRI-84-4253*, U.S. Geological Survey, Denver, CO and Fenix and Scisson, Inc., Mercury, NV. (NNA.890511.0117)

Langkopf, B. S., and P. R. Gnirk, 1986, "Rock-Mass Classification of Candidate Repository Units at Yucca Mountain, Nye County, Nevada," *SAND82-2034*, Sandia National Laboratories, Albuquerque, NM. (HQS.880517.1662)

Lide, D. R., editor, 1990, *CRC Handbook of Chemistry and Physics, 71st Edition,* CRC Press, Boca Raton, FL. (NNA.901127.0187)

Lin, M., M. P. Hardy, and S. J. Bauer, 1993, "Fracture Analysis and Rock Quality Designation Estimation for the Yucca Mountain Site Characterization Project," *SAND92-0449,* Sandia National Laboratories, Albuquerque, NM. (NNA.921204.0012)

Lin, W., and W. Daily, 1984, "Transport Properties of Topopah Spring Tuff," *UCRL-53602,* Lawrence Livermore National Laboratory, Livermore, CA. (NNA.891026.0025)

Lipman, P. W., and E. J. McKay, 1965, Geologic Map of the Topopah Spring SW Quadrangle, Nye County, Nevada, U.S. Geological Survey Quandrangle Map GQ-439, Scale 1:24,000, U.S. Geological Survey. (NNA.900720.0032)

Lobmeyer, D. H., 1986, "Geohydrology of Rocks Penetrated by Test Well USW G-4, Yucca Mountain, Nye County, Nevada," *USGS/WRIR-86-4015,* U.S. Geological Survey, Denver, CO. (NNA.890918.0510)

Lobmeyer, D. H., M. S. Whitfield, Jr., R. G. Lahoud, and L. Bruckheimer, 1983, "Geohydrologic Data for Test Well UE-25b#1, Nevada Test Site, Nye County, Nevada," *USGS/OFR-83-855*, U.S. Geological Survey, Denver, CO and Fenix and Scisson, Inc., Mercury, NV. (NNA.890922.0285)

Long, A., and S. W. Childs, 1993, "Rainfall and Net Infiltration Probabilities for Future Climate Conditions at Yucca Mountain," in *High Level Radioactive Waste Management, Proceedings of the Fourth Annual International Conference, Las Vegas, Nevada, April 26-30, 1993*, pp. 112-121, American Nuclear Society, La Grange Park, IL. (NNA.940203.0016)

Loskot, C. L., and D. P. Hammermeister, 1992, "Geohydrologic Data from Test Holes UE-25 UZ #4 and UE-25 UZ #5, Yucca Mountain Area, Nye County, Nevada," *USGS/OFR-90-369*, U.S. Geological Survey, Denver, CO. (NNA.911219.0001)

MacDonald, G. A., 1972, *Volcanoes*, Prentice-Hall, Inc., Englewood Cliffs, NJ, 510 p. (NNA.940415.0006)

Maldonado, F., and S. L. Koether, 1983, "Stratigraphy, Structure, and Some Petrographic Features of Tertiary Volcanic Rocks at the USW G-2 Drill Hole, Yucca Mountain, Nye County, Nevada," *USGS/OFR-83-732*, U.S. Geological Survey and Fenix and Scisson, Inc., Tulsa, OK. (HQS.880517.1329)

Mansure, A. J., and S. V. Petney, 1991, "Determination of Equivalent Thermal Loadings as a Function of Waste Age and Burnup," *SAND87-2909*, Sandia National Laboratories, Albuquerque, NM. (NNA.901128.0001)

Marshall, B. D., Z. E. Peterman, and J. S. Stuckless, 1993, "Strontium Isotopic Evidence for a Higher Water Table at Yucca Mountain," in *High Level Radioactive Waste Management, Proceedings of the Fourth Annual International Conference, Las Vegas, Nevada, April 26-30, 1993*, pp. 1984-1952, American Nuclear Society, La Grange Park, IL. (NNA.931025.0035)

Martinez, M. J., R. C. Dykhuizen, and R. R. Eaton, 1992, "The Apparent Conductivity for Steady Unsaturated Flow in Periodically Fractured Porous Media," *Water Resources Research*, **28**(11):2879-2887. (NNA.930423.0202)

Maxey, G. B., and T. E. Eakin, 1949, "Ground Water in White River Valley, White Pine, Nye, and Lincoln Counties, Nevada," *Water Resources Bulletin No. 8*, Nevada Department of Conservation and Natural Resources, Carson City, NV. (NNA.870407.0319)

McCord, J. T., 1991, "Application of Second-Type Boundaries in Unsaturated Flow Modeling," *Water Resources Research*, **27**(12). (NNA.930823.0193)

McGuire, R. K., D. B. Bullen, N. Cook, K. J. Coppersmith, J. Kemeny, A. Long, F. J. Pearson Jr., F. Schwartz, M. Sheridan, and R. R. Youngs, 1990, "Demonstration of a Risk-Based Approach to High-Level Waste Repository Evaluation," *EPRI NP-7057*, Electric Power Research Institute, Palo Alto, CA. (NNA.910813.0004)

McGuire, R. K., M. J. Apted, D. B. Bullen, S. Childs, N. G. W. Cook, K. J. Coppersmith, R. L. Keeney, J. M. Kemeny, A. Long, F. J. Pearson Jr., B. Ross, F. W. Schwartz, M. F. Sheridan, and R. R. Youngs, 1992, "Demonstration of a Risk-Based Approach to High-Level Waste Repository Evaluation: Phase 2," *EPRI TR-100384*, Electric Power Research Institute, Palo Alto, CA. (NNA.940225.0126)

Meijer, A., 1990, "Yucca Mountain Project Far-Field Sorption Studies and Data Needs," *LA-11671-MS*, Los Alamos National Laboratory, Los Alamos, NM. (NNA.920131.0363)

Meijer, A., 1992, "A Strategy for the Derivation and Use of Sorption Coefficients in Performance Assessment Calculations for the Yucca Mountain Site," in *Proceedings of the DOE/Yucca Mountain Site Characterization Project Radionuclide Adsorption Workshop at Los Alamos National Laboratory, September 11-12, 1990*, Los Alamos National Laboratory Report, *LA-12325-C*, Los Alamos, NM, pp. 9-36. (NNA.930629.0011)

Meijer, A., 1993, "Far-Field Transport of Carbon Dioxide: Retardation Mechanisms and Possible Validation Experiments," *LA-UR-92-3278*, Los Alamos National Laboratory, Los Alamos, NM. (NNA.940427.0096)

Miller, I., R. Kossik, and M. Cunnane, 1992, "A New Methodology for Repository Site Suitability Evaluation," in *High Level Radioactive Waste Management, Proceedings of the Third International Conference, Las Vegas, Nevada, April 12-16, 1992*, American Nuclear Society, La Grange Park, IL. (NNA.920505.0064)

Montazer, P., E. P. Weeks, F. Thamir, S. N. Yard, and P. B. Hofrichter, 1986, "Monitoring the Vadose Zone in Fractured Tuff, Yucca Mountain, Nevada," *Proceedings of the NWWA Conference on Characterization and Monitoring of the Vadose (Unsaturated) Zone*, National Water Well Association, Worthington, OH. (NNA.900924.0023)

Montazer, P., and W. E. Wilson, 1984, "Conceptual Hydrologic Model of Flow in the Unsaturated Zone, Yucca Mountain, Nevada," *USGS/WRIR-84-4345*, U.S. Geological Survey, Denver, CO. (NNA.890327.0051)

Mossop, S. C., and G. Gafner, 1951, "The Thermal Constants of Some Rocks from the Orange Free State," *Journal of the Chemical, Metallurgical and Mining Society of South Africa*, **52**:61-76. (NNA.940321.0120)

Muller, D. C., and J. E. Kibler, 1984, "Preliminary Analysis of Geophysical Logs from Drill Hole UE-25p#1, Yucca Mountain, Nye County, Nevada," *USGS/OFR-84-649*, U.S. Geological Survey, Denver, CO. (HQS.880517.1353)

Naeser, C. W., and F. Maldonado, 1981, "Fission-Track Dating of Climax and Gold Meadows Stocks, Nye County, Nevada," U.S. Geological Survey Professional Paper 1199E, U.S. Geological Survey, pp. 45-47. (NNA.940421.0048)

National Council on Radiation Protection and Measurements (NCRP), 1987, "Exposure of the Population in the United States and Canada from Natural Background Radiation," NCRP Report No. *94*, NCRP, Bethesda, MD. (NNA.920403.0060)

Nelson, R. W., and C. E. Bruch, 1993, Summary of Performance Assessment (PA) Thermal Modeling Meeting, TRW Environmental Safety Systems, Inc., Yucca Mountain Site Characterization Project, Las Vegas, NV, June 29, 1993. (NNA.931015.0010)

Nelson, P. H., D. C. Muller, U. Schimschal, and J. E. Kibler, 1991, "Geophysical Logs and Core Measurements from Forty Boreholes at Yucca Mountain, Nevada," *Geophysical Investigations MAP GP-1001*, U.S. Geological Survey, Denver, CO. (NNA.920211.0022)

Nilson, R. H., and K. H. Lie, 1990, "Double Porosity Modeling of Oscillatory Gas Motion and Contaminant Transport in Fractured Porous Media," *International Journal for Numerical and Analytical Methods in Geomechanics*, **17**:565-585. (NNA.940301.0030)

Nilson, R. H., E. W. Peterson, K. H. Lie, N. R. Burkhard, and J. R. Hearst, 1991, "Atmospheric Pumping: A Mechanism Causing Vertical Transport of Contaminated Gases through Fractured Permeable Rock," *Journal of Geophysical Research*, **96**(B13):21,933-21,948. (NNA.940301.0029)

Nilson, R. H., P. L. Lagus, W. B. McKinnis, J. R. Hearst, N. R. Burkhard, and C. F. Smith, 1992, "Field Measurements of Tracer Gas Transport Induced by Barometric Pumping," *High Level Radioactive Waste Management, Proceedings of the Third Annual International Conference, Las Vegas, Nevada, April 12-16, 1992*, pp. 710-716, American Nuclear Society, La Grange Park, IL. (NNA.940203.0033)

Nimick, F. B., S. J. Bauer, and J. R. Tillerson, 1984, "Recommended Matrix and Rock-Matrix Bulk, Mechanical, and Thermal Properties for Thermomechanical Stratigraphy of Yucca Mountain," *Keystone Document 6310-85-1*, Sandia National Laboratories, Albuquerque, NM. (NNA.891129.0284)

Nitao, J. J., 1989, "V-TOUGH—An Enhanced Version of the TOUGH Code for the Thermal and Hydrologic Simulation of Large-Scale Problems in Nuclear Waste Isolation," *UCID-21954*, Lawrence Livermore National Laboratory, Livermore, CA. (NNA.900712.0168)

Nitsche, H., R. C. Gatti, E. M. Standifer, S. C. Lee, M. Muller, T. Prussin, R. S. Deinhammer, H. Maurer, K. D. Becraft, S. Leung, and S. A. Carpenter, 1993a, "Measured Solubilities and Speciation of Np, Pu, and Am in a Typical Groundwater (J-13) from the Yucca Mountain Region," *LA-12562-MS*, Los Alamos National Laboratory, Los Alamos, NM. (NNA.930507.0136)

Nitsche, H., K. Roberts, T. Prussin, D. Keeney, S. A. Carpenter, K. Becraft, and R. C. Gatti, 1993b, "Radionuclide Solubility and Speciation Studies for the Yucca Mountain Site Characterization Project," in *High Level Radioactive Waste Management, Proceedings of the Fourth Annual International Conference, Las Vegas, Nevada, April 26-30, 1993*, **2**:1490-1495, American Nuclear Society, La Grange Park, IL. (NNA.940203.0034)

Norris, A. E., 1989, "The Use of Chlorine Isotope Measurements to Trace Water Movements at Yucca Mountain," in *FOCUS '89, Proceedings of the Topical Meeting on Nuclear Waste Isolation in the Unsaturated Zone, September 17-21, 1989, Las Vegas, Nevada*, American Nuclear Society, La Grange Park, IL. (NNA.920218.0022)

Nuclear Regulatory Commission (NRC), 1983, "Disposal of High-Level Radioactive Wastes in Geologic Repositories," *Code of Federal Regulations*, Title 10, Part 60. (NNA.900727.0307)

Ogard, A. E., and J. F. Kerrisk, 1984, "Groundwater Chemistry Along Flowpaths Between a Proposed Repository Site and the Accessible Environment," *LA-10188-MS*, Los Alamos National Laboratory, Los Alamos, NM. (NNA.870406.0021)

Olsson, O., editor, 1992, "Site Characterization and Validation—Final Report," *STRIPA 92-22*, Swedish Nuclear Fuel and Waste Management Company, Stockholm, Sweden. (NNA.940421.0049)

Ortiz, T. S., R. L. Williams, F. B. Nimick, B. C. Whittet, and D. L. South, 1985, "A Three-Dimensional Model of Reference Thermal/Mechanical and Hydrological Stratigraphy at Yucca Mountain, Southern, Nevada," *SAND84-1076,* Sandia National Laboratories, Albuquerque, NM. (NNA.890315.0013)

Paces, J. B., E. M. Taylor, and C. Bush, 1993, "Late Quaternary History and Uranium Isotopic Compositions of Ground Water Discharge Deposits, Crater Flat, Nevada," in *High Level Radioactive Waste Management, Proceedings of the Fourth Annual International Conference, Las Vegas, Nevada, April 26-30, 1993*, pp. 1573-1580, American Nuclear Society, La Grange Park, IL. (NNA.940203.0035)

Park, U-S., and C. G. Pflum, 1990, "Requirements for Controlling a Repository's Releases of Carbon-14 Dioxide; the High Costs and Negligible Benefits," in *Proceedings of the International Topical Meeting on High Level Radioactive Waste Management*, American Nuclear Society, La Grange Park, IL. (NNA.900615.0185)

Parkhurst, D. L., D. C. Thorstenson, and L. N. Plummer, 1980, "PHREEQE—A Computer Program for Geochemical Calculations," *USGS/WRI-80-96*, U.S. Geological Survey, Reston, VA. (HQS.880517.2817)

Pei-Lin Tien, M. D. Siegel, C. D. Updegraf, K. K. Wahi, and R. V. Guzowski, 1985, "Repository Site Data Report for Unsaturated Tuff, Yucca Mountain, NV," *NUREG/CR-4110*, U.S. Nuclear Regulatory Commission, Washington, DC. (HQS.880517.1853)

Peters, R. R., and E. A. Klavetter, 1988, "A Continuum Model for Water Movement in an Unsaturated Fractured Rock Mass," *Water Resources Research*, **24**(3):416-430. (NNA.890523.0139)

Peters, R. R., E. A. Klavetter, I. J. Hall, S. C. Blair, P. R. Heller, and G. W. Gee, 1984, "Fracture and Matrix Hydrogeologic Characteristics of Tuffaceous Materials from Yucca Mountain, Nye County, Nevada," *SAND84-1471*, Sandia National Laboratories, Albuquerque, NM. (NNA.870407.0036) (DTN: SNSAND84147100.000)

Peters, R. R., E. A. Klavetter, J. T. George, and J. H. Gauthier, 1987, "Measuring and Modeling Water Imbibition into Tuff," in *Flow and Transport Through Unsaturated Fractured Media*, edited by D. D. Evans and T. J. Nicholson, American Geophysical Union, Washington, DC. (NNA.900308.0324)

Philip, J. R., and D. A. de Vries, 1957, "Moisture Movement in Porous Materials Under Temperature Gradients," *EOS, Transactions of the American Geophysical Union*, **38**:222-231. (NNA.890713.0173)

Prindle, R. W., and P. L. Hopkins, 1990, "On Conditions and Parameters Important to Model Sensitivity for Unsaturated Flow Through Layered, Fractured Tuff: Results of Analyses for HYDROCOIN Level 3, Case 2," *SAND89-0652*, Sandia National Laboratories, Albuquerque, NM. (NNA.900523.0211)

Pruess, K., 1987, "TOUGH User's Guide," *LBL-20700/SAND86-7104* and *NUREG/CR-4645*, Lawrence Berkeley Laboratory, University of California, Berkeley, CA. (NNA.890315.0010)

Pruess, K., 1991, "TOUGH2–A General-Purpose Numerical Simulator for Multiphase Fluid and Heat Flow," *LBL-29400*, Lawrence Berkeley Laboratory, University of California, Berkeley, CA. (NNA.940202.0088)

Pruess, K., and Y. Tsang, 1993, "Modeling of Strongly Heat-Driven Flow Processes at a Potential High-Level Nuclear Waste Repository at Yucca Mountain, Nevada," in *High Level Radioactive Waste Management, Proceedings of the Fourth Annual International Conference, Las Vegas, Nevada, April 26-30, 1993*, pp. 568-575, American Nuclear Society, La Grange Park, IL. (NNA.940203.0036)

Pruess, K., J. S. Y. Wang, and Y. W. Tsang, 1990, "On Thermohydrologic Conditions Near High-Level Nuclear Wastes Emplaced in Partially Saturated Fractured Tuff: 1. Simulation Studies with Explicit Consideration of Fracture Effects, 2. Effective Continuum Approximation," *Water Resources Research*, **6**(6):1235-1261. (NNA.910328.0073)

Public Law 97-425, 1982, *Nuclear Waste Policy Act of 1982*. (NNA.890626.0312)

Public Law 102-486, 1992, *Energy Policy Act of 1992*, Title VIII, Section 801. (NNA.940321.0121)

Ramirez, A. L., T. A. Buscheck, R. Carlson, W. Daily, K. Lee, W. Lin, N. Mao, T. S. Ueng, H. Wang, and D. Watwood, 1991, "Prototype Engineered Barrier System Field Test (PEBSFT) Final Report," *UCRL-ID-106159*, Lawrence Livermore National Laboratory, Livermore, CA. (NNA.910313.0032)

Rautman, C. A., and A. H. Treadway, 1991, "Geologic Uncertainty in a Regulatory Environment: An Example From the Potential Yucca Mountain Nuclear Waste Repository Site, *Environ. Geol. Water Sci.*, **18**:171-184. ~~(NNA.910828.0001)~~ (NNA.920102.0080) erry 9/28/94

Rautman, C. A., and A. L. Flint, 1992, "Deterministic Geologic Processes and Stochastic Modeling," in *High Level Radioactive Waste Management, Proceedings of the Third Annual International Conference, Las Vegas, Nevada, April 12-16, 1992*, American Nuclear Society, La Grange Park, IL. (NNA.920505.0069)

Rautman, C. A., and T. H. Robey, 1993, "Recent Developments in Stochastic Modeling and Upscaling of Hydrologic Properties in Tuff," in *High Level Radioactive Waste Management, Proceedings of the Fourth Annual International Conference, Las Vegas, Nevada, April 26-30, 1993*, American Nuclear Society, La Grange Park, IL. (NNA.930702.0014)

Rautman, C. A., B. C. Whittet, and D. L. South, 1987, "Definitions of Reference Boundaries for the Proposed Geologic Repository at Yucca Mountain, Nevada," *SAND86-2157*, Sandia National Laboratories, Albuquerque, NM. (NNA.890123.0066)

Rice, W. A., 1984, "Preliminary Two-Dimensional Regional Hydrologic Model of the Nevada Test Site and Vicinity," *SAND83-7466*, Sandia National Laboratories, Albuquerque, NM. (NNA.900810.0286)

Richards, L. A., 1931, "Capillary Conduction of Liquids Through Porous Mediums," *Physics*, 1:318-333. (NNA.890522.0282)

Robison, J. H., 1984, "Ground-Water Level Data and Preliminary Potentiometric Surface Maps, Yucca Mountain and Vicinity, Nye County, Nevada," *USGS/WRIR-84-4197*, U.S. Geological Survey. (NNA.870519.0096)

Roddy, J. W., H. C. Claiborne, R. C. Ashline, P. J. Johnson, and B. T. Rhyne, 1986, "Physical and Decay Characteristics of Commercial LWR Spent Fuel," *ORNL/TM-9591/V1&R1,* Oak Ridge National Laboratory, Oak Ridge, TN. (NNA.891016.0145)

Rood, R. B., 1987, "Numerical Advection Algorithms and Their Role in Atmospheric Transport and Chemistry Models," *Reviews of Geophysics*, 25(1):71-100. (NNA.940301.0031)

Ross, B., 1984, "A Conceptual Model of Deep Unsaturated Zones with Negligible Recharge," *Water Resources Research,* 20:1627-1629. (HQS.880517.1832)

Ross, B., 1990, "Quasi-Linear Analysis of Water Flow in the Unsaturated Zone at Yucca Mountain, Nevada, USA," in *Water Resources in Mountainous Regions, Memoires of the 22nd Congress of the International Association of Hydrogeologists*, edited by A. Parriaux, International Association of Hydrogeologists, Lausanne, Switzerland. (NNA.920207.0007)

Ross, B., S. Amter, and N. Lu, 1992, "Numerical Studies of Rock-Gas Flow in Yucca Mountain," *SAND91-7034*, Sandia National Laboratories, Albuquerque, NM. (NNA.920205.0062)

Ross, B., Y. Zhang, and N. Lu, 1993, "Implications of Stability Analysis for Heat Transfer at Yucca Mountain," in *High Level Radioactive Waste Management, Proceedings of the Fourth Annual International Conference, Las Vegas, Nevada, April 26-30, 1993,* American Nuclear Society, La Grange Park, IL. (NNA.931012.0006)

Rush, F. E., 1971, "Regional Ground-Water Systems in the Nevada Test Site Area, Nye, Lincoln, and Clarke Counties, Nevada," Water Resources-Reconnaissance Report No. *54*, Nevada Department of Conservation and Natural Resources, Carson City, NV. (NNA.870406.0383)

Rush, F. E., W. Thordarson, and L. Bruckheimer, 1983, "Geohydrologic and Drill-Hole Data for Test Well USW H-1, Adjacent to the Nevada Test Site, Nye County, Nevada," *USGS/OFR-83-141*, U.S. Geological Survey, Reston, VA. (NNA.870519.0103)

Rush, F. E., W. Thordarson, and D. G. Pyles, 1984, "Geohydrology of Test Well USW H-1, Yucca Mountain, Nye County, Nevada," *USGS/WRIR-84-4032*, U.S. Geological Survey, Denver, CO. (NNA.870518.0067)

Rutherford, B. M., I. J. Hall, R. R. Peters, R. G. Easterling, and E. A. Klavetter, 1992, "Statistical Analysis of Hydrologic Data for Yucca Mountain," *SAND87-2380,* Sandia National Laboratories, Albuquerque, NM. (NNA.910822.0001)

Ryder, E. E., 1993, "Comparison of Predicted Far-Field Temperatures for Discrete and Smeared Heat Sources," in *High Level Radioactive Waste Management, Proceedings of the Fourth Annual International Conference, Las Vegas, Nevada, April 26-30, 1993*, American Nuclear Society, La Grange Park, IL. (NNA.930702.0022)

Sandia National Laboratories (SNL), 1987, "Nevada Nuclear Waste Storage Investigations Project–Site Characterization Plan–Conceptual Design Report," compiled by H. R. MacDougall, L. W. Scully, and J. R. Tillerson, *SAND84-2641*, Albuquerque, NM. (NN1.880902.0014-NN1.880902.0019)

Sass, J. H., A. H. Lachenbruch, and C. W. Mase, 1980, "Analysis of Thermal Data from Drill Holes UE25a-3 and UE25a-1, Calico Hills and Yucca Mountain, Nevada Test Site," *USGS/OFR-80-826*, U.S. Geological Survey, Menlo Park, CA. (NNA.890715.0552)

Sass, J. H., A. H. Lachenbruch, W. W. Dudley, Jr., S. S. Priest, and R. J. Munroe, 1987, "Temperature, Thermal Conductivity, and Heat Flow Near Yucca Mountain, Nevada: Some Tectonic and Hydrogeologic Implications," *USGS/OFR-87-649*, U.S. Geological Survey, 118 p. (NNA.890123.0010)

Schenker, A. R., D. C. Guerin, and T. H. Robey, 1994, "Stratigraphy and Hydrogeologic Properties Development for the Total-System Performance Assessment 1993," *SAND94-0244*, Sandia National Laboratories, Albuquerque, NM. (NNA.940204.0199)

Schrauf, T. W., and D. D. Evans, 1984, "Relationship Between the Gas Conductivity and Geometry of a Natural Fracture," *NUREG/CR-3680*, University of Arizona, Tucson, AZ. (NNA.900123.0075)

Schwartz, B. M., 1990, SNL Yucca Mountain Project Data Report: Density and Porosity Data for Tuffs from the Unsaturated Zone at Yucca Mountain Nevada," *SAND88-0811*, Sandia National Laboratories, Albuquerque, NM. (NNA.900108.0028)

Scott, R. B., and J. Bonk, 1984, "Preliminary Geologic Map of Yucca Mountain, Nye County, Nevada, with Geologic Sections," *USGS/OFR-84-494*, U.S. Geological Survey, Denver, CO. (HQS.880517.1443)

Scott, R. B., and M. Castellanos, 1984, "Stratigraphic and Structural Relations of Volcanic Rocks in Drill Holes USW GU-3 and USW G-3, Yucca Mountain, Nye County, Nevada," *USGS/OFR-84-491*, U.S. Geological Survey, Denver, CO. (NNA.890804.0017)

Scott, R. B., R. W. Spengler, S. Diehl, A. R. Lappin, and M. P. Chornack, 1983, 'Geologic Character of Tuffs in the Unsaturated Zone at Yucca Mountain, Southern Nevada,' "Role of the Unsaturated Zone in Radioactive and Hazardous Waste Disposal," *Ann Arbor Science*, Ann Arbor, MI, pp. 289-335. (NNA.870406.0034)

Shampine, L. F., and H. A. Watts, 1980, "DEPAC–Design of a User Oriented Package of ODE Solvers," *SAND79-2374*, Sandia National Laboratories, Albuquerque, NM. (NNA.900122.0001)

Shapiro, A. B., 1985, "TOPAZ3D—A Three-Dimensional Finite Element Heat Transfer Code," *UCID-20483*, Lawrence Livermore National Laboratory, Livermore, CA. (NNA.940421.0050)

Shapiro, A. B., and A. L. Edwards, 1990, "TOPAZ2D Heat Transfer Code Users Manual and Thermal Properties Data Base," *UCRL-ID-104558*, Lawrence Livermore National Laboratory, Livermore, CA. (NNA.940321.0125)

Siegel, M. D., P. L. Hopkins, R. J. Glass, and D. B. Ward, 1992, "Design of an Intermediate-Scale Experiment to Validate Unsaturated-Zone Transport Models, in *High Level Radioactive Waste Management, Proceedings of the Third Annual International Conference, Las Vegas, Nevada, April 12-16, 1992,* American Nuclear Society, La Grange Park, IL. (NNA.930205.0016)

Siegel, M. D., D. B. Ward, W. C. Cheng, C. Bryant, C. S. Chocas, and C. G. Reynolds, 1993, "Preliminary Characterization of Materials for Reactive Transport Model Validation Experiment," in *High Level Radioactive Waste Management, Proceedings of the Fourth Annual International Conference, Las Vegas, Nevada, April 26-30, 1993*, American Nuclear Society, La Grange Park, IL. (NNA.930702.0024)

Sinnock, S., Y. T. Lin, and J. P. Brannen, 1984, "Preliminary Bounds on the Expected Postclosure Performance of the Yucca Mountain Repository Site, Southern Nevada," *SAND84-1492*, Sandia National Laboratories, Albuquerque, NM. (NNA.870519.0076)

Sinton, S., 1989, "Characterization of the Large Hydraulic Gradient Beneath the North End of Yucca Mountain, Nevada," *EOS*, Abstract H11B-03 0910H, **70**:321. (NNA.891204.0065)

Snoeberger, D. F., J. Baker, C. J. Morris, and R. B. Rosa, 1974, "Permeability of Surface Alluvium and a Nuclear Chimney at Nevada Test Site," *UCID-16479*, Lawrence Livermore National Laboratory, Livermore, CA. (NNA.940323.0007)

Spaulding, W. G., 1985, "Vegetation and Climates of the Last 45,000 Years in the Vicinity of the Nevada Test Site, South-Central Nevada," U.S. Geological Survey Professional Paper 1329, U.S. Geological Survey, Washington, DC. (HQS.880517.1484)

Spengler, R. W., and J. G. Rosenbaum, 1980, "Preliminary Interpretations of Geologic Results Obtained from Boreholes UE25a-4, -5, -6, and -7, Yucca Mountain, Nevada Test Site," *USGS/OFR-80-929*, U.S. Geological Survey, Reston, VA. (NNA.890823.0106)

Spengler, R. W., and M. P. Chornack, 1984, "Stratigraphic and Structural Characteristics of Volcanic Rocks in Core Hole USW G-4, Yucca Mountain, Nye County, Nevada," with a section on geophysical logs by D. C. Muller and J. E. Kibler, *USGS-OFR-84-789*, U.S. Geological Survey. (NNA.870519.0105)

Spengler, R. W., D. C. Muller, and R. B. Livermore, 1979, "Preliminary Report on the Geology and Geophysics of Drill Hole UE25a-1, Yucca Mountain, Nevada Test Site," *USGS/OFR-79-1244*, U.S. Geological Survey, Denver, CO. (HQS.880517.1491)

Spengler, R. W., F. M. Byers, Jr., and J. B. Warner, 1981, "Stratigraphy and Structure of Volcanic Rocks in Drill Hole USW-G1, Yucca Mountain, Nye County, Nevada," *USGS/OFR-81-1349, DOE/ET/44802/T4*, U.S. Geological Survey, Denver, CO. (HQS.880517.1492)

St. John, C. M., 1985, "Thermal Analysis of Spent Fuel Disposal in Vertical Emplacement Boreholes in a Welded Tuff Repository," *SAND84-7207*, Sandia National Laboratories, Albuquerque, NM. (HQS.880517.2542)

Stock, J. M., J. H. Healy, and S. H. Hickman, 1984, "Report on Televiewer Log and Stress Measurements in Core Hole USW G-2, Nevada Test Site, October-November, 1982," *USGS/OFR-84-172*, U.S. Geological Survey, Menlo Park, CA. (NNA.870406.0157)

Swift, P. N., 1992, "Long-Term Climate Variability at the Waste Isolation Pilot Plant, Southeastern New Mexico, USA," *SAND91-7055*, Sandia National Laboratories, Albuquerque, NM. (NNA.940203.0039)

Thomas, K. W., 1987, "Summary of Sorption Measurements Performed With Yucca Mountain, Nevada, Tuff Samples and Water From Well J-13," *LA-10960-MS*, Los Alamos National Laboratory, Los Alamos, NM. (NNA.890602.0026)

Thordarson, W., 1983, "Geohydrologic Data and Test Results from Well J-13, Nevada Test Site, Nye County, Nevada," *USGS/WRIR-83-4171*, U.S. Geological Survey, Denver, CO. (HQS.880517.1849)

Thordarson, W., F. E. Rush, R. W. Spengler, and S. J. Wadell, 1984, "Geohydrologic and Drill-Hole Data for Test Well USW H-3, Yucca Mountain, Nye County, Nevada," *USGS/OFR-84-149*, U.S. Geological Survey, Denver, CO. (NNA.870406.0056)

Thordarson, W., F. E. Rush, and S. J. Wadell, 1985, "Geohydrology of Test Well USW H-3, Yucca Mountain, Nye County, Nevada," *USGS/WRI-84-4272*, U.S. Geological Survey, Lakewood, CO. (SRX.850418.0031)

Tidwell, V. C., J. D. VonDoemming, and K. Martinez, 1993, "Scale Dependence of Effective Media Properties," in *High Level Radioactive Waste Mananagement, Proceedings of the Fourth Annual International Conference, Las Vegas, Nevada, April 26-30, 1993*, pp. 1059-1064, American Nuclear Society, La Grange Park, IL. (NNA.930615.0056)

Tien, Pei-Lin, M. D. Siegel, C. D. Updegraff, K. K. Wahi, and R. V. Guzowski, 1985, "Repository Site Data Report for Unsaturated Tuff, Yucca Mountain, Nevada," *NUREG/CR-4110*, U.S. Nuclear Regulatory Commission, Washington, DC. (HQS.880517.1853)

Triay, I. R., A Meijer, M. R. Cisneros, G. G. Miller, A. J. Mitchell, M. A. Ott, D. E. Hobart, P. D. Palmer, R. E. Perrin, and R. D. Aguilar, 1991a, "Sorption of Am in Tuff and Pure Minerals Using Synthetic and Natural Groundwaters," *Radiochimica Acta*, **52/53**:141-145. (NNA.920131.0405)

Triay, I. R., D. E. Hobart, A. J. Mitchell, T. W. Newton, M. A. Ott, P. D. Palmer, R. S. Rundbert, and J. L. Thompson, 1991b, "Size Determinations of Plutonium Colloids Using Autocorrelation Photon Spectroscopy," *Radiochimica Acta,* **52/53**:127-131. (NNA. 930607.0060)

Triay, I. R., A. J. Mitchell, and M. A. Ott, 1991c, "Radionuclide Migration as a Function of Mineralogy," in *High Level Radioactive Waste Management, Proceedings of the Second Annual International Conference, Las Vegas, Nevada, April 28-May 3, 1991*, **1**:494-498, American Nuclear Society, La Grange Park, IL. (NNA.920131.0406)

Triay, I. R., B. A. Robinson, R. M. Lopez, A. J. Mitchell, and C. M. Overly, 1993a, "Neptunium Retardation With Tuffs and Groundwaters from Yucca Mountain," in *High Level Radioactive Waste Management, Proceedings of the Fourth Annual International Conference, Las Vegas, Nevada, April 26-30, 1993*, **2**:1504-1508, American Nuclear Society, La Grange Park, IL. (NNA.940203.0037)

Triay, I. R., K. H. Birdsell, A. J. Mitchell, and M. A. Ott, 1993b, "Diffusion of Sorbing and Non-Sorbing Radionuclides," in *High Level Radioactive Waste Management, Proceedings of the Fourth Annual International Conference, Las Vegas, Nevada, April 26-30, 1993*, **2**:1527-1532, American Nuclear Society, La Grange Park, IL. (NNA.930924.0109)

Triay, I., A. Simmons, S. Levy, H. Nuttall, B. Robinson, W. Steinkampf, and B. Viani, "Colloid-Facilitated Radionuclide Transport at Yucca Mountain," (1994) in press, to be published as a LA-MS report. (NNA.930628.0067)

Tsang, Y. W., and P. A. Witherspoon, 1981, "Hydromechanical Behavior of a Deformable Rock Fracture Subject to Normal Stress," *Journal of Geophysical Research*, **86**(B10):9287-9398. (NNA.900403.0018)

Tsang, Y. W., and K. Pruess, 1989, "Preliminary Studies of Gas Phase Flow Effects and Moisture Migration at Yucca Mountain, Nevada," *LBL-28819, DE90 016642*, Lawrence Berkeley National Laboratory, Berkeley, CA, 42 pp. (NNA.940303.0045)

Tsang, Y. W., and K. Pruess, 1990, "Further Modeling Studies of Gas Movement and Moisture Migration at Yucca Mountain, Nevada, *LBL-29127*, Lawrence Berkeley Laboratory, Berkeley, CA, 52 pp. (NNA.910405.0037)

Turrin, B. D., and D. E. Champion, 1991, "$^{40}Ar/^{39}Ar$ Laser Fusion and K-Ar Ages from Lathrop Wells, Nevada, and Cima, California: The Age of the Latest Volcanic Activity in the Yucca Mountain Area," in *High Level Radioactive Waste Management, Proceedings of the Second Annual International Conference, Las Vegas, Nevada, April 28-May 3, 1991*, **1**:68-75, American Nuclear Society, La Grange Park, IL. (NNA.910620.0133)

Udell, K. S., and Fitch, J. S., 1985, "Heat and Mass Transfer in Capillary Porous Media Considering Evaporation, Condensation and Noncondensable Gas Effects," presented at the 23rd ASME/AICHE National Heat Transfer Conference, Denver CO. (NNA.890713.0199)

1948 amj 9/28/94

Uhlig, H. H., ~~1946~~, *Corrosion Handbook*, J. Wiley, New York, NY, p. 645. (NNA.940414.0123)

van Genuchten, R., 1978, "Calculating the Unsaturated Hydraulic Conductivity with a New Closed-Form Analytical Model," *Water Resources Bulletin*, Princeton University Press, Princeton University, Princeton, NJ. (HQS.880517.1859)

Vaniman, D. T., B. M. Crowe, and E. S. Gladney, 1982, "Petrology and Geochemistry of Hawaiite Lavas from Crater Flat, Nevada," *Contributions to Mineralogy and Petrology*, **80**:341-357. (HQS.880517.1906)

Van Konynenburg, R. A., 1991, "Gaseous Release of Carbon-14: Why the High Level Waste Regulations Should be Changed," *High Level Radioactive Waste Management, Proceedings of the Second Annual International Conference, Las Vegas, Nevada, April 28-May 3, 1991*, American Nuclear Society, La Grange Park, IL. (NNA.920413.0140)

Voss, C., Golder Associates, Inc., 1992a, Letter to P. Kaplan SNL, Subject: Transfer of Test Case Data—Attachment A: Composite Transect Dataset: Includes Representative Samples from Surface Outcrop Studies with Data on Porosity, Bulk Density, and Sorptivity, Saturated Hydraulic Conductivity, and Moisture Retention, dated June 15, 1992. (DTN: GS920508312231.010). (MOL.19941005.0125) emj 10/6/94

Voss, C., Golder Associates, Inc., 1992b, Letter to P. Kaplan, SNL, Subject: Transfer of Test Case Data—Attachment B: USW GU-3 Core Analyses, 69 Samples from Tonopah Spring Shardy Base (1263.8 ft) to Prow Pass Partially Welded (1883.5 ft), with Measurements of Porosity, Bulk Density, Particle Density, Sorptivity, and Saturated Conductivity, dated June 15, 1992. (DTN: GS920508312231.011). (MOL.19940930.0001) emj 9/30/94

Voss, C., Golder Associates, Inc., 1993, Letter to T. Robey, SNL, Subject: Third Contribution to the Yucca Mountain Test Case Data Set—Water Retention Using CX-2 on Subsamples of Composite Dataset, dated February 15, 1993. (NNA.940113.0033)

Wang, J. S. Y., and T. N. Narasimhan, 1985, "Hydrologic Mechanisms Governing Fluid Flow in Partially Saturated, Fractured, Porous Tuff at Yucca Mountain," *SAND84-7202*, Sandia National Laboratories, Albuquerque, NM. (NNA.870407.0209)

Wang, J. S. Y., and T. N. Narasimhan, 1986, "Hydrologic Mechanisms Governing Partially Saturated Flow in Fractured Welded Units and Porous Non-Welded Units at Yucca Mountain," *SAND85-7114*, Lawrence Berkeley Laboratory, Berkeley, CA. (NNA.870806.0063)

Wang, J. S. Y., and T. N. Narasimhan, 1988, "Hydrologic Modeling of Vertical and Lateral Movement of Partially Saturated Fluid Flow Near a Fault Zone at Yucca Mountain," *SAND87-7070*, Sandia National Laboratories, Albuquerque, NM. (NNA.871109.0057)

Wang, J. S. Y., N. G. W. Cook, H. A. Wollenberg, C. L. Carnahan, I. Javandel, and C. F. Tsang, 1993, "Geohydrologic Data and Models of Rainier Mesa and Their Implications to Yucca Mountain," in *High Level Radioactive Waste Management, Proceedings of the Fourth Annual International Conference, Las Vegas, Nevada, April 26-30, 1993,* American Nuclear Society, La Grange Park, IL. (NNA.940203.0038)

Wanner, H., and I. Forest, 1992, *Vol. 1 Chemical Thermodynamics of Uranium*, North-Holland Elsevier Science Publishers B.V., The Netherlands. (NNA.940415.0009)

Ward, J. C., 1964, "Turbulent Flow in Porous Media," *Proc. Amer. Soc. Civil Eng.: Journal of the Hydraulics Division,* **90**(HY5):1-12. (NNA.910923.0005)

Weeks, E. P., 1978, "Field Determination of Vertical Permeability to Air," U.S. Geological Survey Professional Paper 1051, Washington, DC, 41 pp. (HQS.880517.1930)

Weeks, E. P., 1987, 'Effect of Topography on Gas Flow in Unsaturated Fractured Rock: Observations and Concepts,' "Flow and Transport Through Unsaturated Fractured Rock," Geophysical Monograph 42, pp. 165-170. (HQS.880517.3214)

Weeks, E. P., and W. E. Wilson, 1984, "Preliminary Evaluation of Hydrologic Properties of Cores of Unsaturated Tuff, Test Well USW H-1, Yucca Mountain, Nevada," *USGS/WRI-84-4193*, U.S. Geological Survey, Denver, CO. (NNA.870407.0037)

Wells, S. G., L. D. McFadden, C. E. Renault, and B. M. Crowe, 1990, "Geomorphic Assessment of the Late Quaternary Volcanism in the Yucca Mountain Area, Southern Nevada: Implications for the Proposed High-Level Radioactive Waste Repository," *Geology*, **18**:549-553. (NNA.901130.0030)

Westrich, H. R., 1982, "The Solubility of LWR Core Debris in Sacrificial Floor Material," *Journal of Nuclear Materials*, **110**:324-332. (NNA.940301.0032)

White, J. W. C., 1993, "Don't Touch That Dial," *Nature*, **364**:186, July 15. (NNA.940427.0097)

Whitfield, M. S., Jr., W. Thordarson, and E. P. Eshom, 1984, "Geohydrologic and Drill-Hole Data for Test Well USW H-4, Yucca Mountain, Nye County, Nevada," *USGS/OFR-84-449*, U.S. Geological Survey, Denver, CO. (NNA.870407.0317)

Whitfield, M. S., Jr., E. P. Eshom, W. Thordarson, and D. H. Schaefer, 1985, "Geohydrology of Rocks Penetrated by Test Well USW H-4, Yucca Mountain, Nye County, Nevada," *USGS/WRI-85-4030*, U.S. Geological Survey, Denver, CO and Fenix and Scisson, Inc., Mercury, NV. (NNA.870407.0328)

Whitfield, M. S., W. Thordarson, D. P. Hammermeister, and J. B. Warner, 1990, "Drilling and Geohydrologic Data for Test Hole USW UZ-1, Yucca Mountain, Nye County, Nevada," *USGS/OFR 90-354*, U.S. Geological Survey, Denver, CO. (NNA.900622.0450)

Wilson, C. N., 1987, "Results From Cycles 1 and 2 of NNWSI Series 2 Spent Fuel Dissolutions Tests," *HEDL-TME 85-22*, Hanford Engineering Development Laboratory, Richland, WA. (HQS.880517.2581)

Wilson, C. N., 1990a, "Results from NNWSI Series 2 Bare Fuel Dissolution Tests," *PNL-7169,* Pacific Northwest Laboratory, Richland, WA. (NNA.900814.0048)

Wilson, C. N., 1990b, "Results from NNWSI Series 3 Bare Fuel Dissolution Tests," *PNL-7170*, Pacific Northwest Laboratory, Richland, WA. (NNA.900329.0142)

Wilson, M. L., 1992, "Comparison of Two Conceptual Models of Flow Using the TSA," in *High Level Radioactive Waste Management, Proceedings of the Third Annual International Conference, Las Vegas, Nevada, April 12-16, 1992*, American Nuclear Society, La Grange Park, IL. (NNA.920505.0061)

Wilson, M. L., 1993, "Sensitivity Analyses for Total-System Performance Assessment," in *High Level Radioactive Waste Management, Proceedings of the Fourth Annual International Conference, Las Vegas, Nevada, April 26-30, 1993*, American Nuclear Society, La Grange Park, IL. (NNA.930702.0013)

Wilson, M. L., F. C. Lauffer, J. C. Cummings, and N. B. Zieman, 1991, "Total-System Analyzer for Performance Assessment of Yucca Mountain," in *High Level Radioactive Waste Management, Proceedings of the Second Annual International Conference, Las Vegas, Nevada, April 28-May 3, 1991*, American Nuclear Society, La Grange Park, IL. (NNA.920427.0051)

Winograd, I. J., B. J. Szabo, T. B. Coplen, and A. C. Riggs, 1988, "A 250,000-Year Climatic Record from Great Basin Vein Calcite: Implications for Milankovitch Theory," *Science*, **242**:1275-1280. (NNA.910522.0030)

Winograd, I. J., T. B. Coplen, J. M. Landwehr, A. C. Riggs, K. R. Ludwig, B. J. Szabo, P. T. Kolesar, and K. M. Revesz, 1992, "Continuous 500,000-Year Climate Record for Vein Calcite in Devils Hole, Nevada, *Science*, **258**:225-260, October 9, 1992. (HQX.921207.0010)

WIPP Performance Assessment Department, 1992, "Preliminary Performance Assessment for the Waste Isolation Pilot Plant, December 1992—Volume 1: Third Comparison with 40 CFR 191, Subpart B," *SAND92-0700/1*, Sandia National Laboratories, Albuquerque, NM. (NNA.940321.0124)

Wittwer, C. S., G. Chen, and G. S. Bodvarsson, 1993, "Studies of the Role of Fault Zones on Fluid Flow Using the Site-Scale Numerical Model of Yucca Mountain," *High Level Radioactive Waste Management, Proceedings of the Fourth Annual International Conference, Las Vegas, Nevada, April 26-30, 1992*, 1:667-674, American Nuclear Society, La Grange, IL. (NNA.931129.0085)

Wolery, T. J., "Calculation of Chemical Equilibrium Between Aqueous Solutions and Minerals: The EQ3/6 Software Package," *UCRL-52658*, Lawrence Livermore National Laboratory, Livermore, CA. (HQS.880517.2586)

Yang, I. C., A. K. Turner, T. M. Sayre, and P. Montazer, 1988, "Triaxial-Compression Extraction of Pore Water from Unsaturated Tuff, Yucca Mountain, Nevada," *USGS/WRI-88-4189,* U.S. Geological Survey, Denver, CO. (NNA.890309.0161)

Yang, I. C., J. S. Davis, and T. M. Sayre, 1990, "Comparison of Pore-Water Extraction by Triaxial Compression Methods and High Speed Centrifugation Methods," in *Proceedings of Conference on Minimizing Risk to the Environment, American Institute of Hydrology 1990*, pp. 250-259. (NNA.920117.0120)

Yeh, T. C. J., L. W. Gelhar, and A. L. Gutjahr, 1985, "Stochastic Analysis of Unsaturated Flow in Heterogeneous Soils," 2, "Statistically Anisotropic Media with Variable Alpha," *Water Resour. Res.*, **21**:457-464. (NNA.870908.0030)

Yeh, T. C., T. C. Rasmussen, and D. D. Evans, 1988, "Simulation of Liquid and Vapor Movement in Unsaturated Fractured Rock at the Apache Leap Tuff Site," *NUREG/CR-5097*, University of Arizona, Tucson, AZ. (NNA.900123.0079)

Younker, J. L., TRW, 1993, Memo to distribution, Subject: Summary of Performance Assessment (PA) Thermal Modeling Meeting, dated October 1, 1993. (NNA.931015.0010)

Younker, J. L., W. B. Andrews, G. A. Fasano, C. C. Herrington, S. R. Mattson, R. C. Murray, L. B. Ballou, M. A. Revelli, A. R. DuCharme, L. E. Shephard, W. W. Dudley, D. T. Hoxie, R. J. Herbst, E. A. Patera, B. R. Judd, J. A. Docka, and L. D. Rickertsen, 1992, "Report of Early Site Suitability Evaluation of the Potential Repository Site at Yucca Mountain, Nevada," *SAIC-91/8000*, Science Applications International Corporation, Las Vegas, NV. (NNA.910708.0111)

Yucca Mountain Project, 1992a, "Data Resulting from Data Acquisition," *Technical Data Information Form,* DTN:GS920508312231.010.

Yucca Mountain Project, 1992b, "Data Resulting from Data Acquisition," *Technical Data Information Form,* DTN: GS920508312231.011.

Yucca Mountain Project, 1992c, "Data Resulting from Data Acquisition," *Technical Data Information Form,* DTN: GS920508312231.012.

Zimmerman, R. M., and W. C. Vollendorf, 1982, "Geotechnical Field Measurements, G-Tunnel, Nevada Test Site," *SAND81-1971*, Sandia National Laboratories, Albuquerque, NM. (HQS.880517.1720)

Zimmerman, R. M., M. L. Blanford, J. F. Holland, R. L. Schuch, and W. H. Barrett, 1986, "Final Report G-Tunnel Small-Diameter Heater Experiments," *SAND84-2621*, Sandia National Laboratories, Albuquerque, NM. (HQS.880517.2365)

Zimmerman, R. M., and R. E. Finley, 1987, "Summary of Geomechanical Measurements Taken In and Around the G-Tunnel Underground Facility, NTS," *SAND86-1015*, Sandia National Laboratories, Albuquerque, NM. (NNA.870526.0015)

Appendix A
TSPA-93 Column Stratigraphy

Table A-1. Simulation #1 (Seed = 69069).

Unit	Top of:	Column #1	Column #2	Column #3	Column #4	Column #5	Column #6	Column #7	Column #8
1	Tiva Canyon welded	1429.93[a]	1443.33	1392.24	1391.67	1335.33	1370.21	1295.49	1267.65
2	Paintbrush nonwelded	1360.93	1324.36	1312.16	1321.31	1264.31	1303.02	1251.20	1214.63
3	Topopah Spring welded	1324.36	1281.68	1263.40	1263.40	1202.44	1260.35	1207.27	1165.86
	Repository base	1078.43	1048.22	1007.50	999.67	971.96	1047.72	973.62	932.87
4	Topopah basal vitrophyre	1055.69	1006.36	984.29	955.08	927.74	N/A	909.47	909.78
5	Calico Hills/Prow Pass vitric	1040.89	995.17	964.69	934.21	912.88	992.12	900.68	888.49
6	Calico Hills/Prow Pass zeolitic	915.30	899.14	864.87	845.25	826.06	903.42	864.25	823.49
7	Prow Pass welded								
6	Calico Hills/Prow Pass zeolitic	N/A							
7	Prow Pass welded		N/A	N/A	N/A	N/A	N/A	N/A	N/A
6	Calico Hills/Prow Pass zeolitic								
8	Bullfrog welded	772.67							
9	Bullfrog nonwelded	N/A							
	Water table	751.51	742.67	748.26	754.99	731.25	731.09	730.91	730.61

N/A = Not applicable.

[a] Units are in meters.

Table A-2. Simulation #2 (Seed = 69071).

Unit	Top of:	Column #1	Column #2	Column #3	Column #4	Column #5	Column #6	Column #7	Column #8
1	Tiva Canyon welded	1429.93[a]	1443.33	1392.24	1391.67	1335.33	1370.21	1295.49	1267.65
2	Paintbrush nonwelded	1360.93	1326.87	1306.07	1312.89	1246.12	1293.88	1211.58	1226.82
3	Topopah Spring welded	1315.21	1278.64	1263.40	1257.30	1208.53	1251.20	1175.00	1193.29
	Repository base	1078.43	1048.22	1007.50	999.67	971.96	1047.72	973.62	932.87
4	Topopah basal vitrophyre	1013.02	969.78	969.05	948.98	897.26	N/A	927.76	870.16
5	Calico Hills/Prow Pass vitric	998.22	958.60	949.45	928.12	882.40	949.45	918.97	848.87
6	Calico Hills/Prow Pass zeolitic	915.30	899.14	864.87	845.25	826.06	903.42	864.25	823.49
7	Prow Pass welded			803.15		733.04			
6	Calico Hills/Prow Pass zeolitic	N/A	N/A	794.00					
7	Prow Pass welded				N/A		N/A	N/A	N/A
6	Calico Hills/Prow Pass zeolitic			N/A		N/A			
8	Bullfrog welded	830.58	794.00						
9	Bullfrog nonwelded	766.57	N/A						
	Water table	751.51	742.67	748.26	754.99	731.25	731.09	730.91	730.61

N/A = Not applicable.

[a] Units are in meters.

Table A-3. Simulation #3 (Seed = 69073).

Unit	Top of:	Column #1	Column #2	Column #3	Column #4	Column #5	Column #6	Column #7	Column #8
1	Tiva Canyon welded	1429.93[a]	1443.33	1392.24	1391.67	1335.33	1370.21	1295.49	1267.65
2	Paintbrush nonwelded	1354.84	1315.21	1284.73	1290.83	1261.80	1278.64	1263.40	1226.82
3	Topopah Spring welded	1324.36	1272.54	1242.06	1239.01	1217.68	1251.20	1217.68	1190.24
	Repository base	1078.43	1048.22	1007.50	999.67	971.96	1047.72	973.62	932.87
4	Topopah basal vitrophyre	988.63	975.88	959.90	952.03	885.07	N/A	924.71	909.78
5	Calico Hills/Prow Pass vitric	973.84	964.69	940.31	931.16	870.20	976.88	915.92	888.49
6	Calico Hills/Prow Pass zeolitic	915.30	899.14	864.87	845.25	826.06	903.42	864.25	823.49
7	Prow Pass welded				781.81				
6	Calico Hills/Prow Pass zeolitic	N/A	N/A		763.52				
7	Prow Pass welded			N/A		N/A	N/A	N/A	N/A
6	Calico Hills/Prow Pass zeolitic				N/A				
8	Bullfrog welded	815.34	784.86						
9	Bullfrog nonwelded	N/A	N/A						
	Water table	751.51	742.67	748.26	754.99	731.25	731.09	730.91	730.61

N/A = Not applicable.

[a] Units are in meters.

Table A-4. Simulation #4 (Seed = 69075).

Unit	Top of:	Column #1	Column #2	Column #3	Column #4	Column #5	Column #6	Column #7	Column #8
1	Tiva Canyon welded	1429.93[a]	1443.33	1392.24	1391.67	1335.33	1370.21	1295.49	1267.65
2	Paintbrush nonwelded	1336.55	1327.40	1327.40	1309.12	1275.59	1281.68	1208.53	1193.29
3	Topopah Spring welded	1303.02	1287.78	1287.78	1266.44	1217.68	1245.11	1171.96	1175.00
	Repository base	1078.43	1048.22	1007.50	999.67	971.96	1047.72	973.62	932.87
4	Topopah basal vitrophyre	970.35	939.30	972.10	958.12	878.97	N/A	939.95	915.88
5	Calico Hills/Prow Pass vitric	955.55	928.12	952.50	937.26	864.11	986.03	931.16	894.59
6	Calico Hills/Prow Pass zeolitic	915.30	899.14	864.87	845.25	826.06	903.42	864.25	823.49
7	Prow Pass welded			754.38					
6	Calico Hills/Prow Pass zeolitic								
7	Prow Pass welded	N/A	N/A		N/A	N/A	N/A	N/A	N/A
6	Calico Hills/Prow Pass zeolitic			N/A					
8	Bullfrog welded								
9	Bullfrog nonwelded Water table	751.51	742.67	748.26	754.99	731.25	731.09	730.91	730.61

N/A = Not applicable.

[a] Units are in meters.

Table A-5. Simulation #5 (Seed = 69077).

Unit	Top of:	Column #1	Column #2	Column #3	Column #4	Column #5	Column #6	Column #7	Column #8
1	Tiva Canyon welded	1429.93[a]	1443.33	1392.24	1391.67	1335.33	1370.21	1295.49	1267.65
2	Paintbrush nonwelded	1397.51	1373.12	1312.16	1299.97	1284.73	1296.92	1248.16	1193.29
3	Topopah Spring welded	1360.93	1336.55	1275.59	1254.25	1239.01	1260.35	1217.68	1171.96
	Repository base	1078.43	1048.22	1007.50	999.67	971.96	1047.72	973.62	932.87
4	Topopah basal vitrophyre	1016.07	972.83	950.76	948.98	918.60	N/A	909.47	909.78
5	Calico Hills/Prow Pass vitric	1001.27	961.64	931.16	928.12	903.73	964.69	900.68	888.49
6	Calico Hills/Prow Pass zeolitic	915.30	899.14	864.87	845.25	826.06	903.42	864.25	823.49
7	Prow Pass welded								
6	Calico Hills/Prow Pass zeolitic	N/A							
7	Prow Pass welded		N/A	N/A	N/A	N/A	N/A	N/A	N/A
6	Calico Hills/Prow Pass zeolitic								
8	Bullfrog welded	766.57							
9	Bullfrog nonwelded	N/A							
	Water table	751.51	742.67	748.26	754.99	731.25	731.09	730.91	730.61

N/A = Not applicable.

[a] Units are in meters.

Table A-6. Simulation #6 (Seed = 69079).

Unit	Top of:	Column #1	Column #2	Column #3	Column #4	Column #5	Column #6	Column #7	Column #8
1	Tiva Canyon welded	1429.93[a]	1443.33	1392.24	1391.67	1335.33	1370.21	1295.49	1267.65
2	Paintbrush nonwelded	1357.88	1310.91	1296.92	1312.16	1254.25	1263.40	1242.06	1187.20
3	Topopah Spring welded	1312.16	1281.65	1275.59	1260.35	1214.63	1254.25	1220.72	1184.15
	Repository base	1078.43	1048.22	1007.50	999.67	971.96	1047.72	973.62	932.87
4	Topopah basal vitrophyre	1025.21	945.40	956.86	970.32	915.55	N/A	912.52	891.49
5	Calico Hills/Prow Pass vitric	1010.41	934.21	937.26	949.45	900.68	955.55	903.73	870.20
6	Calico Hills/Prow Pass zeolitic	915.30	899.14	864.87	845.25	826.06	903.42	864.25	823.49
7	Prow Pass welded			772.67	835.15	763.52			
6	Calico Hills/Prow Pass zeolitic				829.06	760.48			
7	Prow Pass welded	N/A	N/A		769.62	739.14	N/A	N/A	N/A
6	Calico Hills/Prow Pass zeolitic			N/A					
8	Bullfrog welded				N/A	N/A			
9	Bullfrog nonwelded Water table	751.51	742.67	748.26	754.99	731.25	731.09	730.91	730.61

N/A = Not applicable.

[a] Units are in meters.

Table A-7. Simulation #7 (Seed = 69081).

Unit	Top of:	Column #1	Column #2	Column #3	Column #4	Column #5	Column #6	Column #7	Column #8
1	Tiva Canyon welded	1429.93[a]	1443.33	1392.24	1391.67	1335.33	1370.21	1295.49	1267.65
2	Paintbrush nonwelded	1379.22	1321.31	1293.88	1284.73	1263.40	1275.59	1251.20	1205.48
3	Topopah Spring welded	1351.79	1293.88	1266.44	1260.35	1211.58	1232.92	1217.68	1175.00
	Repository base	1078.43	1048.22	1007.50	999.67	971.96	1047.72	973.62	932.87
4	Topopah basal vitrophyre	1022.16	988.07	947.71	945.93	949.08	N/A	921.67	912.83
5	Calico Hills/Prow Pass vitric	1007.36	976.88	928.12	925.07	934.21	973.84	912.88	891.54
6	Calico Hills/Prow Pass zeolitic	915.30	899.14	864.87	845.25	826.06	903.42	864.25	823.49
7	Prow Pass welded			812.29	800.10				
6	Calico Hills/Prow Pass zeolitic			806.20					
7	Prow Pass welded	N/A	N/A	772.67		N/A	N/A	N/A	N/A
6	Calico Hills/Prow Pass zeolitic			754.38	N/A				
8	Bullfrog welded			N/A					
9	Bullfrog nonwelded Water table	751.51	742.67	748.26	754.99	731.25	731.09	730.91	730.61

N/A = Not applicable.

[a] Units are in meters.

Table A-8. Simulation #8 (Seed = 69083).

Unit	Top of:	Column #1	Column #2	Column #3	Column #4	Column #5	Column #6	Column #7	Column #8
1	Tiva Canyon welded	1429.93[a]	1443.33	1392.24	1391.67	1335.33	1370.21	1295.49	1267.65
2	Paintbrush nonwelded	1367.03	1318.26	1330.45	1299.97	1272.54	1284.73	1254.25	1199.39
3	Topopah Spring welded	1324.36	1266.44	1257.30	1245.11	1208.53	1229.87	1190.24	1144.52
	Repository base	1078.43	1048.22	1007.50	999.67	971.96	1047.72	973.62	932.87
4	Topopah basal vitrophyre	988.63	978.92	953.81	952.03	933.84	N/A	900.33	873.21
5	Calico Hills/Prow Pass vitric	973.84	967.74	934.21	931.16	918.97	958.60	891.54	851.92
6	Calico Hills/Prow Pass zeolitic	915.30	899.14	864.87	845.25	826.06	903.42	864.25	823.49
7	Prow Pass welded								
6	Calico Hills/Prow Pass zeolitic	N/A	N/A	N/A					
7	Prow Pass welded				N/A	N/A	N/A	N/A	N/A
6	Calico Hills/Prow Pass zeolitic								
8	Bullfrog welded	842.77	812.29	751.33					
9	Bullfrog nonwelded	N/A	N/A	N/A					
	Water table	751.51	742.67	748.26	754.99	731.25	731.09	730.91	730.61

N/A = Not applicable.

[a] Units are in meters.

Table A-9. Simulation #9 (Seed = 69085).

Unit	Top of:	Column #1	Column #2	Column #3	Column #4	Column #5	Column #6	Column #7	Column #8
1	Tiva Canyon welded	1429.93[a]	1443.33	1392.24	1391.67	1335.33	1370.21	1295.49	1267.65
2	Paintbrush nonwelded	1357.88	1333.50	1324.36	1296.92	1266.44	1284.73	1243.58	1211.58
3	Topopah Spring welded	1321.31	1303.02	1278.64	1263.40	1214.63	1260.35	1208.53	1181.10
	Repository base	1078.43	1048.22	1007.50	999.67	971.96	1047.72	973.62	932.87
4	Topopah basal vitrophyre	1052.64	1006.36	950.76	964.22	878.97	N/A	915.57	900.64
5	Calico Hills/Prow Pass vitric	1037.84	995.17	931.16	943.36	864.11	958.60	906.78	879.35
6	Calico Hills/Prow Pass zeolitic	915.30	899.14	864.87	845.25	826.06	903.42	864.25	823.49
7	Prow Pass welded			772.67	778.76	736.09			
6	Calico Hills/Prow Pass zeolitic	N/A							
7	Prow Pass welded		N/A				N/A	N/A	N/A
6	Calico Hills/Prow Pass zeolitic			N/A	N/A	N/A			
8	Bullfrog welded	778.76							
9	Bullfrog nonwelded	N/A							
	Water table	751.51	742.67	748.26	754.99	731.25	731.09	730.91	730.61

N/A = Not applicable.

[a] Units are in meters.

Table A-10. Simulation #10 (Seed = 69087).

Unit	Top of:	Column #1	Column #2	Column #3	Column #4	Column #5	Column #6	Column #7	Column #8
1	Tiva Canyon welded	1429.93[a]	1443.33	1392.24	1391.67	1335.33	1370.21	1295.49	1267.65
2	Paintbrush nonwelded	1391.41	1342.64	1327.40	1318.26	1254.25	1300.71	1257.30	1202.44
3	Topopah Spring welded	1357.88	1309.12	1303.02	1278.64	1213.10	1274.88	1226.82	1175.00
	Repository base	1078.43	1048.22	1007.50	999.67	971.96	1047.72	973.62	932.87
4	Topopah basal vitrophyre	1043.50	1021.60	984.29	948.98	891.17	N/A	903.38	864.06
5	Calico Hills/Prow Pass vitric	1028.70	1010.41	964.69	928.12	876.30	979.93	894.59	842.77
6	Calico Hills/Prow Pass zeolitic	915.30	899.14	864.87	845.25	826.06	903.42	864.25	823.49
7	Prow Pass welded	870.20							
6	Calico Hills/Prow Pass zeolitic								
7	Prow Pass welded	N/A	N/A	N/A	N/A	N/A	N/A	N/A	N/A
6	Calico Hills/Prow Pass zeolitic								
8	Bullfrog welded	809.24	790.96						
9	Bullfrog nonwelded	778.76	N/A						
	Water table	751.51	742.67	748.26	754.99	731.25	731.09	730.91	730.61

N/A = Not applicable.

[a] Units are in meters.

Table A-11. Thermal/mechanical stratigraphy of Ortiz *et al.* (1985).

Unit	Top of:	Column #1	Column #2	Column #3	Column #4	Column #5	Column #6	Column #7	Column #8
TCw	Tiva Canyon welded	1429.93[a]	1443.33	1392.24	1391.67	1335.33	1370.21	1295.49	1267.65
PTn	Paintbrush nonwelded	1345.02	1318.19	1312.08	1316.38	1257.75	1283.01	1240.39	1205.00
TSw1	Topopah Spring welded	1308.16	1282.03	1267.26	1261.64	1209.11	1257.91	1209.89	1166.36
TSw2	Repository base	1078.43	1048.22	1007.50	999.67	971.96	1047.72	973.62	932.87
TSw3	Topopah basal vitrophyre	1020.36	989.86	958.15	947.69	884.57	N/A	916.21	876.03
CHnv/ PPw	Calico Hills/Prow Pass vitric	1005.57	978.68	938.56	926.82	869.70	981.22	907.42	854.74
CHnz/ PPw	Calico Hills/Prow Pass zeolitic	915.30	899.14	864.87	845.25	826.06	903.42	864.25	832.49
BFw	Bullfrog welded	788.42	N/A	N/A	N/A	N/A	N/A	N/A	N/A
–	Water table	751.51	742.67	748.26	754.99	731.25	731.09	730.91	730.61

N/A = Not applicable.

[a] Units are in meters.

Appendix B
Probability Distribution Functions for Solubility and Sorption

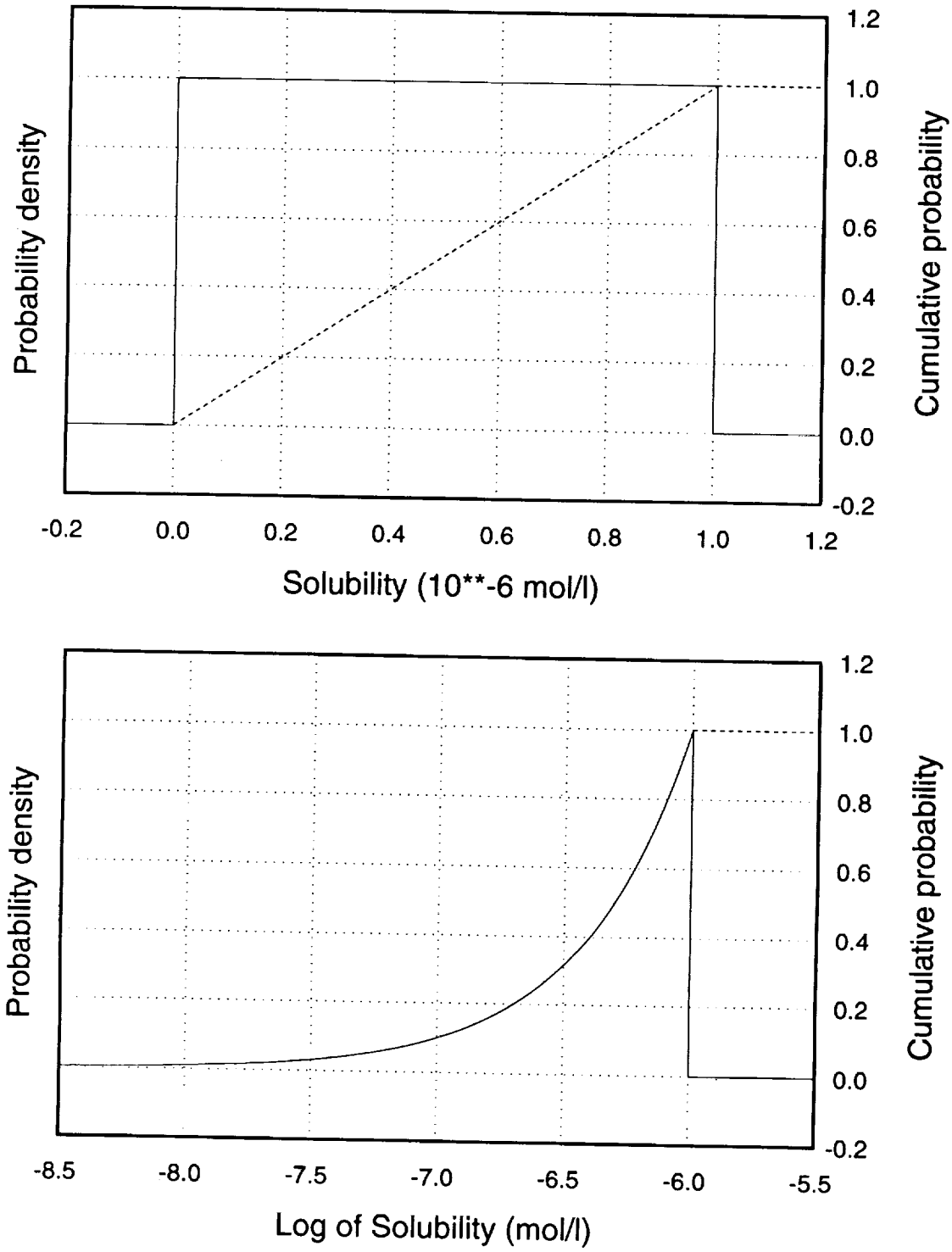

Figure B-1. Solubility distributions for samarium, actinium, plutonium, and americium. Top figure is with linear solubility scale, bottom figure is with logarithmic solubility scale. Solid curve is probability density function, dashed curve is cumulative distribution function.

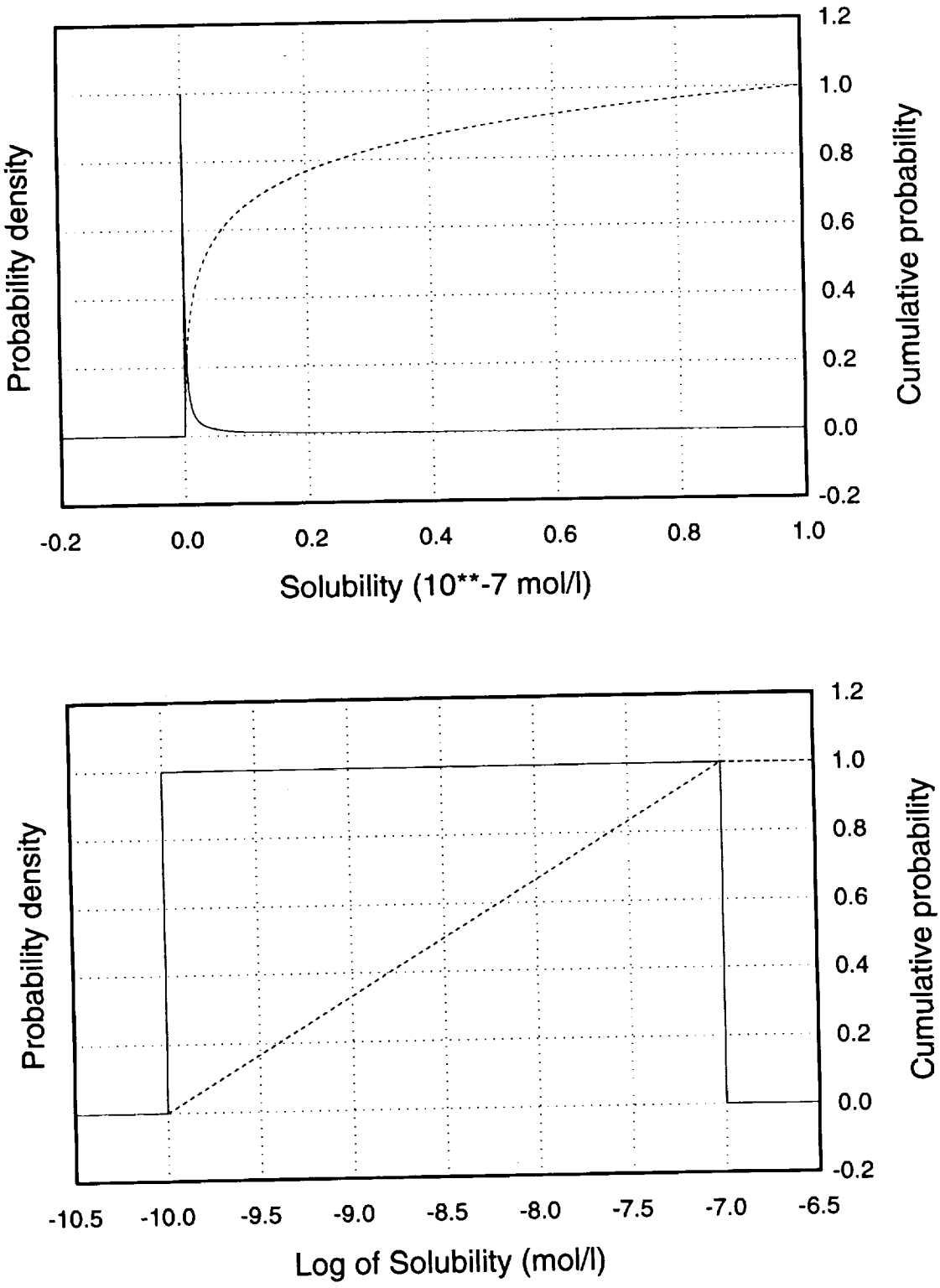

Figure B-2. Solubility distributions for thorium. Top figure is with linear solubility scale, bottom figure is with logarithmic solubility scale. Solid curve is probability density function, dashed curve is cumulative distribution function.

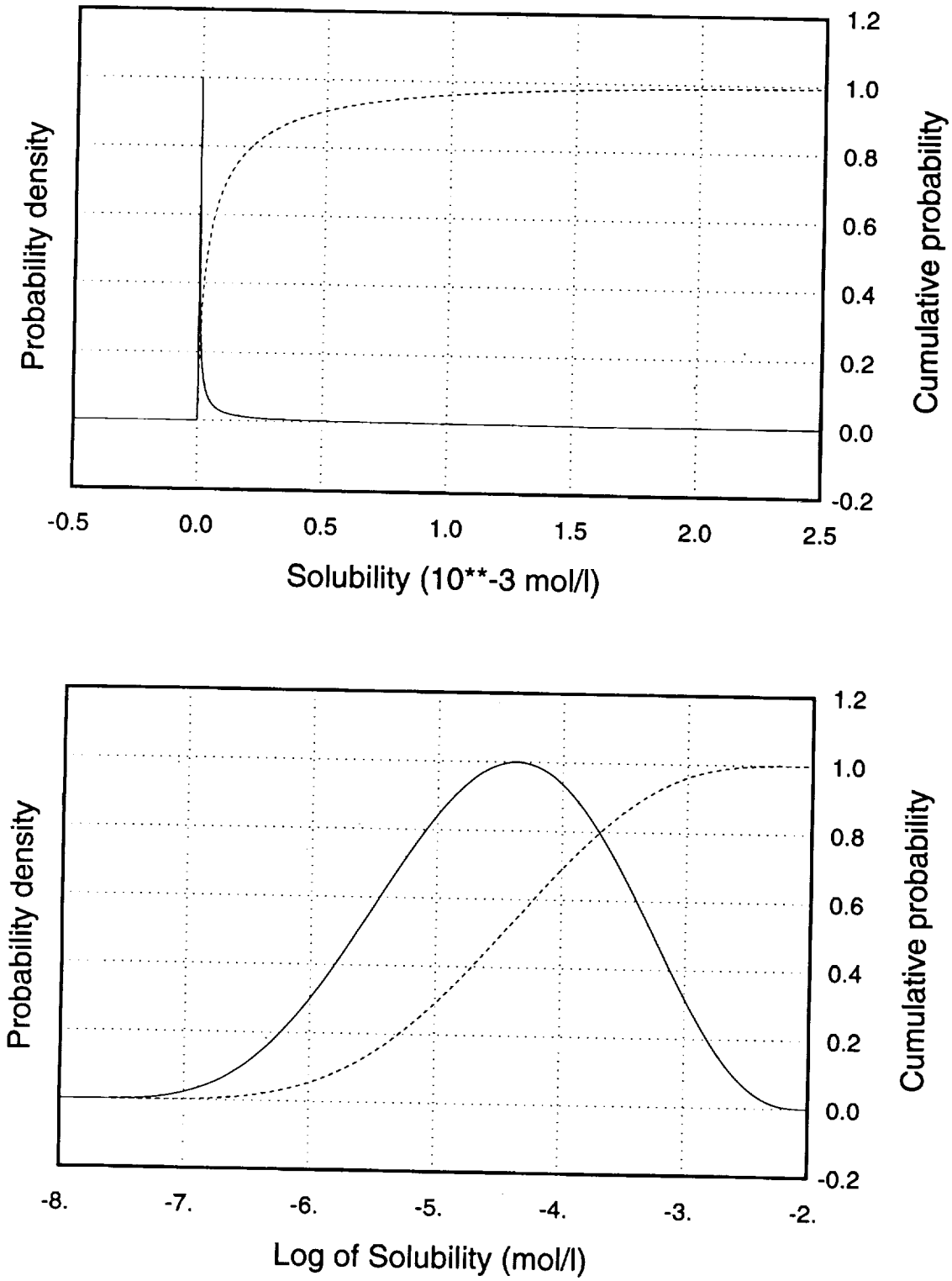

Figure B-3. Solubility distributions for uranium. Top figure is with linear solubility scale, bottom figure is with logarithmic solubility scale. Solid curve is probability density function, dashed curve is cumulative distribution function.

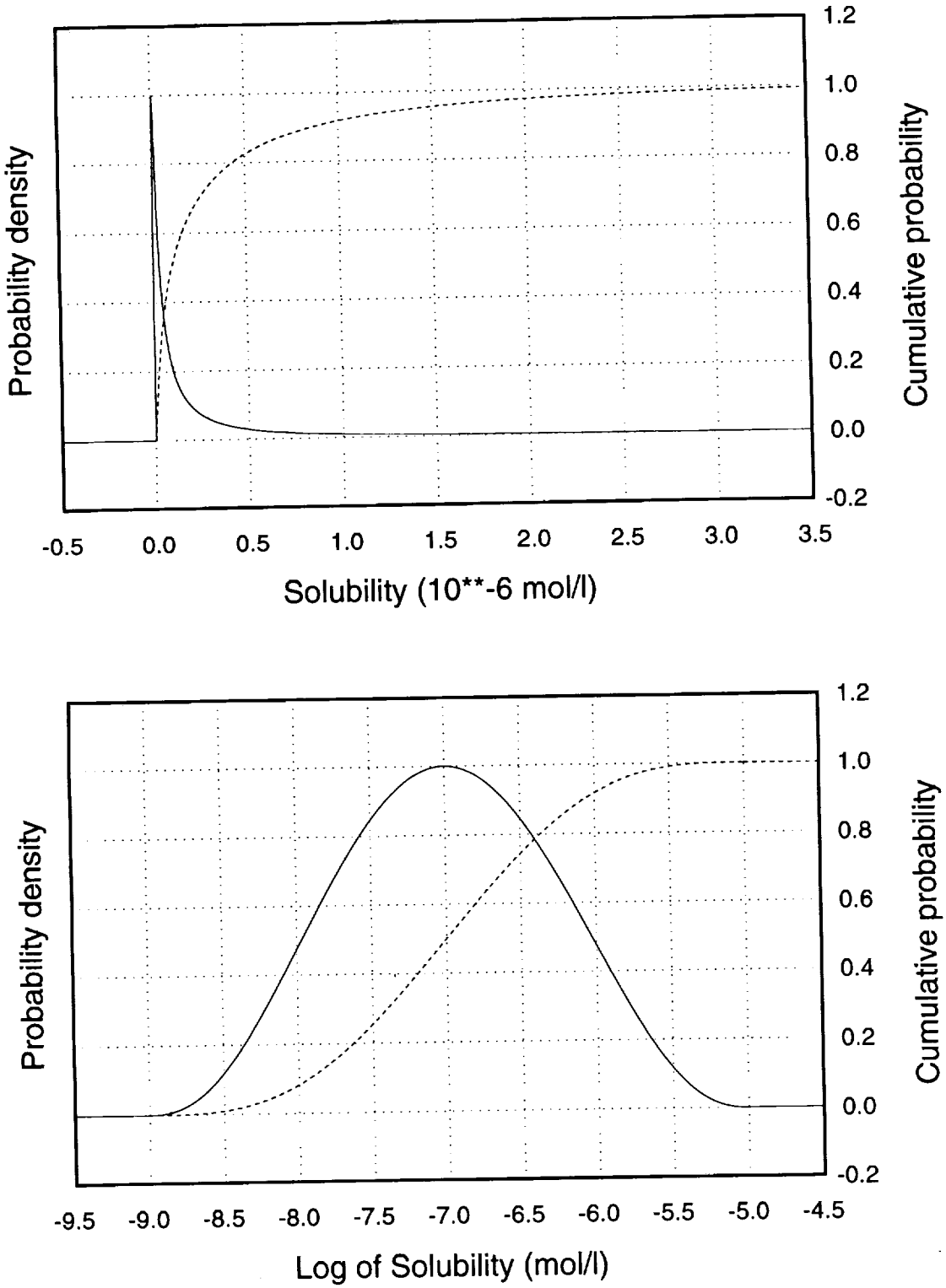

Figure B-4. Solubility distributions for radium. Top figure is with linear solubility scale, bottom figure is with logarithmic solubility scale. Solid curve is probability density function, dashed curve is cumulative distribution function.

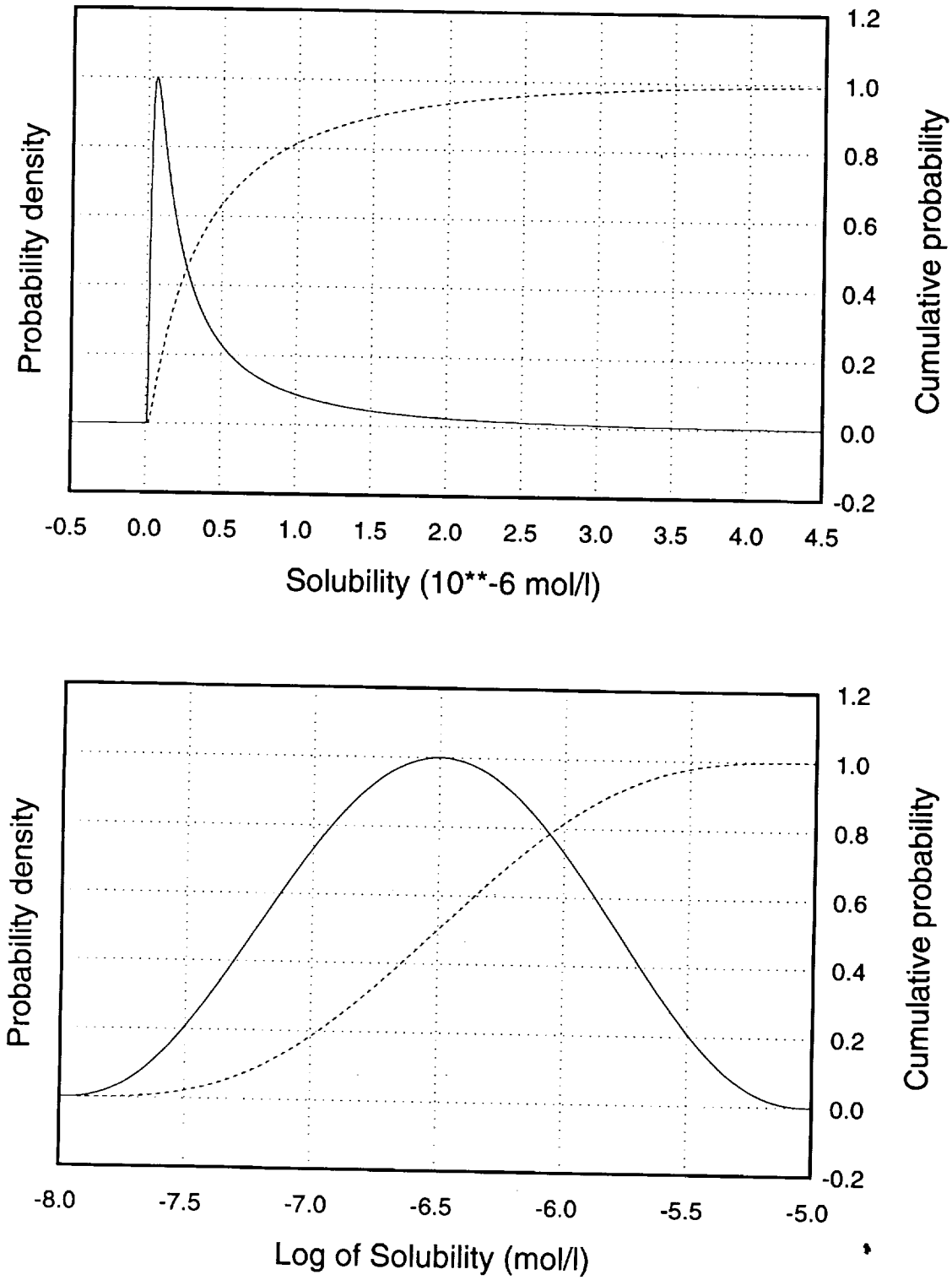

Figure B-5. Solubility distributions for lead. Top figure is with linear solubility scale, bottom figure is with logarithmic solubility scale. Solid curve is probability density function, dashed curve is cumulative distribution function.

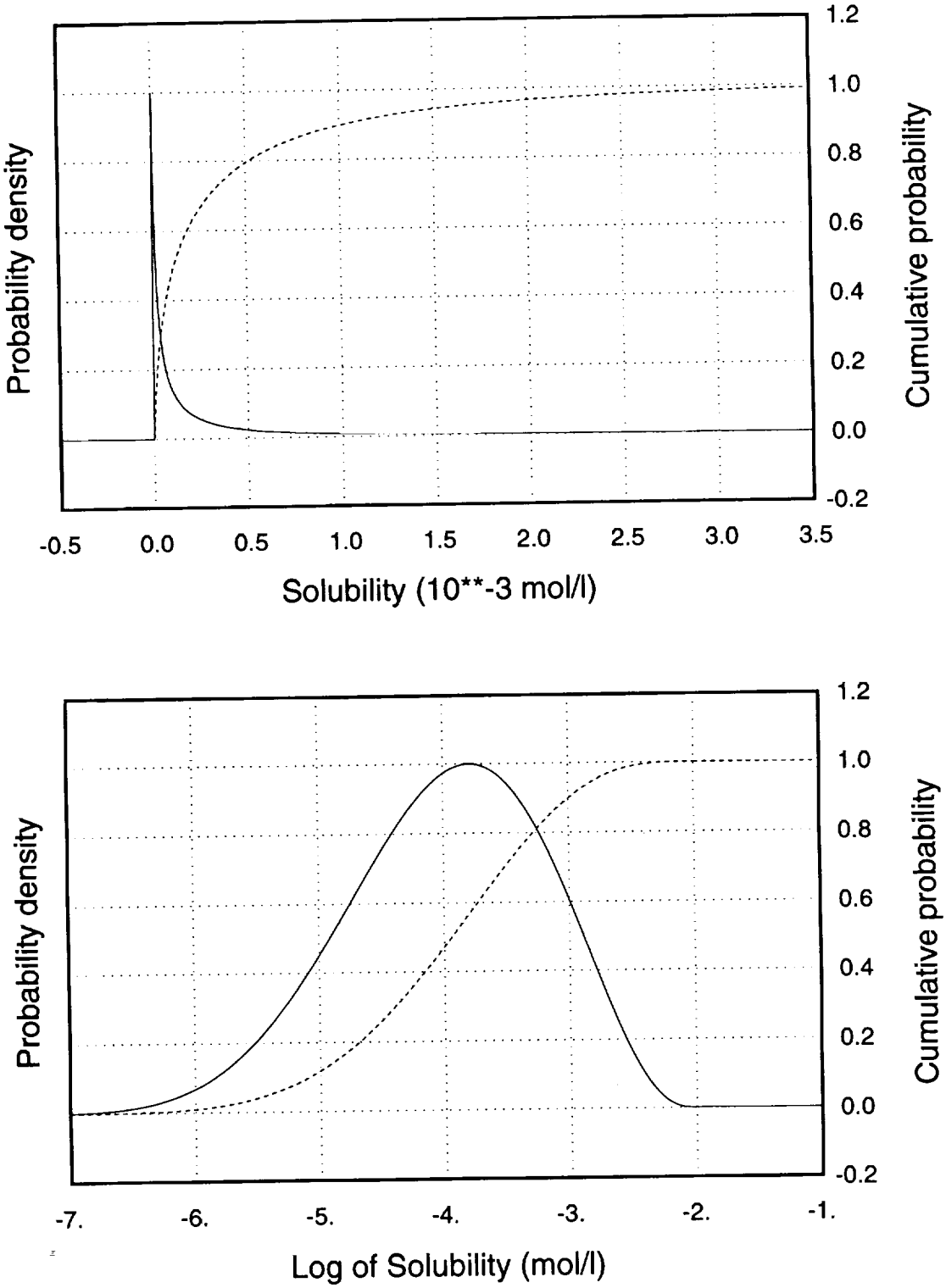

Figure B-6. Solubility distributions for neptunium. Top figure is with linear solubility scale, bottom figure is with logarithmic solubility scale. Solid curve is probability density function, dashed curve is cumulative distribution function.

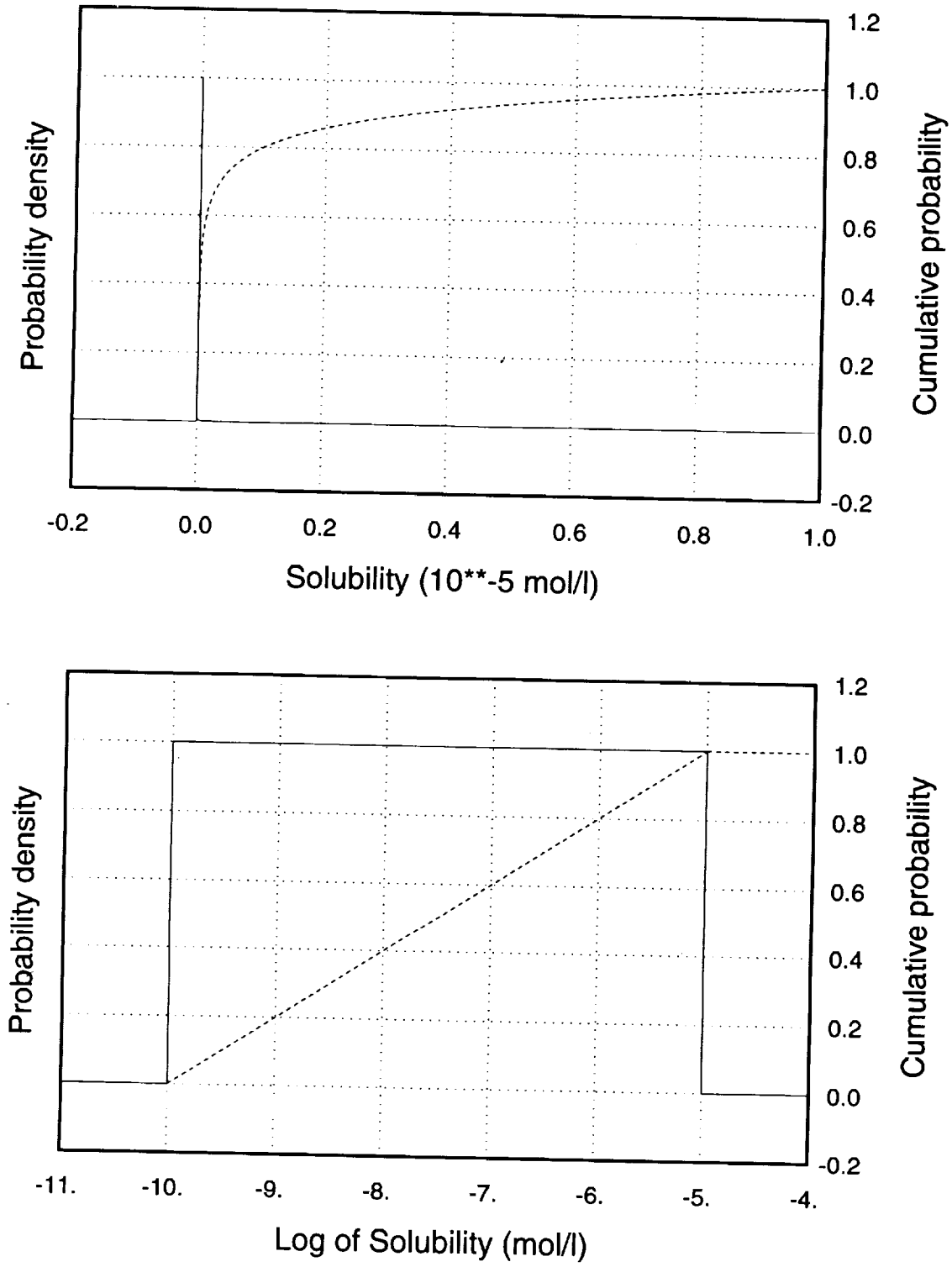

Figure B-7. Solubility distributions for protactinium. Top figure is with linear solubility scale, bottom figure is with logarithmic solubility scale. Solid curve is probability density function, dashed curve is cumulative distribution function.

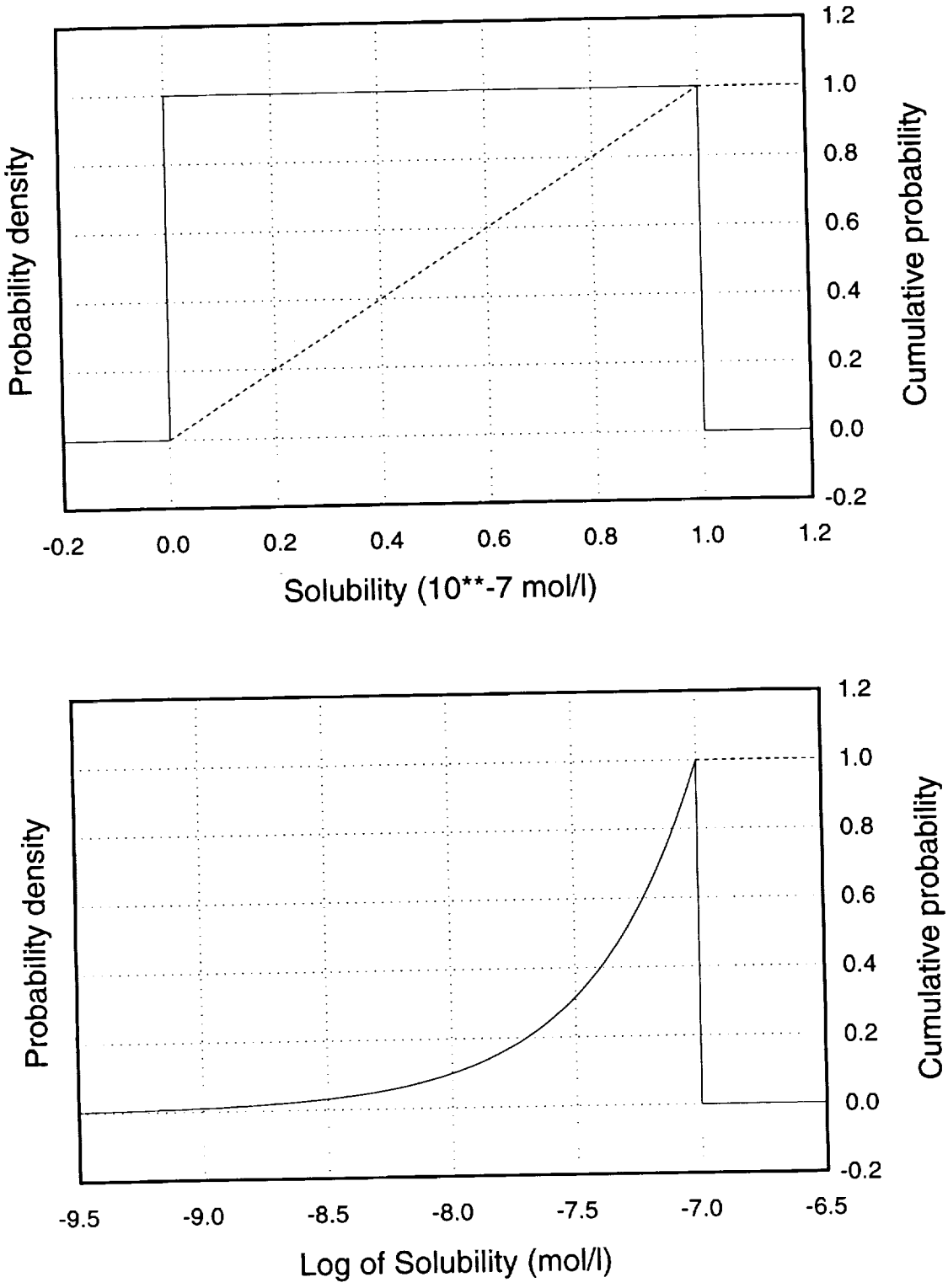

Figure B-8. Solubility distributions for tin. Top figure is with linear solubility scale, bottom figure is with logarithmic solubility scale. Solid curve is probability density function, dashed curve is cumulative distribution function.

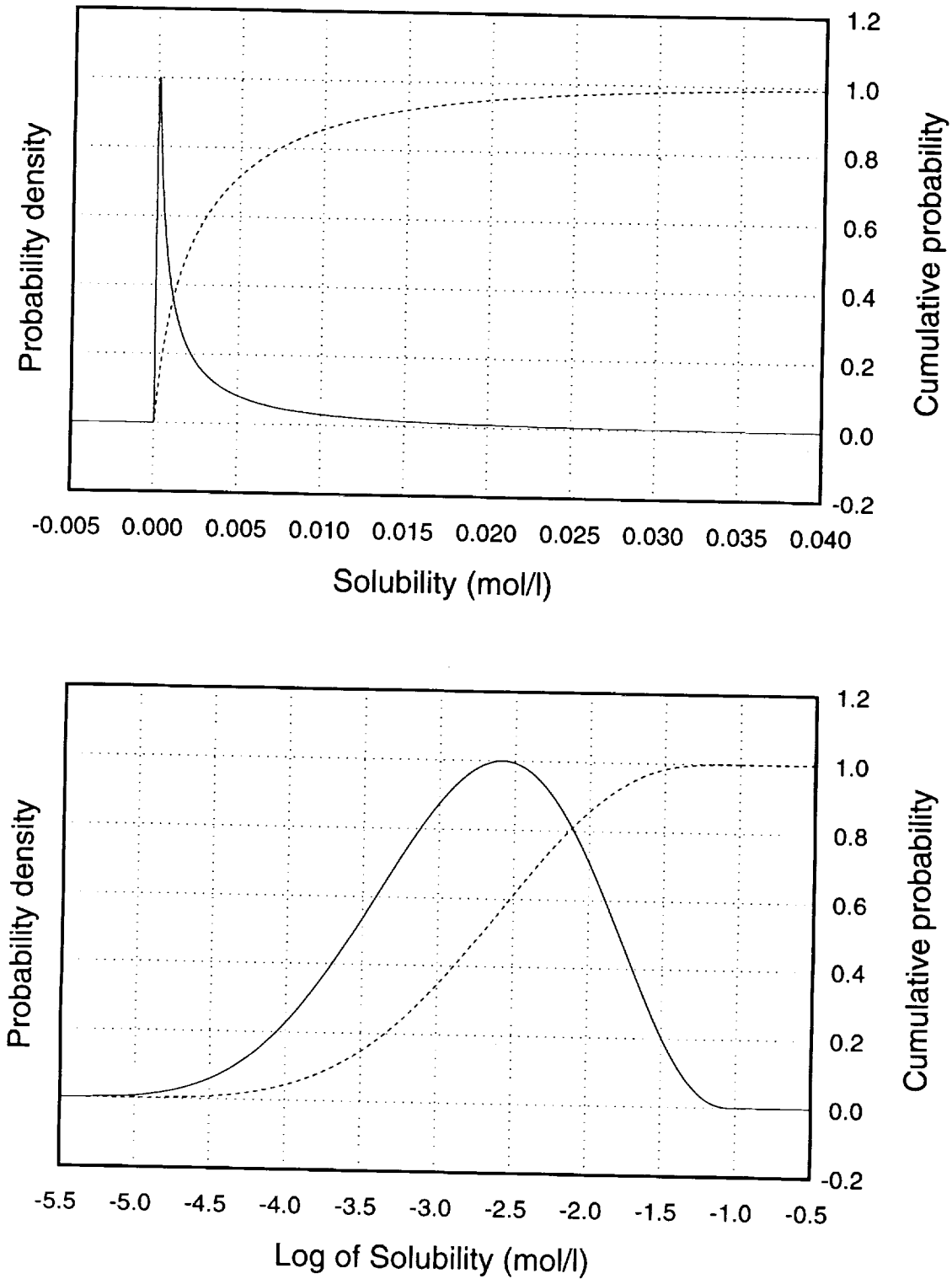

Figure B-9. Solubility distributions for nickel. Top figure is with linear solubility scale, bottom figure is with logarithmic solubility scale. Solid curve is probability density function, dashed curve is cumulative distribution function.

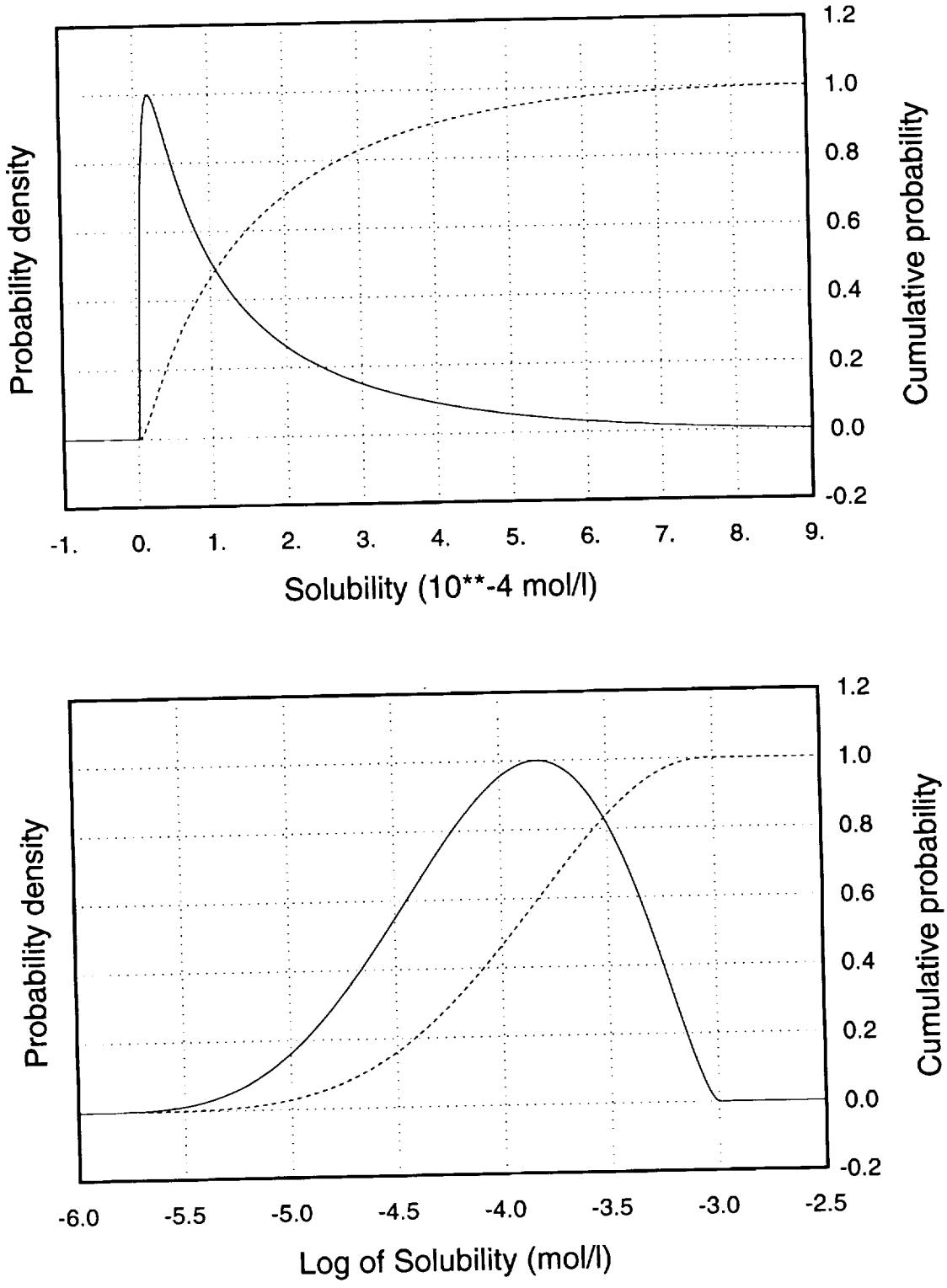

Figure B-10. Solubility distributions for strontium. Top figure is with linear solubility scale, bottom figure is with logarithmic solubility scale. Solid curve is probability density function, dashed curve is cumulative distribution function.

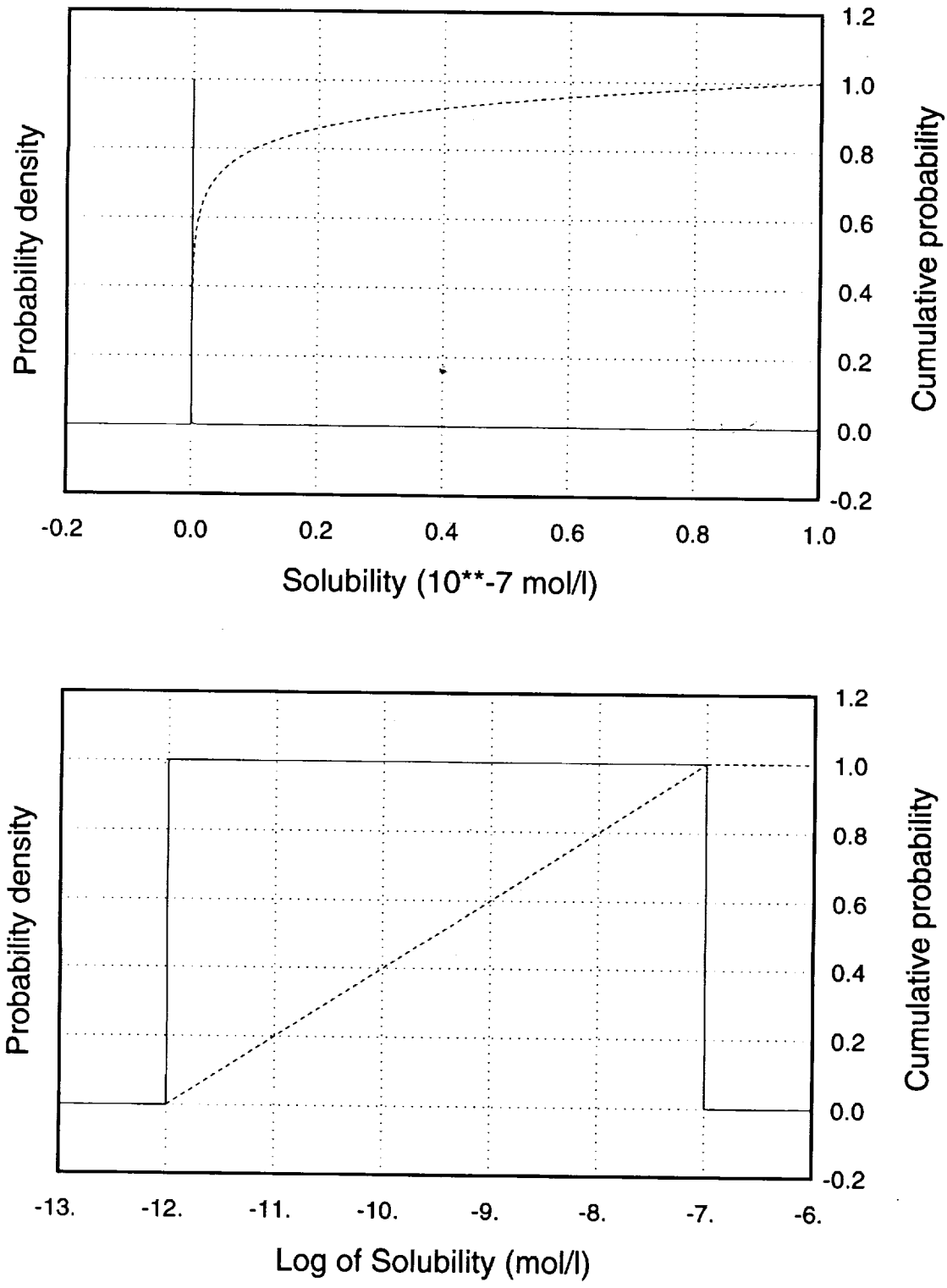

Figure B-11. Solubility distributions for zirconium. Top figure is with linear solubility scale, bottom figure is with logarithmic solubility scale. Solid curve is probability density function, dashed curve is cumulative distribution function.

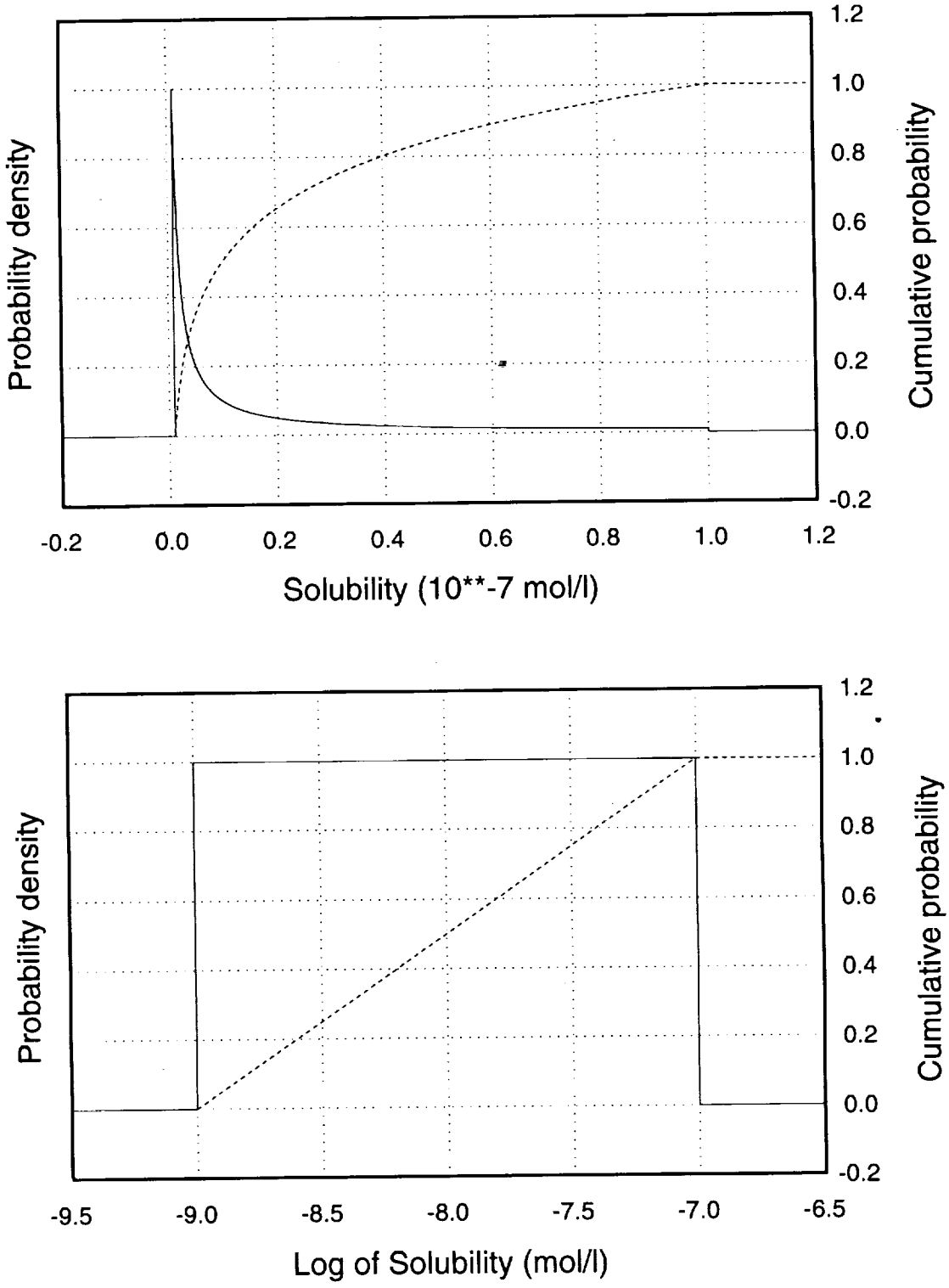

Figure B-12. Solubility distributions for niobium. Top figure is with linear solubility scale, bottom figure is with logarithmic solubility scale. Solid curve is probability density function, dashed curve is cumulative distribution function.

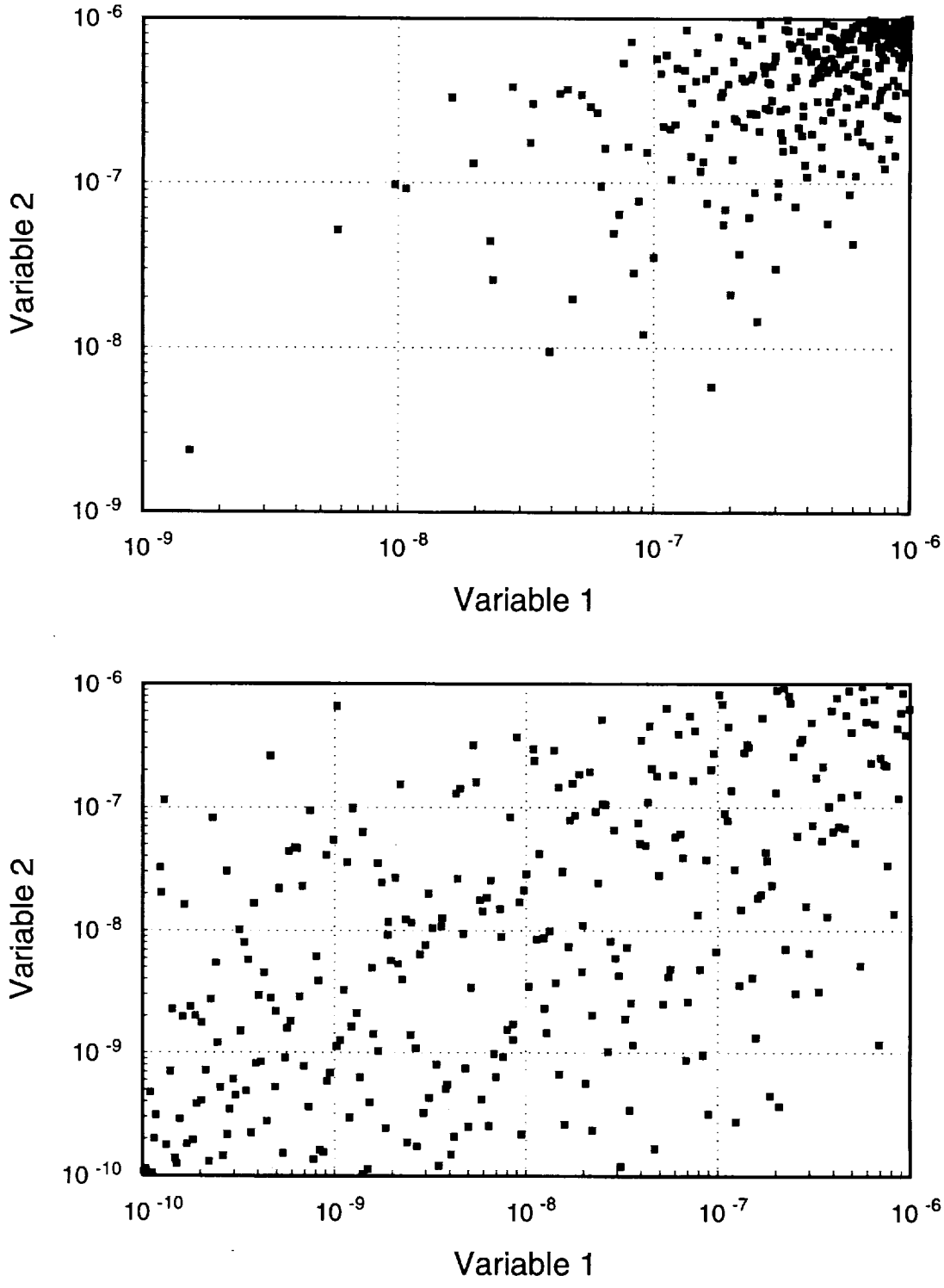

Figure B-13. Scatter plot for 300 samples with rank correlation of 0.6 between two arbitrary variables. Top figure is for samples drawn from uniform distributions, bottom figure is for samples drawn from log-uniform distributions.

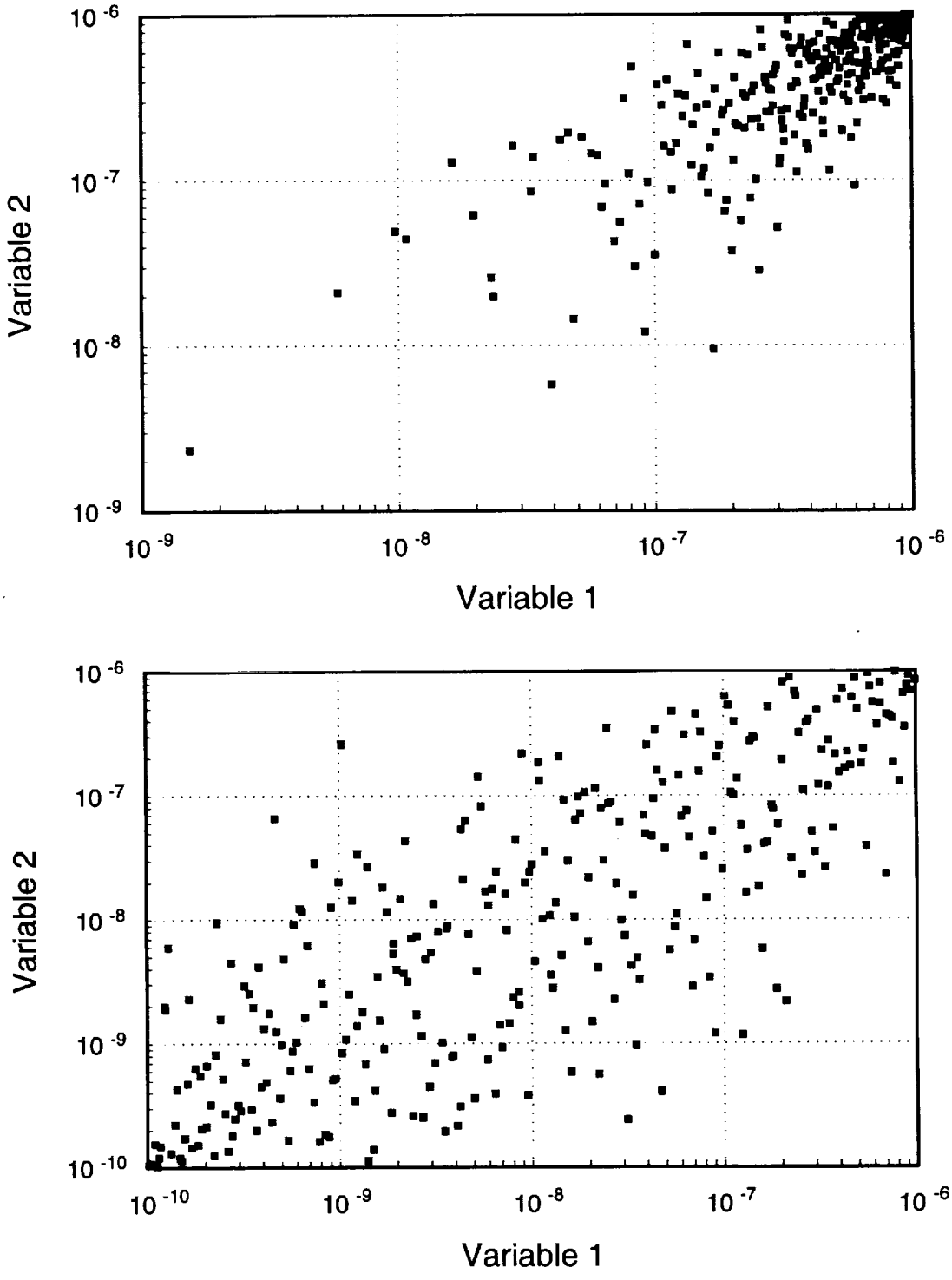

Figure B-14. Scatter plot for 300 samples with rank correlation of 0.8 between two arbitrary variables. Top figure is for samples drawn from uniform distributions, bottom figure is for samples drawn from log-uniform distributions.

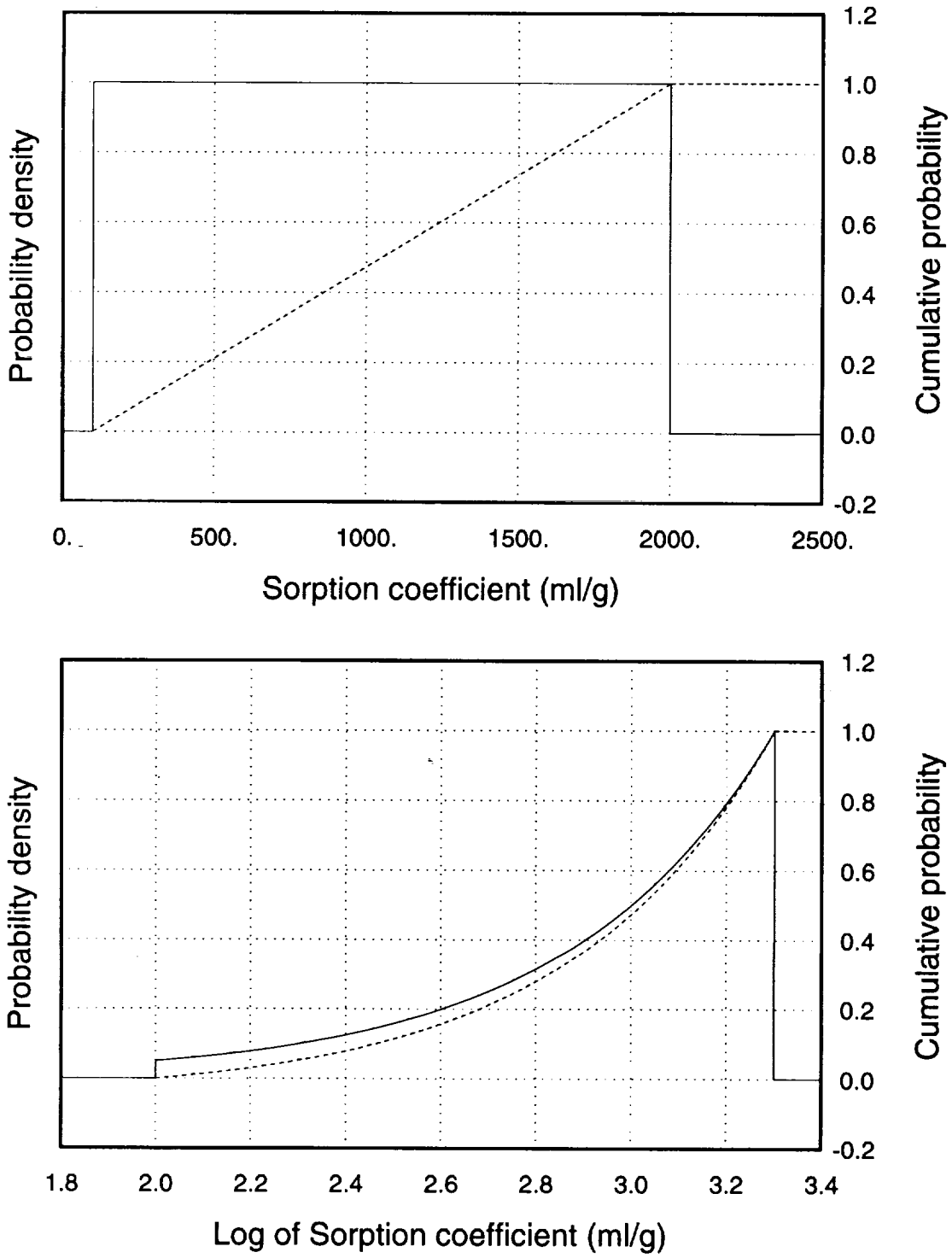

Figure B-15. Sorption-coefficient distributions for zirconium, niobium, samarium, actinium, thorium, and americium on devitrified tuff. Top figure is with linear K_d scale, bottom figure is with logarithmic K_d scale. Solid curve is probability density function, dashed curve is cumulative distribution function.

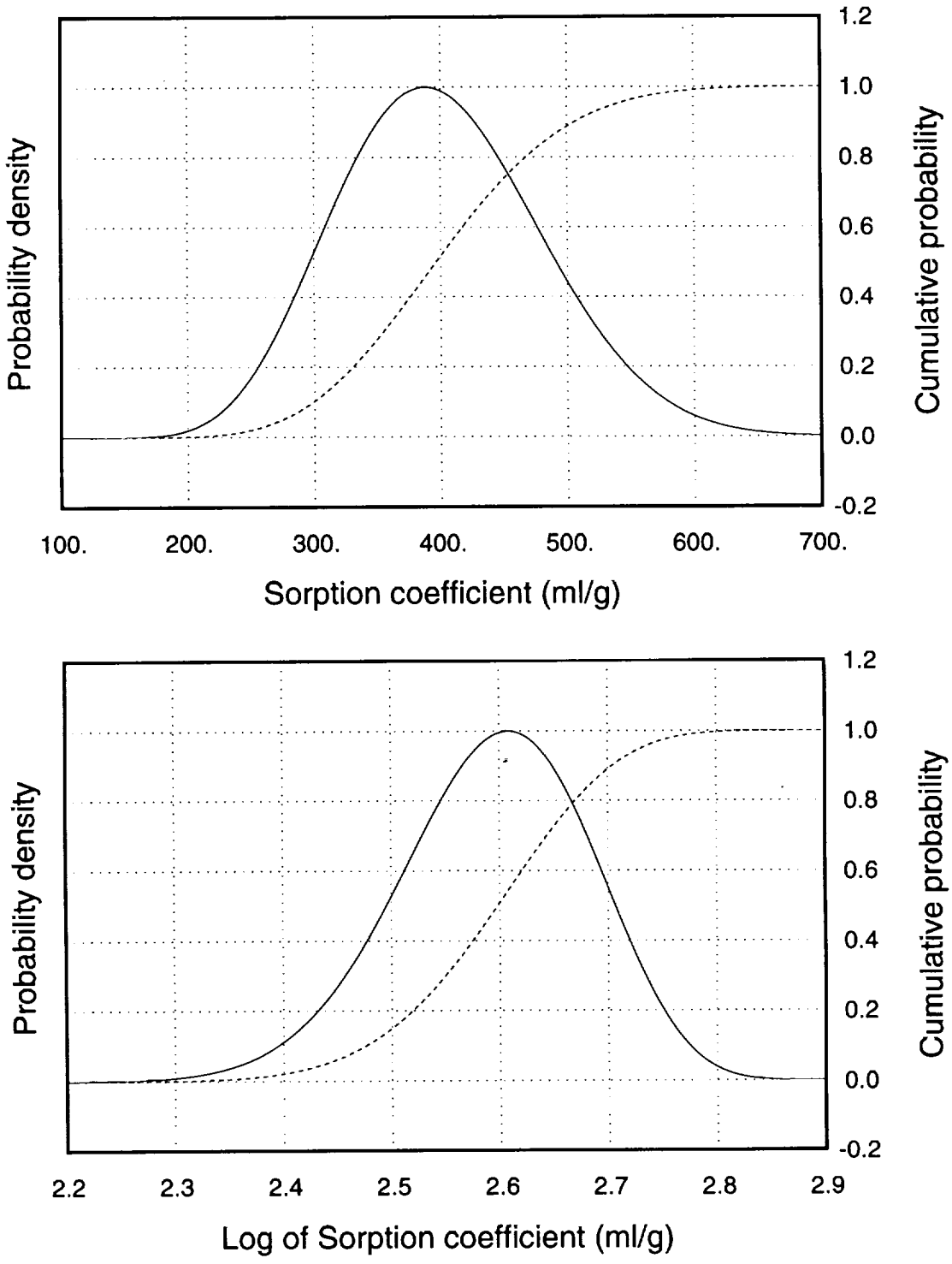

Figure B-16. Sorption-coefficient distributions for zirconium, niobium, samarium, actinium, thorium, and americium on vitric tuff. Top figure is with linear K_d scale, bottom figure is with logarithmic K_d scale. Solid curve is probability density function, dashed curve is cumulative distribution function.

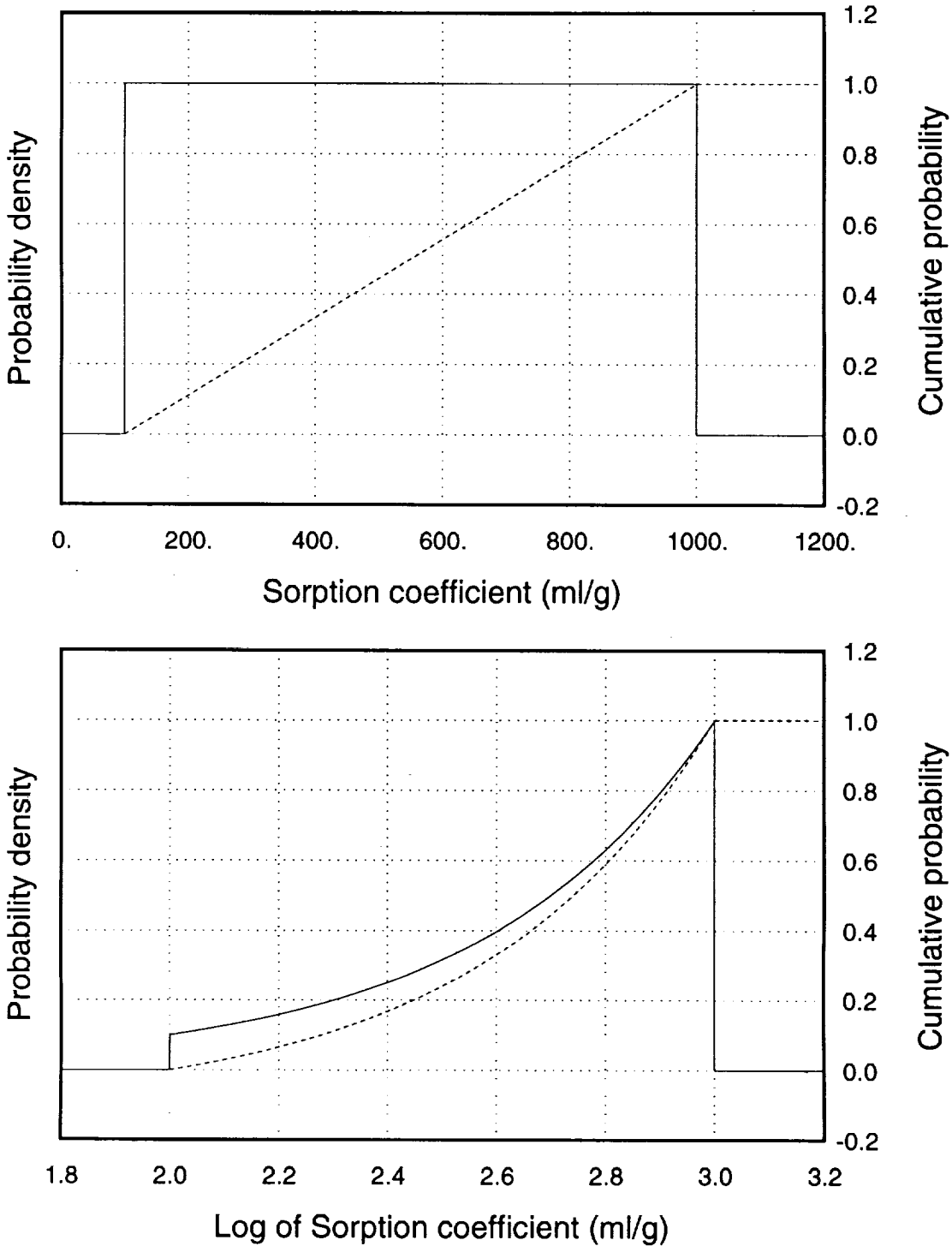

Figure B-17. Sorption-coefficient distributions for zirconium, niobium, samarium, actinium, thorium, and americium on devitrified tuff, and for selenium, lead, and uranium on iron oxides. Top figure is with linear K_d scale, bottom figure is with logarithmic K_d scale. Solid curve is probability density function, dashed curve is cumulative distribution function.

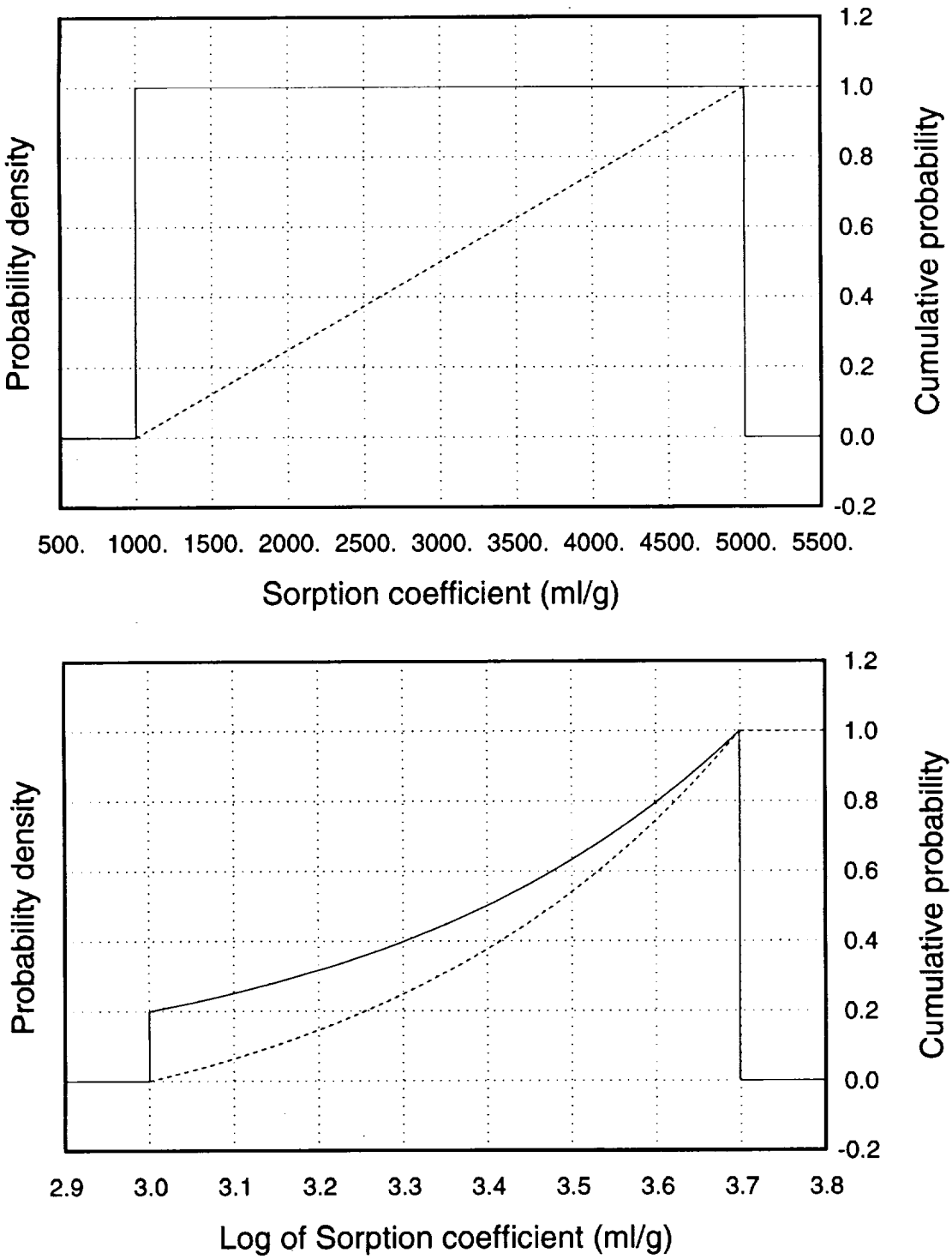

Figure B-18. Sorption-coefficient distributions for radium on zeolitic tuff, and for zirconium, niobium, samarium, actinium, thorium, plutonium, and americium on iron oxides. Top figure is with linear K_d scale, bottom figure is with logarithmic K_d scale. Solid curve is probability density function, dashed curve is cumulative distribution function.

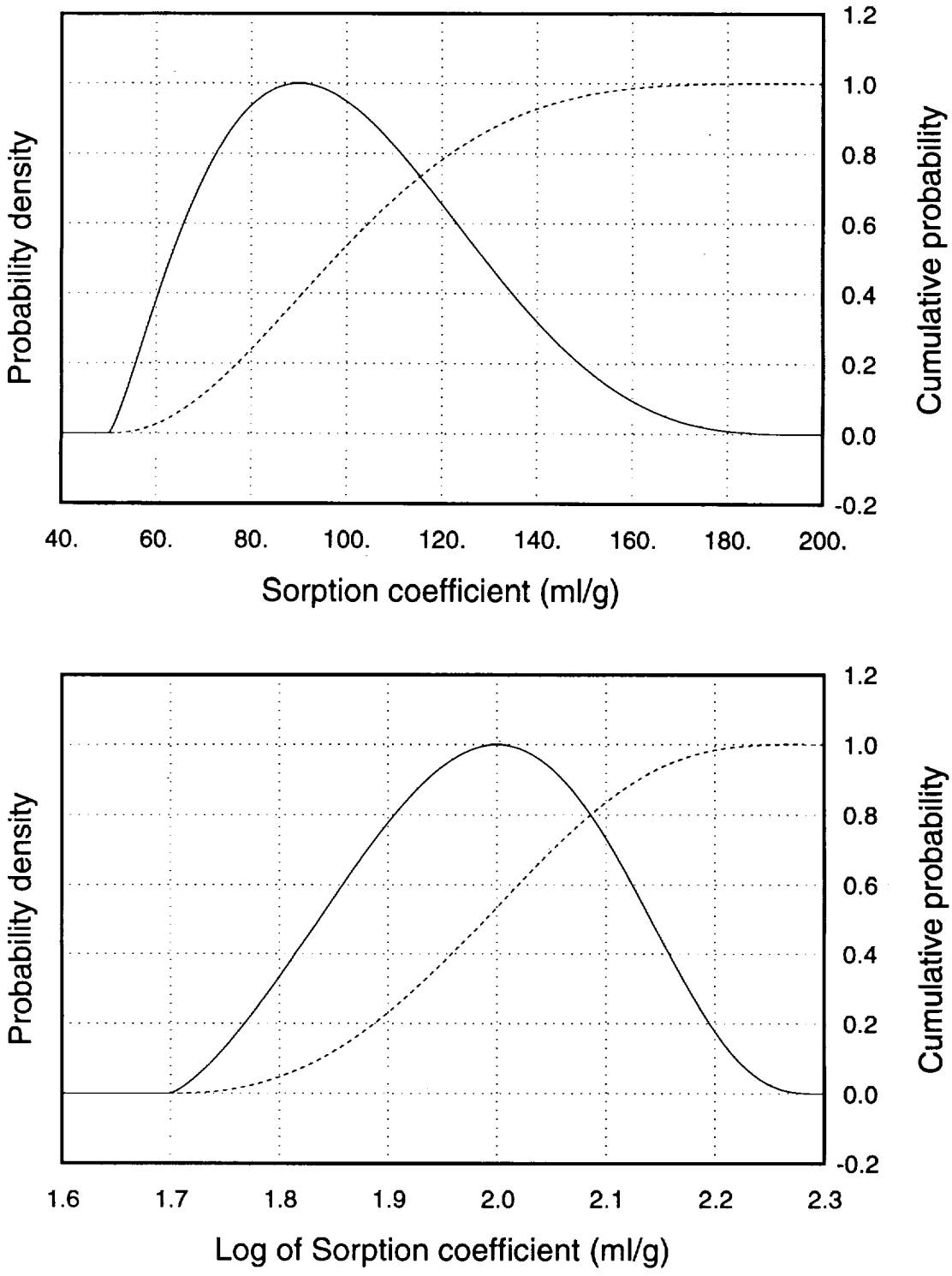

Figure B-19. Sorption-coefficient distributions for plutonium on devitrified tuff and on vitric tuff. Top figure is with linear K_d scale, bottom figure is with logarithmic K_d scale. Solid curve is probability density function, dashed curve is cumulative distribution function.

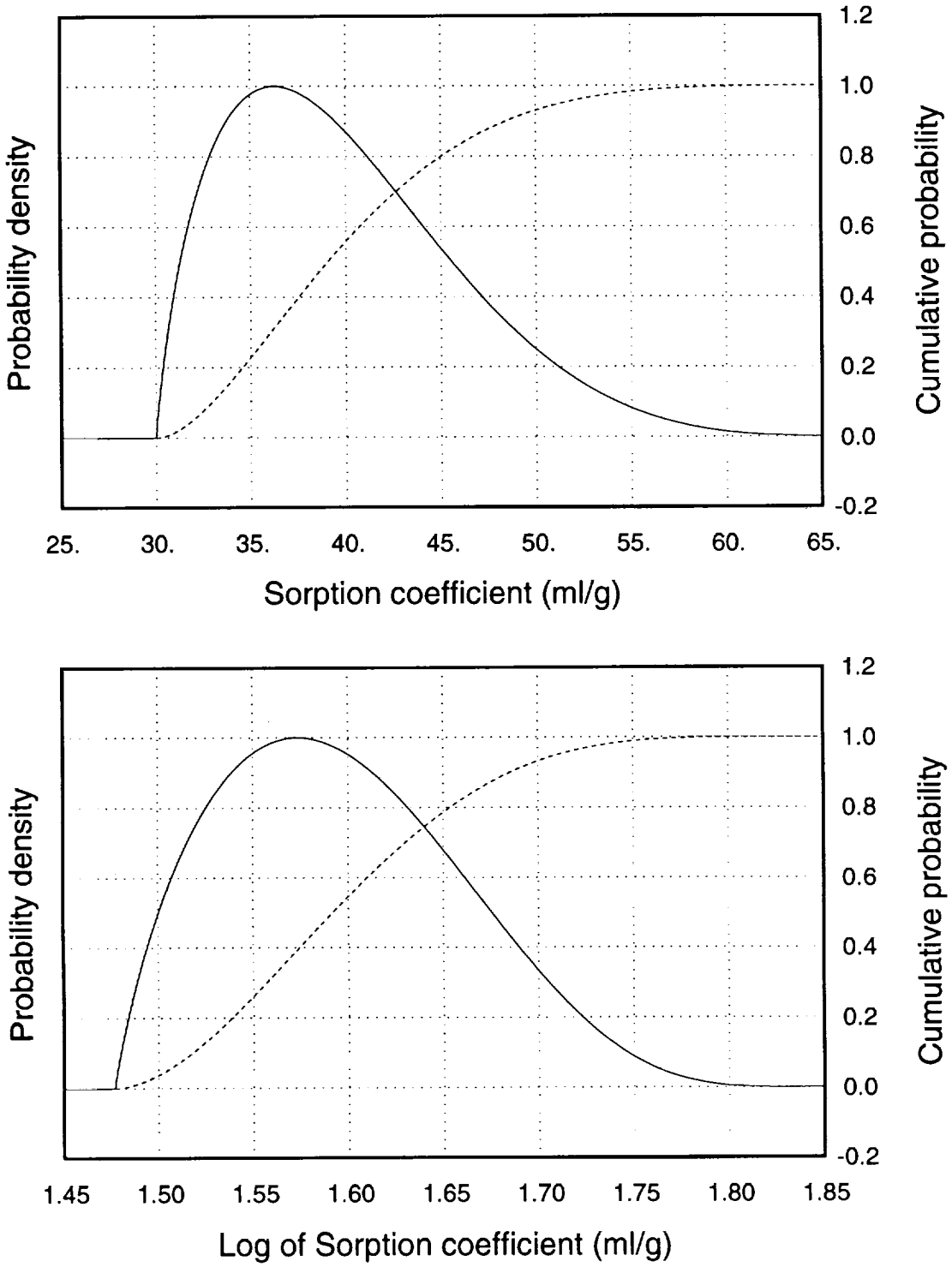

Figure B-20. Sorption-coefficient distributions for plutonium on zeolitic tuff. Top figure is with linear K_d scale, bottom figure is with logarithmic K_d scale. Solid curve is probability density function, dashed curve is cumulative distribution function.

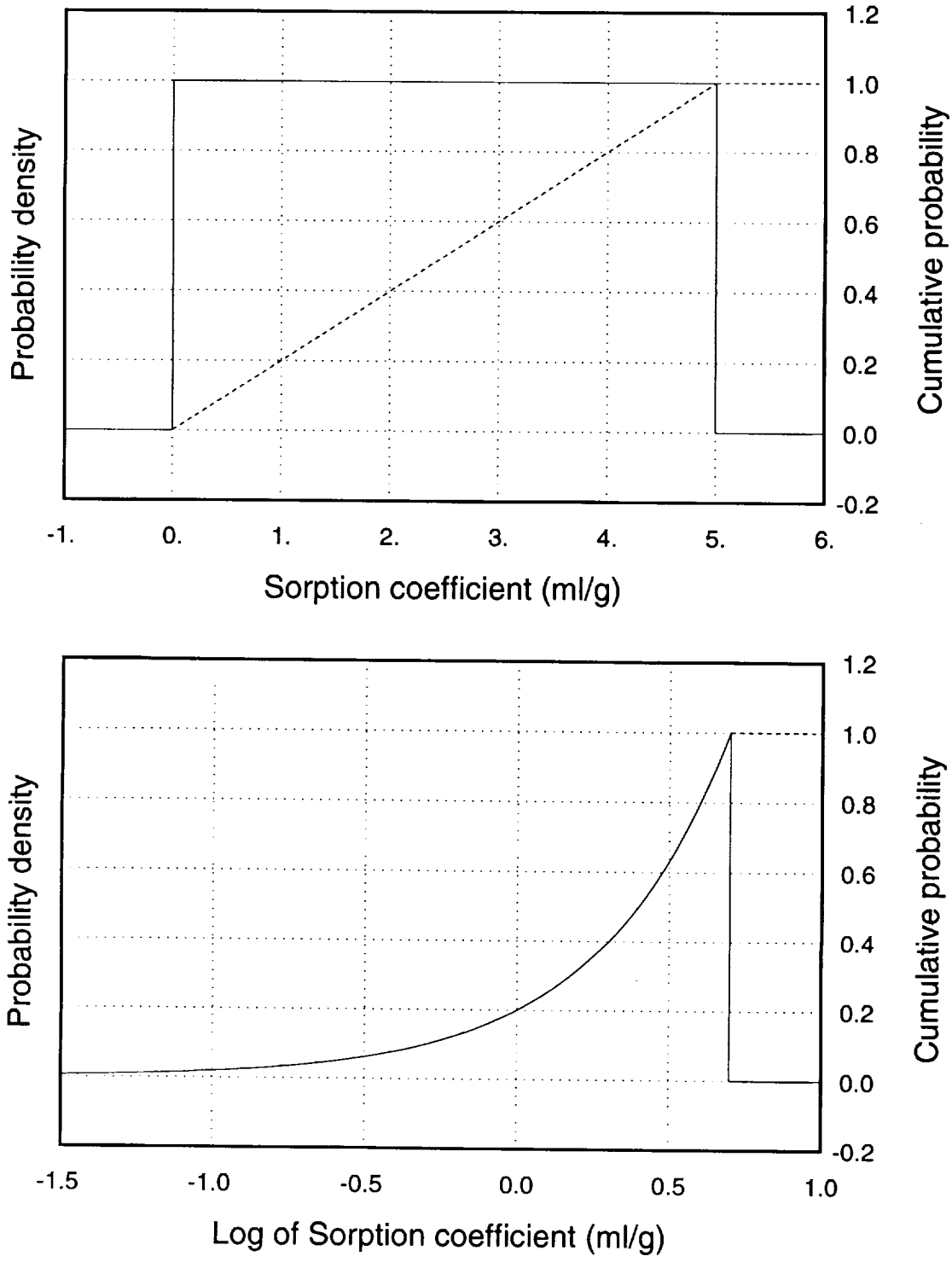

Figure B-21. Sorption-coefficient distributions for selenium and uranium on devitrified tuff. Top figure is with linear K_d scale, bottom figure is with logarithmic K_d scale. Solid curve is probability density function, dashed curve is cumulative distribution function.

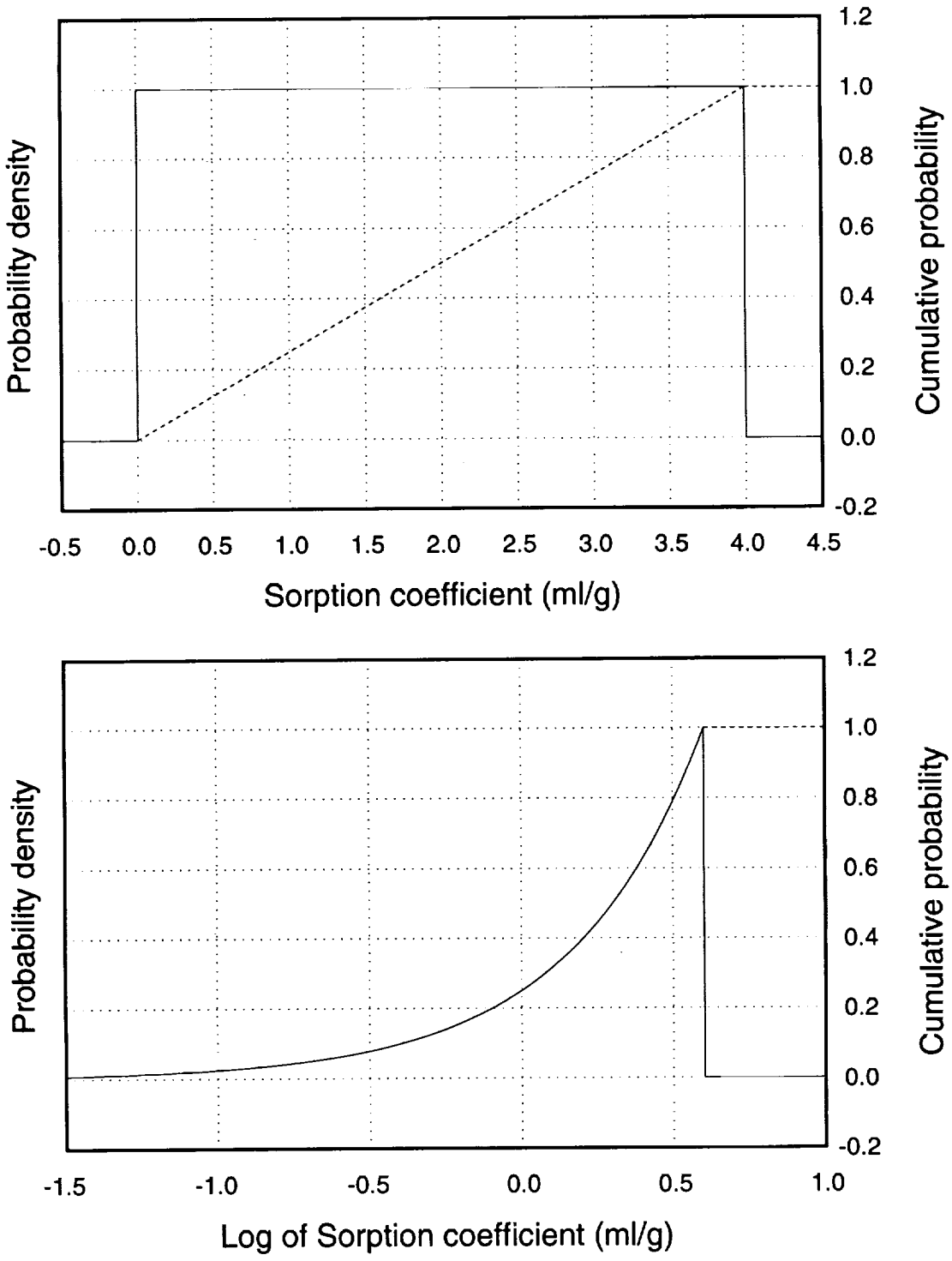

Figure B-22. Sorption-coefficient distributions for selenium and uranium on vitric tuff. Top figure is with linear K_d scale, bottom figure is with logarithmic K_d scale. Solid curve is probability density function, dashed curve is cumulative distribution function.

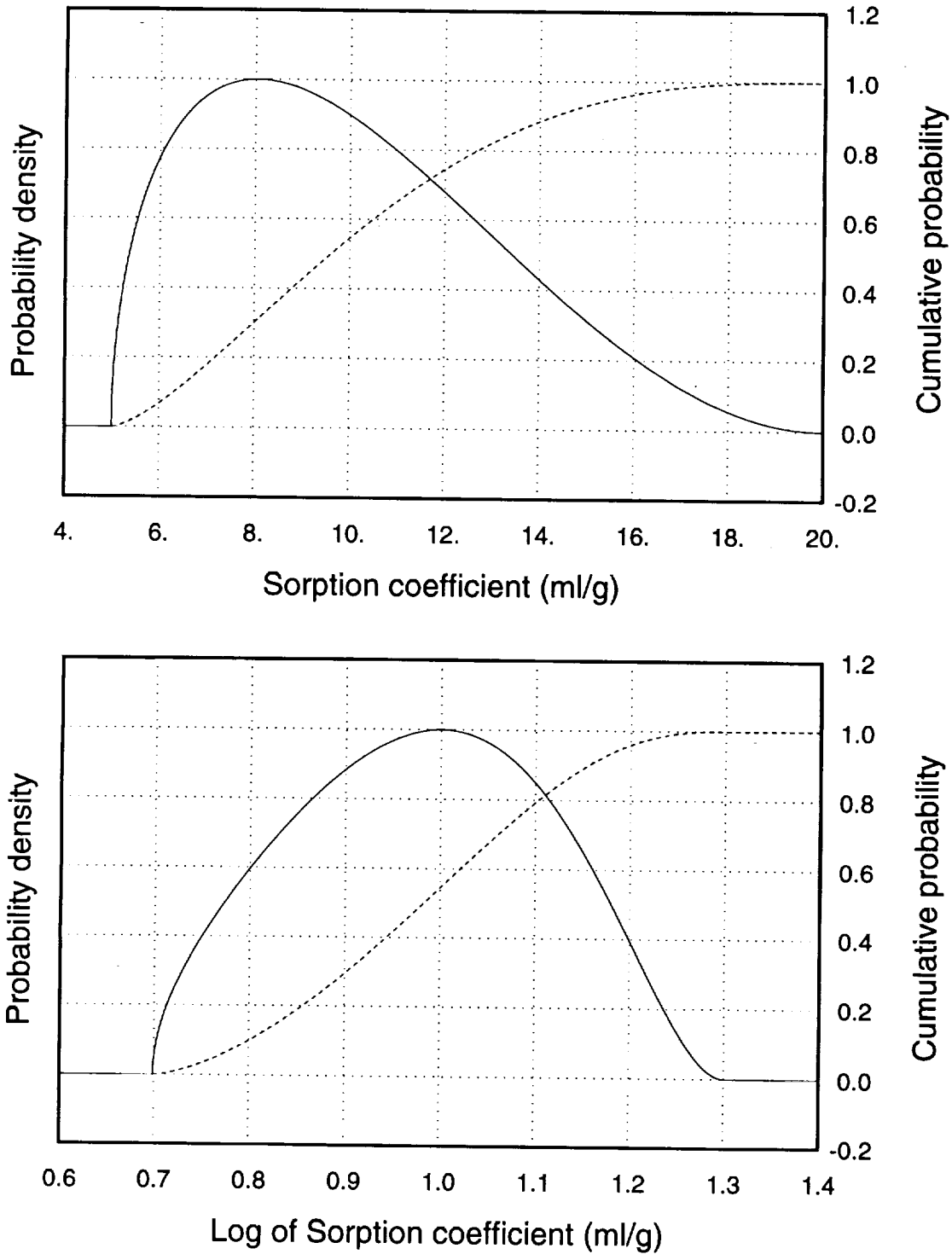

Figure B-23. Sorption-coefficient distributions for selenium and uranium on zeolitic tuff. Top figure is with linear K_d scale, bottom figure is with logarithmic K_d scale. Solid curve is probability density function, dashed curve is cumulative distribution function.

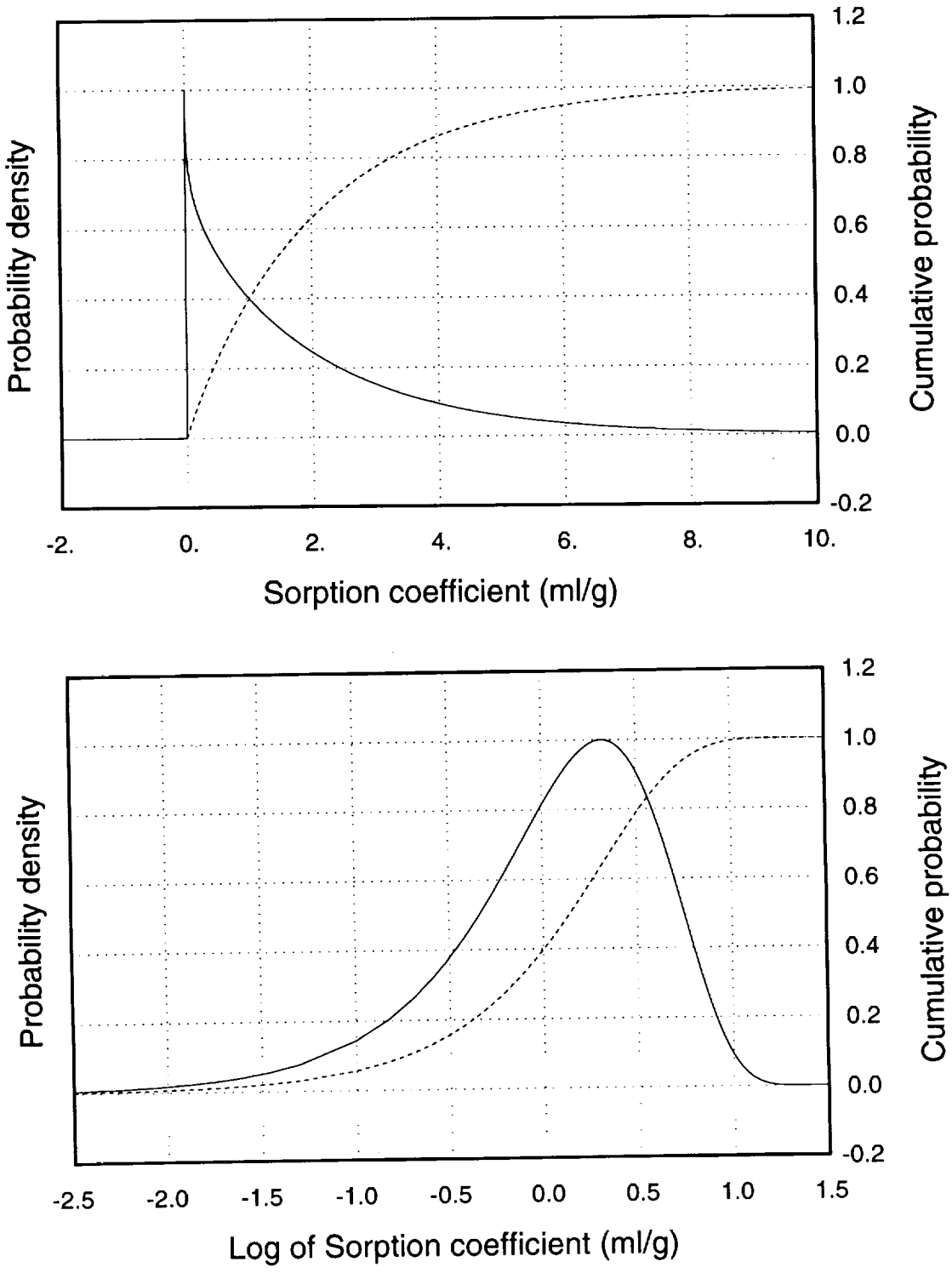

Figure B-24. Sorption-coefficient distributions for protactinium and neptunium on devitrified tuff. Top figure is with linear K_d scale, bottom figure is with logarithmic K_d scale. Solid curve is probability density function, dashed curve is cumulative distribution function.

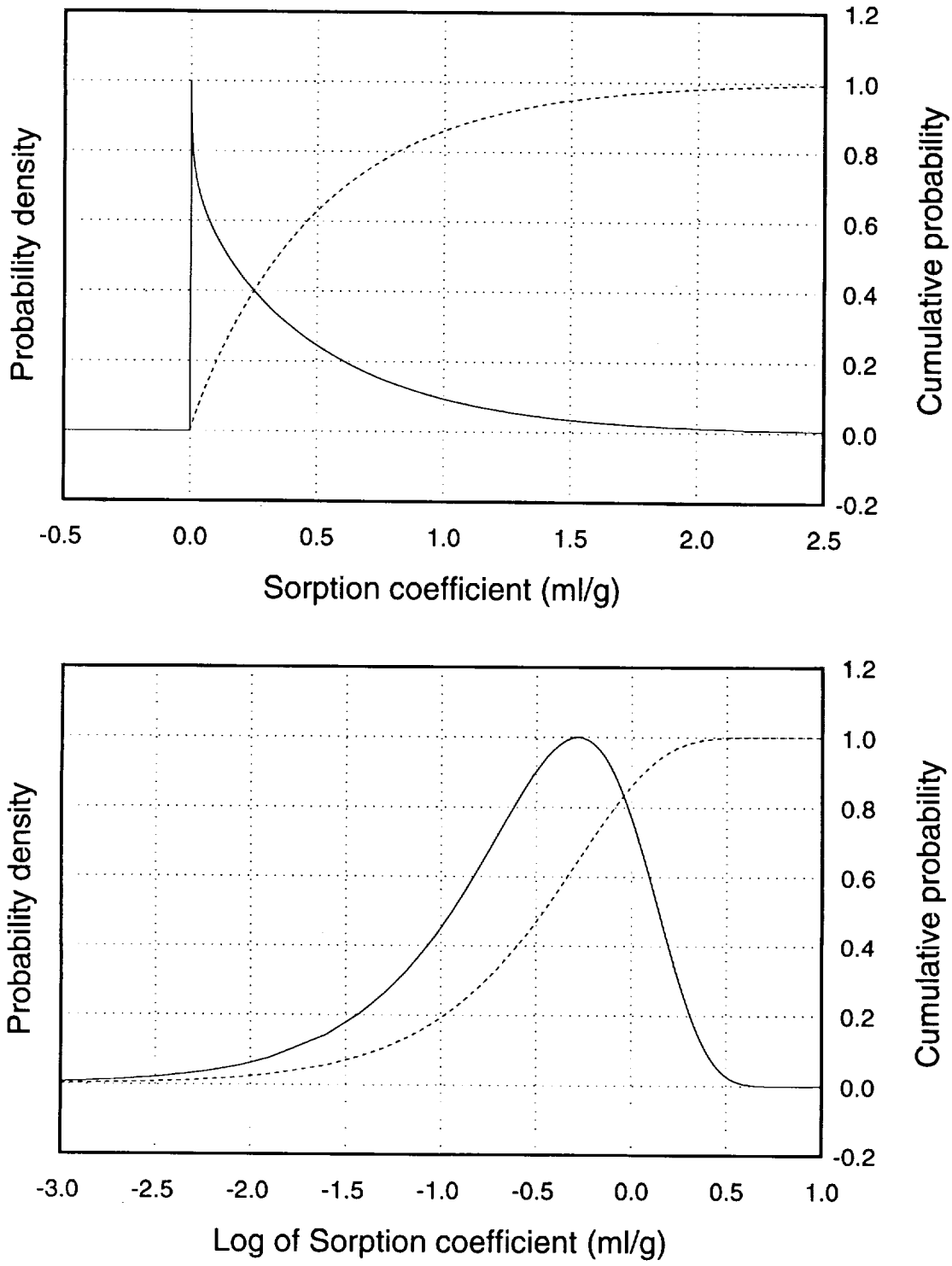

Figure B-25. Sorption-coefficient distributions for protactinium and neptunium on vitric tuff. Top figure is with linear K_d scale, bottom figure is with logarithmic K_d scale. Solid curve is probability density function, dashed curve is cumulative distribution function.

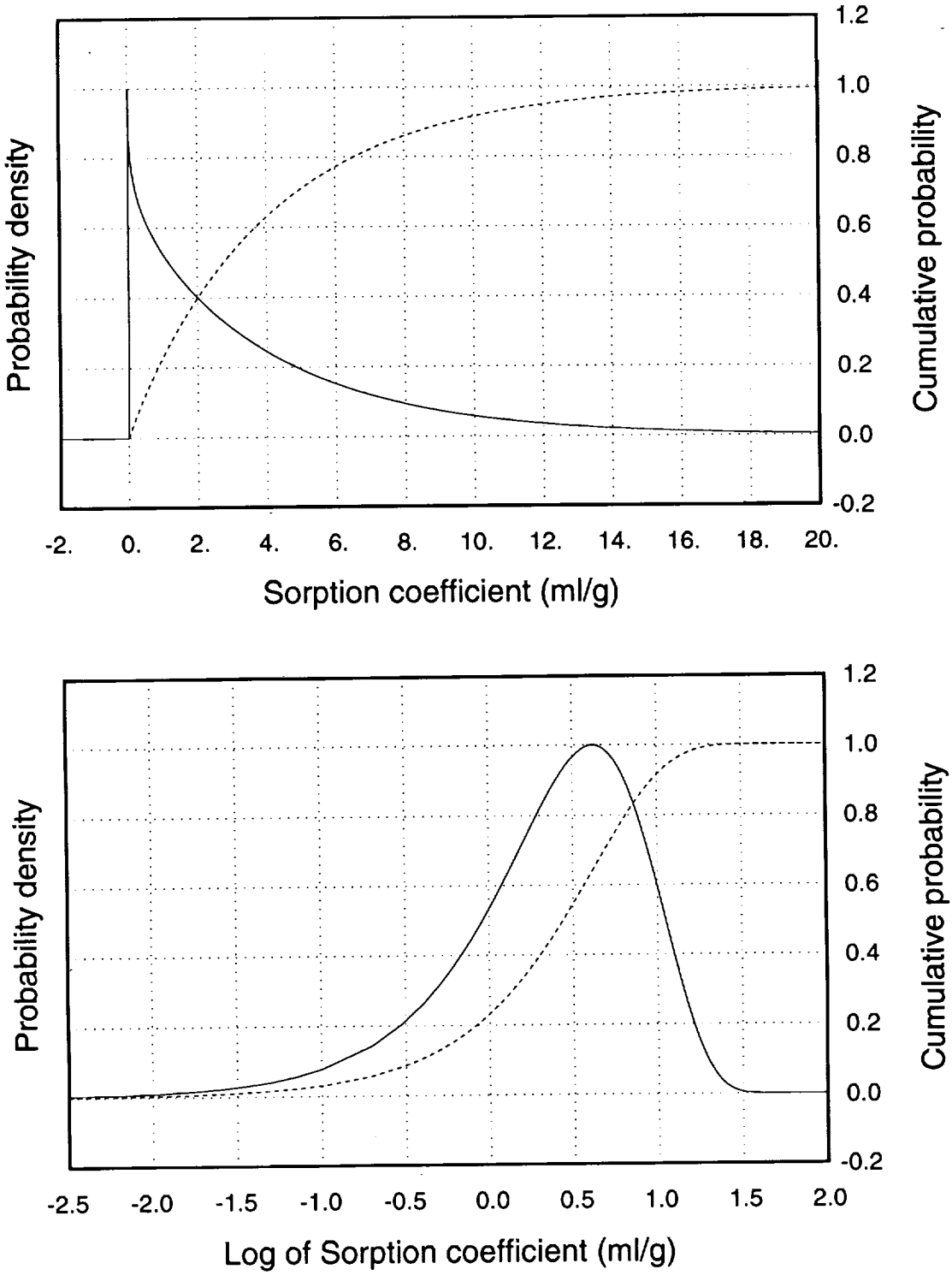

Figure B-26. Sorption-coefficient distributions for protactinium and neptunium on zeolitic tuff. Top figure is with linear K_d scale, bottom figure is with logarithmic K_d scale. Solid curve is probability density function, dashed curve is cumulative distribution function.

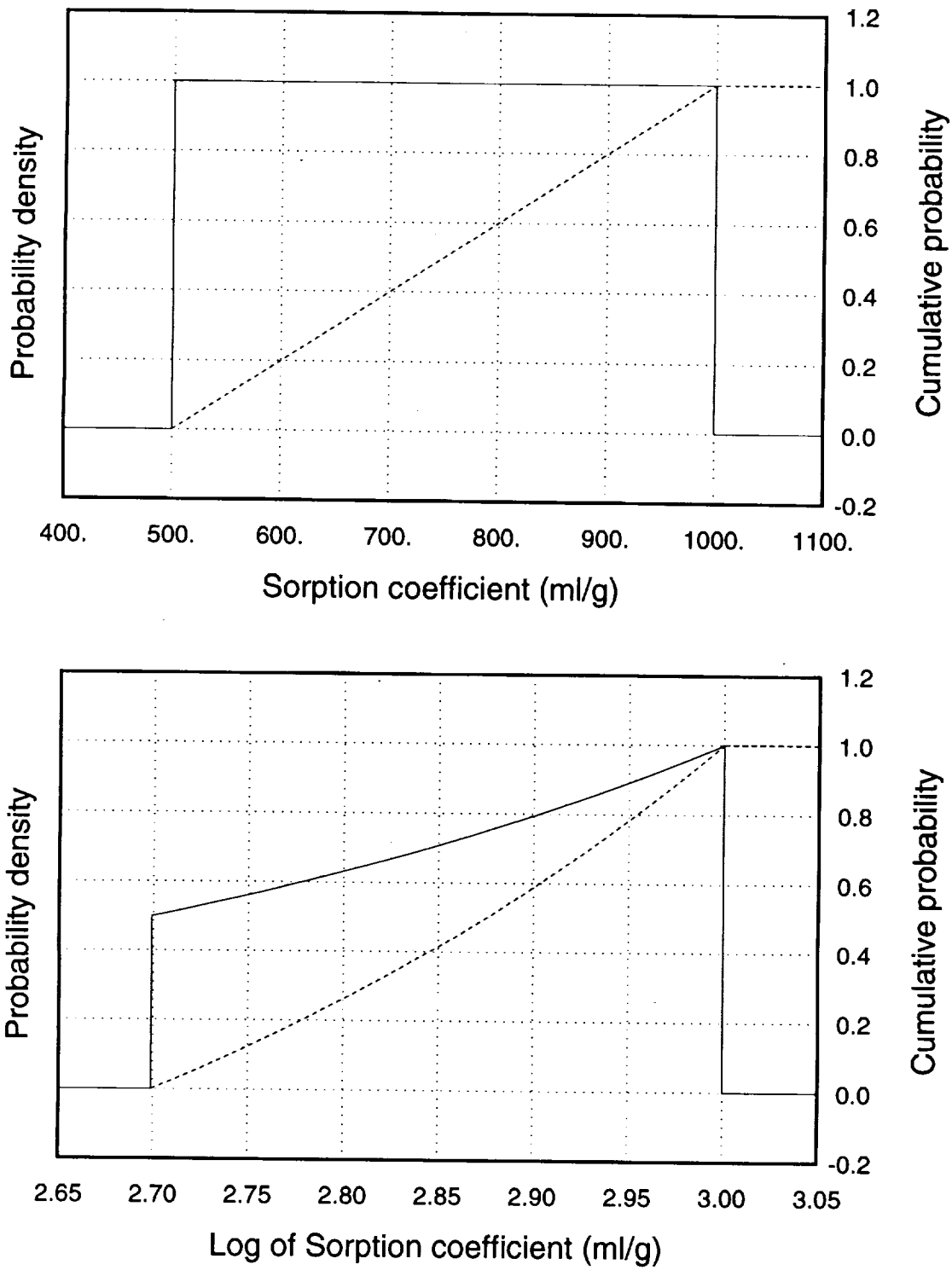

Figure B-27. Sorption-coefficient distributions for protactinium and neptunium on iron oxides. Top figure is with linear K_d scale, bottom figure is with logarithmic K_d scale. Solid curve is probability density function, dashed curve is cumulative distribution function.

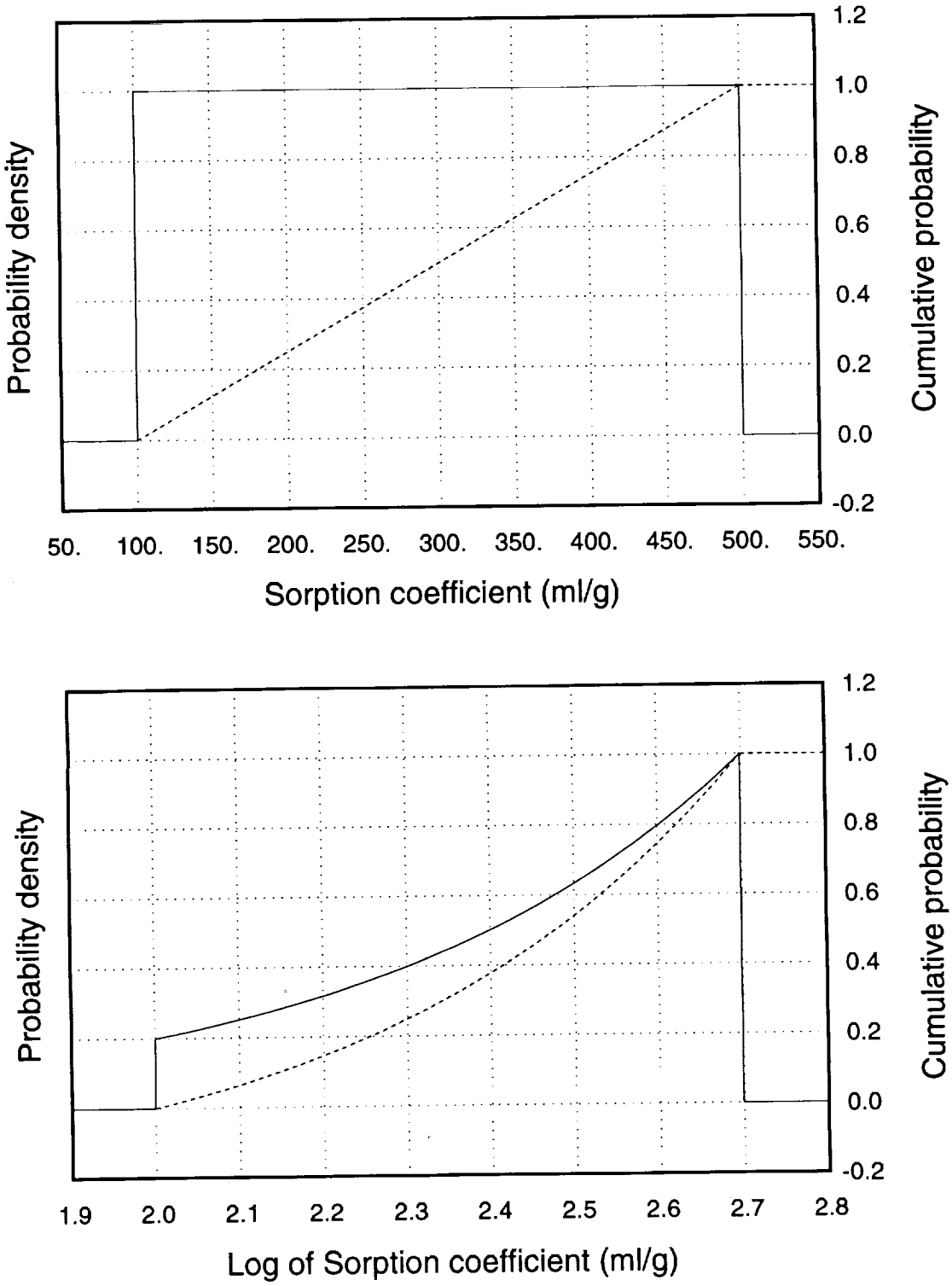

Figure B-28. Sorption-coefficient distributions for lead and radium on devitrified and vitric tuff, and for lead on zeolitic tuff. Top figure is with linear K_d scale, bottom figure is with logarithmic K_d scale. Solid curve is probability density function, dashed curve is cumulative distribution function.

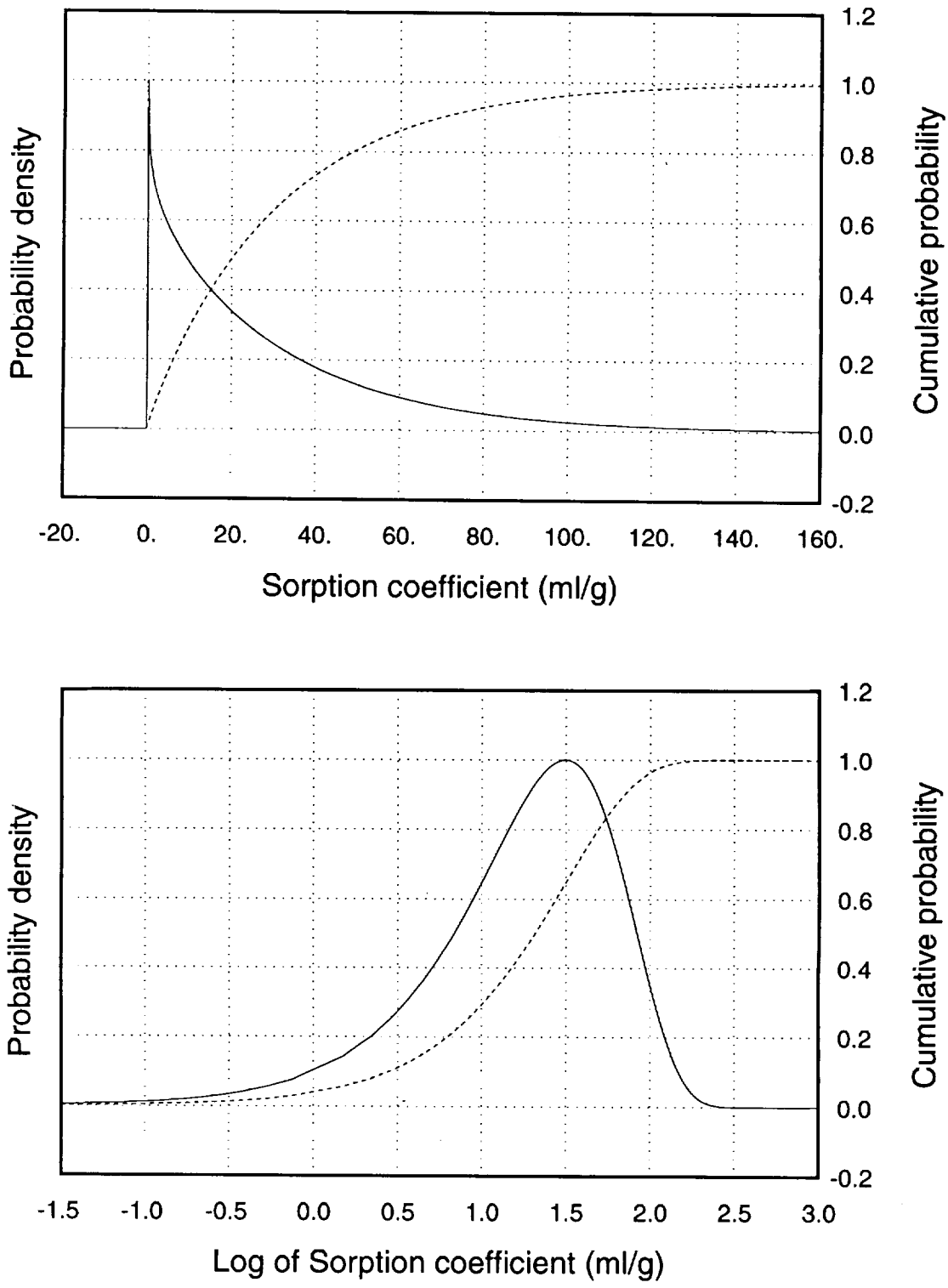

Figure B-29. Sorption-coefficient distributions for radium on iron oxides. Top figure is with linear K_d scale, bottom figure is with logarithmic K_d scale. Solid curve is probability density function, dashed curve is cumulative distribution function.

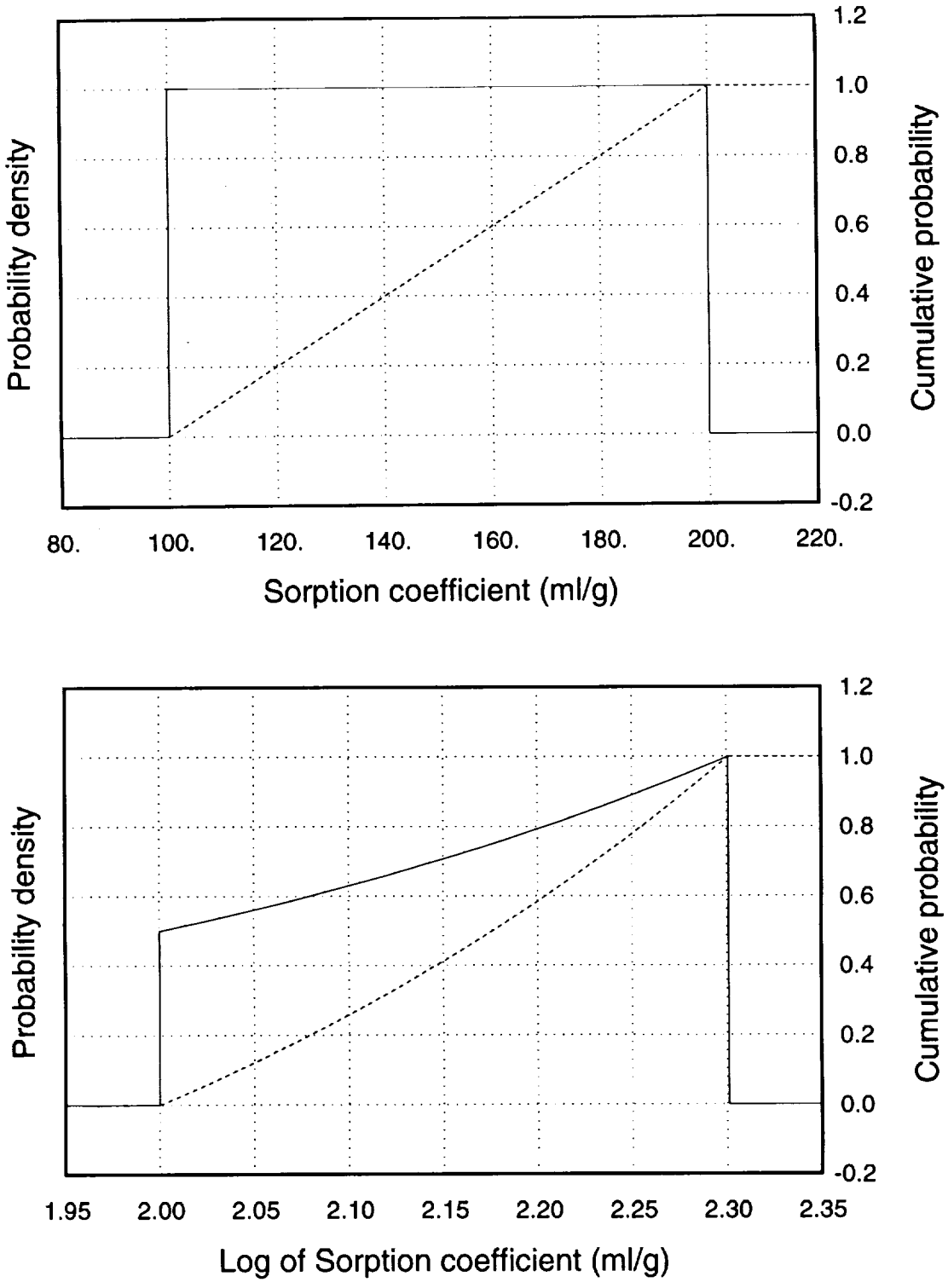

Figure B-30. Sorption-coefficient distributions for cesium on devitrified and vitric tuff. Top figure is with linear K_d scale, bottom figure is with logarithmic K_d scale. Solid curve is probability density function, dashed curve is cumulative distribution function.

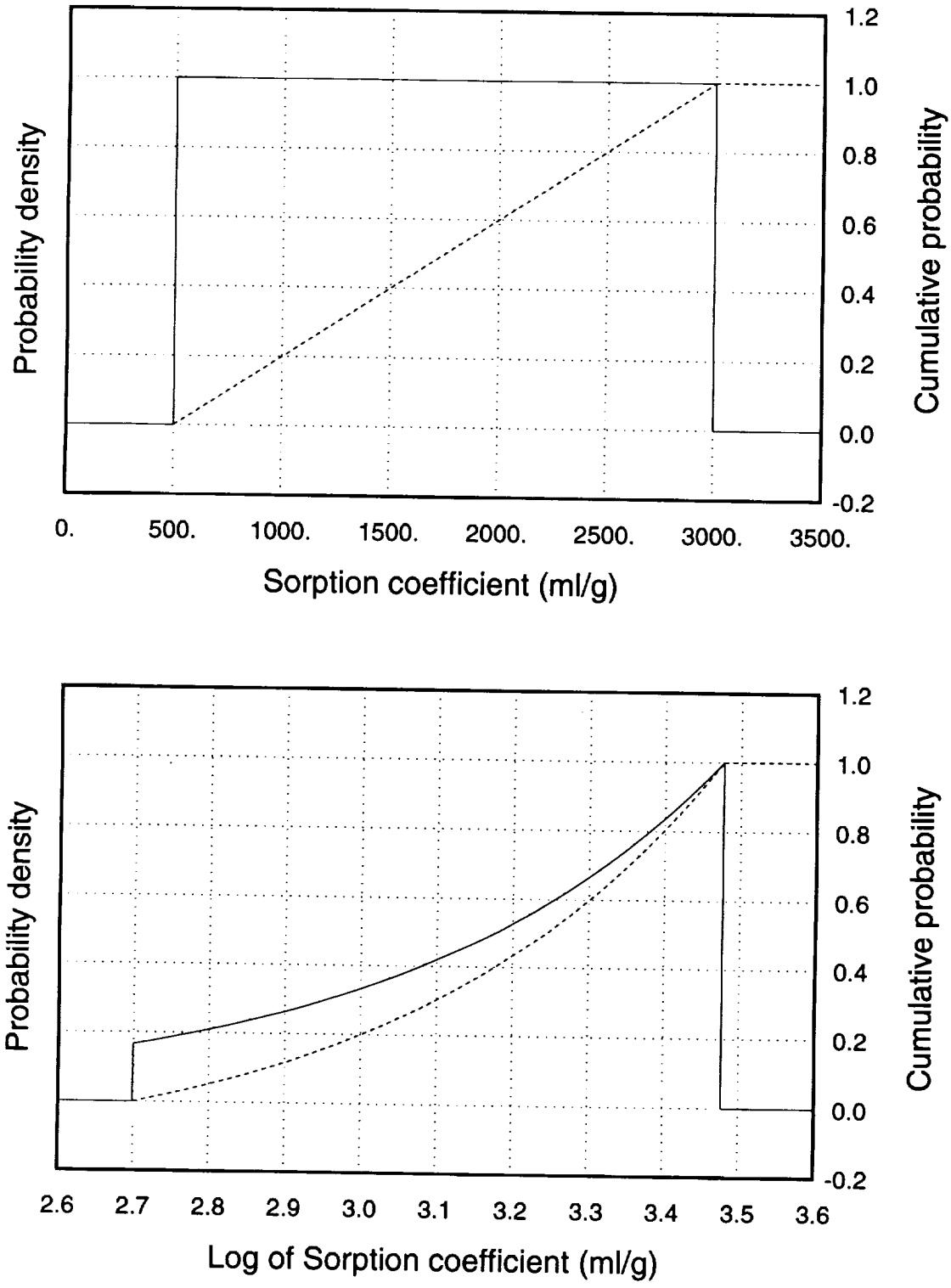

Figure B-31. Sorption-coefficient distributions for cesium on zeolitic tuff. Top figure is with linear K_d scale, bottom figure is with logarithmic K_d scale. Solid curve is probability density function, dashed curve is cumulative distribution function.

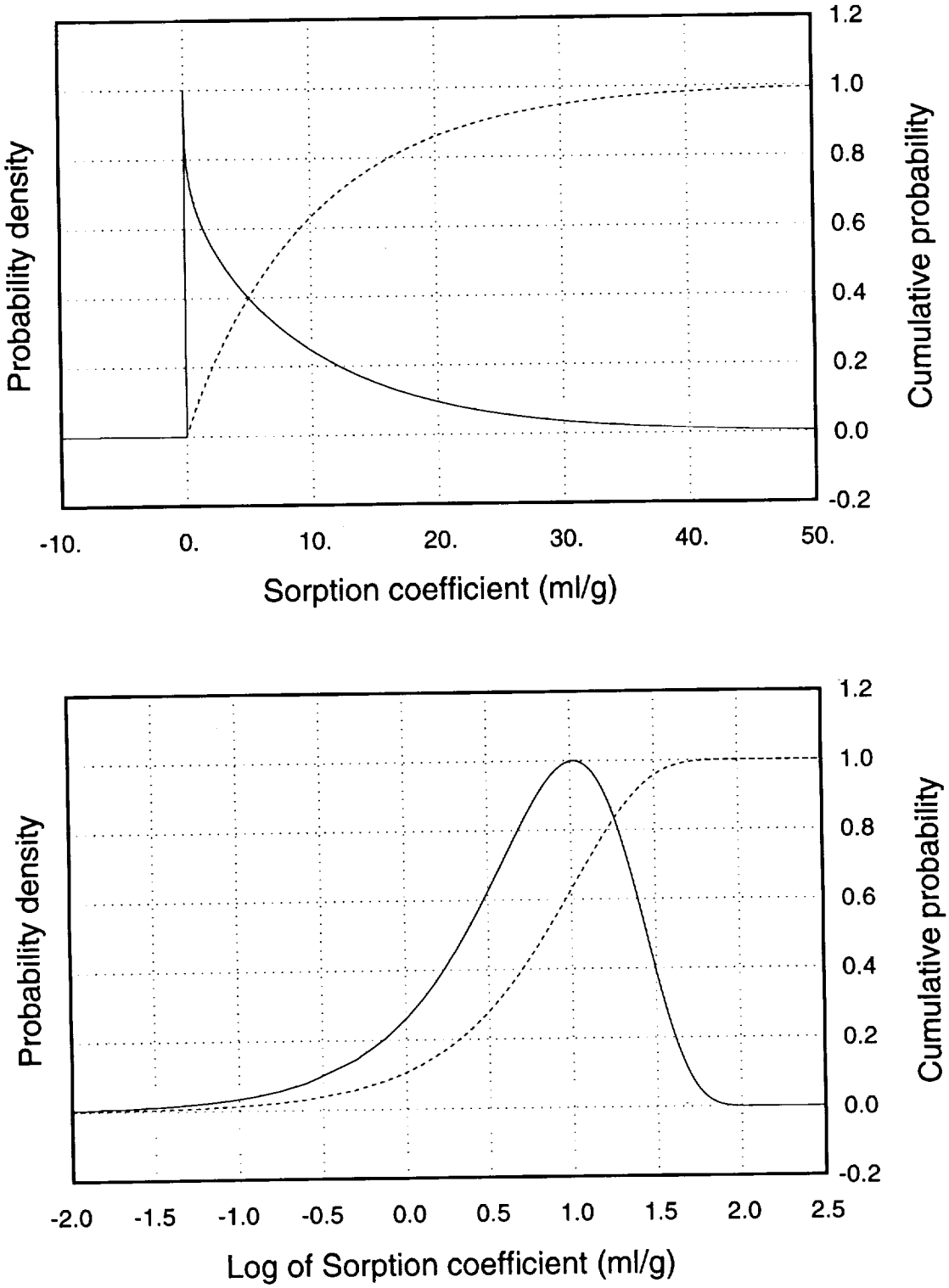

Figure B-32. Sorption-coefficient distributions for cesium on iron oxides. Top figure is with linear K_d scale, bottom figure is with logarithmic K_d scale. Solid curve is probability density function, dashed curve is cumulative distribution function.

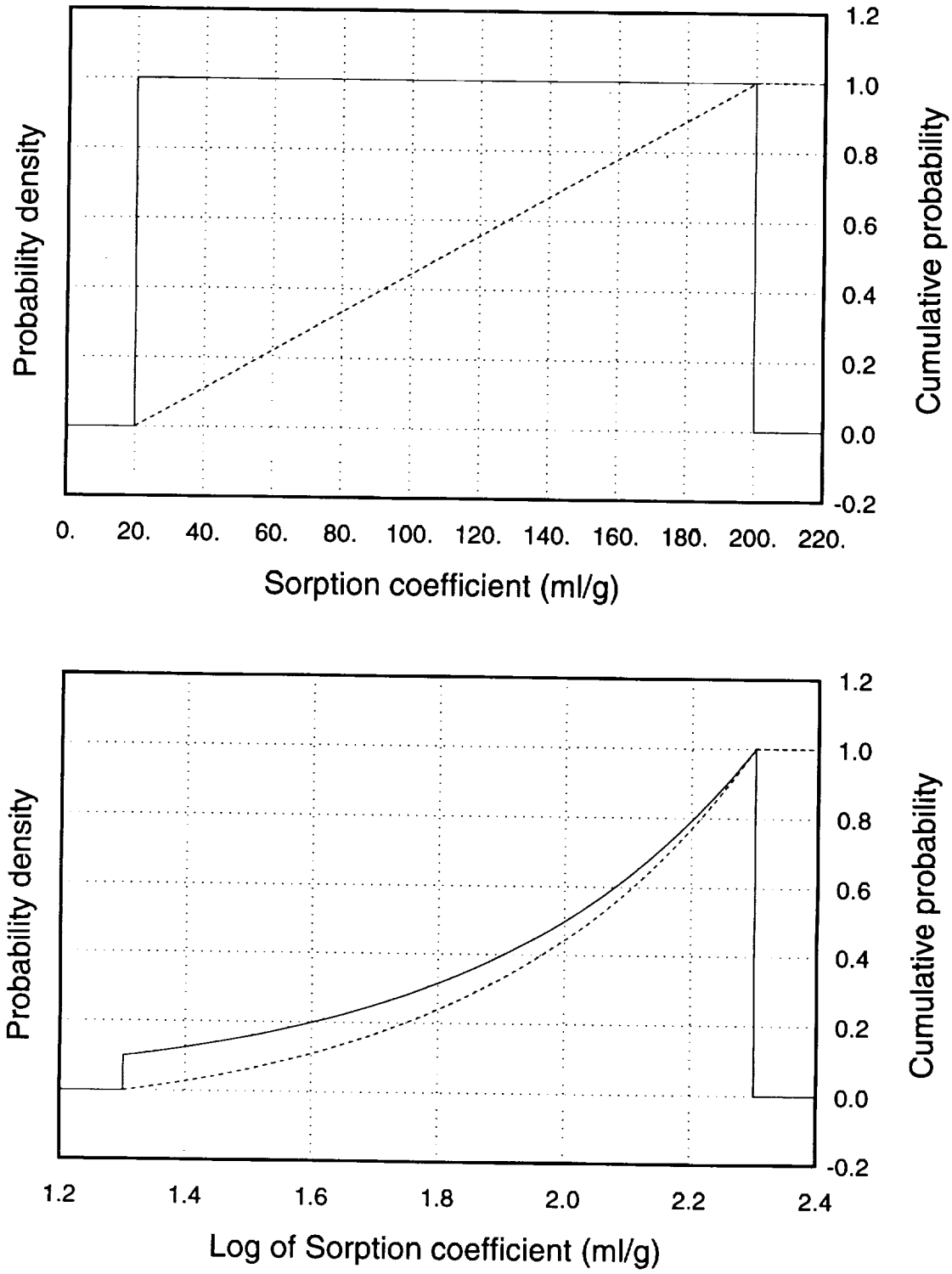

Figure B-33. Sorption-coefficient distributions for tin on devitrified and vitric tuff. Top figure is with linear K_d scale, bottom figure is with logarithmic K_d scale. Solid curve is probability density function, dashed curve is cumulative distribution function.

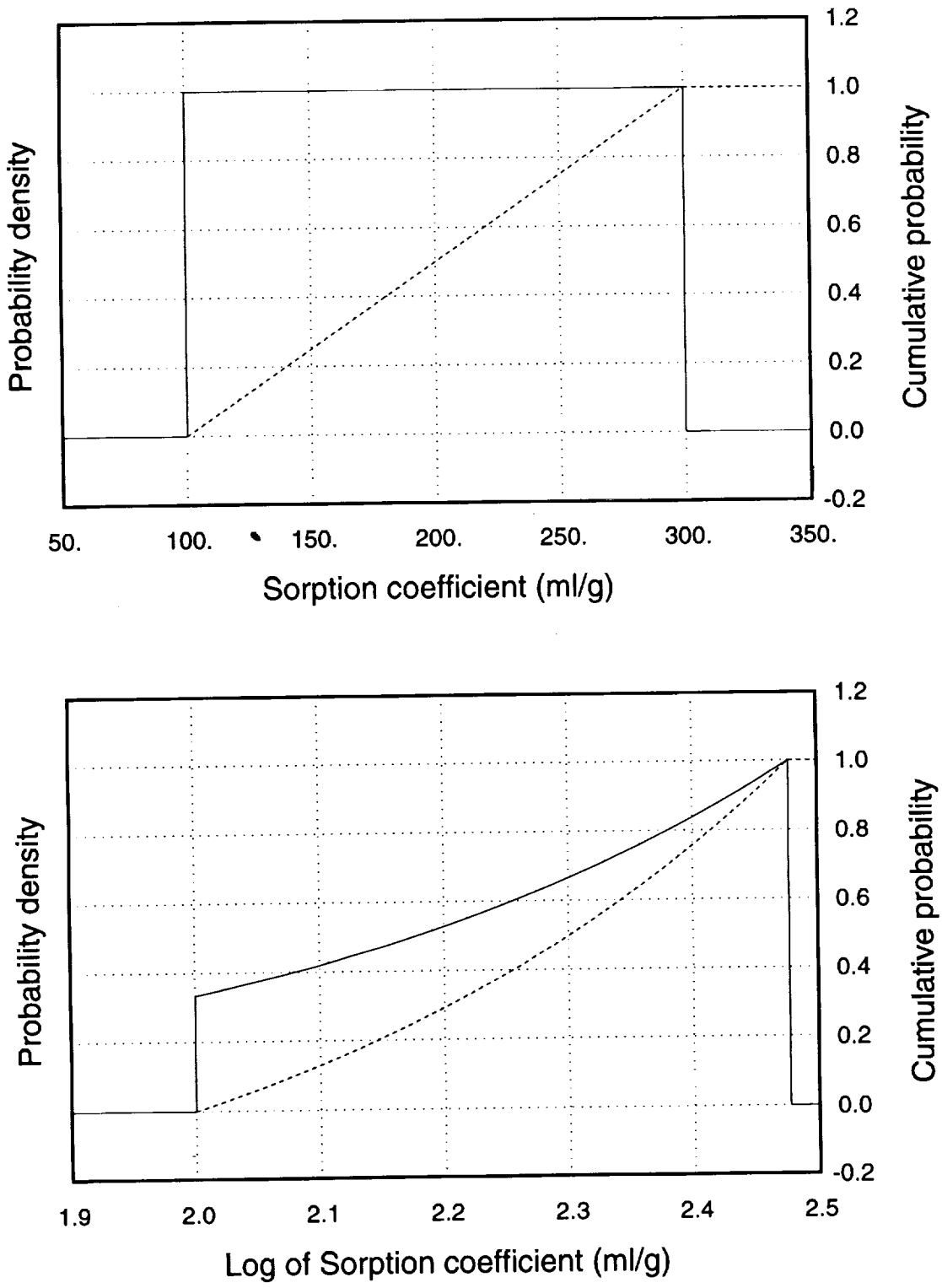

Figure B-34. Sorption-coefficient distributions for tin on zeolitic tuff, and for carbon on iron oxides. Top figure is with linear K_d scale, bottom figure is with logarithmic K_d scale. Solid curve is probability density function, dashed curve is cumulative distribution function.

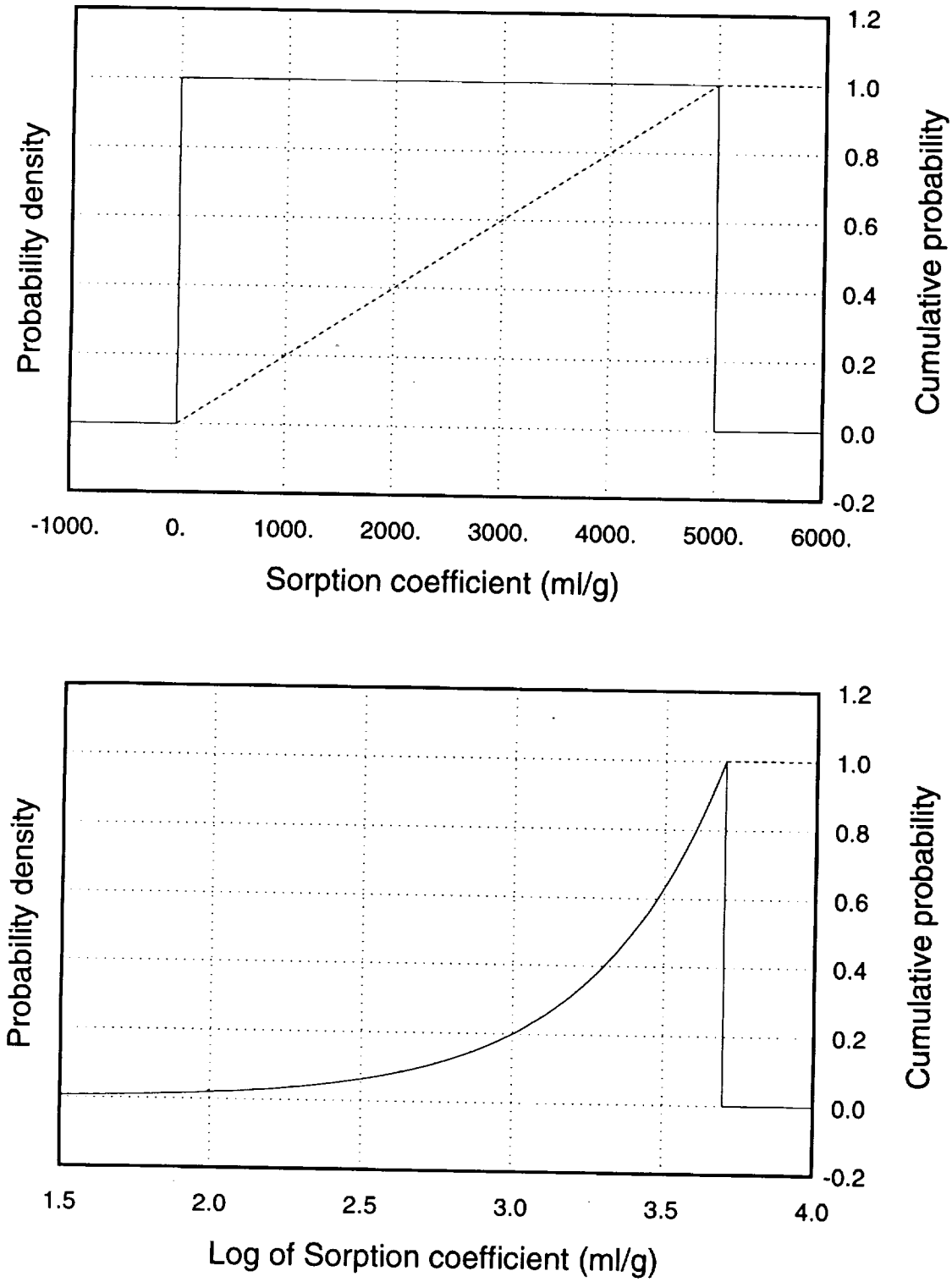

Figure B-35. Sorption-coefficient distributions for tin on iron oxides. Top figure is with linear K_d scale, bottom figure is with logarithmic K_d scale. Solid curve is probability density function, dashed curve is cumulative distribution function.

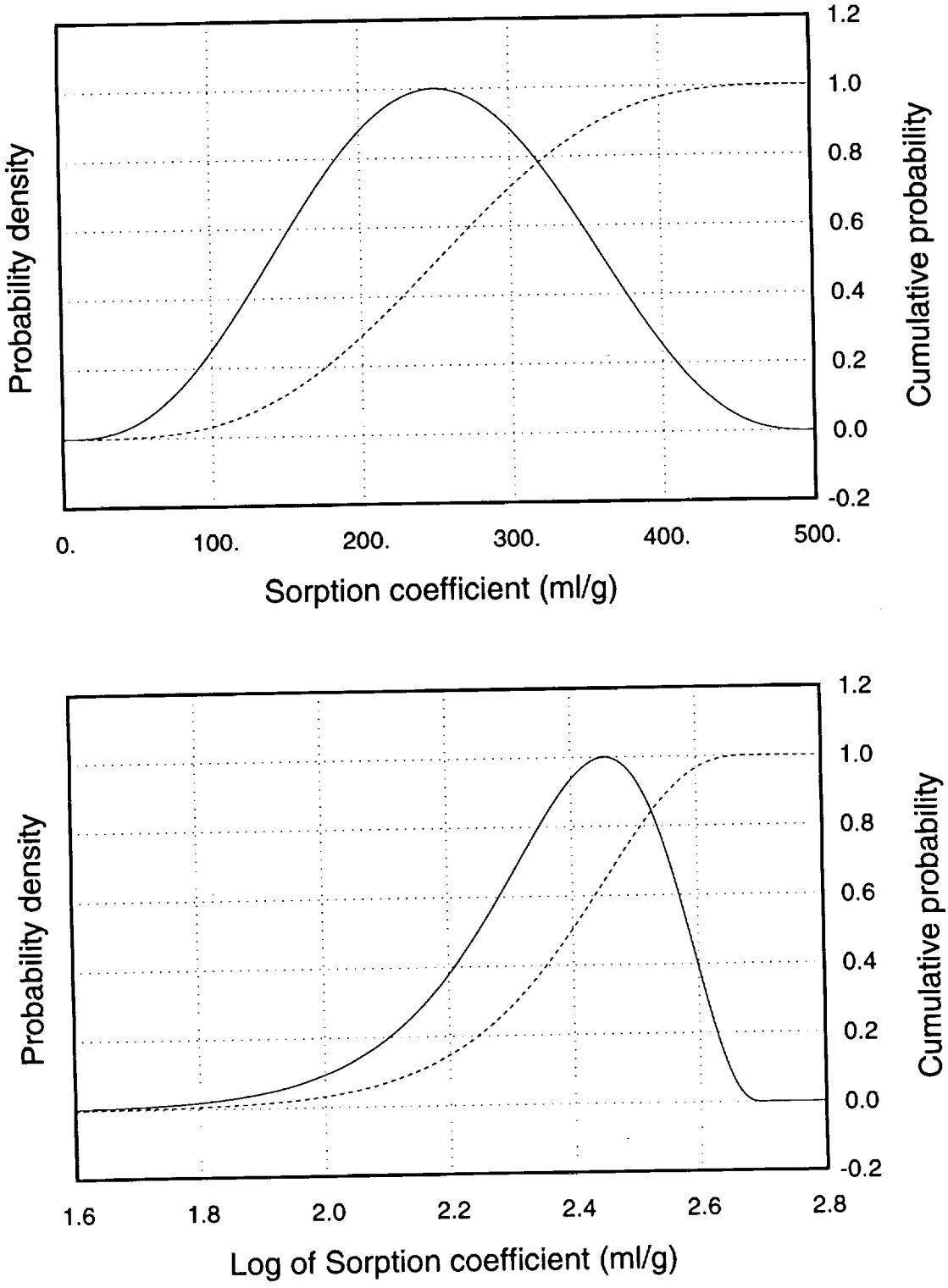

Figure B-36. Sorption-coefficient distributions for nickel on devitrified, vitric, and zeolitic tuff. Top figure is with linear K_d scale, bottom figure is with logarithmic K_d scale. Solid curve is probability density function, dashed curve is cumulative distribution function.

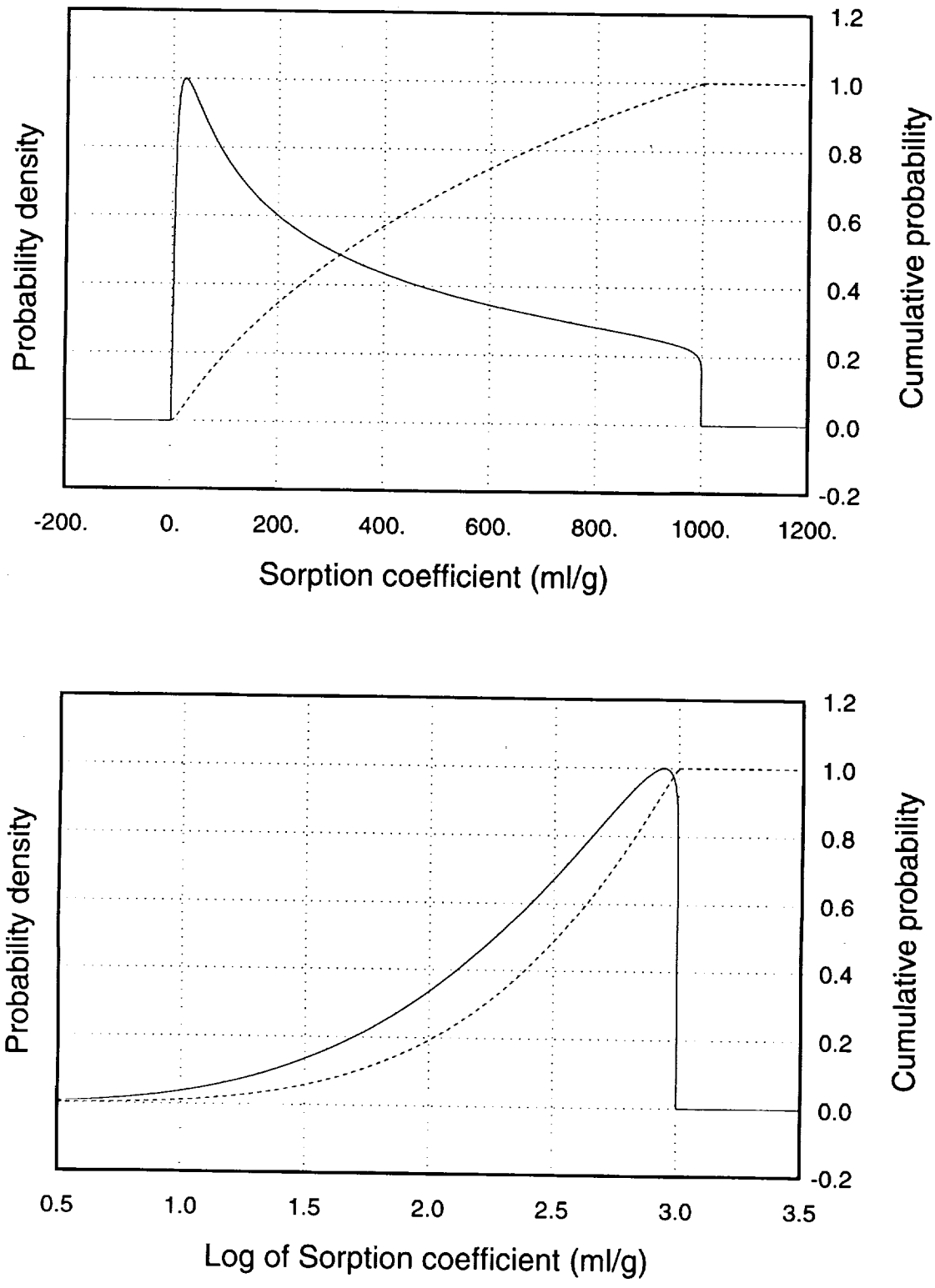

Figure B-37. Sorption-coefficient distributions for nickel on iron oxides. Top figure is with linear K_d scale, bottom figure is with logarithmic K_d scale. Solid curve is probability density function, dashed curve is cumulative distribution function.

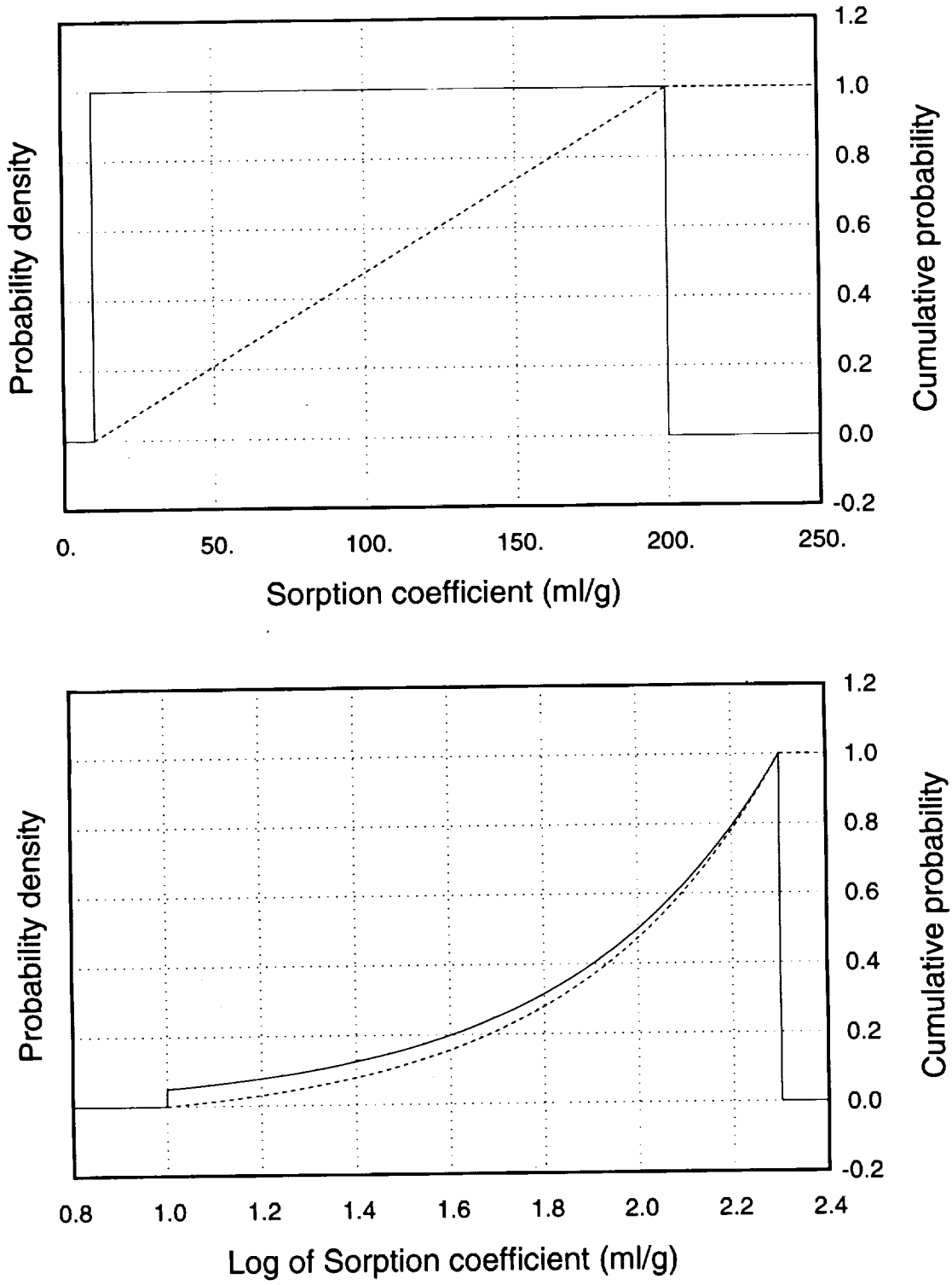

Figure B-38. Sorption-coefficient distributions for strontium on devitrified tuff. Top figure is with linear K_d scale, bottom figure is with logarithmic K_d scale. Solid curve is probability density function, dashed curve is cumulative distribution function.

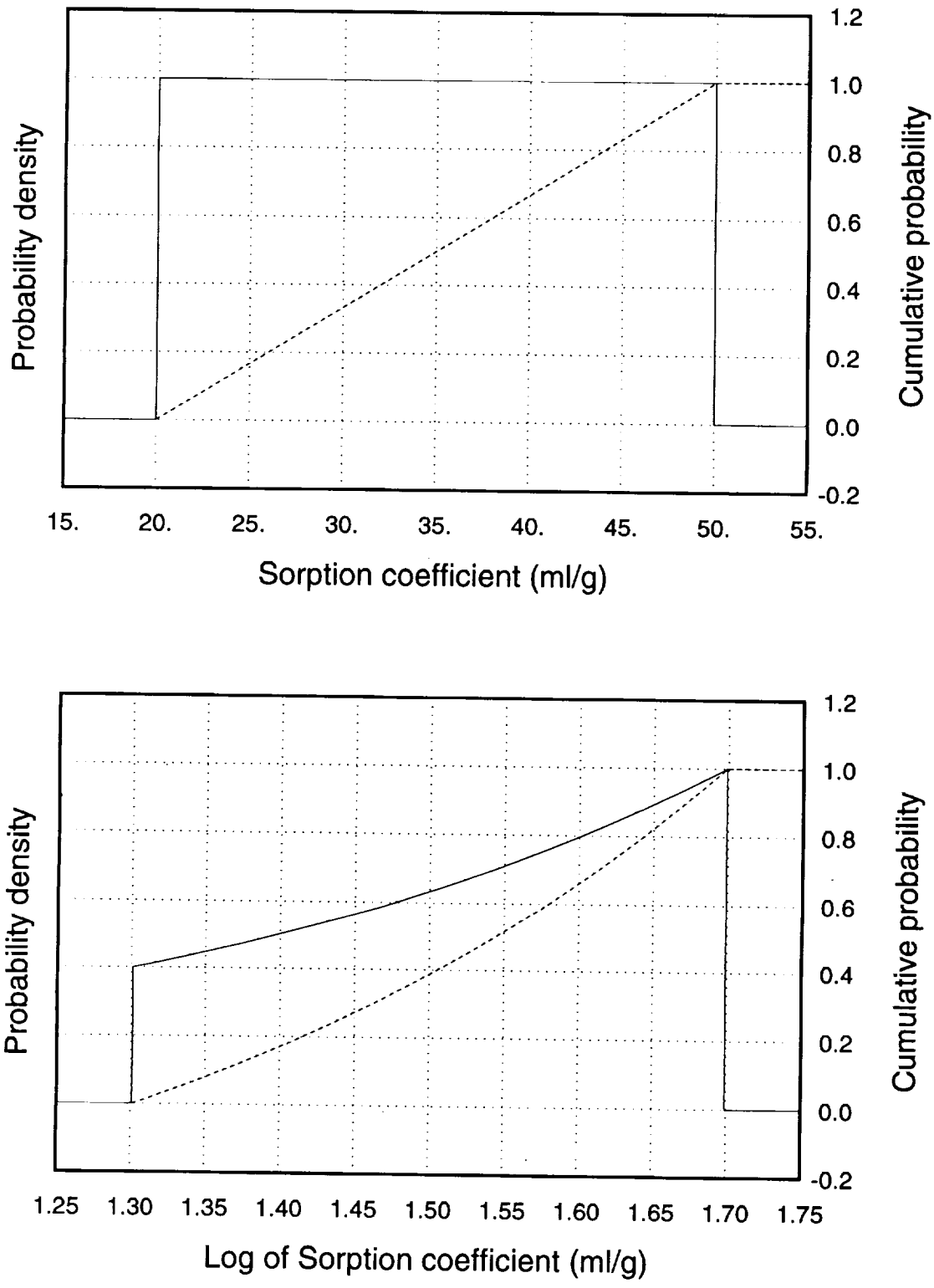

Figure B-39. Sorption-coefficient distributions for strontium on vitric tuff and on iron oxides. Top figure is with linear K_d scale, bottom figure is with logarithmic K_d scale. Solid curve is probability density function, dashed curve is cumulative distribution function.

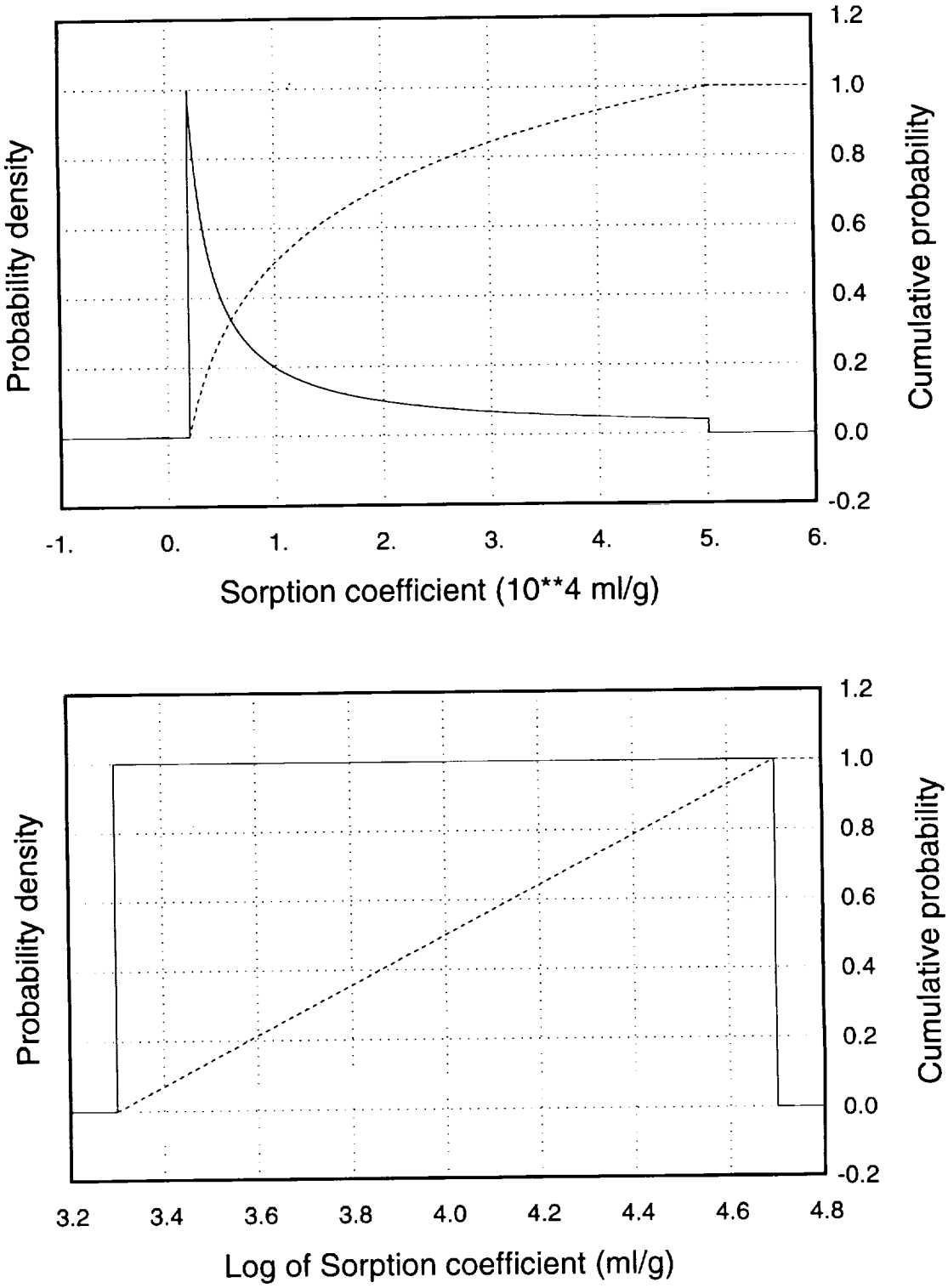

Figure B-40. Sorption-coefficient distributions for strontium on zeolitic tuff. Top figure is with linear K_d scale, bottom figure is with logarithmic K_d scale. Solid curve is probability density function, dashed curve is cumulative distribution function.

Appendix C
Thermal Modeling Approaches

Appendix C
Thermal Modeling Approaches

For TSPA-93, several approaches were used in the thermal modeling of the potential repository. Analytical conduction models that discretely account for each waste package, coupled hydrothermal models that use axisymmetric plate source representations of the heat-generating waste, and nonlinear conduction codes applied to various scales of interest were all employed in defining the thermal environment for the four cases chosen. Included in this appendix are detailed descriptions of the analytical thermal modeling approach used in calculating fraction dry, dry-out volume, and representative container surface temperatures. The nonlinear heat-conduction model used to generate the early-time container surface temperatures is also documented.

C.1 Analytical approach

For the analytical approach, the repository site was assumed to be composed of a single, infinite, homogeneous, isotropic material with constant properties. In addition, no open air spaces or variations in surface topography were considered. Using these simplifications, analytical solutions to the heat conduction equation can be derived.

Based on a closed-form analytical solutions to the heat conduction equation, the specific method chosen for use in this iteration of TSPA employs the ideas of point/cylindrical heat sources, superposition, and the method of images to obtain temperature histories at discrete points in three dimensions.

The development of the method is based on the analytical solution for the uniform distribution of heat-generating material throughout a right-circular cylinder, or a point source, located in an infinite medium with constant material properties (see Figure C-1). The infinite-medium solution for a single uniform cylindrical source is now presented.

The governing equation of the problem displayed in Figure C-1 is:

$$\frac{\partial T}{\partial t} - \alpha \nabla^2 T = S \,, \tag{C.1}$$

where

α = thermal diffusivity of the medium, and

T = temperature rise resulting from the heat source, S.

The heat source S can be expressed in terms of the Heaviside function $H(x)$ as:

$$S(r,z,t) = q(t)H(t)H(r)H(r_m - r)H(l - z)H(l + z)/\rho C_p \,, \tag{C.2}$$

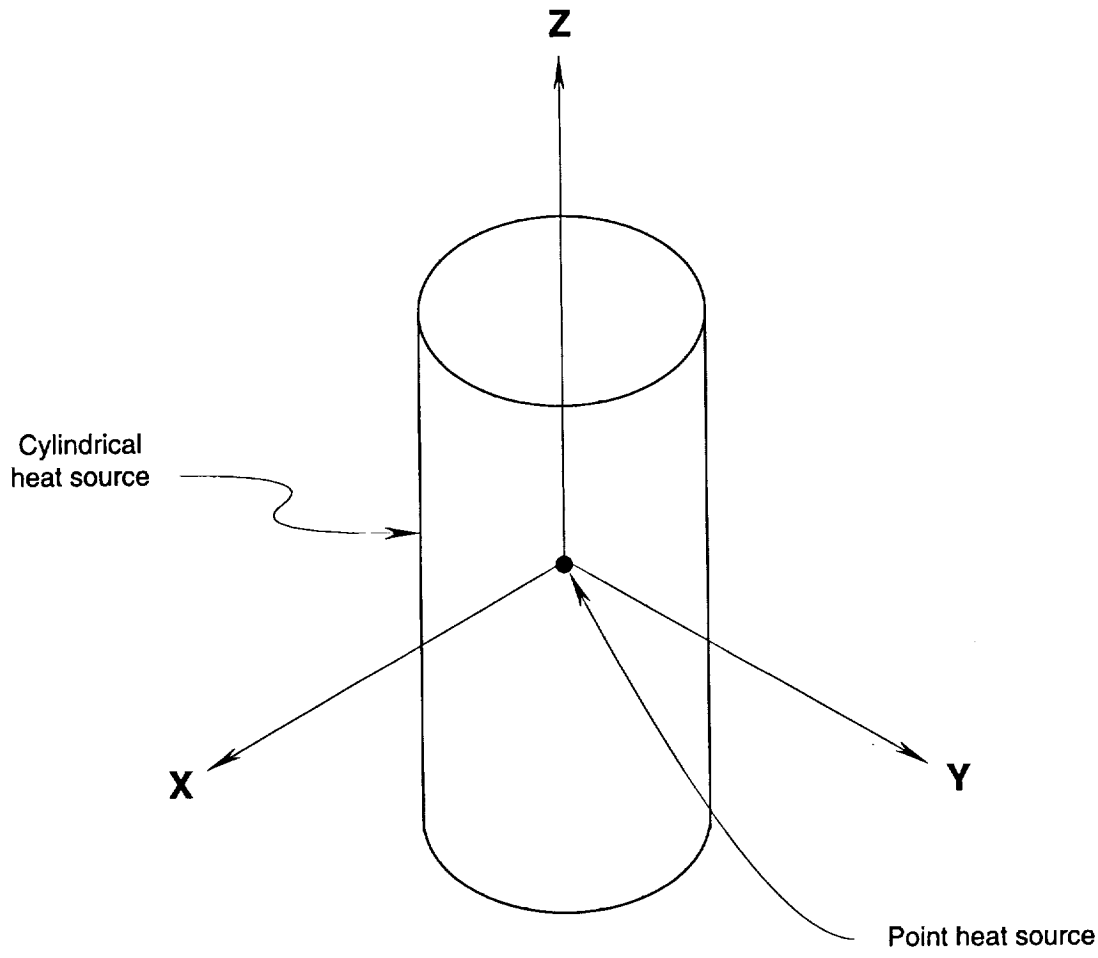

Figure C-1. Coordinate system for the point or cylindrical heat-generating source.

where

r_m = radial dimension of the cylindrical source,

l = half-length of cylindrical source,

ρC_p = volumetric heat capacity of the medium,

x, y, z = coordinates at which the induced temperature rise resulting from a heat source located at the origin is being evaluated for a given time t,

r = $\sqrt{x^2 + y^2}$, and

$H(x)$ = $\begin{cases} 1 \text{ for } x \geq 0 \\ 0 \text{ for } x < 0 \end{cases}$.

The heat-generation rate per unit volume for the cylinder is approximated by:

$$q(t) = Q\sum_{1}^{n} a_i e^{-b_i t} , \tag{C.3}$$

where

a_i = thermal output of the i^{th} exponential term as a fraction of the total thermal output of the heat source at the time of emplacement, (note that $\sum_1^n a_i = 1 = 1$),

Q = initial power density of the source,

n = number of exponential terms in the heat-source curve fit,

t = time, and

b_i = time constant of the i^{th} exponential term.

Applying the initial condition,

$$T(r,z,0) = 0,$$

the solution to equation C.1 can be expressed as

$$T_c(r,z,t) = \frac{Qr_m}{2\rho C_p}\sum_1^n a_i \int_{t_0}^{t} e^{-b_i t'}\left[erf\left(\frac{z+l}{\sqrt{4\alpha(t-t')}}\right) - erf\left(\frac{z-l}{\sqrt{4\alpha(t-t')}}\right)\right] \cdot \int_0^{\infty} e^{-\alpha(t-t')\beta^2} J_0(\beta r) J_1(\beta r_m)\, d\beta dt' \quad , \tag{C.4}$$

where T_c represents the temperature rise at (r,z,t) due to a cylindrical heat source at the origin, β and t' are variables of integration, and J_0 and J_1 are first-kind Bessel functions of orders zero and one, respectively.

Equation C.4 represents the temperature rise (evaluated at r,z,t) due to a single cylindrical heat-generating source located at the origin of the coordinate system. The numerical operations involved in solving equation C.4 require a relatively large amount of computer time. It is understood, however, that if the location at which one is calculating the temperature rise is at least a predetermined distance from the heat source, then desired accuracy can be maintained if the cylindrical heat source is approximated by a point source. In terms of computer time, the savings associated with switching from a cylindrical to a point source are substantial. This is due to the fact that temperature predictions for a point source can be made using transcendental function evaluations rather than the nested numerical integrations required to evaluate equation C.4. The source term for an infinitesimal point source can be expressed as:

$$S(r,z,t) = q(t)\, H(t)\, \delta(r)\, \delta(z) / \rho C_p \, , \tag{C.5}$$

where, $\delta(x)$ is a Dirac delta function. This source term is consistent with the definition of an infinitesimal point source as given by Beyerlein and Claiborne (1982). Using the

same nomenclature as above, the solution to the initial and boundary value problem given by Equations C.1, C.3, and C.5 can be expressed as follows:

$$T_{p(r,z,t)} = \frac{Qe^{-R^2/4\alpha t}}{4k\pi R} \sum_{1}^{n} a_i U\left(\sqrt{b_i t}\,\frac{R}{\sqrt{4\alpha t}}\right), \tag{C.6}$$

where

T_p = temperature rise at (r,z,t) due to a point source located at the origin,

R = spherical radial coordinate, $R = \sqrt{r^2 + z^2}$,

k = thermal conductivity of the medium, and

U = real part of the complex error function as defined in Abramowitz and Stegun (1972).

No significant loss of accuracy in temperature predictions is experienced with this change from a cylindrical to a point heat source. However, the choice of what distance is far enough away for this switch to occur is dependent upon material properties and the size of the cylindrical source. For this study, a radius of 150 m was found to be an adequate distance.

C.1.1 Modeled repository geometry

The repository layout used for this study was developed based on preliminary Advanced Conceptual Design (ACD) drawings provided by Raytheon Services of Nevada that document a conceptual layout based on a TBM mining method (see Figure 4-6). Many of the primary features of the layout published in the SCP–CDR (SNL, 1987) are preserved in this layout. Specifically, the perimeter drift and main access corridors are maintained. The panel structure is replaced by long emplacement drifts mined perpendicular to the mains, and the region that was originally defined as panels 1 and 2 in the SCP–CDR layout is identified as an expansion region for the Exploratory Studies Facility (ESF).

Based on the assumptions of 7.6 m (25 ft) diameter emplacement drifts and a maximum 30% extraction ratio, the modeled distance between the centerlines of emplacement drifts was set to a constant 25.4 m (83.3 ft). For the vertical emplacement scenarios, the containers were assumed to be emplaced in vertically excavated boreholes whose axial lines of symmetry are normal to the centerline of the emplacement drift. To address rock stability issues, minimum allowable borehole spacing was set to 2.29 m (7.5 ft) for the vertical emplacement cases. For the in drift scenarios, the waste packages were assumed to line up axially along a line coincident with the vertical plane of sym-

metry for an emplacement drift, with minimum container spacing dictated by the overall container length.

As indicated in Chapter 10, one of the primary benefits to this analytical approach is that each waste package can be modeled explicitly. This translates into a need to define 7,640 containers for the in drift scenarios and 32,021 for the vertical cases. For the double-blended waste stream, the problem is further complicated by the fact that, in any given emplacement year, two container types displaying different decay characteristics are typically defined. Therefore, in order not to bias the resulting layout toward any specific package type, a random selection from a given year's inventory of packages had to be observed as part of the modeled emplacement scheme. Activation of the heat generation of the spent fuel containers was timed to mimic a fully stepped emplacement scheme. Specifically, containers were activated on a yearly basis beginning at the perimeter drift and working toward the main drift accesses. It was further assumed that emplacement proceeds from south to north. It is noted that for the 114 kW/acre cases, emplacement was isolated to the area on the western side of the mains. For the 57 kW/acre cases, a given year's emplacement was modeled as using drifts on both sides of the mains, again proceeding from south to north.

C.1.2 Modeled container geometry

For all four thermal loading scenarios, the spent-fuel waste containers were modeled as right-circular cylinders. For the vertical emplacement cases, the waste packages were assumed to have a diameter of 0.71 m (28 in.) and a length of 4.76 m (187.5 in.). For the in-drift scenarios a diameter of 1.83 m (72.1 in.) and a length of 4.91 m (193.4 in.) were assumed.

C.1.3 Spent-fuel thermal decay characteristics

The thermal decay characteristics of spent fuel as a function of reactor type, burnup, and age out-of-reactor, as calculated using the ORIGEN2 code, are maintained on the Characteristics Database (DOE, 1992b). Four-term exponential fits valid for a temporal range of 5 to 1000 years were performed by Mansure and Petney (1991). For this iteration of TSPA, modeled time frames out to 30,000 years were requested. Thus, the thermal power functions had to be refitted to accommodate the extended period of interest. Using the same method documented in Mansure and Petney (1991), exponential fits consistent with the form of equation C.3 employing up to 10 terms were generated.

C.1.4 Material properties

As indicated in Section C.1, it was assumed that the waste is isolated in a semi-infinite mass of rock. The properties of this rock were assumed to be equivalent to those for the second unit of the Topopah Spring Member (TSw2) at Yucca Mountain. Specifically, values of 2.1 W/mK and 2.2 J/cm^{3}K as reported in the RIB were assumed for the thermal conductivity and heat capacitance, respectively.

C.1.5 Boundary and initial conditions

Since the analytical solution presented above is based on heat-generating sources in an infinite medium, the method of images had to be employed to construct solutions consistent with a constant-temperature surface boundary. Described in detail in Carslaw and Jaeger (1967), the method of images can be used to construct a temperature solution that is vanishing at the bounding plane (i.e., a constant temperature surface). The constant-temperature surface was assumed to be 311 m above the plane defined by the centerpoints of the modeled heat sources.

Imposed on the temperature-rise solutions obtained from the analytical method described above is a geothermal gradient. For this set of analyses, the geothermal gradient was assumed to be 0.0177°C/m-depth, fixed by a constant surface temperature of 18.7°C. These values are consistent with a straight-line approximation of data included in the RIB for drillhole USW-G4.

C.2 Nonlinear heat conduction model

As discussed in Chapter 10, representative container wall temperatures were obtained by matching the early-time solutions of the COYOTE model (Gartling, 1982) with late-time predictions from the analytical model discussed above in Section C.1. In this section, the inputs and assumptions used in the three-dimensional nonlinear heat-conduction model, COYOTE, will be presented. Prior to a description of the geometry and heat-source strengths used for the four cases, a description of the assumed intact rock and backfill thermal properties will be presented.

C.2.1 Intact rock properties

For this set of analyses, a layered stratigraphy was assumed. The layers were considered to be uniform in thickness over the entire modeled region and contact points for the various units were chosen to be consistent with information reported in the RIB for drillhole USW-G4. Table C-1 documents the distance from the surface to the contact between units (as measured vertically downward from the surface), as well as the thermal conductivity and the heat capacitances for each unit.

It is noted that unpublished comparisons between axisymmetric repository-scale calculations using the COYOTE model and the above property descriptions compare closely with equivalent V-TOUGH calculations. This tends to indicate that the functional descriptions for heat capacitance adopted for use in these calculations provides a good approximation of temperature predictions that would be obtained using a fully coupled hydrothermal code.

Table C-1. Thermal properties and contact depths of stratigraphic units.

Unit	Upper Contact (m)	Lower Contact (m)	Thermal Conductivity (W/mK)	94°C≤T	94°C<T≤114°C	114°C<T
TCw	0	36.0	1.65	2.0313	9.3748	2.0979
PTn	36.0	74.1	0.85	2.2286	29.3110	1.5236
TSw1	74.1	204.2	1.60	2.0775	12.2655	2.0219
TSw2	204.2	393.5	2.10	2.1414	10.4768	2.1839
TSw3	393.5	409.3	1.28	2.0530	4.5193	2.5535
CHn1v	409.3	414.5	1.20	2.5651	35.3680	1.6702
CHn1z	414.5	518.5	1.28	2.6709	35.3854	2.2835
CHn2	518.5	535.2[a]	1.30	2.5512	22.3349	1.9599

[a] For the regions below CHn2, property values are not available in the RIB. Therefore, CHn2 properties will be assumed to persist below 535.2 m.

C.2.2 Backfill rock properties

The emplacement drifts modeled for this TSPA were assumed to be backfilled with crushed tuff at 75 years following emplacement. Furthermore, it was assumed that the circular emplacement drifts that would be created using a TBM will have a highly compacted backfill floor installed prior to waste emplacement. Therefore, two sets of thermal properties for backfill were required for the analyses defined. In all cases, the backfill was assumed to be completely dry and contact-resistance effects were ignored.

C.2.2.1 Backfilled floor

For all four scenarios, it was assumed that a well-compacted backfill floor is installed prior to waste emplacement. According to Fernandez *et al.* (1987), a "reasonable estimated range of porosity" for a "moderately to well compacted" backfill of crushed tuff is 30% to 35%. For these analyses, the well-compacted tuff floor installed in the circular emplacement drifts was assumed to have an effective porosity of 30%.

No data exist on the thermal conductivity of a crushed tuff backfill; however, many theoretical and empirical relationships do exist for mixtures of this type. For these calculations, the thermal conductivity for backfill was estimated on the basis of a geometric mean (Lappin, 1981; Kaviany, 1991). Specifically,

$$k_e = k_s^{(1-\phi)} k_f^{(\phi)}, \tag{C.7}$$

where k_e is the effective thermal conductivity of the backfill, k_s is the thermal conductivity of the intact rock, k_f is the thermal conductivity of the fluid filling the void spaces (in this case air), and is the effective porosity of the backfill. Using values of 2.10 W/mK for k_s, 0.042 W/mK for k_f, and 0.30 for ϕ, a value of 0.65 W/mK can be calculated for the effective thermal conductivity of the compacted backfill floor.

Like the effective conductivity, the effective thermal capacitance for backfill is dependent upon the porosity. Since the backfill is considered dry, the fluid filling the pores is assumed to be air. With the thermal capacitance of air two orders of magnitude smaller than that for intact TSw2, a reasonable approximation for the effective thermal capacitance of backfill becomes

$$(\rho c_p)_e = (1-\phi)(\rho c_p)_s, \tag{C.8}$$

where $(\rho c_p)_e$ is the effective thermal capacitance, ρ is the porosity, and $(\rho c_p)_s$ is the thermal capacitance of the dry rock. Using values of 0.30 for ϕ and 2.18 J/cm^{3}K for $(\rho c_p)_s$, an effective thermal capacitance of 1.53 J/cm^{3}K can be calculated for the well-compacted backfill floor.

C.2.2.2 Noncompacted backfill

At 75 years following emplacement, the drifts in all four scenarios are assumed to be backfilled with a noncompacted, crushed tuff. Little information is available on what the porosity of this backfill might be; a value of 60% was assumed. Using the same inputs as used in Section C.2.2.1 for the thermal conductivities of TSw2 and air, and a value of 0.60 for , equation C.7 yields an equivalent thermal conductivity of 0.20 W/mK for the noncompacted backfill.

Using equation C.8 and the inputs discussed in Section C.2.2.1, but substituting 0.60 for ϕ, a thermal capacitance of 0.87 J/cm^{3}K is calculated for the noncompacted backfill.

C.2.3 Radiation properties

Prior to the backfilling of the emplacement drifts, it is assumed that the drift will be unventilated. Gartling *et al.* (1981) showed that radiative heat transfer in a closed drift is an order of magnitude greater than convective heat transfer in a typical SCP-type emplacement drift. Therefore, radiation was considered the dominant heat transfer mechanism in the open emplacement drifts.

There are two methods that can be employed in modeling radiative heat transfer within the emplacement drifts. A drift equivalent material can be defined for the open air space of the emplacement drift that models the radiative flux across the space, or the radiative heat transfer can be modeled explicitly. For these calculations, it was decided that the drift-equivalent-material approach was most appropriate.

A value of 20 W/mK was used to represent the drift equivalent thermal conductivity. Similarly, a constant heat capacitance of 0.001 J/cm^3 was also applied. These values are consistent with previous calculations (St. John, 1985) and are considered representative of a radiation dominated environment within the emplacement drifts.

C.2.4 Modeled geometry

Two model geometries were assumed, corresponding to the two emplacement modes. The drift diameter and drift spacing were assumed constant for both emplacement modes. Specifically, it was assumed that the circular emplacement drifts have a diameter of 7.6 m (25 ft) and that they are spaced 25.4 m (83.3 ft), corresponding to a 30% extraction ratio.

The cross-sectional view provided in Figure C-2 shows the highly compacted backfill floor. This floor was assumed to extend to a distance 1.83 m (6 ft) from the base of the drift, as measured along the vertically oriented diameter. The level of the backfilled floor is further assumed to be 311 m below the ground surface, and the modeled region extends 1,300 m below the drift floor. As shown in Figure C-3, the top of the heat source for the vertical emplacement options was assumed to be 3.05 m (10 ft) below the drift floor. For the in drift scenarios, a 0.15 m separation is modeled between the backfilled floor and the bottom of the waste package. This is done to account for resting brackets that are proposed to hold the waste packages.

C.2.5 Waste package

The waste packages that form the basis of the source definition used in this study are based on the 4:3 hybrid design documented in the SCP and the 21 PWR package currently being investigated by the Project. Shown in Chapter 4, the hybrid waste package assumed for the vertical emplacement cases was modeled as being 0.71 m (28 in.) in diameter and 4.47 m (176 in.) in length. The reduction in modeled container length was assumed based on the reported average length of a typical BWR assembly (DOE, 1992a) For the in-drift cases, the 21-PWR package was modeled as having a diameter of approximately 1.83 m (72.1 in.) and a length of 4.91 m (193.4 in.).

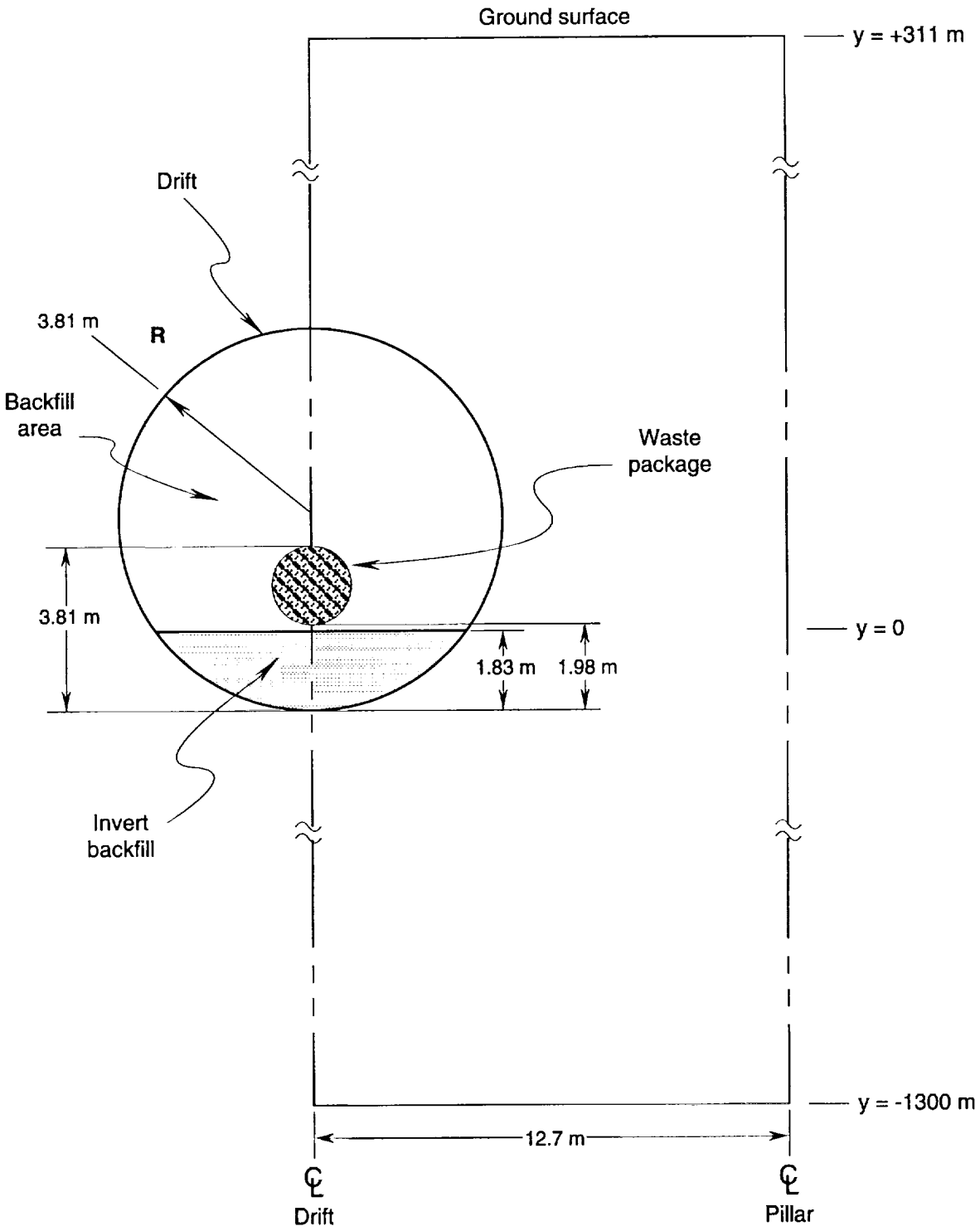

Figure C-2. Geometry for in-drift emplacement option.

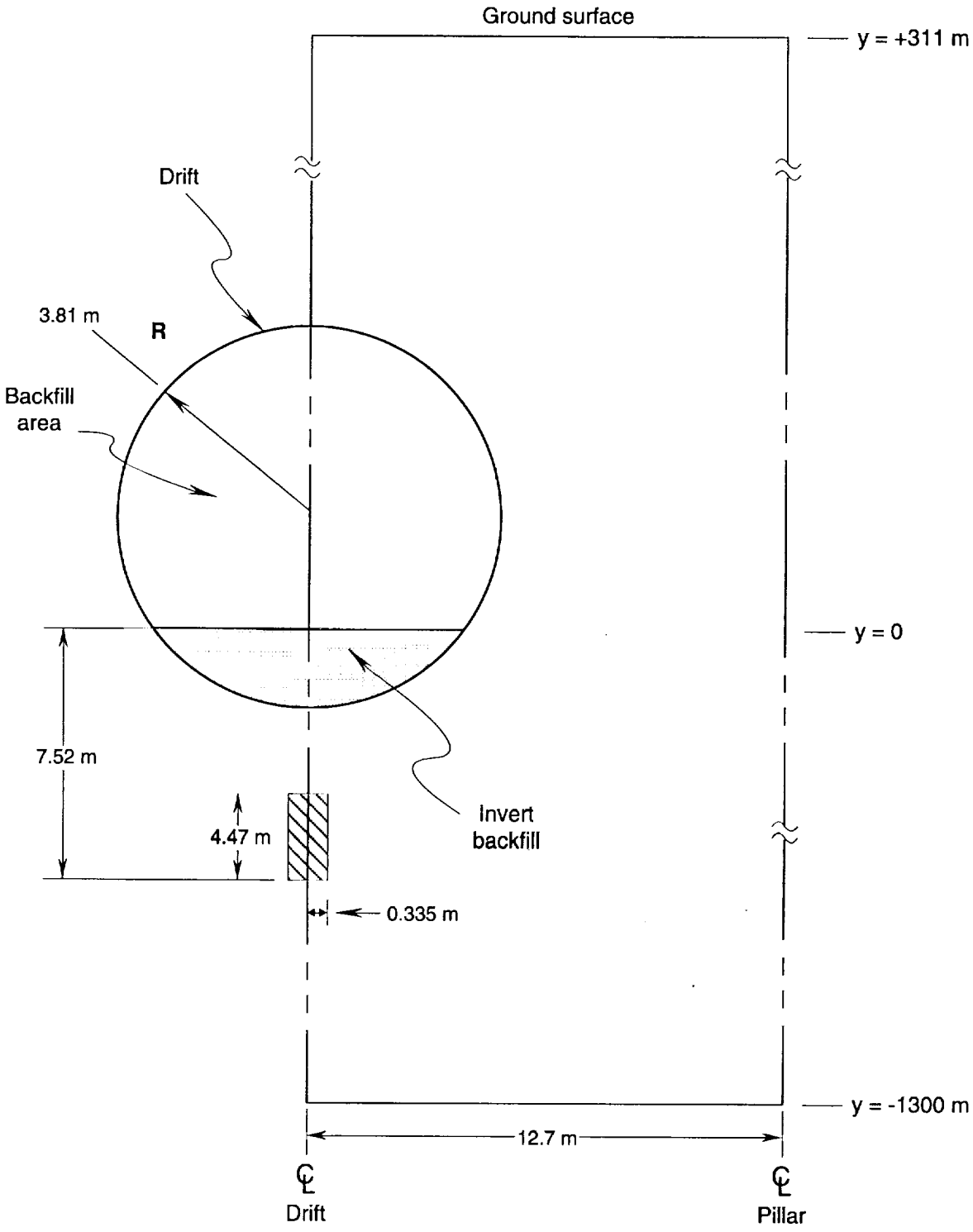

Figure C-3. Geometry for vertical emplacement option with a circular drift cross section.

C.2.6 Spent-fuel characteristics

Since the COYOTE model assumes an infinite array of waste packages based on the definition of only one container, the waste stream used in the analytical models had to be simplified into a single set of characteristics. For these analyses, a weighted burnup of 37,286 MWd/MTU was assumed with an average waste age of 25.8 years out-of-reactor. Using the method documented by Mansure and Petney (1991), an eight-term exponential decay curve of the form of equation C.3 was calculated. This curve appears valid out to 10,000 years. The fitted coefficients for this curve are documented in Table C-2. In addition to defining the decay characteristics, averages for the initial power outputs of each package type were also assumed based on the double-blended waste stream. Specifically, the COYOTE simulations of the vertical-emplacement cases assumed the waste packages to have an initial power output of 2.022 kW. The in-drift simulations assumed an 8.5 kW initial container power output. These initial power outputs combine with the assumed drift spacing of 25.4 m to define specific container spacings for each thermal loading scenario. Table C-3 documents the modeled container spacings for each of the four COYOTE simulations.

Table C-2. Fitted decay constants used in COYOTE calculations.

Term	Qa_i(W/MTU)	b_i (1/yr)
1	4.25537	0.782887×10^{-5}
2	8.65595	0.588968×10^{-4}
3	13.6825	0.937490×10^{-4}
4	0.192549×10^{-2}	0.127082×10^{-3}
5	0.424570×10^{-7}	0.160416×10^{-3}
6	158.298	0.151383×10^{-2}
7	102.027	0.618833×10^{-2}
8	1139.97	0.236043×10^{-1}

Table C-3. Container spacings assumed in COYOTE calculations.

Case	Container Spacing (m)
In Drift, 114 kW/acre	11.88
In Drift, 57 kW/acre	23.76
Vertical Borehole, 114 kW/acre	2.82
Vertical Borehole, 57 kW/acre	5.65

C.2.7 Boundary and initial conditions

The emplacement drifts are assumed to be one drift in an infinite series of simultaneously emplaced drifts. Using symmetry, the vertical boundaries shown in Figures C-2 and C-3 were modeled as adiabatic surfaces. At the ground surface, a constant tem-

perature of 18°C was assumed. At the lower boundary, a constant temperature of 53°C was imposed, consistent with information presented in the RIB. To connect these boundaries, the three-dimensional model was allowed to reach steady-state conditions prior to activating the heat source.

APPENDIX

Information from the Reference Information Base Used in this Report

This report contains no information from the Reference Information Base.

Candidate Information for the Reference Information Base

This report contains no candidate information for the Reference Information Base.

Candidate Information for the Geographic Nodal Information Study and Evaluation System

This report contains no candidate information for the Geographic Nodal Information Study and Evaluation System.

YUCCA MOUNTAIN SITE CHARACTERIZATION PROJECT
DISTRIBUTION LIST

1 D.A. Dreyfus (RW-1)
Director
OCRWM
US Department of Energy
1000 Independence Avenue SW
Washington, DC 20585

1 L.H. Barrett (RW-2)
Acting Deputy Director
OCRWM
US Department of Energy
1000 Independence Avenue SW
Washington, DC 20585

1 J.D. Saltzman (RW-4)
Office of Strategic Planning and International Programs
OCRWM
US Department of Energy
1000 Independence Avenue SW
Washington, DC 20585

1 J.D. Saltzman (RW-5)
Office of External Relations
OCRWM
US Department of Energy
1000 Independence Avenue SW
Washington, DC 20585

1 Samuel Rousso (RW-10)
Office of Program and Resource Mgt.
OCRWM
US Department of Energy
1000 Independence Avenue SW
Washington, DC 20585

1 J. C. Bresee (RW-10)
OCRWM
US Department of Energy
1000 Independence Avenue SW
Washington, DC 20585

1 R.M. Nelson (RW-20)
Office of Geologic Disposal
OCRWM
US Department of Energy
1000 Independence Avenue, SW
Washington, DC 20585

1 S. J. Brocoum (RW-22)
Analysis and Verification Division
OCRWM
US Department of Energy
1000 Independence Avenue SW
Washington, DC 2585

1 D. Shelor (RW-30)
Office of Systems and Compliance
OCRWM
US Department of Energy
1000 Independence Avenue, SW
Washington, DC 20585

1 J. Roberts (RW-33)
Director, Regulatory Compliance Division
OCRWM
US Department of Energy
1000 Independence Avenue, SW
Washington, DC 20585

1 G. J. Parker (RW-332)
Reg. Policy/Requirements Branch
OCRWM
US Department of Energy
1000 Independence Avenue, SW
Washington, DC 20585

1 R. A. Milner (RW-40)
Office of Storage and Transporation
OCRWM
US Department of Energy
1000 Independence Avenue, SW
Washington, DC 20585

1 S. Rousso (RW-50)
Office of Contract Business Management
OCRWM
US Department of Energy
1000 Independence Avenue, SW
Washington, DC 20585

1 T. Wood (RW-52)
Director, M&O Management Division
OCRWM
US Department of Energy
1000 Independence Avenue, SW
Washington, DC 20585

4 Victoria F. Reich, Librarian
Nuclear Waste Technical Review Board
1100 Wilson Blvd, Suite 910
Arlington, VA 22209

5 R.M. Nelson Jr, Acting Project Manager
Yucca Mountain Site Characterization Office
US Department of Energy
P.O. Box 98608--MS 523
Las Vegas, NV 89193-8608

1 C. L. West, Director
Office of External Affairs
DOE Nevada Field Office
US Department of Energy
P.O. Box 98518
Las Vegas, NV 89193-8518

8 Technical Information Officer
DOE Nevada Field Office
US Department of Energy
P.O. Box 98518
Las Vegas, NV 89193-8518

1 P. K. Fitzsimmons, Technical Advisor
Office of Assistant Manager for Environmental Safety and Health
DOE Nevada Field Office
US Department of Energy
P.O. Box 98518
Las Vegas, NV 89193-8518

1 D. R. Elle, Director
Environmental Protection and Division
DOE Nevada Field Office
US Department of Energy
P.O. Box 98518
Las Vegas, NV 89193-8518

1 Repository Licensing & Quality Assurance
Project Directorate
Division of Waste Management
US NRC
Washington, DC 20555

1 Senior Project Manager for Yucca Mountain
Repository Project Branch
Division of Waste Management
US NRC
Washington, DC 20555

1 NRC Document Control Desk
Division of Waste Management
US NRC
Washington, DC 20555

1 Philip S. Justus
NRC Site Representive
301 E Stewart Avenue, Room 203
Las Vegas, NV 89101

1 E. P. Binnall
Field Systems Group Leader
Building 50B/4235
Lawrence Berkeley Laboratory
Berkeley, CA 94720

1 Center for Nuclear Waste Regulatory Analyses
6220 Culebra Road
Drawer 28510
San Antonio, TX 78284

3 W. L. Clarke
Technical Project Officer - YMP
Attn: YMP/LRC
Lawrence Livermore National Laboratory
P.O. Box 5514
Livermore, CA 94551

1 J. A. Blink
Deputy Project Leader
Lawrence Livermore National Laboratory
101 Convention Center Drive
Suite 820, MS 527
Las Vegas, NV 89109

4 J. A. Canepa
Technical Project Officer - YMP
N-5, Mail Stop J521
Los Alamos National Laboratory
P.O. Box 1663
Los Alamos, NM 87545

1 H. N. Kalia
Exploratory Shaft Test Manager
Los Alamos National Laboratory
Mail Stop 527
101 Convention Center Dr., #820
Las Vegas, NV 89101

1 N. Z. Elkins
Deputy Technical Project Officer
Los Alamos National Laboratory
Mail Stop 527
101 Convention Center Dr., #820
Las Vegas, NV 89101

5 L. E. Shephard
Technical Project Officer - YMP
Sandia National Laboratories
Organization 6302, M/S 1333
P.O. Box 5800
Albuquerque, NM 87185

1 J. F. Devine
Asst Director of Engineering Geology
US Geological Survey
106 National Center
12201 Sunrise Valley Drive
Reston, VA 22092

1 L. R. Hayes
Technical Project Officer
Yucca Mountain Project Branch
MS 425
US Geological Survey
P.O. Box 25046
Denver, CO 80225

1 V. R. Schneider
Asst. Chief Hydrologist--MS 414
Office of Program Coordination and Technical Support
US Geological Survey
12201 Sunrise Valley Drive
Reston, VA 22092

1 J. S. Stuckless
Geologic Division Coordinator
MS 913
Yucca Mountain Project
US Geological Survey
P.O. Box 25046
Denver, CO 80225

1 D. H. Appel, Chief
Hydrologic Investigations Program
MS 421
US Geological Survey
P.O. Box 25046
Denver, CO 80225

1 E. J. Helley
Branch of Western Regional Geology
MS 427
US Geological Survey
345 Middlefield Road
Menlo Park, CA 94025

1 R. W. Craig, Chief
Nevada Operations Office
US Geological Survey
101 Convention Center Drive
Suite 860, MS 509
Las Vegas, NV 89109

1 D. Zesiger
US Geological Survey
101 Conventional Center Drive
Suite 860, MS 509
Las Vegas, NV 89109

1 G. L. Ducret, Associate Chief
Yucca Mountain Project Division
US Geological Survey
P.O. Box 25046
421 Federal Center
Denver, CO 80225

1 A. L. Flint
US Geological Survey
MS 721
P.O. Box 327
Mercury, NV 89023

1 D. A. Beck
Water Resources Division, USGS
6770 S Paradise Road
Las Vegas, NV 89119

1 P. A. Glancy
US Geological Survey
Federal Building, Room 224
Carson City, NV 89701

1 Sherman S.C. Wu
US Geological Survey
2255 N. Gemini Drive
Flagstaff, AZ 86001

1 J. H. Sass - USGS
Branch of Tectonophysics
2255 N Gemini Drive
Flagstaff, AZ 86001

1 DeWayne Campbell
Technical Project Officer - YMP
US Bureau of Reclamation
Code D-3790
P.O. Box 25007
Denver, CO 80225

1 J. M. LaMonaca
Records Specialist
US Geological Survey
421 Federal Center
P.O. Box 25046
Denver, CO 80225

1 W. R. Keefer - USGS
913 Federal Center
P.O. Box 25046
Denver, CO 80225

1 M. D. Voegele
Technical Project Officer - YMP
SAIC
101 Convention Center Drive
Suite 407
Las Vegas, NV 89109

2 L. D. Foust
Nevada Site Manager
TRW Environmental Safety Systems
101 Convention Center Drive
Suite 540, MS 423
Las Vegas, NV 89109

1 C. E. Ezra
YMP Support Office Manager
EG&G Energy Measurements Inc
MS V-02
P.O. Box 1912
Las Vegas, NV 89125

1 E. L. Snow, Program Manager
Roy F. Weston Inc
955 L'Enfant Plaza SW
Washington, DC 20024

1 Technical Information Center
Roy F. Weston Inc
955 L'Enfant Plaza SW
Washington, DC 20024

1 D. Hedges, Vice President, QA
Roy F. Weston Inc
4425 Spring Mountain Road
Suite 300
Las Vegas, NV 89102

1 D. L. Fraser, General Manager
Reynolds Electrical & Engineering Co, Inc
MS 555
P.O. Box 98521
Las Vegas, NV 89193-8521

1 [illegible]V. Colston, President and
[illegible]neral Manager
L Vegas Branch
Ra[illegible]ytheon Services Nevada
M[illegible] 416
P Box 95487
[illegible]s Vegas, NV 89193-5487

1 R. L. Bullock
Technical Project Officer - YMP
Raytheon Services Nevada
Suite P-250, MS 403
101 Convention Center Drive
Las Vegas, NV 89109

1 Paul Eslinger, Manager
PASS Program
Pacific Northwest Laboratory
P.O. Box 999
Richland, WA 99352

1 A. T. Tamura
Science and Technology Division
OSTI
US Department of Energy
P.O. Box 62
Oak Ridge, TN 37831

1 Carlos G. Bell Jr
Professor of Civil Engineering
Civil and Mechanical Engineering Dept.
University of Nevada, Las Vegas
4505 S Maryland Parkway
Las Vegas, NV 89154

1 P. J. Weeden, Acting Director
Nuclear Radiation Assessment Div.
US EPA
Environmental Monitoring Systems Lab
P.O. Box 93478
Las Vegas, NV 89193-3478

1 ONWI Library
Battelle Columbus Laboratory
Office of Nuclear Waste Isolation
505 King Avenue
Columbus, OH 43201

1 T. Hay, Executive Assistant
Office of the Governor
State of Nevada
Capitol Complex
Carson City, NV 89710

3 R. R. Loux
Executive Director
Agency for Nuclear Projects
State of Nevada
Evergreen Center, Suite 252
1802 N. Carson Street
Carson City, NV 89710

1 C.H. Johnson
Technical Program Manager
Agency for Nuclear Projects
State of Nevada
Evergreen Center, Suite 252
1802 N. Carson Street
Carson City, NV 89710

1 John Fordham
Water Resources Center
Desert Research Institute
P.O. Box 60220
Reno, NV 89506

1 David Rhode
Desert Research Institute
P.O. Box 60220
Reno, NV 89506

1 Eric Anderson
Mountain West Research-
Southwest Inc
2901 N Central Avenue #1000
Phoenix, AZ 85012-2730

1 The Honorable Cyril Schank
Chairman
Churchill County Board of
Commissioners
190 W First Street
Fallon, NV 89406

1 Dennis Bechtel, Coordinator
Nuclear Waste Division
Clark County Department of
Comprehensive Planning
301 E Clark Avenue, Suite 570
Las Vegas, NV 89101

1 Juanita D. Hoffman
Nuclear Waste Repository
Oversight Program
Esmeralda County
P.O. Box 490
Goldfield, NV 89013

1 Eureka County Board of
Commissioners
Yucca Mountain Information
Office
P.O. Box 714
Eureka, NV 89316

1 Brad Mettam
Inyo County Yucca Mountain
Repository Assessment Office
Drawer L
Independence, CA 93526

1 Lander County Board of
Commissioners
315 South Humbolt
Battle Mountain, NV 89820

1 Vernon E. Poe
Office of Nuclear Projects
Mineral County
P.O. Box 1026
Hawthorne, NV 89415

1 Les W. Bradshaw
Program Manager
Nye County Nuclear Waste
Repository Program
P.O. Box 153
Tonopah, NV 89049

1 Florindo Mariani
White Pine County Nuclear
Waste Project Office
457 Fifth Street
Ely, NV 89301

1 Judy Foremaster
City of Caliente Nuclear Waste
Project Office
P.O. Box 158
Caliente, NV 89008

1 Phillip A. Niedzielski-Eichner
Nye County Nuclear Waste
Repository Project Office
P.O. Box 221274
Chantilly, VA 22022-1274

1 Jason Pitts
Lincoln County Nuclear Waste
Project Office
Lincoln County Courthouse
Pioche, NV 89043

1 Economic Development Dept.
City of Las Vegas
400 E. Stewart Avenue
Las Vegas, NV 89101

1 Commmunity Planning and Development
City of North Las Vegas
P.O. Box 4086
North Las Vegas, NV 89030

1 Community Development and Planning
City of Boulder City
P.O. Box 61350
Boulder City, NV 89006

1 Commission of the European Communities
200 Rue de la Loi
B-1049 Brussells
BELGIUM

2 M. J. Dorsey, Librarian
YMP Research and Study Center
Reynolds Electrical & Engineering Co Inc
MS 407
P.O. Box 98521
Las Vegas, NV 89193-8521

1 Amy Anderson
Argonne National Laboratory
Building 362
9700 S Cass Avenue
Argonne, IL 60439

1 Steve Bradhurst
P.O. Box 1510
Reno, NV 89505

1 Michael L. Baughman
35 Clark Road
Fiskdale, MA 01518

1 Glenn Van Roekel
Director of Community Development
City of Caliente
P.O. Box 158
Caliente, NV 89008

1 Ray Williams, Jr
P.O. Box 10
Austin, NV 89310

1 Nye County District Attorney
P.O. Box 593
Tonopah, NV 89049

1 William Offutt
Nye County Manager
Tonopah, NV 89049

1 Charles Thistlethwaite, AICP
Inyo County Planning Department
Drawer L
Independence, CA 93526

1 R. F. Pritchett
Technical Project Officer - YMP
Reynolds Electrical & Engineering Company Inc
MS 408
P.O. Box 98521
Las Vegas, NV 89193-8521

1 Dr. Moses Karakouzian
1751 E Reno #125
Las Vegas, NV 89119

3 Brenda Bailey White
CCS
5301 Central NE
Suite 1520
Albuquerque, NM 87108

1 Clarence R. Allen
NWTRB
1000 E. California Blvd.
Pasadena, CA 91106

1 Johan Andersson
SKI
Division of Nuclear Waste
Sehlstedtgatan II
Box 27106
S-102 52 Stockholm
SWEDEN

1 Michael J. Apted
Intera Sciences
3609 S. Wadsworth Blvd
Denver, CO 80235

1 Dwayne Chesnut
Lawrence Livermore National Laboratory
P.O. Box 808
M/S L202
Livermore, CA 94551

1 Richard Codell
US Nuclear Regulatory Commission
M/S 4-H-3
Washinton, DC 20555

1 Seth M. Coplan
US Nuclear Regulatory Commission
M/S 4-H-3
Washington, DC 20555

1 Kevin Coppersmith
Geomatrix Consultants
100 Pine Street, 10th Floor
San Francisco, CA 94111

1 C.F. Costa
Nuclear Radiation Assessment Division
US EPA
Environmental Monitoring Systems Laboratory
P.O. Box 93478
Las Vegas, NV 89193-3478

1 Allen G. Croff
Chemical Technology Division
Oak Ridge National Laboratory
4500N, MS-6235
P.O. Box 2008
Oak Ridge, TN 37831-6235

1 Bruce M. Crowe
Los Alamos National Laboratory
101 Convention Center Drive
Suite 820
Las Vegas, NV 89109

1 Department of Comprehensive Planning
Clark County
225 Bridger Avenue, 7th Floor
Las Vegas, NV 89155

1 D.W. Engel
Pacific Northwest Laboratory
P.O. Box 999
M/S K7-34
Richland, WA 99352

1 Leonard J. Fiorenzi
P.O. Box 257
Eureka, NV 89316

1 A.B. Gureghian
CNWRA
6220 Culebra Road
San Antonio, TX 78228-0510

5 William G. Halsey
Lawrence Livermore National Laboratory
P.O. Box 808
M/S L-204
Livermore, CA 94551

1 M.E. Harr
School of Civil Engineering
Purdue University
1284 Civil Engineering Building
West Lafayette, IN 47907-1284

1 Dwight Hoxie
US Geological Survey
101 Convention Center Drive
Suite 860
Las Vegas, NV 89109

1 Edwin E. Kinter
Bradley Hill Road
P.O. Box 682
Nortwich, VT 05055

1 Donald Langmuir
Nuclear Waste Technical Review Board
109 So. Lookout Mountain Cr.
Golden, CO 80401

1 Lincoln County Commission
Lincoln County
P.O. Box 90
Pioche, NV 89043

1 Ian Miller
Golder Associates Inc
4104 148 Avenue NE
Redmond, WA 98052

1 R.W. Nelson
INTERA-M&O
101 Convention Center Drive
Suite P110
Las Vegas, NV 89109

1 Claudia Newbury
Yucca Mountain Project Office
US Department of Energy
P.O. Box 98608
M/S 523
Las Vegas, NV 89193-8518

1 D. Warner North
NWTRB
Decision Focus Inc
4984 El Camino Real
Los Altos, CA 94062

2 William J. O'Connell
Lawrence Livermore National Laboratory
P.O. Box 808, M/S L-195
Livermore, CA 94551

1 Michael Revelli
Lawrence Livermore National Laboratory
P.O. Box 808
M/S L-206
Livermore, CA 94551

1 Benjamin Ross
Disposal Safety Inc
1660 L STreet NW, Suite 314
Washington, DC 20036

2 SAIC-T & MSS Library
101 Convention Center Drive
Suite 407
Las Vegas, NV 89109

1 Frank W. Schwartz
195 Thornbury Lane
Powell, OH 43065

1 Bjorn Selinder
190 W. First Street
Fallon, NV 89406

1 Ardyth Simmons
Yucca Mountain Project
US DOE
P.O. Box 98608
M/S 523
Las Vegas, NV 89193-8518

1 Scott Sinnock
TRW
101 Convention Center Drive
Suite P110
Las Vegas, NV 89109

1 Ellis D. Verink
Nuclear Waste Technical Review Board
4401 NW 18th Place
Gainesville, FL 32605

1 Joseph Wang
Lawrence Berkeley Laboratory
Earth Sciences Division
1 Cyclotron Road
Berkeley, CA 94720

1 R.V. Watkins, Chief
Project Planning and Management
USGS
P.O. Box 25046
421 Federal Center
Denver, CO 80225

1 Ed Weeks -USGS
P.O. Box 25046
Federal Center M/S 413
Lakewood, CO 80225

1 C.L. West, Director
Office of External Affairs
DOE Field Office, Nevada
US DOE
P.O. Box 98518
Las Vegas, NV 89193-8518

1 Robert F. Williams
EPRI Nuclear Power Division
P.O. Box 10412
Palo Alto, CA 94303

1 George Zyvoloski
Geoanalysis Group
Los Alamos National Lab
M/S F665
Los Alamos, NM 87545

1 Jean Younker
TRW
101 Convention Center Drive
Suite P110
Las Vegas, NV 89109

1 Dr. June Fabryka-Martin
Los Alamos National Lab
MS J-514
Los Alamos, NM 87545

1 Dr. F. Owen Hoffman
Oak Ridge National Lab
P.O. Box 2008
Oak Ridge, TN 37831-6036

1 Dr. Arjun Makhijani
Institute for Energy and Environmental Research
6935 Laurel Avenue
Takoma Park, MD 20912

1 Dr. James E. Martin
Assistant Professor of
Radiological Health
University of Michigan
School of Public Health
Ann Arbor, MI 48109

1 Dr. H. Robert Meyer
C.N.S.I.
750 East Park Drive
Suite 200
Harrisburg, PA 17111

1 Jess Riley
Heinman Research Labs
P.O. Box 35457
Charlotte, NC 28207

1 James E. Watson Jr
Environ. Science and Engineering
Campus Box 7400
University of North Carolina
Chapel Hill, NC 27599-7400

1 Dr. William M. Murphy
Center for Nuclear Waste
Regulatory Analyses
Southwest Research Institute
6220 Culebra Road
San Antonio, TX 78238-5166

1 Miroslav Kucerka, Consultant
Radioactive Waste Management
Botevova 3104
143 00 Praha 4
Czech Republic

1 Dr. John Kessler
Nuclear Power Division
EPRI
P.O. Box 10412
Palo Alto, CA 94303-0813

1 Per-Eric Ahlstrom
Research Director
Swedish Nuclear Fuel and
Waste Management Co
Box 5864 S-102 48
Stockholm, Sweden

1 W.A. Seddon
AECL Technologies
9210 Corporate Boulevard
Suite 410
Rockville, MD 20850

1 Dr. Wilfried Albert
NAGRA
Hardstrasse 73
CH-5430 Wettingen
Switzerland

1 Runo Barrdahl
Swedish Radiation Protection
Institute
P.O. Box 60204
S-104 01 Stockholm
Sweden

1 Dr. John E. Gale
Fracflow Consultants Inc
36 Pearson Street
St. John's, Newfoundland
Canada A1A 3R1

1 Dr. Furruccio Gera
ISMES S.P.S.
Via dei Crociferi 44
00187 Rome, Italy

1 Dr. Gunnar Gustafson
Department of Geology
Chalmers University of Technology
and University of Goteborb
S-412 96 Goteborg
Sweden

1 Dr. Alan W. Herbert
AEA Technology
Theoretical Studies Department
Harwell Laboratory B424.4
Oxfordshire OX11 ORA
United Kingdom

1 David Hodgkinson
INTERA
Chiltern House
45 Station Road
Henley-on-Thames, Oxon
RG9 1AT
United Kingdom

1 Dr. Yong Soo Hwang
Korea Atomic Energy
Research Institute
P.O. Box 7
Daeduk-Danji
Taejeon, Korea

1 Dr. Katsumi Kamemura
Shinozuka Research Institute
5F Maguna Kogyo Building 1-31-13
Yoyogi, Shibuya-ku
Tokyo, 151, Japan

1 Dr. Bill Lanyon
Geo-Science Limited
Falmouth Business Park
Bickland Water Road
Falmouth, Cornwall
TR11 4SZ, United Kingdom

1 Dr. Jussi Palmu
Imatran Voima Oy
Rajatorpantie 8
P.O. Box 112
SF-01601 Vantaa, Finland

1 Dr. Carmen Bajos Parada
ENRESA
Emilio Vargas 7
28043 Madrid, Spain

1 Dr. Gunnar Ramqvist
ELTEKNO AB
Gruvvagen 1
S-714 00 Kopparberg
Sweden

1 Dr. Robert Rundberg
Los Alamos National Lab
Mail Stop J-514
Los Alamos, NM 87545

1 James A. Steadman
Building Research Establishment
Structural Performance Division
Garston, Watford WD2 7JR
United Kingdom

1 Dr. Ove Stephansson
Department of Engineering Geology
Royal Institute of Technology
S-100 44 Stockholm, Sweden

1 Dr. Juhani Vira
Teollisuuden Voiman Oy
Annankatu 42 C
SF-00100 Helsinki
Finland

1 Peter Wallman
Golder Associates
4104 148 Avenue NE
Redmond WA 98052

1 Minoro Yamakuma
Geoscience Research Project
PNC Tokyo, Japan

1 David Leaver
Polestar
Four Main Street
Los Altos, CA 94022

1 James Gansemer
Lawrence Livermore National Laboratory
P.O. Box 808
Livermore, CA 94551

1 Lynn C. Lewis
Lawrence Livermore National Laboratory
P.O. Box 808
Livermore, CA 94551

1 Alan D. Lamont
Lawrence Livermore National Laboratory
P.O. Box 808
Livermore, CA 94551

1 Ines Triay
Los Alamos National Laboratory
P.O. Box 1663
Los Alamos, NM 87545

1 David Morris
Los Alamos National Laboratory
P.O. Box 1663
Los Alamos, NM 87545

1 Ning Lu
USGS
P.O. Box 25046, MS 421
Denver Federal Center
Lakewood, CO 80225

1 Gary LeCain
USGS
P.O. Box 25046
Denver Federal Center
Lakewood, CO 80225

1 Edward Kwicklis
USGS
P.O. Box 25046
Denver Federal Center
Lakewood, CO 80225

1 Jerry McNeish
INTERA
M/S 423
101 Convention Center Drive
Las Vegas, NV 89109

1 April V. Gil
Yucca Mountain Project
M/S 523
101 Convention Center Drive
Las Vegas, NV 89109

1 Joseph J. Dlugosz
Yucca Mountain Project
M/S 523
101 Convention Center Drive
Las Vegas, NV 89109

1 Wendy R. Dixon
Yucca Mountain Project
M/S 523
101 Convention Center Drive
Las Vegas, NV 89109

1 Jeanne C. Nesbit
Yucca Mountain Project
M/S 523
101 Convention Center Drive
Las Vegas, NV 89109

1 Susan B. Jones
Yucca Mountain Project
M/S 523
101 Convention Center Drive
Las Vegas, NV 89109

1 William B. Simecka
Yucca Mountain Project
M/S 523
101 Convention Center Drive
Las Vegas, NV 89109

1 Dennis R. Williams
Yucca Mountain Project
M/S 523
101 Convention Center Drive
Las Vegas, NV 89109

1 C. Thomas Statton
Yucca Mountain Project
M&O/WCFS
M/S 423
101 Convention Center Drive
Las Vegas, NV 89109

1 Yvonne Tsang
Lawrence Berkeley Laboratory
Earth Sciences Division
1 Cyclotron Road
Berkeley, CA 94720

1 Tom Bjerstedt
Yucca Mountain Project
US DOE
P.O. Box 98608
M/S 523
Las Vegas, NV 89193-8518

1 Maxwell Blanchard
Yucca Mountain Project
P.O. Box 98608
M/S 523
Las Vegas, NV 89193-8518

2 Jeremy Boak
Yucca Mountain Project
US DOE
P.O. Box 98608
M/S 523
Las Vegas, NV 89193-8518

1 Garry D. Brewer
Nuclear Waste Technical Review Board
University of Michigan
Dana Bldg, Room 3516
Ann Arbor, MI 48109-1115

1 Daniel B. Bullen
Iowa State University
P.O. Box 1768
Ames, IA 50010

1 Thomas A. Buscheck
Lawrence Livermore National Laboratory
P.O. Box 808
M/S L206
Livermore, CA 94550

1 John E. Cantlon, Chairman
Nuclear Waste Technical Review Board
1795 Bramble Drive
East Lansing, MI 48823

1 K.W. Causseaux
NHP Reports Chief
U.S. Geological Survey
421 Federal Center
P.O. Box 25046
Denver, CO 80225

1 Pat Domenico
NWTRB
1100 Wilson Boulevard, Suite 910
Arlington, VA 22209

2 A.L. Dudley
SPECTRA Research Institute
1603 University NE
Albuquerque, NM 87102

1 William Dudley
US Geological Survey
P.O. Box 25046
M/S 425
Denver, CO 80225

1 J. Russell Dyer
Yucca Mountain Project Office
US DOE
P.O. Box 98608
M/S 425
Las Vegas, NV 89193-8518

1 Norman A. Eisenberg
US Nuclear Regulatory Commission
M/S 4-H-3
Washington, DC 20555

1 W.W.-L. Lee
Environmental Evaluation Group
7007 Wyoming NE
Suite F-2
Albuquerque, NM 87109

1 R.E. Lowder
MAC Tec
101 Conventional Center Drive
Suite 1100
Las Vegas, NV 89109

1 R.R. Luckey
USGS
Building 53
Denver Federal Center
Room H2314/MS 5421
Denver, CO 80225

1 Annette MacIntyre
Lawrence Livermore National Laboratory
P.O. Box 808
M/S L-194
Livermore, CA 94551

1 Edward A. Mason
Amoco Resource Center
P.O. Box 451
46 Admirals Lane
Osterville, MA 02655-0451

1 Russell McFarland
NWTRB
100 Wilson Blvd, Suite 910
Arlington, VA 22209

1 Robin McGuire
Risk Engineering Inc
5255 Pine Ridge Road
Golden, CO 80403

1 John J. McKetta
NWTRB
Department of Chemical Engineering
CRE Building 1450
Austin, TX 78712-1062

1 Ian McKinley
NAGRA
Hardstrasse 73
Wettingen, CH-5430
SWITZERLAND

1 Fred W. McLafferty
Department of Chemistry
Cornell University
2600 Baker Laboratory
Ithaca, NY 14853-1301

1 Arend Meijer
GCX Inc
P.O. Box 87198-2427
Albuquerque, NM 87198

1 Dr. Martin Mifflin
Water Resources Center
Desert Research Center
2505 Chandler Avenue, Suite 1
Las Vegas, NV 89120

1 Suresh Pahwa
INTERA
6850 Austin Center Blvd
Suite 300
Austin, TX 78731

1 Planning Department
Nye County
P.O. Box 153
Tonopah, NV 89049

1 F. Joseph Pearson Jr
1304 Walnut Hill Lane
Suite 210
Irving, TX 75038

1 Chris Pflum
SAIC
101 Conventional Center Drive
Las Vegas, NV 89109

1 T.H. Pigford
University of California
Department of Nuclear Engineering
Berkeley, CA 94720

1 P.T. Prestholt
NRC Site Representative
301 E. Stewart Avenue, Room 203
Las Vegas, NV 89101

1 Dennis L. Price
NWTRB
1011 Evergreen Way
Blackburg, VA 24060

1 Karsten Pruess
Lawrence Berkeley Laboratory
Earth Sciences Division
1 Cyclotron Road
Berkeley, CA 94720

1 Norman C. Rasmussen
MIT
Department of Nuclear Engineering
Bldg 24-205
Cambridge, MA 02139

1 Leon Reiter
NWTRB
1100 Wilson Blvd, Suite 910
Arlington, VA 22209-2297

1 Everett Springer
Los Alamos National Laboratory
P.O. Box 1663
M/S J495
Los Alamos, NM 87545

1 Roger Staehle
University of Minnesota
Department of Chemical Engineering
and Materials Science
22 Red Fox Road
North Oaks, MN 55127

1 Jane Summerson
US DOE
Forrestal RW-22, 7F-091/FORS
Washington, DC 20555

1 Aaron Thode
Los Alamos National Lab
M/S F607
P.O. Box 1663
Los Alamos, NM 87545

1 K.T. Thomas
National Academy of Sciences
2001 Wisconsin Ave NW
Harris Bldg, Room 456
Washington, DC 20007

1 C.F. Tsang
Lawrence Berkeley Laboratory
Earth Sciences Division
1 Cyclotron Road
Berkeley, CA 94720

1 Greg Valentine
Los Alamos National Lab
P.O. Box 1663
M/S F665
Los Alamos, NM 87545

1 Richard Van Konynenburg
Lawrence Livermore National Lab
P.O. Box 808
Livermore, CA 94551

1 Abraham Van Luik
Intera-M&O
101 Convention Center Drive
Suite #P110
Las Vegas, NV 89109

1 C. John Mann
Department of Geology
245 Natural History Building
1301 West Green Street
Urbana, Illinois 61801

1 Henry Loo
Westinghouse Idaho Nuclear Co.
P.O. Box 4000
M/S 5219
Idaho Falls, ID 83415

1 Kjell Andersson
Karinta-Konsult
P.O. Box 6048
S-183 06
Taby, Sweden

1 Dr. G. Ross Heath
College - Ocean/Fishery Sciences
583 Henderson Hall
University of Washington
Seattle, WA 98195

1 Carl Anderson
National Academy of Sciences
2101 Constitution Ave NW
Harris Building, Room 456
Washington, DC 20418

1 Dorothy M. Clark
Secretary, Science Advisory Board
US EPA
401 M Street SW, A-101F
Washington, DC 20460

1 Kathleen W. Conway
Science Advisory Board - EPA
401 M Street SW, A-101F
Washington, DC 20460

1 Dr. Chris Whipple
Clement International
160 Spear Street
Suite 1380
San Francisco, CA 94105-1535

13 Priscilla Bunton
US DOE, OCRWM (RW-331)
1000 Independence Ave SW
Washington, DC 20585

1 Linda Desell
US DOE, OCRWM (RW-331)
Suite 200
1000 Independence Ave SE
Washington, DC 20585

1 Robert J. Budnitz, President
Future Resources Associates Inc
2000 Center Street, Suite 418
Berkeley, CA 94704

1 Thomas A. Cotton
JK Research Associates Inc
4429 Butterworth Place, NW
Washington, DC 20016

1 Srikanta Mishra
M&O/ INTERA
M/S 423
101 Convention Center Drive
Las Vegas, NV 89109

120 Eric Smistad
Yucca Mountain Project
M/S 523
101 Convention Center Drive
Las Vegas, NV 89109

1 Margaret Federline
Nuclear Regulatory Commission
Washington, DC 20555-0001

1 Dr. Alan Hooper
United Kingdom Nirex Limited
Curie Avenue, Harwell
Didcot, Oxfordshire OX11 0RH
United Kingdom

1 Dr. Michael J. Bell
IAEA
Wagramerstrasse 5
P.O. Box 100
A-1400 Vienna
Austria

1 Dr. Neil Chapman
INTERA
Park View House
14B Burton Street
Melton Mowbray, Leicestershire
United Kingdom LE13 1AE

1 Dr. James G.T. Chyr
Taiwan Power Company
AF 2 Alley 15
Lane 196 Sec 4
Roosevelt Road
Taipei, Taiwan
Republic of China

1 Dr. Nestor R. Correa
NAGRA
Hardstrasse 73
CH-5430 Wettingen
Switzerland

1 Kenneth W. Dormuth, AECL
Whiteshell Laboratories
Pinawa, Manitoba
Canada ROE 1L0

1 Dr. Esko Eloranta
Finnish Centre for Radiation
P.O. Box 268
SF-00101 Helsinki
Finland

1 Dr. Helmut D. Fuchs
Gesellschaft fur Nuklear-
Service mbH
Lange Laube 7
D-3000 Hannover 1
Germany

1 Ito Fumio
c/o Prof. Swoboda
University of Innsbruck
Technikerstr 13
A-6020 Innsbruck
Austria

1 Dr. Hilkka Leino-Forsman
VTT, Technical Research
Centre of Finland
Otakaari 3 A
P.O. Box 200
SF-02151 Espoo, Finland

1 Dr. Robert W. Lieb
NAGRA
Hardstrasse 73
CH-5430 Wettingen
Switzerland

1 Dr. J.W. Lloyd
School of Earth Sciences
Edgbaston, Birmingham
B 15 2TT, United Kingdom

1 D. Ganpat S. Lodha, AECL
Whiteshell Laboratories
Pinawa, Manitoba
Canada ROE 1L0

1 Douglas E. Metcalfe
Waste Management Division
P.O. Box 1046, Station B
270 Albert Street
Ottawa, Canada K1P 5S9

1 Dr. Ivars Neretnieks
Department of Chemical
Engineering
Royal Institute of Technology
Teknikringen 26
S-100 44 Stockholm
Sweden

1 Dr. Jean-Pierre Olivier
OECD/NEA
12 Boulevard des Iles
92130 Issy Les Molineaux
France

1 Dr. Olle Olsson
Conterra AB
P.O. Box 493
S-751 06 Uppsala, Sweden

1 Maria Onofrei, AECL
Whiteshell Laboratories
Pinawa, Manitoba
Canada ROE 1L0

1 Dr. Liu Wen-Chung
Radwaste Adminstration
Atomic Energy Council
6F 65 Lane 144 Keeling Load
Section 4 Taipei
Taiwan

1 Dr. Sidney H. Whitaker
AECL
Whiteshell Laboratories
Pinawa, Manitoba
Canada ROE 1L0

1 Dr. Roger Yearsley
Inspectorate of Pollution
Room A5.02
Romney House
43 Marsham Street
London SW1P 3Py
United Kingdom

1 Dr. Piet Zuidema
NAGRA
Hardstrasse 73
CH-543o Wettingen
Switzerland

1 Dr. Arthur Motta
Nuclear Engineering Department
Pennsylvania State University
231 Sackett Building
University Park, PA 16802

1 Dr. M.R. Chandratillake
Capcis March Limited
Bainbridge House, Granby Row
Manchester M1 2PW
United Kingdom

1 Serge Runge
Eurisys Consultants S.A.
14 rue du Printemps
74017 Paris, France

1 Peter Suci
Montana State University
Bozeman, MT

1 Dr. David Kreamer
Geoscience Department - UNLV
4505 South Maryland Parkway
Las Vegas, NV 89159

1 Richard Forester
USGS
P.O. Box 25046
Denver Federal Center
Lakewood, CO 80225

1 Zell Peterman
USGS
P.O. Box 25046
Denver Federal Center
Lakewood, CO 80225

1 Kevin McCoy
B&W Fuel Company
101 Convention Center Drive
Suite P110
Las Vegas, NV 89109

1 John Nitao
Lawrence Livermore National Laboratory
P.O. Box 808
Livermore, CA 94551

1 Anne-Marie Meike
Lawrence Livermore National Laboratory
P.O. Box 808
Livermore, CA 94551

1 G.S. Bodvarsson
Lawrence Berkeley Laboratory
1 Cyclotron Road
Berkeley, CA 94720

1 Jiamin Wan
Lawrence Berkeley Laboratory
1 Cyclotron Road
Berkeley, CA 94720

1 Robert Andrews
INTERA
M/S 423
101 Convention Center Drive
Las Vegas, NV 89109

1 Tim Dale
INTERA
M/S 423
101 Convention Center Drive
Las Vegas, NV 89109

1 Dan McCright
Lawrence Livermore National Laboratory
P.O. Box 808
M/S L-204
Livermore, CA 94551

1 Ray Stout
Lawrence Livermore National Laboratory
P.O. Box 808
M/S L-204
Livermore, CA 94551

INTERNAL DISTRIBUTION

	MS	
4	1330	G. M. Gerstner-Miller, 6352 100/12541/SAND93-2675/QA
20	1330	WMT Library, 6352
1	0827	P. J. Hommert, 1502
1	1375	D. A. Dahlgren, 4400
5	0899	Technical Library, 7141
1	0619	Technical Publications, 7151
10	1119	Document Processing for DOE/OSTI, 7613-2
1	9018	Central Technical Files, 8523-2
1	0827	J. C. Cummings, 1502
1	0827	J. S. Rottler, 1511
1	0827	P. L. Hopkins, 1511
1	0827	M. J. Martinez, 1511
1	0835	R. R. Eaton, 1513
1	0835	R. D. Skocypec, 1513
1	1324	P. D. Davies, 6115
1	1324	R. J. Glass, 6115
1	1324	C. A. Rautman, 6115
1	1324	V. C. Tidwell, 6115
1	1324	C. Ho, 6115
1	1320	M. D. Siegel, 6119
1	1333	F. J. Schelling, 6302
10	1326	H. A. Dockery, 6312
5	1326	R. W. Barnard, 6312
1	1326	G. E. Barr, 6312
1	1326	J. H. Gauthier, 6312
1	1326	P. G. Kaplan, 6312
1	1326	T. H. Robey, 6312
1	1326	L. H. Skinner, 6312
1	1326	W. G. Perkins, 6312
1	1326	A. R. Schenker, 6312
1	1326	S. A. Shannon, 6312
60	1326	M. L. Wilson, 6312
1	1325	L. S. Costin, 6313
1	1325	R. E. Finley, 6313
1	1325	E. Dunn, 6313
1	1325	J. F. Holland, 6313
1	1325	J. Pott, 6313
1	1325	C. S. Chocas, 6313
1	1325	E. E. Ryder, 6313
1	1325	S. R. Sobolik, 6313
1	1330	M. C. Brady, 6314
1	1345	T. Brown, 6331

1	1328	M. E. Fewell, 6342
1	1328	C. T. Stockman, 6342
1	1328	R. P. Rechard, 6342
1	1328	M. G. Marietta, 6342
1	0755	B. D. Zak, 6612
1	1315	T. E. Blejwas, 7500
1	9043	R. Nilson, 8745

*U.S. GOVERNMENT PRINTING OFFICE 1994-0-573-026/00003

SAND93-2675

The number in the lower right-hand corner is an accession number used for Office of Civilian Radioactive Waste Management purposes only. It should not be used when ordering this publication.

Org.	Bldg.	Name	Rec'd by	Org.	Bldg.	Name	Rec'd by

Sandia National Laboratories